



The 33<sup>rd</sup> Thai Institute of Chemical Engineering  
and Applied Chemistry International Conference

# TIChE 2024

E-proceedings



Smart Solution to Environmental  
Sustainability for Better World

March 7-8, 2024  
Krungsri River Hotel,  
Phra Nakhon Si Ayutthaya, Thailand





The 33<sup>rd</sup> Thai Institute of Chemical Engineering and Applied Chemistry  
International Conference (TIChE2024)

## E-PROCEEDINGS

Smart Solution to Environmental Sustainability for Better World

March 7-8, 2024

TIChE2024, Phra Nakhon Si Ayutthaya, Thailand

## **DISCLAIMER**

The papers in this book represent the research presented at **the 33<sup>rd</sup> Thai Institute of Chemical Engineering and Applied Chemistry International Conference (TIChE2024)**. They convey the opinions of the authors and are published in their revised form as submitted. The committee does not guarantee the accuracy, completeness, or usefulness of the information provided. Unauthorized use may infringe on privately owned patents or publication rights. For permission to reprint or use information from these manuscripts, please contact the individual author(s).

## Message from President of TIChE

Dear Esteemed Colleagues, Distinguished Guests and Delegates of the 33<sup>rd</sup> TIChE conference

On behalf of The Thai Institute of Chemical Engineering and Applied Chemistry, I extend our heartfelt gratitude to each of you for your invaluable contributions to the success of the 33<sup>rd</sup> Annual TIChE Conference, themed "Smart Solutions to Environmental Sustainability for a Better World."

As we gather for the 33<sup>rd</sup> Annual TIChE Conference, I am also delighted to announce two significant programs that will undoubtedly enrich our event and highlight the exceptional talent within our community.



Firstly, it is with great pleasure that we will unveil the winners of the 2023-2024 National Design Project Competition. This prestigious competition serves as a platform for the senior chemical engineering students from around the nation to apply their knowledge to the real industrial design problem. The dedication and ingenuity demonstrated by participants are truly commendable, and we eagerly anticipate celebrating their achievements. This year, the competition is supported by SCG Chemicals Plc. and PTT Plc.

In addition, we are thrilled to recognize the outstanding projects submitted to the TIChE Senior Project Contest. This contest provides a platform for senior students to showcase their remarkable research and project work, reflecting their commitment to academic excellence and practical innovation. We commend the participants for their hard work, creativity, and dedication to advancing the field of chemical engineering and applied chemistry.

As we applaud the winners of these esteemed competitions, let us also extend our appreciation to all participants for their contributions and dedication to excellence. Your passion and commitment inspire us all to push the boundaries of knowledge and innovation in pursuit of a better world.

And of course, our sincere appreciation goes to the Department of Chemical Engineering, RMUTT, for their unwavering support and collaboration in organizing this esteemed gathering. Their dedication and commitment have been instrumental in bringing together professionals and scholars to exchange ideas and insights on pressing environmental challenges.

We also extend our deepest appreciation to our esteemed keynotes and plenary speakers whose expertise and passion will illuminate our discussions and inspire innovative solutions. Your invaluable contributions enrich the dialogue and propel us towards actionable outcomes in the realm of environmental sustainability.

To our sponsors, and supporters, we express our gratitude for your generous contributions and unwavering commitment to advancing the frontiers of chemical engineering and applied chemistry. Your support enables us to foster meaningful dialogue and drive impactful change in our quest for a more sustainable world.

As we convene at the enchanting Krungsri River Hotel in Ayutthaya, Thailand, I am filled with optimism and anticipation for the transformative conversations and collaborations that lie ahead. Together, we have the power to shape a brighter, greener future for generations to come.

Once again, thank you for your dedication, enthusiasm, and unwavering commitment to environmental sustainability. Your presence enriches our community and strengthens our collective resolve to build a better world.

With deepest gratitude and warm regards,

A handwritten signature in black ink, appearing to read "S. Chalothorn", written over a light blue rectangular background.

Surachate Chalothorn  
President

The Thai Institute of Chemical Engineering and Applied Chemistry

## Message from President of RMUTT

Welcome distinguished guests to the 33<sup>rd</sup> Thai Institution of Chemical Engineering and Applied Chemistry International Conference (TICChE2024) which was held on 7-8<sup>th</sup> March, 2024 at Krungsri River Hotel, Ayutthaya, Thailand. TICChE2024 was hosted by the Department of Chemical and Materials Engineering, Faculty of Engineering, Rajamangala University of Technology Thanyaburi and the Thai Institute of Chemical Engineering and Applied Chemistry in the theme of “Smart Solution to Environmental Sustainability for Better World”.



The objective of TICChE2024 is to facilitate knowledge exchange, research data and experience sharing between researchers, engineers, scientists, students, and interested audiences working in the fields of chemical engineering, applied chemistry, and related areas. The rapid development of advanced technologies in chemical engineering will be a valuable knowledge exchange between our participants as well as academic network.

On behalf of Rajamangala University of Technology Thanyaburi, I would like to express my sincere gratitude to the TICChE2024 conference participants and organizers for their tireless work during the preparation period. I am confident that the conference will serve as a productive platform for researchers and attendees to exchange knowledge, strengthening the network for upcoming national and international research initiatives.

A handwritten signature in black ink that reads "Sommai Pivsa-Art".

Sommai Pivsa-Art, Ph.D.  
President  
Rajamangala University of Technology Thanyaburi

## COMITTEES

### Conference Chair

Mr. Surachate	Chalothorn	The Thai Institute of Chemical Engineering and Applied Chemistry, Thailand
---------------	------------	--

### Conference Co-Chair

Assoc.Prof.Dr. Natacha	Phetyim	Rajamangala University of Technology Thanyaburi, Thailand
------------------------	---------	---

### International Organizing Committee

Prof.Dr. Kiyoshi	Yoshikawa	Kyoto University, Japan
Prof.Dr. Hideaki	OHGAKI	
Prof.Dr. Hiroshi	Kamitakahara	
Dr. Taro	SONOBE	
Prof.Dr. Ken	Kokubo	CNT-Application Research Center, Japan
Prof.Dr. Yuji	ASO	Kyoto Institute of Technology, Japan
TS. Roslan	Arshad	Universiti Sultan Zainal Abidin, Besut Campus, Terengganu, Universiti Sultan Zainal Abidin, Malaysia
Assoc.Prof.Dr. Fatma	Yalcinkaya	Technical University of Liberec, Czech Republic
Asst.Prof.Dr. Rafael Omar	Torres Mendieta	Technical University of Liberec, Czech Republic
Prof.Dr. Injoo	Chin	Inha University, Korea
Prof.Dr. Yong Ku	Kwon	
Assoc.Prof.Dr. Ryuichi	Ashida	Kyoto University, Japan
Prof.Dr. Wega	Trisunaryanti	Universitas Gadjah Mada Yogyakarta, Indonesia
Prof.Dr. Tarcicius Yoyok	Wahyu Subroto	
Prof.Dr. Hiroshi	Takiyama	Tokyo University of Agriculture and Technology, Japan

Prof.Dr. Hongxun	Hao	Tianjin University, China
Prof.Dr. Jerry	Heng	Imperial College London, United Kingdom
Prof.Dr. Kevin	Roberts	University of Leeds, United Kingdom
Assoc.Prof.Dr. Koichi	Igarashi	Osaka Metropolitan University, Japan
Prof.Dr. Tu	Lee	National Central University, Taiwan
Prof.Dr. Woo-Sik	Kim	Kyung Hee University, Korea
Prof.Dr. Marjatta	Louhi-Kultanen	Aalto University, Finland
Dr.Keonakhone	Khounvilay	National University of Laos, Laos
Assoc.Prof.Dr. Sevgi	Polat	University of Marmara, Turkey
Assoc.Prof.Dr. Huaiyu	Yang	Loughborough University, United Kingdom
Prof.Dr. João	Maia	Case Western Reserve University, USA

### **Local organizing committee**

Mr.Surachate	Chalothorn	
Mr.Pukpong	Wungrattanasopon	
Prof.Dr. Tawatchai	Charinpanitkul	
Prof.Dr. Pramoch	Rangsunvigitt	
Prof.Dr. Varong	Pavarajarn	
Assoc.Prof.Dr. Kejvalee	Pruksathorn	
Assoc.Prof.Dr. Phavanee	Narataruksa	The Thai Institute of Chemical
Prof.Dr. Mali	Hunsom	Engineering and Applied Chemistry,
Assoc.Prof.Dr. Kulchanat	Prasertsit	Thailand
Asst.Prof.Dr. Pornchai	Bumroongsri	
Asst.Prof.Dr. Weerawat	Patthaveekongka	
Asst.Prof.Dr. Monpilai	Narasingha	
Dr. Narisara	Thongboonchoo	
Dr. Terasut	Sookkumnerd	
Prof.Dr. Benjapon	Chalermainsuwan	

Mr. Visoot	Duenkwang	
Assoc.Prof.Dr. Sumonman	Niamlang	
Assoc.Prof.Dr. Natacha	Phetyim	
Assoc.Prof.Dr. Weraporn	Pivsa-Art	
Asst.Prof.Dr. Thirawat	Mueansichai	
Asst.Prof.Dr. Rinlada	Sirisangsawang	
Asst.Prof.Dr. Chaiyapop	Siraworakun	
Asst.Prof.Dr. Weerinda	Mens	Rajamangala University of
Asst.Prof.Dr. Sasiradee	Jantasee	Technology Thanyaburi, Thailand
Asst.Prof. Sarawut	Jitpinit	
Asst.Prof. Yanyong	Sookklay	
Dr. Puttiporn	Thiamsinsangwon	
Asst.Prof.Dr. Nithinart	C. Juntadech	
Dr. Panrawee	Rungskunroch	
Dr. Phornwalan	Nanthananon	
Assoc.Prof.Dr. Chaiyan	Chaiya	

### Scientific Committee

Assoc.Prof.Dr. Lek	Wantha	Suranaree University of Technology, Thailand
Assoc.Prof.Dr. Pornnapa	Kasemsiri	
Assoc.Prof.Dr. Sutasinee	Neramittagapong	Khon Kaen University, Thailand
Assoc.Prof.Dr. Arthit	Neramittagapong	
Assoc.Prof.Dr. Chanatip	Samart	Thammasat University, Thailand
Assoc.Prof.Dr. Worapon	Kiatkittipong	
Assoc.Prof.Dr. Supakij	Suttiruengwong	Silpakorn University, Thailand
Asst.Prof.Dr. Veerayut	Lersbamrungsuk	
Dr. Wanwitoo	Wanmolee	
Asst.Prof.Dr. Suchata	Kirdponpattara	King Mongkut's University of
Asst.Prof.Dr. Santi	Chuetor	Technology North Bangkok,
Assoc.Prof.Dr. Chaiwat	Prapainainar	Thailand
Asst.Prof.Dr. Sakhon	Ratchahat	Mahidol University, Thailand
Assoc.Prof.Dr. Chakkrit	Umpuch	
Assoc.Prof.Dr. Chatchai	Kunyawut	Ubon Ratchathani University, Thailand
Asst. Prof. Dr. Lerdluck	Kaewvimol	Rajamangala University of Technology Krungthep, Thailand



Dr. Natthawan

Prasongthum

Thailand Institute of Scientific and  
Technological Research, Thailand

### Peer Review Committee

Assoc.Prof.Dr. Lek  
Dr. Terasut

Wantha  
Sookkummerd

Suranaree University of Technology,  
Thailand

Asst.Prof.Dr. Amata  
Assoc.Prof.Dr. Prakob  
Asst.Prof.Dr. Patcharaporn

Anantpinijwatna  
Kitchaiya  
Weerachawanasak

King Mongkut's Institute of  
Technology Ladkrabang, Thailand

Assoc.Prof.Dr. Anawat  
Asst.Prof.Dr. Jindarat  
Assoc.Prof.Dr.Somnuk  
Dr. Kantharakorn

Sungpet  
Pimsamarn  
Jarudilokkul  
Macharoen

King Mongkut's University of  
Technology Thonburi, Thailand

Assoc.Prof.Dr. Chaiwat  
Asst.Prof.Dr. Karn  
Asst.Prof.Dr. Lida  
Dr. Matthew  
Assoc.Prof.Dr. Patcharin  
Asst.Prof.Dr. Santi  
Asst.Prof.Dr. Suchata  
Dr. Supachai  
Assoc.Prof.Dr. Supak

Prapainainar  
Pana-Suppamassadu  
Simasatitkul  
Hartley  
Worathanakul  
Chuetor  
Kirdponpattara  
Jadsadajerm  
Tontisirin

King Mongkut's University of  
Technology North Bangkok,  
Thailand

Assoc.Prof.Dr. Anusith  
Asst.Prof.Dr. Manop  
Prof.Dr. Metta  
Assoc.Prof.Dr. Nanthiya  
Assoc.Prof.Dr. Paweena  
Assoc.Prof.Dr. Chanin

Thanapimmetha  
Charoenchaitrakool  
Chareonpanich  
Hansupalak  
Prapainainar  
Panjapornpon

Kasetsart University,Thailand

Prof.Dr. Benjapon

Chalermnsinsuwan

Chulalongkorn University, Thailand

Assoc.Prof.Dr. Chakkrit  
Asst. Prof. Channarong  
Assoc.Prof.Dr. Chatchai  
Asst. Prof. Dr. Karnika  
Assoc.Prof.Dr. Wipada  
Assoc.Prof.Dr. Supatpong  
Dr. Natthaya

Umpuch  
Puchongkawarin  
Kunyawut  
Ratanapongleka  
Dechapanya  
Mattaraj  
Punsuwan

Ubon Ratchathani University,  
Thailand

Assoc.Prof.Dr. Chanchira

Jubsilp

Assoc.Prof.Dr. Nawadon Assoc. Prof. Dr. Unchalee	Petchwattana Suwanmanee	Srinakharinwirot University, Thailand
Dr. Chaowat	Autthanit	Rajamangala University of Technology Phra Nakhon, Thailand
Asst. Prof. Choowong Asst. Prof. Dr. Nutchapon Asst.Prof.Dr. Weerawat Asst.Prof.Dr. Veerayut Dr. Wasu Dr. Sarawut	Chaisuk Chotigkrai Patthaveekongka Lersbamrungsuk Chaitree Phupaichitkun	Silpakorn University, Thailand
Assoc.Prof.Dr. Ekrachan	Chaichana	Nakhon Pathom Rajabhat University, Thailand
Assoc.Prof.Dr. Yuvarat Asst. Prof. Dr.Somboon Dr. Totsaporn	Ngernyen Sukpancharoen Suwannaruang	Khon Kaen University, Thailand
Assoc.Prof.Dr. Kulchanat Dr. Songtham	Prasertsit Photaworn	Prince of Songkla University, Thailand
Asst. Prof. Dr. Lerdluck Assoc.Prof.Dr. Kanokwan Assoc.Prof.Dr. Piyaporn	Kaewvimol Ngaosuwan Kampeerapappun	Rajamangala University of Technology Krungthep, Thailand
Asst.Prof.Dr. Nithinart Assoc.Prof.Dr. Natacha Assoc.Prof.Dr. Weraporn Asst.Prof.Dr. Thirawat Asst.Prof.Dr. Rinlada Asst.Prof.Dr. Chaiyapop Asst.Prof.Dr. Weerinda Asst.Prof.Dr. Sasiradee Asst.Prof. Sarawut Asst.Prof. Yanyong Assoc.Prof.Dr. Chaiyan	C. Juntadech Phetyim Pivsa-Art Mueansichai Sirisangsawang Siraworakun Mens Jantasee Jitpinit Sookklay Chaiya	Rajamangala University of Technology Thanyaburi, Thailand
Dr. Pamornrat Asst.Prof.Dr. Watcharapong Asst.Prof.Dr. Weerawun	Chantam Khaodee Weerachaipichasgul	Naresuan University, Thailand
Assoc.Prof.Dr. Akkarat Assoc.Prof.Dr. Piyachat Asst.Prof.Dr. Settakorn	Wongkaew Wattanachai Upasen	Burapha university, Thailand

Asst.Prof.Dr. Srisuda	Nithettham	
Asst.Prof.Dr. Woranart	Jonglertjunya	
Asst.Prof.Dr. Poomiwat	Phadungbut	Mahidol University, Thailand
Assoc.Prof.Dr. Atthapon	Srifa	
Mr. Jiraprat	Kitsuwan	Rayong Technical College, Thailand
Asst.Prof.Dr. Attaso	Khamwichit	Walailak University, Thailand

## LIST OF CONTENT

	<b>Page</b>
Preface	a
Committees	c
 <b>Papers of TIChE2024</b>	
Polymeric adsorbent from silicone rubber for carbon dioxide capture	1
Equilibrium molecular interactions of phosphonium-based ionic liquids with CO <sub>2</sub> and H <sub>2</sub> S for gas separation	9
Effect of temperature on the methanol synthesis through ethanol-assisted CO <sub>2</sub> hydrogenation in fixed bed reactor	17
Density, viscosity, and CO <sub>2</sub> absorption capacity of tri-amine blends 2-amino-2-methyl-1-propanol (AMP), piperazine (PZ), and monoethanolamine (MEA)	25
Potential of advanced tri-amine blends of 2-amino-2-methyl-1-propanol (AMP), methyl diethanolamine (MDEA), and piperazine (PZ) for post-combustion carbon capture	32
Esterification of oleic acid with glycerol using solid acid catalysts	40
A green sulfonated activated carbon catalyst for esterification of oleic acid with glycerol	54
Effect of surface functional group on siliceous zirconia for glycerol acetylation with acetic acid	64
Valorization of glycerol via esterification with acetic acid using 12-tungstophosphoric acid catalyst	76
Performance improvement of wet scrubbing unit for resin production	85
Simulation of hydrocracking process: impact of process parameters on product yields and properties	91
Process simulation of the reactive distillation using various ethanol-to-lactic acid ratios for the purification of lactic acid produced by fermentation	100
Simulation and techno-economic comparison of subcritical dimethyl ether, supercritical carbon dioxide and organic solvent extraction of rice bran oil manufacture	108
Process simulation and techno-economic evaluation of free lutein production from marigold flowers by dimethyl ether extraction and de-esterification.	116
Synthesis and characterization of core-shell zeolitic imidazolate frameworks by seed-mediated growth method	124
Effect of cerium promoter in the silica supported copper catalyst on the selective hydrogenation of furfural to furfuryl alcohol	132
Life cycle assessment of bio-hydrogenated diesel from palm fatty acid distillate and refined palm stearin	140
Techno-economic study of green diesel production from palm oil by-product using recycled solvent	147

## LIST OF CONTENT

	<b>Page</b>
Detection and replacement of states with spikes and noise by long short-term memory models or neural networks	154
Economic evaluation of intensified furfural production process with reactive-azeotropic dividing wall column using aspen plus program	163
Hollow fiber membrane modeling and simulation in the application of gas separation process	170
Extraction of thunbergia laurifolia lindl. with subcritical fluid technique	180
Methane reforming with CO <sub>2</sub> in gliding arc plasma minireactor integrated with NiO and CoO catalysts on Al <sub>2</sub> O <sub>3</sub> ball support	186
Investigation of the polymerization of ethylene and ethylene/1-hexene over zirconocene/MMAO catalyst supported on Ga-modified silica	194
Utilization of industrial waste cellulose for solid fuel production in pilot plant scale	202
Continuous conversion of fatty acid methyl esters to bio-jet fuel via hydroisomerization /hydrocracking over NiGa/modified beta zeolite catalysts	210
Sustainable heat exchanger network synthesis using linearization method	218
Effect of dip coating conditions on film thickness and CO <sub>2</sub> /CH <sub>4</sub> separation performance of pebax/PEI pomposite hollow fiber membrane	226
Characterization and properties of K-ZrO <sub>2</sub> catalyst derived from UiO-66 for glycerolysis of methyl palmitate	234
High-temperature catalytic oxidative cleavage of oleic acid to produce azelaic and pelargonic acids	241
Simulation-assisted transfer learning for steam consumption prediction in industrial steam monitoring with limited data scenario	248
Fabrication of thin film composite nanofibrous membrane using electrospinning and dip coating technique for selective protein purification	257
UV- enhanced catalytic oxidative cleavage of oleic acid.	265
Enhancement of oleic acid content in palm oil via chemical interesterification for application as bio-transformer oil	273
L-lysine production by corynebacterium glutamicum TISTR 461 using cassava pulp hydrolysate as a carbon source	281
Adsorption of moisture by rice husk silica and commercial silica	288
Methanol production via CO <sub>2</sub> hydrogenation with 1-propanol assisted in fixed bed reactor	296
The assessment of the relationship between fine particulate matter and related meteorological conditions	304
Tuning magnetic properties and particle size of iron oxide by changing Fe <sup>2+</sup> /Fe <sup>3+</sup> precursor ratios and rotation speed	312
Fe-doped in LaNiO <sub>3</sub> perovskite catalysts for dry reforming of methane	320

## LIST OF CONTENT

	<b>Page</b>
Evaluation of HEK293.2sus growth in 5 commercial media	328
Comparative study of lignin isolated from bagasse using different solid-to-liquid ratios of dilute sulfuric acid pretreatment	333
Preparation and synthesis of carboxymethyl cellulose from rice straw	341
The role of nonionic surfactants in lubricity of green diesel	349
Hydrodynamics simulation of sorbent riser and regenerator for carbon dioxide capture process using $K_2CO_3/Al_2O_3$ in circulating fluidized bed reactor	357
Removal of iodine compounds in periodate oxidation of water-soluble carbohydrates	369
Performance analysis and optimization of sorption-enhanced chemical looping oxidative steam reforming of methanol for high-temperature proton exchange membrane fuel cell	376
Study the parameters for acetylation over glycerol and acetic acid involving exploring indion 225-H as alternative ion-exchange resin.	385
Preparation of sulfonated activated carbon from polymer waste for conversion of fructose to 5-hydroxymethylfurfural	396
A Pouch-type liquid-to-gas phase transition actuator: performance tests and cost analysis	402
Synergistic effects of plastic wastes and sludge for producing fuel via co-pyrolysis in a batch reactor	410
Enhancement of porous carbon from oil palm empty fruit bunch and $CO_2$ capture application	418
Chemical recycling of waste PET into terephthalic acid by alkaline hydrolysis	425
Coaching for research and development in chemical engineering senior projects	432
Ethanol purification comparison between adsorption and azeotropic distillation: A rough simulation and economic analysis using Aspen Plus V.11	440
Adsorption of uremic toxins in hemodialysis using bio-based hybrid granular activated carbon for dialysate regeneration	448
UV-vulcanized natural rubber grafted with methyl methacrylate for production of ultrafine powder as toughening fillers in polylactic acid	457
The assessment of greenhouse gases for lerdsin hospital	466
Rice bran wax as a renewable resource for biolubricant formulation	472
Influence of chitosan content on antibacterial property of chitosan/polyvinyl alcohol composites	480
Conversion of furfuryl alcohol to butyl levulinate using alumina-supported tungsten catalysts	489
The development of metal/carbon quantum dots/cellulose nanocomposites for glucose sensing by fluorimetric and colorimetric detection	497

## LIST OF CONTENT

	<b>Page</b>
Assessing sustainability performance of thailand provinces via super-efficiency data envelopment analysis	505
Machine learning for predictive modelling of hydrogen production from biomass gasification	513
Transdermal drug delivery system of hesperidin-loaded cubosomes for anti-aging	521
Travelling salesman problem considering traffic data and IoTs for smart waste collection system: case study of a university	529
Zinc-organic framework and titanium dioxide nanocomposite for use as photocatalyst for dye degradation	537
Bioethanol production from rice straw using simultaneous saccharification and fermentation process	545
Effect of enantiomeric configuration of chiral cofomer in chiral resolution by cocrystallization	553
Inhibitory effects of schinus terebinthifolia leave extract on polyphenol oxidase activity and enzymatic browning	561
Catalytic conversion of palm refined oil to bio-hydrogenated diesel over monometallic and bimetallic supported on ZSM-5	569
Enhancing polycaprolactone (PCL) by incorporating lignin to improve properties	578
Data augmentation enhanced multilayer perceptron neural network model for catalytic CO <sub>2</sub> methanation	586
Development of convolutional neural network for leaked gas detection and classification in chemical processes	594
A study of pig farm waste to promote the circular economy concept	601
Examining the connection between nutrients and water hyacinth invasion in the lower tha chin river	609
Predictive model for the fatigue life of a low-cost leaf cup mold.	617
Study on coefficient of performance model for industrial refrigeration system	625
Adsorption behavior of industrial dye by activated carbon derived from bagasse ash	633

## Polymeric Adsorbent from Silicone Rubber for Carbon Dioxide Capture

**Attachai Pornpaiboonsuk<sup>1</sup>, Benjapon Chalermssinsuwan<sup>2</sup>,  
and Sirilux Poompradub<sup>2,3,4,\*</sup>**

<sup>1</sup> Program in Petrochemistry and Polymer Science, Faculty of Science, Chulalongkorn University, Bangkok 10330, Thailand

<sup>2</sup> Department of Chemical Technology, Faculty of Science, Chulalongkorn University, Bangkok 10330, Thailand

<sup>3</sup> Center of Excellence in Green Materials for Industrial Application, Faculty of Science, Chulalongkorn University, Bangkok 10330, Thailand

<sup>4</sup> Center of Excellence on Petrochemical and Materials Technology, Chulalongkorn University, Bangkok 10330, Thailand

E-mail: \*sirilux.p@chula.ac.th

### Abstract

One of the major greenhouse gases contributing to the global warming comes from carbon dioxide (CO<sub>2</sub>) which is commonly produced through fossil fuel combustion, industrial processes, transportation, volcanic eruption and forest fire. It is very crucial to solve the problem by reducing CO<sub>2</sub> before emission to atmosphere which can be done by adsorption of silica, zeolite, metal-organic frameworks or polymeric material. In this work, the polymeric adsorbent material of rubber scrap from silicone manufacture was chosen to study as the CO<sub>2</sub> adsorbent. The characterization of silicone rubber was examined by using thermogravimetric analysis, durometer and tensile testing machine. The effect of hardness (50-70 shore A) on the CO<sub>2</sub> adsorption capacity was investigated and the regeneration of adsorbent material was established by 5 adsorption-desorption cycles. The result showed that the CO<sub>2</sub> adsorption capacity increased with the increase of hardness of silicone rubber. Moreover, CO<sub>2</sub> adsorption capacity of silicone rubber was higher than that of natural rubber under the same condition. This result referred that silicone rubber can be used as an alternative adsorbent material for CO<sub>2</sub> capture.

**Keywords:** Silicone rubber; CO<sub>2</sub> capture; CO<sub>2</sub> adsorption; Polymeric adsorbent

### 1. Introduction

Carbon dioxide (CO<sub>2</sub>) is a vital gas for life on earth and presents in natural sources. However, it would be dangerous when it is uncontrollably emitted from different manmades and natural sources such as fossil fueled power plants, industrial processes, transportation, volcanic eruption and forest fire. The accumulation of CO<sub>2</sub> in the atmosphere as one of the most important global greenhouse gasses may cause global warming, sea level rise and ocean acidification as signs of sever climate changes.[1] It is very crucial to solve the problem by reducing CO<sub>2</sub> before emission to atmosphere. For controlling CO<sub>2</sub> emission in atmosphere, various CO<sub>2</sub> capture methods are available such as absorption, adsorption, cryogenic distillation, and membrane separation. Currently, the most commonly used method for carbon capture and separation in the industry is the amine absorption because of the longest development history, mature technology and stable operation. However, this technique has many disadvantages such as the instability of amine and its high energy requirement for



regeneration. Other problems include equipment corrosion and amine poisoning. Therefore, many researchers have focused on the porous adsorption materials such as silica, metal–organic frameworks and zeolites because such adsorbent materials can achieve intrinsically lower energy consumption and less toxicity than amine solution. [2] In recent years, the polymeric adsorbent is attractively interesting and developing due to their ease of regeneration, good thermal stability and low energy requirement. In order to increase the adsorption capacity and selectivity of the adsorbent toward CO<sub>2</sub>, the heteroatoms such as nitrogen or oxygen play an important role to increase the active sites as Lewis base for CO<sub>2</sub> capture. [3]

A lot of silicone rubber scrap/waste were produced from production and laboratory in silicone manufacturer. It is very interesting to reduce and utilize the silicone rubber scrap/waste as sustainable material for support circular economy. Therefore, this study focuses on the scrap of silicone rubber using as the novel alternative CO<sub>2</sub> adsorbent. The characterization of silicone rubber was analyzed by thermal and mechanical properties using thermal gravimetric analysis, durometer, and tensile testing machine. Additionally, the optimization of hardness were studied to investigate the maximum CO<sub>2</sub> adsorption capacity for silicone rubber scrap.

## 2. Material and Method

### 2.1 Materials

The silicone rubbers sheet with 50, 60 and 70 hardness Shore A were provided and supported by Shin-Etsu Silicones (Thailand) Limited (Rayong), Thailand. 99.99% Nitrogen gas (N<sub>2</sub>) and mixed gas (12% CO<sub>2</sub>/88% N<sub>2</sub>) were purchased from Thai-Japan Gas Co., Ltd. (Thailand).

### 2.2 Preparation of silicone rubber particles

Silicone rubber sheet from manufacturer was ground by a two roll mill and sieved by using mesh sieve No.20. The obtained particle size of silicone rubber was less than 840 μm. The sample code was S50, S60 and S70, respectively according to the hardness value.

### 2.3 Mechanical and thermal properties

The hardness of silicone rubber was performed at room temperature (~25 °C) according to JIS K 6249. The Bareiss Digitest BS09 (Germany) instrument was used with the shore A method and the thickness of sample was 6 mm. The hardness was repeatedly measured for 3 times and obtained an average value.

The tensile test was performed in accordance with JIS K 6249 using a Shimadzu AG-X (Japan). Dumbbell-shaped specimens were prepared by a pneumatic cutter. Testing was conducted with a 1000 N load cell at the rate of 500 mm/min. Three test pieces of each sample were tested, and the average tensile strength and elongation at break values were reported.

The thermal stabilities of samples were analyzed by thermogravimetric analysis TG/DTA Perkin Elmer Pyris diamond (USA) with a heating rate of 10 °C/min from 40 to 1000 °C under N<sub>2</sub> atmosphere.

## 2.6 Adsorption - desorption

For CO<sub>2</sub> adsorption, the silicone material was contained in a stainless reactor under an ambient temperature and pressure. First, the pre-treatment of sample was done by heating at 80 °C under vacuum for 20 min to remove the adsorbed gas in the sample. After that, the sample was cooled down to ambient temperature under a N<sub>2</sub> flow. Then, the mixed gas (12: 88 (v/v) CO<sub>2</sub>: N<sub>2</sub>) was flowed in the reactor at 80 mL/min. The CO<sub>2</sub> concentration and gas temperature were detected by sensor at the outlet of reactor. The CO<sub>2</sub> adsorption capacity was calculated from the difference between the CO<sub>2</sub> adsorption capacity of the sample and blank based on Eq. (1).

$$q = \frac{1}{M} \left[ \int_0^t Q(c_0 - c) dt \right] \frac{P}{RT} \quad (1)$$

where  $q$  is the adsorption capacity of CO<sub>2</sub> (mmol/g),  $M$  is the mass of adsorbent (g),  $Q$  is the gas flow rate (mL/min),  $c_0$  and  $c$  are inlet and outlet CO<sub>2</sub> concentration (%vol), respectively,  $t$  is the denoted time (min),  $P$  is the gas pressure (atm),  $R$  is the gas constant (82.0573 cm<sup>3</sup> atm/Kmol) and  $T$  is the gas temperature (K)

## 2.7 Regeneration

The stability of silicone material was studied through the adsorption and desorption process. Once the sample got the saturated CO<sub>2</sub> adsorption, the desorption was done under pure N<sub>2</sub> gas with the flow rate of 80 mL/min at 80 °C for 20 min. The adsorption–desorption cycles were repeated 5 times to investigate the regeneration capability of the silicone material.

## 3. Results and discussion

### 3.1. Mechanical properties of silicone materials

Figure 1 shows the mechanical properties of silicone materials. The mechanical properties of silicone depended on the proportion of polydimethylsiloxane (PDMS) and silica in silicone scrap rubber. Based on the information from silicone material provider, S70 had the highest silica content of 20%w/w followed by 17%w/w for S60 and 15%w/w for S50. The hardness values of silicone materials were 50 (S50), 60 (S60) and 70 (S70), respectively. These results indicated that high silica content in silicone materials could improve the mechanical properties of adsorbent materials. The tensile strength of S50, S60 and S70 was 10.8, 9.8 and 9.7 N/mm<sup>2</sup>, respectively and the elongation at break of those samples was the silica content 699, 538 and 469 %, respectively. It was shown that the tensile strength and elongation at break of silicone materials tended to decrease with increasing the silica content. During stretched silicone rubber, silica particles obstructed the alignment of PDMS in silicone rubber resulting in the decrease of the tensile strength and elongation at break of silicone rubber. In addition, the silicone rubber was more brittle by the increase of the silica content. Consequently, S70 has the highest hardness, then the sample became brittle resulting in lowest tensile strength and elongation at break.

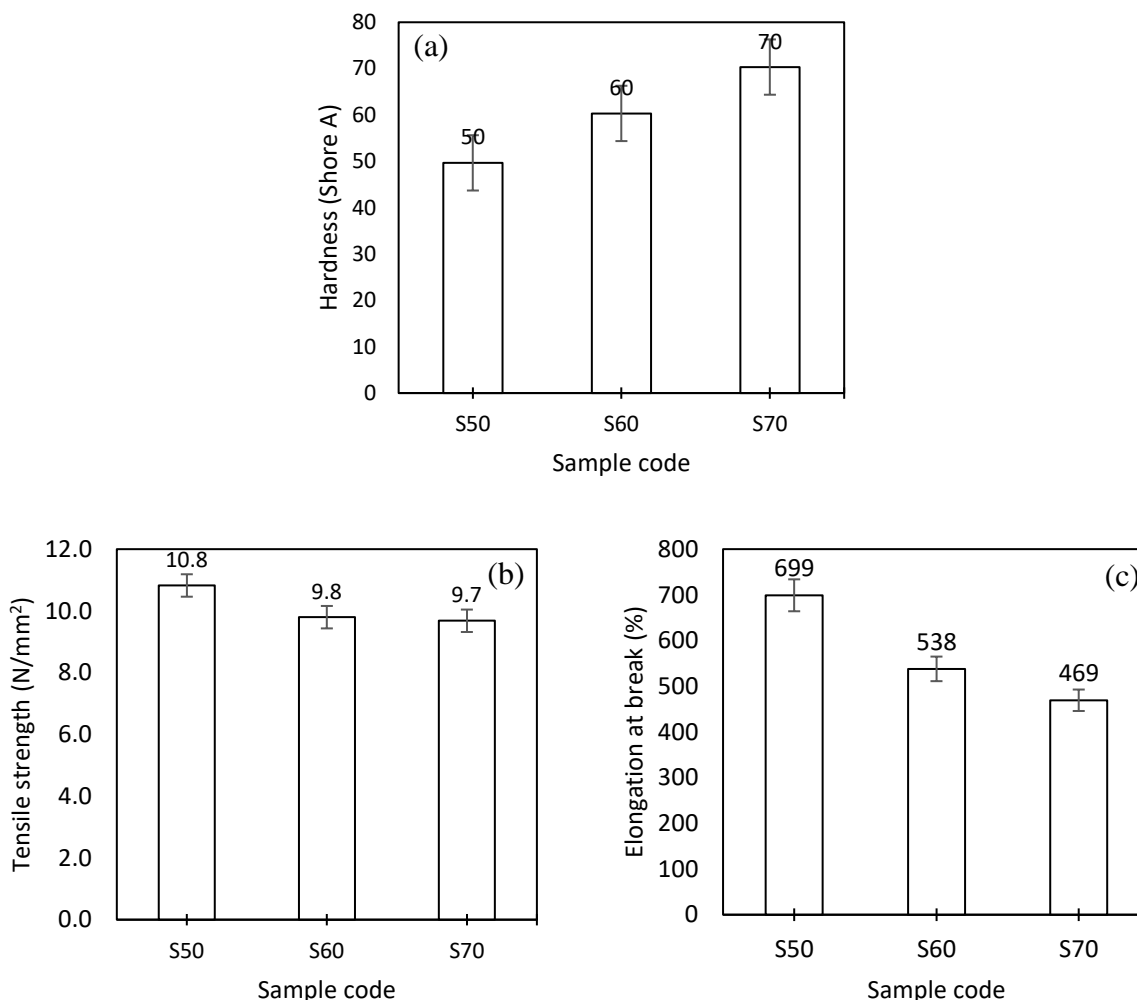


Fig. 1 Mechanical properties of silicone material (a) hardness, (b) tensile strength and (c) elongation at break.

### 3.2. Thermal properties of silicone materials

The thermogravimetric (TG) curves of the silicone materials (S50, S60 and S70) were shown in Figure 2. For all silicone materials, the initial weight loss started from 220 °C to 350 °C belonged to the decomposition of residual silicone monomer. Then, the main weight loss occurred from 350 °C to 700 °C due to the weight loss of polydimethylsiloxane (PDMS). The total weight loss of silicone materials were 22.86%, 22.75% and 20.83% for S50, S60 and S70, respectively. After that silicone rubber completely decomposed at 800 °C and formed as silica. The final residue weight was 70.94 % for S50, 71.68 % for S60 and 71.76% for S70 referred to silica powder.

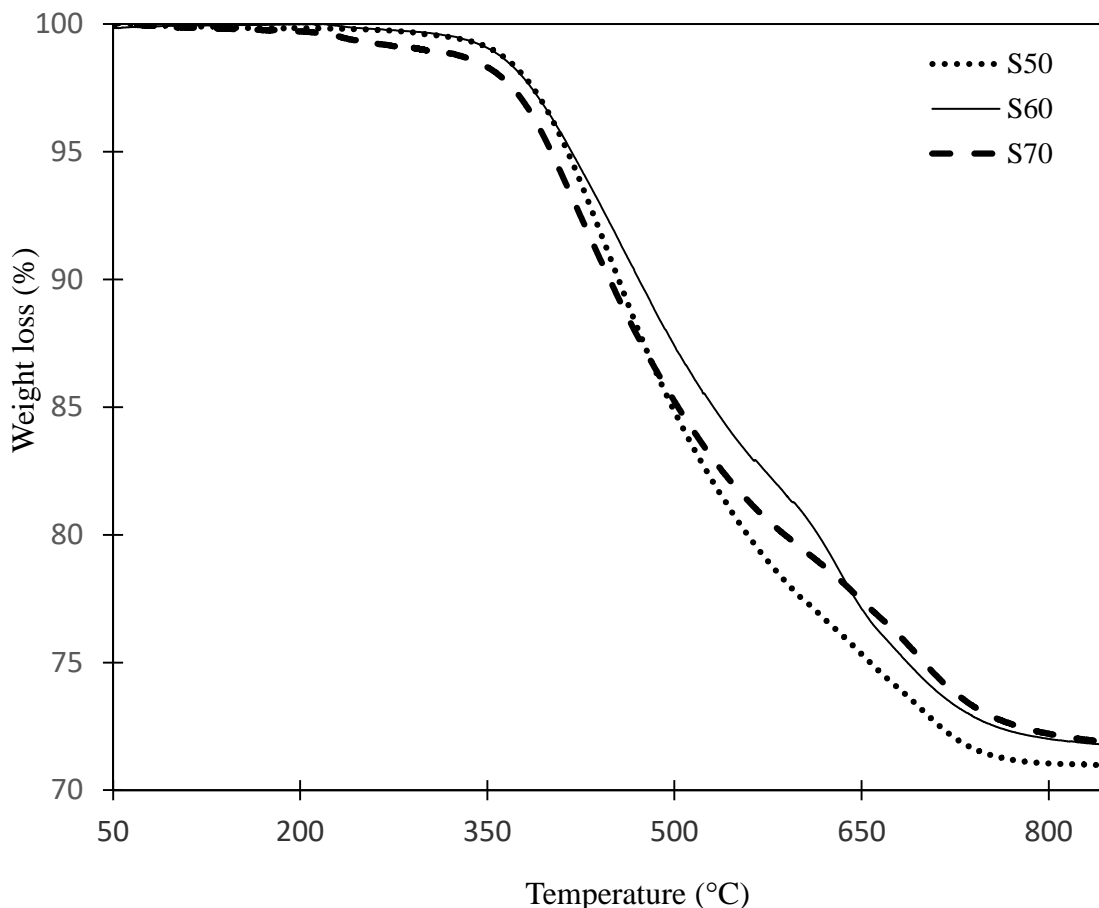


Fig. 2 Thermogravimetric curves of the silicone materials.

### 3.3. CO<sub>2</sub> adsorption capacity

Figure 3 shows the breakthrough curves of silicone materials. A breakthrough curve was plotted between the percentage of the CO<sub>2</sub> concentration and time. Initially, the amount of CO<sub>2</sub> was not detected in the outlet gas because the inlet CO<sub>2</sub> was completely adsorbed on the silicone material. The curves slightly and continuously increased, since the CO<sub>2</sub> adsorption capacity of silicone material slightly decreased, resulting in CO<sub>2</sub> concentration at the outlet gas decreased. Finally, the curves became constant at 12 % (outlet CO<sub>2</sub> concentration equals that of the inlet) because the silicone material were saturated with CO<sub>2</sub>.

The total CO<sub>2</sub> adsorption capacity of silicone materials was calculated from the breakthrough curves and summarized in Table 1. The highest CO<sub>2</sub> adsorption capacity was obtained by S70 (7.00 mg CO<sub>2</sub>/g sorbent), followed by S60 (4.73 mg CO<sub>2</sub>/g sorbent) and S50 (4.62 mg CO<sub>2</sub>/g sorbent), respectively. These results indicated that the silicone material can be used as the adsorbent material for CO<sub>2</sub> capture. It was because the chemical structure of silicone

material presents the oxygen atom, which is acting as the active site like Lewis base to enhance CO<sub>2</sub> capture. Apart from oxygen atom in silicone's chemical structure, the presence of silica content in silicone rubber also helps to improve the CO<sub>2</sub> adsorption capacity and mechanical properties. In addition, the CO<sub>2</sub> adsorption capacity of S70 (7.00 mg CO<sub>2</sub>/g sorbent) was higher than that of natural rubber (1.81 mg CO<sub>2</sub>/g sorbent) [5] by an approximately 3.9 times because the natural rubber had no silica and oxygen atom in its structure resulting in its low CO<sub>2</sub> adsorption capacity.

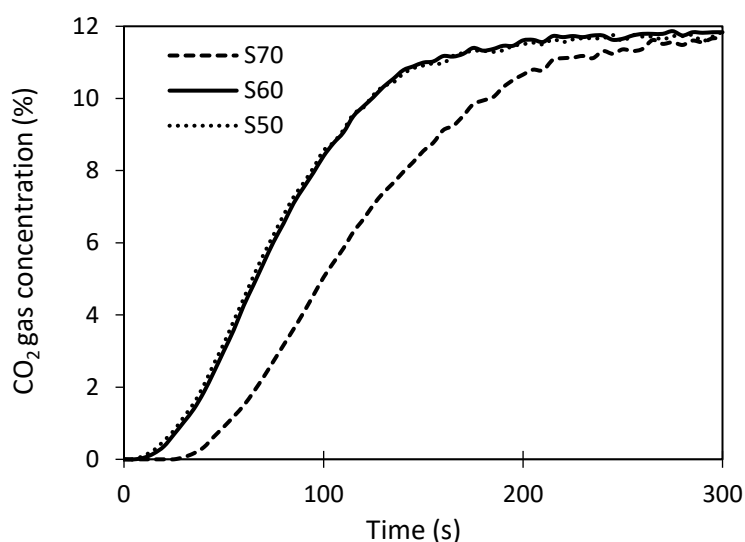


Fig. 3 Breakthrough curves of the S50, S60 and S70

Table 1. Comparison of CO<sub>2</sub> adsorption capacity.

Sample Name	Experimental condition		CO <sub>2</sub> adsorption capacity (mg CO <sub>2</sub> /g sorbent)	Reference
	CO <sub>2</sub> (vol.%)	Silica content (%)		
S50	12	15	4.62	Present work
S60	12	17	4.73	Present work
S70	12	20	7.00	Present work
Natural rubber	12	-	1.81	[5]

### 3.4. Regeneration of silicone material

Five adsorption–desorption cycles were studied for S70. The results presented in Figure 4 showed that the CO<sub>2</sub> adsorption capacity of S70 was slightly decreased after 3 cycles from 7.02 mg CO<sub>2</sub>/g sorbent to 6.91 mg CO<sub>2</sub>/g sorbent and its seemed to be constant up to 5 cycles. These results implied that the silicone rubber has stable adsorption capacity.

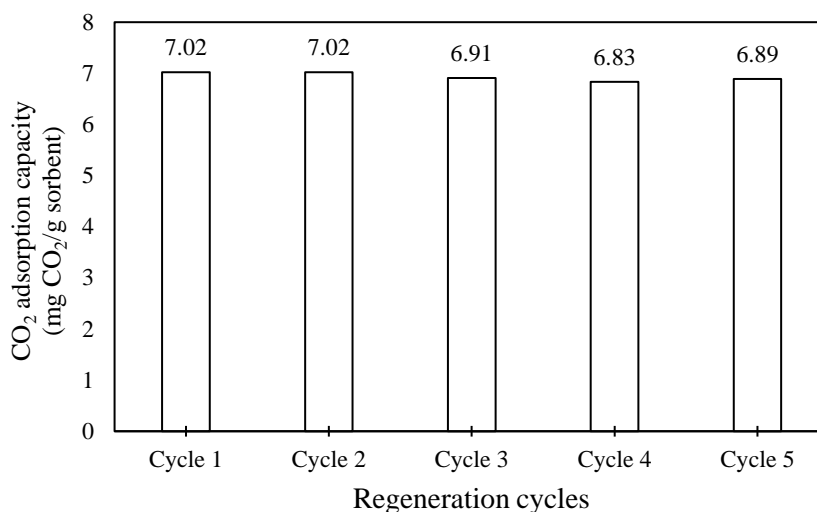


Fig. 4 CO<sub>2</sub> adsorption capacity of S70 over 5 adsorption-desorption cycles.

## 4. Conclusion

In this work, the silicone material was selected to study CO<sub>2</sub> adsorption as the adsorbent material. The CO<sub>2</sub> adsorption capacity of silicone material increased with the increase of silica content. The highest CO<sub>2</sub> adsorption capacity of S70 was obtained up to 7.00 mg CO<sub>2</sub>/g sorbent at ambient temperature and atmosphere pressure. Additionally, the S70 showed the good thermal and mechanical properties, and it also can be reused up to 5 cycles. Accordingly, the silicone material can be used as an alternative adsorbent material for CO<sub>2</sub> capture.

## Acknowledgement

The authors thank the Center of Excellence in Green Materials for Industrial Application, Faculty of Science, Chulalongkorn University for instrument support throughout this work.

## References

- [1] Sattari, A., Ramazani, A., Aghahosseini, H., and Aroua, M.K. (2021). The application of polymer containing materials in CO<sub>2</sub> capturing via absorption and adsorption methods. *Journal of CO<sub>2</sub> Utilization*, 48, 101526.
- [2] Chi, S., Ye Y., Zhao, X., Liu, J., Jin, J., Du, L. and Mi, J. (2023). Porous molecular sieve polymer composite with high CO<sub>2</sub> adsorption efficiency and hydrophobicity. *Separation and Purification Technology*, 307, 122738.
- [3] Tiwari, D., Kaur, S., Bhunia, H., and Bajpai, P.K. (2018). CO<sub>2</sub> adsorption on oxygen enriched nanostructured carbons derived from silica templated resorcinol-formaldehyde. *Journal of Industrial and Engineering Chemistry*, 65, 146-155.
- [4] Sethy, N.K., Arif, Z., Mishra, P.K., and Kumar, P. (2019). Synthesis of SiO<sub>2</sub> nanoparticle from bamboo leaf and its incorporation in PDMS membrane to enhance its separation properties. *Journal of Polymer Engineering*, 39(7), 679-687.
- [5] Panploo, K., Chalermssinsuwan, B., and Poompradub, S. (2020). Effect of amine types and temperature of a natural rubber based composite material on the carbon dioxide capture. *Chemical Engineering Journal*, 402, 125332.

## Equilibrium Molecular Interactions of Phosphonium-Based Ionic Liquids with CO<sub>2</sub> and H<sub>2</sub>S for Gas Separation

Umar Muhammad Yahaya<sup>1</sup>, Hossein Haghani<sup>1,\*</sup>, and Teerawat Sema<sup>1,\*</sup>

<sup>1</sup>Department of Chemical Technology, Chulalongkorn University, Pathumwan, Bangkok, 10330, Thailand.  
Emails: hossein.h@chula.ac.th, teerawat.se@chula.ac.th

### Abstract

Molecular dynamics (MD) simulation was conducted to investigate the equilibrium behavior of tetrabutylphosphonium acetate ([P<sub>4444</sub>][AcO]) and tetrabutylphosphonium diethylphosphate ([P<sub>4444</sub>][DEP]) with CO<sub>2</sub>/H<sub>2</sub>S at 333.15 K and 1.01 bar. The GAFF (General Amber Force Field) was selected from the available forcefields to explore potential modifications that could enhance the consistency between simulated properties and experimental data. Analysis of the radial distribution function confirmed a physical interaction between the ionic liquids and the gases. The two ionic liquids have a large free volume that decreases after the absorption of CO<sub>2</sub> but increases with H<sub>2</sub>S which could be attributed to the angular geometry and polarity of H<sub>2</sub>S. This is supported by the significant negative Coulombic Energy observed in the two ionic liquid systems after absorption of H<sub>2</sub>S and its subsequent lower diffusivity. The molar diffusivity of the gases is higher in [P<sub>4444</sub>][DEP] and the self-diffusivity coefficient of CO<sub>2</sub> is 97.2% greater than that of H<sub>2</sub>S in the same ionic liquid. This work revealed that [P<sub>4444</sub>][DEP] can be considered and further studied for devising low-cost phosphonium-based ionic liquid for CO<sub>2</sub> capture.

**Keywords:** MD simulation, phosphonium-based ionic liquids, gas separation

### 1. Introduction

Gas processing plants separate carbon dioxide (CO<sub>2</sub>), hydrogen sulfide (H<sub>2</sub>S), and other acid gases from gas mixtures. The removal of these gases from the gas mixtures to meet transport and selling specifications is necessary to avoid health and technical problems [1]. The methods employed for this purpose include chemical solvents, physical solvents, and membranes. Chemical solvents, like amines, react with acid gases to form stable compounds that can be easily separated [2]. Physical solvents, such as glycols, absorb acid gases through physical interactions without chemical reactions [3]. Membrane separation relies on the selective permeation of gases through semi-permeable membranes [4]. However, each method presents its challenges. Consequently, the exploration of alternative materials is underway.

Molecular Dynamics (MD) simulation is a technique used to investigate the dynamics and thermodynamic properties at the molecular level [5]. MD simulation principle integrates the equation of motion on each particle in the system to trace their trajectories which pave the way for analyzing the time evolution of the particles. This technique is employed in studying various systems such as that of gas absorption by Ionic Liquids (ILs) [6].

ILs are ionic compounds that are liquids at temperatures below 100 °C [7]. They have essential properties like non-flammability, non-volatility, and higher thermal stability which facilitates their usage as green solvents for various purposes [8]. Phosphonium-based Ionic Liquids (PILs) are ionic liquids with quaternary phosphonium cation. It was reported that



PILs have a higher capacity for dissolving CO<sub>2</sub> on a mole fraction basis than imidazolium-based ILs of the same anion [9].

In this study, MD simulation was employed to investigate the equilibrium interaction of tetrabutylphosphonium acetate ([P<sub>4444</sub>][AcO]) and tetrabutylphosphonium diethylphosphate ([P<sub>4444</sub>][DEP]) with CO<sub>2</sub>/H<sub>2</sub>S at 333.15 K and 1.01 bar. Following this introductory part is a brief explanation of the forcefield employed and the simulation method adopted. The radial distribution function, self and molar diffusivities, Coulombic energy, and free volume in the systems were investigated. The concluding remark is provided at the end.

## 2. Forcefield and Simulation Method

### 2.1 Forcefield

General Amber Force Field (GAFF) [10] is parametrized on all the organic molecules was chosen to explore potential modifications that could enhance the consistency between simulation and experimental data. The interactions between a pair of atoms are taken care of by the bonded and nonbonded potential terms. The bonded potential terms are mimicked by bond stretching, angle bending, and dihedral as seen in Eq. (1):

$$E_{bonded} = \sum_{bonds} k_r (r - r_{eq})^2 + \sum_{angles} k_\theta (\theta - \theta_{eq})^2 + \sum_{dihedrals} \frac{V_n}{2} [1 + \cos(n\varphi - Y)] \quad (1)$$

Where  $r_{eq}$  and  $\theta_{eq}$  are the equilibrium bond length and angle,  $k_r$ ,  $k_\theta$  and  $V_n$  are the bond, angle, and dihedral force constants,  $n$  is multiplicity,  $\varphi$  is the dihedral angle and  $Y$  is phase angle for the torsional angle parameter. The nonbonded interactions are represented by 12-6 Lennard-Jones potentials and Coulombic electrostatic interaction terms as seen in Eq. (2):

$$E_{nonbonded} = \sum_{i < j} \left[ \frac{A_{ij}}{R_{ij}^{12}} - \frac{B_{ij}}{R_{ij}^6} + \frac{q_i q_j}{\epsilon R_{ij}} \right] \quad (2)$$

Where  $R$  is the distance between atom  $i$  and  $j$ ,  $A$  is the depth of the potential energy well and  $B$  is related to the atomic size and curvature of the potential energy well,  $q_i$  and  $q_j$  are the charges of the atoms and  $\epsilon$  is the permittivity of the medium.

### 2.2 Simulation Method

Avogadro [11] was used to model the molecular structures used in this study (Figure 1) which are then submitted to the ACPYPE server [12] to generate the topology with GAFF. GROMACS 2023.1 [13] was used to conduct all the simulations. The temperature of the system was controlled by the velocity-rescaled modified Berendsen method [14] with a 4.0 ps coupling time and pressure is controlled with the stochastic cell rescaling Berendsen method [15] with a 5 ps relaxation time. Periodic boundary conditions were applied in three dimensions, and a 1.4 nm cutoff was used for Lennard-Jones interactions. Coulombic interactions were computed by the particle-mesh Ewald method with a 0.168 nm grid spacing and a real space cutoff of 1.4 nm. We chose a 2-fs time step for integrating the equations of motion using the leapfrog algorithm, saved the trajectory every 10 ps, and visualize them with UCSF Chimera [16]. LINCS algorithm is employed to constrain all the covalent bonds in the system [17].

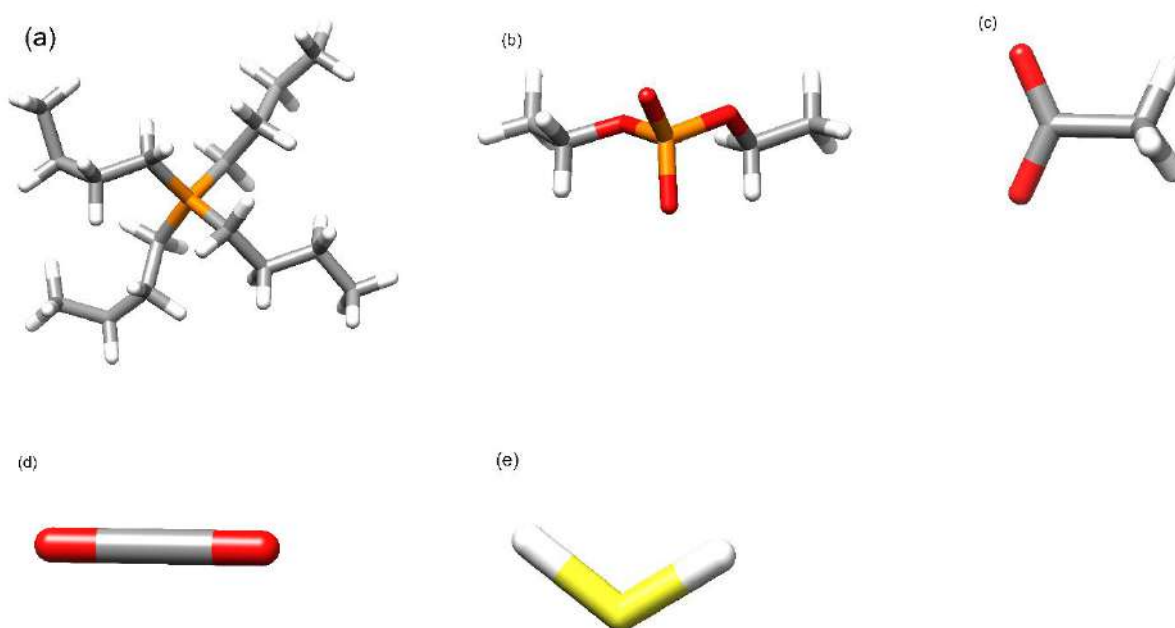


Fig. 1 The Structure of (a) tetrabutylphosphonium, (b) diethylphosphate, (c) acetate, (d) carbon dioxide, and (e) hydrogen sulfide.

Initially, pure systems of the two PPILs with 200 ion pairs were formed using Packmol [18] and simulated for validating the model against available experimental work. Then a system of either of the ionic liquid and CO<sub>2</sub>/H<sub>2</sub>S in 1:1 mole proportion were inserted in the center of a cubic box at 1 nm from its wall. The system was subjected to energy-minimization, followed by temperature equilibration in canonical ensemble for 2 ns at 333.15 K then 10 ns pressure equilibration in isothermal-isobaric ensemble at 1.01 bar. MD production was run for 100 ns in the same isothermal-isobaric ensemble state. Since we intend to investigate the equilibrium behavior MD production was continued for another 100 ns and the last 40 ns was considered for analysis as the system reached equilibrium in that period.

### 3. Results and Discussion

The density of the pure [P<sub>4444</sub>][AcO] ionic liquid is given in Table 1. Interestingly, there is an experimental density of this ionic liquid reported elsewhere [19] and our result deviated by 2.9% only. Experimental density of [P<sub>4444</sub>][DEP] is scarce in the literature.

Table 1. Experimental and simulated densities of ionic liquids.

PPILs	$\rho$ (kgm <sup>-3</sup> )		% Error
	Experiment	Simulation	
[P <sub>4444</sub> ][AcO]	916.4	889.8	2.9
[P <sub>4444</sub> ][DEP]	-	955.3	-

### 3.1 Equilibrium Interactions Behavior

To characterize how the studied ionic liquids interact with the acid gases, we evaluate the cation-anion radial distribution function as shown in Figure 2. The cation-anion radial distribution function of the two ionic liquids remains virtually the same in pure and with interacting gases. This signifies the absence of change in the structural arrangement of the cations and anions before and after absorption of the gases as such only physical interaction exists between the ionic liquids and the gases.

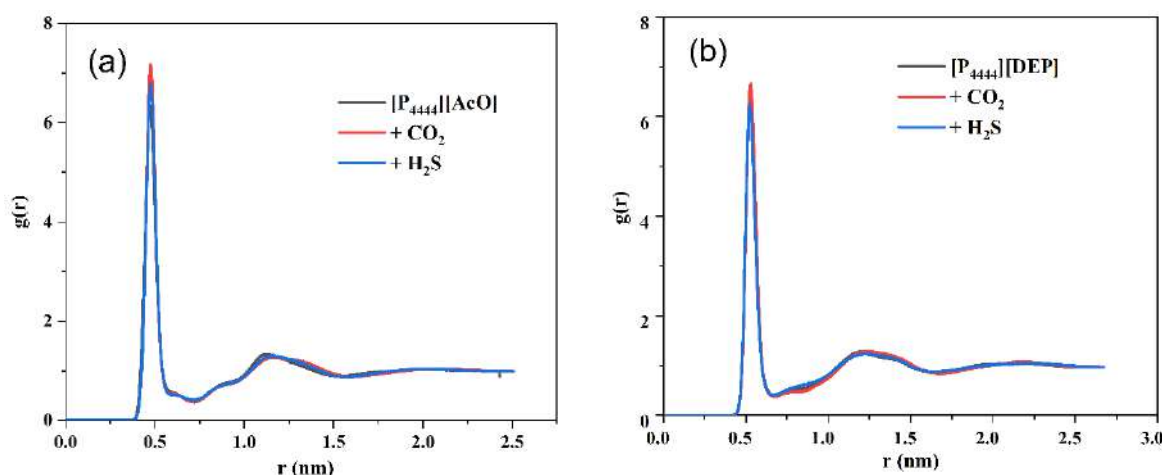


Fig. 2 Cation-anion radial distribution functions of (a)  $[P_{4444}][AcO]$  and (b)  $[P_{4444}][DEP]$ .

### 3.2 Short-range Coulombic Energies

The short-range coulombic interaction energies are presented in Figure 3. When two particles attract each other their Coulombic potential energy of interaction is negative but positive in case of repulsion. The magnitude of the energy determines the extent of the interaction providing insight into the nature and dynamics of their relationship. As seen in Figure 3, all the short-range Coulombic interaction energies are negative indicating the electrostatic attraction between the ions and with the absorbed gas at equilibrium. In pure  $[P_{4444}][DEP]$ , the average Coulombic energy is  $-23500 \text{ kJmol}^{-1}$ . After absorption of  $CO_2$  and  $H_2S$ , the energy reduced to  $-25560 \text{ kJmol}^{-1}$  and  $-28060 \text{ kJmol}^{-1}$  respectively. This testifies that favorable electrostatic attraction exists between the gases and  $[P_{4444}][DEP]$ . In the  $[P_{4444}][AcO]$  system, the average Coulombic interaction energy in pure is  $-47999 \text{ kJmol}^{-1}$  while after absorption of  $CO_2$  and  $H_2S$  it changed to  $-46757 \text{ kJmol}^{-1}$  and  $-51920 \text{ kJmol}^{-1}$  respectively. The trends of ion pair Coulombic interaction energy in pure and after  $CO_2/H_2S$  absorption is  $[P_{4444}][AcO] > [P_{4444}][DEP]$ . And the energy is greater in  $H_2S$ -PPILs system than  $CO_2$ -PPILs system. As a result of this high  $H_2S$ -PPILs interaction energy  $H_2S$  was found to have lower diffusivity in the ionic liquids than  $CO_2$ . The PPILs under investigation have lower interaction energy in pure form than after absorption of either  $CO_2$  or  $H_2S$  except in  $[P_{4444}][AcO]$  where the interaction energy of the pure ionic liquid is slightly greater than after its absorption of  $CO_2$  see Figure 3. The decrease in Coulombic interaction energy in  $[P_{4444}][AcO]-CO_2$  is attributed to the less favorable interaction between  $[P_{4444}][AcO]$  and  $CO_2$ , which, in turn, promotes higher diffusivity of  $CO_2$  than  $H_2S$ .

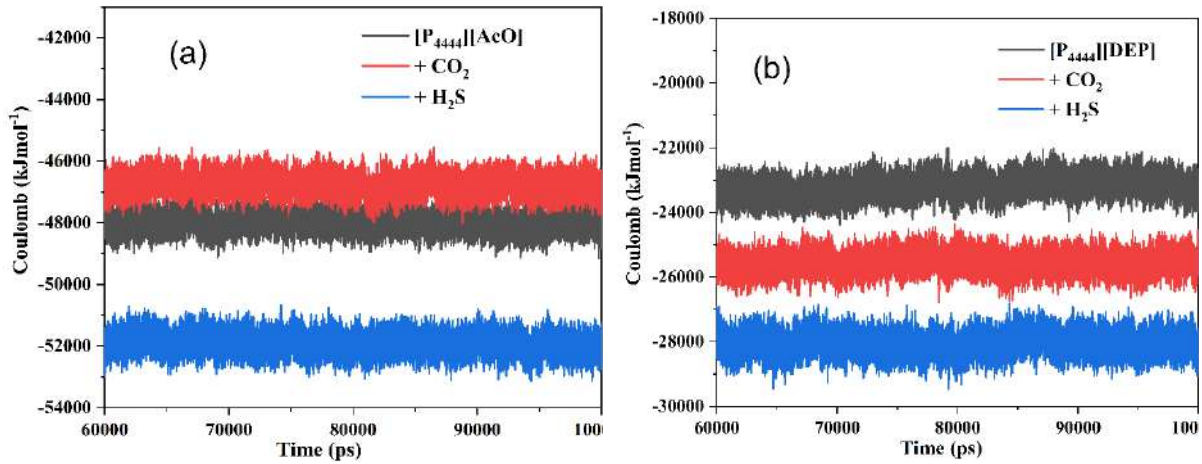


Fig. 3 Coulombic energy of (a) [P<sub>4444</sub>][AcO] and (b) [P<sub>4444</sub>][DEP] systems.

### 3.3 Self-diffusivity Coefficient

The deviation of the position of a particle from a reference is measured by Mean squared Deviation (MSD). It is defined by Eq. (3):

$$MSD(t) = \sum_{i=1}^N \langle |r_i(t) - r_i(0)|^2 \rangle \quad (3)$$

Where  $I = 1, \dots, N$  are the number of particles,  $r_i(t)$  and  $r_i(0)$  is the positions of  $i^{th}$  particle at time  $t$  and  $0$  respectively. To improve statistical accuracy, the time-average method is used to obtain diffusivity from MSD curves of the gases, Figure 4. The curves scaled linearly with time indicating the establishment of Einstein diffusivity hence the self-diffusivity coefficient,  $D$  is defined and obtained by Eq. (4):

$$D = \frac{1}{6N} \frac{d}{dt} \lim_{t \rightarrow \infty} \sum_{i=1}^N \langle |r_i(t) - r_i(0)|^2 \rangle \quad (4)$$

The mobility of the ions is reported to be dependent on the cation-anion interaction and/or molecular weight [6]. Table 2 is the self-diffusivity coefficients of the ions and the gases. [P<sub>4444</sub>] is the common cation for the two ionic liquids under investigation, it has the highest diffusivity in [P<sub>4444</sub>][DEP] also [DEP] diffuses faster than [AcO]. The higher diffusivities values of the ions in [P<sub>4444</sub>][DEP] is connected to the lowest cation-anion interaction energy and higher size of the anion in this ionic liquid. [P<sub>4444</sub>][AcO] has high ion pair interaction energy as such its ions show lower diffusivity values. In the two PPIL under investigation, CO<sub>2</sub> shows higher diffusivity than H<sub>2</sub>S and the diffusivity is higher in [P<sub>4444</sub>][DEP] due to lower interaction energy with this ionic liquid. H<sub>2</sub>S has lower diffusivity due to higher interaction energy with the ionic liquids in each case.

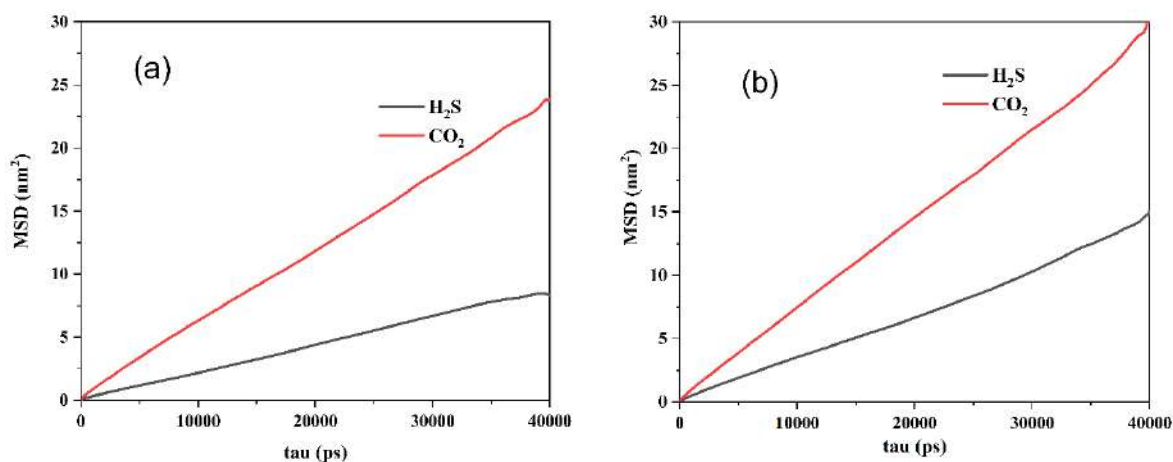


Figure 4. Mean squared deviation of CO<sub>2</sub> and H<sub>2</sub>S for (a) [P<sub>4444</sub>][AcO] and (b) [P<sub>4444</sub>][DEP].

Table 2. Self-diffusivity coefficient (D) of the ions and gases.

PPIL	Self-Diffusivity Coefficient, D ("x"10 <sup>-5</sup> cm <sup>2</sup> s <sup>-1</sup> )			
	D <sub>+</sub>	D <sub>-</sub>	D <sub>CO2</sub>	D <sub>H2S</sub>
[P <sub>4444</sub> ][AcO]	0.00052	0.00047	0.10100	0.03290
[P <sub>4444</sub> ][DEP]	0.00058	0.00067	0.11760	0.05965

### 3.4 Molar Diffusivity

The molar diffusivity is a measure of the number of particles and their diffusivity values in a system. Figure 5 shows the molar diffusivity of the gases in the two PPILs. From this figure, we can understand that there is a greater number of CO<sub>2</sub> molecules moving with higher diffusivity values in the two PPILs than H<sub>2</sub>S. This is consistent with the high diffusivity value of CO<sub>2</sub> we observed in both ionic liquids.

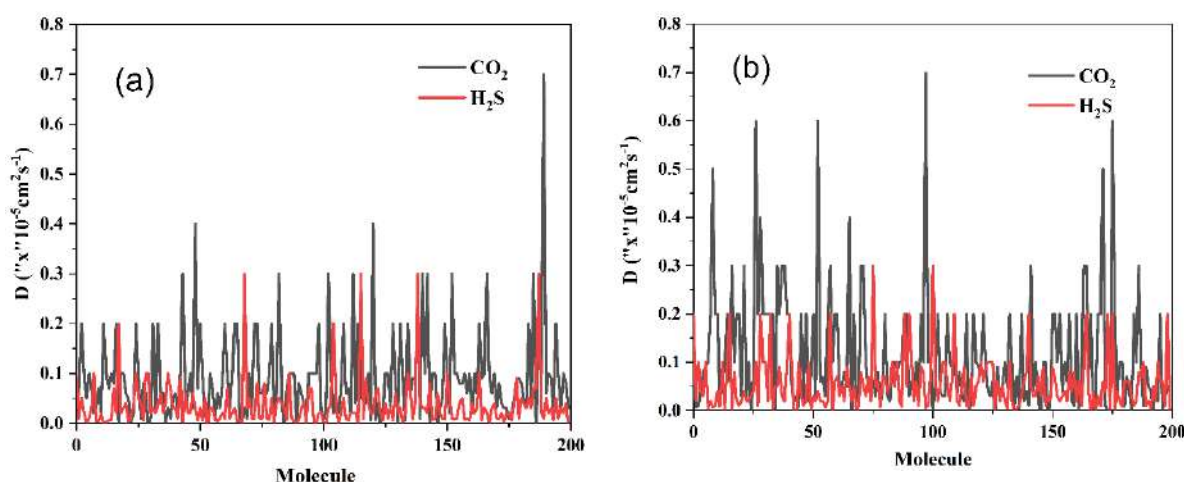


Fig. 5 Molar diffusivity of CO<sub>2</sub> and H<sub>2</sub>S in (a) [P<sub>4444</sub>][AcO] and (b) [P<sub>4444</sub>][DEP].

### 3.5 Free Volume Change

The Free Volume (FV) is evaluated as a function of time and reported as a fraction of the total volume. Table 3 gives the Total Volume (TV) and Free Volume (FV) of the studied PPILs in pure and after absorption of the gases. It can be observed that the FV increases with H<sub>2</sub>S in the two PPILs. This increase is attributed to the high dipole moment of H<sub>2</sub>S which causes higher PPIL-H<sub>2</sub>S interaction energy as it binds firmly to the ionic liquids where the angular geometry of H<sub>2</sub>S causes an overall increase in the FV. The observation is reversed with CO<sub>2</sub> due to its linear geometry and absence of dipole moment.

Table 3. Total Volume (TV), and Free Volume (FV) in the ionic liquid systems.

	[P <sub>4444</sub> ][AcO]			[P <sub>4444</sub> ][DEP]		
	Pure	+ CO <sub>2</sub>	+ H <sub>2</sub> S	Pure	+ CO <sub>2</sub>	+ H <sub>2</sub> S
TV (nm <sup>3</sup> )	118.86	129.69	128.74	143.43	153.9	153.15
FV (%)	39.65	39.55	39.96	39.28	39.08	39.48

### 4. Conclusion

In this work, we employ MD simulation to investigate the equilibrium interaction behavior of [P<sub>4444</sub>][AcO], and [P<sub>4444</sub>][DEP] with CO<sub>2</sub>/H<sub>2</sub>S at 333.15 K and 1.01 bar. The two ionic liquids have significant free volume which enhances CO<sub>2</sub>/H<sub>2</sub>S absorption by physical interactions as proved by the analysis of radial distribution function. [P<sub>4444</sub>][DEP] has low cation-anion interaction energy and high CO<sub>2</sub>/H<sub>2</sub>S diffusivity but low [P<sub>4444</sub>][DEP]-CO<sub>2</sub>/H<sub>2</sub>S interaction energy which may hinder higher gas solubility. [P<sub>4444</sub>][AcO] has high cation-anion and [P<sub>4444</sub>][AcO]-CO<sub>2</sub>/H<sub>2</sub>S interaction energies. The diffusivities of the gases are low in this ionic liquid. H<sub>2</sub>S interacts more strongly with all ionic liquids than CO<sub>2</sub> because of that it has low diffusion coefficient. The diffusivity of CO<sub>2</sub> in [P<sub>4444</sub>][DEP] is 97.2% higher than that of H<sub>2</sub>S in the same ionic liquid. The free volume of two PPILs increases after absorption of H<sub>2</sub>S which is connected to the angular geometry and polarity of the gas. Our work shows that CO<sub>2</sub> and H<sub>2</sub>S have high diffusivity in [P<sub>4444</sub>][DEP] due to low cation-anion interaction energy in this ionic liquid. Therefore, this ionic liquid should be considered for devising low-cost phosphonium-based ionic liquid for CO<sub>2</sub> capture.

### Acknowledgments

The authors wish to acknowledge the Graduate School of Chulalongkorn University for financial support and NSTDA Supercomputer center (ThaiSC) and the National e-Science Infrastructure Consortium for their support of computing facilities.

### References

- [1] Ramdin, M., et al. (2014). Solubility of CO<sub>2</sub>/CH<sub>4</sub> gas mixtures in ionic liquids. *Fluid Phase Equilibria*, 375, 134-142.
- [2] Al-Baghli, N. A., et al., (2001). A rate-based model for the design of gas absorbers for the removal of CO<sub>2</sub> and H<sub>2</sub>S using aqueous solutions of MEA and DEA. *Fluid phase equilibria*, 185(1-2), 31-43.
- [3] Jimoh, T. A., et al. (2023). Introduction to Carbon Capture by Solvent-based Technologies. *Ref. Modul. Earth Syst. Environ. Sci*, 2023.

- [4] Liang, L., Gan, Q., and Nancarrow, P. (2014). Composite ionic liquid and polymer membranes for gas separation at elevated temperatures. *Journal of Membrane Science*, 450, 407-417.
- [5] Hollingsworth, S. A., and Dror, R. O. (2018). Molecular dynamics simulation for all. *Neuron*, 99(6), 1129-1143.
- [6] Gupta, K. M., and Jiang, J. (2014). Systematic Investigation of Nitrile Based Ionic Liquids for CO<sub>2</sub> Capture: A Combination of Molecular Simulation and ab Initio Calculation. *The Journal of Physical Chemistry C*, 118(6), 3110-3118.
- [7] Lei, Z., et al. (2017). Introduction: ionic liquids. ACS Publications, 6633-6635.
- [8] Gutowski, K. E. (2018). Industrial uses and applications of ionic liquids. *Physical Sciences Reviews*, 3(5), 20170191.
- [9] Carvalho, P. J., et al. (2010). High carbon dioxide solubilities in trihexyltetradecylphosphonium-based ionic liquids. *The Journal of Supercritical Fluids*, 52(3), 258-265.
- [10] Wang, J., et al. (2004). Development and testing of a general amber force field. *Journal of computational chemistry*, 25(9), 1157-1174.
- [11] Hanwell, M. D., et al. (2012). Avogadro: an advanced semantic chemical editor, visualization, and analysis platform. *Journal of cheminformatics*, 2012. 4(1), 1-17.
- [12] Sousa da Silva, A. W., and Vranken, W. F. (2012). ACPYPE-Antechamber python parser interface. *BMC research notes*, 5, 1-8.
- [13] Van Der Spoel, D., et al. (2005). GROMACS: fast, flexible, and free. *Journal of computational chemistry*, 26(16), 1701-1718.
- [14] Berendsen, H. J., et al. (1984). Molecular dynamics with coupling to an external bath. *The Journal of chemical physics*, 81(8), 3684-3690.
- [15] Bernetti, M., and Bussi, G. (2020). Pressure control using stochastic cell rescaling. *The Journal of Chemical Physics*, 153(11).
- [16] Pettersen, E. F., et al. (2004). UCSF Chimera—a visualization system for exploratory research and analysis. *Journal of computational chemistry*, 25(13), 1605-1612.
- [17] Hess, B., et al. (1997). LINCS: A linear constraint solver for molecular simulations. *Journal of computational chemistry*, 18(12), 1463-1472.
- [18] Martínez, L., et al. (2009). PACKMOL: A package for building initial configurations for molecular dynamics simulations. *Journal of computational chemistry*, 30(13), 2157-2164.
- [19] Otero, I., et al. (2017). How does the addition of a third ion affect the molecular interactions and the thermodynamic properties of acetate-based ionic liquids? *The Journal of Physical Chemistry B*, 121(41), 9725-9736.

## Effect of temperature on the methanol synthesis through ethanol-assisted CO<sub>2</sub> hydrogenation in fixed bed reactor

**Chanapat Boonprakom<sup>1</sup>, Kritchart Wongwailikhit<sup>1,2</sup>, Rungthiwa Methaapanon<sup>1,2</sup>, and Apinan Soottitantawat<sup>1,2\*</sup>**

<sup>1</sup>Center of Excellence in Particle and Materials Processing Technology, Department of Chemical Engineering, Faculty of Engineering, Chulalongkorn University, Bangkok 10330, Thailand

<sup>2</sup>Bio-Circular-Green-economy Technology & Engineering Center, Department of Chemical Engineering, Faculty of Engineering, Chulalongkorn University, Bangkok 10330, Thailand

E-mail: apinan.s@chula.ac.th

### Abstract

As a fundamental chemical compound, methanol plays a pivotal role in producing various chemicals in numerous industries, including the chemical and synthesis industry, pharmaceuticals, electronics, and coatings. Currently, a significant portion of methanol is derived from natural gas. To address environmental concerns and improve economic efficiency, there is a growing interest in directly synthesizing methanol from carbon dioxide, a process known as CO<sub>2</sub> hydrogenation. CO<sub>2</sub> hydrogenation is an exothermic reaction, which typically operates under high-pressure and high-temperature conditions. The standard synthesis temperature ranges from 250°C to 300°C, resulting in a lower conversion of CO<sub>2</sub> to methanol at equilibrium. High pressures in the 50-100 bar range are also required, making the process energy-intensive. In this study, an alternative approach is explored, known as alcohol-assisted methanol synthesis. This method involves using alcohols as solvents to facilitate the reaction, reducing the required temperature and pressure while improving methanol yield. Methanol synthesis with the assistance of ethanol in a gas phase has been thoroughly investigated in a fixed-bed reactor. The effect of temperature is studied, assessing their impact on both methanol yield and CO<sub>2</sub> conversion. This study has gained valuable insights that can contribute to energy reduction in methanol production via the CO<sub>2</sub> hydrogenation process. This research serves as a guiding pathway for the future development and improvement of this process.

**Keywords:** Methanol; Hydrogenation; Alcohol-assisted;

### 1. Introduction

Methanol is a crucial chemical feedstock, with a global production ranging from 40 to 60 million tons annually. It plays a pivotal role in various industries, including the chemical, pharmaceutical, and electrical appliance industries. Additionally, it serves as a fuel additive, enhancing the combustion efficiency of diesel engines and contributing to the reduction of particulate matter, hydrocarbons, and carbon monoxide emissions from diesel engines. Therefore, methanol is a highly sought-after chemical in numerous industries (Chen et al., 2021).

The continuous increase in carbon dioxide (CO<sub>2</sub>) emissions is attributed to various industries and the combustion of fossil fuels. This phenomenon leads to the accumulation of greenhouse gases, contributing to the greenhouse effect and resulting in a rise in global temperatures. These environmental impacts have severe consequences, such as ocean acidification, rising sea levels, and elevated surface temperatures (Kanuri et al., 2022). To



mitigate the release of carbon dioxide (CO<sub>2</sub>) into the atmosphere, various strategies have been proposed, such as carbon capture, separation, and utilization (Meesattham & Kim-Lohsoontorn, 2022). One approach to reducing carbon dioxide emission is converting CO<sub>2</sub> into value-added chemicals, providing an avenue to generate economic value from this greenhouse gas.

The direct hydrogenation of methanol from carbon dioxide (CO<sub>2</sub>) gas employs a Cu/ZnO/Al<sub>2</sub>O<sub>3</sub> catalyst, which is an exothermic reaction. Due to thermodynamic constraints, the synthesis temperature typically ranges from 250 to 300 °C, resulting in a low conversion of CO<sub>2</sub> at equilibrium. To enhance the conversion of CO<sub>2</sub>, high pressures of 50-100 bar are required, making this process energy-intensive. CO<sub>2</sub> hydrogenation is the reaction mechanism as shown in equation (1) and reverse water gas shift reaction (RWGS) as shown in equation (2) (Kanuri et al., 2022).



Following Le Chatelier's principle, methanol synthesis from the CO<sub>2</sub> hydrogenation reaction is an exothermic reaction, which occurs efficiently at low temperatures. Since it is a reaction reducing the number of components, it is favorable at high pressures. Furthermore, conducting the reaction at higher temperatures increases by-products like alcohols and hydrocarbons. Therefore, producing methanol at low temperatures is a suitable option. According to the principles of thermodynamics, the practice may yield higher methanol production (Meesattham & Kim-Lohsoontorn, 2022).

Therefore, alternative methods, known as methanol synthesis with alcohol-assisted, have been explored. This approach employs alcohols as solvents to accelerate the reaction, reduce reaction temperature and pressure, and enhance methanol yield. As shown in equations (3)-(6), alcohol assisted the reaction mechanism. The detection of ethyl acetate resulting from the catalytic dehydrogenation of ethanol was reported, as shown in equation (7). The synthesis of methanol using an alcohol-assisted method can be conducted at temperatures of 150-170 °C and pressures of 30-50 bar, which are lower conditions compared to the conventional methanol synthesis via CO<sub>2</sub> hydrogenation reactions. Furthermore, the alcohol-assisted methanol synthesis enhances CO<sub>2</sub> conversion and increases the methanol yield (Meesattham & Kim-Lohsoontorn, 2022). Therefore, operating under conditions with lower energy requirements is advantageous for cost reduction in operations.



The report studied different types of alcohols used as solvents to expedite the reaction, including ethanol, 1-propanol, 1-butanol, and 1-pentanol. As the size of the alcohol molecules increases, it impacts the solubility of carbon dioxide in the alcohol, leading to a decrease in carbon dioxide conversion and methanol yield. The CO<sub>2</sub> conversion and methanol yield remain constant over 24 hours. Therefore, a reaction time of approximately 24 hours is necessary to achieve equilibrium (Meesattham & Kim-Lohsoontorn, 2022).

Fixed-bed reactors are suitable for gas-phase reactions, and in industry, methanol is commonly produced in the gas phase using fixed-bed reactors. This is because fixed-bed reactors do not require the separation of the catalyst, making operations convenient without being affected by the dispersion of the starting gas. Moreover, they can accommodate a large quantity of catalysts. The characteristics of fixed-bed reactors make them well-suited for scalable processes (Din et al., 2019).

This project investigates the synthesis of methanol through CO<sub>2</sub> hydrogenation via ethanol-assisted methanol synthesis in a fixed-bed reactor. The starting material is pure carbon dioxide gas, and the catalyst used is Cu/ZnO. Ethanol is introduced into the gas phase to study the effect of temperature on methanol production in the hydrogenation reaction of carbon dioxide, with ethanol present in the gas phase in the fixed-bed reactor. The effect of temperature is studied, assessing their impact on methanol yield and CO<sub>2</sub> conversion. This study has gained valuable insights that can contribute to energy reduction in methanol production via the CO<sub>2</sub> hydrogenation process. This research serves as a guiding pathway for the future development and improvement of this process.

## 2. Methods

### 2.1. Fixed-bed Reactor

The apparatus used for reaction testing is of the fixed-bed reactor type. The material is made of stainless steel with a diameter of 1/2 inch and a height of 78 cm. Figure 1 illustrates the process flow diagram of the fixed-bed reactor system, and Figure 2 shows the heating measurement system inside the reactor.

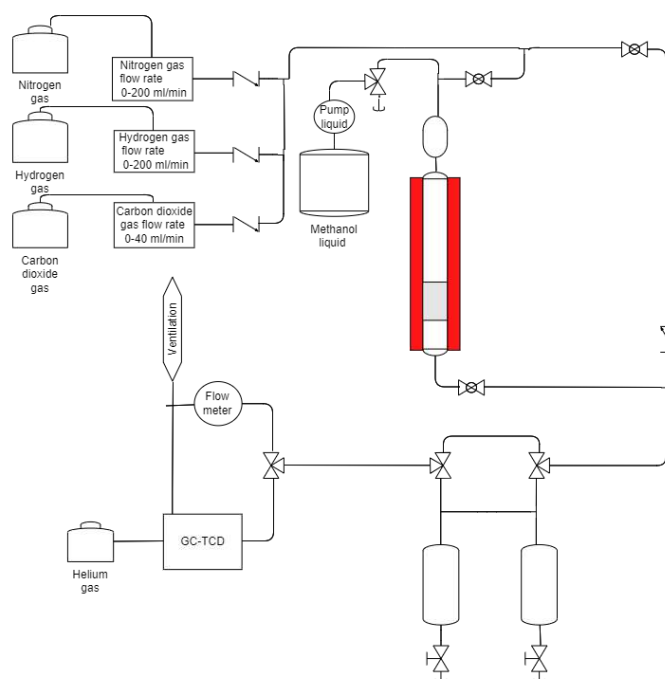


Fig.1 Process flow diagram of the fixed-bed reactor system.

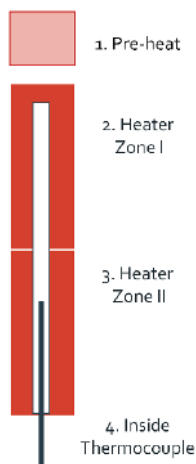


Fig.2 The diagram of the temperature control system.

## 2.2. Packing Catalysis

The catalyst for the reaction had been placed at the end of the thermocouple to ensure precise temperature measurement. For this experiment, a Cu/ZnO catalyst from the industry, with a size of 1-1.6 mm (prepared by grinding and sieving to achieve the desired size), weighed 20 g. Additionally, aluminum oxide with a height of 4.5 cm and wool with a height of 4.5 cm had been prepared. The wool had been tightly wound around the thermocouple. Aluminum oxide and the previously prepared Cu/ZnO catalyst were added, followed by the addition of a grinding ball with a height of 18 cm Figure 3.

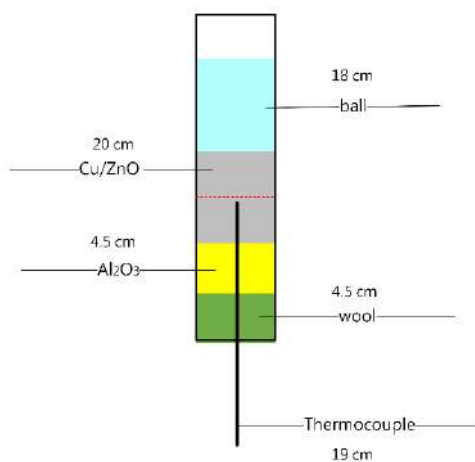


Fig.3 The catalysis packing in the fixed-bed reactor.

## 2.3. Pressure Check

Nitrogen gas had been fed into the apparatus at a rate of 200 ml/min, and the pressure had gradually increased until it reached 30 bar. After reaching the desired pressure, the nitrogen gas was closed, and the system was left undisturbed for approximately 1 hour. The pressure had been monitored during this time, and if there had been a continuous decrease, each valve

point of the apparatus had been inspected using a spray at the valves. Air bubbles had been observed to check for gas leakage in the system.

## 2.4. Reduced Catalysts

The reduced catalysts were prepared by flowing nitrogen gas at 200 ml/min and hydrogen gas at 10 ml/min at a pressure of 5 bar and a temperature of 230 °C. Throughout this process, the temperature had been controlled not to exceed 300 °C. The reduction process took approximately 4 hours or until the temperature stabilized. When the temperature had stabilized, the hydrogen gas flow rate was adjusted to 200 ml/min, and the valve was opened to remove water from the system.

## 2.5. Operation Reaction

A 20 g catalyst was subjected to the reaction at a GHSV of 298 mL/g<sub>cat</sub>.hr with a hydrogen to carbon dioxide molar ratio of 5:1. The reaction was conducted at a pressure of 30 bar and temperatures of 140, 170, 200, and 230 °C. Initially, hydrogen and carbon dioxide gases were introduced, followed by the addition of ethanol through a feed line passing through a pre-heat at 230 °C to ensure ethanol was in the gas phase. Samples were then collected every 3 hours up to 24 hours and analyzed using Gas Chromatography with Thermal Conductivity Detection (GC-TCD). The concentration values were measured using GC-TCD, and the gas flow rate from the outlet was recorded, as shown in Figure 4. The report presented the effect of temperature on methanol yield and CO<sub>2</sub> conversion, calculated through equations (8)-(9).

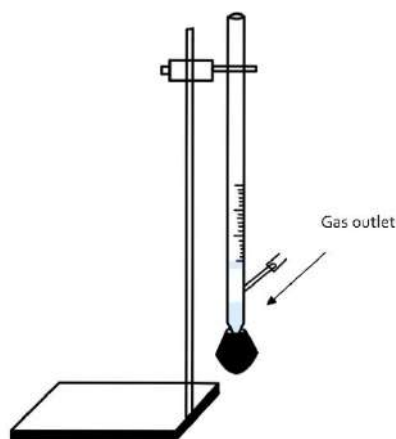


Fig.4 Measurement of gas outlet flow rate.

$$CO_2 \text{ conversion} = \frac{\text{mol of converted } CO_2}{\text{mol of initial } CO_2} \times 100 \quad (8)$$

$$\% \text{Methanol Yield} = \frac{\text{mol of methanol in product}}{\text{mol of initial } CO_2} \times 100 \quad (9)$$

## 3. Results and Discussion

The experimental results in the fixed-bed reactor for non-ethanol assisted reactions, both methanol yield and CO<sub>2</sub> conversion increased as the temperature increased, as shown in Figures 5 and 6. In the experiments conducted at 230°C, the methanol yield was 24.58%, and the CO<sub>2</sub>

conversion was 28.33%, representing the highest values compared to temperatures at 140, 170, and 200 °C. Furthermore, while the rate of CO<sub>2</sub> hydrogenation increases with the rise in reaction temperature up to a certain degree, it begins to decline at higher temperatures due to a decrease in the thermodynamic equilibrium constant with increasing temperature. Consequently, this reaction is not suitable for operation at very high temperatures. According to (Fujitani & Nakamura, 2000), the rate of methanol synthesis by CO<sub>2</sub> hydrogenation increases with temperature up to 220 °C. However, any further increase in temperature depresses the rate of the reaction. This discrepancy becomes quite understandable when considering other concurrent reactions that occur alongside the CO<sub>2</sub> hydrogenation to methanol. One such significant reaction is the RWGS reaction as shown in equation (2), which accompanies CO<sub>2</sub> hydrogenation, as illustrated in the reaction equation. Given its endothermic nature, the RWGS reaction favors higher temperatures. Therefore, an increase in the reaction temperature will shift the CO<sub>2</sub> hydrogenation towards the reverse water gas shift reaction.

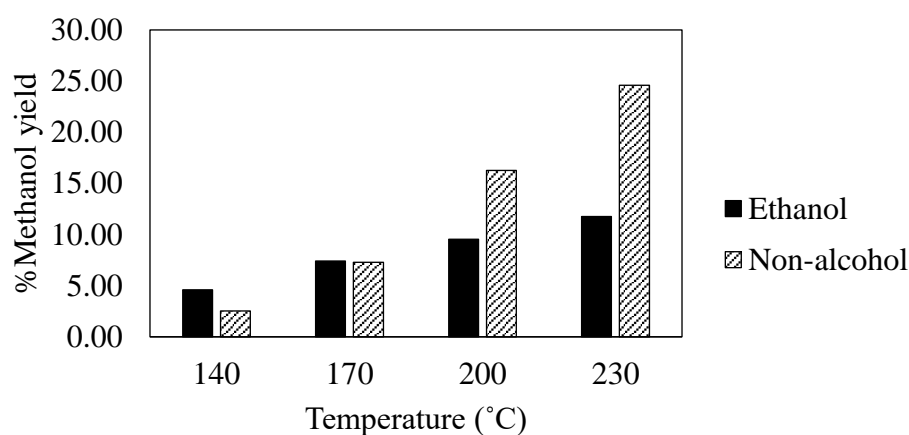


Fig. 5 Methanol yield at temperatures of 140, 170, 200, and 230 °C, reaction pressure of 30 bar, and GHSV of 298 mL/g<sub>cat</sub>.hr in non-ethanol and ethanol-assisted reactions.

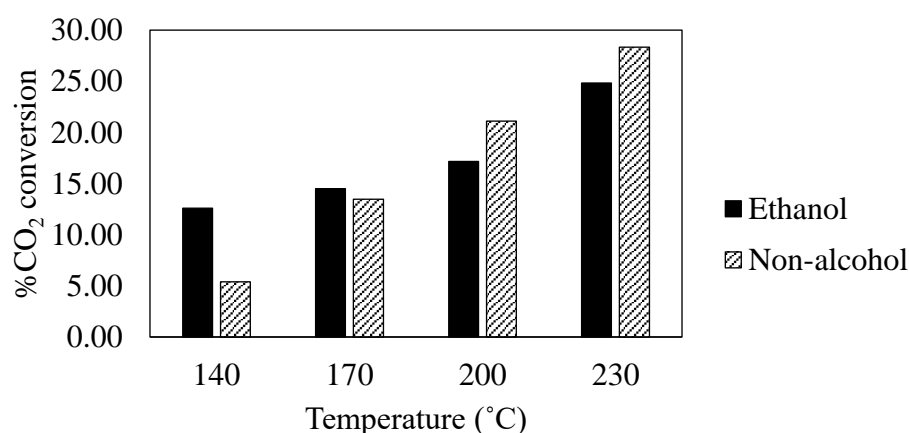


Fig. 6 CO<sub>2</sub> conversion at temperatures of 140, 170, 200, and 230 °C, reaction pressure of 30 bar, and GHSV of 298 mL/g<sub>cat</sub>.hr in non-ethanol and ethanol-assisted reactions.

The experimental results for ethanol-assisted reactions showed an increase in both methanol yield and CO<sub>2</sub> conversion as the temperature increased. At 230°C, the methanol yield was 11.76%, and the CO<sub>2</sub> conversion was 24.83%, representing the highest values compared to temperatures at 140, 170, and 200°C in ethanol-assisted reactions. However, when comparing the experimental results of non-ethanol and ethanol-assisted reactions at 140 °C, the methanol yield was 2.54% for the non-ethanol reaction and 4.58% for the ethanol-assisted reaction. The CO<sub>2</sub> conversion was 5.39% for the non-ethanol reaction and 12.58% for the ethanol-assisted reaction. The results are presented in Figures 5 and 6, showing that the ethanol-assisted reaction exhibited higher methanol yield and CO<sub>2</sub> conversion than the non-ethanol reaction at 140°C. Therefore, it was hypothesized that alkyl formate served as a significant pathway in the ethanol-assisted reaction. This pathway facilitated the synthesis of methanol at low temperatures. According to (Zhang et al., 2008), the reaction temperature experienced a significant decrease, attributed to the catalytically active nature of alcohol and the emergence of a novel reaction pathway. In this context, the alcohol employed in the reaction remained unconsumed as it underwent self-regeneration through the hydrogenation of alkyl formate. This process effectively acted akin to a catalytic solvent.

#### 4. Conclusions

The study examined the effect of temperature on methanol synthesis using ethanol-assisted methods at reaction temperatures of 140, 170, 200, and 230 °C. Methanol yield and CO<sub>2</sub> conversion were determined when the reaction was conducted at 140°C, with methanol yield at 4.58% and CO<sub>2</sub> conversion at 12.58%. Methanol yield and CO<sub>2</sub> conversion increased when using ethanol-assisted synthesis at lower temperatures. Ethanol-assisted methanol synthesis involves a change in the reaction mechanism, enabling methanol synthesis at low temperatures. According to the report, ethanol used in this reaction was not consumed due to its self-regeneration by hydrogenation of alkyl formate, acting like a catalytic solvent.

However, ethyl acetate was found to be a by-product resulting from the dehydrogenation of ethanol, leading to acetaldehyde and potentially affecting the purity of the final products in the process. Methanol production is a complex process. We previously reported that using ethanol-assisted synthesis resulted in higher methanol yields than non-ethanol reactions. However, the main drawback is the difficulty in obtaining pure products. The cost implications are evident in increased production costs due to the need for additional distillation columns and higher public utility expenses.

#### References

- [1] Chen, F., Zhang, P., Xiao, L., Liang, J., Zhang, B., Zhao, H., Kosol, R., Ma, Q., Chen, J., & Peng, X. (2021). Structure–Performance Correlations over Cu/ZnO Interface for Low-Temperature Methanol Synthesis from Syngas Containing CO<sub>2</sub>. *ACS Applied Materials & Interfaces*, *13*(7), 8191-8205.
- [2] Din, I. U., Shaharun, M. S., Alotaibi, M. A., Alharthi, A. I., & Naeem, A. (2019). Recent developments on heterogeneous catalytic CO<sub>2</sub> reduction to methanol. *Journal of CO<sub>2</sub> Utilization*, *34*, 20-33.
- [3] Fujitani, T., & Nakamura, J. (2000). The chemical modification seen in the Cu/ZnO methanol synthesis catalysts. *Applied Catalysis A: General*, *191*(1-2), 111-129.
- [4] Kanuri, S., Roy, S., Chakraborty, C., Datta, S. P., Singh, S. A., & Dinda, S. (2022). An insight of CO<sub>2</sub> hydrogenation to methanol synthesis: Thermodynamics, catalysts,

operating parameters, and reaction mechanism. *International Journal of Energy Research*, 46(5), 5503-5522.

- [5] Meesattham, S., & Kim-Lohsoontorn, P. (2022). Low-temperature alcohol-assisted methanol synthesis from CO<sub>2</sub> and H<sub>2</sub>: The effect of alcohol type. *International Journal of Hydrogen Energy*, 47(54), 22691-22703.
- [6] Zhang, Y., Yang, R., & Tsubaki, N. (2008). A new low-temperature methanol synthesis method: Mechanistic and kinetics study of catalytic process. *Catalysis today*, 132(1-4), 93-100.

## Density, Viscosity, and CO<sub>2</sub> Absorption capacity of Tri-amine blends 2-amino-2-methyl-1-propanol (AMP), Piperazine (PZ), and Monoethanolamine (MEA)

**Wadeeva Pornsawasklin<sup>1</sup>, Sopita Unprasert<sup>1</sup>, Rattapanorn Apaiyakul<sup>1</sup>,  
Teerawat Sema<sup>1,\*</sup>**

<sup>1</sup>Department of Chemical Technology, Faculty of Science, Chulalongkorn University, Pathumwan, Bangkok,  
10330, Thailand

E-mail: teerawat.se@chula.ac.th

### Abstract

Amine based carbon dioxide (CO<sub>2</sub>) absorption technology has been commercially proved over a decade in several locations around the world. Its key is to use a highly effective solvent, which can capture larger amount of CO<sub>2</sub> than the conventional aqueous solution of 30%wt. monoethanolamine (MEA). This study focuses on a formulation of tri-amine blend, which consists of 2-amino-2-methyl-1-propanol (AMP), piperazine (PZ), and MEA. A mixture design based on the Design-Expert software was applied to design the blends with various weight ratios of each amine. With total amine concentrations of 20%wt., 30%wt., and 40%wt., twenty-one aqueous solutions of AMP-PZ-MEA were proposed. Density and viscosity of the blends were measured by Stabinger viscometer SVM 3001 (Anton Paar, Austria) at 293–363 K. It was found that density of AMP-PZ-MEA was in a same range with that of benchmark 30%wt. MEA. At 303 K, 5%wt. AMP:17.5%wt. PZ:17.5%wt. MEA had the highest density of 1.0166 g/cm<sup>3</sup>, which is slightly greater than that of 30%wt. MEA (1.0085 g/cm<sup>3</sup>). On the other hand, viscosity of AMP-PZ-MEA was much larger than that of 30%wt. MEA. At 303 K, 5%wt. AMP:30%wt. PZ:5%wt. MEA showed the largest value of 6.9078 mPa.s, which is approximately four-time higher than viscosity of 30%wt. MEA (1.7186 mPa.s). At CO<sub>2</sub> concentration of 12%v/v. and 313 K, a promising 5%wt. AMP:30%wt. PZ:5%wt. MEA had absorption capacity of 0.841 mol CO<sub>2</sub>/mol amine, which is 67.5% greater than that of 30%wt. MEA.

**Keywords:** CO<sub>2</sub> capture; capacity; amine; density; viscosity

### 1. Introduction

CO<sub>2</sub> is the most released greenhouse gas into the atmosphere when compared to other greenhouse gases. The emission of CO<sub>2</sub> in large amounts directly contributes to the increase in atmospheric temperature and leads to global warming [1]. The CO<sub>2</sub> capture technology by absorption with amine solvents is widely used because of its high efficiency. Moreover, amine solvents are easily obtainable and can be regenerated [2]. The commonly used amine solvent in the industry is MEA due to its high reaction kinetics. However, it has limitations, such as low CO<sub>2</sub> absorption capacity and high solvent regeneration [3]. Using a blended solvent could enhance the performance of MEA. From the study, it is found that AMP has high CO<sub>2</sub> absorption capacity and low solvent regeneration, while PZ can react quickly with CO<sub>2</sub>. Therefore, combining AMP and PZ with MEA aims to improve the limitations of MEA. Nevertheless, AMP and PZ precipitate at high concentration [4]. This research investigates the behavior of the blended solvent AMP-PZ-MEA in terms of precipitation behavior, density,



viscosity, and CO<sub>2</sub> absorption capacity to find suitable blending ratios for developing a high-performance solvent. Moreover, the characteristics of the high-performance solvent are density and viscosity in acceptable region, high absorption capacity, high reaction kinetic, low solvent regeneration, and high mass transfer coefficient.

## 2. Material and methods

### 2.1 Chemicals

AMP ( $\geq 98\%$ ) and MEA (98%) were purchased from Merk, Germany. PZ (98%) was obtained by Sigma-Aldrich, Switzerland. Kemaus, Australia supplied 1 M hydrochloric acid (HCl) standard solution. CO<sub>2</sub> (99.5%) and Nitrogen (N<sub>2</sub>, 99.5%) were obtained by Thai-Japan Gas Co., Ltd.

### 2.2 Operating conditions

The Design–Expert software was applied to design the blends with various weight ratios of each amine. With total amine concentrations of 20%wt., 30%wt., and 40%wt., twenty–one aqueous solutions of AMP–PZ–MEA were proposed. Density and viscosity were measured over 293–343 K. CO<sub>2</sub> absorption capacity was operated at CO<sub>2</sub> concentration of 12%v/v. (CO<sub>2</sub> partial pressure 12 kPa) and temperature at 313 K [4].

### 2.3 Density and viscosity

Density and viscosity of AMP–PZ–MEA were measured by Stabinger viscometer SVM 3001 (Anton Paar, Austria) at temperature range of 293–343 K. It was validated by pure MEA over 293–343 K. The density and viscosity of pure MEA in accordance with the literature data with average absolute deviation percentage (%AAD) of 0.35% and 2.40%, respectively [5].

### 2.4 CO<sub>2</sub> absorption capacity

The CO<sub>2</sub> absorption capacity was measured in term of an equilibrium CO<sub>2</sub> loading (mol CO<sub>2</sub>/mol amine). The result was reported that CO<sub>2</sub> absorption capacity (mol CO<sub>2</sub>/L-solution). 25 mL of AMP–PZ–MEA was loaded into an absorption reactor, which is regulated temperature by water bath (WD11, Hanyang Scientific Equipment CO., Ltd, Korea). In this study, CO<sub>2</sub> concentration is 12%v/v which was a flue gas stream from fossil fired energy production. CO<sub>2</sub> and N<sub>2</sub> gas stream were mixed and fed into blended solvent as modulated by CO<sub>2</sub> analyzer (SprintIR-6 100%, CO<sub>2</sub> METER, Canada). Then, CO<sub>2</sub> had reacted with amine AMP–PZ–MEA until equilibrium. The amine sample with 1 mL was taken to define CO<sub>2</sub> loading by titration with 1 M HCl standard solution using Chittick apparatus [6]. This process was sampled every 30 minutes until equilibrium CO<sub>2</sub> loading. The CO<sub>2</sub> absorption capacity was validated by 30%wt. MEA at 313 K. The results of this validation comply with the literature with %AAD of 1.76% [7].

### 3. Results and discussion

#### 3.1 Density

The density of AMP–PZ–MEA at total amine concentrations of 20%wt., 30%wt., and 40%wt. over temperature range 293–343 K were plotted in Figs. 1(a), 1(b), and 1(c), respectively. The results of three total amine concentrations showed that the temperature increased as the density decreased. The raising of temperature affects to liquid molecules have higher kinetics energy, volume of liquid increased [6].

For 20%wt., 30%wt., and 40%wt. total amine concentration of AMP–PZ–MEA, the results indicated that the ratios of 5/10/5 (20%wt.), 5/20/5 (30%wt.), and 5/30/5 (40%wt.) had the highest density of three total amine concentration. According to the theoretical background, PZ possessed density greater than AMP, water, and MEA, respectively [8]. Consequently, density elevated as PZ concentration increased. Furthermore, as the total amine concentration increased, the amount of water in the solvent decreased, resulting in density increased. Therefore, 5/30/5 of total amine concentration 40%wt. has the highest density because it has the highest total amine concentration and PZ concentration. The density of AMP–PZ–MEA at total amine concentrations of 20%wt. (0.9790–1.0094 g/cm<sup>3</sup>), 30%wt. (0.9751–1.0173 g/cm<sup>3</sup>), and 40%wt. (0.9727–1.0280 g/cm<sup>3</sup>). had slightly lower than 20%wt. MEA (0.9815–1.0073 g/cm<sup>3</sup>), 30%wt. MEA (0.9862–1.0166 g/cm<sup>3</sup>), and 40%wt. MEA (0.9889–1.0184 g/cm<sup>3</sup>), respectively.

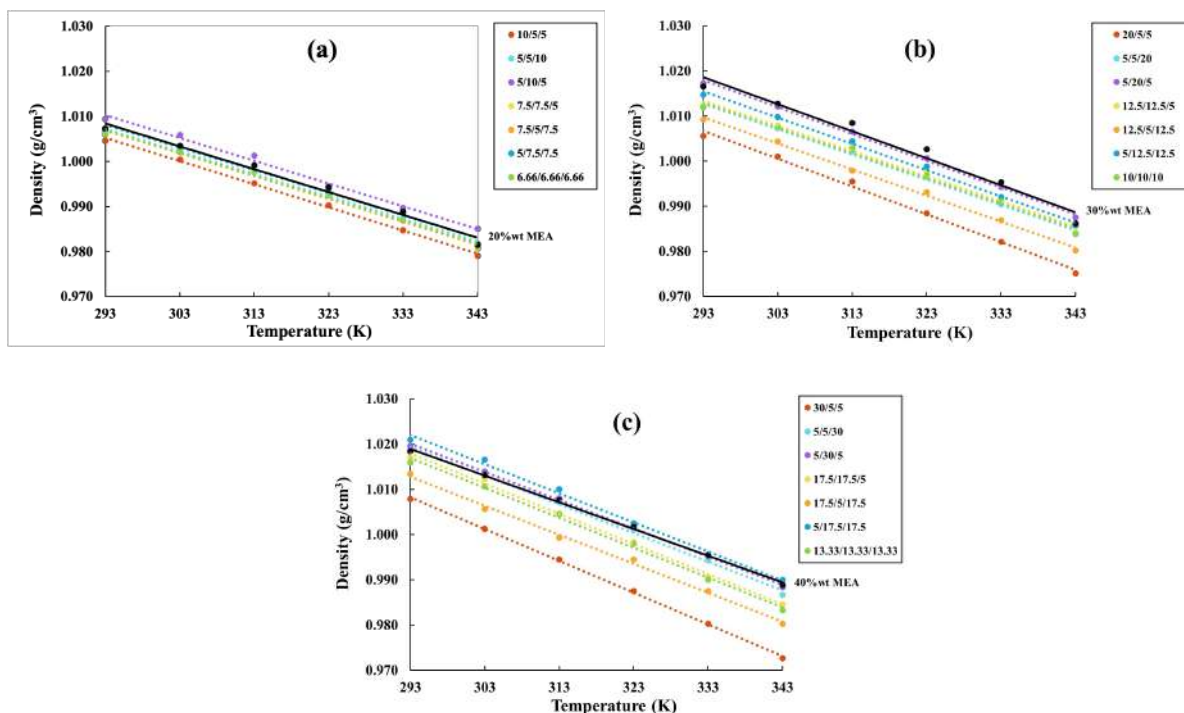


Fig. 1. Density of AMP–PZ–MEA solvents over temperature range 293–343 K and total amine concentration of (a) 20%wt., (b) 30%wt., and (c) 40%wt. compared with 20%wt., 30%wt., and 40%wt. MEA, respectively.

### 3.2 Viscosity

The viscosity of AMP–PZ–MEA was measured over temperature range 293–343 K. The total amine concentration of 20%wt., 30%wt., and 40%wt. showed in Figs. 2(a), 2(b), and 2(c), respectively. The experimental results of all total amine concentration indicated that viscosity decreased as temperature increased. As, the increasing temperature affects the liquid molecules having higher thermal energy, leading to faster movement of molecules. This results in a decrease viscosity.

The viscosity of AMP–PZ–MEA at total amine concentrations of 20%wt. (0.7371–2.8901 mPa.s), 30%wt. (0.9781–5.1524 mPa.s), and 40%wt. (1.2580–11.3253 mPa.s). had slightly higher than 20%wt. MEA (0.6054–1.8955 mPa.s), 30%wt. MEA (0.9157–3.0491 mPa.s), and 40%wt. MEA (1.0595–4.2059 mPa.s), respectively. Furthermore, as the total amine concentration increased, the amount of water decreased, resulting in an increased viscosity. Therefore, the 5/30/5 has the highest PZ concentration and total amine concentration, illustrated the highest viscosity. The viscosity of 0-20 mPa.s is a good range [9], and the viscosity of all solvent formulations within this range.

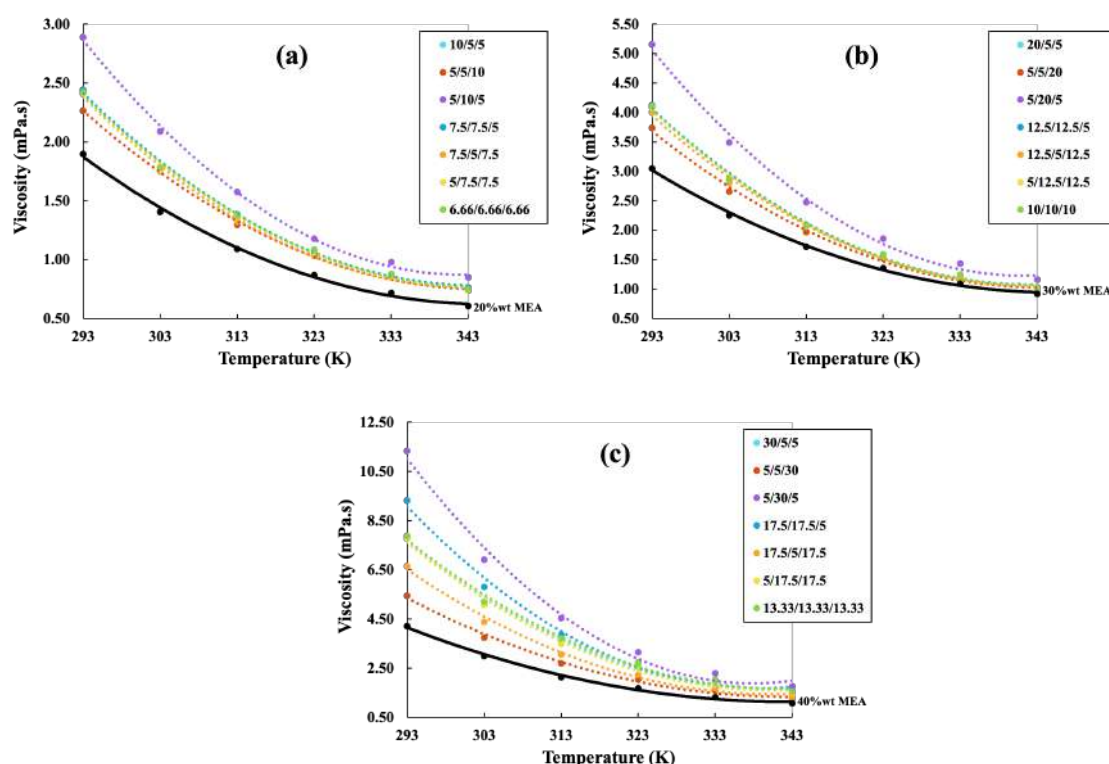


Fig. 2. Viscosity of AMP–PZ–MEA solvents over temperature range 293–343 K and total amine concentration of (a) 20%wt., (b) 30%wt., and (c) 40%wt. compared with 20%wt., 30%wt., and 40%wt. MEA, respectively.

### 3.3 CO<sub>2</sub> absorption capacity

CO<sub>2</sub> absorption capacity of AMP–PZ–MEA blended solvent with total amine concentrations 20%wt., 30%wt., and 40%wt. and benchmark MEA were measured in term of equilibrium CO<sub>2</sub> loading (mol CO<sub>2</sub>/mol amine) at temperature 313 K and CO<sub>2</sub> partial pressure 12 kPa. In the part of result reporting, they were reported in mol CO<sub>2</sub>/L-solution.

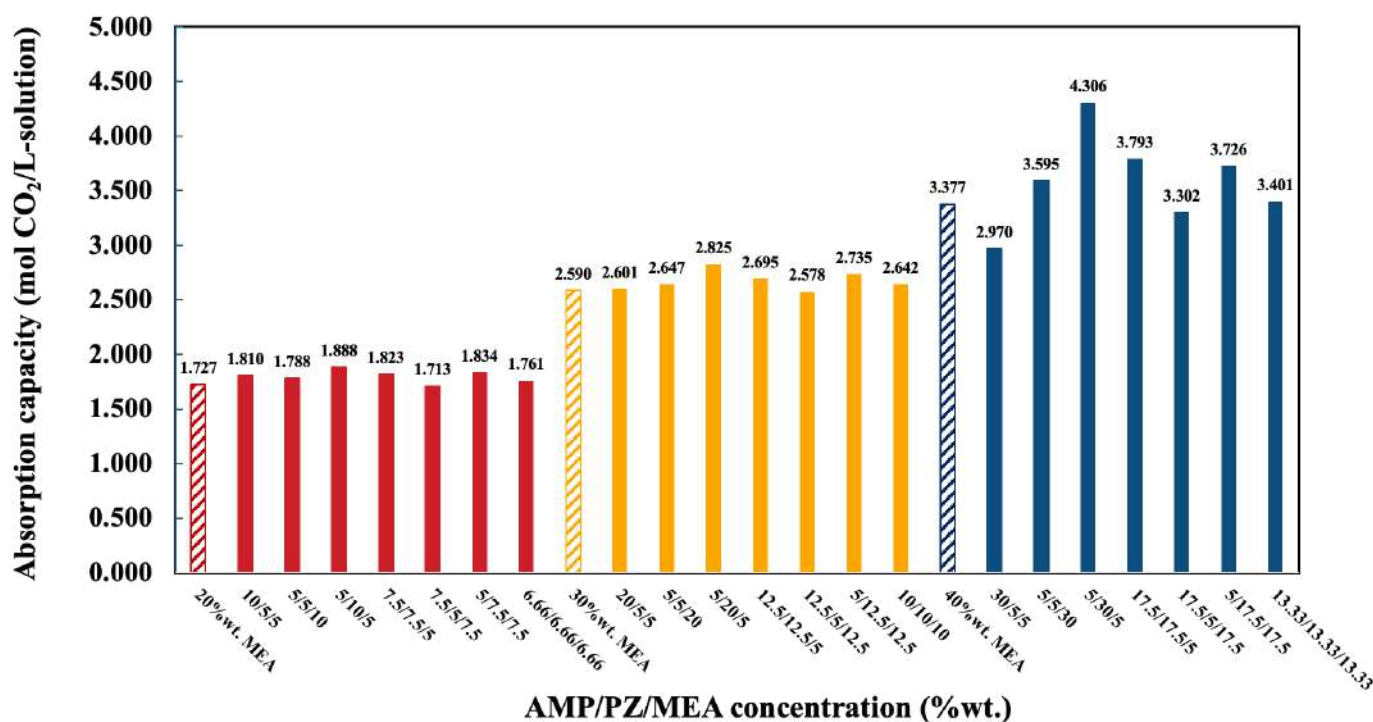


Fig. 3. CO<sub>2</sub> absorption capacity of AMP–PZ–MEA solvent at 313 K and CO<sub>2</sub> partial pressure 12 kPa.

The CO<sub>2</sub> absorption capacity of AMP–PZ–MEA at total amine concentration 20%wt., 30%wt., and 40%wt. and 20%wt., 30%wt., and 40%wt. MEA were showed in Fig. 3. For 20%wt., 30%wt., and 40%wt. total amine concentration of AMP–PZ–MEA, the result showed that 5/10/5 (20%wt.), 5/20/5 (30%wt.), and 5/30/5 (40%wt.) had the highest CO<sub>2</sub> absorption capacity, respectively. Due to, they had the highest PZ concentration when compared with another formulars in the similar group. PZ is the cyclic amine which has two amino groups, so it can react with CO<sub>2</sub> better than AMP and MEA. However, precipitation of PZ at high concentration should be careful. Additionally, increasing of total amine concentration, the CO<sub>2</sub> absorption capacity was found increase. Therefore, the 5/30/5 (40%wt.) had the highest CO<sub>2</sub> absorption capacity of 4.306 mol CO<sub>2</sub>/L-solution.

By comparison of AMP–PZ–MEA at total amine concentration 5/10/5 (20%wt.), 5/20/5 (30%wt.), and 5/30/5 (40%wt.) with 20%wt., 30%wt., and 40%wt. MEA found that 5/10/5

(20%wt.), 5/20/5 (30%wt.), and 5/30/5 (40%wt.) greater than the benchmark of 9.32%, 9.07% and 27.51%, respectively.

For 5/30/5, it has the highest absorption capacity, which is interesting. However, caution should be exercised as this ratio exhibits the highest viscosity when compared to other formulas in the research. Excessive viscosity may lead to increased difficulty for CO<sub>2</sub> to diffuse through the solvent. From this research, the density, viscosity, and absorption capacity of AMP–PZ–MEA are basic parameters used to indicate the performance of the solvent, further investigation other parameters such as mass transfer coefficient, heat regeneration, and corrosion are necessary to develop an optimal and suitable solvent.

#### 4. Conclusion

The study investigated the density, viscosity, and absorption capacity of AMP–PZ–MEA as fundamental parameters indicating solvent performance. The results showed that density decreased with increasing temperature due to higher kinetic energy and expanded liquid volume. The ratios of 5/10/5, 5/20/5, and 5/30/5 exhibited the highest density, attributed to PZ greater density compared to AMP, water, and MEA, respectively. Moreover, as total amine concentration increased, water content decreased, resulting in higher density. Viscosity decreased with rising temperature, but increased with higher total amine concentration, affecting CO<sub>2</sub> diffusion through the solvent. The viscosity of AMP–PZ–MEA within an acceptable range for solvent suitability. The highest CO<sub>2</sub> absorption capacity is 5/30/5 of 40%wt. total amine concentration. Due to, it has a highest total amine concentration and PZ concentration. Additionally, AMP–PZ–MEA of 5/30/5 (40%wt.) have a CO<sub>2</sub> absorption capacity greater than 40%wt. MEA benchmark up to 27.51%.

## References

- [1] Khan, S., Hailegiorgis, S., Man, Z., Garg, S., Shariff, A., Farrukh S., Ayoub, M., and Ghaedi, H. (2018). High-pressure absorption study of CO<sub>2</sub> in aqueous N-methyldiethanolamine (MDEA) and MDEA-piperazine (PZ)-1-butyl-3-methylimidazolium trifluoromethanesulfonate [bmim][OTf] hybrid solvents. *Journal of Molecular Liquids*, 249, 1236–1244
- [2] Aghel, B., Janati, S., Wongwises, S., Shadloo, M. (2022). Review on CO<sub>2</sub> capture by blended amine solutions. *International Journal of Greenhouse Gas Control*, 119, 103715.
- [3] Lui, Y., Fan, W., Wang, K., and Wang, J. (2016). Studies of CO<sub>2</sub> absorption/regeneration performances of novel aqueous monoethanolamine (MEA)-based solutions. *Journal of Cleaner Production*, 112, 4012–4021.
- [4] Nwaoha C., Saiwan, C., Tontiwachwuthikul, P., Supap, T., Rongwong, W., Idem, R., AL-Marri, A., and Benamor, A. (2016). Carbon dioxide (CO<sub>2</sub>) capture: Absorption-desorption capabilities of 2-amino-2-methyl-1-propanol (AMP), piperazine (PZ) and monoethanolamine (MEA) tri-solvent blends. *Journal of Natural Gas Science and Engineering*, 33, 742–750.
- [5] Li, H., and Lei, Y. (1994). Densities and Viscosities of solutions of Monoethanolamine + N-Methyldiethanolamine + Water and Monoethanolamine + 2-amino-2-methyl-1-propanol + Water. *Journal of Chemical Engineering Data*, 39, 444–447.
- [6] Apaiyakul, R., Nimmanterdwong, P., Kanchanakungvalkul, T., Puapan, P., Gao, H., Liang, Z., Tontiwachwuthikul, P., and Sema, T. (2022). Precipitation behavior, density, viscosity, and CO<sub>2</sub> absorption capacity of highly concentrated ternary AMP-PZ-MEA solvents. *International Journal of Greenhouse Gas Control*, 120, 103775.
- [7] Shen, K., and Le, M. (1992). Solubility of Carbon Dioxide in Aqueous Mixtures of Monoethanolamine with Methyldiethanolamine. *Journal of Chemical Engineering Data*, 37, 96–100.
- [8] Apaiyakul, R., Nimmanterdwong, P., Kanchanakungvalkul, T., Puapan, P., Ngamprasertsith, S., Liu, H., Gao, H., Liang, Z., Tontiwachwuthikul, P., and Sema, T. (2024). Analysis and insights of the second-generation ternary AMP-PZ-MEA solvents for post-combustion carbon capture: Absorption-regeneration performance. *International Journal of Greenhouse Gas Control*, 132, 104038
- [9] Yang, C., Li, T., Tantikhajorngosol, T., Sema, T., Xiao, M., and Tontiwachwuthikul, P. (2023). Evaluation of novel aqueous piperazine-based physical-chemical solutions as biphasic solvents for CO<sub>2</sub> capture: Initial absorption rate, equilibrium solubility, phase separation and desorption rate. *Chemical Engineering Science*, 277, 118852.

## Potential of Advanced Tri-amine blends of 2-amino-2-methyl-1-propanol (AMP), methyldiethanolamine (MDEA) and piperazine (PZ), for Post-Combustion Carbon Capture

Sopita Unprasert<sup>1</sup>, Wadeya Pornsawasklin<sup>1</sup>, Rattanaporn Apaiyakul<sup>1</sup>,  
Teerawat Sema<sup>1,\*</sup>

<sup>1</sup>Department of Chemical Technology, Faculty of Science, Chulalongkorn University, Pathumwan, Bangkok, 10330, Thailand

E-mail: teerawat.sc@chula.ac.th

### Abstract

Post-combustion carbon capture technology, which uses an absorption process by amine solvent, has widely been implemented to capture CO<sub>2</sub> for decades. This study measured the physical properties and absorption capacity of CO<sub>2</sub> in mixed amine solution of 2-amino-2-methyl-1-propanol (AMP), piperazine (PZ), and methyldiethanolamine (MDEA). Since AMP and PZ precipitate at high amine concentration, the mixed solvents were preliminary screened based on a visualized solid sediment formation. The possible total amine concentration range of 20-40%wt., which can maintain a clear solution, was obtained. A mixture design then applied to systematically formulate the mixed amine solution. As a result, 21 aqueous solutions at different weight ratios of AMP, PZ, and MDEA were suggested. Physical properties (i.e., density and viscosity) of the mixtures are measured by an Anton Paar SVM3001 at temperatures of 293-343 K. The results showed that density and viscosity of the AMP-PZ-MDEA solvent increased with concentration of PZ increased but decreased as concentration of MDEA increased. Additionally, both measured densities and viscosities dropped as temperature increased. Absorption capacity of the mixed solvent at CO<sub>2</sub> partial pressure of 12.1 kPa and 313 K was also experimentally determined. It was observed that CO<sub>2</sub> absorption capacity of AMP-PZ-MDEA can be improved by increasing PZ concentration. Interestingly, 5%wt. AMP : 30%wt. PZ : 5%wt. MDEA (40%wt. total amine concentration) showed the highest CO<sub>2</sub> absorption capacity (0.728 mol CO<sub>2</sub>/mol amine), which is much higher than that of 30%wt. monoethanolamine or MEA (0.518 mol CO<sub>2</sub>/mol amine).

**Keywords:** Carbon capture; amine; absorption; advanced solvent

## 1. Introduction


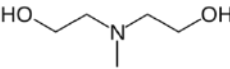
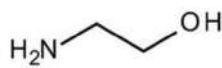
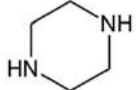
Due to the negative impacts of global warming, controlling carbon dioxide (CO<sub>2</sub>) emission from various industries is imperative. An effective technology widely used for this purpose is amine absorption, specifically utilizing amine solutions [1]. Different types of amines, such as AMP (2-amino-2-methyl-1-propanol) and PZ (piperazine) [2], exhibit varying efficiencies in capturing and reusing CO<sub>2</sub>. AMP, while having high CO<sub>2</sub> absorption capacity, utilizes low heat for regeneration, but faces limitations in reaction kinetics. To address these limitations, PZ is often mixed with AMP due to its superior reaction kinetics with CO<sub>2</sub>. However, both AMP and PZ tend to solidify at high concentration. This research develops a tri-solvent solution, combining AMP, PZ, and MDEA (methyldiethanolamine), with an elevation of the overall amine concentration. This enhances the overall CO<sub>2</sub> capture efficiency. Additionally, MDEA [3], known for low heat requirements in regeneration, aids in reducing the overall heat load. The study evaluates the density, viscosity, and absorption capacity of the AMP-PZ-MDEA tri-solvent and compares it with the traditional MEA (monoethanolamine) solvent to assess its potential for improved CO<sub>2</sub> capture performance.

## 2. Materials and methods

### 2.1 Materials

AMP (98%) and MEA (99%) were purchased from Merck, Germany. PZ (99%) was obtained from Sigma-Aldrich, Switzerland. MDEA was supplied from Hebei Gualang Biotechnology Co., Ltd, China. Hydrochloric acid, HCl (1.00 M) was supplied from Kemaus, Australia. CO<sub>2</sub> (99.5%) and Nitrogen (N<sub>2</sub>, 99.5%) were both delivered by Thai-Japan Gas Co., Ltd, Thailand. All materials were use as received without further purification. The chemical structure of amines used in this work are presented in Table 1.

Table 1. Chemical structure of amines used in the present work [4].

Amine	Molecular weight (g/mol)	Chemical structure	Amine classification
AMP	89.14		Sterically hindered primary amine
MDEA	119.16		Tertiary amine
MEA	61.08		Primary amine
PZ	86.14		Cyclical secondary diamine



## 2.2 Methods

### 2.2.1 Density and viscosity

Density and kinematic viscosity measurements were carried out using an Anton Paar SVM 3001 over temperature ranging from 293 K to 343 K and at CO<sub>2</sub> unloading condition of various AMP-PZ-MDEA weight percentage ratios (i.e., 10/5/5, 5/5/10, 5/10/5, 7.5/5/7.5, 5/7.5/7.5, 7.5/7.5/5, 6.66/6.66/6.66, 10/10/10, 20/5/5, 5/5/20, 5/20/5, 12.5/5/12.5, 5/12.5/12.5, 12.5/12.5/5, 30/5/5, 5/5/30, 5/30/5, 17.5/5/17.5, 5/17.5/17.5, 17.5/17.5/5, and 13/13/13). Be informed that these concentration ratios were obtained from a mixture design (Design Expert software) with following constrains: total minimum amine solvent 20%wt., total maximum amine solvent 40%wt., and minimum concentration of each amine 5%wt. Before and after each measurement, the equipment was cleaned and calibrated by 30%wt. MEA. For an unloaded 30%wt. MEA solution, 1.0085 g/cm<sup>3</sup> and 1.7186 mPa.s were obtained with 0.34% average absolute deviation percentage (%AAD) for density and 5.56%AAD for viscosity [5].

### 2.2.2 CO<sub>2</sub> absorption capacity

In the CO<sub>2</sub> absorption capacity experimental, 25 mL of amine blended solvent was introduced into the absorption reactor, which was immersed in a temperature-controlled water bath at 313 K and atmospheric pressure. A mixed gas stream of CO<sub>2</sub> and N<sub>2</sub> at the partial pressure of CO<sub>2</sub> 12.1 kPa was bubbled into the reactor. After CO<sub>2</sub> reacted with amine solvents for 6-8 hr, 1 mL of amine sample was taken from the reactor for measuring the CO<sub>2</sub> loading (which is a titration with 1.00 M of HCl standard solution using Chittick apparatus to endpoint of methyl orange) [6]. This procedure was taken every 30 minutes until the measured CO<sub>2</sub> loading (in a unit of mol CO<sub>2</sub>/mol amine) was constant or reached equilibrium. The experiment was validated by 30%wt. MEA. The obtained result agrees with the literature with 1.76%AAD [7].

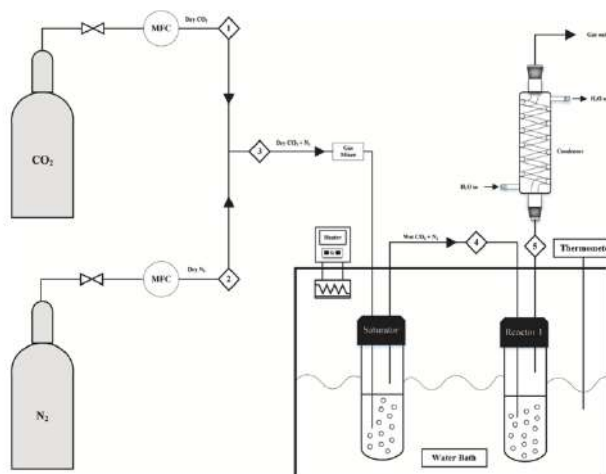


Fig. 1. Process flow diagram of CO<sub>2</sub> absorption experiment.[8]

### 3. Result and discussion

#### 3.1 Density

Density of tri-solvents was measured range of temperature is 293-343 K at different concentration ratios (i.e., 10/5/5, 5/5/10, 5/10/5, 7.5/5/7.5, 5/7.5/7.5, 7.5/7.5/5, 6.66/6.66/6.66, 10/10/10, 20/5/5, 5/5/20, 5/20/5, 12.5/5/12.5, 5/12.5/12.5, 12.5/12.5/5, 30/5/5, 5/5/30, 5/30/5, 17.5/5/17.5, 5/17.5/17.5, 17.5/17.5/5, and 13/13/13 AMP-PZ-MDEA). The results are shown in Figs. 1(a), 1(b), and 1(c). It was found that the density decreased as the temperature increased over the studied temperature range. Due to rising temperature, the volume of liquid expands and occupies more space [9].

Figures 1(a), 1(b) and 1(c), shows that as PZ concentration increase, the density increases accordingly. This is due to PZ has higher density than MDEA, water and AMP respectively. Therefore, the 5/30/5 for 40%wt. has the highest density because it has the highest PZ concentration. In addition, the total amine concentration increase, water in solvent decrease so the density increase. Furthermore, when comparing the density of blended solvent at various concentrations with the benchmark MEA (20%wt. MEA, 30%wt. MEA, and 40%wt. MEA), it was found that the density is similar.

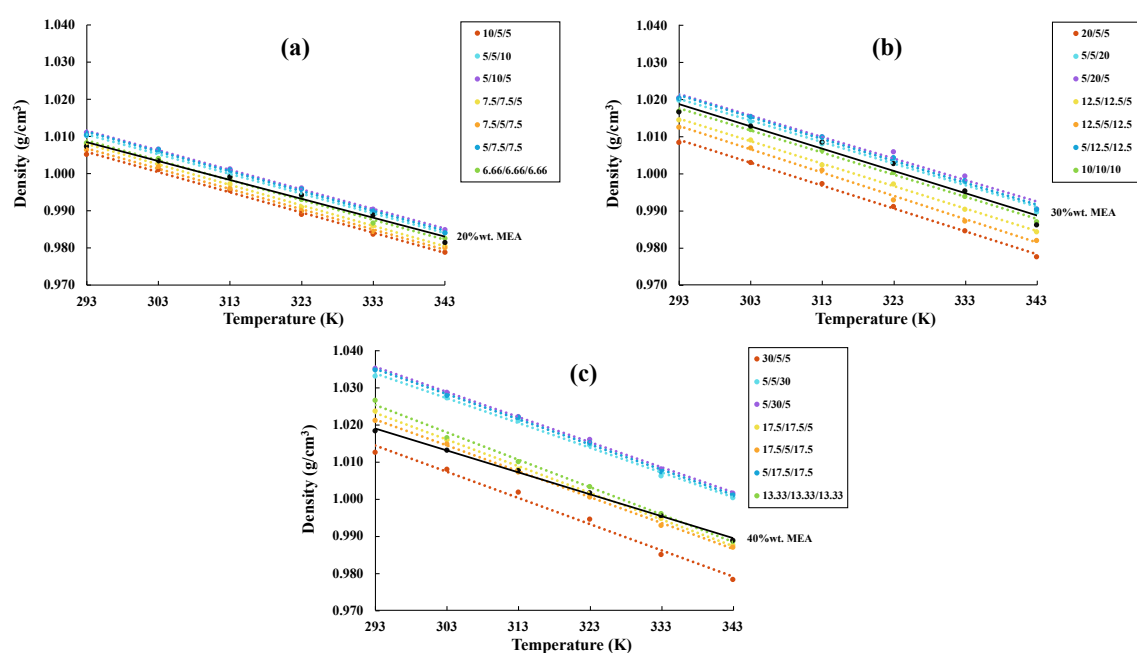


Fig. 2. Density of AMP-PZ-MDEA at various temperatures and total amine concentrations (a) 20%wt., (b) 30%wt., and (c) 40%wt..

#### 3.2 Viscosity

Viscosity of tri-solvent was measured range of temperature is 293-343 K in different concentrations ratios (i.e., 10/5/5, 5/5/10, 5/10/5, 7.5/5/7.5, 5/7.5/7.5, 7.5/7.5/5, 6.66/6.66/6.66, 10/10/10, 20/5/5, 5/5/20, 5/20/5, 12.5/5/12.5, 5/12.5/12.5, 12.5/12.5/5, 30/5/5, 5/5/30, 5/30/5, 17.5/5/17.5, 5/17.5/17.5, 17.5/17.5/5, and 13/13/13 AMP-PZ-MDEA). The results are shown in Figs. 2(a), 2(b), and 2(c). It was found that viscosity decrease as temperature increase.

Since, temperature elevation affect the liquid has more thermal energy therefore liquid easier to flow [10].

Figures 2(a), 2(b), and 2(c), show viscosity increases as PZ concentration increases. Due to, PZ originally is a solid has higher than AMP and MDEA, respectively. The results indicated that 5/10/5, 5/20/5, and 5/30/5 AMP-PZ-MDEA are highest viscosity in the similar total concentration. Furthermore, 40%wt. has the highest viscosity, followed by 30%wt. and 20%wt. respectively.

Additionally, the viscosity of AMP-PZ-MDEA at total amine concentration 20%wt., 30%wt., and 40%wt. were compared with 20%wt., 30%wt., and 40%wt. the conventional MEA found that the viscosity of AMP-PZ-MDEA is higher than the conventional MEA. According to theory, the viscosity of AMP, MDEA, and PZ have greater than MEA. Viscosity is important physical property affecting the liquid flow inside the packed tower [11] and CO<sub>2</sub> diffusion. In case of too high viscosity affects the liquid flow slow down and CO<sub>2</sub> diffusion through the solvent is more difficult. Then, reaction between solvent and CO<sub>2</sub> will be decreased. The viscosity of 0-10 mPa.s is a great region and 10-20 mPa.s is a good region [12]. Even though, the viscosity of AMP-PZ-MDEA is higher than the conventional MEA but it still is in a 0-10 mPa.s (great region) except 5/30/5 AMP-PZ-MDEA is in a 10-20 mPa.s (good region). Consequently, the blended solvent can be utilized in the absorption process.

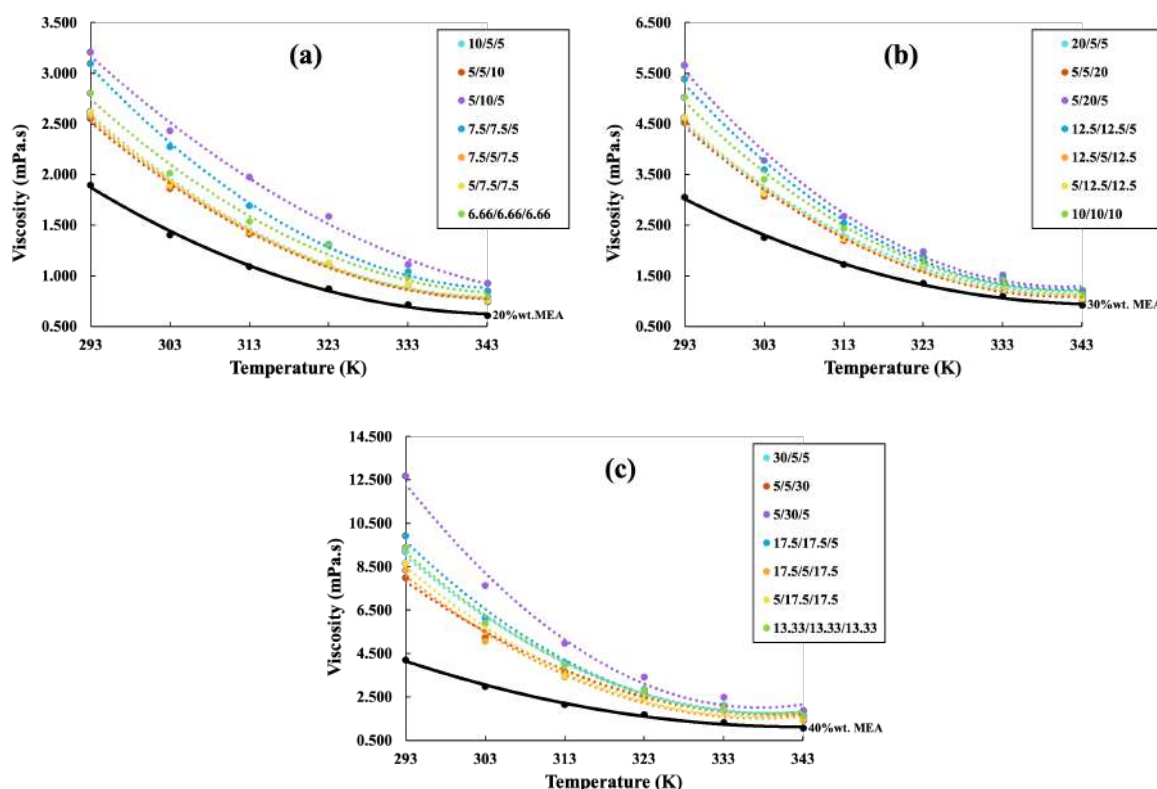


Fig. 3. Viscosity of AMP-PZ-MDEA at various temperatures and total amine concentrations (a) 20%wt., (b) 30%wt., and (c) 40%wt..

### 3.3 Absorption capacity

The equilibrium CO<sub>2</sub> loading or absorption capacity, commonly used in the form of mol CO<sub>2</sub>/mol amine. The absorption capacity of AMP-PZ-MDEA at 313 K and CO<sub>2</sub> partial pressure 12.1 kPa at atmosphere pressure. The absorption capacity of AMP-PZ-MDEA is presented in Fig. 3. The results showed that the absorption capacity of 20%wt., 30%wt., and 40%wt. AMP-PZ-MDEA are higher than that of conventional 20%wt., 30%wt., and 40%wt. MEA. At 10/5/5, 5/5/10, and 5/10/5 AMP-PZ-MDEA with the similar total amine concentration (20%wt.), Additionally, PZ concentration increases as absorption capacity increases because PZ has two amino group. It able to absorb more CO<sub>2</sub> [13]. Therefore, the absorption capacity of 5/10/5 is higher than 5/5/10 and 10/5/5 AMP-PZ-MDEA, respectively. Due to, concentration of PZ is the highest.

From Fig. 3., the highest absorption capacity of 20%wt. is 5/7.5/7.5 and 7.5/7.5/5 AMP-PZ-MDEA (0.73 mol CO<sub>2</sub>/mol amine) which has higher absorption capacity than that of 20%wt. MEA (0.52 mol CO<sub>2</sub>/mol amine) at 40.38%. For 30%wt., 5/20/5 and 5/12.5/12.5 AMP-PZ-MDEA (0.72 mol CO<sub>2</sub>/mol amine) have higher absorption capacity than 30%wt. MEA (0.52 mol CO<sub>2</sub>/mol amine) at 38.46%. Total amine concentration 40%wt., which 5/30/5 and 17.5/17.5/5 AMP-PZ-MDEA (0.73 mol CO<sub>2</sub>/mol amine), has higher than 40%wt. MEA (0.51 mol CO<sub>2</sub>/mol amine) at 43.14%. Consequently, these formulars are interesting because they have high absorption capacity. However, density, viscosity, and absorption capacity are preliminary parameter used to evaluate the efficiency of solvent. Further studies investigate other parameters, such as mass transfer coefficient, regeneration heat duty, and corrosion for get the suitable formular in the absorption process.

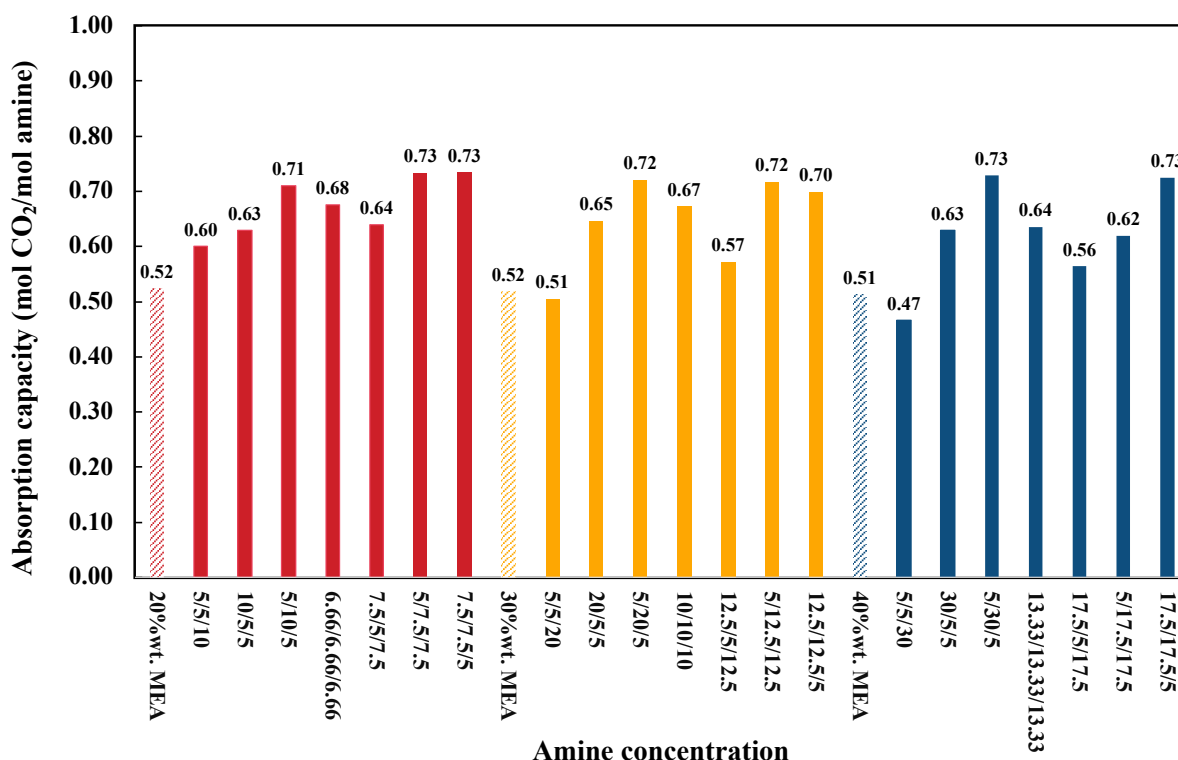


Fig. 4. CO<sub>2</sub> absorption capacity of AMP-PZ-MDEA solvent at 313 K and CO<sub>2</sub> partial pressure 12 kPa.

#### 4. Conclusion

Parameters of this experiment are physical properties and absorption capacity of AMP-PZ-MDEA tri-solvent. The density decreases as temperature increase because the raising of temperature affects the volume expansion. Additionally, PZ concentration increases as density increases. Therefore, the highest density is 5:30:5 AMP-PZ-MDEA (40%wt.). Due to, it has high concentration of PZ. Moreover, the viscosity decreased as temperature increased but elevated as PZ concentration increased. The increasing of viscosity lead to diffusion through the solvent of CO<sub>2</sub> is more difficult. However, all of formulas have the viscosity in great region except 5/30/5 AMP-PZ-MDEA is in a good region. The absorption capacity of AMP-PZ-MDEA tri-solvent is 9.6 - 43.14% higher than that of the conventional MEA and 5/7.5/7.5, 7.5/7.5/5 (for 20%wt.), 5/20/5, 5/12.5/12.5 (for 30%wt.), 5/30/5, and 17.5/17.5/5 (for 40%wt.) AMP-PZ-MDEA have the highest absorption capacity.

#### References

- [1] Cucciaa L., Dugay J., Bontemps D., Louis-Louisy M., Vial J. (2012). Analytical method for the monitoring of post-combustion CO<sub>2</sub> capture process using amine solvents: A review. *International Journal of Greenhouse Gas Control*, 72, 138-151.
- [2] Dumée L., Scholes C., Stevens G., Kentish S. Purification of aqueous amine solvents used in post combustion CO<sub>2</sub> capture. (2018). *International Journal of Greenhouse Gas Control*, 10, 443-455.
- [3] Khan A., Halder G., Saha A. (2007). Experimental investigation on efficient carbon dioxide capture using piperazine (PZ) activated aqueous methyldiethanolamine (MDEA) solution in a packed column. *International Journal of Greenhouse Gas Control*, 64, 163-173.
- [4] Zhang R., Zhang X., Yang Q., Yu H., Liang Z., Luo X. (2017). Analysis of the reduction of energy cost by using MEA-MDEA-PZ solvent for post-combustion carbon dioxide capture (PCC). *Applied Energy*, 205, 1002-1011.
- [5] Hartono A., Mba O. E., Svendsen H. (2014). Physical properties of partially CO<sub>2</sub> loading aqueous monoethanolamine (MEA). *Journal of Chemical Engineering*, 59, 1808-1816.
- [6] Nwaoha C., Saiwan C., Tontiwachwuthikul P., Supap T., Rongwong W., Idem R., Al-marri M., Benamor A. (2016). Carbon dioxide (CO<sub>2</sub>) capture: absorption-desorption capabilities of 2-amino-2-methyl-1-propanol (AMP), piperazine (PZ) and monoethanolamine (MEA) tri-solvent blends. *Journal of Natural Gas Science and Engineering*, 33, 742-750.
- [7] Shen K. P., Li M. (1992). Solubility of carbon dioxide in aqueous mixtures of monoethanolamine with methyldiethanolamine. *Journal of Chemical Engineering*, 37, 96-100.
- [8] Apaiyakul R., Chalermssinsuwan B., Ngamprasertsith S., Tontiwachwuthikul P., Gao H., Liang Z., Sema T. (2024). Comprehensive investigation on carbon dioxide absorption capacity, cyclic capacity, and regeneration heat duty of blended 2-amino-2-methyl-1-propanol (AMP) and N-methyl-4-piperidinol (MPDL) solvent, *International Journal of Greenhouse Gas Control*, 131, 104019.

- [9] Apaiyakul R., Nimmanterdwong P., Kanchanakungvalkul T., Puapan P., Gao H., Liang Z., Tontiwachwuthikul P., Sema T. (2022). Precipitation behavior, density, viscosity, and CO<sub>2</sub> absorption capacity of highly concentrated ternary AMP-PZ-MEA solvents, *International Journal of Greenhouse Gas Control*, 120, 103775.
- [10] Apaiyakul R., Ranong P., Kiattinirachara T., Posoknistakul P., Pakchotanon P., Jiraratananon R., Tontiwachwuthikul P., Sema T. (2021). Density, viscosity, physical CO<sub>2</sub> diffusivity, and CO<sub>2</sub> absorption capacity of novel blended N-methyl-4-piperidinol and piperazine solvent, *Energy Reports*, 7, 844-853.
- [11] Apaiyakul R., Nimmanterdwong P., Kanchanakungvalkul T., Puapan P., Ngamprasertsith S., Liu H., Gao H., Liang Z., Tontiwachwuthikul P., Sema T. (2024). Analysis and insights of the second-generation ternary AMP-PZ-MEA solvents for post-combustion carbon capture: Absorption-regeneration performance, *International Journal of Greenhouse Gas Control*, 132, 104038.
- [12] Yang C., Li T., Tantikhajongosol P., Sema T., Xiao M., Tontiwachwuthikul T. (2023). Evaluation of novel aqueous piperazine-based physical-chemical solutions as biphasic solvents for CO<sub>2</sub> capture: Initial absorption rate, equilibrium, solubility, phase separation and desorption rate, *Chemical Engineering Science*, 277, 118852.
- [13] Muchan P., Saiwan C., Narku-Tettet J., Idem J., Supap T., Tontiwachwuthikul P. (2017). Screening tests of aqueous alkanolamine solutions based on primary, secondary, and tertiary structure for blended aqueous amine solution selection in post combustion CO<sub>2</sub> capture. *Chemical Engineering Science*, 170, 574-582.

## Esterification of Oleic Acid with Glycerol using Solid Acid Catalysts

**La-onghip Yuwansri<sup>1</sup>, Kanokwan Ngaosuwana<sup>2</sup>, Charuphatthana Oatsawamongkhon<sup>1</sup>,  
Kittitara sridet<sup>1</sup>, Weerinda Mens<sup>1,\*</sup>, Rinlada Sirisangsawang<sup>1</sup>, Doonyapong  
Wongsawaeng<sup>3</sup>, Suttichai Assabumrungrat<sup>4,5</sup>**

<sup>1</sup> Department of Chemical and Materials Engineering, Faculty of Engineering, Rajamangala University of Technology Thanyaburi, Pathum Thani, 12110, Thailand

<sup>2</sup> Chemical Engineering Division, Department of Engineering, Rajamangala University of Technology Krungthep, Bangkok, 10120, Thailand

<sup>3</sup> Research Unit on Plasma Technology for High-Performance Materials Development, Department of Nuclear Engineering, Faculty of Engineering, Chulalongkorn University, Bangkok 10330, Thailand

<sup>4</sup> Center of Excellence on Catalysis and Catalytic Reaction Engineering, Department of Chemical Engineering, Faculty of Engineering, Chulalongkorn University, Bangkok, 10330, Thailand

<sup>5</sup> Bio-Circular-Green economy Technology & Engineering Center, BCGeTEC, Department of Chemical Engineering, Faculty of Engineering, Chulalongkorn University, Bangkok, 10330, Thailand

### Abstract

Esterification of oleic acid (OA) with glycerol to produce monoacylglycerols (MAG) for the food, cosmetic, and pharmaceutical industries was investigated using different solid acid catalysts. The catalysts were characterized by XRD, BET, and SEM-EDX. The effects of operating parameters including catalyst type ( $\gamma$ -Al<sub>2</sub>O<sub>3</sub>, ZSM5, ZnO/ $\gamma$ -Al<sub>2</sub>O<sub>3</sub>, and ZnO/ZSM5), reaction temperature, and reaction time were investigated. Reactions were conducted at glycerol-to-oleic acid molar ratio (GL/OA) of 4:1 and catalyst loading of 0.5 wt.% of the total reaction mixture in the range of 150–200 °C using a batch reactor. Samples were collected during the reaction period, and MAG, diacylglycerol (DAG), triacylglycerol (TAG), and OA concentrations were analyzed using HPLC. The results indicated that impregnation of ZnO on the supports ( $\gamma$ -Al<sub>2</sub>O<sub>3</sub> and ZSM5) providing higher oleic acid conversion. Among the catalysts tested, zinc oxide-supported ZSM5-zeolite (ZnO/ZSM5) gave the highest catalytic activity. 94.1% oleic acid conversion was obtained at the reaction temperature of 180 °C, catalyst loading of 0.5 wt.%, and reaction time of 2 h. In addition, increasing the reaction temperature significantly increased the DAG and TAG selectivity due the nature of consecutive reaction.

**Keywords:** Esterification; Oleic acid; Glycerol; Monoacylglycerols (MAG); Zinc oxide supported ZSM5.

## 1. Introduction

The increasing surplus of glycerol (GL), a byproduct resulting from the continuous growth of the biodiesel and oleochemical industries has led to extensive research and comprehensive investigations by transformation into the valuable products (Kong, Aroua, Daud, Cognet, & Pérès, 2016). Converting glycerol into the valuable products represents a promising opportunity for bio-circular societies. With its indispensable role as a critical raw material in the pharmaceutical and food sectors, GL plays a pivotal role in various applications within these industries. Monoacylglycerols (MAG), distinguished by their excellent surfactant properties, finds diverse applications as an emulsifier in the food, pharmaceutical, and cosmetic industries. The MAG synthesis can be achieved through various alternative methods, such as the glycerolysis of triglycerides using either enzyme or base catalysts (Holmberg, Lassen, & Stark, 1989; Kumoro, 2012), transesterification of methyl ester with glycerol (Ferretti, Soldano, Apesteguía, & Di Cosimo, 2010), and esterification of fatty acid with glycerol (Kan, Barrault, & Wu, 2001). However, the most widely employed method currently is the esterification of fatty acids with glycerol.

Homogeneous and heterogeneous acid catalysts have been demonstrated to enhance the esterification of fatty acids with glycerol (Jyoti, Keshav, Anandkumar, & Bhoi, 2018). For homogenous acid catalysts, such as sulfuric acid (Vitiello et al., 2021), *p*-toluenesulfonic acid, and 2-phenyl benzimidazole-5-sulfonic acid (Moliner, Ladero, Tamayo, & García-Ochoa, 2014) were used. However, it is difficult to separate the catalyst from products, and the liquid acid catalysts often cause reactor corrosion (Harmer & Sun, 2001). Therefore, heterogeneous acid catalysts offer non-corrosive characteristics, environmental friendliness, and fewer challenges in disposal. It can be more easily separated from products and can be tailored to deliver enhanced activity, selectivity, and prolonged catalyst lifetimes (Jothiramalingam & Wang, 2009). Numerous heterogeneous catalysts were applied for the esterification of glycerol with free fatty acids, such as zeolites (da Silva-Machado, Cardoso, Pérez-Pariente, & Sastre, 2000), layered double hydroxide (Hamerski, Prado, da Silva, Voll, & Corazza, 2016), and zinc oxide (Singh, Patidar, Ganesh, & Mahajani, 2013).

ZnO is an acid transition-metal oxide employed as heterogeneous catalyst for the esterification of free fatty acids (Kwong & Yung, 2016). Nevertheless, when in powder form, zinc oxide tends to leach out into the reaction mixture, presenting a substantial challenge in downstream processing and compliance with environmental regulations (Singh et al., 2013). This leaching issue is more dominated when ZnO is immobilized onto a support material. (Singh, Bhoi, Ganesh, & Mahajani, 2014). Singh et al. (2013) conducted a study on the development and performance evaluation of ZnO supported  $\beta$ -zeolite catalyst, for esterification of oleic acid and glycerol. The use of zeolite as a support significantly mitigates the leaching of ZnO. During the esterification of oleic acid, this catalyst exhibited high selectivity, reaching 70–80% for MAG within the conversion range of 60–90% (Singh et al., 2013). However, the disadvantage is the longer reaction time required to complete the reaction. Therefore, studying different types of supported materials for ZnO active sites represents a promising alternative for further investigation. Support catalysts with acidic properties commonly employed in the esterification including ion-exchange resins (Pouilloux, Abro, Vanhove, & Barrault, 1999), activated carbon (Konwar et al., 2016),  $\gamma$ -Al<sub>2</sub>O<sub>3</sub> (Yuan, Jiang, & Li, 2019),  $\beta$ -zeolite (Singh et al., 2013), zeolite (ZSM5 or  $\beta$ -zeolite) (Resende et al., 2020). Zeolites are commonly used as support catalysts in the esterification. Singh et al. (2014) reported that PbO/ZSM5 might be a preferred catalyst for the transesterification reaction of oils free of fatty acids (e.g., sunflower



oil). In contrast, ZnO/ ZSM5 could be the preferred choice for the esterification of free fatty acids with alcohol to produce fatty acid methyl ester (FAME). The FAME yield of jatropha oil on ZnO/ZSM5 was approximately 93.8%, indicating high efficiency at a temperature of 200 °C with an oil-to-methanol molar ratio of 1:30, 1 hr of reaction time, a catalyst loading of 1.0 wt %, and a speed of 600 rpm (Singh et al., 2014). Typically, silica is commonly used as a support catalyst due to its large surface area, although it no stability (Hu & Gao, 2010). However, zeolite-ZSM5 offers better stability (Teh et al., 2015). The selection of a support catalyst can potentially enhance the activity of the catalyst.

Therefore, this study aimed to explore the effect of catalyst supports ( $\gamma$ -Al<sub>2</sub>O<sub>3</sub> and ZSM5) with a ZnO loading of 25% for esterification of oleic acid (OA) with glycerol. The catalysts were characterized by XRD, BET, and SEM-EDS. The effects of operating parameters including catalyst type ( $\gamma$ -Al<sub>2</sub>O<sub>3</sub>, ZSM5, ZnO/ $\gamma$ -Al<sub>2</sub>O<sub>3</sub>, and ZnO/ZSM5), reaction temperature, and reaction time were investigated. The production of MAG, DAG and TAG were monitored and analysis using high performance liquid chromatography (HPLC).

## 2. Materials and Methods

### 2.1 Materials and Catalyst

Oleic acid (72.0% purity) and glycerol (99.5% purity) were purchased from Daejung. Zinc acetate (Zn(CH<sub>3</sub>COO)<sub>2</sub>·2H<sub>2</sub>O) was obtained from KemAus, Neutral aluminum oxide and acidic aluminum oxide ( $\gamma$ -Al<sub>2</sub>O<sub>3</sub>) was obtained from Alfa Aesar, and Zeolite ZSM-5 and the acidic HPLC mobile phase modifier include trifluoroacetic acid (TFA) were obtained from Sigma-Aldrich. Chemicals for reaction mixture analysis included: acetonitrile, methanol, tetrahydrofuran (HPLC grade) as a mobile phase for HPLC analysis, and acetone as a solvent for preparing sample obtained from Honeywell. The 1-Glyceryl mononadecanoate ( $\geq$  99.0% purity), 1-3 Glyceryl dinadecanoate ( $\geq$  99.0% purity) and Glyceryl trinadecanoate ( $\geq$  97.0% purity) as a standard for HPLC analysis were also purchased from Sigma-Aldrich.

### 2.2 Catalyst Preparation

The ZnO was loaded onto the support by wet impregnation method using zinc acetate (Zn(CH<sub>3</sub>COO)<sub>2</sub>·2H<sub>2</sub>O) as the ZnO precursor. Requisite volume of the prepared solution was impregnated on ZSM5 support to obtain 25 wt% ZnO in the final catalyst. The obtained mixture was dried in water bath with continuous stirring and subsequently in an oven at 80°C for overnight and finally calcined at 500°C for 3 h in a tubular reactor in the presence of air flow. The same procedure was employed for the preparation of ZnO/ $\gamma$ -Al<sub>2</sub>O<sub>3</sub> as mentioned above.

### 2.3 Catalyst Characterization

The X-ray diffraction analysis of catalysts powder was performed using a Bruker D8 Advance diffractometer. The X-ray diffraction data are recorded by using Cu K $\alpha$  radiation ( $\lambda = 1.5406 \text{ \AA}$ ) at 40 kV and 30 mA. The intensity data are collected over a  $2\theta$  range of 5-80° with a step size of 0.02°. The Brunner-Emmet-Teller (BET) surface area, pore size, and pore volume of the catalysts were determined using N<sub>2</sub> adsorption and desorption isotherms using a Micromeritics Corporation adsorption apparatus. For SEM analysis, a field emission gun scanning electron microscope using a Hitachi S3400N with a resolution of about 50 and 20  $\mu\text{m}$  was used to study the surface morphology of the samples. Catalysts acid sites measurements were performed by temperature programmed desorption of ammonia (NH<sub>3</sub>-TPD) with a conventional flow apparatus equipped with a thermal conductivity detector (TCD). A given amount of the sample, was pretreated in flowing helium at 500 °C for 1 h, cooled to 150 °C, and then exposed to NH<sub>3</sub> (20 mL/min) for 30 min. Samples adsorbed by NH<sub>3</sub> were subsequently purged with He at the same temperature for 1 h to remove the physi-sorbed NH<sub>3</sub>. The TPD

measurements were conducted in flowing He (30 mL/min) from 100 to 700 °C at a heating rate of 10 °C/min.

## 2.4 Catalytic tests

The schematic representation of the experimental setup is shown in Fig. 1. A standard 250 mL four-neck round-bottom flask assembled with stirrer to give uniform mixing of reaction mixture (stirring rate was kept constant as 340 rpm), condenser, and thermocouple type K was used to carry out the esterification. The glycerol and oleic acid (GL/OA molar ratio of 4:1) were stirred at 340 rpm and heated in an oil bath at the required temperature. When the desired temperature was reached, the catalyst was then added to start the reaction. The samples, approximately 1.5 mL each, were collected at specific time intervals. The mixture is centrifuged to separate the top organic layer from the sample and analyze by the acid titration and HPLC method.

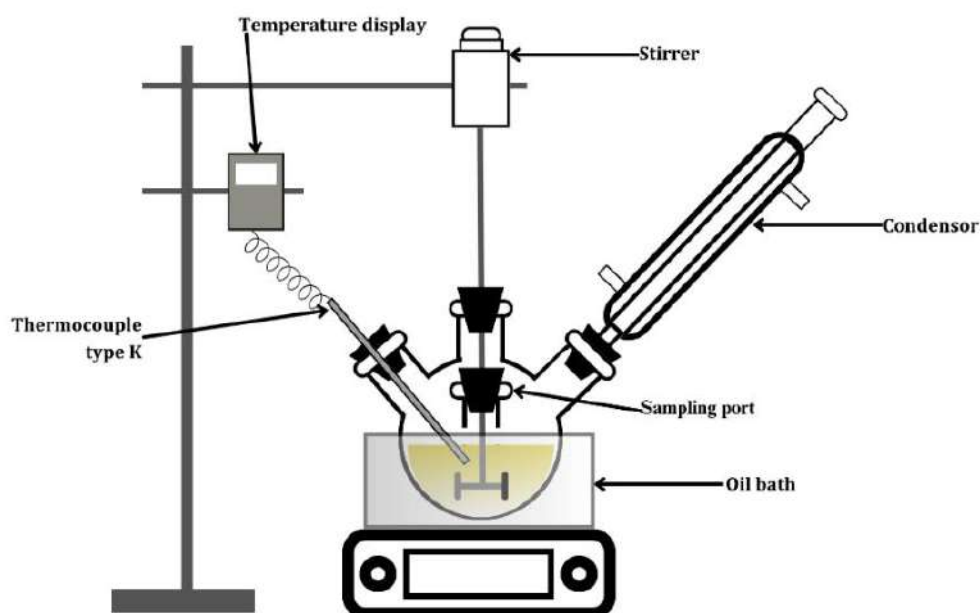


Fig. 1 Schematic representation of experimental setup.

## 2.5 Analytical methods

Acid value determination was used to monitor the conversion progress according to ASTM D4662-03 method. The product mixtures were titrated with NaOH-ethanol-solution (0.1 mol/L). Quantitative analyses of the products were carried out using a Thermo Scientific Surveyor Plus HPLC system equipped with a photodiode array (PDA) detector. An InertSustain C18 column (4.6 I.D. ×250 mm, 25 μm) was used for the analysis. The temperature of the detector oven was set at 40 °C. The column operated in isocratic mode with acetonitrile, water, and trifluoroacetic acid (TFA), employing as the mobile phases at a wavelength of 210 nm. The total flow rate of the mobile phase was consistently set at 0.7 mL/min. The mobile phase composition comprised a mixture of acetonitrile/water (87:13% vol/vol) with 0.1% vol/vol TFA using for oleic acid (OA) and monoacylglycerol (MAG) determination. However,

diacylglycerol (DAG) and triacylglycerol (TAG) analyses involved the use of acetone/acetonitrile (40:60% vol/vol) as the mobile phase. The total flow rate of the mobile phase was set constantly at 0.8 mL/min and held for 40 min. The oleic acid conversion ( $X_{OA}$ ), selectivity of monoacylglycerol ( $S_{MAG}$ ), selectivity of diacylglycerol ( $S_{DAG}$ ), selectivity of triacylglycerol ( $S_{TAG}$ ), yield of monoacylglycerol ( $Y_{MAG}$ ), yield of diacylglycerol ( $Y_{DAG}$ ), and yield of triacylglycerol ( $Y_{TAG}$ ) were determined according to the Eqs. (1)-(7),

$$X_{OA} (\%) = \left(1 - \frac{C_{OA}}{C_{OA,0}}\right) \times 100 \quad (1)$$

$$S_{MAG} = \frac{C_{MAG}}{C_{MAG} + 2C_{DAG} + 3C_{TAG}} \quad (2)$$

$$S_{DAG} = \frac{2C_{DAG}}{C_{MAG} + 2C_{DAG} + 3C_{TAG}} \quad (3)$$

$$S_{TAG} = \frac{3C_{TAG}}{C_{MAG} + 2C_{DAG} + 3C_{TAG}} \quad (4)$$

$$Y_{MAG} (\%) = \text{Conv}_{OA} (\%) \times S_{MAG} \quad (5)$$

$$Y_{DAG} (\%) = \text{Conv}_{OA} (\%) \times S_{DAG} \quad (6)$$

$$Y_{TAG} (\%) = \text{Conv}_{OA} (\%) \times S_{TAG} \quad (7)$$

where  $X_{OA}$  is the conversion of oleic acid,  $C_{OA,0}$  is the initial concentration of oleic acid,  $C_{OA}$ ,  $C_{MAG}$ ,  $C_{DAG}$ ,  $C_{TAG}$  are the concentration of oleic acid, monoacylglycerol, diacylglycerol, and triolein in terms of time,  $S_{MAG}$ ,  $S_{DAG}$ ,  $S_{TAG}$  are the selectivity of monoacylglycerol, diacylglycerol, and triacylglycerol while  $Y_{MAG}$ ,  $Y_{DAG}$ , and  $Y_{TAG}$  are the yield of monoacylglycerol, diacylglycerol, and triacylglycerol, respectively.

### 3. Results and discussion

#### 3.1 Characterization of catalysts

Powder X-ray diffraction patterns for ZnO/ZSM5, ZnO/ $\gamma$ -Al<sub>2</sub>O<sub>3</sub>,  $\gamma$ -Al<sub>2</sub>O<sub>3</sub>, ZSM5 and ZnO are shown in Fig. 2. The diffraction peak of ZnO obtained from the ZnO/ZSM5 at  $2\theta = 31.76, 34.31, 36.25, 47.51, 56.60$  and  $62.88^\circ$  correspond to the lattice planes (100), (002), (101), (102), (110) and (103), respectively (Singh et al., 2013). Moreover, the peaks appeared at  $34.31^\circ$ , assigned as (002), are related to the zinc oxide. This can be explained by the confines of ZnO inside the zeolite, and the overlapping by the zeolite peaks (Ref Cod 01-087-1619) (Alswat, Ahmad, Saleh, Hussein, & Ibrahim, 2016). On the other hand, the XRD pattern of ZnO/ $\gamma$ -Al<sub>2</sub>O<sub>3</sub> revealed the absence of distinct peaks corresponding to crystalline of ZnO.

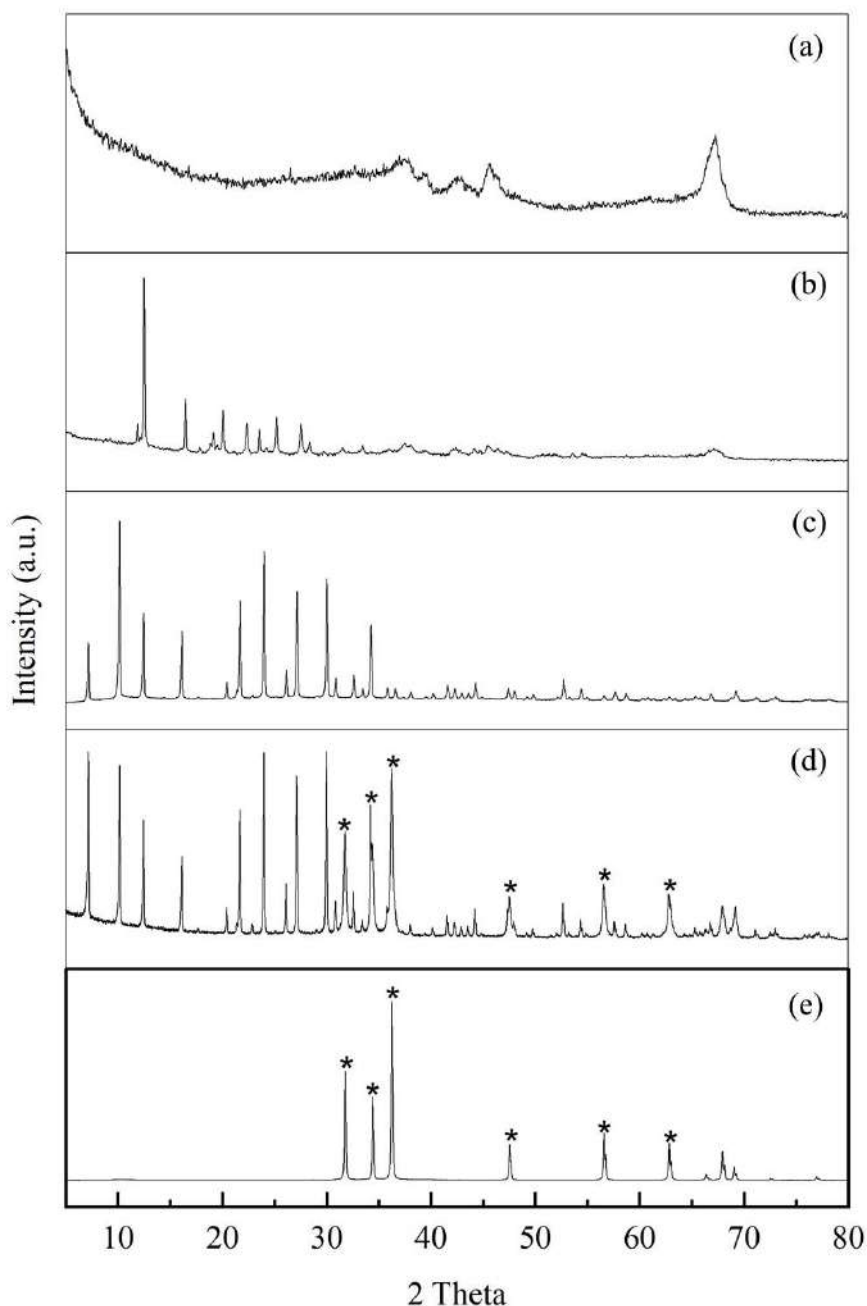


Fig. 2 XRD patterns of (a)  $\gamma$ - $\text{Al}_2\text{O}_3$ , (b)  $\text{ZnO}/\gamma\text{-Al}_2\text{O}_3$ , (c) ZSM5, (d)  $\text{ZnO}/\text{ZSM5}$ -, and (e) ZnO.

The scanning electron microscope (SEM) images for  $\gamma\text{-Al}_2\text{O}_3$ , ZSM-5,  $\text{ZnO}/\gamma\text{-Al}_2\text{O}_3$  and  $\text{ZnO}/\text{ZSM5}$  catalysts are shown in Figs. 3-4. It was evident from the SEM analysis that the shapes of the  $\gamma\text{-Al}_2\text{O}_3$  (support) pellets revealed coarse rock/sand-like shapes in Fig. 3(a). In this sample, the average size of the particles is 90.9  $\mu\text{m}$ . The SEM images for the  $\text{ZnO}/\gamma\text{-Al}_2\text{O}_3$  indicated the regions of different color intensities with light grey representing the ZnO on a relatively darker  $\gamma\text{-Al}_2\text{O}_3$  background as shown in Fig. 3(b).  $\text{ZnO}/\gamma\text{-Al}_2\text{O}_3$  was locally present as agglomerates, which led to low metal distribution. However, in the ZSM5 catalyst, the

average particle size was 53.5  $\mu\text{m}$ , as illustrated in Fig. 4(a). It was evident from the SEM analysis that the shapes of the ZSM5 (support) particles were nonuniform, and the particle size distribution was large with sizes in Fig. 4 (a). It is clear that ZSM5 exhibited a cubic morphology with smooth surfaces. On the other hand, ZnO nanoparticles maintained the granular spherical morphology dominated by particle agglomerations as illustrated in Fig 4(b). The SEM images for the ZnO/ZSM5 indicated regions of different color intensities with light grey representing the ZnO on a relatively darker ZSM5 background. Fig. 5 shows the EDX elemental maps for ZnO/ $\gamma$ -Al<sub>2</sub>O<sub>3</sub>, the elements Al, O, and Zn are represented by green, red, and blue colors, respectively. On the other hand, in the case of ZnO/ZSM5 (Fig. 6), Zn was well-distributed over the external surface of the support.

The elemental mapping and EDX results of ZnO/ $\gamma$ -Al<sub>2</sub>O<sub>3</sub> and ZnO/ZSM5 also indicated that the Zn elements uniform distributed over the  $\gamma$ -Al<sub>2</sub>O<sub>3</sub> and ZSM5 supports. The surface components are known from the EDX analysis, for ZnO/ $\gamma$ -Al<sub>2</sub>O<sub>3</sub> catalyst contained 36.31 wt.% of O, 56.65 wt.% of Al, and 7.04 wt.% of Zn. For ZnO/ZSM5 catalyst contained 27.19 wt.% of O, 18.44 wt.% of Al, 16.90 wt.% of Si, and 34.47 wt.% of Zn.

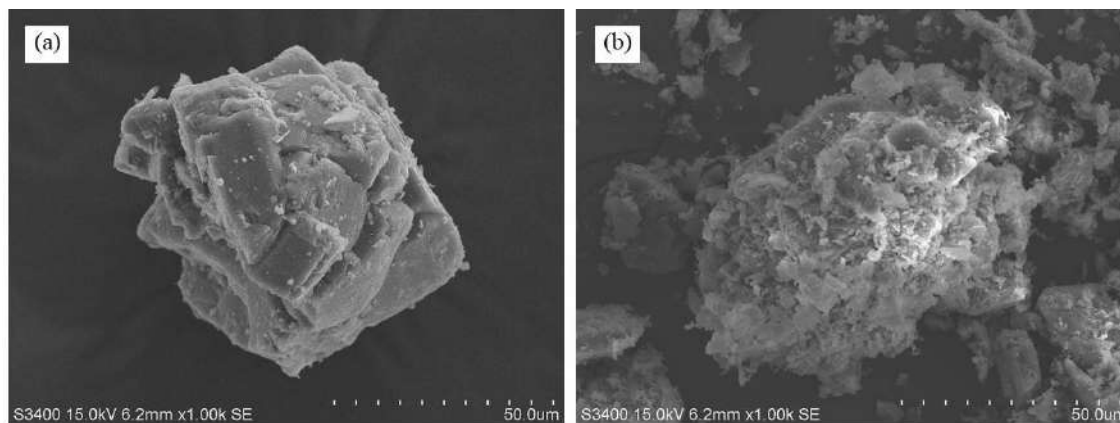


Fig. 3 SEM images of (a)  $\gamma$ -Al<sub>2</sub>O<sub>3</sub>, and (b) ZnO/ $\gamma$ -Al<sub>2</sub>O<sub>3</sub>.

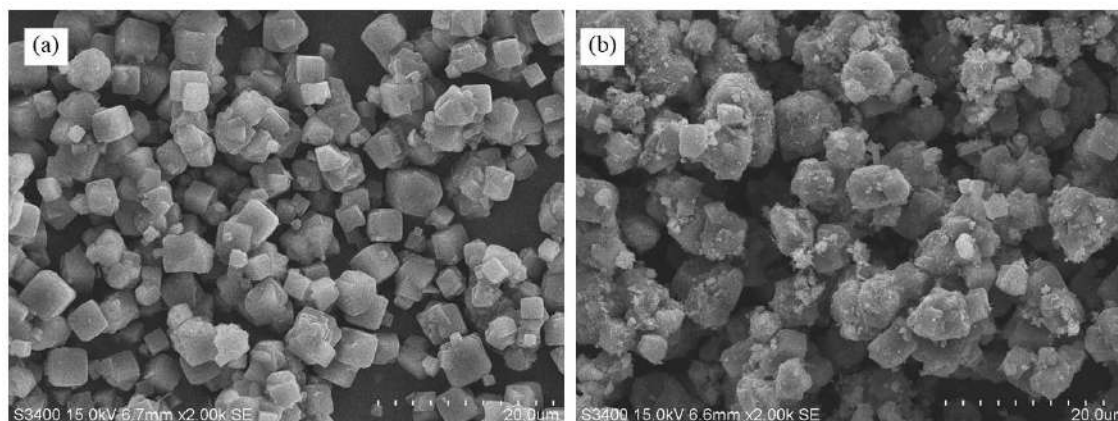


Fig. 4 SEM images of (a) ZSM5, and (b) ZnO/ZSM5.



Fig. 5 Elemental mapping of the ZnO/ $\gamma$ -Al<sub>2</sub>O<sub>3</sub> catalyst (metal indicated in elemental mapping by the following colors: O (red), Al (green), and Zn (blue)).

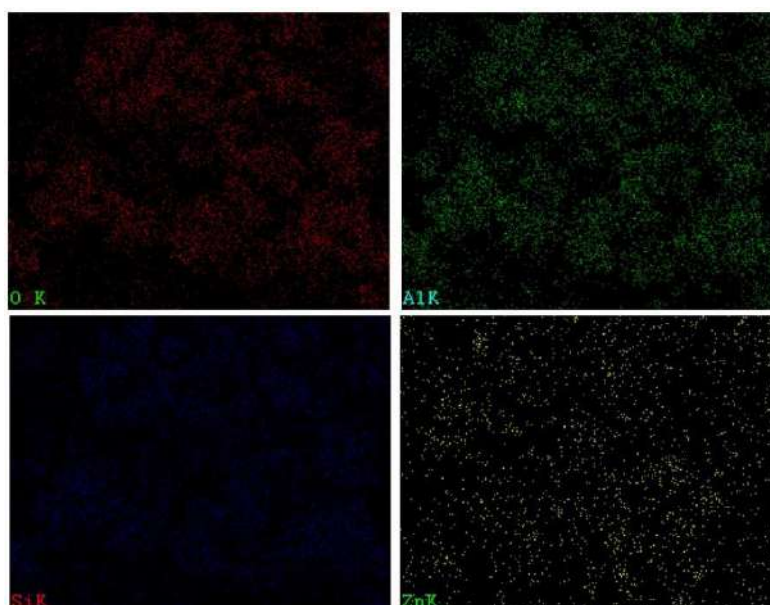


Fig. 6 Elemental mapping of the ZnO/ZSM-5 catalyst (metal indicated in elemental mapping by the following colors: O (red), Al (green), Si (blue) and Zn (yellow)).

### 3.2 Effect of catalyst type

The esterification of oleic acid with glycerol requires active acid catalyst to achieve high rates. To compare the catalytic performance, the reaction was conducted under similar conditions without using catalyst, and with using  $\gamma$ -Al<sub>2</sub>O<sub>3</sub>, ZSM5, ZnO/ $\gamma$ -Al<sub>2</sub>O<sub>3</sub>, and ZnO/ZSM5 catalysts. In selecting the operating conditions, Singh et al. reported promising results for the synthesis of monoglycerides using a ZnO-supported  $\beta$ -zeolite catalyst. The esterification of oleic acid was obtained under optimal conditions, including a Gly/OA mole ratio of 4:1, a catalyst concentration of 2 wt.% of the total weight, a reaction temperature of 150°C, and a reaction time of 360 min, resulted in a conversion rate of 88.9%. Notably, the S<sub>MAG</sub> was observed to be as high as 66.8%, while the S<sub>DAG</sub> was 27.4% (Singh et al., 2013). Therefore, these optimal conditions were chosen for studying the effect of catalyst type. The effect of catalyst type is presented in Fig 7. In this study,  $\gamma$ -Al<sub>2</sub>O<sub>3</sub> demonstrated a higher conversion compared to ZSM5. It should be noted that  $\gamma$ -Al<sub>2</sub>O<sub>3</sub> has a BET surface area and pore size of 92.38 m<sup>2</sup>/g and 98.47 Å, respectively, which higher surface area than ZSM5. For ZSM5

exhibits a smaller surface area of 9.58 m<sup>2</sup>/g and a larger pore size of 113.26 Å. However, the acidity of the catalysts also effects on reaction activity. According to Shabani et al. (2022), the reported that acidity of  $\gamma$ -Al<sub>2</sub>O<sub>3</sub> was 1.17 mmol NH<sub>3</sub>/g (weak acid sites = 0.68 mmol NH<sub>3</sub>/g and strong acid sites = 0.49 mmol NH<sub>3</sub>/g) (Shabani, Moosavian, Royae, & Zamani, 2022), while ZSM5 had a higher acidity of 5.664 mmol NH<sub>3</sub>/g (weak acid sites = 4.217 mmol NH<sub>3</sub>/g and medium acid sites = 1.447 mmol NH<sub>3</sub>/g). When ZnO was loaded, the ZnO/ZSM catalyst had an acidity value of 4.265 mmol NH<sub>3</sub>/g (weak acid sites = 2.472 mmol NH<sub>3</sub>/g, medium acid sites = 0.632 mmol NH<sub>3</sub>/g and strong acid sites = 1.161 mmol NH<sub>3</sub>/g). It can be seen that loading ZnO on ZSM5 indicate the formation of strong acidic sites, consequently enhancing its catalytic activity.

However, ZnO/ZSM5 catalyst exhibited the highest values for X<sub>OA</sub>, Y<sub>MAG</sub>, and Y<sub>DAG</sub>, of 37.1%, 26.8%, and 10.3%, respectively. Following that, ZnO/ $\gamma$ -Al<sub>2</sub>O<sub>3</sub> showed the X<sub>OA</sub>, Y<sub>MAG</sub>, and Y<sub>DAG</sub> of 31.77%, 23.15%, and 8.61%, respectively. ZnO supported on ZSM-5 demonstrated a significantly increased reaction rate due to the larger number of acid sites derived from ZnO loading. Therefore, 25% ZnO/ZSM5 was used to further study the effect of operating parameters for the esterification of OA.

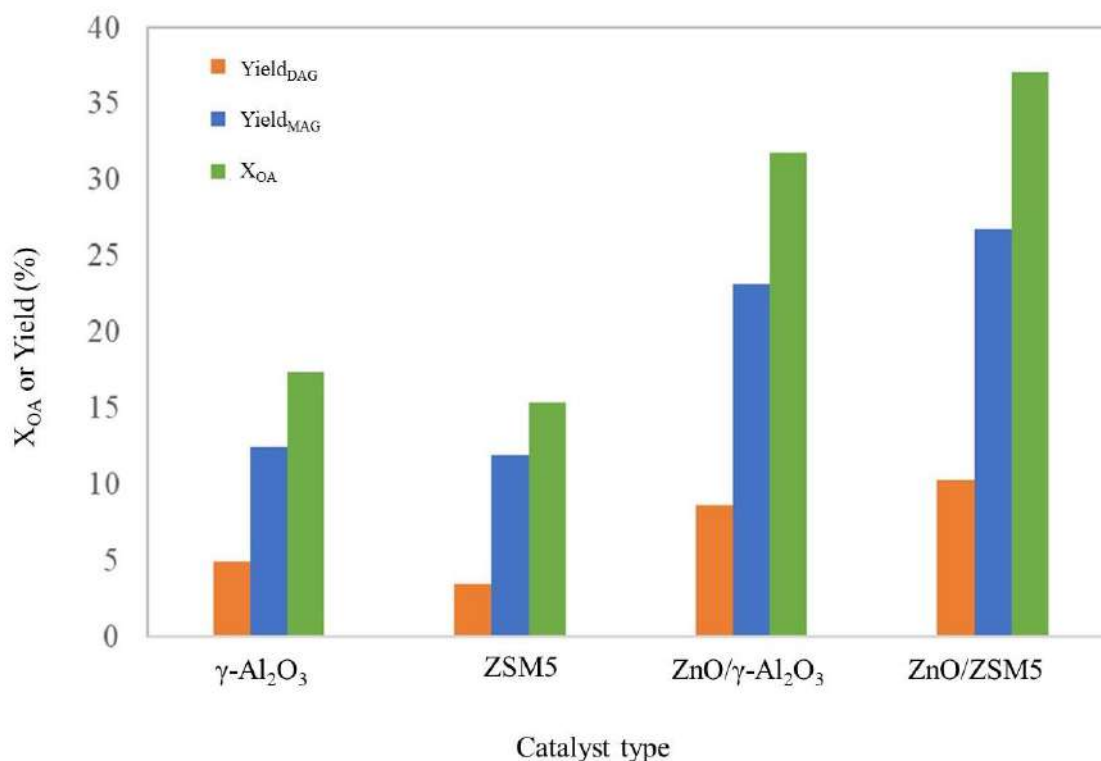


Fig. 7 Effect of catalyst type for esterification of OA (Gly/OA mole ratio 4:1; reaction temperature 150 °C; reaction time 60 min; catalyst loading 0.5 wt.% of total weight).

### 3.3 Effect of operating parameters

Fig. 8 shows the effect of reaction temperature on the esterification of oleic and glycerol using ZnO/ZSM5 loading of 0.5 wt.% of total weight of reactants at GL/OA molar ratio of 4:1, and varying reaction time. The effect of temperature on the esterification rate has been studied

by varying in the range of 150 to 180 °C. The increase in the reaction temperature significantly increase the oleic conversion based on the Arrhenius's law. Moreover, it is well known that the reaction temperature also affects the glycerol solubility in the oleic acid. Thus, higher temperatures enhance the effective glycerol concentration in the OA phase favoring drive the esterification rate (Noureddini, Harkey, & Gutsman, 2004). This result revealed that, the oleic acid conversion ( $X_{OA}$ ) increased from 30% to 79.4% when the reaction temperature increased from 150 °C to 180 °C at reaction time of 15 min. In addition, increasing the reaction temperature significantly increased the DAG and TAG selectivity due the nature of consecutive reaction as shown in Fig. 9. At a reaction time of 90 min, it was seen that. increasing the reaction temperature from 150 to 200 °C enhances the  $S_{DAG}$  and  $S_{TAG}$  due to amounts of DAG and TAG were also formed due to secondary reactions (Konwar et al., 2016).

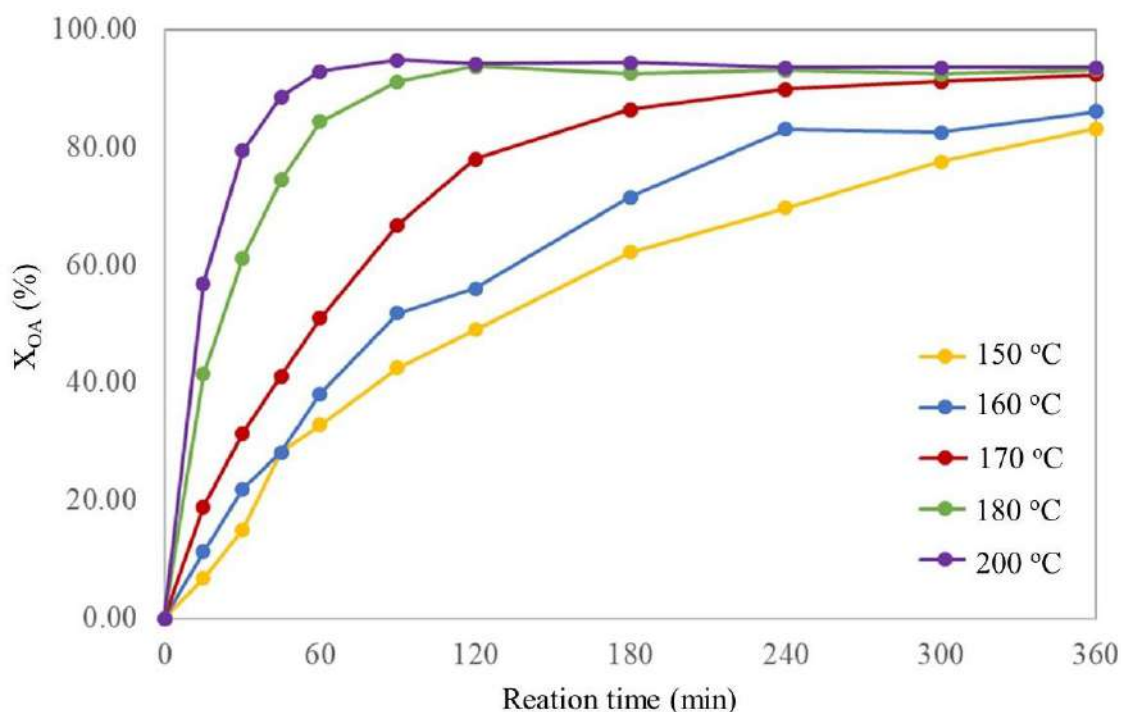


Fig. 8 Conversion of oleic acid at different reaction temperature (GL/OA mole ratio 4:1; ZnO/ZSM5 catalyst concentration of 0.5 wt.% of total weight)



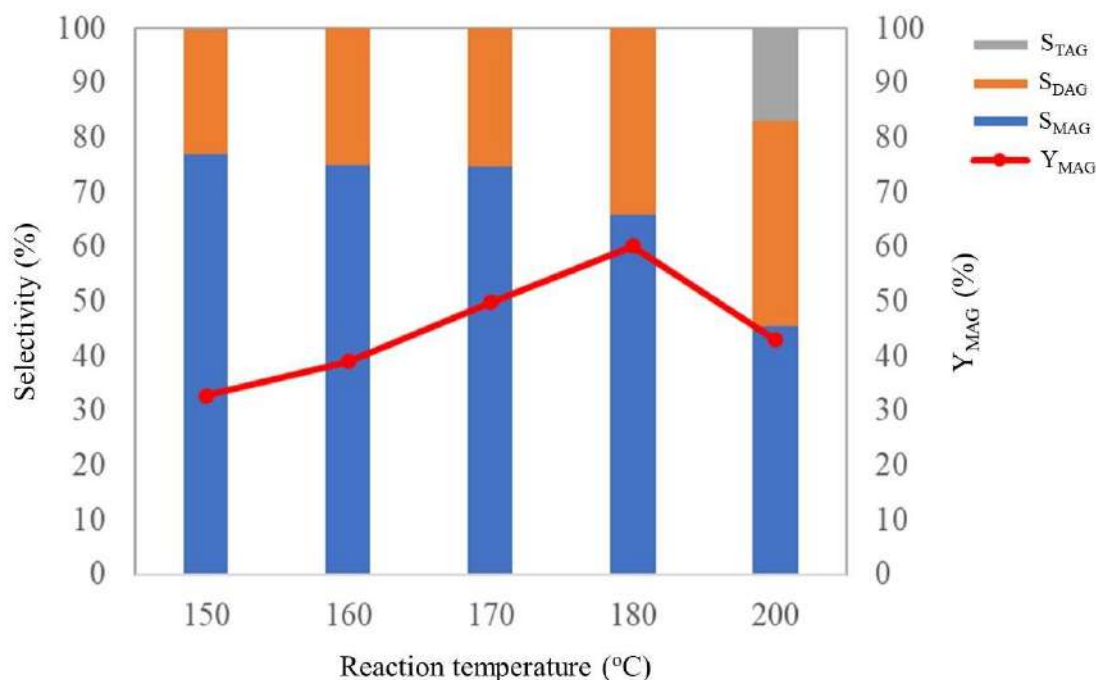


Fig. 9 The effect of reaction temperature using on MAG, DAG and TAG selectivity at 90 min (GL/OA mole ratio 4:1; reaction time 90 min; ZnO/ZSM5 catalyst concentration of 0.5 wt.% of total weight)

Table 1 is a comparison of catalyst performance in esterification of oleic acid with glycerol by different heterogeneous catalysts. It can be noted that ZnO/ZSM5 prepared by wet impregnation method is a promising heterogeneous catalyst for monoglyceride synthesis from glycerol.

Table 1. Comparison of catalyst performance in esterification of oleic acid with glycerol by different heterogeneous catalysts

Catalyst	The conditions	X <sub>OA</sub> (%)	S <sub>MAG</sub> (%)	S <sub>DAG</sub> (%)	S <sub>TAG</sub> (%)	Ref.
ZnO/ZSM5	Gly/OA mole ratio = 4:1 Catalyst concentration = 0.5 (wt.% of total weight) Reaction temperature = 180 °C Reaction time = 90 min	91.2	66.0	34.0		This study
ZnO/ $\beta$ -zeolite	Gly/OA mole ratio = 4:1 Catalyst concentration = 2 (wt.% of total weight) Reaction temperature = 150 °C Reaction time = 360 min	88.9	66.8	27.4		(Singh et al., 2013)

Catalyst	The conditions	X <sub>OA</sub> (%)	S <sub>MAG</sub> (%)	S <sub>DAG</sub> (%)	S <sub>TAG</sub> (%)	Ref.
Amberlyst 35	Gly/OA mole ratio = 4:1 Catalyst concentration = 2 (wt.% of total weight) Reaction temperature = 150 °C Reaction time = 360 min	65.1	78.6	19.3		(Singh et al., 2013)
Ti-SBA-16 (Meso porous Titanosilicates)	Gly/OA mole ratio = 1:1 Catalyst concentration = 3 (wt.% of OA) Reaction temperature = 180 °C Reaction time = 180 min	72.8	32.8	57.9	9.2	(Kotwal, Kumar, & Darbha, 2013)
Fe-Zn DMC (Fe-Zn double- metal cyanide (DMC))	Gly/OA mole ratio = 1:1 Catalyst concentration = 7 (wt.% of OA) Reaction temperature = 180 °C Reaction time = 480 min	63.4	67.3	31.7		(Kotwal, Deshpande, & Srinivas, 2011)
ZrO <sub>2</sub> -SiO <sub>2</sub> - Me&Et- PhSO <sub>3</sub> H (hydrophobic mesoporous zirconia-silica)	Gly/OA mole ratio = 1:1 Catalyst concentration = 5 (wt.% of total weight) Reaction temperature = 160 °C Reaction time = 240 min	63.4	59.4	34.6	6.0	(Kong, Pérès, Wan Daud, Cognet, & Aroua, 2019)

#### 4. Conclusions

Esterification of oleic acid with glycerol to produce monoacylglycerols (MAG) was investigated using the different solid acid catalysts. The wet impregnation method for ZnO loading preparation was used to prepare ZnO/support. The effects of operating parameters including catalyst type ( $\gamma$ -Al<sub>2</sub>O<sub>3</sub>, ZSM5, ZnO/ $\gamma$ -Al<sub>2</sub>O<sub>3</sub>, and ZnO/ZSM5), reaction temperature, and reaction time were investigated. Loading ZnO on the support provided higher catalytic activity due to ZnO can increase the number of acid sites. Among the catalysts tested, zinc oxide-supported ZSM5-zeolite (ZnO/ZSM5) gave the highest catalytic activity. 94.1% oleic acid conversion was obtained at the reaction temperature of 180 °C, catalyst loading of 0.5 wt.%, and reaction time of 2 h. In addition, increasing the reaction temperature significantly increased the DAG and TAG selectivity.

#### Acknowledgement

This research has received funding support from the NSRF via the Program Management Unit from Human Resources & Institutional Development, Research and Innovation (Grant number B05F640085).

#### References

Alswat, A. A., Ahmad, M. B., Saleh, T. A., Hussein, M. Z. B., & Ibrahim, N. A. (2016). Effect of zinc oxide amounts on the properties and antibacterial activities of zeolite/zinc oxide nanocomposite. *Materials Science and Engineering: C*, 68, 505-511. doi:<https://doi.org/10.1016/j.msec.2016.06.028>

- da Silva-Machado, M., Cardoso, D., Pérez-Pariente, J., & Sastre, E. (2000). Esterification of lauric acid with glycerol using modified zeolite beta as catalyst. In *Studies in Surface Science and Catalysis* (Vol. 130, pp. 3417-3422): Elsevier.
- Ferretti, C. A., Soldano, A., Apesteguía, C. R., & Di Cosimo, J. I. (2010). Monoglyceride synthesis by glycerolysis of methyl oleate on solid acid–base catalysts. *Chemical Engineering Journal*, 161(3), 346-354.
- Hamerski, F., Prado, M. A., da Silva, V. R., Voll, F. A. P., & Corazza, M. L. (2016). Kinetics of layered double hydroxide catalyzed esterification of fatty acids with glycerol. *Reaction Kinetics, Mechanisms and Catalysis*, 117(1), 253-268. doi:10.1007/s11144-015-0942-0
- Harmer, M. A., & Sun, Q. (2001). Solid acid catalysis using ion-exchange resins. *Applied Catalysis A: General*, 221(1-2), 45-62. doi:10.1016/S0926-860X(01)00794-3
- Holmberg, K., Lassen, B., & Stark, M. B. (1989). Enzymatic glycerolysis of a triglyceride in aqueous and nonaqueous microemulsions. *Journal of the American Oil Chemists' Society*, 66(12), 1796-1800.
- Hu, S.-H., & Gao, X. (2010). Stable Encapsulation of Quantum Dot Barcodes with Silica Shells. *Advanced Functional Materials*, 20(21), 3721-3726. doi:https://doi.org/10.1002/adfm.201000711
- Jothiramalingam, R., & Wang, M. K. (2009). Review of recent developments in solid acid, base, and enzyme catalysts (heterogeneous) for biodiesel production via transesterification. *Industrial and Engineering Chemistry Research*, 48(13), 6162-6172. doi:10.1021/ie801872t
- Jyoti, G., Keshav, A., Anandkumar, J., & Bhoi, S. (2018). Homogeneous and heterogeneous catalyzed esterification of acrylic acid with ethanol: reaction kinetics and modeling. *International journal of chemical kinetics*, 50(5), 370-380.
- Kan, Q. B., Barrault, J., & Wu, T. H. (2001). Esterification of glycerol by oleic acid and selective hydrogenation of oleic acid methylester over acid and Ru-Sn-B supported mesoporous AIMCM-41. *Chinese Chemical Letters*, 12(9), 823-826.
- Kong, P. S., Aroua, M. K., Daud, W. M. A. W., Cognet, P., & Pérès, Y. (2016). Enhanced microwave catalytic-esterification of industrial grade glycerol over Brønsted-based methane sulfonic acid in production of biolubricant. *Process Safety and Environmental Protection*, 104, 323-333. doi:https://doi.org/10.1016/j.psep.2016.09.014
- Kong, P. S., Pérès, Y., Wan Daud, W. M. A., Cognet, P., & Aroua, M. K. (2019). Esterification of Glycerol With Oleic Acid Over Hydrophobic Zirconia-Silica Acid Catalyst and Commercial Acid Catalyst: Optimization and Influence of Catalyst Acidity. *Frontiers in Chemistry*, 7. doi:10.3389/fchem.2019.00205
- Konwar, L. J., Mäki-Arvela, P., Kumar, N., Mikkola, J.-P., Sarma, A., & Deka, D. (2016). Selective esterification of fatty acids with glycerol to monoglycerides over –SO<sub>3</sub>H functionalized carbon catalysts. *Reaction Kinetics, Mechanisms and Catalysis*, 119. doi:https://10.1007/s11144-016-1040-7
- Kotwal, M., Deshpande, S. S., & Srinivas, D. (2011). Esterification of fatty acids with glycerol over Fe–Zn double-metal cyanide catalyst. *Catalysis Communications*, 12(14), 1302-1306. doi:https://doi.org/10.1016/j.catcom.2011.05.008
- Kotwal, M., Kumar, D. A., & Darbha, S. (2013). Three-dimensional, mesoporous titanosilicates as catalysts for producing biodiesel and biolubricants. *Journal of Molecular Catalysis A: Chemical*, 377, 65–73. doi:10.1016/j.molcata.2013.04.029

- Kumoro, A. C. (2012). Experimental and modeling studies of the reaction kinetics of alkaline-catalyzed used frying oil glycerolysis using isopropyl alcohol as a reaction solvent. *Research Journal of Applied Sciences, Engineering and Technology*, 4(8), 869-876.
- Kwong, T.-L., & Yung, K.-F. (2016). One-step production of biodiesel through simultaneous esterification and transesterification from highly acidic unrefined feedstock over efficient and recyclable ZnO nanostar catalyst. *Renewable Energy*, 90, 450-457. doi:<https://doi.org/10.1016/j.renene.2016.01.028>
- Molinero, L., Ladero, M., Tamayo, J., & García-Ochoa, F. (2014). Homogeneous catalytic esterification of glycerol with cinnamic and methoxycinnamic acids to cinnamate glycerides in solventless medium: Kinetic modeling. *Chemical Engineering Journal*, 247, 174-182.
- Noureddini, H., Harkey, D. W., & Gutsman, M. R. (2004). A Continuous Process for the Glycerolysis of Soybean Oil. *JAOCs, Journal of the American Oil Chemists' Society*, 81(2), 203-207. doi:[10.1007/s11746-004-0882-y](https://doi.org/10.1007/s11746-004-0882-y)
- Pouilloux, Y., Abro, S., Vanhove, C., & Barrault, J. (1999). Reaction of glycerol with fatty acids in the presence of ion-exchange resins: Preparation of monoglycerides. *Journal of Molecular Catalysis A: Chemical*, 149(1), 243-254. doi:[https://doi.org/10.1016/S1381-1169\(99\)00187-9](https://doi.org/10.1016/S1381-1169(99)00187-9)
- Resende, R. F., Vieira, S. S., Santos, N. A. V., Fernandes, A., Ribeiro, M. F., & Magriotis, Z. M. (2020). Effect of the amount of SO<sub>4</sub><sup>2-</sup>/La<sub>2</sub>O<sub>3</sub> on HZSM-5 activity for esterification reaction. *Catalysis Today*, 344, 150-157. doi:<https://doi.org/10.1016/j.cattod.2018.11.072>
- Shabani, M. R., Moosavian, M. A., Royaei, S. J., & Zamani, Y. (2022). Acid Gas Converting to Organosulfur and Hydrogen in Methanol Thiolation Using Alkali Promoted Catalysts: Case Study. *Catalysis Surveys from Asia*, 26(1), 46-57. doi:[10.1007/s10563-021-09345-5](https://doi.org/10.1007/s10563-021-09345-5)
- Singh, D., Bhoi, R., Ganesh, A., & Mahajani, S. (2014). Synthesis of Biodiesel from Vegetable Oil Using Supported Metal Oxide Catalysts. *Energy & Fuels*, 28(4), 2743-2753. doi:[10.1021/ef500045x](https://doi.org/10.1021/ef500045x)
- Singh, D., Patidar, P., Ganesh, A., & Mahajani, S. (2013). Esterification of Oleic Acid with Glycerol in the Presence of Supported Zinc Oxide as Catalyst. *Industrial & Engineering Chemistry Research*, 52(42), 14776-14786. doi:[10.1021/ie401636v](https://doi.org/10.1021/ie401636v)
- Teh, L. P., Triwahyono, S., Jalil, A. A., Mukti, R. R., Aziz, M. A. A., & Shishido, T. (2015). Mesoporous ZSM5 having both intrinsic acidic and basic sites for cracking and methanation. *Chemical Engineering Journal*, 270, 196-204. doi:<https://doi.org/10.1016/j.cej.2015.01.084>
- Vitiello, R., Taddeo, F., Russo, V., Turco, R., Buonerba, A., Grassi, A., . . . Tesser, R. (2021). Production of sustainable biochemicals by means of esterification reaction and heterogeneous acid catalysts. *ChemEngineering*, 5(3), 46.
- Yuan, Y., Jiang, W., & Li, J. (2019). Preparation of solid acid catalyst SO<sub>4</sub><sup>2-</sup>/TiO<sub>2</sub>/γ-Al<sub>2</sub>O<sub>3</sub> for esterification: A study on catalytic reaction mechanism and kinetics. *Chinese Journal of Chemical Engineering*, 27(11), 2696-2704. doi:<https://doi.org/10.1016/j.cjche.2018.11.021>

## A Green Sulfonated Activated Carbon Catalyst for Esterification of Oleic Acid with Glycerol

**Chaiwichit Sennoi<sup>1</sup>, Kanyarat Duangngen<sup>1</sup>, Wanatchporn Kaewfa<sup>1</sup>, Weerinda Mens<sup>1\*</sup>, Kanokwan Ngaosuwan<sup>2</sup>, Chaiyan Chaiya<sup>1</sup>, Sasiradee Jantasee<sup>1</sup>, Lida Simasatitkuland<sup>3</sup> Suttichai Assabumrungrat<sup>4,5</sup>**

<sup>1</sup> Department of Chemical and Materials Engineering, Faculty of Engineering, Rajamangala University of Technology Thanyaburi, Pathum Thani, 12110, Thailand

<sup>2</sup> Chemical Engineering Division, Department of Engineering, Rajamangala University of Technology Krungthep, Bangkok, 10120, Thailand

<sup>3</sup> Department of Industrial Chemistry, Faculty of Applied Science, King Mongkut's University of Technology North Bangkok, Bangkok 10800, Thailand

<sup>4</sup> Center of Excellence on Catalysis and Catalytic Reaction Engineering, Department of Chemical Engineering, Faculty of Engineering, Chulalongkorn University, Bangkok, 10330, Thailand

<sup>5</sup> Bio-Circular-Green economy Technology & Engineering Center, BCGeTEC, Department of Chemical Engineering, Faculty of Engineering, Chulalongkorn University, Bangkok, 10330, Thailand

E-mail: weerinda.a@en.rmutt.ac.th\*(Corresponding author)

### Abstract

A green sulfonated activated catalyst was successfully synthesized through sulfonation of activated carbon (SAC). The sulfonation temperature (140-200°C) was investigated and the catalytic activity was tested via esterification of oleic acid and glycerol to produce mono-olein (MO). The carbon-based catalysts were characterized by X-ray diffraction (XRD) and scanning electron microscope energy-dispersive X-ray spectroscopy (SEM-EDS). The catalyst's total acid density was determined using a modified Boehm titration approach. The effects of operating parameters including reaction temperature, catalyst loading and reaction time were investigated. The sulfonation temperature varied from 140 to 200 °C as named SAC-140, SAC-160, SAC-180, and SAC-200 catalysts. It was found that SAC-180 catalyst exhibited the highest initial rate due to the highest total acid site density. As-prepared SAC-180 catalyst showed the excellent catalytic performance to obtain 70.75 % of oleic acid conversion at reaction temperature of 170°C, catalyst loading of 2 %wt. and reaction time 3 hr. In addition, increasing the reaction temperature of 130 to 170 °C exhibited positive improvement of the MO selectivity.

**Keywords:** Esterification; Oleic acid; Glycerol; Mono-olein (MO); Sulfonated activated carbon catalyst.

## 1. Introduction

The biodiesel market continues to expand due to the increasing demand for sustainable and innovative products. As a result, the capacity for biodiesel production is increasing worldwide, leading to a significant rise in glycerol production (Badday, Abdullah, Lee, & Khayoon, 2012). It was estimated that approximately glycerol is produced during the transesterification process in the biodiesel plant by 10 wt.% of total biodiesel production. For every 10 kg of biodiesel produced, 1 kg of crude glycerol is generated. Glycerol has to be completely removed from the mixture because the high temperatures makes many chemical compounds harmful for the engines such as acrolein, the disposal of crude glycerol contaminated with salts, free fatty acids, and methanol presents an environmental and economic challenge (Alashek, Keshe, & Alhassan, 2022). This indicates that overly produced glycerol has an effect on the market price of glycerol. Therefore, this is one reason to develop processes to generate value added products from glycerol. The Glycerol has potential to be transformed and converted to monoglyceride (MG) by catalytic processes via esterification reactions. Although selectivity catalyst such as hydrochloric acid, sulphuric acid and phosphoric acid have been utilized for esterification, the challenge remains in removing these homogeneous catalysts from the final products (Lilja et al., 2002; Rastegari & Ghaziaskar, 2015).

Numerous studies have explored heterogeneous acid catalysts to overcome the drawbacks associated with homogeneous catalysts. Solid acids such as zeolites,  $-SO_3H$  modified zeolites, mesoporous silica, metal oxide modified zeolites have been investigated as potential catalysts. Nevertheless, the preparation of these catalysts is both cost and energy-intensive, requiring several complex steps. Additionally, various literature sources have highlighted the significance of catalyst properties, such as steric factors, acidity, and hydrophilicity/hydrophobicity, in influencing glycerol esterification and MG yields (Konwar et al., 2016). As a result, there is a rising interest in the synthesis of solid catalysts such as carbonaceous materials due to their cost-effectiveness, abundance, and ability to adjust surface structures. Carbon-based catalysts have been extensively used in biodiesel production. For instance, A significantly high biodiesel synthesis yield of 97.3% using a high surface area activated carbon derived from bamboo. They demonstrated that the presence of  $-SO_3H$  species on the carbon surface predominantly enhanced catalytic activity (Tang & Niu, 2019). Therefore, this study aimed to explore the effect of sulfonation temperature (140-200 °C) for esterification of oleic acid (OA) with glycerol. The catalysts were characterized by XRD, and SEM-EDS. The effects of operating parameters including reaction temperature and reaction time were investigated.

## 2. Materials and Methods

### 2.1 Materials

Oleic acid (72.0% purity) and glycerol (99.5% purity) were obtained from Daejung, Activated carbon and sulphuric acid 98% were obtained from carbokarn company limited (Thailand) and KemAus, respectively. Sulphuric acid (98 %), phenolphthalein (98%), sodium hydroxide ( $\geq 97\%$ ), and methanol (98 %) were obtained from Merck.

## 2.2 Catalyst Preparation

The green sulfonated activated carbon catalysts were prepared based sulfonic acid-functionalized carbonaceous material. The activated carbon (AC) was dried at 110 °C for 12 hr. Then 1 g of AC was added to 30 mL of H<sub>2</sub>SO<sub>4</sub> in portion wise, placed in a magnetic stirrer for 2 hr. It was then kept in hot air oven at 140-200 °C for 18 h. The sample was rinsed with deionized water after cooling down to room temperature until pH was 7. The product AC-SO<sub>3</sub>H was vacuum-dried for overnight at 80 °C and stored in a desiccator for further use. The SO<sub>3</sub>H acid density was determined using titration. Here 0.1 g of catalyst was mixed with 0.1 M NaOH for 20 ml then agitated for 1 hr. The sample was centrifuged and then the top of solution was titrated with 0.1 M HCL by using phenolphthalein as indicator.

## 2.3 Catalyst Characterization

The X-ray diffraction analysis of catalysts powder was performed using a Bruker D8 Advance diffractometer. The X-ray diffraction data are recorded by using Cu K $\alpha$  radiation ( $\lambda = 1.5406 \text{ \AA}$ ) at 40 kV and 30 mA. For SEM analysis, a field emission gun scanning electron microscope using a Hitachi S3400N with a resolution of about 50 and 20  $\mu\text{m}$  was used to study the surface morphology of the samples.

## 2.4 Catalytic tests

The schematic representation of the experimental setup is shown in Fig. 1. A standard 250 mL four-neck round-bottom flask assembled with a magnetic bar, condenser, and thermometer type K. The glycerol and oleic acid (GL/OA molar ratio of 5:1) were stirred at 340 rpm and heated in an oil bath at the required temperature (130 -170 °C). When the desired temperature was reached, the catalyst was then added to start the reaction. The samples, approximately 1.5 mL each, were collected at specific time intervals. The mixture is centrifuged to separate the top organic layer from the sample and analyze by the acid titration.

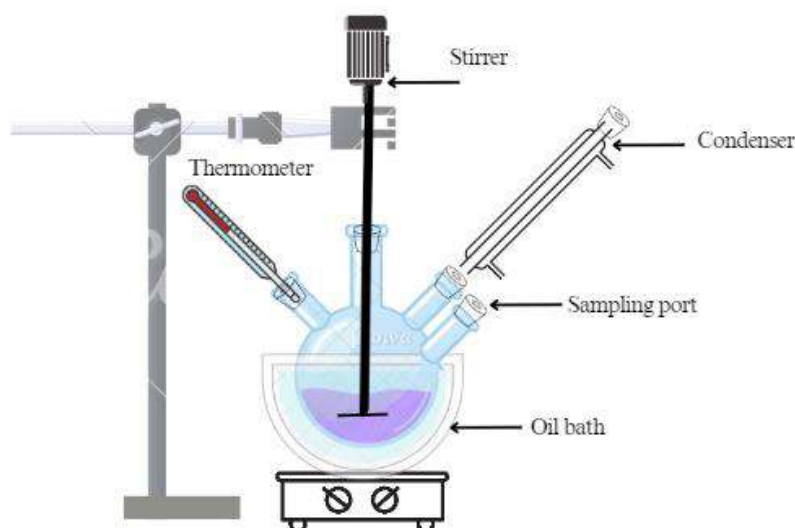


Fig. 1 Schematic representation of experimental setup.

## 3. Results and Discussion

### 3.1 Catalyst Characterization

X-ray diffraction (XRD) indicated that different sulfonated carbons have confirmed that these materials exhibit a structure consistent with amorphous carbon material (Konwar, Mäki-Arvela, & Mikkola, 2019). In Fig. 2, shows the presence of different peaks specific for each sample: doped carbon can be seen at  $25^\circ$  and  $45^\circ$ , which confirms that the support is carbonaceous in nature corresponding to the literature of Konwar et al. (2016) The AC-SO<sub>3</sub>H-180 catalyst curve exhibits peak  $2\theta = 50^\circ$  which suggest proper sulfonation with H<sub>2</sub>SO<sub>4</sub> (Radhika, Subadevi, Krishnaveni, Liu, & Sivakumar, 2018).

The elemental structure for the AC-SO<sub>3</sub>H catalysts are shown in Fig. 4a, the doped resulted AC-SO<sub>3</sub>H catalyst is perceived to be C = 82.32%, O = 10.95% and S = 7.37% as shown in table 1. It is evident in the SEM micrographs that have been provided for sulfonated carbon on activated carbon. Moreover, It was show that the AC-SO<sub>3</sub>H-180 was highly amorphous and porosity

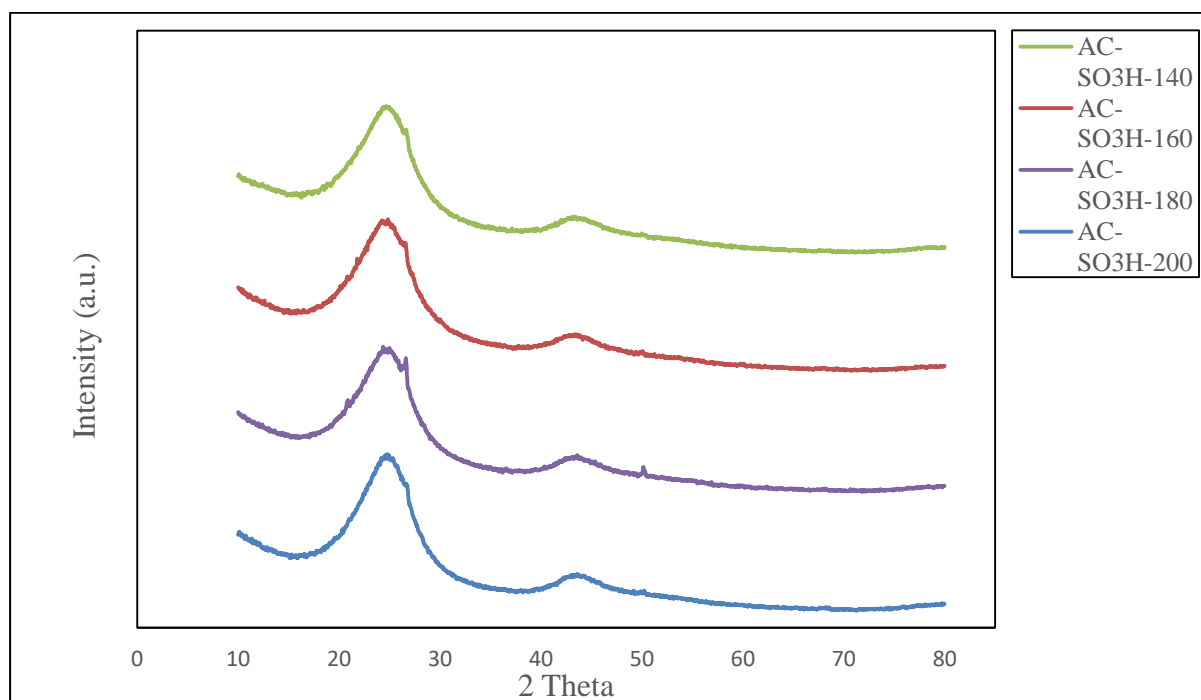


Fig. 2 X-ray diffraction (XRD) for AC-SO<sub>3</sub>H catalysts analysis



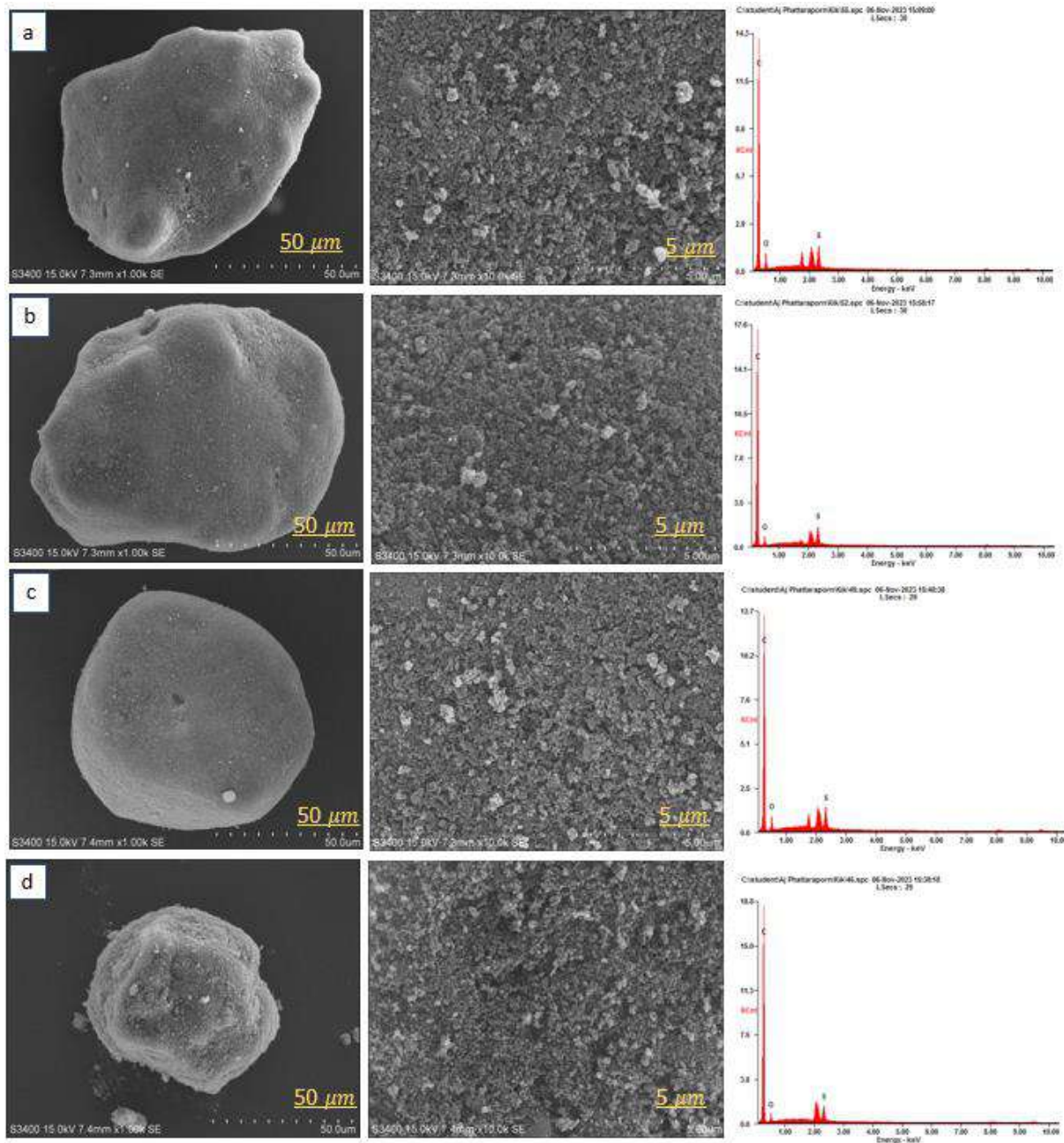


Fig.3 SEM-EDS images of (a) AC-SO<sub>3</sub>H-140, (b) AC-SO<sub>3</sub>H-160, (c) AC-SO<sub>3</sub>H-180, (d) AC-SO<sub>3</sub>H-200

Table 1 EDS analysis of catalysts.

Catalyst	Content of element; wt%		
	C	O	S
AC-SO <sub>3</sub> H-140	82.32	10.95	6.74
AC-SO <sub>3</sub> H-160	85.97	7.76	6.28
AC-SO <sub>3</sub> H-180	82.31	10.32	7.37
AC-SO <sub>3</sub> H-200	87.24	7.14	5.62

### 3.2 The Effect of temperature for catalyst preparation.

The catalytic activities of the AC-SO<sub>3</sub>H catalysts were confirmed by conducting the esterification of oleic acid with glycerol as shown in Fig. 4. Additionally, esterification experiments were conducted with only the AC support to assess the reaction activity under comparable conditions in the absence of the sulfonated catalysts. AC support had the lowest oleic acid (OA) conversion at 90 min while AC-SO<sub>3</sub>H-180 had the highest OA conversion among all the AC-SO<sub>3</sub>H catalysts. This indicates that sulfonation temperature has a dominant effect on the catalytic activities of the sulfonated AC catalysts. It should be noted that total acid site density appeared to affect significantly the activities for OA esterification. The catalysts with higher SO<sub>3</sub>H acid site densities trended to have higher conversions of OA, total acid site density shown in Table 2. Therefore, AC-SO<sub>3</sub>H-180 was used to further study the effect of operating parameters for the esterification of OA.

Table 2 Catalysts acid value.

Catalysts	Total acid site density (mmol/g)
AC	0.042
AC-SO <sub>3</sub> H-140	0.959
AC-SO <sub>3</sub> H-160	0.944
AC-SO <sub>3</sub> H-180	0.963
AC-SO <sub>3</sub> H-200	0.961

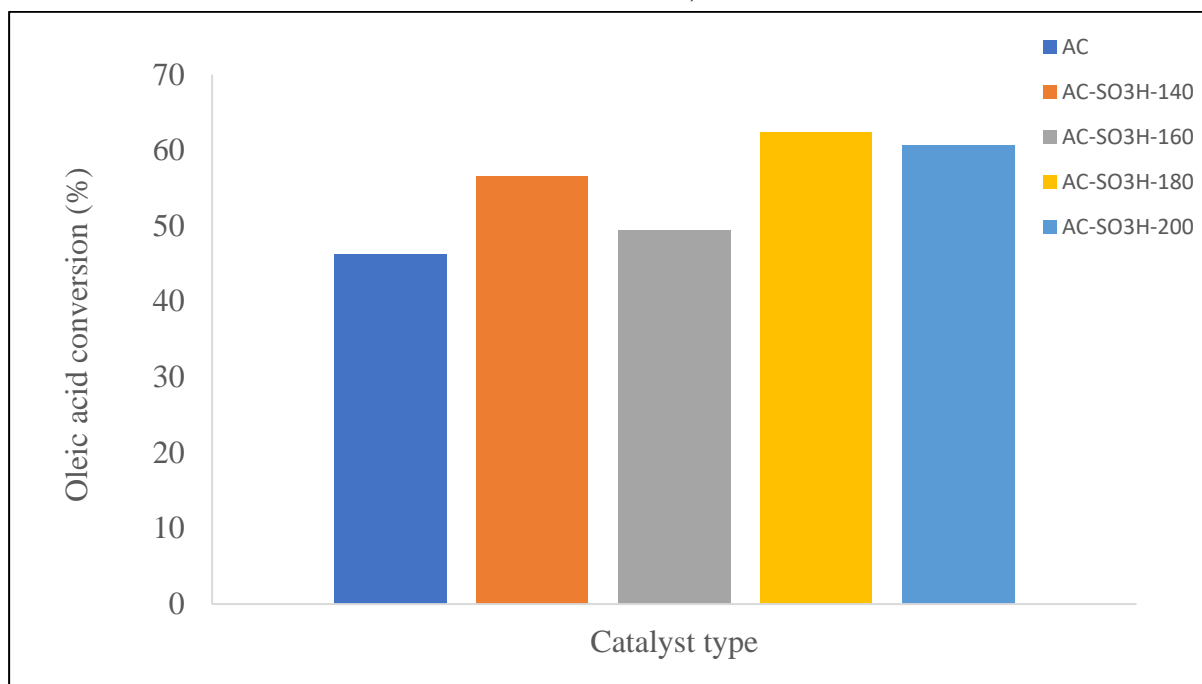


Fig 4. The effect of temperature for catalyst preparation (Gly/OA mole ratio 5:1; reaction temperature 150 °C; reaction time 180 min; catalyst loading 1.0 wt.% of total weight).

### 3.3 The Effect of operating condition

To investigate the effect of AC-SO<sub>3</sub>H-180 catalyst loading, four different amounts of catalyst (0.5 wt %, 1 wt %, 2 wt %, 3 wt %) were selected to perform reaction at Gly/OA mole ratio of 1:5, and reaction temperature of 150 °C. Fig. 5 shows an increase in the amount of catalyst, increasing the OA conversion up to 2% wt., and then a constant decrease. The maximum conversion was recorded at 2 wt. %, the reduced conversion of OA with excess catalyst may be attributed to an increase in the viscosity of the reaction mixture (Kedir, Wondimu, & Weldegrum, 2023).

Fig. 6 shows the effect of reaction temperature on the esterification of oleic and glycerol using AC-SO<sub>3</sub>H-180 loading of 2 wt.% of total weight of reactants at GL/OA molar ratio of 5:1, and varying reaction time. The temperature is an important factor for conversion of oleic acid. The oleic acid conversion increased from 23.4% to 70.7% when the reaction temperature increased from 130 °C to 170 °C at reaction time of 120 min. It can be seen that the increase in the reaction temperature significantly increase the oleic conversion based on the Arrhenius's law. Additionally, it is widely recognized that reaction temperature influences the solubility of glycerol in oleic acid (Mamtani, Shahbaz, & Farid, 2021). Therefore, higher temperatures enhance the effective glycerol concentration in the OA phase favoring drive the esterification rate (Sudiby, Rochmadi, & Fahrurrozi, 2017).

Table 3 is a comparison of catalyst performance in esterification of oleic acid with glycerol by different heterogeneous catalysts. Although the oleic acid (OA) conversion for AC-SO<sub>3</sub>H-180 (60.4%) might seem lower compared to [ME/SO<sub>3</sub>H]-MCM-41 (96.0%), it still demonstrates a reasonable level of conversion, especially considering the simplicity of the

process. It can be noted that AC-SO<sub>3</sub>H-180 is a green promising heterogeneous catalyst for esterification of oleic and glycerol.

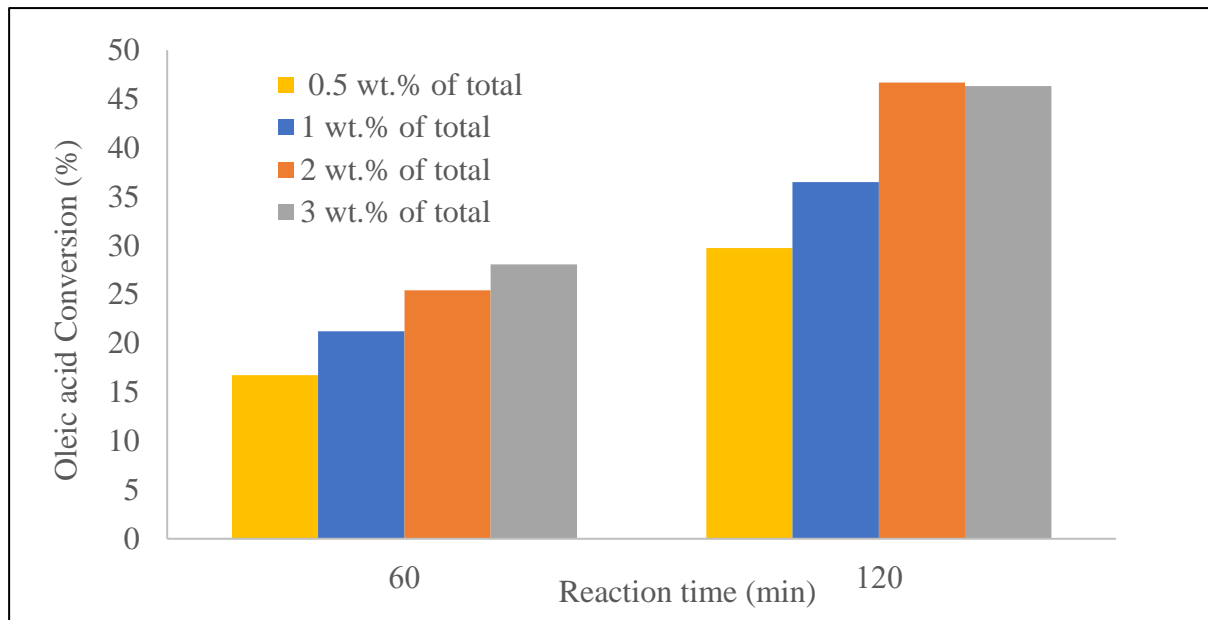


Fig. 5 Conversion of oleic acid at different catalyst loading (GL/OA mole ratio 5:1; AC-SO<sub>3</sub>H-180 catalyst concentration of 1 wt.% of total weight and reaction temperature of 150 °C)

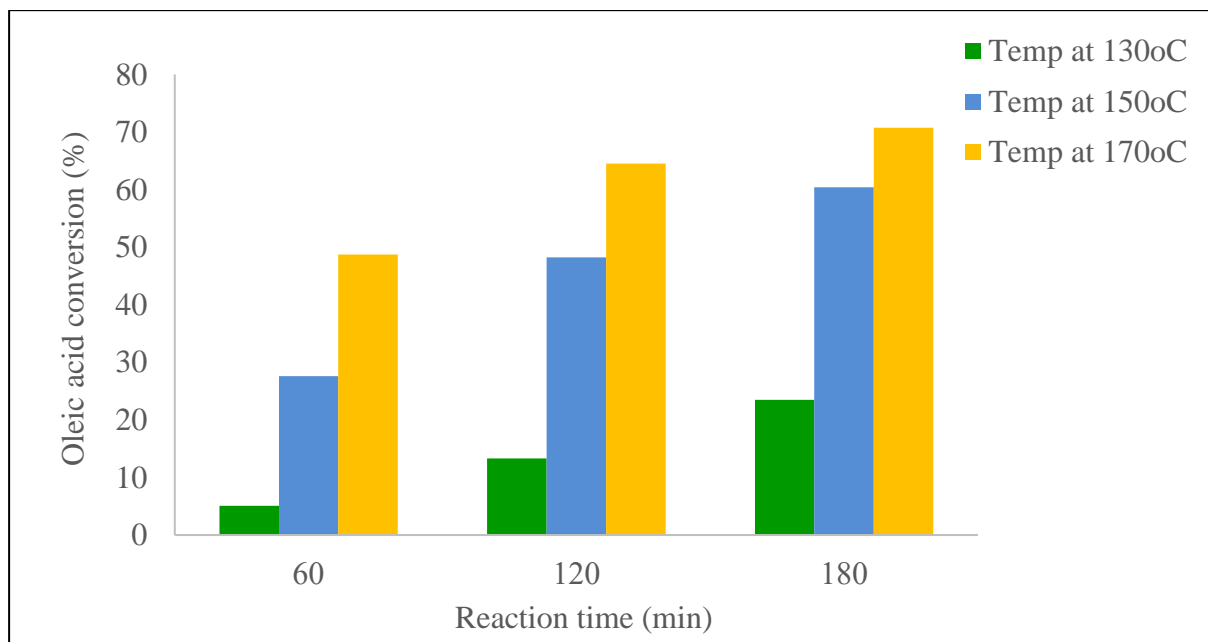


Fig. 6 Effect of reaction temperature ((GL/OA mole ratio 5:1; AC-SO<sub>3</sub>H-180 catalyst concentration of 2 wt.% of total weight)

Table 3 Comparison of catalyst performance in esterification of oleic acid with glycerol by different heterogeneous catalysts

Catalysts	T (°C)	GL:O A	Reaction time (min)	OA conversion %	Ref.
AC-SO <sub>3</sub> H -180	150	5:1	180	60.4	This work
[ME/SO <sub>3</sub> H]- MCM-41 (Modified MCM- 41 with sulfonic acid)	150	1:1	360	96.0	(Díaz, Márquez- Alvarez, Mohino, Pérez-Pariente, & Sastre, 2000)
ZnO/Zeolite	150	4:1	360	62	(Singh, Patidar, Ganesh, & Mahajani, 2013)

#### 4. Conclusion

The esterification of oleic acid conversion was investigated using a sulfonation activated carbon catalyst (AC-SO<sub>3</sub>H). It found that AC-SO<sub>3</sub>H -180 catalyst exhibited the highest oleic acid conversion due to the highest total acid site density corresponding to the total acid density and SEM-EDS results. As-prepared SAC-180 catalyst shows excellent catalytic performance, 70.75% of oleic acid conversion was obtain at reaction temperature of 170 °C, catalyst loading of 2 %wt. and reaction time 180 min. It can be noted that AC-SO<sub>3</sub>H-180 is a green promising heterogeneous catalyst for esterification of oleic and glycerol .Emerging research on the use of abundantly and naturally available resources such as carbon as catalyst has the potential to significantly enhance the effectiveness of biomass-based catalysts for sustainable monoglyceride production.

#### Acknowledgment

This research has received funding support from the NSRF via the Program Management Unit from Human Resources & Institutional Development, Research and Innovation (Grant number B05F640085).

#### References

- Alashek, F., Keshe, M., & Alhassan, G. (2022). Preparation of glycerol derivatives by entered of glycerol in different chemical organic reactions: A review. *Results in Chemistry*, 4, 100359. doi: <https://doi.org/10.1016/j.rechem.2022.100359>
- Badday, A. S., Abdullah, A. Z., Lee, K. T., & Khayoon, M. S. (2012). Intensification of biodiesel production via ultrasonic-assisted process: A critical review on fundamentals and recent development. *Renewable and Sustainable Energy Reviews*, 16(7), 4574-4587. doi: <https://doi.org/10.1016/j.rser.2012.04.057>

- Díaz, I., Márquez-Alvarez, C., Mohino, F., Pérez-Pariente, J. n., & Sastre, E. (2000). Combined Alkyl and Sulfonic Acid Functionalization of MCM-41-Type Silica: Part 2. Esterification of Glycerol with Fatty Acids. *Journal of Catalysis*, *193*(2), 295-302. doi: <https://doi.org/10.1006/jcat.2000.2899>
- Kedir, W. M., Wondimu, K. T., & Weldegrum, G. S. (2023). Optimization and characterization of biodiesel from waste cooking oil using modified CaO catalyst derived from snail shell. *Heliyon*, *9*(5), e16475. doi: <https://doi.org/10.1016/j.heliyon.2023.e16475>
- Konwar, L. J., Mäki-Arvela, P., Kumar, N., Mikkola, J.-P., Sarma, A. K., & Deka, D. (2016). Selective esterification of fatty acids with glycerol to monoglycerides over –SO<sub>3</sub>H functionalized carbon catalysts. *Reaction Kinetics, Mechanisms and Catalysis*, *119*(1), 121-138. doi:10.1007/s11144-016-1040-7
- Konwar, L. J., Mäki-Arvela, P., & Mikkola, J.-P. (2019). SO<sub>3</sub>H-Containing Functional Carbon Materials: Synthesis, Structure, and Acid Catalysis. *Chemical Reviews*, *119*(22), 11576-11630. doi:10.1021/acs.chemrev.9b00199
- Lilja, J., Murzin, D. Y., Salmi, T., Aumo, J., Mäki-Arvela, P., & Sundell, M. (2002). Esterification of different acids over heterogeneous and homogeneous catalysts and correlation with the Taft equation. *Journal of Molecular Catalysis A: Chemical*, *182-183*, 555-563. doi: [https://doi.org/10.1016/S1381-1169\(01\)00495-2](https://doi.org/10.1016/S1381-1169(01)00495-2)
- Mamtani, K., Shahbaz, K., & Farid, M. M. (2021). Glycerolysis of free fatty acids: A review. *Renewable and Sustainable Energy Reviews*, *137*, 110501. doi: <https://doi.org/10.1016/j.rser.2020.110501>
- Radhika, G., Subadevi, R., Krishnaveni, K., Liu, W. R., & Sivakumar, M. (2018). Synthesis and Electrochemical Performance of PEG-MnO<sub>2</sub>-Sulfur Composites Cathode Materials for Lithium-Sulfur Batteries. *J Nanosci Nanotechnol*, *18*(1), 127-131. doi:10.1166/jnn.2018.14568
- Rastegari, H., & Ghaziaskar, H. S. (2015). From glycerol as the by-product of biodiesel production to value-added monoacetin by continuous and selective esterification in acetic acid. *Journal of Industrial and Engineering Chemistry*, *21*, 856-861. doi: <https://doi.org/10.1016/j.jiec.2014.04.023>
- Singh, D., Patidar, P., Ganesh, A., & Mahajani, S. (2013). Esterification of Oleic Acid with Glycerol in the Presence of Supported Zinc Oxide as Catalyst. *Industrial & Engineering Chemistry Research*, *52*(42), 14776-14786. doi:10.1021/ie401636v
- Sudibyo, H., Rochmadi, R., & Fahrurrozi, M. (2017). Kinetic Study of Palm Fatty Acid Distillate Esterification with Glycerol over Strong Acidic Cation Exchanger Tulsion 42SM. *Engineering Journal*, *21*(1), 45-61.
- Tang, X., & Niu, S. (2019). Preparation of carbon-based solid acid with large surface area to catalyze esterification for biodiesel production. *Journal of Industrial and Engineering Chemistry*, *69*, 187-195. doi: <https://doi.org/10.1016/j.jiec.2018.09.016>

## Effect of Surface Functional Group on Siliceous Zirconia for Glycerol Acetylation with Acetic Acid

**Kochakorn Boonkhong<sup>1,\*</sup>, Weerinda Mens<sup>2</sup>, Kanokwan Ngaosuwan<sup>3</sup>,  
Worapon Kiatkittipong<sup>4</sup>, Doonyapong Wongsawaeng<sup>5</sup>, Santi Chueter<sup>6</sup>,  
Apiluck Eiad-ua<sup>7</sup> and Suttichai Assabumrungrat<sup>1,8</sup>**

<sup>1</sup> Center of Excellence on Catalysis and Catalytic Reaction Engineering, Department of Chemical Engineering, Faculty of Engineering, Chulalongkorn University, Bangkok 10330, Thailand

<sup>2</sup> Department of Chemical and Materials Engineering, Faculty of Engineering, Rajamangala University of Technology Thanyaburi, Pathum Thani 12110, Thailand

<sup>3</sup> Chemical Engineering Division, Engineering Faculty, Rajamangala University of Technology Krungthep, Bangkok 10120, Thailand

<sup>4</sup> Department of Chemical Engineering, Faculty of Engineering and Industrial Technology, Silpakorn University, Nakhon Pathom 73000, Thailand

<sup>5</sup> Research Unit on Plasma Technology for High-Performance Materials Development, Department of Nuclear Engineering, Faculty of Engineering, Chulalongkorn University, Bangkok 10330, Thailand

<sup>6</sup> Department of Chemical Engineering, Faculty of Engineering, King Mongkut's University of Technology North Bangkok, Bangkok 10800, Thailand

<sup>7</sup> College of Materials Innovation and Technology, King Mongkut's Institute of Technology Ladkrabang, Chalongsong Rd., Ladkrabang (KMILT), Bangkok 10520, Thailand

<sup>8</sup> Bio-Circular-Green-economy Technology & Engineering Center (BCGeTEC), Department of Chemical Engineering, Faculty of Engineering, Chulalongkorn University, Bangkok 10330, Thailand

E-mail: \* Corresponding: kochakornbooncong@gmail.com

### Abstract

Glycerol acetylation with acetic acid produces a mixture of mono-, di-, and tri-acetins, which have significant commercial value and are used in various industries such as cosmetics, plastic, and food. In the present study, siliceous zirconia (SZ) was functionalized with sulfuric acid and 12-tungstophosphoric acid to generate sulfonated SZ catalysts. The catalysts were characterized using X-ray diffraction (XRD), thermogravimetric analysis (TGA), scanning electron microscope energy-dispersive X-ray spectroscopy (SEM-EDS), and Fourier Transform Infrared Spectroscopy (FTIR). The effects of operating parameters including surface groups on the SZ catalyst, reaction temperature, and reaction time were investigated at a glycerol-to-acetic acid molar ratio of 1:9. The sulfuric acid-loaded SZ catalyst showed excellent catalytic performance to obtain 97.8% of glycerol conversion, and 51.8% of di-acetin yield at a reaction temperature of 110°C and reaction time 60 min. In addition, increasing the reaction temperature showed a significant increase in di-acetin selectivity.

**Keywords:** Acetylation; Glycerol; Acetic acid; Acetins; Heterogeneous catalyst.

### 1. Introduction

Currently, global biodiesel production amounts to approximately 21 million tons per year. In the process of biodiesel synthesis through the transesterification of oil and alcohol, glycerol (Gly) is generated as the primary by-product, constituting approximately 10% of the

biodiesel yield (Mamtani, Shahbaz, & Farid, 2021; Rashid, Anwar, Moser, & Ashraf, 2008). As a result, this sector produces a Gly surplus that raises economic and environmental concerns. Hence, there is a pressing need for novel approaches to convert glycerol into high-value chemicals, aiming to enhance the economic viability of biodiesel production and address environmental concerns. The acetylation process of glycerol with acetic acid offers a pathway to produce valuable products, including mono-, di-, and tri-acetins, all of which carry considerable commercial significance (Sedghi et al., 2022). These compounds find practical applications across various industries, such as cosmetics, plastics, and food production. (Shehayeb et al., 2021).

The glycerol acetylation to acetins is commonly carried out using homogeneous acid catalysts, such as sulfuric acid (H<sub>2</sub>SO<sub>4</sub>) (Abida & Ali, 2020a) or p-toluenesulfonic acid (PTA) (Bachiller-Baeza & Anderson, 2004). While these catalysts facilitate high process efficiency, their utilization presents several drawbacks, including challenges in product separation and purification, catalyst reuse, and equipment corrosion protection (Malaika, Ptaszyńska, Gaidukevič, & Kozłowski, 2022). Therefore, heterogeneous acid catalysts offer non-corrosive characteristics, environmental friendliness, and fewer challenges in disposal (Sun, Tong, Yu, & Wan, 2016). Moreover, solid catalysts can be more easily separated from products and can be reused. A variety of the heterogeneous acid catalysts such as sulfated zirconia (SZ), MoO<sub>3</sub>-SiO<sub>2</sub> (Hlatshwayo, Ndolomingo, Bingwa, & Meijboom, 2021), ZrO<sub>2</sub>, TiO<sub>2</sub>-ZrO<sub>2</sub>, WO<sub>3</sub>/TiO<sub>2</sub>-ZrO<sub>2</sub>, and MoO<sub>3</sub>/TiO<sub>2</sub>-ZrO<sub>2</sub> (Reddy, Sudarsanam, Raju, & Reddy, 2010), have been explored for the Gly acetylation. SZ has been known to give high activity and selectivity in Gly acetylation. However, due to the high crystallinity of ZrO<sub>2</sub> and often low specific surface area, the accessibility of active sites remains limited. To decrease this limitation, employing a combination of ZrO<sub>2</sub> with an amorphous support such as silica oxide may offer advantages. The use of a high surface area support facilitates the accessibility of active species, while zirconia serves to chemically stabilize heteropolyacids (Kuzminska, Kovalchuk, Backov, & Gaigneaux, 2014).

Therefore, this study aimed to explore the effect of surface functional groups on siliceous zirconia (SZ) for glycerol acetylation with acetic acid. SZ was functionalized with sulfuric acid and 12-tungstophosphoric acid to generate sulfonated SZ catalysts. The catalysts were characterized using X-ray diffraction (XRD), thermogravimetric analysis (TGA), scanning electron microscope energy-dispersive X-ray spectroscopy (SEM-EDS), and Fourier Transform Infrared Spectroscopy (FTIR). The effects of operating parameters including surface groups on the SZ catalyst, reaction temperature, and reaction time were investigated at a glycerol-to-acetic acid molar ratio of 1:9. The production of mono-, di-, and tri-acetins were analyzed using gas chromatography (GC).

## 2. Materials and Methods

### 2.1 Materials

In this research, various chemicals were employed, including Glycerol (AR grade) 99.5% and Sulphuric Acid (AR grade) 98.0% obtained from Quality Reagent Chemical (QREC). Acetic acid (Glacial) 100.0% and Tungstophosphoric acid hydrate were sourced from Supelco, along with Tetraethoxysilane (TEOS) 98.0%, Zirconium dichloride oxide 98.0%, and



Glycerol monoacetate from Thermo Scientific. Additionally, Diacetin (Technical grade) 50.0%, Glyceryl triacetate (>99.0%), Isopropyl acetate, and Glycerol (GC grade) (>99.0%) were obtained from Sigma-Aldrich. Ammonia (30.0%) was procured from Panreac AppliChem ITW Reagents.

## 2.2 Catalyst Preparation

The catalyst was prepared by the sol-gel method (Abida & Ali, 2020a). Zirconium oxychloride ( $ZrOCl_2 \cdot 8H_2O$ ) was dissolved in DI water, with a volume of 20 mL. Subsequently, the solution was transferred to a beaker under constant stirring at a temperature of 35 °C. Once this step is completed, ammonium hydroxide solution (1 M) was added dropwisely until reaching a pH of 10, and continuous stirring for 15 min. Next, tetraethoxyorthosilicate (TEOS, 98%) was slowly added with a Si/Zr ratio of 1:1 under continuous stirring for 1 hr at 35 °C. After completing this step, the resulting mixture was filtered and washed with DI water until the pH was 7. The product was then dried at 110 °C for 12 hr. Finally, the catalyst, named SZ, undergoes a process in a carbolite furnace at a temperature of 550 °C for 4 hr, and it was designated as SZ-550. After synthesizing SZ successfully, the process can incorporate sulphuric acid ( $H_2SO_4$ ) and tungstophosphoric acid hydrate (TPA) to introduce the sulfate ion into the matrix. This involves adding  $H_2SO_4$  and TPA at a concentration of 1 molar (3 ml) and stirring the mixture at 35°C for 24 hr. The resulting mixture was dried at 110 °C for 12 hr and then calcined using carbolite furnaces at a temperature of 550 °C for 4 hr. This procedure resulted in the formation of two catalysts, SSZ-550 and TSZ-550.

## 2.3 Catalyst Characterization

The X-ray diffraction (XRD) measurements were conducted using a Bruker D8 Advance diffractometer equipped with Cu  $K\alpha$  radiation ( $\lambda = 1.5418 \text{ \AA}$ ). Thermogravimetric Analysis (TGA) analytical technique was employed to examine weight variations in samples during heating, utilizing the SDT Q600 instrument within a temperature range from room temperature up to 900°C. The Scanning Electron Microscope (SEM) was employed for the examination of surface structures. The specific model utilized is the S-3400N by Hitachi, with a serial number 340637-09. Additionally, Energy-Dispersive X-ray Spectroscopy (EDS) was employed for chemical analysis. The chemical composition is analyzed using the Apollo X model by EDAX, and the instrument was identified by the serial number 2371. The Fourier-transform infrared spectroscopy (FTIR) method, utilizing the Bruker Alpha II instrument, was employed to analyze functional groups on the surface in the range of 2,600 to 600  $cm^{-1}$ .

## 2.4 Acetylation of glycerol with acetic acid

The acetylation of glycerol with acetic acid was carried out in a three-necked glass reactor. The reaction occurred in a 250 mL three-necked glass reactor equipped with a magnetic bar, condenser, and thermometer. Glycerol and acetic acid were mixed in a molar ratio of 1:9 in the glass reactor and heated in an oil bath to the required temperature. When the desired temperature was reached, the catalyst (3% by weight relative to the glycerol) was then added to start the reaction. The samples, approximately 1.5 mL each, were collected at a specific time

interval. The mixture was centrifuged to separate the catalyst powder from the sample and analyzed by the GC method.

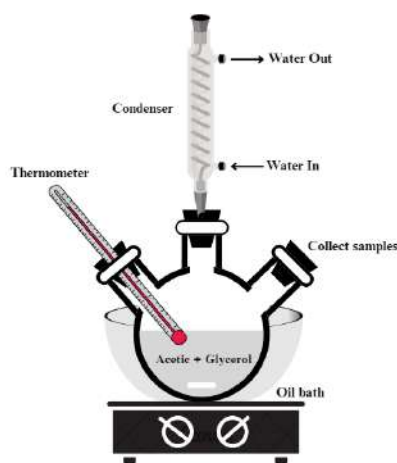


Fig. 1 Schematic representation of experimental setup.

## 2.5 Methods

Quantitative analyses of the products were carried out using a gas chromatograph (GC-2010 plus) from SHIMADZU CORPORATION with an auto-injector. A Zebron capillary column (ZB-5HT INFERNO) was used. The column dimensions are 30 m × 0.25 mm × 0.25 μm. Helium was used as a carrier gas with a flow rate of 0.7 mL/min. The injection volume was 1 μL of a standard sample (20-100 mg) dissolved in 20 mL of isopropyl acetate. The inlet and detector temperature were set at 250 °C. The column temperature program was set as follows, 70°C hold for 5 min, followed by a ramping of 1 °C/min until reaching 130 °C, where it was held for an additional 10 min (Nebel, Mittelbach, & Uray, 2008).

## 3. Results and Discussion

### 3.1 Characterization of catalysts

The XRD patterns of siliceous zirconia (SZ-550), H<sub>2</sub>SO<sub>4</sub>-siliceous zirconia (SSZ-550), and TPA-siliceous zirconia (TSZ-550) are depicted in Fig. 2. SZ-550 catalyst only exhibited the typical broad band of amorphous solids associated to the framework of mesoporous silica as shown in Fig. 2(a). After the SZ-550 matrix was modified with H<sub>2</sub>SO<sub>4</sub>, the crystallization of sulfur was obtained, as shown in Fig. 2 (b). The main peaks indicate the crystallization of H<sub>2</sub>SO<sub>4</sub> as the primary phase at 2θ = 22.3, 23.08, 25.4, 25.84, 27.2, 27.8, 31.4, 32.5, 37.04, 38.1, 46.2, 47.8, 56.6, and 57.5 (Radhika, Subadevi, Krishnaveni, Liu, & Sivakumar, 2018). For ZrSiO<sub>2</sub> as the secondary phase showed the characteristic peaks at 2θ = 22.2, 22.5, 31.1, 36.2, 37.1, 37.5, 40.8, 45.3, 48.2, 52.9 and 53.7 (De la Rosa-Cruz, Diaz-Torres, Salas, Castano, & Hernandez, 2001). Additionally, the XRD pattern of TSZ showed the characteristic peaks of tungsten Keggin-structure at 2θ values of 22.8, 24.9, 31.2, 34.4, 36.5 and 42.5 (Huang, Wang, & Liu, 2020).

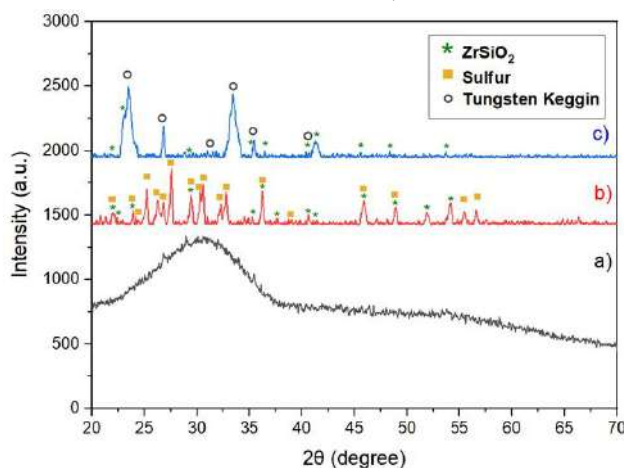


Fig. 2. XRD patterns of (a) SZ-550, (b) SSZ-550, and (c) TSZ-550.

Thermogravimetric analysis (TGA) was employed to investigate the thermal characteristics of all three catalysts, as shown in Fig. 3. For siliceous zirconia (SZ), the DTA curve presents two endothermic peaks centered at 50 and 210 °C, assigned to the loss of water and carboxylate ligands, respectively (Al-Hazmi, Choi, & Ablett, 2014). Fig. 3 (a) demonstrates that the weight loss is correlated with the nature of the carboxylate ligands of the precursors and clearly shows that the weight loss starts at room temperature and is complete around 550 °C. It can be concluded that the calcination temperature should be conducted at 550 °C. Furthermore, the TGA curve of the SSZ-550 catalyst shown in Fig. 3 (b), according to the presented data, SSZ-550 was quite thermally stable. The weight loss was reported at the temperature of 680 °C. Additionally, it can be observed from Fig. 3 (c) that the TSZ-550 samples differed from the SSZ-550. It showed higher weight loss at specific temperatures of TG analysis than the SSZ-550. Therefore TSZ-550 was quite thermally unstable.

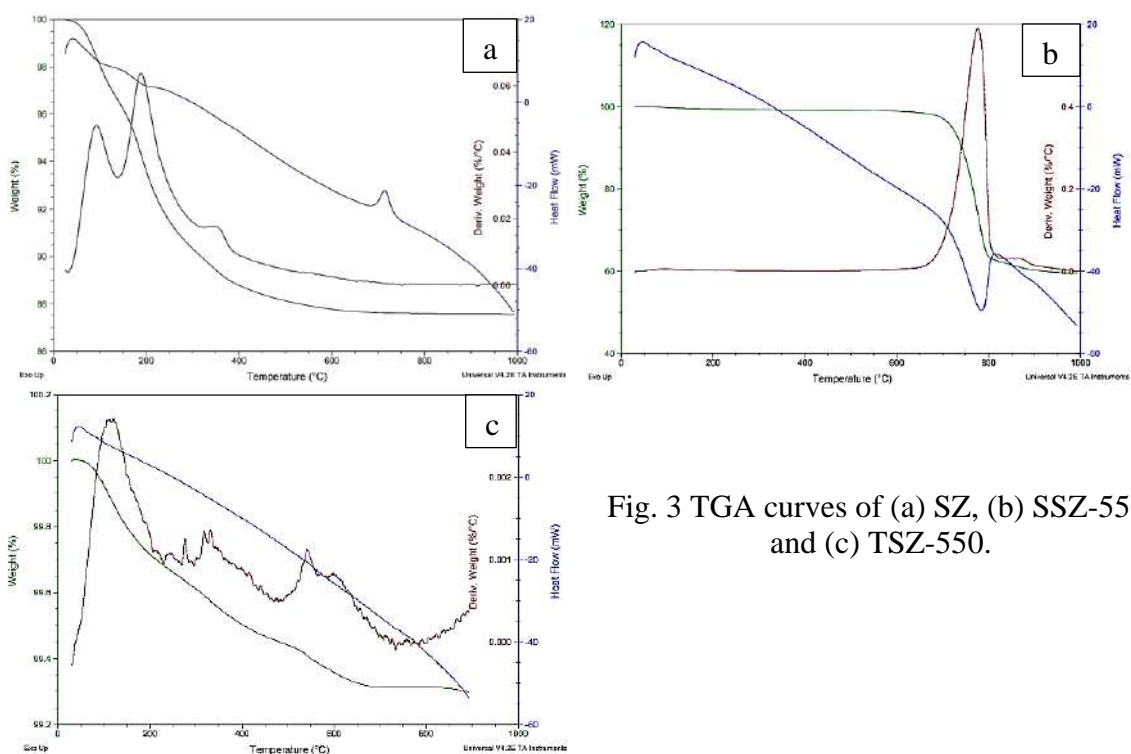


Fig. 3 TGA curves of (a) SZ, (b) SSZ-550, and (c) TSZ-550.

The scanning electron microscope (SEM) images of SZ-550, SSZ-550, and TSZ-550 catalysts are depicted in Fig. 4. The particle sizes of these catalysts were measured, revealing average particle sizes of 63.88  $\mu\text{m}$  for SZ-550, 72.22  $\mu\text{m}$  for SSZ-550, and 86.11  $\mu\text{m}$  for TSZ-550, as illustrated in Fig. 4(a), 4(b), and 4(c), respectively. While the particles of the SZ-550 catalyst exhibited uniformity, both SSZ-550 and TSZ-550 catalysts displayed particle aggregation. The elemental mapping and EDS results of three catalysts are presented in Table 1. For the SSZ-550 catalyst, the results showed the incorporation of both sulfur and oxygen, potentially indicating the formation of  $\text{SO}_3\text{H}$  groups within the SZ matrix. SSZ-550 contained 13.81% of sulfur, 37.11% of oxygen, 10.65% of silica, and 38.44% of zirconium. In addition, the composition analysis of TSZ-550, results demonstrated the presence of tungsten (W), phosphorus (P), oxygen (O), silica (Si), and zirconium (Zr) providing conclusive evidence for the existence of TPA ( $\text{H}_3\text{PW}_{12}\text{O}_{40}$ ), with tungsten being the primary element which refers to heteropoly acid.

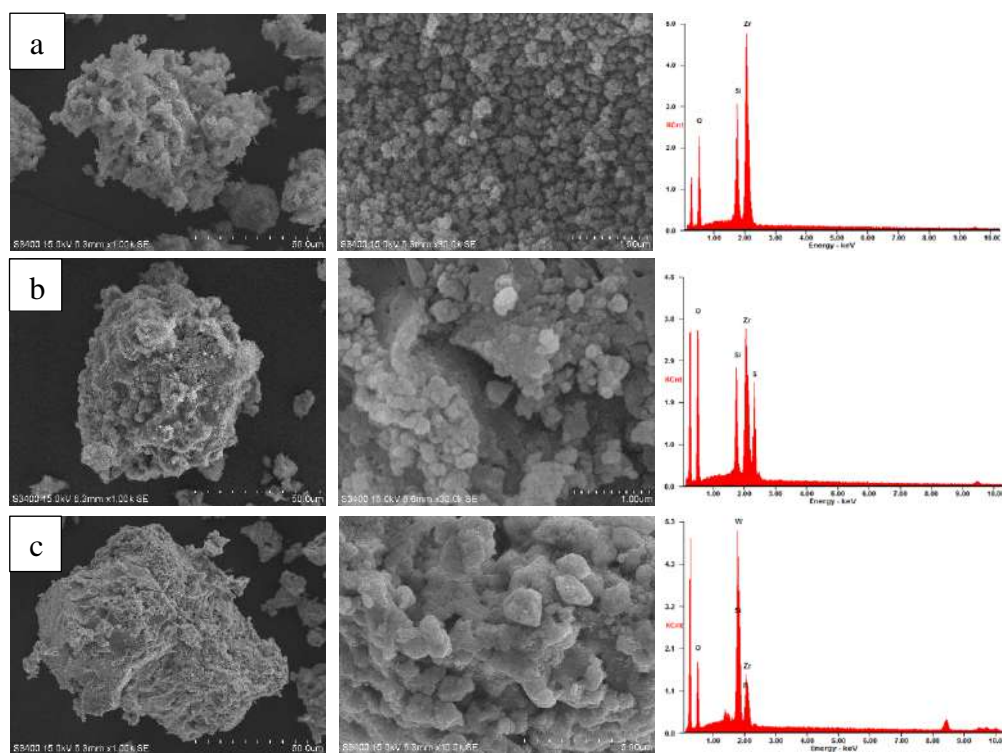


Fig. 4 SEM-EDS images of (a) SZ-550, (b) SSZ-550, and (c) TSZ-550.

Table 1 EDS analysis of catalysts.

Catalyst	Content of element; wt%					
	Zr	Si	O	S	W	P
a) SZ-550	61.34	13.09	25.57	-	-	-
b) SSZ-550	38.44	10.65	37.11	13.81	-	-
c) TSZ-550	15.32	2.49	12.4	-	69.48	0.31

The analysis of functional groups on the surface can be conducted using the FTIR technique. The FTIR spectra of SZ-550, SSZ-550, and TSZ-550 were presented in Fig. 5. In Fig. 5 (a) the FTIR spectra of SSZ-550, the sample show a band at  $\sim 810 \text{ cm}^{-1}$  and  $1087 \text{ cm}^{-1}$  due to the vibrations of M–O–M and O–M–O (where M=Zr/Si) (Verma, Rani, & Kumar, 2018). In the FTIR spectra, new bands in the range of approximately  $1010\text{--}1080 \text{ cm}^{-1}$  were observed in Fig. 2 (b), indicating stretching vibrations corresponding to S–O and S=O bonds. These findings support the incorporation of sulfate groups into the siliceous zirconia matrix. A similar observation was noted by Abida and Ali (Abida & Ali, 2020b), where the bands within the range of  $1028\text{--}1266 \text{ cm}^{-1}$  were reported, indicating the anchoring of sulfate ions onto the siliceous zirconia matrix. The FTIR spectrum of TSZ-550 presented in Fig. 5(c), It was shown that the bands at  $1084 \text{ cm}^{-1}$ ,  $983 \text{ cm}^{-1}$ , and  $890 \text{ cm}^{-1}$  were observed, indicating characteristic bands of 12-tungstophosphoric acid (Rao, Sekharnath, Sudhakar, Rao, & Subha, 2014).

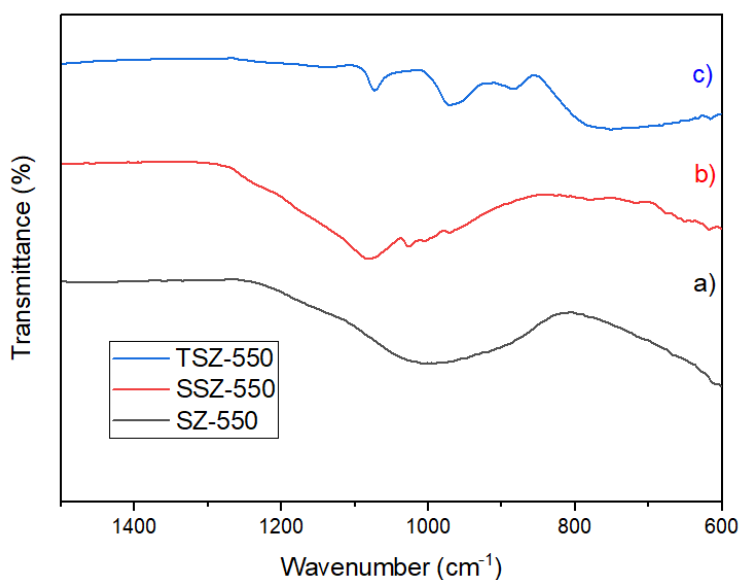


Fig.5 FT-IR spectras of (a) SZ-550, (b) SSZ-550 and (c) TSZ-550

### 3.2 Catalytic activity

The glycerol acetylation with acetic acid requires an active acid catalyst to achieve high rates. To compare the catalytic performance, the reaction was conducted under similar conditions without using catalysts, and with using SZ-550, SSZ-550, and TSZ-550 catalysts. The effect of catalyst type is presented in Fig. 6 and Fig. 7. At a reaction time of 90 min, the SSZ-550 catalyst exhibited the highest values for glycerol conversion ( $X_{\text{Gly}}$ ), and di-acetin yield ( $Y_{\text{DA}}$ ) of 64.51%, and 15.82%, respectively. Following that, TSZ-550 showed the  $X_{\text{Gly}}$ , and  $Y_{\text{DA}}$  of 33.17%, and 4.83%, respectively. This should be due to the acid functional group on the SZ matrix possessing the positive properties to catalyze the acetylation of glycerol with acetic acid. The SSZ-550 demonstrated a significant increase in the reaction rate due to the larger number of acid sites derived from  $\text{H}_2\text{SO}_4$  loading. Therefore, SSZ-550 was used to further study the effect of operating parameters for glycerol acetylation with acetic acid.

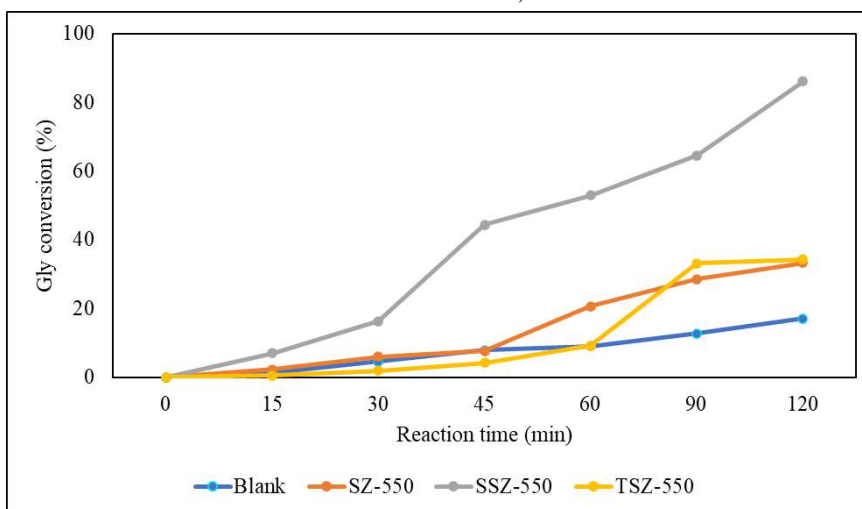


Fig. 6 Effect of catalyst type on the conversion of glycerol (Gly/AC mole ratio of 1:9; catalyst concentration of 3 wt.% of Gly, reaction temperature of 80 °C).

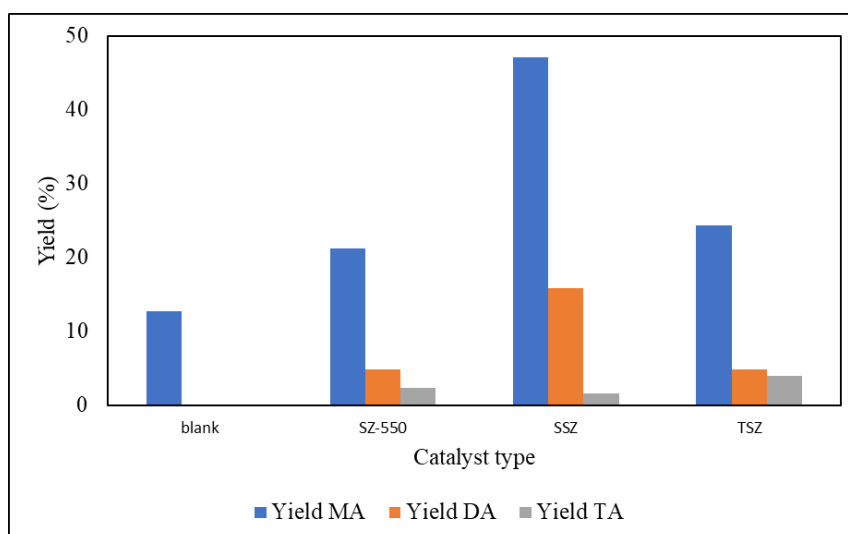


Fig. 7 Effect of catalyst type on acetins yield (Gly/AC mole ratio of 1:9; catalyst concentration of 3 wt.% of Gly, reaction temperature of 80 °C, and reaction time of 90 min).

Fig. 8 shows the effect of reaction temperature on glycerol conversion using SSZ-550 loading of 3 wt.% of Gly at Gly/AC mole ratio of 1:9, different reaction temperatures of 80°C to 110°C, and varying reaction time. At a reaction time of 60 min, the values of  $X_{Gly}$  were 52.9 and 97.8 at 80°C and 110 °C, respectively. The  $X_{Gly}$  was significantly increased when increasing the reaction temperature which corresponds the Arrhenius's law. In addition, the  $Y_{DA}$  reached 51.81% at a reaction temperature of 110 °C, while  $Y_{DA}$  was obtained at only 10.75% at 80°C as shown in Fig. 9. It was seen that increasing the reaction temperature from 80 to 110 °C enhances the  $S_{DA}$  and  $S_{TA}$  because amounts of DA and TA were also formed due to secondary reactions as shown in Fig. 10. (Keogh, Jeffrey, Tiwari, & Manyar, 2022).

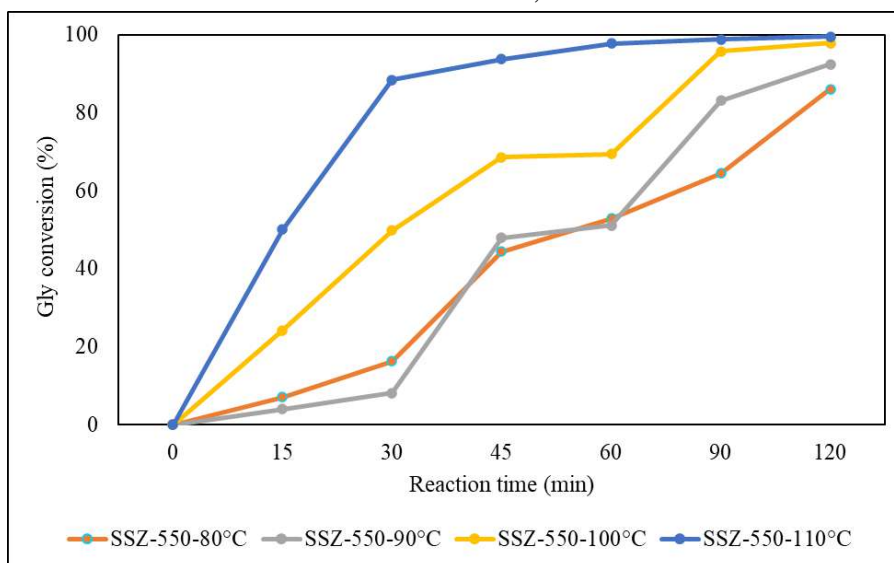


Fig.8 Conversion of glycerol at different reaction temperatures (Gly/AC mole ratio of 1:9; SSZ-550 catalyst concentration of 3 wt.% of Gly).

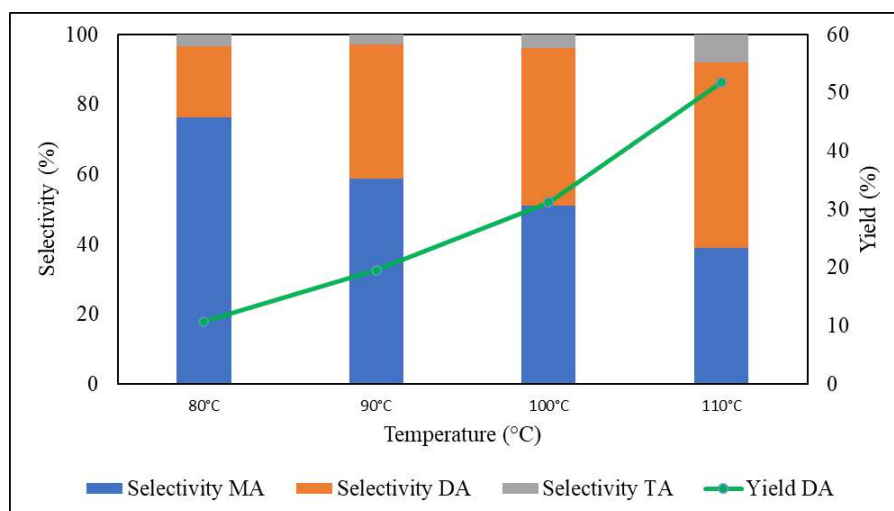


Fig. 9 Selectivity and yield at different reaction temperatures (Gly/AC mole ratio of 1:9; SSZ-550 catalyst concentration of 3 wt.% of Gly and reaction time of 60 min).

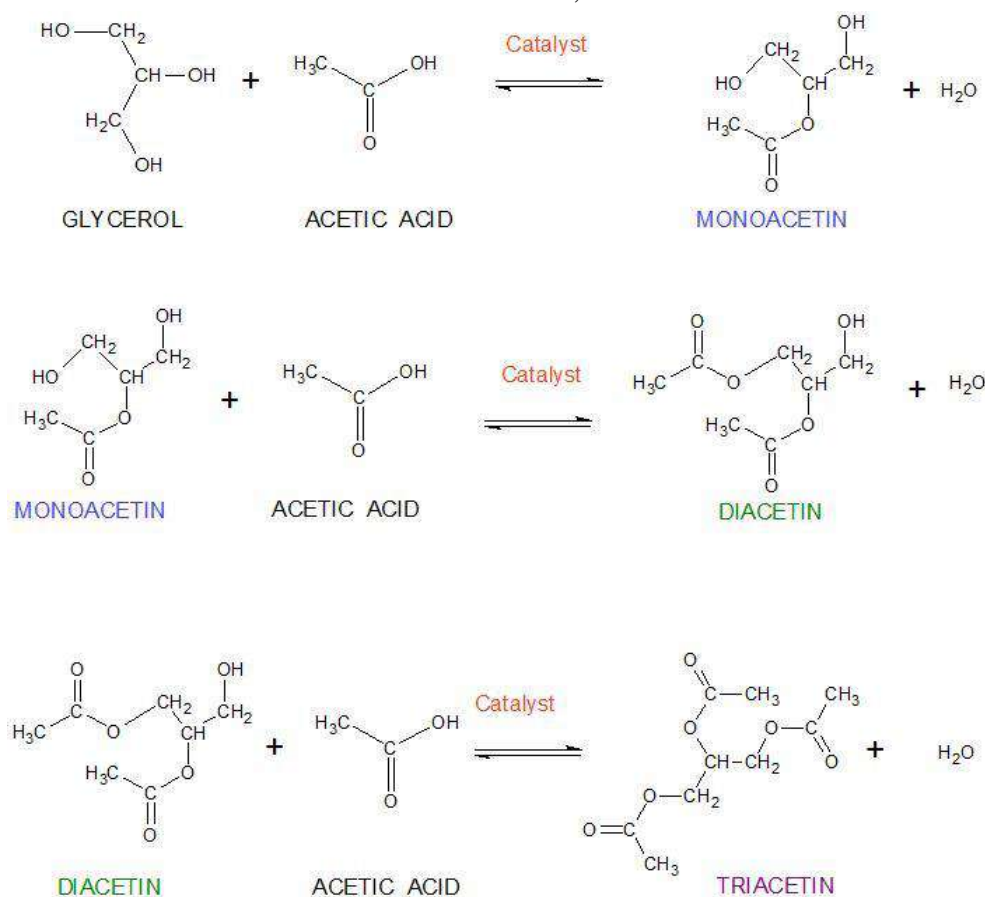


Fig. 10 Acetylation of glycerol reaction mechanism with Acetic Acid.  
(Kaya Ekinici & Oktar, 2019)

#### 4. Conclusions

The acetylation process of glycerol to produce acetins was investigated using various acid catalysts. Siliceous zirconia was prepared by the sol-gel method providing the surface acid functional groups of the sulfonated group. The effects of operating parameters including catalyst type (SZ-550, SSZ-550, and TSZ-550), reaction temperature, and reaction time were investigated. Based on the similar reaction condition, SSZ-550 demonstrated the highest performance compared to TSZ-550 and SZ-550. This suggests that SSZ-550 exhibited the best catalytic performance with high glycerol conversion and yields of DA and TA within just 60 min due to the high content of SO<sub>3</sub>H groups on the SZ surface. A 97.8 % glycerol conversion was obtained at the reaction temperature of 110 °C, SSZ-550 catalyst loading of 3 wt.% of Gly, and reaction time of 60 min. In addition, increasing the reaction temperature significantly increased the DA and TA yields.

#### Acknowledgment

The authors would like to express appreciation for the support of the NRCT-JSPS Grant via National Research Council of Thailand (NRCT) [Grant number N10A660366].



## Reference

- [1] Abida, K., & Ali, A. (2020a). Sulphuric acid-functionalized siliceous zirconia as an efficient and reusable catalyst for the synthesis of glycerol triacetate. *Chemical Papers*, 74, 3627-3639.
- [2] Abida, K., & Ali, A. (2020b). Sulphuric acid-functionalized siliceous zirconia as an efficient and reusable catalyst for the synthesis of glycerol triacetate. *Chemical Papers*, 74(10), 3627-3639. doi:10.1007/s11696-020-01189-z
- [3] Al-Hazmi, M. H., Choi, Y., & Apblett, A. W. (2014). Preparation of Zirconium Oxide Powder Using Zirconium Carboxylate Precursors. *Advances in Physical Chemistry*, 2014, 429751. doi:10.1155/2014/429751
- [4] Bachiller-Baeza, B., & Anderson, J. (2004). FTIR and reaction studies of the acylation of anisole with acetic anhydride over supported HPA catalysts. *Journal of Catalysis*, 228(1), 225-233.
- [5] De la Rosa-Cruz, E., Diaz-Torres, L., Salas, P., Castano, V., & Hernandez, J. (2001). Evidence of non-radiative energy transfer from the host to the active ions in monoclinic ZrO<sub>2</sub>: Sm<sup>3+</sup>. *Journal of Physics D: Applied Physics*, 34(14), L83.
- [6] Hlatshwayo, X. S., Ndolomingo, M. J., Bingwa, N., & Meijboom, R. (2021). Molybdenum-modified mesoporous SiO<sub>2</sub> as an efficient Lewis acid catalyst for the acetylation of alcohols. *RSC advances*, 11(27), 16468-16477.
- [7] Huang, X., Wang, W., & Liu, X. (2020). H<sub>3</sub>PW<sub>12</sub>O<sub>40</sub>-doped pyromellitic diimide prepared via thermal transformation as an efficient visible-light photocatalyst. *Journal of materials science*, 55, 8502-8512.
- [8] Kaya Ekinçi, E., & Oktar, N. (2019). Production of value-added chemicals from esterification of waste glycerol over MCM-41 supported catalysts. *Green processing and synthesis*, 8(1), 128-134.
- [9] Keogh, J., Jeffrey, C., Tiwari, M. S., & Manyar, H. (2022). Kinetic Analysis of Glycerol Esterification using Tin Exchanged Tungstophosphoric Acid on K-10. *Industrial & Engineering Chemistry Research*.
- [10] Kuzminska, M., Kovalchuk, T. V., Backov, R., & Gaigneaux, E. M. (2014). Immobilizing heteropolyacids on zirconia-modified silica as catalysts for oleochemistry transesterification and esterification reactions. *Journal of Catalysis*, 320, 1-8. doi:https://doi.org/10.1016/j.jcat.2014.09.016
- [11] Malaika, A., Ptaszyńska, K., Gaidukevič, J., & Kozłowski, M. (2022). The impact of surface groups of functionalized graphene on glycerol acetylation. *Fuel*, 313, 122987. doi:https://doi.org/10.1016/j.fuel.2021.122987
- [12] Mamtani, K., Shahbaz, K., & Farid, M. M. (2021). Glycerolysis of free fatty acids: A review. *Renewable and Sustainable Energy Reviews*, 137, 110501. doi:https://doi.org/10.1016/j.rser.2020.110501
- [13] Nebel, B., Mittelbach, M., & Uray, G. (2008). Determination of the composition of acetyl glycerol mixtures by <sup>1</sup>H NMR followed by GC investigation. *Analytical chemistry*, 80(22), 8712-8716.
- [14] Radhika, G., Subadevi, R., Krishnaveni, K., Liu, W.-R., & Sivakumar, M. (2018). Synthesis and electrochemical performance of PEG-MnO<sub>2</sub>-sulfur composites cathode materials for lithium-sulfur batteries. *Journal of Nanoscience and Nanotechnology*, 18(1), 127-131.
- [15] Rao, U. S., Sekharnath, K., Sudhakar, H., Rao, K. C., & Subha, M. (2014). Mixed matrix membranes of sodium alginate and hydroxy propyl cellulose loaded with

- phosphotungstic heteropolyacid for the pervaporation separation of water–isopropanol mixtures At 30 0 C. *Int J Sci Technol Res*, 3, 129-137.
- [16] Rashid, U., Anwar, F., Moser, B. R., & Ashraf, S. (2008). Production of sunflower oil methyl esters by optimized alkali-catalyzed methanolysis. *Biomass and Bioenergy*, 32(12), 1202-1205. doi:10.1016/j.biombioe.2008.03.001
- [17] Reddy, P. S., Sudarsanam, P., Raju, G., & Reddy, B. M. (2010). Synthesis of bio-additives: Acetylation of glycerol over zirconia-based solid acid catalysts. *Catalysis Communications*, 11(15), 1224-1228.
- [18] Sedghi, R., Shahbeik, H., Rastegari, H., Rafiee, S., Peng, W., Nizami, A.-S., . . . Pan, (2022). Turning biodiesel glycerol into oxygenated fuel additives and their effects on the behavior of internal combustion engines: A comprehensive systematic review. *Renewable and Sustainable Energy Reviews*, 167, 112805.
- [19] Shehayeb, S., Zaher, S., Ghannam, L., Srouf, H., Kanj, A., Shayah, J., & Karamé, I. (2021). Sustainable valorization of the abundant biodiesel byproduct-The glycerol. In *Handbook of Greener Synthesis of Nanomaterials and Compounds* (pp. 807-860): Elsevier.
- [20] Sun, J., Tong, X., Yu, L., & Wan, J. (2016). An efficient and sustainable production of triacetin from the acetylation of glycerol using magnetic solid acid catalysts under mild conditions. *Catalysis today*, 264, 115-122.
- [21] Verma, S., Rani, S., & Kumar, S. (2018). Tetragonal zirconia quantum dots in silica matrix prepared by a modified sol–gel protocol. *Applied Physics A*, 124(5), 387.

## Valorization of Glycerol via Esterification with Acetic Acid to Produce Di- and Tri-acetin

Wirat Kandee<sup>1,a</sup>, Kanokwan Ngaosuwan<sup>2,b,\*</sup>, Weerinda Mens<sup>3</sup>,  
Doonyapong Wongsawaeng<sup>4</sup>, Worapon Kiatkittipong<sup>5</sup>, Armando T. Quitain<sup>6</sup>,  
Tetsuya Kida<sup>7</sup>, Suttichai Assabumrungrat<sup>1,8</sup>

<sup>1</sup>Center of Excellence in Catalysis and Catalytic Reaction Engineering, Department of Chemical Engineering, Faculty of Engineering, Chulalongkorn University, Bangkok 10330, Thailand

<sup>2</sup>Chemical Engineering Division, Faculty of Engineering, Rajamangala University of Technology Krungthep, Bangkok 10120, Thailand

<sup>3</sup>Department of Chemical and Materials Engineering, Faculty of Engineering, Rajamangala University of Technology Thanyaburi, Pathum Than 12110, Thailand

<sup>4</sup>Research Unit on Plasma Technology for High-Performance Materials Development, Department of Nuclear Engineering, Faculty of Engineering, Chulalongkorn University, Bangkok 10330, Thailand

<sup>5</sup>Department of Chemical Engineering, Faculty of Engineering and Industrial Technology, Silpakorn University, Nakhon Pathom 73000, Thailand

<sup>6</sup>Center for International Education, Kumamoto University, 2-39-1 Kurokami, Chuo-ku, Kumamoto 860-8555, Japan Research Organization for Advanced Science and Technology (IROAST), Kumamoto University, 2-39-1 Kurokami, Chuo-ku, Kumamoto 860-8555, Japan

<sup>7</sup>Faculty of Advanced Science and Technology, Kumamoto University, 2-39-1 Kurokami, Chuo-ku, Kumamoto 860-8555, Japan

<sup>8</sup>Bio-Circular-Green-economy Technology & Engineering Center (BCGeTEC), Faculty of Engineering, Chulalongkorn University, Bangkok 10330, Thailand

E-mail: <sup>a</sup>wirat.kand@outlook.com, <sup>b</sup>kanokwan.n@mail.rmutk.ac.th

### Abstract

A renewable fuel, biodiesel, is an environmentally friendly and alternative resource for local availability which has potential to replace diesel. However, 10 kg of biodiesel production via transesterification produces 1 kg of glycerol as a byproduct. Crude glycerol from this process requires the distillation unit to increase purity of glycerol which is an extensive energy requirement. The glycerol esterification is one of potential process to produce bio-additive fuel as diacetin (DA) and triacetin (TA). The solid acid catalysts, namely, graphene oxide (GO), reduced graphene oxide (rGO) and 12 – tungstophosphoric acid (TPA) were selected to catalyze the glycerol esterification using acetic acid to glycerol molar ratio of 6:1, catalyst loading of 1 wt.% and reaction temperature of 110 °C for 2 h. It was found that TPA and rGO offered high glycerol conversion as well as high selectivity of DA and TA. The characterization results of catalyst supported their catalytic activities in term of active function groups including sulfonated group for rGO and heteropoly acid group for TPA.

**Keywords:** Glycerol esterification; 12-Tungstophosphoric acid (TPA); Graphene oxide (GO); Reduced graphene oxide (rGO); Acetin

### 1. Introduction

Biodiesel is a renewable fuel and has potential to replace diesel. It is an environmentally friendly and alternative source for local availability. It can be produced through a transesterification between a triglyceride derived from vegetable or animal fat or oil with alcohol. Glycerol is a byproduct from this biodiesel production process, which is 10 wt.% of glycerol produced following the stoichiometric basis [1]. The selling of crude glycerol can

reduce the cost of biodiesel production by only 6%. In addition, the huge amount of crude glycerol is generated leading to the relatively low profit from selling this glycerol. The effective usage and valorization of this glycerol could considerably improve the profitability of biodiesel production. One of the good choices to valorize glycerol is its glycerol esterification with acetic acid according to the following equations:



The products of this reaction are mono-, di- and triacetin (MA, DA and TA, respectively). Glycerol is mostly used in the food, cosmetic, plastic and pharmaceutical industries. Acetin derivative from glycerol esterification is widely used, especially DA and TA. DA and TA can be used as biodiesel additive as fuel enhancer to improve the viscosity and anti-knock properties of fuel as well as fuel additive to reduce the noxious gas emissions [2]. Glycerol esterification with acetic acid is a crucial process, traditionally catalyzed by homogeneous acid catalysts. However, these catalysts pose environmental and cost challenges. The change to heterogeneous catalysts, such as solid acid catalysts, presents a more practical and eco-friendly approach. 12-Tungstophosphoric acid (TPA) has recently gained considerable attention among heteropoly acids (HPAs) and could be replaced the mineral liquid acids such as H<sub>2</sub>SO<sub>4</sub>, HCl, HNO<sub>3</sub>, etc. [3]. However, the formation of water as a byproduct can have a great impact on the catalytic performance of some solid acid catalysts such as supported heteropoly acids (HPAs) because of high hydrophilic properties [4].

Heteropoly acids (HPAs) are versatile green catalysts. They showed high oxidizing ability, high acidity, good thermal stability, strong Brønsted acidity, Keggin structure, less corrosiveness and easy improvement of acidity. They have wide range of acid-catalyzed reactions [4]. However, the leaching of this HPAs is a main consideration for utilizing this species. To overcome their solubility issues as well as increase the water resistance, the supporting material namely graphene oxide (GO) is selected. GO is known for its high potential and acid catalysis capability. The previous report showed that using GO as a catalyst in the esterification of glycerol and acetic acid can achieve complete glycerol conversion with 90% and high selectivity of DA and TA. The unprecedented catalytic performance is related to the oxygen-containing groups related to the acid functional group (carboxylic and phenolic groups), particularly the SO<sub>3</sub>H groups. Therefore, the comparison on their catalytic activity for glycerol esterification with acetic acid should be investigated under the similar operating condition. This research marks the first report on the catalytic performance of heterogeneous GO, rGO and TPA catalysts for this process. The catalyst characteristics were also investigated to support their catalytic activities.

## 2. Materials and methods

**2.1 Chemical:** Graphite powder (99.0%), 12-tungstophosphoric acid (H<sub>3</sub>PW<sub>12</sub>O<sub>40</sub>), acetic acid and isopropyl acetate (99%), were obtained from Sigma-Aldrich. Sulfuric acid (98.0%) and

glycerol (99.5%) were purchased from QReC-chemical. Potassium permanganate (99.5%) and sodium carbonate ( $\geq 99.0\%$ ) were obtained from Kemaus. Sodium nitrate ( $\geq 99.0\%$ ) was obtained from Dae Jung. Hydrogen peroxide solution (30.0%) and hydrochloric acid (37.0%) were obtained from Fisher chemical. Ethanol (98.0%) was obtained from RCI-Labscan. Hydrazine solution (64% in H<sub>2</sub>O) was obtained from Thermo scientific.

**2.2 Preparation of graphene oxide (GO):** The synthesis of graphene oxide (GO) was carried out using the modified Hummer's method [5, 6]. The procedure involved adding 1 g of graphite powder, 0.5 g of NaNO<sub>3</sub>, and 23 mL of sulfuric acid (H<sub>2</sub>SO<sub>4</sub>) to a 500 mL flask, which was placed in an ice bath at 0-5 °C and stirred for 10 min. Subsequently, 3 g of KMnO<sub>4</sub> was slowly introduced to the mixture, maintaining the temperature at 0-5 °C for 2 h. After removing from the ice bath, and the temperature gradually increased to 35 °C, with continuous stirring for 30 min. H<sub>2</sub>SO<sub>4</sub> was added, and after another 30 min, deionized (DI) water (46 mL) was slowly incorporated into the solution. The resulting hydration increased the temperature to 90-98 °C, and stirring continued for an additional 30 min. The reaction was stopped by adding 140 mL of deionized water and 10 mL of 30 wt.% hydrogen peroxide. The brown/yellowish product was separated from the solution through vacuum filtration. The GO powders were washed twice with a 5% HCl solution (200 mL) and DI water before being air-dried in an oven at 60 °C for 12 h.

**2.3 Preparation of the reduce graphene oxide (rGO):** rGO was synthesized following the previous research [7]. GO 500 mg was sonicated in DI water 500 mL for 2 h. Then, 5% Na<sub>2</sub>CO<sub>3</sub> 12 mL was added to increase the solution pH to 9–10. Afterwards, 20 mL of 64% hydrazine hydrate (41.2 wt. equiv.) was added to the suspension. The mixture was refluxed for 24 h. The solution was cooled down to room temperature and washed with DI water (100 mL) and MeOH (200 mL) and dried at 40 °C under vacuum overnight.

**2.4 Glycerol esterification:** The experiment involved conducting acetic acid and catalyst reactions in a three-neck round-bottom glass, varying the acetic acid to glycerol molar ratio of 6:1 and catalyst concentration of 1 wt.%. Reaction temperatures of 110°C was explored, maintaining a stirring speed of 700 rpm for 120 min. Glycerol was preheated separately. The sequence reaction setup, acetic acid and the catalyst were heated in the three-neck round-bottom flask, while the separated glycerol was preheated in the flask. When the reaction temperature was reached to the desired temperature, the preheated glycerol was introduced in the three-neck round-bottom flask and stirring with magnetic bar. The glycerol esterification process employed silicone oil as a heating medium. the mixture product was analyzed by gas chromatography (GC) to determine the content of mono-, di-, and triacetin.

**2.5 Determination content of glycerol and acetin:** 20 mL of isopropyl acetate solvent was prepared in 50 mL beaker. Reaction mixture samples were weighed to  $0.04 \pm 0.004$  g, dissolved sample in isopropyl acetate solvent and shake to allow the solution to be mixed. Then, the 1  $\mu$ L of sample solution was injected in GC following GC condition. MA, DA and TA content obtained from glycerol esterification with acetic acid was analyzed by GC using a DB-5 column (30 m  $\times$  0.320 mm, 0.25  $\mu$ m) starting at a temperature of 50 °C with a holding time of 5 min. Then, the temperature was increased to 130 °C at 1 °C/min and held for 10 min. Carrier gas helium flow 0.7 mL/min, 120 °C 5 min, then 1 °C/min up to 130 °C. Acetins yield was calculated using Equations (4) and (5). To determine conversion of glycerol and acetins selectivity were defined as follows:

$$\text{Conversion (\%)} = \frac{(\text{initial mol of glycerol}) - (\text{mol of glycerol at time (t)})}{(\text{initial mol of glycerol})} \times 100 \quad (4)$$

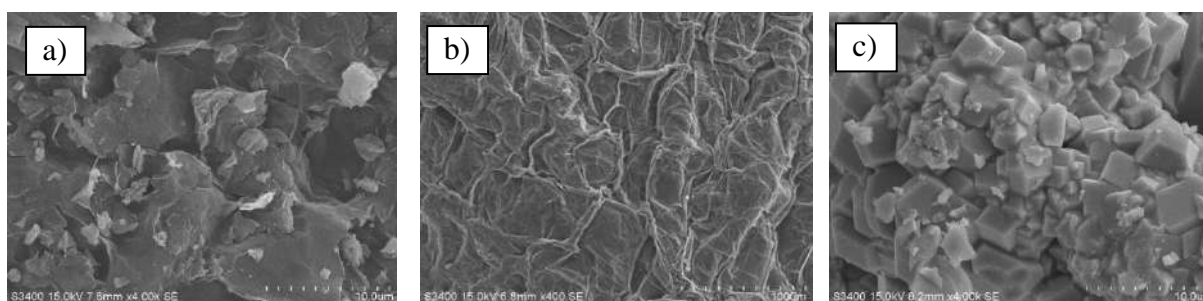
$$\text{Selectivity (\%)} = \frac{\text{moles of desired acetin product}}{\text{mol of total acetin product}} \times 100 \quad (5)$$

### 3. Results and discussion

#### 3.1 Characterization results

The catalyst characterization results including of SEM, SEM-DEX and XRD was investigated as illustrated in Fig. 1, Table 1 and Fig. 2, respectively. Acidity of catalysts in Table 2

##### 3.1.1 SEM-EDX



**Fig. 1** SEM images of (a) GO), (b) rGO) and (c) TPA

Fig. 1 (a) depicts the structure of GO before reduction, revealing a little change in sample morphology following the exfoliation. Consequently, all the altered carbons maintained their flake-like structures [8]. Fig. 1(b) reveals the morphology of reduced graphene oxide (rGO). A typical flake-like structure characterized by exfoliated layers, creases, twists, wrinkles, and crumbles, along with holes and gaps between carbon planes contributing to its developed texture. Post-thermal treatment, the thickness of rGO was notably smaller than that of graphene oxide (GO) flakes, attributed to factors such as the elimination of oxygen-containing functional groups and the removal of interlamellar water in graphite oxide, influenced by relative humidity. Fig (c) presents bulk aggregated clusters with the orderly appearance and crystallites [9].

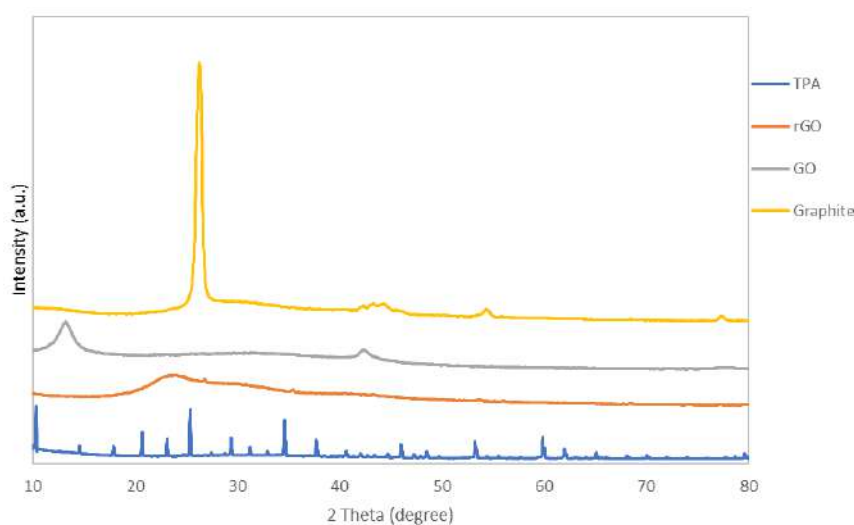
**Table 1** SEM-EDX analysis results of all catalysts

Catalyst	Elements composition (wt.%)				
	C	O	S	W	P
GO	61.78	31.31	1.69	1.21	4.01
rGO	56.72	25.34	15.92	0.89	1.13
TPA	1.52	15.19	0.43	76.59	6.27

Table 1 shows the evolution of composition of rGO compared with that of GO. The result showed the incorporation of both sulfur and oxygen, potentially indicating the formation of SO<sub>3</sub>H groups within the GO structure. GO contained 1.69% of sulfur and 31.31% of oxygen, while 15.92% of sulfur and 25.34% of oxygen observed for rGO. The thermal exfoliation of GO (rGO) with high temperature induced the changes in the composition of the parent sample,

introducing varying amounts of sulfur and oxygen to GO [2, 10]. This suggests that modifying graphene-based samples with temperature is a highly efficient method of functionalization and successful the reduction of oxygen functional group. Significantly, the direct consequence of rGO was an increase in sample acidity, supporting the formation of acidic groups in the processes of GO, including sulfonic and carboxylic functionalities [11]. The composition of TPA in the result revealed the presence of C, O, W, and P conclusively confirming the existence of TPA ( $H_3PW_{12}O_{40}$ ), with W or tungsten being the most abundant element which could be refer to heteropoly acid.

### 3.1.2 XRD



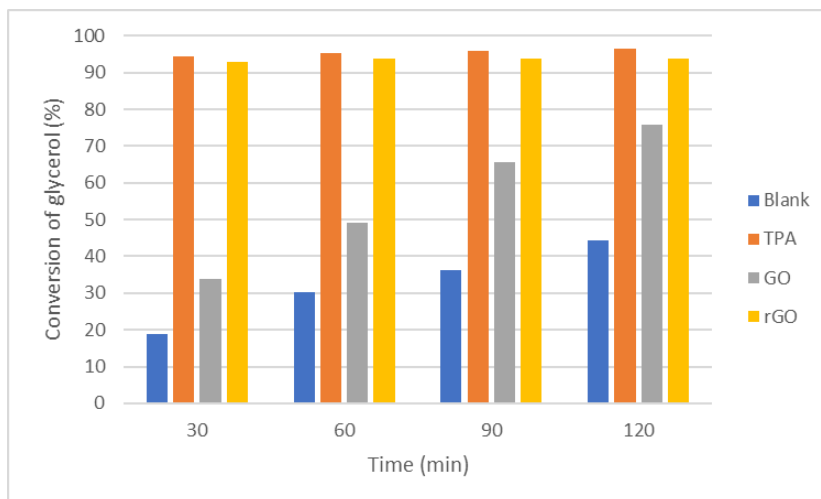
**Fig. 2** XRD patterns of the (a) graphite, (b) GO, (c) rGO and (d) TPA

The XRD patterns of graphite, graphene oxide (GO), reduced graphene oxide (rGO) and TPA are depicted in Fig. 2. In the XRD pattern of GO, a significant crystalline peak at  $13.6^\circ$  is evident, corresponding to a d-spacing of  $8.42^\circ\text{\AA}$ , attributed to oxygenated functional groups introduced during the modified Hummer's method and interlamellar water molecules trapped between adjacent hydrophilic graphene oxide layers. The less intense peak at  $2\theta = 42.1^\circ$  commonly observed in graphitic substances indicates the presence of some unexfoliated graphite particles [13]. For the XRD pattern of rGO, the intensity of the GO peak diminishes, and a new peak at  $23.6^\circ$  emerges, corresponding to a decreased d-spacing of  $6.6^\circ\text{\AA}$ . This reduction in d-spacing in rGO indicates the successful elimination of oxygen-containing functional groups, confirming the effectiveness of the reduction process. Additionally, the XRD patterns of TPA (12-Tungstophosphoric acid) showed the characteristic peaks of the Keggin ion at  $2\theta$  values of  $10.3^\circ$ ,  $17.9^\circ$ ,  $23.2^\circ$ ,  $25.8^\circ$ ,  $29.7^\circ$ ,  $36.3^\circ$ , and  $38.9^\circ$ . This consistency aligns with reported literature, confirming the presence of tungsten Keggin-structure-related peaks at  $2\theta = 10.5^\circ$ ,  $18.3^\circ$ ,  $23.7^\circ$ ,  $26.1^\circ$ ,  $30.2^\circ$ ,  $35.6^\circ$ , and  $38.8^\circ$  [14].

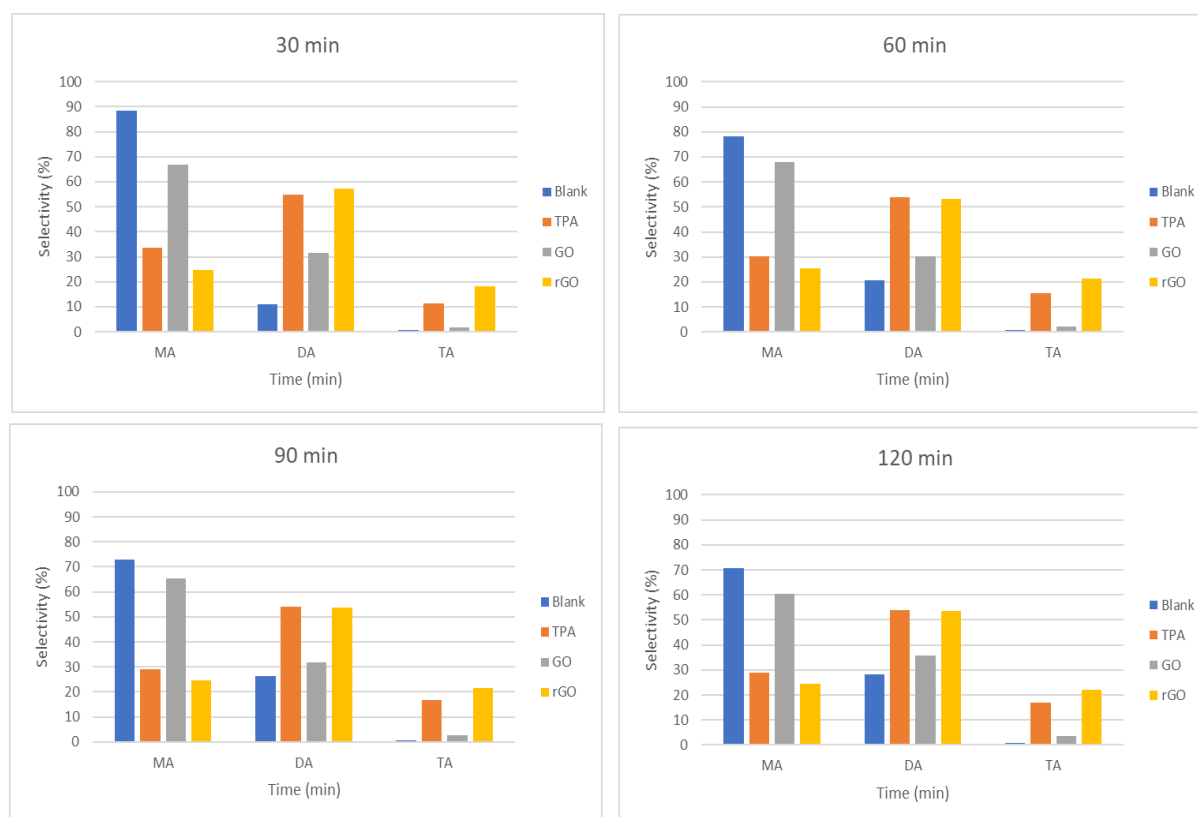
### 3.2 Catalytic activity

In the experimental setup, the operation at a reaction temperature of  $110^\circ\text{C}$  and an acetic acid to glycerol molar ratio of 6:1 was used to serve as a driving force to propel the forward esterification. The catalytic performances of the samples were assessed based on glycerol

conversion and selectivity's of acetin products (MA, DA, and TA). The obtained results, including the blank test, are shown in Figs. 3-4.



**Fig. 3** Catalytic activity for esterification of glycerol and acetic acid in term of conversion of glycerol obtained in the reaction with blank, GO, rGO and TPA catalysts.



**Fig. 4** Catalytic activity for esterification of glycerol and acetic acid in term of selectivity of acetic products obtained in the reaction with blank, GO, rGO and TPA catalysts.



Fig. 3 presents the results of glycerol conversion along the reaction time using GO, rGO and TPA catalysts compared to the blank system (without catalyst). The glycerol conversion for all runs was increased along the reaction time from 0 to 120 min. However, the longer the reaction time, the smaller the differences in the sample activities were observed due to approaching/reaching the reaction equilibrium. The glycerol conversion derived from the blank run was reached 44% at 120 min. This indicated that the autocatalytic reaction was occurred from the acetic acid reactant. When, the GO was used to catalyze esterification, the glycerol conversion was increased to 76% at 120 min. The similar highest glycerol conversion was observed for both rGO and TPA catalyzed esterification of glycerol and acetic acid as 93 and 95% at the initial reaction stage of 30 min, respectively. The previous report also found the similar trend for using the TPA [15] and rGO [16]. This should be because the acid functional group and acid properties of rGO and TPA poses the positive properties to catalyze esterification of glycerol and acetic acid. TPA is the one of heteropoly acid catalyst having high Brønsted acid strength and high acid site density [4]. Back titration was used to determine acidity for all catalysts. It was found that the acidity of TPA was only obtained as 3.996 mmol/g.cat while the acid site derived from GO and rGO catalysts could not dissolve in NaOH solution. Malaika et. al [2] reported the acidity of rGO as 0.82 mmol/g.cat derived from sulfonated functional groups to facilitate its catalytic activity. Gao et. al [5] also found the acidity of GO as 0.378 mmol/g.cat. Therefore, the order of catalytic activity for glycerol esterification was in accordance to their acidity. In addition, EDX revealed that the high S content of 15.92 wt.% was found from rGO while only 1.69 % was observed for GO. This demonstrates the higher acidity for rGO was due to the high concentration of SO<sub>3</sub>H groups on its surface. TPA also exhibits the catalytic effect in glycerol esterification comparable to rGO, even though it lacks SO<sub>3</sub>H groups on its surface. This suggests other functionalities, particularly the tungsten (W) in structure as detected on TPA which refers the heteropoly acid catalyst. This species was found to give high catalytic activity for glycerol esterification [14].

Fig. 4 illustrates the distribution of various products during glycerol esterification at the selected reaction times using different catalysts and compared to the blank test (without catalyst). The esterification of glycerol and acetic acid led to the production of MA, DA and TA, respectively. At the initial stage (30 min), the GO catalyst was predominated in selectivity for MA showing approximately 67.8% selectivity of MA while the blank exhibiting about 88.4% selectivity to MA. Conversely, the MA selectivity at 30 min of using TPA and rGO catalysts was lower about 33.66% and 24.65%, respectively. These catalysts primarily catalyzed esterification for transformation of glycerol into diacetin (DA) with a selectivity of about 53% at 60 min, while also produced significant triacetin (TA) amounts (selectivity of about 15 and 21%, respectively) at 60 min and increased by approximately 3-5% at 120 min with achieving a glycerol conversion of about 95% at 120 min. The observed selectivity found that formation of acetin derivative throughout consecutive reactions. The initial selectivity to MA was decreased over time in all cases, while the selectivity of DA and TA were increased. This suggests that glycerol esterification over graphene oxide and TPA catalysts occurs in three steps: (1) MA formation, (2) followed by MA reacted with acetic acid converted to DA, and (3) DA conversion to TA with corresponding to Eqs. (1)– (3). Based on the selectivity profiles along the reaction time for rGO and TPA catalysts expressed the order magnitude of selectivity from high to low were DA, MA and TA for all catalysts. This observation could propose the order of the net reaction rate constant involving each step for high to low as the net reaction rate of DA > MA > TA. In contrast to, the DA+TA over GO catalyst at the initial reaction stage

(30 min) was relatively low. It was around 32% at 60 min. Over the reaction time, especially for the more active GO catalyst, DA+TA increased, reaching approximately 40% at 120 min. This can be concluded that the rGO and TPA were the most active catalysts providing the rapid conversion of glycerol to MA to higher DA and TA, making them effective in converting substantial glycerol amounts into MA, DA and TA within a short reaction time. When considering both the catalytic activity (Fig. 3-4), it was found that high activity was associated with high acidity. Previously report was concluded that the higher acetins formed in glycerol esterification over carbon materials [17-18], corresponds well with the number of its SO<sub>3</sub>H group or acidity.

#### 4. Conclusions

The glycerol valorization using esterification to produce acetin derivatives (MA, DA and TA) was successfully carried out using acid catalysts. Graphene-based catalyst GO and rGO were prepared through thermal exfoliation of graphite providing the surface acid functional groups of carboxylic and sulfonated group. While TPA was a tungsten-containing material referred to the heteropoly acid catalyst. Based on the similar reaction condition, TPA demonstrated highest performance, slightly higher compared to rGO. This suggests that other functionalities, particularly the tungsten (W) in structure detected on TPA exhibited the best catalytic performance with high glycerol conversion and yields of DA and TA within just 60 min. rGO was also highly effective, incorporating a substantial number of SO<sub>3</sub>H leading to a significant increase in the total acidity of the parent material. The rGO displayed the highest content of SO<sub>3</sub>H groups derived from S content on the surface. Catalytic data from the glycerol and acetic acid esterification indicated the crucial role of strong acidic sites in the process.

#### 5. Acknowledgement

The authors would like to express appreciation for the support of the NRCT-JSPS Grant via National Research Council of Thailand (NRCT) [Grant number N10A660366].

#### References

- [1] Kim, I., Kim, J., & Lee, D. (2014). A comparative study on catalytic properties of solid acid catalysts for glycerol acetylation at low temperatures. *Applied Catalysis B: Environmental*, 148, 295-303.
- [2] Malaika, A., Ptaszyńska, K., Gaidukevič, J., & Kozłowski, M. (2022). The impact of surface groups of functionalized graphene on glycerol acetylation. *Fuel*, 313, 122987.
- [3] San Kong, P., Aroua, M. K., Daud, W. M. A. W., Lee, H. V., Cognet, P., & Pérès, Y. (2016). Catalytic role of solid acid catalysts in glycerol acetylation for the production of bio-additives: a review. *RSC advances*, 6(73), 68885-68905.
- [4] Zhu, S., Gao, X., Dong, F., Zhu, Y., Zheng, H., & Li, Y. (2013). Design of a highly active silver-exchanged phosphotungstic acid catalyst for glycerol esterification with acetic acid. *Journal of catalysis*, 306, 155-163.

- [5] Gao, X., Zhu, S., & Li, Y. (2015). Graphene oxide as a facile solid acid catalyst for the production of bioadditives from glycerol esterification. *Catalysis communications*, 62, 48-51.
- [6] Guerrero-Contreras, J., & Caballero-Briones, F. (2015). Graphene oxide powders with different oxidation degree, prepared by synthesis variations of the Hummers method. *Materials Chemistry and Physics*, 153, 209-220.
- [7] Cheng, J., Qiu, Y., Zhang, J., Huang, R., Yang, W., & Fan, Z. (2017). Conversion of lipids from wet microalgae into biodiesel using sulfonated graphene oxide catalysts. *Bioresource technology*, 244, 569-574.
- [8] Singh, H., & Ali, A. (2023). Esterification as well as transesterification of waste oil using potassium imbued tungstophosphoric acid supported graphene oxide as heterogeneous catalyst: Optimization and kinetic modeling. *Renewable Energy*, 207, 422-435.
- [9] Dizaji, A. K., Mokhtarani, B., & Mortaheb, H. R. (2019). Deep and fast oxidative desulfurization of fuels using graphene oxide-based phosphotungstic acid catalysts. *Fuel*, 236, 717-729.
- [10] Tran, D. T. (2020). rGO/persulfate metal-free catalytic system for the degradation of tetracycline: effect of reaction parameters. *Materials Research Express*, 7(7), 075501.
- [11] Nongbe, M. C., Ekou, T., Ekou, L., Yao, K. B., Le Grogne, E., & Felpin, F. X. (2017). Biodiesel production from palm oil using sulfonated graphene catalyst. *Renewable Energy*, 106, 135-141.
- [12] Kozhevnikov, I. V. (1998). Catalysis by heteropoly acids and multicomponent polyoxometalates in liquid-phase reactions. *Chemical Reviews*, 98(1), 171-198.
- [13] Chamoli, P., Das, M. K., & Kar, K. K. (2017). Green synthesis of silver-graphene nanocomposite-based transparent conducting film. *Physica E: Low-dimensional Systems and Nanostructures*, 90, 76-84.
- [14] Kumar, C. R., Rambabu, N., Lingaiah, N., Prasad, P. S., & Dalai, A. K. (2014). Hafnium salts of dodeca-tungstophosphoric acid catalysts for liquid phase benzylation of anisole with dibenzylether. *Applied Catalysis A: General*, 471, 1-11.
- [15] Kale, S. S., Armbruster, U., Eckelt, R., Bentrup, U., Umbarkar, S. B., Dongare, M. K., & Martin, A. (2016). Understanding the role of Keggin type heteropolyacid catalysts for glycerol acetylation using toluene as an entrainer. *Applied Catalysis A: General*, 527, 9-18.
- [16] de la Calle, C., Fraile, J. M., García-Bordejé, E., Pires, E., & Roldán, L. (2015). Biobased catalyst in biorefinery processes: sulphonated hydrothermal carbon for glycerol esterification. *Catalysis Science & Technology*, 5(5), 2897-2903.
- [17] Sánchez, J. A., Hernández, D. L., Moreno, J. A., Mondragón, F., & Fernández, J. J. (2011). Alternative carbon based acid catalyst for selective esterification of glycerol to acetylgllycerols. *Applied Catalysis A: General*, 405(1-2), 55-60.
- [18] Malaika, A., Ptaszyńska, K., & Kozłowski, M. (2021). Conversion of renewable feedstock to bio-carbons dedicated for the production of green fuel additives from glycerol. *Fuel*, 288, 119609.

## Performance Improvement of Wet Scrubbing Unit for Resin Production

Nirut Arnaratana<sup>1</sup>, Teerawat Sema<sup>2,\*</sup>

<sup>1</sup> Petrochemistry and Polymer Science Program, Faculty of Science, Chulalongkorn University, 10330, Thailand

<sup>2</sup> Department of Chemical Technology, Faculty of Science, Chulalongkorn University, 10330, Thailand

Email: \*teerawat.se@chula.ac.th

### ABSTRACT

Alkyd resin plant is a facility where the resin is produced at larger scale. Around 200,000 tons per year of alkyd resin are produced and used as coatings and finishes in the protective coatings industry. In the resin production process, several waste gases (e.g., toluene and xylene) are emitted. Wet scrubber is therefore implemented to absorb those waste gases aiming at pollution control. The undesired performance of wet scrubber causes unpleasant odor and pollution impact. The studied plant uses water and aqueous solution of 5%wt. sodium hydroxide as an absorbent. Due to the low solubility of some waste gases in the absorbent, unpleasant odor has been experienced. This work aims to improve the performance of wet scrubber unit for alkyd production by a manipulation of the operating conditions. As a result, the waste gas from resin processing to wet scrubber system was simulated using Aspen Plus at waste gas flow rate of 60 kg/hr. Since the knockout drum is a crucial unit that reduces the load of waste gas treatment in the wet scrubber, performance improvement of the knockout drum was preliminary investigated by varying (i) operating temperature (30-50 °C) and (ii) nitrogen carrier flow rate 5-20 kg/hr. Simulation result shows that flow rates of xylene and toluene in the discharge gas stream trend to be low when decreasing the temperature and nitrogen flow rate.

**Keywords:** Resin process; knockout drum; wet scrubber.

### 1. INTRODUCTION

Wet gas scrubbers, also known as wet scrubbers, are widely used in industrial plants for the treatment of waste gases from production processes, such as acid vapors and various chemical vapors. Due to their simple system and low investment requirements, wet scrubbers are often chosen for air pollution control. These systems are designed to capture and remove pollutants, including particulate matter and gases, from industrial exhaust streams. Wet scrubbers find application in diverse industries such as chemical manufacturing, petrochemicals, pharmaceuticals, and metal processing. There are many types of wet gas purification systems, such as packed tower, sprayed tower, Venturi, and cyclone gas purification systems. However, the most popular system in the industry is the packed tower [1] The process relies on the contact between the waste gas containing contaminants and the absorbent, usually water, on a packing material designed to increase the contact surface between the contaminated waste gas and the liquid absorbent. When the liquid absorbent comes into contact with the filling material, it decreases in volume, with some flowing as a thin film on the surface of the filling material. This phenomenon increases the contact surface area between the liquid absorbent and the released gas, consequently enhancing the efficiency of capturing waste gases. There are three types of flow directions for waste gases and liquid absorbers: counterflow, concurrent flow, and crossflow [2]. The selection of which depends on the objectives of each industry. The efficiency of a wet scrubber can be enhanced by incorporating a knockout drum. This device facilitates

the transformation of waste gas or vapor steam from the process into a liquid phase, thereby reducing the load of waste gas on the wet scrubber and improving emission control [3]. In this research, Aspen plus software has been applied in several studies to simulate the effects of nitrogen rate, temperature, and flow rate of waste gas in knockout drum were discussed.

## 2. METHODOLOGY

The alkyd resin plant generates xylene and toluene waste gases during the process. The total waste gas flow rate of 60 kg/hr is directed into a knockout drum to separate the vapor phase and liquid phase. The vapor phase is then directed into a wet scrubber, while the liquid phase is packaged in bulk for disposal.

### 2.1 Process description and configuration

Fig. 1 presents a simulated process flow diagram for scrubber unit in alkyd resin plant production, which is built using ASPEN Plus software. The NRTL thermodynamic model was used in this simulation. Waste gas (including toluene and xylene) are the inlet gases to knockout drum. The temperature of the inlet gas is 45 °C, and the temperature of knockout drum is 40 °C. Some of the inlet gas condenses into the liquid phase, while the gas phase goes to the wet scrubber. In knockout drum, the temperature is 40 °C. It receives xylene and toluene at a temperature of 45 °C from the process xylene and toluene condense into the liquid phase, while a portion of xylene and toluene in the gas phase is directed to the wet scrubber for gas treatment.

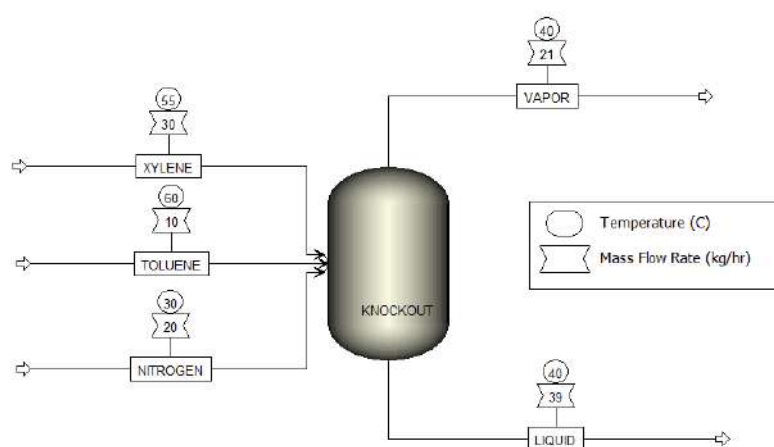


Fig. 1 Simulated process flow diagram of knockout drum

### 2.2 Equipment description

For the studied Alkyd resin plant, the knockout drum is a vertical tank made from stainless steel with a height of 2 meters and a length of 1.35 meters. This tank is equipped with a chilled water coil to supply water at a temperature of 12-14 °C. At the bottom of the tank, there is a 1-inch drain valve for draining liquid condensate. Additionally, at the top of the tank, there is an outlet valve for directing wet gas to the wet scrubber.

### 2.3 Operating Condition

The operating conditions in the alkyd process vary with temperatures of the knockout drum and nitrogen flow rate. The temperature ranges between 30 - 50 °C, representing the minimum and maximum operating temperatures for the knockout drum, respectively. The nitrogen flow rate is currently at 20 kg/hr in the processing of alkyd resin. In this research study, the effect of nitrogen rates at 10 kg/hr and 5 kg/hr is explored, as shown in Table 1.

Table 1. Operating conditions of the knockout drum

No	Temperature (°C)	N <sub>2</sub> flow rate (kg/hr)
1	30	20
2	40	20
3	50	20
4	30	10
5	40	10
6	50	10
7	30	5
8	40	5
9	50	5

## 3. RESULTS AND DISCUSSION

The ASPEN Plus software provides a tool capable of process optimization for adjustable variables. The temperature of the knockout drum is set between 30 °C and 50 °C, and the nitrogen flow rate ranges from 5 to 20 kg/hr. The effect of different operation parameters are discussed as followings:

### 3.1 Temperature of knockout drum

The temperature of the knockout drum is an essential parameter in the separation of gas from liquid [4]. A higher temperature increases the rate of separation and reduces phase separation time [5]. For the alkyd process, Table 2. presents the relationship between temperature and the flow rate of waste gas in the liquid and vapor phases. The flow rates of xylene and toluene in the discharge gas stream trend to be low when decreasing the temperature. (in other words, their mass flow rate in the discharge liquid stream increase).

### 3.2 Nitrogen flow rate

Nitrogen is a crucial raw material for the synthesis of the resin process, and it significantly influences product properties such as colour and appearance [6]. According to the simulation using ASPEN Plus, nitrogen varies at 5 kg/hr, 10 kg/hr, and 20 kg/hr under different temperatures of 30 °C, 40 °C, and 50 °C, respectively. The results indicate that increasing the nitrogen flow rate leads to higher flow rate of xylene and toluene in the vapor phase, which correlates with the temperature of the knockout drum. Table 3 illustrates the effect of nitrogen flow rate at a knockout drum temperature of 30 °C, resulting in lower flow rates of xylene and toluene in the vapor phase compared to the normal operating conditions shown in Table 4. The

worst conditions occur at the maximum knockout drum temperature of 50°C and a nitrogen flow rate of 20 kg/hr, as indicated in Table 5, where the flow rates of xylene and toluene are higher.

Table 2. Discharge flow rate of waste gas at difference temperature and constant nitrogen rate 20 kg / hr

Inlet		Discharge					
		Liquid flow rate (kg/hr)			Vapor flow rate (kg/hr)		
Feed component	Flow rate (kg/hr)	30 °C	40 °C	50 °C	30 °C	40 °C	50 °C
Toluene	10.000	9.575	9.318	8.944	0.425	0.682	1.056
Xylene	30.000	29.570	29.259	28.763	0.430	0.741	1.237
Nitrogen	20.000	0.020	0.018	0.017	19.980	19.982	19.983

Table 3. Discharge flow rate at difference nitrogen flow rates and constant temperature 30 °C

Inlet		Discharge					
		Liquid phase			Vapor phase		
Feed component	Flow rate (kg/hr)	Toluene	xylene	Nitrogen	Toluene	Xylene	Nitrogen
Nitrogen	20	9.575	29.570	0.020	0.425	0.430	19.980
	10	9.653	29.632	0.021	0.347	0.368	9.979
	5	9.892	29.817	0.021	0.108	0.106	4.979

\*Toluene inlet flow rate 10 kg/hr and xylene inlet flow rate 30 kg/hr

Table 4. Discharge flow rate at difference nitrogen flow rates and constant temperature 40 °C

Inlet		Discharge					
		Liquid phase			Vapor phase		
Feed component	Flow rate (kg/hr)	Toluene	xylene	Nitrogen	Toluene	Xylene	Nitrogen
Nitrogen	20	9.318	29.259	0.018	0.682	0.741	19.982
	10	9.653	29.632	0.019	0.347	0.368	9.981
	5	9.826	29.817	0.019	0.174	0.183	4.981

\*Toluene inlet flow rate 10 kg/hr and xylene inlet flow rate 30 kg/hr

Table 5. Discharge flow rate at difference nitrogen flow rates and constant temperature 50 °C

Inlet		Discharge					
		Liquid phase			Vapor phase		
Feed component	Flow rate (kg/hr)	Toluene	xylene	Nitrogen	Toluene	Xylene	Nitrogen
Nitrogen	20	8.944	28.763	0.017	1.056	1.237	19.983
	10	9.458	29.387	0.017	0.542	0.613	9.983
	5	9.726	29.696	0.017	0.274	0.304	4.983

\*Toluene inlet flow rate 10 kg/hr and xylene inlet flow rate 30 kg/hr

### 3.3 Sensitivity Analysis

The effect of main operating conditions, which are temperature of knockout drum and flow rate of nitrogen gas, are discussed in this section. To enhance waste gas treatment in the resin process, assumptions have been developed during the simulation. The temperature of the knockout drum varies between 30 °C and 50 °C, and the nitrogen flow rate ranges from 5 kg/hr to 20 kg/hr. Additionally, the total waste gas flow rate is fixed at 60 kg/hr for all cases. The effect of temperature in the range of 0 °C to 100 °C is shown in Figure 2. The flow rate of xylene in vapor phase increase 99.46% and liquid phase reduce 39.96 % Moreover, the flow rate of toluene in vapor phase increase 98.67% and 59.61 % reduce of liquid phase, can be observed that the flow rate of waste gas increases with the temperature, while the flow rate of the fluid phase decreases with the temperature. A similar trend was observed by Marcantonio and colleagues [7].

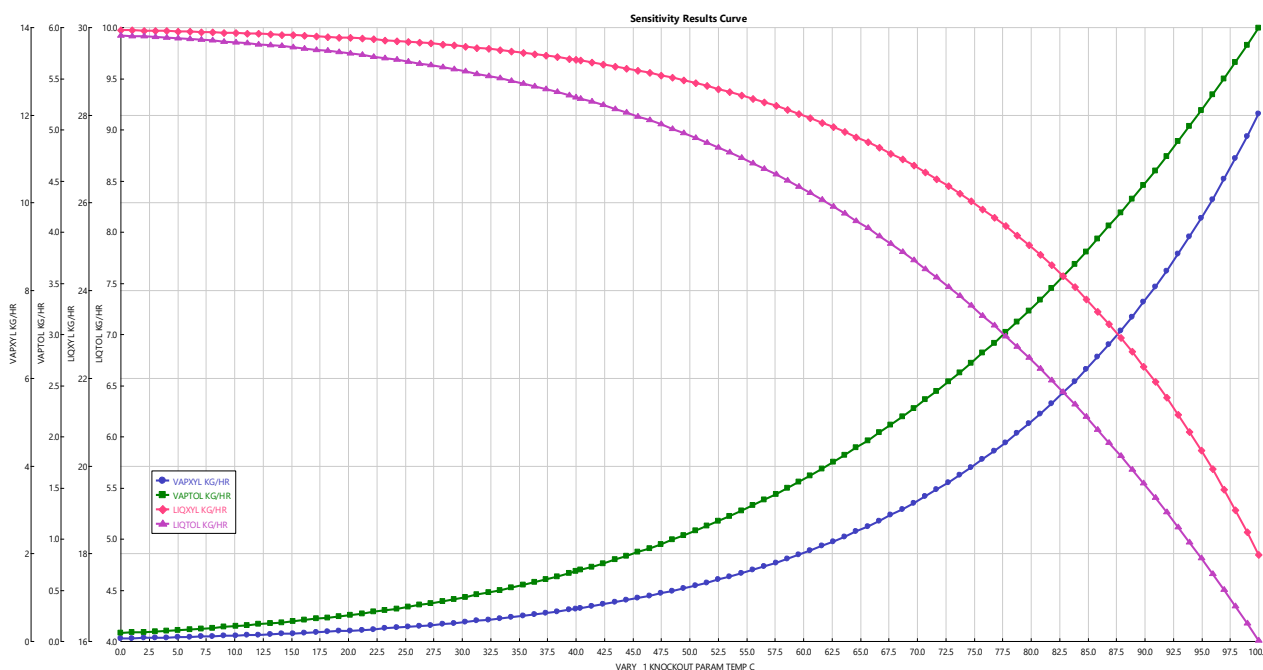


Fig. 2 Sensitivity analysis of waste gas flow rate respect to temperature.

## 4. CONCLUSION

In this work a simulation of waste gas of knockout drum from alkyd resin process using ASPEN Plus software was developed. The conclusions are given as follows:

1. The ASPEN Plus software has proven to be effective in simulating the flow rate of waste gas from the knockout drum in the alkyd resin process and predicting the operating conditions.
2. The nitrogen flow rate in the alkyd resin process should be carefully determined, taking into consideration the efficiency of the knockout drum. In actual operating conditions of the alkyd resin plant, at a knockout drum temperature of 40 °C, the vapor phase flow rate of xylene reduces by 50.34%, and toluene reduces by 49.12% when changing the nitrogen flow rate from 20 kg/hr to 10 kg/hr.

These findings suggest that the knockout drum is an effective method for reducing waste gas from the alkyd resin process, addressing both unpleasant odor and pollution impact.



## 5. ACKNOWLEDGEMENTS

TOA Paint (Thailand) Public Company Limited for scholarship funding.

## REFERENCES

- [1] EPA Air Pollution Control Cost manual, Office of Research and Development, U.S. Environmental Protection Agency, Research Triangle Park, North Carolina, Publication No. EPA/452/B-02-001
- [2] Treybal, Robert E. (1980). Mass Transfer Operations (Third Edition), McGraw-Hill Book Company, New York, pp.139-333.
- [3] Abdullah A. Al-Dughaiter, Ahmed A. Ibrahim, Waheed A. Al-Masry (2011). Investigating pressure drop across wire mesh mist eliminators in bubble column, Journal of Saudi Chemical Society (15), 1-9.
- [4] Maurice, Stewart, (2014). Surface Production Operations, 3rd, Gulf professional publishing is an imprint of Elsevier, pp 559-634.
- [5] Song Ye, Lena Hohl, Matthias Kraume, (2023). Effect of temperature on mixing and separation of stirred liquid/liquid dispersions over a wide range of dispersed phase fractions, [Online URL: <https://doi.org/10.1016/j.ces.2023.118676>] accessed on January 12, 2024.
- [6]. Himadri Panda (2000). Alkyd resin technology handbook, Asia Pacific Business Press, pp.60 -72.
- [7]. Vera Marcantonio, Enrico Bocci, Pieter Ouweltjjes (2020). Evaluation of sorbents for high temperature removal of tars, hydrogen sulphide, hydrogen chloride and ammonia from biomass-derived syngas by using aspen plus, International Journal of Hydrogen Energy, (45), 6651-6662.

## Simulation of Hydrocracking Process: Impact of Process Parameters on Product Yields and Properties

Krongkiat Na Lumphoon<sup>1</sup>, Sakdinun Nuntang<sup>2</sup>, Prathana Nimmanterdwong<sup>3</sup>,  
Benjapon Chalermssinsuwan<sup>4,\*</sup>

<sup>1</sup> Program of Petrochemistry and Polymer Science, Faculty of Science, Chulalongkorn University, Bangkok 10330, Thailand

<sup>2</sup> Program of Industrial Chemistry Innovation, Faculty of Science, Maejo University, Chiang Mai 50290, Thailand

<sup>3</sup> Department of Chemical Engineering, Faculty of Engineering, Mahidol University, Nakhon Pathom 73170, Thailand

<sup>4</sup> Department of Chemical Technology, Faculty of Science, Chulalongkorn University, Bangkok 10330, Thailand

\*E-mail: benjapon.c@chula.ac.th

### Abstract

Residue hydrocracking (RHC) is a crucial refinery process that converts heavy oil residues into valuable distillate products such as diesel and gasoline. This process significantly enhances the value of heavy crude oil by upgrading low-value residues into more marketable products. RHC is a complex process involving high temperatures, pressures, and catalysts to break down the large hydrocarbon molecules found in heavy residues. This study aims to simulate the hydrocracking process to maximize diesel production, considering various process parameters using Aspen HYSYS. The investigated process parameters include feed quality (such as light vacuum gas oil (LVGO), heavy vacuum gas oil (HVGO), and short residue (SR)), feed rate, gas-to-oil ratio, recycle gas H<sub>2</sub> purity, and combined feed ratio (CFR). A simulation model was developed using the factorial design approach to examine the impact of these process parameters on diesel production. The simulation results indicated that feed quality exerts the most significant influence on diesel production, followed by CFR, feed rate, gas-to-oil ratio, and recycled gas H<sub>2</sub> purity. Implementing these conditions is predicted to maximize yield diesel production using feed quality as SR, HVGO, and LVGO, respectively. The simulation results also demonstrated that optimizing process parameters can enhance diesel production. These simulation outcomes are valuable as they provide a practical tool for optimizing hydrocracking process operations to maximize diesel production. Additionally, the study emphasizes the crucial role of feed quality in determining diesel production.

**Keywords:** Hydrocracking process; Aspen HYSYS; Factorial design; Diesel production; Process optimization.

## 1. Introduction

In the realm of petroleum refining, the main ingredient at play is crude oil, which falls into three distinct categories: light, medium, and heavy crude oil. Post-refining, these variants of crude oil render two fundamental products: white oil, commonly referred to as gasoline, and black oil, known as long residue, representing a less lucrative commodity. The current trend in the industry is an increased focus on advancing technologies for the further refinement of heavy crude oil, driven by its economical advantages. Nonetheless, the petroleum refining sector tends to shy away from heavy crude oil due to its elevated proportion of black oil, a less valuable output.[1]

Hydrocracking serves as the pivotal technique for transforming lesser-value products like vacuum gas oil (VGO) or short residue (SR) into high-value entities such as naphtha, kerosene, and diesel. This intricate process employs two fixed-bed reactors: a hydrotreating reactor responsible for eliminating sulfur and nitrogen compounds, and a hydrocracking reactor facilitating hydroisomerization and hydrocracking reactions to produce diesel characterized by low sulfur and aromatics content, coupled with a high smoke point. [2]

This current study endeavors to construct a model of the hydrocracking process utilizing the Aspen HYSYS software, grounded in a reference study leveraging authentic refinery data. The analytical pursuit revolves around determining optimal process conditions, evaluating percentage alterations, maximizing diesel output, and substantiating the viability of the hydrocracking process. The overarching objective is to underscore the potential of hydrocracking in enhancing refinery profitability through the maximization of high-value product generation, particularly diesel. [3]

## 2. Methodology

### 2.1. Process description and configuration

The hydrocracking process is carried out in a fixed-bed reactor with a catalyst at high temperature and pressure to convert heavy oil into middle distillates in a high hydrogen atmosphere. Since the hydrocracking reaction involves both cracking and hydrogenation, a dual-function catalyst is required, consisting of a hydrogenation component dispersed on a porous acidic support to promote cracking. Typical catalysts are silica-alumina (or low or high silica zeolite) with base metal components such as Ni, Pt, Pd, W, and Mo. The silica-alumina component promotes cracking, while the metals promote hydrogenation. [4]

The process typically uses two reactors in series: a hydrotreater (HT) and a hydrocracker (HC) as can be seen in Fig. 1. The hydrotreater is used to pretreat feedstock, which is typically heavy vacuum gas oil (HVGO), a mixture of various hydrocarbons classified as paraffins, olefins, aromatics, naphthene, and compounds with ring structures. The HVGO also contains sulfur and nitrogen, as well as various metal compounds.[5]

The hydrotreater removes sulfur and nitrogen compounds and converts some of the olefins to paraffins. The hydrocracker then cracks the remaining heavy molecules into lighter products, such as gasoline, diesel fuel, and jet fuel. It is used to convert heavy, low-value feedstocks into more valuable products. The process is also used to produce high-quality fuels that meet environmental regulations.

The chemical reaction occurs both in Hydrotreater and Hydrocracker are as follows respectively:

Hydrodesulfurization, hydrodenitrogenation, hydrogenation, ring dealkylation, ring opening and hydrocracking. This process involves breaking carbon-carbon bonds and saturating carbon-carbon double bonds, resulting in the production of high-quality fuels like diesel, and jet fuel.

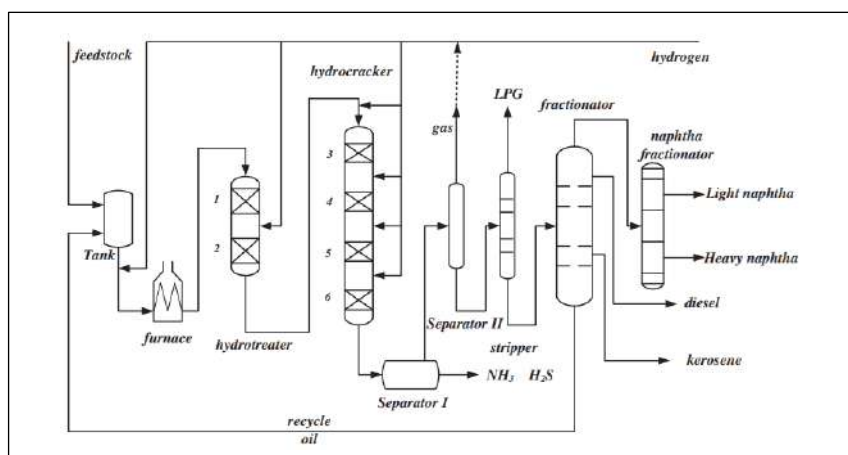


Fig. 1 Simplified hydrocracking process diagram

## 2.2. Operating conditions

The hydrocracking process was simulated using Aspen Hysys software as illustrates in Fig. 2. The feedstock properties are shown in Tables 1 and 2. The feed rate was 4270 tons per day and the single-pass conversion was 67.48%. The yield of diesel was 26.65%. The operating conditions for the process are shown in Table 3. The amount of catalyst used for the hydrotreater (HT) was 10% wt of the amount of catalyst used for the hydrocracker (HC). The temperature of the HVGO before entering the reactor was 360.87 °C and the pressure was 130 bar. [6]

Table 1. Distillation ranges of each feedstock

Distillation (%)	HVGO		LVGO		SR	
	TBP (K)	TBP (°C)	TBP (K)	TBP (°C)	TBP (K)	TBP (°C)
0	541.56	268.6	573.2	300.0	833.2	560.0
5	601.64	328.6	581.8	308.6	855.2	582.0
10	628.85	355.9	590.6	317.5	861.1	588.0
30	673.25	400.3	628.2	355.1	886.2	613.1
50	708.47	435.5	667.0	393.9	918.6	645.5
70	741.07	468.1	707.9	434.7	965.2	692.1
90	780.32	507.3	756.9	483.7	1032.3	759.1
95	797.93	524.9	771.7	498.6	1042.3	769.1
100	815.54	542.5	793.1	520.0	1097.1	823.9

Table 2. Properties of each feedstock

Properties	HVGO	LVGO	SR	Unit of measure
Density	0.9135	0.8631	0.9959	g/cm <sup>3</sup>
Sulfur	2.2	1.5	4.8	%wt
Nitrogen	637	349	2711	ppmwt

Table 3. The operating conditions for the HT and HC process

Reactor outlet bed	Outlet bed temperature (°C)
HT Bed 1	387.82
HT Bed 2	392.82
HC Bed 1	379.67
HC Bed 2	379.01
HC Bed 3	379.65
HC Bed 4	380.72

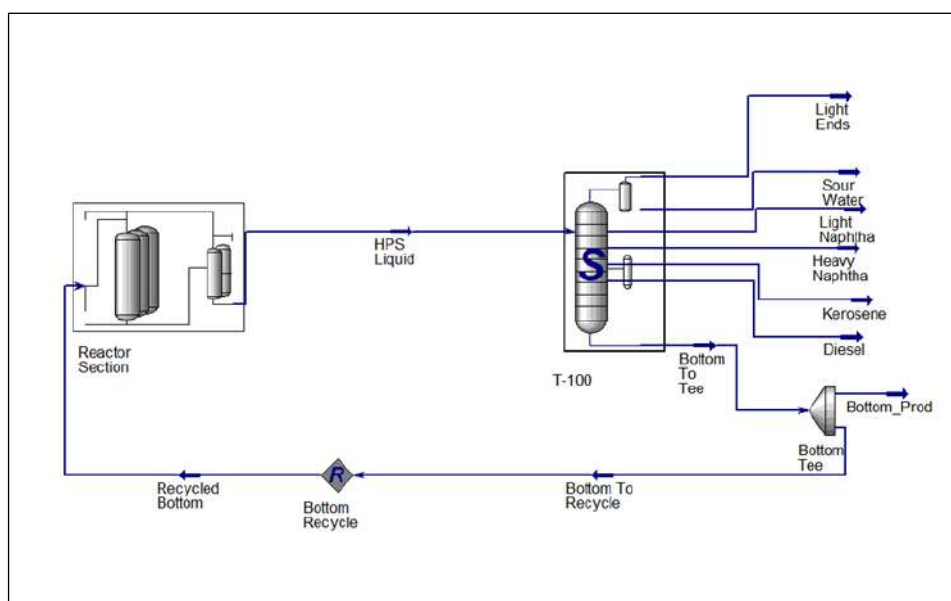


Fig. 2 Simulated hydrocracking process diagram

### 3. Experimental Design

The effect of process variables on the hydrocracking process was studied using Aspen HYSYS software. As stated before, the feedstock qualities are shown in Tables 1 and 2, while the studied variables and their ranges are presented in Table 4.

Table 4. The process variables studied in the hydrocracking process

Feedstock quality	Feed rate	Hydrogen-to-oil ratio	Recycle gas purity	Combine feed ratio
	(tons/day)	(Std m <sup>3</sup> /m <sup>3</sup> )	(mol percent H <sub>2</sub> )	
Light Vacuum Gas Oil	3000-5000	2000-4000	80-100	1.0-2.0
Heavy Vacuum Gas Oil	3000-5000	2000-4000	80-100	1.0-2.0
Short Residue	3000-5000	2000-4000	80-100	1.0-2.0

The study evaluated the impact of various process variables on the hydrocracking process. Key parameters included conversion (percentage of feedstock converted), diesel yield (amount of diesel produced), cetane index (measure of diesel quality), and catalyst deactivation (loss of catalyst activity over time). This comprehensive analysis aimed to optimize the process, potentially improving diesel production and quality while minimizing catalyst degradation.

#### 4. Simulation Data

In comparing the results obtained from the reference Flow paper by Zhou et al. in Fig.3 [6] with those of the simulation conducted using Aspen HYSYS, model validation using process parameter as Table.1, Table.2 and Table.3 while using catalyst load in HT equal 10% of total mass load of HC Catalyst. The reference paper, based on industrial measurements, reported a single-pass conversion ratio of 67.48% and a yield of diesel at 26.65%. In contrast, the simulation results from Aspen HYSYS indicated a slightly higher single-pass conversion ratio of 67.53% and a marginally lower yield of diesel at 26.62%. Calculations of the percentage error reveal a 0.074% deviation for the single-pass conversion ratio and a slight 0.113% deviation for the yield of diesel. These differences suggest a close alignment between the simulation results and the values reported in the reference paper with minor variations.

	Volume Flow [m <sup>3</sup> /h]	Mass Flow [kg/h]	Volume [%]	Mass [%]
NH <sub>3</sub>	<empty>	0.0000	<empty>	0.0000
H <sub>2</sub> S	<empty>	2250.7570	<empty>	1.3848
C1+C2	<empty>	825.1583	<empty>	0.5077
C3	2.6485	1345.4228	1.4886	0.8278
C4	2.9786	1680.1899	1.6741	1.0338
C5+ in LPG	1.1657	704.6175	0.6552	0.4335
Light Naphtha	16.7552	10763.9931	9.4171	6.6227
Heavy Naphtha	33.6498	24626.2751	18.9126	15.1516
Kerosene	25.5176	21194.3310	14.3420	13.0401
Diesel	50.7916	43273.8480	28.5471	26.6248
Bottom	63.3219	52766.9989	35.5896	32.6456
Total	199.1521	159431.5316	111.9321	98.0924
Total C4+	194.1804	155010.1935	109.1378	95.3721
Total C5+	191.2018	153330.0036	107.4636	94.3383
Conversion	<empty>	<empty>	64.4104	67.5344

Fig.3 Validation results obtained from the reference paper by Zhou et al.

After the model validation, simulation data was generated for 243 different case studies based on process variables from experimental design. The conversion percentage is often calculated based on the weight of the feedstock compared to the weight of the products. In hydrocracking, the process not only breaks down the heavy hydrocarbons but also adds hydrogen molecules to the product molecules. As a result, the weight of the products can exceed the weight of the original feedstock, leading to a conversion percentage greater than 100%.

Conversion is a measure of the amount of reaction or the amount of work that is accomplished in the unit as shown in Eq. 1

$$\text{Conversion}(\%) = \frac{\text{Fresh feed} - \text{Unconverted oil}}{\text{Fresh feed}} \times 100 \quad (\text{Eq. 1})$$

Diesel yield can be maximized by optimizing the conversion in stages I and II, the quality of recycle feed, and the extent of secondary cracking of diesel. The exact calculation method can vary depending on the specific hydrocracking process and catalysts used.

The cetane index is a number used to denote the quality of diesel fuel. It is calculated using distillation properties of the diesel to infer performance in the engine. The relationship is given by the following Eq. 2

$$\text{Cetane Index} = 2386.26(D) + 0.1740(T10) + 0.1215(T50) + 0.01850(T90) + 297.42 \quad (\text{Eq. 2})$$

Where  $D$  is the density at 15°C,  $T10$ ,  $T50$ , and  $T90$  are the temperatures at which 10%, 50%, and 90% of the diesel has distilled, respectively.

Catalyst deactivation is the gradual loss of the catalyst's activity while maintaining the same conversion severity. As the deactivation increases the catalyst temperature has to increase in order to obtain a fixed conversion and desired products. In this study, WABT at start of run (SOR) is 368.2°C and WABT at end of run (EOR) is 430 °C.

In Table 5, the p-values from the ANOVA test indicate that the feed rate has a significant effect on all response parameters, as the p-values are extremely small. The gas-to oil ratio also has a significant effect on conversion, yield diesel, and catalyst deactivation, but not on the cetane Index, as its p-value is greater than 0.05. The recycle gas H<sub>2</sub> purity does not appear to have a significant effect on any of the response parameters, as its p-values are 1 or almost 1. Both the combine feed ratio and feed quality have significant effects on all response parameters, as indicated by their extremely small p-values. For all the responses, the feed quality exerts the most significant influence on diesel production, followed by combine feed ratio, feed rate, gas-to-oil ratio, and recycled gas H<sub>2</sub> purity.

Table 5. Effect of variables process parameter on p-value of each response parameter

Source	p-value			
	Conversion	Yield Diesel	Cetane Index	Catalyst deactivation
Feed Rate	1.86E-192	9.74E-26	5.85E-65	2.65E-249
Gas-to Oil Ratio	1.37E-61	1.12E-26	6.88E-02	2.86E-05
Recycle Gas H <sub>2</sub> Purity	9.99E-01	1.00E+00	9.99E-01	1.00E+00
Combine Feed Ratio	1.02E-223	1.27E-265	6.72E-96	2.53E-67
Feed Quality	9.19E-278	5.01E-250	1.68E-142	0.00E+00

## 5. Optimizing process variables

The analysis leveraged Design-Expert software to construct quadratic equations for each feedstock quality (LVGO, HVGO, SR). These equations captured the complex

relationships between process variables (feed rate, hydrogen-to-oil ratio, recycle gas purity and combine feed ratio) and key performance indicators (conversion, diesel yield, cetane index and catalyst degradation) based on a dataset of 243 simulated cases. By analyzing these equations, the optimal combination of process variables was identified for each feedstock quality, leading to significant improvements in diesel production, quality, and catalyst lifespan as summarized in Tables 6 to 9.

The analysis delved deeper into the relationship between single-pass conversion ratio (SPCR) and combine feed ratio (CFR) for each feedstock quality (LVGO, HVGO, SR). SPCR reflects the conversion efficiency of the feedstock within a single pass through the reactor, while CFR determines the proportion of feedstocks and unconverted oil blended before processing. In summary, the single stage with recycled hydrocracking process achieves higher conversion rates and diesel yields, and produces diesel of higher quality, compared to the single stage hydrocracking process. However, it requires a higher CFR, meaning that more unconverted oil needs to be recycled. The choice between the two processes would depend on the specific requirements and constraints of the refinery.

Table 6. The optimized process variables studied in the single stage with recycled hydrocracking process

Feedstock quality	Feed rate	Gas-to-oil ratio	Recycle gas purity	Combine feed ratio
	(tons/day)	(Std m <sup>3</sup> /m <sup>3</sup> )	(mol percent H <sub>2</sub> )	
Light Vacuum Gas Oil	3000	4000	97.8	2.0
Heavy Vacuum Gas Oil	3000	4000	86.7	2.0
Short Residue	3000	4000	81.6	2.0

Table 7. Results of the optimized process variables studied in the single stage with recycled hydrocracking process

Feedstock quality	Conversion	Diesel yield	Cetane Index	Catalyst degradation
	(%)	(%)		(Remaining days)
Light Vacuum Gas Oil	108.044	50.2914	61.1861	7095.54
Heavy Vacuum Gas Oil	104.024	47.7854	60.6598	5343.8
Short Residue	50.7623	35.4734	59.1779	4442.49



Table 8. The optimized process variables studied in the single stage hydrocracking process

Feedstock quality	Feed rate	Gas-to-oil ratio	Recycle gas purity	Combine feed ratio
	(tons/day)	(Std m <sup>3</sup> /m <sup>3</sup> )	(mol percent H <sub>2</sub> )	
Light Vacuum Gas Oil	3000	2000	81.40	1.0
Heavy Vacuum Gas Oil	3000	4000	84.5	1.0
Short Residue	3000	4000	99.1	1.0

Table 9. Results of the optimized process variables studied in the single stage hydrocracking process

Feedstock quality	Conversion	Diesel yield	Cetane Index	Catalyst degradation
	(%)	(%)		(Remaining days)
Light Vacuum Gas Oil	73.9181	24.4974	53.0517	7420.7
Heavy Vacuum Gas Oil	71.0477	23.0137	53.1353	5518.06
Short Residue	36.6699	23.3128	57.4447	4296.61

## 6. Conclusion

In this work, Aspen HYSYS simulations and data analysis unveil a fascinating conundrum in single-stage hydrocracking. While recycle demonstrably boosts conversion and diesel yield, it accelerates catalyst degradation. This trade-off necessitates tailoring process configuration based on priority. Maximum diesel yield favors recycle, aligning with past studies showing yield increases. However, prioritizing catalyst life necessitates eschewing recycle due to slower deactivation, as evidenced in literature. Beyond illuminating this crucial choice, this study empowers optimization through its comprehensive approach, positioning itself as a valuable investment in advancing hydrocracking performance and efficiency.

## Acknowledgments

This study was supported by Program of Petrochemistry and Polymer Science, Faculty of Science, Chulalongkorn University and the National Research Council of Thailand / Chulalongkorn University for providing the Mid-Career Research Grant (N42A660438).

## References

- [1] Bhutani N., Ray A., and Rangaiah G. P. (2006). Modeling, Simulation, and Multi-objective Optimization of an Industrial Hydrocracking Unit. *Industrial Engineering Chemistry Research* 45, 1354-1372.
- [2] Jorge A., and Sergio S., Miguel A. R. (2005). Kinetic modeling of hydrocracking of heavy oil fractions. *Catalysis Today* 109, 76-92.
- [3] Jan M., and Ireneusz M. (2005). Study on Single-stage Hydrocracking of Vacuum Residue in the Suspension of Ni-Mo Catalyst. *Applied Catalysis A: General* 283, 147-155.
- [4] Mohanty S., Saraf D.N. and Kunzru D. (1991). Modeling of a hydrocracking reactor. *Fuel Processing Technology* 29, 1-17.
- [5] Ramakanta S., Byung J., Ji S., Young-Pyo J., and Chul W. (2015). A review of recent advances in catalytic hydrocracking of heavy residues. *Journal of Industrial and Engineering Chemistry* 27, 12-24.
- [6] Zhou H., Lu J., Cao Z., Shi J., Pan M., Li W., Jiang Q. (2011). Modeling and optimization of an industrial hydrocracking unit to improve the yield of diesel or kerosene. *Fuel* 90, 3521-3530.

## Process simulation of the reactive distillation using various ethanol-to-lactic acid ratios for the purification of lactic acid produced by fermentation

Salisa Dachboon, Suchanya Junsen, Sasithon Singbun, and Anawat Sungpet\*

Department of Chemical Engineering, Faculty of Engineering, King Mongkut's University of Technology Thonburi, 126 Pracha Uthit Rd., Bang Mod, Thung Khru, Bangkok, 10140, Thailand  
E-mail: \* [anawat.sun@kmutt.ac.th](mailto:anawat.sun@kmutt.ac.th)

### Abstract

The objective of this study was to know the effects of the molar ratios between ethanol to lactic acid on the process that used reactive distillation columns to purify lactic acid obtained from the fermentation. Aspen Plus V.10 was used to simulate the process to produce 88 wt. % lactic acid. The molar ratios of ethanol to lactic acid were 3:1, 4:1, and 5:1. The simulation results showed that if the reboiler duty was the same for all ratios, the purity of lactic acid decreased with the increase of the molar ratio. This was because the temperature profiles in the column decreased, leading to the lesser extent of the reactions. When the reboiler duty was adjusted to generate similar temperature profiles, the purity of lactic acid increased to the specified value. When the conversion %, the lactic acid production rate, and the energy utilization were considered, the molar ratio of 3:1 provided the highest conversion % and the production rate. The reboiler duty of the columns was also the least.

**Keywords:** Lactic acid; Process simulation; Reactive distillation; Purification

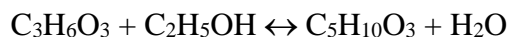
### 1. Introduction

Fermentation of biomass such as corn stover can produce lactic acid, which has applications in many industries, for example, pharmaceuticals, and textiles. It is also used to produce polylactic acid, which is a biodegradable polymer. Lactic acid is one of the biochemicals that will be produced in the Eastern Economic Corridor (EEC) Thailand [1] as the demand for lactic acid is increasing rapidly.

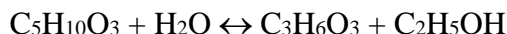
Even though lactic acid has a wide range of applications, the commercial utilization of the lactic acid produced by fermentation is limited due to the expensive downstream processing, which costs around 30 to 40 % of the total production cost [2]. The cost of separation and final purification stages is estimated to be 50 % of the total production cost [3]. The high affinity between lactic acid and water, and the low volatility of lactic acid pose a great challenge to the separation and purification. Furthermore, the oligomerization of lactic acid at high temperatures is another challenging difficulty.

Reactive distillation combines chemical reactions and distillation separation in a single column, providing many advantages when compared with conventional separation and purification methods. Examples of the advantages are the low capital investment and operating costs, and an increase in conversion and selectivity.

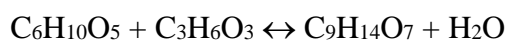
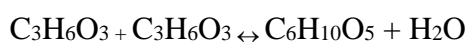
A two-step reaction process can be used for the separation and purification of lactic acid from fermentation broth by reactive distillation. Lactic acid is first reacted with alcohol to form a more volatile ester. The reversible esterification reaction is facilitated by an acid catalyst. The reaction of lactic acid with ethanol is shown by the following equation.



The ethyl lactate is subsequently hydrolyzed back into lactic acid and ethanol by the hydrolysis reaction. The reaction shown below is also catalyzed by an acid catalyst.



The undesirable oligomerization reactions are expressed by the following equations.



The alcohol-to-lactic acid molar ratio is an important parameter in esterification. The laboratory experiments showed that the ethyl lactate yield increased with the ethanol/lactic acid molar ratio because the excess of ethanol shifts the equation to the right, toward the desired product [4]. It was also found that the equilibrium conversion increases with the initial ethanol-to-lactic acid molar ratio [5]. The conversion increased from 9 % for the molar ratio of 1 to 35 % when the molar ratio of 6 was used. The effect of lactic acid to methanol molar ratio on the recovery of lactic acid in a batch distillation process was studied [6]. The products from the esterification column, i.e. methyl lactate and water, were distilled in the hydrolysis column. The yield of lactic acid increased as the lactic acid to methanol molar ratio decreased from 1:4 to 1:2 because the decrease led to a decrease in the unreacted methanol, increasing the boiling temperature of the reaction mixture. The higher boiling temperature resulted in the higher transfer of methyl lactate in the reboiler of the esterification part to the reboiler of the hydrolysis part. As shown from the literature review the the molar ratio of alcohol to lactic acid affected the production of lactic acid, the objective of this study was to know the effects of the molar ratios between ethanol to lactic acid on the process that used reactive distillation columns to purify lactic acid obtained from the fermentation.

## 2. Method

### 2.1. Description of Process Units

The process consists of four main units, i.e. the preconcentrator, the esterification column, the hydrolysis column, and the ethanol recovery column as shown in Figure 1. The feed was the lactic acid solution obtained from the fermentation of corn stover [7]. The molar percentages of water, lactic acid, and acetic acid were 96.85, 2.02, and 1.13, respectively. Acetic acid was only the impurity in the feed because the concentrations of 5-hydroxymethylfurfural (HMF) and furfural were very small. The solution was concentrated by the preconcentrator before it was fed into the esterification column. The reduction of water in the solution promoted the esterification reaction to produce the products. The feed stage of the preconcentrator was stage number 2. The column had a pressure of 0.2 atm. The distillate rate obtained from the preconcentrator was 199.83 kmol/h and consisted of 99.11 mol % water. The bottom rate was 10.17 kmol/h. It consisted of 52.51, 41.70, and 5.79 mol % of water, lactic acid, and acetic acid, respectively. This bottom stream was fed into the esterification column.

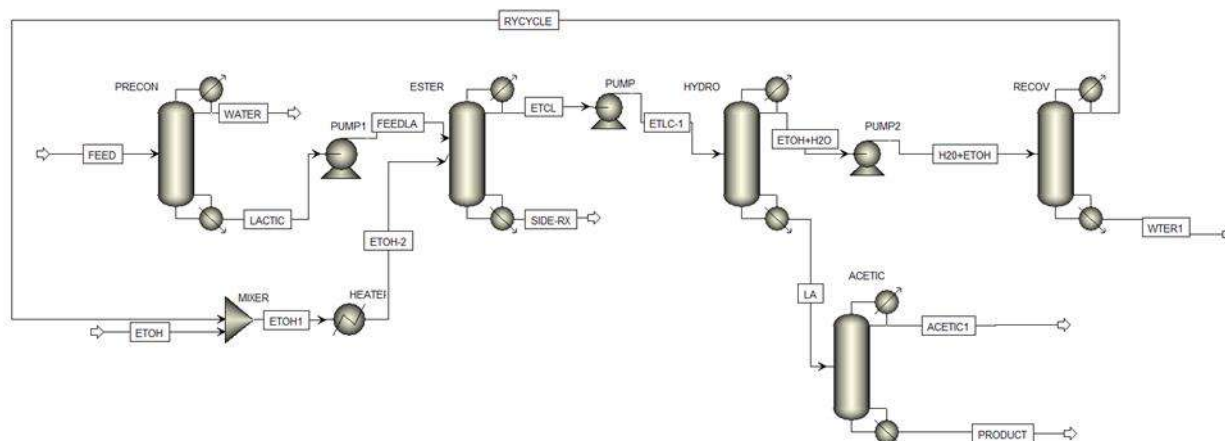


Fig. 1 Process flow sheet of lactic acid separation and purification.

Lactic acid was converted to ethyl lactate in the esterification column. The pressure of the column was 0.2 atm. The feed obtained from the preconcentrator was fed into stage number 2 of the column at a rate of 10.17 kmol/h. Ethanol fed into the column at stage number 28 was the fresh ethanol and the recycled ethanol from the ethanol recovery column. The number of total stages was 29. The reactions were specified to occur from stage 3 to stage 27.

Ethyl lactate was hydrolyzed back to lactic acid and ethanol in the hydrolysis column. The pressure of the column was 1 atm. The ethyl lactate solution was fed into stage number 8 of the column. The total number of stages was 29. The reactions were specified to take place from stage 2 to stage 7, and from stage 9 to stage 28.

The acetic acid column was necessary for the production of lactic acid with a minimum purity of 88 wt. %. The column pressure was 1 atm. The bottom stream from the hydrolysis column was fed into stage number 5 of the acetic column, which had a total number of stages equal to 14.

The ethanol recovery column consisted of 38 stages, and the pressure was 1 atm. It separated ethanol from other impurities and partially supplied ethanol for the esterification column.

## 2.2. Reaction Kinetics and Phase Equilibria

The kinetic parameters of the reactions mentioned in the introduction section were from Navinchandra, et al. [8]. Although the feed stream included acetic acid as the impurity and would result in the presence of ethyl acetate in the esterification column, the esterification of acetic acid was excluded. If ethyl acetate were formed in the esterification column, it probably would be in the distillate stream as acetic acid did because both compounds had similar boiling points. Ethyl acetate would then be converted back to acetic acid in the hydrolysis column, which would require the separation from lactic acid by the acetic acid column in the same manner employed by this work. The UNIQUAC model was used to account for nonideal vapor-liquid and vapor-liquid-liquid equilibriums of the systems. The Hayden-O'Connell second virial coefficient model was used for the vapor phase nonideality. The fugacity coefficients were computed by the Aspen Plus built-in association parameters. The parameters that were not in the Aspen database were estimated by UNIFAC.

### 3. Results and Discussion

The temperature profiles in the esterification and hydrolysis columns greatly affected the reactions. When the molar ratio of ethanol to lactic acid was 3:1, the reboiler duty of the esterification column was 405 kW, and the reboiler duty of the hydrolysis column was 290 kW. These conditions provided the production of lactic acid with 88 wt. % purity from the process. As the molar ratio increased to 4:1, the temperature profiles of the columns changed, leading to a decrease in the lactic acid purity. The process simulation failed when the molar ratio increased to 5:1. The temperature profiles in the esterification and the hydrolysis columns radically changed, leading to the failure of the recovery column. The reboiler duties of the esterification and hydrolysis columns must be altered to produce lactic acid with 88 wt. % purity.

#### 3.1. Esterification column

Ethyl lactate production rate from the ethanol-to-lactic acid ratio of 4:1 was less than that obtained from the 3:1 ratio as shown in Table 1. Lactic acid was converted to dilactic acid to a higher extent.

Table 1. The molar flow rate (kmol/h) of the main products from the esterification column at various ethanol-to-lactic acid molar ratios: Reboiler duty of column = 405 kW.

Component	Ethanol-to-Lactic Acid Molar Ratio	
	3:1	4:1
<b>Distillate product</b>		
Lactic acid	0.023	0.012
Ethanol	8.876	14.390
Ethyl lactate	3.997	2.884
Water	13.702	12.970
Dilactic acid	$4.386 \times 10^{-4}$	0
Trilactic acid	0	0
<b>Bottom product</b>		
Dilactic acid	0.043	0.635
Trilactic acid	0.044	0.024

This was because the increase in the ethanol flow rate into the column led to a decrease in the temperature profile as shown in Fig. 1. The lower conversion of lactic acid to ethyl lactate as the ethanol-to-lactic acid molar ratio increased from 2.52 to 9.2 was also experimentally observed [9]. To produce ethyl lactate at a similar flow rate obtained from the ethanol-to-lactic acid molar ratio of 3:1, the reboiler duty was increased from 405 kW to 434 kW for the 4:1 ratio, and 460 kW for the 5:1 ratio. Table 2 presents the results after the increase of the reboiler duty. The rates of ethyl lactate production at the ratios of 4:1 and 5:1 were comparable to that produced from the 3:1 ratio. It was partly because the side reactions occurred to a lesser extent, as indicated by the decrease in the molar flow rate of dilactic acid. Nonetheless, the limited side reactions because of the more appropriate temperatures may not be only the reason. The temperature profiles of the ratios 4:1 and 5:1 after the increase in the reboiler duty were not the same as that of the 3:1 ratio as shown in Fig. 2. Another possibility was the excess ethanol in the column promoted the forward reaction.

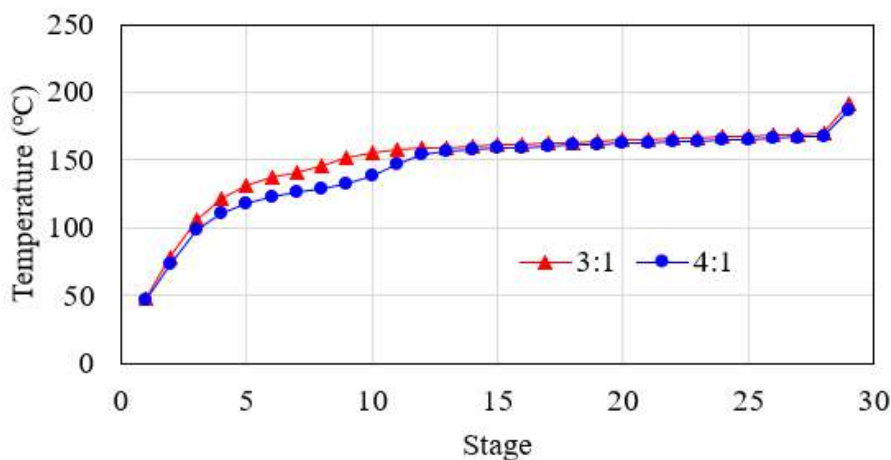


Fig. 1 Temperature profiles of the esterification column when the ethanol-to-lactic acid molar ratios are 3:1 and 4:1: Reboiler duty of column = 405 kW.

Table 2. The molar flow rate (kmol/h) of the main products from the esterification column at various ethanol-to-lactic acid molar ratios: Reboiler duty of column = 434 kW for the 4:1 ratio, and 460 kW for the 5:1 ratio.

Component	Ethanol-to-Lactic Acid Molar Ratio		
	3:1	4:1	5:1
<b>Distillate product</b>			
Lactic acid	0.023	0.018	0.0143
Ethanol	8.876	13.458	17.845
Ethyl lactate	3.997	4.129	4.0635
Water	13.702	13.170	12.926
<b>Bottom product</b>			
Dilactic acid	0.043	0.015	0.063
Trilactic acid	0.044	0.021	0.012

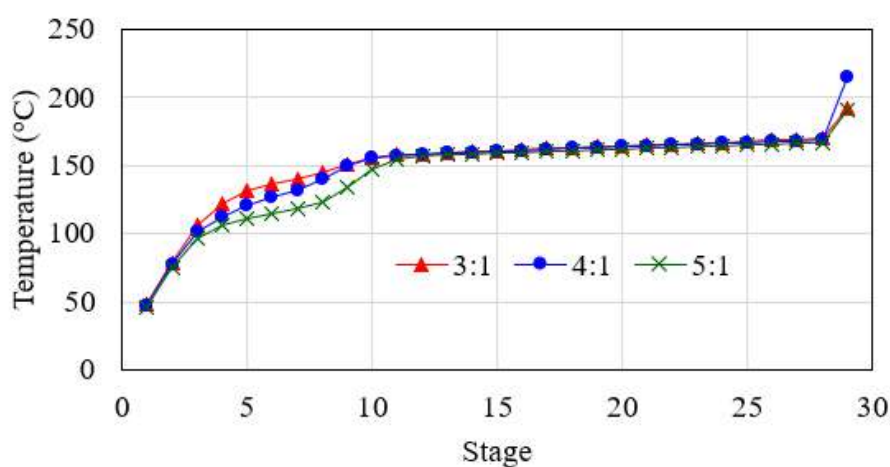


Fig. 2 Temperature profiles of the esterification column when the ethanol-to-lactic acid molar ratios are 3:1 and 4:1: Reboiler duty of column = 405 kW for the 3:1 ratio, 434 kW for the 4:1 ratio, and 460 kW for the 5:1 ratio.

### 3.2. Hydrolysis Column

The lactic acid molar flow rate produced from the ethanol-to-lactic acid ratio of 4:1 was significantly less than the rate obtained from the 3:1 ratio as shown in Table 3.

Table 3. The molar flow rate (kmol/h) of the main products from the hydrolysis column at various ethanol-to-lactic acid molar ratios: Reboiler duty of column = 290 kW.

Component	Ethanol-to-Lactic Acid Molar Ratio	
	3:1	4:1
<b>Distillate product</b>		
Ethanol	12.692	13.032
Water	6.095	5.338
<b>Bottom product</b>		
Lactic acid	3.659	1.150
Ethanol	0.013	2.573
Ethyl lactate	0.037	1.669
Water	3.493	6.455
Acetic acid	0.588	0.588
Dilactic acid	0.163	0.038

The unsuitable temperature in the column was probably a reason for the lower conversion of ethyl lactate hydrolysis. The temperature profile in the column at the ethanol-to-lactic acid ratio of 4:1 was slightly lower than that of the 3:1 ratio as shown in Fig. 3.

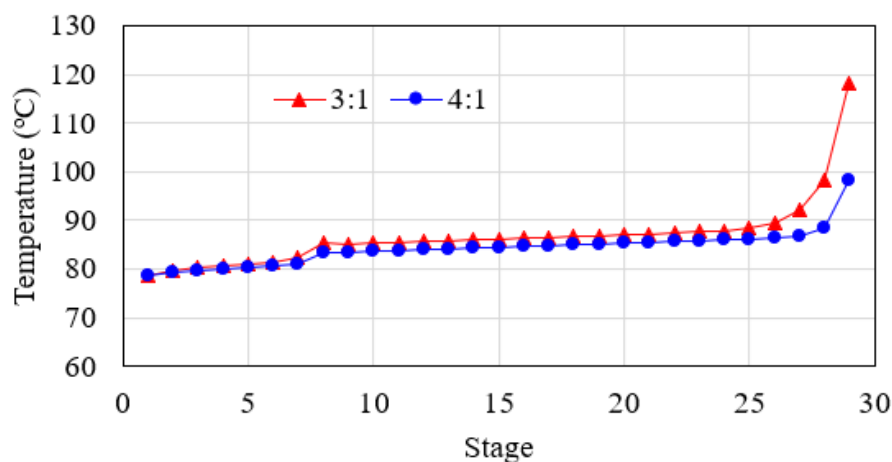


Fig. 3 Temperature profiles of the hydrolysis column when the ethanol-to-lactic acid molar ratios are 3:1 and 4:1: Reboiler duty of column = 290 kW.

The hydrolysis of ethyl lactate was increased as the reboiler duty was increased. For the 4:1 ratio, the reboiler duty of the hydrolysis column was increased to 350 kW. The reboiler duty was increased to 425 kW for the 5:1 ratio. The temperature profiles of both ratios were consequently similar to that of the 3:1 ratio. The molar flow rates of lactic acid correspondingly increased as shown in Table 4.



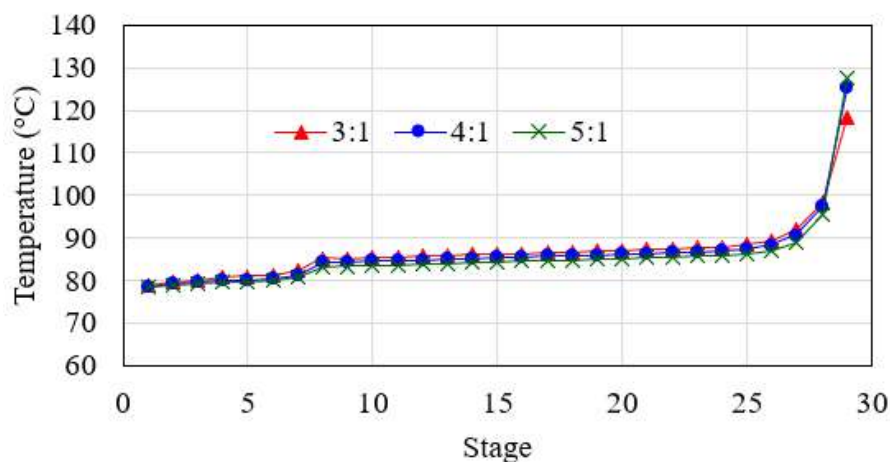


Fig. 4 Temperature profiles of the hydrolysis column when the ethanol-to-lactic acid molar ratios are 3:1 and 4:1: Reboiler duty of column = 290 kW for the 3:1 ratio, 350 kW for the 4:1 ratio, and 425 kW for the 5:1 ratio.

Table 4. The molar flow rate (kmol/h) of the main products from the hydrolysis column at various ethanol-to-lactic acid molar ratios: Reboiler duty of column = 350 kW for the 4:1 ratio, and 425 kW for the 5:1 ratio.

Component	Ethanol-to-Lactic Acid Molar Ratio		
	3:1	4:1	5:1
<b>Distillate product</b>			
Ethanol	12.692	16.748	20.600
Water	6.095	6.851	7.470
<b>Bottom product</b>			
Lactic acid	3.659	3.202	3.033
Ethanol	0.013	0.310	0.367
Ethyl lactate	0.037	0.801	0.943
Water	3.493	3.062	2.382
Acetic acid	0.588	0.588	0.588
Dilactic acid	0.163	0.072	0.051

Even though the temperature profiles were very similar, the lactic acid production rates obtained from the 4:1 and 5:1 ratios were still less than that of the 3:1 ratio. It was very likely that the excess ethanol in the hydrolysis column, as evidenced by the significantly higher ethanol flow rates in the bottom product streams of the 4:1 and 5:1 ratios, caused the reaction to shift backward.

#### 4. Conclusions

The process simulation of lactic acid purification from the feed containing 96.85, 2.02, and 1.13 molar percentages of water, lactic acid, and acetic acid, respectively, was performed. The process consisted of two reactive distillation columns for the esterification and the hydrolysis reactions. The objective of the simulation was to learn about the effects of the ethanol-to-lactic

acid ratio fed to the process. When compared with the ethanol-to-lactic molar ratio of 3:1, the utilization of a higher ratio of 4:1 reduced the temperature in both the esterification and the hydrolysis columns. As a consequence, the production of ethyl lactate in the esterification column and lactic acid in the hydrolysis column were lower. The increase in the temperature in the columns resulted in higher molar flow rates of ethyl lactate in the esterification column, and the lactic acid in the hydrolysis column. The excess ethanol in the esterification column was probably another reason that helped shift the reaction to the product side. However, the excess ethanol in the hydrolysis column led to lower lactic acid production rates due to the backward shifting of the reaction.

## References

- [1] What is EEC? EEC MISSION.  
<https://www.eeco.or.th/th/filedownload/2959/f73de7f9e3571ea9f307e48aec38c445.pdf>
- [2] Lopez-Garzon, C.S., & Straathof, A. J. J., (2014). Recovery of carboxylic acids produced by fermentation. *Biotechnology Advances*, 32(5), 873-904.
- [3] Komesu, A., Martins, P.F.M., Lunelli, B.H., Oliveria, J., Filho, R. M., & Maciel, M. R. W., (2015). The effect of evaporator temperature on lactic acid purity and recovery by short path evaporation. *Separation Science and Technology*, 50(10), 1548-1553.
- [4] Komesu, A., Martinez, P. F. M., Lunelli, B. H., Filiho, R. M., & Maciel, M. R. W., (2015). Lactic acid purification by reactive distillation system using design of experiments. *Chemical Engineering and Processing: Process Intensification*, 95, 26-30.
- [5] Delgado, P., Sanz, M. T., Beltran, S., (2007). Kinetic study for esterification of lactic acid with ethanol and hydrolysis of ethyl lactate using an ion-exchange resin catalyst. *Chemical Engineering Journal*, 126, 111-118.
- [6] Seo, Y., Hong, W. H., Hong, T. H., (1999). Effects of Operation Variables on the Recovery of Lactic Acid in a Batch Distillation Process with Chemical Reactions. *Korean Journal of Chemical Engineering*, 16(5), 556-561.
- [7] Hu, J., Lin, Y., Zhang, Z., Xiang, T., Mei, Y., Zhao, S., Liang, Y., & Peng, N., (2016). High-titer lactic acid production by lactobacillus pentosus F10421 from corn stover using fed-batch simultaneous saccharification and fermentation. *Bioresource Technology*, 214, 74-80.
- [8] Navinchandra, S. A., Kolah, A. K., Vu, D. T., Lira, C. T., & Dennis J. M., (2006). A Kinetic Model for the Esterification of Lactic Acid and Its Oligomers, *Industrial & Engineering Chemistry Research*, 45(15), 5251-5257.
- [9] Miller, D. J., Asthana, N., Kolah, A., Lira, C. T., (2010). Process for Production of Organic Acid Esters. U.S. Patent No. 7652167 B2.

## Simulation and Techno-Economic Comparison of Subcritical Dimethyl Ether, Supercritical Carbon Dioxide and Organic Solvent Extraction of Rice Bran Oil Manufacture

**Dhanakorn Damrongsakul, Chonlatep Usaku, Phannipha Daisuk and Artiwan Shotipruk\***

Bio-Circular-Green-economy Technology & Engineering Center, BCGeTEC, Department of Chemical Engineering, Faculty of Engineering, Chulalongkorn University, Phayathai Road, Patumwan, Bangkok 10330, Thailand.

E-mail: \*Artiwan.Sh@chula.ac.th

### Abstract

This study aims to evaluate the economic feasibility using subcritical dimethyl ether (SUBDME) and supercritical carbon dioxide (SC-CO<sub>2</sub>) as alternative solvents to replace the conventional toxic solvent hexane of extraction rice bran oil (RBO). Large-scale RBO extraction processes were simulated in Aspen Plus through semi-batch operations, with extraction conditions obtained from published literature. The simulation results, including mass balances, energy consumptions, and equipment costs, were further analyzed to assess economic feasibility. Techno-economic analysis revealed that SUBDME and hexane extraction processes were the most economical compared to SC-CO<sub>2</sub>. Raw material and utility prices were identified as the most impactful variables on the cost of manufacturing (COM), making SC-CO<sub>2</sub> extraction less profitable overall. Profitability analysis indicated that SUBDME could compete favorably with commercial RBO extraction by hexane with the NPV of 182.2x10<sup>6</sup> US\$ and the payback period of 3.49 years.

**Keywords:** Rice bran oil; Subcritical DME extraction; Simulation; Techno-economic analysis

### 1. Introduction

Rice bran oil (RBO) is obtained from rice bran (RB), a by-product generated during the rice milling process, whose varies between 10% and 22% by weight of RB [1]. Scientific reports indicated that RBO offers several health benefits as it contains plentiful natural antioxidants including  $\gamma$ -oryzanol, tocopherols, tocotrienols, and phytosterols [2]. Exhibiting reduction in low-density lipoprotein (LDL) cholesterol levels, prevention of cardiovascular disease, and anti-inflammatory effects [3], RBO is widely used as nutritional supplements and in medicinal and cosmetic applications [4]. In RBO, Oleic acid, a monounsaturated fatty acid (MUFA), constitutes 38.4% to 42.3%. Polyunsaturated fatty acid (PUFA) constitutes 33.1% to 37.0% linoleic acid, and a small amount of linolenic acid, approximately 0.5% to 2.2%. Palmitic acid is the main saturated fatty acid (SFA) component in RBO, ranging from 17.0% to 21.5%, while stearic and myristic acids are minor SFAs, containing 1.0% to 3.0% and 0.4% to 1.0%, respectively [5].

Extraction of RBO is carried out with an organic solvent, typically hexane. However, hexane is widely known for its high toxicity, environmental impact and human health issues [6]. To reduce the risk of toxicity to the environment and human health, non-conventional

extraction solvents and methods have been proposed. Supercritical carbon dioxide (SC-CO<sub>2</sub>) extraction has been considered a renewable green technology, by adjusting above critical temperature of 31 °C and critical pressure of 73.8 bar. In the wide range above critical conditions, CO<sub>2</sub> can modify its density and solvent power for the extraction of RBO. Additionally, removal CO<sub>2</sub> from the extracted oil is easily achieved by reverting CO<sub>2</sub> to a gaseous form, via depressurization to atmospheric conditions [7]. Recently, researchers have investigated another extraction technique known as subcritical dimethyl ether (SUBDME). DME can be readily turned into liquid phase under pressure of 5.9 bar at room temperature [8], which is lower than the operating condition of SC-CO<sub>2</sub>, possibly reduce the energy consumption. This has a potential opportunity to reduce the energy consumption for RBO extraction process, which could lower and optimize the production cost of RBO manufacturing, all while maintaining its status as an environmentally friendly technology.

In this work aims to evaluate the economic feasibility of alternative RBO extraction techniques, specifically DME extraction method, in comparison to traditional organic solvent extraction and SC-CO<sub>2</sub> extraction. Aspen plus V11 software was employed to simulate the flow processes in a commercial production scale at extraction conditions obtained from lab-scale experiments in literatures, and the energy consumptions and economic assessments for various processes were then analyzed.

## 2. Materials and Methods

### 2.1 Rice bran component estimation

In this work, the physical properties of non-conventional component of RB are required to estimate thermodynamic properties by Aspen plus which include the density and specific heat capacity whose values of 1.38 g/cm<sup>3</sup> [9] and 0.41 BTU/lb<sub>m</sub>·°F [10], respectively. The typical composition of RB was sourced from published literature [11]. In RB, moisture and lipids content were selected as main components, constituting 9.26 wt.% and 22.2 wt.%, respectively. The  $\gamma$ -oryzanol, representing 12,510 mg per kg<sub>RB</sub>, were manually added the molecule structure, which was imported from NCBI databank and physicochemical properties were predicted by Aspen Plus.

### 2.2 Process modelling and simulation

The quantity of RB feed stream was based on the RBO production of Thai Edible Oil Co. Ltd, with the maximum feed loading capacity of 200,000 tons/year. The solvent to feed ratios for different extraction processes were taken from selected literatures, as summarized in Table 1 along with information regarding process conditions and extraction yields. The UNIF-LL thermodynamic model was employed for SUBDME extraction, as it is typically applied in liquid-liquid equilibrium at pressures lower than 10 bar. For SC-CO<sub>2</sub> extraction, which CO<sub>2</sub> exists at supercritical condition above critical pressure of 73.8 bar, the RK-ASPEN model was generally employed to handle mixtures of hydrocarbons and light gases (such as CO<sub>2</sub>) at high pressures [12]. For hexane extraction, NRTL model was used, which handles combination of polar and non-polar compounds, particularly when they are farther away from their critical conditions. Solvents and make-up solvents of each extraction process are transported as liquid phase and stored in a storage vessel. For all extraction processes, solvents were recycled, with a loss assumed as 2% of the total solvent per

extraction cycle. Crude product is stored at 30 °C as a crude RBO product, in which the maximum allowable solvent contamination is 1.5 wt.% of the extracted product [13]. Pumps and compressors were assumed to have an isentropic efficiency of 80% [14]. Semi-continuous operation was assumed employing multiple extraction vessels, to make approximate the continuous RBO production on industrial scale. Each extraction undergoes three operational steps: loading of RB, batch RBO extraction, and unloading of defatted and product. Loading and unloading times are 30 minutes for SC-CO<sub>2</sub> and SUBDME extraction while for organic solvent extraction, loading and unloading takes 15 minutes [14].

Table 1 Extraction conditions based on selected literatures and laboratory results.

Extraction technique	Pressure (bar)	Temperature (°C)	Extraction time (min)	Solvent to RB	RBO yield (%)	Oryzanol recovery	Ref.
SUBDME	7	30	10	6.53 g:1 g <sub>RB</sub>	20.2	91 %	This work
SC-CO <sub>2</sub>	300	40	240	70 g:1 g <sub>RB</sub>	17.6	89 %	[15]
Hexane	-	40	90	3.27 g:1 g <sub>RB</sub>	19.78	18.53 g/kg <sub>CRBO</sub>	[16]

### 2.2.1 SUBDME extraction

The process flow diagram for RBO extraction with subcritical DME is shown in Fig. 1. Initially, liquid DME (6 bar, 25 °C) solvent is adjusted to the extraction conditions of 6 barg and 30 °C using a pressure pump (PUMP) and a heater (HX1). To extract RBO, the solvent and RB are then fed into extraction vessels (EXT) at a mass ratio of 6.53 g<sub>solvent</sub>:1 g<sub>RB</sub>. After reaching an extraction time of 10 minutes for each cycle (total of 31,680 cycles per year), the solid residue is discharged at the bottom of EXT. The oil-solvent mixture is depressurized and heated through a back pressure regulator valve (VALVE1) and a heater (HX2) to isolate the solvent from the crude product stream. The solvent separation occurs at a flash separator vessel (SEP1). The crude product flows to a flow regulator valve (VALVE2) to reduce the pressure to atmospheric pressure, while heat supplied at the heater (HX3) to evaporate the residual DME. Crude product is separated at a flash separator vessel (SEP2). DME is recompressed and then cooled by a compressor (CP) and a cooler (HX4). The stream (RC-4) is then mixed with recycle stream (RC-1) from SEP1, and the stream exiting the mixer (MIXER2) was then passed to a cooler (HX5) where it is cooled to the initial liquid DME stage. Finally, the extracted oil is cooled by a cooler (HX6) as a crude RBO product.

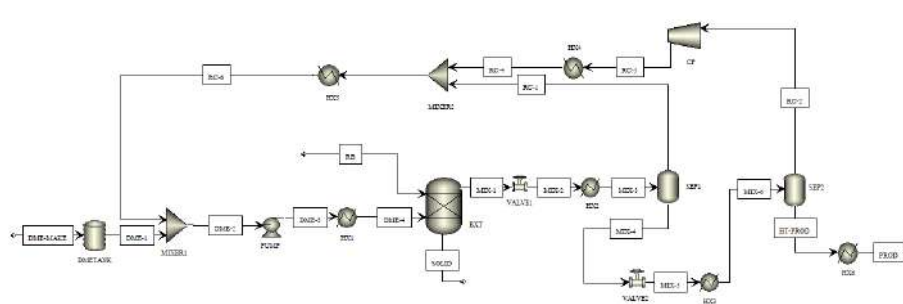


Fig. 1 Process flow diagram of RBO extraction by DME extraction technique

### 2.2.2 SC-CO<sub>2</sub> extraction

As shown in the process flow diagram for SC-CO<sub>2</sub> extraction of RBO in Fig. 2, liquid CO<sub>2</sub> (45 bar, 9 °C) is compressed to the desired working pressure and is heated to supercritical conditions of 300 bar at 40 °C [15] using a high-pressure pump (PUMP) and a heater (HX1). The SC-CO<sub>2</sub> and RB are then fed into extractor vessels (EXT) at a mass ratio of 70 g<sub>solvent</sub>:1 g<sub>RB</sub> [15]. Once the extraction time of 240 minutes is reached [15], corresponding to approximately 7,920 cycles per year, solid is discharged at the bottom of EXT while the mixture of oil and solvent is depressurized through a back pressure regulator valve (VALVE1) to 45 bar and is heated (HX1) to evaporate CO<sub>2</sub> before it is fed into a flash separator vessel (SEP1) to isolate CO<sub>2</sub> from the product. The crude product is sent to a flow regulator valve (VALVE2) to reduce pressure to atmospheric stage which residue of CO<sub>2</sub> is evaporated and isolated at a flash separator vessel (SEP2). Subsequently, the pressure and temperature of CO<sub>2</sub> are adjusted to the initial stage by a compressor (CP) and a cooler (HX3) prior to being recycled to the process. Finally, the extracted oil is cooled by a cooler (HX5) and stored as a crude RBO product.

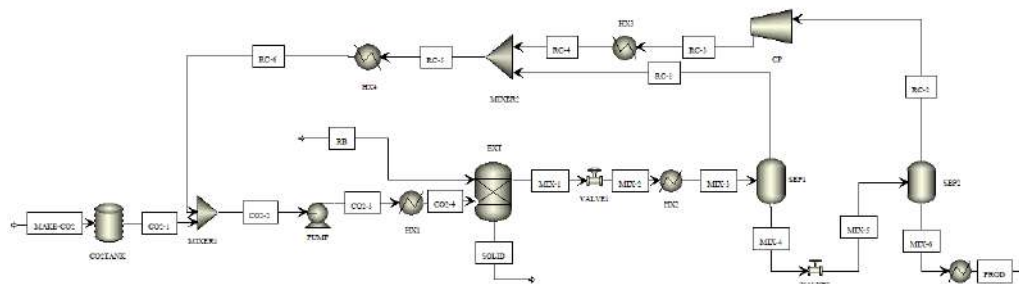


Fig. 2 Process flow diagram of RBO extraction by SC-CO<sub>2</sub> extraction technique

### 2.2.3 Organic solvent extraction

The process flow diagram for organic solvent extraction is illustrated in Fig. 3. The hexane, stored at 25 C and 0.1 bar, is heated to extraction conditions at 40 °C [16] using a heater (HX1) then the solvent and RB are fed to extractor vessels (EXT) at a mass ratio of 3.27 g<sub>solvent</sub>:1 g<sub>RB</sub> [16]. After reached the extraction time of 90 minutes [16], which can operate 15,840 cycles per year, solid is discharged at the bottom of EXT. On the other hand, the mixture of oil and solvent is heated by a heater (HX2) then sent to a flash separator vessel (SEP) to isolate the solvent from crude extract. The solvent (160 °C) is cooled to the initial stages (25 °C and 0.1 bar) by a cooler (HX3). Finally, the extracted oil is cooled by a cooler (HX4) and stored as a crude RBO product.

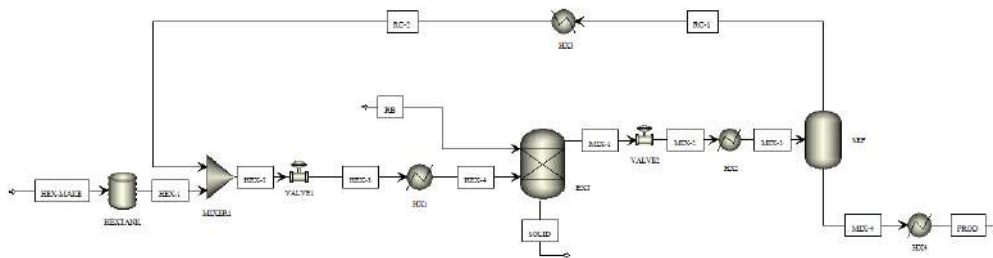


Fig. 3 Process flow diagram of RBO extraction by organic solvent extraction technique

## 2.3 Economic assessment

In this study, the plant is designed to operate 330 working days per year or 7,920 h/year. Economic performance will be evaluated based on the Fixed Capital Investment cost (FCI) and the Cost of Manufacturing (COM), e.g. cost of raw material ( $C_{RM}$ ), cost of utility ( $C_{UT}$ ), and labor cost ( $C_{OL}$ ). The ATEX (Atmosphere Explosible) factor for DME and hexane extraction was two times the base cost of the equipment due to the requirement of special precautions such as the use of explosion proof equipment. The parameters used in the assessment of the economic profitability include Net Present Value (NPV) over 20 years of plant life with the discount rate of 5 percent per year [17], Profitability Index (PI), Internal Rate of Return (IRR) and Payback Period (PB). The input prices of raw material, solvents, products, and utilities, summarized in Table 2, were from Alibaba and Turton et al. (2018).

Table 2 Raw material streams, product and the cost of utilities

Stream / Utility	Value	Cost per unit	Ref.
Rice bran	150	US\$/ton	[18]
Liquid dimethyl ether	652	US\$/ton	[19]
Liquid carbon dioxide	220	US\$/ton	[20]
Hexane	1,040	US\$/ton	[21]
Crude rice bran oil	1,806.6	US\$/ton	[13]
Cooling water	0.378	US\$/GJ	[17]
Chilled water	4.77	US\$/GJ	[17]
Low pressure steam	2.03	US\$/GJ	[17]
Medium pressure steam	2.78	US\$/GJ	[17]
Electricity	0.074	US\$/kWh	[17]

## 3. Results and Discussion

### 3.1 The simulated results of RBO extraction processes by Aspen plus

According to the calculations performed using Aspen Plus, Table 3 presents the conditions and mass flows of the main process streams. For the raw material and solvent loadings, SC-CO<sub>2</sub> extraction exhibited the highest mass flow of solvent and RB due to the fewer extraction cycles per year, resulting from the long extraction time compared to the SUBDME and hexane extractions. The final product stream boasted a total purity of product (RBO and  $\gamma$ -oryzanol) in mass percentage of 98.6% (SUBDME), 99.85% (SC-CO<sub>2</sub>) and 98.52% (Hexane). SC-CO<sub>2</sub> provided the highest purity as most of the CO<sub>2</sub> was readily isolated from the extracted material and recovered in the recycle stream, whereas DME required heating to isolate solvent, however with a milder temperature of around 60 °C, compared to hexane removal, which necessitated approximately 160 °C according to the simulation.

Table 3 Mass balance and operating conditions of RBO extraction.

Stream	SUBDME			SC-CO <sub>2</sub>			Hexane		
	DME-4	RB	PROD	CO2-4	RB	PROD	HEX-4	RB	PROD
Temp.(°C)	30	25	30	40	25	30	40	25	30
Pressure(bar)	7	1	1	300	1	1	1	1	1

Mass flow (kg/batch)	41,252	6,313.1	1,366.7	1.77x10 <sup>6</sup>	25,252.5	4,732.7	82,772.7	12,626.3	2,582.0
Solvent(wt.%)	99.93	-	1.40	99.99	-	0.15	99.88	-	1.48
Water(wt.%)	0.07	9.62	-	0.01	9.62	-	0.12	9.62	-
Oil(wt.%)	-	22.2	93.34	-	22.20	93.91	-	22.2	96.73
γ-oryzanol (wt.%)	-	1.25	5.26	-	1.25	5.94	-	1.25	1.79
Solid(wt.%)	-	66.93	-	-	66.93	-	-	66.93	-

### 3.2 Economic assessment

Total FCI and COM are illustrated in Table 4. Total FCI for the SUBDME, SC-CO<sub>2</sub> and hexane extractions were 6.34x10<sup>6</sup>, 33.72x10<sup>6</sup> and 3.36x10<sup>6</sup> US\$, respectively. The SUBDME and SC-CO<sub>2</sub> processes incurred higher equipment costs than hexane due to the need for a compressor to recompress the solvent to its initial feeding conditions at high pressure. The major difference occurred in SC-CO<sub>2</sub> extraction, primarily because of the larger size of equipment needed to support the very high quantity of raw material and solvent loading.

Regarding COM, C<sub>RM</sub> was directly related to the amount of RB and solvent that had to fed to the process, results in the SUBDME and hexane extractions providing lower C<sub>RM</sub> of 47.4x10<sup>6</sup> US\$/year and 44.2x10<sup>6</sup> US\$/year, respectively, while SC-CO<sub>2</sub> process provided the highest C<sub>RM</sub> of 91.6x10<sup>6</sup> US\$/year. C<sub>UT</sub> was increasingly spent on a high-pressure technology of SC-CO<sub>2</sub> process, amounting to 35.4x10<sup>6</sup> US\$/year. This is due to the relatively high energy consumption needed to generate supercritical conditions of CO<sub>2</sub>, and cooling utilities were required in large quantities to reduce the temperature of the recovered solvent to the initial feeding stage at low temperature of 9 °C. In contrast, the mild conditions of SUBDME and hexane processes utilized lower energy to reach the extraction conditions and provided a low C<sub>UT</sub> of 1.5x10<sup>6</sup> US\$/year and 1.3x10<sup>6</sup> US\$/year, respectively.

The money invested to produce 1 kg of extracted product was evaluated, which was found that SUBDME and hexane processes yielded similar values of 1.44 US\$kg<sup>-1</sup><sub>product</sub> and 1.43 US\$kg<sup>-1</sup><sub>product</sub> due to the high extraction yields and low manufacturing costs, while SC-CO<sub>2</sub> extraction provided the highest value of 4.36 US\$kg<sup>-1</sup><sub>product</sub> due to lower extraction yield and very high manufacturing costs associated with extracting RBO.

Table 4 Comparison of direct cost estimates for each of the three RBO extraction processes

Cost	Unit	SUBDME	SC-CO <sub>2</sub>	Hexane
Fixed Capital (FCI)	US\$	6,341,400	33,720,700	3,358,000
Raw Materials (C <sub>RM</sub> )	US\$/year	47,426,479	91,612,336	44,249,381
Utilities (C <sub>UT</sub> )	US\$/year	1,517,369	35,411,932	1,314,495
Labor (C <sub>OL</sub> )	US\$/year	357,143	357,143	357,143
Cost of Manufacturing (COM)	US\$/year	62,317,385	163,284,575	57,685,288
Product sale	US\$/year	78,222,099	67,716,536	72,793,418
Unit Cost of Manufacturing	US\$/kg <sub>product</sub>	1.44	4.36	1.43

### 3.3 Feasibility analysis



The cumulative cash flow estimation is illustrated in Fig. 4, represents the construction stages of the industrial plant, concluding within two years. SUBDME and hexane extraction processes emerged as the most economically feasible cases. The estimated PB to recover the initial investment were reached in 3.49 and 3.45 years, respectively after the initial investments were made. Additionally, the NPV after 20 operating years amounted to  $182.2 \times 10^6$  US\$ and  $173.2 \times 10^6$  US\$ with IRR 31.86% and 33.10%, for SUBDME and hexane extraction, respectively. These metrics suggest that these processes are profitable and desirable. Moreover, the PI was higher than 1, indicating that these processes are worth investing in. Conversely, SC-CO<sub>2</sub> was not yield a profit as the COM exceeded the revenue from product sales. The NPV was  $-1,288.9 \times 10^6$  US\$ and PI was -6.298, signaling that this process is not worth investing in.

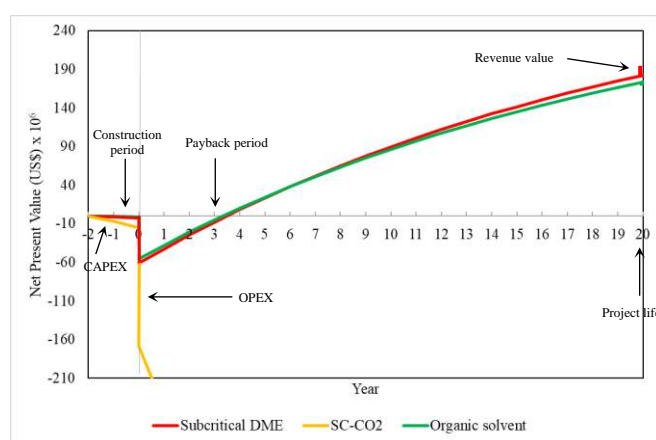


Fig. 4 Cumulative cash flow over project life of RBO extraction processes.

#### 4. Conclusions

SUBDME extraction presents a promising alternative for RBO extraction, offering economic advantages due to higher productivities and greater environmental friendliness, compared to the current commercial RBO extraction using hexane. This is evidenced by comparable NPV, IRR, and PI values, indicating no significant differences. On the other hand, RBO extraction by SC-CO<sub>2</sub> was shown to be the least RBO extraction process on a commercial scale, being extremely energy-intensive and costly, with the highest COM stemming from utility and solvent costs.

#### 5. References

1. Pourali, O., F. Salak Asghari, and H. Yoshida, Simultaneous rice bran oil stabilization and extraction using sub-critical water medium. *Journal of Food Engineering*, 2009. **95**(3): p. 510-516.
2. Bhatnagar, A.S., et al., Processing of commercial rice bran for the production of fat and nutraceutical rich rice brokens, rice germ and pure bran. *LWT - Food Science and Technology*, 2014. **58**(1): p. 306-311.
3. Cho, Y.-H., et al., Characterization and quantification of  $\gamma$ -oryzanol in Korean rice landraces. *Journal of Cereal Science*, 2019. **88**: p. 150-156.
4. Rigo, L.A., et al., Rice Bran Oil, in *Wheat and Rice in Disease Prevention and Health*. 2014. p. 311-322.

5. Lai, O.-M., et al., Nutritional Studies of Rice Bran Oil, in Rice Bran and Rice Bran Oil. 2019. p. 19-54.
6. Rosenthal, A., D.L. Pyle, and K. Niranjana., Aqueous and Enzymatic Processes for Edible Oil Extraction. *Enzyme and Microbial Technology*, 1996. **19**(6): p. 402–420.
7. Pinto, T.I., et al., Supercritical Carbon Dioxide Extraction, Antioxidant Activity, and Fatty Acid Composition of Bran Oil from Rice Varieties Cultivated in Portugal. *Separations*, 2021. **8**(8).
8. Zheng, Q. and M. Watanabe, Advances in low-temperature extraction of natural resources using liquefied dimethyl ether. *Resources Chemicals and Materials*, 2022. **1**(1): p. 16-26.
9. Soares, J.F., et al., Extraction of rice bran oil using supercritical CO<sub>2</sub> and compressed liquefied petroleum gas. *Journal of Food Engineering*, 2016. **170**: p. 58-63.
10. Tao, Jiaxun, "Rice Bran Stabilization by Improved Internal and External Heating Methods." (1989). *LSU Historical Dissertations and Theses*. 4812.
11. Oliveira, R., et al., Effects of the extraction conditions on the yield and composition of rice bran oil extracted with ethanol—A response surface approach. *Food and Bioproducts Processing*, 2012. **90**(1): p. 22-31.
12. Khalati, E., P. Oinas, and L. Favén, Techno-economic and safety assessment of supercritical CO<sub>2</sub> extraction of essential oils and extracts. *Journal of CO<sub>2</sub> Utilization*, 2023. **74**.
13. ExportersIndia. Crude rice bran oil price. 2023, October 20; Available from: [https://www.alibaba.com/product-detail/China-Supplier-Wholesale-Food-Addictive-Reagent\\_1600615168945.html?s=p](https://www.alibaba.com/product-detail/China-Supplier-Wholesale-Food-Addictive-Reagent_1600615168945.html?s=p).
14. Todd, R. and S. Baroutian, A techno-economic comparison of subcritical water, supercritical CO<sub>2</sub> and organic solvent extraction of bioactives from grape marc. *Journal of Cleaner Production*, 2017. **158**: p. 349-358.
15. Wang, C.H., et al., Designing supercritical carbon dioxide extraction of rice bran oil that contain oryzanols using response surface methodology. *J Sep Sci*, 2008. **31**(8): p. 1399-407.
16. Li, D., et al., The enhancement of rice bran oil quality through a novel moderate biorefining process. *Lwt*, 2021. **151**.
17. Turton, R., Shaeiwitz, J. A., Bhattacharyya, D., & Whiting, W. B. (2018). *Analysis, synthesis, and design of chemical processes*.
18. Alibaba. Rice bran price. 2023, October 20; Available from: [https://www.alibaba.com/product-detail/High-Quality-Wholesale-Rice-Bran-best\\_1600369483287.html](https://www.alibaba.com/product-detail/High-Quality-Wholesale-Rice-Bran-best_1600369483287.html).
19. Alibaba. Liquid dimethyl ether (food grade) price. 2023, October 20; Available from: [https://www.alibaba.com/product-detail/Quality-and-quantity-guaranteed-dimethyl-ether\\_1600696583366.html?](https://www.alibaba.com/product-detail/Quality-and-quantity-guaranteed-dimethyl-ether_1600696583366.html?)
20. Alibaba. Liquid CO<sub>2</sub> (food grade) price. 2023, October 20; Available from: [https://www.alibaba.com/product-detail/Factory-Supply-Price-12800kg-High-Purity\\_1600707644358.html?spm=a2700.7735675.0.0.a9b0JedIJedI44&s=p](https://www.alibaba.com/product-detail/Factory-Supply-Price-12800kg-High-Purity_1600707644358.html?spm=a2700.7735675.0.0.a9b0JedIJedI44&s=p).
21. Alibaba. Hexane extraction solvent (food grade) price. 2023, October 20; Available from: [https://www.alibaba.com/product-detail/China-Supplier-Wholesale-Food-Addictive-Reagent\\_1600615168945.html?s=p](https://www.alibaba.com/product-detail/China-Supplier-Wholesale-Food-Addictive-Reagent_1600615168945.html?s=p).

## Process simulation and techno-economic evaluation of free lutein production from marigold flowers by dimethyl ether extraction and de-esterification

**Yada Meayrin<sup>1</sup>, Chonlatep Usaku<sup>1</sup>, Phannipha Daisuk<sup>1</sup> and Artiwan Shotipruk<sup>1,\*</sup>**

<sup>1</sup> Bio-Circular-Green-economy Technology & Engineering Center (BCGeTEC), Department of Chemical Engineering, Faculty of Engineering, Chulalongkorn University, Phayathai Road, Patumwan, Bangkok 10330, Thailand.  
E-mail: \*Artiwan.Sh@chula.ac.th

### Abstract

Marigold flower extract is known to be the richest source of lutein, which has numerous applications in the food, pharmaceutical, cosmetic, and health sectors. After extraction, lutein naturally contained in marigold oleoresin in ester forms needs to be converted to free lutein by reacting with an alkali solution (e.g., KOH). Recently extractions with liquefied dimethyl ether (DME) have been shown to be effective and could potentially replace use of organic solvent for extraction of marigold flowers. The possibility for simultaneous DME extraction and de-esterification has also been demonstrated, requiring fewer process steps, and thus improve the process efficiency.

This study utilized Aspen Plus V.11 software to model a free lutein manufacturing process from marigold flowers, with an annual input marigold flower of 2,000 tons per year. Techno-economic and economic assessments were conducted for both the two-step extraction and simultaneous extraction/de-esterification processes. The analysis included estimation of energy and utility consumption, as well as capital expenditure (CAPEX) and operating expenditure (OPEX). Results indicated that the simultaneous extraction process was more technically and economically efficient for lutein extraction, yielding free lutein content of 86.16 wt% in the final product. From 100 g of D\_MG, the simultaneous process produced 32.28 g of free lutein-rich product, costing 3.09 USD/kg produced. In the total of CAPEX, the simultaneous process incurred costs of 1.9 M\$/year, while the total of OPEX for the simultaneous process amounted to 93 M\$/year.

**Keywords:** Marigold flowers; Lutein; Liquefied dimethyl ether; Techno-economic analysis

### 1. Introduction

Lutein (C<sub>40</sub>H<sub>56</sub>O<sub>2</sub>) is a dihydroxy carotenoid compound, has surged in popularity in recent years for its use as nutritional supplements to prevent age-related macular degeneration. Moreover, lutein has been shown to exhibit anti-glycemic and antioxidant activities, the functional properties that make it an appealing ingredient for incorporation into various products across different industries, including pharmaceuticals and dietary supplements [1]. Lutein comprises approximately 60-70% of total xanthophylls (or oxygenated carotenoids) in marigold (*Tagetes erecta*) flowers, the richest and purest source of natural lutein [2]. In the flowers, lutein is chemically bound to various fatty acids, primarily lutein fatty acid diesters. Through the process of de-esterification of the flower extract (oleoresin), these primary lutein fatty acid esters are transformed into free lutein. The global market for lutein extracted from marigold flowers is projected to reach US\$ 225 million by 2027, with a compound annual growth rate (CAGR) of around 5% [3].

Traditionally, natural carotenoids are extracted using organic solvents such as hexane, isopropanol, and methylene chloride. Of these, hexane is favored for its low polarity, stability, and ease of removal via evaporation due to low boiling point and heat of vaporization. However, use of hexane poses environmental concerns owing to their flammability, volatility, toxicity, and reliance on non-renewable resources. As regulations such as European Directives and REACH have tightened control over petrochemical solvents like hexane [4], industries are compelled to adopt eco-friendly extraction techniques utilizing green solvents derived from biomass or eco-friendly petrochemicals that are non-toxic and biodegradable. DME, the simplest form of ether, possesses distinctive characteristics such as a remarkably low boiling point of  $-24.8^{\circ}\text{C}$ . In its liquefied state, DME can be utilized as an extraction solvent, while at room temperature, DME does not persist in the extracted materials. The absence of biological toxicity in DME has sparked significant interest in its potential as an environmentally friendly solvent for food production. In a prior study, we demonstrated DME's effectiveness in extracting lutein esters from marigold flowers. In this same study, a simultaneous DME extraction and de-esterification was also proposed to effectively produce free lutein, rich product, eliminating multiple operations compared with a two-step process, where DME extraction was subsequently followed by esterification [5].

This study aims to conduct techno-economic analysis of free lutein production using liquefied DME as extraction solvent. Two extraction options were simulated: sequential and simultaneous extraction/de-esterification processes. From the simulated results, energy and utilities consumption, alongside equipment design were determined to estimate Operating Expense (OPEX) and Capital Expenditure (CAPEX) for the two options. The cost-effectiveness for the integrated single-step process over the multiple sequential steps is evaluated, and the technological challenges in free lutein production are highlighted.

## 2. Material and Methodology

### 2.1 Process modeling and simulation

Marigold (*T. erecta*) planting information report in Thailand indicates a production of approximately 28,904 tons per year [6]. In this study, each process option was evaluated based on the process design to handle 2,000 tons per year of dried marigold flower powder. The Aspen Plus process simulator was utilized to simulate the lutein extraction processes. According to the composition of dried marigold flowers summarized in Table 1, the total carotenoids comprise approximately 68% w/w of the total extract, with zeaxanthin and  $\beta$ -carotene constituting 10% of the total carotenoids. As lutein di-palmitate was used as the model lutein ester in the simulation as it has been shown to be the main lutein ester component (ca. 50% w/w) [7]. Other components including the insoluble components, constituting 47.61% of the marigold flower were defined as a set of non-conventional components.

Table 1. General composition of marigold flower [7]

Components	Composition (wt.%)
Moisture	3.98
Lutein	8.19
Lutein ester	34.97
Zeaxanthin	3.77
$\beta$ -carotene	1.48
Other	18.36
Insoluble compound	29.25

## 2.2 Process simulation

The dried marigold extraction process closely follows the experimental and simulation procedures proposed by Boonnou et al. (2017) [8], whose process specifications are summarized in Table 2. The simulations are based on the processes operated 24 h/day for 330 days per year or 7,920 h/year, assuming semi-continuous operations with multi-extractor vessels to mimic industrial-scale production. The SOLID activity coefficient model was employed to simulate phase equilibrium for the solid-solvent system for the conversion of lutein esters to free lutein via de-esterification. As free lutein, lutein esters, and zeaxanthin components listed in Table 1 are not currently in the simulator's database, it is essential to import the .mol files of these molecules into the software. The .mol file provides a graphic-functional representation of the molecules, allowing for the estimation of their physical and chemical properties through a group contribution method. Since some chemical-physical features require predictive estimates, UNIFAC was used for evaluation.

Table 2. Process conditions and specifications

Extraction technique	Condition*	Amount of free lutein	Material flows associated for simulation
Sequential process	DME extraction; DME to dried marigold ratio 33:0.5, 35 °C, 400 rpm, 30min. De-esterification; ethanol to oleoresin ratio 4:0.2, 2.5% KOH, 35 °C, 150 rpm, 240 min	16.72 mg free lutein/ g dried marigold	<b>Only liquified DME extraction:</b> N <sub>extraction</sub> 5,940 Cycles per year Feed dried marigold 336.7 kg/batch Feed DME 22,223 kg/batch <b>Sequential process:</b> N <sub>extraction</sub> 3,751 Cycles per year Feed dried marigold 533.11 kg/batch Feed DME 35,185.19 kg/batch Feed solvent <sub>KOH-EtOH</sub> 5,369.97 kg/batch
Simultaneous process	DME to dried marigold ratio 33:0.5, ethanol to dried marigold ratio 10:0.5, 5% KOH, 35 °C, 400 rpm and 60 min	20.71 mg free lutein/ g dried marigold	N <sub>extraction</sub> 4,320 Cycles per year Feed dried marigold 115.74 kg/batch Feed DME 7,638.89 kg/batch Feed solvent <sub>KOH-EtOH</sub> 6,443.96 kg/batch

\*based on experimental study by Boonuan et al. (2017) [8]

### 2.2.1 Sequential extraction process

The sequential extraction process begins with liquefied DME extraction. The process was simulated based on 2,000 ton of dried marigold flower feed per year. The diagram in Fig. 1 illustrates the process flow and the unit operations involved, including a pumping (PUMP) and heating system (HX) to generate liquefied DME, extractors (EXTRACT), and a separation system (SEP and VALVE), and compressors for DME recycling. Pump and compressors (Isentropic type) were assumed to have an efficiency of 80%. Initially, DME from a storage tank (5.3 bars at 20°C) is pressurized to 7 bars and then heated it to 37°C in HX-1 before being loaded into the extractors (EXTRACT), preloaded with dried marigold powder at a solvent to feed mass ratio of 33g: 0.5g<sub>MG</sub> [8]. The exiting stream from the extractors is then directed to a separator for the separation of extracted oleoresin and DME that is to be recycled. It is assumed that the solvent undergoes a loss of 2% of the total solvent per extraction cycle. The oleoresin is stored in a tank before being sent to the de-esterification process to convert lutein esters into free lutein.

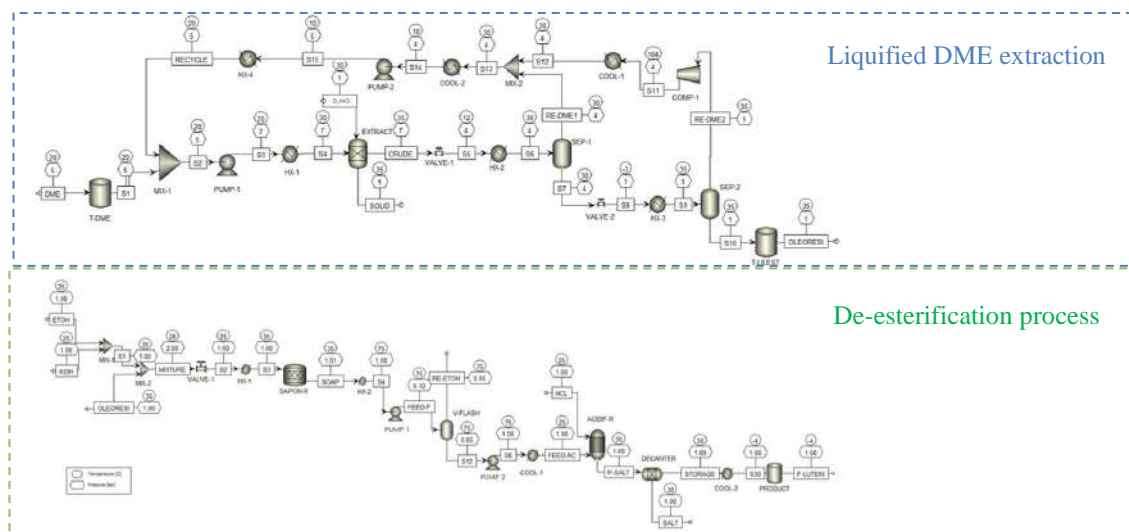


Fig. 1 Process flow diagram of the sequential process

Following liquefied DME extraction, de-esterification process necessitates the conversion of lutein esters in the crude oleoresin to free lutein. The flow diagram for this process is shown in Fig. 1. Crude lutein ester was mixed with KOH-EtOH in the MIXER-1. De-esterification was carried out in the SAPON-R unit (at 35 °C, 1 bar) thereby converting the lutein ester into free lutein and soaps (resulted from saponification of free fatty acids). Figure 2. as shown the de-esterification process. The lutein fatty acid esters consist of R1 and R2 function are converted to free lutein and by-product is fatty acid salt (soap). This reaction product stream was then heated to 75 °C using a heat exchanger (HX-2) before flowing it to the vacuum flash (V-FLASH) unit. The vacuum flash unit separated the more volatile component (ethanol) of the feed to vapor phase. The liquid stream from the V-FLASH unit was sent to the acidification unit, ACIDIF-R, where the de-esterified product was neutralized by acidification using HCl. This leads to the formation of two distinct layers: a top free lutein-rich layer and the bottom layer containing aqueous solution of inorganic salts. After separation, the free lutein product was stored on an ice bath at 4 °C. Each cycle of this sequential process involves 30 minutes for extraction, 240 minutes for de-esterification, and an additional 60 minutes for the preparation, loading, and unloading of the feed raw material.

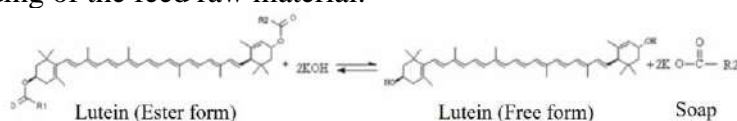


Fig. 2 De-esterification of lutein fatty acid esters

### 2.2.2 Simultaneous DME extraction and de-esterification

In a simultaneous process, both DME extraction and de-esterification of lutein esters take place in a single unit. Since exact unit operation is not available in ASPEN plus software, the process is instead represented in the simulator as two separate units: a reactor (SAPONR, where the mixture of marigold flower powder, DME as extractant solvent, and KOH-EtOH solution at 3.27g DME:0.5 g<sub>MG</sub>:10g KOH-EtOH solution (5% KOH) from MIX-1 unit is fed) and a decanter (where DME and the extract are separated), as shown in the process flow diagram in Fig. 3. Each cycle for this simultaneous process takes 60 min for extraction/de-esterification, with additional 60 min for preparation, loading and unloading of the feed raw material.

Separation of residue solid and acidification then took place in a similar manner as described in the previous sections.

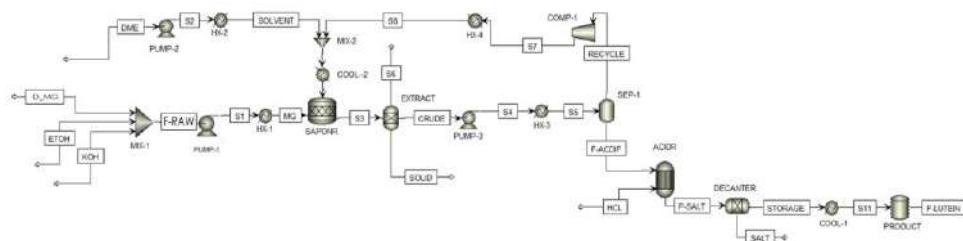


Fig. 3 Process flow diagram of the simultaneous process

### 2.3 Economic assessment

Table 3 summarizes the unit costs of dried marigold flower powder, solvents and chemicals, utilities, as well as the product prices for lutein esters and free lutein, needed for the process cost estimation. The economic assessment of the sequential and the simultaneous processes of the free lutein production was carried out, covering the determination of the capital investment (CAPEX) and operating costs (OPEX) over 20 years of plant life.

Table 3. Cost involved in the economic assessment.

Category	Material	Cost	Units	Ref.
Raw materials	Dried marigold flower	32.42	US\$/kg	[9]
Solvents	Liquified dimethyl ether	652	US\$/ton	[10]
	Ethanol	683	US\$/ton	[10]
	KOH	850	US\$/ton	[10]
	HCl	156	US\$/ton	[10]
Utilities	Cooling water	0.378	US\$/GJ	[11]
	Chilled water	4.77	US\$/GJ	[11]
	Low pressure steam	2.03	US\$/GJ	[11]
	Electricity	0.074	US\$/kWh	[11]
Product	Crude lutein ester	280	US\$/kg	[12]
	Free lutein extraction	357.15	US\$/kg	[12]

## 3. Results and Discussion

### 3.1 Aspen plus simulation of free lutein extraction processes

Table 4 summarizes the results from ASPEN-plus mass balance simulation for sequential and simultaneous processes. For initial liquified DME extraction process, the results revealed that 76.10 wt% the flower the obtained extract was lutein esters and 17.82 wt% was free lutein. Further processing of the lutein ester through de-esterification increased the content of free lutein to 80.91 wt%, leaving 11.09 wt% of lutein esters unconverted.

Interestingly, despite the longer residence time needed for de-esterification in the sequential process, the combined volume of both reactor vessels in the two-step process was smaller than that of the reactor required in the single-step simultaneous process. Conversely, simultaneous process showed higher content of free lutein at 86.16 wt%, with 4.59% of lutein ester remaining unconverted. Despite achieving the desired product quality, the simultaneous process required more solvent compared to the sequential process as it required 1.2 times the amount of KOH-EtOH solution. Nonetheless, the simultaneous process maintained a solvent recovery rate of 98.54%, and it requires less DME feed volume and shorter extraction cycle

times all together. Out of 100 g of D-MG, 32.28 g of lutein rich product was obtained from simultaneous process, whereas only 19.51 g was obtained from the sequential process, a 1.6-fold improvement in the product yield.

Table 4. Aspen-plus mass balance results for sequential and simultaneous lutein extraction processes.

Stream	Sequential process					Simultaneous Process			
	In DMG	Subcritical DME		De-esterification		In DMG	In DME	In KOH-EtOH	Out Product
Temp.(°C)	30	19.58	35	25	4	30	19.58	25	4
Pressure(bar)	1	5.3	1	1	1	1	5.3	1	1
Mass flow (kg/batch)	<b>533</b>	35,185	186	5,370	<b>104</b>	<b>116</b>	7,639	6,444	<b>37.45</b>
<b>Composition (wt.%)</b>									
Water	3.98	0.07	0.03	-	0.71	3.98	0.07	-	0.80
DME	-	99.93	1.03	0.05	0.87	-	99.93	0.05	1.46
KOH-EtOH	-	-	-	99.95	1.56	-	-	99.95	1.87
Free lutein	8.19	-	<b>17.82</b>	-	<b>80.91</b>	8.19	-	-	<b>86.16</b>
Lutein ester	34.97	-	<b>76.10</b>	-	<b>11.09</b>	34.97	-	-	<b>4.59</b>
Zeaxanthin	3.77	-	3.61	-	3.47	3.77	-	-	3.72
$\beta$ -carotene	1.48	-	1.41	-	1.39	1.48	-	-	1.40
Solid	47.61	-	-	-	-	47.61	-	-	-

### 3.2 Economic assessment

The economic assessment results for the sequential and simultaneous processes are shown in Table 5. For each process, the total CAPEX was calculated from the sum of the costs of the main equipment and corresponding installation costs, estimated following the Association for the Advancement of Cost engineering (ACE) guidelines [13]. As seen from the estimation, the total CAPEX of the sequential process (2.3 M\$/year) was higher than that of the simultaneous process (1.9 M\$/year), as the former process required additional equipment, thus the total equipment cost and the capital cost are higher. On the other hand, the estimate for the total OPEX were comparable, amounting to 94.3 M\$/year for the sequential process, which is only slightly higher than that of the simultaneous process (93 M\$/year).

Moreover, the comparison other cost metrics (defined and presented in Table 5) reveals that the FCI and TCI associated with the sequential process exceed those of the simultaneous process due to prolonged extraction time in the sequential process (1.5 hr. for extraction, plus 4 hr. of de-esterification), leading to smaller number of batches per year and consequently, a smaller amount of extract mass obtained per unit time. The contribution of the four components: CRM, FCI, COL, and CUT to COM followed the order of CRM > FCI > COL > CUT for both evaluated processes. Notably, the significant contribution from CRM was expected due to the considerable cost of marigold flower raw material (US\$ 32.42/kg).-Despite utilities being a function of the amount of raw material processed per batch, the contribution of CUT saw only a marginal increase with scale-up, mainly due to more significant variations in the contributions of other components, as indicated in Table 5.



Table 5. Economic assessment of lutein extraction.

<b>Economic evaluation</b>	<b>Sequential process</b>	<b>Simultaneous Process</b>
Raw material purchase cost (USD/kg <sub>D_MG</sub> )	4.52 (3.99)	3.10
<b>CAPEX</b>		
Total equipment cost (USD)	1,945,480 (1,361,600)	1,625,680
Capital cost (USD/year)	183,659 (128,539)	153,469
<b>OPEX</b>		
Raw Materials (C <sub>RM</sub> ) (USD/year)	<b>79,065,711</b> (73,667,479)	<b>78,649,346</b>
Utilities (C <sub>UT</sub> ) (USD/year)	<b>214,262</b> (23,994)	<b>186,587</b>
Labor (C <sub>OL</sub> ) (USD/year)	<b>369,458</b> (357,143)	<b>369,458</b>
Direct Supervision and clerical labor (USD/year)	36,946 (35,714)	17,110
Laboratory charges (USD/year)	36,946 (35,714)	17,110
Maintenance and repair (USD/year)	45,776 (32,038)	38,251
Operating supplies (USD/year)	4,578 (3,204)	3,825
Plant overhead cost (USD/year)	226,090 (212,447)	113,231
Interest (USD/year)	114,440 (80,094)	95,628
Local taxes (USD/year)	91,552 (64,075)	76,503
Insurance (USD/year)	22,888 (16,019)	19,126
<b>Total OPEX (M\$/year)</b>	<b>94.3</b> (87.7)	<b>93.3</b>
<b>Total CAPEX (M\$/year)</b>	<b>2.3</b> (1.6)	<b>1.9</b>
<b>Fixed Capital (FCI)* (US\$)</b>	<b>7,729,880</b> (4,909,000)	3,574,880
Total capital investment (TCI)	9,662,350 (6,136,250)	4,468,600
<b>Operating costs (COM) (M\$/year)</b>	<b>99.7</b> (92.5)	<b>97.6</b>
Product sale (M\$/year)	22.1 (23.14)	31.5

\*FCI is the cost required for the installation of the unit operation, consisting of direct costs and indirect costs. Direct costs include the costs of purchasing and installing the equipment, cost of electrical system, instrumentation, building and service facilities. Indirect costs comprise the cost of engineering and supervision, legal and construction expenses, and contractor's fee and contingency.

#### 4. Conclusions

The techno-economic analysis of free lutein extraction processing, supported by conceptual process design and Aspen Plus simulations for energy and mass balances, demonstrated that

the simultaneous process was a more technically and economically viable technology for extracting free lutein, compared with the sequential process. The simultaneous process offers increased product yield and reduced production costs compared to the sequential process. Specifically, the simultaneous process achieves a free lutein extraction yield of 86.16 wt% with a production cost of 3.09 USD/kg of crude free lutein. The total OPEX, nevertheless, of both processes are very high. When considering the sequential process, it could be drawn from the economic assessment in Table 5 that the large contribution of this cost was from the liquefied DME extraction process, and the major portion of the cost of operating the extraction process itself was the marigold flower powder raw material. Such high OPEX indeed led to a payback period exceeding 20 years (result not shown). To further improve the profitability of the process, it is possible to incorporate an in-house preparation of marigold flower powder to mitigate the initial investment burden by reducing the need to purchase dried flowers from a vendor.

## References

- [1] Khoo, H. E., Ng, H. S., Yap, W.-S., Goh, H. J. H., & Yim, H. S. (2019). Nutrients for prevention of macular degeneration and eye-related diseases. *Antioxidants*, 8(4), 85.
- [2] Šivel, M., Kráčmar, S., Fišera, M., Klejdus, B., & Kubán, V. (2014). Lutein content in marigold flower (*Tagetes erecta* L.) concentrates used for production of food supplements. *Food Science and Technology*, Vol. 32, 521-525.
- [3] Rahman, K. M., & Melville, L. (2023). Global market opportunities for food and feed products from microalgae. In *Handbook of Food and Feed from Microalgae* (pp. 593-602). Academic Press.
- [4] Lores, M., Celeiro, M., Rubio, L., Llompart, M., & Garcia-Jares, C. (2018). Extreme cosmetics and borderline products: An analytical-based survey of European regulation compliance. *Analytical and bioanalytical chemistry*, 410, 7085-7102.
- [5] Goto, M., Kanda, H., & Machmudah, S. (2015). Extraction of carotenoids and lipids from algae by supercritical CO<sub>2</sub> and subcritical dimethyl ether. *The journal of supercritical Fluids*, 96, 245-251.
- [6] Mansuriwong, P., Wongvarodom, V., & Te-chato, S. (2023). Marigold Planting Information Report. Available Source, Rajamangala University of Technology Srivijaya Research Journal, 15(2), 521-536.
- [7] Hadden, W. L., Watkins, R. H., Levy, L. W., Regalado, E., Rivadeneira, D. M., van Breemen, R. B., & Schwartz, S. J. (1999). Carotenoid composition of marigold (*Tagetes erecta*) flower extract used as nutritional supplement. *Journal of agricultural and food chemistry*, 47(10), 4189-4194.
- [8] Boonnoun, P., Tunyasitkun, P., Clowutimon, W., & Shotipruk, A. (2017). Production of free lutein by simultaneous extraction and de-esterification of marigold flowers in liquefied dimethyl ether (DME)-KOH-EtOH mixture. *Food and Bioproducts Processing*, 106, 193-200.
- [9] Organic Thailand. Online Store. (Accessed 2023, October 20) Available from: <https://www.organicthailand.com/en/product/35616-55418/marigold-flower-powder-1kg>
- [10] Market Price & Insight, (2023, October 20). "Solvent price". ECHEMI. <https://www.echemi.com/market-insights-products.html>.
- [11] Turton, R., Shaeiwitz, J. A., Bhattacharyya, D., & Whiting, W. B. (2018). Analysis, synthesis, and design of chemical processes.
- [12] Alibaba (2023, October 20). "Crude lutein (food grade) price". IEPA. [https://www.alibaba.com/product-detail/Natural-Marigold-extract-20-Lutein-Oil\\_1600764524862.html?spm=a2700.galleryofferlist.normal\\_offer.d\\_price.51cc5cdc01UBpX](https://www.alibaba.com/product-detail/Natural-Marigold-extract-20-Lutein-Oil_1600764524862.html?spm=a2700.galleryofferlist.normal_offer.d_price.51cc5cdc01UBpX)
- [13] Association for the Advancement of Cost Engineering International, Cost Estimate Classification System - As Applied in Engineering, Procurement, and Construction for the Process Industries, AACE International Recommended Practice No. 18R-97 (revised June 15, 1998). [www.aacei.org](http://www.aacei.org)

## Synthesis and Characterization of Core-Shell Zeolitic Imidazolate Frameworks by Seed-Mediated Growth Method

**Nattanon Threerattanakulpron<sup>1\*</sup>, Nikom Klomkliang<sup>1\*\*</sup>, Somsak Supasitmongkol<sup>2</sup>**

<sup>1</sup> School of Chemical Engineering, Suranaree University of Technology, Nakhon Ratchasima 30000, Thailand

<sup>2</sup> National Energy Technology Center (ENTEC), National Science and Technology Development Agency (NSTDA), 114 Thailand Science Park, Phahonyothin Rd., Khlong Nueng, Khlong Luang, Pathum Thani 12120, Thailand

E-mail: \*gew.nattanon@gmail.com, \*\*nikom.klo@sut.ac.th

### Abstract

This study focuses on the synthesis of bimetallic ZIFs, starting with Core ZIF-8 and ZIF-67. A study of the core materials led to the development of ZIF-8@ZIF-67 and ZIF-67@ZIF-8 core-shell structures. Fourier-transform infrared spectroscopy (FTIR) and X-ray diffraction analysis (XRD) were employed to analyze these cores. The thermal stability of these formations was evaluated through thermogravimetric analysis (TGA) to elucidate the effects of heat, while their morphology was thoroughly investigated using transmission electron microscopy (TEM) and scanning electron microscopy (SEM). ZIF-8@ZIF-67 and ZIF-67@ZIF-8 were successfully synthesized and had surface area of 1723.7 and 1640.4 m<sup>2</sup>/g and pore volume of 0.7239 and 0.7998 cm<sup>3</sup>/g, respectively, based on the BET method. The seed-mediated growth synthesis effectively preserved the dodecahedron structure of core materials. The creation of a core-shell structure was shown with a uniform distribution of Co and Zn particles on the surface. The integrity of the dodecahedron structure was maintained, boasting an excellent surface area and pore volume. Further enhancement of the physical and chemical properties was achieved by adding Cu particles to the core-shell materials through co-precipitation.

**Keywords:** ZIF-8; MOFs; Seed-mediated growth; Bimetallic

### 1. Introduction

Metal-organic frameworks (MOFs) have become significant because of their distinct chemical and physical characteristics. They are of interest to researchers in many different domains. These include a high surface area, huge porosity, robust pore structures as well as thermal and chemical stability under diverse environmental conditions [1]. The distinct structure of these materials comprises metal nodes interconnected by organic ligands, forming a well-defined framework. In this research project, we study and synthesize a type of MOF known as zeolitic imidazolate frameworks (ZIFs), which are composed of transition metals and imidazole [2]. Specifically, we focus on ZIF-8 and ZIF-67 due to the ease of synthesis at room temperature and the versatility of their applications, these materials have garnered widespread interest. Previous research has demonstrated the versatility of ZIFs in various applications such as energy storage, energy conversion, gas storage separation, and catalysis [3]. For instance, their use in hydrogen gas storage is particularly advantageous due to the large surface area. As catalysts, they are often employed as supporters, the large pore sizes minimizing the occurrence of pore blockage while also offering extensive surface area.

Further studies focused on how to enhance the physical and chemical properties of Single-metal ZIFs. A popular strategy adopted is the use of mixed metal or bimetallic MOFs, which involves incorporating desired heavy metals into the single-metal ZIF frameworks. For

example, the core-shell materials demonstrated significantly higher CO<sub>2</sub> adsorption (58.3 cm<sup>3</sup> g<sup>-1</sup>) in comparison to its single-metal counterpart (44.8 cm<sup>3</sup> g<sup>-1</sup>), showcasing the potential of this strategy [4]. and Zn/Co ZIFs were effective for adsorbing gases (N<sub>2</sub>, CO<sub>2</sub>, and CH<sub>4</sub>) and could be used for converting CO<sub>2</sub> into cyclic carbonates [5]. According to these investigations, single-metal ZIFs are inferior to bimetallic ZIFs in terms of their chemical and physical characteristics.

In this study, we investigated the synthesis of core-shell materials from single-metal ZIFs using the seed-mediated growth technique. The X-ray diffraction (XRD) technique was utilized to examine the structural characteristics of the crystals and determine any modifications to the initial dodecahedron structures of core materials during the synthesis process. The materials were then subjected to analysis using energy-dispersive X-ray spectroscopy (EDS) to create elemental mapping while SEM and TEM to capture images of the crystal structures and observe the distribution of Co, Cu, and Zn on the material surface. The materials' thermal characteristics were then studied using thermogravimetric analysis (TGA), and the chemical properties and functional groups were studied using FT-IR. Following the successful synthesis, the core-shell structures were produced. Copper nitrate hexahydrate was then added to the two types of materials using the co-precipitation technique and analyzed using the same techniques as for the core-shell synthesis to study the behavior of the Cu particles added to the materials.

## 2. Experimental section

### 2.1. Synthesis of ZIF-8 framework.

Zn(NO<sub>3</sub>)<sub>2</sub> · 6H<sub>2</sub>O (810 mg, 3.5 mmol) in 40 mL of methanol and 2-methylimidazole (526 mg, 2.4 mmol) was dissolved in another 40 mL of methanol. The two solutions were combined and agitated for 12 hours at room temperature, resulting in a turbid white solution. The solution was then separated by centrifugation and washed many times with methanol. The mixture was subsequently dried for 6 hours at 70 °C in an oven, resulting in the formation of a delicate white solid.

### 2.2. Synthesis of ZIF-67 framework

Co(NO<sub>3</sub>)<sub>2</sub> · 6H<sub>2</sub>O (582 mg, 2 mmol) in 50 mL of methanol and 2-methylimidazole (656 mg, 8 mmol) was dissolved in another 50 mL of methanol. The two solutions were combined and agitated for 12 hours at room temperature, resulting in a purple solution. The solution was then separated by centrifugation and washed many times with methanol. The mixture was subsequently dried for 6 hours at 70 °C in an oven, resulting in the formation of a delicate purple solid.

### 2.3. Synthesis of core-shell ZIF-8@ZIF-67 framework.

The core-shell was produced through the seed-mediated growth process. Initially, ZIF-8 (160 mg, 0.697 mmol) was dissolved in 20 mL of methanol using a sonication bath for 30 minutes. Concurrently, in 6 mL of methanol, 2-methylimidazole (1790 mg, 21 mmol) and Co(NO<sub>3</sub>)<sub>2</sub> · 6H<sub>2</sub>O (433 mg, 1.5 mmol) were dispersed. This solution was then gradually added to the ZIF-8 solution, followed by stirring for 30 minutes. The mixture was then placed to a Teflon-lined autoclave and heated at 100 °C for 12 hours. The resultant purple solution was separated using centrifugation and washed several times with methanol. Finally, the mixture was subsequently dried for overnight at 100 °C in an oven, resulting in the formation of a delicate purple solid

## 2.4. Synthesis of core-shell ZIF-67@ZIF-8 framework.

The process began with dissolving of ZIF-67 (40 mg, 0.18 mmol) in 20 mL of methanol using a sonication bath for 30 minutes. Simultaneously,  $\text{Zn}(\text{NO}_3)_2 \cdot 6\text{H}_2\text{O}$  (595 mg, 2mmol) and 2-methylimidazole (656 mg, 8 mmol) were dispersed in 40 mL of methanol. This solution was then gradually added to the ZIF-67 solution, followed by stirring for 30 minutes. To ensure complete dissolution, the mixture was further treated in the sonication bath for an additional 30 minutes. The resulting purple solution was separated using centrifugation and washed several times with methanol. Subsequently, the solution was subsequently dried for overnight at 100 °C in an oven, resulting in the formation of a delicate purple solid.

## 2.5. Synthesis of core-shell materials incorporated with Cu

Core-shell materials (200 mg) were dissolved in 50 mL of methanol using a sonication bath for 30 minutes. Once core-shell was completely dissolved in methanol. The solution was agitated for 30 min. after the addition of 140 mg of  $\text{Cu}(\text{NO}_3)_2 \cdot 3\text{H}_2\text{O}$ . Then, 20 mL of DI water were used to dissolve 109.77 mg of  $\text{NaBH}_4$ , which was subsequently and progressively added to the purple solution, followed by continuous stirring for 1 hour. Centrifugation was used to separate the purple solution that was produced, and it was then repeatedly washed with methanol and DI water. Ultimately, a fine purple solid formed after the mixture was dried for 12 hours at 50 °C in an oven.

## 2.6. Characterization

Field emission scanning electron microscope (FE-SEM) (thorough JEOL JSM 7800F instrument) was used for studying the structure and morphology of specimens. Before analysis, the samples must be dried and then coated with a gold layer to enhance their electrical conductivity. The analysis is carried out under vacuum conditions to capture high-resolution images of the samples. The operation was controlled via a computerized system.

Powder X-ray diffraction (PXRD) was used to examine the phase structure of the prepared ZIF-8@ZIF-67 and ZIF-67@ZIF-8 (through Bruker D2 phaser with  $\text{CuK}\alpha$  radiation 1.5418 Å and a step size of 0.02° in 5-40°).

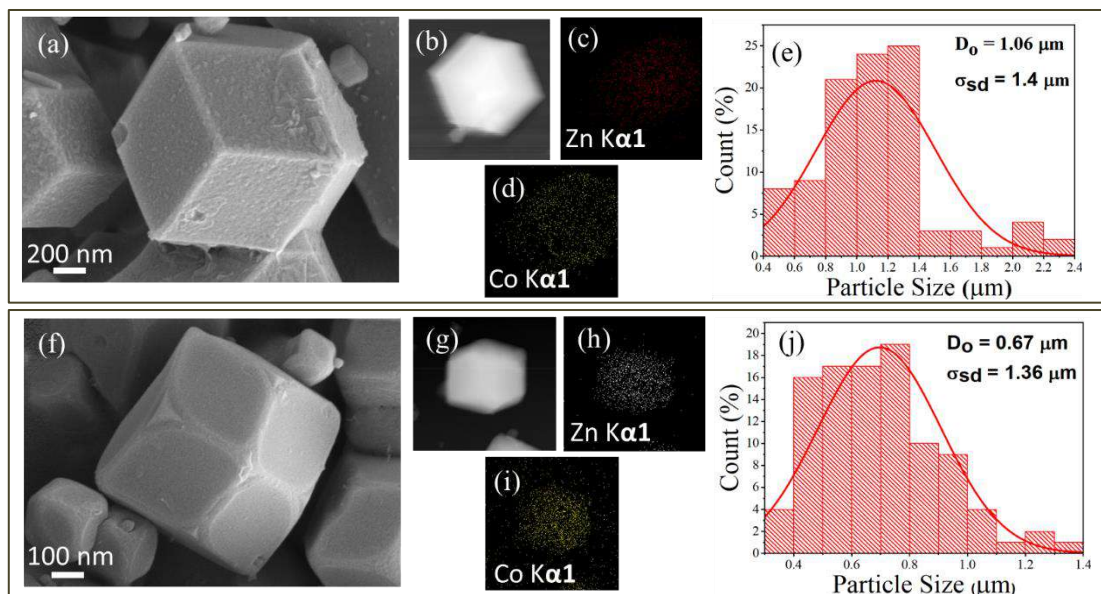
The measurement of  $\text{N}_2$  adsorption and desorption isotherms at -196 °C was conducted with the Micromeritics ASAP 2020 plus instrument. The samples were degassed for 6 hours at a temperature of 120 °C in preparation for the measurements. The BET method was employed to determine the specific area, which was calculated from the relative pressure in the range of 0.05-0.30, as well as the total pore volume was calculated at 0.99 relative pressure. (4V/A by BET).

Thermogravimetric analysis (TGA/Mettler Toledo DSC1) was employed as a technique to study the behavior of samples in response to increasing temperature within the system. The impact of temperature on weight loss was measured through the use of this method, allowing for the determination of which particles or structures in the sample changed at specific temperature ranges. Temperature rose from 50 to 600 °C at a rate of 10 °C/min during the analysis, with  $\text{O}_2$  gas flowing through at a rate of 30 mL/min.

The analysis of chemical bonds or functional groups on molecular surfaces can be achieved through Fourier transform Infrared (FTIR) Spectroscopy, which operated within the 4000-400  $\text{cm}^{-1}$  wavelength interval.

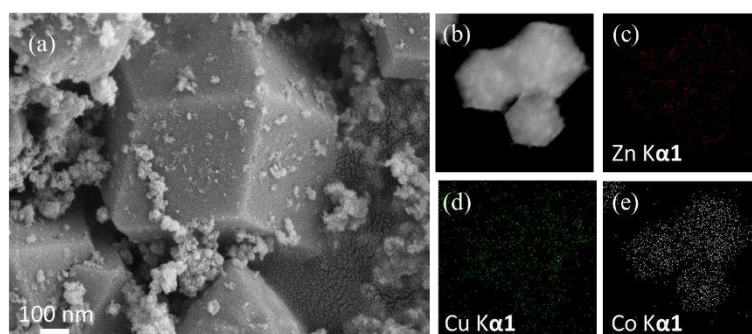
### 3. Results and discussion

#### 3.1 Field Emission Scanning Electron Microscope (FE-SEM)



**Fig. 1.** (a) SEM image, (b) TEM images, (c,d) elemental mapping (e) particle size distribution of ZIF-8@ZIF-67 frameworks and (f) SEM image, (g) TEM images, (h,i) elemental mapping (j) particle size distribution of ZIF-67@ZIF-8 frameworks.

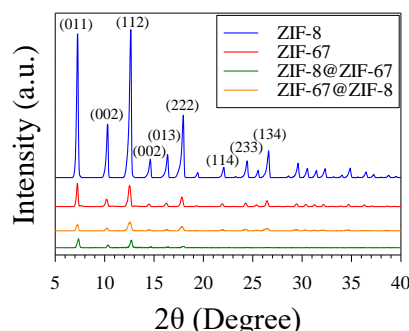
Figure 1 depicts the crystalline structure of core-shell materials. The synthesized materials exhibit a dodecahedron structure with a particle size distribution ranging from 0.4 to 2.4  $\mu\text{m}$ . Core-shell materials have average material sizes of 1.06  $\mu\text{m}$  and 0.67  $\mu\text{m}$ , respectively. Elemental mapping analysis was conducted to examine the distribution of metal nodes, specifically Zn in ZIF-8 and Co in ZIF-67. The analysis indicates that in the Core-shell materials, Zn and Co particles are distributed throughout the surface. This provides evidence that ZIF-8 and ZIF-67 are compatible materials after synthesis by seed-mediated growth.



**Fig. 2.** (a) SEM image, (b) TEM images, (c-e) elemental mapping of Cu-ZIF-67@ZIF-8 frameworks.

Figure 2 presents SEM images as evidence of the crystalline structure of the Cu-ZIF-67@ZIF-8 material. Examination of these images reveals that the core-shell structure of ZIF-67@ZIF-8 maintains its dodecahedron shape even during the incorporation of Copper(II) nitrate trihydrate using the co-precipitation technique. This suggests that the addition of Cu ions does not alter the physical and chemical structure of the material. The material remains a Metal-Organic Framework (MOF) with an excellent distribution of metal nodes and Cu ions.

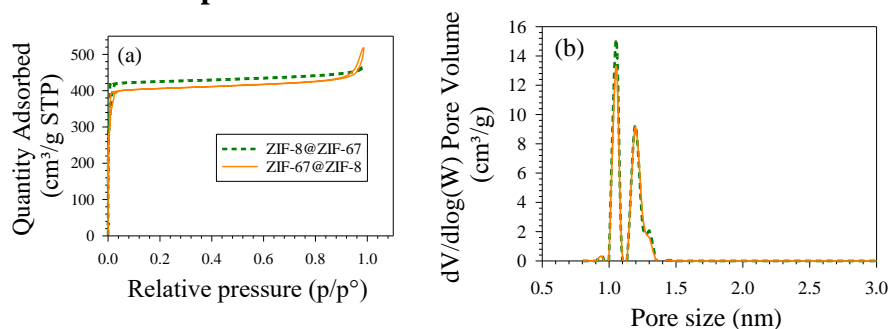
### 3.2 X-ray diffraction (PXRD)



**Fig. 3.** Powder X-ray diffraction (PXRD) patterns of ZIF-8, ZIF-67, ZIF-8@ZIF-67 and ZIF-67@ZIF-8 frameworks.

Figure 3 presents the XRD pattern of single-metal ZIFs and core-shell materials. The observed peak positions at  $2\theta$  are 7.52 (011), 10.53 (002), 12.90 (112), 14.86 (002), 16.60 (0.13), 18.21 (222), 22.21 (114), 24.66 (233), and 26.82° (134) [6]. Upon examining the peak positions of core materials, they align with previous research, indicating that the prepared samples are pure and exhibit sharp peaks with a highly crystalline structure. In the case of the core-shell materials, it is evident that there are no additional peak positions present apart from those of core materials. This suggests that during the core-shell materials synthesis using the seed-mediated growth technique, the original structure of the core is not destroyed in the process.

### 3.3 BET surface area and pore size distribution



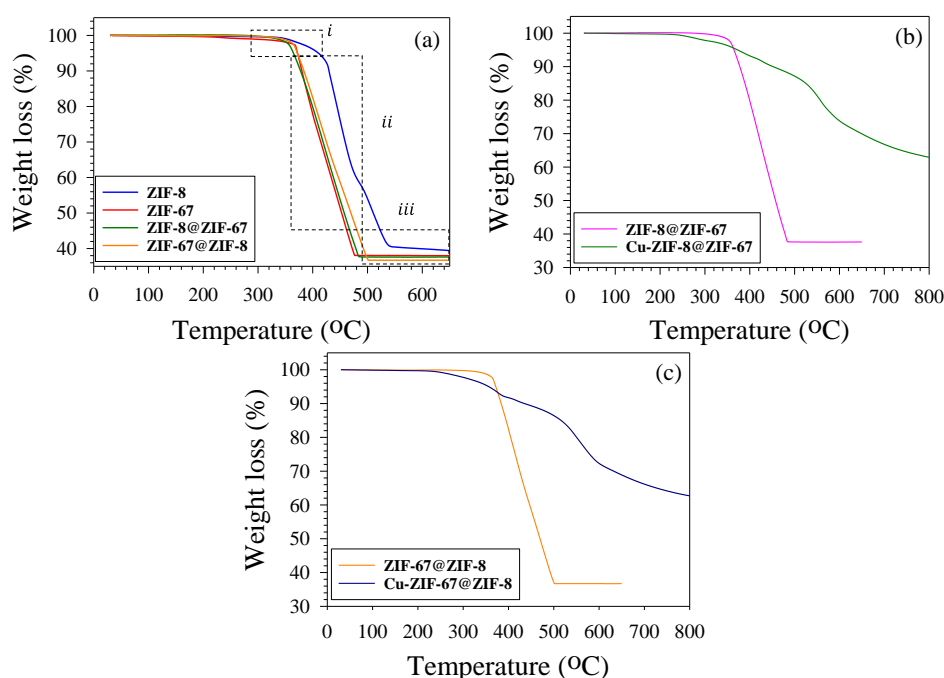
**Fig. 4.** (a) N<sub>2</sub> adsorption isotherms at -196 °C and (b) pore size distribution of ZIF-8@ZIF-67 and ZIF-67@ZIF-8 frameworks.

**Table 1** Surface area, pore volume, pore size of the core-shell ZIF-8@ZIF-67 and ZIF-67@ZIF-8 frameworks.

Catalyst	Surface area (m <sup>2</sup> /g)	Average pore size (nm)	Total pore volume (cm <sup>3</sup> /g)	Reference
ZIF-8@ZIF-67	1723.7	1.68	0.7239	Our work
	1402.1	1.2	0.8752	[7]
ZIF-67@ZIF-8	1640.4	1.95	0.7998	Our work
	1271.8	1.02	0.6797	[7]

Core-shell materials are represented in Figure 4, displaying their N<sub>2</sub> adsorption isotherms at -196 °C and pore size distribution. It reveals that N<sub>2</sub> adsorption occurs sharply at low relative pressures, indicating a Type I adsorption isotherm which is adsorption in microporous sizes. The BET measurements of core-shell reveal that their specific surface areas and pore volumes are 1723.7 and 1640.4 m<sup>2</sup>/g and 0.7015 and 0.7093 cm<sup>3</sup>/g, as shown in Table 1. In contrast to the single-metal ZIF-8 and ZIF-67, which had pore volumes of 0.7633 and 0.7324 cm<sup>3</sup>/g and surface areas of 1323.62 and 1392.30 m<sup>2</sup>/g, respectively [8]. The surface areas and pore volumes of the core-shell structures are significantly higher than those of the original single-metal forms due to the formation of a shell structure in ZIFs materials and the absence of pore blockage. This observation aligns with the results from the XRD and FTIR analyses, supporting the effectiveness of seed-mediated growth synthesis in maintaining the structural integrity of the materials.

### 3.4 Thermogravimetric analysis (TGA)



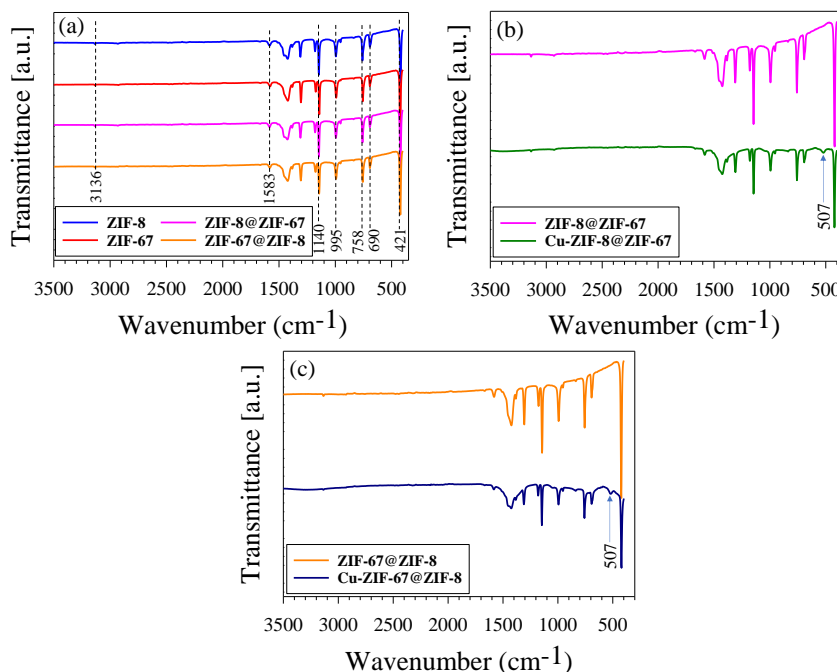
**Fig. 5.** TGA of (a) ZIF-8, ZIF-67, ZIF-8@ZIF-67 and ZIF-67@ZIF-8, (b) ZIF-8@ZIF-67 and Cu-ZIF-8@ZIF-67, (c) ZIF-67@ZIF-8 and Cu-ZIF-67@ZIF-8 frameworks.

Figure 5(a) shows the TGA analysis of single-metal ZIFs and core-shell materials under oxygen flow. The weight loss in the region *i* (330–370 °C) is 2–5% due to the release of water, methanol, and non-reactive 2-methylimidazole species. This is accompanied by an exothermic decomposition. In the region *ii* (370–480 °C), the weight loss is significant, reaching 62%. This is attributed to the thermal decomposition of 2-methylimidazole, which is bonded to the metal nodes (Co and Zn) within the structure. The thermal stability of the metal nodes of the materials is in the range of 475–550 °C indicating region *iii*. All materials exhibit similar thermal behavior because ZIF-8 and ZIF-67 have the same organic ligand. The results indicate that the structure decomposition starts with 2-methylimidazole. In Figure 5(b, c), when copper particles are added to core-shell materials, the weight loss at 240 °C is 4% due to the decomposition of copper nitrate trihydrate, sodium borohydride, and impurities on the material surface. When the temperature reaches 400–650 °C, the material weight decreases by 30%. This is the onset of structure decomposition, starting with 2-methylimidazole. The behavior of decomposition is



similar to core-shell materials. and the thermal stability is 650 °C. The TGA results indicate that the addition of Cu significantly improves the thermal stability of the materials.

### 3.5 Fourier Transform Infrared Spectrometer (FT-IR)



**Fig. 6.** (a) FTIR of ZIF-8, ZIF-67, ZIF-8@ZIF-67 and ZIF-67@ZIF-8, (b) ZIF-8@ZIF-67 and Cu-ZIF-8@ZIF-67, (c) ZIF-67@ZIF-8 and Cu-ZIF-67@ZIF-8 frameworks.

The FTIR spectra of single-metal and core-shell materials in Figure 6(a), the presence of Zn-N and Co-N bonds between the metal nodes and 2-methylimidazole ligand is shown by a noticeable peak at 421  $\text{cm}^{-1}$ . The C=N and C-H bonds are evident at 1583 and 3136  $\text{cm}^{-1}$ , respectively. In addition, the vibrations of aromatic  $\text{Sp}^2$  C-H bending are seen at 690 and 758  $\text{cm}^{-1}$ . The vibrations of in-plane bending of the ring are represented by the peaks at 995 and 1145  $\text{cm}^{-1}$  [9]. The FTIR analysis of core-shell materials shows that the 2-methylimidazole linker does not undergo any structural changes during the formation of the core material using the seed-mediated growth technique. This is because the bonding structures of the core and core-shell materials are consistent, especially the peak at 421  $\text{cm}^{-1}$ . This indicates the formation of Zn-imidazolate and Co-imidazolate bonds within the composite materials. Figure 6(b-c) shows the spectra of core-shell materials, Cu-ZIF-8@ZIF-67, and Cu-ZIF-67@ZIF-8 after Cu particles were added to the core-shell materials. The overall peak positions are similar to those of the core and core-shell materials. The small peak at 507  $\text{cm}^{-1}$  indicates the vibrations of the Cu center particles on the surface of the material [10]. This indicates that the Cu particles were added successfully to the material using the co-precipitation technique. The results of the analysis show that the addition of copper(II) nitrate trihydrate does not destroy the existing structure.

### 4. Conclusion

Through the application of the seed-mediated growth approach, core-shell ZIF-8@ZIF-67 and ZIF-67@ZIF-8 were produced. It was found that the original structure of the core materials was not destroyed, and a core-shell structure was successfully formed. This conclusion is supported by the results of SEM, XRD, BET, TGA, and FTIR analyses.

Furthermore, to enhance the physical and chemical properties, a method was designed to incorporate Cu metal into the materials using the co-precipitation technique. Within the core-shell materials, Cu particles were observed to be well-dispersed on the surface. TGA experiments also indicated that the addition of Cu particles significantly enhances thermal stability. This improvement is highly beneficial for various applications.

### Acknowledgement

This work was supported by the Thailand Graduate Institute of Science and Technology (TGIST) scholarship, managed by the National Science and Technology Development Agency (NSTDA). (Contract no. SCA-CO-2562-9759-TH).

### References

- [1] Nandi, S., De Luna, P., Daff, T. D., Rother, J., Liu, M., Buchanan, W., . . . Vaidhyanathan, R. A single-ligand ultra-microporous MOF for precombustion CO<sub>2</sub> capture and hydrogen purification. *Science Advances*, 1(11), e1500421. doi:10.1126/sciadv.1500421
- [2] Zhu, H. W., Xu, C. L., Wu, D. H., Wei, B. Q., Vajtai, R., & Ajayan, P. M. (2002). Direct Synthesis of Long Single-Walled Carbon Nanotube Strands. *Science*, 296(5569), 884-886. doi:10.1126/science.1066996
- [3] Banerjee, R., Phan, A., Wang, B., Knobler, C., Furukawa, H., O'Keeffe, M., & Yaghi, O. M. (2008). High-Throughput Synthesis of Zeolitic Imidazolate Frameworks and Application to CO<sub>2</sub> Capture. *Science*, 319(5865), 939-943. doi:10.1126/science.1152516
- [4] Li, T., Sullivan, J. E., & Rosi, N. L. (2013). Design and Preparation of a Core–Shell Metal–Organic Framework for Selective CO<sub>2</sub> Capture. *Journal of the American Chemical Society*, 135(27), 9984-9987. doi:10.1021/ja403008j
- [5] Zhou, K., Mousavi, B., Luo, Z., Phatanasri, S., Chaemchuen, S., & Verpoort, F. (2017). Characterization and properties of Zn/Co zeolitic imidazolate frameworks vs. ZIF-8 and ZIF-67. *Journal of Materials Chemistry A*, 5(3), 952-957. doi:10.1039/C6TA07860E
- [6] Kaur, G., Rai, R. K., Tyagi, D., Yao, X., Li, P.-Z., Yang, X.-C., . . . Singh, S. K. (2016). Room-temperature synthesis of bimetallic Co–Zn based zeolitic imidazolate frameworks in water for enhanced CO<sub>2</sub> and H<sub>2</sub> uptakes. *Journal of Materials Chemistry A*, 4(39), 14932-14938. doi:10.1039/C6TA04342A
- [7] Panchariya, D. K., Rai, R. K., Anil Kumar, E., & Singh, S. K. (2018). Core–Shell Zeolitic Imidazolate Frameworks for Enhanced Hydrogen Storage. *ACS Omega*, 3(1), 167-175. doi:10.1021/acsomega.7b01693
- [8] Chen, B., Yang, Z., Zhu, Y., & Xia, Y. (2014). Zeolitic imidazolate framework materials: recent progress in synthesis and applications. *Journal of Materials Chemistry A*, 2(40), 16811-16831. doi:10.1039/C4TA02984D
- [9] Kaur, H., Mohanta, G. C., Gupta, V., Kukkar, D., & Tyagi, S. (2017). Synthesis and characterization of ZIF-8 nanoparticles for controlled release of 6-mercaptopurine drug. *Journal of Drug Delivery Science and Technology*, 41, 106-112. doi:<https://doi.org/10.1016/j.jddst.2017.07.004>
- [10] Wang, Y., Wu, Y., Xie, J., Ge, H., & Hu, X. (2013). Multi-walled carbon nanotubes and metal–organic framework nanocomposites as novel hybrid electrode materials for the determination of nano-molar levels of lead in a lab-on-valve format. *Analyst*, 138(17), 5113-5120. doi:10.1039/C3AN00598D

## Effect of Cerium Promoter in the Silica Supported Copper Catalyst on the Selective Hydrogenation of Furfural to Furfuryl Alcohol

**Luksiga Noomsalee, Theerisara Suramanon, Pimlapat Nakvichein,  
and Choowong Chaisuk\***

Department of Chemical Engineering, Faculty of Engineering and Industrial Technology, Silpakorn University, Nakhon Pathom, 73000, Thailand  
E-mail: \*CHAIKUK\_C@su.ac.th

### Abstract

The selective hydrogenation of furfural to furfuryl alcohol on the Cu-Ce/SiO<sub>2</sub> catalyst was studied in this work. The cerium with 0.1-10 wt% loadings was added in the 20 wt% Cu/SiO<sub>2</sub> catalyst. The catalysts were characterized by the X-ray diffraction (XRD), N<sub>2</sub> physisorption, temperature programmed reduction (TPR) and N<sub>2</sub>O decomposition. The catalytic reaction was tested under 20 bar of hydrogen at 160 °C for 2 h. Addition of the Ce hardly affected the crystalline structure and the pore characteristics of the catalysts, except the 0.1 wt% Ce loading. The presence of Ce can lower the reduction temperature of the Cu/SiO<sub>2</sub> catalyst. An undetectable copper metal active sites by N<sub>2</sub>O decomposition indicated a weak interaction between copper metal and silica support resulting in the aggregation of copper metal to form the particles with larger size. The 0.5 wt% Ce was suitable content to maintain high reaction rate and high selectivity to furfuryl alcohol. An overload of the Ce content produced the other byproducts and therefore decreased significantly the selectivity of furfuryl alcohol. The impregnation of Ce after Cu showed the promising catalytic activity and selectivity compared to both the impregnation of Ce before Cu and the co-impregnation of Ce and Cu.

**Keywords:** Furfural hydrogenation; Furfuryl alcohol; Cu-Ce/SiO<sub>2</sub> catalyst.

### 1. Introduction

Thailand is a country with a large number of agricultural crops and therefore there is a lot of agricultural waste or biomass. Biomass is mainly composed of three compounds: cellulose, lignin and hemicellulose. The hemicellulose can be converted to a furfural (FAL) that produces high value-added products such as furfuryl alcohol (FOL), furan, tetrahydrofuran, 2-methylfuran, 2-methyltetrahydrofuran, tetrahydrofurfuryl alcohol, and cyclo-products [1]. Due to the attractive economic value and wide range of applications, furfuryl alcohol is an important derivative of furfural through hydrogenation process. It is used widely in the fine chemical and the polymer industries for many applications such as thermosetting resins, synthetic fibers, lysine, vitamin C, and lubricants [2, 3]. On the industry of furfuryl alcohol production from furfural, the traditional catalyst is Cu-Cr. However, the heavy environmental pollution and energy crisis limits the wide use of Cu-Cr catalysts, and the high toxicity has enforced the researchers to develop the high active Cr-free catalysts [4]. Therefore, Cr free catalysts have been developed to overcome these limitations. Various metal-based catalysts without Cr including Pt, Pd, Co, Cu and Ni have been studied. Among all catalysts, Cu-based catalysts have been the most frequently employed metal for hydrogenation of furfural due to inexpensive material and satisfactory hydrogenation selectivity [5]. However, the disadvantage of Cu metal is that its activity for the furfural hydrogenation is lower than that of noble metal. Addition of the suitable promoter is one of alternative ways to improve the catalytic performance. A cerium

was interesting promoter. It was reported that the Lewis acidic and basic sites coexisting on the low vacancy surfaces of CeO<sub>2</sub> can favor the dissociation of H-H bond [6]. A silica was selected as the catalyst support because it had a large surface area to highly disperse the active components [7]. In this work, the effect of Ce content in the Cu/SiO<sub>2</sub> catalyst on the catalytic property for liquid-phase selective hydrogenation of furfural was investigated.

## 2. Materials and Methods

The Cu-Ce/SiO<sub>2</sub> catalysts were prepared by impregnation method. First, the commercial SiO<sub>2</sub> powder was mixed with the aqueous solution of copper nitrate. This slurry was stirred at 70 °C for 6 h. The obtained material was dried at 110 °C for 12 h in oven. The powder was crushed and calcined in 30 ml/min of air flow at 400 °C for 3 h. After calcination, a 2 ml of the aqueous solution of ammonium cerium (IV) nitrate was impregnated into this powder and held at room temperature for 6 h. The obtained material was dried at 110 °C for 12 h in oven. The powder was crushed and calcined in 30 ml/min of air flow at 400 °C for 3 h. The final product was the Cu-Ce/SiO<sub>2</sub> catalysts. The Cu content was fixed as 20 wt% while the Ce content was varied as 0.1, 0.5, 1, 5 and 10 wt%. In this work, the symbol of Cu-*x*Ce/SiO<sub>2</sub> represented the catalyst prepared by the re-impregnation of Ce after Cu on the commercial SiO<sub>2</sub> support with *x* wt% Ce loading.

The catalysts were characterized by X-ray diffraction (XRD), N<sub>2</sub> physisorption, temperature programmed reduction (TPR) and N<sub>2</sub>O decomposition. The bulk crystalline phases of the catalysts were measured using the XRD technique by Bruker AXS Model D8 Discover in the range 2θ from 20° to 80° with Cu Kα. The crystalline sizes were calculated by the Scherer equation. The specific BET surface area was measured by N<sub>2</sub> physisorption using Micromeritics ASAP 2010. The catalysts were firstly pretreated in helium gas flow with 50 ml/min at 180 °C for 3 h to remove water bound to the surface of the catalyst. After pretreatment, a sample cell was installed to an adsorption part containing liquid nitrogen in a dewar. The volume of N<sub>2</sub> was measured at a different partial pressure of N<sub>2</sub> at -196 °C. The bulk reduction behavior of the catalysts was measured by TPR using a Micromeritics AutoChem 2910 instrument. Before the measurement, the catalyst was pretreated at 150 °C for 1 h under N<sub>2</sub> gas flow in order to eliminate the adsorbed water. The reduction step was proceeded under 10% H<sub>2</sub> in N<sub>2</sub> with 30 ml/min from 100 to 800 °C with the ramp heating rate of 10 °C/min and held at 800 °C for 1 h. During the reduction step, the water produced in the process was trapped by the liquid nitrogen. Decomposition of N<sub>2</sub>O was conducted to determine Cu active sites. It was measured by a Micromeritics AutoChem 2910 instrument. Before the measurement, the catalyst was reduced in H<sub>2</sub> with 25 ml/min at 300 °C for 3 h. The Cu active sites were measured at 90 °C with injected-pulses of N<sub>2</sub>O. The experiments were stopped when the sample was saturated.

The catalyst was tested by liquid-phase hydrogenation of furfural to furfuryl alcohol. This reaction occurred in 25 ml of stainless-steel reactor with magnetic stirrer. Prior to the reaction test, a 0.05 g of catalyst was ex-situ reduced by H<sub>2</sub> at 300 °C for 3 h. This catalyst was initially introduced into a liquid mixture consisting of a 0.1 ml of furfural reactant and a 10 ml of isopropanol solvent. The reaction was operated using a 20 bar of H<sub>2</sub> pressure and 160 °C. The reaction time was fixed as 2 h. After the reaction, the liquid product was collected and analyzed by GC-FID.

### 3. Results and Discussion

The XRD pattern of the Cu- $x$ Ce/SiO<sub>2</sub> catalysts is shown in Fig. 1. The XRD peaks of CuO referred by several previous works [8-11] were apparent for all catalysts. The crystalline size of CuO was calculated and recorded in table 1. Only the Cu-0.1Ce/SiO<sub>2</sub> catalyst showed larger crystalline size of the CuO. It showed the XRD peaks at 25.8, 33.5, 36.5 and 43.5° ascribed as Cu<sub>2</sub>(OH)<sub>3</sub>NO<sub>3</sub> [12]. The formation of this phase possibly interfered the dispersion of CuO particles on the catalyst surface. The XRD peaks of CeO<sub>2</sub> reported by the literatures [10, 11] were clearly observed for the catalysts with high Ce content (5 and 10 wt% Ce loadings). The pore characteristics and the specific BET surface area were determined by adsorption and desorption of N<sub>2</sub> as shown in Fig. 2 and table 1, respectively. Addition of the Ce hardly affected the specific BET surface area except the Cu-0.1Ce/SiO<sub>2</sub> catalyst. Type IV of physisorption isotherms with hysteresis loop was corresponding to the characteristics of mesoporous materials with pore diameters between 2 and 50 nm. The hysteresis loop was type H2 pores (ink-bottle pores) with narrow mouths according to the IUPAC classification [13].

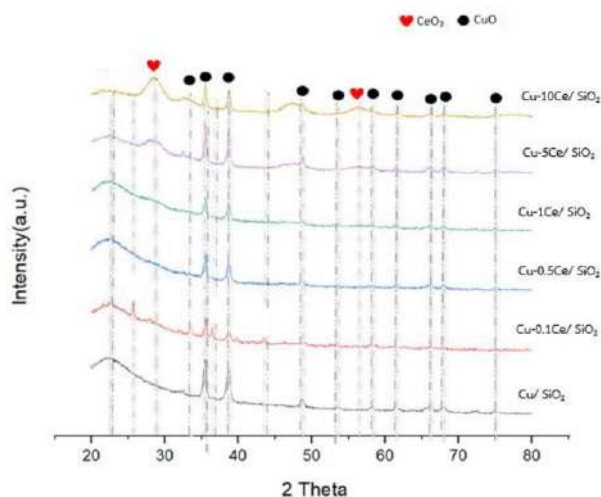


Fig. 1 The XRD pattern of the Cu- $x$ Ce/SiO<sub>2</sub> catalysts.

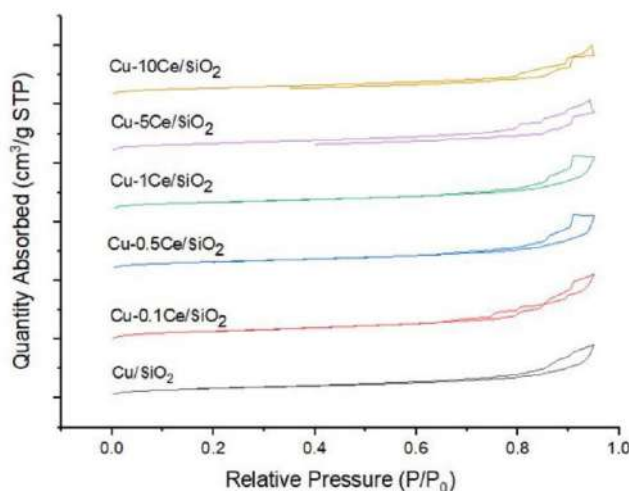


Fig. 2 The N<sub>2</sub> adsorption/desorption isotherms of the Cu- $x$ Ce/SiO<sub>2</sub> catalysts.

Table 1. The CuO crystalline size, the BET surface area, the mean pore size diameter and the total reducibility of the Cu-*x*Ce/SiO<sub>2</sub> catalysts obtained by the results of XRD, N<sub>2</sub> physisorption and TPR, respectively.

Catalyst	CuO crystalline size (nm)	BET surface area (m <sup>2</sup> /g)	Mean pore size diameter (nm)	Total reducibility (%)
Cu/SiO <sub>2</sub>	38.8	106	10.7	94.4
Cu-0.1Ce/SiO <sub>2</sub>	53.9	135	10.8	91.8
Cu-0.5Ce/SiO <sub>2</sub>	31.4	114	10.6	83.4
Cu-1Ce/SiO <sub>2</sub>	34.5	112	10.6	91.2
Cu-5Ce/SiO <sub>2</sub>	34.5	111	10.2	95.2
Cu-10Ce/SiO <sub>2</sub>	36.4	108	10.3	86.0

Figure 3 shows the TPR profiles of the Cu-*x*Ce/SiO<sub>2</sub> catalysts. All catalysts showed the reduction peaks in the range of 150-400 °C. These peaks were assigned as the reduction of CuO particles dispersed on the silica support. It was noted that the bulk CuO was reduced in a range of 200-325 °C confirmed by the literature [14]. Typically, the reduction of the Cu oxide to Cu metal had two possible pathways. One was single step reduction of the Cu oxide to Cu metal. The Cu-0.5Ce/SiO<sub>2</sub> catalyst showed this behavior. The other was two step reduction. The CuO was first reduced to Cu<sub>2</sub>O and subsequently reduced to Cu metal. This was the reduction behavior of all catalysts, except the Cu-0.5Ce/SiO<sub>2</sub> catalyst. The TPR peaks were significantly shifted to low temperature when adding the Ce promoter. A position of the TPR peak was dependent on the size of metal oxide. Basically, the larger the particle size, the higher the reduction temperature. As reported in the literature [15], the reduction temperature of CuO dispersed on the support was addressed in a range of 130-260 °C. This implied that the Ce can reduce the size of copper oxides and therefore the reduction temperature was decreased. It was remarked that total reducibility as shown in table 1 was calculated by an assumption that the only CuO species was reduced. However, a small broad peak at 400-550 °C was found on the catalysts with high Ce content (5 and 10 wt% Ce loadings). This peak was represented to the reduction of the CeO<sub>2</sub> particles. It was reported that the reduction peak at about 500 °C contributed to the reduction of Ce<sup>4+</sup> on surface and subsurface [16].

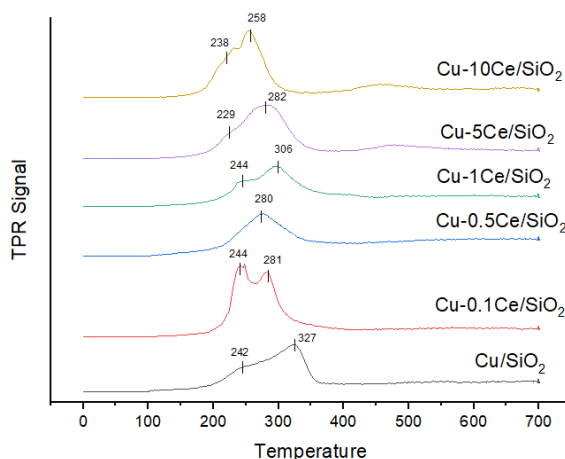


Fig. 3 The TPR profiles of the Cu-*x*Ce/SiO<sub>2</sub> catalysts.

The Cu active sites were measured by N<sub>2</sub>O decomposition. Unfortunately, a very low amount of decomposed N<sub>2</sub>O was detected for all catalysts. This meant a low amount of Cu active sites or large size of Cu metal on the catalyst surface. This was due to a weak interaction between copper metal and silica support resulting in the aggregation of copper metal to form the particles with larger size. Figures 4 and 5 show the catalytic activity and selectivity for the selective hydrogenation of furfural to furfuryl alcohol on the Cu-*x*Ce/SiO<sub>2</sub> catalysts. It was remarked that the conversion of furfural was very low corresponding to a low amount of Cu active sites measured by the decomposition of N<sub>2</sub>O and therefore the reaction rate was evaluated. A suitable content of Ce promoter in this work was 0.5 wt%. The Cu-0.5Ce/SiO<sub>2</sub> catalyst can maintain both high activity and selectivity. This was possible that its reduction characteristics was different from those of the other catalysts. A low content of Ce (0.1 wt%) showed very low activity because a large size of CuO was formed as confirmed by the XRD results. At a high content of Ce (5 and 10 wt%), the selectivity to furfuryl alcohol was decreased when compared to a moderate content of Ce (0.5 and 1 wt%). The other byproducts including 2-methylfuran, 2-methyltetrahydrofuran, and tetrahydrofurfuryl alcohol were formed. This was consistent with the other works [17-19].

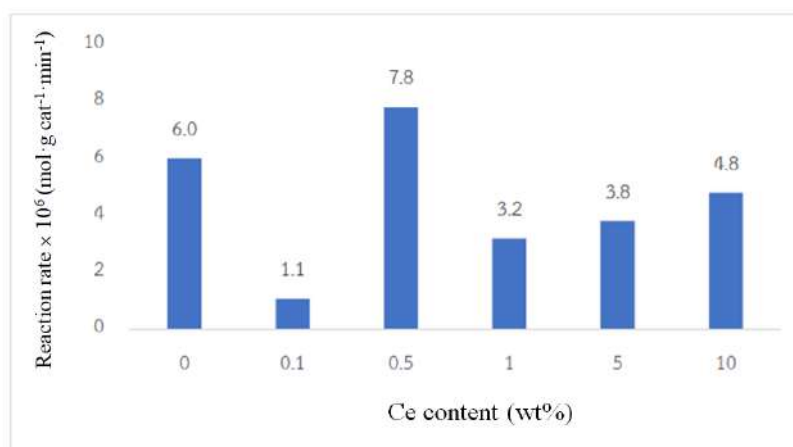


Fig. 4 Effect of Ce loading on the reaction rate for furfural hydrogenation.

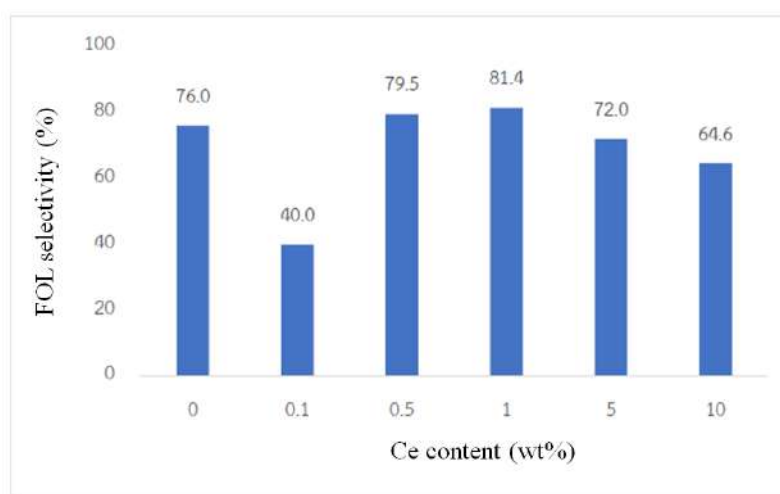


Fig. 5 Effect of Ce loading on the FOL selectivity for furfural hydrogenation.

Two Cu-0.5Ce/SiO<sub>2</sub> catalysts synthesized by the different preparation method was also evaluated. One was the Cu-0.5Ce/SiO<sub>2</sub> (B) prepared by sequential impregnation method. The Ce was impregnated on the silica support before impregnating the Cu. Another was the Cu-0.5Ce/SiO<sub>2</sub> (C) prepared by co-impregnation of the Cu and Ce. Three catalysts showed the same pore characteristics and had the BET surface area in a range of 110-115 m<sup>2</sup>/g. Compared to the Cu-0.5Ce/SiO<sub>2</sub> catalyst, both Cu-0.5Ce/SiO<sub>2</sub> (B) and Cu-0.5Ce/SiO<sub>2</sub> (C) showed the shift of the TPR peaks of CuO to lower temperature and lower total reducibility (not shown here). The amount of decomposed N<sub>2</sub>O cannot detected as well. The comparative results of three catalysts for reaction test are shown in Figs. 6 and 7. The Cu-0.5Ce/SiO<sub>2</sub> catalyst exhibited the highest reaction rate and furfuryl alcohol selectivity. A decrease of reaction rate and furfuryl alcohol selectivity of both Cu-0.5Ce/SiO<sub>2</sub> (B) and Cu-0.5Ce/SiO<sub>2</sub> (C) was because Cu particles with small size was formed corresponding with the TPR results. The furfural reactant with large molecular size was difficult to adsorb on Cu particles with small size while hydrogen reactant preferred to adsorb on them. The reaction rate was dependent on the concentration of furfural on the surface of catalyst and therefore it was decreased with decreasing the furfural concentration. The presence of more hydrogen on the surface of catalyst promoted the formation of byproduct through hydrogenation and hydrogenolysis and therefore the selectivity to furfuryl alcohol was decreased.

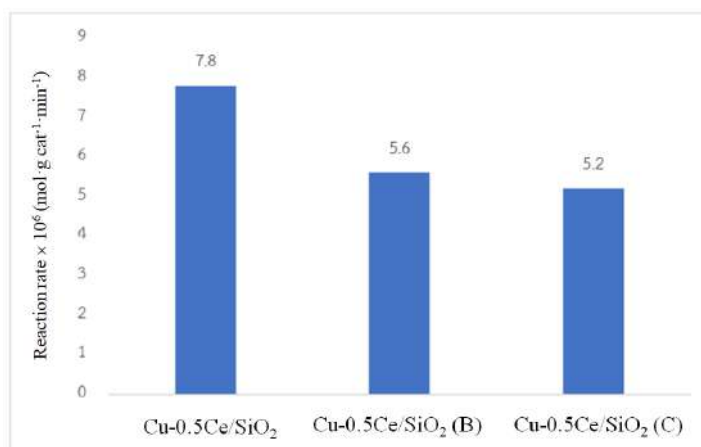


Fig. 6 Effect of the preparation method on the reaction rate for furfural hydrogenation.

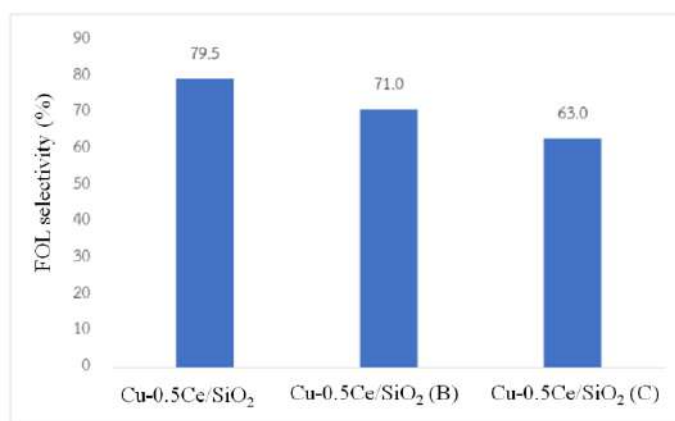


Fig. 7 Effect of the preparation method on the FOL selectivity for furfural hydrogenation.



#### 4. Conclusions

The effect of Ce promotor in the Cu-Ce/SiO<sub>2</sub> catalyst on selective hydrogenation of furfural to furfuryl alcohol was studied. The optimum content of the Ce promotor was 0.5 wt%. The Cu-0.5Ce/SiO<sub>2</sub> catalyst can maintain high reaction rate and high selectivity to furfural alcohol. This was dependent on a suitable particle size of Cu metal dispersed on the catalyst surface. Either larger size of Cu metal in the catalyst with low Ce content or smaller size of Cu metal and in the catalysts with high Ce content showed a decrease of the catalytic activity and a decrease of the selectivity to furfuryl alcohol. A trade-off between the concentrations of the furfural and hydrogen on the catalyst surface was a key factor to obtain a promising catalytic performance.

#### Acknowledgements

This work was financially supported by Department of Chemical Engineering, Faculty of Engineering and Industrial Technology, Silpakorn University.

#### References

- [1] Yan, K., Wu, G., Lafleur, T., and Jarvis, C. (2014). Production, properties and catalytic hydrogenation of furfural to fuel additives and value-added chemicals. *Renewable and Sustainable Energy Reviews*, 38, 663-676.
- [2] Huber, G.W., Iborra, S., and Corma, A. (2006). Synthesis of transportation fuels from biomass: chemistry, catalysts, and engineering. *Chemical Reviews*, 106(9), 4044-4098.
- [3] Kijeński, J, Winiarek, P., Paryjczak, T., Lewicki, A., and Mikołajska, A. (2002). Platinum deposited on monolayer supports in selective hydrogenation of furfural to furfuryl alcohol. *Applied Catalysis A: General*, 233(1-2), 171-182.
- [4] Burnett, L.W., Johns, I.B., Holdren, R.F., and Hixon, R.M. (1948). Production of 2-methylfuran by vapor-phase hydrogenation of furfural. *Industrial & Engineering Chemistry*, 40(3), 502-505.
- [5] Wang, Y., Miao, Y., Li, S., Gao, L., and Xiao, G. (2017). Metal-organic frameworks derived bimetallic Cu-Co catalyst for efficient and selective hydrogenation of biomass-derived furfural to furfuryl alcohol. *Molecular Catalysis*, 436, 128-137.
- [6] Zou, Y., Zhang, M., Liu, Y., Ma, Y., Zhang, S., and Qu, Y. (2022). Highly selective transfer hydrogenation of furfural into furfuryl alcohol by interfacial frustrated Lewis pairs on CeO<sub>2</sub>. *Journal of Catalysis*, 410, 54-62.
- [7] Li, F., Cao, B., Ma, R., Liang, J., Song, H., and Song, H. (2016). Performance of Cu/TiO<sub>2</sub>-SiO<sub>2</sub> catalysts in hydrogenation of furfural to furfuryl alcohol. *Canadian Journal of Chemical Engineering*, 94(7), 1368-1374.
- [8] Etefagh, R., Azhir, E., and Shahtahmasebi, N. (2013). Synthesis of CuO nanoparticles and fabrication of nanostructural layer biosensors for detecting *Aspergillus niger* fungi. *Scientia Iranica*, 20(3), 1055-1058.
- [9] Santos-Cruz, D., Mayén-Hernández, S.A., de Moure-Flores, F., Campos-Álvarez, J., Pal, M., and Santos-Cruz, J. (2017). CuO<sub>x</sub> thin films by direct oxidation of Cu films deposited by physical vapor deposition. *Results in Physics*, 7, 4140-4144.
- [10] Kabure, A. A., Mane, S. R., and Shirke, B. S. (2020). The lpg gas-sensing performance of CeO<sub>2</sub>-CuO nanocomposite film synthesized by microwave assisted sol-gel method. *International Journal of Recent Scientific Research*, 11(5), 38560-38567.

- [11] Jiménez-Gómez, C.P., Cecilia, J.A., Márquez-Rodríguez, I., Moreno-Tost, R., Santamaría-González, J., Mérida-Robles, J., and Maireles-Torres, P. (2017). Gas-phase hydrogenation of furfural over Cu/CeO<sub>2</sub> catalysts. *Catalysis Today*, 279, 327-338.
- [12] Wang, A.L., Ye, C.L., Jia, X.Y., and Yin, H.B. (2021). Methanol dehydrogenation to methyl formate catalyzed by Cu/SiO<sub>2</sub> catalysts: Impact of precipitation procedure and calcination temperature. *Russian Journal of Applied Chemistry*, 94(9), 1302-1312.
- [13] Xiang, Q., Yu, J., Wang, W., and Jaroniec, M. (2011). Nitrogen self-doped nanosized TiO<sub>2</sub> sheets with exposed {001} facets for enhanced visible-light photocatalytic activity. *Chemical Communications*, 47(24), 6906-6908.
- [14] Fierro, G., Lojacono, M., Inversi, M., Porta, P., Lavecchia, R., and Cioci, F. (1994). A Study of anomalous temperature-programmed reduction profiles of Cu<sub>2</sub>O, CuO, and CuO-ZnO catalysts. *Journal of Catalysis*, 148(2), 709-721.
- [15] Boccuzzi, F., Chiorino, A., Martra, G., Gargano, M., Ravasio, N., and Carrozzini, B. (1997). Preparation, characterization, and activity of Cu/TiO<sub>2</sub> catalysts. I. Influence of the preparation method on the dispersion of copper in Cu/TiO<sub>2</sub>. *Journal of Catalysis*, 165(2), 129-139.
- [16] He, J., Zhang, H., Wang, W., Yao, P., Jiao, Y., Wang, J., and Chen, Y. (2021). Soot combustion over CeO<sub>2</sub> catalyst: the influence of biodiesel impurities (Na, K, Ca, P) on surface chemical properties. *Environmental Science and Pollution Research*, 28(20), 26018-26029.
- [17] Jiménez-Gómez, C.P., Cecilia, J.A., Márquez-Rodríguez, I., Moreno-Tost, R., Santamaría-González, J., Mérida-Robles, J., and Maireles-Torres, P. (2017). Gas-phase hydrogenation of furfural over Cu/CeO<sub>2</sub> catalysts. *Catalysis Today*, 279, 327-338.
- [18] Du, H., Ma, X., Yan, P., Jiang, M., Zhao, Z., and Zhang, Z.C. (2019). Catalytic furfural hydrogenation to furfuryl alcohol over Cu/SiO<sub>2</sub> catalysts: A comparative study of the preparation methods. *Fuel Processing Technology*, 193, 221-231.
- [19] Jackson, M.A., White, M.G., Haasch, R.T., Peterson, S.C., and Blackburn, J.A. (2018). Hydrogenation of furfural at the dynamic Cu surface of CuOCeO<sub>2</sub>/Al<sub>2</sub>O<sub>3</sub> in a vapor phase packed bed reactor. *Molecular Catalysis*, 445, 124-132.

## Life cycle assessment of bio-hydrogenated diesel from palm fatty acid distillate and refined palm stearin

**Pakawat Prachapitukkun<sup>1</sup>, Wisunsaya Pipattananon<sup>1</sup>, Supanida Thanasomboon<sup>1</sup>,  
Kanyarat Tantawisut<sup>1</sup>, Rapeepat Tuengja<sup>1</sup>, Suwimol Wongsakulphasatch<sup>1</sup>,  
Lida Simasatitkul<sup>2</sup>, Paweena Prapainainar<sup>3</sup>, Kandis Sudsakorn<sup>3</sup>,  
Suttichai Assabumrungrat<sup>4</sup>, Chaiwat Prapainainar<sup>1\*</sup>**

<sup>1</sup> Department of Chemical Engineering, Faculty of Engineering, King Mongkut's University of Technology North Bangkok 10800, Thailand, <sup>2</sup> Department of Industrial Chemistry, Faculty of Applied Science, King Mongkut's University of Technology North Bangkok 10800, Thailand,

<sup>3</sup> Department of Chemical Engineering, Faculty of Engineering, Kasetsart University 10900, Thailand,

<sup>4</sup> Department of Chemical Engineering, Faculty of Engineering, Chulalongkorn University 10330, Thailand

\*Corresponding author: chaiwat.r@eng.kmutnb.ac.th

### Abstract

Energy demand has been growing, especially in the transportation sector, while environmental concerns have also been under focus. Green diesel, a renewable energy, can be an alternative to fossil fuel to tackle both issues. Prior to using green diesel, environmental impact assessment is required to ensure environmental friendliness of its production. This study focuses on the environmental impact of production processes of green diesel alternatively called bio-hydrogenated diesel (BHD) produced from hydro-processing technology by comparing between two feedstocks (palm fatty acid distillate (PFAD) and refined palm stearin (RPS) with those of diesel from fossil fuel. BHD production processes were simulated using ASPEN Plus to analyze material and energy balances with the production rate of 50-ton BHD/day, while reaction information was attained from experiments. The environmental impact analysis was within the Cradle-to-Gate system boundary starting from palm oil plantation, cultivation to the production of BHD. Life cycle assessment (LCA) was carried out using ReCiPe 2016 method with LCSof where databases were collected from relevant research studies. LCA results in this study focusing on the end point results are typically shown as an impact on human health, ecosystem quality, and resource depletion.

**Keywords:** Bio-hydrogenated diesel; Palm oil; Life cycle assessment; Palm fatty acid distillate; Refined palm stearin

### 1. Introduction

In 2019, Enerdata, a global energy data provider [1], found that the world's overall energy consumption has increased by 67% since 2000 indicating a significant rise in energy demand. Energy from petroleum is considered unsustainable, contributing significantly to environmental issues [2]. Consequently, there is a growing need for sustainable energy sources. Biodiesel is first-generation biofuel produced from plant oil or animal fat. Although biodiesel is considered more environmentally friendly compared to traditional diesel, it has many limitations and requires blending with diesel fuel for transportations uses [3]. Bio-hydrogenated diesel (BHD) have been developed as second generation of biofuel and can be produced from plant oils. Thailand can produce palm oil at a capacity of 18.9 million tons yearly in 2023 [4], and Thailand

is the world's third-largest producer of palm oil [5]. Therefore, palm-based BHD production can be a renewable energy source for Thailand. For the transportation sector, it is important to evaluate the environmental impact if BHD is to be fully adopted and compared to the current petroleum-based fuel, especially diesel.

BHD can be produced from various palm oil products and by-products [5]. Palm fatty acid distillate (PFAD) and refined palm stearin (RPS), triglycerides, are by-products from the palm oil refining industry that share similar features for BHD production. Kaitkittipong et al. (2013) [5] reported an experimental study of BHD production and found that the product yield of BHD and reaction conversion reached the highest values of 81% and 91%, respectively for PFAD. Boonrod et al. (2018) [6] reported the environmental impact and energy usage of BHD production from PFAD and FAME from palm oil through a life cycle assessment and found that BHD from PFAD required less energy for its production but had a greater environmental impact than that from FAME. Permpool et al. (2021) [7] studied the environmental impact of three types of diesels: BHD, FAME, and petroleum-based, by comparing the impact categories considered for the endpoint assessment: human health, ecosystem, and resource, using life cycle assessment (LCA). It was found that petroleum diesel has the highest environmental impacts, followed by FAME and BHD.

In this work, a comparative study between the use of PFAD and RPS as feedstocks under the same technological conditions is carried out and investigated. This research studies the environmental impacts throughout the life cycle assessment. The boundary for this study is Cradle-to-Gate, from palm oil plantation to BHD production. The results will be presented in terms of endpoint indicators with three dimensions: human health, ecosystem, and resources. The results from this work will be valuable for making informed decisions in the future development of bio-hydrogenated diesel, considering both technological and environmental aspects.

## 2. Methods: LCA method

The LCA study compared BHD production from PFAD and RPS based on the series of ISO 14040 (2006).

### 2.1. Goal and scope

The goal of the study was to assess the relevant environmental impacts at endpoint stage of the BHD production processes using PFAD and RPS as raw materials.

### 2.2. System boundary and functional unit

The first route is BHD from PFAD feedstock, and second route is BHD from RPS feedstock. The system boundaries were "Cradle-to-Gate" consisting of four main steps for BHD from PFAD: palm oil plantation, palm oil production, palm oil refining, and BHD production. For BHD from RPS, there are five main steps: palm oil plantation, palm oil production, palm oil refining, palm oil fractionation, and BHD production. The use phase of BHD as a fuel in diesel engine was not included in the study. The system boundary of BHD from PFAD and BHD from RPS can be shown in Fig. 1(a) and Fig. 1(b). The functional unit (FU) of this study was defined as 1 kg of BHD for comparison.

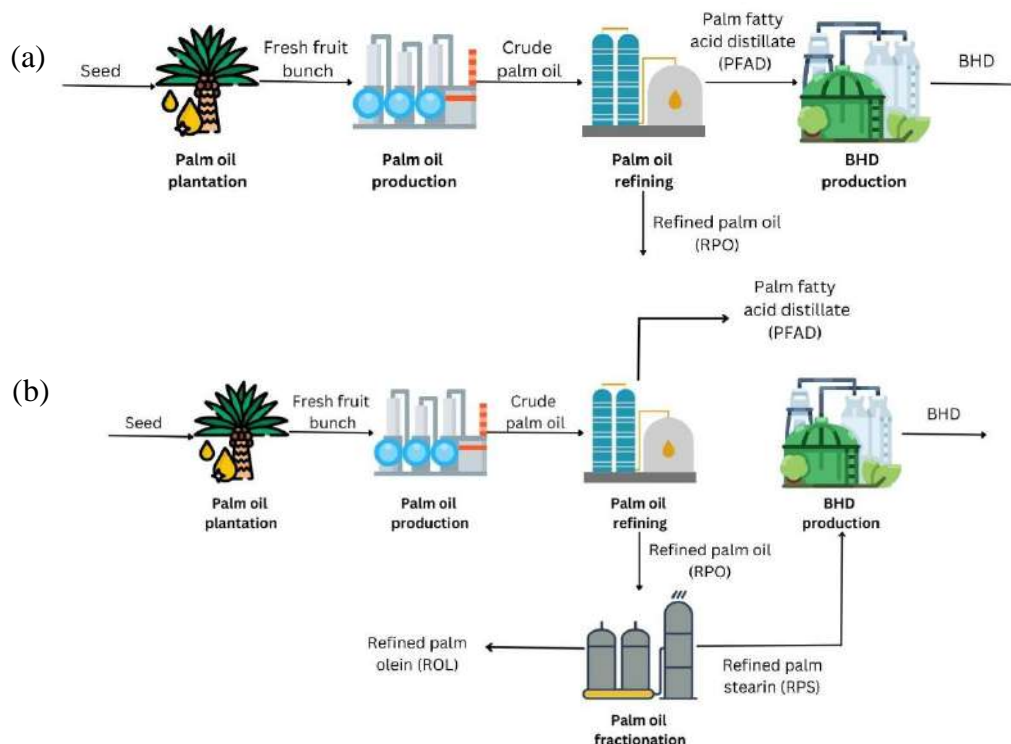


Fig. 1 System boundary of BHD derived from (a) PFAD (b) RPS.

### 2.3. Inventory data collection and assumptions.

Life cycle inventory (LCI) involves data on the input and output of the usage of raw materials, energy, and the emissions of various wastes throughout the lifecycle of BHD production process from palm oil plantation to BHD production. Inventory data used in this study are collected from various sources, including data from literature, Eco-invent provided in the LCSof software, material and energy balance results from BHD production using chemical process simulation software, Aspen Plus. Inventory data used in this work can be summarized in Table 1.

Table 1. Life cycle inventory (LCI) database references.

Process	Feedstock	Main product	Ref.
Palm oil plantation	Seed	Fresh fruit bunch	Kittithammavong (2013) [8]
Palm oil production	Fresh fruit bunch	Crude palm oil	Pleanjai et al. (2004) [9]
Palm oil refining	Crude palm oil	PFAD, RPO	Boonrod et al. (2018) [6]
Palm oil fractionation	RPO	RPS, ROL	Boonrod et al. (2018) [6]
BHD production	PFAD	BHD-PFAD	From this work
BHD production	RPS	BHD-RPS	From this work

## 2.4. Impact assessment

To evaluate the environmental impact of BHD productions from PFAD and RPS feedstocks, database from LCSoft software and Thailand databases are required. ReCiPe 2016 methods were used to assess environmental impact. Microsoft Excel was used for data processing and calculation. The endpoint indicators are final measures of environmental impact that reflect the damage or benefit, they show the ultimate outcomes of environmental changes and allow for a more integrated and consistent comparison of different impact categories [10]. The endpoint impacts considered in this work are human health, ecosystem, and resource. Human health may include considerations of air and water pollution, exposure to hazardous substances, and other factors that could impact human well-being. Ecosystems including terrestrial and aquatic environments may affect biodiversity, soil quality, water quality, and other aspects of ecosystems. Resource focuses on the consumption and depletion of natural resources, which evaluates the impact on non-renewable resources, such as minerals and fossil fuels, as well as the potential for overexploitation of renewable resources [11].

## 3. Results and Discussion

Environmental impact analysis of BHD production from PFAD and RPS were considered from Cradle-to-Gate, meaning that from palm oil plantation to BHD production shown in Figure 1 of the whole life cycle of 1 kg BHD produced. The results of life cycle impact assessment can be shown in the sections below.

### 3.1. Characterization results of impact categories

ReCiPe 2016 was used in the characterization of the selected endpoints, which are three impact categories: human health, ecosystem, and resource. The results are shown in Table 2 and Table 3.

Table 2. Characterization results of BHD production from PFAD based on 1 kg BHD produced.

Indicator	Unit	Palm oil plantation	Palm oil production	Palm oil refining	BHD production
Human health	DALY	$1.34 \times 10^{-2}$	$3.44 \times 10^{-4}$	$2.89 \times 10^{-1}$	$2.74 \times 10^{-2}$
Ecosystem	species/yr	$8.07 \times 10^{-7}$	$8.96 \times 10^{-7}$	$2.86 \times 10^{-4}$	$6.33 \times 10^{-5}$
Resource	\$	$3.00 \times 10^{-1}$	$6.26 \times 10^{-1}$	$5.71 \times 10^2$	23.2

From Table 2, the highest impact for human health, ecosystem and resource indicators occurs at the palm oil refining stage at  $2.89 \times 10^{-1}$  DALY,  $2.86 \times 10^{-4}$  species/yr, and  $5.71 \times 10^2$ , respectively. It implies that high energy usage is in this step and the energy used are mainly from heat and electricity. The step with the lowest impact for human health is palm oil production stage at  $3.44 \times 10^{-4}$  DALY, for ecosystem and resource is palm oil plantation stage at  $8.07 \times 10^{-7}$  species/yr, and  $3.00 \times 10^{-1}$ , respectively, which was the result of lower energy usage in these steps and lower emissions, including more environmentally friendly waste compared to other steps.

Table 3. Characterization result of BHD production from RPS based on 1 kg BHD produced.

Indicator	Unit	Palm oil plantation	Palm oil production	Palm oil refining	Palm oil fractionation	BHD production
Human Health	DALY	$1.56 \times 10^{-3}$	$3.03 \times 10^{-4}$	$3.36 \times 10^{-2}$	1.95	$6.85 \times 10^{-1}$
Ecosystem	species/yr	$9.42 \times 10^{-8}$	$8.38 \times 10^{-7}$	$3.32 \times 10^{-5}$	$4.50 \times 10^{-3}$	$1.58 \times 10^{-3}$
Resource	\$	$3.35 \times 10^{-2}$	$3.24 \times 10^{-1}$	$6.63 \times 10^1$	$1.63 \times 10^3$	$5.74 \times 10^2$

From Table 3, the impacts on human health, ecosystem, and resource indicators for BHD from RPS are like from PFAD with the highest impact occurring during the palm oil refining stage at 1.95 DALY,  $4.50 \times 10^{-3}$  species/yr, and  $\$1.63 \times 10^3$ , respectively. This indicates that energy usage was highest at this step, mainly in the form of heat and electricity. The steps with the lowest impact on human health are the palm oil production stage, with a value of  $3.03 \times 10^{-4}$  DALY, for ecosystem and resource is palm oil plantation stage at  $9.42 \times 10^{-8}$  species/yr and  $\$3.35 \times 10^{-2}$ , respectively.

The comparison of the endpoint impact between the two processes can be shown in Fig. 2(a) and Fig. 2(b)

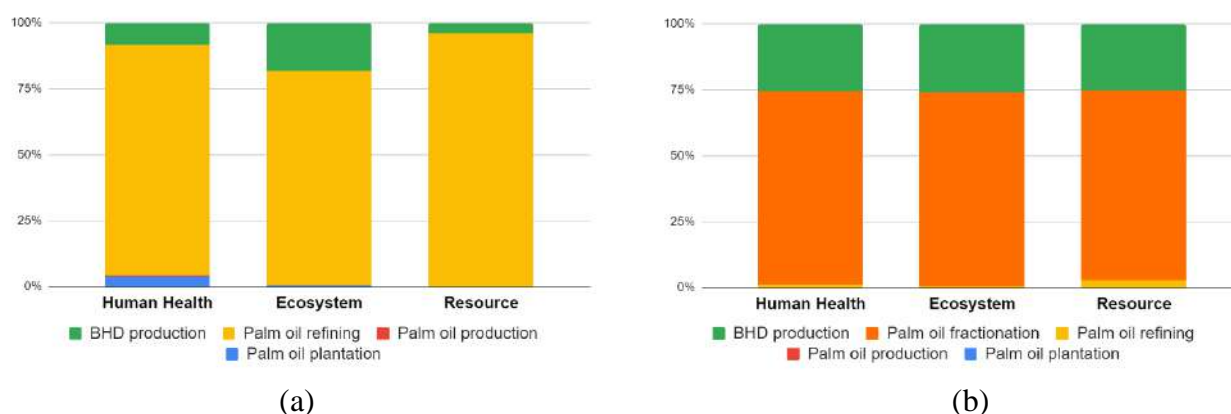


Fig. 2 Comparison of the environmental impacts of BHD obtained from (a) PFAD (b) RPS

Fig. 2(a) and Fig. 2(b) show overall impact of the three categories. In Fig. 2(a), the largest impact on BHD production with PFAD feedstock was observed in the palm oil refining step, contributed approximately higher than 80 percent to all the impacts, followed by BHD production. This is due to the high energy requirement in the palm oil refining process as PFAD accounts for 4% (Refined palm oil 96%) of the overall product coming from this step. This can be explained by the high energy intensity of this step, which involves the use of steam and electricity. Both energy sources in Thailand are mainly derived from fossil fuels. The impacts from BHD production from RPS were different from those of PFAD as it requires an additional step to produce RPS, which is palm oil fractionation. The largest contributor is palm oil fractionation step around 75 percent, followed by the BHD production step, as shown in Fig. 2(b). This can be because palm oil fractionation step involves a unit operation with very high energy intensity, specifically a distillation column, leading to a substantial demand for energy, primarily sourced from fossil fuels.

#### 4. Conclusions

In the LCA analysis considering Cradle-to-Gate scope for BHD production from plantation to BHD production, endpoint impacts; human health, ecosystems, and resources were examined. When PFAD was used as a feedstock, palm oil refining contributed the highest compared to other steps with approximately 80 percent in all three categories. In the case of RPS, the biggest contributor is palm oil fractionation step around 75 percent across in all three impacts. These impacts are primarily attributed to the use of energy, mainly derived from fossil fuels. In summary, a recommendation for improving environmental impacts is to consider utilizing renewable energy sources for heat and electricity. This approach can result in lower environmental impacts compared to using energy derived from petroleum-based fuels. Additionally, another option involves reducing energy consumption by opting for process modification and intensification.

#### 5. Acknowledgements

The authors acknowledge the Office of National Higher Education Science Research and Innovation Policy Council – PMU C, PTT EXPLORATION AND PRODUCTION PUBLIC Co., Ltd., CHERDCHAI CORPORATION Co., Ltd., POLAWAT ENGINE Co., Ltd., and VERASUWAN CO Ltd. (C10F640103) for funding support.

#### 6. References

- [1] Enerdata. (2021, April 28). Global Energy Transition Statistics 2020. Enerdata. <https://yearbook.enerdata.net/> (Accessed on 2024, February 1)
- [2] Bangkokbiznews. (2021, October 11). The Problem and Solutions to the 'Energy Crisis' in Europe. Tisco. <https://www.bangkokbiznews.com/pr-news/business/965157> (Accessed on 2024, February 5)
- [3] Kantama, A., Prapainainar C., Narataruk P., and Hunpinyo P. (2014). Feasibility Study of Bio-hydrogenated Diesel (BHD) Production: A Case Study in Thailand. *Advanced Materials Research Vols. 931-932 (2014)* pp 162-167.
- [4] Infoquest. (2023, June 2). DIT revealed that the government is planning to export excess palm oil and provide income insurance to maintain price stability in the domestic market. Infoquest. <https://www.infoquest.co.th/2023/306375> (Accessed on 2024, February 5)
- [5] Kiatkittipong, W., Phimsen, S., Kiatkittipong, K., Wongsakulphasatch, S., Laosiripojana, N., and Assabumrungrat, S. (2013). Diesel-like hydrocarbon production from hydroprocessing of relevant refining palm oil. *Fuel Processing Technology*, 116, 16–26. doi: 10.1016/j.fuproc.2013.04.018
- [6] Boonrod B., Prapainainar C., Narataruk P., Kantama, A., Saibautrong W., Sudsakorn K., Mungcharoen T., and Prapainainar P. (2016). Evaluating the environmental impacts of bio-hydrogenated diesel production from palm oil and fatty acid methyl ester through life cycle assessment. *Journal of Cleaner Production*, doi: 10.1016/j.jclepro.2016.07.128
- [7] Permpool, N., Mahmood, A., Ghani, H. U., and Gheewala, S. H. (2021). An Eco-Efficiency Assessment of Bio-Based Diesel Substitutes: A Case Study in Thailand. *Sustainability*, 13(2), 576. <https://doi.org/10.3390/su1302057> (Accessed on 2024, February 1)



- [8] Kittithammavong V. (2013). Life Cycle Assessment of Biofuels from Transesterification Process [Degree of Master of Engineering Program in Environmental Engineering Department of Environmental Engineering Faculty of Engineering, Chulalongkorn University] Chulalongkorn University.
- [9] Pleanjai S., Gheewala S., and Garivait S. (2004). Environmental Evaluation of Biodiesel Production from Palm Oil in a Life Cycle Perspective [The Joint Graduate School of Energy and Environment, King Mongkut's University of Technology Thonburi, Bangkok, Thailand]. CiteSeerX.  
<https://citeseerx.ist.psu.edu/document?repid=rep1&type=pdf&doi=9ac5da01c2eeb6144cec4ce001cd27e58eba7a37> (Accessed on 2024, February 6)
- [10] LinkedIn community (2024, January 24). What are the advantages and disadvantages of using midpoint and endpoint indicators in LCA. LinkedIn.  
<https://www.linkedin.com/advice/0/what-advantages-disadvantages-using-midpoint> (Accessed on 2024, February 8)
- [11] Committed to health and sustainability (2011, June 16). LCIA: the ReCiPe model. National Institute for Public Health and the Environment. <https://www.rivm.nl/en/life-cycle-assessment-lca/recipe> (Accessed on 2024, February 6)

## Techno-economic Study of Green Diesel Production from Palm Oil By-product using Recycled Solvent

**Rangsihorn Dilokratanakorn<sup>1</sup>, Wisunsaya Pipattananon<sup>1</sup>, Supanida Thanasomboon<sup>1</sup>,  
Kanyarat Tantawisut<sup>1</sup>, Rapeepat Tuengja<sup>1</sup>, Suwimol Wongsakulphasatch<sup>1</sup>,  
Paweena Prapainainar<sup>2</sup>, Kandis Sudsakorn<sup>2</sup>, Suttichai Assabumrungrat<sup>3</sup>,  
Chaiwat Prapainainar<sup>1,\*</sup>**

<sup>1</sup> Department of Chemical Engineering, Faculty of Engineering,  
King Mongkut's University of Technology North Bangkok, Bangkok 10800, Thailand

<sup>2</sup> Department of Chemical Engineering, Faculty of Engineering, Kasetsart University, Bangkok 10900, Thailand

<sup>3</sup> Department of Chemical Engineering, Faculty of Engineering, Chulalongkorn University, Bangkok 10330,  
Thailand

\*Corresponding author: chaiwat.r@eng.kmutnb.ac.th

### Abstract

Bio-hydrogenated diesel (BHD) or green diesel is a second generation of biofuel, having a straight chain alkane structure with 15 – 18 carbon atoms, which is in the same range as petroleum diesel. However, the production process is still limited because the hydro-processing requires high operating conditions and high energy. This study aims to compare the effects of different starting materials, palm fatty acid distillate (PFAD) and refine palm stearin (RPS), which are the by-products from a palm oil refining process. Impact of using BHD product as recycle stream to lower the operating condition and reduce energy consumption is also focused. The study was divided into four cases: PFAD and RPS as feedstocks with and without recycle stream with the production capacity of 50 tons/day of feed. From lab-scale experimental results, BHD production using solvent can be done under lower operating condition from 50 bar to 17 and 34 bar for PFAD and RPS, respectively. Based on the experimental data, the simulation study was carried out using ASPEN Plus, while BHD product-recycle stream was added as solvent in the continuous processes. The results showed that main products from PFAD was pentadecane (C15) and heptadecane (C17), whereas that of RPS produced primarily pentadecane. It is worth mentioning that, in the case of using a solvent, the main product for both feedstocks is hexadecane (C16) as cracking reaction may occur, and the energy consumption is increasing to 39-45% for heating duty, and 32-42% for cooling duty as increasing flowrate in process.

**Keywords:** Green diesel; Hydro-processing; Solvent; Palm fatty acid distillate; Refine palm stearin.

### 1. Introduction

With Thailand experiencing rapid economic growth, there is a rising daily demand for energy and fuel. Importing fuel oil from abroad, aside from being costly, brings about environmental concerns related to its use and production. In response to these issues, a growing number of people are turning to alternative energy and fuels derived from renewable sources, such as biodiesel and synthetic biodiesel [1]. Biodiesel is the first generation of biofuels, which can be derived from renewable resources such as palm oil, vegetable oil, animal fat, or algae.

This alternative diesel fuel shares combustion properties very similar to petroleum diesel, naturally biodegrades through biological processes, is non-toxic to the environment, and represents a form of bioenergy [2]. The second-generation biofuels are often referred to as green diesel, renewable diesel, or bio-hydrogenated diesel (BHD), which can be produced by reacting triglyceride or fatty acid with hydrogen gas. BHD can be blended with diesel to fuel cars or used as a direct substitute for petroleum diesel [3]. BHD production from fatty acid can be referred as hydro-processing process involving hydrodeoxygenation, decarboxylation, and decarbonylation, while BHD from triglyceride includes hydrogenation and hydrogenolysis as shown in Fig. 1 [4]. In hydro-processing process, solvent can be added at the reaction step to influence the reaction, enhance mass transfer, facilitate alkane desorption, and prevent the formation of undesired products [5]. In industrial scale, the use of a solvent comes with its drawbacks, which may increase energy consumption and process costs. The choice of solvent is also a crucial decision with implications for the overall efficiency and sustainability of the hydro-processing system [5].

Thongkumkoon et al. [6] successfully reported experimental study of BHD production from palm products in a batch-type reactor filled with 25 cm<sup>3</sup> of feedstock and 0.5 g of sulfided metal catalyst without using solvent under the operating condition of 4 MPa, 300-400 °C, and 1-3 hr. reaction time. The diesel yield from palm fatty acid distillate (PFAD) and refined palm stearin (RPS) is 69.7% and 69.5% respectively. [6]

In Thailand, palm stands out as one of the prime choices for fuel processing [7]. The production of green diesel can use PFAD and refined palm stearin (RPS), which comprise mainly of palmitic acid and oleic acid composition around 49-59 wt.% and 27-36 wt.% respectively [6]. These feedstocks are not in competition with the food sector, and using them for energy resource production can add value to palm products and contributes to the sustainable energy landscape in Thailand [6, 8]. Therefore, green diesel production from palm products appears to be a viable solution to the problem of insufficient fossil fuels. This research aims to compare the material balance and energy consumption associated with the use of different feedstocks (PFAD, RPS) and the effect of using recycle product as a solvent. The Aspen Plus v12 program is employed to simulate the green diesel production process.



Fig. 1 Reaction of green diesel production from triglyceride and fatty acid [4]

## 2. Method

The process for production of synthetic green diesel from palm oil by-products was focused on PFAD and RPS, while solvent was derived from the recycling of the product to assist in the reaction. This design process divides the operation into four case studies, which are BHD

production from PFAD (PH), from RPS (RH), from PFAD with solvent (PHS), and from RPS with solvent (RHS).

## 2.1. Operating condition and feedstock

The appropriate operating conditions for the hydro-processing reactor in the production of green diesel are determined based on research and academic articles. The specified operating conditions are presented in Table 1, while the components of the feedstock are from Thongkumkoon et al. [6] and Kantama [8]. The reaction performances were based on the reference cited in Table 1.

Table 1. Operating conditions for green diesel production processes.

Parameter	PH	RH	PHS	RHS
Temperature [°C]	370	370	375	375
Pressure [bar]	50	50	17	34
Feed to solvent ratio	-	-	1: 0.785	1:1
Reference	[6]	[6]	Experiments conducted by our research group	

## 2.2. Assumption and block flow diagram

The main scope of operations and assumptions are as follows: production capacity of 50 tons per day of feedstock, steady state operation, hydrogen feed at stoichiometric ratio, Redlich-Kwong-Soave (RK-SOAVE). A block flow diagram in this study can be presented in Figure 2, where recycle stream were used only when solvent was required in the reactor.

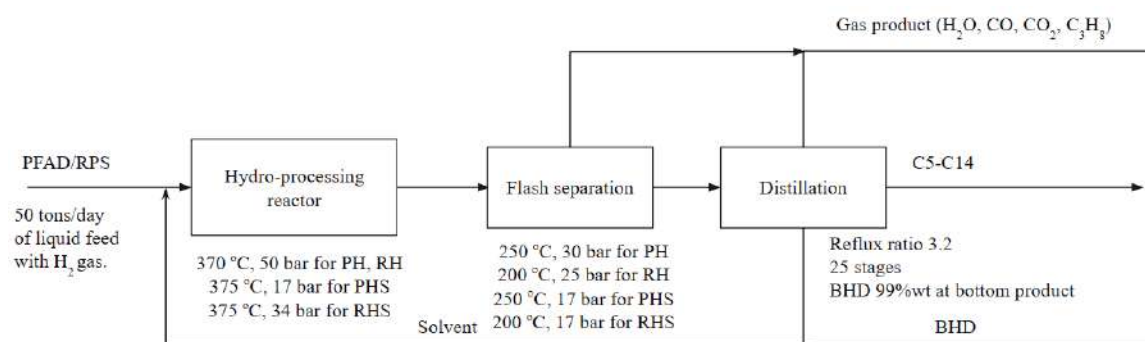


Fig.2 Block flow diagram of green diesel production from PFAD and RPS with solvent in this study.

## 3. Results and discussion

### 3.1. Model validation

The reactor model in this research was a balance-based model, RSTOIC, where fractional conversion of chemical reaction can be input as model specification. The resulting product distribution from the simulation model was compared to that from experimental results from

Thongkumkoon et al. [6] (PH and RH) and from our group (PHS and RHS) for validation by calculation the absolute fraction of variance ( $R^2$ ). It was found that the feedstocks, PFAD and RPS, have  $R^2$  values higher than 99% in all cases. The product distribution from experimental results is shown in Figure 3.

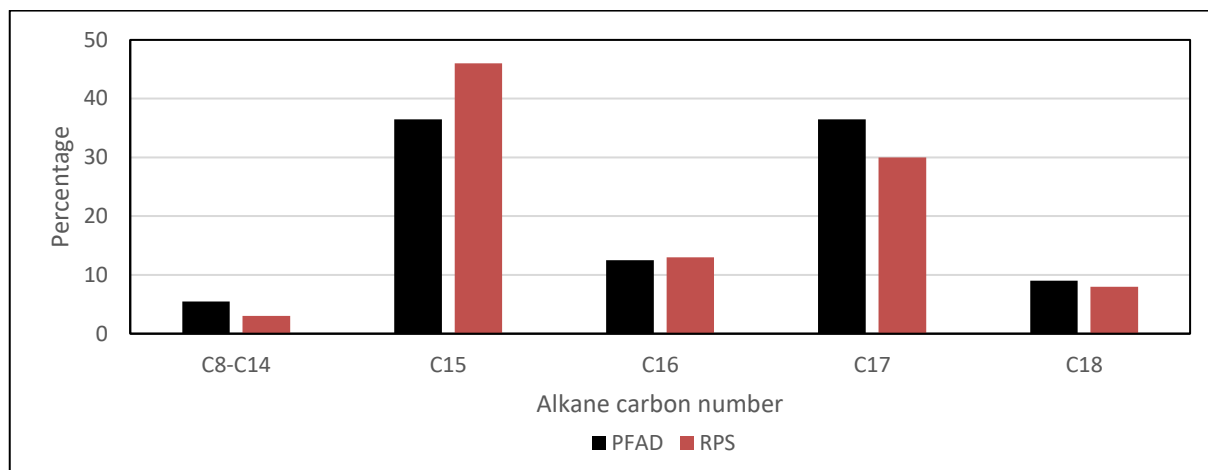


Fig. 3 The product distribution from green diesel production by PFAD and RPS [6]

### 3.2. BHD production rate

After creating a model of the green diesel production process, it was observed that when feeding the initial substances in each case study at a rate of 50 tons per day, the resulting amounts of green diesel in each case at 39.44, 38.53, 34.43, and 33.89 tons per day, respectively (as illustrated in Figure 4). The hydrogen requirement for stoichiometric of RPS is higher than that of PFAD due to hydrogenolysis from triglycerides to fatty acids [9]. The reduction in the green diesel quantity is attributed to the recycling of the product, which leads to increased cracking reactions due to high operating temperature leading to cracking of alkanes [10] and a higher demand for hydrogen gas in the chemical reaction. This, in turn, results in an increased production of by-products. The composition of green diesel primarily comprises alkanes with a carbon number of 15 and higher, constituting over 99% by mass.

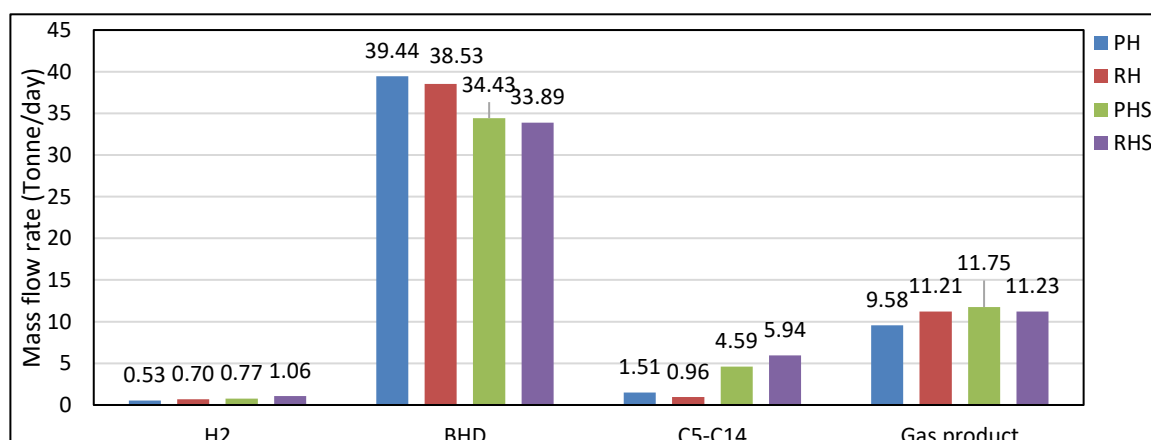


Fig.4 Mass flow rates from the four case studies.

### 3.3. Energy consumptions

Figure 5 reveals that, in the case of product recycling, the utilization of hot and cold utilities is notably higher than that of the case with no recycle, attributable to the increased flow of substances within the system. Specifically, the heating energy usage experiences a 39% increase for PFAD and 45% for RPS, while the cooling energy usage sees a surge of 32% for PFAD and 42% for RPS. On the other hand, in the PHS case, electricity consumption decreases. This is attributed to the recycle solvent, which reduces reacting pressure and feed density, resulting in lower energy consumption by the pump and compressor. When considering the effect of feedstock, using RPS requires higher energy than PFAD.

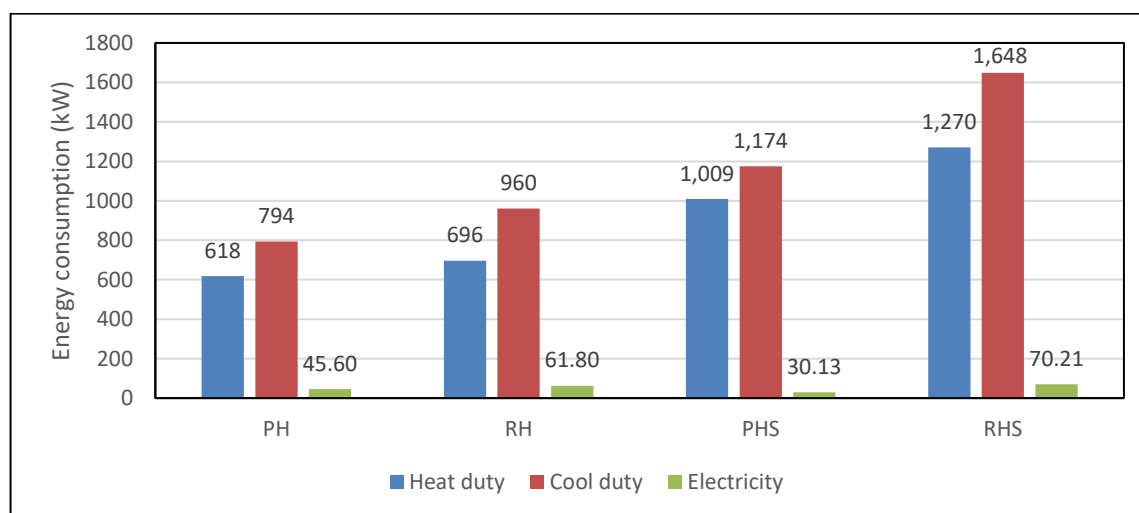


Fig. 5 Comparison of energy consumption

Table 3 illustrates that the primary energy consumer in the process is the heater, accounting for 73-78% of the heating duty. This high energy consumption is a consequence of the high-temperature production process. Implementing heat recovery measures can help mitigate this consumption. Additionally, the reactor necessitates cooling utility due to the exothermic nature of the green diesel production reaction, which could potentially serve as a heat source to reduce overall energy consumption.

Table 3 Total energy consumption in each unit.

Unit [kW]	PH	RH	PHS	RHS
Heater	483.87	505.38	754.13	729.43
Cooler	-556.00	-634.57	-118.10	-244.61
Reactor	-142.50	-236.70	-110.17	-368.59
Distillation				
- Reboiler	128.95	190.14	254.62	522.64
- Condenser	-95.78	-89.14	-191.77	-305.38

#### 4. Conclusion

The BHD production from hydro-processing process was simulated using ASPEN Plus and validated against experimental data obtained from the previous research. The findings indicated that recycling the product as a solvent resulted in a reduction in operating pressure but an increase in cracking reactions. This, in turn, led to a lower yield of green diesel and a higher formation of by-products. Moreover, the recycling of the product had a significant impact on the energy consumption of the process. Notably, heating and cooling duties increased due to the higher flow rate of substances within the system. It was observed that the efficiency and economics of the green diesel production process could be enhanced through heat recovery and the optimization of process parameters.

#### 5. Acknowledgement

The authors acknowledge the Office of National Higher Education Science Research and Innovation Policy Council – PMU C, PTT EXPLORATION AND PRODUCTION PUBLIC Co., Ltd., CHERDCHAI CORPORATION Co., Ltd., POLAWAT ENGINE Co., Ltd., and VERASUWAN Co, Ltd. (C10F640103) for funding support.

#### 6. References

- [1] Energy Policy and Planning Office (EPPO). (2021). Thailand Energy Situation in 2021. [Online URL: <https://www.eppo.go.th/index.php/>] accessed on December 24 2023
- [2] Cavuoto D., Zaccheria F., Ravasio N. (2020). Some Critical Insights into the Synthesis and Applications of Hydrophobic Solid Catalysts. *Catalysts*.; 10(11):1337. <https://doi.org/10.3390/catal10111337>
- [3] Kumar A., Anand R., (2019). Chapter 15 - Progress in biofuel generation and its application in fuel cell. in: A.K. Azad, M. Rasul (Eds.). *Advanced Biofuels*. Woodhead Publishing. pp. 371–403. Editors.
- [4] Sotelo-Boyas, R., Trejo-Zarraga, F., Jesus Hernandez-Loyo, F. de. (2012). Hydroconversion of Triglycerides into Green Liquid Fuels. *InTech*. doi: 10.5772/48710
- [5] Lucantonio S., Di Giuliano A., Rossi L., Gallucci K. (2023). Green Diesel Production via Deoxygenation Process: A Review. *Energies* 2023, 16, 844. <https://doi.org/10.3390/en16020844>
- [6] Skonrach T., Worapon K., Unalome W., Navadol L., Pornlada D. (2019). Catalytic activity of trimetallic sulfided Re-Ni-Mo/ $\gamma$ -Al<sub>2</sub>O<sub>3</sub> toward deoxygenation of palm feedstocks, *Renewable Energy*, Volume 140, Pages 111-123, ISSN 0960-1481, <https://doi.org/10.1016/j.renene.2019.03.039>.
- [7] The Bangkok Insight. (2019). [Online URL: <https://www.thebangkokinsight.com/179454/>] accessed at December 6 2023
- [8] Angsana K. (2014). Study of Bio-hydrogenated Diesel Production from Palm Fatty Acid Distillate and Biodiesel. King Mongkut's University of Technology North Bangkok.



- [9] Nitchakul H., Paweena P., Chaiwat P. (2022). Review of green diesel production from fatty acid deoxygenation over Ni-based catalysts. *Molecular Catalysis*. Volume 523. 111696. ISSN 2468-8231. <https://doi.org/10.1016/j.mcat.2021.111696>.
- [10] N. Asikin-Mijan, H.V. Lee, G. Abdulkareem-Alsultan, A. Afandi, Y.H. Taufiq-Yap. 2017. Production of green diesel via cleaner catalytic deoxygenation of *Jatropha curcas* oil. *Journal of Cleaner Production*. Volume 167. Pages 1048-1059. ISSN 0959-6526. <https://doi.org/10.1016/j.jclepro.2016.10.023>.



## **DETECTION AND REPLACEMENT OF STATES WITH SPIKES AND NOISE BY LONG SHORT-TERM MEMORY MODELS OR NEURAL NETWORKS**

**IttikornYutto<sup>1</sup>, Paisan Kittisupakorn<sup>2</sup>**

Control and Systems Engineering Research Center, Department of Chemical Engineering,  
Faculty of Engineering, Chulalongkorn University, Bangkok 10330, Thailand  
E-mail: ittikorn2095@gmail.com, PAISAN.K@CHULA.AC.TH

### **Abstract**

Spike signals are often discussed in the context of neuroscience, but it's found that they are also encountered in control systems. Both fields share a similarity in that spike signals have a common characteristic of immediate and temporary changes in signal amplitude. The difference lies in the source of the spike signals and the purpose of detection. In control systems, the sources of spike signals can be varied, such as signal interference, environmental factors like temperature changes or vibrations, sensor defects or damage like sensor degradation or calibration issues, etc. The purpose of detecting spike signals in control systems is to find and eliminate them, as spike signals can have several detrimental effects on the control system. For example, they can introduce incorrect data into control circuits, result in inaccurate measurements and feedback, leading to inappropriate control outcomes or overreactions that cause the system to become unbalanced and less efficient. This work presents a new method using LSTM or Neural Network (NN) models for detecting spikes and noise signals, and for replacing these signals in second-order systems.

**Keywords:** Long Short-Term Memory (LSTM), second-order systems, spike signals

### **1. Introduction**

Spike signals are often discussed predominantly in neuroscience literature. However, it is found that spike signals are also encountered in the field of control systems. When discussing the similarities and differences of spike signals in each domain, the similarity lies in the fact that spike signals exhibit immediate and temporary changes in the amplitude of the signal. The difference lies in the origin of the spike signal and the objective of the detection.

In the field of neuroscience, the source of spike signals by (Lewicki, 1998) can be identified as the result of neural cells communicating with each other in the nervous system. The objective of spike detection is to gain a fundamental understanding of neural activity that occurs in the nervous system. Spike detection allows researchers to detect and analyze electrical signals or spikes originating from individual neural cells. By studying these spikes, researchers can gain insights into the functioning of neural networks, information processing within the nervous system, and internal communication within the brain. Spike detection is crucial for tasks such as neural mapping, studying neural encoding mechanisms, and investigating the effects of various stimuli on neural activity. The algorithms used for spike detection in different fields are often categorized or classified based on their characteristics. by (Brendel et al., 2020; Nenadic & Burdick, 2005; Xia & Ni, 2018; Zhang et al., 2022)

In the field of control systems, spike signals can have multiple causes. These include electromagnetic interference (EMI), environmental factors such as temperature changes or vibrations, sensor defects or damage, and calibration issues. The objective of spike signal detection in control systems is to detect and eliminate them from the signal because spike signals can have various detrimental effects on control systems. For example, they can introduce incorrect data into the control circuit, leading to inaccurate measurements and feedback. This can result in inappropriate control responses, system imbalance, and reduced efficiency. Spike signals can also lead to errors in estimating system parameters. Additionally, they can trigger false alarms or unnecessary corrective actions, increasing operational and maintenance costs, affecting the quality, accuracy, and efficiency of control. The algorithms used for spike signal detection in this field are aimed at detecting and removing or reducing spike signals to minimize their undesired impact on control systems.

In the field of research, various algorithms have been developed for spike signal detection, including the "depiking" algorithm by (Feuerstein, Parker, & Boutelle, 2009). This algorithm consists of two steps: spike position identification and time interval segmentation. The identified spikes are then replaced with new values using a quadratic SG filter. The main characteristic of the "depiking" algorithm is the detection of spike signals and the prediction of their values to replace the designated spike regions. Additionally, Kalman filtering is employed by (Park et al., 2019), which involves predicting the current state based on the estimated state from the previous time step. The predicted value is then combined with the sensor measurements using a Kalman gain to determine the estimated state at the current time. However, both Kalman filtering and quadratic SG filter have their limitations. In the case of quadratic SG filtering, it is a filtering technique that considers data within a specified window. It also relies on linear modeling, which may limit its ability to capture complex relationships or non-linear behaviors in the data. On the other hand, Kalman filtering poses challenges in model identification and tuning, and its equations assume a Gaussian distribution of noise. If the system exhibits non-linear behavior or the noise does not follow a Gaussian distribution, it may degrade the filtering performance of Kalman filtering.

This work presents a novel approach utilizing LSTM or Neural Network (NN) models for spike and noise detection, as well as the capability to replace signals that are free from spikes and noise in a second or third-order system.

## 2. Materials And Methods

### 2.1. Data

#### 2.1.1. Actual signals of the system

The data used is simulated from two first-order equations for calculating the energy balance of hot and cold fluids in a heat exchange. It describes the temperature change in the system over time. For the hot fluid or hot stream, the rate of temperature change depends on the sum of the impact of heat loss to the cold fluid and the impact of the inflow of the hot fluid. For the cold fluid or cold stream, the rate of temperature change depends on the sum of the impact of heat

gain from the hot fluid and the impact of the inflow of the cold fluid. The temperature data for both the hot and cold streams were simulated with 15,000 samples each, as shown in Fig. 1.

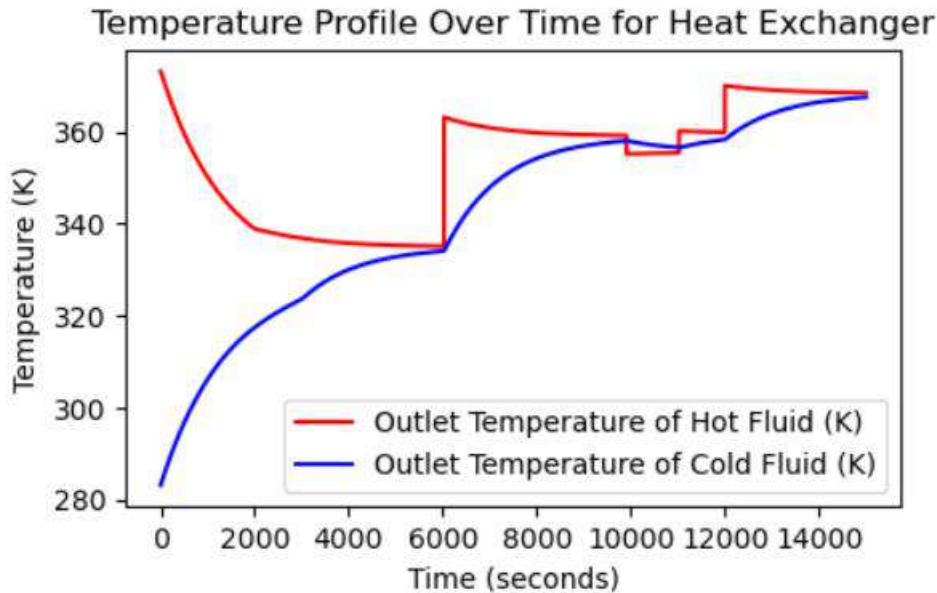


Fig. 1 Actual signals of the system.

### 2.1.2. Spike signals

In the context of control systems, the characteristics of spike signals are scrutinized for their transient, sharp nature, which significantly differentiates them from standard operational signals. These spikes, marked by a sudden increase in signal amplitude followed by a rapid decrease, are often the result of external disturbances such as electromagnetic interference, sensor defects, or environmental changes. The precise identification and subsequent analysis of these spikes are critical for maintaining system integrity and performance.

In the simulation of spike signals, it involves randomization both in the location of the spike occurrence and in the size of the spike signal. The number of spikes depends on the amount of real signal data of the system, and the size is randomly within a specified range of signal sizes.

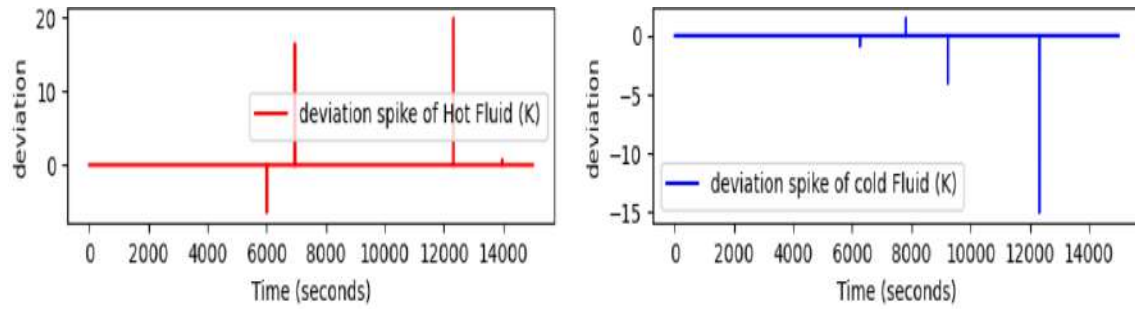


Fig. 2 Position and magnitude of spike signals.

## 2.2. LSTM model

### 2.2.1. Structure and Equation of LSTM model

From the figure 3, it shows the computational structure of an LSTM layer with three inputs: the current time input data ( $x_t$ ), the previous time step's cell state ( $c_{t-1}$ ), and the previous time step's hidden state ( $h_{t-1}$ ). Within the LSTM, there are six equations being calculated: the forget gate ( $f_t$ ), the input gate ( $i_t$ ), the output gate ( $o_t$ ), the temporary cell state ( $\bar{c}_t$ ), the current cell state ( $C_t$ ), and the current hidden state ( $h_t$ ), as described by the equations for 1,2,3,4,5 and 6 respectively. The output consists of both the current cell state ( $C_t$ ) and the current hidden state ( $h_t$ ), which are then passed on to the fully connected layer (both the LSTM and the fully connected layer are part of the same layer called the hidden layer). The output from the fully connected layer is further processed in the output layer. It undergoes multiplication with weights and biases and passes through an activation function in that layer. The resulting output is then subjected to linear transformation to become the predicted output or the desired value we aim to predict.

$$f_t = \sigma(W_f x_t + U_f h_{t-1} + b_f) \quad (\text{forget gate}) \quad (1)$$

$$i_t = \sigma(W_i x_t + U_i h_{t-1} + b_i) \quad (\text{input gate}) \quad (2)$$

$$o_t = \sigma(W_o x_t + U_o h_{t-1} + b_o) \quad (\text{output gate}) \quad (3)$$

$$\bar{C}_t = \tanh(W_c x_t + U_c h_{t-1} + b_c) \quad (\text{temporary cell state}) \quad (4)$$

$$C_t = f_t * C_{t-1} + i_t * \bar{C}_t \quad (\text{current cell state}) \quad (5)$$

$$h_t = o_t * \tanh(C_t) \quad (\text{current hidden state}) \quad (6)$$

$W$  denotes the weights for inputs,  $U$  represents the weights for recurrent connections, and  $b$  is the bias component. The symbols  $f$ ,  $i$ , and  $o$  are used to identify the forget gate, input gate, and output gate, respectively. The sigmoid function, denoted by  $\sigma$ , acts as the activation function for these gates, limiting values within the range of 0 to 1. Similarly, the hyperbolic tangent function, or  $\tanh$ , serves as another activation mechanism, compressing values to fall between -1 and 1. Both activation functions play a crucial role in enhancing the network's non-linearity, as described by the equations for 7 and 8 respectively.

$$\sigma(x) = \frac{1}{1+e^{-x}} \quad (\text{sigmoid function}) \quad (7)$$

$$\tanh(x) = \frac{e^x - e^{-x}}{e^x + e^{-x}} \quad (\text{hyperbolic tangent function}) \quad (8)$$

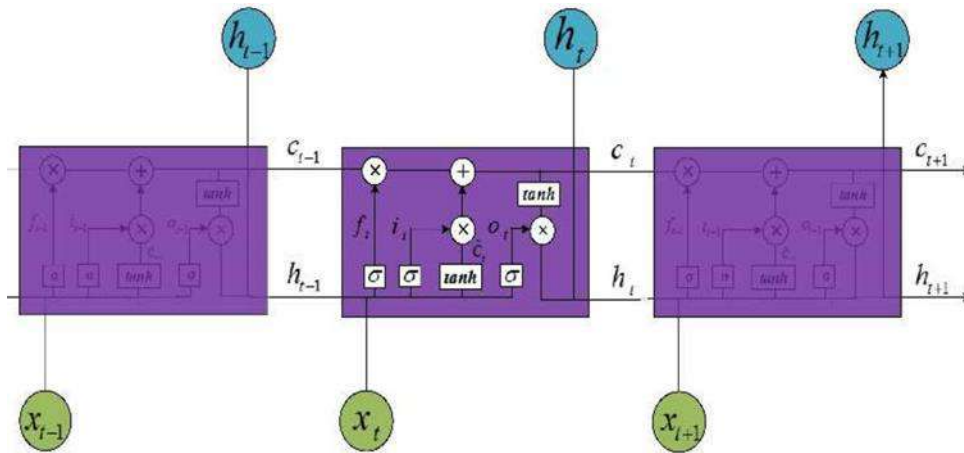


Fig. 3 The typical structure of LSTM (Song et al., 2020)

### 2.2.2. Data Preprocessing

The dataset used to train and test the model comprises a combination of real system signal data and spike signal data. This dataset is divided into 70% for training data and 30% for testing data. Both the training and testing data sets must undergo normalization using a min-max scaler, fitted with the minimum and maximum values from the training data. Subsequently, the training and testing data sets are used to define features and labels before being utilized for further model training, as depicted in Fig. 4.

The benefit of normalizing the dataset before training with an LSTM model is a crucial step that helps the training process proceed efficiently and yields better results. The main benefits of normalization are as follows: scaling the data appropriately and bringing various values into a similar range helps mitigate the issue of uneven data distribution. This, in turn, can reduce training difficulties and time. Additionally, normalization ensures that the model's weight updates occur at a consistent rate, reducing the likelihood of problems such as gradient vanishing or exploding gradients. These are common issues in models using Recurrent Neural Network (RNNs) and LSTMs due to their sensitivity to data variations. Normalization enables LSTMs to learn and memorize data more effectively without encountering these problems. Ultimately, this leads to the development of more accurate and efficient predictive models.

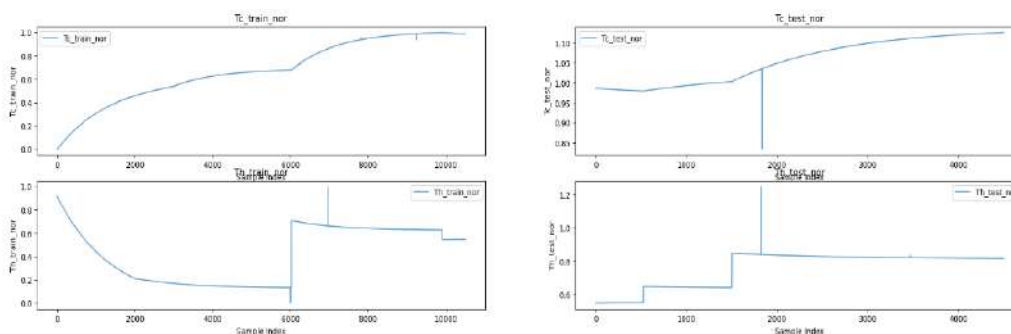


Fig. 4 Normalization of train data and test data.

### 2.2.3. Model Design and Selection

The criteria for selecting LSTM models are based on the characteristics of the time series data, which have complex sequential relationships, and the task's objective to detect and replace states with spikes and noise. LSTMs surpass in managing long-term dependencies within time series data, unlike traditional Recurrent Neural Network (RNNs) that encounter the vanishing gradient problem, leading to substantial challenges in learning long-term patterns. LSTMs are designed with specific gate mechanisms that can retain crucial information for extended periods, which are the true states of the system, and discard irrelevant data, which are characteristics of spike signals. This ensures a robust capability for memory and prediction. This makes LSTMs excel in modeling complex sequential relationships and trends, which other models might not capture accurately or might lose predictive efficiency over time. Furthermore, LSTMs' ability to mitigate overfitting and underfitting through their complex architecture makes them a more reliable choice for analyzing time series datasets, particularly in scenarios where accuracy and the capability to predict future states from historical data are essential. This advantage emphasizes the rationale for choosing LSTMs for time series prediction tasks, highlighting their increased efficiency and effectiveness in handling the complexity of sequential data compared to similar models. The selected structure of the LSTM model includes three layers in the hidden layer: 1. LSTM layer, 2. LSTM layer, 3. Dense fully connected layer, in that order.

Hyperparameters adjusted to improve LSTM model prediction include units, dropout rate, learning rate, batch size, and epochs. Increasing units enhances the model's ability to learn complex data patterns but may cause overfitting and longer training times. Conversely, reducing units may oversimplify the model, hindering its capacity to capture unique data features. Adjusting the dropout rate helps prevent overfitting by randomly dropping neurons, with increased rates reducing inter-neuron dependencies but risking underfitting. Conversely, decreasing the dropout rate may enable deeper learning but increases the risk of overfitting. Modifying the learning rate affects the speed of weight adjustments during training; higher rates accelerate training but may destabilize the model, while lower rates slow training but offer better stability. Batch size, the data size used in each training step, impacts the precision and efficiency of model updates, with larger sizes reducing fluctuations but potentially slowing training, and smaller sizes speeding up updates but increasing fluctuations. Finally, epochs, the total training rounds, influence the model's learning and performance, with more epochs

enhancing learning but risking overfitting, and fewer epochs reducing training time but potentially limiting learning.

#### 2.2.4. Evaluation Metrics

Mean Absolute Error (MAE) is a metric used to measure the error of a continuous value prediction model, particularly emphasizing severe errors or abnormal data. It calculates the average error without squaring the errors, preventing excessive weighting of large errors. Additionally, MAE provides straightforward insights into the model's quality, making it useful for analyzing and comparing prediction accuracy in complex and fluctuating scenarios.

#### 2.2.5. Implementation Details

Working in Jupyter Notebook on Anaconda Navigator, operating on a machine equipped with an AMD Ryzen 9 4900H CPU, and using Python along with TensorFlow for deep learning model development.

### 3. Results And Discussions

This research aimed to develop algorithms capable of detecting and replacing states with spikes and noise in second or third-order systems using LSTM or Neural Network (NN) models. The LSTM model was configured with specific hyperparameters including 20 units, a dropout rate of 0.1 to prevent overfitting, and a conservative learning rate of 0.00001 to allow for gradual convergence. The model was trained over 30 epochs with a batch size of 20, a size determined to balance between computational efficiency and the need for accurate.

The training results indicate a consistent decrease in loss and mean absolute error, which suggests that the model was learning effectively over time. The final epochs displayed a loss of 0.0328, with the last epoch significantly faster due to the completion of the training loop. This steady decline in error metrics illustrates the model's capacity to adapt to the data's patterns while also inferring the underlying system dynamics.

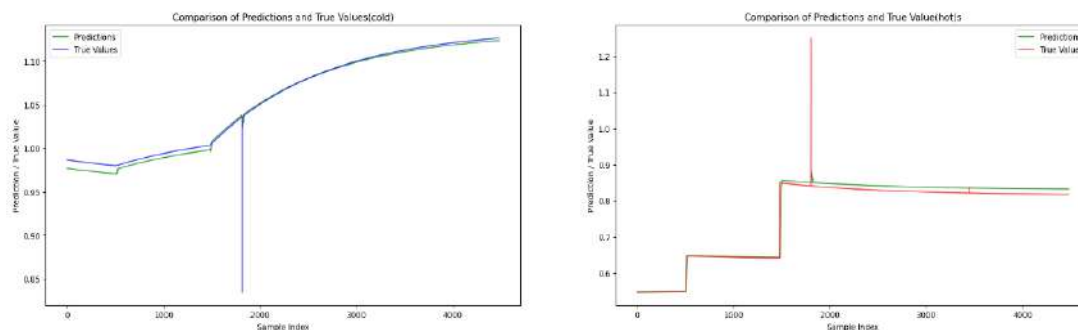


Fig. 5 The results of the prediction are compared with the actual values of the system.

From the figure 5, LSTM model are presented in two separate plots, comparing the predictions made by the LSTM model against the actual system values. The first plot illustrates the model's performance on data without the presence of spikes (cold data), indicating a close match between the predicted and true values. This demonstrates the model's capability to accurately replicate the normal behavior of the system.

These findings underscore the LSTM model's potential in enhancing the reliability of control systems by providing a mechanism to detect anomalies and replace them with predicted states that are free from spikes and noise. However, the research also acknowledges the model's limitations, particularly when facing highly erratic or non-linear noise distributions. Future work may explore the integration of more complex or hybrid models to further improve the accuracy and reliability of spike and noise detection in dynamic systems.

This research contributes to the field by offering a novel approach to managing spikes and noise, which are pervasive issues in control systems. By employing LSTM models, we have demonstrated that it is possible to not only detect these anomalies but also to predict and replace them with high fidelity, thereby ensuring the integrity and performance of the controlled system. The results encourage continued exploration into advanced neural network architectures for even more resilient and adaptive control system applications.

#### 4. Conclusion

This study aimed to develop LSTM algorithms for detecting and replacing noisy spikes in control systems. Our LSTM model, with carefully tuned hyperparameters, showed a promising decrease in loss and MAE during training, indicating a strong learning capacity.

The findings affirm the LSTM's potential in stable environments but also highlight the need for further refinement for complex conditions. Future efforts should focus on enhancing the model's robustness against extreme variations. In essence, this research marks a step forward in the application of LSTM models for improving control system reliability.



## References

Article in a journal

- [1] Brendel, W., Bourdoukan, R., Vertech, P., Machens, C. K., & Denève, S. (2020). Learning to represent signals spike by spike. *PLoS Comput Biol*, 16(3), e1007692. <https://doi.org/10.1371/journal.pcbi.1007692>
- [2] Feuerstein, D., Parker, K. H., & Boutelle, M. G. (2009). Practical methods for noise removal: applications to spikes, nonstationary quasi-periodic noise, and baseline drift. *Anal Chem*, 81(12), 4987-4994. <https://doi.org/10.1021/ac900161x>
- [3] Lewicki, M. S. (1998). A review of methods for spike sorting: the detection and classification of neural action potentials. *Network*, 9(4), R53-78.
- [4] Nenadic, Z., & Burdick, J. W. (2005). Spike detection using the continuous wavelet transform. *IEEE Trans Biomed Eng*, 52(1), 74-87. <https://doi.org/10.1109/tbme.2004.839800>
- [5] Park, S., Gil, M. S., Im, H., & Moon, Y. S. (2019). Measurement Noise Recommendation for Efficient Kalman Filtering over a Large Amount of Sensor Data. *Sensors (Basel)*, 19(5). <https://doi.org/10.3390/s19051168>
- [6] Song, X., Liu, Y., Xue, L., Wang, J., Zhang, J., Wang, J., Jiang, L., & Cheng, Z. (2020). Time-series well performance prediction based on Long Short-Term Memory (LSTM) neural network model. *Journal of Petroleum Science and Engineering*, 186, 106682. <https://doi.org/10.1016/j.petrol.2019.106682>
- [7] Xia, Y.-X., & Ni, Y.-Q. (2018). A wavelet-based despiking algorithm for large data of structural health monitoring. *International Journal of Distributed Sensor Networks*, 14(12), 1550147718819095. <https://doi.org/10.1177/1550147718819095>
- [8] Zhang, Y., Han, J., Liu, T., Yang, Z., Chen, W., & Zhang, S. (2022). A robust spike sorting method based on the joint optimization of linear discrimination analysis and density peaks. *Sci Rep*, 12(1), 15504. <https://doi.org/10.1038/s41598-022-19771-8>

## **Economic Evaluation of Intensified Furfural Production Process with Reactive-azeotropic Dividing Wall Column Using Aspen Plus Program**

**Ratchaphon Chaloeamkamsit, Malinee Rupsom, Manisawa Sungkaew,  
Patcharapuek Pattaramanon, and Choowong Chaisuk\***

Department of Chemical Engineering, Faculty of Engineering and Industrial Technology, Silpakorn University,  
Nakhon Pathom, 73000, Thailand  
E-mail: \*CHAIKUK\_C@su.ac.th

### **Abstract**

The conventional process to produce the furfural from bagasse was modified in this work. The sections of reaction and separation were combined to reduce the fixed capital cost and the energy consumption. The separation process with three simple distillation columns to purify the furfural proposed by Silva et al. was referred for the synthesis of the prototype process. Some process parameters such as number of stages, reflux ratio, and steam flow rate were varied by sensitivity analysis of Aspen Plus program. The furfural product with 99 wt% purity was obtained by the prototype process. The process intensification via reactive distillation (RD) and reactive-azeotropic dividing wall column (RDWC) was investigated. After tuning the suitable parameters, both modified processes can maintain a 99 wt% purity of the furfural with high product recovery and decrease about 86% of the usage of cold utility. Economic indicators including total capital cost (TCC), total operating cost (TOC), net present value (NPV), internal rate of return (IRR), and discounted payback period (DPP) were evaluated. The TCC savings of the RD and RDWC processes were 37.4 and 68.6%, respectively. However, both modified processes showed about 26% increase of the TOC. The NPV, IRR and DPP showed positive results after modification and therefore an investment to modify the furfural production process was promising.

**Keywords:** Furfural production process; Reactive-azeotropic dividing wall column; Economic evaluation; Aspen Plus program.

### **1. Introduction**

Furfural is generally produced by the dehydration of five-carbon sugar derived from lignocellulosic biomass such as xylose and arabinose [1]. It can be utilized in a wide range of industries such as pharmaceuticals, plastics, pesticides, oil refining [2-4]. The conventional process of furfural production commonly consists of four major steps: hydrolysis of hemicellulose into xylose, dehydration of xylose into furfural, furfural recovery, and purification in sequential order [5]. This process shows high energy consumption and high amount of steam utility. In addition, the furfural and water form an azeotrope, which necessitates complex separation via many unit operations [6]. One of alternative ways to improve the process is an intensification that is a process design leading to smaller, cleaner, safer, and more energy-efficient process technology such as reactive distillation and dividing wall distillation columns [7]. In this work, two interesting intensified configurations consisting of a reactive distillation (RD) and a reactive-azeotropic dividing wall column (RDWC) were investigated to compare with the conventional process. All processes were simulated using Aspen Plus program. The economic indicators and the energy consumption were basically evaluated.

## 2. Materials and Methods

In this work, all of process flowsheets were simulated using Aspen Plus Program V8.8. The conventional process consisted of two sections including the reaction and separation sections. In the reaction section, the CSTR model was simulated using the kinetic expression referred by the work of Chen et al. [8]. In the separation section, three distillation columns with the RadFrac model were simulated using thermodynamic model of NRTL to predict immiscible liquid phases. This conventional separation flowsheet was obtained from Silva et al. [9]. Both sections were initially verified and some parameters were adjusted to improve the performance of the process. This was so-called the prototype process. After improvement, the process was modified by two intensified configurations, a reactive distillation (RD) and a reactive-azeotropic dividing wall column (RDWC). After modification, the economic indicators including total capital cost (TCC), total operating cost (TOC), net present value (NPV), internal rate of return (IRR), and discount payback period (DPP) were evaluated.

## 3. Results and Discussion

The process flowsheets of both reaction and separation sections were simulated and verified. For the reaction section, the decomposition of xylose to furfural and water was occurred. The homogeneous catalyst for this reaction was the acetic acid. The reaction rate was shown as follows:

$$(-r_{xylose}) = \left[ 6.216 \times 10^8 \exp\left(-\frac{108.6}{T}\right) \right] C_{xylose}$$

the xylose conversion obtained by our simulation results was slightly different from the experimental data reported by Chen et al. [8]. An error was about 6%. Figure 1 shows the flowsheet of the conventional separation process consisting of three distillation column and a decanter. The concept of this system was similar to heterogeneous azeotropic distillation process. The simulated feed components consisted of furfural, acetic acid, formic acid, methanol and water. The steam was injected to the C-101 column in order to reduce the energy consumption. The methanol was separated by the C-102 column and the furfural product was purified by the C-103 column. The remaining chemicals was removed as the waste water at the bottom of the C-101 column. Our simulation results were rather similar to the data reported by Silva et al. [9]. The purity of the furfural product was approximately 98.5 wt%.

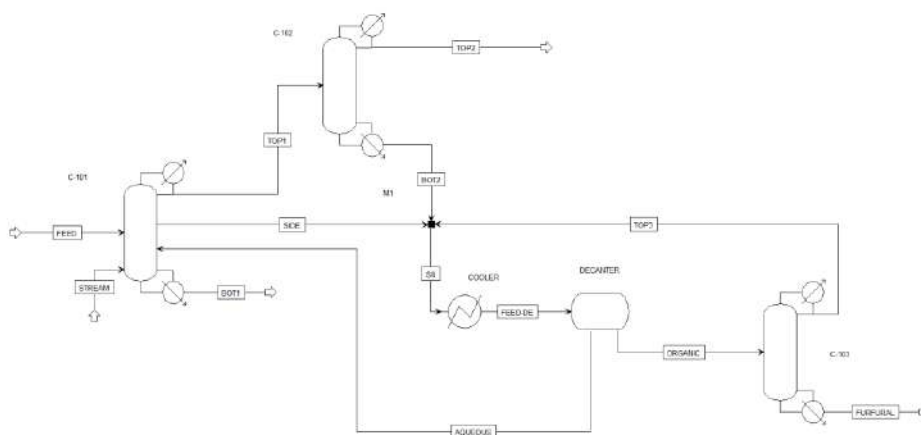


Fig. 1 The flowsheet of the conventional separation process.

After verification of both sections, the data of the feed stream was changed. Two feed streams were sugarcane bagasse hydrolysate and purified acetic acid. The 10000 kg/h of sugarcane bagasse hydrolysate consisted of 2.1 wt% xylose, 97.4 wt% water, 0.4 wt% acetic acid and 0.1 wt% furfural. The mass ratio of the sugarcane bagasse hydrolysate stream and the purified acetic acid stream was about 47. The acetic acid was added to be both homogenous catalyst and entrainer. The residual curve map of furfural, water and acetic acid is shown in Fig. 2. Based on the NRTL model, the azeotrope of mixture of furfural and water was about 35 wt% of furfural. An immiscible area in the residual curve indicated the possibility to overcome the limitation of a simple distillation by the concept of heterogeneous azeotropic distillation process.

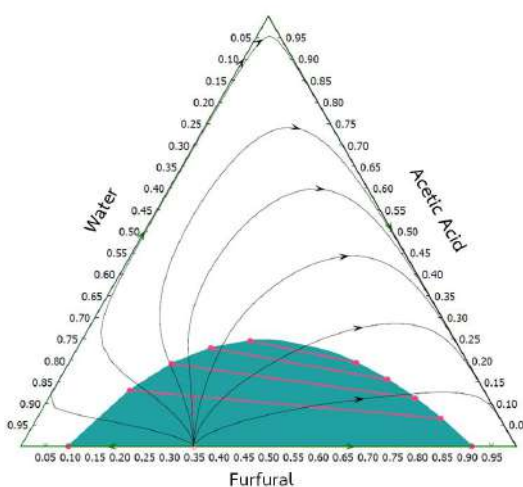


Fig. 2 The residual curve map of the system of furfural, water and acetic acid.

The reaction and separation sections were connected and simulated by the above feed stream. Because of the different feed components, it was found that after simulation the furfural was lost to the top of the C-102 column. Hence, the conventional separation process was adjusted by removing the C-102 column out of the process flowsheet. To achieve high purity of the furfural product, some parameters were adjusted to improve the performance of the process. The adjusted process flowsheet was so-called the prototype process as shown in Fig. 3. The production rate in this process was 108.8 kg/h with 99 wt% purity of the furfural.

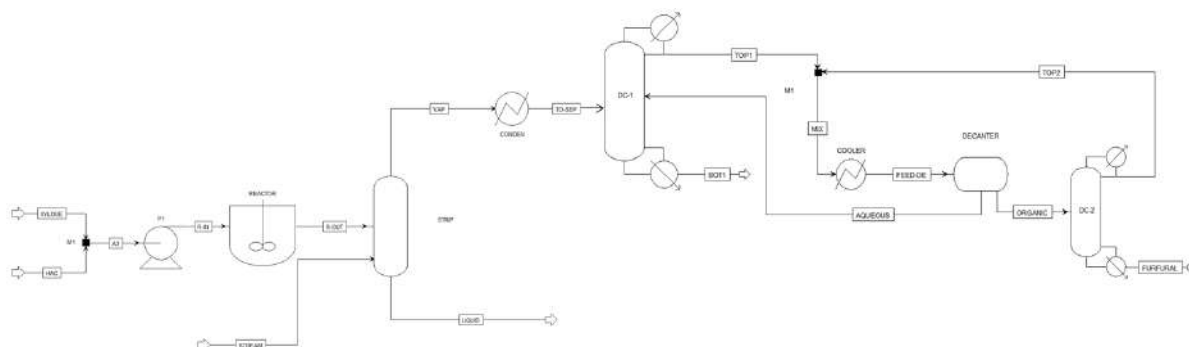


Fig. 3 The flowsheet of the prototype process with both reaction and separation sections.

The RD process to combine the reaction and separation sections is shown in Fig. 4. Sugarcane bagasse hydrolysate and acetic acid were fed into RD column for simultaneous reaction and separation. A mixture of the furfural and the water was recovered at the top of the RD column. The decanter and the DC column were used to purify the furfural product. The RDWC process was operated by a single column with an inside partition wall [10] as shown in Fig. 5. This column was divided into three sections consisting of reaction section (C1), rectifying section (C2) and purification section (C3). By simulating the process flowsheet of the RDWC process, the dividing wall column was represented by the three columns of the RadFrac model. The height of the wall was determined to balance the number of stages of two sides in the single column. Some parameters of the dividing wall column were adjusted to control a suitable composition of a stream entering the decanter.

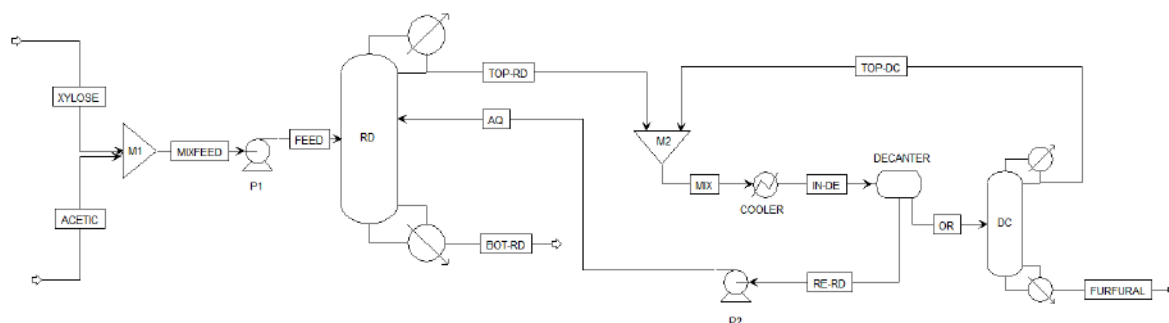


Fig. 4 The flowsheet of the reactive distillation (RD) process.

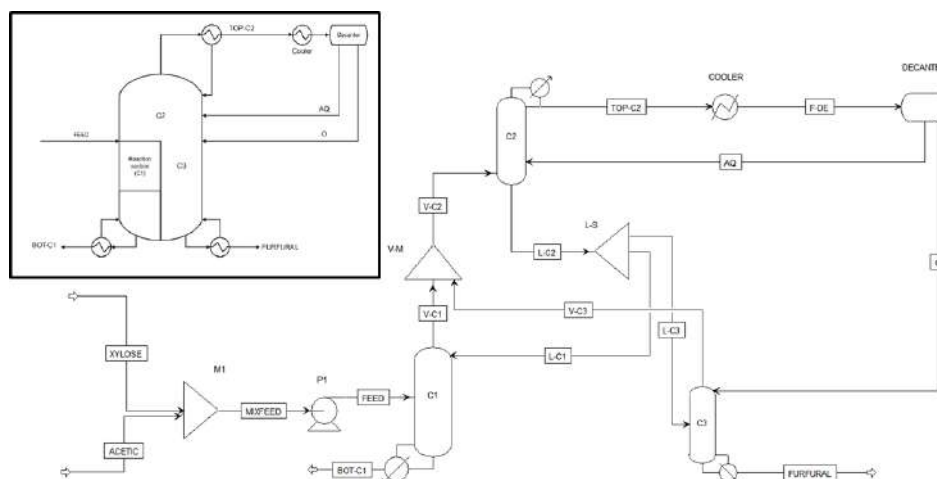


Fig. 5 The flowsheet of the reactive-azeotropic dividing wall column (RDWC) process.

After simulation of both intensified processes, the sensitivity analysis to study the effect of some parameters on the process performance was also made. The simulation results of both intensified processes after the sensitivity analysis were compared to those of the prototype process as shown in table 1. Considering the energy consumption including heat duties of condenser and reboiler, both intensified processes can reduce both hot and cold utilities as shown in Fig. 6, especially a decrease about 86% of the usage of cold utility. All of the cold

utilities were only the cooling water. The hot utilities were low-pressure and medium-pressure steam in the prototype process, were medium-pressure and high-pressure steam in the RD process and high-pressure steam and hot oil in the RDWC process. The different cost of each utility was already used for economic evaluation.

Table 1. The simulation results of the prototype, RD and RDWC processes.

Simulation results	Prototype	RD	RDWC
Xylose conversion (%)	69.8	85.8	85.8
Production rate (kg/h)	108.8	126.0	126.0
Furfural purity (wt%)	99.0	99.0	99.0
Furfural recovery (wt%)	99.5	99.5	99.5

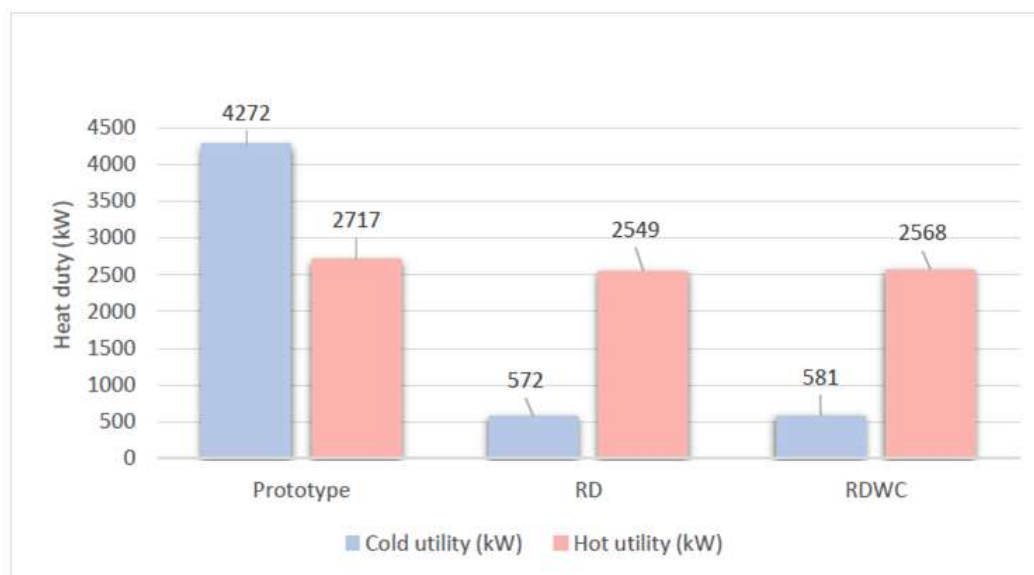


Fig. 6 The energy consumption in the prototype, RD and RDWC processes.

Figure 7 shows the total capital cost (TCC) and the total operating cost (TOC) of three processes. The sources of equipment cost data for evaluating the TCC were obtained by Aspen Process Economic Analyzer V9.0. The operating hour per year was 8760 h/y. The investment for the RDWC process was cheaper than that for the prototype and RD processes. This implied that the purchase cost of the single dividing wall column was lower than that of two columns. However, the disadvantage of both intensified processes was more expensive operating cost than the prototype process. This was due to complex operation in the special columns. The economic indicators including net present value (NPV), internal rate of return (IRR), and discounted payback period (DPP), was evaluated as shown in Figs 8 and 9. The discount rate of return was assumed to be 10% for calculating the DPP and NPV. The project life time was fixed as 20 years for calculating the IRR. It indicated that it was totally worth to invest the RDWC process. This process showed a positive NPV and the payback of investment in a short time. Also, the IRR was rather high.

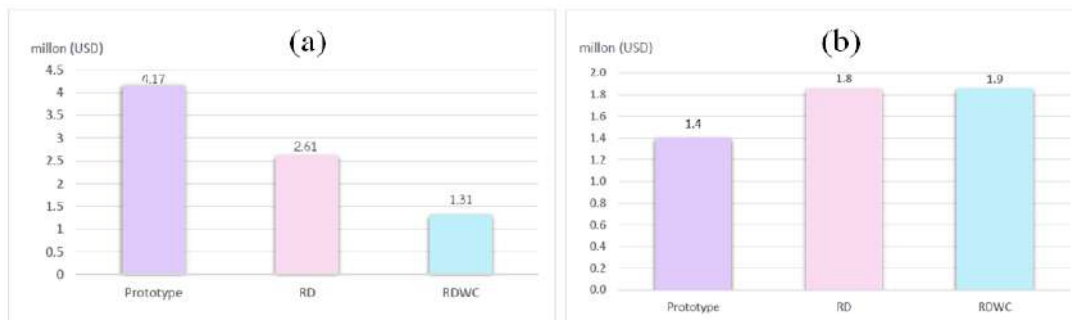


Fig. 7 (a) The total capital cost and (b) The total operating cost for three processes.

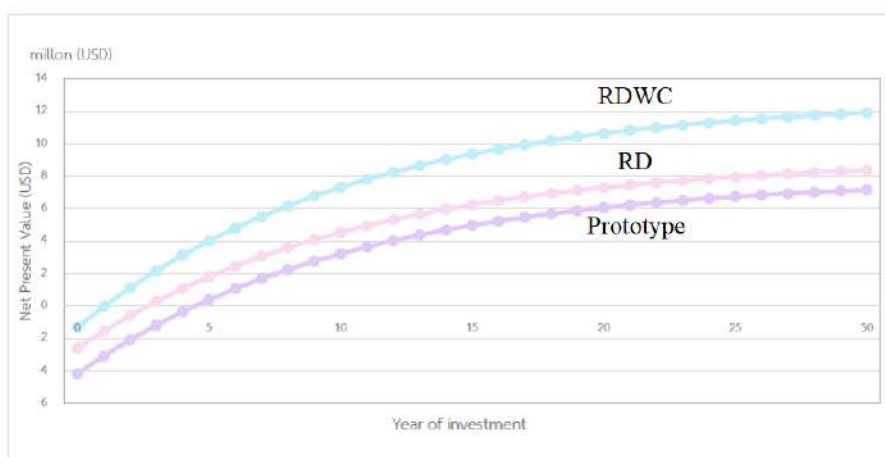


Fig. 8 The net present value for three processes.

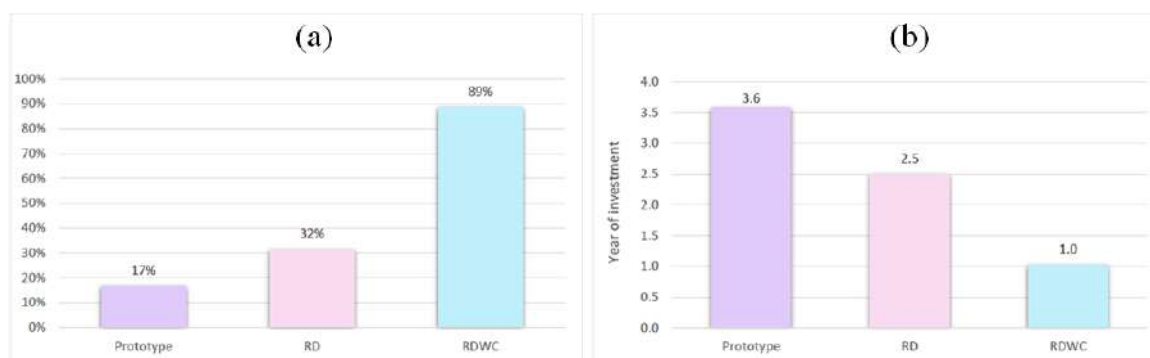


Fig. 9 (a) The internal rate of return and (b) The discount payback period for three processes.

#### 4. Conclusion

The modification of the furfural production process was focused in this work. Two intensified process including reactive distillation (RD) and reactive-azeotropic dividing wall column (RDWC). Both processes were compared to the prototype process, which was developed from the conventional process consisting of reaction and separation sections proposed by Chen et al. [8] and Silva et al. [9]. After simulation and sensitivity analysis, all processes can produce the furfural product with a 99.0 wt% furfural purity. Although all

processes showed the same furfural recovery (99.5 wt%), the production rate of both intensified processes was significantly higher than that of the prototype process. This affected directly the profit. The economic considerations including net present value (NPV), internal rate of return (IRR), and discount payback period (DPP) indicated a worth to invest the intensified process, especially the RDWC process. However, a high operating cost involving the complex operation of a single column with an inside partition wall to support a simultaneous reaction and separation was concerned.

### Acknowledgements

This work was financially supported by Department of Chemical Engineering, Faculty of Engineering and Industrial Technology, Silpakorn University.

### References

- [1] Yan, K., Wu, G., Lafleur, T., and Jarvis, C. (2014). Production, properties and catalytic hydrogenation of furfural to fuel additives and value-added chemicals. *Renewable and Sustainable Energy Reviews*, 38, 663-676.
- [2] Zhang, L., Xi, G., Yu, K., Yu, H., and Wang, X. (2017). Furfural production from biomass-derived carbohydrates and lignocellulosic residues via heterogeneous acid catalysts. *Industrial Crops and Products*, 98, 68-75.
- [3] Dashtban, M., Gilbert, A., and Fatehi, P. (2012). Production of furfural: Overview and challenges. *Journal of Science & Technology for Forest Products and Processes*, 2(4), 44-53.
- [4] Machado, G., Leon, S., Santos, F., Lourega, R., Dullius, J., Mollmann, M.E., and Eichler, P. (2016). Literature Review on Furfural Production from Lignocellulosic Biomass. *Natural Resources*, 7(3), 115-129.
- [5] Yong, K.J., Wu, T.Y., Lee, C.B.T.L., Lee, Z.J., Liu, Q., Jahim, J.M., Zhou, Q., and Zhang, L. (2022). Furfural production from biomass residues: Current technologies, challenges and future prospects. *Biomass and Bioenergy*, 161, 106458.
- [6] Wiranarongkorn, K., Im-orb, K., Panpranot, J., Maréchal, F., and Arpornwichanop, A. (2021). Exergy and exergoeconomic analyses of sustainable furfural production via reactive distillation. *Energy*, 226, 120339.
- [7] Mahdi, T., Ahmad, A., Nasef, M.M., and Ripin, A. (2014). State-of-the-art technologies for separation of azeotropic mixtures. *Separation & Purification Reviews*, 44(4), 308-330.
- [8] Chen, Z., Zhang, W., Xu, J., and Li, P. (2015). Kinetics of xylose dehydration into furfural in acetic acid. *Chinese Journal of Chemical Engineering*, 23(4), 659-666.
- [9] Silva, J.F.L., Selicani, M.A., Junqueira, T.L., Klein, B.C., Vaz Júnior, S., and Bonomi, A. (2017). Integrated furfural and first generation bioethanol production: Process simulation and techno-economic analysis. *Brazilian Journal of Chemical Engineering*, 34(3), 623-634.
- [10] Shi, L., Huang, K., Wang, S., Yu, J., Yuan, Y., Chen, H., and Wong, D.S.H. (2015). Application of vapor recompression to heterogeneous azeotropic dividing-wall distillation columns. *Industrial & Engineering Chemistry Research*, 54(46), 11592-11609.



## Hollow Fiber Membrane Modeling and Simulation in the Application of Gas Separation Process

**Teeranuth Srisarunya<sup>1</sup>, Chalida Klaysom<sup>1\*</sup> and Pongtorn Charoensuppanimit<sup>2\*</sup>**

<sup>1</sup> Center of Excellence in Particle and Material Processing Technology, Department of Chemical Engineering, Faculty of Engineering, Chulalongkorn University, Bangkok, 10300, Thailand

<sup>2</sup> Control and Systems Engineering Research Laboratory, Department of Chemical Engineering, Faculty of Engineering, Chulalongkorn University, Bangkok 10330, Thailand  
E-mail: chalida.kl@chula.ac.th, Cpongton@yahoo.com

### Abstract

A new hollow fiber membrane consisting of a porous support layer and a dense selective layer was developed for CO<sub>2</sub> separation process. Before industrial application, new membranes must undergo rigorous testing in an enhanced laboratory or a pilot scale, which requires well-equipped facilities and can be costly as well as time-consuming. Modeling and simulation provide a more practical and less costly way to initially test these membranes, avoiding the physical and financial limitations of traditional experimental approaches. This research introduced a mathematical model to describe the separation behavior of hollow fiber membranes operated in a shell-side feed and counter-flow configuration. The succession-of-state method together with the bisection algorithm were applied to investigate membrane performance and product quality. The models were coded via MATLAB and validated with pre-published experimental studies that involve CO<sub>2</sub> separation applications data available in literature and the experimental studies of CO<sub>2</sub>/CH<sub>4</sub> separation using our developed hollow fiber membrane. The result revealed that the mathematical model was unable to adequately describe the gas separation behavior in the novel hollow fiber membrane. The discrepancy is attributed to the assumptions of the modeling. Moreover, mathematical modeling by the shortcut method was insufficient in achieving the acceptable results. The recommendation for further study is to apply the full method in order to improve accuracy and ensure the reliability of the model.

**Keywords:** Membrane gas separation; hollow fiber membrane; membrane modeling; succession of state

### 1. Introduction

Membrane technology has been applied in various applications such as desalination, gas separation, water purification, food and beverage processing, and pharmaceutical [1]. Among various membrane forms, hollow fiber (HF) membranes have gained prominence in the industrial gas separation process nowadays due to their high surface area and cost effectiveness especially in a large capacity. These membranes typically comprise two essential layers: porous support layer and a dense selective layer [2]. The porous support layer that enhances membrane strength, is usually created through a phase inversion method, and the dense selective layer that improves separation efficiency, is often fabricated using the dip-coating technique [3].

The transition from laboratory development to commercial-scale production of hollow fiber membranes is critical yet fraught with challenges. Laboratory experiments associated with membrane development are notably time-consuming and expensive, and scaling up these membranes presents significant hurdles in fabrication and optimizing operational conditions.

To address these limitations, mathematical modeling emerges as a crucial tool. It bypasses experimental constraints and enables efficient estimation of membrane performance.

The modeling of hollow fiber membrane has been conducted by Lock et al. [4]. Modeling of countercurrent flow configuration was modeled using Fick's law of diffusion to describe mass transport for the gas separation behavior in hollow fiber membrane. The succession of state method was applied to simplify membrane calculation. Additionally, the non-linear counterflow model utilized the bisection algorithm, by which the model's solution is numerically determined.

This study aims to leverage a mathematical model to elucidate the behavior of the novel HF membranes in application of CO<sub>2</sub> separation. The models were calculated and implemented using MATLAB. Furthermore, the model's accuracy is affirmed through comparison with existing literature and further validated against our experimental data. This approach underscores the model's robustness and reliability, offering valuable insights into the membrane's efficacy in gas separation.

## 2. Methods

### 2.1 Transport mechanism

The solution diffusion model has been widely utilized to elucidate the transport mechanism occurring in hollow fiber membranes [5]. This model comprises three distinct steps that facilitate the separation of gases through the membrane. First, all feed gas molecules are absorbed into the membrane, a crucial initial stage in the process. Following absorption, gases undergo diffusion through the membrane material, driven by concentration gradients. This diffusion process enables the transport of gas molecules from the region of higher concentration within the membrane to the regions of lower concentration outside the membrane. In the final step, some selectively permeable gas species pass through the membrane, referred to as the permeate, while the remaining gases are retained on the feed side, known as the retentate. The permeate, now enriched with the selectively transported gases, is collected on the other side of the membrane, resulting in the desired separation outcome. In other words, the membrane gas separation mechanism can be explained by the principle known as "Fick's law of diffusion" where the driving force is partial pressure difference between the feed side and permeate side as shown in Eq. (1) [6].

$$y_{T,n} V_T = Q_n A_m (p_h x_{s,n} - p_l y_{T,n}) \quad (1)$$

where,  $y_{T,n}$  denotes permeate composition of gas  $n$ ,  $V_T$  denotes permeate flow rate,  $Q_n$  denotes gas permeance of each component,  $A_m$  denotes membrane area,  $p_h$  denotes pressure at the feed side,  $x_{s,n}$  denotes retentate composition of gas  $n$ , and  $p_l$  denotes pressure at the permeate side. It is worth mentioning that the solution-diffusion model for gas separation through membranes simplifies the process modeling by applying ideal gas law and independent gas actions. It also presumes a uniform pressure across the membrane and expresses the driving force for permeation as merely a concentration gradient. This model neglects alternative transport mechanisms, such as pore flow or surface diffusion, and overlooks complex interactions, such as concentration polarization and plasticization in polymeric membranes. Yet, these simplifications can lead to inaccuracy in predicting the actual transport behavior of gases through the membrane [7].

## 2.2 Succession of state

Succession of state is a technique that can be applied to solve the membrane differential equation. This approach aims to transform the complex differential equation into a series of elements.[8] The calculation procedures begin by defining the inlet conditions. The entire membrane area is then divided into multiple elements, each with constant driving forces. In addition, the succession of state contributes to calculating material balance and mass transfer equations to obtain the outlet conditions. Once the outlet condition is obtained, it serves as the inlet condition for the next element as shown in Fig. 1. The calculation proceeds sequentially through each element until the entire membrane area is accounted for [4-6, 9].

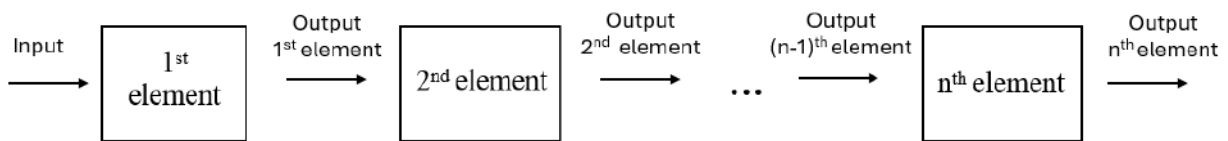


Fig. 1 Illustration of criteria using succession of state method

## 2.3 Simulation methodology

### 2.3.1 Model's assumptions

The schematic of flow direction in membrane module is demonstrated in Fig. 2. The membrane is operated in the countercurrent flow configuration, in which the feed enters on the shell side and flows axially along the membrane's length. Concurrently, the permeate stream moves in the opposite direction to the feed, ensuring efficient separation.

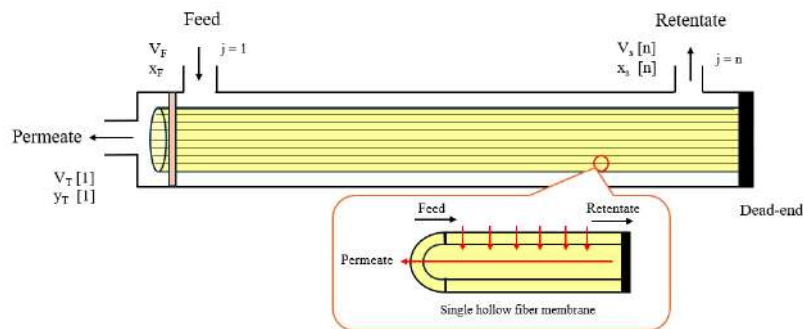


Fig. 2 Schematic of countercurrent flow configuration in membrane module

To simplify the calculation, the following assumptions are made.

- (1) Gas permeance is constant which is independent of the change in pressure, composition, and temperature.
- (2) The entire process is carried out at a constant temperature, implying isothermal condition.
- (3) The used membrane has no defects, ensuring no mixing occurs between the gas entering on the shell side and the gas collected on the tube side.
- (4) The pressure drop in the shell side is neglected since the flow channel in the shell side is large and relatively short.

These assumptions aim to reflect the experimental setup for model verification and the conditions anticipated in practical applications. It's important to note that, for simplicity, certain parameters are omitted, which may impact the model's accuracy. These considerations will be further explored and addressed in the discussion part.

To analyze the membrane performance more precisely, the method of succession of states is employed. The membrane area is segmented into defined elements. Each segment is assigned an index 'j'. This indexing helps to accurately identify and describe each segment's position along the membrane's longitudinal direction, facilitating detailed analysis and modeling of the membrane's behavior.

### 2.3.2 Workflow of calculation

The workflow in Fig. 3 illustrates the procedure of calculation applied in the study reported by Lock et al. In this study, we primarily focus on shortcut calculation due to their efficiency and computational simplicity. The modeling process begins with the utilization of simple equations and algorithms. In the algorithm, the calculation begins with providing the necessary inlet conditions (e.g., feed gas composition as  $x_F$ , feed flow rate as  $V_F$ , pressure between feed and permeate side, gas permeance, packing density, and membrane area after divided into the number of elements)

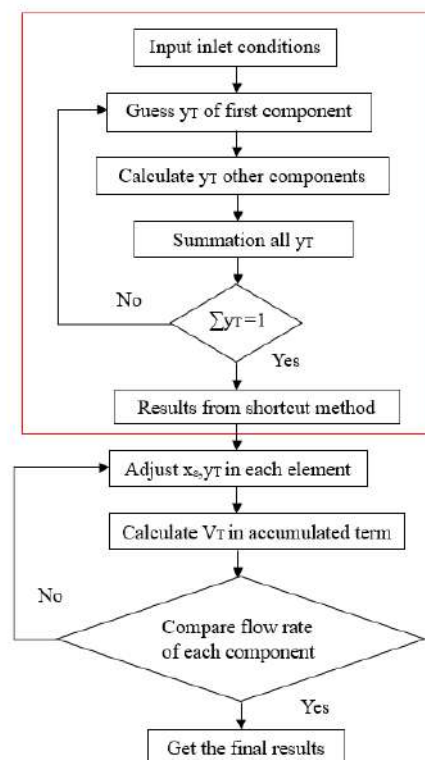


Fig. 3 The workflow of the membrane calculation

In the counter flow mathematical model, it is crucial to start with an initial guess regarding the gas composition on the permeate side at the entry point of the feed gas into the module—specifically, at the first element ( $j=1$ ). This necessity arises because the composition of the gases

at this juncture is initially unknown, a situation illustrated in Fig. 4 [4, 9]. One effective technique for solving this is the bisection method. This process of interval division is repeated, narrowing down the search range until a sufficiently precise solution is achieved within a predetermined tolerance level. This method provides a reliable means of approximating the initial conditions necessary for the counterflow model, ensuring accuracy in the simulation of gas permeation through the membrane [4, 9].

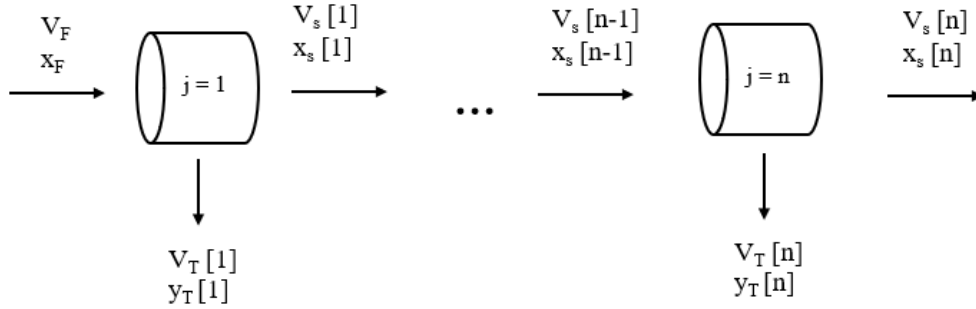


Fig. 4 Schematic of crossflow membrane as an initial guess for counter flow modeling.

The simulation algorithm starts with guessing the permeate composition at the first component. The initial guessing interval of permeate composition at the feed side should fall between the composition of the feed gas and a maximum permeate composition, which is set at 1. Local stage cut,  $\theta^*$ , can be determined by the mass transfer equation using Fick's law of diffusion as shown in Eq. (2). In other words, the local stage cut is the ratio of the permeate flow rate,  $V_T$ , to the feed flow rate,  $V_s$ . The permeate flow rate is calculated using Eq. (3). The other permeate gas compositions can be calculated in Eq. (4). The further step is the summation of all gas permeate compositions depicted in Eq. (5) which must equal to one as shown in Eq. (6).

$$y_{T,n}[j]\theta^* V_s[j-1] = Q_n A_m (p_h x_{s,n}[j-1] - p_l y_{T,n}[j]) \quad (2)$$

$$\theta^* = \frac{V_T[j]}{V_s[j-1]} \quad (3)$$

$$y_{T,n+1} = \frac{p_h x_{s,n+1}[j-1]}{((V_T[j]/Q_{n+1} A_m) + p_l)} \quad (4)$$

$$\text{sum} = \sum_{n=1}^N y_{T,n}[j] \quad (5)$$

$$\delta = \text{sum} - 1 \quad (6)$$

$$\delta \leq \epsilon \quad (7)$$

The simulation iterates Eq. (2) to Eq. (6) until the tolerance is satisfied – the tolerance limit of  $\epsilon = 0.00001$  is set in accordance with Eq. (7). After obtaining the outlet results at the first element, it becomes the input condition for the next element. The simulation algorithm for the subsequent element is almost identical to that of the first element, with the exception of the

interval used to guess the initial gas permeate composition. It is crucial to note that the boundary condition for the next element must lie between the retentate and the permeate compositions from the previous element. This iterative process continues throughout the entire membrane area. After obtaining preliminary results using the shortcut method, it's necessary to adjust certain parameters for more accurate calculation. First, refining the estimates for retentate and permeate compositions using the material balance equations, as presented in Eqs. (8) and (9). Subsequently, these revised compositions are used to calculate the new flow rates for both retentate,  $V_{s(new)}$ , and permeate,  $V_{T(new)}$ . These calculations incorporate the accumulated permeate flow rate from the preceding element, as shown in Eqs. (10) to (12). The calculation starts at the feed side denoted as the first element and continues to the final element at the retentate end.

$$x_{s,n(new)}[j] = \frac{x_{s,n(old)}[j-1]V_{s(old)}[j-1] + A_m Q_n p_l y_{T,n(old)}[j]}{V_{s(old)}[j] + A_m Q_n p_h} \quad (8)$$

$$y_{T,n(new)}[j] = \frac{y_{T,n(old)}[j+1]V_{T(old)}[j+1] + A_m Q_n p_l x_{s,n(old)}[j]}{V_{T(old)}[j] + A_m Q_n p_l} \quad (9)$$

$$\Delta V_{new} = \sum_{n=1}^N Q_n A_m (p_h x_{s,n(new)}[j] - p_l y_{T,n(new)}[j]) \quad (10)$$

$$V_{snew}[j] = V_{snew}[j-1] - \Delta V_{new} \quad (11)$$

$$V_{Tnew}[j] = V_{Tnew}[j+1] + \Delta V_{new} \quad (12)$$

This iterative procedure is repeated until the changes in the component flow rates of both permeate and retentate fall within the specified tolerance limit, i.e.,  $\epsilon = 0.0001$  as provided in Eqs. (13) and (14).

$$\left| \frac{y_{T,n(new)}[1]V_{T(new)}[1] - y_{T,n(old)}[1]V_{T(old)}[1]}{y_{T,n(old)}[1]V_{T(old)}[1]} \right| < \epsilon \quad (13)$$

$$\left| \frac{x_{s,n(new)}[X]V_{s(new)}[X] - x_{s,n(old)}[X]V_{s(old)}[X]}{x_{s,n(old)}[X]V_{s(old)}[X]} \right| < \epsilon \quad (14)$$

## 2.4 Experimental conditions

To assess the accuracy and the dependability of the mathematical model, it is essential to demonstrate that the model's prediction closely aligns with the experimental data, maintaining an error margin within acceptable accuracy. Validation is conducted through a comparison with the published experimental results of CO<sub>2</sub> separation processes using hollow fiber membranes [10]. Furthermore, to verify the model's robustness, we compared its prediction against experimental data obtained from own developed hollow fiber membranes. Tables 1 and 2 illustrate input parameters from the experimental studies for the model validation.

Table 1 The experimental parameters from literature study for model validation [10]

<b>Experimental parameters in literature</b>	
Gas separation process	CO <sub>2</sub> /CH <sub>4</sub> /O <sub>2</sub>
Feed flow rate (l/min)	Vary from 1.5 to 5 l/min
CO <sub>2</sub> permeance (GPU)	77.8
CH <sub>4</sub> permeance (GPU)	2.1
O <sub>2</sub> permeance (GPU)	17.9
feed composition	34.5/64.5/1
Packing density	50%
Membrane module diameter (mm)	0.8
Length of hollow fiber membrane (cm)	38
Pressure at feed side (bar)	9 bar
Pressure at permeate side (bar)	1.1 bar

Table 2 The experimental parameters from CO<sub>2</sub> separation our developed hollow fiber membrane for model validation

<b>Details for membrane module</b>	
Gas separation process	CO <sub>2</sub> /CH <sub>4</sub>
Membrane material	PDMS (polydimethylsiloxane)
Membrane Module	Two opened ends using He as carrier gas feed at permeate stream.
Membrane module area (cm <sup>2</sup> )	2500
<b>Experimental parameters</b>	
Feed flow rate (ml/min)	500
CO <sub>2</sub> permeance (GPU)	29.1-49.7
CH <sub>4</sub> permeance (GPU)	28.7-30.8
feed composition	50/50
Packing density	50%
Membrane module diameter (cm)	3.5
Length of hollow fiber membrane (m)	0.14
Pressure at feed side (bar)	Vary from 1 bar to 2 bar

Pressure at permeate side (bar)

1 bar

### 3. Results and Discussion

Makaruk and Harasek utilized hollow fiber membrane in order to separate CO<sub>2</sub> from the gas mixture consisting of CO<sub>2</sub>, CH<sub>4</sub>, and O<sub>2</sub> [10]. In addition, they studied the effect of feed flowrate (1.5 - 5 l/min) on the amount of CH<sub>4</sub> as a product in the retentate stream. Figure 4 showcases a comparison between the outcomes of model simulations and the experimental data from literature studies [10]. The findings reveal that utilizing a shortcut method for modeling does not adequately validate the experiments. This inadequacy stems from the shortcut method's reliance on an initial guess of crossflow in the counterflow modeling. As mentioned in section 2.3, the purpose of the criteria for the crossflow initialization is to circumvent the complication in counterflow mathematical model [4]. At the initial stage when the feed gas enters the module, the permeation is influenced by the composition of the gas that has already permeated. Nevertheless, this information is initially not defined. To achieve more precise and consistent results with the experimental data, the study suggests moving towards the full algorithm, which is currently in progress. The full algorithm was provided for adjusting parameters to calculate mass balance and mass transfer within the membrane element, aiming to obtain more accurate and reasonable results in a counterflow configuration.

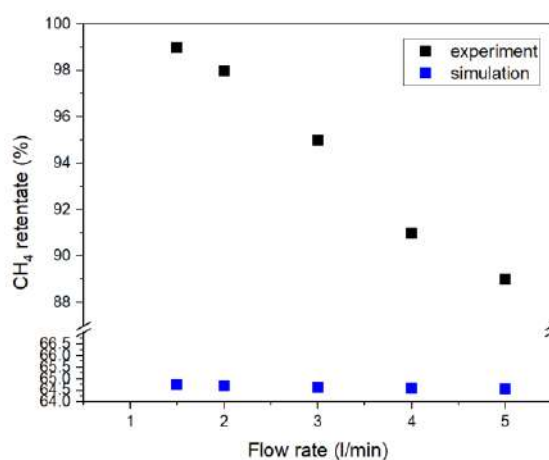


Fig. 5 Model validation with pre-published experimental studies [10]

From the experimental study using developed hollow fiber membrane for CO<sub>2</sub>/CH<sub>4</sub> separation, The effect of feed pressure on the product quality (methane purity) illustrate in Fig. 5. In general, methane purity can be determined by the amount of methane in the retentate stream over the total retentate flow rate. Increasing feed pressure implies a higher driving force, leading to increased CO<sub>2</sub> removal from the gas stream. Therefore, the methane product on the retentate stream will be purer [6]. However, the simulation results indicate that methane purity is not influenced by the change in feed pressure. This variation can be attributed to multiple factors, including the assumptions made within the mathematical model and the distinct characteristics of the membrane module housing use in our experiment. In certain mathematical models, it is common to assume membrane gas permeance to be constant in order to simplify calculation. However, the operating conditions, which are transmembrane pressure



temperature, including specific capabilities of each polymer for separation influence the change of gas permeance [2]. Additionally, simulation methods often ignore the behaviors of multicomponent gas mixtures, relying instead on calculations with pure gases, which may not accurately reflect actual membrane performance [11]. Another reason for the deviation between simulation and experimental results is the distinct characteristics of the membrane module housing. This difference is particularly notable between the assumptions made in the simulation, as depicted in Fig. 2, and the setup used in our experiment. In the simulation, there is no inlet permeate stream in the membrane module housing, while helium (He) is applied as the carrier gas introduced at the inlet of the permeate stream in our experimental study. This variability in the experimental setup compared to the simulation assumptions can lead to discrepancies in results. The suggestions for the further study are to modify the assumptions of the mathematical modeling. Applying the non-ideal effect, including gas permeability which depends on operating parameters and also applying the correlation between the gas mixture will improve membrane performance estimation and accuracy of the calculation [12].

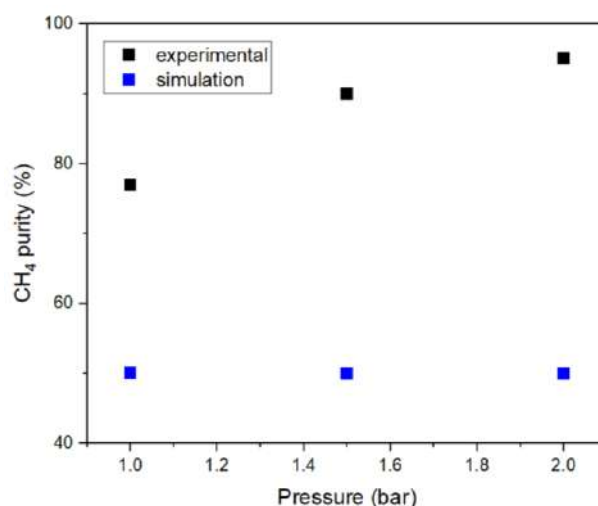


Fig. 6 Model validation with CO<sub>2</sub>/CH<sub>4</sub> experiment data using the novel hollow fiber membrane

#### 4. Conclusion

The utilization of mathematical model to simulation saves time and effort compared to experimental approaches. In this study, the succession of state method along with the bisection method are applied to describe the behavior of the developed hollow fiber membrane for CO<sub>2</sub> separation processes. However, the simulation results after experimental validation demonstrate that the current modeling method is insufficient for accurate description, particularly the quantification of membrane performance. For further studies, it is essential to continue with the full method algorithm and adjust the model assumptions that influence the accuracy of the results. This adjustment is necessary to ensure that the model can better fit with experimental studies and improve the robustness of the mathematical modeling.

#### References

- [1] Baker, R.W. (2004) Gas Separation, Membrane Technology and Applications. pp. 301-353.

- [2] Li, G., et al. (2021). A review - The development of hollow fibre membranes for gas separation processes. *International Journal of Greenhouse Gas Control*, 104, 103195.
- [3] Sukitpaneent, P. and T.-S. Chung. (2014). Fabrication and use of hollow fiber thin film composite membranes for ethanol dehydration. *Journal of membrane science*, 450, 124-137.
- [4] Lock, S.S.M., et al. (2015). Modeling, simulation and economic analysis of CO<sub>2</sub> capture from natural gas using cocurrent, countercurrent and radial crossflow hollow fiber membrane. *International Journal of Greenhouse Gas Control*, 36, 114-134.
- [5] Ahmad, F., et al. (2015). Hollow fiber membrane model for gas separation: Process simulation, experimental validation and module characteristics study. *Journal of Industrial and Engineering Chemistry*, 21, 1246-1257.
- [6] Ahmad, F., et al. (2012). Process simulation and optimal design of membrane separation system for CO<sub>2</sub> capture from natural gas. *Computers & Chemical Engineering*, 36, 119-128.
- [7] Ismail, A.F., et al. Understanding the solution-diffusion mechanism in gas separation membrane for engineering students. in *Regional Conference on Engineering Education RCEE*. 2005.
- [8] Jeon, J.-Y., B.-R. Park, and J.-H. Kim. (2022). Numerical Simulation and Optimization of 4-Component LDG Separation in the Steelmaking Industry Using Polysulfone Hollow Fiber Membranes. *Membranes*, 12(1), 97.
- [9] Lock, S., K. Lau, and A. Shariff. (2015). Effect of recycle ratio on the cost of natural gas processing in countercurrent hollow fiber membrane system. *Journal of Industrial and Engineering Chemistry*, 21, 542-551.
- [10] Makaruk, A. and M. Harasek. (2009). Numerical algorithm for modelling multicomponent multipermeator systems. *Journal of Membrane Science*, 344(1-2), 258-265.
- [11] Sadrzadeh, M., K. Shahidi, and T. Mohammadi. (2009). Effect of operating parameters on pure and mixed gas permeation properties of a synthesized composite PDMS/PA membrane. *Journal of Membrane Science*, 342(1-2), 327-340.
- [12] Da Conceicao, M., et al. (2023). Gas Separation Membrane Module Modeling: A Comprehensive Review. *Membranes*, 13(7), 639.

## Extraction of *Thunbergia laurifolia* Lindl. With Subcritical Fluid Technique

**Nichapa Areepong<sup>1</sup>, and Veronica Winoto<sup>1,\*</sup>**

<sup>1</sup> Department of Chemical Engineering, Faculty of Engineering, Thammasat School of Engineering, Thammasat University, Pathumthani, Thailand.

E-mail: \* wveronic@engr.tu.ac.th

### Abstract

*Thunbergia laurifolia* Lindl. or Rang Jued is a local Thai plant that belongs to *Acanthaceae* family. It was widely used as herbal Thai tea or medical treatment. Moreover, this plant has been reported that the extracts of leaves had antioxidants which were phenolic compounds. In this work, the antioxidant activity of *T. laurifolia* leaves was investigated under subcritical conditions. The preliminary extraction was prepared by various amounts of *T. laurifolia* powder between 0.1 to 0.5 grams, extraction temperature between 160 to 240°C, and extraction time between 1 to 9 minutes. Subcritical extraction technique was applied with 99.9% ethanol as a solvent. The total phenolic content (TPC) was evaluated by using the Folin-Ciocalteu method with UV-visible spectrophotometer at 750 nm. The results indicated that the effect of temperature and time affected the TPC. The highest TPC obtained was 45.42 mg GAE per g. The optimum condition was at 0.1:50 of TL:EtOH, 240°C of temperature, and 1 min of reaction time.

**Keywords:** *Thunbergia laurifolia* Lindl.; Subcritical Fluid; Extraction; Antioxidant; Total Phenolic Content.

### 1. Introduction

*Thunbergia laurifolia* Lindl. or Rang Jued is a local Thai plant that belongs to *Acanthaceae* family. Moreover, *T. laurifolia* is called laurel clock vine because the shape of flowers is trumpet shaped. The flowers have three colors consisting of white, yellow, and purple. The purple flower has been reported that there were several pharmacological properties particularly from the whole plant: stems, roots, and leaves [1-3]. In Thailand, *T. laurifolia* is widely processed into by-products in the form of herbal tea, powder, and capsules. According to the by-products, most of them were advised by Thai medical doctors for patients who suffer from alcohol, drugs, and addictive behaviors including food poisoning [4]. The leaves extract has been reported to have several biological properties for example 1. The anti-inflammatory properties have investigated, and it was found that the efficiency of *T. laurifolia* leaves extract with aqueous solution has higher efficiency than *Garcinia mangostanarind* extract, 2. The anti-diabetic; the previous study injected an aqueous leaves extract into diabetic rats where results showed a decreasing level of blood glucose, 3. The detoxifying; it has been reported that leaves extract reduced some effects of cadmium toxicity and prevented Pb neurotoxicity, and 4. The antioxidant properties; *T. laurifolia* has antioxidants such as phenolic compounds which were found in aqueous, ethanol, and acetone extraction. In addition, the *T. laurifolia* extract has been investigated to have a higher yield of TPC and free radical scavenging [2].

Furthermore, *T. laurifolia* extract consists of several phenolic compounds such as rosmarinic acid, caffeic acid, gallic acid, quercetin, catechin, or rutin where rosmarinic and caffeic acid had higher concentrations [4]. The study shows that rosmarinic acid was the major

antioxidant which was found in *T. laurifolia*. It has been reported that the highest rosmarinic acid was  $38.82 \pm 2.54$  mg/g dry weight [5]. Moreover, it was confirmed that rosmarinic acid ( $1896.7 \pm 89.3$  mg/100 g leaves) and caffeic acid ( $13.2 \pm 0.7$  mg/100 g) were dominant antioxidants [6]. The polyphenols and antioxidant activity of *T. laurifolia* were studied in the form of an infused tea with various drying conditions. The increment of drying temperature increased TPC and TFC significantly as well as DPPH inhibitory effect [4]. However, the appropriate drying methods have been proven to help preserve bioactive compounds. Four different drying methods were investigated including oven-drying at 50°C and 100°C, freeze-drying, and ambient air-drying. The results showed that oven-drying at 100°C preserved the total phenolic compound better than other methods [6].

There were several extraction methods such as Soxhlet, maceration, microwave-assisted, ultrasound-assisted, supercritical technique, and subcritical technique with different types of solvents [7]. The subcritical fluid technique is a novel technique with fluid under a critical point but above its boiling point such as 78.3°C ethanol, 100°C water, 64.7°C methanol, and 56°C acetone. The advantages of subcritical techniques are shorter extraction time, environmentally friendly, and high quality of the extract [8]. The previous studies reported that subcritical ethanol extraction of oil recovering from coconut meal demonstrated higher total phenolic content and antioxidant activity than Soxhlet extraction with hexane, which means subcritical ethanol extraction is an effective method with good antioxidant properties [9]. Additionally, defatted rice bran was studied by extraction with subcritical technique. It has been concluded that at the same extraction condition for the length of time, subcritical aqueous ethanol was more efficient than subcritical water [10]. From Table 1, the studies exhibited the optimum condition and the effective results. Hence, the subcritical technique with *T. laurifolia* has extracted potential and shows the effectiveness of the extract solution.

In this research, *T. laurifolia* was selected as a material for subcritical extraction by using ethanol as a solvent. The effect of temperature, time, and amount of *T. laurifolia* powder was varied in this study. The amount of TPC was further analyzed to investigate the effect of each parameter.

Table 1. The antioxidant extraction with different methods and plants.

Methods and Plants	Conditions	Antioxidant	Ref.
Tea infusion <i>T. laurifolia</i>	2 g TL: 300 ml water for 30 min 90°C	TPC $744.8 \pm 5.79$ mg GAE/L	[4]
Maceration <i>T. laurifolia</i>	20 g TL: 200 ml EtOH for 72 h room temperature	Rosmarinic acid $38.82 \pm 2.54$ mg/g dry weight	[5]
Shaking <i>T. laurifolia</i>	1 g TL: 50 ml MeOH for 72 h room temperature	TPC $834.1 \pm 32.6$ mg GAE/100g	[6]
Subcritical fluid Coconut meal	8:1 solid to solvent for 45 min 100°C	TPC $47.8$ µg GAE/g oil	[9]
Subcritical fluid Defatted rice bran	1.5 g DRB: 75 ml 20% v/v EtOH for 5 min 237°C	TPC $53.5$ mg GAE/g bran	[10]

## 2. Materials and Methods

### 2.1. Chemicals and material

Ethanol 99.99% (C<sub>2</sub>H<sub>5</sub>OH), Folin-Ciocalteu reagent, Gallic acid monohydrate (C<sub>7</sub>H<sub>6</sub>O<sub>5</sub>·H<sub>2</sub>O), and Sodium Carbonate (Na<sub>2</sub>CO<sub>3</sub>) were purchased from QREC Thailand Asia. *Thunbergia laurifolia* Lindl. (*T. laurifolia*) leaves were purchased from Sisaket, Thailand.

### 2.2. Preparation of *T. laurifolia* powder

*T. laurifolia* fresh leaves were removed from stems and washed with still water until it was cleaned. After that, spread them on a tray and dried by using hot air-drying oven at 80°C for 1.5 h with fan speed of 100%. Then, using a mortar and pestle ground them into a fine powder and sieve it.

### 2.3. Subcritical fluid extraction

The subcritical extraction was carried out in a stainless-steel reactor. Then, *T. laurifolia* leaves powder ranging from 0.1 to 0.5 g was mixed with 50 ml of EtOH. The reaction temperature was performed at 160, 200, and 240°C with the reaction time at 1, 5, and 9 min. The approximate heating-up time is 15 min. After the reaction occurred, the vessel was cooled down immediately in an ice bath. The extract solution was kept in a glass bottle until further analysis.

### 2.4. Total Phenolic Content (TPC) analyzation

The total phenolic content was performed according to Ibrahim et al. (2015) method [11]. Each 1 ml of sample was added to the test tube followed by 1 ml of Folin-Ciocalteu reagent and samples were left for 5 min. Then, 10 ml of Na<sub>2</sub>CO<sub>3</sub> (7%w/v) was added. After mixing, the samples were incubated for 30 min. The absorbance was measured by using UV-visible spectrophotometer at 750 nm. Gallic acid was used as a standard for a calibration curve with concentrations at 0, 5, 10, 20, 40, 60, 80, 100, 200, and 300 µg/ml ( $y = 0.0078x + 0.0648$  with  $R^2 = 0.996$ ). The TPC was expressed as mg gallic acid equivalent per gram of sample.

## 3. Results and Discussion

### 3.1. Effect of *T. laurifolia* powders amount

The experiment was carried out with various amounts of *T. laurifolia* (TL) powders (0.1, 0.3, and 0.5 g) with 50 ml ethanol. Table 2 shows the extraction conditions and total phenolic content (TPC). The results demonstrated that when the temperature was at 200°C, 1 min extraction time, and high amount of TL powder, the TPC decreased from 34.46 to 25.51 mg GAE/g. Likewise, at 240°C temperature, 9 min extraction time, TPC was slightly decreased from 36.00 to 29.32 mg GAE/g. Therefore, using a high temperature with a lower amount of TL increased TPC. Since the solvent volume was fixed so, the higher amount of TL powder couldn't dissolve well in the solvent due to the limited available contact surface. According to the previous study, by increasing the solvent amount the substances dissolved more easily than by decreasing the solvent amount [8].

Table 2. The subcritical extraction conditions and TPC results.

Temperature (°C)	Time (min)	TL:50 EtOH	TPC (mg GAE/g)
160	1	0.1	19.27
160	1	0.3	24.50
160	1	0.5	19.62
160	5	0.1	36.96
160	5	0.3	19.18
160	5	0.5	21.62
160	9	0.1	19.65
160	9	0.3	35.14
160	9	0.5	18.01
200	1	0.1	34.46
200	1	0.3	29.44
200	1	0.5	25.51
200	5	0.1	32.92
200	5	0.3	27.77
200	5	0.5	28.43
200	9	0.1	27.92
200	9	0.3	31.74
200	9	0.5	29.51
240	1	0.1	45.42
240	1	0.3	35.65
240	1	0.5	30.74
240	5	0.1	35.42
240	5	0.3	30.65
240	5	0.5	27.01
240	9	0.1	36.00
240	9	0.3	34.05
240	9	0.5	29.32

### 3.2. Effect of extraction time

The extraction time was varied to 1, 5, and 9 min. At 200°C extraction temperature with 0.1 g TL powder at 3 different extraction times from 1 to 9 min, the TPC were 34.46, 32.92, and 27.92 mg GAE/g, respectively. In addition, at 240°C extraction temperature with 0.1 g of TL powder at extraction time varied from 1 to 9 min, TPC decreased from 45.42 to 36.00 mg GAE/g. However, lower extraction time enhanced higher TPC. Similarly to subcritical ethanol extraction with defatted rice bran, TPC at 5 min extraction time was higher than at 10 min extraction by 25% [10].

### 3.3. Effect of extraction temperature

The experiment was carried out at 160, 200, and 240°C. From Table 2 the results showed that TPC ranged from 19.27-36.29 mg GAE/g, 25.51-34.46 mg GAE/g, and 27.01-45.42 mg GAE/g at 3 different extraction temperatures 160, 200, and 240°C, respectively. The increment of temperature with low amounts of TL powder and extraction time increased TPC. The effect

of extraction temperature was significant for TPC. The higher TPC was obtained more at higher temperatures. Accordingly, it can be concluded that among the 3 effects, temperature is the most important effect that significantly affected TPC value, while the concentration of ethanol as a solvent was a minor effect. While the temperature of ethanol increases within the subcritical range, it decreases viscosity and surface tension, which can improve diffusivity. Additionally, the bioactive compounds can be dissolved through the particles [10, 12].

#### 4. Conclusions

Subcritical ethanol extraction of *T. laurifolia* leaves powder was studied. The 3 parameters that affected the TPC such as the amount of *T. laurifolia* leaves powder of 0.1, 0.3, and 0.5 g, extraction temperature ranging from 160 to 240°C, and extraction time at 1, 5, and 9 min were investigated. The results showed that the highest TPC obtained was 45.42 mg GAE per g. The optimum condition was at 0.1:50 of TL:EtOH, 240°C of extraction temperature, and 1 min of extraction time. In conclusion, the shorter the reaction time and lower the amount of *T. laurifolia* powder can provide the best TPC result at high temperatures. Hence, subcritical ethanol extraction is an alternative technique for extraction and preservation of antioxidants from *T. laurifolia* leaves. Furthermore, *T. laurifolia* extracts have the potential to be applied as active ingredients in pharmaceuticals.

#### Acknowledgements

This research is supported by Department of Chemical Engineering, Thammasat School of Engineering, Thammasat University.

#### References

- [1] Woottisin, N., Kongkiatpaiboon, S., Sukprasert, S., & Sathirakul, K. (2020). Development and validation of stability indicating HPLC method for determination of caffeic acid, vitexin and rosmarinic acid in thunbergia laurifolia leaf extract. *Pharmacognosy Journal*, 12(3).
- [2] Jungsi, M., & Siripongvutikorn, S. (2016). *Thunbergia laurifolia*, a traditional herbal tea of Thailand: botanical, chemical composition, biological properties and processing influence. *International Food Research Journal*, 23(3), 923.
- [3] Oonsivilai, R., Cheng, C., Bomser, J., Ferruzzi, M. G., & Ningsanond, S. (2007). Phytochemical profiling and phase II enzyme-inducing properties of *Thunbergia laurifolia* Lindl. (RC) extracts. *Journal of Ethnopharmacology*, 114(3), 300-306.
- [4] Essiedu, J. A., Gonu, H., Adadi, P., & Withayagiat, U. (2023). Polyphenols and Antioxidant Activity of Thunbergia laurifolia Infused Tea under Drying Conditions. *Journal of Food Quality*, 2023.
- [5] Suwanchaikasem, P., Chaichantipyuth, C., & Sukrong, S. (2014). Antioxidant-guided isolation of rosmarinic acid, a major constituent from *Thunbergia laurifolia*, and its use as a bioactive marker for standardization. *Chiang Mai J. Sci*, 41, 117-127.
- [6] Oh, H. K. F., Siow, L. F., & Lim, Y. Y. (2019). Approach to preserve phenolics in Thunbergia laurifolia leaves by different drying treatments. *Journal of food biochemistry*, 43(7), e12856.
- [7] Fadimu, G. J., Ghafoor, K., Babiker, E. E., Al-Juhaimi, F., Abdulraheem, R. A., & Adenekan, M. K. (2020). Ultrasound-assisted process for optimal recovery of phenolic

- compounds from watermelon (*Citrullus lanatus*) seed and peel. *Journal of Food Measurement and Characterization*, 14, 1784-1793.
- [8] Yoswathana, N., & Eshtiaghi, M. N. (2015). Optimization of subcritical ethanol extraction for xanthone from mangosteen pericarp. *International Journal of Chemical Engineering and Applications*, 6(2), 115.
- [9] Plangklang, T., Khuwijitjaru, P., Klinchongkon, K., & Adachi, S. (2021). Chemical composition and antioxidant activity of oil obtained from coconut meal by subcritical ethanol extraction. *Journal of Food Measurement and Characterization*, 15(5), 4128-4137.
- [10] Chiou, T. Y., Neoh, T. L., Kobayashi, T., & Adachi, S. (2012). Properties of extract obtained from defatted rice bran by extraction with aqueous ethanol under subcritical conditions. *Food Science and Technology Research*, 18(1), 37-45.
- [11] Ibrahim, U. K., Yusof, M. I. S., Zamil, K. A. A., Kamarrudin, N., Maqsood-ul-Haque, S. N. S., & Ab Rashid, S. R. (2015). Total phenolic content and antioxidant activity of local fruit wastes in malaysia. *Advanced Materials Research*, 1113, 471-476.
- [12] Bodoira, R., Velez, A., Andreatta, A. E., Martínez, M., & Maestri, D. (2017). Extraction of bioactive compounds from sesame (*Sesamum indicum* L.) defatted seeds using water and ethanol under sub-critical conditions. *Food Chemistry*, 237, 114-120.



## Methane Reforming with CO<sub>2</sub> in Gliding Arc Plasma Minireactor Integrated with NiO and CoO Catalysts on Al<sub>2</sub>O<sub>3</sub> Ball Support

Thayarat Suwannasri<sup>1</sup>, Sumaeth Chavadej<sup>2</sup>, Hidetoshi Sekiguchi<sup>3</sup>  
and Nongnuch Rueangjitt<sup>4,5,\*</sup>

<sup>1</sup> Graduate Program in Industrial Chemistry, Faculty of Science, Chiang Mai University, Chiang Mai, 50200, Thailand

<sup>2</sup> The Petroleum and Petrochemical College, Chulalongkorn University, Bangkok, 10330, Thailand

<sup>3</sup> Department of Chemical Engineering, Faculty of Engineering, Tokyo Institute of Technology, Tokyo, 152-8552, Japan

<sup>4</sup> Department of Industrial Chemistry, Faculty of Science, Chiang Mai University, Chiang Mai, 50200, Thailand

<sup>5</sup> Materials Science Research Center (MSRC), Faculty of Science, Chiang Mai University, Chiang Mai, 50200, Thailand

E-mail: \*nongnuch.r@cmu.ac.th

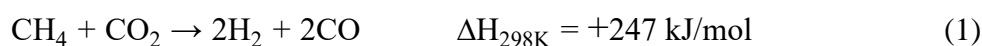
### Abstract

An integrated effect of non-thermal plasma and catalyst on methane reforming with CO<sub>2</sub> was investigated in gliding arc plasma minireactor with supported catalysts. This research work focused the effects of metal oxide types (NiO and CoO) and metal oxide loading (1, 2 and 3 M concentration of metal salt solution) on the plasma-catalytic performance. NiO and CoO catalysts on Al<sub>2</sub>O<sub>3</sub> ball support were prepared by a wet impregnation method, and were characterized by SEM-EDS and BET surface area & pore analyzer. The results showed that the catalytic activity of NiO/Al<sub>2</sub>O<sub>3</sub> catalyst was comparatively greater than CoO/Al<sub>2</sub>O<sub>3</sub> catalyst. At the same metal oxide loading, NiO/Al<sub>2</sub>O<sub>3</sub> catalyst provided higher CH<sub>4</sub> and CO<sub>2</sub> conversions than CoO/Al<sub>2</sub>O<sub>3</sub> ones. The higher amount of NiO and CoO loaded on Al<sub>2</sub>O<sub>3</sub> ball support synergistically resulted in the higher H<sub>2</sub> and CO selectivities. The catalyst of 1M NiO/Al<sub>2</sub>O<sub>3</sub> exhibited the highest CH<sub>4</sub> and CO<sub>2</sub> conversions of 22.87% and 8.82% with the H<sub>2</sub> and CO selectivities of 53.41% and 24.38% while the 3M NiO/Al<sub>2</sub>O<sub>3</sub> catalyst exhibited the highest H<sub>2</sub> and CO selectivities of 58.07% and 26.83% with the CH<sub>4</sub> and CO<sub>2</sub> conversions of 20.66% and 3.26%, respectively.

**Keywords:** non-thermal plasma; gliding arc plasma; methane reforming; supported catalysts

### 1. Introduction

Global warming is a serious environmental problem, caused by increasing greenhouse gases emission. Carbon dioxide (CO<sub>2</sub>) and methane (CH<sub>4</sub>) are two main components of greenhouse gases which are produced from many sectors such as fossil fuel, energy industry, agriculture and natural gas [1]. The development of alternative energy has attracted interest to reduce greenhouse gas emissions. CH<sub>4</sub> reforming with CO<sub>2</sub> utilizes two greenhouse gases to produce valuable synthesis gas (H<sub>2</sub> and CO) (Eq. (1)), which is a very important chemical intermediate for producing various chemicals including methanol synthesis and Fischer-Tropsch process [2].



Thermodynamic limitations of CH<sub>4</sub> reforming with CO<sub>2</sub> are still the main challenge that it can not be used on industrial scale because it is very endothermic reaction, and requires high temperature (900-1,200 K) to convert reactants at high conversion which brings to high energy cost and causes carbon deposit on catalyst and catalyst deactivation [3,4,6]. Therefore, it needs to look for another energy source to overcome the limitations.

Non-thermal plasma is a great alternative energy source for many chemical reactions. Non-thermal plasma can provide high energy efficiency and high selectivity [5]. Non-thermal plasma can be created by supplying electric energy to two electrodes, and electric field accelerates electrons to collide gas molecules, creating reactive species (ions, excited species and radicals), and form new compounds [6]. Moreover, electron temperature is about 1 eV (~10,000 K), whereas gas temperature remains close to room temperature. These are remarkable advantages of non-thermal plasma; it can overcome inert and stable reactants (CH<sub>4</sub> and CO<sub>2</sub>) at mild condition and can operate without external heating [5,6]. Many types of non-thermal plasma have been investigated for CH<sub>4</sub> reforming with CO<sub>2</sub> such as dielectric barrier discharge (DBD), corona discharge and gliding arc discharge [7-10]. Among various types of non-thermal plasma, gliding arc discharge shows the best performance for CH<sub>4</sub> reforming with CO<sub>2</sub> in terms of conversions and energy efficiency [11]. Since the electron temperature of gliding arc discharge provides effectively vibration excitation of CO<sub>2</sub>, and relates to high gas temperature that enhances the thermodynamically favorable process for CH<sub>4</sub> reforming with CO<sub>2</sub> [6].

Different catalyst types have been investigated for plasma-catalytic CH<sub>4</sub> reforming with CO<sub>2</sub> to improve the conversion efficiency and product selectivity. Among various catalyst types, metal oxides on alumina (Al<sub>2</sub>O<sub>3</sub>) support are the most commonly used in plasma-catalytic CH<sub>4</sub> reforming with CO<sub>2</sub> [8,10,13,14]. This is because of the advantages of Al<sub>2</sub>O<sub>3</sub>; availability, cheap and high surface area. Zeng et al. [12] investigated the effect of different supported metal catalysts (Ni, Co, Cu and Mn) with using Al<sub>2</sub>O<sub>3</sub> support on the performance of plasma process. It found that combining plasma with Ni/ $\gamma$ -Al<sub>2</sub>O<sub>3</sub> and Mn/ $\gamma$ -Al<sub>2</sub>O<sub>3</sub> catalysts significantly enhanced CH<sub>4</sub> conversion. The highest CH<sub>4</sub> conversion (19.6%) was achieved over Ni/ $\gamma$ -Al<sub>2</sub>O<sub>3</sub>. Mei et al. [14] reported that Ni/ $\gamma$ -Al<sub>2</sub>O<sub>3</sub> provided higher and more stable conversion as compared to Ag/ $\gamma$ -Al<sub>2</sub>O<sub>3</sub> and Pt/ $\gamma$ -Al<sub>2</sub>O<sub>3</sub>.

In this research work, plasma integrated with supported catalysts for CH<sub>4</sub> reforming with CO<sub>2</sub> has been investigated in a gliding arc plasma minireactor. The effects of metal oxide type (NiO and CoO) and metal oxide loading (1, 2 and 3 M metal salt solution) on Al<sub>2</sub>O<sub>3</sub> ball support has been evaluated the performance of plasma-catalytic CH<sub>4</sub> reforming with CO<sub>2</sub> in terms of conversions of CH<sub>4</sub> and CO<sub>2</sub>, selectivities and yields of H<sub>2</sub> and CO and specific energy consumption.

## 2. Materials and Methods

### 2.1 Catalyst preparation

The metal oxide supported catalysts were prepared by a wet impregnation method. The Al<sub>2</sub>O<sub>3</sub> ball support was dried at 110°C for 12 hr and calcined at 500°C for 5 hr. Al<sub>2</sub>O<sub>3</sub> support was impregnated in metal salt solutions (Ni(NO<sub>3</sub>)<sub>2</sub>·6H<sub>2</sub>O and CoSO<sub>4</sub>·7H<sub>2</sub>O salt solution for nickel and cobalt precursor, respectively) with 1, 2 and 3 M concentrations for 12 hr. The metal oxide on Al<sub>2</sub>O<sub>3</sub> was dried and calcined at the same condition with previous step. To investigate the characteristic of catalysts, surface morphology and element distribution was tested by scanning electron microscope (SEM) operated at 15 kV and energy dispersive spectroscopy

(EDS). The specific surface area, total pore volume and average pore radius were determined by BET surface analyzer.

## 2.2 Plasma-catalytic CH<sub>4</sub> reforming with CO<sub>2</sub>

The experiment was performed by using gliding arc plasma minireactor and metal oxide catalysts, as shown in Fig. 1. The reactor was made from acrylic material with a width of 8 cm, and length of 11 cm, and consisted of two knife-shaped electrodes made from stainless steel. The reactor was oriented horizontally. The electrodes were connected with AC power supply, monitored by power analyzer. The metal oxide catalysts were introduced into the gap on silicone sheet, with a width of 3 cm and a length of 3 cm. In this work, a mixed CH<sub>4</sub>/CO<sub>2</sub> ratio of 70/30 was used as feed gas. The flow rate of mixed CH<sub>4</sub>/CO<sub>2</sub> was controlled by digital mass flow controller. All experiments were performed under the following condition: total feed flow rate of 25 cm<sup>3</sup>/min, applied voltage of 16.25 kV, frequency of 300 Hz and electrode gap distance of 4.5 mm. After the reaction, the flow rate of outlet gas was measured by a soap bubble flow meter. The product gas reached a steady state after turning on plasma (about 10 min). The concentrations of feed gas and outlet gas were measured by Gas Chromatograph (GC). The experiments were repeated at least two times and calculated the average concentration in terms of conversions of CH<sub>4</sub> and CO<sub>2</sub>, selectivities and yields of H<sub>2</sub> and CO and specific energy consumption.

## 2.3 Gas product analysis

The conversions of CH<sub>4</sub> and CO<sub>2</sub>, selectivities and yields of H<sub>2</sub> and CO, H<sub>2</sub>/CO ratio and energy consumption (W·s/molecule) are calculated according to these equations.

$$\text{CH}_4 \text{ conversion (\%)} = \frac{\text{mole of CH}_4 \text{ in} - \text{mole of CH}_4 \text{ out}}{\text{mole of CH}_4 \text{ in}} \times 100 \quad (2)$$

$$\text{CO}_2 \text{ conversion (\%)} = \frac{\text{mole of CO}_2 \text{ in} - \text{mole of CO}_2 \text{ out}}{\text{mole of CO}_2 \text{ in}} \times 100 \quad (3)$$

$$\text{H}_2 \text{ selectivity (\%)} = \frac{\text{mole of H}_2 \text{ produced}}{2 \times \text{mole of CH}_4 \text{ converted}} \times 100 \quad (4)$$

$$\text{CO selectivity (\%)} = \frac{\text{mole of CO produced}}{(\text{mole of CH}_4 \text{ converted}) + (\text{mole of CO}_2 \text{ converted})} \times 100 \quad (5)$$

$$\text{H}_2 \text{ yield (\%)} = \frac{\text{mole of H}_2 \text{ produced}}{(\text{mole of CH}_4 \text{ in}) + (\text{mole of CO}_2 \text{ in})} \times 100 \quad (6)$$

$$\text{CO yield (\%)} = \frac{\text{mole of CO produced}}{(\text{mole of CH}_4 \text{ in}) + (\text{mole of CO}_2 \text{ in})} \times 100 \quad (7)$$

$$\text{H}_2/\text{CO} = \frac{\text{mole of H}_2 \text{ produced}}{\text{mole of CO produced}} \quad (8)$$

$$\text{Energy consumption} = \frac{P \times 60}{N \times M} \quad (9)$$

P refers to power (W), N refers to Avogadro's number ( $6.02 \times 10^{23}$  molecule $\cdot$ g $\cdot$ mol $^{-1}$ ) and M refers to rate of reactant converted or of syngas produced molecule (g $\cdot$ mol $^{-1}$ )

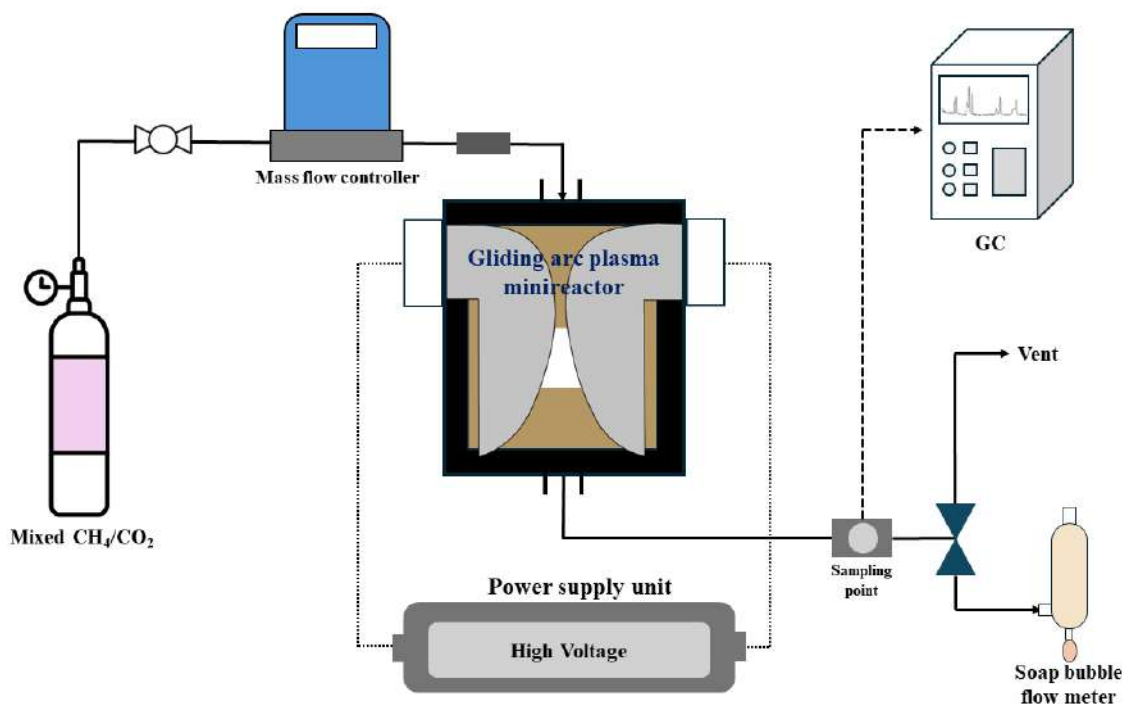


Fig. 1 Schematic diagram of plasma-catalytic of CH<sub>4</sub> reforming with CO<sub>2</sub>

### 3. Results and Discussion

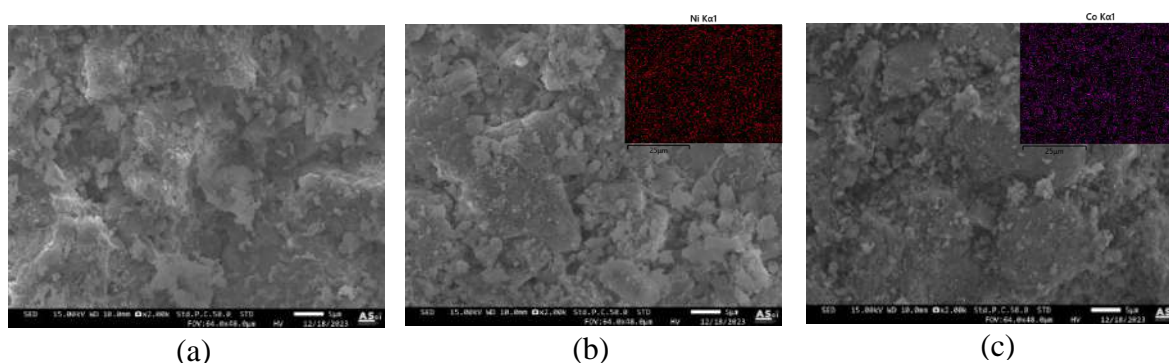
#### 3.1 Catalyst characterization

Table 1 shows the textural properties of catalysts including Al<sub>2</sub>O<sub>3</sub> ball, NiO/Al<sub>2</sub>O<sub>3</sub> and CoO/Al<sub>2</sub>O<sub>3</sub>. The Al<sub>2</sub>O<sub>3</sub> ball support had a specific surface area of 246.79 m<sup>2</sup>/g, a total pore volume of 0.521 cm<sup>3</sup>/g and an average pore radius of 42.22 Å. The specific surface area of catalysts decreased when metal oxide was supported on Al<sub>2</sub>O<sub>3</sub> balls. Moreover, the higher amounts of NiO and CoO loaded on Al<sub>2</sub>O<sub>3</sub> ball tended to give a decreasing specific surface area and total pore volume. It is certainly due to the fact that the porous Al<sub>2</sub>O<sub>3</sub> ball support is coated or deposited with NiO and CoO crystallites on either exterior or interior surface of porous Al<sub>2</sub>O<sub>3</sub> ball. As well as, this can be explained by the pore blocking and penetration of metal oxide in Al<sub>2</sub>O<sub>3</sub> ball surface [15]. It also can be clearly seen that the specific surface area and total pore volume of NiO/Al<sub>2</sub>O<sub>3</sub> catalyst samples was higher than CoO/Al<sub>2</sub>O<sub>3</sub> one.

The surface morphologies of catalysts were characterized by using SEM. Figure 2 shows the SEM images of Al<sub>2</sub>O<sub>3</sub> ball, 1M NiO/Al<sub>2</sub>O<sub>3</sub> and 1M CoO/Al<sub>2</sub>O<sub>3</sub> catalysts. The elemental area mapping results by SEM-EDS present the uniform dispersion of Ni and Co elements on Al<sub>2</sub>O<sub>3</sub> ball surface, as shown in Fig. 2(b) and 2(c), respectively. Additionally, the higher concentration of NiO and CoO relatively corresponded to the analysis results of elemental area mapping by SEM-EDS. The amounts of Ni and Co elements are shown in Table 1.

Table 1. BET surface analysis and EDS elemental analysis

Catalyst Type	Surface Area (m <sup>2</sup> /g)	Pore Volume (cm <sup>3</sup> /g)	Pore Radius (Å)	Ni (%wt.)	Co (%wt.)
Al <sub>2</sub> O <sub>3</sub> ball	246.79	0.5210	42.22	-	-
1M NiO/Al <sub>2</sub> O <sub>3</sub>	223.47	0.5289	47.34	13.69	-
2M NiO/Al <sub>2</sub> O <sub>3</sub>	176.25	0.4267	48.42	14.27	-
3M NiO/Al <sub>2</sub> O <sub>3</sub>	176.88	0.4247	48.02	20.60	-
1M CoO/Al <sub>2</sub> O <sub>3</sub>	151.44	0.3425	45.23	-	18.12
2M CoO/Al <sub>2</sub> O <sub>3</sub>	119.36	0.3143	52.66	-	22.20
3M CoO/Al <sub>2</sub> O <sub>3</sub>	103.62	0.2875	55.50	-	53.33

Fig. 2 SEM images of (a) Al<sub>2</sub>O<sub>3</sub> ball, (b) 1M NiO/Al<sub>2</sub>O<sub>3</sub>, and (c) 1M CoO/Al<sub>2</sub>O<sub>3</sub>

### 3.2 Plasma-catalytic of CH<sub>4</sub> reforming with CO<sub>2</sub>

#### 3.2.1 Effect of metal oxide on Al<sub>2</sub>O<sub>3</sub> ball support

Figure 3 shows the effect of NiO and CoO catalysts on Al<sub>2</sub>O<sub>3</sub> ball support on the plasma-catalytic CH<sub>4</sub> reforming with CO<sub>2</sub>. It found that NiO/Al<sub>2</sub>O<sub>3</sub> catalyst exhibited higher CH<sub>4</sub> and CO<sub>2</sub> conversions than CoO/Al<sub>2</sub>O<sub>3</sub> catalyst, except for 3M NiO/Al<sub>2</sub>O<sub>3</sub> (Fig. 3(a)). This result was similar to the result from thermal catalytic dry reforming that Ni-based catalyst showed better activity than Co-based catalyst [16]. This might be because the reaction pathway between plasma species with NiO was different from that with CoO. Moreover, it is worth noting that CH<sub>4</sub> conversion of all catalysts are much higher than CO<sub>2</sub> conversion. It indicates that the dissociation energy of C-H bond from CH<sub>4</sub> (438 kJ/mol) is lower than C=O bond from CO<sub>2</sub> (532 kJ/mol), and the reverse water gas shift (RWGS) occurs as a side reaction (Eq.(10)) [17].



The selectivities of the main product are shown in Fig. 3(b). Compared to the reaction with Al<sub>2</sub>O<sub>3</sub> ball, H<sub>2</sub> selectivity was slightly improved when using NiO/Al<sub>2</sub>O<sub>3</sub> and CoO/Al<sub>2</sub>O<sub>3</sub>, whilst CO selectivity did not much change. The highest H<sub>2</sub> and CO selectivities were achieved with 3M NiO/Al<sub>2</sub>O<sub>3</sub> (58.07% and 26.83% respectively). In addition, the selectivity and yield of H<sub>2</sub> were obviously higher than that of CO, partly due to the occurrence of RWGS at low temperature [13]. The formed CO molecule can react with water molecule, resulting in a lower

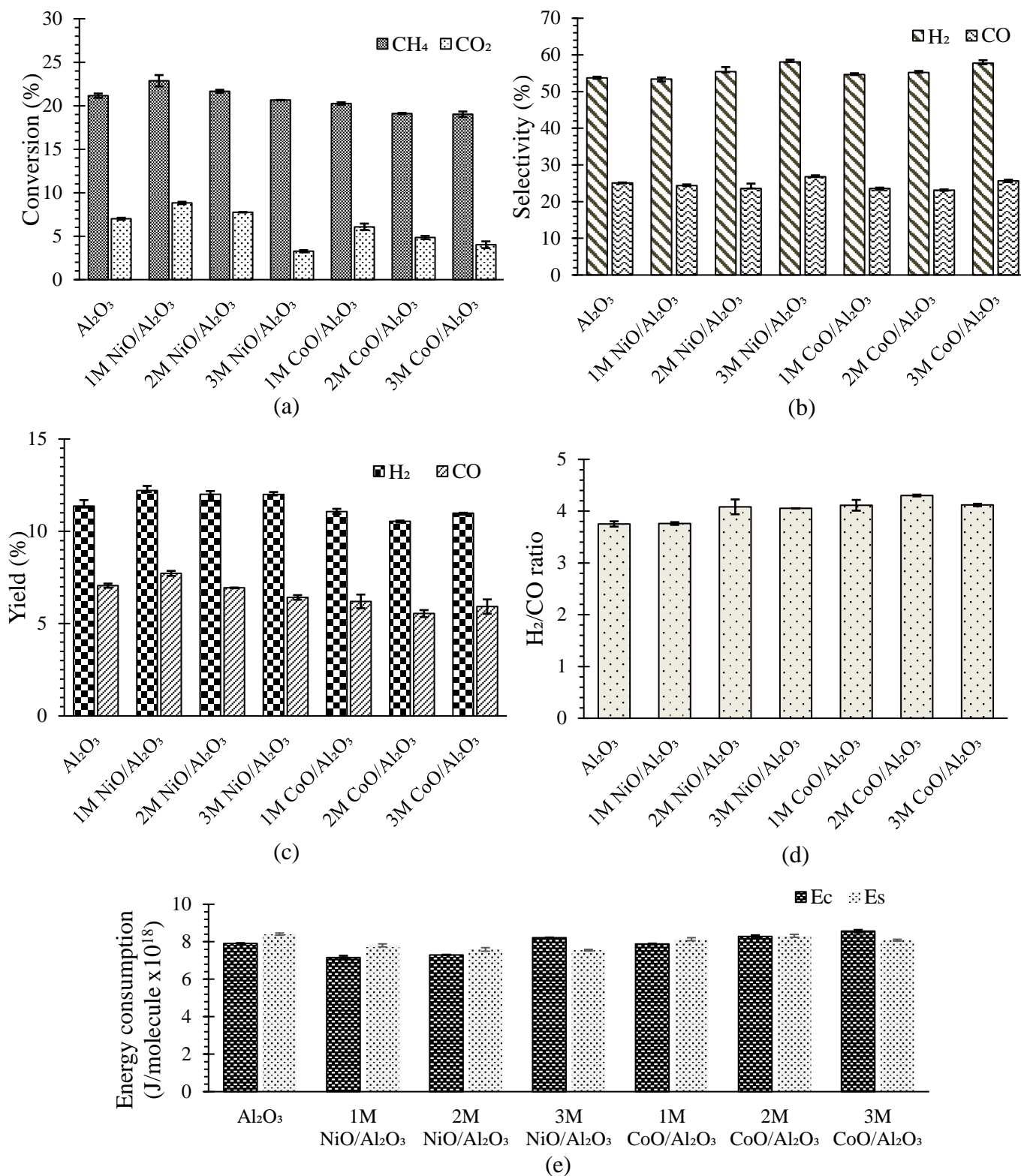


Fig. 3 Effects of metal oxide type and metal oxide loading on Al<sub>2</sub>O<sub>3</sub> ball support: (a) conversions of CH<sub>4</sub> and CO<sub>2</sub>, (b) selectivities of H<sub>2</sub> and CO, (c) yields of H<sub>2</sub> and CO, (d) H<sub>2</sub>/CO ratio, and (e) energy consumption

CO<sub>2</sub> conversion and higher H<sub>2</sub> produced. Moreover, the conversion and yield of CoO/Al<sub>2</sub>O<sub>3</sub> catalyst was reduced when compared to unmodified Al<sub>2</sub>O<sub>3</sub>. This probably referred to the results of much less surface area and pore volume of CoO/Al<sub>2</sub>O<sub>3</sub> than unmodified Al<sub>2</sub>O<sub>3</sub>. H<sub>2</sub>/CO molar ratio of Al<sub>2</sub>O<sub>3</sub> ball was 3.75, and slightly increased when using NiO and CoO on Al<sub>2</sub>O<sub>3</sub> ball. Figure 3(e) shows that energy consumption of the studied plasma catalytic reaction. The energy consumption of reactant converted ( $E_c$ ) and energy consumption of syngas produced ( $E_s$ ) of Al<sub>2</sub>O<sub>3</sub> ball were  $7.9 \times 10^{-18}$  and  $8.4 \times 10^{-18}$  J/molecule, respectively. Using NiO/Al<sub>2</sub>O<sub>3</sub> catalyst was found to reduce both  $E_c$  and  $E_s$ , whilst introducing CoO/Al<sub>2</sub>O<sub>3</sub> catalyst into reactor consumed more energy in converting reactant, compared to Al<sub>2</sub>O<sub>3</sub> ball.

### 3.2.2 Effect of metal oxide loading on NiO/Al<sub>2</sub>O<sub>3</sub> and CoO/Al<sub>2</sub>O<sub>3</sub> catalysts

To study the effect of metal oxide loading, Al<sub>2</sub>O<sub>3</sub> ball support was impregnated with three different metal salt solution concentrations (1, 2 and 3 M). It noticed that CH<sub>4</sub> and CO<sub>2</sub> conversions obviously decreased with increasing metal oxide loading. CH<sub>4</sub> and CO<sub>2</sub> conversions of NiO/Al<sub>2</sub>O<sub>3</sub> catalyst decreased from 22.87% to 20.66% and 8.82% to 3.26%, respectively. The same results were also observed for CoO/Al<sub>2</sub>O<sub>3</sub> catalyst. This can indicate that the higher amount of Ni and Co atoms can stick on the Al<sub>2</sub>O<sub>3</sub> ball surface, thus the structural properties including specific surface area and total pore volume were reduced, as shown in Table 1 [10]. This result was also reported in Martin-del-Campo's work [10] that the higher Ni loading exhibited the negative effect to CH<sub>4</sub> and CO<sub>2</sub> conversions.

The opposite result was found for product selectivity, the higher amounts of NiO and CoO on Al<sub>2</sub>O<sub>3</sub> ball support clearly affected the higher H<sub>2</sub> and CO selectivities. Both 3M NiO/Al<sub>2</sub>O<sub>3</sub> and 3M CoO/Al<sub>2</sub>O<sub>3</sub> presented the highest H<sub>2</sub> and CO selectivities at the same metal oxide concentration. In the case of product yield, the increment of NiO and CoO amounts did not affect H<sub>2</sub> yield, but slightly decreased CO yield. In Fig. 3(d), the highest H<sub>2</sub>/CO molar ratio was 4.08 and 4.30 for 2M NiO/Al<sub>2</sub>O<sub>3</sub> and 2M CoO/Al<sub>2</sub>O<sub>3</sub> catalysts, respectively. The energy consumption is shown in Fig. 3(e). It found that the higher NiO and CoO loadings had an unfavorable effect for both energy consumption of reactant converted ( $E_c$ ) and energy consumption of syngas produced ( $E_s$ ). The higher amount of metal oxide reduced the opportunity of plasma to react with species adsorbed on catalyst surface, and resulted in more consumed energy. The lower metal oxide amount exhibited the better performance for plasma-catalytic CH<sub>4</sub> reforming with CO<sub>2</sub>.

## 4. Conclusions

The CH<sub>4</sub> reforming with CO<sub>2</sub> by gliding arc discharge plasma integrated with NiO and CoO catalysts on Al<sub>2</sub>O<sub>3</sub> ball support was investigated at atmosphere pressure and ambient temperature. NiO/Al<sub>2</sub>O<sub>3</sub> catalyst exhibited higher CH<sub>4</sub> and CO<sub>2</sub> conversions than CoO/Al<sub>2</sub>O<sub>3</sub> catalyst at the same metal loading. The highest CH<sub>4</sub> and CO<sub>2</sub> conversions were achieved when using 1M NiO/Al<sub>2</sub>O<sub>3</sub> (22.87% and 8.82%, respectively). The higher amount of metal oxide loading was not a favorable effect for the plasma-catalytic reaction possibly because the textural properties were declined by the pore blocking of metal oxide. Oppositely, the higher metal oxide loading was beneficial for H<sub>2</sub> and CO selectivities. In addition, the lower energy consumption can be achieved when using metal oxide catalyst and less amount of metal oxide.

## Acknowledgement

The authors would like to thank the Graduate School, Chiang Mai University for TA/RA Scholarship.

## References

- [1] Thailand. (2022). Greenhouse Gas Emission by Sector. Thailand biennial update report. [Online URL: <https://unfccc.int/documents/624750>] accessed on December 23, 2023.
- [2] Schmidt, L.D., Deutschmann O., and Goralski Jr., C. T. (1998). Modelling the partial oxidation of methane to syngas at millisecond contact times. *Studies in Surface and Catalysis*, 119, 685-692.
- [3] Hussien, A. G. S., Polychronopoulou, K. (2022). A review on the different aspects and challenges of the dry reforming of methane (DRM) reaction. *Nanomaterials*, 12, 2-8.
- [4] Lavoie, J. (2014). Review on dry reforming of methane, a potentially more environmentally-friendly approach to the increasing natural gas exploitation. *Chemical and Process Engineering*, 2, 2-16.
- [5] Fridman, A. (2008). *Plasma Chemistry*. Cambridge University Press, pp. 3-10.
- [6] Snoeckx, R., and Bogaerts, A. (2017). Plasma technology – a novel solution for CO<sub>2</sub> conversion. *The Royal Society of Chemistry*, 46, 5805-5863.
- [7] Nguyen, H. H., and Kim K. (2015). Combination of plasma and catalytic reactions for CO<sub>2</sub> reforming of CH<sub>4</sub> by dielectric discharge process. *Catalysis Today*, 256, 88-95.
- [8] Aziznia, A., Bozorgzadeh, H. R., Seyed-Matin, N., Baghalha, M., and Mohamadizadeh, A. (2012). Comparison of dry reforming of methane in low temperature hybrid plasma-catalytic corona with thermal catalytic reactor over Ni/ $\gamma$ -Al<sub>2</sub>O<sub>3</sub>. *Journal of Natural Gas Chemistry*, 21, 466-475.
- [9] Rueangjitt, N., Sreethawong, T., and Chavadej, S. (2009). Plasma-catalytic reforming of methane in AC microsized gliding arc discharge: Effect of input power, reactor thickness, and catalyst existence. *Chemical Engineering Journal*, 155, 874-880.
- [10] Martin-del-Campo, J., Uceda, M., Coulombe, S., and Kopyscinski, J. (2021). Plasma-catalytic dry reforming of methane over Ni-supported catalysts in a rotating gliding arc – Spouted bed reactor. *Journal of CO<sub>2</sub> Utilization*, 46, 1-13.
- [11] Liu, J., Gao, Y., Sun, B., Zhu, B., and Li, X. (2022). Mechanism study on gliding arc (GA) plasma reforming: A combination approach of experiment and modeling. *Plasma Process Polymers*, 19, 1-2.
- [12] Zeng, Y., Zhu, X., Mei, D., Ashford, B., and Tu, X. (2015). Plasma-catalytic dry reforming of methane over  $\gamma$ -Al<sub>2</sub>O<sub>3</sub> supported metal catalysts. *Catalysis Today*, 256, 80-87.
- [13] Andersen, J. A., Christensen, J. M., Østberg, M., Bogaerts, A., and Jensen, A. D. (2020). Plasma-catalytic dry reforming of methane: Screening of catalytic material in a coaxial packed-bed DBD reactor. *Chemical Engineering Journal*, 397, 1-8.
- [14] Mei, D., Sun, M., Liu, S., Zhang, P., Fang, Z., and Tu, Z. (2023). Plasma-enabled catalytic dry reforming of CH<sub>4</sub> into syngas, hydrocarbons and oxygenated: Insight into the active metals of  $\gamma$ -Al<sub>2</sub>O<sub>3</sub>. *Journal of CO<sub>2</sub> Utilization*, 67, 1-11.
- [15] Auzza, M., Ahlafi, H., Moussout, H., Mounir, C., Fadel, A., and Addad, A. (2020). Catalytic reduction of nitro-phenolic compounds over Ag, Ni and Co nanoparticles catalysts supported on  $\gamma$ -Al<sub>2</sub>O<sub>3</sub>. *Journal of Environmental Chemical Engineering*, 8, 1-12.
- [16] Budiman, A. W., Song, S., Chang, T., Shin, C., and Choi, M. (2012). Dry reforming of methane over cobalt catalysts: A literature review of catalyst development. *Catalysis Surveys from Asia*, 16, 183-197.
- [17] Luo, Y. (2002). *Chemical bond energies*, 1st, Taylor & Francis Group, pp. 19, 342.



## Investigation of the polymerization of ethylene and ethylene/1-hexene over zirconocene/MMAO catalyst supported on Ga-modified silica

Thanapoom Osathalert, Bunjerd Jongsomjit\*

Center of Excellence on Catalysis and Catalytic Reaction Engineering (CECC)  
Department of Chemical Engineering, Faculty of Engineering  
Chulalongkorn University, Bangkok 10330, Thailand  
E-mail: \*bunjerd.j@chula.ac.th

### Abstract

Silica is commonly used as a support material in metallocene catalytic systems (MTC) and has many different kinds of surface functional groups. The presence of various functional groups on silica may result in the deactivation of active sites due to their inherent undesirable properties. Considerable effort has been dedicated to the development of active supported metallocene species, which exhibit enhanced stability and activity. In this study, methylaluminoxane (MAO) cocatalyst supported on two distinct types of structured mesoporous silica supports, namely CAB-O-SIL and MCF-Si, which were modified with 1% of Ga in ethylene polymerization and ethylene/1-hexene copolymerization was investigated. First, the modification of calcined CAB-O-SIL and MCF-Si was conducted with 1 wt% of Ga impregnated on the support, and then the support was sequentially impregnated with MAO cocatalyst using the proper immobilization technique. Under slurry polymerization conditions, ethylene and ethylene/1-hexene were polymerized over cocatalyst and the zirconocene supported catalysts using toluene as solvent with  $[Al]_{MAO}/[Zr]_{cat}$  molar ratio = 2,000 at 70°C and 3.5 bar of ethylene pressure. The higher activity in ethylene/1-hexene copolymerization was similarly observed with the supported catalyst containing Ga modification on both CAB-O-SIL and MCF-Si supports. The results indicated that incorporating Ga could enhance the capability of supports to immobilize metallocene catalysts.

**Keywords:** mesocellular foam; Ga-modified; ethylene polymerization; metallocene catalyst; methylaluminoxane

### 1. Introduction

The continuous increase in polyolefin production can be attributed to their exceptional product properties and environmental compatibility. In addition to components for the automotive and electrical industries, they are frequently utilized as packaging materials, foils, and filaments. The industrial production of polyolefins involves the utilization of two catalyst approaches: the traditional heterogeneous Ziegler-Natta catalysts supported on  $MgCl_2$ , or the Phillips catalysts, which are chromium catalysts attached to  $SiO_2$  or  $Al_2O_3$  bases. In polymer science, the discovery of metallocene and methylaluminoxane (MAO) catalysts for olefin polymerization has ushered in a new millennium. In addition to the traditional Ziegler-Natta and Phillips systems, metallocene and other catalysts have been synthesized; these catalysts produce polymers with unique structures and enable greater control over the tacticity, molar mass, and

molar mass distribution of the polymer [1,2]. Metallocene is an organometallic catalyst with a single site which is activated by MAO that enables the synthesis of polyolefins while keeping great regulation over molecular weight and distribution [3]. Many researches have been reported on silica supports to see if they can stop side reactions and keep the shape of olefin polymerization while heterogeneous ethylene polymerization is happening [4].

A variety of metallocene catalysts have been demonstrated using inorganic carriers, most commonly titania, silica, or alumina. In addition, mesoporous substances contain distinct pore configurations. For example, fumed silica (CAB-O-SIL), which consists of branched chains formed from amorphous silica particles on the nanometer scale, and silica-mesocellular foam (MCF-Si), which contains both an interconnected pore structure and a three-dimensional spherical pore structure, are both viable alternatives. For industrial applications, the development of supported metallocene is critical, as it permits their use in gas and slurry phases and prevents contamination issues in reactors. According to available reports, silica has emerged as a highly desirable support material applied, thus, far for supported metallocene catalysts. However, depending on the polymerization activity and properties of the resultant polymers, the properties of silica may not exactly fulfill all desired objectives. Due to the acidity of various surface OH groups and other intrinsically undesirable properties, the formation of multiple active sites is possible. Many efforts have been applied to the development of active, supported metallocene species that exhibit enhanced stability and activity. Utilizing a support modified with acidic metals such as Ga presents an intriguing option for improving catalytic performance and holds promise for further advancement in ethylene polymerization. [5,6].

The investigation in this research has been divided into two different parts. After the impregnation of (MAO) on different silica supports, such as SBA-15 and MCF-Si modified with Ga, an evaluation was first conducted of the MAO's physical and chemical properties. Second, the application of these supported catalysts for the polymerization of ethylene and ethylene/1-hexene was investigated.

## 2. Materials and Methods

### 2.1. Chemical

All chemical processes and polymerizations were carried out in an argon environment, employing Schlenk techniques and/or a glove box. The following analytical reagents have been purchased from Sigma-Aldrich: hydrochloric acid, 1,3,5-trimethylbenzene (TMB), tetraethyl orthosilicate (TEOS), methylaluminoxane (MAO), toluene, 1-hexene, gallium nitrate [Ga(NO<sub>3</sub>)<sub>3</sub>] zirconocene catalysts and Pluronic P123 (Mw 5800).

### 2.2. Silica cabosil calcination

The silica supports were calcined for 6 hours at 400°C under a N<sub>2</sub> flow with a ramp rate of 10°C/min.

### 2.3. Silica mesocellular foam synthesis

In order to produce the synthetic MCF-Si, 2 g of P123 was mixed with a hydrochloric solution at 40 °C while being stirred until the mixture became uniform. Following the addition and stirring of 7 g of TMB for 2 hours as white solution. After accumulating 2 hours, 4 g of TEOS solution was dropped slowly while stirring for 5 minutes. Then, the milky solution was aged in the oven at 40 °C for 20 hours. After that, the required temperature was raised to 100 °C for a duration of 24 hours. Finally, the white sediment was washed with 50 ml each of ethanol and DI water until the pH of the filtered solution was neutral. Subsequently, the sediment was been exposed to light overnight at room temperature.

### 2.4. Ga-modified silica support

Ga was introduced via  $[\text{Ga}(\text{NO}_3)_3]$ . Silica support was impregnated with Ga at concentrations of 0.2 or 1.0 wt%. After 12 hours of drying at 110°C in an oven, the support was calcined for 2 hours at 400°C in air.

### 2.5. Support impregnation

Every investigation was performed within a glove box containing a dry argon gas-purified inert atmosphere. In a reactor equipped with a magnetic agitating bar, 1 g of supported catalyst and 10 mL of MAO in a 10 mL toluene solution were initially introduced. After 30 minutes of agitation at room temperature, the solution was subsequently vacuum-dried and stirred until it was completely dried.

### 2.6. Ethylene polymerization

In a 100 mL reactor, ethylene polymerization was conducted via 0.01 g of supported catalyst, 1500 mL of zirconocene catalyst solution, 2 mL of MAO in a 26.5 mL toluene solution, and MAO. In case of copolymerization, 5 mL of 1-hexene was added. Ethylene and ethylene/1-hexene were polymerized for a duration of 15 minutes at a temperature of 70°C and an ethylene pressure of 3.5 bar, which was consistent with slurry polymerization conditions.

## 3. Results and discussion

The surface morphology of supported catalysts was determined utilizing the SEM technique as shown in **Figure 1**. The morphology of Cab-Si is composed of amorphous silica at the nanometer scale. After impregnation process with 1 wt% of Ga, the morphology of Cab-Si exhibited no significant change.



Fig. 1 The SEM image of Cab-Si and Cab-Si after impregnation with 1% Ga, respectively

No significant changes in morphologies were observed for Cab-Si and 1 wt% Ga Cab-Si following immobilization with MAO as shown in **Figure 2**.

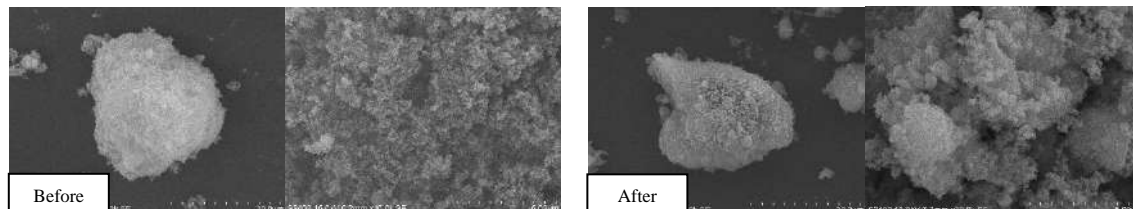


Fig. 2 The SEM image of Cab-Si and 1 wt% Ga Cab-Si after impregnation with MAO,

**Figure 3** shows micrographs illustrating the various morphologies of MCF-Si before and after the impregnation process employing 1 wt% of Ga. MCF-Si exhibits a spherical pore structure that is structured in three dimensions. MCF-Si's morphology remained largely unchanged following the impregnation procedure, which is similar to that of Cab-Si.

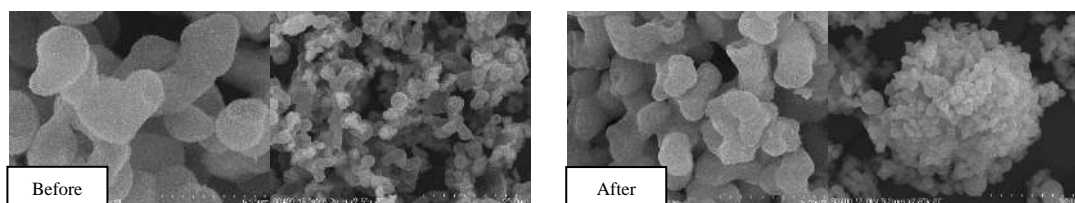


Fig. 3 The SEM image of MCF-Si before and after impregnation with 1 wt% of Ga

Likewise, no significant changes in morphologies were observed for MCF-Si and 1 wt% of Ga MCF-Si subsequent to immobilization with MAO as shown in **Figure 4**.

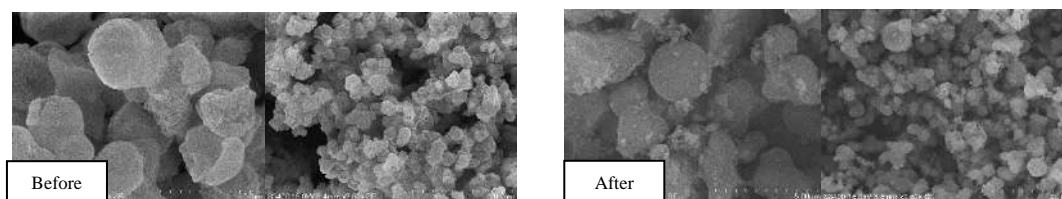


Fig. 4 The SEM image of MCF-Si and 1 wt% Ga MCF-Si after impregnation with MAO

The EDX technique was used in order to analyze the elemental distribution of catalysts. The EDX method was implemented in order to analyze the elemental composition of catalysts. The dispersion of the elements Si, O, and Al for Cab-Si and MCF-Si within the granules of the supported catalysts is effectively illustrated in **Figures 5** and **7**. In case of supports modified by 1 wt% of Ga analyze the elemental composition of Si, O, Ga and Al as shown in **Figures 6** and **8**. In addition, **Table 1** shows the elemental composition (less than 5 microns) as discovered through EDX measurement. The Cab-Si-MAO supported catalyst exhibited a greater Si/Al ratio of 3.25 compared to the 2.42 Si/Al ratio of the 1 wt% of Ga-Cab-Si-MAO supported catalyst. In contrast, the 1 wt% Ga-MCF-Si-MAO supported catalyst

catalyst. In contrast, The 1% Ga-MCF-Si-MAO supported catalyst exhibited a greater Si/Al ratio of 2.70 compared to the 2.36 Si/Al ratio of the MCF-Si-MAO supported catalyst.

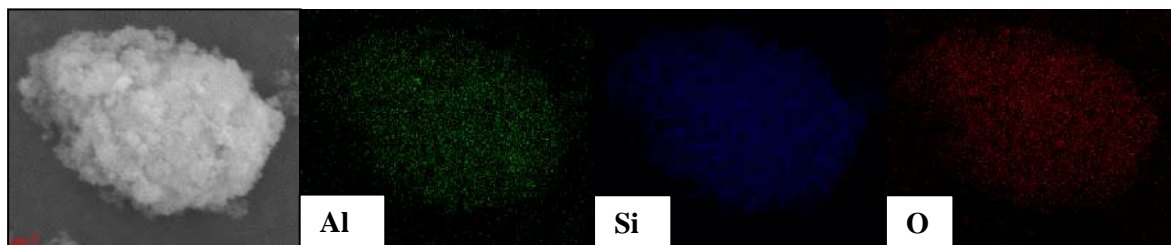


Fig. 5 The SEM and EDX images of Cab-Si-MAO

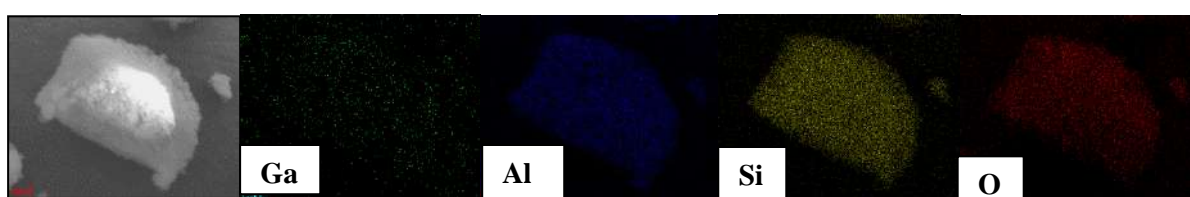


Fig. 6 The SEM and EDX images of 1% Ga-Cab-Si-MAO

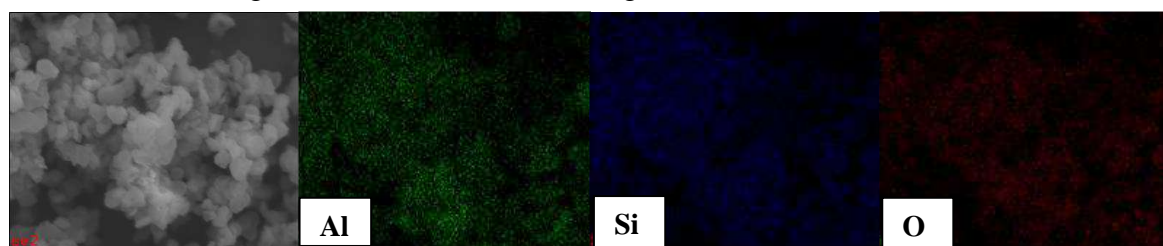


Fig. 7 The SEM and EDX images of MCF-Si-MAO

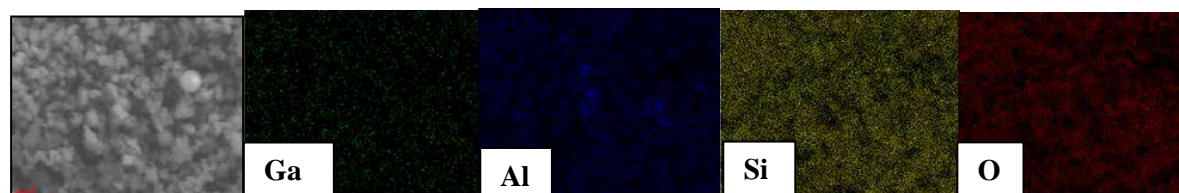


Fig. 8 The SEM and EDX images of 1% Ga-MCF-Si-MAO

Table 1. The distribution of the elements on the catalysts from EDX technique

Type of support	Element content (wt%)				Si/Al ratio
	%Si	%O	%Al	%Ga	
<b>Cab-Si-MAO</b>	40.96	46.44	12.60	-	3.25
<b>1% Ga-Cab-Si-MAO</b>	38.66	44.06	16.00	1.26	2.42
<b>MCF-Si-MAO</b>	41.77	43.11	15.12	-	2.76
<b>1% Ga-MCF-Si-MAO</b>	43.59	39.73	16.12	0.56	2.70

The crystal structure of catalysts was determined through using the technique of wide-angle X-ray diffraction (XRD), as illustrated in **Figure 9**. Similar peaks were observed in the XRD patterns of Cab-Si, 1% Ga-Cab-Si, Cab-Si-MAO, 1% Ga-Cab-Si-MAO, MCF-Si, 1% Ga-MCF-Si, MCF-Si-MAO, and 1% Ga-MCF-Si-MAO. It was found that the morphology of both supported catalysts remained unchanged following the impregnation technique. The amounts of Ga and MAO on both silica are different because of the structure and morphology of each silica support are different.

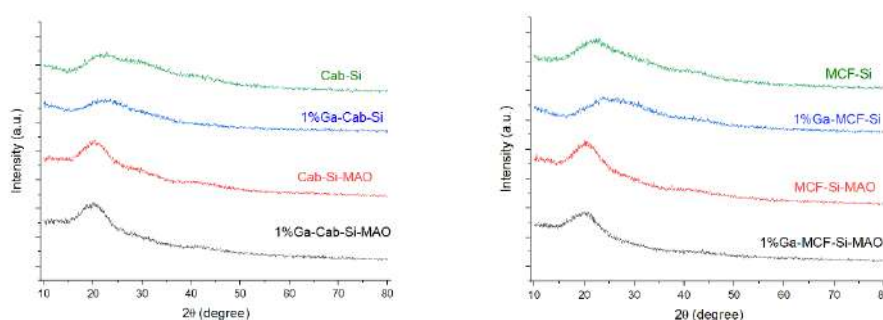


Fig. 9 The wide-angle XRD patterns of supported catalysts.

The yield and activity of the polymer products resulting from the polymerization of ethylene and ethylene/1-hexene are detailed in **Table 2**. Due to the comonomer effect, which increases the number of active sites and causes a highly exothermic reaction, the ethylene polymerization yield and activity were lower than those of the ethylene/1-hexene polymerization. In addition, supported catalysts modified with Ga exhibited higher yields and activities of polymer products compared to the original support that had not been modified with Ga.

Table 2. The yield and activity of polymerization obtained from different supports

Type support	Type of Reaction	Yield (g)	Activity (g.PE/gcat*h)
Cab-Si	HOMO	0.55	20
1%Ga-Cab-Si	HOMO	1.03	40
Cab-Si	COPO	2.29	90
1%Ga-Cab-Si	COPO	3.50	140
MCF-Si	HOMO	0.50	20
1%Ga-MCF-Si	HOMO	1.36	50
MCF-Si	COPO	2.13	90
1%Ga-MCF-Si	COPO	4.75	190

**Figures 10 and 11** illustrate, respectively, the morphological characteristics of polymer products obtained via ethylene and ethylene/1-hexene polymerization. Supported catalyst structure affects the morphology of the polymer. Comonomer insertion also contributed to the fact that crystalline polymer was produced during ethylene/1-hexene polymerization as compared to ethylene polymerization. In fact, comonomer insertion results in a decrease in crystallinity resulting in lower  $T_m$ .

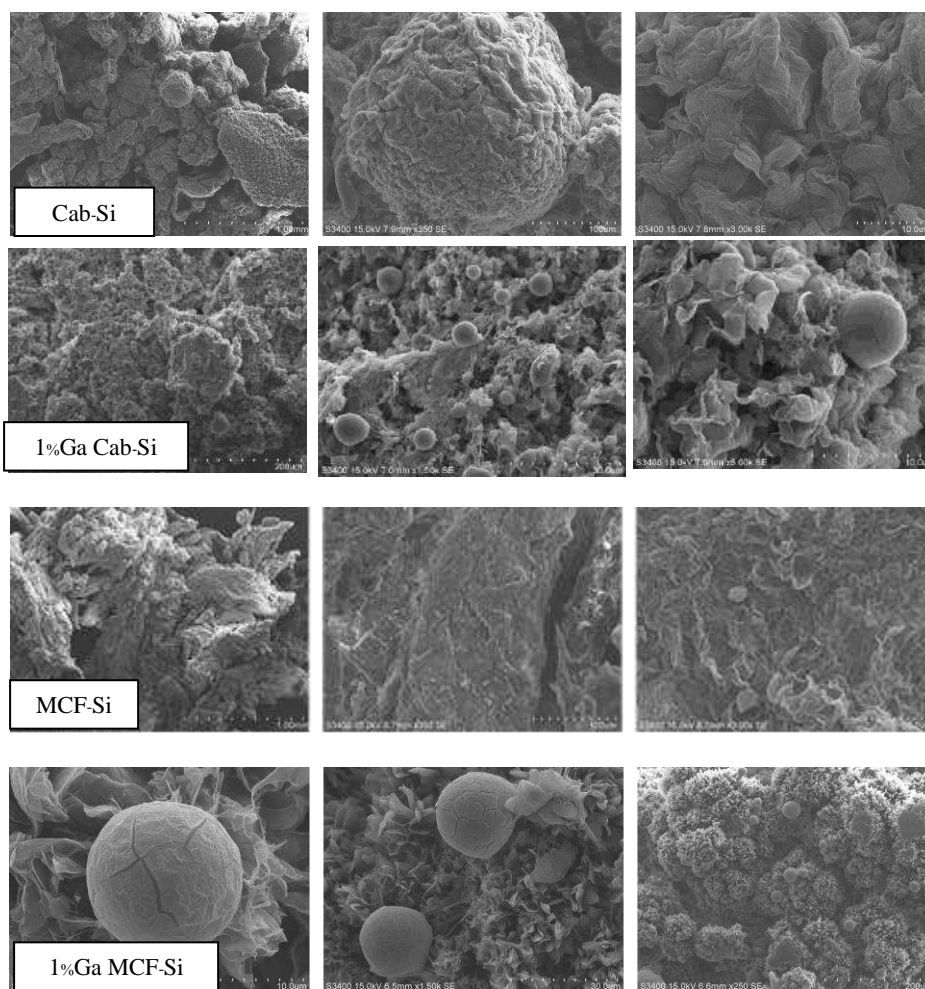
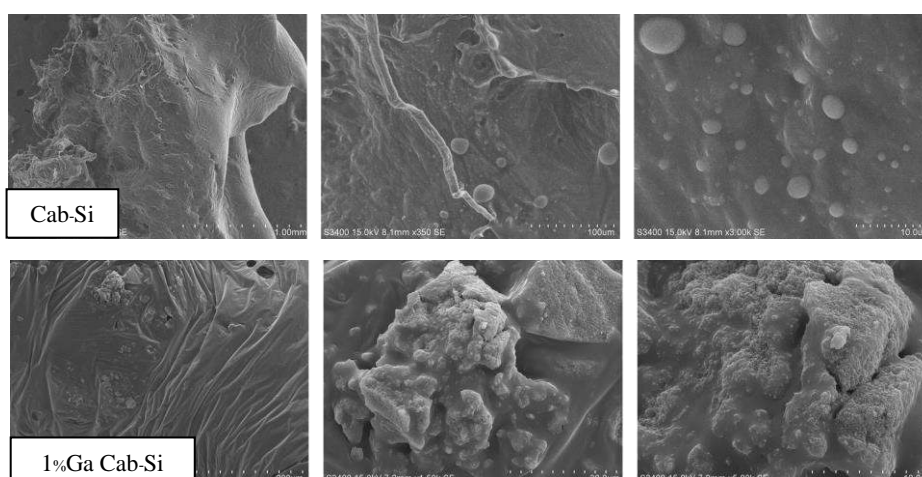


Fig. 10 The SEM image of polymers product of supported catalyst in ethylene polymerization



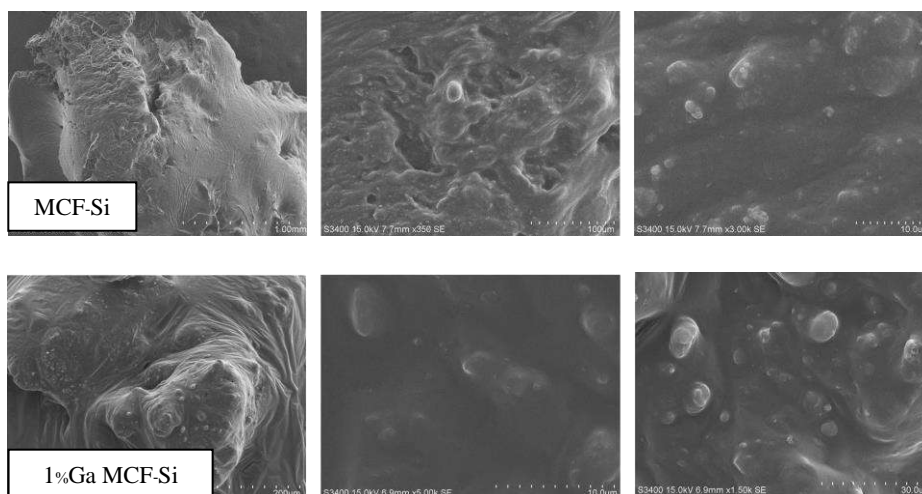


Fig. 11 The SEM image of polymers product of supported catalyst in 1-hexene polymerization

#### 4. Conclusions

The physical and chemical analyses revealed that the morphology of neither the supported catalyst impregnated with Ga nor the catalyst itself changed. In contrast, the Si/Al ratio of the supported catalyst modified treated with Ga and immobilized with MAO is lower than that of the supported catalyst not treated with Ga indicating more attached MAO with Ga modification. As a consequence, the supported catalyst that treated by Ga exhibited increased yield and activity of the polymer products.

#### 5. ACKNOWLEDGEMENTS

The author would like to thank the Thai Polyethylene, Co, Ltd (TPE) and PTTGlobal for providing some chemicals for this study.

#### References

- [1] Fink G, Steinmetz B, Zechlin J, Przybyla C, Tesche B. Propene Polymerization with Silica-Supported Metallocene/MAO Catalysts. *Chemical Reviews*. 2000;100(4):1377-90.
- [2] Manianglung C, Jeon HI, Ko YS. Synergistic effect of amine and borane in immobilized metallocene catalysts on ethylene polymerization. *Catalysis Today*. 2024;425:114352.
- [3] A. Shamiri, M.H. Chakrabarti, S. Jahan, M.A. Hussain, W. Kaminsky, P.V. Aravind, W.A. Yehye. The influence of Ziegler-Natta and metallocene catalysts on polyolefin structure, properties, and processing ability. *Mater. (Basel)* 7 (2014) 5069–5108.
- [4] P. G. Belelli, M. a. L. Ferreira and D. E. Damiani. Silica-supported metallocene for ethylene polymerization. *Applied Catalysis A: General*. 2002;228(1):189-202.
- [5] Klinthongchai Y, Prichanont S, Praserttham P, Jongsomjit B. Synthesis, characteristics and application of mesocellular foam carbon (MCF-C) as catalyst for dehydrogenation of ethanol to acetaldehyde. *Journal of Environmental Chemical Engineering*. 2020;8(3):103752.
- [6] Wannaborworn M, Jongsomjit B. Ethylene/1-Octene Copolymerization over Ga-modified SiO<sub>2</sub>-supported Zirconocene/MMAO Catalyst Using In Situ and Ex Situ Impregnation Methods. *Iranian Polymer Journal*. 2009;18:969-79.



## Utilization of Industrial Waste Cellulose for Solid Fuel Production in Pilot Plant Scale

Supawan Inthawong<sup>1</sup>, Atayut Asavarahapun<sup>2</sup>, Lek Wantha<sup>1</sup> and Atichat Wongkoblal<sup>1,\*</sup>

<sup>1</sup> School of Chemical Engineering, Institute of Engineering, Suranaree University of Technology, Nakhon Ratchasima 30000, Thailand

<sup>2</sup> Nitro Chemical Industry Ltd., 84/2 Moo 4, Rama II road, Bangtorud Sub-district, Maung District, Samut Sakhon, 74000, Thailand

E-mail: \* atichat@sut.ac.th

### Abstract

In this work, the production of solid fuel produced from mixing of industrial waste cellulose and coal is investigated. In the laboratory study, lime can be used as a binder between cellulose and coal, however in the pilot scale, the solid fuel is easily broken. This may be due to that the extruder force used in the laboratory equipment is less than that performed in the pilot machine. Therefore, the tapioca starch is introduced to use as the binder in this study. The optimal ratio between cellulose, lime, coal, and tapioca starch is investigated. It is found that coal 98% and cellulose 2% with 10% of starch has homogeneous texture and stable form. The size of cellulose less than 1 mm. and coal diameter of 300 microns are suitable for the solid fuel casting. The physical and thermal properties of all materials and chemical used in this study are analyzed, for example, moisture content, ash, volatile matter, fixed carbon and heating value. The heating value of sawdust was 15,519 J/g, while that of cellulose was 15,582 J/g. The heating value of coal was the greatest at 19,920 J/g. There is no heating value of lime evaluated. Solid fuel compositions (cellulose, lime, coal, with and without starch) are mixed in different ratios, and then it is extruded by using the charcoal compressor. The solid fuel briquettes without starch are easily broken, but the briquettes with starch are hard enough to maintain its form. The heating value of mixture materials were then determined. The coal-based solid fuel with and without starch have heating values of 16,901 and 16,745 J/g, respectively and greater than the heating value of sawdust-based solid fuel with starch of 14,734 J/g. When comparing solid briquettes with different compositions in the combustion test in the laboratory, it is found that solid fuels are not easy to ignite due to the main composition of coal. The further study for continues burning in industrial boiler will be investigated at the factory.

**Keywords:** Cellulose; Coal; Heating Value; Solid Fuel; Solid Waste

## 1. Introduction

A new economic model of Bio-Circular-Green Economic (BCG) has been established by the research community and promoted by the Thai government for sustainability-society. This is due to Thailand's biological richness, [1,2] and the most population in agricultural sector [3]. The global community is aware of health and environmental anxieties because the current environmental problems can affect the world, in terms of global warming, air pollution, and inefficient waste management. Therefore, the products derived from natural resources are become great demand. The trend of both healthy and environmentally sustainable product is increasing. Thailand would use the strengthening research and industry to make high-value products from agricultural or biological resources to generate sustainable economic growth.

In order to manage the industrial waste, this research project intends to develop the solid fuel production by using cellulose waste. It will focus on the utilization of waste materials in the nitrocellulose industry. In this industry, cellulose from cotton linter or wood pulp are used as raw material for nitrocellulose or cellulose nitrate production. However the cellulose must be loosened by picking machine and the cellulose dust are occurred, some are fallen on the floor as shown in Figure 1 and some are sent to the bag filler. There will be cellulose dust as waste from the manufacturing process, and this waste is disposed through incineration, which wastes energy and causes air pollution due to the emission of carbon dioxide (CO<sub>2</sub>). In previous study [4], the nitrocellulose waste is combined with sawdust or coal and additional lime as binder. The suitable solid fuel to combined with nitrocellulose is coal, and about 25% of lime is suitable to combine basic fuel and nitrocellulose. If the composition of lime is greater than 25%, the heating value is decreased and it becomes unstable form. However, lime is not the good binder for the larger briquettes, it cannot glue between coal and cellulose. It has shown in the literature that cassava starch is used as a binder for fuel briquettes produced from flamboyant pod, and corn cob [5] and for charcoal briquettes produced from waste rice straw [6]. Therefore, in this study the tapioca starch will be used as a binder and the suitable ratio of cellulose and coal will be investigate. The investigation in the laboratory will be applied to the pilot scale machine. The outcome of this study will be the utilization of waste cellulose as an energy source.



Fig. 1 The cellulose dust from picking machine.

## 2. Materials and Methods

### 2.1 Raw Materials

The cellulose dust is sieved with size of less than 1 mm, and coal are grided to less than 300 microns for the assessment of their physical and thermal properties.

### 2.2 Methods

#### 2.2.1 Material Characterization

Coal was analyzed for moisture, ash, volatile matter, and fixed carbon content in order to determine the quality of materials used in solid fuel compositions. The heating value of coal cellulose and tapioca starch were tested using a bomb calorimeter.

#### 2.2.2 Solid Fuel Production

The solid fuel composition of coal, cellulose was weighed according to the ratios designed in Table 1 and tapioca starch was added about 10% of total weight of coal and cellulose. The cassava starch of 10% was used as studied in the literature [5,6]. In the previous study, the greater composition of coal is, then the more stable of pellet is [4]. Then we started from the coal content of 98% and decreased its composition to 95, 90, 88 and 85%. During the mixing process, we observed the fuel textures how the homogeneous it is. The sample was moistened with a small amount of water to aid in mixing and dried at 60 °C for 24 hours before being extruded in a 1 centimeter-diameter cylindrical mold using a hydraulic press.

Table 1. Lists the weight ratios of cellulose and coal.

Test	% F and C	
	Coal (F)	Cellulose (C)
1	98	2
2	95	5
3	90	10
4	88	12
5	85	15

#### 2.2.3 Solid Fuel Production in Charcoal Compressor

To investigate the production of solid fuel in pilot scale, the commercial charcoal compressor as shown in Figure 2 is used, the composition of solid fuel in our previous study [4] are introduced. However, without tapioca starch, the solid fuel briquettes were easily broken, then the sample with starch in section 3.2.2 were used in charcoal compressor. In the combustion test, solid fuel briquettes were burned in the stove to see how easy to ignite.



Fig. 2 The charcoal compressor.

#### 2.2.4 Solid Fuel Combustion

In the combustion test, solid fuel pellet samples were burned in the crucible, while the fuel briquettes were combusted in the stove. The ignition of all samples was observed.

### 3. Results and Discussion

#### 3.1 Physical and Thermal Properties

The properties of coal used in solid fuel composition, was initially analyzed using proximate analysis. The two sets of the proximate analysis are the combustible components, which are volatile matter and fixed carbon, and the non-combustible components, which comprise of moisture and ash. The testing results are shown in Table 2.

Table 2. Proximate analysis of coal.

Test Item	Coal
moisture (%)	20.1
ash (%)	1.2
volatile matter (%)	38.8
fixed carbon (%)	39.9

The heating value of coal, sawdust and cellulose are presented in Table 3, this value is an analysis of the amount of heat released during the combustion of a specific amount of sample. The heating value of coal was greater than cellulose and sawdust which are biomass samples.

Table 3. Heating value of solid fuel composition.

Test Item	Cellulose	Coal	Sawdust
Heating value (J/g)	15,582	19,920*	15,519*

\* from ref. [4]

In our previous study [4], coal-based solid fuel with a ratio of 1:1:2 of nitrocellulose, lime and coal, yielded the maximum heating value at 13,458 J/g due to the high coal content and high heating value of coal itself. In the case of sawdust, the ratio of nitrocellulose, lime and

sawdust of 2:1:1 yielded the highest heating value of 9,453 J/g. Lime was used as a binder in solid fuel pellets. When these ratios of either coal or sawdust were used in the charcoal compressor, it was found that the solid fuel is easily broken due to the extruder force used in the laboratory equipment is less than that performed in the charcoal compressor. The sample obtained by using sawdust was not stable and easier broken compared to that using coal. The heating value obtained from these two samples were also investigated, again the heating value of the coal-based sample of 16,745 J/g was greater than that of the sawdust-based solid fuel of 14,325 J/g as shown in Table 4. This experimental value was greater than the previous study [4], this may be due to that the cellulose used in this study has heating value of 15,582 J/g which is greater than that of nitrocellulose in previous study of 11,449 J/g.

Having seen the broken of solid fuel, the tapioca starch was introduced as the new binder in this investigation. We added 10% of starch in the above sample ratio for both coal-based and sawdust-based solids, and then produced the solid fuel using the pilot machine. It was found that these solid fuels were performed stronger structure and firm. The heating value became greater due to the additional heating value of tapioca starch as shown in Table 4. In previous study [4], it was observed that as the amount of lime increased, the heating value dropped because lime has no heating value. But in this study, the addition of starch will increase the heating value because the tapioca starch is one of the biomasses.






Table 4. Heating value of coal- and sawdust-based solid fuels in the presence and absence of tapioca starch.

Test	Sample	Heating value (J/g)	
		With starch	Without starch
1	Coal	16,901	16,745
2	Sawdust	14,734	14,325

### 3.2 Physical Appearance of Solid Fuel

Because lime is not the good binder and the cellulose is used instead of nitrocellulose which releases NO<sub>x</sub> during combustion. Then the new composition of cellulose and coal with 10% of tapioca starch are investigated as shown in Table 1. In the process of extruding solid fuel pellets, samples are placed into a 1-centimeter-diameter cylindrical mold and then extruded by a hydraulic press. From Table 5, It can be observed that most solid fuel textures are non-homogeneous except sample no. 1. It tends to clump together as fibers. In terms of strength, the greater cellulose content, the stronger it is. This is due to the reinforcement of fibrous in the coal structure.

Table 5. Physical Appearance of Solid Fuel in laboratory hydraulic press with 10% starch.

Test	%Coal: %Cellulose	Coal-Based Solid Fuel	
		Appearance	Observation
1	98:2		Solid fuel textures are homogeneous, smoother surface and stable but brittle because of less reinforcement of fiber.
2	95:5		Solid fuel textures are non-homogeneous, stronger structure than sample no. 3
3	90:10		Solid fuel textures are non-homogeneous and easily broken.
4	88:12		Solid fuel textures are non-homogeneous, the fibrous can be observed on solid surface. It is hard due to reinforce fiber.
5	85:15		Solid fuel textures are non-homogeneous, the fibrous can be observed on solid surface. It is hard due to reinforce fiber.

### 3.3 The Production of Solid Fuel using Charcoal Compressor

In previous section, the composition of coal 98% and cellulose 2% with 10% of tapioca starch is suitable to produce the solid fuel from waste cellulose because it is more stable form. Therefore, this composition is mixed and used in the charcoal compressor equipment, the solid fuel texture was homogeneous as shown in Figure 3 due to that it contained most composition of coal. a single briquettes of solid fuel combustion test, it was discovered that the solid fuel is not easy to ignite due to it composes of coal. However, in the industrial used, the solid fuel is burnt in the boiler where the combustion is continuous occurred. The further study in the combustion chamber of boiler will be investigated with the nitrocellulose company.



Fig. 3 Solid fuel from the charcoal compressor.

### 3.4 Ignition test

In the combustion test of coal-based solid fuel pellets and briquettes, it was discovered that due to the non-homogeneous texture of the solid fuel, while igniting the cellulose area was burned first and smoke was observed. Though the cellulose has caught on fire and been entirely consumed by the flames, the coal may still have not ignited. Experiments containing a high proportion of cellulose, such as tests 4 and 5, were shown to be more easily combustible, however coal remains.

### 4. Conclusions

In this investigation, the composition of coal or sawdust with lime and cellulose were used to produce the solid fuel in the pilot scale. The commercial charcoal compressor was introduced, it was found that the solid fuel without tapioca starch as the binder cannot be firm after passing this machine. Then the starch was added 10% and the structure of solid fuel maintained stable. The heating value was also increased due to an additional biomass in the solid. The new composition between coal and cellulose with 10% of starch were investigated and the percentage of coal and cellulose of 98% and 2% can give the homogeneous texture of solid fuel in the hydraulic press equipment in laboratory. This mixture was also investigated using the charcoal compressor, the structure of solid fuel was good and can be applied to use in the industry. Although, it was not easy to ignite due to the content of coal, its strength can be maintained its form. The suggestion is to test the solid fuel in the industrial boiler for further study.

### 5. Acknowledgements

This work was supported by (i) Suranaree University of Technology (SUT), (ii) Thailand Science Research and Innovation (TSRI), and (iii) National Science Research and Innovation Fund (NSRF) - Grant number 179270 (FF7-706-65-36-134(B)). We also acknowledge Nitro Chemical Industry Co., Ltd. for providing cellulose.

### References

- [1] Office of National Higher Education Science Research and Innovation Policy Council. *BCG in Action* [Online]. Available: <https://www.nxpo.or.th/th/en/bcg-in-action/> [Accessed: 25 December 2022]
- [2] The National Science and Technology Development Agency. *Bio-Circular-Green Economy to be declared a national agenda - Thailand the hub of bioeconomy in ASEAN* [Online]. Available: <https://www.nstda.or.th/thaibioeconomy/138-bio-circular-green-economy-to-be-declared-a-national-agenda.html> [Accessed: 25 December 2022]

- [3] The International Trade Administration. *Thailand – Agriculture* [Online]. Available: <https://www.trade.gov/country-commercial-guides/thailand-agriculture> [Accessed: 5 January 2023]
- [4] Supawan Inthawong, Pakamas Kohmuean, Atayut Asavarahapun and Atichat Wongkoblaph, *Development of Solid Fuel Produced from Waste Cellulosic Materials*, The 32<sup>nd</sup> Thai Institute of Chemical Engineering and Applied Chemistry Conference TIChE2023 Proceedings, Kanchanaburi, Thailand, March 16-17, 2023.
- [5] Oladosu K.O., Babalola S.A., Kareem M'W', Ajimotokan H.A., Kolawole M.Y., Issa W.A., Olawore A.S. and Ponle E.A., *Optimization of fuel briquette made from bi-composition biomass for domestic heating applications*, Scientific African, 21, September 2023.
- [6] Narzary, A., Brahma, j. and Das, Amarendra K., *Utilization of waste rice straw for charcoal briquette production using three different binder*, Cleaner Energy System, 5, August 2023.



## Continuous Conversion of Fatty Acid Methyl Esters to Bio-Jet Fuel via Hydroisomerization /Hydrocracking over NiGa/Modified Beta Zeolite Catalysts

Norratat Ruthaisirirot<sup>1</sup>, Napida Hinchiranan<sup>1,2,3,\*</sup>

<sup>1</sup> Department of Chemical Technology, Faculty of Science, Chulalongkorn University, Bangkok, Thailand

<sup>2</sup> Center of Excellence on Petrochemical and Materials Technology (PETROMAT), Chulalongkorn University, Bangkok, Thailand

<sup>3</sup> Center of Excellence in Catalysis for Bioenergy and Renewable Chemicals (CBRC), Chulalongkorn University, Bangkok, Thailand

\* Corresponding author

Email: [Norratat\\_sky@hotmail.com](mailto:Norratat_sky@hotmail.com), [napida.h@chula.ac.th](mailto:napida.h@chula.ac.th)

### Abstract

Currently, the consumption of fossil fuels used for internal combustion engines in the transportation sector tends to be declined according to the replacement of electric vehicles. This consequently causes an oversupply of biodiesel in the future. To maintain the balance in the palm oil market, the biodiesel derived from palm oil has a potential to be supplied as the feedstock for producing the bio-jet fuel in accordance with the policy of International Civil Aviation Organization (ICAO) to support the use of sustainable aviation fuels (SAF). In this regard, this research focuses on the continuous hydroconversion of biodiesel derived from palm oil to bio-jet fuel in a fixed bed reactor. Due to the drawbacks of nickel (Ni)-based catalysts, such as agglomeration, extensive hydrogenolysis and coke formation during the hydroprocess, the effect of incorporation of gallium (Ga) as a second metal in bimetallic Ni-based catalysts supported on the modified beta zeolite obtained from hydrofluoric acid/ammonium fluoride (HF/NH<sub>4</sub>F) solution on the catalytic properties and reactivity was investigated. At 360 °C, 2.45 h<sup>-1</sup> weight hourly space velocity, and 30 bar H<sub>2</sub> pressures at flow rate of 60 mL/min., the results showed that the iso-/n-alkanes ratio in the liquid product obtained from the system using Ni/modified beta zeolite was improved from 0.32 for Ni/unmodified beta zeolite to 0.48. Furthermore, the addition of Ga effectively suppressed the hydrogenolysis of the Ni-based catalyst, leading an increase in the selectivity to jet fuel range from 35.7 to 44.9%.

**Keywords:** Hydroisomerization; Bio-jet; Nickel; Gallium; Fatty acid methyl esters.

### 1. Introduction

According to the enhancement of utilization of electric vehicles, the demand of conventional fuels for internal combustion engines tends to be declined [1]. Typically, the first-generation of biodiesel is produced via transesterification process of animal or vegetable oils with methanol in the presence of acid or base catalysts to form fatty acid methyl esters (FAMES). Despite FAMES possessing a high cetane number and low sulfur content, their properties are incompatible with combustion engines. These limitations include low heating value, instability, high viscosity, and acidity. These undesired properties are caused by the high oxygen content and unsaturated bonds found in the molecular structure of FAMES [2]. Consequently, the use of FAMES to replace petroleum liquid fuels faces significant obstacles.

Hence, reducing these undesired compounds and enhancing the market value of FAMES have become more attractive objectives. Catalytic conversion processes offer efficient pathways to transform FAMES to bio-jet fuel range, aligning with the International Civil Aviation Organization's (ICAO) policy to promote the use of sustainable aviation fuels (SAF) derived from hydroconversion of triglyceride-based materials [3]. Noble metals like platinum (Pt) are widely acknowledged as a remarkable catalyst for hydroprocessing reactions due to their high activity and selectivity [4, 5]. However, Pt catalysts have disadvantages in terms of high cost and susceptibility to be poisoned by sulfur and other contaminants containing in feedstocks [6]. In contrast, non-noble metals like nickel (Ni) are more practical in commercialization due to its lower cost, robustness against poisoning, and comparable catalytic activity. Moreover, Ni-based catalysts facilitate the removal of oxygenated functional groups [7-9] and produce hydrocarbons containing the suitable carbon number for the jet fuel application.

Unfortunately, monometallic Ni-base catalysts are easily deactivated by coke and agglomerate during hydroprocess. These drawbacks can induce undesired products and reduced efficiency of hydroconversion to convert FAMES as bio-jet fuel. Incorporation of a second metal in Ni-based catalysts to form bimetallic catalysts offers a highly effective approach to enhance the performance of hydroconversion in terms of activity, selectivity, and resistance to coking. This improvement is attributed to the fact that the second metal, acting as a promoter, could alter the geometric and electronic structures of Ni. Dai et al. [10] investigated that the catalytic performance of NiGa/SAPO-11 and monometallic Ni/SAPO-11 via hydroisomerization of n-hexadecane in fixed bed reactor. Their findings revealed that the NiGa/SAPO-11 catalyst exhibited the better activity than its monometallic catalysts. The addition of Ga into the supported Ni-based catalysts promoted Ni species to become more active for hydrogenation/dehydrogenation. Moreover, Ga components covered and shielded some acid sites of the supports, to reduce the acidity of the catalysts. This adjustment optimized the isomerization ability of the acid sites and the ability hydrogenation/dehydrogenation of the metal sites, resulting in an optimal synergistic catalytic state, to achieve the maximum n-hexadecane conversion of 96.76% and i-hexadecane selectivity of 91.42%.

Not only the active metal phase, but catalyst support also plays a crucial role in determining the performance of the catalysts. Zeolite is commonly used as a support for hydroprocessing due to its high surface area and acidity, which are beneficial for catalytic reactions. However, the small pore size of zeolites poses a significant challenge, leading the severe mass transfer limitation resulting to the adversely affect the activity, selectivity, and stability of the catalysts [11]. Furthermore, n-alkanes can readily diffuse deeply into the micropores of zeolites, where cracking reactions occur in parallel with isomerization. This induces the formation of smaller molecules through (s, p)  $\beta$ -scission at the microporous Brønsted acid sites. To overcome these limitations, Hunsiri et al. [12] studied the modification of beta zeolite using hydrofluoric acid/ammonium fluoride (HF/NH<sub>4</sub>F) solution as a support for Ni-based catalysts for hydroisomerization of palm olein, to produce branched-chain biofuels for bio-jet fuel production. The modified beta zeolite with 0.25 M HF in the HF/NH<sub>4</sub>F solution resulted in a higher pore volume, to facilitate hydroisomerization. In addition, the better Ni dispersion, by suppressing the agglomeration of Ni particles during catalyst preparation could prevent the over cracking of the reactants and products. These advantages provide a 43.4 wt% bio-jet fuel yield with 22.1 wt% iso-alkanes fraction. Thus, this study aims to investigate the effect of Ga in the Ni-based bimetallic catalysts supported on the modified beta zeolite on hydroisomerization/hydrocracking of FAMES to produce bio-jet fuel range.

## 2. Experimental

### 2.1 Preparation of modified bata zeolite

The NH<sub>4</sub>-beta zeolite (TOSOH Co.; SiO<sub>2</sub>/Al<sub>2</sub>O<sub>3</sub> mol ratio=27) was modified by leaching process in the presence of HF/NH<sub>4</sub>F following the procedure reported in previous study [12]. NH<sub>4</sub>F (10 g) was dissolved in a 0.25 M HF solution (60 mL). The solution was mixed with 5 g NH<sub>4</sub>-beta zeolite and stirred at room temperature for 1 h. After centrifugation and washing with deionized water (DI) until pH neutral, the wet sample was dried at 110 °C in an oven overnight. Then, the dried sample was calcined at 550 °C for 4 h to obtain the modified beta zeolite, which was denoted as beta-HF.

### 2.2. Preparation of bimetallic Ni-Ga/beta-HF catalysts

The bimetallic 5Ni5Ga/beta-HF catalysts were prepared using the incipient wetness impregnation method. In detail, the specific quantities of nickel (II) nitrate hexahydrate (Ni(NO<sub>3</sub>)<sub>2</sub>·6H<sub>2</sub>O) and gallium (III) nitrate hydrate (Ga(NO<sub>3</sub>)<sub>2</sub>·H<sub>2</sub>O) were dissolved in 6.5 mL DI water and dropped onto 5 g beta-HF. Subsequently, the impregnated samples were dried at 110 °C in an oven overnight, followed by calcination at 500 °C for 2 h. The calcined catalysts were *ex-situ* reduction in a horizontal tubular furnace at 600 °C for 2 h under H<sub>2</sub> atmosphere. Finally, the catalysts were passivated in a presence of 5/95 (v/v) oxygen (O<sub>2</sub>)/nitrogen (N<sub>2</sub>) mixed gas at room temperature overnight. For the preparation of monometallic Ni- or Ga-based catalysts, the method was similar to that used for bimetallic catalysts. Only the Ni or Ga precursor at 10 wt% was used and then dropped onto the specified supports. They were denoted as 10Ni/beta, 10Ni/beta-HF and 10Ga/beta-HF catalysts.

### 2.3. Catalyst characterization

The structural properties of the catalysts were characterized by X-ray diffraction (XRD; Bruker D8 Advance) technique. The 2θ was adjusted between 5 and 80° with a step size of 0.2 degree. The reduction temperature of the calcined catalysts was evaluated by using H<sub>2</sub>-temperature programmed reduction profile recorded by Chemisorption analyzer (BELCAT II). Briefly, a sample (50 mg) was pretreated at 110 °C to remove the moisture before analysis. The measurement step was conducted at the range of 200 to 800 °C with a heating rate of 10 °C/min under the 5/95 (v/v) hydrogen (H<sub>2</sub>)/argon (Ar) mixed gas.

### 2.4. Hydroisomerization/hydrocracking of FAMES

FAMES derived from palm oil were manufactured by Bangchak Corporation Public Co., Ltd., Bangkok, Thailand. It consisted of 49.3% methyl palmitate (C<sub>17</sub>H<sub>34</sub>O<sub>2</sub>), 43.8% methyl oleate (C<sub>19</sub>H<sub>36</sub>O<sub>2</sub>), 5.9% methyl stearate (C<sub>19</sub>H<sub>38</sub>O<sub>2</sub>), and 1.1% methyl myristate (C<sub>15</sub>H<sub>30</sub>O<sub>2</sub>). The hydroisomerization/hydrocracking of FAMES was conducted in a continuous-downflow stainless steel fixed-bed reactor (ø=10 mm; L= 300 mm). Before starting the reaction, 2.0 g passivated catalysts were placed between a layer of quartz wool at top and glass beads (5 g) at bottom of the reactor, which was located at the middle of the vertical tubular furnace. When the reactor was heated to 360 °C, the H<sub>2</sub> gas was fed into the reactor at a flow rate of 60 mL/min. The pressure inside the reactor was controlled to be constant at 30 bar by a back pressure regulator. FAMES was then introduced into the reactor via a high-pressure liquid micro-pump at a weight hourly space velocity (WHSV) of 2.45 h<sup>-1</sup>. Each test was conducted with a time on

stream for 3 h. The liquid product was collected after waiting for 1 h to ensure that some liquid trapped in the catalyst or inside the reactor was removed.

Qualitative analysis of the liquid products was carried out using a gas chromatography-mass spectroscopy technique (GC-MS; Shimadzu, GCMS-QP2020NX). The sample (10,000 ppm of liquid product in ethyl acetate) was injected at 300 °C and the column temperature was heated from 40 °C to 280 °C with a heating rate of 5 °C/min. The liquid product was also quantitatively analyzed using a gas chromatography equipped with flame ionization detector (GC-FID; Agilent 7890A) using a similar method for GC-MS as mentioned above to calculate the degree of FAMES conversion.

### 3. Results and discussion

#### 3.1. Catalyst characterization

X-ray diffraction (XRD) analysis was conducted to examine the diffraction patterns of each Ni-based catalyst as shown in Fig. 1. It was evidence that even after leaching the zeolite with NH<sub>4</sub>F/HF (10Ni/beta-HF), it still exhibited characteristic diffraction peaks ( $2\theta = 6.60\text{--}9.17^\circ$  and  $21.82\text{--}23.14^\circ$ ). These peaks were attributed to the (101) plane, indicating a highly distorted structure resulting from various isomorphs, and the (302) plane, suggesting lattice contraction/expansion of the beta zeolite framework [12], respectively. This pattern closely resembled that of the parent zeolite (10Ni/beta). This indicated that the etching zeolite preserved the structure of zeolite. To study the impact of support and Ga loading on Ni crystalline size, the Ni crystallite size was estimated using Scherrer's equation [13] as summarized in Table 1. The Ni crystalline size in the 10Ni/beta and 10Ni/beta-HF catalysts were 20.4 and 17.5 nm, respectively. It was observed that the modified support yields the smaller Ni particle sizes possibly due to its larger pore size [12], which induced the formation of smaller-sized Ni particles. When Ga was loaded into the catalyst, the Ni particle size was also decreased to 12.4 nm for the 5Ni5Ga/beta-HF catalyst. It was possible that the addition of Ga inhibited the Ni agglomeration, resulting in a smaller size of Ni particle [10]. This result suggested that the addition of Ga improved the Ni dispersion. It was further confirmed by H<sub>2</sub>-TPR technique. As depicted in Fig. 2, the 5Ni5Ga/beta-HF catalyst showed the reduction profile indicating a higher temperature than the 10Ni/beta-HF catalyst. This result indicated a stronger interaction between Ni and the support material possibly related to the better Ni dispersion.

Table 1. The Ni crystalline size in each Ni-based catalyst.

Catalysts	Ni crystalline size (nm) <sup>a</sup>
10Ni/beta	20.4
10Ni/beta-HF	17.5
5Ni5Ga/beta-HF	12.4
10Ga/beta-HF	-

<sup>a</sup> Calculated by XRD using Scherrer's equation.

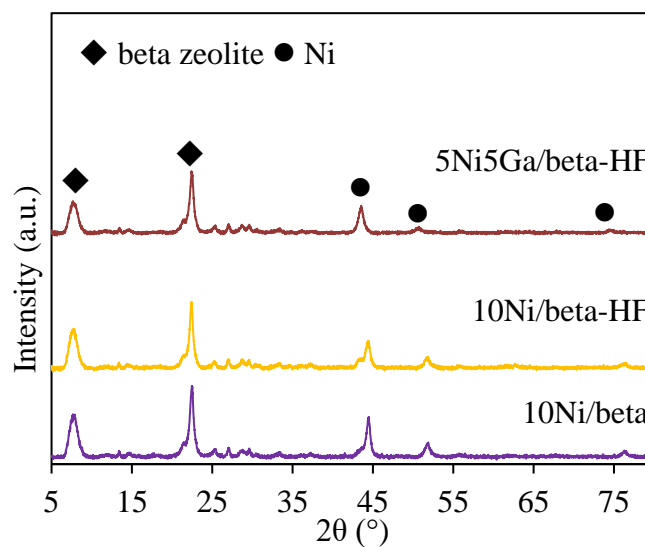


Fig. 1 XRD pattern of each Ni-based catalyst.

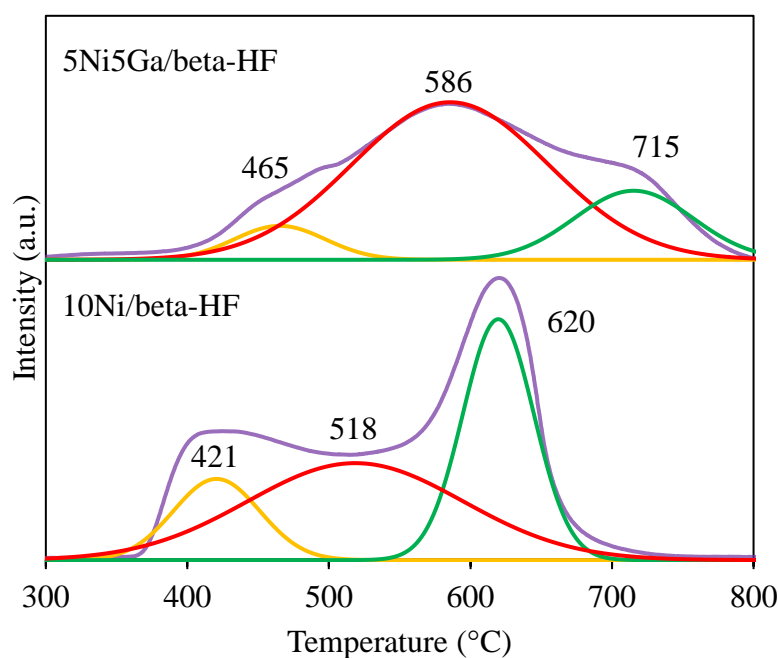


Fig. 2 H<sub>2</sub> - TPR profiles of 10Ni/beta-HF and 5Ni5Ga/beta-HF catalysts.

### 3.2. Catalytic performance

To study the catalytic performance on FAMES conversion into bio-jet fuel, the 10Ni/beta, 10Ni/beta-HF, 5Ni5Ga/beta-HF, and 10Ga/beta-HF catalysts were comparatively evaluated in terms of FAMES conversion and jet fuel range selectivity. As reported in Table 2, all catalysts exhibited the high catalytic performance on FAMES conversion to achieved 94.9% to 98.1%.

The 10Ni/beta and 10Ni/beta-HF catalysts were first compared to study the effect of support. Although the jet-fuel range selectivity obtained from the system using 10Ni/beta (37.6%) and 10Ni/beta-HF (35.7%) catalysts did not show a significant difference, the product compositions based on structural similarity, as shown in Table 3 indicated that the 10Ni/beta-HF catalyst provided the liquid product having the higher iso-/n-alkanes (i/n) ratio of 0.48. While the liquid product collected from the system using 10Ni/beta catalyst had i/n ratio of 0.32. This suggested that the synergistic effect of the larger pore size of beta-HF associated with the enhanced Ni dispersion and a higher Bronsted acid to Lewis acid ratio (B/L ratio) of modified support [12] contributed the higher catalytic performance to convert n-alkanes to branched isomers.

In the case of bimetallic catalysts, the addition of Ga to the catalyst exhibited a positive effect on the jet-fuel range selectivity (Table 3). Specifically, the jet-fuel range selectivity was improved from 35.7% over 10Ni/beta-HF to 44.9% over 5Ni5Ga/beta-HF catalyst. This result suggested that the catalytic performance of 10Ni/beta-HF can be further improved by the addition of Ga, leading the higher jet-fuel range selectivity. However, the jet-fuel range selectivity declined to 22.4% when the monometallic 10Ga/beta-HF catalyst was applied.

The studied catalysts with different metal compositions also showed different product compositions based on structural similarity as shown in Table 3. The quantities of iso-alkanes in the liquid product obtained over the catalysts followed in the sequence of 5Ni5Ga/beta-HF > 10Ni/beta-HF > 10Ga/beta-HF. This implied that Ga could enhance the isomerization ability of Ni-based catalysts [10]. On the other hand, the amounts of oxygen compounds obtained from all catalysts displayed a different order of 10Ga/beta-HF > 5Ni5Ga/beta-HF > 10Ni/beta-HF. This result implied that Ga did not promote hydrodeoxygenation, as evidenced by a higher amount of oxygen compounds of 10Ga/beta-HF (65.9%) compared to 10Ni/beta-HF (21.2%).

Table 2. Effect of catalyst types on the FAMEs conversion and compositions in the liquid product based on the carbon number derived from hydroisomerization/hydrocracking of FAMEs.

Catalysts	FAMEs conversion	Gasoline ( $\leq C_8$ )	Jet (C <sub>9</sub> -C <sub>14</sub> )	Diesel ( $\geq C_{15}$ )
10Ni/beta	98.0	18.6	37.6	43.8
10Ni/beta-HF	98.1	23.2	35.7	41.1
5Ni5Ga/beta-HF	97.5	25.0	44.9	30.1
10Ga/beta-HF	94.9	12.7	22.4	64.9

Table 3. Effect of catalyst types on the product compositions based on structural similarity and i/n ratio obtained from hydroisomerization/hydrocracking of FAMEs.

Catalysts	n-Alkanes	iso-Alkanes	Cyclics	Aromatics	Oxy. comp.	Unsat. comp.	i/n ratio
10Ni/beta	36.8	11.7	7.60	27.4	15.3	1.30	0.32
10Ni/beta-HF	29.6	14.1	11.0	23.0	21.2	1.03	0.48
5Ni5Ga/beta-HF	13.7	14.7	11.8	28.5	28.8	2.43	1.07
10Ga/beta-HF	8.60	5.22	3.38	14.6	65.9	2.27	0.61

#### 4. Conclusions

In summary, Ni-based catalysts were synthesized through the incorporation of a second metal (Ga), while beta zeolite was modified via acid treatment (HF/NH<sub>4</sub>F) to use as the catalyst's support. The physicochemical characterizations of the prepared catalysts were examined. XRD analysis revealed that the modification of beta zeolite via acid treatment did not significantly affect its structure. However, this modification provided the smaller crystalline size of Ni particles deposited on the surface of the modified beta catalyst. This indicated the effective suppression of the agglomeration of Ni particles and provided a higher iso-/n-alkanes ratio at 0.48. Additionally, H<sub>2</sub>-TPR analysis indicated the shifted of the reduction peaks toward the higher temperature, which implied that the incorporation of Ga could reduce the crystalline size of Ni by the synergistic interaction between Ni and Ga, thereby enhancing catalytic performance. Specifically, the 5Ni5Ga/beta-HF catalyst exhibited the highest selectivity for jet-fuel range of 44.9%, with iso-/n-alkanes ratio of 1.07.

#### 5. Acknowledgements

The authors gratefully acknowledge the Department of in Chemical Technology, Faculty of Science, Chulalongkorn University for the financial support.

#### References

- [1] Europe's gasoline, diesel car sales loss majority market share to EVs for first time, 2023.[Online: <https://www.spglobal.com/commodityinsights/en/market-insights/latest-news/oil/020123-europes-gasoline-diesel-car-sales-lose-majority-market-share-to-evs-for-first-time?fbclid=iwar2hjpb27yzpvj7rjo5r0-c4nirvauzoajpatqfoxcaugb4sqhmtyw8smqi>] accessed 22 September 2023.
- [2] Xiao, Y., Shang, J., Zhai, M., Qiao, C. (2021). Hydrodeoxygenation of fatty acid methyl esters and simultaneous products isomerization over bimetallic Ni-Co /SAPO-11 catalysts. *International Journal of Energy Research* 45(6), 9648-9656.
- [3] น้ำมันอากาศยานแบบยั่งยืน (sustainable aviation fuels) โอกาสที่ไม่ควรมองข้าม ของอุตสาหกรรมเชื้อเพลิงชีวภาพและการบินของไทย, 2021.[Online: <https://www.scbeic.com/th/detail/product/7523>] accessed 21 July 2023.
- [4] Hengsawad, T., Srimingkwanchai, C., Butnark, S., Resasco, D.E., Jongpatiwut, S. (2018). Effect of Metal–Acid Balance on Hydroprocessed Renewable Jet Fuel Synthesis from Hydrocracking and Hydroisomerization of Biohydrogenated Diesel over Pt-Supported Catalysts. *Industrial & Engineering Chemistry Research* 57(5), 1429-1440.
- [5] Kim, M.Y., Kim, J.-K., Lee, M.-E., Lee, S., Choi, M. (2017). Maximizing Biojet Fuel Production from Triglyceride: Importance of the Hydrocracking Catalyst and Separate Deoxygenation/Hydrocracking Steps. *ACS Catalysis* 7(9), 6256-6267.
- [6] Chaveanghong, S., Nakamura, T., Takagi, Y., Cagnon, B., Uruga, T., Tada, M., Iwasawa, Y., Yokoyama, T. (2021). Sulfur poisoning of Pt and PtCo anode and cathode catalysts in polymer electrolyte fuel cells studied by operando near ambient pressure hard X-ray photoelectron spectroscopy. *Phys Chem Chem Phys* 23(6), 3866-3873.
- [7] Chintakanan, P., Vitidsant, T., Reubroycharoen, P., Kuchonthara, P., Kida, T., Hinchiranan, N. (2021). Bio-jet fuel range in biofuels derived from hydroconversion of palm olein over Ni/zeolite catalysts and freezing point of biofuels/Jet A-1 blends. *Fuel* 293, 120472.

- [8] Yang, H., Du, X., Zhou, L., Li, D., Hu, C. (2023). Enhanced deoxygenation performance and coke resistance of Ni-based catalysts for jatropha oil conversion by rare earth elements. *Fuel* 334.
- [9] Liu, C.-y., Yang, H., Jing, Z.-y., Xi, K.-z., Qiao, C.-z. (2016). Hydrodeoxygenation of fatty acid methyl esters and isomerization of products over NiP/SAPO-11 catalysts. *Journal of Fuel Chemistry and Technology* 44(10), 1211-1216.
- [10] Dai, X., Cheng, Y., Si, M., Wei, Q., Huang, W., Yang, H., Zhou, Y. (2022). A non-noble metal supported catalyst with potential prospect for hydroisomerization of n-hexadecane: Second metal incorporated NiMe/SAPO-11 catalyst with superior hydroisomerization performance. *Fuel* 324, 124517.
- [11] Suárez, N., Pérez-Pariente, J., Márquez-Álvarez, C., Grande Casas, M., Mayoral, A., Moreno, A. (2019). Preparation of mesoporous Beta zeolite by fluoride treatment in liquid phase. Textural, acid and catalytic properties. *Microporous and Mesoporous Materials* 284, 296-303.
- [12] Hunsiri, W., Chaihad, N., Ngamcharussrivichai, C., Tungasmita, D.N., Reubroycharoen, P., Hinchiranan, N. (2023). Branched-chain biofuels derived from hydroisomerization of palm olein using Ni/modified beta zeolite catalysts for biojet fuel production. *Fuel Processing Technology* 248, 107825.
- [13] Richardson, J. (2003). X-ray diffraction study of nickel oxide reduction by hydrogen. *Applied Catalysis A: General* 246(1), 137-150.



## Sustainable Heat Exchanger Network Synthesis Using Linearization Method

Dzata Hadi Nugrah<sup>1</sup>, and Kitipat Siemanond<sup>2\*</sup>

<sup>1</sup>Petroleum and Petrochemical Collage, Chulalongkorn University, Bangkok, Thailand and <sup>2</sup>Petroleum and Petrochemical Collage, Chulalongkorn University, Bangkok, Thailand.  
E-mail: \* kitipat.s@chula.ac.th

### Abstract

The Paris Agreement aims to reduce global warming by 45% by 2030 and reach a net-zero target by 2050, CO<sub>2</sub> emissions have also become the trend right now to reduce global warming and gain credit from it. Heat Exchanger Network Synthesis (HENS) is a method to reduce energy use, affecting environmental, social, and economic impact. Stage-wise superstructure (SWS) is a mathematical programming model using Mixed Integer Nonlinear Programming (MINLP) to synthesize HENS. The area term in SWS becomes an obstacle for the computational process because of nonlinearity. This research will be focused on the sustainable aspect by adding a CO<sub>2</sub> emission variable into the SWS model and reducing nonlinear terms. The credit gained from CO<sub>2</sub> emission reduction by exchanger-heat recovery will be subtracted from overall cost in the objective function. The linearization method will be applied to reduce nonlinear terms in the model by converting the continuous model to a discrete model. Linearization terms will significantly reduce the processing time problems and make more robust HENS models to generate the most cost-effective design.

**Keywords:** Heat Exchanger Network Synthesis; CO<sub>2</sub> Emission; Sustainability; Linearization.

### 1. Introduction

Global warming is a world problem right now. The Paris Agreement aims to reduce 45% emissions by 2030 and reach the net zero target by 2050 world, result reduces temperature to 1.5 degrees Celsius. Decreasing energy in several resources such as natural gas and coal, opens the eyes of people worldwide to begin to find alternative energy resources. In another way we also need to investigate the sustainability aspect of energy usage. Energy recovery is one of the solutions to use our energy sustainably. Heat Exchanger Network Synthesis (HENS) is used to generate energy recovery. It can be connected to minimizing Total Annual Cost (TAC). Carbon credit is currently an alternative to maximize profit from credit to reducing CO<sub>2</sub> emissions. The stage-wise superstructure (SWS) model from Yee and Grossman [1] is a mathematical programming model using MINLP to synthesize HENS. The area term in SWS becomes an obstacle for the computational process because of nonlinearity. SWS model from Yee and Grossman [1] were popular models that we used to find the optimal HEN design for this study. Moreover, the area variable specific on the Logarithmic Mean Temperature Difference (LMTD) term still becomes problematic in finding solutions due to the non-convex and nonlinearity. Chen approximation [3] changed the area term to become less nonlinear, this method still has limitations in finding the solution.

This research will focus on developing the area term in HEN model to minimize TAC. Faria and Bagajewicz [2] present the linearization method by converting the temperature difference

variable to parameter. On this research some constraints, and logic were slightly different from the Faria and Bagajewicz [2].

## 2. HEN Model

This research reduced the nonlinear from the model by adding the assumption that is listed below this.

- Heat exchangers use countercurrent model
- Heat capacities value is constant
- Heat transfer coefficients value is constant

### 2.1. Objective Function

Objective Function to reduce the Total Annual Cost (TAC) by minimizing the variable that becomes a parameter of Capital Expenditure (CAPEX) and Operation Expenditure (OPEX). TAC is the trade-off between utilities, CO<sub>2</sub> carbon credit, unit number, and area.

$$\begin{aligned}
 \min & \left( C_{cu} \sum_I q_{cu}(I) - C_{cucarbon} \sum_{J,K} q(I, J, K) \right. \\
 & + C_{hu} \sum_J q_{hu}(J) - C_{hucarbon} \sum_{I,K} q(I, J, K) \\
 & + C_{he} \sum_{I,J,K} z(I, J, K) + \sum_I z_{cu}(I) + \sum_J z_{hu}(J) \\
 & + C_{Ahe} \sum_{I,J,K} a(I, J, K) + C_{Acu} \sum_I a_{cu}(I) \\
 & \left. + C_{Ahu} \sum_J a_{hu}(J) \right) \quad (1)
 \end{aligned}$$

### 2.2. Overall heat balance for each stream

$$(T_{INI}(I) - T_{OUTI}(I)) \cdot F(I) = \sum_{J,K} q(I, J, K) + q_{cu}(I) \quad (2)$$

$$(T_{OUTJ}(J) - T_{INJ}(J)) \cdot F(J) = \sum_{I,K} q(I, J, K) + q_{hu}(J) \quad (3)$$

### 2.3. Heat balance at each stage

$$(t_{i,k} - t_{i,k+1}) \cdot F(I) = \sum_j q(I, J, K) \quad (4)$$

$$(t_j(J, K) - t_j(J, K + 1)) \cdot F(J) = \sum_I q(I, J, K) \quad (5)$$

### 2.4. Superstructure inlet temperature

$$T_{INJ}(J) = t_j(J, NOK + 1) \quad (6)$$

$$T_{INJ}(J) = t_j(J, NOK + 1) \quad (7)$$

## 2.5. Feasibility of temperatures

$$ti(I, K) \geq ti(I, K + 1) \quad (8)$$

$$tj(J, K) \geq tj(J, K + 1) \quad (9)$$

$$TOUTI(I) \leq ti(I, NOK + 1) \quad (10)$$

$$TOUTJ(J) \geq tj(J, K1) \quad (11)$$

## 2.6. Hot and Cold Utility Load

$$(ti(I, NOK + 1) - TOUTI(I)) \cdot F(I) = qcu(I) \quad (12)$$

$$(TOUTJ(J) - tj(J, K1)) \cdot F(J) = qhu(J) \quad (13)$$

## 2.7. Logical Constrains

$$q(I, J, K) - \Omega \cdot z(I, J, K) \leq 0 \quad (14)$$

$$qhu(J) - \Omega \cdot zhu(J) \leq 0 \quad (15)$$

$$qcu(I) - \Omega \cdot zcu(I) \leq 0 \quad (16)$$

$$z(I, J, K), zcu(I), zhu(J) = 0, 1 \quad (17)$$

## 2.8. Approach Temperature

$$\Delta t(I, J, K) \leq (ti(I, K) - tj(J, K)) + \Gamma \cdot (1 - z(I, J, K + 1)) \quad (18)$$

$$\Delta t(I, J, K + 1) \leq (ti(I, K + 1) - tj(J, K + 1)) + \Gamma \cdot (1 - z(I, J, K)) \quad (19)$$

$$\Delta t_{cu}(I) \leq (ti(I, NOK + 1) - T_{outCU}) + \Gamma \cdot (1 - zcu(I)) \quad (20)$$

$$\Delta t_{hu}(J) \leq (T_{outHU} - tj(J, K1)) + \Gamma \cdot (1 - zhu(J)) \quad (21)$$

## 2.9. Minimum Approach Temperatures

$$\Delta t(I, J, K) \geq EMAT \quad (22)$$

$$\Delta t_{cu}(I) \geq EMAT \quad (23)$$

$$\Delta t_{hu}(J) \geq EMAT \quad (24)$$

$$d\Delta t(I, J, K) = ti(I, K) - tj(J, K) \quad (25)$$

## 2.10. Area Calculation

$$a_{ijk} = \frac{q_{ijk} \left( \frac{1}{UH(i)} + \frac{1}{UC(j)} \right)}{\left( \Delta t_{ijk} \cdot \Delta t_{ijk+1} \frac{\Delta t_{ijk} \cdot \Delta t_{ijk+1}}{2} \right)^{1/3}} \quad (26)$$

$$a_{i,cu} = \frac{q_{i,cu} \left( \frac{1}{UH(i)} + \frac{1}{UCU} \right)}{\left( \Delta t_{cu_i} \cdot (TOUTI(i) - TINCUI) \frac{\Delta t_{cu_i} \cdot (TOUTI(i) - TINCUI)}{2} \right)^{1/3}} \quad (27)$$

$$a_{j,hu} = \frac{q_{j,hu} \left( \frac{1}{UC(j)} + \frac{1}{UHU} \right)}{\left( \Delta t_{hu_j} \cdot (TINHU - TOUTJ(j)) \frac{\Delta t_{hu_j} \cdot (TINHU - TOUTJ(j))}{2} \right)^{1/3}} \quad (28)$$

Eq. (26-28) is the equation of area calculation using the approach by Chen [5], this equation helps reduce nonlinearity. Eq. (1-25) are adapted from SWS model proposed by Yee and Grossman [1].

### 3. Linearization Model

This model was inspired by Faria and Bagajewicz [2]. The model is slightly different where Eq. (31-34) to discrete the temperature difference,  $N+1$  and  $M+1$  at Eq. (30,32) is the logic for discrete temperature difference.  $Rn$  and  $Rm$  are number of discrete at each stage, Eq. (33,34)  $Rn$  and  $Rm$  use to limit the discrete number to equal 1 match between  $\Delta td1_{I,J,K,N}$  and  $\Delta td2_{I,J,K,M}$ . Eq. (35-38) are the constrains to substitute  $\Delta td1_{I,J,K,N}$  and  $\Delta td2_{I,J,K,M}$  into area term in Eq. (26-28),  $G_{I,J,K,N,M}$  at Eq. (35) are represent of LMTD.

$$\sum_N Rn_{I,J,K,N} \cdot \Delta td1_{I,J,K,N} \leq \Delta t_{I,J,K} \leq \sum_N Rn_{I,J,K,N} \cdot \Delta td1_{I,J,K,N+1} \quad (29)$$

$$\sum_N Rn_{I,J,K+1,N} \cdot \Delta td1_{I,J,K+1,N} \leq \Delta t_{I,J,K+1} \leq \sum_N Rn_{I,J,K+1,N} \cdot \Delta td1_{I,J,K+1,N+1} \quad (30)$$

$$\sum_M Rm_{I,J,K,M} \cdot \Delta td2_{I,J,K,M} \leq \Delta t_{I,J,K} \leq \sum_M Rm_{I,J,K,M} \cdot \Delta td2_{I,J,K,M+1} \quad (31)$$

$$\sum_M Rm_{I,J,K+1,M} \cdot \Delta td2_{I,J,K+1,M} \leq \Delta t_{I,J,K+1} \leq \sum_M Rm_{I,J,K+1,M} \cdot \Delta td2_{I,J,K+1,M+1} \quad (32)$$

$$\sum_N Rn_{I,J,K,N} = 1 \quad (33)$$

$$\sum_M Rm_{I,J,K+1,M} = 1 \quad (34)$$

$$q_{I,J,K} \cdot \left( \frac{1}{UH(I)} + \frac{1}{UC(J)} \right) - \sum_{N,M} B_{I,J,K,N,M} \cdot G_{I,J,K,N,M} \leq 0 \quad (35)$$

$$\sum_N B_{I,J,K,N,M} - \Psi \cdot Rm_{I,J,K,M} \leq 0 \quad (36)$$

$$\sum_M B_{I,J,K+1,N,M} - \Psi \cdot Rn_{I,J,K+1,N} \leq 0 \quad (37)$$

$$\sum_{N,M} B_{I,J,K,N,M} - a_{I,J,K} = 0 \quad (38)$$

### 4. CO<sub>2</sub> Emissions Variable

Carbon credit relates to reduction of CO<sub>2</sub> emission from heat exchanger load or energy saving from utility in HEN. The price of carbon in this research uses is 0.04\$/kg of CO<sub>2</sub> [3]. Calculation of carbon credit comes from total energy that HEN recovers or from hot and cold utility saving.

Table 1 CO<sub>2</sub> production of electricity and heat from several technology and energy source [4]

Technology and Source for Hot and Cold Utility	Overall CO <sub>2</sub> Emission (After Calculated with Efficiency of Combustion) (kg CO <sub>2</sub> (kWh) <sup>-1</sup> )
--	---

<b><i>electricity production</i></b>	
Coal-fired power plant	0.955
Methane	0.467
Oil and Diesel	0.748
<b><i>heat production</i></b>	
Coal to Steam	0.401
Methane to steam	0.221

Hot utility heat source is from methane to steam combustion from Table 1, this is an assumption of no specific information of what source and technology of hot utility and cold utility from study case Table 4. Cold utility energy source come from electricity, this research took example of Thailand electricity source composition, the data presented in Table 2.

Table 2 Share of Electricity Generation by Energy Source from EGAT 2023 [7].

<b>Type of Fuel</b>	<b>Percentage (%)</b>
Natural gas	60.47
Coal	19.31
Renewable energy	17.78
Fuel oil and palm oil	0.19
Diesel oil	1.37
Other (Laos, Malaysia, Lamtakong Jolbha Vadhana)	0.88
<b>Total</b>	<b>100.00</b>

Natural gas, coal, and diesel oil data from Table 2 are the main sources of CO<sub>2</sub> emission from Thailand electricity. Energy composition percentage used in calculation for CO<sub>2</sub> emission shows in Table 3.

Table 3 CO<sub>2</sub> Variables Input Calculation

<b>Carbon price * Energy Composition percentage * CO<sub>2</sub> Emission</b>	
Ccucarbon	$0.04\$/\text{kgCO}_2 * ((0.6047 * 0.467\text{kgCO}_2/\text{kWh}) + (0.1931 * 0.955\text{kgCO}_2/\text{kWh}) + (0.0137 * 0.748\text{kgCO}_2/\text{kWh}))$
Chucarbon	$0.04\$/\text{kgCO}_2 * (1 * 0.221\text{kgCO}_2/\text{kWh})$

Note: Table 3 is calculation variable for objective function at Eq (1).

## 5. Result and Discussion

Study case processing with GAMS software (version 24.2.1), MINLP model is solve using DICOPT (version 24.2.1) in laptop (AMD RYZEN™ 7 5800H CPU @3.20 GHz, Ram 16 GB). This researcher also does the comparison with different EMAT to observe the effect of changes in the EMAT due to Total Annual cost and amount of energy recovery at stream which is related to CO<sub>2</sub> emission reduced.

Table 4 Study Case from Faria and Bagajewicz [2]

<b>Stream</b>	<b>Ti K</b>	<b>To K</b>	<b>H kW/(m<sup>2</sup>K)</b>	<b>F kW/K</b>
H1	433.15	366.15	0.06	2.634
H2	522.15	411.15	0.06	3.162

H3	500.15	339.15	0.06	4.431
H4	472.15	339.15	0.06	5.319
C1	333.15	433.15	0.06	2.286
C2	389.15	495.15	0.06	1.824
C3	311.15	494.15	0.06	2.532
C4	355.15	450.15	0.06	5.184
C5	366.15	478.15	0.06	4.170
CU	311.15	355.15	0.06	
HU	544.15	422.15	0.06	

*EMAT = 10*

Table 5 Cost Variables of Study Case [2]

	Che (\$)	CA (\$/m <sup>2</sup> )	C(\$/kWyear)
HE	5291.9	77.79	
CU		77.79	53349* <sup>1</sup>
HU		77.79	566167* <sup>2</sup>

Note: \*<sup>1</sup> cost variable for Ccu and \*<sup>2</sup> cost variable for Chu

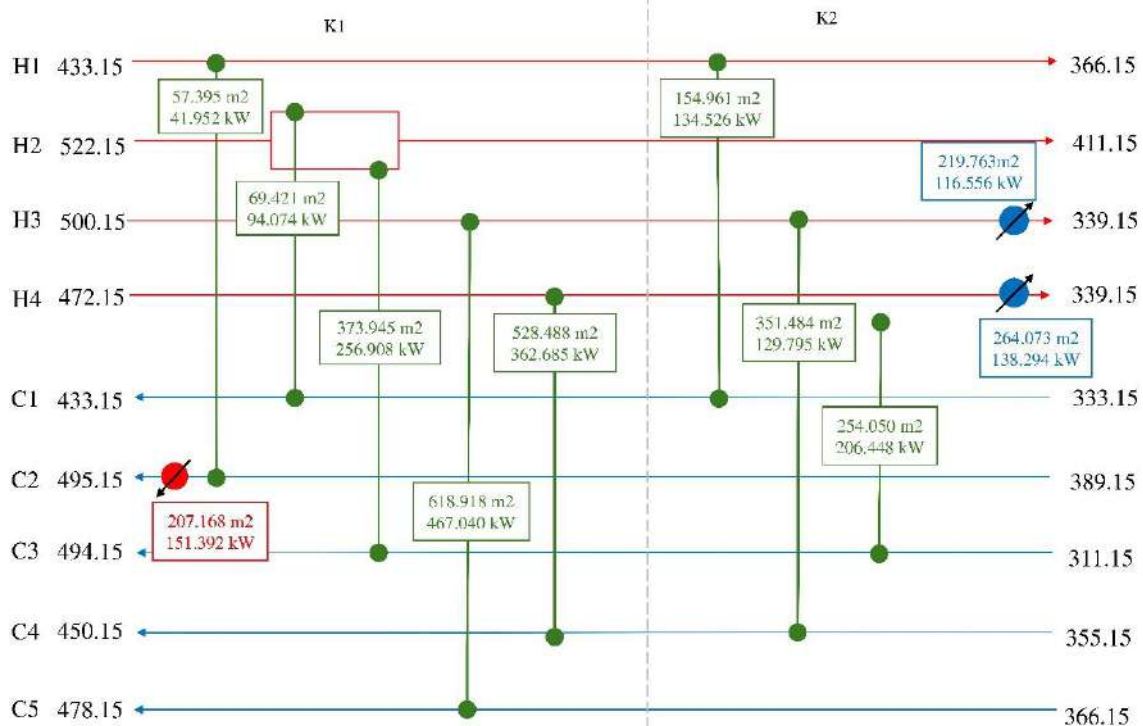


Figure 1 This Research Result of study case with  $EMAT = 10$

Fig (1) shows the area and number of energy used at each heat exchanger and utilities. The design for heat exchanger network has eight units of heat exchangers, one hot utility, and two cold utilities. The result from the study case had TAC of **99,280.37 k\$/year**, which is lower than reference [1]. Parameter cost and the  $EMAT$  of the study case referenced from Table (4,5). The total energy recovery from HEN or savings in hot and cold utilities is 3386.87 kW, equivalent to reducing **10,355.26 ton CO<sub>2</sub>/year**.

Table 6 This Research Result Comparison with Different EMAT Value

EMAT	Energy Recovery (kW)	Total Annual Cost (k\$/year)
7	3,411.18	91,852.39
8	3,393.59	97,044.89
9	3,390.50	98,150.66
10	3,386.87	99,280.37
11	3,370.06	104,509.37

Table 6 shows the difference between EMAT values due to TAC, in this case lowering the EMAT value result lowers the objective function result.

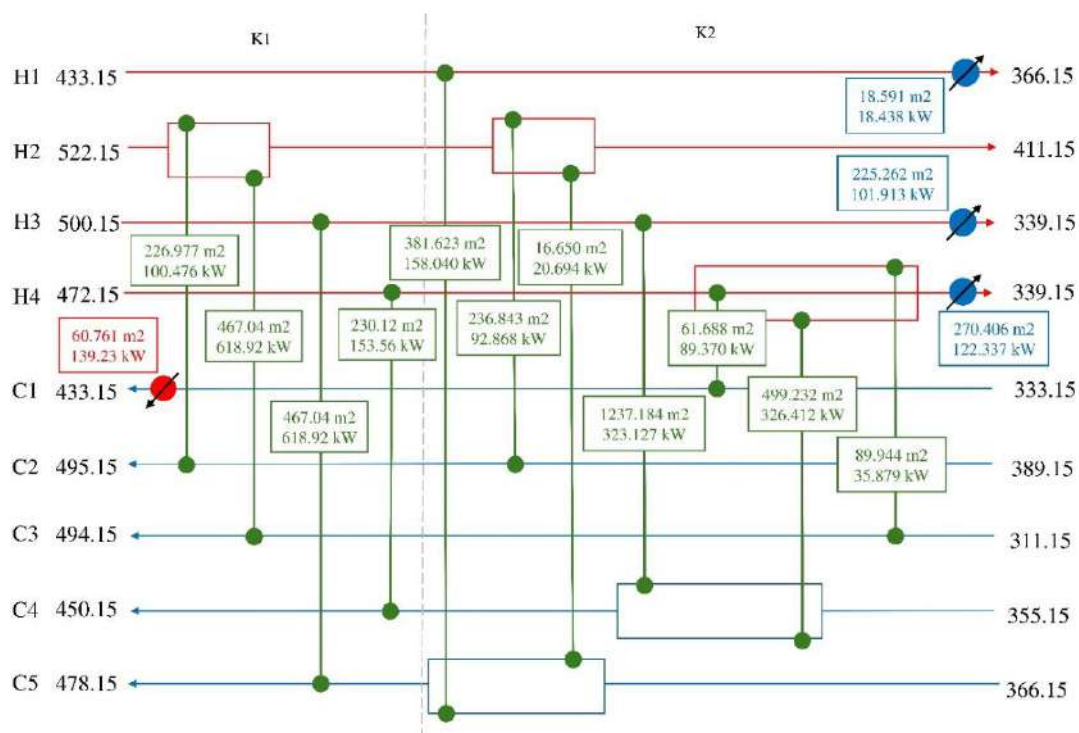


Figure 2 This Result of Study Case with EMAT = 7

The amount of CO<sub>2</sub> emissions reduced is relied on the number of total energy used, change the EMAT is method to minimizing objective function. Increasing or decreasing the EMAT does not always show the minimum TAC it is dependent on each case. Fig (2) shows the different HEN design of study case with EMAT = 7 the TAC is **91,852.39 k\$/year**, this significantly minimizing the TAC with total energy recovery 3411.18 kW, equivalent of reducing **10,429.74 ton CO<sub>2</sub>/year**.

## 6. Conclusions

The research presented the HEN model combined with linearization method and CO<sub>2</sub> emission variable. Discrete temperature differences and the upper bound limit of  $\Omega$ ,  $\Gamma$ , and  $\Psi$  are the key to this method. Moreover, constrain variables must have efficient logic to help simplify the process. The model from this research successfully generated minimized TAC and reduced CO<sub>2</sub> emission for sustainability energy and environment. EMAT value also affects the

energy recovery, and the amount of CO<sub>2</sub> emission reduces. Choosing the EMAT value has limitation due to the technology of heat exchanger.

## Nomenclature

Set:

I = hot streams

J = cold streams

K = stages

N, M = discretized parameter

Parameters:

TINI = inlet temperature of hot stream

TOUTI = outlet temperature of hot stream

TINJ = inlet temperature of Cold stream

TOUTJ = outlet temperature of Cold stream

Ccu = cold utilities cost

Chu = hot utilities cost

CA = area cost

Che = fixed cost of heat exchanger

F<sub>I</sub> = heat capacity flowrate of hot stream I on the hot side of stage K

F<sub>J</sub> = heat capacity flowrate of cold stream J on the hot side of stage K

H = heat transfer coefficient

NOK = number of stages

Bexp = exponent value from cost

Ω = upper bound for exchanged heat

Γ = upper bound for temperature difference

Ψ = upper bound for areas

EMAT = exchanger minimum approach temperature

Δtd = discretized temperature difference in stage K

Variables:

Δt<sub>I, J, K</sub> = temperature difference in stage k for match between stream I and J

ΔTcu = temperature difference for match between stream I and cold utility

ΔThu = temperature difference for match between stream J and hot utility

q<sub>I, J, K</sub> = exchanged heat for hot and cold stream match in stage K

qcu = cold utility for stream I

qhu = hot utility for stream J

Ccucarbon = calculation of CO<sub>2</sub> emission

R, B, G = variable linearization to discrete the temperature difference

z = binary variable for (I, J) match in stage k

zcu = binary variable for cold utility in hot stream

zhu = binary variable for hot utility in cold stream

## Reference

- [1] Yee, T. F., & Grossmann, I. E. (1990). Simultaneous optimization models for heat integration—II. Heat exchanger network synthesis. *Computers & Chemical Engineering*, 14(10), 1165-1184.
- [2] Faria, D. C., Kim, S. Y., & Bagajewicz, M. J. (2015). Global Optimization of the Stage-wise Superstructure Model for Heat Exchanger Networks. *Industrial & Engineering Chemistry Research*, 54(5), 1595-1604.
- [3] Osmani, A., & Zhang, J. (2014). Economic and environmental optimization of a large scale sustainable dual feedstock lignocellulosic-based bioethanol supply chain in a stochastic environment. *Applied Energy*, 114, 572-587.
- [4] Ditzl, P., & Šulc, R. (2024). Calculations of CO<sub>2</sub> emission and combustion efficiency for various fuels. *Energy*, 290, 130044.
- [5] Chen, J. J. J. (1987). Comments on improvements on a replacement for the logarithmic mean. *Chemical Engineering Science*, 42, 2488-2489.
- [6] Brooke, A.; Kendrick, D.; Meeraus, D.; Raman, R. GAMS - A User guide; GAMS Development Corporation: Washington D.C., 2007.
- [7] Share of electricity generation by energy source in EGAT's system. EGAT. <https://www.egat.co.th/home/en/statistics-fuel-usage/>



## Effect of Dip Coating Conditions on Film Thickness and CO<sub>2</sub>/CH<sub>4</sub> Separation Performance of Pebax/PEI Composite Hollow Fiber Membrane

**Nathakrit Prasongporn<sup>1</sup>, Kajornsak Faungnawakij<sup>2</sup>, and Chalida Klaysom<sup>1,\*</sup>**

<sup>1</sup> Center of Excellence in Particle and Material Processing Technology (CEPT), Department of Chemical Engineering, Faculty of Engineering, Chulalongkorn University, Bangkok, 10330, Thailand

<sup>2</sup> Nanocatalysis and Molecular Simulation Research Group (NCAS), National Nanotechnology Center (NANOTEC), National Science and Technology Development Agency (NSTDA), Pathum Thani, 12120, Thailand

E-mail: \* chalida.klaysom@gmail.com, +66-917546080

### Abstract

A composite hollow fiber (HF) membrane was created, combining a porous polyether imide (PEI) support layer with a dense, selective Pebax layer. The key to its separation efficiency lies in the thickness and structure of this selective layer. The layer was applied to the support using a dip coating method, a straightforward technique offering easy control over film thickness. This study explored how different dip coating conditions, like polymer concentration and number of coating cycles, impact the membrane. The PEI support layer of the HF membrane is dipped in a dip coating solution, and the resulting Pebax-coated HF membranes were further crosslinked using a solution of toluene diisocyanate (TDI) in n-hexane to improve both their mechanical resilience and CO<sub>2</sub>/CH<sub>4</sub> separation ability. Various attributes of the final membrane were thoroughly examined, including the selective layer thickness, the mechanical strength of the membrane, as well as membrane performance (e.g., selectivity and permeance). The result revealed that the thickness of the selective film was easily controlled by adjusting coating concentrations and coating cycles. A membrane with a thicker layer exhibited a better mechanical strength, and improved selectivity but at a cost of gas permeance. Detailed and systematic investigation to obtain the optimal film thickness is highly recommended.

**Keywords:** dip coating; film thickness; hollow fiber membrane; Pebax; membrane gas separation

### 1. Introduction

In recent years, membrane technology has emerged as a promising candidate for efficient gas separation processes. It provides a more energy-efficient and cost-effective alternative to conventional gas separation technologies, including chemical absorption, pressure swing adsorption, and cryogenic distillation [1]. The main advantages of membrane-based technology include lower energy consumption, process simplicity, smaller unit size, easy upscaling, and lower environmental impact [2, 3]. Among various gas separation applications, the separation of gases such as carbon dioxide (CO<sub>2</sub>) and methane (CH<sub>4</sub>) from natural gas is of particular significance due to their roles in environmental concerns and industrial processes [4, 5].

Choosing materials to fabricate the membranes' selective layer is a key factor in successfully separating specific gas mixtures. One of the materials suitable for the CO<sub>2</sub>/CH<sub>4</sub> separation is polyether block amide (PEBA), trade name "Pebax". It is a thermoplastic elastomer multiblock copolymer containing linear chains of rigid polyamide (PA) segments interspaced with flexible polyether (PEO) segments [6, 7]. The hard PA blocks provide

mechanical stability while soft PEO blocks increase the affinity for CO<sub>2</sub> and improve CO<sub>2</sub>/CH<sub>4</sub> species separation performance [8-10].

The efficiency of membrane-based separation is determined by two key factors: permeance and selectivity. However, these factors are inversely related; membranes with high permeance often exhibit low selectivity, and vice versa [11, 12]. Achieving a membrane that offers both high flow rates (or permeance) and high selectivity necessitates a design with minimal mass transfer resistance, often achieved through thin membranes. However, crafting a thin, self-supporting film that can endure typical operational pressures poses significant challenges. An optimal approach to address this issue is the development of thin film composite membranes. These membranes comprise a very thin, densely selective layer atop a porous support structure, offering an effective way to balance and enhance both permeance and selectivity while maintaining structural integrity [13, 14]. The porous support is usually created via phase inversion, whereas the selective layer is fabricated through plasma polymerization, dip-coating, dual-layer spinning, and interfacial polymerization [15].

Dip-coating involves the immersion of a porous support into a polymer solution, followed by controlled withdrawal to form a thin, dense, selective layer of the membrane. It is a straightforward, cheap, and time-effective coating technique that allows control of film thickness by tuning the dipping conditions such as polymer concentration, viscosity of the dip-coating solution, withdrawal speed, dwell time, and number of coating cycles [16-18]. Therefore, understanding the relationship between dip coating conditions and film thickness is essential for tailoring membranes with optimal separation performance.

In this work film composite hollow fiber (HF) membranes were fabricated. The support was fabricated in hollow fiber (HF) configuration using polyether imide (PEI) and the Pebax was coated on top via a dip-coating method. To use in CO<sub>2</sub>/CH<sub>4</sub> separation, the selective film was cross-linked. This study focuses on investigating how dip coating conditions, specifically the concentration of the polymer and the number of coating cycles, influence the thickness of the selective layer film. Additionally, it aims to assess the impact of these variables on the separation efficiency of crosslinked Pebax/PEI composite hollow fiber membranes (HFMs).

## 2. Materials and Methods

### 2.1. Materials

Polyether block amide (Pebax, MH-1657) was purchased from Arkema Inc. (Germany). Ethyl Alcohol (EtOH, ≥99.9%), was purchased from QRec (New Zealand). The solvents for the crosslinking solution were toluene diisocyanate (TDI, 98%) purchased from TCI (Japan), and n-hexane (95%) purchased from QRec (New Zealand). PEI-HF supports were fabricated using Polyetherimide (PEI) granule purchased from Sigma-Aldrich (USA) and n-Methyl-2-Pyrrolidone (NMP, 99.5%) purchased from RCI Labscan Ltd. (Thailand).

### 2.2. Preparation of Pebax Dip-coating Solution

Pebax MH-1657 granules were dissolved in a solvent mixture of ethyl alcohol and water (70/30 wt.%) to a concentration of 7 and 10 wt.% by continuous heating and stirring at 60°C until homogenized.

### 2.3. Dip-coating and Forming of Selective Layer

To investigate the effect of the dip-coating solution concentration and the number of dipping cycles, the porous PEI HF support layers were dipped into the prepared 7 and 10 wt.% Pebax coating solution from 3 to 10 dip-coating cycles at room temperature. Each dip-coating cycle comprised of 10 seconds immersion, 1 minute of dwelling, 1 minute of withdrawal, and drying for 5 minutes in an oven at 60°C to let the solvent evaporate completely before repeating the next dip-coating cycle. The finalized dip-coated PEI/Pebax composite HF membranes were dried overnight in the oven at 60°C to fully remove the solvent.

#### 2.4. Crosslinking of PEI/Pebax Composite HF Membranes

The PEI/Pebax composite HF membranes were immersed in a crosslinking solution of 2.17% v/v TDI in n-hexane for 60 minutes. Then the crosslinked membranes were washed thoroughly in a circulating water bath for 15 minutes before being dried in an oven at 60°C overnight.

#### 2.5. Characterization of PEI/Pebax Composite HF Membranes

The morphology of the membrane was investigated by a S-3400N scanning electron microscope (SEM) (Hitachi, Japan). The mechanical strength of the membrane was investigated using a 5566-model universal testing machine (UTM) (Instron, USA). The crystallinity of the membranes was characterized by x-ray diffraction (XRD) analysis using a D8 Advance diffractometer (Bruker, Germany) with Cu-K $\alpha$  radiation ( $\lambda=1.5418 \text{ \AA}$ ).

#### 2.6. Membrane Performance Test

The prepared membranes were packed in a size ¼” stainless-steel module. The module was attached to a custom-developed gas separation system shown in Fig. 1. To investigate the performance, the membranes were tested with a gas mixture of CO<sub>2</sub> and CH<sub>4</sub> at a 40/60 molar ratio at a constant operating temperature of 35°C and pressure at 20 bar. The gas composition was controlled by a mass flow controller. The flow diagram is shown in Fig. 2. The gas mixture was fed with a flow rate of 50 ml/min to the shell side of HF membrane module. Helium gas was fed into the inside of the HF membrane to carry the permeate gas to the chromatography. The flow rate and gas composition were measured by a VP-2 film flow meter (Horiba Tec, Japan) and a GC-2014C gas chromatography (Shimadzu, Japan) respectively.



Fig. 1 A custom-developed gas separation system

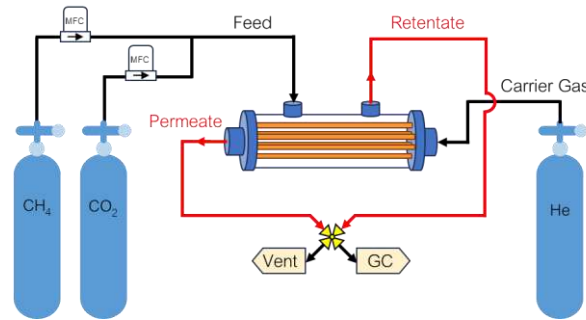


Fig. 2 Flow diagram of the gas separation system

The gas permeability and selectivity of the Pebax/PEI composite HF membranes can be calculated from Eq. (1) and Eq. (2) respectively.

$$\mathcal{P}_i = \frac{J_i \ell}{(p_{i,0} - p_{i,X})} \quad (1)$$

when  $\mathcal{P}_i$  is permeance of gas  $i$  [GPU]  
 $J_i$  is flux of gas  $i$  [ $\text{cm}^3/\text{cm}^2 \cdot \text{s}$ ]  
 $\ell$  is membrane selective layer thickness [cm]  
 $(p_{i,0} - p_{i,X})$  is transmembrane pressure of gas  $i$  [bar]

when 1 GPU is  $10^{-6} \frac{\text{cm}^3_{\text{STP}}}{\text{cm}^2 \cdot \text{s} \cdot \text{cmHg}}$

$$\alpha_{ij} = \frac{\mathcal{P}_i}{\mathcal{P}_j} \quad (2)$$

when  $\alpha_{ij}$  is selectivity of gas  $i$   
 $\mathcal{P}_i$  is permeance of gas  $i$   
 $\mathcal{P}_j$  is permeance of gas  $j$

### 3. Results and Discussion

#### 3.1. Effect of Polymer Concentration and coating cycle on Film Thickness

The influence of polymer concentration on the film thickness coated on HF supports was investigated (see Fig.3) and the results are summarized in Table 1. It was found that an increase in the concentration of dip-coating solution resulted in an increased film thickness.

Table 1. Summarized selective layer thickness and membrane diameter

Pebax concentration (wt.%)	Number of coating cycle			
	9 cycles		10 cycles	
	Selective layer thickness ( $\mu\text{m}$ )	Membrane diameter ( $\mu\text{m}$ )	Selective layer thickness ( $\mu\text{m}$ )	Membrane diameter ( $\mu\text{m}$ )
7%	200.67	812.36	260.70	928.30
10%	282.15	966.67	330.59	1047.55

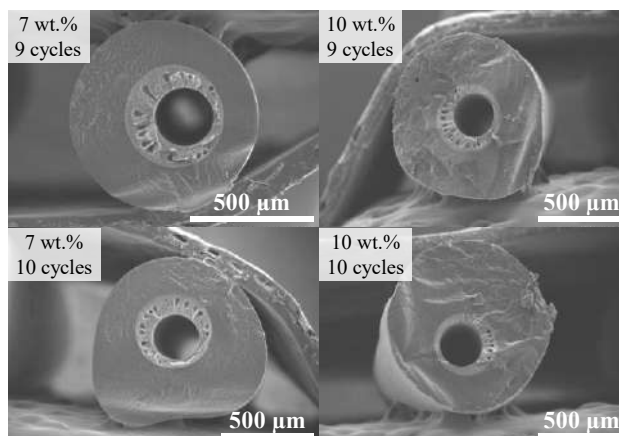


Fig. 3 SEM images of Pebax/PEI HFMs dip-coated at 7 wt.% (left) and 10 wt.% (right) with 9 (top) and 10 dip-coating cycles (bottom).

Additionally, the film thickness and overall diameter (support + coated layer) of membranes increased with the increasing coating cycles. The selective layer thickness and membrane diameter are summarized in Fig. 4.

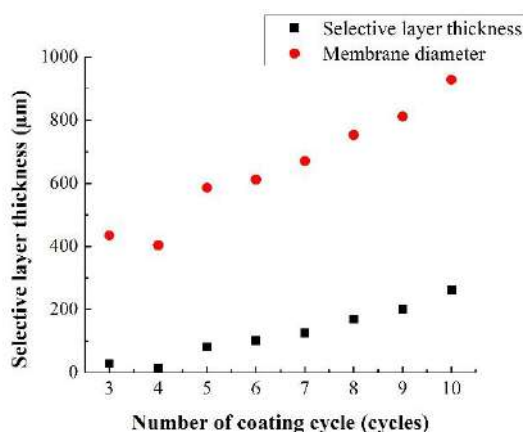


Fig. 4 Effect of the number of coating cycles on selective layer thickness and membrane diameter

### 3.2. Effect of Number of Coating Cycles on Membrane Strength

The dipping cycles and the film thickness were also found to directly affect the mechanical strength of the membranes as illustrated in Fig.5. When increasing the number of coating cycles, the mechanical strength of the membrane, which can be represented by tensile stress at yield of the membrane, increased.

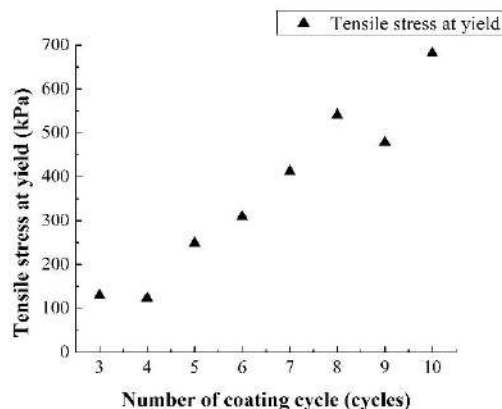


Fig. 5 Effect of number of coating cycle on mechanical strength

### 3.3. Effect of Number of Coating Cycles on Membrane Separation Performance

The membranes were chemically crosslinked to improve mechanical strength and selectivity before the performance test. The successfully crosslinked membranes can be verified using the XRD technique (Fig. 6) as the intensity of crystallinity peak at  $2\theta = 24^\circ$  [19, 20] has changed after the crosslink. The performance of the crosslinked membranes with different coating cycles is compared in Fig.7. Increasing the number of coating cycles resulted in a decline in gas permeance but an enhancement in the  $\text{CO}_2/\text{CH}_4$  selectivity. The increased thickness of the selective layer extends the diffusion path for gas molecules, leading to greater resistance in membrane transport. Consequently, gas diffusion through a thicker membrane becomes more challenging [21]. Given that the Pebax selective layer exhibits a higher affinity for  $\text{CO}_2$  compared to  $\text{CH}_4$ , the selectivity for  $\text{CO}_2$  over  $\text{CH}_4$  is further enhanced in membranes with thicker selective layers.

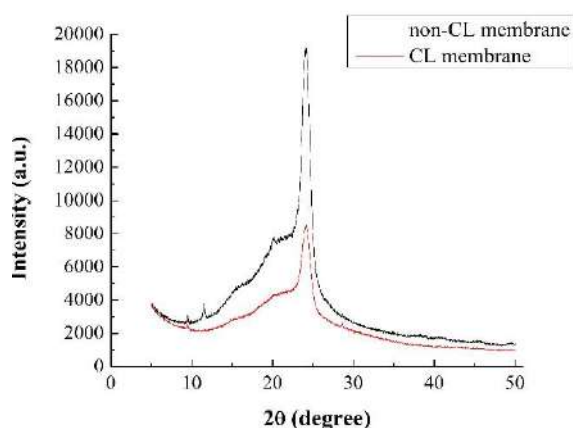


Fig. 6 XRD result of non-CL and CL Pebax/PEI TFC-HFM

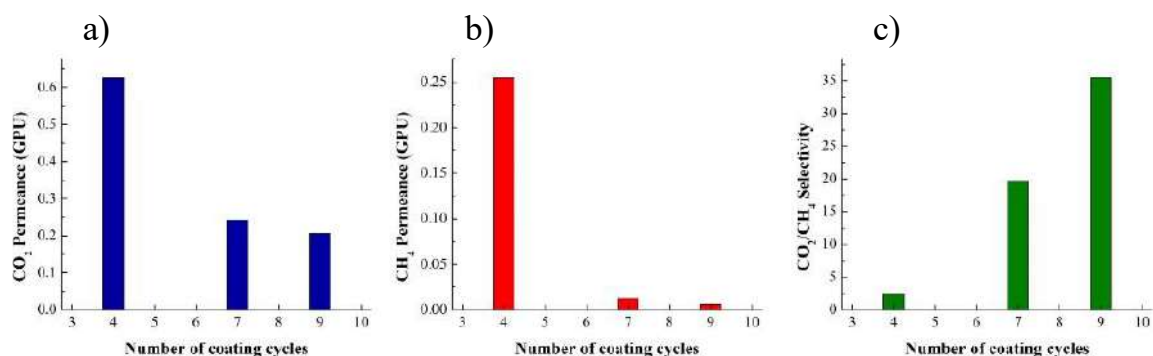


Fig. 7 Separation performance of Pebax/PEI – HFMs prepared at different coating cycles; a) CO<sub>2</sub> permeance, b) CH<sub>4</sub> permeance, and c) CO<sub>2</sub>/CH<sub>4</sub> selectivity.

#### 4. Conclusions

Pebax MH-1657/PEI HFMs were prepared using a dip-coating technique. The effect of dip-coating conditions on film thickness and CO<sub>2</sub>/CH<sub>4</sub> separation performance were investigated, this includes polymer concentration and number of coating cycles. For the polymer concentration, increasing the concentration results in increased selective film thickness. For the number of coatings cycles, increasing the number of coating cycles directly increases the selective film thickness which in turn increases the mechanical strength of the membrane as a result. Additionally, increasing the number of coatings cycles results in a decrease in gas permeance and an increase in membrane CO<sub>2</sub>/CH<sub>4</sub> selectivity. However, the separation performance results still need more investigation and clarification on the effect of changes in operating pressure which will be studied further.

#### Acknowledgments

The authors would like to thank the Center of Excellence in Particle and Material Processing Technology (CEPT), Chulalongkorn University, and the National Science and Technology Development Agency (NSTDA) especially the National Nanotechnology Center (NANOTEC) for providing facilities for this study.

#### References

- [1] Sidhikku Kandath Valappil, R., N. Ghasem, and M. Al-Marzouqi. (2021). Current and future trends in polymer membrane-based gas separation technology: A comprehensive review. *Journal of Industrial and Engineering Chemistry*, 98, 103-129.
- [2] Sun, Y. and M. Gou. (2022). Highly efficient of CO<sub>2</sub>/CH<sub>4</sub> separation performance via the pebax membranes with multi-functional polymer nanotubes. *Microporous and Mesoporous Materials*, 342, 112120.
- [3] Kargari, A. and S. Rezaeinia. (2020). State-of-the-art modification of polymeric membranes by PEO and PEG for carbon dioxide separation: A review of the current status and future perspectives. *Journal of Industrial and Engineering Chemistry*, 84, 1-22.
- [4] Zhang, Y., et al. (2013). Current status and development of membranes for CO<sub>2</sub>/CH<sub>4</sub> separation: A review. *International Journal of Greenhouse Gas Control*, 12, 84-107.

- [5] Younas, M., et al. (2020). Post-combustion CO<sub>2</sub> capture with sweep gas in thin film composite (TFC) hollow fiber membrane (HFM) contactor. *Journal of CO<sub>2</sub> Utilization*, 40, 101266.
- [6] Ardestani, M.A., et al. (2010). Fabrication of PEBA/ceramic nanocomposite membranes in gas sweetening. *Desalination*, 250(3), 1140-1143.
- [7] Sridhar, S., et al. (2007). Development of crosslinked poly(ether-block-amide) membrane for CO<sub>2</sub>/CH<sub>4</sub> separation. *Colloids and Surfaces A: Physicochemical and Engineering Aspects*, 297(1), 267-274.
- [8] Taheri, P., M.S. Maleh, and A. Raisi. (2021). Cross-linking of poly (ether-block-amide) by poly (ethylene glycol) diacrylate to prepare plasticizing-resistant CO<sub>2</sub>-selective membranes. *Journal of Environmental Chemical Engineering*, 9(5), 105877.
- [9] Quan, S., et al. (2017). CO<sub>2</sub>-selective mixed matrix membranes (MMMs) containing graphene oxide (GO) for enhancing sustainable CO<sub>2</sub> capture. *International Journal of Greenhouse Gas Control*, 56, 22-29.
- [10] Liu, Y.-C., et al. (2019). Characterization and molecular simulation of Pebax-1657-based mixed matrix membranes incorporating MoS<sub>2</sub> nanosheets for carbon dioxide capture enhancement. *Journal of Membrane Science*, 582, 358-366.
- [11] Liang, C.Z., T.-S. Chung, and J.-Y. Lai. (2019). A review of polymeric composite membranes for gas separation and energy production. *Progress in Polymer Science*, 97, 101141.
- [12] Robeson, L.M. (2008). The upper bound revisited. *Journal of Membrane Science*, 320(1), 390-400.
- [13] Liu, M., et al. (2022). Thin film composite membranes for postcombustion carbon capture: Polymers and beyond. *Progress in Polymer Science*, 126, 101504.
- [14] Zhao, B., et al. (2023). Inner-selective polyethersulfone-polydimethylsiloxane (PES-PDMS) thin film composite hollow fiber membrane for CO<sub>2</sub>/N<sub>2</sub> separation at high pressures. *Separation and Purification Technology*, 323, 124439.
- [15] Li, G., et al. (2021). A review - The development of hollow fibre membranes for gas separation processes. *International Journal of Greenhouse Gas Control*, 104, 103195.
- [16] Beyribey, B., J. Bayne, and J. Persky. (2022). The effect of dip-coating parameters on the thickness and uniformity of BCZY electrolyte layer on porous NiO-BCZY tubular supports. *Ceramics International*, 48(5), 6046-6051.
- [17] Yu, H.J., et al. (2023). A new dip-coating approach for plasticization-resistant polyimide hollow fiber membranes: In situ thermal imidization and cross-linking of polyamic acid. *Chemical Engineering Journal*, 473, 145378.
- [18] Nandi, B.K., R. Uppaluri, and M.K. Purkait. (2009). Effects of dip coating parameters on the morphology and transport properties of cellulose acetate-ceramic composite membranes. *Journal of Membrane Science*, 330(1), 246-258.
- [19] Lu, S.C., et al. (2022). Aminosilane-Functionalized Zeolite Y in Pebax Mixed Matrix Hollow Fiber Membranes for CO<sub>2</sub>/CH<sub>4</sub> Separation. *Polymers (Basel)*, 15(1).
- [20] Tang, P.-H., et al. (2021). Carbon Dioxide Enrichment PEBAX/MOF Composite Membrane for CO<sub>2</sub> Separation. *Membranes*, 11(6), 404.
- [21] Shen, Y. and A. Lua. (2010). Effects of Membrane Thickness and Heat Treatment on the Gas Transport Properties of Membranes Based on P84 Polyimide. *Journal of Applied Polymer Science*, 116, 2906-2912.



## Characterization and properties of K-ZrO<sub>2</sub> Catalyst Derived from UiO-66 for Glycerolysis of Methyl Palmitate

Wasupol Saksritiwa<sup>1,2</sup>, Jeffrey Chi-Sheng Wu<sup>2\*</sup>, Apinan Soottitantawat<sup>1\*</sup>

<sup>1</sup>Particle Research Laboratory, Department of Chemical Engineering, Faculty of Engineering, Chulalongkorn University, Bangkok 10330, Thailand

<sup>2</sup>Department of Chemical Engineering, National Taiwan University, Taipei 10617, Taiwan  
E-mail: wasupol1998@gmail.com<sup>1,2</sup>, cswu@ntu.edu.tw<sup>2\*</sup>, apinan.s@chula.ac.th<sup>1\*</sup>

### Abstract

The glycerolysis process required a high temperature to react. So, the catalyst plays a pivotal role in enhancing process efficiency by increasing productivity and reducing energy consumption. However, homogeneous catalysts are not economically viable for recovery and reuse. Therefore, the use of heterogeneous catalysts has been explored to address these issues. Nevertheless, the catalytic activity of heterogeneous catalysts is limited by factors such as active site dispersion, stability, and the quantity of active sites. To address these limitations, K-ZrO<sub>2</sub> metal-organic frameworks (MOFs) have emerged as a promising solution. K-ZrO<sub>2</sub> is a mesoporous catalyst substance synthesized through a direct heat-treatment process that involves loading KNO<sub>3</sub> on the UiO-66 metal-organic framework. Consequently, this research aims to investigate the catalysts properties and characterization concerning calcined temperature and quantity of loaded KNO<sub>3</sub>, with the objective of enhancing understanding of catalyst.

**Keywords:** Glycerolysis; Catalyst; UiO-66 derived K-ZrO<sub>2</sub>

### 1. Introduction

Glycolysis, a reaction that requires high temperatures, is commonly employed to produce MGs and DGs, which find applications in the food and pharmaceutical industries [1].

Catalysts are primarily classified as either heterogeneous or homogeneous based on the phase criteria of the reactant and catalyst. However, homogeneous catalysts are not economically viable for recovery and reuse in the transesterification process. Therefore, the use of heterogeneous catalysts has been explored to address these issues. Nevertheless, the catalytic activity of heterogeneous catalysts is limited by factors such as active site dispersion, stability, and the quantity of active sites [4-6]. Metal-organic frameworks (MOFs) have emerged as a technology to overcome the challenges associated with both heterogeneous and homogeneous catalysts.

MOFs are substances characterized by the coordination between metal ions and organic ligands, resulting in complex topological structures. These materials offer significant porosity, uniform pore size, and the ability to customize their characteristics and activity by incorporating different metal ions, organic ligands, or loaded ion substances onto MOFs [2].

K-ZrO<sub>2</sub> is a mesoporous catalyst substance synthesized through a direct heat-treatment process that involves loading KNO<sub>3</sub> on the UiO-66 metal-organic framework. This process results in the formation of carbon molecules, which serve as mesoporous templates and provide base-resistant reinforcement for zirconia. The resulting K-ZrO<sub>2</sub> catalysts exhibit high surface area and basicity properties [3-4].

## 2. Experimental

### 2.1. Materials and Chemicals

Zirconium (IV) chloride ( $ZrCl_4$ ) 98%, anhydrous, N,N-Dimethylformamide (DMF),  $\geq 99.8\%$ , Methanol and Potassium nitrate ( $KNO_3$ ) was provided by Thermo Scientific, UK. 1,4-benzenedicarboxylic acid (BDC) was provided by Acros Organics, Belgium. N-heptane 99% was provided by Baker analyzed, USA.

### 2.2. Catalyst preparation

The preparation of UiO-66, 1.4 g of  $ZrCl_4$  and 1.02 g of 1,4-benzenedicarboxylic acid (BDC) were initially blended with 62 mL of dimethylformamide (DMF). The resulting mixture was heated in a stainless-steel vessel with a Teflon liner at 120 °C for 24 hours to activate it. Subsequently, the catalyst was purified through sequential refluxing with DMF and methanol. Finally, the dry catalyst was obtained by subjecting it to treatment at 100 °C for 3h.

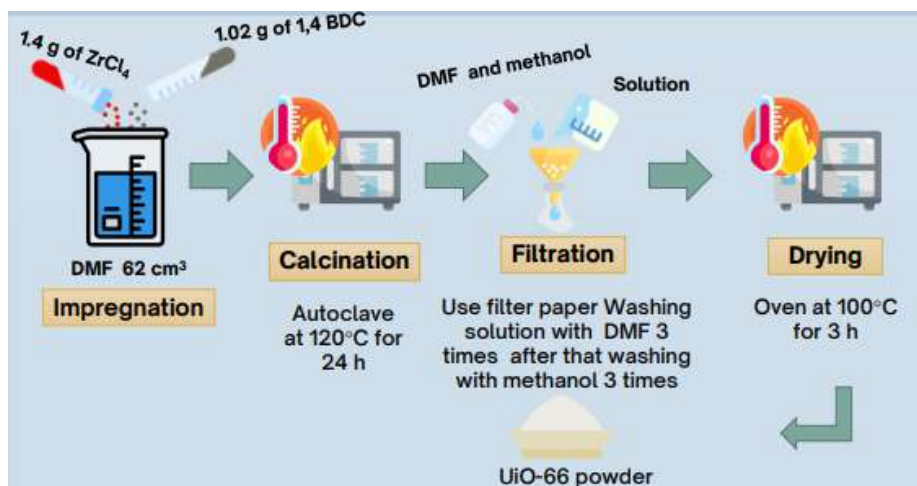


Fig. 1 Preparation of UiO-66 catalyst

The preparation of modified UiO-66 ( $K-ZrO_2$ ), 800 mg of UiO-66 was suspended in 100 mL of dry n-heptane and sonicated for 15 minutes until a homogeneous solution was achieved. Subsequently, 0.8 mL of an aqueous  $KNO_3$  solution with varying concentrations was added dropwise to the mixture over a period of 15 minutes, while stirring continuously. The resulting solution was stirred continuously for 8 hours, followed by filtration to separate the catalysts and solution. Finally, white catalyst powder was obtained by drying the catalyst in air at 100 °C. The resulting samples were labeled as U-AK-1 A, depending on the amount of potassium nitrate added. The sample without any added potassium nitrate was denoted as U, representing the pure UiO-66 sample.  $K-ZrO_2$  was synthesized from U-AK-1 using a two-step heat treatment process. First, it was calcined at various temperatures in nitrogen for 3 hours, followed by a heat treatment at 400 °C in air for 6 hours. The resulting  $K-ZrO_2$  samples were denoted as  $K-ZrO_2$ -x-y, where x, y represents the mg contents of K and the calcination temperature under  $N_2$ , respectively.

This study employed catalysts with varying amounts of potassium nitrate added (0 mg, 60 mg, 120 mg, and 180 mg). Subsequently, these catalysts were subjected to calcination in a nitrogen atmosphere at temperatures of 550°C, 650°C, and 750°C for a duration of 3 hours.

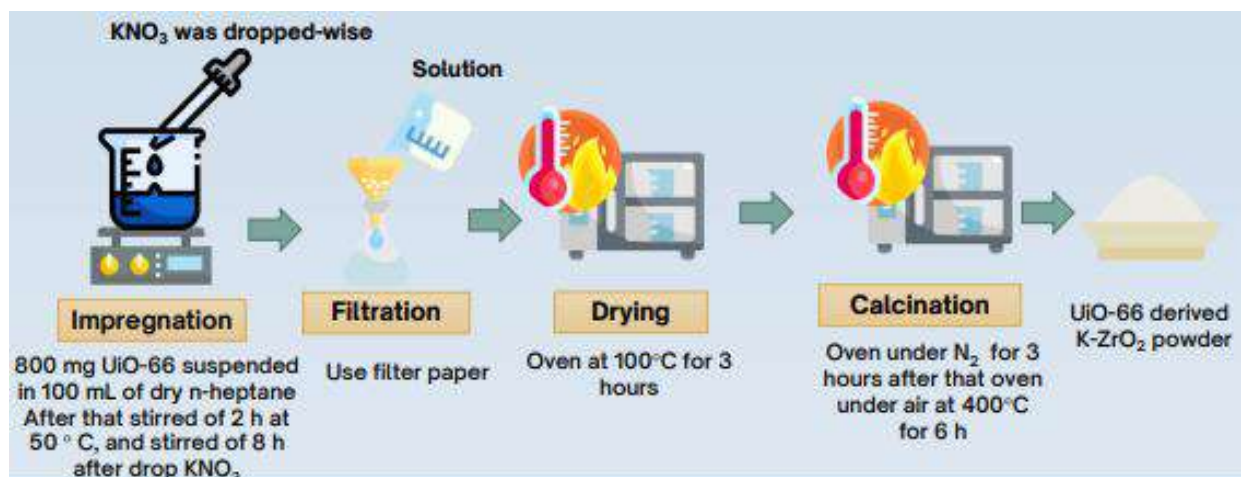


Fig. 2 Preparation of K-ZrO<sub>2</sub> catalyst

### 2.3. Catalyst Characterization

The crystallographic structure and arrangement of atoms in a crystalline substance of UiO-66 and K-ZrO<sub>2</sub> were determined by X-ray diffraction XRD.

The decomposition UiO-66 after loading Potassium from KNO<sub>3</sub> was measured by changes in sample's weight as a function of temperature at 0 to 800 degree Celsius under Nitrogen atmosphere.

The morphology and elemental composition of UiO-66 and K-ZrO<sub>2</sub> were investigated using a Scanning Electron Microscope and energy dispersive x-ray spectroscopy (SEM-EDX).

## 3. Result and discussion

### 3.1. X-ray diffraction (XRD, Rigaku-Ultima IV)

Fig. 3 shows the X-ray diffraction patterns from the UiO-66 sample, revealing characteristic peaks at approximately 7.3, 8.5, 17.2, 22.4, 25.8, and 30.7 degrees. However, it is observed that the X-ray diffraction patterns of the UiO-66 sample obtained from the experiment (Fig. 3) exhibit noise. This heightened noise may be attributed to the presence of residual DMF or reactant residues within the UiO-66 catalyst.

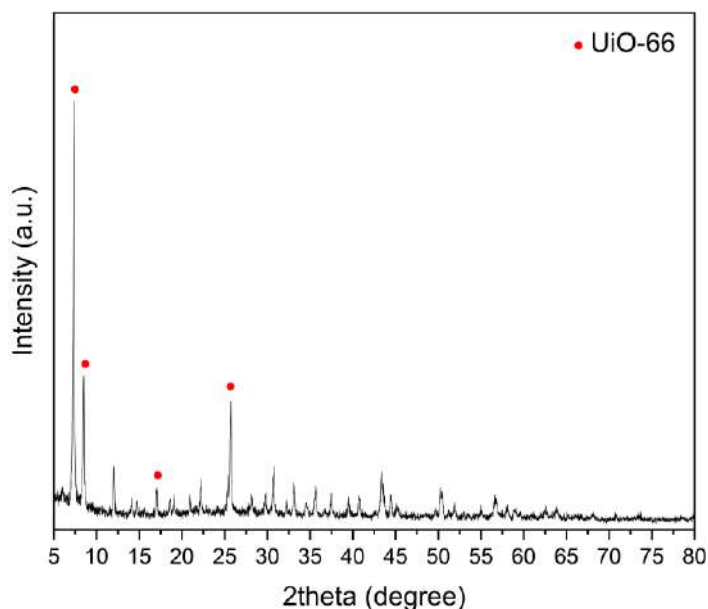


Fig. 3 X-ray diffraction patterns of UiO-66 from experiment

### 3.2. Thermogravimetric Analysis (TGA)

Fig. 4, shows that the decomposition of carbon residue begins at a temperature of 400°C, compared with different amount of  $\text{KNO}_3$  loaded from UiO-66 which decomposed into carbon hybrid zirconia 500 and 600 °C. As base-stable materials, UiO-66 which loaded  $\text{KNO}_3$  carbon layer can protect frameworks from collapse compared with pure UiO-66.

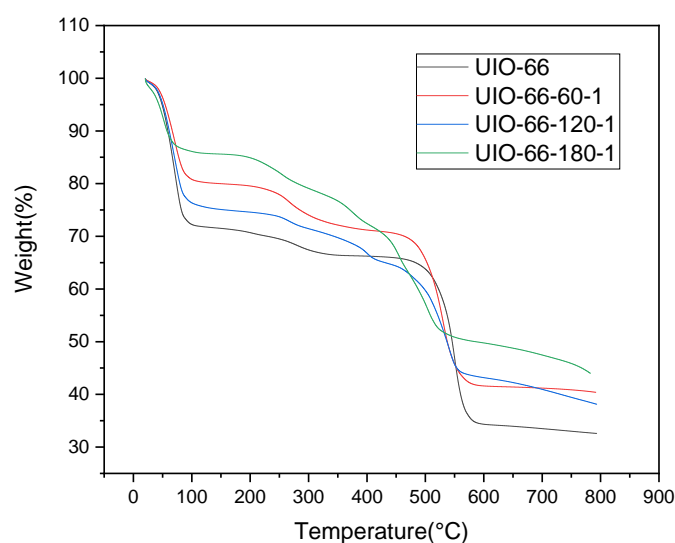


Fig. 4 TGA profiles of UiO-66 loaded with different amounts of  $\text{KNO}_3$

### 3.3. Scanning Electron Microscope (SEM)

The SEM technique cannot be used to explain the differing concentration loading of Potassium on UiO-66 catalysts and pure UiO-66. Fig. 5A illustrates that pure UiO-66 catalysts adhere to a pellet model. In Fig. 5B, the introduction of K into the catalyst demonstrates uniform dispersion of the accelerator. Meanwhile, in Fig. 5C, KZrO<sub>2</sub>-60-550, at the maximum loading of potassium; 120 mg, results in metal accumulation in the catalyst and agglomeration.

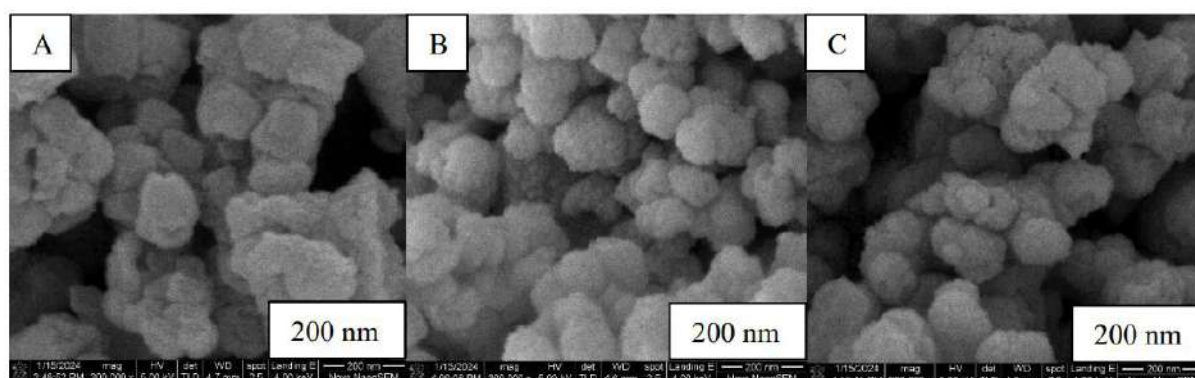


Fig. 5 SEM of (A) UiO-66; SEM of (B) KZrO<sub>2</sub>-60-550; SEM of (C) KZrO<sub>2</sub>-120-550

### 3.4. Energy Dispersive X-ray Spectroscopy (EDX)

Fig 6 shows that the EDX method is useful for distinguishing between the surface composition of potassium-filled UiO-66 and UiO-66 catalysts. Inconsistencies were found in Table 1 regarding EDX defragmentation for different doses of KNO<sub>3</sub>-loaded UiO-66 catalysts (60, 120, 180 mg percent of potassium). This discrepancy may be due to insufficient distribution of KNO<sub>3</sub> within the pores during the synthesis process. In addition, the EDX analysis reveals the decomposition of carbon compounds after firing UiO-66, which can lead to observed anomalies. Moreover, Table 1 shows that the percentage of carbon elements and chlorine dropped to near zero after calcining UiO-66 to KZrO<sub>2</sub>

Table 1. Classification of Catalysts and Elemental Composition by Weight from EDX

Type of catalyst	%Weight(Zr)	%Weight(O)	%Weight(K)	%Weight(C)	%Weight(Cl)
UIO-66	26.93	28.60	-	43.67	0.79
K-ZrO <sub>2</sub> -60-550	63.61	29.93	6.45	-	-
K-ZrO <sub>2</sub> -120-550	65.26	31.60	3.14	-	-
K-ZrO <sub>2</sub> -180-550	45.29	37.85	16.18	-	-

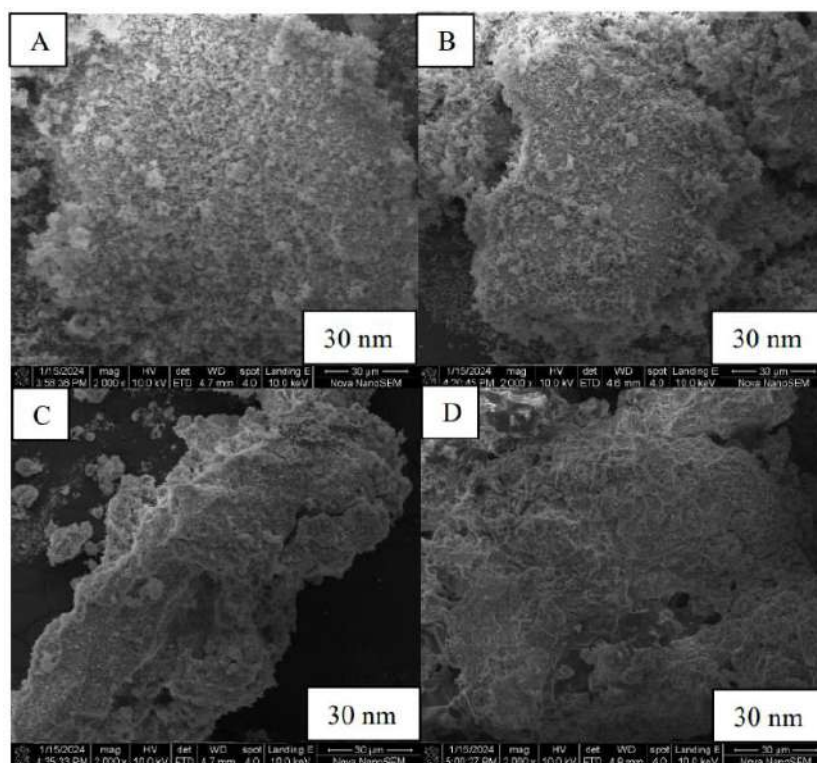


Fig. 6 EDX mapping (A) of UiO-66; EDX mapping (B) of KZrO<sub>2</sub>-60-550;  
EDX mapping (C) of KZrO<sub>2</sub>-120-550; EDX mapping (D) of KZrO<sub>2</sub>-180-550

#### 4. Conclusion

In this work, we successfully to synthesis KZrO<sub>2</sub>, which necessitated the synthesis of UiO-66 to utilize X-ray diffraction (XRD) for verifying the correctness of the UiO-66 catalyst. Subsequently, Thermogravimetric Analysis (TGA) is employed to discern the characteristics of UiO-66 while loading KNO<sub>3</sub> to determine its variance from pure UiO-66 and confirm the effect of high calcined. EDX and SEM methods were utilized to investigate the catalyst's surface. However, the SEM method cannot be employed to explain the different concentrations of K loading on UiO-66 catalysts compared to pure UiO-66. Table 1 reveals the percentage weight loss, predominantly attributed to carbon components in TGA. Additionally, Table 1 format displays the weight percentages of potassium loaded onto KZrO<sub>2</sub> in varying degrees of success, illustrating differences between KNO<sub>3</sub> on UiO-66.

## References

- [1] Miao, S. and D. Lin (2019). Monoglycerides: Categories, Structures, Properties, Preparations, and Applications in the Food Industry. *Encyclopedia of Food Chemistry*: 155-163.
- [2] Ma, X., et al. (2021). "Current application of MOFs based heterogeneous catalysts in catalyzing transesterification/esterification for biodiesel production: A review." *Energy Conversion and Management* 229.
- [3] Cai X, Xie Z, Li D, Kassymova M, Zang S– Q, Jiang H– L. Nano– sized metal– organic frameworks: Synthesis and applications. *Coordination Chemistry Reviews*. 2020;417:213366.
- [4] Wang, P., et al. (2017). "MOF derived mesoporous K-ZrO<sub>2</sub> with enhanced basic catalytic performance for Knoevenagel condensations." *RSC Advances* 7(88): 55920-55926.
- [5] Guldhe, A., et al., Biodiesel synthesis from microalgal lipids using tungstated zirconia as a heterogeneous acid catalyst and its comparison with homogeneous acid and enzyme catalysts. *Fuel*, 2017. 187: p. 180-188.
- [6] Xie, W., X. Yang, and M. Fan, Novel solid base catalyst for biodiesel production: Mesoporous SBA-15 silica immobilized with 1,3-dicyclohexyl-2-octylguanidine. *Renewable Energy*, 2015. 80: p. 230-237.

## High-Temperature Catalytic Oxidative Cleavage of Oleic Acid to Produce Azelaic and Pelargonic Acids

**Nichkamon Suwannit and Varong Pavarajarn\***

Center of Excellence in Particle and Materials Processing Technology, Department of Chemical Engineering,  
Faculty of Engineering, Chulalongkorn University, Phayathai Road, Patumwan Bangkok, 10330, Thailand  
\*Email: varong.p@chula.ac.th.

### Abstract

Azelaic acid (AA) and pelargonic acid (PA) are medium-chain fatty acids that are used as building blocks in organic synthesis in various industries. Simultaneous production of AA and PA from oleic acid (OA), which is abundantly available in nature, is possible via oxidative cleavage at the carbon-carbon double bond. However, it is still a great challenge to achieve high conversion and yields of AA and PA from this reaction. In this work, oxidative cleavage of oleic acid by hydrogen peroxide was investigated at a temperature higher than that previously reported, in the range of 80-160°C, under autogenous pressure. Tungsten (VI) oxide was used as a catalyst. Tertiary butanol was used as a co-solvent. The results showed that a complete conversion of oleic acid could be achieved. The analysis by gas chromatography with tandem mass spectroscopy (GC-MS) revealed various products, including various medium-chain fatty acids and 9, 10-dihydroxystearic acid. The yields of both AA and PA were increased as the temperature was increased.

**Keywords:** Oxidative cleavage; Oleic acid; Medium-chain fatty acids; Tungsten (VI) oxide

### 1. Introduction

Nowadays, the oleochemical industry is continuously growing. Leveraging abundant resources found in nature, both from plants and animals, oleochemicals are utilized to produce high-value products. One notable example is long-chain unsaturated fatty acids such as oleic acid, linolenic acid, and ricinoleic acid. In particular, oleic acid can be used to produce AA and PA through oxidative cleavage reactions, as shown in Figure 1. Such products serve as crucial starting materials in chemical synthesis, which are commonly employed in polymer manufacturing industries (polyamides, polyesters, and polyurethanes), as well as in plasticizers, adhesives, and lubricants. Furthermore, AA is an important ingredient in the pharmaceutical and cosmetic industries to promote healthier skin [1-3].

The oxidative cleavage reaction of unsaturated fatty acids is a reaction that breaks the carbon-carbon double bonds and forms carbon-oxygen double bonds [4]. The oxidative cleavage reaction can be caused by oxidative agents [5]. Hydrogen peroxide (H<sub>2</sub>O<sub>2</sub>) is an interesting oxidative agent because it is environmentally friendly in that it naturally decomposes into water and oxygen [6, 7]. The hydrogen peroxide can be converted to hydroxyl radicals (OH•), which have a high oxidation potential [8]. This mechanism can be facilitated by utilizing various means such as light, UV light, lasers, and heat, which increase the rate of generation of hydroxyl radicals [9, 10]. When hydrogen peroxide is used as the oxidizing agent, tungsten oxide (WO<sub>3</sub>) is used as a catalyst in the oxidative cleavage reaction because of its low toxicity, high stability, and high product yield in the bond cleavage process.



In this work, we investigate how temperature affects the hydrothermal conditions-induced oxidative bond cleavage ability. To improve the yield and conversion of the intended product, we also employ hydrogen peroxide as an oxidizing agent and tungsten oxide as a catalyst. By adopting a straightforward procedure and catalyst, we hope that this study will provide guidelines and basic knowledge for the production of AA and PA from industrially obtained oleic acid using a simple process and catalyst.

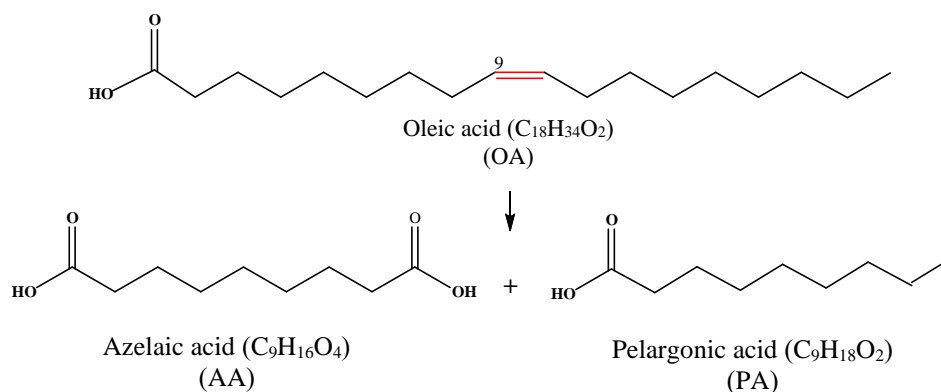


Fig.1 Oxidative cleavage of oleic acid

## 2. Materials and Methods

### 2.1 Material

Oleic acid ( $C_{18}H_{34}O_2$ , 87% industrial grade), hydrogen peroxide ( $H_2O_2$ , 30% AR Grade, ANaPure), tert-butanol ( $(CH_3)_3COH$ , AR Grade, Loba Chemie), and the commercial catalyst tungsten (VI) oxide ( $WO_3$ , Loba Chemie). The material for esterification was n-hexane ( $C_6H_{14}$ , AR Grade, QReC), along with hydrochloric acid ( $HCl$ , 37% AR Grade, QReC), methanol ( $CH_3OH$ , AR Grade, QReC), and deionized water.

### 2.2 Methods

#### 2.2.1 Oxidation reaction of oleic acid under autogenous pressure

A reaction was conducted in a thermal vessel with a total solution volume of 30 ml, composed of 0.253 mM oleic acid, 8.666 mM hydrogen peroxide ( $H_2O_2$ ), 6.417 mM tertiary butanol, and 1.0% (w/v) tungsten (VI) oxide. The thermal vessel was then placed in an oven with temperatures varying between 80°C and 160°C for a reaction duration of 6 hours under autogenous pressure. Once the reaction was completed, the tungsten (VI) oxide catalyst was separated by centrifugation at 3,000 rpm for 5 minutes. The liquid samples were subsequently analyzed using GC-MS.

## 2.2.2 Sample preparation before analysis with esterification reaction

The sample preparation method followed Ishihara's method [11]. First, 0.4 mL of the sample, 3 mL of methanol, and 0.6 mL of hydrochloric acid (9% w/w in methanol) were added to the analysis flask. The mixture was then heated in a bath at a constant temperature of 80 °C for 2 hours. Afterward, the solution was allowed to cool to room temperature. Following this, 2 mL of hexane and 2 mL of deionized water were added. It was observed that the solution separated into two phases: the organic phase and the water phase. The upper phase, which is the organic phase, was selected for GC-MS analysis.

## 2.2.3 Analytical methods

The oxidation cleavage products were a mixture of AA and PA then analyzed by gas chromatography-mass spectrometry (GC-MS) using The Agilent 7000C GC/MS Triple Quad GC-MS unit has an HP-5ms column (30 m × 0.25 mm, 0.25 μm thick) injector volume 0.5 μL. The initial column temperature was 80 °C and held for 2 min increased to 280 °C at a rate of 20 °C/min and held for 6 min. The flow rate of the He Carrier was 1.0 mL/min average velocity of 36.966 cm/s. The sample was injected at a split ratio of 50/1

## 3. Results and Discussion.

The experimental results show oxidative cleavage of oleic acid at reaction temperatures ranging from 80 to 160 °C, where the conversion value of oleic acid is shown in Table 1. The maximum conversion value was obtained from the reaction at a high temperature of 130 °C, which was followed by 80, 160, 150, and 140 °C, in that order. However, high conversion values do not necessarily indicate that oleic acid will become the main product; all by-products also occur, as shown in Figure 2.

Table 1. shows the conversion of oleic acid at temperatures of 80, 130, 140, 150, and 160 °C, using a molar ratio of H<sub>2</sub>O<sub>2</sub> to oleic acid of 8:1 and a reaction time of 6 hours under autogenous pressure.

Entry	Reaction temperature (°C)	Conversion of oleic acid (mol%)
1	80	95.21
2	130	97.36
3	140	86.77
4	150	94.17
5	160	95.07

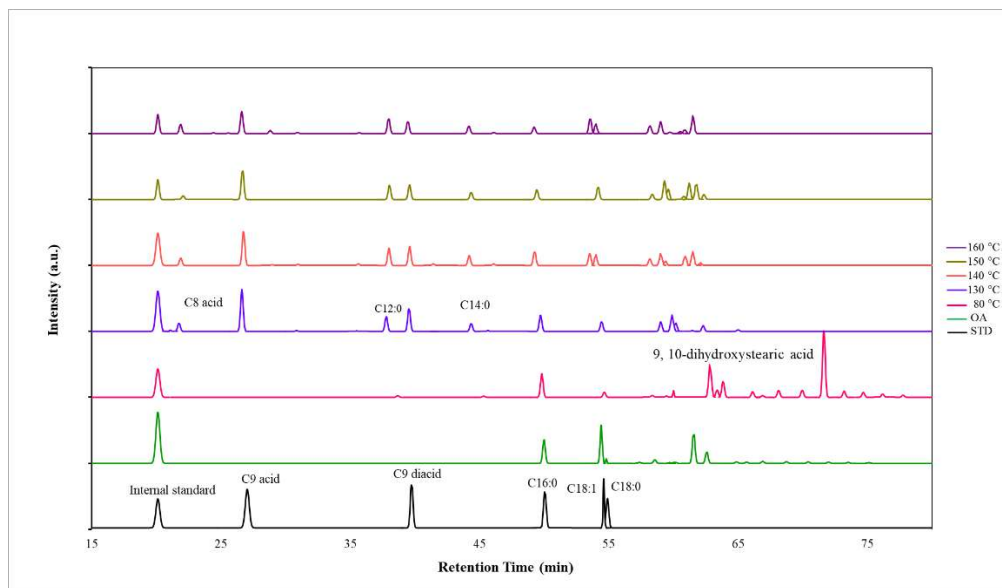


Fig.2 Chromatogram of GC-MS comparing standard oleic acid and the oxidative cleavage reaction of oleic acid at temperatures 80, 130, 140, 150, and 160 °C, reaction time 6 hours under autogenous pressure.

Chromatograms of reactions at various temperatures between 80 and 160 °C are displayed in Figure 2. The reactions are compared from reactant to reaction. As may be observed, C16:0 and C18:0 are also present in the reactants. It was discovered that very little AA and PA were produced as results of the reaction when it was conducted at a temperature of 80 °C, and other by-products were created. However, it can be seen that at a higher temperature of 80 °C, it clearly forms AA and PA and also by-products, i.e., caprylic acid (C8 acid), lauric acid (C12:0), myristic acid (C14:0), and 9, 10-dihydroxystearic acid (9,10-DSA). Observing a tendency for stearic acid (C18:0) and palmitic acid (C16:0) to decrease at high temperatures, to determine whether it is possible to produce both products (AA and PA), we performed an experiment by replacing oleic acid with C16:0 and C18:0 using an experimental temperature of 80 °C and 130 °C at a reaction time of 6 hours. It seems that there is no AA or PA.

When temperatures rise, one important by-product of methyl esters fatty acid oxidation is C8 acid, which can be synthesized from the 9-hydroxyperoxide of oleic and linolenic acids [12]. Moreover, it can be observed that the presence of 9,10-dihydroxystearic acid is reduced when the reaction is carried out at a higher temperature. According to Figure 3, the presence of 9,10-DSA was pronounced at 80°C and gradually decreased with increasing temperature. In particular, at 140°C, the content of 9,10-DSA decreased significantly. German and Colombo implied that AA PP, C8 diacid, and C8 acid can be generated through the oxidative cleavage process of 9,10-dihydroxystearic acid [13, 14]. This suggests that the reaction at 140°C has the potential for 9,10-DSA to convert to AA and PA, resulting in a higher yield compared to other temperatures. This consistency is depicted in Figures 3 and 4.

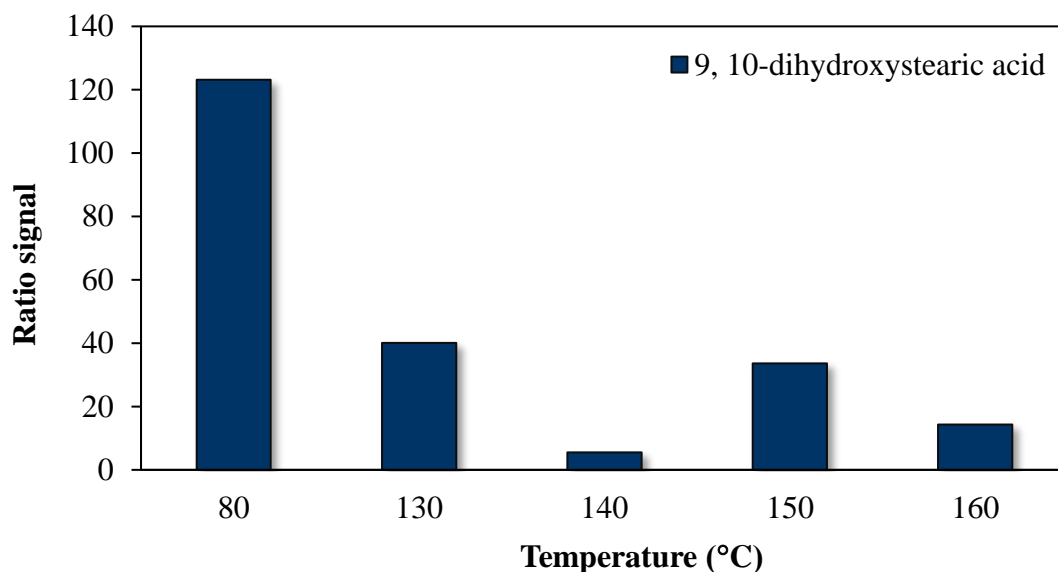


Fig. 3 9, 10-dihydroxystearic acid is formed from reactions at temperatures of 80, 130, 140, 150, and 160 °C; reaction time: 6 hours under autogenous pressure.

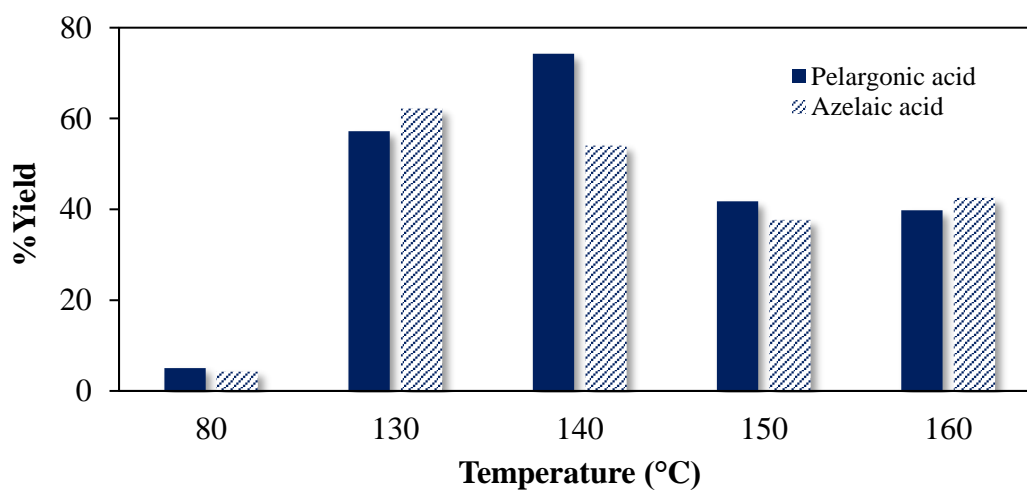


Fig. 4 Pelargonic acid and azelaic acid yield at temperatures of 80, 130, 140, 150, and 160 °C; reaction time: 6 hours under autogenous pressure.

In the experimental results, temperature significantly affects the yields of both PA and AA. The PA yield at 80 °C was observed to be 5.01%, steadily increasing to a maximum of 74.29% at 140 °C. This suggests that increasing temperatures promote PA production. However, when the temperature exceeds 140 °C, the PA yield sharply drops to 41.77% at 150°C and further decreases to 39.81% at 160 °C. These results are depicted in Figure 4. The decrease in PA yield indicates that excessively high temperatures may generate other by-products, leading to a reduction in overall yield. In contrast, AA yields follow a different trend. They increase steadily from 4.25% at 80°C to a peak of 62.22% at 130°C. However, when the temperature surpasses 130°C, the yield rapidly declines to 54.06% at 140°C, continuing to

decrease to 37.69% at 150°C before slightly rising to 42.56% at 160°C. This suggests that while moderate temperatures enhance AA production, excessive heat may impede AA formation, possibly due to side reactions or decomposition.

#### 4. Conclusions

The study highlights temperature-dependent yields of AA and PA, with increased temperature enhancing PA production but excessive heat reducing yields due to by-product formation. In contrast, AA production benefits from moderate temperatures but is hindered by excessive heat, likely due to side reactions or decomposition. These observations underscore the pivotal role of temperature control in modulating the yield of desired products and mitigating the formation of unwanted by-products during the oxidative cleavage of oleic acid. Optimal PA yield occurs at 140°C, while moderate temperatures around 130°C enhance AA production. Precise temperature control is essential for optimizing desired product yields.

#### References

- [1] Vondran, J., et al. (2022). From tandem to catalysis—organic solvent nanofiltration for catalyst separation in the homogeneously W-catalyzed oxidative cleavage of renewable methyl 9, 10-dihydroxystearate. *Catalysis Science & Technology*, 12(11), 3622-3633.
- [2] Yun, D., et al. (2021). Reactive species and reaction pathways for the oxidative cleavage of 4-octene and oleic acid with H<sub>2</sub>O<sub>2</sub> over tungsten oxide catalysts. *ACS Catalysis*, 11(5), 3137-3152.
- [3] Li, X., J.C.P. Syong, and Y. Zhang. (2018). Sodium stannate promoted double bond cleavage of oleic acid by hydrogen peroxide over a heterogeneous WO<sub>3</sub> catalyst. *Green Chemistry*, 20(15), 3619-3624.
- [4] Kerenkan, A.E., F. Béland, and T.-O. Do. (2016). Chemically catalyzed oxidative cleavage of unsaturated fatty acids and their derivatives into valuable products for industrial applications: a review and perspective. *Catalysis Science & Technology*, 6(4), 971-987.
- [5] Yun, D., Z. Zhang, and D.W. Flaherty. (2022). Catalyst and reactor design considerations for selective production of acids by oxidative cleavage of alkenes and unsaturated fatty acids with H<sub>2</sub>O<sub>2</sub>. *Reaction Chemistry & Engineering*, 7(9), 2054-2065.
- [6] Turnwald, S., et al. (1998). Oleic acid oxidation using hydrogen peroxide in conjunction with transition metal catalysis. *Journal of materials science letters*, 17, 1305-1307.
- [7] Behr, A., N. Tenhumberg, and A. Wintzer. (2013). Efficient ruthenium-catalysed oxidative cleavage of methyl oleate with hydrogen peroxide as oxidant. *RSC advances*, 3(1), 172-180.
- [8] Zhang, P., et al. (2018). Mechanisms of hydroxyl radicals production from pyrite oxidation by hydrogen peroxide: Surface versus aqueous reactions. *Geochimica et Cosmochimica Acta*, 238, 394-410.
- [9] Sharma, H. and D.S. Sharma. (2017). Detection of hydroxyl and perhydroxyl radical generation from bleaching agents with nuclear magnetic resonance spectroscopy. *Journal of Clinical Pediatric Dentistry*, 41(2), 126-134.

- [10] Gierer, J. and K. Jansbo. (1993). Formation of hydroxyl radicals from hydrogen peroxide and their effect on bleaching of mechanical pulps. *Journal of wood chemistry and technology*, 13(4), 561-581.
- [11] Ichihara, K.i. and Y. Fukubayashi. (2010). Preparation of fatty acid methyl esters for gas-liquid chromatography [S]. *Journal of lipid research*, 51(3), 635-640.
- [12] Romano, R., et al. (2021). Oxidative stability of high oleic sunflower oil during deep-frying process of purple potato Purple Majesty. *Heliyon*, 7(3).
- [13] German, D., et al. (2024). Oxidative Cleavage of 9, 10-Dihydroxystearic Acid on Supported Au, Pd and PdAu Nanoparticle-Based Catalysts. *Reactions*, 5(1), 120-134.
- [14] Colombo, D., et al. (2021). Oxidation of threo-9, 10-Dihydroxystearic Acid Mediated by *Micrococcus luteus* as a Key Step in the Conversion of Oleic Acid into Pelargonic and Azelaic Acids. *ChemCatChem*, 13(14), 3275-3282.

## Simulation-Assisted Transfer Learning for Steam Consumption Prediction in Industrial Steam Monitoring with Limited Data Scenario

Chayanit Chuay-ock, Chanin Panjapornpon\*, and Santi Bardeeniz

Department of Chemical Engineering, Faculty of Engineering, Kasetsart University, Bangkok 10900, Thailand  
E-mail: \* fengcnp@ku.ac.th

### Abstract

Steam consumption is a primary utility in industrial operations, serving as a crucial heat source that necessitates an accurate monitoring system. However, one of challenges in implementing effective steam monitoring arises from the missing information. In a practical industrial setting, only the measurement of total steam usage is accessible, while specific information regarding the steam utilization of each individual equipment unit is frequently unavailable. To address this challenge, this study proposes a novel approach for predicting steam consumption across multiple equipment units using simulation-assisted transfer learning allocator. The proposed method leverages simulation data to train two output streams, gaining pre-trained knowledge and operational constraints. The knowledge is then employed in transfer learning phase, utilizing partial layer freezing technique, to obtain the third output stream. Simultaneously, the target domain is supervised by total steam consumption to adjust the learnable parameters towards the true function. By combining these strategies, the study aims to enhance adaptation and improve the accuracy of estimating steam consumption among different equipment units within industrial processes, even missing information of individual steams. Furthermore, the proposed model verifies the practicability and reliability through a case study of a large-scale crude glycerol purification process.

**Keywords:** Missing information; Limited data; Simulation-assisted allocator; Transfer learning; Steam consumption prediction

### 1. Introduction

Energy serving as an input factor within industrial production processes now significantly influences operational efficiency and cost effectiveness (Shi et al., 2024). Particularly, steam consumption stands out as a fundamental component in the realm of industrial processes, commonly used as a vital heat source essential for various operations. Nevertheless, a notable challenge in establishing effective steam monitoring systems arises due to the restricted availability of data. Within a practical industrial setting, only the quantification of overall steam consumption is available, without detailed data on the steam utilization of each equipment unit. In order to tackle this challenge, it is vital to accurately forecast the amount of steam that will be used, especially when determining the specific allocation of total steam usage for each individual piece of equipment.

Process simulation is the virtual replication of real-world processes or systems, commonly within computational domains. In the industrial sector, process simulation enables users to observe the consequences of varying conditions and strategies, thereby providing valuable insights for analysis and enhancement. Numerous engineering research studies commonly utilize modeling and simulation techniques as valuable tools to study several industrial equipment and processes. For instance, a simulation technique has been utilized to simulate a

cryogenic distillation process of atmospheric air under conditions of both steady-state and dynamic operation (Yerolla et al., 2022). Consequently, numerous process variables, including product purity, product recovery, and various behaviors, are obtained through various modifications in the process. In addition, a process simulation of syngas production from regasified liquefied natural gas was developed to obtain process monitoring and performance enhancement (Sunny et al., 2016). In response to the limited data and missing information, a process simulation thereby emerges as a promising solution to handle information deficiencies. Therefore, this affords valuable insights into steam utilization across individual equipment units. As research attention shifts towards artificial intelligence, numerous studies of an artificial neural network (ANN) model have been employed to predict energy consumption, thereby promoting efficient and ecologically sustainable improvement within the industrial sector (Zhang et al., 2022). Some researchers have utilized the integration of simulation and ANN models to predict building energy consumption (Sharif & Hammad, 2019). Additionally, the ANN model has been applied to determine the complex relationship between energy consumption and its influencing factors, highlighting the network capability in precisely forecasting energy consumption (Olanrewaju et al., 2012). Some researchers adopted a transfer learning technique, which remarkably improves the predictive performance due to its capacity to mitigate uncertainties and handles the challenge of limited sample size (Du et al., 2023). Therefore, simulation techniques and ANN models have played a crucial role in gaining insights into and predicting energy consumption trends. However, it is recognized that relying solely on the simulation domain may introduce limitations in achieving precise prediction, particularly in the practical industrial domain.

Therefore, this study proposes a modeling framework for simulation-assisted transfer learning for steam consumption allocation. The proposed technique uses data obtained from simulation to train two output streams. By pre-training these outputs, the model gains knowledge of the operational constraints of the industrial process. Upon completing the pre-training phase, transfer learning with partial layer freezing is applied to maintain the knowledge gained from simulation domains. The model then progresses to the final phase of training by fine-tuning the network to create the third output stream based on the total steam consumption obtained from a real industrial process. These strategies aim to enhance adaptation and improve the accuracy of estimating steam consumption among different equipment units within industrial processes, even when information is missing. In addition, the proposed model verifies its practicability and reliability through a case study of a large-scale crude glycerol purification process. The following are the main contributions of this study:

1. The simulation model of crude glycerol purification process is a virtual replication of an industrial process. The simulation model provides synthetic datasets to handle missing information which is steam utilization by each individual equipment unit.
2. Steam consumption prediction is performed by utilizing an integration of ANN model and simulation-assisted transfer learning techniques.
3. Simulation-Assisted Transfer Learning Allocator (SATLA) is developed by the above-mentioned model to estimate steam consumption among different equipment units.



## 2. Methodology

### 2.1 Description of Crude Glycerol Purification Process

The process involves a series of techniques to achieve high-purity glycerol suitable for industrial applications. Distillation stands out as a practical method, primarily used to eliminate water and methanol based on their boiling points. Before distillation, acidification induces a phase separation mechanism, eliminating matter organic non-glycerol (MONG) and producing inorganic salts. Next, the acidified crude glycerol undergoes subsequent neutralization with an NaOH solution to recover glycerol from free triglycerides. Finally, vacuum distillation effectively removes impurities while minimizing thermal degradation. The block diagram of crude glycerol purification process is shown in Fig. 1.

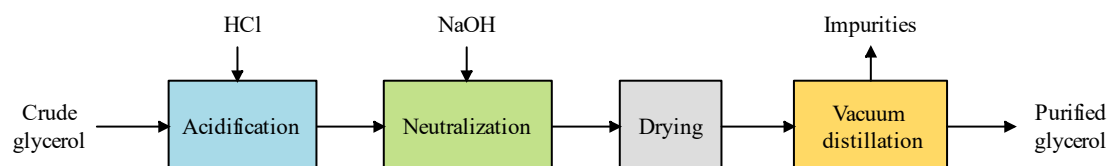


Fig. 1 Block diagram of crude glycerol purification process.

### 2.2 Process Simulation

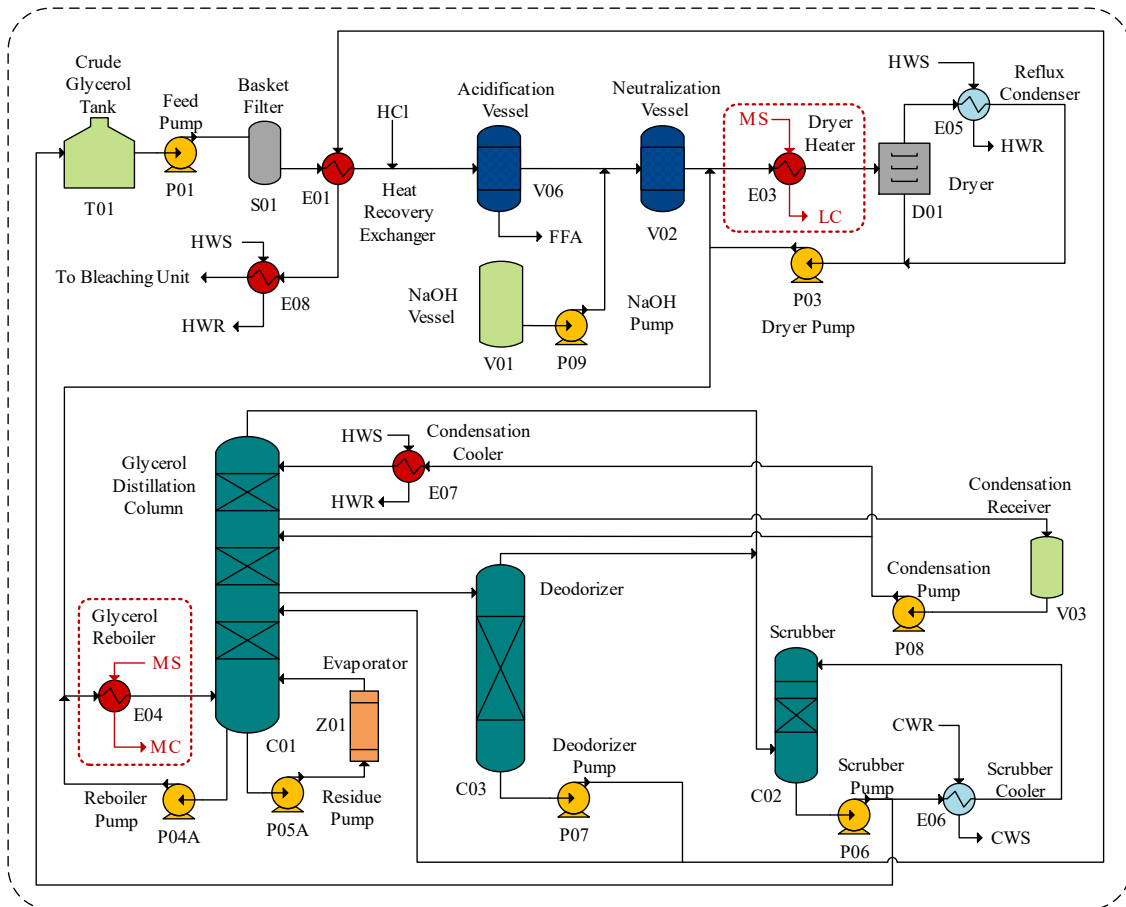
The simulation model for the crude glycerol purification process is constructed using the UniSim Design Suite simulation software, depicted in Fig. 2. In this process, a steam totalizer is responsible for distributing steam to three distinct equipment units, which are E03, E04, and vacuum system (VAC). Notably, the steam totalizer is designed to provide measurable usage data, whereas the three equipment units (E03, E04, and VAC) are considered non-measurable in terms of their steam usage. In this study, the simulation model is crucially employed to acquire simulated data, addressing the challenge posed by non-measurable steam usage. Moreover, the study employs 20 keys process variables, as shown in Table 1, to develop both the simulation model and deep learning approaches.

Table 1. Key process variables for simulation model and deep learning in crude glycerol purification.

No.	Description	No	Description
1	Crude glycerol feed rate	11	Inlet temperature of condensation cooler
2	Inlet temperature of dryer	12	Mass flowrate from P08 to E07
3	Inlet temperature of reflux condenser	13	Temperature of condensation receiver
4	Mass flowrate from P03 to E04	14	Mass flowrate from P07 to C01
5	Temperature at E08 to bleaching unit	15	Top pressure of deodorizer
6	Pressure of MS* at glycerol reboiler	16	Top pressure of scrubber
7	Bottom temperature of distillation column	17	Outlet temperature of scrubber cooler
8	Bottom pressure of distillation column	18	Pressure of MS* at totalizer
9	Top pressure of distillation column	19	Temperature of MS* at totalizer
10	Top temperature of distillation column	20	Mass flowrate of MS* at totalizer

MS\* denotes medium-pressure steam.

### GLYCERINE DISTILLATION



### VACUUM SYSTEM

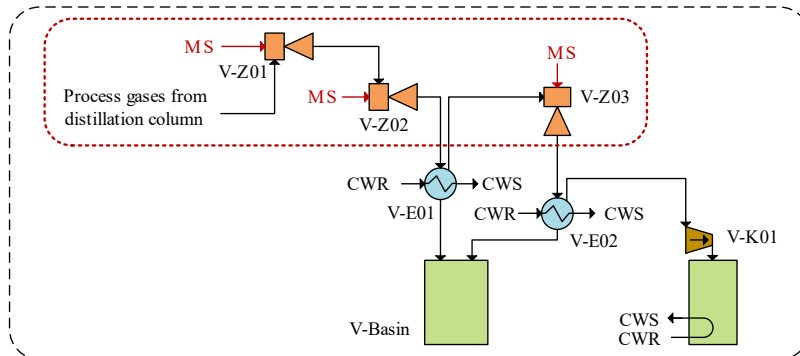


Fig. 2 Process flow diagram of crude glycerol purification process.

### 2.3 Modeling Framework for SATLA

Fig. 3 depicts the framework for developing the SATLA model. The simulation model for the crude glycerol purification process was developed based on real-world process data, sampled at four-hour intervals. However, detailed process information about the vacuum systems is not available in this study due to practical limitations in the industrial setting. Thus, the simulation model is constrained, providing steam usage data specifically for E03 and E04.

The subsequent step involves employing a deep learning approach. The process data and simulated data of E03 and E04 are utilized to develop two distinct models for each, leveraging ANN. In this approach, the Bayesian optimization method is applied to acquire the optimal hyperparameters. After obtaining pre-trained knowledge from models E03 and E04, the transfer learning approach is implemented. Subsequently, new process data, sampled at one-minute intervals, is acquired for the implementation of the SATLA technique. The layers from models E03 and E04 undergo a partial layer freezing technique. Learnable layers are then introduced to represent steam usage for VAC. An additional layer in MATLAB is employed, thereby constraining the model by total steam consumption. This allows the model to adapt using insight gained from E03 and E04 models, with a specific focus on capturing steam usage patterns within VAC. The model performance is evaluated by using RMSE, MAPE, and  $R^2$ .

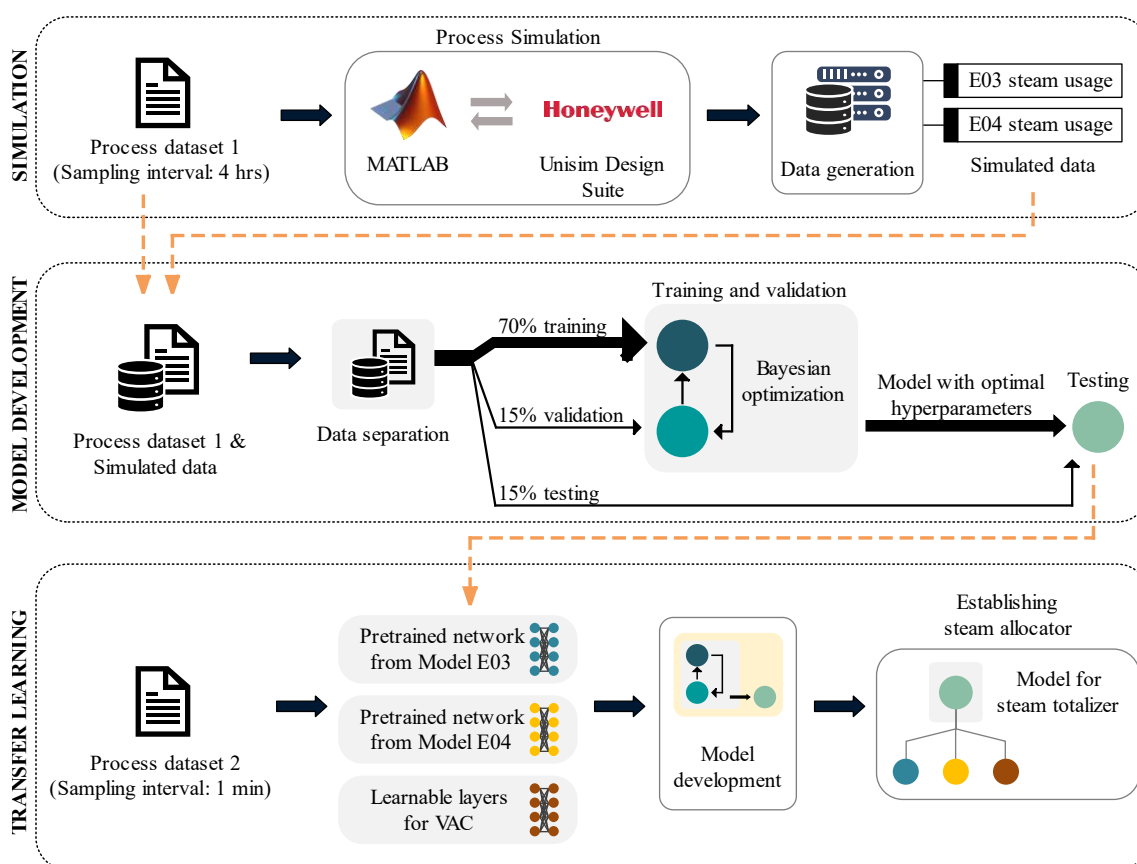


Fig. 3 Modeling framework of SATLA.

### 3. Results and Discussion

#### 3.1 Model Performance in Predicting Steam Consumption for E03 and E04

The initial phase of this study focuses on the exploration of deep learning models, particularly ANN, to predict steam consumption in the crude glycerol purification process. This involves employing simulation data to develop prediction models. The models receive input from various variables, including process temperature, pressure, and mass flowrate, as illustrate in Table 1. The output layer of each model thus utilizes the acquired knowledge and patterns to

generate a prediction for steam usage of each equipment unit. The models are trained and validated, and their hyperparameters are optimized by the Bayesian optimization method (Liu et al., 2019). The optimized values for these hyperparameters are detailed in Table 2. For model E03, the optimal number of layers is two, while for model E04, it is three layers. This difference can be attributed to the complexity of E04, the glycerol reboiler, in comparison to E03, the dryer heater. Subsequently, the models' performance is evaluated. The results for models E03 and E04, are presented in Table 3. In the evaluation of model E03, an MAPE of 1.4% is coupled with a notably high  $R^2$  at 0.9939. Also, model E04 performs well with a smaller MAPE of 1.2%, while maintaining a commendable  $R^2$  of 0.9710.

### 3.2 Performance Evaluation of the SATLA Technique

To develop a prediction model for the steam totalizer, the SATLA technique leverages the knowledge acquired from models E03 and E04 through transfer learning, involving the introduction of a new process dataset. A key aspect of this technique is the integration of learnable layers designed to represent the non-measurable VAC. Simultaneously, the pre-trained networks of models E03 and E04 undergo a freezing process. Additionally, the Bayesian optimization method is applied to determine the optimal hyperparameters for the VAC learnable layers, with the results presented in Table 4. The performance of the steam totalizer prediction model is evaluated. Table 3 provides the model's accuracy including MAPE, RMSE, and  $R^2$ . Furthermore, line plots and scatter plots depicting the predicted value against the actual value are shown in Fig. 4. The result indicates that the SATLA technique is highly effective in developing accurate prediction models, particularly in scenarios with limited data availability. The close alignment between predicted and actual values, along with a minimal MAPE of 1.47% and a substantial  $R^2$  of 0.9424, proves the accuracy and reliability of the model.

### 3.3 SATLA Results

After developing the steam totalizer model, three distinct network architectures are constructed. Each architecture specializes in capturing specific aspects of steam usage at individual equipment units. Therefore, a steam allocator named SATLA is developed by freezing each network architecture and then concatenating them to form a comprehensive model. The results are depicted in Fig. 5.

Table 2. Optimal hyperparameters for models E03 and E04.

Model	Hyperparameter	Searching domain	Optimal value
E03	Initial Learn Rate	[0.00001, 1]	0.2583
	Numbers of Layers	[1, 3]	2
	Numbers of Neurons in Layer 1	[1, 100]	100
	Numbers of Neurons in Layer 2	[1, 100]	39
E04	Initial Learn Rate	[0.00001, 1]	0.0658
	Numbers of Layers	[1, 3]	3
	Numbers of Neurons in Layer 1	[1, 200]	28
	Numbers of Neurons in Layer 2	[1, 200]	196
	Numbers of Neurons in Layer 3	[1, 200]	125

Table 3. Model performance for steam consumption prediction.

Model		MAPE	RMSE	R <sup>2</sup>
<b>E03*</b>	Validation	1.0443	3.7345	0.9969
	Testing	1.4255	4.9485	0.9939
<b>E04*</b>	Validation	0.8047	100.7932	0.9404
	Testing	1.2192	67.8450	0.9710
<b>Totalizer<sup>†</sup></b>	Validation	1.5575	73.4067	0.9541
	Testing	1.4656	74.1204	0.9424

\* denotes model developed from simulation data.

† denotes model developed using the SATLA technique.

Table 4. Optimal hyperparameters for VAC learnable layers.

Hyperparameter	Searching domain	Optimal value
Initial Learn Rate	[0.00001, 1]	0.0071
Numbers of Layers	[1, 3]	3
Numbers of Neurons in Layer 1	[1, 200]	101
Numbers of Neurons in Layer 2	[1, 200]	200
Numbers of Neurons in Layer 3	[1, 200]	179

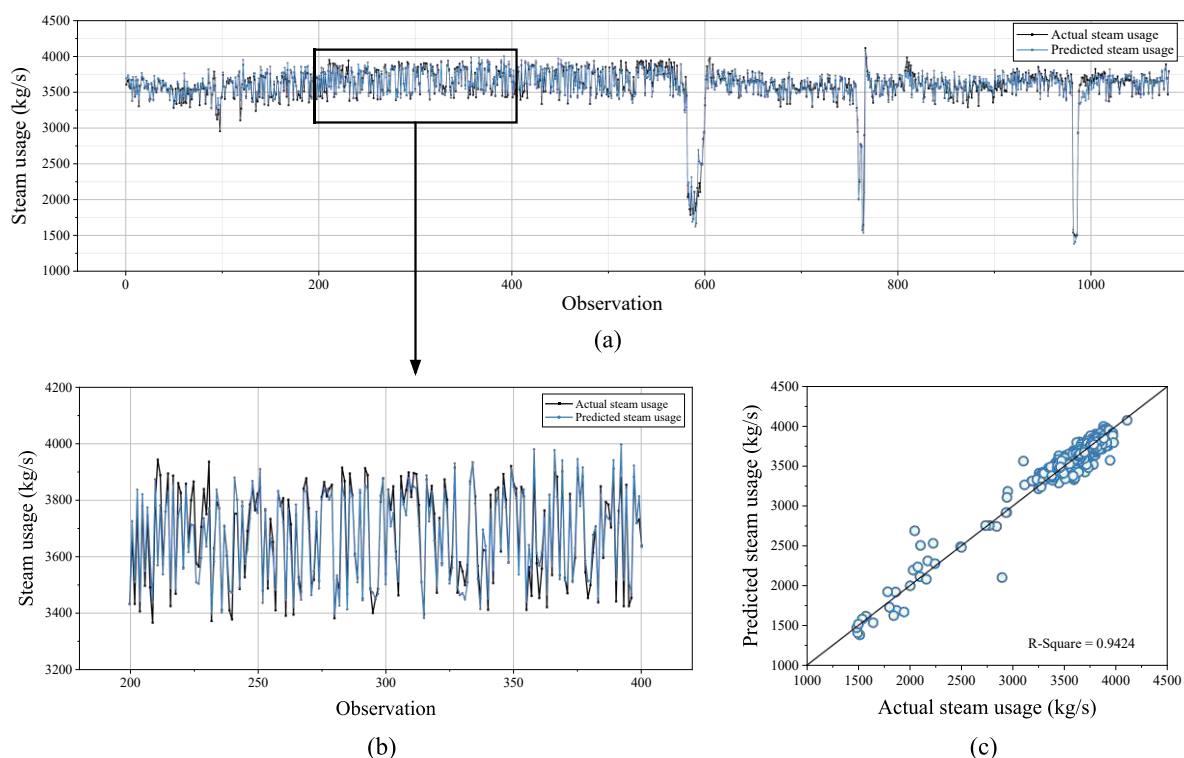


Fig. 4 Results of total steam consumption prediction model based on the SATLA technique: (a) all testing data, (b) subset with 200 to 400 observations, (c) scatter plot.

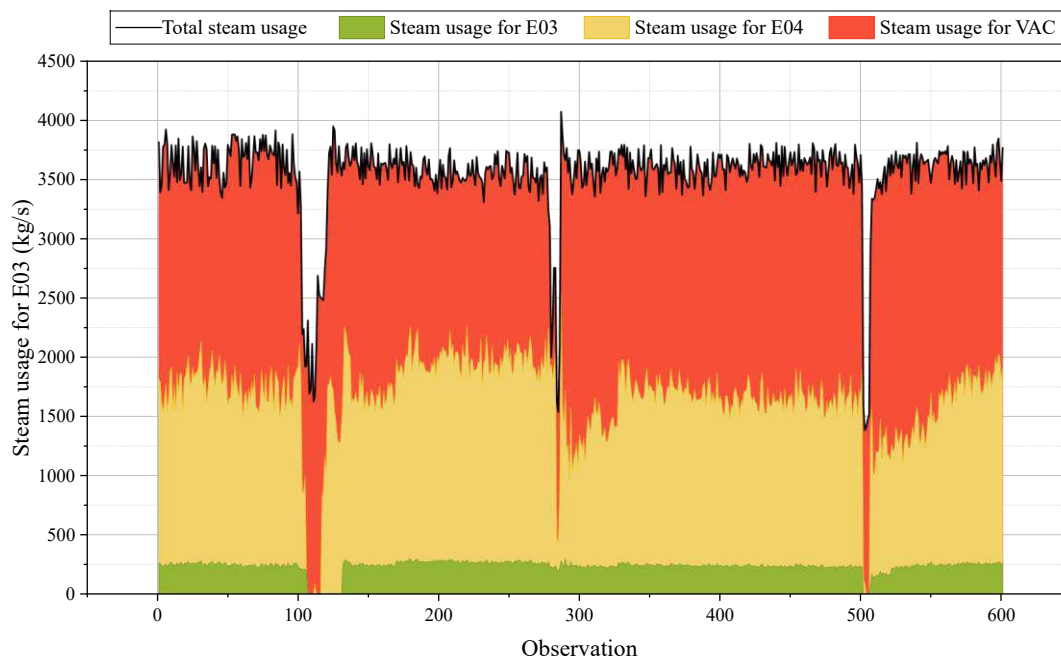


Fig. 5 Result of SATLA.

#### 4. Conclusion

In this study, the primary aim is to develop a robust methodology for predicting steam consumption in the crude glycerol purification process, a challenging task complicated by missing information. To address this, we propose the SATLA technique that utilizes a simulation model as a tool to handle the missing information. Moreover, the integration of deep learning, specifically ANN, and a transfer learning technique demonstrates the effectiveness of incorporating total steam consumption as a constraint. The proposed technique establishes its accuracy and reliability in predicting steam consumption across various equipment units within industrial processes, achieving a minimal MAPE value of 1.47% and a high R-square value of 0.9424. These findings contribute a valuable method to handle the challenge posed by limited data and missing information.

#### Acknowledgement

The authors express their sincere gratitude for the support received from the Department of Chemical Engineering, Faculty of Engineering, Kasetsart University, which provided funding for this study. Additionally, the authors would like to acknowledge Honeywell and GRD Tech Co., Ltd for providing the UniSim Design Suite, a process simulation software used in this study.

#### References

- [1] Du, S., Wang, M., Yang, J., Zhao, Y., Wang, J., Yue, M., Xie, C., & Song, H. (2023). An enhanced prediction framework for coalbed methane production incorporating deep learning and transfer learning. *Energy*, 282, 128877.

- [2] Liu, Y., Qin, H., Zhang, Z., Pei, S., Wang, C., Yu, X., Jiang, Z., & Zhou, J. (2019). Ensemble spatiotemporal forecasting of solar irradiation using variational Bayesian convolutional gate recurrent unit network. *Applied Energy*, 253, 113596.
- [3] Olanrewaju, O. A., Jimoh, A. A., & Kholopane, P. A. (2012). Integrated IDA–ANN–DEA for assessment and optimization of energy consumption in industrial sectors. *Energy*, 46(1), 629–635.
- [4] Sharif, S. A., & Hammad, A. (2019). Developing surrogate ANN for selecting near-optimal building energy renovation methods considering energy consumption, LCC and LCA. *Journal of Building Engineering*, 25, 100790.
- [5] Shi, G., Pan, S., Zou, R., & Yu, A. (2024). STGNets: A spatial–temporal graph neural network for energy consumption prediction in cement industrial manufacturing processes. *Powder Technology*, 434, 119280.
- [6] Sunny, A., Solomon, P. A., & Aparna, K. (2016). Syngas production from regasified liquefied natural gas and its simulation using Aspen HYSYS. *Journal of Natural Gas Science and Engineering*, 30, 176–181.
- [7] Yerolla, R., Muhammed, R. C. A., Naseef, Y., & Besta, C. S. (2022). Simulation of cryogenic distillation of atmospheric air using Aspen HYSYS. *IFAC-PapersOnLine*, 55(1), 860–865.
- [8] Zhang, X., Hou, L., Liu, J., Yang, K., Chai, C., Li, Y., & He, S. (2022). Energy consumption prediction for crude oil pipelines based on integrating mechanism analysis and data mining. *Energy*, 254, 124382.

## **Fabrication of Thin Film Composite Nanofibrous Membrane using Electrospinning and Dip Coating Technique for Selective Protein Purification**

**Alkaif Rafi Dina Gamgali<sup>1</sup>, Chalida Klayson<sup>2</sup>, and Ratthapol Rangkupan<sup>3,\*</sup>**

<sup>1</sup> Department of Nanoscience and Technology, Chulalongkorn University, Bangkok, Thailand

<sup>2</sup> Center of Excellence in Particle and Material Processing Technology, Department of Chemical Engineering, Chulalongkorn University, Bangkok, Thailand

<sup>3</sup> Metallurgy and Materials Science Research Institute, Chulalongkorn University, Bangkok, Thailand

E-mail: \*ratthapol.r@chula.ac.th

### **Abstract**

Membrane technology is highly effective in isolating proteins from other molecules through size exclusion or diffusion. However, many protein separation membranes are made from relatively hydrophobic polymers like polysulfone, a widely used material in the traditional membrane production method known as phase inversion. These membranes are prone to fouling caused by various impurities that are exacerbated by their non-uniform pore sizes and inherent hydrophobic properties. This research aimed to fabricate a thin film composite nanofibrous (TFCN) membrane with highly selective and improved anti-fouling properties by using a versatile electrospinning and dip coating method. Polyacrylonitrile-co-methyl acrylate (PAN-co-MA) electrospun nanofiber support was dip-coated with various concentrations (1.5, 3, and 5 wt%) of Pebax®. The results showed that the PAN nanofibrous was successfully coated with Pebax®. The highest solute rejection of 56.63±4.99% with a permeance flux of 2.21±0.15 L.m<sup>-2</sup>.h<sup>-1</sup>.bar<sup>-1</sup> was achieved by the thin film with 5% Pebax®. This membrane exhibited good potential as an ultrafiltration or nanofiltration membrane for the purification of protein. Further studies on the hydrophilicity, specific molecular weight cut-off, and anti-fouling properties of the TFCN are recommended to explore its capacity as a new, lightweight, and highly efficient membrane.

**Keywords:** Electrospinning; nanofibrous membrane; protein purification; thin film.

### **1. Introduction**

The rapid increase in the human population has led to a higher consumption of food derived from both plants and animals. This consumption results in significant amounts of food waste, which includes a considerable quantity of discarded protein [1]. There are several works that have been done to deal with food waste problems and transform the food waste into various products such as biofertilizer, food stock for animal husbandry, and bioenergy [2]. To mitigate food waste and meet protein demand regarding the growing population, it is also essential to purify and recover the high protein content found in food waste. Recovering protein not only addresses the demand for protein but also indirectly reduces food waste disposed to the environment [3,4].

Protein can be extracted from food waste using various methods, including chemical, biochemical, and physical techniques [3]. Membrane technology, a physical method, has shown exceptional efficacy in protein recovery due to its lower energy requirements, cost-effectiveness, and adjustable performance [5]. Membrane technology offers significant benefits as a promising method for recovering protein from food waste. However, it faces challenges



due to its susceptibility to fouling. Over time, the continuous operation of the membrane system can reduce protein yield due to the blockage of pores by smaller protein fractions or the formation of a cake layer [6,7]. The propensity for membrane fouling is mainly related to specific characteristics, such as low hydrophilicity and a closed pore structure. These are often a result of the phase inversion method used in production, which tends to favor hydrophobic polymers. Developing membranes with enhanced fouling resistance and selectivity is essential for achieving sustained, high-quality protein recovery over long-term operations.

Electrospinning presents a promising avenue for membrane fabrication due to its simple process and the wide range of polymers that can be used. This method allows for the production of nanofibrous membranes with customizable characteristics by adjusting processing parameters. These membranes typically feature high porosity and interconnected nano-sized fibers, facilitating direct molecule transport through the membrane [10]. However, their high porosity and large pore size can limit their use as standalone filtration membranes for small molecules. To overcome this, modifications such as adding a composite with a thin film layer can enhance membrane selectivity [11]. Selecting materials that increase the hydrophilicity of both the nanofibrous membrane and the thin film selective layer is crucial for achieving a high flux membrane with superior selectivity for protein recovery.

Polyacrylonitrile (PAN), known for its excellent spinnability, hydrophilicity, and chemical resistance, is an attractive material for crafting nanofibrous membranes via electrospinning. [12]. Additionally, Poly(ether-block-amide) (Pebax® 1657) films, recognized for their density and mechanical strength, can serve as a thin film to augment the selectivity and mechanical durability of the membrane [13]. This research aims to explore the combination of nanofibrous membranes with a thin film selective layer for protein recovery. The study examines various membrane characteristics, including surface morphology, structure, and chemical bonds, using SEM, confocal microscopy, and ATR-FTIR. Performance evaluations, including permeance flux and filtration assays with PEG as a representative molecule, were conducted to assess membrane efficacy.

## 2. Materials & Methods

### 2.1 Materials

Poly (acrylonitrile-co-methyl acrylate) (PAN-co-MA) with a molecular weight of 150,000 g/mol (methyl acrylate 8.5%) was purchased from Haihang Industry, China. Poly(ether-block-amide) (Pebax® 1657) was purchased from Arkema. N,N-Dimethylformamide (DMF) was obtained from Carlo Erba Reagents, France. Polyethylene glycol (PEG) with molecular weights of 35,000 Da was supplied by Sigma-Aldrich. Hydrochloric acid (HCL, 36-38% AR) was obtained from SDFCL, India. Ethyl alcohol (absolute) was obtained from Duksan Pure Chemicals, Korea. Iodine was purchased from Kanto Chemical Co. Inc., Japan. Potassium iodide and Barium chloride were supplied from Guangdong Chemical, China.

### 2.2 Membrane Fabrication

The preparation of a thin-film composite nanofibrous membrane (TFCN) involves two steps, the fabrication of a nanofibrous support layer and the formation of thin film. The details of each step are as follows.

### 2.2.1 Fabrication of Nanofibrous Support

The nanofibrous support layer was fabricated using an electrospinning process as depicted in Fig. 1.

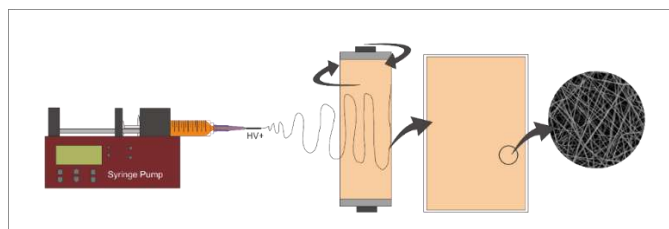


Fig. 1 Schematic illustration of the electrospinning process of the nanofibrous support layer

Firstly, PAN-co-MA was dissolved in DMF with a total solution concentration of 8 wt% overnight at 50 °C to get a well-dissolved polymer solution for electrospinning. The electrospinning parameters were set at 23 kV for applied voltage on the needle tip with the needle size of 0.55 mm. The polymer solution was ejected through the needle with a flow rate of 20  $\mu$ l/min. On the collector side, the rotating collector drum was rotated at a speed of 20 rpm with a fixed distance between the collector and the needle tip of 20 cm. The electrospinning process was running out for 6 h to get sufficient thickness of the nanofibrous support. The fabricated support was heat-pressed for 3 min at 100 °C.

### 2.2.2 Thin Film Formation

Pebax® thin film was deposited on the prepared support via a dip coating technique. Firstly, the coating solution was prepared by dissolving Pebax® in ethanol/water (7:3) with a total concentration of 1.5, 3, and 5% under a stirring condition for 24 h at 80 °C that coded as P1.5, P3, and P5 respectively. After that, the prepared nanofibrous support layer was dip-coated in each concentration of Pebax® and dried at 65 °C for 6 h in the oven.

## 2.3 Material Characterization

The morphology and structure of the fabricated support and TFCN membranes were observed using scanning electron microscopy (SEM, Hitachi S-3400N) and confocal microscopy (LEXT 3D Measuring Laser Microscope OLS5000). Attenuated total reflectance Fourier transform infrared spectroscopy (ATR-FTIR, Bruker Alpha II) was employed to examine the chemical structure of the membranes.

## 2.4 Membrane Performance Test

The performance of the fabricated membrane in terms of water permeance and solute rejection was carried out by dead-end filtration equipment with a membrane-effective area of 6.25 cm<sup>2</sup> as illustrated in Fig. 2.

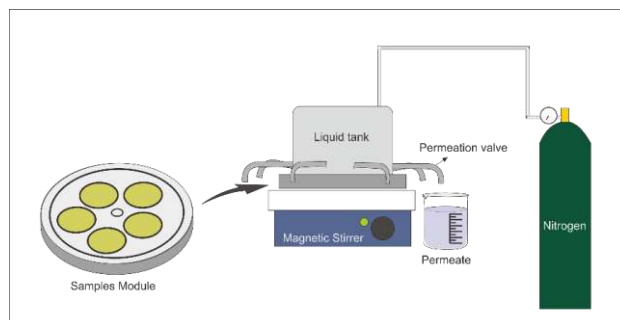


Fig. 2 Illustration of a dead-end module to measure membrane performance.

The TFCN membrane sample with a diameter of 2.5 cm was placed inside the dead-end module. PEG with a molecular weight of 35,000 Da was used as representative molecules for the target protein. The filtration of 500 ppm of PEG aqueous solution was carried out at a controlled pressure of 1 bar. The permeate volume and filtration time were recorded. The permeance flux and permeance were calculated using Eq. (1)

$$\text{Permeance Flux} = \frac{V}{T \times A \times P} \quad (1)$$

Where V is the volume (L), T is time (h), A is the total area of the sample (m<sup>2</sup>), and P is the pressure applied in the setup (bar).

Solute rejection is also determined using the following expression;

$$\text{Solute Rejection} = \left(1 - \frac{C_p}{C_f}\right) \times 100 \quad (2)$$

Where C<sub>p</sub> is the concentration of permeate (ppm) and C<sub>f</sub> is the concentration of feed (ppm). The concentration of PEG in feed and permeate was measured using UV-vis spectrophotometry at a wavelength of 535 nm.

### 3. Results and Discussion

#### 3.1. Material Characteristics

The PAN nanofibrous support membrane and TFCN membrane were successfully fabricated as can be observed in Fig. 3. The nanofibrous structure of the pristine PAN support membrane is highly porous, with an average fiber diameter of 138±9 nm. The SEM images reveal varying morphologies for TFCN coated with different concentrations of Pebax®. Specifically, the membrane coated with 5% Pebax® exhibited a uniform and even film. In contrast, nanofiber structure remains visible when coated at lower concentration of Pebax®.

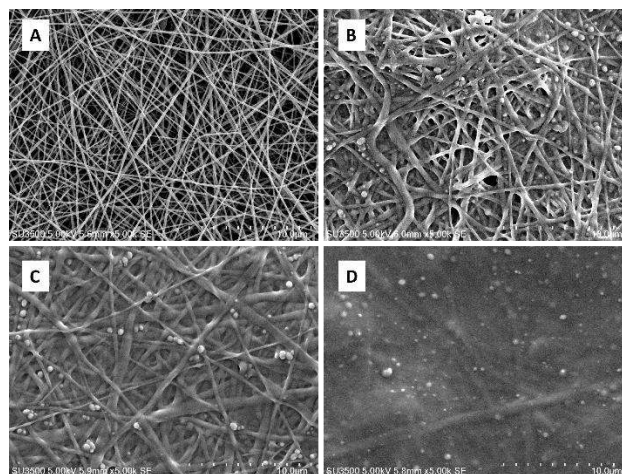


Fig. 3 SEM images of (A) PAN nanofibrous support and the TFCN membrane coated with (B) 1.5 wt.%, (G) 3.0 wt.%, and (D) 5.0 wt.% Pebax®.

The different morphology of the thin film that was deposited on top of the PAN nanofibrous layer was correlated with the concentration of the Pebax® aqueous solution. Dense thin film form in 5% Pebax® is closely affected by the high viscosity of the solution leading to a slow evaporation rate of the solvent. In contrast, the low viscosity of the Pebax® solution due to low concentration provides high solvent evaporation that favors thin film with less support coverage and defect formation [17,18].

Confocal images for all membrane samples depict that the surface roughness of the membranes was more than 1  $\mu\text{m}$  and the roughness tends to increase with the concentration of the coating solution. Additionally, confocal images of TFCN membranes highlight an uneven distribution of the Pebax® thin film atop the nanofibrous support layer, as illustrated in Fig. 4. This irregularity may result from the Pebax® solution infiltrating the surface during the coating process [18].

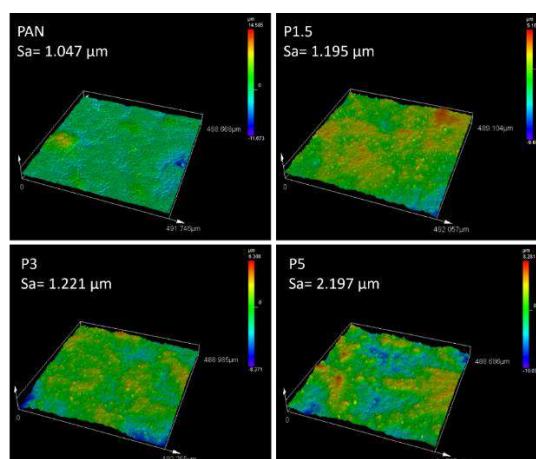


Fig 4. 3D surface confocal images of (A) PAN nanofibrous support and the TFCN membrane coated with (B) 1.5 wt.%, (G) 3.0 wt.%, and (D) 5.0 wt.% Pebax®, namely P1.5, P3 and P5, respectively.

FTIR analysis was conducted to pinpoint specific functional groups within the samples, as illustrated in Fig. 5. The FTIR spectrum of PAN nanofibrous support membrane shows the peak at  $2237\text{ cm}^{-1}$  and  $1736\text{ cm}^{-1}$  that indicate the peak for bond of  $\text{C}\equiv\text{N}$  and  $\text{C}=\text{O}$  respectively which are typical peaks of PAN-co-MA copolymer [14]. In contrast, the FTIR spectra of the TFCN membrane samples displayed distinct patterns compared to the PAN support. Notably, the TFCN samples exhibited peaks at  $3297\text{ cm}^{-1}$ ,  $2857\text{ cm}^{-1}$  -  $2937\text{ cm}^{-1}$ ,  $1636\text{ cm}^{-1}$ ,  $1143\text{ cm}^{-1}$ , and  $1096\text{ cm}^{-1}$ . These peaks represent the N-H, C-H, C=O, C-O, and C-N bonds, respectively, indicating the presence of Pebax®, which comprises polyamide and polyethylene oxide.

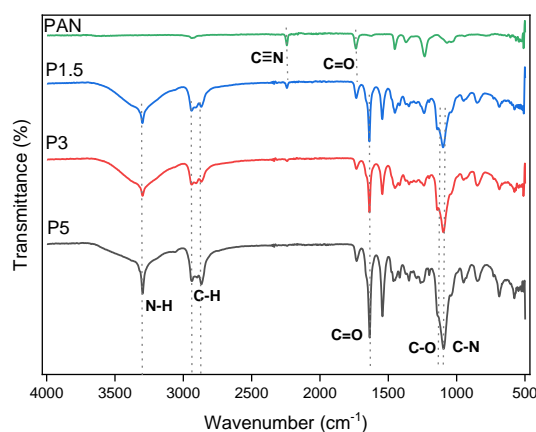


Fig. 5 FTIR spectrum of pristine PAN and TFCN membrane

### 3.2. Membrane Performance

Membrane performance in terms of water permeance flux and solute rejection against PEG with a molecular weight of 35000 Da was carried out using dead-end equipment. The permeate flux through the membranes markedly decreased following the application of the coating, and this decrease was more pronounced at higher concentrations of the coating solution, as shown in Fig. 6. Conversely, the ability of the membranes to reject solutes significantly improved as the concentration of the coating solution increased.

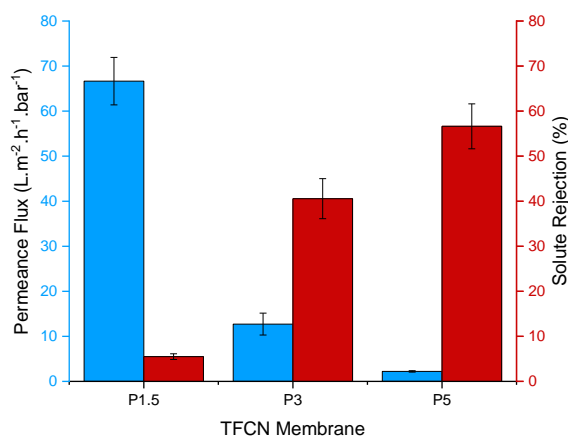


Fig. 6 Permeance flux and solute rejection of TFCN membrane

The permeability of the membrane is directly related to the density and thickness of its thin film. A denser and thicker film impedes fluid transport through the membrane, whereas a thinner film facilitates higher permeate flux [19]. The differences in rejection were also affected by the structure of the thin film [19]. Investigating the membrane's hydrophilicity, molecular weight cutoff, and antifouling properties is intriguing. Further modifications are recommended to further enhance the membrane characteristics and performance that meet the requirement in protein recovery application.

#### 4. Conclusion

A thin film nanocomposite membrane that consists of PAN nanofibrous support layer and Pebax® active separation layer was successfully fabricated using the electrospinning and dip coating method. Varying concentrations of Pebax® in the coating solution lead to distinct thin film structures, significantly influencing the TFCN membrane's performance. An increase in Pebax® concentration results in thicker and denser thin films. The thin film containing 5% Pebax® reached a peak solute rejection rate of around 57% and a permeance flux of 2.21 Lm<sup>-2</sup>h<sup>-1</sup>bar<sup>-1</sup>, showcasing its efficacy as a promising ultrafiltration or nanofiltration membrane for protein purification.

#### References

- [1] Peydayesh, M., Bagnani, M., Soon, W. L., and Mezzenga, R. (2022). Turning food protein waste into Sustainable Technologies. *Chemical Reviews*, 123(5), 2112-2154.
- [2] Musharavati, F., Ahmad, A., Javed, M. H., Sajid, K., and Naqvi, M. (2024). Sustainability assessment of biofuel and value-added product from organic fraction of municipal solid waste. *Environmental Research*, 246, 118121.
- [3] Piercy, E., Verstraete, W., Ellis, P. R., Banks, M., Rockström, J., Smith, P., Witard, O. C., Hallet, J., Hogstrand, C., Knott, G., Karwati, A., Rasoarahona, H. F., Leslie, A., He, Y., and Guo, M. (2023). A sustainable waste-to-protein system to maximise waste resource utilisation for developing food-and feed-grade protein solutions. *Green Chemistry*, 25(3), 808-832.
- [4] Henchion, M., Hayes, M., Mullen, A. M., Fenelon, M., and Tiwari, B. (2017). Future protein supply and demand: strategies and factors influencing a sustainable equilibrium. *Foods*, 6(7), 53.
- [5] Yadav, D., Karki, S., Gohain, M. B., and Ingole, P. G. (2023). Development of micropollutants removal process using thin-film nanocomposite membranes prepared by green new vapour-phase interfacial polymerization method. *Chemical Engineering Journal*, 472, 144940.
- [6] Tian, S., Yu, B., Du, K., and Li, Y. (2022). Purification of wheat germ albumin hydrolysates by membrane separation and gel chromatography and evaluating their antioxidant activities. *Lwt*, 161, 113365.
- [7] Rastogi, Y., and Gogate, P. R. (2022). Intensified recovery of whey proteins using combination of enzyme in free or immobilized form with ultrafiltration. *Chemical Engineering and Processing-Process Intensification*, 179, 109076.
- [8] Chiang, S. A., Liu, S. H., Hsiao, Y. S., Fu, C. C., and Juang, R. S. (2022). Nonsolvent-induced phase separation preparation of porous TOPO-mixed polyethersulfone membranes for selective clearance of p-cresol from simulated serum. *Separation and Purification Technology*, 290, 120911.

- [9] Filip, P. (2023). Explicit Expressions for a Mean Nanofibre Diameter Using Input Parameters in the Process of Electrospinning. *Polymers*, 15(16), 3371.
- [10] Liang, Y., Ma, H., Taha, A. A., and Hsiao, B. S. (2020). High-flux anti-fouling nanofibrous composite ultrafiltration membranes containing negatively charged water channels. *Journal of Membrane Science*, 612, 118382.
- [11] Ding, S., Li, P., Zhang, T., and Wang, X. (2022). Coordination of copper ion crosslinked composite beads with enhanced toxins adsorption and thin-film nanofibrous composite membrane for realizing the lightweight hemodialysis. *Advanced Fiber Materials*, 4(3), 556-570.
- [12] Vatanpour, V., Pasaoglu, M. E., Kose-Mutlu, B., and Koyuncu, I. (2023). Polyacrylonitrile in the Preparation of Separation Membranes: A Review. *Industrial & Engineering Chemistry Research*, 62(17), 6537-6558.
- [13] Rajati, H., Alvandi, H., Rahmatabadi, S. S., Hosseinzadeh, L., and Arkan, E. (2023). A nanofiber-hydrogel composite from green synthesized AgNPs embedded to PEBAX/PVA hydrogel and PA/Pistacia atlantica gum nanofiber for wound dressing. *International journal of biological macromolecules*, 226, 1426-1443.
- [14] Eldin, M. M., Elaassar, M. R., Elzatahry, A. A., and Al-Sabah, M. M. B. (2017). Poly (acrylonitrile-co-methyl methacrylate) nanoparticles: I. Preparation and characterization. *Arabian journal of chemistry*, 10(8), 1153-1166.
- [15] Estahbanati, E. G., Omidkhah, M., and Amooghin, A. E. (2017). Preparation and characterization of novel Ionic liquid/Pebax membranes for efficient CO<sub>2</sub>/light gases separation. *Journal of Industrial and Engineering Chemistry*, 51, 77-89.
- [16] Fam, W., Mansouri, J., Li, H., and Chen, V. (2017). Improving CO<sub>2</sub> separation performance of thin film composite hollow fiber with Pebax® 1657/ionic liquid gel membranes. *Journal of Membrane Science*, 537, 54-68.
- [17] Jomekian, A., Behbahani, R. M., Mohammadi, T., and Kargari, A. (2016). CO<sub>2</sub>/CH<sub>4</sub> separation by high performance co-casted ZIF-8/Pebax 1657/PES mixed matrix membrane. *Journal of Natural Gas Science and Engineering*, 31, 562-574.
- [18] Martínez-Izquierdo, L., Malankowska, M., Téllez, C., and Coronas, J. (2021). Phase inversion method for the preparation of Pebax® 3533 thin film membranes for CO<sub>2</sub>/N<sub>2</sub> separation. *Journal of Environmental Chemical Engineering*, 9(4), 105624.
- [19] Yu, X., Shen, L., Zhu, Y., Li, X., Yang, Y., Wang, X., Zhu, M., and Hsiao, B. S. (2017). High performance thin-film nanofibrous composite hemodialysis membranes with efficient middle-molecule uremic toxin removal. *Journal of Membrane Science*, 523, 173-184.

## UV- Enhanced Catalytic Oxidative Cleavage of Oleic Acid.

Nonrawit Janam<sup>1</sup>, Varong Pavarajarn<sup>1,\*</sup>

<sup>1</sup> Center of Excellence in Particle and Materials Processing Technology, Department of Chemical Engineering, Faculty of Engineering, Chulalongkorn University, Bangkok 10330, Thailand  
E-mail: \*Varong.p@chula.ac.th.

### Abstract

Oleic acid, a prominent fatty acid, serves as a vital precursor in various industrial processes. This study explores its conversion potential into valuable compounds, such as propionic acid, butyric acid, caproic acid, pelargonic acid, and azelaic acid. Traditionally, these acids were synthesized from oleic acid using ozone-based ozonolysis, a method fraught with safety hazards and high energy demands. In contrast, this research investigates an alternative approach employing hydrogen peroxide as an oxidizing agent, coupled with UV radiation and a tungsten oxide catalyst. The study delineates the impact of UV radiation on the oxidative cleavage of oleic acid, demonstrating enhanced conversion under UV radiation. Experimental results indicate that UV-assisted oxidative cleavage achieves maximum conversion efficiency at 80°C, outperforming non-UV conditions. Notably, UV radiation enables efficient conversion even at lower temperatures, significantly reducing energy consumption. Gas chromatography-mass spectrometry analysis (GC-MS) corroborates this analysis, showcasing the effectiveness of UV-enhanced catalytic oxidative cleavage in oleic acid transformation. Overall, this study highlights the efficacy of UV-C radiation in facilitating the oxidative cleavage of oleic acid, offering a promising avenue for environmentally sustainable and energy-efficient industrial processes.

**Keywords:** Oxidative cleavage; Oleic acid; Tungsten-based catalysts; Radical reaction pathway; UV-C.

### 1. Introduction

Oleic acid is a long-chain fatty acid classified as a fatty acid characterized by a carboxyl group (R-COOH). They are unsaturated fatty acids with double bonds between carbon atoms at positions 9 and 10 from the methyl end of the chain. It is also referred to as C18:1 or 9-octadecenoic acid. Oleic acid is present in various natural sources, including olive oil, sunflower oil, palm oil, and animal fats. It can serve as a precursor for producing other fatty acids or compounds by cleavage chemical bonds. Usually, oleic acid can be used as a raw material in the production process. Propionic acid (C3) can be synthesized by breaking chemical bonds and forming valuable compounds. It is utilized to produce food preservatives [Campbell et al., 2009], herbicides, and certain pharmaceuticals [Ihre et al., 1996]. Butyric acid (C4) is a precursor in making food and aromatic compounds [Armstrong & Yamazaki, 1986]. Caproic acid (C6) is an antibacterial agent [Huang et al., 2011] and an addition in animal feed. The study undertaken by [Zentek et al., 2011] also employed it as a biofuel [Yanowitz et al., 2011]. Pelargonic acid, also known as C9-acid or Nonanoic acid, serves as an intermediate chemical



in the production of lubricants and plasticizer herbicides [Turnwald et al., 1998]. Azelaic acid (C<sub>9</sub>-diacid, Nonane dioic) is a versatile compound that can be used as a precursor for synthesizing polymers, lubricants, and cosmetics. Additionally, it is commonly applied as a therapy for acne [Enferadi-Kerenkan et al., 2017]. Nevertheless, these acids are uncommon in their occurrence and were traditionally synthesized from oleic acid, an unsaturated fatty acid that can be obtained from different sources, including fossil feedstocks, using a chemical process known as ozonolysis, which involves oxidative cleavage without the use of a catalyst [Sun et al., 2007; Zhu et al., 2011]. Ozonolysis is a chemical process that involves the oxidative cleavage of unsaturated organic compounds by ozone (O<sub>3</sub>), which is a high oxidant that can break the double bonds in oleic acid and produce smaller molecules, such as aldehydes, ketones, or carboxylic acids. However, ozonolysis also has some drawbacks, such as the safety risks of handling ozone that was used oxidizing agent, toxic to humans in the respiratory system, and difficulty in controlling the occurrence of runaway reactions caused affects commercial applications. In addition, the ozonolysis process necessitates substantial energy and costly, sophisticated equipment, leading to a substantial initial investment. Hydrogen peroxide has recently been employed as a potent oxidizing agent that is both ecologically acceptable and effective, can react with many organic and inorganic substances, and can control the occurrence of runaway reaction well because the action of H<sub>2</sub>O<sub>2</sub> must be broken down into O<sub>2</sub> before O<sub>2</sub> enters the Oxidative Cleavage reaction, and this is also another reason why H<sub>2</sub>O<sub>2</sub> is more environmentally friendly. However, hydrogen peroxide is not a high oxidant like ozone; it requires a catalyst for the catalytic reaction.

Hydroxyl radicals (OH·) a highly oxidant more of ozone, can attack the double bond in oleic acid, resulting in the cleavage of the molecule and the formation of various fatty acids or other compounds. The production of hydroxyl radicals is a method that can be used ultraviolet (UV) radiation. UV radiation is a form of electromagnetic radiation with a shorter wavelength and higher energy than visible light. UV radiation can induce the generation of hydroxyl radicals (OH·) by dissociating hydrogen peroxide. Therefore, from the above theory, using UV to help create hydroxyl radicals increase Oxidation ability. This work will study the efficacy of UV-C radiation in the reaction that took place in a batch reactor within the ambient temperature. The oxidant was hydrogen peroxide, with tertiary butanol as the co-solvent. The catalyst employed was tungsten (IV) oxide. To examine the effect of ultraviolet (UV) radiation (UV-C) on breaking down oleic acid by oxidation and to improve the reaction conditions at low temperatures. The product profile was examined using gas chromatography coupled with tandem mass spectrometry (GC-MS).

## 2. Materials and Methods

The effect of ultraviolet (UV) radiation on the transformation of oleic acid via the oxidation cleavage reaction mechanism. Chemicals in this work: The composition of the substance is 86%w/w of oleic acid (C<sub>18</sub>H<sub>34</sub>O<sub>2</sub>), and it is classified as a commercial-grade product. The catalyst is Tungsten Oxide with a purity of 99.8%w/w (WO<sub>3</sub>) on a metal basis. It is an analytical reagent (AR) grade produced by Alfa Aesar. The substance is hydrogen

peroxide ( $\text{H}_2\text{O}_2$ ) with a concentration of 30% w/w to use an oxidant system. It is of analytical reagent (AR) grade produced by ANaPURE. Tert-butyl alcohol, also known as  $(\text{CH}_3)_3\text{COH}$ , is a high-quality chemical compound commonly referred to as AR-Grade produced by Loba Chemie. It was used as a co-solvent, and the heat transfer media is commercial-grade silicone oil.

Intarasuk et al. [2021] propose a ratio of oleic acid, t-butanol, and hydrogen peroxide at a molar ratio of 0.051:1.000:0.413. It can give a conversion of oleic acid a maximum of around 66% at 80°C with a catalyst loading of 1% w/v, which will be used in this work. In the total volume of 100 ml, the resultant mixture was introduced into the three-necked round bottom flask in the specified proportion run reaction at 360 minutes, stirred at around 2,000 rpm. Set up the experimental equipment in the same configuration depicted in Figure 1. The experiment conducted in this study consists of four experiments.

- Experiment 1: Condition the temperature of 80 °C without UV-C radiation as a base case.
- Experiment 2: Condition the temperature of 80 °C, accompanied by UV-C radiation to identify effect of UV radiation comparing with base case.
- Experiment 3: Condition to a temperature of 60 °C, accompanied by UV-C radiation to identify the effect of UV radiation when thermal energy is less than the base case which is experiment 1.
- Experiment 4: Condition to UV-C irradiation at 25 °C (ambient temperature) to identify the effect of UV radiation without thermal heat integration.

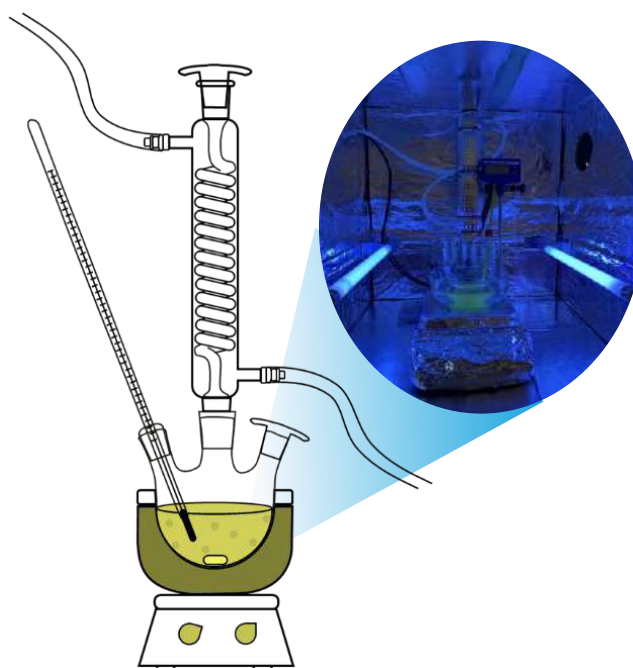


Fig. 1 Experimental UV- Enhanced Catalytic Oxidative Cleavage.

In the experimental procedure, the mixture was heated at a temperature specific to each condition, utilizing a silicon oil bath. Hydrogen peroxide was introduced into the mix once the temperature reached the desired target. The UV fluorescence used in this work is UV type C (UV-C), as the UV-C has the highest energy comparing types A and B. It is to examine whether the effect of UV radiation at high energy can improve the reaction conditions. The 15 W, 4 lamps are activated for condition to UV-C radiation. If the light is without UV-C radiation, it is switched off. The mixture was maintained under these conditions for 360 minutes. After the time was up, the catalyst was separated from the mixture utilizing the centrifugal apparatus at about 2500 rpm for 5 minutes.

The methodologies analysis for this work involved injecting the material using Agilent Technologies Triple Quadrupole GC-MS/MS (Agilent 7000C GC/MS). The gas chromatography (GC) column employed was the HP-5ms. It had dimensions of 30 m in length and  $0.25 \times 10^{-3}$  m in diameter, with a particle size of  $0.25 \times 10^{-6}$  m. The volume of the injected sample was  $0.5 \times 10^{-6}$  L. The column was initially heated to a temperature of 80 °C and maintained at that temperature for 2 minutes. Subsequently, the temperature was raised to 280 °C at the Heat rate of 20 °C/min, and the sample was maintained at this temperature. The duration is 6 minutes. The Injector is kept at 260 °C, while the Detector is held at 280 °C. The flow rate of the Helium (He) carrier gas is  $1.0 \times 10^{-3}$  L/min.

### 3. Results and Discussion

Figure 2 shows the comparison of %Conversion at 80 °C in different working conditions under UV-C and without UV-C radiation. The reaction time of the oxidative cleavage of oleic acid with  $\text{WO}_3$  as a catalyst was 360 minutes. The conversion of oleic acid in conditions under UV-C radiation and without UV-C were 100% and 94%, respectively. The results showed that the conversion of oleic acid using UV-C incorporated was higher than a condition without UV-C radiation by 6% because the energy of UV-C radiation would increase the decomposition of  $\text{H}_2\text{O}_2$  into hydroxyl radicals. This was attributed to the enhanced breakdown of  $\text{H}_2\text{O}_2$  into hydroxyl radicals due to the energy from UV-C radiation. UV-C energy ranges from 4.43 to 12.4 eV. The energy needed to break the O-H bond in  $\text{H}_2\text{O}_2$  to form hydroxyl radicals is around 5.15 eV, as stated by [Crosley et al., 2017]. This indicates that UV-C can break down  $\text{H}_2\text{O}_2$  into hydroxyl radicals, as illustrated in Equation 1 by [Cataldo, 2014]. The hydroxyl radical possesses strong oxidizing characteristics and a high affinity for gaining electrons to oxidize other substances. The standard potentials rank highest at 2.80 V, followed by ozone at 2.07 V and hydrogen peroxide at 1.77 V [LibreTexts, 2020]. It makes increasing the oxidative cleavage reaction better than producing through only temperature at the same condition and duration of work. It makes it possible to increase the oxidative cleavage reaction better than producing through only temperature at the same condition and duration of work, which can enhance conversion up to 100% at 80 °C compared to without UV-C radiation.

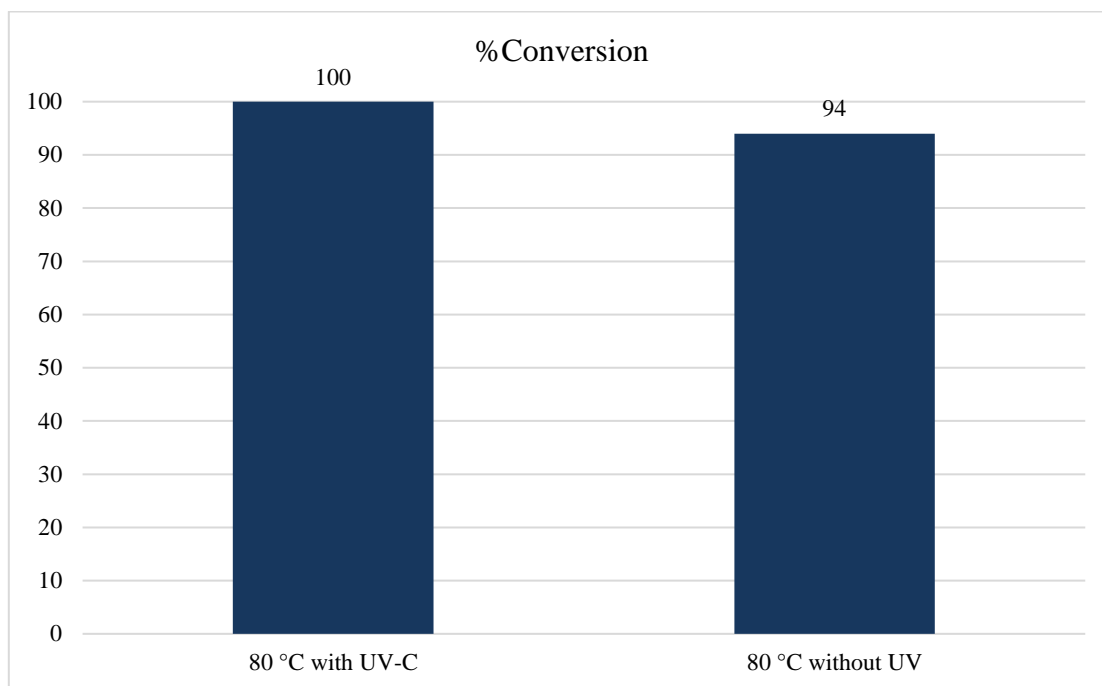
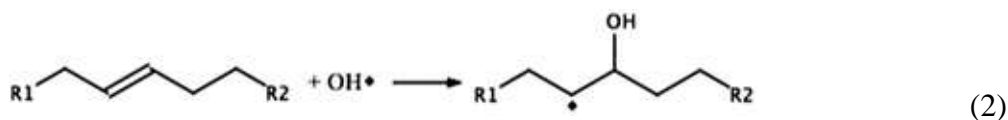
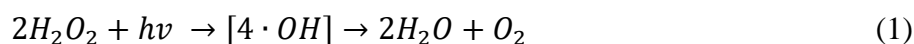


Fig. 2 The conversion at 80 °C operating with and without UV-C radiation.

And a possible reaction scheme for the hydroxyl radicals reaction of unsaturated fatty acid. H(hydrogen atoms) abstraction by hydroxyalkyl radicals will result in the formation of alkyl (R) radicals. These R radicals could react with hydroxyl radicals or O<sub>2</sub> to subsequently form stable reaction products with oxygenated functional groups. It is also possible that these R radicals (and hydroxyalkyl radicals) participate in chain propagation chemistry by reacting with neighboring unsaturated fatty acid molecules (and their reaction products) via radical addition to the C=C double bond, thus triggering a radical chain polymerization mechanism that rapidly consumes the molecular species showed in Equation 2 [Nah et al., 2013].



Furthermore, by reducing the temperature conditions, it was revealed that UV-C affected the conversion of different temperatures in Figures 3 and 4. The decrease in temperature also leads to a reduction in the conversion of oleic acid. The conversion of oleic acid at 80°C, 60°C, and 25°C (ambient temperature) achieved 100%, 98%, and 97%, respectively. So, the findings indicated that UV radiation impacts the transformation of oleic acid by facilitating the decomposition of H<sub>2</sub>O<sub>2</sub> to hydroxyl radicals by breaking the O-H bond, which is the best choice for this reaction in operating, which is UV-C radiation and heat.

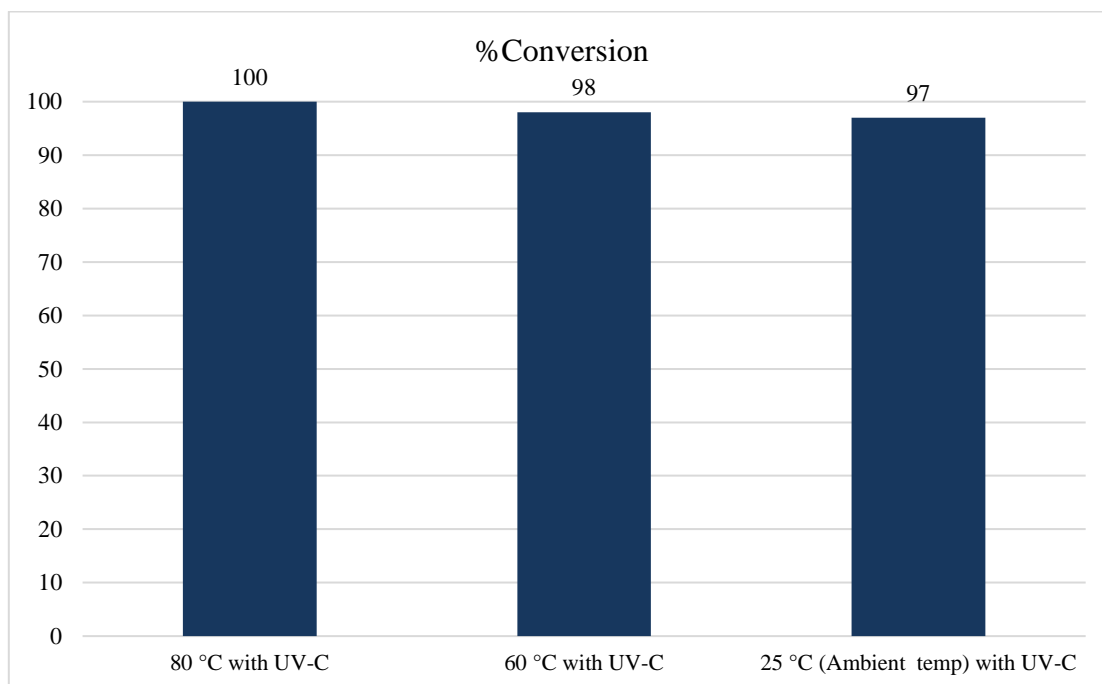


Fig. 3 The conversion under different temperature conditions with UV-C radiation.

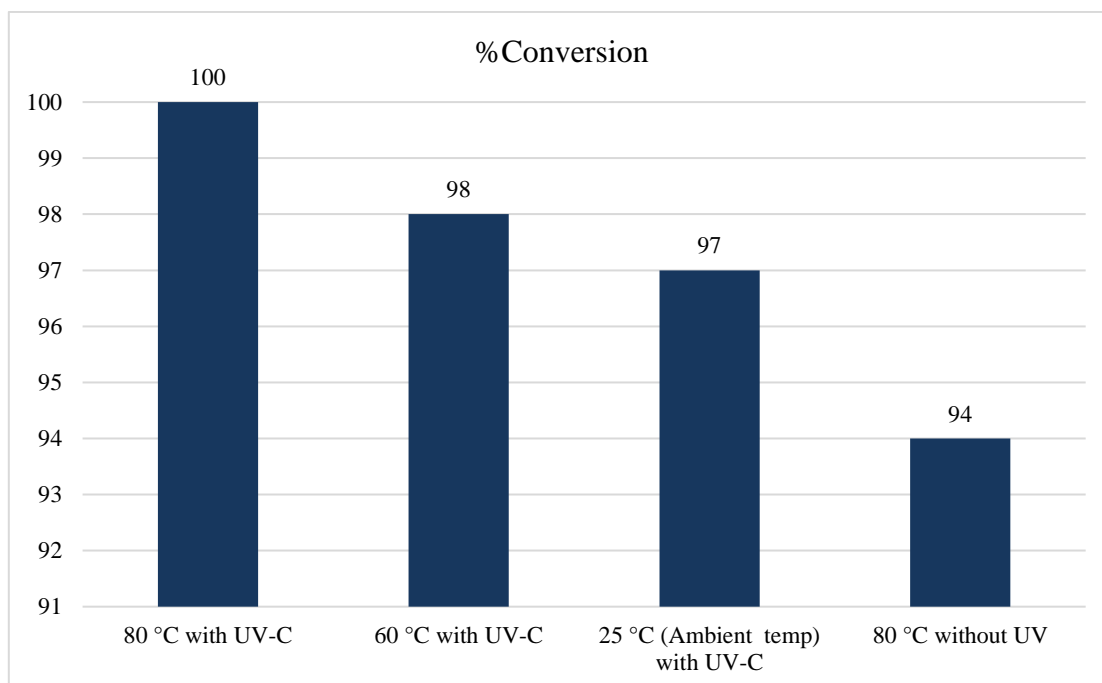


Fig. 4 the results of the under different conditions.

#### 4. Conclusions

This study investigated the oxidative cleavage of oleic acid with WO<sub>3</sub> as a catalyst under different working conditions and temperatures. The results showed that the conversion of oleic acid was enhanced by the presence of UV-C radiation, which increased the production of hydroxyl radicals from hydrogen peroxide. The hydroxyl radicals were highly effective in oxidizing the oleic acid and its reaction products, leading to 100% conversion at 80°C. The conversion of oleic acid was also influenced by the temperature, as lower temperatures reduced the reaction rate. However, the use of UV-C radiation compensated for the lower temperatures by generating more hydroxyl radicals. The study demonstrated that UV-C radiation can improve the oxidative cleavage of oleic acid. This has potential applications in the production of chemical substances and bioproducts from renewable sources that do not require operating conditions at high temperatures.

#### 5. References

- [1] Armstrong, D. W., & Yamazaki, H. (1986). Natural flavours production: a biotechnological approach. *Trends in Biotechnology*, 4(10), 264-268.
- [2] Campbell, J. L., Rustad, L. E., Boyer, E. W., Christopher, S. F., Driscoll, C. T., Fernandez, I. J., Groffman, P. M., Houle, D., Kieckbusch, J., & Magill, A. H. (2009). Consequences of climate change for biogeochemical cycling in forests of northeastern North America. *Canadian Journal of Forest Research*, 39(2), 264-284.
- [3] Cataldo, F. (2014). Hydrogen peroxide photolysis with different UV light sources including a new UV-LED light source. *New Frontiers in Chemistry*, 23(2), 99.
- [4] Crosley, D. R., Araps, C. J., Doyle-Eisele, M., & McDonald, J. D. (2017). Gas-phase photolytic production of hydroxyl radicals in an ultraviolet purifier for air and surfaces. *Journal of the Air & Waste Management Association*, 67(2), 231-240.
- [5] Enferadi-Kerenkan, A., Ello, A. S., & Do, T.-O. (2017). Synthesis, organo-functionalization, and catalytic properties of tungsten oxide nanoparticles as heterogeneous catalyst for oxidative cleavage of oleic acid as a model fatty acid into diacids. *Industrial & Engineering Chemistry Research*, 56(38), 10639-10647.
- [6] Huang, C. B., Alimova, Y., Myers, T. M., & Ebersole, J. L. (2011). Short-and medium-chain fatty acids exhibit antimicrobial activity for oral microorganisms. *Archives of oral biology*, 56(7), 650-654.  
<https://www.ncbi.nlm.nih.gov/pmc/articles/PMC3119748/pdf/nihms-275213.pdf>
- [7] Ihre, H., Hult, A., & Söderlind, E. (1996). Synthesis, characterization, and <sup>1</sup>H NMR self-diffusion studies of dendritic aliphatic polyesters based on 2, 2-bis (hydroxymethyl) propionic acid and 1, 1, 1-tris (hydroxyphenyl) ethane. *Journal of the American Chemical Society*, 118(27), 6388-6395.
- [8] Intarasuk, C., Pavarajarn, V., Sirimittagoon, S., & Chantanuson, R. (2021). Selective Oxidative Cleavage of Oleic Acid on Alumina Supported Metal Catalyst. MATEC Web of Conferences,
- [9] LibreTexts. (2020). *Comparing Strengths of Oxidants and Reductants*. Retrieved August 15 from [https://chem.libretexts.org/Bookshelves/Analytical\\_Chemistry/Supplemental\\_Modules\\_\(Analytical\\_Chemistry\)/Electrochemistry/Redox\\_Chemistry/Comparing\\_Strengths\\_of\\_Oxidants\\_and\\_Reductants](https://chem.libretexts.org/Bookshelves/Analytical_Chemistry/Supplemental_Modules_(Analytical_Chemistry)/Electrochemistry/Redox_Chemistry/Comparing_Strengths_of_Oxidants_and_Reductants)

- [10] Nah, T., Kessler, S. H., Daumit, K. E., Kroll, J. H., Leone, S. R., & Wilson, K. R. (2013). OH-initiated oxidation of sub-micron unsaturated fatty acid particles. *Physical Chemistry Chemical Physics*, 15(42), 18649-18663. <https://pubs.rsc.org/en/content/articlepdf/2013/cp/c3cp52655k>
- [11] Sun, Z., Ramsay, J. A., Guay, M., & Ramsay, B. A. (2007). Carbon-limited fed-batch production of medium-chain-length polyhydroxyalkanoates from nonanoic acid by *Pseudomonas putida* KT2440. *Applied microbiology and biotechnology*, 74, 69-77. <https://link.springer.com/content/pdf/10.1007/s00253-006-0655-4.pdf>
- [12] Turnwald, S., Lorier, M., Wright, L., & Mucalo, M. (1998). Oleic acid oxidation using hydrogen peroxide in conjunction with transition metal catalysis. *Journal of materials science letters*, 17, 1305-1307.
- [13] Yanowitz, J., Christensen, E., & McCormick, R. L. (2011). Utilization of renewable oxygenates as gasoline blending components.
- [14] Zentek, J., Buchheit-Renko, S., Ferrara, F., Vahjen, W., Van Kessel, A., & Pieper, R. (2011). Nutritional and physiological role of medium-chain triglycerides and medium-chain fatty acids in piglets. *Animal Health Research Reviews*, 12(1), 83-93. <https://www.cambridge.org/core/services/aop-cambridge-core/content/view/0022D08B9613B5EF09F928FBBF9A2303/S1466252311000089a.pdf/div-class-title-nutritional-and-physiological-role-of-medium-chain-triglycerides-and-medium-chain-fatty-acids-in-piglets-div.pdf>
- [15] Zhu, J., Du, J., & Xie, X. (2011). Method for Producing Nonandioic Acid, Pelargonic Acid by Ozonization-Oxidative Decomposition of Oleic Acid. *CN Patent*, 101, 14.

## Enhancement of Oleic Acid Content in Palm Oil via Chemical Interesterification for Application as Bio-Transformer Oil

**Nataporn Inkong<sup>1</sup>, Boonyawan Yoosuk<sup>2</sup>, and Napida Hinchiranan<sup>1,3,4,\*</sup>**

<sup>1</sup> Department of Chemical Technology, Faculty of Science, Chulalongkorn University, Bangkok, Thailand

<sup>2</sup> National Energy Technology Center (ENTEC), National Science and Technology Development Agency (NSTDA), Pathumthani, Thailand

<sup>3</sup> Center of Excellence on Petrochemical and Materials Technology (PETROMAT), Chulalongkorn University, Bangkok, Thailand

<sup>4</sup> Center of Excellence in Catalysis for Bioenergy and Renewable Chemicals (CBRC), Chulalongkorn University, Bangkok, Thailand

E-mail: \* Gamnataporn@gmail.com, napida.h@chula.ac.th

### Abstract

Mineral oil, a product obtained from petroleum refinery, has excellent electrical insulation properties, efficient heat dissipation, and stability at high temperatures. However, it is non-biodegradable and toxic to the environment. Thus, palm oil is expected to replace the use of mineral oil as a liquid insulator for transformers to reduce fossil fuel consumption. However, it has high viscosity and pour point due to palmitic acid (C16:0) and oleic acid (C18:1), which the main saturated and unsaturated components in palm oil. Since the unsaturated portion promotes the good cold flow properties of the oils, the enhancement of the unsaturated part in the palm oil structure via chemical interesterification (CIE) involving a rearrangement or exchange of the fatty acids on the glycerol backbone of the triacylglycerol molecule of palm oil was the aim of this research. Herein, the refined, bleached, and deodorised palm oil (RBDPO) mixed with methyl oleate (MO, C18:1) at 50/50 (w/w) were used as feedstocks for CIE process. The reaction was fed into the reactor and the reaction was conducted in the presence of sodium methoxide (NaOCH<sub>3</sub>) 0.5 wt% based on the feedstock content) at 70-110 °C for 0.5-1.5 h. The content of triacylglycerol with the carbon number of C54 (TAG-C54) was enhanced from 5.29% in feedstocks to 16.82% when the CIE was conducted at 110 °C for 1.5 h. The product with high TAG-C54 content could be used as an alternative in bio-transformer oil production.

**Keywords:** Chemical interesterification; Methyl oleate; Palm oil; Oleic acid

### 1. Introduction

Palm oil is obtained from the extraction of oil palm fruits, particularly from the outer layer called as mesocarp. It is semi-solid at room temperature and bright orange-red [1]. Generally, palm oil consists of saturated and unsaturated fatty acids in equal fractions. Saturated fatty acids fraction contains 39.3-47.5 wt% palmitic acid (C16:0) and 3.5-6.0 wt% stearic acid (C18:0), while unsaturated fatty acids portion composes with 36-44 wt% oleic acid (C18:1) and 9-12 wt% linoleic acid (C18:2) [2]. Mostly, the fatty acids in palm oil are present in the form of triacylglycerols (TAGs) in an amount of 94-98% [3], TAG is consisted of three fatty acids linking with glycerol by an ester bond. The position of fatty acids in TAG is indicated according to a stereospecific numbering system (*sn*) such as *sn*-1, *sn*-2 and *sn*-3 as shown in Fig. 1. At *sn*-1 and *sn*-3 positions, unsaturated fatty acids are located, while *sn*-2 position is the position of the saturated fatty acids [2]. The arrangement of fatty acids within TAG plays an important role to affect the thermal behavior of oils in terms of crystallization and melting point. The higher portion of saturated fatty acids induces the oil to be quickly crystallized [4] with the high



oxidative and thermal stability. In the other hand, the oil with the higher content of unsaturated fatty acids shows the low pour point and cloud point.

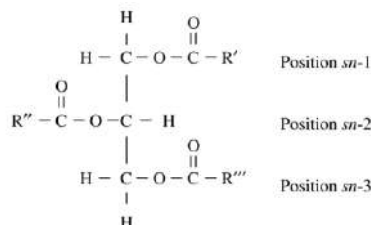


Fig. 1 Triacylglycerol structure (R= fatty acid) [2].

Mineral oil produced from petroleum refinery has excellent electrical insulation properties, efficient heat dissipation, and stability at high temperatures [5]. However, it is non-biodegradable and toxic to the environment with low fire point (160-170 °C) and flash point (170-180 °C). Meanwhile, the palm oil has advantages in the aspect of environmental friendly, biodegradable with high fire point (> 300 °C) and flash point (> 350 °C) [6]. However, its high viscosity (39.4 cSt) and pour point (23.6 °C) [7] are required to be improved before applying as transformer oil, which the viscosity and pour point of transformer oil are limit to be less than 50 cSt and -10 °C, respectively according to the international standard IEC 62770. Since the poor cold flow properties (high viscosity and pour point) are related to the degree of saturation, this work aims to improve the TAG structure of palm oil via chemical interesterification (CIE) to have the higher level of unsaturation. This process involves with the exchange of fatty acids between different esters, acids, and alcohols to form new esters [8]. The change in position of fatty acids can occur in 2 ways: 1) intraesterification, involving the change of the position of fatty acids within the same glycerol molecule and 2) interesterification, which is related to the exchange of fatty acids with another glycerol molecule. The reaction mechanism of interesterification is proposed as shown in Fig. 2.

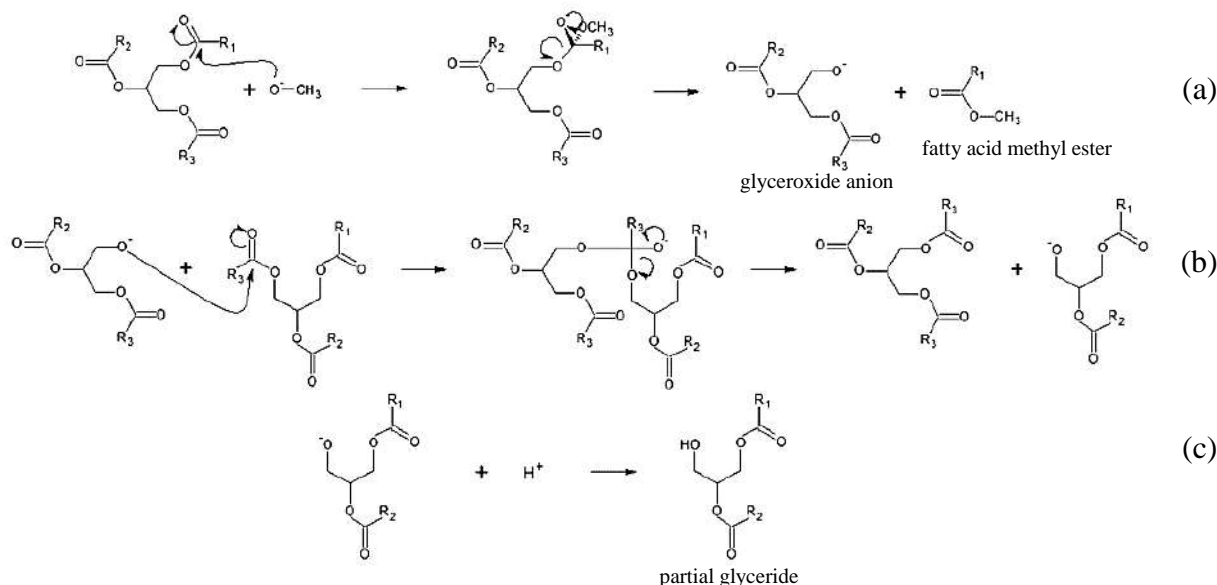


Fig. 2 Chemical interesterification mechanism: (a) initiation, (b) propagation and (c) termination [9].

The initiation is activated by catalyst. The methoxide radical generated from methoxide catalyst attacks the carbonyl carbon of the ester bond to form a tetrahedral intermediate (Fig. 2(a)). Propagation is the formation of fatty acid methyl ester and glyceroxide anion acting as a nucleophile to attack the carbonyl carbons of other TAGs (Fig. 2(b)). For the termination step, the reaction is terminated by adding acid [9] or hot water [10] to deactivate the catalyst and glyceroxide anion. The proton then reacts with glyceroxide anion to form partial glyceride (Fig. 2(c)). From poor cold flow properties of palm oil, this research aims to increase the oleic content in the TAG structure of palm oil via CIE by using methyl oleate (MO). The reaction parameters affecting level of MO conversion and carbon number of the obtained product such as reaction time and reaction temperature were investigated. In the case that the TAG contains oleic acid for all *sn* position, the total carbon number of the obtained modified triacylglycerol would be 54 (TAG-C54).

## 2. Materials and Methods

### 2.1. Materials

Refined, bleached, and deodourised palm oil (RBDPO) obtained from Patum Vegetable Oil Co., Ltd. (Thailand) consists of 0.29% free fatty acids (FFA), 0.16 % monoacylglycerols (MAG), 7.39% diacylglycerols (DAG) and 92.16% triacylglycerols (TAG). Methyl oleate (MO (C18:1), 70% purity) was manufactured by Sigma–Aldrich (Germany). Sodium methoxide anhydrous powder was obtained from Acros Organics (Germany).

### 2.2. CIE of RBDPO with MO

RBDPO and MO were mixed at a ratio of 50/50 (w/w) in 250 mL pressure reducing filter flask. The ratio between RBDPO and MO was followed the previous literature reported by Ramli et. al. [10]. The mixture was then heated under vacuum (20 mbar) for 40 min to eliminate the trace of water. Then, sodium methoxide (NaOCH<sub>3</sub>) 0.5 wt% based on the feedstock (RBDPO and MO) content was added into the reaction mixture to start the reaction under a reduced pressure (20 mbar) for desired reaction time (0.5-1.5 h) and temperature (70-110 °C). To terminate the reaction, 5 mL hot water was added into the reaction mixture [11].

### 2.3. Analysis of compositions in RBDPO and products

Before analysis, 0.05 mg sample was mixed with 250 µL of N,O-Bis(trimethylsilyl) trifluoroacetamide (BSTFA) and 200 of µL pyridine. The mixture was heated at 40 °C for 10 min and then 1000 µL *n*-heptane was added. The obtained resulting mixture was analyzed to determine its composition by gas chromatography flame ionization detection (GC-FID, Shimadzu gas chromatograph GC-2010) equipped with Elite5HT column (12 m, 0.32 mm i.d. and 0.10 µm) using helium as a carrier gas at a flow rate of 10 mL/min. 1 µL sample was injected into the GC-FID at a injector temperature of 300 °C with a split ratio of 1:25. The oven temperature was initially held at 80 °C for 2 min and programmed to increase to 340 °C at a rate of 8 °C/min, and then kept at this temperature for 10 min. The detector temperature was controlled at 360 °C.

## 3. Results and Discussion

Palm oil consisted of acyl groups classified as diacylglycerols (DAG) and triacylglycerols (TAG). DAG can be divided into three categories based on the sum of carbon atoms in the acyl chains: C32, C34 and C36 as shown in Fig. 3(a). For TAG, it is categorized into four groups

based on the sum of carbon atoms in the acyl chains: C48, C50, C52 and C54 as shown in Fig. 1. In the case that the acyl chain is entirely composed of palmitic acid (C16:0), the carbon number is C48. If all three acyls of TAG are oleic acid (C18:1), the carbon number is C54. In addition, the C50 and C52 groups are TAG mostly consisting of fatty acids with 18 carbon atoms (stearic acid (C18:0), oleic acid (C18:1) and linoleic acid (C18:2)) combining with fatty acids containing 16 carbon atoms (palmitic acid (C16:0)). Moreover, monoacylglycerols (MAG) are also found in the composition of palm oil. The structure of MAG is shown in Fig. 3(b).

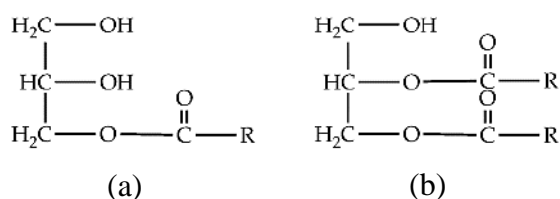


Fig. 3 Structure (a) diacylglycerols (DAG) and (b) monoacylglycerol (MAG).  
(R = fatty acid) [12].

### 3.1. Feedstock composition

Composition of the mixed feedstock (RBDPO/MO = 50/50 (w/w)) before CIE is shown in Table 1. TAG generated from RBDPO was 45.11 wt%. This mixture also contained 3.44 wt% DAG from RBDPO and other components consisting of 0.72 wt% MAG from RBDPO and 3.24 wt% FFA

Table 1. Composition of the mixed feedstock

Compositions	wt%
MO	47.49
TAG	45.11
TAG-C48	0.87
TAG-C50	17.33
TAG-C52	21.32
TAG-C54	5.29
DAG	3.44
DAG-C32	0.23
DAG-C34	1.98
DAG-C36	1.23
Others	3.96
MAG	0.72
FFA	3.24
SUM	100

Note: MO = methyl oleate, TAG = triacylglycerols, DAG = diacylglycerols, MAG = monoacylglycerols and FFA = free fatty acid.

### 3.2. Effect of reaction time

The effect of the reaction time on the compositions in the obtained product was shown in Fig. 4. The increased MO conversion was accompanied by a higher others content and an

increase in DAG content [10]. After CIE, the degree of MO conversion (Fig. 4(a)) tended to increase from 1.66% to 12.9% when the reaction time was extended from 0.5 h to 1.5 h. It was caused by the replacement of C18:1 generated from MO to hydroxyl group in DAG and acyl group in TAG. The increase in others fraction from 3.96 wt% in feedstock to 11.0 wt% in the product obtained at 1.5 h confirmed the release of the acyl group from TAG as shown in Fig. 4(a).

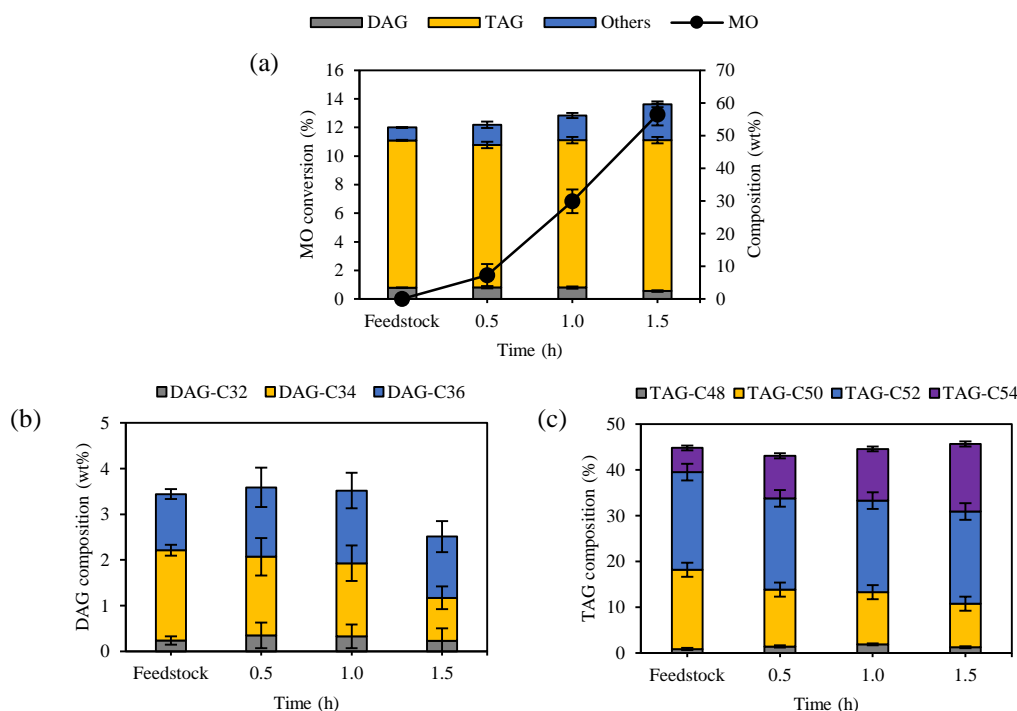


Fig. 4 Effect of reaction time on (a) the level of MO conversion and product compositions, (b) DAG compositions and (c) TAG compositions (Condition:  $T = 90\text{ }^{\circ}\text{C}$  and  $0.5\% \text{ NaOCH}_3$ ).

The change in the compositions in DAG and TAG fractions was also observed in Fig. 4(b) and 4(c), respectively. At 1.5 h, the level of DAG decreased to 2.42 wt%. This result was consistent with the TAG change that amount of TAG increased from 43.5 wt% to 46.2 wt% when the reaction time was 1.5 h. It indicated that the longer time induced the more removal of acyl groups from the glycerol backbone of TAG due to the reaction between MO and DAG or TAG. The longer reaction time promoted the better reactivity between MO and the hydroxyl group in DAG to generate TAG. Moreover, the levels of TAG-C50 and TAG-C52 decreased and the level of TAG-C54 increased at longer reaction time. The increase in the TAG-C54 was caused by 2 reasons: 1) the reaction between the hydroxyl group in DAG and MO and 2) the replacement of C18:1 generated from MO to the acyl group in TAG-C50 and TAG-C52. At 1.5 h, the amount of TAG-C54 increased from 9.3 wt% to 14.8 wt%.

### 3.3. Effect of reaction temperature

Figure 5 shows the effect of reaction temperature on the change of the compositions in the liquid product. The higher reaction temperature to  $90\text{ }^{\circ}\text{C}$  increased the degree of MO conversion and others to 12.9% and 11.0 wt%, respectively. This result was also revealed by a previous literature [13]. This indicated that C18:1 generated from MO replaced the hydroxyl group in

DAG and the acyl group in TAG. However, the increase in the reaction temperature to 110 °C decreased the level of MO conversion. This indicated a competition between MO and others consisting of FFA and MAG to replace the acyl group in TAG.

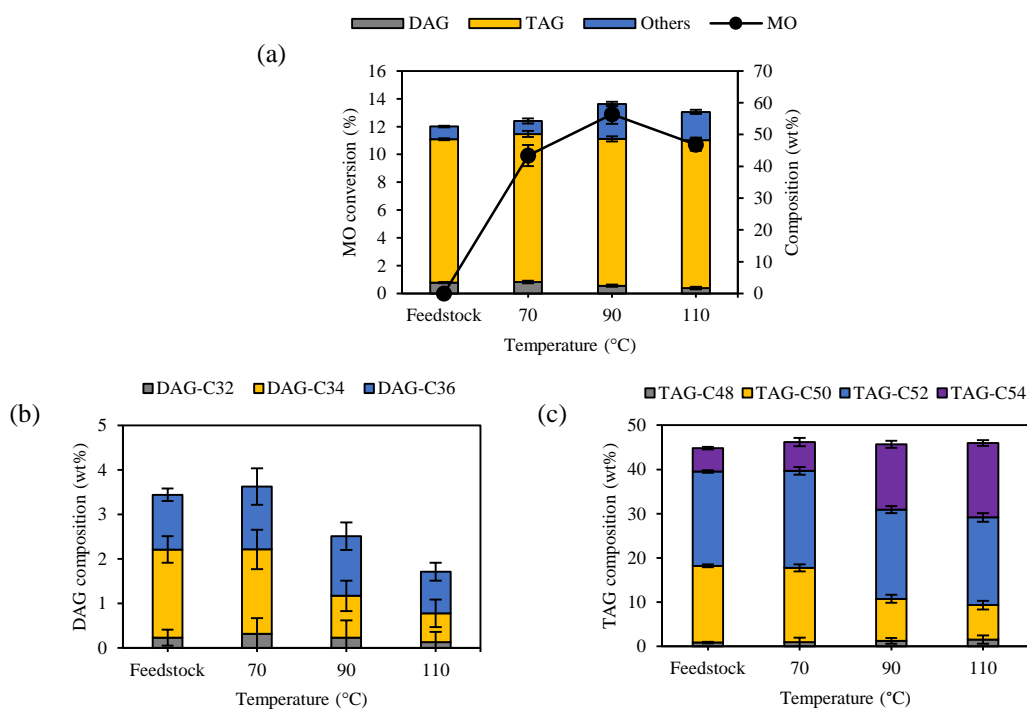


Fig. 5 Effect of reaction temperature on (a) the level of MO conversion and product compositions, (b) DAG compositions and (c) TAG compositions (Condition: Time = 1.5 h and 0.5% NaOCH<sub>3</sub>).

The level of DAG and TAG compositions as shown in Fig. 5(b) and 5(c) indicated that the level of DAG content decreased to 2.40 wt% and 1.71 wt% at the reaction temperature of 90 and 110 °C, respectively, whereas the amount of TAG increased to 46.2 wt% and 46.5 wt%, respectively. This indicated that the higher reaction temperature promoted the acyl group replacement in DAG, especially DAG-C34 and DAG-C36. The proportion of TAG-C54 at 70, 90 and 110 °C increased to 6.52 wt%, 14.77 wt% and 16.82 wt%, respectively. It was corresponded to the decrease in the amount of TAG-C50 and TAG-C52. Moreover, this result indicated the acyl group in TAG-C50 and TAG-C52 was replaced by C18:1 generated from MO and the acyl group from others fraction. Although the level of MO conversion at 90 °C was greater, the reduction of others fraction, DAG, TAG-C50 and TAG-C52 at 110 °C was less than those obtained from the system at 90 °C. Additionally, the increase in TAG-C54 at reaction temperature of 110 °C higher than 90 °C. This result suggested that the replacement in DAG, TAG-C50 and TAG-C52 was due to the reaction between others fraction and the group of DAG, TAG-C50 and TAG-C52, it could be that others fraction consisting of C18:0, C18:1 or C18:2 content.

#### 4. Conclusions

Chemical impregnation (CIE) of RBDPO with MO increased the level of TAG-C54 group in the product delivered from palm oil. Therefore, the increase in TAG-C54 represents a change in the structure of TAG in palm oil. The optimum condition for increasing the TAG-C54 portion

were the reaction temperature of 110 °C, reaction time of 1.5 h and 0.5% of NaOCH<sub>3</sub>. Moreover, the higher reaction temperature and the longer reaction time enhanced the replacement of MO (C18:1) in the acyl group of TAG-C50 and TAG-C52.

## References

- [1] Okogeri, O. (2013). Adulteration of crude palm oil with red dye from the leaf sheath of sorghum bicolor. *Food Science and Quality Management*, 17, 1-6.
- [2] Berry, S. E. (2009). Triacylglycerol structure and interesterification of palmitic and stearic acid-rich fats: an overview and implications for cardiovascular disease. *Nutrition research reviews*, 22(1), 3-17.
- [3] Tan, C. P., and Nehdi, I. A. (2012). The physicochemical properties of palm oil and its components. In *Palm oil*, pp. 377-391. AOCS Press.
- [4] de Almeida, E. S., da Silva Damaceno, D., Carvalho, L., Victor, P. A., dos Passos, R. M., de Almeida Pontes, P.V., Cunha-Filho, M., Sampaio, K.A. and Monteiro, S. (2021). Thermal and physical properties of crude palm oil with higher oleic content. *Applied Sciences*, 11(15), 7094.
- [5] Yaacob, M., and Alsaedi, M. (2015). Use palm oil as alternative with insulation oil in high voltage equipment. *Physical Science International Journal*, 5(3), 172-178.
- [6] Ritu, P., Brahmin, A., and Kaur, S. (2021). A Review on Utilization of Vegetable Oils as Transformer Oils. *Int. Res. J. Eng. Technol*, 8, 2598-2601.
- [7] Verma, P., Sharma, M. P., and Dwivedi, G. (2016). Evaluation and enhancement of cold flow properties of palm oil and its biodiesel. *Energy Reports*, 2, 8-13.
- [8] Nugrahini, A. D., and Soerawidjaja, T. H. (2015). Directed interesterification of coconut oil to produce structured lipid. *Agriculture and agricultural science procedia*, 3, 248-254.
- [9] Gamallo, O. D., Júnior, H. F. M., de Carvalho, M. G., and Saldanha, T. (2020). Chemical interesterification of palm oil and palm kernel oil in the presence of the DAPTS-MCM-41 catalyst. Regiospecific distribution and composition in triacylglycerols. *Brazilian Journal of Chemical Engineering*, 37, 773-782.
- [10] Ramli, M. R., Siew, W. L., and Cheah, K. Y. (2009). Production of high oleic palm oils on a pilot scale. *Journal of the American Oil Chemists' Society*, 86(6), 587-594.
- [11] Oliveira, P. D., Rodrigues, A. M., Bezerra, C. V., and Silva, L. H. (2017). Chemical interesterification of blends with palm stearin and patawa oil. *Food chemistry*, 215, 369-376.
- [12] Kontogiorgos, V. (2021). *Introduction to food chemistry*. Springer Nature. pp. 97–121.

- [13] Farfán, M., Álvarez, A., Gárate, A., and Bouchon, P. (2015). Comparison of chemical and enzymatic interesterification of fully hydrogenated soybean oil and walnut oil to produce a fat base with adequate nutritional and physical characteristics. *Food technology and biotechnology*, 53(3), 361-366.

## L-lysine Production by *Corynebacterium Glutamicum* TISTR 461 Using Cassava Pulp Hydrolysate as a Carbon Source

Pattareeya Promnguluem<sup>1</sup>, Lek Wantha<sup>1, \*</sup>, Waewdao Dathong<sup>2</sup> and Apichat Boontawan<sup>3, \*</sup>

<sup>1</sup> School of Chemical Engineering, Institute of Engineering, Suranaree University of Technology, Nakhon Ratchasima, 30000, Thailand,

<sup>2</sup> Biology Program, Faculty of Science and Technology, Nakhon Ratchasima Rajabhat University, Nakhon Ratchasima 30000, Thailand and

<sup>3</sup> School of Biotechnology, Institute of Agricultural Technology, Suranaree University of Technology, Nakhon Ratchasima, 30000, Thailand.

E-mail: <sup>1</sup> b6016456@g.sut.ac.th and <sup>1, \*</sup> lekwa@sut.ac.th (\*Corresponding author)

### Abstract

L-lysine is one of the essential amino acids for humans and animals. In general, a fermentation process is used to produce L-lysine. Glucose is utilized as a carbon source for fermentation. Various starch feedstocks are converted to glucose. However, cassava pulp is an interesting feedstock for L-lysine production because it is waste in the starch industry. The cassava pulp was converted to glucose by enzymatic hydrolysis. After that, the cassava pulp hydrolysate was filtered, centrifuged, and concentrated. The condensed hydrolysate (glucose) was utilized as the carbon source for L-lysine production. *Corynebacterium glutamicum* TISTR 461 was cultured on a nutrient agar, inoculum medium, and main medium in an Erlenmeyer flask, respectively. The conditions were maintained in a shaker at 200 rpm and 30 °C for 72 h. This fermentation investigated the effects of glucose, initial glucose concentration, and incubated pH for L-lysine production. The glucose from the AR grade gave a higher L-lysine concentration (11.52 g/L) than hydrolysate (7.65 g/L). The optimum condition for L-lysine production was 100 g/L of initial glucose concentration at incubated pH of 7.2 and provided L-lysine concentration of 8.17 g/L.

**Keywords:** Cassava pulp; L-lysine; *Corynebacterium glutamicum*.

### 1. Introduction

In 2019, 10.2% of the cultivated cassava global production in Thailand. 82.1% of the domestic cassava was used as a raw material in industries like sweeteners, starch, food, and beverages [1]. For starch production, there is waste namely cassava pulp [2]. Cassava pulp is sold as an animal feed because of its low prices. When observing the components of the cassava pulp, there is a high starch and some cellulose [3]. These carbon sources could be the raw materials in other processes such as ethanol production, acid production, and amino acid production. It also increases the value of cassava pulp and reduces waste in the starch industry.

For the fermentation process, carbon sources can be glucose, fructose, sucrose, molasses, and starch hydrolysate [4]. However, the high amino acid was produced by using glucose compared to another carbon source [5]. There are many ways to produce glucose from cheap carbon sources like acid hydrolysis, base hydrolysis, and enzymatic hydrolysis. Nevertheless, chemical process provide environmental problems and harmful conditions [6]. This caused to selected enzymatic hydrolysis to avoid problems. Normally, cellulase,  $\alpha$ -amylase, and amyloglucosidase were used to digest cellulose, and starch to glucose, respectively.



Amino acid is a basic compound in animals and plants. It is useful for the growth of muscle, the production of hormones, immunity, and neurons [7]. L-lysine is one of the essential amino acids that cannot be synthesized by the human body. So, it is a component of supplementary, feed additive, cosmetic, and pharmaceutical [8]. The L-lysine was produced by fermentation because it provided only L-amino acid [9]. *Corynebacterium glutamicum* is a popular bacterium for the L-lysine fermentation process. Because this strain is fast growing, not acid-fast, non-sporulating, and nonpathogenic [10]. It also uses cheap carbon sources as a raw material [11]. The quality of L-lysine depended on *C. glutamicum*. The parameters in broth such as initial glucose concentration, incubated pH, incubated temperature, incubated time, and DO (dissolved oxygen) must be controlled at optimum conditions for the bacteria.

Thus, this research investigates the parameters of initial glucose concentration and incubated pH on a laboratory scale. In the future, these results will be used in a 5 L of Bioreactor to develop the optimum conditions for L-lysine production.

## 2. Materials and Methods

### 2.1. Raw materials

Cassava pulp was received from Korat Flour Industry Co., Ltd., Nakhon Ratchasima, Thailand. The cassava pulp (wet basis) was dried under the sunlight for 4 days, ground, and sieved into less than particle sizes of 150  $\mu\text{m}$ . The cassava pulp (dry basis (%w/w): starch, 62.91; moisture, 9.54; cellulose, 7.00; other, 20.55) was stored in a desiccator and used for the experiment.

### 2.2. Enzymes and Microorganism

The cellulase (activity: 12,524 U/mL),  $\alpha$ -amylase (activity: 162,078 U/mL), and amyloglucosidase (activity: 230,110 U/g/mL) were purchased from Nutitech co, Ltd., Bangkok, Thailand. The *Corynebacterium glutamicum* TISTR 461 was purchased from the Thailand Institute of Scientific and Technological Research (TISTR), Bangkok, Thailand.

### 2.3. Preparation of Cassava Pulp Hydrolysate

The 5 %w/w of cassava slurry was prepared by adding 250 g of cassava pulp into 4750 g of distilled water. The mixture was gelatinized at a temperature of 85 °C and pH 6.0 for 10 min. Then, the slurry was cooled to a temperature of 60 °C. The 237  $\mu\text{L}$  of cellulase was added into the slurry at pH 5.5 for 6 hr. After that, the slurry was liquefied at temperature of 90 °C and pH 6.0 for 2 hr 30 min by adding 28  $\mu\text{L}$  of  $\alpha$ -amylase. Finally, the temperature of the slurry was cooled at a temperature of 60 °C. The slurry was saccharified by adding 88  $\mu\text{L}$  of amyloglucosidase at pH 6 for 4 hr. The amount of enzyme based on optimum usage from product information. The cassava pulp hydrolysate was filtered, centrifuged at 8000 rpm for 10 min, and concentrated by rotary evaporator at a temperature of 40 °C and vacuum pressure of 45 mbar. The cassava pulp hydrolysate was stored in a freezer to avoid contamination.

### 2.4. Medium and Culture Conditions

*C. glutamicum* TISTR 461 was cultured on nutrient agar at a temperature of 30 °C for 48 hr. Two loops full of *C. glutamicum* were transferred and inoculated in 40 mL of seed culture medium at a temperature of 30 °C, pH 7.2, and agitation speed of 200 rpm for 20 hr. The 5 mL

of seed culture medium was transferred into 45 mL of the main medium for preparation of 10% v/v inoculum. The main medium was incubated at the temperature of 30 ° C, pH 7.2, and agitation speed of 200 rpm by using a shaking water bath for 72 hr. The pH of the main medium was maintained by 5 M of NaOH every 4 hr. The initial glucose concentration and incubated pH of the main medium were investigated. The L-lysine production was done in 250 mL of Erlenmeyer flask.

Nutrient agar was prepared the following (g/L): beef extract, 3; peptone, 5; agar, 15. Seed culture medium was prepared the following (g/L): glucose, 30; peptone, 10; yeast extract, 5; NaCl, 3; MgSO<sub>4</sub>.7H<sub>2</sub>O, 5; MnSO<sub>4</sub>.SO<sub>4</sub>, 5; K<sub>2</sub>HPO<sub>4</sub>, 1.5; KH<sub>2</sub>PO<sub>4</sub>, 0.5; biotin 2.5x10<sup>-6</sup>. Main medium was prepared the following (g/L): glucose, 110; peptone, 10; yeast extract, 5; meat extract, 5; MgSO<sub>4</sub>, 0.25; MnSO<sub>4</sub>, 0.01; (NH<sub>4</sub>)<sub>2</sub>SO<sub>4</sub>, 15; K<sub>2</sub>HPO<sub>4</sub>, 1.5; KH<sub>2</sub>PO<sub>4</sub>, 0.5; CaCO<sub>3</sub>, 10; FeSO<sub>4</sub>, 0.01; CH<sub>3</sub>COONa, 2; vitamin B1, 1.25 x10<sup>-6</sup>; biotin 2.5 x10<sup>-6</sup>.

## 2.5. Analytical Methods

The moisture, starch, and cellulose contents of cassava pulp were determined by AOAC (2000) [12], Rojas, M.J. [13], and TAPPI (1999) [14].

Glucose concentration was determined by the DNSA method [15]. The broth was centrifuged at 8,000 rpm for 10 min. The 1 mL of supernatant and 2 mL of DNS reagent (1 g of 3,5-dinitrosalicylic, 20 mL of 2 M NaOH, 30 g of Na-K tartrate and added distilled water to 100 mL of solution) were mixed into a test tube. The mixture was heated in boiling water for 5 min. Then, the mixture was cooled and diluted 100 times. The diluted mixture was measured at an absorbance value at a wavelength of 540 nm by a UV-visible spectrometer.

L-lysine concentration was determined by the Ninhydrin-ferric reagent method [16]. The 20 µL of supernatant, 660 µL of reagent A (373 mL of methylcellosolve, 30 mL of 50 % (w/w) FeCl<sub>3</sub> and 600 mL of 0.1 M KCl which was adjusted pH to 1 by 1 N of HCl) and 370 µL of reagent B (1 g of ninhydrin, 100 mL of 0.1 M KCl which was adjusted pH to 1 by 1 N of HCl) were mixed into a test tube. The mixture was heated in boiling water for 20 min and cooled with tap water. The 4 mL of Dimethyl sulfoxide (DMSO) and 6 mL of deionized water were added to the mixture. The mixture was measured an absorbance value at a wavelength of 470 nm by a UV-visible spectrometer.

The *C.glutamicum* TISTR 461 was determined by dry cell weight (DCW) [17]. The resulting precipitate from the DNSA method was collected. The precipitate was washed twice with distilled water and dried at a temperature of 105 °C until the weight of DCW was constant.

## 3. Results and Discussion

After enzymatic hydrolysis, the glucose concentration of hydrolysate of glucose was 40 g/L. The hydrolysate was separated to remove residues and condensed by a rotary evaporator to receive 150 g/L of glucose concentration. The hydrolysate was diluted and used as a carbon source at different initial concentrations.

### 3.1. Effect of source of glucose to L-lysine production

Figure 1 shows the effect of the source of glucose to L-lysine production at initial glucose concentration of 110 g/L and incubated pH of 7.2. After 72 hr of incubated time, the L-lysine concentration using AR grade of glucose as a carbon source (11.52 g/L) was higher than hydrolysate (7.65 g/L). The remained glucose of AR grade was 35.96 g/L whereas hydrolysate was 27.73 g/L. However, the utilization of glucose using hydrolysate was higher, but the L-

lysine concentration was lower. Under enzymatic hydrolysis, the hydrolysate may be contained components such as xylose, arabinose, dehydration of lignin, acetic acid, and lactic acid [18]. These components inhibited the growth of microorganisms [19].

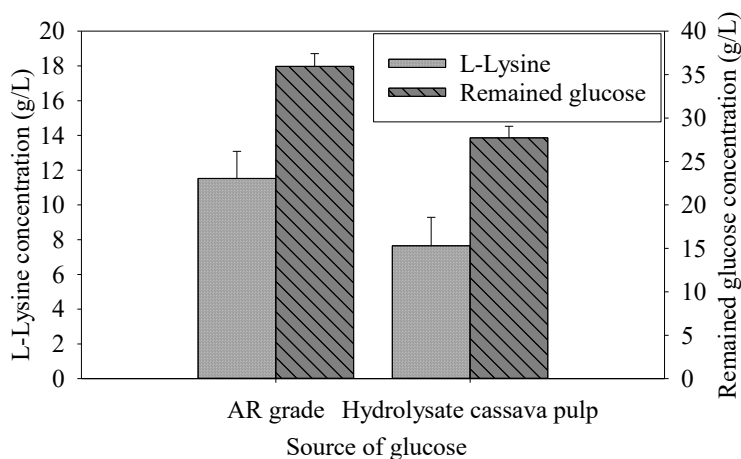


Fig. 1 The effect of the source of glucose to L-lysine production at initial glucose concentration of 110 g/L and incubated pH of 7.2

### 3.2. Effect of initial glucose concentration to L-lysine production

Figure 2 shows the effect of the initial glucose concentration to L-lysine production at different initial glucose concentrations of 40-110 g/L and incubated pH of 7.2. When the initial glucose concentration increases, the L-lysine concentration increases and then slightly decreases. While DCW (dry cell weight) is stable and has a little decline, glucose concentration increases. The maximum L-lysine concentration is 8.17 g/L at the initial concentration of 100 g/L. Thus, the initial glucose concentration of 100 g/L is an optimum condition for L-Lysine production. This effect is due to inhibitors like a higher initial glucose concentration [20] and some desirable components in hydrolysate [21]. This inhibited the growth of bacteria associated with L-lysine production [22].

### 3.3. Effect of incubated pH to L-lysine production

Figure 3 shows the effect of the incubated pH to L-lysine production at initial glucose concentrations of 100 g/L and different incubated pH of 6.5-8.0. During increasing incubated pH, the DCW increases. The trend of remaining glucose concentration also decreases but increases suddenly at a pH of 7.2. This result according to L-Lysine concentrations and provides the maximum L-Lysine concentration of 8.17 g/L. Thus, the incubated pH media at 7.2 is an optimum condition. It is an important parameter to L-Lysine production because incubated pH affected bacteria growth.[20]

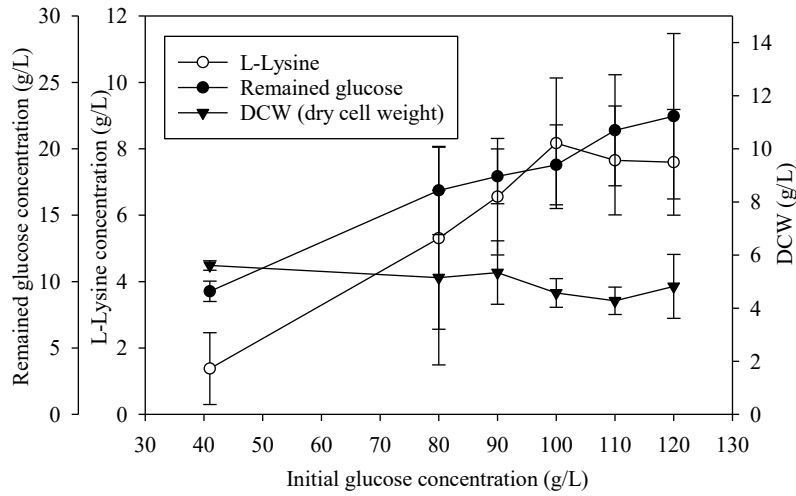


Fig. 2 The effect of the initial glucose concentration to L-lysine production at different initial glucose concentrations of 40-110 g/L and incubated pH of 7.2

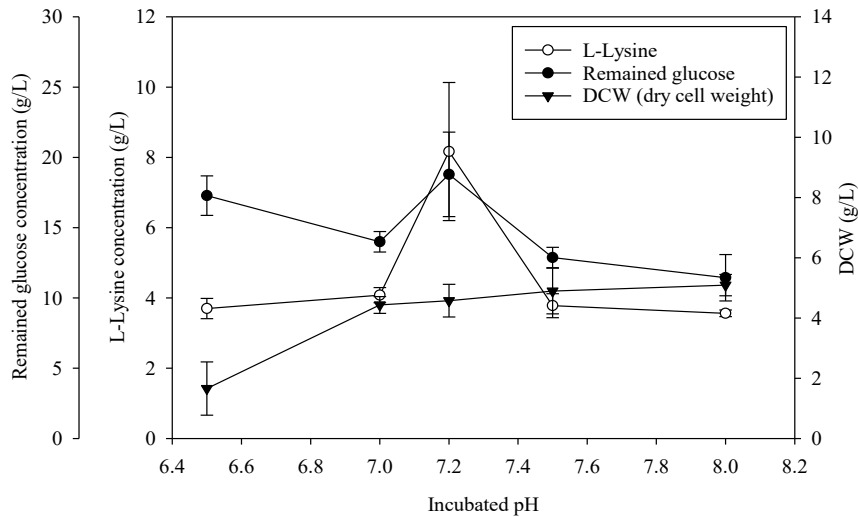


Fig. 3 The effect of the incubated pH to L-lysine production at initial glucose concentrations of 100 g/L and different incubated pH of 6.5-8.0

#### 4. Conclusions

This study shows that L-Lysine production using *C.glutamicum* TISTR 461 can be produced from hydrolysate, as a carbon source, obtained enzymatic cassava pulp. The initial glucose concentration and incubated pH affect productivity of L-lysine. This can be used as the condition to improve the fermentation of L-lysine production. In the future, these will lead to study the L-lysine fermentation in different sizes of bioreactor.

## Acknowledgements

This work was supported by (i) Suranaree University of Technology (SUT), (ii) Thailand Science Research and Innovation (TSRI), and (iii) National Science, Research and Innovation Fund (NSRF) - Grant no. 179270.

## References

- [1] Sowcharoensuk, C. (2021, Sep 21). Industry Outlook 2022-2024: Cassava Industry. Bank of Ayudhya Public Company Limited. <https://www.krungsri.com/en/research/industry/industry-outlook/agriculture/cassava/IO/io-cassava-21>
- [2] Ditkunchaimongkol, N. (2015). The study of efficiency and cost of cassava plup hydrolysis by acid and enzymes. National Science Research Conference, pp. 249-259. Chonburi, Thailand.
- [3] Deeprasert, S., Boonmunma, S., Boottongmol, W., Chinchoedwong, B., and Loha, V. (2012). Utilization of cassava soild waste for sugar production. Thaksin University Journal, 15(3), 39-46.
- [4] Anastassiadis, S. (2007). L-lysine fermentation. Recent Pat Biotechnol, 1(1), 11-24. doi:10.2174/187220807779813947
- [5] Hussain, A., Mukhtar, H., and Ikram-Ul-Haq. (2015). Optimization of Fermentation Medium for L-Lysine Production by Corynebacterium Glutamicum. Pakistan Journal of Botany, 47, 345-349.
- [6] Oyeyinka, S. A., Adeloye, A. A., Olaomo, O. O., and Kayitesi, E. (2020). Effect of fermentation time on physicochemical properties of starch extracted from cassava root. Food Bioscience, 33. doi:10.1016/j.fbio.2019.100485
- [7] Hou, Y., and Wu, G. (2018). Nutritionally Essential Amino Acids. Advances in Nutrition, 9(6), 849-851. doi:10.1093/advances/nmy054
- [8] Liu, J., Xu, J. Z., Rao, Z. M., and Zhang, W. G. (2022). Industrial production of L-lysine in Corynebacterium glutamicum: Progress and prospects. Microbiol Research, 262, 127101. doi:10.1016/j.micres.2022.127101
- [9] Irshad, S., Faisal, M., Hashmi, A., Javed, M., Baber, M., Awan, A., and Anjum, A. (2015). Mass production and recovery of l-lysine by microbial fermentation using Brevibacterium flavum. Journal Animal and Plant Sciences, 25, 290-294.
- [10] Razak, M. A., and Viswanath, B. (2015). Optimization of fermentation upstream parameters and immobilization of Corynebacterium glutamicum MH 20-22 B cells to enhance the production of L-lysine. Biotech, 5(4), 531-540.
- [11] Gopinath, V., and Nampoothiri, K. M. (2014). Corynebacterium glutamicum. In C. A. Batt & M. L. Tortorello (Eds.), Encyclopedia of Food Microbiology (Second Edition) (pp. 504-517). Oxford: Academic Press.
- [12] Association of Official Analytical Collaboration (AOAC). (2000). Official Methods of Analysis. Food Processing, 44, 46-48.
- [13] Rojas, M. J., Amaral-Fonseca, M., Fernandez-Lafuente, R., de Lima Camargo Giordano, R., and Tardioli, P. W. (2019). Recovery of starch from cassava bagasse for cyclodextrin production by sequential treatment with  $\alpha$ -amylase and cyclodextrin glycosyltransferase. Biocatalysis and Agricultural Biotechnology, 22. doi:10.1016/j.bcab.2019.101411

- [14] American National Standards Institute (1999). TAPPI Standard: Regulations and Style Guidelines. *International Nonwovens Journal*, 8(2). doi:10.1177/155892509908-800208
- [15] Ayoola, A., Adeeyo, O., Efevbokhan, V., and Ajileye, O. (2012). A comparative study on glucose production from sorghum bicolor and manihot esculenta species in Nigeria. *International Journal of Science and Technology*, 2(6), 353-357.
- [16] Hsieh, C. L., Hsiung, K. P., and Su, J. C. (1995). Determination of lysine with ninhydrin-ferric reagent. *Analytical biochemistry*, 224(1), 187-189.
- [17] Xia, J., Xu, Z., Xu, H., Liang, J., Li, S., and Feng, X. (2014). Economical production of poly(epsilon-l-lysine) and poly(l-diaminopropionic acid) using cane molasses and hydrolysate of streptomyces cells by *Streptomyces albulus* PD-1. *Bioresour Technology*, 164, 241-247. doi:10.1016/j.biortech.2014.04.078
- [18] Shi, X., Chen, Y., Ren, H., Liu, D., Zhao, T., Zhao, N., and Ying, H. (2014). Economically enhanced succinic acid fermentation from cassava bagasse hydrolysate using *Corynebacterium glutamicum* immobilized in porous polyurethane filler. *Bioresour Technology*, 174, 190-197. doi:10.1016/j.biortech.2014.09.137
- [19] Thongchul, N., Navankasattusas, S., and Yang, S. T. (2010). Production of lactic acid and ethanol by *Rhizopus oryzae* integrated with cassava pulp hydrolysis. *Bioprocess and Biosystems Engineering*, 33(3), 407-416. doi:10.1007/s00449-009-0341-x
- [20] Razak, M. A., and Viswanath, B. (2015). Optimization of fermentation upstream parameters and immobilization of *Corynebacterium glutamicum* MH 20-22 B cells to enhance the production of L-lysine. *Biotechnology*, 5(4), 531-540.
- [21] Fu, J., Li, C., Ju, X., Bai, J., Zhou, Y., Zhang, Y., and Ji, L. (2022). Efficient production of epsilon-poly-L-lysine from cassava bagasse hydrolysate used as carbon source by *Streptomyces albulus* US3-18. *Bioprocess and Biosystems Engineering*, 45(8), 1407-1419. doi:10.1007/s00449-022-02755-3
- [22] Haleem Sha, A., Hameed, A., Ahmad, S., and Khan, G. M. (2002). Optimization of Culture Conditions for L-Lysine Fermentation by *Corynebacterium glutamicum*. *Biological Sciences*, 2(3), 151-156. doi:10.3923/jbs.2002.151.156

## **Adsorption of Moisture by Rice Husk Silica and Commercial Silica** **Maninya Warunlawan, Thumpussorn Akarajarasroj, and Weerawat Clowutimon\***

Department of English Program, Satriwithaya School, 82 Dinso Rd, Wat Bowon Niwet, Phra Nakhon, Bangkok, 10200  
E-mail: weerawat@satriwit.ac.th

### **Abstract**

Adsorption of moisture by rice husk silica and commercial silica was investigated in this study. Rice husk silica was extracted from rice husk using a strong base solution and neutralized by a strong acid solution. After the drying process, the silica was characterized by XRF and BET. Subsequently, the adsorption experiments were carried out in a batch to determine adsorption equilibrium time and adsorption isotherm. It was found that the purity and the surface area of rice husk silica were 90% and 214 m<sup>2</sup>/g, respectively. The adsorption process of both silicas reached equilibrium within 36 hr. Furthermore, the adsorption isotherms were found to be linear in the range of moisture content studied and the adsorption capacity of rice husk silica was around 63% of that of commercial silica.

**Keywords:** Adsorption; rice husk silica; air moisture content.

### **1. Introduction**

Rice is one of the most abundantly produced and consumed foods worldwide. It is a major source of sustenance for more than three billion people annually [1]. After harvesting, rice grain is separated from rice husk (RH) for human consumption using the milling process. This residue, RH, is generally incinerated as fuel in biomass power plants, and the byproduct of this process is rice husk ash (RHA). Generally, RHA has been utilized in various applications, for example, as a filler in rubbers [2] or as an additive to concrete for increased permeability [3]. However, the amount of RHA used in these applications is rather small, compared to the amount produced from biomass power plants. Conversion of RHA to other high value products is therefore required to reduce the tremendous effect of the ever-present waste generation and environmental pollution [4].

The properties of RHA are such that it contains rather high amounts of silica (85-98% wt) [5] compared to other plant ash. RHA is therefore considered an important natural silica source. Generally, silica is a lightweight and highly porous material with a large external surface

area [6], making it suitable for use as an adsorbent, especially for heavy metal, dye, and moisture [7]. For example, Khan et al. [8] studied the removal of arsenic ion from water using rice husk silica (RHS), the results of which indicated that RHS could effectively adsorb and eliminate approximately 60% of arsenic ion.

Although the use of RHS as an adsorbent in several applications has been investigated, a comparison of the adsorption efficiency of RHS and commercial silica has not been reported. In this research, a comparative analysis of the adsorption efficiency of RHS and commercial silica is undertaken to provide insights for further economical evaluation of large-scale RHS production.

## 2. Experiment

### 2.1 Materials

RH was obtained from local milling (Phra Nakhon Si Ayutthaya, Thailand). Commercial silica was purchased from Pro Dry Chemical Co., Ltd (Samut Prakarn, Thailand). All chemicals used in the preparation of rice husk silica, i.e., sodium hydroxide and hydrochloric acid were supplied by Fisher Scientific (USA).

### 2.2 Preparation of RHS

The method for preparation of RHS is depicted in Fig.1. Initially, RHA was pretreated by adding 100 g of RH to a beaker containing 1000 mL of 1 M HCl. The beaker was then heated up to 70°C for 1 hour using a hot plate (C-MAG HS 4, IKA), after which the heat source was removed and the beaker cooled down to room temperature. The RH was then separated from the solution by filtration. It was subsequently washed with deionized water until it reached a pH of 7. The RH was dried in an oven (OF-01E, JEIO TECH) overnight.

For the process of converting pretreated RH to RHA, 20 g of RH was placed in a 300 mL crucible and burnt in a furnace (Thermo Scientific FB1415M, TEquipment) at 700 °C for 2 hours. The conversion into RHS was performed by adding 10 g of RHA to a beaker containing 100 mL of 1 M NaOH solution, and the mixture was stirred at 70 °C for 24 hours. Afterwards, a filtration assembly was used to filter the solution. The remaining ash on the filter paper was then washed with 100 mL of hot water, and the filtrate was neutralized using 1 M of HCl to form silica gel. The solution was left overnight to completely congeal. After that, the gel was then crushed and washed with 100 mL of distilled water. Subsequently, the gel was dried in an



oven at 100 °C for 24 hours. The dried silica was ground to fine particles with diameters between 125 and 160  $\mu\text{m}$ .

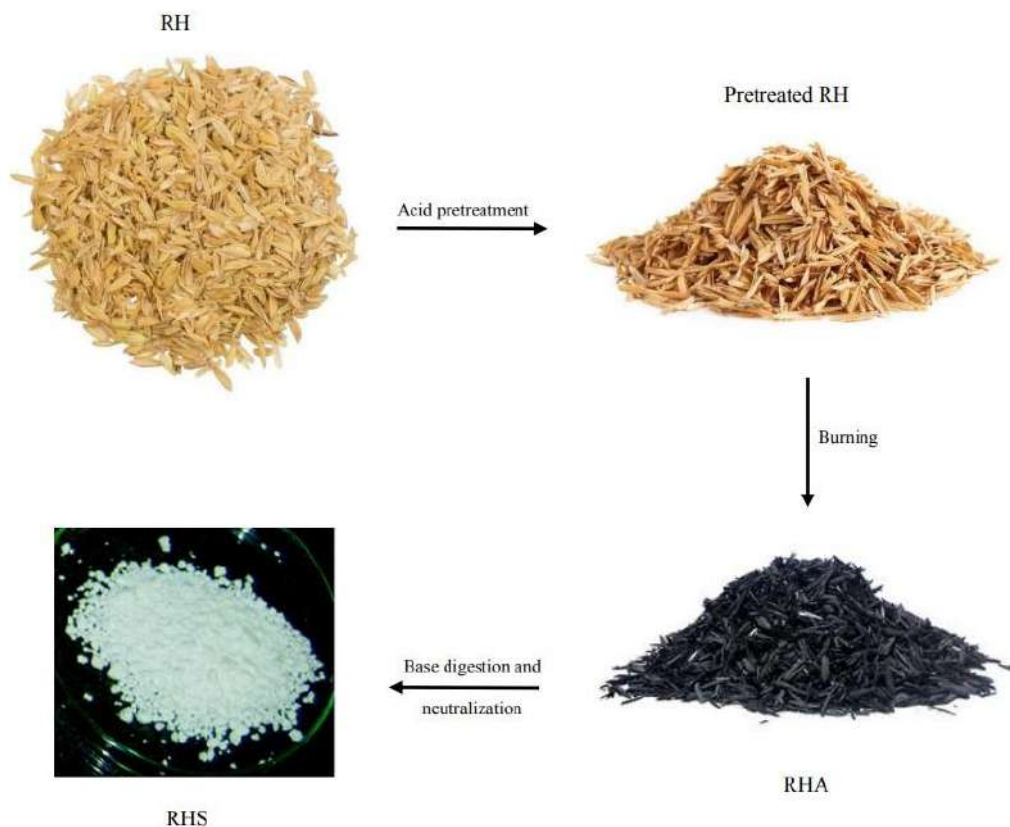


Fig. 1 Schematic diagram for the preparation of RHS

### 2.3 Characterization of RHS

The RHS was characterized by X-ray Fluorescence (XRF) to analyze the composition and by Brunauer-Emmett-Teller analysis (BET) to determine the pore volume, pore diameter and surface area.

### 2.4 Adsorption experiments

Batch adsorption experiments were conducted by placing 6 vials, each containing 1.5 g of commercial silica, and 6 vials, each containing 1.5 g of RHS, in a plastic box with a beaker of water aerated with an air compressor to promote a humid environment (as shown in Fig. 2). The temperature was controlled at  $30 \pm 1$  °C. To determine equilibrium time and adsorption equilibrium, the effect of contact time (6 – 48 hours) and moisture content (68 - 85%) were investigated. The amount of moisture adsorbed per unit mass of adsorbent ( $q$ ), in mg/g, was determined by Eq. 1

$$q = \frac{w_f - w_i}{w_s} \quad (1)$$

where  $w_i$  and  $w_f$  are the initial and final weights of bottle and  $w_s$  is the amount of adsorbent in the bottle.

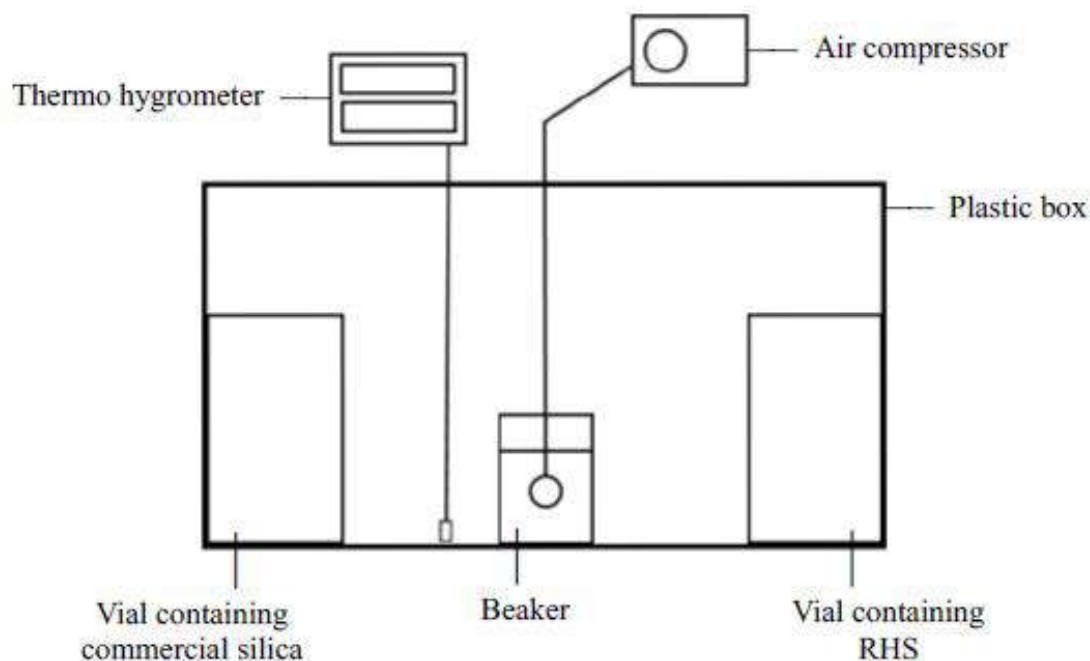


Fig. 2 Schematic diagram of adsorption experiment

### 3. Results and discussion

#### 3.1 Characterization of RHS

RHS was characterized by XRF to determine its composition. The result is presented in Table 1.

**Table 1 Composition of RHS**

Component	Percent
SiO <sub>2</sub>	90.15
Na <sub>2</sub> O	7.98
CaO	0.72
FeO	0.54
NiO	0.31
CuO	0.30

As shown in the table, the main compositions of RHS are SiO<sub>2</sub> and Na<sub>2</sub>O, around 90% and 8%, respectively. These results are consistent with other studies [9-11].

Characterization results of RHS by BET analysis to determine pore volume, pore diameter and surface area are presented in Table 2. As indicated in the table, the surface area of RHS is 213.9 m<sup>2</sup>/g, which accords well with the results of other studies [11-12]. The pore diameter and pore volume are also within the range presented in other studies [11, 13-14].

**Table 2 BET characterization results of RHS**

Parameter	
Total surface area	213.9 m <sup>2</sup> /g
Total pore volume	0.35 cm <sup>3</sup> /g
Pore diameter	11.15 nm

### 3.2 Adsorption experiments

Adsorption kinetics of moisture was carried out to determine the equilibrium time using batch adsorption at 85% moisture content. The results are presented in Fig. 3. As shown in this figure, the amounts of moisture adsorbed by both silicas are linearly proportional to contact time up to 36 hours, after which they plateau, indicating equilibrium of adsorption. The contact time, which is 36 hours, is the most suitable duration for studying adsorption isotherm.

The adsorption isotherms of moisture of both silicas were studied by varying moisture content. The results are presented in Fig. 4. As this figure demonstrates, the amount of moisture adsorbed slightly increases as the moisture content increases. This is due to the increase in contact between water vapor and adsorbents from the accumulation of moisture content in the controlled environment. Compared to commercial silica, however, the adsorption efficiency of RHS is relatively lower at approximately 63%. This may result from the lower surface area of RHS (200 vs 600 m<sup>2</sup>/g, approximately). In future studies, experimentation with increasing the surface area of RHS is recommended to determine whether it yields better adsorption efficiency. In addition, the mass production of RHS should be considered for commercial purposes.

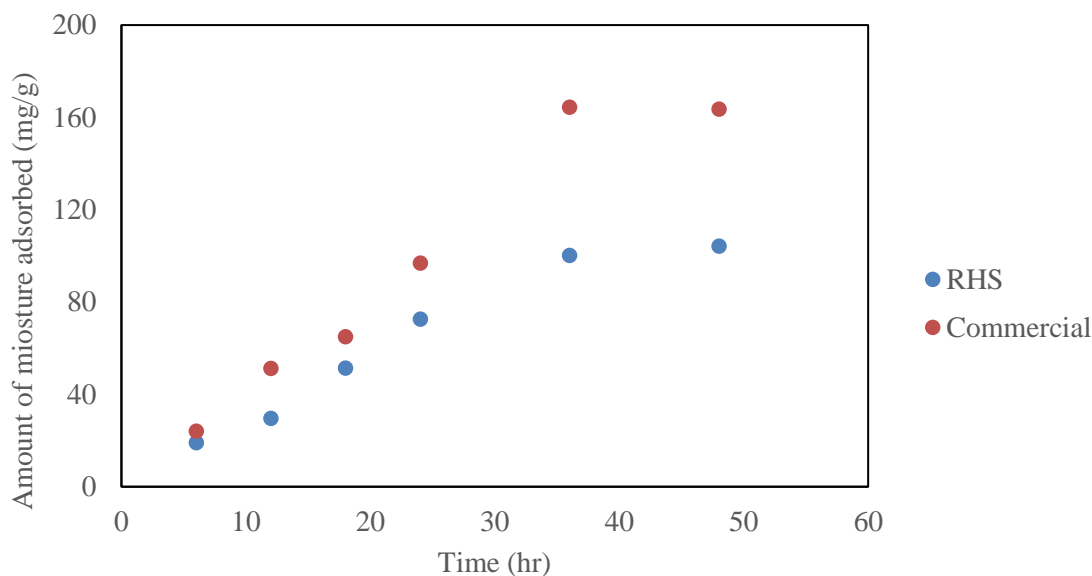


Fig. 3 Amount of moisture adsorbed by rice husk silica and commercial silica at various time (at 85% moisture content)

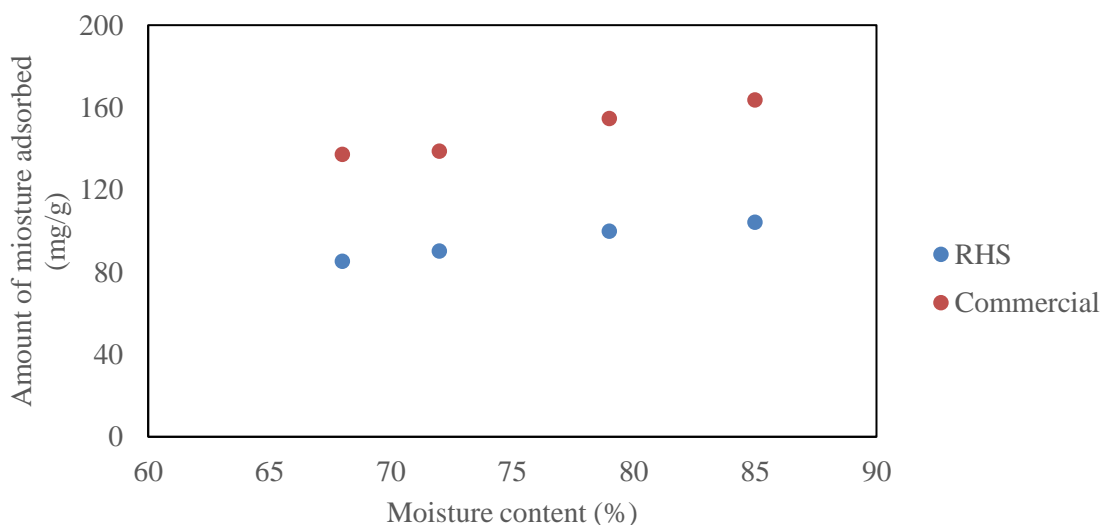


Fig. 4 Adsorption isotherm of moisture of rice husk silica and commercial silica

#### 4. Conclusion

In this research, adsorption efficiency of RHS compared to commercial silica was studied. A moisture adsorption experiment was conducted with varied contact time. The results found that the adsorption of both types of silica reached equilibrium within 36 hours and the adsorption isotherms were linear. RHS was shown to have 63% of the adsorption efficiency of commercial silica. This is probably due to the lower surface area.

## 5. Acknowledgements

The authors thank Satriwithaya School for financial support and Biochemical Engineering Laboratory, Department of Chemical Engineering, Chulalongkorn University for equipment support.

## References

- [1] Bodie, A. R., Micciche, A. C., Atungulu, G. G., Rothrock, M. J., Ricke, S. C., (2019). Current Trends of Rice Milling Byproducts for Agricultural Applications and Alternative Food Production Systems. *Frontiers in Sustainable Food Systems*, 3, 1-13.
- [2] Sun, L., Gong, K., (2001). Silicon Based Materials from Rice Husks and Their Applications. *Industrial and Engineering Chemistry Research*, 40, 5861-5877.
- [3] Sensale, G.R., (2006). Strength Development of Concrete with Rice Husk Ash. *Cement and Concrete Composites*, 28(2), 158-160.
- [4] Liu, Y., Guo, Y., Zhu, Y., An, D., Gao, W., Wang, Z., Ma, Y., Wang, Z., (2011). A Sustainable Route for the Preparation of Activated Carbon and Silica from Rice Husk Ash. *Journal of Hazardous Materials*, 186(2-3), 1314-1319.
- [5] Naskar, M. K., Kundu, D., Chatterjee, M., (2011). Coral-like Hydroxy Sodalite Particles from Rice Husk Ash as Silica Source. *Materials letters*, 65, 3408-3410.
- [6] Jongpradist, P., Homtragoon, W., Sukkarak, R., Kongkitkul, W., Jamsawang, P., (2018). Efficiency of Rice Husk Ash as Cementitious Material in High-Strength Cement-Admixed Clay. *Advances in Civil Engineering*, 2018, 1-11.
- [7] Chandrasekhar, S., Satyanarayana, K.G., Pramada, P.N., Raghavan, P., Gupta, T. N., (2003). Review Processing, Properties and Applications of Reactive Silica from Rice Husk—An Overview. *Journal of Materials Science*, 38, 3159-3168.
- [8] Khan, T., Wahap, S.A.B.A., Chaudhuri, M., (2012). Adsorption of Arsenite from Water by Rice Husk Silica. *Nature Environment and Pollution Technology*, 11(2), 229-233.
- [9] Kalapathy, U., Proctor, A., Shultz, J., (2000). A Simple Method for Production of Pure Silica from Rice Hull Ash. *Bioresource Technology*, 73, 257-262.
- [10] Kalapathy, U., Proctor, A., Shultz, J., (2002). An Improved Method for Production of Silica from Rice Hull Ash. *Bioresource Technology*, 85, 285-289.
- [11] Teinkarodjanakul, N., Clowutimon, W., Assawasangrat, P. (2010). Adsorption of Free Fatty Acid in Crude Palm Oil by Rice Hull Products. *Ladkrabang Engineering Journal*, 27(2), 37-42.



- [12] Dhaneswara, D., Fatriansyah, J. F., Situmorang, F. W., Haqoh, A. N., (2020). Synthesis of Amorphous Silica from Rice Husk Ash: Comparing HCl and CH<sub>3</sub>COOH Acidification Methods and Various Alkaline Concentrations. *International Journal of Technology*, 11(1), 200-208.
- [13] Bakar, R. A., Yahya, R., Gan, S. N., (2016). Production of High Purity Amorphous Silica from Rice Husk. *Procedia Chemistry*, 19, 189-195.
- [14] Azat, S., Sartova, Z., Bekseitova, K., Askaruly, K., (2019) Extraction of High Purity Silica from Rice Husk via Hydrochloric Acid Leaching Treatment. *Turkish Journal of Chemistry* 43(5), 1258-1269.
-

## Methanol production via CO<sub>2</sub> hydrogenation with 1-propanol assisted in fixed bed reactor

Narakorn Ninkaew<sup>1</sup>, Kritchart Wongwailikhit<sup>1,2</sup>, Rungthiwa Methaapanon<sup>1,2</sup>, and Apinan Soottitantawat<sup>1,2\*</sup>

<sup>1</sup>Center of Excellence in Particle and Materials Processing Technology, Department of Chemical Engineering, Faculty of Engineering, Chulalongkorn University, Bangkok 10330, Thailand

<sup>2</sup>Bio-Circular-Green-economy Technology & Engineering Center, Department of Chemical Engineering, Faculty of Engineering, Chulalongkorn University, Bangkok 10330, Thailand

E-mail: apinan.s@chula.ac.th

### Abstract

Carbon capture, utilization, and storage (CCUS) is developed to reduce anthropogenic CO<sub>2</sub> emissions from industrial processes that have the capability to capture and efficiently utilize the substantial quantities of CO<sub>2</sub> that are released by industrial processes. Furthermore, the utilization of carbon dioxide conversion to chemicals or CO<sub>2</sub> conversion to higher-valued products, such as methanol. An exothermic chemical reaction, hydrogenation frequently occurs in the presence of a catalyst and is composed of hydrogen molecules and an element or molecule. A typical synthesis temperature ranging from 250 °C to 300 °C leads to a minimal equilibrium conversion of CO<sub>2</sub> as a consequence of thermodynamic constraints. In this study, the concept of alcohol-assisted methanol synthesis is investigated as an alternate strategy by using primary alcohols, especially 1-propanol, to avoid the product purification problem. Methanol was synthesised on a Cu/ZnO/Al<sub>2</sub>O<sub>3</sub> catalyst at temperatures of 140, 170, 200, and 230 °C using a CO<sub>2</sub>:H<sub>2</sub> 1:5 ratio, changing 1-propanol ratios of 1:1 and 1:0, GHSV 420 h<sup>-1</sup>, and 30 bars in fixed bed reactor. 1-propanol is used as the alcohol due to its reactivity, providing a 47.80% methanol yield with 63.93% CO<sub>2</sub> conversion and 67.54% methanol selectivity. At 170 °C, the sample with 1-propanol has a higher CO<sub>2</sub> conversion (14.74%) and methanol yield (12.86%) than the sample without alcohol.

**Keywords:** Methanol; Hydrogenation; Alcohol-assisted;

### 1. Introduction

Significant global warming is impacted by climate change. The environment has been greatly impacted by human activities, Global warming is the increase in the Earth's temperature caused by the greenhouse effect, which is enhanced by human activities such as combustion, transportation, and industrial processes that produce carbon dioxide.

Carbon dioxide (CO<sub>2</sub>), methane (CH<sub>4</sub>), nitrous oxide (N<sub>2</sub>O), hydrofluorocarbons (HFCs), chlorofluorocarbons (CFCs), and sulfur hexafluoride (SF<sub>6</sub>) are critical greenhouse gases that must be reduced. As a result of the process's extensive deforestation for practical subsistence, the effectiveness of the carbon dioxide removal cycle is diminished. In conclusion, global warming is the result of human behavior on a global scale. Carbon dioxide (CO<sub>2</sub>) is most important greenhouse gases have amount 87 percent of all greenhouse gases and tend to continuing to increase results in an increase in global temperatures of 1-3

degrees Celsius, which has many consequences, such as the melting of the polar ice caps. The weather is unseasonably variable and various disasters occurred.

Also, global warming has led to health problems in recent years. Dangerously, pollution and dust lead to the third-highest death rate for cancer and other diseases among Thais. Carbon dioxide levels have been elevated for long time, exceeding the established guideline of 800-1000 PM. Health will be impacted indirectly. Whether the issue is bodily degradation caused by the production of free radicals, from inducing chronic inflammation, a substantial body of clinical data indicates that it is associated with sleep quality. Causes allergic reactions Because of the indirect impact that the elevated carbon dioxide levels in the atmosphere will produce in inflammation of the respiratory mucosa as well as immune system functionality.

In order to mitigate environmental and health concerns, researchers are interested in methods of carbon dioxide elimination which considers sustainability when addressing issues related to environmental impact. Methanol is one such product developed through the investigation of Carbon Capture, Usage and Storage (CCUS). Methanol, which is the simplest alcohol ( $\text{CH}_3\text{OH}$ ), is a chemical component found in countless commonplace items such as plastics, paints, automobile components, and building materials. In addition to being utilized to power vehicles such as cars, trucks, buses, ships, fuel cells, boilers, and cook stoves, methanol is a clean energy resource.

Methanol is an extremely useful molecule that can be utilized as a fuel or as a component in the synthesis of other substances. In recent years, there has been an increasing level of interest in the so-called "Power-to-Fuel" method for producing methanol from  $\text{CO}_2$ . Methanol, which has numerous applications, is among the most valuable compounds produced via  $\text{CO}_2$  hydrogenation using the "Power-to-Fuel" method. Formaldehyde, acetic acid, methyl methacrylate, dimethyl terephthalate, methylamines, dimethyl ether, methyl-tert-butyl ether, and chloromethane are among the compounds from which methanol is commonly extracted and utilized as a solvent or raw material. Additionally, it is possible to produce light olefins (ethylene and propylene) by the methanol-to-olefin process. Furthermore, methanol exhibits potential as a substitute fuel in the transportation industry and in applications involving fuel cells. Methanol can be generated by the following three primary processes: syngas production, syngas conversion into methanol, and purification via distillation. The majority of syngas is produced through the reforming of natural gas or through the synthesis of carbon-based raw materials, including biogas, coal, petroleum, heavy oil, or asphalt. Purification via distillation constitute a substantial portion of the whole methanol manufacturing process, accounting for around 50 to 80 percent of the overall expenditure. Additionally, the development of coke and soot is a possibility and can provide a significant concern.

Currently, the majority of methanol is produced through the catalytic conversion of synthesis gas (syngas), which is typically produced through the steam reforming of natural gas. Syngas, a mixture of hydrogen, carbon dioxide, and  $\text{CO}_2$ , is converted to methanol at temperatures and pressures of 50–100 bar using copper and zinc oxide ( $\text{Cu/ZnO}$ ) catalysts.

The methanol synthesis process can be described by three equilibrium reactions:





Equations (1) and (2) represent the exothermic hydrogenation of CO<sub>2</sub>, and CO to methanol, and Equation (3) represents the water-gas shift (WGS) reaction that is activated by the copper-based methanol synthesis catalysts.

Alcohol type as catalytic solvent is significant effect on methanol synthesis reaction. By adding alcohol to the reaction, a novel technique for producing methanol at a low temperature from syngas and CO<sub>2</sub>, is known as alcohol-assisted methanol synthesis. By altering the reaction pathway and substantially lowering the reaction temperature, the introduction of alcohol enables the production of methanol under low-temperature conditions.

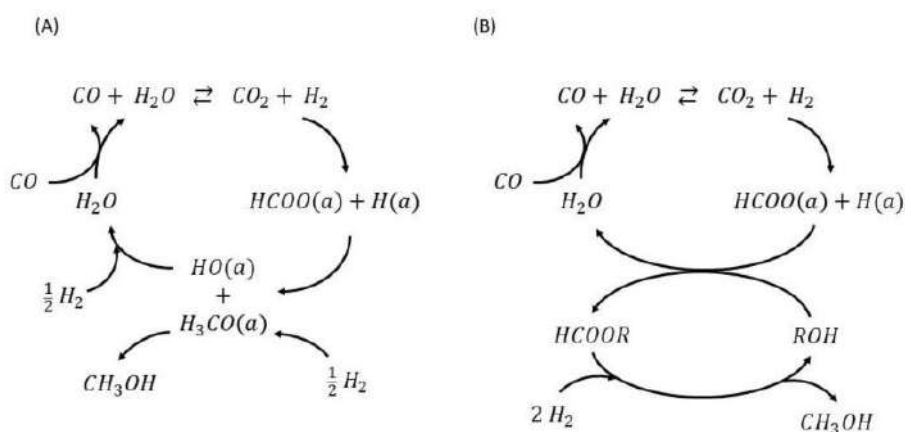
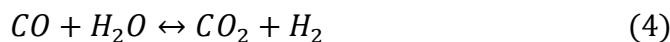


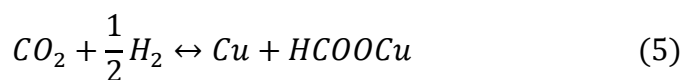
Fig. 1 Illustration of two commonly accepted pathways for methanol synthesis via (A) CO<sub>2</sub>, hydrogenation (B) alcohol-assisted methanol synthesis.

Alcohol-assisted methanol synthesis from syngas consists of the reactions in Equations (4)-(8).

Water-gas shift:



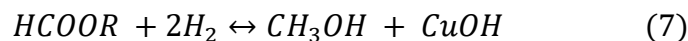
Formic species synthesis from CO<sub>2</sub>, and H<sub>2</sub>:



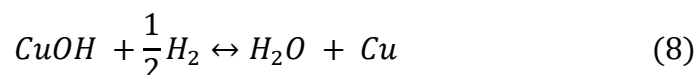
Esterification of formic acid by alcohol to alkyl formate:



Hydrogenation of alkyl formate to methanol and alcohol:



Cu reactivation:



The methanol productivity obtained in the current research can be compared to results reported in other studies. Sutida et al. [3] studied stilising alcohol as a catalyst solvent considerably increases methanol yield while assisting in the reduction of reaction temperature and pressure (150 C and 50 bar). Alcohol by virtue of its reactivity is ethanol, which yields a substantial amount of methanol (47.80%), converts CO<sub>2</sub> by 63.93%, and is methanol-selective to 67.54%. Conversely, ethanol produces ethyl acetate as an unintended byproduct through side reactions; this compound subsequently reacts with methanol to form an azeotrope. Giorgia et al. [4] examined a novel Cu/Zn/Al/Zr catalyst that facilitates the conversion of CO<sub>2</sub> and H<sub>2</sub> to methanol. The catalyst was evaluated at laboratory scale using a cylindrical fixed bed reactor and 0.5 g of catalyst under isothermal conditions (T = 250 °C). The parameters analysed included a gas hourly space velocity ranging from 4000 to 13,000 h<sup>-1</sup>, a pressure of 3.0 to 7.0 MPa, and an H<sub>2</sub>/CO<sub>2</sub> molar ratio between 3 and 6. Methanol yields of up to 13% and CO<sub>2</sub> conversion of up to 26% are achieved.

## 2. Materials and Methods

### 2.1 Catalyst preparation

Before using the Cu/ZnO/Al<sub>2</sub>O<sub>3</sub> catalyst (size 1-1.6 mm) in a packaging catalyst process continuous fixed bed reactor, 20 grams of the catalyst's total weight should be crushed into a 20-cm-tall particle on bed support. Prepare 2.9 grams of aluminum oxide (Al<sub>2</sub>O<sub>3</sub>), 0.26 grams of fiber, and 6.4 grams of ball, as illustrated in Figure 2.

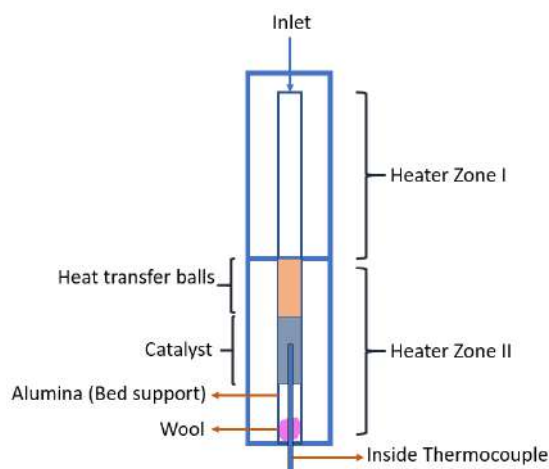


Fig. 2 Catalyst packing tube

After encasing the thermocouple in wool, proceed to add aluminium oxide, the catalyst, and the ball in that order. Then, in order to test for gas leakage in the system, increase pressure to 50 bar and spray foamy liquid onto each valve while introducing N<sub>2</sub> at a flow rate of 200 ml/min into the reactor. This will allow for the observation of bubbles. Reduce catalyst flow by N<sub>2</sub> to 200 ml/min and H<sub>2</sub> to 10 ml/min at a pressure of 5 bar and a temperature of 230 °C for 4 hours. Achieving a constant temperature while increasing the rate signifies the completion of the catalyst reduction process. opening the valve and draining the liquid from the system.

## 2.2 The performance test of 1-propanol assisted methanol synthesis



Fig. 3 Test station

Table 1. Condition operating

Temperature (°C)	CO <sub>2</sub> /C <sub>3</sub> H <sub>8</sub> O ratio
140	1:1
170	1:1
200	1:1
230	1:1
140	1:0
170	1:0
200	1:0
230	1:0

In Table 1, a fixed reactor was supplied with a mixture of CO<sub>2</sub>:H<sub>2</sub> (1:5) and 1-propanol (1:0, 1:1) as the catalytic solvent. The reactor was subsequently pressured to 30 bar and operated at a temperature range of 170, 200, and 230 °C. Following the reaction, the reactor was returned to ambient temperature, as illustrated in Figure 3. On-line detection of the effluent gas and liquid was accomplished by using 6890N gas chromatography. The parameters utilized to quantify the reactivity of catalysts were methanol production, CO<sub>2</sub> conversion, and product selectivity, which were computed using Equations (10) to (13).

$$\%Conversion\ CO_2 = \frac{Mole\ flow\ CO_{2\ in} - Mole\ flow\ CO_{2\ out} \times 100}{Mole\ flow\ CO_{2\ in}} \quad (10)$$

$$\%Yield\ methanol = \frac{Mole\ flow\ methanol_{out} \times 100}{Mole\ flow\ CO_{2\ in}} \quad (11)$$

$$\%selectivity\ methanol = \frac{Mole\ flow\ methanol_{out} \times 100}{Mole\ flow\ total\ product} \quad (12)$$

$$\%selectivity\ CO = \frac{Mole\ flow\ CO_{out} \times 100}{Mole\ flow\ total\ product} \quad (13)$$

### 3. Results and Discussion

#### 3.1 Effect of temperature

At various temperatures, reactions in 1-propanol were conducted under a constant overall pressure. The combined influence of reaction temperature and overall gas pressure on CO<sub>2</sub> conversion, methanol yield, and methanol selectivity is illustrated in Figure 4. At 140, 170, 200, and 230 °C, the total gas pressure remains constant. It has been observed that methanol yield and CO<sub>2</sub> conversion increase significantly with temperature within the investigated temperature range. The synthesis of methanol from CO<sub>2</sub> is an exothermic process, with the endothermic reverse water-gas shift reaction occurring as a byproduct. Methanol formation rates are comparatively higher than CO formation rates at lower temperatures.

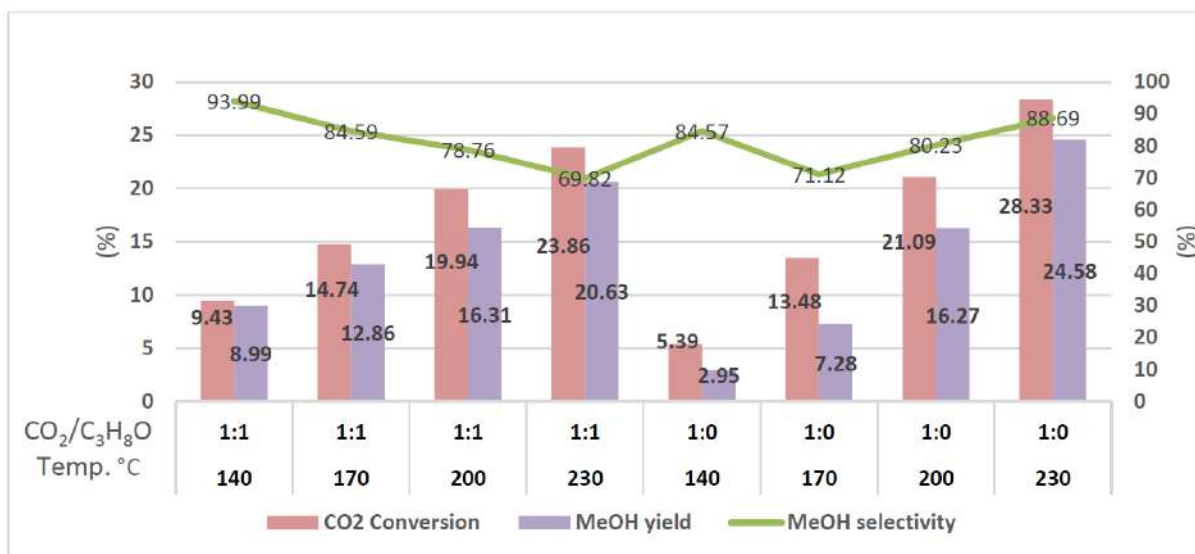


Fig. 4 CO<sub>2</sub> conversion, Methanol yield and methanol selectivity in alcohol-assisted methanol synthesis from CO<sub>2</sub> and H<sub>2</sub> with various temperature and ratio alcohol.

(Conditions: Cu/ZnO/Al<sub>2</sub>O<sub>3</sub> 20 g, alcohol: 1-propanol, pressure 30 bar, total flow 100 ml/min, GHSV 420 h<sup>-1</sup>, feed gas: CO<sub>2</sub>/H<sub>2</sub> = 1/5).

In this study, we investigated the impact of temperature on the efficacy of the catalyst during the synthesis of methanol at low temperatures (Fig. 1). Temperature variations do have an impact on the specific surface area and activities of the catalyst. While mass transfer is influenced by temperature and pressure, the impact of solvent solubility and vapour pressure on catalyst properties during the drying process is a more intricate matter. At an operational temperature of 230 °C, however, both CO<sub>2</sub> conversion and methanol yield attain their maximum values of 24.58% and 28.33%, respectively.

### 3.2 Effect of alcohol

The impact of alcohol type on the synthesis of methanol using alcohol-assisted methods from CO<sub>2</sub> and H<sub>2</sub> was examined. The choice of alcohols employed as solvents had a substantial impact on both the energy consumption and the overall cost of methanol production. In contrast to secondary alcohols, which have a boiling point comparable to that of water, the utilization of primary alcohols, which have a higher boiling point, substantially enhanced the thermal efficiency of the process. In an ideal scenario, solvents with an even higher boiling point would be employed to facilitate the separation process, thereby potentially enabling the reactor to selectively evaporate methanol and water. In order to achieve reasonable reaction rates at low reaction temperatures, the solvent must also be adequately active in the alcohol-promoted reaction. Further equilibrium conversion could be achieved through the development of catalyst systems with increasing activity, which could permit even lower reaction temperatures. [5]

Alcohol-consuming side reactions were inevitable despite the use of alcohol as the catalyst solvent; for example, dehydrogenation of 1-propanol could produce propyl propionate and propyl formate from esterification of formic acid and 1-propanol, respectively. To examine the

impact of temperature, the temperature of the reaction was decreased to 140 °C. The methanol yields slightly decreased to 2.54%, likely due to a slower reaction rate. However, methanol selectivity significantly increased (84.57%). The Cu/ZnO catalyst was typically utilised in conventional methanol synthesis at temperatures between 250 and 300 °C, as CO<sub>2</sub> hydrogenation to methanol did not take place at lower temperatures (140-150 °C). 1-propanol facilitated the occurrence of the alcohol-assisted methanol synthesis reaction at a reduced temperature. At 170 °C, the sample with 1-propanol has a higher CO<sub>2</sub> conversion (14.74%) and methanol yield (12.86%) than the sample without alcohol.

#### 4. Conclusions

It was discovered that methanol yield and CO<sub>2</sub> conversion increase significantly with temperature within the investigated temperature range. However, at an operating temperature of 230 °C, both CO<sub>2</sub> conversion and methanol yield reach their peak values of 24.58% and 28.33%. Alcohol serves as the catalytic solvent in a novel low-temperature methanol synthesis method from CO<sub>2</sub> and H<sub>2</sub> via a 1-propanol promoter, as stated in the conclusion. The effects of the alcohol used in alcohol-assisted methanol, dehydrogenation of 1-propanol could produce propyl propionate and propyl formate from esterification of formic acid and 1-propanol, respectively. 1-propanol accelerated the alcohol-assisted methanol synthesis reaction at a lower temperature. Solvents with an even higher boiling point would be employed to facilitate the separation process. At 170 °C, the sample with 1-propanol has a higher CO<sub>2</sub> conversion (14.74%) and methanol yield (12.86%) than the sample without alcohol. Subsequent investigations should aim to decrease the duration of space velocity time when operating at low temperatures, as this influences the rate of reaction in an experiment. In order to achieve a greater methanol yield, substances typically require an extended residence time as they require more time to transit through the system.

#### References

- [1] Armitage, J.M., Quinn, C.L., Wania, F. (2011). Global climate change and contaminants-an overview of opportunities and priorities for modelling the potential implications for long-term human exposure to organic compounds in the Arctic. *Journal of Environmental Monitoring*, 1532–1546.
- [2] Leonzio, G., E. Zondervan, and P.U. Foscolo. (2019). Methanol production by CO<sub>2</sub> hydrogenation: analysis and simulation of reactor performance. *International Journal of Hydrogen Energy*, 7915-7933.
- [3] Meesattham, S. and P. Kim-Lohsoontorn. (2022) Low-temperature alcohol-assisted methanol synthesis from CO<sub>2</sub> and H<sub>2</sub>: The effect of alcohol type. *International Journal of Hydrogen Energy*, 22691-22703.
- [4] Giorgia L, Mauro M, Sarah L, Francesca F, Alberto P, Luciano Atzori, Antonio C and Manuele G. (2022) CO<sub>2</sub> hydrogenation to methanol with an innovative Cu/Zn/Al/Zr catalyst: Experimental tests and process modeling. *Journal of CO<sub>2</sub> Utilization*, 7, 450
- [5] Prasert R, Tetsuji Y, Tharapong V, Yoshiharu Y, Motoaki I, and Noritatsu T. (2022) Continuous Low-Temperature Methanol Synthesis from Syngas Using Alcohol. *Energy & Fuels*, 17, 817-821

## The Assessment of The Relationship Between Fine Particulate Matter and Related Meteorological Conditions

Panida Soontornsathun<sup>1</sup>, Kornvipa Sirisawat<sup>1</sup>, Natsuda Klinklan<sup>1</sup>,  
Wladyslaw Szymanski<sup>1,3</sup>, and Viganda Varabuntoonvit<sup>1,2,\*</sup>

<sup>1</sup> Chemical Engineering Department, Kasetsart University, Bangkok, Thailand

<sup>2</sup> The Center of Excellence on Petrochemical and Materials Technology,  
Kasetsart University, Bangkok, Thailand

<sup>3</sup> Faculty of Physics, Aerosol Physics and Environmental Physics Division,  
University of Vienna, Austria

E-mail: \* fengvgv@ku.th

### Abstract

The issue of PM<sub>2.5</sub> in Thailand stands as a pressing national concern, demanding urgent solutions. Particularly in the Bangkok metropolitan region, PM<sub>2.5</sub> values consistently surpass established standards, directly impacting the daily lives of residents. These levels tend to escalate during the winter season, spanning from October to March each year. Meteorological factors significantly influence the occurrence and accumulation of PM<sub>2.5</sub>; therefore, this research aims to investigate the correlation between these factors and PM<sub>2.5</sub> levels in Bangkok. This research explores the correlation between meteorological factors and PM<sub>2.5</sub> levels specifically in the Bangkok area. The Deep Neural Network (DNN) model was developed to predict PM<sub>2.5</sub> concentration using meteorological factors. Additionally, the study tests the accuracy of the model predictions by using the Cascade Virtual Impactor (CAVI) to measure PM<sub>2.5</sub> and compare it with the model predictions. The results demonstrate the predictive efficiency of the DNN model for PM<sub>2.5</sub>, showcasing an R-squared ( $R^2$ ) value of 0.6637 and a Root Mean Squared Error (RMSE) value of 12.8610. The value predicted from the DNN model when compared to the results from the Environment Agency and BKK measurements within the same area, exhibits a 59.06% discrepancy. Additionally, the values obtained from the measurement of CAVI show a difference of 35.33% when compared to the predicted average value. The results indicate that the predicted values still exhibit low accuracy. Therefore, further efforts should concentrate on refining the model and structuring the dataset systematically for data training purposes. Experimentation with adjusting the model to accommodate time series data, such as using an LSTM model, should also be considered.

**Keywords:** Air Pollution; Particulate Matter; PM<sub>2.5</sub>; Weather; Meteorological Factors

### 1. Introduction

Thailand is currently facing the problem of air pollution, especially PM<sub>2.5</sub> values, which tend to increase, especially in the Bangkok Metropolitan Region. The PM<sub>2.5</sub> problem has an impact on human's daily life. Whether it is a matter of daily life problems or even health problems. Factors affecting the distribution of PM<sub>2.5</sub> aerosol are meteorological factors like wind speed, wind direction, temperature, and relative humidity. Normally, there are 3 methods for measuring PM<sub>2.5</sub> in the ambient air such as mechanical method, optical method, and electrical method. However, the above methods will let you know only the PM<sub>2.5</sub> value at that

time but cannot know the amount of PM that will occur in the future. Therefore, predicting the density of PM<sub>2.5</sub> particles that will occur in the future is important because it will help effectively deal with the air pollution problem. It also helps inform the public and the media about PM<sub>2.5</sub> problems that will occur in the future on time.

In predicting PM<sub>2.5</sub> value, meteorological data can be used to analyze. The technique or method that is popularly used for analysis is called "Machine Learning" which is a technique that allows the computer system to learn things by itself from the data and environment received from the learning system. which can be classified into many different types of simulation models. In this research, we will use the Deep Neural Network (DNN) model, which is a model that adds a certain number of layers. Resulting in more variables used for feature extraction. To increase efficiency in analyzing and predicting results. The accuracy of the model is checked using the Root Mean Square (RMSE) and R square error ( $R^2$ ) values.

The purpose of this study was to develop a DNN model that could predict PM<sub>2.5</sub> values in urban areas, using the Bangkok area as a case study. By referring to PM<sub>2.5</sub> values and meteorological data from the following measurement stations: 1. Din Daeng Community Housing Station (Pollution Control Department) 2. Din Daeng District Station (Environment Department, BMA) and 3. Chatuchak District Station which is in front of Kasetsart University (Environment Department, BMA). Moreover, still measuring PM<sub>2.5</sub> in the ambient air at Kasetsart University with the Cascade Virtual Impactor (CAVI). Then compare PM<sub>2.5</sub> obtained by CAVI measuring with PM<sub>2.5</sub> of the Environment Department, BMA, and PM<sub>2.5</sub> values obtained from the prediction model, respectively. The values obtained from the measurements were more precise than those obtained from the prediction model.

## 2. Methodology

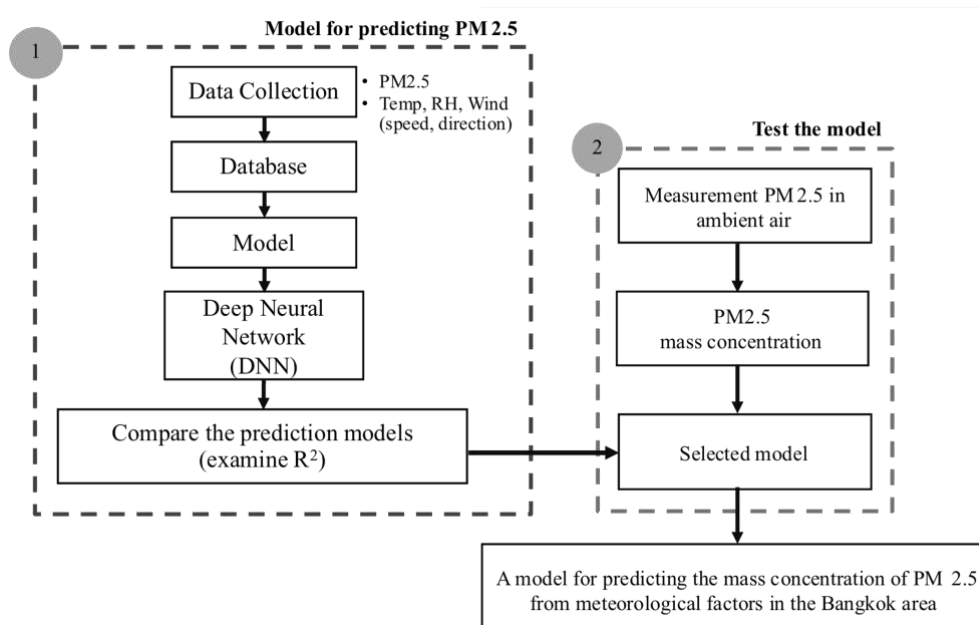


Fig. 1 Workflow to creating the model for predicting PM<sub>2.5</sub>



First part, the Deep Neural Networks (DNN) model was created to predict the mass concentration of PM<sub>2.5</sub> from meteorological factors in the Bangkok area. Staring collects the PM<sub>2.5</sub> and meteorological factors from the air monitoring stations in Bangkok. Then, clean the data and follow up by creating the model. The second part, measuring the mass concentration of PM<sub>2.5</sub> with the Cascade Virtual Impactor (CAVI) at Phahon Yothin Gate, Kasetsart University to test the accuracy of the model in predicting PM<sub>2.5</sub> values.

## 2.1 Data Collection

PM<sub>2.5</sub> and meteorological (temperature, relative humidity, wind speed, wind direction, pressure, and rainfall) measurement data were collected in hourly format from Din Daeng Community Housing Station, Pollution Control Department and Din Daeng District Station, Environment Department, BMA since July 1, 2022, to On June 30, 2023, for a total period of 1 year. Besides, it also collects from Chatuchak District Station (Environment Department, BMA) in front of Kasetsart University from January 1, 2023, to June 30, 2023, a total period of 6 months. After that, these raw data were data cleaned first, and some missing data were removed and data sets were selected to train the model. In addition, we measure the mass concentration of PM<sub>2.5</sub> mass concentration by using the Cascade Virtual Impactor (CAVI) at Phahon Yothin Gate, Kasetsart University.

## 2.2 DNN Model

An artificial neural network system (Neural Network) to nest in many layers and to learn sample data. These data will be used to detect patterns or classify data. Generally speaking, artificial neural network methods can only learn a few layers to establish neural networks. Our brain can think and process complex things like the human brain. Hidden layers must have many layers to send information. This makes it possible to calculate more complex things because there is no training data or computer skills are not high enough. Recently, with the development of technology, computer efficiency has increased and network data layers have become easier. The more layers stacked, the more complex and in-depth the network becomes. Machine learning-based learning patterns typically do not automatically process raw data input. However, it requires some domain knowledge of handcrafted features.[10-12]

To establish the DNN model, we used MATLAB 2003a software. Starting from the "Read Table" command to run PM<sub>2.5</sub> data, and then divide it into training data and test data. Training data is parameter input data and testing data is parameter output data. Then, use the MATLAB deep learning toolbox, and adjust validation data, test data, and layer size to fit the training model. In the training model, such as the number of epochs, training algorithm, etc., use the training options command and execute the training model using functions. Training Network: Train the model using a dataset for predicting PM<sub>2.5</sub>. Use trained models to predict PM<sub>2.5</sub>. And investigate the prediction accuracy of the selected model.[10]

## 2.3 PM measurement using CAVI

Cascade Virtual Impactor or CAVI, collected the particles by using a gravimetric system or mechanical methods, relying on the principle of differences in air flow rates to separate particles according to their size and fall onto the filter. CAVI can separate particulate matter diameters smaller than 10, 2.5, and 1 micrometer as PM<sub>10</sub>, PM<sub>2.5</sub>, and PM<sub>1</sub>. The total flow rate is equal to 12.5 l/min. More detail about CAVI was described by Vejpongsa et al., 2017.[6]

CAVI measurement starts by preparing the filters before, the tissue quart membrane filters are put into a furnace at a temperature of 350 °C for 1 hour and put into a desiccator. After that, the aerosols in the ambient air were measured with CAVI at Phahon Yothin Gate, Kasetsart University for 24 hours, after which the filters were weighed with a 5-position scale.

## 2.4 Validation Parameters

In this study, the model was accurately evaluated using R-squared ( $R^2$ ) and root mean squared error (RMSE).

### 2.4.1 R-Squared ( $R^2$ )

R-Squared ( $R^2$ ) is one of the most popular metrics used to measure performance or the accuracy of the linear regression, machine learning model.  $R^2$  is the variance that the model can explain as a proportion from the total variance of the data set (The calculation formula is total variance equal to explained variance plus error). Normally, the value of R-Squared is between 0 and 1. If the  $R^2$  value is closer to 1, it means that the model has high performance in predicting results.

### 2.4.2 Root Mean Square Error (RMSE)

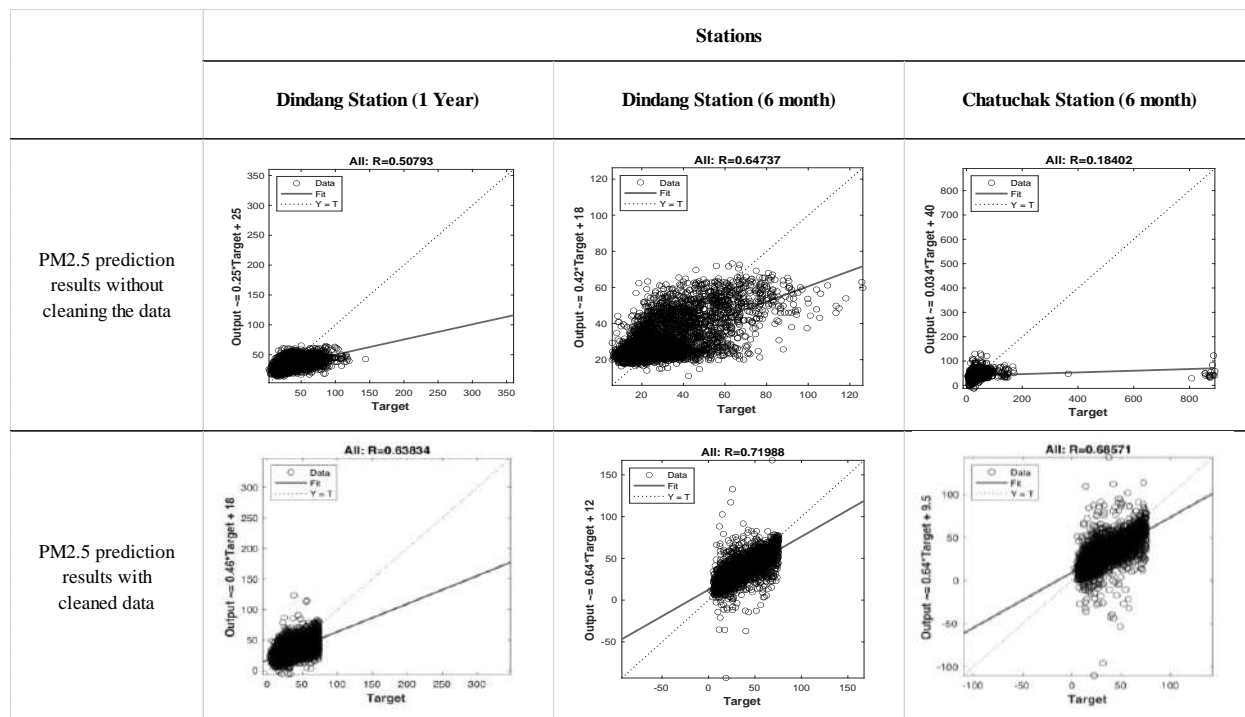
The difference between the numerical value predicted by the model and the average actual value is compared by measuring the error, and then the quadratic curve is obtained. If the obtained RMSE value is low, the predicted value is close to the actual value. This means that the model has high prediction efficiency, and vice versa. A high RMSE means that the predicted value is very different from the actual value, indicating low model efficiency.

## 3. Result and Discussion

### 3.1 Results of PM<sub>2.5</sub> Prediction with DNN Model

This research studies and compares the accuracy of Deep Neural Network (DNN) learning models to predict PM<sub>2.5</sub> dust concentrations from meteorological factors. Using hourly data from Din Daeng Community Housing Station (Pollution Control Department) is data for a period of 1 year and data from Din Daeng District Station and Chatuchak District Station. (Environment Department, BMA ) for a period of 6 months. The results of the experiment were as follows: Using the Deep Neural Network (DNN) model to predict the concentration of PM<sub>2.5</sub> dust, it was found that if an orderly data set was used There is no missing data. It will make the model more accurate, with  $R = 0.71968$ , even when compared to data from the same station with a larger dataset (This is caused by a data set from the Din Daeng Community Housing Station. Pollution Control Department has a 1-year data set with missing data and unusual data, such as quite a lot of Nan, 0, and \*). In addition, Normalizing Data and Preprocessing Data will make the model more accurate.

Table 3.1 Comparison of model accuracy when using three datasets



The values used to measure the performance and accuracy of the Deep Neural Network (DNN) model that the model renders are the  $R^2$  value and the Root mean square value (RMSE). The  $R^2$  value is a measure of the model's error. If the value is close to 1, it means that the model is accurate and the Root mean square difference (RMSE) is a value that indicates the discrepancy between the prediction of the value obtained from the model with the actual value. If the MSE value is small means that the model is accurate.

Table 3.2 Displays the Root mean square difference (RMSE) and  $R^2$  values before predictions

Data	Train		Test	
	RMSE	$R^2$	RMSE	$R^2$
1. Din Daeng Community Housing Station (Pollution Control Department)	10.9659	0.7014	14.1886	0.4773
2. Din Daeng District Station (Environment Department, BMA)	8.7780	0.8126	13.9028	0.5214
3. Chatuchak District Station (Environment Department, BMA)	10.1491	0.8176	16.4475	0.4688

### 3.2 Comparison results of the DNN Model with the Cascade Virtual Impactor

The comparison of PM<sub>2.5</sub> was measured by Cascade Virtual Impactor (CAVI) with PM<sub>2.5</sub> which was obtained from the monitoring station of the Environment Department, BMA, and PM<sub>2.5</sub> predicting from DNN models with the same areas. By placing measuring devices around Phahol Yothin Gate, Kasetsart University. The distance of installation of the CAVI from the Environment Department's monitoring station is about 102.41 meters. The measurement will be carried out 2 times as shown in Table 3.3



Fig. 2 Distance between the installation point of the CAVI and the Environment Department, BMA measuring device.

Table 3.3 The mass concentration of PM<sub>2.5</sub> obtained from measurements and predictions from models.

Round	Mass concentration of PM <sub>2.5</sub> ( $\mu\text{g}/\text{m}^3$ )		
	Measured by CAVI	Measured by the Environment Department, BMA	Prediction by DNN
1	19.32079	15	22.4138
2	22.63293	16	26.8976

From Table 3.3, it can be seen that the PM<sub>2.5</sub> values measured by the CAVI are closer to the PM<sub>2.5</sub> measured by the Environment Department, BMA than the values predicted by the model. Because the model obtained is not yet suitable for predicting the mass concentration of PM<sub>2.5</sub>.

#### 4. Conclusion

This study created a deep neural network (DNN) for predicting PM<sub>2.5</sub> based on meteorological factors. The model values with the most ordered data or the fewest abnormalities in the data were discovered. The model with the highest accuracy has a R-value of 0.7199. Through the model research permits researchers to comprehend preprocessing, data normalization, and data cleaning. The forecast of PM<sub>2.5</sub> concentration will be more accurate if data from earlier periods are used in the model. When the cleaning data exists, the RMSE value will decrease compared to the previous value. This time, the RMSE value of the training data is 8.778. In addition, as compared to the PM<sub>2.5</sub> values received from measurements collected by the Environment Agency in the same location with the PM<sub>2.5</sub> predicted by the DNN model, it was discovered that the results obtained from measuring PM<sub>2.5</sub> with the CAVI machine proved more accurate.

#### References

Article in a journal

- [1] Doreswamy, K S, H., KM, Y., Gad, I. (2020). Forecasting Air Pollution Particulate Matter (PM<sub>2.5</sub>) Using Machine Learning Regression Models. *Procedia Computer Science*, 171, 2057-2066. DOI: 10.1016/j.procs.2020.04.221
- [2] Eren, B., Aksangür, İ., and Erden, C. (2023). Predicting next hour fine particulate matter (PM<sub>2.5</sub>) in the Istanbul Metropolitan City using deep learning algorithms with a time windowing strategy. *Urban Climate*, 48. DOI: 10.1016/j.uclim.2023.101418
- [3] Muruganandam, N. S., & Arumugam, U. (2022). Seminal Stacked Long Short-Term Memory (SS-LSTM) Model for Forecasting Particulate Matter (PM<sub>2.5</sub> and PM<sub>10</sub>). *Atmosphere*, 13(10). DOI: 10.3390/atmos13101726
- [4] Niu, M., Zhang, Y., and Ren, Z. (2023). Deep Learning-Based PM<sub>2.5</sub> Long Time-Series Prediction by Fusing Multisource Data—A Case Study of Beijing. *Atmosphere*, 14(2), 340. DOI: 10.3390/atmos14020340
- [5] Vejpongsa, I., Suvachittanont, S., Klinklan, N., Thongyen, T., Veres, M., Szymanski, W.W., (2017). Deliberation between PM<sub>1</sub> and PM<sub>2.5</sub> as air quality indicators based on comprehensive characterization of urban aerosols in Bangkok, Thailand. *Particuology*. 35. 10.1016/j.partic.2017.05.001.
- [6] Wen, Z., Wang, Q., Ma, Y., Jacinthe, P., Liu, G., Li, S., Shang, Y., Tao, H., Fang, C., Lyu, L., Zhang, B., and Song, K. (2023). Remote estimates of suspended particulate matter in global lakes using machine learning models. *International Soil and Water Conservation Research*. DOI: 10.1016/j.iswcr.2023.07.002
- [7] Winalai, C., Nanthasen, S., & Chadsuthi, S. (2022). THE EFFECT OF WEATHER ON PM<sub>2.5</sub> IN THE BANGKOK AREA AND BANGKOK METROPOLITAN REGION USING MACHINE LEARNING. *Life Sciences and Environment Journal*, 23(2), 409–421. DOI: 10.14456/lsej.2022.31

Conference Paper:

- [8] K. Thaweephol and N. Wiwatwattana. (2019). Long Short-Term Memory Deep Neural Network Model for PM<sub>2.5</sub> Forecasting in the Bangkok Urban Area. 17<sup>th</sup> International Conference on ICT and Knowledge Engineering (ICT&KE), Bangkok, Thailand, 1-6. DOI: 10.1109/ICTKE47035.2019.8966854

Web page:

- [9] L, M. P. (2019). Deep Learning แบบฉบับคนสามัญ EP 1 : Neural Network History. <https://medium.com/mmp-li/deep-learning-แบบฉบับคนสามัญ-ep-1-neural-network-history-f7789236a9a3> accessed on January 15, 2024.
- [10] Nessessence. (2018). Deep learning คืออะไร ? <https://www.thaiprogrammer.org/2018/12/deep-learning-คืออะไร/> accessed on January 15, 2024.
- [11] Sheel, D. (2020). Deep Learning คืออะไร? <https://new.abb.com/news/detail/58004/deep-learning> accessed on January 16, 2024.

## Tuning magnetic properties and particle size of iron oxide by changing Fe<sup>2+</sup>/Fe<sup>3+</sup> precursor ratios and rotation speed

**Chaline Kraithat<sup>1</sup>, Weerinda Mens<sup>1</sup>, Chaiyan Chaiya<sup>1</sup>, Rittichai Phaoniam<sup>2</sup>, Sasiradee Jantasee<sup>1,\*</sup>**

<sup>1</sup> Department of Chemical and Materials Engineering, Faculty of Engineering, Rajamangala University of Technology Thanyaburi, Pathum Thani 12110, Thailand

<sup>2</sup> Department of Mechanical and Industrial Engineering, Faculty of Engineering, Rajamangala University of Technology Krungthep, Bangkok 10120, Thailand

\*E-mail: sasiradee\_j@rmutt.ac.th

### Abstract

Iron oxide is widely used in a variety of applications, such as catalysts, contrast agents, medicine delivery, and crack-detecting spray, because it comes in several forms. For application in crack-detecting spray, iron oxide having a high saturation magnetization (Ms) and a low magnetic retentivity (Mr) is required. There are two common phases of iron oxide: magnetite (Fe<sub>3</sub>O<sub>4</sub>) and maghemite (Fe<sub>2</sub>O<sub>3</sub>), each of which has specific characteristics. Moreover, the magnetic properties and particle size of iron oxide can be modified by using different iron precursors and synthesis conditions. Thus, the influences of the Fe<sup>2+</sup>/Fe<sup>3+</sup> precursor ratio and rotating speed on the phase, particle size, and magnetic characteristics of iron oxide were investigated in this work. Mixtures of Fe<sup>2+</sup>/Fe<sup>3+</sup> in the ratios of 1:1, 1:2, and 2:1 were used as a precursor. The precursor solution was precipitated in NH<sub>4</sub>OH at 80 °C with rotating speeds of 300 and 3,000 rpm. When the amount of Fe<sup>2+</sup> precursor was increased, the iron oxide particle size reduced while the Ms and Mr increased. At a rotating speed of 300 rpm, the Fe<sup>2+</sup>/Fe<sup>3+</sup> precursor ratio of 2:1 produced the iron oxide with the highest Ms and Mr of 80.90 emu/g and 6.40 emu/g, respectively. Using a high shear reactor to increase the rotating speed to 3,000 rpm can reduce particle size and increase the Ms to 91.85 emu/g, which is closer to the MS of iron oxide particles in commercial grade crack-detecting spray.

**Keywords:** Iron oxide; magnetic particle; magnetization; particle size.

### 1. Introduction

Crack detection sprays play a crucial role in the widely employed nondestructive testing (NDT) method known as magnetic particle testing. This testing method comprises two main parts: a device for generating a magnetic field and detection reagents containing solvent chemicals facilitating the movement of magnetic substances, along with magnetic powder (Zolfaghari et al., 2018). Pure iron particles are utilized for magnetic particle testing. To meet industry standards and specifications for NDT, magnetic particle inspection powders should exhibit a clearly visible color and maintain consistent sizes. In particle testing, iron particles with sizes ranging from 0.1 to 75 μm are preferred. Spherical particles are favored for their suitability, as they can effectively distribute magnetism in all directions, resulting in improved efficiency compared to particles of other shapes. Additionally, the magnetic properties of these particles must be robust enough to promptly respond to magnetic field leakage sources at the surface of the workpiece.



Iron oxide is a chemical compound composed of iron and oxygen, exhibiting various phase forms, including wüstite (FeO), magnetite (Fe<sub>3</sub>O<sub>4</sub>) classified as iron (II) oxide, and alpha phase hematite ( $\alpha$ -Fe<sub>2</sub>O<sub>3</sub>), beta phase ( $\beta$ -Fe<sub>2</sub>O<sub>3</sub>), gamma phase maghemite ( $\gamma$ -Fe<sub>2</sub>O<sub>3</sub>), epsilon phase ( $\epsilon$ -Fe<sub>2</sub>O<sub>3</sub>) classified as iron (III) oxide. Widely employed across various applications, iron oxide finds use in catalysts (Stevens et al., 2005), contrast agents (Patel et al., 2008), drug delivery systems (Alexiou et al., 2006), and crack detection sprays (Luk et al., n.d.), owing to its versatile forms. Notably, magnetite and maghemite are commonly utilized forms.

Iron oxide can be synthesized through various methods, such as co-precipitation (Karaagac et al., 2012), emulsion method (Tomitaka et al., 2014), hydrothermal method (Ahmad et al., 2015), sol-gel method (Rahman et al., 2019), microwave irradiation (Parsons et al., 2009), polyol method (Changming et al., 2011), and aerosol method (Cabañas et al., 1993). The most common technique to produce iron oxide is coprecipitation because of its simplicity, high yield performance and high crystallization. The Fe<sup>2+</sup>/Fe<sup>3+</sup> ratio has a major effect on the properties of iron oxide in a typical coprecipitation reaction. Utilizing iron (III) chloride hexahydrate and iron (II) chloride tetrahydrate, (Karaagac et al., 2012) discovered that a larger ratio resulted in higher saturation magnetization (Ms). When the ratio of Fe<sup>2+</sup> to Fe<sup>3+</sup> was less than 2/1, the magnetic particle exhibited superparamagnetic behavior with zero coercivity (Hc) and zero remanence (Mr). Moreover, the kind of precipitate solutions and iron precursors have an effect on particle morphology and size as well (Fatima et al., 2018). The effects of different iron precursors, capping agents, and capping agent concentrations on the forms of Fe<sub>3</sub>O<sub>4</sub> were investigated. The spherical magnetic nanoparticle appears to be produced by the iron precursor iron (III) chloride hexahydrate and ammonium acetate, with a particle size of around 216 nm. Using KOH, magnetic nanoparticles produced octahedron and cubic forms, with particle sizes ranging from 4.9  $\mu$ m to 158 nm. The types of alkaline solutions employed to precipitate iron oxide particles influenced the development of magnetic particles. Two types of alkaline solutions were compared: NH<sub>4</sub>OH and NaOH. When NH<sub>4</sub>OH was used, the magnetic particles were more homogeneous and simpler to separate than when NaOH was used, because the particles were less pure due to their varied sizes. NH<sub>4</sub>OH also formed magnetic particles with improved magnetic characteristics. Furthermore, synthesis parameters such as temperature, pH, and mixing velocity impacted the purity, size distribution, and shape of the magnetic particles. The solid crystallization reaction required a well-distributed alkaline solution with strong mixing power, resulting in a narrower size distribution and smaller particles. The effects of stirring velocity at 10,000, 18,000, and 25,000 rpm on the particle size of magnetic nanoparticles produced by the coprecipitation technique were investigated (Valenzuela et al., 2009). When magnetite nanoparticles were manufactured at a velocity of 25,000 rpm, non-magnetic magnetite was formed with hematite and goethite. On the other hand, with varied stirring velocities of 10,000 rpm, the magnetite phase can emerge in the absence of another secondary phase. Magnetic stirring and homogenization at 10,000 rpm generated spherical or ellipsoidal magnetite nanoparticles.

In order to determine the appropriate conditions for the synthesis of magnetic particles for crack-detecting sprays, this study evaluated the effects of the Fe<sup>2+</sup>/Fe<sup>3+</sup> precursor ratio and rotation speed on the phase, particle size, and magnetic properties of iron oxide as a precursor, Fe<sup>2+</sup>/Fe<sup>3+</sup> mixtures with ratios of 1:1, 1:2, and 2:1 were employed. The precipitation was carried out in basic conditions, with NH<sub>4</sub>OH at 80 °C and rotational speeds of 300 and 3,000 rpm.



## 2. Methodology

### 2.1 Chemicals

All the chemicals were commercially available and of analytical grade. Specifically, iron (II) chloride tetrahydrate ( $\text{FeCl}_2 \cdot 4\text{H}_2\text{O}$ ), was procured from Sigma-Aldrich, while iron (III) chloride hexahydrate ( $\text{FeCl}_3 \cdot 6\text{H}_2\text{O}$ ), was obtained from Daejung. Additionally, ammonia 30% was purchased from Panreac Applichem.

### 2.2 Synthesis of iron oxide

The synthesis of iron oxide involved combining  $\text{FeCl}_2 \cdot 4\text{H}_2\text{O}$  and  $\text{FeCl}_3 \cdot 6\text{H}_2\text{O}$  in molar ratios of  $\text{Fe}^{2+}$  to  $\text{Fe}^{3+}$  at 1:1, 1:2, and 2:1. The precursors were dissolved in 100 ml of deionized water at 80 °C and stirred for 10 minutes. Subsequently, the precursor solution was subjected to precipitation in  $\text{NH}_4\text{OH}$  using either a mechanical stirrer reactor at rotating speeds of 300 rpm or a homogenizer at rotating speeds of 3,000 rpm for 30 minutes at 80 °C. Following this, the resulting black solid was separated, washed with deionized water, and then dried at 80 °C for 12 hours. The agglomerated product underwent grinding.

### 2.3 Characterization of iron oxide prepared

We used the Scanning electron microscopy (SEM) to measure the morphology and surface characteristics of the iron oxide with a Hitachi S-3400 at STREC, Chulalongkorn University, Thailand. X-ray diffraction (XRD) patterns were scanned within the  $2\theta$  range of  $20^\circ$ - $80^\circ$  to confirm the phase of the iron oxide with a Bruker D8 Discover at STREC, Chulalongkorn University, Thailand. The magnetic properties of the magnetic particles including magnetization and retentivity were investigated using a Vibrating Sample Magnetometer (VSM), with data collected at room temperature under a magnetic field strength of 10,000 Gauss, utilizing 100 points per loop with a 7403 Lake Shore at the Faculty of Science, Khon Kaen University, Thailand. Particle size and zeta potential were analyzed using a Particle Size Analyzer Model Master 3000, employing the Dynamic Light Scattering Method Model ZetaSizer Nano ZS at TUCSEAR, Thammasat University, Thailand.

## 3. Result and discussion

### 3.1 Morphology of iron oxides

Iron oxide was prepared in this study using various iron precursors and synthesis conditions. The iron precursors included iron (II) chloride tetrahydrate and iron (III) chloride hexahydrate, mixed in  $\text{Fe}^{2+}/\text{Fe}^{3+}$  ratios of 1:1, 1:2, and 2:1 using a rotating speed of 300 rpm. Morphological analysis conducted via SEM, as depicted in Fig. 1A)-1C), revealed that iron oxide particles predominantly exhibited irregular shapes with rough surfaces across all  $\text{Fe}^{2+}/\text{Fe}^{3+}$  ratios. The  $\text{Fe}^{2+}/\text{Fe}^{3+}$  ratios did not exert a significant impact on the morphology of iron oxide. Additionally, employing a homogenizer at a rotating speed of 3000 rpm yielded more uniformly spherical shapes and consistent particle sizes (Fig. 1D) compared to iron oxide synthesized using a mechanical stirrer with a lower rotating speed. This improvement can be attributed to the homogenizer's ability to create a uniform and homogeneous mixture by inducing turbulence and cavitation through high pressure in a confined space. Consequently, this process ensures the even distribution of solution contents, resulting in more uniform particle sizes. Therefore, it can be suggested that utilizing a homogenizer with a high rotating

speed has the potential to produce iron oxide particles with more spherical and uniform characteristics.

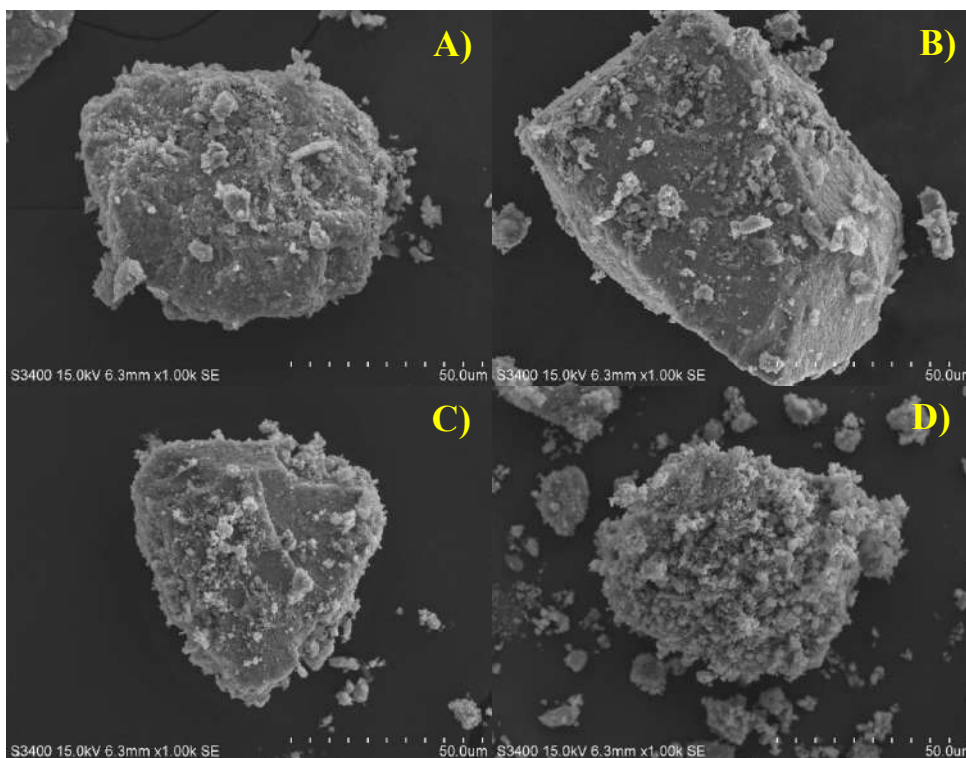


Fig. 1 SEM images of iron oxide particles prepared by  $\text{Fe}^{2+}/\text{Fe}^{3+}$  ratio of; A) 1:1, B) 1:2, C) 2:1 and D) 2:1 with 3000 rpm.

### 3.2 Crystallinity of iron oxides

X-ray diffraction analysis was employed to assess the crystallinity of the prepared iron oxide. The samples were scanned within the  $2\theta$  range of  $20^\circ$  to  $80^\circ$ , and the resulting diffraction peaks are presented in Fig. 2. Iron oxide synthesized with  $\text{Fe}^{2+}/\text{Fe}^{3+}$  ratios of 2:1 exhibited peaks corresponding to the  $\text{Fe}_3\text{O}_4$  magnetite phase, as indicated by the standard peaks from the International Center for Diffraction Data (ICDD) at  $30.28^\circ$ ,  $35.67^\circ$ ,  $43.36^\circ$ ,  $57.36^\circ$ , and  $62.99^\circ$ . These peaks align with the (220), (311), (400), (511), and (440) crystal planes of  $\text{Fe}_3\text{O}_4$  (Fadli et al., 2019), (Fatima et al., 2018). There were no impurities or secondary phase peaks detected in the iron oxide prepared from the  $\text{Fe}^{2+}/\text{Fe}^{3+}$  ratios of 2:1. Furthermore, an increase in the  $\text{Fe}^{2+}$  content was observed to enhance the crystallinity of the iron oxide.

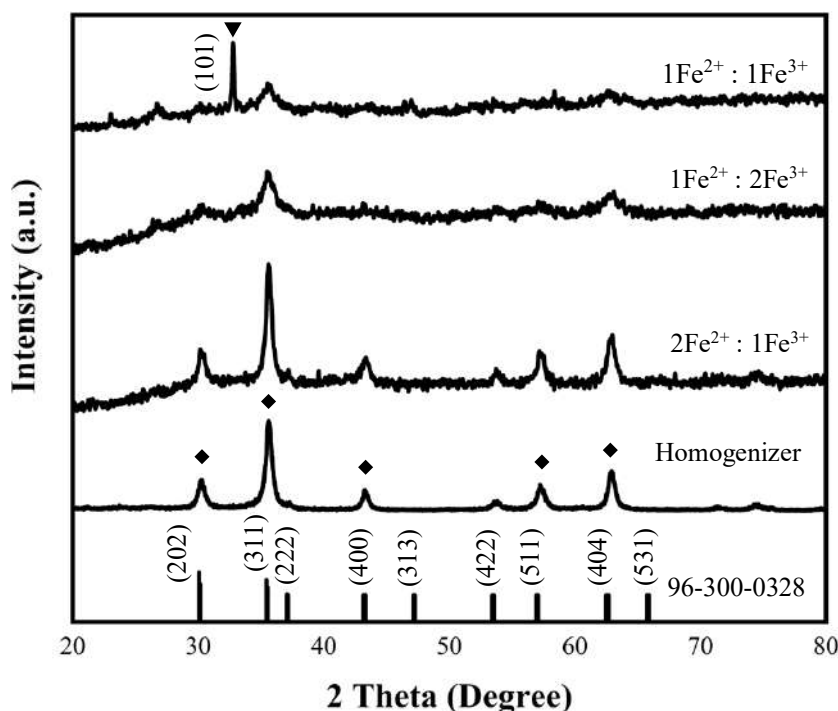


Fig. 2 XRD patterns of iron oxide particles.

### 3.3 Magnetization of iron oxides

In Fig. 3, the magnetization versus magnetic field graphs for all iron oxides are illustrated, revealing hysteresis loops characteristic of a superparamagnetic nature. The  $\text{Fe}^{2+}/\text{Fe}^{3+}$  ratio of 1:1 and 1:2 demonstrated lower saturation magnetization compared to the significant threefold increase observed with the ratio of 2:1. Saturation points were measured at 21.30 and 30.90 emu/g for ratios of 1:1 and 1:2, respectively, while the  $\text{Fe}^{2+}/\text{Fe}^{3+}$  ratio of 2:1 displayed a remarkable increase in saturation magnetization, reaching 80.90 emu/g. It is worth noting that the use of a homogenizer resulted in the highest magnetization and remanence. Iron oxide with smaller particle sizes exhibited higher magnetization, albeit with slightly elevated zero remanence.

### 3.4 Particle size and zeta potential of iron oxides

The particle size of iron oxide, prepared with  $\text{Fe}^{2+}/\text{Fe}^{3+}$  ratios of 1:2, 1:1, and 2:1, was determined using a Particle Size Analyzer as presented in Table 1, yielding sizes of 104  $\mu\text{m}$ , 76.30  $\mu\text{m}$ , and 65.60  $\mu\text{m}$ , respectively. These results underscore the significant influence of the  $\text{Fe}^{2+}/\text{Fe}^{3+}$  ratio on particle size. Notably, an increase in the  $\text{Fe}^{2+}$  content led to a reduction in the particle size of iron oxide. Furthermore, employing a homogenizer at 3000 rpm resulted in the production of iron oxide with the smallest particle size measured at 46.6  $\mu\text{m}$ . This reduction can be attributed to the homogenizer's ability to create a uniform and homogeneous mixture by inducing turbulence and cavitation, thereby yielding more uniform and smaller particle sizes. In terms of applications, magnetic powders used for crack detection sprays typically require particle sizes ranging between 10-75  $\mu\text{m}$ . The particle size results obtained in this study align reasonably well with these requirements.

Dynamic Light Scattering was used to measure the zeta potential of iron oxides, a crucial parameter in the formulation of crack detection sprays. Zeta potential characterizes the surface electrical charge of particles in a solution. It is influenced by various factors, including pH and the presence of multivalent cations such as  $\text{Fe}^{2+}$  and  $\text{Fe}^{3+}$ . The zeta potential of magnetite tends to be positive in acidic solutions and becomes increasingly negative as pH rises (Sun et al., 1998). This polarity variation in zeta potential suggests the presence of repulsive forces between nanoparticles, hindering their aggregation. The zeta potentials of all iron oxides shown in Table 1 exhibit positive zeta potential values, indicating high stability in solution. The direct adsorption of  $\text{Fe}^{2+}$  onto the magnetite surface contributes to positive zeta potential values in acidic environments. Altering the  $\text{Fe}^{2+}/\text{Fe}^{3+}$  ratio and changing mixing speed did not produce any notable impact on the zeta potential, which consistently maintained a positive values. A zero zeta potential denotes a lack of electrostatic repulsion among nanoparticles, potentially leading to increased aggregation and reduced stability (Sun et al., 1998). The upward shift of the zeta potential away from zero further reinforces the stability of nanoparticles, confirming their efficacy in crack detection applications.

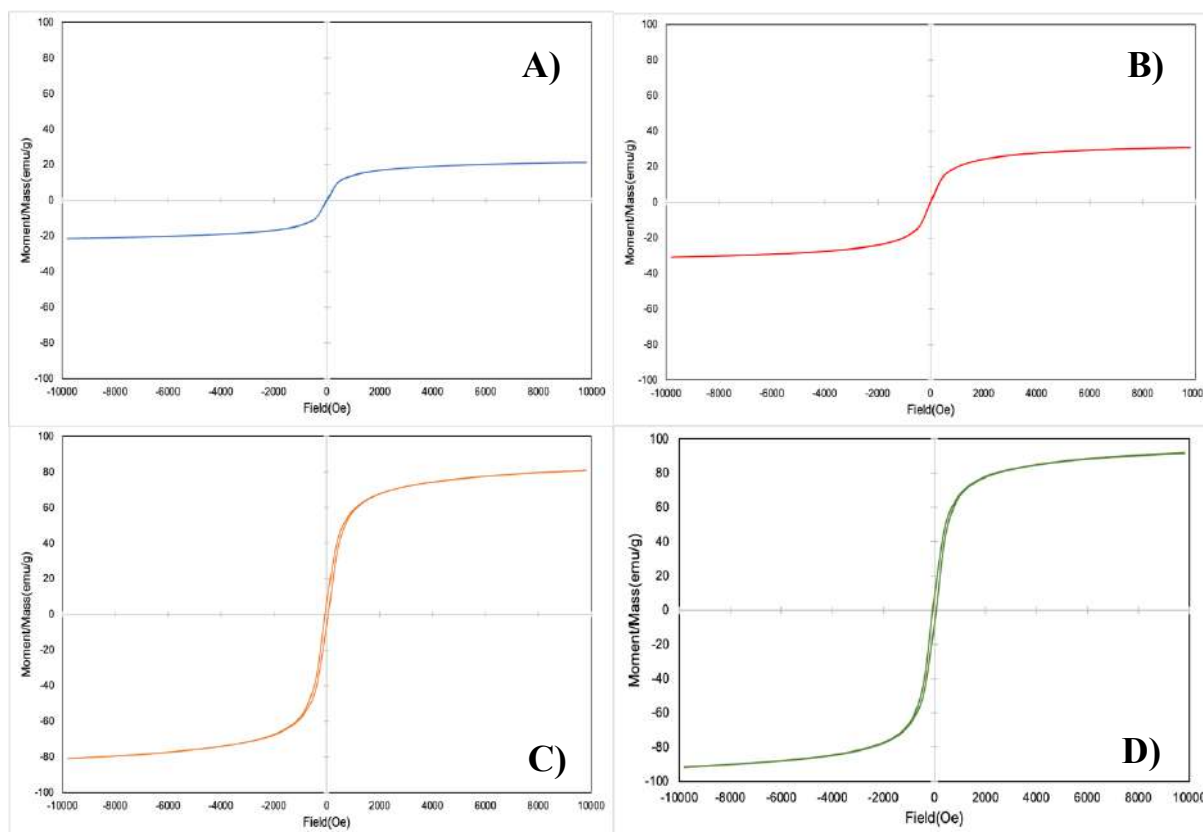


Fig. 3 VSM profile of iron oxides prepared from  $\text{Fe}^{2+}/\text{Fe}^{3+}$  ratios of; A) 1:1, B) 1:2, C) 2:1, and D) 2:1 with 3000 rpm.

Table 1. Particle size, zeta potential, and magnetization properties of iron oxides.

Precursor ratio	Rotating speed (rpm)	Particle size ( $\mu\text{m}$ )	Zeta potential (mV)	Ms (emu/g)	Mr (emu/g)
1:1	300	76.30	34.20	21.30	0.30
1:2	300	104.00	32.70	30.90	0.20
2:1	300	65.60	35.00	80.90	6.40
2:1	3000	46.60	37.00	91.83	8.21

#### 4. Conclusion

Iron oxides were synthesized utilizing varying  $\text{Fe}^{2+}/\text{Fe}^{3+}$  ratios, employing both mechanical stirring at a rotational speed of 300 rpm and a homogenizer at 3000 rpm. The synthesized iron oxides were subjected to comprehensive analysis to evaluate their morphology, crystallinity, particle size, and magnetic characteristics. It was observed that the manipulation of the  $\text{Fe}^{2+}/\text{Fe}^{3+}$  ratio significantly influenced the crystallinity, particle size, and magnetic properties of the iron oxide, while the morphology remained unaffected. An increase in the  $\text{Fe}^{2+}$  content led to the production of iron oxide with enhanced crystallinity and magnetization, accompanied by a reduction in particle size. Furthermore, the utilization of a homogenizer facilitated the creation of a uniform and homogeneous mixture, resulting in iron oxide with a more spherical morphology, smaller particle size, and higher magnetization compared to samples synthesized using mechanical stirring.

#### Acknowledgement

The financial supports from Thailand Science Research and Innovation (TSRI) managed by Rajamangala University of Technology Thanyaburi (FRB67E0729).

#### References

- Ahmad, T., & Phulb, R. (2015). Magnetic iron oxide nanoparticles as contrast agents: Hydrothermal synthesis, characterization and properties. *Solid State Phenomena*, 232, 111–145. doi: 10.4028/www.scientific.net/SSP.232.111
- Alexiou, C., Jurgons, R., Seliger, C., & Iro, H. (2006). Medical applications of magnetic nanoparticles. *Journal of Nanoscience and Nanotechnology*, 6(9–10), 2762–2768. doi: 10.1166/jnn.2006.464
- Cabañas, M. V., Vallet-Regi, M., Labeau, M., & González-Calbet, J. M. (1993). Spherical iron oxide particles synthesized by an aerosol technique. *Journal of Materials Research*, 8(10), 2694–2701. doi: 10.1557/JMR.1993.2694
- Changming Cheng. Fangjie Xu. Hongchen Gu. (2011). *Facile synthesis and morphology evolution of magnetic iron oxide nanoparticles in different polyol processes*. New Journal of Chemistry. Retrieved from <https://pubs.rsc.org/en/content/articlelanding/2011/nj/c0nj00986e>

- Fadli, A., Komalasari, Adnan, A., Iwantono, Rahimah, & Addabsi, A. S. (2019). Synthesis of Magnetite Nanoparticles via Co-precipitation Method. *IOP Conference Series: Materials Science and Engineering*, 622(1). doi: 10.1088/1757-899X/622/1/012013
- Fatima, H., Lee, D. W., Yun, H. J., & Kim, K. S. (2018). Shape-controlled synthesis of magnetic Fe<sub>3</sub>O<sub>4</sub> nanoparticles with different iron precursors and capping agents. *RSC Advances*, 8(41), 22917–22923. doi: 10.1039/c8ra02909a
- Karaagac, O., & Kockar, H. (2012). Iron oxide nanoparticles co-precipitated in air environment: Effect of [Fe<sup>2+</sup>]/[Fe<sup>3+</sup>] ratio. *IEEE Transactions on Magnetics*, 48(4), 1532–1536. doi: 10.1109/TMAG.2011.2173313
- Luk, B. L., & Chan, H. S. (n.d.). *Human Factors and Ergonomics in Dye Penetrant and Magnetic Particles Nondestructive Inspection Methods*.
- Parsons, J. G., Luna, C., Botez, C. E., Elizalde, J., & Gardea-Torresdey, J. L. (2009). Microwave-assisted synthesis of iron(III) oxyhydroxides/oxides characterized using transmission electron microscopy, X-ray diffraction, and X-ray absorption spectroscopy. *Journal of Physics and Chemistry of Solids*, 70(3–4), 555–560. doi: 10.1016/j.jpics.2008.12.017
- Patel, D., Moon, J. Y., Chang, Y., Kim, T. J., & Lee, G. H. (2008). Poly(d,l-lactide-co-glycolide) coated superparamagnetic iron oxide nanoparticles: Synthesis, characterization and in vivo study as MRI contrast agent. *Colloids and Surfaces A: Physicochemical and Engineering Aspects*, 313–314, 91–94. doi: 10.1016/j.colsurfa.2007.04.078
- Rahman, M. T., Hoque, M. A., Rahman, G. T., Azmi, M. M., Gafur, M. A., Khan, R. A., & Hossain, M. K. (2019). Fe<sub>2</sub>O<sub>3</sub> nanoparticles dispersed unsaturated polyester resin based nanocomposites: effect of gamma radiation on mechanical properties. *Radiation Effects and Defects in Solids*, 174(5–6), 480–493. doi: 10.1080/10420150.2019.1606809
- Stevens, P. D., Fan, J., Gardimalla, H. M. R., Yen, M., & Gao, Y. (2005). Superparamagnetic nanoparticle-supported catalysis of Suzuki cross-coupling reactions. *Organic Letters*, 7(11), 2085–2088. doi: 10.1021/ol050218w
- Sun, Z.-X., Su, F.-W., Forsling, W., & Samskog, O. (1998). Surface Characteristics of Magnetite in Aqueous Suspension. In *JOURNAL OF COLLOID AND INTERFACE SCIENCE* (Vol. 197).
- Tomitaka, =Asahi, Jo, J., Aoki, I., & Tabata, Y. (2014). Preparation of biodegradable iron oxide nanoparticles with gelatin for magnetic resonance imaging. *Inflammation and Regeneration*, 34(1), 045–055. doi: 10.2492/inflammregen.34.045
- Valenzuela, R., Fuentes, M. C., Parra, C., Baeza, J., Duran, N., Sharma, S. K., Knobel, M., & Freer, J. (2009). Influence of stirring velocity on the synthesis of magnetite nanoparticles (Fe<sub>3</sub>O<sub>4</sub>) by the co-precipitation method. *Journal of Alloys and Compounds*, 488(1), 227–231. doi: 10.1016/j.jallcom.2009.08.087
- Zolfaghari, A., Zolfaghari, A., & Kolahan, F. (2018). Reliability and sensitivity of magnetic particle nondestructive testing in detecting the surface cracks of welded components. *Nondestructive Testing and Evaluation*, 33(3), 290–300. doi: 10.1080/10589759.2018.1428322

## Fe-doped in LaNiO<sub>3</sub> Perovskite Catalysts for Dry Reforming of Methane

Suparatthakorn Puangjinda<sup>1</sup>, Merika Chanthanumataporn<sup>1,2,\*</sup>,

<sup>1</sup> Center of Excellence on Catalysis and Catalytic Reaction Engineering, Department of Chemical Engineering, Faculty of Engineering, Chulalongkorn University, Bangkok, 10330, Thailand

<sup>2</sup> Bio-Circular-Green-economy Technology & Engineering Center, BCGeTEC, Department of Chemical Engineering, Faculty of Engineering, Chulalongkorn University, Bangkok, Thailand 10330

E-mail: \* merika.c@chula.ac.th

### Abstract

The dry reforming of the CH<sub>4</sub> reaction can transform CH<sub>4</sub> and CO<sub>2</sub> into hydrogen (H<sub>2</sub>) and carbon monoxide (CO), aiming to reduce greenhouse gas emissions in chemical industries and others. The mixture of H<sub>2</sub> and CO, called synthesis gas, is known to be used in methanol production and the Fischer-Tropsch process to generate hydrocarbon fuels. The challenges in dry reforming of CH<sub>4</sub> include coke formation on the catalyst surface and low H<sub>2</sub> selectivity. It was previously reported that doping a small amount of Fe in LaNiO<sub>3</sub> perovskites structure can enhance a metal-support interaction that aids in the dispersion of active sites, inhibiting sintering, and improving catalytic stability, activity, and carbon resistance in the dry reforming of CH<sub>4</sub>. Different catalysts possess various chemical and physical characteristics that can modify their performance and influence the activity of various processes.[1, 2] The LaNi<sub>0.5</sub>Fe<sub>0.5</sub>O<sub>3</sub> perovskite was synthesized using the hydrothermal and sol-gel methods. Both prepared catalysts will be characterized using Brunauer-Emmett-Teller (BET) and scanning electron microscopy (SEM) to examine morphology, as well as x-ray diffraction (XRD) to analyze crystal structure, phase formation, surface area, and morphology.

**Keywords:** Coke formation; sol-gel; hydrothermal; Dry reforming of methane; LaNiFeO<sub>3</sub>; Perovskite catalysts

### 1. Introduction

Global warming has become an increasingly serious problem due to the emission of greenhouse gases by numerous industrial sectors worldwide. There has been a rise in greenhouse gas emissions from various industrial sectors in Thailand. Notably, the chemical industry has recognized the escalating challenges and has initiated research to reduce the production of greenhouse gases through chemical reactions, including partial oxidation, steam reforming, and dry reforming of methane. Methane serves as a primary precursor in these

chemical reactions, which aim to lower the generation of greenhouse gases. Substances such as methane, carbon dioxide, and carbon monoxide are involved in chemical processes.[3-5]

Carbon monoxide (CO) and hydrogen are generated through the dry reforming of methane, which converts methane and carbon dioxide into synthesis gas. Serving as a precursor for various chemical processes, synthesis gas enables the synthesis of a diverse range of chemical compounds. Subsequent chemical reactions can lead to the production of various products, including methanol, ethanol, fuels, and hydrocarbons.[6-8]

Ni-based catalysts are commonly employed in methane dry reforming (DRM) processes. However, these catalysts can lead to challenges such as coke production and metal sintering at elevated temperatures during DRM processes. To address these issues, the perovskite structure is employed as the foundational framework for synthesizing Ni-based catalysts in a bimetallic configuration. The strategic choice of the perovskite structure stems from its potential as a highly promising activity precursor for DRM processes. Additionally, this approach enhances the catalyst's resistance to coking by modifying either the A or B components of the  $ABO_3$  perovskite structure, thereby optimizing performance in DRM processes. [3, 7, 9]

The objective of this work is to examine the chemical and physical properties of  $LaNiFeO_3$  catalysts to compare the sol-gel and hydrothermal processes and ascertain the attributes of the catalysts' surface area, XRD, and elemental distribution. that it is appropriate for methane dry reforming.

## 2. Material and Synthesis Method

Materials used in this study are Nickel (II) nitrate hexahydrate ( $Ni(NO_3)_2 \cdot 6H_2O$ ), Lanthanum nitrate hexahydrate ( $La(NO_3)_3 \cdot 6H_2O$ ), Iron(III) nitrate nonahydrate ( $Fe(NO_3)_3 \cdot 9H_2O$ ), Citric acid monohydrate ( $C_6H_8O_7 \cdot H_2O$ ), Ethanol Absolute 99.9% ( $C_2H_6O$ ), Ammonia solution 25% ( $NH_4OH$ ), Glycine ( $C_2H_5NO_2$ )

### 2.1. Synthesized $LaNi_{(1-x)}Fe_xO_3$ by hydrothermal method

Nickel (II) nitrate hexahydrate ( $Ni(NO_3)_2 \cdot 6H_2O$ ), Lanthanum nitrate hexahydrate 99% ( $La(NO_3)_3 \cdot 6H_2O$ ), and glycine the iron (III) nitrate hexahydrate ( $Fe(NO_3)_3 \cdot 9H_2O$ ) were dissolved in 150 ml of deionized water. The glycine was added to the mixture solution to stir for 30 min at room temperature. Ammonia solution ( $NH_4OH$ ) was to adjust  $pH = 7.7$ , the solution was transferred into Teflon-lined with 150 ml capacity. The Teflon liner was closed in the stainless-steel autoclave and kept at  $180\text{ }^\circ\text{C}$  for 24 hours. The product was washed with deionized water and ethanol several times until the solution was clear. the catalyst was dried at  $110\text{ }^\circ\text{C}$  for 12 h and calcined at  $550\text{ }^\circ\text{C}$  for 2 h and  $850\text{ }^\circ\text{C}$  for 4 h to obtain the  $LaNi_{0.5}Fe_{0.5}O_3$  catalyst.



## 2.2. Synthesized $\text{LaNi}_{(1-x)}\text{Fe}_x\text{O}_3$ by sol-gel method

Nickel (II) nitrate hexahydrate ( $\text{Ni}(\text{NO}_3)_2 \cdot 6\text{H}_2\text{O}$ ), Lanthanum nitrate hexahydrate 99% ( $\text{La}(\text{NO}_3)_3 \cdot 6\text{H}_2\text{O}$ ), iron (III) nitrate hexahydrate ( $\text{Fe}(\text{NO}_3)_3 \cdot 9\text{H}_2\text{O}$ ) were dissolved together in 200 mL of deionized water. Then citric acid (CA) and ethylene diamine tetraacetic acid (EDTA) were added into the above solution with a molar ratio of metal ion: CA: EDTA = 1: 1: 1.5. Aqueous ammonia was dropped slowly into the mixture solution until  $\text{pH} = 4.0-5.0$  with vigorous stirring. The mixture was maintained at  $80^\circ\text{C}$  until complete evaporation of water and formation of transparent gel, followed by drying at  $100^\circ\text{C}$  for 12 h. The obtained xerogel was calcined in a two-step process. In the first step, the precursor was combusted at  $300^\circ\text{C}$  for 4 h in air to eliminate the organic constituents. Afterward, the temperature further rose to  $550^\circ\text{C}$  for 2 h and  $850^\circ\text{C}$  for 4 h forming a  $\text{LaNi}_{0.5}\text{Fe}_{0.5}\text{O}_3$  catalyst. [10]

## 2.3. Characterization

BET was measured surface area, pore volume, and pore size. FE-SEM-EDS was used to measure the morphology and disperse of elements in catalysts. X-ray diffractometer was used to measure the structure phase of catalysts by using the  $2\theta = (20-80^\circ)$  range at 298 K with  $\text{CuK}\alpha$  radiation source.

## 3. Results and discussion

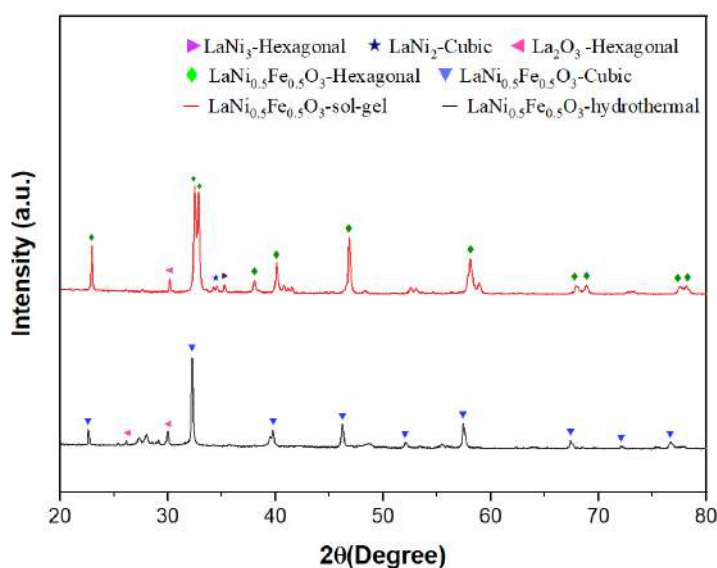


Fig 1. X-ray diffractometer (XRD) of  $\text{LaNi}_{0.5}\text{Fe}_{0.5}\text{O}_3$  the sol-gel method and hydrothermal method

Fig 1. shows X-ray diffractometer (XRD) of  $\text{LaNi}_{0.5}\text{Fe}_{0.5}\text{O}_3$  is between the sol-gel method and hydrothermal method. The  $\text{LaNi}_{0.5}\text{Fe}_{0.5}\text{O}_3$  catalyst was synthesized by the sol-gel method, exhibiting an Hexagonal phase with  $2\theta$  angles at  $22.9^\circ$ ,  $32.4^\circ$ ,  $32.8^\circ$ ,  $40.0^\circ$ ,  $46.8^\circ$ ,  $58.1^\circ$ ,  $67.9^\circ$ ,  $68.8^\circ$ ,  $77.4^\circ$ , and  $78.1^\circ$ . [10] However,  $\text{LaNi}_3$ ,  $\text{LaNi}_2$ , and  $\text{La}_2\text{O}_3$  are also observed among the impurities present in this sample at  $2\theta$  angles at  $30.1^\circ$ ,  $34.3^\circ$ , and  $35.2^\circ$ . The  $\text{LaNi}_{0.5}\text{Fe}_{0.5}\text{O}_3$  catalyst was synthesized by the hydrothermal method, exhibiting an Cubic phase with  $2\theta$  angles at  $22.9^\circ$ ,  $32.6^\circ$ ,  $40.2^\circ$ ,  $46.7^\circ$ ,  $58.1^\circ$ ,  $68.3^\circ$ , and  $77.7^\circ$ . In addition,  $\text{La}_2\text{O}_3$  is also observed among the impurities present in this sample at  $2\theta$  angles at  $26.2^\circ$ , and  $30.1^\circ$ .

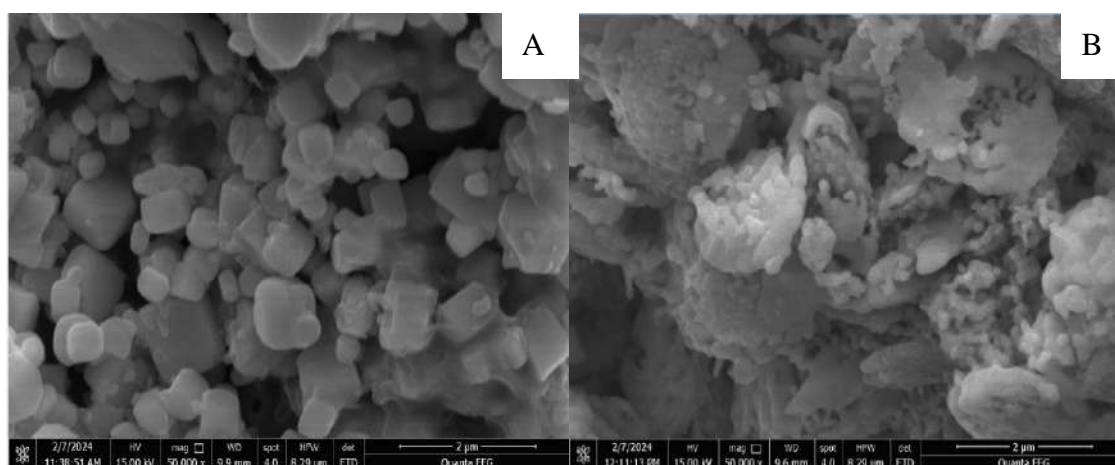


Fig 2. SEM images of  $\text{LaNi}_{0.5}\text{Fe}_{0.5}\text{O}_3$ ; (A)  $\text{LaNi}_{0.5}\text{Fe}_{0.5}\text{O}_3$ -sol-gel, and (B)  $\text{LaNi}_{0.5}\text{Fe}_{0.5}\text{O}_3$ -hydrothermal at 50,000X

Fig 2. shows morphology and shape of catalysts. Different shapes are produced by different synthesis methods. Cubic shape, polygonal shape, and high-forming agglomerations are observed in the The  $\text{LaNi}_{0.5}\text{Fe}_{0.5}\text{O}_3$ -sol-gel. Furthermore, granular shape and high-forming agglomerations are displayed by  $\text{LaNi}_{0.5}\text{Fe}_{0.5}\text{O}_3$ -hydrothermal. [11-13]

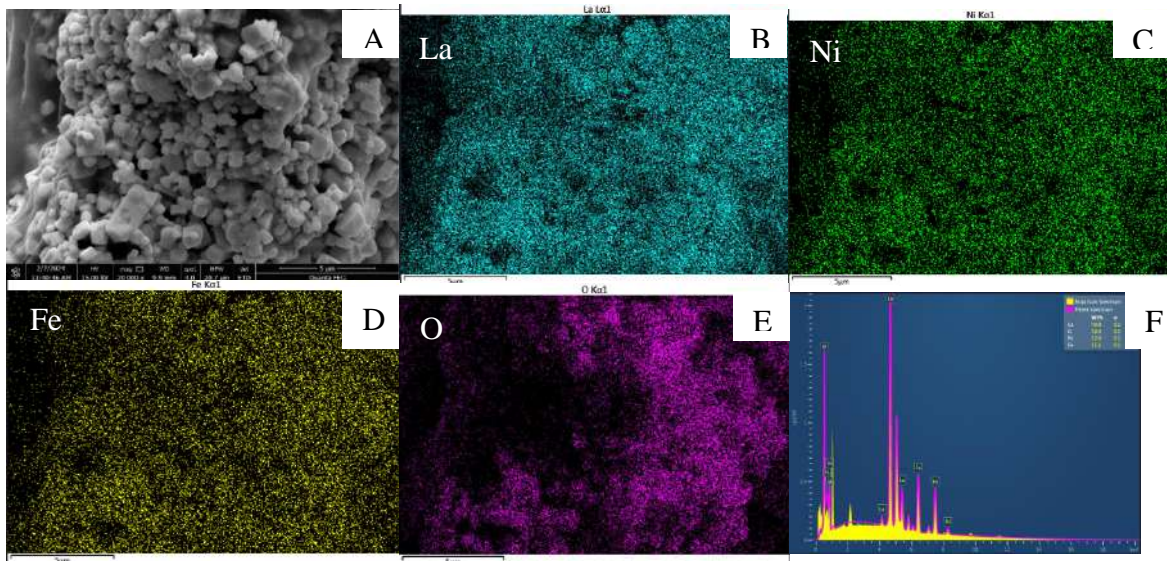


Fig 3. FESEM image (A) and EDS mapping mapping (B-F) of  $\text{LaNi}_{0.5}\text{Fe}_{0.5}\text{O}_3$ -sol-gel

Fig 3. shows the distribution of elements in the  $\text{LaNi}_{0.5}\text{Fe}_{0.5}\text{O}_3$ -sol-gel catalyst. Elementals consist of 59%lanthanum (La), 12.6%Nickel (Ni), 11.1%iron (Fe), 16.4%oxygen ( $\text{O}_2$ ), and 0.9% other, which distributed the surface area of  $\text{LaNi}_{0.5}\text{Fe}_{0.5}\text{O}_3$ - sol-gel catalyst.[11]

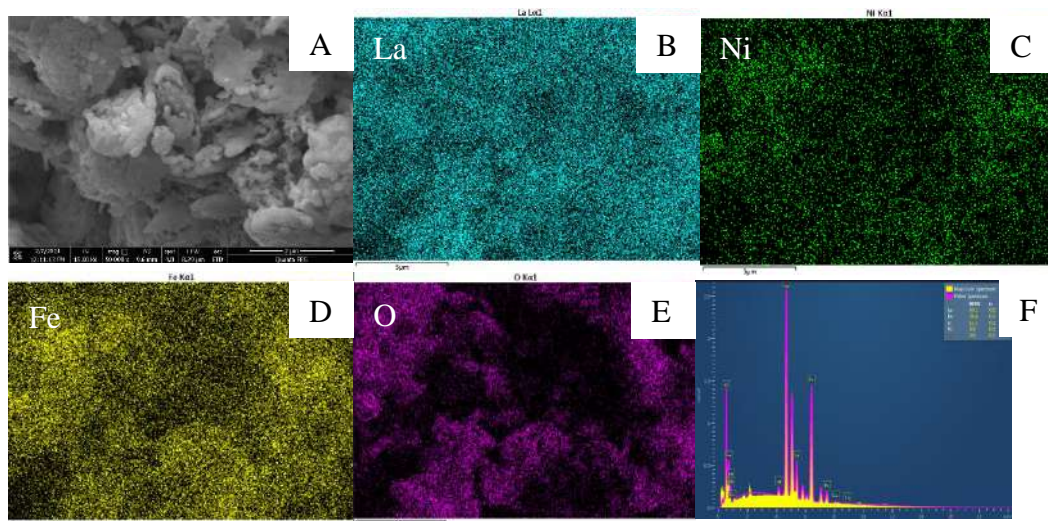


Fig 4. FESEM image (A) and EDS mapping mapping (B-F) of  $\text{LaNi}_{0.5}\text{Fe}_{0.5}\text{O}_3$ -hydrothermal

Fig 4. shows the distribution of elements in the  $\text{LaNi}_{0.5}\text{Fe}_{0.5}\text{O}_3$ -hydrothermal catalyst. Elementals consist of 60.1%lanthanum (La), 3.6%Nickel (Ni), 24.6%Iron (Fe), 11.1%Oxygen ( $\text{O}_2$ ), and 0.6% other what distributed the surface area of  $\text{LaNi}_{0.5}\text{Fe}_{0.5}\text{O}_3$ -hydrothermal catalyst.[11]

Table 1. surface area of  $\text{LaNi}_{0.5}\text{Fe}_{0.5}\text{O}_3$  catalysts.

samples	Surface Area ( $\text{m}^2/\text{g}$ )	Pore volume( $\text{cm}^3/\text{g}$ )	Pore size ( $\text{\AA}$ )
$\text{LaNi}_{0.5}\text{Fe}_{0.5}\text{O}_3$ -Sol-gel	0.2138	0.001092	204.2269
$\text{LaNi}_{0.5}\text{Fe}_{0.5}\text{O}_3$ - Hydrothermal	6.0152	0.016829	111.9107

Table 1. compared surface area of the synthesized catalysts between The  $\text{LaNi}_{0.5}\text{Fe}_{0.5}\text{O}_3$  -Sol-gel and  $\text{LaNi}_{0.5}\text{Fe}_{0.5}\text{O}_3$  -Hydrothermal. The  $\text{LaNi}_{0.5}\text{Fe}_{0.5}\text{O}_3$  -Sol-gel has a surface area, Pore volume less than The  $\text{LaNi}_{0.5}\text{Fe}_{0.5}\text{O}_3$  -Hydrothermal.[10] The decrease in the catalysts' surface area is a consequence of oxygen replacing the large surface area of the catalysts due to their high oxygen content.

The synthesized catalysts were preliminarily tested in methane dry reforming. However, the reaction does not take place since the prepared catalyst cannot be reduced to the form of Ni-Fe metal. The reduced catalysts were analyzed by XRD to investigate crystalline phases.

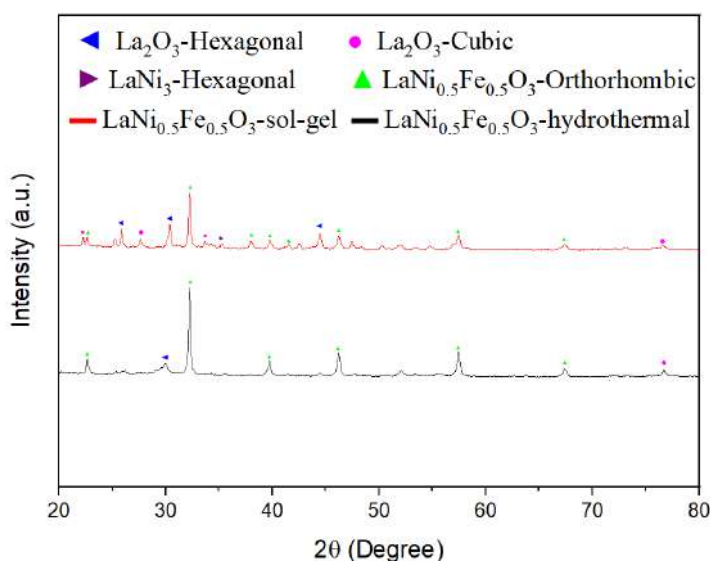


Fig 5 X-ray diffractometer (XRD) of  $\text{LaNi}_{0.5}\text{Fe}_{0.5}\text{O}_3$  the sol-gel method and hydrothermal method after reduction in the atmosphere of  $\text{H}_2/\text{N}_2 = 1:1$ ,  $T = 700^\circ\text{C}$  for 1 hour.

Fig 5. shows X-ray diffractometer (XRD) of  $\text{LaNi}_{0.5}\text{Fe}_{0.5}\text{O}_3$  is between the sol-gel method and hydrothermal method after reduction in the atmosphere. The  $\text{LaNi}_{0.5}\text{Fe}_{0.5}\text{O}_3$  catalyst was synthesized by the sol-gel method, exhibiting an orthorhombic phase with  $2\theta$  angles at  $22.8^\circ$ ,  $32.48^\circ$ ,  $39.9^\circ$ ,  $40.1^\circ$ ,  $43.4^\circ$ ,  $46.6^\circ$ ,  $58^\circ$ , and  $68^\circ$ . However,  $\text{LaNi}_3$  and  $\text{La}_2\text{O}_3$  are also observed among the impurities present in this sample at  $2\theta$  angles at  $22.3^\circ$ ,  $26.2^\circ$ ,  $27.4^\circ$ ,  $29.2^\circ$ ,  $33.7^\circ$ ,  $35.2^\circ$ ,  $46.3^\circ$ , and  $78.8^\circ$ . The  $\text{LaNi}_{0.5}\text{Fe}_{0.5}\text{O}_3$  catalyst was synthesized by the hydrothermal method, exhibiting an orthorhombic phase with  $2\theta$  angles at  $22.8^\circ$ ,  $32.48^\circ$ ,  $40.1^\circ$ ,  $46.6^\circ$ ,  $58^\circ$ , and  $68^\circ$ . In addition,  $\text{La}_2\text{O}_3$  is also observed among the impurities present in this sample at  $2\theta$  angles at  $29.2^\circ$ , and  $78.8^\circ$ . According to studies by Yongjin Luo et al. and Yuta Morishima et al., the rhombohedral phase was observed after the reduction.[10, 14]

## Conclusion

$\text{LaNi}_{0.5}\text{Fe}_{0.5}\text{O}_3$ -hydrothermal can perform activities for dry reforming of methane more than  $\text{LaNi}_{0.5}\text{Fe}_{0.5}\text{O}_3$ -Sol-gel due  $\text{LaNi}_{0.5}\text{Fe}_{0.5}\text{O}_3$ -Hydrothermal having a larger surface area and porous volume than  $\text{LaNi}_{0.5}\text{Fe}_{0.5}\text{O}_3$ -sol-gel. The decrease in the catalysts' surface area is a consequence of oxygen replacing the large surface area of the catalysts due to their high oxygen content. The synthesized catalysts were preliminarily tested in methane dry reforming. However, the reaction does not take place since the prepared catalyst cannot be reduced to the form of Ni-Fe metal. The reduced catalysts were analyzed by XRD to investigate crystalline phases

## Reference

1. Koozegar Kaleji, B. and M. Gorgani, *Comparison of sol-gel and hydrothermal synthesis methods on the structural, optical and photocatalytic properties of Nb/Ag codoped TiO<sub>2</sub> mesoporous nanoparticles*. International Journal of Environmental Analytical Chemistry, 2020. **102**(14): p. 3357-3372.
2. Cano-Casanova, L., et al., *Effect of the Preparation Method (Sol-Gel or Hydrothermal) and Conditions on the TiO<sub>2</sub> Properties and Activity for Propene Oxidation*. Materials (Basel), 2018. **11**(11).
3. Bhattar, S., et al., *A review on dry reforming of methane over perovskite derived catalysts*. Catalysis Today, 2021. **365**: p. 2-23.
4. Usman, M., W.M.A. Wan Daud, and H.F. Abbas, *Dry reforming of methane: Influence of process parameters—A review*. Renewable and Sustainable Energy Reviews, 2015. **45**: p. 710-744.
5. Zhao, X., et al., *Biogas Reforming to Syngas: A Review*. iScience, 2020. **23**(5): p. 101082.
6. Aramouni, N.A.K., et al., *Catalyst design for dry reforming of methane: Analysis review*. Renewable and Sustainable Energy Reviews, 2018. **82**: p. 2570-2585.
7. Cheng, K., et al., *Advances in Catalysis for Syngas Conversion to Hydrocarbons*. 2017. p. 125-208.
8. Martín, M.M., *Syngas*, in *Industrial Chemical Process Analysis and Design*. 2016. p. 199-297.
9. Salaev, M.A., L.F. Liotta, and O.V. Vodyankina, *Lanthanoid-containing Ni-based catalysts for dry reforming of methane: A review*. International Journal of Hydrogen Energy, 2022. **47**(7): p. 4489-4535.
10. Luo, Y., et al., *Studies on B sites in Fe-doped LaNiO<sub>3</sub> perovskite for SCR of NO<sub>x</sub> with H<sub>2</sub>*. International Journal of Hydrogen Energy, 2014. **39**(28): p. 15836-15843.
11. Chang, H.H., et al., *Application of scanning electron microscopy and X-ray microanalysis: FE-SEM, ESEM-EDS, and EDS mapping for studying the characteristics of topographical microstructure and elemental mapping of human cardiac calcified deposition*. Anal Bioanal Chem, 2014. **406**(1): p. 359-66.
12. Zeng, L., et al., *Fe-doped LaNi<sub>1-x</sub>Fe<sub>x</sub>O<sub>3</sub> perovskite oxides for enhanced visible-light-driven photocatalytic activity*. Journal of Solid State Chemistry, 2021. **297**.
13. Zhang, L., et al., *LaNiO<sub>3</sub> nanocube embedded in mesoporous silica for dry reforming of methane with enhanced coking resistance*. Microporous and Mesoporous Materials, 2018. **266**: p. 189-197.
14. Morishima, Y., E. Niwa, and T. Hashimoto, *Analysis of thermal stability of LaNi<sub>1-x</sub>Fe<sub>x</sub>O<sub>3-δ</sub> (x = 0.0, 0.2, 0.4) by thermogravimetry and high-temperature X-ray diffraction under controlled oxygen partial pressures*. Journal of Thermal Analysis and Calorimetry, 2015. **123**(3): p. 1769-1775.

**Evaluation of HEK293.2sus Growth in 5 Commercial Media**  
**Napasorn Ritnetikul<sup>1</sup>, Nuttamon Intharatanod<sup>1</sup>, Asawin Meechai<sup>\*</sup>, Sarawuth**  
**Noppiboon<sup>2</sup> and Lalintip Hocharoen<sup>2\*</sup>**

<sup>1</sup>Department of Chemical Engineering, Faculty of Engineering, King Mongkut's University of Technology Thonburi, Bangmod, Bangkok, 10140, Thailand

<sup>2</sup>Bioprocess Research and Innovation Centre (BRIC), National Biopharmaceutical Facility, King Mongkut's University of Technology Thonburi, Bangkhuntein, Bangkok 10150, Thailand

\*Corresponding author. E-mail: asawin.mee@kmutt.ac.th, lalintip.hoc@mail.kmutt.ac.th

## Abstract

Human embryonic kidney 293 (HEK 293) cells are widely used as cell factories for production of recombinant therapeutic proteins because of their stable growth and high protein production on large scale. At present, various commercial culture media are available for HEK 293, yet there is no report on comparative cell growth performance among these media. In this work, we compared the growth of HEK293.2sus cells cultured in BalanCD HEK293, CDM4HEK293, CD293, FreeStyle 293, and 293 SFM II in shake flasks. First,  $3 \times 10^5$  cells/mL of HEK 293.2sus cells were seeded into 20 mL of each culture medium supplemented with 4mM L-glutamine and 0.01 %v/v anti-clumping in a 125-mL Erlenmeyer flask, and cultured at 37 °C, 5% CO<sub>2</sub>, 100 rpm for 9 days. The cultures were sampled every day over the culture period for analysis of viable cell density, specific growth rate and %viability. The results revealed that CDM4HEK293 was the best media for HEK293.2sus growth, providing the max cell density, the %viability at max cell density, and the specific growth rate around  $5.62 \times 10^6$  cells/mL, 88.73%, and 0.44 day<sup>-1</sup>, respectively.

**Keywords:** cell culture, HEK293.2sus, biopharmaceuticals

## 1. Introduction

Biopharmaceuticals, encompassing therapeutic substances derived from an array of biological sources, including organs, tissues, mammalian cells, insect cells, yeast, and bacteria, undergo intricate development through biological processes. The predominant choice for the production of most biopharmaceuticals on the market revolves around mammalian cell lines. This preference is rooted in the remarkable capacity of mammalian cells to express proteins endowed with complex post-transcriptional modifications (PTMs), a critical factor influencing the properties and stability of proteins, especially on a large scale [1]. Within the realm of mammalian cell lines, the human embryonic kidney (HEK293) cell line stands out in biopharmaceutical research. Its frequent utilization is attributed to its inherent versatility and the presence of numerous derivative cell lines renowned for their stability and ability to express proteins at high levels [2]. The prominence of HEK293 and its derivatives underscores their pivotal role as reliable platforms for the production of intricate therapeutic proteins, positioning them as invaluable assets in the quest for advanced biomedical solutions.

In the domain of biological processes, the significance of expanding the number of cells becomes evident as it directly influences the quantity of substances or products generated. A focal point in this endeavor is the exploration of cell culture media, a pivotal factor in maximizing cell growth and product formation [1]. The selection of appropriate media in cell

culture is contingent upon the specific nutritional requirements of different cell types, underscoring the highly specialized nature of this aspect. Consequently, understanding the impact of different media on the growth of cells is imperative for optimizing conditions tailored to specific cell types.

In line with this, our research endeavors sought to cultivate HEK293.2sus cells, a derivative of the well-established HEK293, in five distinct commercially available media within shake flasks. The evaluation encompassed a comprehensive analysis of cellular performance parameters, including viable cell density, specific growth rate, and the percentage of cell viability. This examination aimed to provide insights into the optimal conditions for robust growth and productivity of HEK293.2sus cells.

## 2. Materials and Methods

### Materials

The cell line under investigation in this study was HEK293.2sus (ATCC, CRL-1573.3), a commonly employed human embryonic kidney cell line. To explore the optimal conditions for its cultivation, a range of culture media and supplements were meticulously examined. The diverse media evaluated included BalanCD HEK293 (Fujifilm, Catalog No: 94137), CDM4HEK293 (Cytiva, Catalog No: SH30858.02), CD293 (Gibco, Catalog No: 11913-019), 293 SFM II (Gibco, Catalog No: 11686-029), and FreeStyle 293 (Gibco, Catalog No: 12338-018). Nutritional supplements included anti-Clumping (Gibco, Catalog No: 0010057AE) and L-glutamine (Gibco, Catalog No: 25030081). Trypan blue was employed for cell viability assessment.

### Methods

#### Seed preparation

To initiate the experimentation, a working cell bank vial of HEK293.2sus was thawed, and a cell density of  $3 \times 10^5$  cells/mL was carefully inoculated into 20 mL volumes of each culture medium. These media were supplemented with 4 mM L-glutamine and 0.01% v/v anti-clumping agent in 125 mL Erlenmeyer flasks. Cultures were maintained under controlled conditions at 100 rpm, 37°C, and 5% CO<sub>2</sub>. Sub-cultures were performed at regular intervals, every 3-4 days, over a span of three passages to ensure the establishment of stable and reproducible cell lines.

#### Shake flask cultures

HEK293.2sus cells, having undergone the aforementioned seed preparation, were further seeded into 20 mL volumes of each culture medium. Again, the media were enriched with 4 mM L-glutamine and 0.01% v/v anti-clumping agent, and the cells were cultured in 125 mL Erlenmeyer flasks. This phase of the experiment extended over a period of 9 days, and all cultures were maintained under conditions of 100 rpm, 37°C, and 5% CO<sub>2</sub>. In order to ensure the robustness and reliability of the results, duplicate experiments were conducted.



## Culture analysis

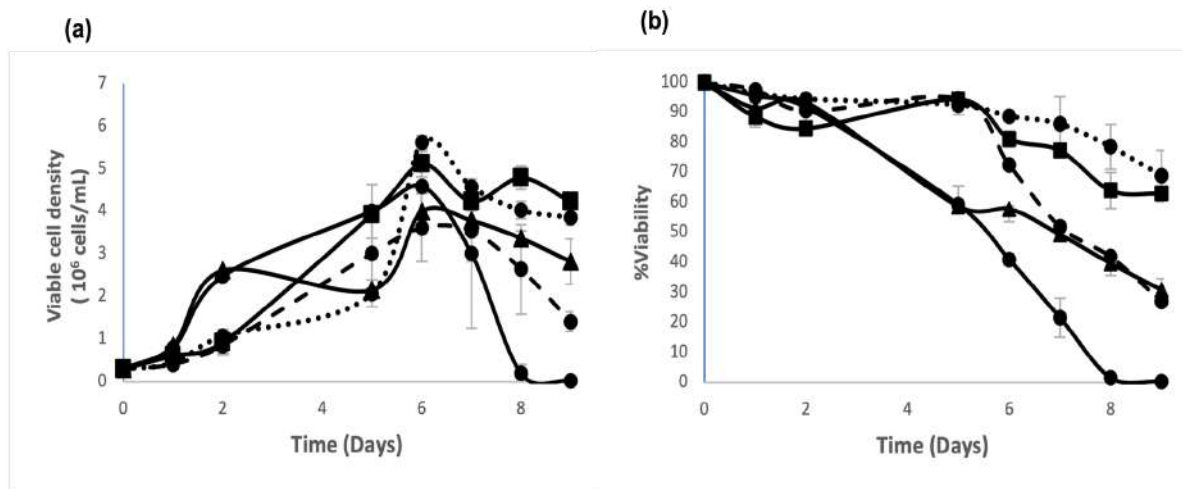
A comprehensive daily sampling regimen was implemented for the subsequent analysis of critical parameters, including cell density, specific growth rate, and percent viability. The quantification of viable and non-viable cells was achieved through the application of the trypan blue exclusion method coupled with the use of a hemocytometer. The determination of viable cell density, percentage viability, and the specific growth rate during the exponential phase was then conducted. This analysis aimed to provide a thorough understanding of the dynamic interplay between HEK293.2sus cells and the diverse culture media and supplements under scrutiny. The experimental design was structured to yield detailed insights into the complexity of cell behavior, thereby contributing valuable knowledge to the optimization of cell culture processes.

## 3. Results and Discussion

In this investigation, the HEK293.2sus cell line underwent cultivation in five distinct media within shake flasks, with a rigorous sampling protocol spanning 9 days (excluding the weekend, days 3-4) to monitor cell density and percentage viability (refer to Figure 1). Furthermore, critical parameters such as maximum cell density, percentage viability at the maximum cell density, and specific growth rates were evaluated and compared across the diverse culture media (see Table 1).

The findings from this extensive analysis revealed distinct performance variations based on the choice of culture medium. Notably, CDM4HEX293 and CD293 emerged as superior choices, yielding cultures characterized by both high cell density and robust viability. In contrast, cultures cultivated in BalanCD and FreeStyle 293 exhibited less favorable outcomes, marked by lower cell density and diminished viability. This divergence underscores the profound impact that the selection of culture medium has on the overall growth and health of HEK293.2sus cells.

A closer examination of specific growth rates emphasized the differences between these media formulations. Cells cultured in CDM4HEX293 and CD293 demonstrated significantly higher specific growth rates compared to those in BalanCD and FreeStyle 293. This observation suggests not only that these media support higher cell densities but also promote a more efficient and rapid proliferation of the HEK293.2sus cells. The heightened specific growth rates in CDM4HEX293 and CD293 emphasize their potential as optimal choices for supporting the robust expansion of this cell line. SFMII appears to be a suitable culture medium for HEK293 in terms of both cell viability and growth rate as well. However, when compared to CDM4HEK293, it falls short. Thus, we are particularly interested in CDM4HEK293 for our future study on a larger scale.



**Figure 1** The time courses of viable cell density (a) and % viability (b) of HEK293.2sus in 5 commercial media.

●— BalanCD    ●····· CDM4    ■— CD293    ▲— FreeStyle    ●- - SFM II

**Table 1** Comparison of max viable cell density, %viability at max viable cell density and specific growth rate of 5 commercial media

Media	Maximum Viable Cell Density (10 <sup>6</sup> cells/mL)	%Viability at Max Viable Cell Density	Specific Growth Rate (day <sup>-1</sup> )
BalanCD	4.59 ± 0.057	40.91 ± 1.888	0.30 ± 0.028
CDM4HEK293	5.62 ± 0.163	88.73 ± 1.520	0.44 ± 0.064
CD293	5.12 ± 0.304	81.12 ± 2.737	0.44 ± 0.014
FreeStyle 293	4.00 ± 0.424	57.82 ± 0.962	0.21 ± 0.014
293 SFM II	3.62 ± 0.424	72.47 ± 3.903	0.41 ± 0.021

Furthermore, it became evident that CDM4HEK293 exhibited the highest growth performance in HEK293.2sus cell cultures within shake flasks, surpassing the outcomes achieved with other commercially available culture media. The precise explanation for why one medium outperforms another cannot be provided explicitly due to a lack of sufficient information regarding the nutritional composition of each medium. However, we believe that the superior performance of CDM4HEK293 could be attributed to the notably higher glucose content present in this medium. A previous report supporting this notion indicated that CDM4HEK293 contains 1.5 times more glucose than CD 293 [3]. Although this speculation requires validation through future experiments incorporating additional glucose measurements, the current study strongly suggests that CDM4HEK293 stands out as the most suitable medium for fostering the growth of HEK293.2sus cells. Additionally, other nutrients such as amino

acids, vitamins and minerals present within these media also play a vital role in cell growth and viability. Regrettably, we couldn't address this aspect due to the absence of nutritional information regarding the media under study.

The prospect of scaling up these findings to larger bioreactors is highly promising. The demonstrated efficacy of CDM4HEK293 in shake flasks positions it as a compelling candidate for further investigation at an expanded scale. Future studies could delve into optimizing conditions for large-scale bioprocessing, taking into account the specific attributes of CDM4HEK293 that contribute to its superior performance in supporting HEK293.2sus cell cultures. Overall, this study lays a robust foundation for future endeavors aimed at refining cell culture strategies and advancing bioprocess optimization for enhanced efficiency and productivity.

#### 4. Conclusion

In conclusion, the utilization of CDM4HEK293 as a growth medium has demonstrated its exceptional suitability for fostering the expansion of HEK293.2sus cell cultures within shake flasks. This medium has exhibited remarkable performance metrics, including achieving the highest maximum viable cell density recorded at  $5.62 \times 10^6$  cells/mL. Notably, the viability of cells reached its pinnacle at the maximum viable cell density, registering an impressive 88.73%. Furthermore, the specific growth rate observed under these conditions was notably high, standing at  $0.44 \text{ day}^{-1}$ . These compelling outcomes underscore the efficacy of CDM4HEK293 in facilitating robust cell growth, making it a promising choice for optimizing bioprocesses involving HEK293.2sus cell lines. The superior performance metrics observed with this medium substantiate its potential as a key component in enhancing the efficiency and productivity of cell culture processes within the context of shake flask applications.

#### References

- [1] O'Flaherty, R., Bergin, A., Flampouri, E., Mota, L. M., Obaidi, I., Quigley, A., . . . Butler, M. (2020). Mammalian cell culture for production of recombinant proteins: A review of the critical steps in their biomanufacturing. *Biotechnology Advances*, 43, 107552. doi:<https://doi.org/10.1016/j.biotechadv.2020.107552>
- [2] Abaandou, L., Quan, D., & Shiloach, J. (2021). Affecting HEK293 Cell Growth and Production Performance by Modifying the Expression of Specific Genes. *Cells*, 10(7), 1667. Retrieved from <https://www.mdpi.com/2073-4409/10/7/1667>
- [3] Unknown Author, (2017) Evaluation of HEK 293 cell growth and adenovirus productivity in HyClone TM CDM 4 HEK 293 medium. GE Healthcare Application Note 29264715. [Online URL: <https://cdn.cytivalifesciences.com/api/public/content/digi-21159-pdf>] Assessed on December 30, 2022.

## Comparative Study of Lignin Isolated from Bagasse Using Different Solid-to-Liquid Ratios of Dilute Sulfuric Acid Pretreatment

Pakkawadee Sarapaiwanich<sup>1</sup>, Malinee Sriariyanun<sup>2</sup>, Santi Cheutor<sup>1</sup>, and Suchata Kirdponpattara<sup>1,\*</sup>

<sup>1</sup> Department of Chemical Engineering, Faculty of Engineering, King Mongkut's University of Technology North Bangkok, Bangkok, Thailand

<sup>2</sup> Department of Chemical and Process Engineering, The Sirindhorn International Thai-German Graduate School of Engineering (TGGSE), King Mongkut's University of Technology North Bangkok, Bangkok, Thailand  
E-mail: \*suchata.k@eng.kmutnb.ac.th

### Abstract

Sugarcane bagasse is a valuable by-product of the sugar production industry, as it contains a significant amount of lignin, which has a range of beneficial properties, including UV protection, antioxidant ability, and antimicrobial activity. However, the method and conditions used to extract lignin can significantly impact its properties. This research aims to investigate lignin extraction from sugarcane bagasse using a dilute sulfuric acid (DSA) pretreatment. The effect of solid-to-liquid ratios (1:2.5, 1:5, and 1:10) on extracted lignin characteristics was investigated. The bagasse pretreated with a solid-to-liquid ratio of 1:10 (DSA10) gave the highest yield of acid-soluble lignin (ASL). However, DSA2.5 and DSA5 presented the highest value of antioxidant activity and total phenolic compound, respectively. The extracted lignin might contain a high content of impurities.

**Keywords:** Acid-soluble lignin; Dilute sulfuric acid; Pretreatment; Sugarcane bagasse

### 1. Introduction

Sugarcane bagasse, a by-product of sugarcane processing in the sugar production industries, is generated in large quantities annually. Typically, it is exterminated by burning because it takes a short period and is easy to handle, leading to environmental pollution. The bagasse comprises cellulose (32-43%), hemicellulose (19-24%), lignin (25-32%), and others (6%-18%) [1]. Global lignin production is projected to rise to 225 million tons per year by 2030 as a by-product of biofuel production, thereby attracting increased attention to lignin as a sustainable resource [2].

Lignin is a biodegradable polymer in plant cells. Large quantities of lignin are produced not only in sugar production but also in the pulp and paper process and the biorefinery industry [3]. There are three monomers, including 1) p-coumaryl alcohol, found in plants in the grass family; 2) coniferyl alcohol, found in narrow-leafed plants (softwood) and broad-leaved plants (Hardwood); and 3) sinapyl alcohols are found primarily on broad-leaved plants consisting of aliphatic hydroxy groups, phenolic groups, methoxy groups, and aromatic ring. Lignin has been reported to present antimicrobial and antioxidant activities [4]. Additionally, lignin is non-toxicity [5]. Lignin composition and characteristics are influenced mainly by the species and extraction method. Lignin has been widely utilized in many fields, such as fuel in combustion or electricity generation, resin adhesives, soil improvers, and rubber reinforcers [3]. Recently, lignin has been used as an antimicrobial coating material in healthcare and agriculture [6].

Lignin is divided into acid-soluble lignin (ASL) and acid-insoluble lignin (AIL). ASL can dissolve into many solvents, which can be applied in versatile fields.

Several techniques have been used to extract lignin from biomass, each of which has its advantages and disadvantages, such as acid pretreatment using the shortest time with high temperature, alkaline pretreatment having high efficiency of lignin exaction with long reaction time, organosolv being able to remove both lignin and hemicellulose with costly solvent, and steam explosion being a cost-effective process with inhibitor generation [7]. However, acid pretreatment is still challenging in operational conditions: dilute acid with high temperatures, concentrate acid with low temperatures, and solid-to-liquid ratio. Srirakul et al. (2017) [8] studied the lignin extraction from bagasse using 4 vol% sulfuric acid at 121°C for 30 minutes, achieving lignin removal of 39.8%. For dilute acid pretreatment, 43.8% of extracted lignin was obtained using 1 vol% sulfuric acid at 170°C for 5 minutes [9].

Different techniques and operational conditions influence the characteristics of extracted lignin. Tons of literature paid attention only to the percent removal of the extracted lignin, as the desired products typically were cellulose and hemicellulose. A few studies have focused on the extracted lignin as a product and examined its properties such as antioxidant characteristics, antimicrobial activity, etc.

This research aims to study the properties of ASL extracted from bagasse using 1 vol% dilute sulfuric acid pretreatment with different solid-to-liquid ratios (1:2.5, 1:5, and 1:10). The characteristics of extracted lignin were analyzed by a Fourier Transform Infrared Spectrometer (FTIR). Total phenolic compound and antioxidant activity were also examined.

## 2. Materials and Methods

### 2.1. Materials

Sugarcane bagasse was purchased from Nonthaburi, Thailand. Chemicals used in the study, such as methanol (99.8%), gallic acid, 2,2-diphenyl-1-picrylhydrazyl (DPPH), and Folin-Ciocalteu reagent were purchased from Merck (Germany). Sulfuric acid (95-98%) and calcium hydroxide were purchased from J.T. Baker (US) and Qrec (Newzealand), respectively.

### 2.2. Dilute sulfuric acid (DSA) pretreatment

A 30 g bagasse having a particle size of 250  $\mu\text{m}$  was pretreated with 1% sulfuric acid solution in the solid-to-liquid ratios of 1:2.5, 1:5, and 1:10 at 121°C for 30 minutes. The samples were named as shown in Table 1. After the pretreatment, the mixture was filtrated to separate the pretreated solid from the liquid. Calcium hydroxide was added into the liquid to adjust pH to 6 to precipitate acid-soluble lignin. Then, the precipitate was obtained by centrifugation at 5,000 rpm for 30 minutes. Finally, the obtained solid was dried in an oven at 60°C for 12 hours and kept in a desiccator.

### 2.3. Characterization of lignin

#### 2.3.1. Fourier Transform Infrared Spectrometer (FTIR) technique

The FTIR spectra of the extracted lignin were examined against standard lignin in wave numbers from 4,000 to 400  $\text{cm}^{-1}$  using the FTIR spectrometer INVENIO (Bruker, Germany). Alkaline lignin supplied by Sigma-Aldrich (US) was used as a standard.

### 2.3.2. Total phenolic compound (TPC)

A 0.2 mL lignin extracted (3 mg/mL) was mixed with 0.8 mL of Folin-Ciocalteu reagent (0.2 N) and incubated in darkness at room temperature for 20 minutes. After that, 1 mL of sodium carbonate 8.5% w/v was added to the mixture and incubated at room temperature in darkness for 90 minutes. Then, the mixture was centrifuged at 5,000 rpm for 20 minutes. The supernatant was measured absorbance with a UV-visible spectrophotometer (Mapada V-1100D, China) at 765 nm using gallic acid as a standard.

### 2.3.3. Antioxidant activity (DPPH)

A 0.5 mL lignin extracted (1 mg/mL) was mixed with 2.5 ml of DPPH (90  $\mu$ mol/L) and incubated at room temperature in darkness for 30 minutes. After that, the mixture was measured with the UV-visible spectrophotometer at 517 nm using gallic acid as a standard. Results are reported in units of Scavenging activity (%) calculated by Eq. 1.

$$\text{Scavenging activity (\%)} = \frac{(OD_S - OD_L)}{OD_S} \times 100 \quad (1)$$

Where  $OD_S$  and  $OD_L$  are the absorbances of the standard and lignin samples, respectively.

Table 1. Solid-to-liquid ratios in dilute sulfuric acid pretreatment.

Sample name	Solid (g) to liquid (mL) ratio
DSA2.5	1:2.5
DSA5	1:5
DSA10	1:10

## 3. Results and Discussion

### 3.1. Lignin content

Lignin was extracted from bagasse through diluted sulfuric acid pretreatment using different solid-to-liquid ratios (DSA2.5, DSA5, DSA10). According to [10], Betancur et al. (2009) optimized the acid pretreatment conditions for sugarcane bagasse. They found that using a solid-to-liquid ratio of 1:2.8 resulted in high xylose concentration hydrolysate production. The hypothesis of this study is the lignin extracted by different solid-to-liquid ratios impacting its yields and characteristics. Hence, the solid-to-liquid ratios of 1:2.5, 1:5, and 1:10 were used to extract lignin from sugarcane bagasse.

The yields of extracted lignin are summarized in Table 2. The extracted lignin could be specified as acid-soluble lignin (ASL), which could be further applied in many fields due to its solubility. Canilha et al. (2011) [11] reported that sugarcane bagasse contained acid-soluble lignin of 5.2% biomass. This value was used as a reference value for calculating the yield of extracted lignin (% ASL in biomass). The result demonstrated that an increase in solid-to-liquid ratios increased the amount of extracted lignin. The highest lignin yield was obtained from DSA10. A small volume of dilute acid could not wet all the bagasse particles, resulting in a small area of contact between solid and liquid contact (Fig. 1). This might be a reason that limited the lignin extraction from the bagasse.

However, the increment of the solid-to-liquid ratio up to 10 sharply increased the lignin yield almost 4 times compared with that of 1:5 (DSA5). Surprisingly, the yield calculated based on ASL in the lignin of DSA10 was higher than the ASL existing in the bagasse, implying high impurities in the extracted lignin. It could be explained that the bagasse was soaking wet by the acid solution; therefore, the acid contacted and directly reacted with the fiber, resulting in the decomposition and the generation of the impurities.

Table 2. Lignin content.

Sample name	Yield of extracted lignin (% biomass)	Yield of extracted lignin (% ASL in biomass)
DSA2.5	2.00 ± 0.01	38.46 ± 1.92
DSA5	2.90 ± 0.01	55.77 ± 1.92
DSA10	11.70 ± 0.24	224.36 ± 45.56



Fig. 1 Image of bagasse after adding 1% sulfuric acid solution

Table 3. FTIR peaks of lignin (standard).

Wave number (cm <sup>-1</sup> )	Functional groups
3378	O-H (Aliphatic and phenolic hydroxyls) [12]
2918	C-H (Methoxyl group) [13]
1640	C=O (Carbonyl group) [13]
1582,1499,1411	Aromatic structure in lignin [14]
1431	C-H (Deformation in lignin) [12]
1255	C=O (Stretching of syringyl unit) [15]
1201	C=O (Stretching of guaiacyl unit) [15]
1113	C-O (Stretching in ester groups (HGS)) [15]
1063	Aromatic C-H (Deformation in syringyl) [15]
1020	Aromatic C-H (Deformation for guaiacyl) [15]
850	Aromatic C-H (Deformation in HGS) [15]

### 3.2. Fourier Transform Infrared Spectrometer (FT-IR) technique

The chemical structure of the extracted lignin was examined and compared with alkaline lignin (used as a standard). The alkaline lignin spectra presented all the significant peaks, as gathered in Table 3. Spectra of DSA2.5 and DSA5 showed 1640, 1431, and 850  $\text{cm}^{-1}$ , indicating carbonyl, C-H (Deformation in lignin), and C-H (Deformation in HGS), respectively. For the guaiacyl deformation at 1020  $\text{cm}^{-1}$ , a bit shift was observed in DSA2.5 and DSA5. A significant move from 1020 to 1101  $\text{cm}^{-1}$  was noticed in DSA10. The aromatic peaks (1499  $\text{cm}^{-1}$ ) and guaiacyl (1201  $\text{cm}^{-1}$ ) were absent in all the extracted lignin. The spectra of DSA10 demonstrated the chemical structure without aliphatic, phenolic hydroxyls, methoxyl, aromatic, syringyl, and guaiacyl structures. Consequently, the solid-to-liquid ratio of 1:10 might be a harsh condition for extracting lignin from the bagasse, leading to lignin structure decomposition and deformation. Also, impurities might be generated.

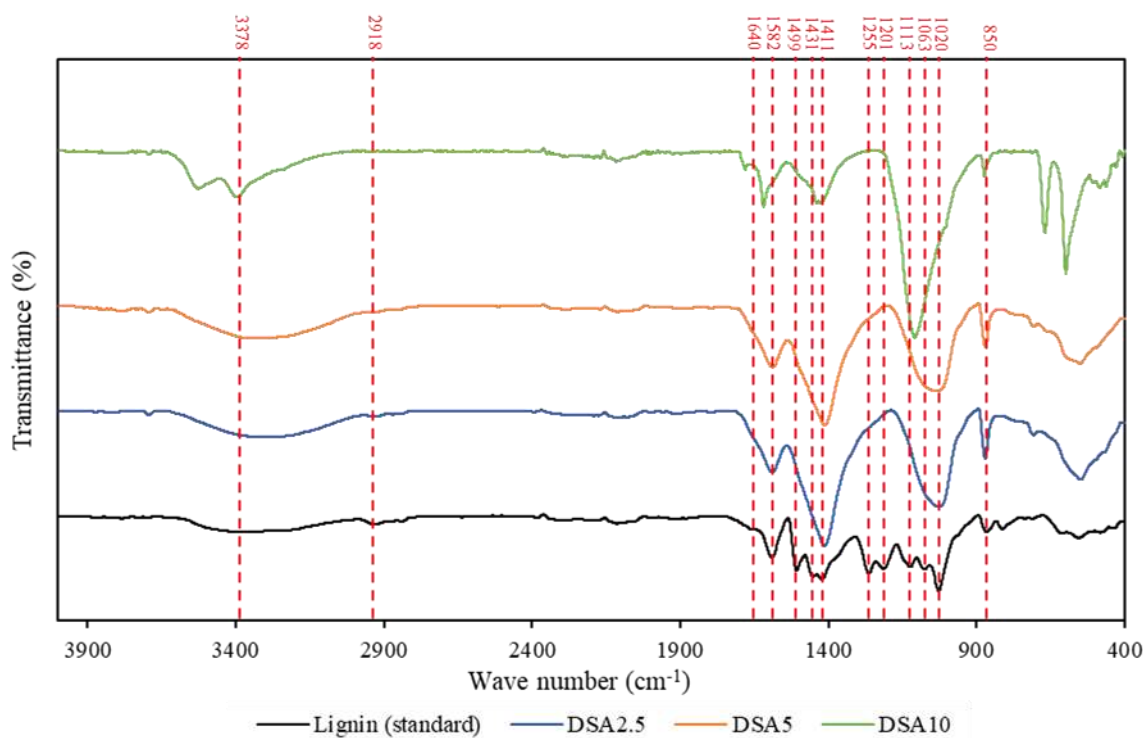


Fig. 2 FTIR spectra of the extracted lignin

### 3.3. Total phenolic compound (TPC)

The TPC values of the extracted lignin are gathered in Table 4. Based on the lignin structure, the phenolic compound is the main compound contained in the structure, indicating antioxidant activity [16, 17]. The phenolic OH groups in the lignin structure directly impact antioxidant activity [17]. The TPC values of the sample were arranged in the following order: DSA5 > DSA2.5 > DSA10. The optimal solid-to-liquid ratio was 1:5 to obtain the highest value of TPC. Increasing the ratio to 1:10 dramatically decreased the TPC value by approximately 60%. As mentioned before, the lignin structure could be destroyed by an excess volume of the acid solution, leading to the generation of impurities and a low TPC value. As seen in the FTIR result, the pattern of the peak at 3378  $\text{cm}^{-1}$  representing phenolic OH of DSA10 differed from the standard. Compared with the literature, Aadil et al. (2014) [18] reported that the TPC of alkaline lignin extracted from Acacia wood was  $73.01 \pm 3.2 \mu\text{g}$  of GAE per mg. Moreover,



Ramakoti [19], reported that the TPC of organosolv lignin extracted from *Bambusa bambos* wood was  $94.30 \pm 1.4$   $\mu\text{g}$  of GAE per mg. In comparison to the previous reports, lignin extracted by dilute acid in this present work showed the lowest TPC value. As mentioned above, the acid might damage the lignin structure, resulting in fewer phenolic OH groups.

### 3.4. Antioxidant activity (DPPH)

According to the literature [20], lignin was proposed as a promising natural antioxidant for many applications. The antioxidant activity of the extracted lignin was analyzed (Table 4). DSA2.5 gave the highest antioxidant value, lower than lignin extracted from bamboo [18]. The bamboo was pretreated by organosolv, having an antioxidant activity of  $38.10 \pm 1.6\%$ . In contrast, black liquor alkaline lignin had an antioxidant activity of 7.3%. Magalhaes et al. (2008) [22] claimed that the source of biomass, purity, molecular weight, and extraction technique could affect the antioxidant activity of the extracted lignin.

Table 4. Total phenolic compound (TPC) and Antioxidant activity (DPPH).

Sample name	TPC ( $\mu\text{g}$ GAE/ mg)	DPPH (%Scavenging activity)
DSA2.5	$26.99 \pm 0.46$	$3.87 \pm 0.24$
DSA5	$43.10 \pm 0.30$	$2.62 \pm 0.09$
DSA10	$17.21 \pm 0.26$	$0.52 \pm 0.40$

## 4. Conclusions

The study extracted ASL from sugarcane bagasse by pretreatment with DSA. The solid-to-liquid ratio affected the amount and properties of the extracted lignin. The lignin structure was decomposed by an excess of DSA volume and generated impurities. The FTIR spectra confirmed that the extracted ASL contained a high content of impurities. DSA5 had the highest TPC value, and a higher yield of extracted lignin compared to DSA2.5. Therefore, 1:5 was the suitable solid-to-liquid ratio to extract ASL from sugarcane bagasse. ASL could be further purified to improve its characteristics for utilization in many applications.

## Acknowledgments

This research is supported by facilities from the Faculty of Engineering, King Mongkut's University of Technology North Bangkok.

## References

- [1] Sakdaronnarong, C., and Jonglertjunya, W. (2012). Rice straw and sugarcane bagasse degradation mimicking lignocellulose decay in nature: An alternative approach to biorefinery. *ScienceAsia*, 38, 364-372.
- [2] Chen, M., Li, Y., Liu, H., Zhang, D., Shi, Q, S., Zhong, X, Q., Guo, Y., and Xie, X, B. (2023). High value valorization of lignin as environmental benign antimicrobial. *Materials Today Bio*.
- [3] Nasrullah, A., Bhat, A, H., Khan, A, S., and Ajab, H. (2017). Comprehensive approach on the structure, production, processing, and application of lignin. *Lignocellulosic Fibre and Biomass-Based Composite Materials*, pp. 165-178.

- [4] Wang, L., Ji, X., Cheng, Y., Tao, Y., LU, J., Du, J., and Wang, H. (2022). All-biodegradable soy protein isolate/lignin composite cross-linked by oxidized sucrose as agricultural mulch films for green farming. *International Journal of Biological Macromolecules*, 223, 120-128.
- [5] Chelliah, R., Wei, S., Vijayalakshmi, S., Barathikannan, K., Sultan, G., Liu, S., and Oh, D, H. (2023). A Comprehensive Mini-Review on Lignin-Based Nanomaterials for Food Applications: Systemic Advancement and Future Trends. *Molecules*, 28, 1-18.
- [6] Zhou, Y., Han, Y., Li, G., Yang, S., Xiong, F., and Chu, F. (2018). Preparation of Targeted Lignin-Based Hollow Nanoparticles for the Delivery of Doxorubicin. *Nanomaterials*, 9, 1-13.
- [7] Nanda, S., Mohammad, J., Reddy, S, N., Kozinski, J, A., and Dalai, A, K. (2013). Pathways of lignocellulosic biomass conversion to renewable fuels. *Biomass Conv Bioref*.
- [8] Sritrakul, N., Nitisinprasert, S., and Keawsompong, S. (2018). Evaluation of dilute acid pretreatment for bioethanol fermentation from sugarcane bagasse pith. *Agriculture and Natural Resources*, 51, 512-519.
- [9] Miyamoto, T., Mihashi, A., Yamamura, M., Tobimatsu, M., Suzuko, S., Takada, R., Kobayashi, T., and Umezawa, T. (2018). Comparative analysis of lignin chemical structures of sugarcane bagasse pretreated by alkaline, hydrothermal, and dilute sulfuric acid methods. *Industrial Crops & Products*, 121, 124-131.
- [10] Betancur, G, J., and Jr, N, P. (2009). Sugar cane bagasse as feedstock for second generation ethanol production. Part I: Diluted acid pretreatment optimization. *Electronic Journal of Biotechnology*, 13, 1-9.
- [11] Canilha, L., Santos, V, T., Rocha, G, J., Silva, J, A., Giulietti, M., Silva, S, S., Felipe, M, A., and Carvalho, W. (2011). A study on the pretreatment of a sugarcane bagasse sample with dilute sulfuric acid, *Journal of Industrial Microbiology and Biotechnology*, 38, 1467-1475.
- [12] Xiao, T., Yuan, H., Ma, Q., Guo, W., and Wi, Y. (2019). An approach for in situ qualitative and quantitative analysis of moisture adsorption in nanogram-scaled lignin by using micro-FTIR spectroscopy and partial least squares regression, *International Journal of Biological Macromolecules*, 132, 1106-1111.
- [13] Cao, J., Xiao, G., Xu, X., Shen, D., and Jin, B. (2013). Study on carbonization of lignin by TG-FTIR and high-temperature carbonization reactor, *Fuel Processing Technology*, 103, 41-47.
- [14] Olgun, C., and Ates, S. (2023). Characterization and Comparison of Some Kraft Lignins Isolated from Different Sources, *Forests*, 14, 1-15.
- [15] Cherif, M, F., Trache, D., Brosse, N., Benaliouche, F., and Tarchoun, A, F. (2020). Comparison of the Physicochemical Properties and Thermal Stability of Organosolv and Kraft Lignins from Hardwood and Softwood Biomass for Their Potential Valorization, *Waste and Biomass Valorization*, 11, 6541-6553.
- [16] Aryal, S., Baniya, M, K., Danekhu, K., Kunwar, P., Gurung, R., and Koirala, N. (2019). Total Phenolic Content, Flavonoid Content and Antioxidant Potential of Wild Vegetables from Western Nepal, *Plants*, 19, 1-12.
- [17] Chen, J., Yang, J., Ma, L., Shahzad, N., and Kim, C, K. (2020). Structure-antioxidant activity relationship of methoxy, phenolic hydroxyl, and carboxylic acid groups of phenolic acids, *Scientific Reports*, 10.

- [18] Aadil, K. R., Barapatre, A., Sahu, S., Jha, H., and Tiway, B. N. (2014). Free radical scavenging activity and reducing power of *Acacia nilotica* wood lignin, *International Journal of Biological Macromolecules*, 67, 220-227
- [19] Ramakoti, B., Dhanagopal, H., Deepa, K., Rajesh, M., Ramaswamy, S., and Tanilarasan, K. (2019). Solvent fractionation of organosolv lignin to improve lignin homogeneity: Structural characterization, *Bioresource Technology Reports*, 7
- [20] An, L., Wang, G., Jia, H., Liu, C., Sui, W. and Si, C. (2017). Fractionation of enzymatic hydrolysis lignin by sequential extraction for enhancing antioxidant performance, *International Journal of Biological Macromolecules*, 99, 674-681.
- [21] Kang, S., Li, B., Chang, J., and Fan, J. (2011). Structure-antioxidant activity relationship of methoxy, phenolic hydroxyl, and carboxylic acid groups of phenolic acids, *Bioresources*, 6, 243-252.
- [22] Magalhaes, L. M., Segundo, M. A., Reis, S., and Lima, J. (2008). Methodological aspects about in vitro evaluation of antioxidant properties, *Analytica Chimica Acta*, 613, 1-19.

## Preparation and Synthesis of Carboxymethyl Cellulose from Rice Straw

Chidchanok Sereenonchai<sup>1</sup>, Santi Chuetor<sup>1,\*</sup>, Verawat Champreda<sup>2</sup>, Suchata Kirdponpattara<sup>1</sup>, Neelu Raina<sup>1</sup>, Navadol Laosiripojana<sup>3</sup> and Suttichai Assabumrungrat<sup>4</sup>

<sup>1</sup> Department of Chemical Engineering, Faculty of Engineering, King Mongkut's University of Technology North Bangkok (KMUTNB), Bangkok 10800, Thailand

<sup>2</sup> Biorefinery and Bioproducts Research Group, National Center for Genetic Engineering and Biotechnology, Thailand Science Park, Pathumthani 12120, Thailand

<sup>3</sup> Joint Graduate School for Energy and Environment (JGSEE), King Mongkut's University of Technology Thonburi (KMUTT), Bangkok 10140, Thailand

<sup>4</sup> Center of Excellence in Catalysis and Catalytic Reaction Engineering, Department of Chemical Engineering, Faculty of Engineering, Chulalongkorn University, Bangkok 10330, Thailand

E-mail: \*santi.c@eng.kmutnb.ac.th

### Abstract

Rice straw (RS) is an abundant agricultural by-product in Thailand; often being disposed through burning thus causing PM<sub>2.5</sub> and related environmental problems. Utilization of RS (cellulose-rich biomaterial) to produce value-added products, such as carboxymethyl cellulose (CMC), serves to increase the value of agricultural wastes and manage it without harming the environment. This research aims to find optimal conditions of alkaline peroxide pretreatment of RS for producing CMC. RS was first treated with different concentrations of hydrogen peroxide including 2.5, 5, and 7.5% (v/v), the solid:liquid ratio was 1:10 and the pH was adjusted to 11.5 (using 5M NaOH). The mixture was then incubated at 45 °C for different durations including 8, 16, and 24 h. The obtained cellulose-rich samples were used to cellulose-based material for CMC synthesis. The physical and chemical characterizations were conducted including FTIR, and XRD to examine the presence of functional groups and crystallinity index respectively. Moreover, the degree of substitution, and the whiteness index were also evaluated in order to find the suitable conditions for CMC synthesis from RS. The results indicated that the suitable condition of alkaline peroxide pretreatment for CMC production was 5% (v/v) of hydrogen peroxide after 16 h with CMC having the highest DS value (0.63) and the highest whiteness index. The FTIR results indicated the substitution of carboxymethyl group in cellulose sample extracted from RS. Therefore, RS is a potential raw material for CMC synthesis.

**Keywords:** Alkaline peroxide pretreatment; carboxymethyl cellulose; cellulose derivative; rice straw

### 1. Introduction

Rice straw (RS) is a lignocellulosic biomass material that accounts for a large amount of waste generated in Thailand. RS is usually disposed of by burning in order to prepare the land for the next rice crop, typically causing air pollution and environmental impacts. RS generally composes of several biomolecules including cellulose, hemicellulose, and lignin that can be converted into value-added products. Therefore, using RS as a raw material for the production of carboxymethyl cellulose is a great way to utilize RS without affecting the environment and to add value to RS as lignocellulosic biomass substrate.

Carboxymethyl cellulose (CMC) is a cellulose derivative made by improving the properties of cellulose by replacing its original structural groups with carboxymethyl groups. CMC is a

white, odorless powder. It is often used in various industries such as the food, pharmaceutical, and textile industry by acting as a viscosity agent, stabilizer, and binder [1]. The production process of CMC is simpler than other cellulose ethers due to its synthesis being achievable under atmospheric pressure conditions and employing commercially available chemicals. This attribute contributes towards making CMC as the largest segment within the cellulose ether industry [2].

To produce the CMC from RS biomass, it needs to be pretreated in order to separate cellulose from other components. One of the most important stages for CMC synthesis is pretreatment, which is typically responsible for fractionating the biomolecules in RS and prepare the cellulose for subsequent stage. In the current study, the pretreatment method used in this research is alkaline peroxide because it is a technique that can separate cellulose under mild process conditions (low temperature and atmospheric pressure), therefore it is a method that uses low energy [3]. The experiments were conducted at different hydrogen peroxide concentrations (2.5%, 5%, and 7.5% (v/v)) and at different time periods (8, 16, and 24 h) to find the most suitable pretreatment conditions for using the separated cellulose fraction from RS to produce carboxymethyl cellulose and study the potential of RS as a preliminary biomaterial for CMC production.

## 2. Materials and Methods

### 2.1. Materials

Rice straw (RS) was obtained from a local field in Thailand. RS was ground with a grinder and passed through sieve (No.35) in order to obtain a particle size of  $<500\mu\text{m}$ . Sodium hydroxide was purchased from MERCK. Methanol, ethanol, 2-Propanol and glacial acetic acid were purchased from QReC. Hydrogen peroxide was purchased from Fisher Chemical. Sodium monochloroacetate was purchased from Alfa Aesar. All chemicals used were of analytical grade.

### 2.2. Alkaline peroxide pretreatment

RS was mixed with hydrogen peroxide using different hydrogen peroxide concentrations: 2.5, 5, and 7.5% (v/v), with a solid:liquid ratio of 1:10. Then the pH was adjusted to 11.5 using 5M NaOH. The samples were placed in an incubator without agitation at a temperature of 45 °C for different durations including 8, 16, and 24 h. After the pretreatment, the suspension was filtered to separate the solid fraction and washed with distilled water until pH 7 was attained. Then the solid fraction thus obtained was extracted cellulose (CEL). It was dried overnight at 70 °C. The samples were namely CEL-2.5-8 etc.

### 2.3. Synthesis of Carboxymethyl cellulose

The process of CMC synthesis was followed according to Biswas et al. (2014) [4]. The CMC synthesis process was divided into two main steps: alkalization and etherification. In the alkalization step, 1 g of extracted cellulose obtained from the alkaline peroxide pretreatment was mixed with 20 mL of isopropanol and 5 mL of 6M NaOH for 24 h. In the etherification step, 1.08 g of sodium monochloroacetate was added to the suspension and left undisturbed for 30 min. The samples were placed in an incubator at 50 °C for 3 h. Then the samples were filtrated to separate the solids. The solid fraction was washed with 70% ethanol, 80% methanol, and 95% ethanol respectively. The solid fraction was immersed in 70% ethanol and the pH was

adjusted to 7 using glacial acetic acid. Then the solid fraction was dried overnight at 70 °C and CMC was thus obtained.

## 2.4. Characterization of Carboxymethyl cellulose

### 2.4.1. Biochemical composition

Rice straw (RS) and extracted cellulose (CEL) were determined for their biochemical compositions by following the National Renewable Energy Laboratory (NREL) protocol (Determination of Structural Carbohydrates and Lignin in Biomass).

### 2.4.2. X-ray diffraction analysis (XRD)

The crystal structure of the extracted cellulose (CEL) and the synthesized CMC was analyzed using X-ray diffraction (Rigaku, SmartLab), and the crystallinity index (CrI) of CEL was calculated using Eq. (1) given below. Crystallinity index was calculated at  $2\theta = 22^\circ$  for the crystalline region ( $I_{002}$ ) and  $2\theta = 18^\circ$  for the amorphous region ( $I_{amorphous}$ )

$$CrI = \left[ \frac{I_{002} - I_{amorphous}}{I_{002}} \right] \times 100 \quad (1)$$

### 2.4.3. Fourier transform infrared analysis (FTIR)

The functional group of the extracted cellulose (CEL) and the synthesized CMC were analyzed using Fourier transform infrared spectrometer (Bruker, INVENIO-S) with a wavenumber of 4000-400  $\text{cm}^{-1}$ .

### 2.4.4. Whiteness index (WI)

The color of the extracted cellulose (CEL) and the synthesized CMC was measured using a ColorQuest Spectrophotometer (HunterLab) by repeating 3 times and the whiteness index was calculated using Eq. (2) where  $L^*$ ,  $a^*$ , and  $b^*$  represented lightness, redness, and yellowness respectively.

$$WI = 100 - [(100 - L^*)^2 + a^{*2} + b^{*2}]^{\frac{1}{2}} \quad (2)$$

### 2.4.5. Determination of degree of substitution (DS)

The degree of substitution (DS) is the average number of hydroxyl groups that were substituted by carboxymethyl groups. Determination of the DS value of CMC was performed according to the Standard Test Methods for Sodium Carboxymethylcellulose (D 1439-97).

## 3. Results and Discussion

### 3.1. Chemical composition of extracted cellulose

The biochemical compositions of rice straw (RS) before and after alkaline peroxide pretreatment were analyzed. Table 1. exhibited the biochemical compositions of each sample at different parameters. After pretreatment it was found that the cellulose content in extracted cellulose (CEL) increased due to break down of hydrogen peroxide into hydroxyl radical and superoxide anion radical, which can cause lignin to decompose [5]. The obtained results indicated that increasing the hydrogen peroxide concentration resulted in an increase in cellulose content because of delignification during the pretreatment. The increase in hydrogen

peroxide concentration produced more number of radicles ( $\text{OH}^\cdot$ ), which can solubilize more lignin. The obtained results showed consistency with the results reported by Tereen et al. (2020) [6]. However, increasing the pretreatment time slightly affected the cellulose content.

Table 1. Chemical composition and crystallinity index of RS and extracted cellulose.

	Cellulose content [%]	Hemicellulose content [%]	Lignin content [%]	Solid recovery [%]	Crystallinity index [%]
RS	32.39	20.22	23.44	-	56.35
CEL-2.5-8	52.09	23.08	16.58	50.2	66.45
CEL-5-8	64.18	17.94	16.31	41.5	69.84
CEL-7.5-8	65.24	15.32	11.91	40.8	69.44
CEL-2.5-16	54.15	24.04	17.19	51.0	67.49
CEL-5-16	64.07	17.03	17.17	44.2	71.07
CEL-7.5-16	68.42	14.42	18.50	37.2	70.91
CEL-2.5-24	53.34	21.93	23.43	53.1	68.45
CEL-5-24	57.94	16.33	22.51	45.9	71.59
CEL-7.5-24	68.80	14.25	15.57	38.7	70.03

### 3.2. X-ray diffraction analysis (XRD)

The results of XRD analysis showed that the crystallinity index of extracted cellulose (CEL) from alkaline peroxide pretreatment was higher than untreated RS because hydrogen peroxide under alkaline conditions reacted with the amorphous part and dissolved along with the liquid part [7]. Therefore, the extracted cellulose obtained after pretreatment had a higher crystallinity index as shown in Table 1. Increasing the concentration of hydrogen peroxide resulted in an increase in crystallinity index. However at a concentration of 7.5% (v/v) hydrogen peroxide, the crystallinity index decreased because the hydrogen peroxide reacted with the crystalline region, causing the crystalline region to degrade [8]. This resulted in the crystallinity index to decrease as compared to that at the concentration of 5% (v/v) hydrogen peroxide. Figure 1 illustrates the XRD spectra of RS, extracted cellulose and CMC.

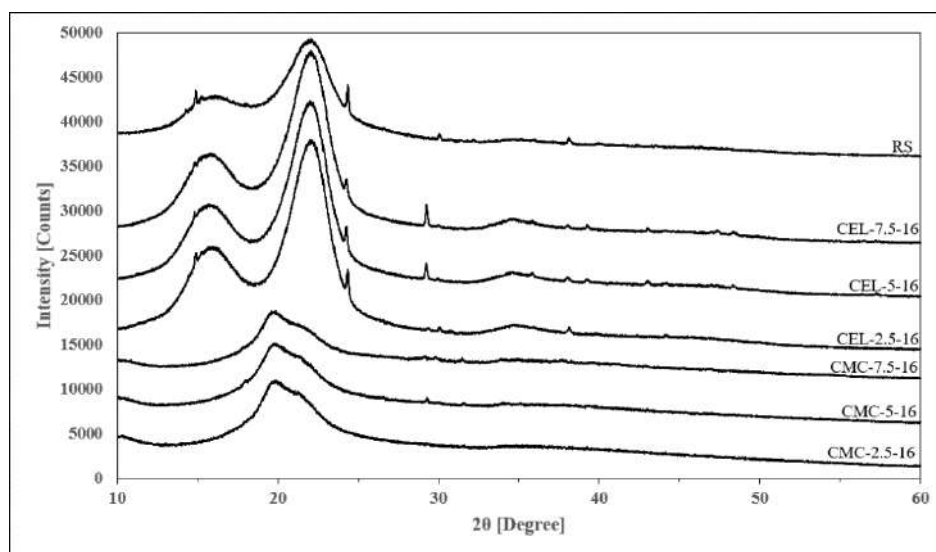


Fig. 1 X-ray diffractograms of RS, extracted cellulose, and synthesized CMC

### 3.3. Fourier transform infrared analysis (FTIR)

The FTIR results demonstrated the functional groups in the samples. The band that differentiated RS from the extracted cellulose (CEL) was located at  $1726\text{ cm}^{-1}$  and disappeared in the pretreated RS. This band can be attributed to the vibrations of carboxylic groups in lignin [6]. The band at  $3333\text{ cm}^{-1}$  corresponds to the stretching of -OH group. The bands at  $2917$  and  $1367\text{ cm}^{-1}$  correspond to stretching and deformation vibration of -CH group respectively. The band at  $895\text{ cm}^{-1}$  is characteristic of  $\beta$ -glycosidic linkage between glucose units in cellulose. The FTIR spectrum characteristic of the extracted cellulose was similar to the spectra of commercial cellulose as reported by Abderrahim et al. (2015) [9]. The results of functional group analysis using FTIR when comparing the cellulose spectrum and the CMC spectrum were markedly different. In the CMC spectrum peaks at  $1590$  and  $1413\text{ cm}^{-1}$  (Fig. 2), caused by stretching of -COO and scissoring of -CH<sub>2</sub>, respectively can be clearly observed [10]. These were peaks that indicated the presence of a carboxymethyl group, indicating that the carboxymethyl group had been substituted into the cellulose structure.

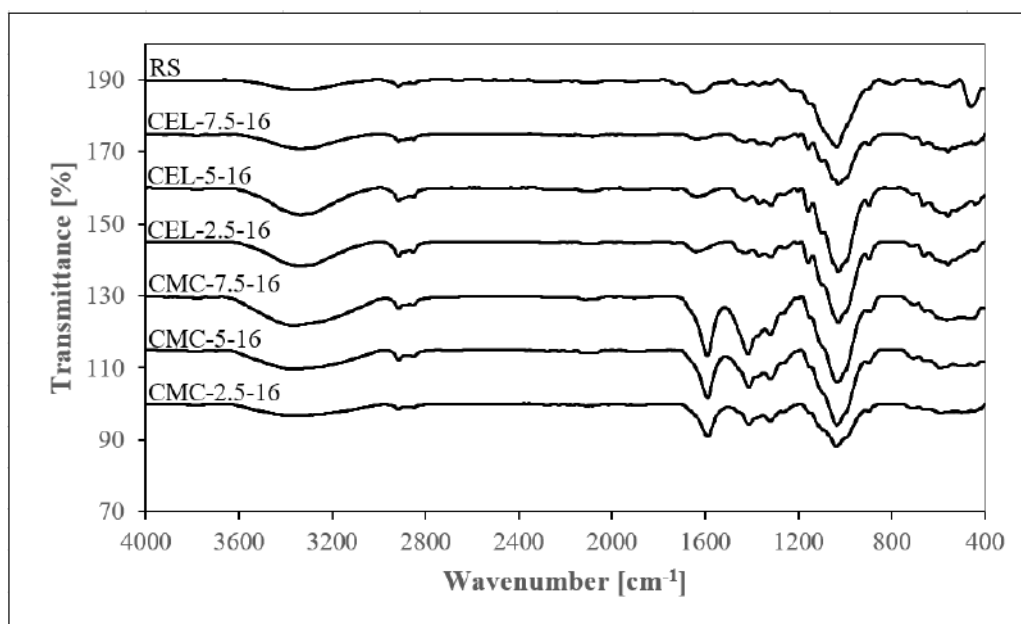


Fig. 2 FTIR spectra of RS, extracted cellulose, and synthesized CMC

### 3.4. Whiteness index (WI)

The whiteness index was evaluated for RS, extracted cellulose (CEL) and CMC samples. The pretreatment of RS with alkaline peroxide increased the whiteness index of the extracted cellulose compared to untreated RS. The experimental results indicated that increasing the concentration of hydrogen peroxide resulted in the extracted cellulose thereby increasing the whiteness index, which can be due to the removal of lignin and decolorization during the alkaline peroxide pretreatment process [11]. Increasing the time did not increase the whiteness index. The optimal condition that resulted in the highest whiteness index of extracted cellulose was hydrogen peroxide concentration of 7.5% (v/v) for 16 h duration. The synthesized CMC had a lower whiteness value compared to the extracted cellulose due to the color formation caused by carboxylation reaction in the CMC synthesis process [12].



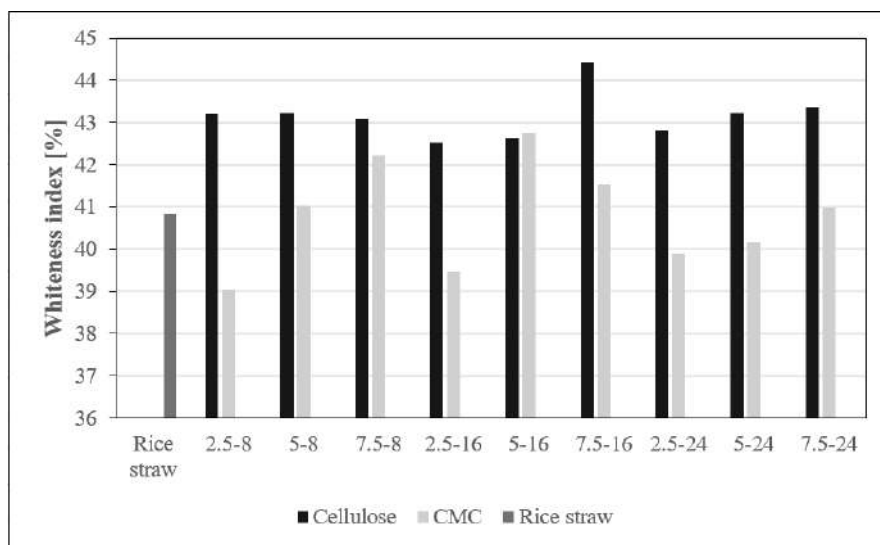


Fig. 3 Whiteness index of RS, extracted cellulose, and synthesized CMC

### 3.5. Degree of substitution (DS)

The degree of substitution was analyzed for synthesized CMC. The CMC synthesized in this study had a DS value in the range of 0.38-0.63, which was close to the normal DS value (DS 0.4-1.3) of CMC obtained by that using Sodium monochloroacetate (NaMCA) as a reagent [10]. CMC-2.5-16, CMC-5-16, and CMC-7.5-16 samples had the crystallinity index of 29.83%, 26.50%, and 32.17%, respectively, when observed at the DS values of these samples. Besides, it could be observed that the DS value increased while the crystallinity index decreased. This occurred because the reagent in the CMC synthesis process activates the non-crystalline part of cellulose [13].

Table 2. Degree of substitution (DS) of Carboxymethyl cellulose.

Sample	DS
CMC-2.5-8	0.51
CMC-5-8	0.38
CMC-7.5-8	0.46
CMC-2.5-16	0.56
CMC-5-16	0.63
CMC-7.5-16	0.50
CMC-2.5-24	0.60
CMC-5-24	0.53
CMC-7.5-24	0.50

## 4. Conclusions

Rice straw (RS), a lignocellulosic biomaterial has the potential to be a substrate for the production of value-added products such as carboxymethyl cellulose (CMC) as depicted in this study. RS needed to be pretreated in order to separate cellulose that was used as a raw material to synthesize CMC. The alkaline peroxide pretreatment is a promising technique for cellulose-rich material for CMC synthesis. The suitable alkaline peroxide pretreatment conditions for RS

for CMC production were studied. The experimental results showed that the most suitable pretreatment condition for pretreatment was hydrogen peroxide concentration of 5% (v/v) at 16 h. Under this condition, the biochemical compositions, XRD, FTIR, whiteness index and DS results were suitable for CMC synthesis from RS. The optimal conditions resulted in the highest DS value of 0.63 and the whitest product color. The obtained results indicated that RS can be an alternative raw material for high value-added products by lignocellulosic valorization.

## 5. Acknowledgement

This research was funded by King Mongkut's University of Technology North Bangkok and National Science and Technology Development Agency, Thailand with Contract no. GRAD011/2566

## 6. References

- [1] Kunjalukkal Padmanabhan, S., Lamanna, L., Friuli, M., Sannino, A., Demitri, C., and Licciulli, A. (2023). Carboxymethylcellulose-based hydrogel obtained from bacterial cellulose. *Molecules*, 28(2), 829. <https://doi.org/10.3390/molecules28020829>
- [2] Pushpamalar, V., Langford, S. J., Ahmad, M., and Lim, Y. Y. (2006). Optimization of reaction conditions for preparing carboxymethyl cellulose from sago waste. *Carbohydrate Polymers*, 64(2), 312–318. <https://doi.org/10.1016/j.carbpol.2005.12.003>
- [3] Bazargan, A., Wang, Z., Barford, J. P., Saleem, J., and McKay, G. (2020). Optimization of the removal of lignin and silica from Rice husks with alkaline peroxide. *Journal of Cleaner Production*, 260, 120848. <https://doi.org/10.1016/j.jclepro.2020.120848>
- [4] Biswas, A., Kim, S., Selling, G. W., and Cheng, H. N. (2014). Conversion of agricultural residues to carboxymethylcellulose and carboxymethylcellulose acetate. *Industrial Crops and Products*, 60, 259–265. <https://doi.org/10.1016/j.indcrop.2014.06.004>
- [5] Ho, M. C., Ong, V. Z., and Wu, T. Y. (2019). Potential use of alkaline hydrogen peroxide in lignocellulosic biomass pretreatment and Valorization – A Review. *Renewable and Sustainable Energy Reviews*, 112, 75–86. <https://doi.org/10.1016/j.rser.2019.04.082>
- [6] Tareen, A. K., Punsuvon, V., and Parakulsuksatid, P. (2020). Investigation of alkaline hydrogen peroxide pretreatment to enhance enzymatic hydrolysis and phenolic compounds of oil palm trunk. *3 Biotech*, 10. <https://doi.org/https://doi.org/10.1007%2Fs13205-020-02169-6>
- [7] Kontogianni, N., Barampouti, E. M., Mai, S., Malamis, D., and Loizidou, M. (2019). Effect of alkaline pretreatments on the enzymatic hydrolysis of wheat straw. *Environmental Science and Pollution Research*, 26(35), 35648–35656. <https://doi.org/10.1007/s11356-019-06822-3>
- [8] Zhan, Y., Cheng, J., Liu, X., Huang, C., Wang, J., Han, S., Fang, G., Meng, X., and Ragauskas, A. J. (2022). Assessing the availability of two bamboo species for fermentable sugars by alkaline hydrogen peroxide pretreatment. *Bioresource Technology*, 349, 126854. <https://doi.org/10.1016/j.biortech.2022.126854>
- [9] Abderrahim, B., Abderrahman, E., Mohamed, A., Fatima, T., Abdessalam, T., and Krim, O. (2015). Kinetic Thermal Degradation of Cellulose, Polybutylene Succinate and a Green Composite: Comparative Study. *World Journal of Environmental Engineering*, 3. <https://doi.org/10.12691/wjee-3-4-1>

- [10] Adinugraha, M. P., Marseno, D. W., and Haryadi. (2005). Synthesis and characterization of sodium carboxymethylcellulose from Cavendish banana pseudo stem (*Musa Cavendishii* Lambert). *Carbohydrate Polymers*, 62(2), 164–169.  
<https://doi.org/10.1016/j.carbpol.2005.07.019>
- [11] Seo, P.-N., Han, S.-Y., Park, C.-W., Lee, S.-Y., Kim, N.-H., and Lee, S.-H. (2018). Effect of alkaline peroxide treatment on the chemical compositions and characteristics of lignocellulosic nanofibrils. *BioResources*, 14(1), 193–206.  
<https://doi.org/10.15376/biores.14.1.193-206>
- [12] Klunklin, W., Jantanasakulwong, K., Phimolsiripol, Y., Leksawasdi, N., Seesuriyachan, P., Chaiyaso, T., Insomphun, C., Phongthai, S., Jantrawut, P., Sommano, S. R., Punyodom, W., Reungsang, A., Ngo, T. M., and Rachtanapun, P. (2020). Synthesis, characterization, and application of carboxymethyl cellulose from asparagus stalk end. *Polymers*, 13(1), 81. <https://doi.org/10.3390/polym13010081>
- [13] Aravamudhan, A., Ramos, D. M., Nada, A. A., and Kumbar, S. G. (2014). Natural polymers. *Natural and Synthetic Biomedical Polymers*, 67–89.  
<https://doi.org/10.1016/b978-0-12-396983-5.00004-1>

## The Role of Nonionic Surfactants in Lubricity of Green Diesel

Anawat Phatthanaphon\*, and Attaphon Maneedaeng

School of Chemical Engineering, Institute of Engineering, Suranaree University of Technology,  
Nakhon Ratchasima, 30000, Thailand  
E-mail: \*m6500894@g.sut.ac.th

### Abstract

This study investigated the influence of nonionic surfactants on the lubricity of bio-hydrogenated diesel (BHD), potential environmentally friendly alternative fuel with several properties surpassing petroleum diesel. However, key obstacle to the practical implementation of the BHD is poor lubricating properties, which can lead to engine wear and tear. This investigation explored the addition of sorbitan esters (Span) series surfactants such as Span 20, Span 80, and Span 120 were added to BHD. The amphipathic molecular structure of Span can be adsorbed onto contact surfaces, resulting in forming a protective layer that reduces wear. The study found that adding amounts of Span without exceeding 5% by volume significantly improved the lubricating properties of BHD investigated by High Frequency Reciprocating Rig under ISO 12156-1:2018 standard procedure. The wear scar diameter (WSD) decreased from 516  $\mu\text{m}$  to 161-203  $\mu\text{m}$ , and the average film formation was 94-98% with an average friction coefficient decreases from 0.296 to 0.147-0.164. This result indicates Span series surfactants can facilitate the formation of a protective layer on the contact surface to prevent wear during the rubbing process. Further analysis of disc specimen using a LEXT OLS5100 3D Laser Measuring Microscope confirmed the positive impact of BHD with surfactants on lubrication behavior on the worn surface. This study highlights the potential of nonionic surfactant of Span series as a BHD additive to enhance lubricity and reduce engine wear.

**Keywords:** Bio-Hydrogenated Diesel; Tribology; Surfactant; Lubrication

### 1. Introduction

In response to environmental concerns, many countries are prioritizing emissions reduction and sustainable development initiatives, leading to a growing adoption of alternative energy sources to replace fossil fuels in transportation and industrial sectors. Green diesel, also called bio-hydrogenated diesel (BHD) is considered as a highly efficient alternative fuel substitute for petroleum diesel due to its potential as a viable environmentally friendly energy source. Moreover, it is compatible with existing compression ignition engines without requiring modifications [1]. BHD possesses a paraffinic hydrocarbon molecular structure, leading to combustion characteristics closely resembling those of conventional diesel fuels. BHD boasts several properties superior to conventional diesel and other fuels [2]. Notably, its high heating value and higher cetane index translate to reduced ignition delay and enhanced combustion efficiency, while its lower sulfur content and emissions rate contribute to a cleaner burning process [3, 4]. These attributes position BHD as a promising alternative for the transportation.

However, the lack of aromatic and oxygen compounds in composition of BHD results in poor lubricating properties [5-7], which do not meet the standards specified in the specifications for appearance and quality of diesel and biodiesel in the national regulations by the Department of Energy Business, Ministry of Energy, Thailand, 2020, which specify a maximum wear scar diameter of 460  $\mu\text{m}$ . The lubricating properties of a fuel directly influence its ability to

minimize friction and engine wear. Therefore, the use of BHD in an engine can lead to increased wear and tear, impacting both engine performance and the longevity of its components.

Numerous studies in recent years have focused on improving the lubricating properties of low-lubricity fuels like BHD and ultra-low sulfur diesel (ULSD). These attempts use friction modifiers and anti-wear additives mixed into the fuel to enhance lubricity performance [8]. One key mechanism involves adsorption of the friction modifiers onto the metal surfaces, forming a protective layer that minimizes direct contact between metal components. Friction modifiers are amphipathic molecules composed of polar head groups (Hydrophilic head) and non-polar aliphatic tail groups (Hydrophobic tail). The hydrophilic head is adsorbed to the metal surface, while the outward-facing hydrophobic tail encourages an orderly molecular arrangement, ultimately leading to a barrier film formation between the contact surface [9, 10]. Chemically, surfactants are a widely used type of amphipathic molecule. Previous studies have investigated the use of surfactants to enhance lubrication properties in various applications. Margielewski and Plaza demonstrated that Polyalkoxy Glycol Dithiophosphates (PGDPs) adsorbed onto metal surfaces, forming a protective film that improves the lubricity of the lubricant [11]. Upadhyay et al. revealed that the addition of Sodium Dodecyl Sulphate (SDS) to PAO6 synthetic oil decreased the friction coefficient. The SDS molecules formed thread-like micelles on metal surfaces, thereby reducing the contact area and minimizing friction [12]. Furthermore, Uchôa et al. found that adding glycerin to ULSD increases its polarity due to the presence of hydroxyl groups. This enhanced polarity improves adhesion to metal surfaces, resulting in the formation of a protective film that reduces wear scars by up to 48% [13].

Despite the aforementioned studies, the use of surfactants specifically for enhancing fuel lubricity remains relatively unexplored. To address this gap, this study delves into the impact of surfactants on fuel lubricity as a novel approach for improving BHD quality. Our focus is on nonionic surfactants because of their superior emulsification properties relative to ionic surfactants, whose primary strength lies in cleaning applications. Additionally, the lack of ionic dissociation at the hydrophilic head of nonionic surfactants minimizes the risk of metal corrosion, further differentiating them from ionic surfactants. Unlike previous research, which have focused on exploring general applications of surfactants for lubricity improvement. This research aims to comprehensively investigate the influence of nonionic surfactants on low-lubricity fuels, with the ultimate goal of establishing guidelines for optimizing BHD quality in accordance with relevant standards.

## 2. Materials and Methods

### 2.1. Chemicals

The commercial bio-hydrogenated diesel (BHD) produced by hydrogenation of palm oil was purchased from Verasuwan Co., Ltd, Thailand. The nonionic surfactants used in this work (Span 20, Span 80, and Span 120) were purchased from Guangdong Huana Chemistry Co., Ltd. (China) with purity greater than 98.0%. These Span series have the hydrophilic sorbitan group act as a polar head in common, but with different hydrophobic fatty acid chain (Fig. 1). Span series were selected due to their composition as fatty acid esters of anhydro sorbitols, which have good oil soluble emulsifying properties [14]. The chemical used to clean the specimen holder was acetone (AR grade) with purity of 99.5% was purchased from RCI Labscan. In addition, Sodium Bromide (Analytical grade) with purity of 99.5% was used for the preparation of sodium bromide saturated solution, which was purchased from QReC.

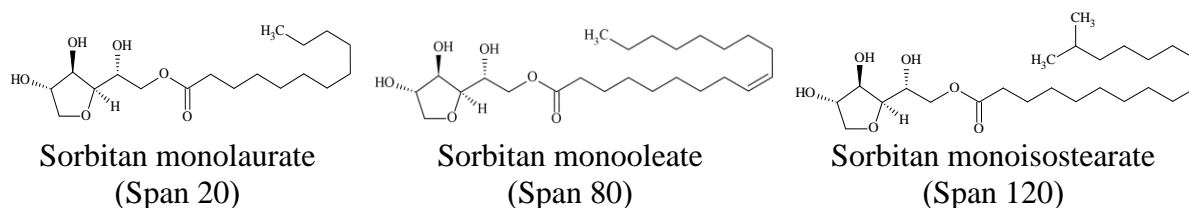


Fig 1. Chemical structure of nonionic surfactants in Span series employed in the study.

## 2.2. Tribological testing

Tribological measurements were performed on the High-Frequency Reciprocating Rig (HFRR) of PCS Instruments. The test is a ball-on-disc method, in which a steel ball slides against a steel disc immersed in the liquid to be tested. Both the ball and disc are made of AISI 52100 steel. The test conditions follow the ISO 12156-1:2018 standard. 2 mL of fuel was added in the reservoir of HFRR. Then, the nonrotating steel ball was held with a vibrator arm and loaded with a 200 g mass until it contacted a test disc completely submerged in the fuel at 60 °C. After then, the ball was vibrated against the disc with a 1 mm stroke at a frequency of 50 Hz for 75 minutes. Laboratory ambient conditions within the cabinet were controlled at 20–26°C temperature and a relative humidity range of 48–58% using a sodium bromide saturated solution for humidity control.

Subsequent to test completion, the ball specimen was removed from the vibrator arm and cleaned by immersion in ultrasonic bath with acetone. The wear scar on the surface of the ball specimen was evaluated using a metallurgical microscope with a magnification of 100x. In this work, each sample was tested three times. However, if the wear scar diameter measurements deviated by more than  $\pm 20 \mu\text{m}$ , a fourth test was necessary to confirm the repeatability of the results. Additionally, the worn surface on the disc specimen was characterized using LEXT OLS5100 3D Laser Measuring Microscope (Olympus, Tokyo, Japan) at 20x magnification.

## 3. Results and Discussion

### 3.1. Lubricity

The lubricating behavior of pure BHD can be observed from the friction coefficient (COF), percentage of film formation, and wear scar diameter (WSD), all obtained from tribological testing using HFRR with ISO12156-1:2018. As seen in Fig. 2(a), the percentage of film formation on the surface is only between 40-60%, indicating insufficient lubrication on the metal surface between the ball and disc. Moreover, Fig. 2(b) reveals fluctuations in the COF, indicate poor film stability. Consequently, large wear scars with an average diameter of 516  $\mu\text{m}$  are observed as shown in Fig. 2(c).

The inclusion of Span series surfactants in BHD led to a notable decrease in WSD, as shown in Fig. 3(a), which reveals a reduction of WSD from 516  $\mu\text{m}$  in pure BHD to a range of 161-203  $\mu\text{m}$ , indicating enhanced BHD lubricity. This enhanced lubricity is due to the structure of the Span series surfactant consists of hydrophilic hydroxyl groups, a hydrophobic fatty acid tail, and ester linkages that connect these two contrasting moieties. The presence of hydroxyl groups indicates an oxygen-containing polar compound that participates in creating hydrogen bonding with BHD molecules [11, 14]. These hydrogen bonds facilitate attractive intermolecular interactions between the BHD molecules and the metal surface, resulting in enhanced adhesion and adsorption of the BHD onto the metal surface [9, 13].

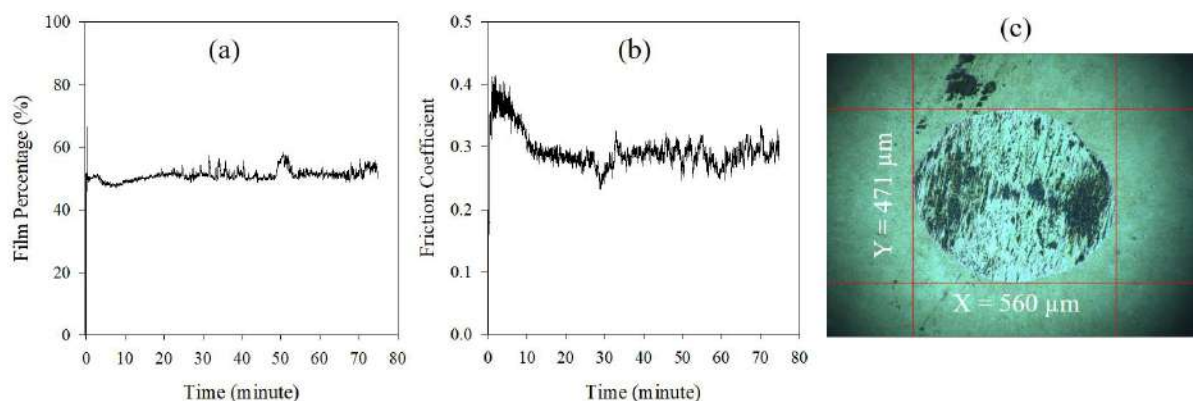


Fig. 2 Fluctuations of (a) film percentage and (b) COF as well as (c) WSD image of pure BHD.

Furthermore, regarding the effect of hydrophobic tail structure of Span series group on wear scar diameter, a key indicator of lubricity. Specifically, the experiment revealed that Span 80 exhibited lower wear scar diameter compared to both Span 20 and Span 120 because the distinct structural limitations of Span 20 and Span 120. Notably, Span 80 has a long hydrophobic tail, leading to a high number of carbon atoms. Consequently, the molecular weight increases enhancing the van der Waals interactions between adjacent molecules [15], resulting in a stronger protective layer compared to Span 20, which has a shorter hydrophobic tail and weaker interactions. However, although Span 120 has the same number of carbon atoms as Span 80, it exhibits a higher propensity for wear scar formation due to the hindrance caused by its branched structure disrupts the molecular arrangement on the surface and hinder complete coverage [16]. This incomplete coverage diminishes the lubricity of the metal surface compared to Span 80.

More importantly, this enhanced adsorption on the metal surface indicates the formation of a protective layer on the metal surface to prevent wear during the rubbing process [4, 9]. Fig. 3(b) provides evidence for film formation. It shows that adding Span series surfactants to the BHD increased the percentage of film formation to be between 94-98%. Similarly, Sriprathum et al. in 2023 studied the addition of fatty acid methyl esters (FAME) to BHD improves its lubricating properties due to the protective layer formed by FAME, which consists of a functional group of ester in the molecules [7]. According to Fig. 3(c) shows the average of the coefficient of friction of BHD decreases from 0.296 to the average range of 0.147-0.164, indicating the operation of a boundary lubrication mechanism [6]. Further observations revealed a negligible change in lubrication behavior with increasing surfactant concentration. This could be attributed to two phenomena: first, surfactant adsorption behavior reaching equilibrium on the surface, and second, micelle formation due to excess surfactant that potentially destabilizes the protective layer [17, 18]. Therefore, incorporating a small amount of Span series surfactant into BHD offers an effective approach to enhance BHD lubricity.

Microscopic analysis of wear scar on the ball surface, as shown in Fig. 4, emphasizes that the addition of only a small amount of surfactant, no more than 5% by volume, significantly reduces the wear scar compared to pure BHD. This reduction in wear scar generally indicates improved lubricity. Moreover, it reinforces the theory that the presence of polar compound adsorbed on the metal surface can form a protective layer that reduce adhesion and limit friction or wear.

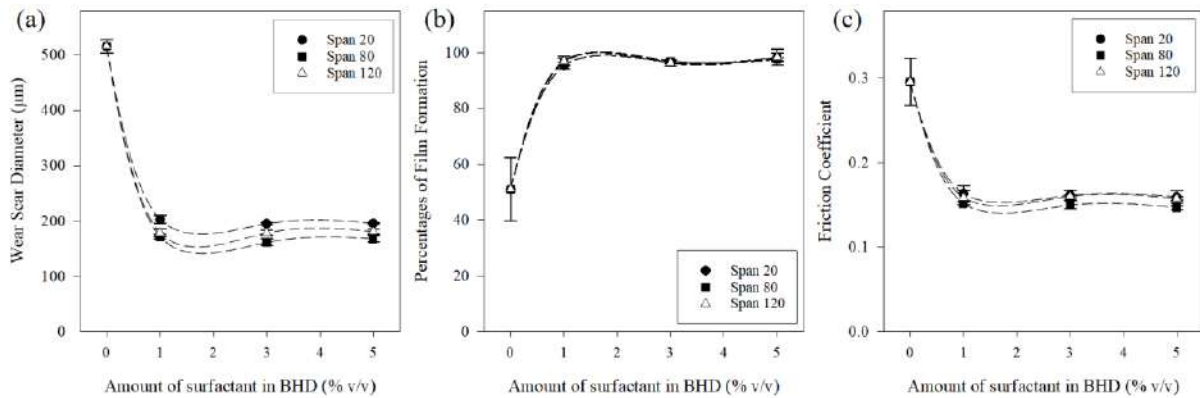


Fig. 3 Variation of (a) wear scar diameter, (b) percentage of film formation, and (c) friction coefficient of adding Span series surfactant to the BHD.

Surfactant Chemical	1% by volume in BHD	3% by volume in BHD	5% by volume in BHD
Span 20	Y = 179 µm X = 227 µm	Y = 168 µm X = 223 µm	Y = 172 µm X = 200 µm
Span 80	Y = 140 µm X = 204 µm	Y = 132 µm X = 190 µm	Y = 141 µm X = 195 µm
Span 120	Y = 153 µm X = 204 µm	Y = 156 µm X = 205 µm	Y = 150 µm X = 209 µm

Fig. 4 A worn on the ball was observed metallurgical microscope with magnification of 100x.

### 3.2. Analysis of the worn surface

Understanding the appearance of wear scar on the disc is crucial alongside analyzing the lubrication behavior of the ball for understanding tribological mechanisms. As shown in Fig. 5, depicts the wear scar observed after tribological testing of pure BHD. The 3D Laser Measuring Microscope image at magnification of 20x in Fig. 5 reveals readily observable wear scars on the disc surface. Therefore, the observed damage confirms the poor lubricating properties of the BHD due to the absence of polar compounds like oxygen in its paraffinic structure.



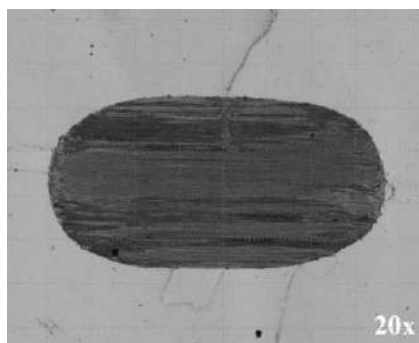


Fig. 5 Worn surface of pure BHD on the disc observed by 3D Laser Measuring Microscope

Interestingly, the addition of Span series surfactant to the BHD significantly reduced wear scars on the discs compared to tests with pure BHD, as depicted in Fig. 6. This trend aligns with the results observed with the WSD on the ball in Fig. 2(a), suggesting a superior lubricating performance of the BHD with surfactant. Furthermore, 3D laser microscope images reveal dark stains around the worn surface. Previous studies have confirmed that the main chemical composition of almost all the black residues on the disc are carbon deposits. The reasoning behind this is likely due to the heat generated during friction during the test, which causes the carbon in the disc to decompose and form the black residues [13, 19]. However, observations revealed increasing surfactant concentration led to a tendency for increased deposit formation on worn surfaces. In order to gain a deeper understanding of the lubrication mechanisms, the worn surface on the disc will be further examined chemically and physically using Fourier Transform Infrared Spectroscopy, Scanning Electron Microscope, and 3D Laser Measuring Microscope.

Surfactant Chemical	1% by volume in BHD	3% by volume in BHD	5% by volume in BHD
Span 20			
Span 80			
Span 120			

Fig. 6 Worn on the disc was observed 3D laser measuring microscope with 20x magnification.

#### 4. Conclusion

This study employed the High-Frequency Reciprocating Rig (HFRR) test under ISO 12156-1:2018 standards to investigate the lubrication performance of bio-hydrogenated diesel (BHD) supplemented with nonionic surfactants of the sorbitan esters (Span) series such as Span 20, Span 80, and Span 120. Our study demonstrates the addition of surfactant to BHD significantly improves lubrication behavior compared to pure BHD. This enhancement is attributed to the amphiphilic structure of the surfactants, which increases the polarity of the BHD, leading to better adsorption and formation of a protective layer on the metal surface. The worn surface analysis on disc confirmed that the addition of nonionic surfactant demonstrated a reduction in wear. However, this benefit was accompanied by an increased tendency for the formation of deposits on the worn surface, necessitating further investigation. Based on these findings, nonionic surfactant of Span series has demonstrated potential as efficient additives for BHD to enhance lubricity and reduce engine wear.

#### Acknowledgement

This work was supported by (i) Suranaree University of Technology (SUT), (ii) Thailand Science Research and Innovation (TSRI), and (iii) National Science, Research and Innovation Fund (NSRF) - Grant no. 179270. The author, AP, also wishes to express gratitude to Suranaree University of Technology for generously providing a grant in support of him pursuit of a Master's degree.

#### References

- [1] Singh, D., K. A. Subramanian, and M. O. Garg (2018). Comprehensive review of combustion, performance and emissions characteristics of a compression ignition engine fueled with hydroprocessed renewable diesel. *Renewable and Sustainable Energy Reviews*, 81, 2947-2954.
- [2] Sugiyama, K., et al. (2011). Effects of Hydrotreated Vegetable Oil (HVO) as Renewable Diesel Fuel on Combustion and Exhaust Emissions in Diesel Engine. *SAE International Journal of Fuels and Lubricants*, 5, 205-217.
- [3] D' Ambrosio, S., A. Mancarella, and A. Manelli (2022). Utilization of Hydrotreated Vegetable Oil (HVO) in a Euro 6 Dual-Loop EGR Diesel Engine: Behavior as a Drop-In Fuel and Potentialities along Calibration Parameter Sweeps. *Energies*, 15(19), 7202.
- [4] Szeto, W. and D.Y.C. Leung (2022). Is hydrotreated vegetable oil a superior substitute for fossil diesel? A comprehensive review on physicochemical properties, engine performance and emissions. *Fuel*, 327, 125065.
- [5] Fathurrahman, N.A., et al. (2023). Lubricity Properties of Palm Oil Biodiesel Blends with Petroleum Diesel and Hydrogenated Vegetable Oil. *Lubricants*, 11(4), 176.
- [6] Mittelbach, M. (2015). Fuels from oils and fats: Recent developments and perspectives. *European Journal of Lipid Science and Technology*, 117.
- [7] Sriprathum, S., et al (2023). Comprehensive analysis of properties of green diesel enhanced by fatty acid methyl esters. *RSC Adv*, 13(45), 31460-31469.
- [8] Cyriac, F., et al. (2021). Influence of structural factors on the tribological performance of organic friction modifiers. *Friction*, 9(2), 380-400.
- [9] Telegdi, J. (2020). Formation of Self-Assembled Anticorrosion Films on Different Metals. *Materials (Basel)*, 13(22).

- [10] Yu, H., et al. (2023). Effect of functional groups on tribological properties of lubricants and mechanism investigation. *Friction*, 11(6), 911-926.
- [11] Margielewski, L. and S. Płaza (2010), Surfactant dithiophosphates lubricating oil additives. *Tribology - Materials, Surfaces & Interfaces*, 4(2), 43-53.
- [12] Upadhyay, R.K. and L.A. Kumaraswamidhas (2014). On the influence of surfactant over friction properties of steel. *Chemical Physics Letters*, 608, 167-172.
- [13] Uchôa, I.M. A., M.S. Deus, and E.L. Barros Neto (2021). Formulation and tribological behavior of ultra-low sulfur diesel fuels microemulsified with glycerin. *Fuel*, 292, 120257.
- [14] Naskar, M.K., A. Patra, and M. Chatterjee (2006). Understanding the role of surfactants on the preparation of ZnS nanocrystals. *Journal of Colloid and Interface Science*, 297(1), 271-275.
- [15] Kumar, V., et al. (2019). Tribological Properties of Some Fatty Acids. *Journal of Physics: Conference Series*, 1240(1), 12133.
- [16] Stachowiak, G. W. and A. W. Batchelor (2014). Boundary and Extreme Pressure Lubrication, in *Engineering Tribology*, 4th, pp. 371-428. Butterworth-Heinemann: Boston.
- [17] Taheri, R., et al. (2017). Surface Film Adsorption and Lubricity of Soybean Oil In-Water Emulsion and Triblock Copolymer Aqueous Solution: A Comparative Study. *Lubricants*, 5(1), 1.
- [18] Kalam, S., et al. (2021). Surfactant Adsorption Isotherms: A Review. *ACS Omega*, 6(48), 32342-32348.
- [19] Farias, A., J. Medeiros, and S. Alves (2014). Micro and Nanometric Wear Evaluation of Metal Discs Used on Determination of Biodiesel Fuel Lubricity. *Materials Research*, 17.

## Hydrodynamics simulation of sorbent riser and regenerator for carbon dioxide capture process using $K_2CO_3/Al_2O_3$ in circulating fluidized bed reactor

Nattida Pakdee\*, Pornpote Piumsomboon, Benjapon Chalermssinsuwan

<sup>1</sup>Department of Chemical Technology, Faculty of Science, Chulalongkorn University

\*E-mail: 6370065323@student.chula.ac.th

### Abstract

Now, the world is facing global warming caused by the release of greenhouse gases into the atmosphere. The most released gas is carbon dioxide. The carbon dioxide capture and storage technology is used to reduce the amount of carbon dioxide gas released into the atmosphere. In this research, potassium carbonate support on aluminum as an adsorbent is used to capture carbon dioxide from flue gas. The adsorbent is loaded into a circulating fluidized bed reactor that consists of an adsorber and a regenerator. The objective of the research is to find a proper drag model for better representing the hydrodynamic model of the regenerator and to study the effect of variables for adsorption and regeneration of the carbon dioxide capture process in the circulating fluidized bed reactor by using computational fluid dynamics. User Define Function (UDF) was used for two reactors and different drag models were used in each model. By simulating the flow behavior of the adsorbent in the riser and downer reactors, it was found that the Gidaspow drag model provided proper hydrodynamics in the riser. The distribution of the sorbent in the riser is similar to the experiment result. Then Wen and Yu, Syamlal O'brien, and Gidaspow drag models were employed to investigate the hydrodynamics in the downer. The Wen & Yu, and Syamlal O'brien drag models show gaps in the downer. However, the Gidaspow drag model reduces the flotation of the sorbent in the downer which is coherent with the observation. Thus, it was concluded that the Gidaspow drag model could be used for both the riser and downer.

**Keywords:** Carbon dioxide capture, Regeneration, Circulating fluidized bed, Hydrodynamics

### 1. Introduction

Nowadays, the world is facing problems with climate change and global warming due to the rise of the global temperature caused by the increase of greenhouse gases in the atmosphere. The major greenhouse gases are carbon dioxide, methane, nitrous oxide, and fluorinated gases. Carbon dioxide ( $CO_2$ ) is the main greenhouse gas emitted to the environment from the burning of fossil fuels to produce power and electricity. Carbon capture and storage technology (CCS) reduces carbon dioxide emissions, a major cause of climate change, and will extend the use of fossil fuels as a major source of energy [1,2].

There are three types of carbon capture technology: pre-combustion  $CO_2$  capture, oxy-fuel  $CO_2$  combustion capture, and post-combustion  $CO_2$  capture. Post-combustion carbon dioxide capture is a technology that has received much attention since it can directly reduce carbon dioxide in the flue gas emitted from thermal power plants with less process modification. Post-combustion technology includes five major processes: absorption, adsorption, cryogenic, membrane, and microbial. The adsorption process has high potential since it has low toxicity, low energy consumption for regeneration, but low efficiency for adsorption [6].



Potassium carbonate supported on alumina ( $K_2CO_3/Al_2O_3$ ) has garnered attention in industrial processes owing to its unique properties and versatility. One of the primary reasons for selecting  $K_2CO_3/Al_2O_3$  lies in its exceptional capacity for capturing acidic gases such as carbon dioxide ( $CO_2$ ) and hydrogen sulfide ( $H_2S$ ) from gas streams. This adsorbent demonstrates high chemical stability and reactivity, making it particularly suitable for applications requiring efficient removal of acidic impurities.

The role of alumina ( $Al_2O_3$ ) within the  $K_2CO_3/Al_2O_3$  adsorbent composite is multifaceted. Alumina serves as a crucial support material, providing mechanical strength and structural integrity to the adsorbent matrix. Moreover, alumina possesses inherent surface properties that enhance the adsorption and retention of potassium carbonate ( $K_2CO_3$ ), thereby improving the overall adsorption performance of the composite material. Additionally, the presence of alumina can mitigate issues related to  $K_2CO_3$  agglomeration and degradation, prolonging the operational lifespan of the adsorbent.

Advantages of  $K_2CO_3/Al_2O_3$  include its excellent adsorption capacity and selectivity towards acidic gases, enabled in part by the synergistic interaction between potassium carbonate and alumina. This combination not only enhances adsorption efficiency but also facilitates the regeneration of the adsorbent, thereby minimizing downtime and operational costs. Furthermore, the presence of alumina imparts thermal stability to the adsorbent, ensuring reliable performance under diverse operating conditions.

Despite its many advantages,  $K_2CO_3/Al_2O_3$  is not without limitations. One notable drawback is its susceptibility to degradation in the presence of moisture, which can compromise its adsorption efficiency over time. Additionally, the regeneration process of  $K_2CO_3/Al_2O_3$  adsorbent can be energy-intensive and costly, posing challenges in terms of operational sustainability.

Comparatively, alternative adsorbents such as amine-based solutions offer higher selectivity for certain gases and may exhibit better resistance to moisture. However, they often come with higher operating costs and pose environmental concerns due to solvent toxicity and degradation issues. In contrast,  $K_2CO_3/Al_2O_3$  presents a viable alternative with a favorable balance of performance, cost-effectiveness, and environmental impact.

Computational fluid dynamics (CFD) modeling is known as a technique to predict the dynamics of the fluid and transport phenomena in multiphase flows, especially where the flow behavior is difficult and expensive to investigate through experimental techniques. So, computational fluid dynamics becomes an attractive and feasible method for the process design, process performance analysis, and optimization of multiphase reactors. It has become a tool for understanding the hydrodynamics and transfer mechanisms in multiphase flow systems [3].

Fluidized bed technology has several advantages such as well mixing and high heat and mass transfer rates between gas and solid particles. Furthermore, heat can be removed quickly during exothermic reactions. Thus, it has been applied to developing the adsorption reactor for carbon dioxide capture.

Furthermore, fluidization flow regimes have impacts on reactor performance and will change when the fluid velocity changes. By increasing gas velocity in the system, there are five main flow regimes in fluidization starting from low to high velocities. The first fluidization regime is the bubbling fluidization regime. It takes place when the gas velocity exceeds the minimum fluidization velocity ( $U_{mf}$ ). The particles start moving and bubbles appear in the reactor. The second regime is the slugging fluidization regime. Bubbles will be as large as the diameter of the reactor. The third regime is the turbulent fluidization regime. The behavior of solid particles in this regime is dense in the bottom area and dilute in the top area. The fourth

regime is the fast fluidization regime. In this regime, the core-annular has dense solid particles. The last regime is the pneumatic transport fluidization regime. The solid particle is dilute and can be transported out of the reactor.

Recently, a novel fluidization regime was found. The regime is in between turbulent and fast fluidization regimes. It is a circulating turbulent fluidized bed (CTFB) regime. The regime has many advantages, such as good solid distribution, high contact area between gas-solid particles, and uniform temperature distribution. The proposed reactor has adopted this regime and applied it to capture CO<sub>2</sub> with solid sorbents and operated continuously [4].

In fluid dynamics, drag is a force acting opposite to the relative motion of any object moving with respect to a surrounding fluid. It exists between two fluid surfaces or between a fluid and a solid surface. Previously, computational fluid dynamics was used to predict the drag force between solid sorbent and gas flow in a fluidized bed reactor. The drag models, such as Gidaspow, Wen & Yu, Syamlal O'brien, and the energy-minimization multi-scale (EMMS), were calculated to determine the momentum exchange between solid and gas flow in a fluidized bed which influenced the hydrodynamic behavior inside the adsorber.

From the previous work of our research group, dynamic models of adsorber and regenerator were developed for CO<sub>2</sub> capture. To control the circulating solid sorbent between the adsorber and the regenerator, a control valve model was also developed at the loop seal of the system. However, the hydrodynamics of the regenerator have not yet been thoroughly studied. The objectives of the research are to investigate the hydrodynamics of the adsorber and regenerator for a CO<sub>2</sub> capture process by finding the proper drag models for the downer and evaluating the CO<sub>2</sub> capture performance of the system.

## 2. Mathematical model

The Eulerian- Eulerian model based on the kinetic theory of granular flow was employed to simulate the gas-solid system of adsorber and regenerator for CO<sub>2</sub> capture process. The solid phase and gas phase are calculated with conservation equations.

### 2.1 Conservation equation

The conservation equations of momentum and mass for solid-gas flow are as follows.

#### Mass conservation equation

Gas phase:

$$\frac{\partial}{\partial t}(\varepsilon_g \rho_g) + \nabla \cdot (\varepsilon_g \rho_g \mathbf{v}_g) = 0 \quad (1)$$

Solid phase:

$$\frac{\partial}{\partial t}(\varepsilon_s \rho_s) + \nabla \cdot (\varepsilon_s \rho_s \mathbf{v}_s) = 0 \quad (2)$$

the sum of the volume fraction is 1.

#### Momentum conservation equation

Gas phase:

$$\frac{\partial}{\partial t}(\varepsilon_g \rho_g \mathbf{v}_g) + \nabla \cdot (\varepsilon_g \rho_g \mathbf{v}_g \mathbf{v}_g) = -\varepsilon_g \nabla P + \nabla \cdot \boldsymbol{\tau}_g + \varepsilon_g \rho_g \mathbf{g} - \beta_{gs}(\mathbf{v}_g - \mathbf{v}_s) \quad (3)$$

Solid phase:

$$\frac{\partial}{\partial t}(\varepsilon_s \rho_s \mathbf{v}_s) + \nabla \cdot (\varepsilon_s \rho_s \mathbf{v}_s \mathbf{v}_s) = -\varepsilon_s \nabla P + \nabla \cdot \boldsymbol{\tau}_s - \nabla P_s + \varepsilon_s \rho_s \mathbf{g} + \beta_{gs}(\mathbf{v}_g - \mathbf{v}_s) \quad (4)$$

#### Energy conservation equation

Gas phase:

$$\frac{\partial}{\partial t}(\rho_g h_g) + \nabla \cdot (\rho_g h_g \mathbf{v}_g) = \nabla \cdot [(k_g + k_{t,g}) \nabla T_g] + S_{h,g} \quad (5)$$

Solid phase:

$$\frac{\partial}{\partial t}(\rho_S h_S) + \nabla \cdot (\rho_S h_S v_S) = \nabla \cdot [(k_S + k_{t,s}) \nabla T_S] + S_{h,s} \quad (6)$$

## 2.2 Conservation of species

Gas phase:

$$\frac{\partial}{\partial t}(\rho Y_{g,i}) + \nabla \cdot (\rho v Y_{g,i}) = -\nabla \cdot J_{g,i} + R_{g,i} + S_{g,i} \quad (7)$$

Solid phase:

$$\frac{\partial}{\partial t}(\rho Y_{s,i}) + \nabla \cdot (\rho v Y_{s,i}) = -\nabla \cdot J_{s,i} + R_{s,i} + S_{s,i} \quad (8)$$

## 2.3 Fluctuating kinetic energy conservation equation

Solid phase:

$$\frac{3}{2} \left[ \frac{\partial}{\partial t} (\varepsilon_s \rho_s \theta) + \nabla \cdot (\varepsilon_s \rho_s \theta v_s) \right] = (-\nabla P_s I + \tau_s) : \nabla v_s + \nabla \cdot (\kappa_s \nabla \theta) - \gamma_s + \phi_{gs} \quad (9)$$

## 2.4 Drag model

Gidaspow drag model

$$\beta_{\text{Gidaspow}} = \begin{cases} \beta_{\text{Wen\&Yu}} & \varepsilon_g \geq 0.8 \\ \beta_{\text{Ergun}} & \varepsilon_g < 0.8 \end{cases}$$

$$\beta_{\text{Wen\&Yu}} = \frac{3 \varepsilon_g (1 - \varepsilon_g) \rho_g |\overline{u_s} - \overline{u_g}|}{4 d_s} C_{D0} \varepsilon_g^{-2.65} \quad (10)$$

$$\beta_{\text{Ergun}} = 150 \frac{(1 - \varepsilon_g)^2 \mu_g}{\varepsilon_g d_s^2} + 1.75 \frac{(1 - \varepsilon_g) \rho_g |\overline{u_s} - \overline{u_g}|}{d_s} \quad (11)$$

$$C_{D0} = \begin{cases} \frac{24}{Re_s} (1 + 0.15 Re_s^{0.687}) & Re_s \leq 1000 \\ 0.44 & Re_s > 1000 \end{cases}$$

Syamlal-O'brien drag model

$$\beta = \frac{3 \varepsilon_s \varepsilon_g \rho_g}{4 v_{r,s}^2 d_p} C_{D0} |\overline{u_s} - \overline{u_g}| \quad (12)$$

$$C_{D0} = \left( 0.63 + \frac{4.8}{\sqrt{Re_s / u_{r,s}}} \right)^2$$

$$Re_s = \frac{\rho_g d_p |\overline{u_s} - \overline{u_g}|}{u_g}$$

$$u_{r,s} = 0.5 \left( A - 0.06 Re_s + \sqrt{(0.06 Re_s)^2 + 0.12 Re_s (2B - A) + A^2} \right)$$

$$A = \alpha_g^{4.14}$$

$$C_{D0} = \begin{cases} P \varepsilon_g^{1.28} & (\varepsilon_g \leq 0.85) \\ \varepsilon_g^Q & (\varepsilon_g > 0.85) \end{cases}$$

$$P = 0.8, Q = 2.65$$

### Energy-minimization multi-scale (EMMS)

$$\beta_{gs} = 150 \frac{(1-\varepsilon_g)^2 \mu_g}{\varepsilon_g d_s^2} + 1.75 \frac{\varepsilon_s \rho_g |v_g - v_s|}{d_s} \quad \varepsilon_g < 0.74 \quad (13)$$

$$\beta_{gs} = \frac{3}{4} C_D \frac{\varepsilon_s \varepsilon_g \rho_g |v_g - v_s|}{d_s} \omega(\varepsilon) \quad \varepsilon_g \geq 0.74 \quad (14)$$

$Re < 1000$ ;

$$C_{D0} = \frac{24}{Re_k} (1 + 0.15 Re_k^{0.687}) Re_k = \frac{\rho_g |v_g - v_s| d_p}{\mu_g}$$

$Re \geq 1000$ ;

$$C_{D0} = 0.44$$

$0.74 \leq \varepsilon_g < 0.82$ ;

$$\omega(\varepsilon) = -0.5760 + \frac{0.0214}{4(\varepsilon_g - 0.7463)^2 + 0.0044}$$

$0.82 \leq \varepsilon_g < 0.97$ ;

$$\omega(\varepsilon) = -0.0101 + \frac{0.0038}{4(\varepsilon_g - 0.7789)^2 + 0.0040}$$

$\varepsilon_g < 0.97$ ;

$$\omega(\varepsilon) = -31.8295 + 32.8295 \varepsilon_g$$

## 2.5 Computational Fluid Dynamics (CFD) Simulation Model

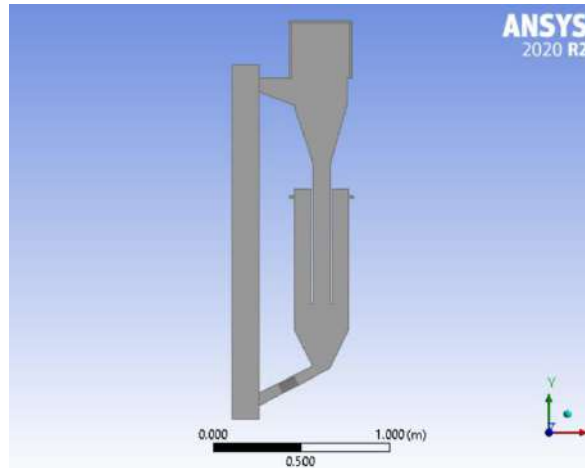
**Table 1. Properties of phase and conditions used in cold model simulations.**

Parameters	Value	Unit
Solid sorbent	Sand	-
Gas inlet	Air	-
Solid particle density	2,650	kg/m <sup>3</sup>
Solid particle diameter	380	μm
Gas density	1.2	kg/m <sup>3</sup>
Gas viscosity	2×10 <sup>-5</sup>	kg/m·s
Initial solid particle inside the CFB	21	kg
Outlet system pressure	101,325	Pa

**Table 2. Properties of phase and conditions used in reaction model simulations.**

Parameters	Value	Unit
Solid sorbent	K <sub>2</sub> CO <sub>3</sub> /Al <sub>2</sub> O <sub>3</sub>	-
Gas inlet	20% CO <sub>2</sub> /15% H <sub>2</sub> O/65% N <sub>2</sub>	-
Solid particle density	3,560	kg/m <sup>3</sup>
Solid particle diameter	380	μm





**Figure 1.** Schematic drawing of CFB reactor.

In the simulation process, the Ansys Fluent program was used to simulate the flow of solid sorbent in the adsorber and regenerator. Figure 1 shows the circulating fluidized bed adsorber and regenerator. The system consists of four important components, which are the adsorber (riser), solid separator (cyclone), regenerator (downer), and loop seal. The adsorber (riser) has a diameter of 0.15 m and a height of 2 m. The regenerator (downer) has a diameter of 0.30 m, a height of 0.90 m, and a thickness of 0.05 m. The simulation is divided into two parts. Part 1 is a cold flow simulation. The data used in the simulation is shown in Table 1, and Part two is a hot flow simulation where the reactions are included. The data used in the simulation is shown in Table 2. When the flue gas enters the riser, potassium carbonate ( $K_2CO_3$ ) adsorbs carbon dioxide from the flue gas and reacts with water converted to potassium bicarbonate ( $KHCO_3$ ) through a forward reaction [5].



The potassium bicarbonate is transported to a cyclone where it is separated from flue gas and falls into the downer. Then, it is converted into Potassium carbonate through a backward reaction and returned to the riser by a loop seal, ending the sorbent circulation cycle.



The kinetics of the reaction can be calculated by rate of reaction.

$$r_{\text{forward}} = k_{fw} [CO_2][H_2O] \varepsilon \quad ; \quad k_{fw} = 7.83 * 10^{-3} \left[ e^{\frac{-(-3609)}{RT}} \right]$$

$$r_{\text{backward}} = k_{bw} \left( \frac{1}{[CO_2]} \right)^{0.15} \left( \frac{1}{[H_2O]} \right)^{0.15} \varepsilon \quad ; \quad k_{bw} = 7.83 * 10^{-3} \left[ e^{\frac{-0.000502}{RT}} \right]$$

The equations for %  $CO_2$  removal and %  $CO_2$  regeneration

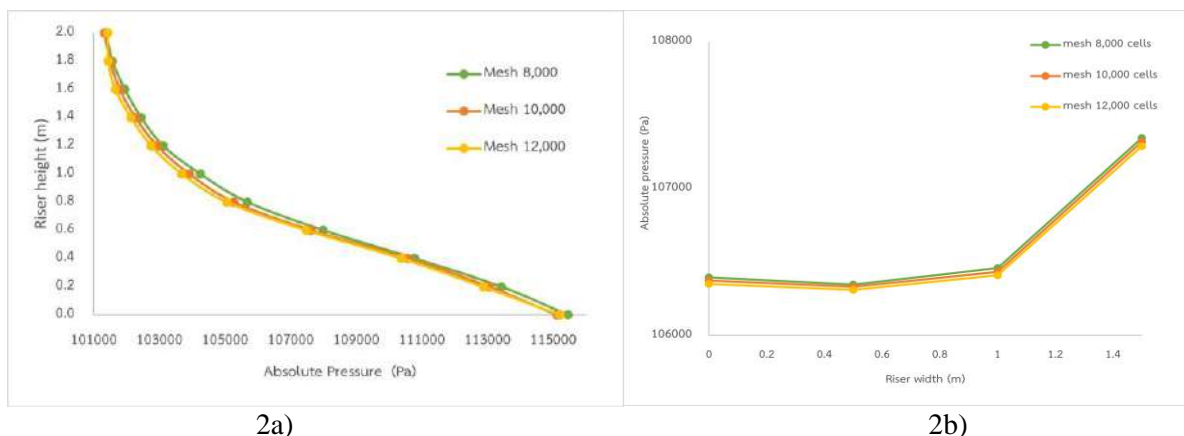
$$\%CO_2 \text{ removal} = \frac{\text{Mass flow of } CO_2 \text{ (in)} - \text{Mass flow of } CO_2 \text{ (out)}}{\text{Mass flow of } CO_2 \text{ (in)}} \times 100 \quad (18)$$

$$\% \text{Regeneration} = \frac{\text{Mass flow of } KHCO_3 \text{ (before)} - \text{Mass flow of } KHCO_3 \text{ (after)}}{\text{Mass flow of } KHCO_3 \text{ (before)}} \times 100 \quad (19)$$

### 3. Results & Discussion

#### 3.1 Validation of the CFD Model

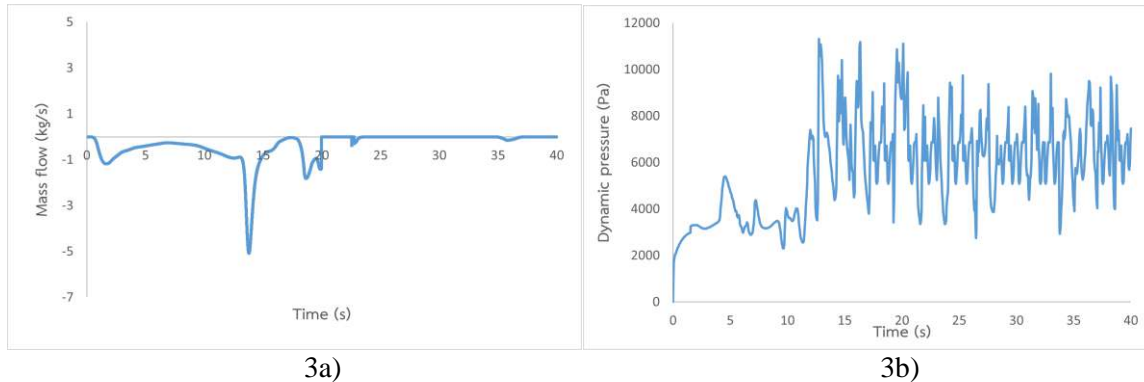
##### 3.1.1. Grid independence test



Figures 2a and 2b show the complete pressure distribution along the axial height and the width of the riser to the number of cells used in the simulation. 8,000, 10,000, and 12,000 cells were employed to identify the proper number of simulation cells. The results show that the finer calculation cells give slightly lower values of pressure distribution than the coarser calculation cells. As the number of cells used for calculation increases, the calculation resolution increases, resulting in the absolute pressure values of 10,000 and 12,000 cells having very close pressure values.

##### 3.1.2. Quasi-steady state test

Figures 3a and 3b plotted the times corresponding to the pressure and mass flow rate at a height of 0.2 meters inside the riser to identify when the system reaches quasi-steady state condition. The figures showed that at the start of the simulation (from 0 to 20 seconds), the pressure inside the riser increased and decreased rapidly over a short time, resulting in a relatively high initial oscillation. Over time (from 20 to 40 seconds), the pressure inside the riser reduced in oscillation. Figure 3b also shows the plot of the solid flow rate at a height of 0.2 meters with time. The figure shows the same behavior as Figure 3a. At the beginning, the flow rate has high oscillating due to an uneven flow and there is also no solid recirculation. Later on, there is a solid return from the downer into the riser. The responses of the pressure and solid flow rate in the system are similar. It can be concluded that the hydrodynamics inside the reactor reaches a quasi-steady state after 20 seconds. The system variables are obtained by averaging their values during the time of 20 to 40 seconds.



3a) Dynamic pressure in the riser with respect to time  
3b) Mass flow rate in the riser with respect to time

### 3.1.3 Drag models in downer investigation

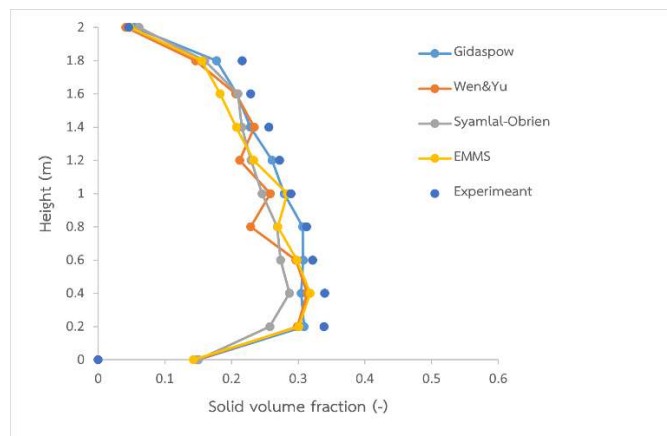


Figure 4 Solid volume fraction along the height

Typically, the adsorption unit would be composed of an adsorber and a regenerator. In the simulation, the adsorption unit is also divided into two sections: the riser (adsorber) section and the downer (regenerator) section. Due to the different operating conditions in each section, different drag models were employed in each section. Typically, the fluid in the riser section will be operated in the fast fluidization regime while that in the downer section will be in the bubbling fluidized bed regime. In this study, the Gidaspow drag model is used to predict the hydrodynamic behavior of gas-solid inside the riser since the model could predict the steady flow and the dispersion of solids along the height of the riser very close to the experimental data as shown in Figure 4. However, several drag models were employed to find the best-fit model for representing the hydrodynamics in the downer. Four drag models, which are the Gidaspow drag model, the Wen & Yu drag model, the Syamlal-O'Brien drag model, and the EMMS drag model, were investigated.

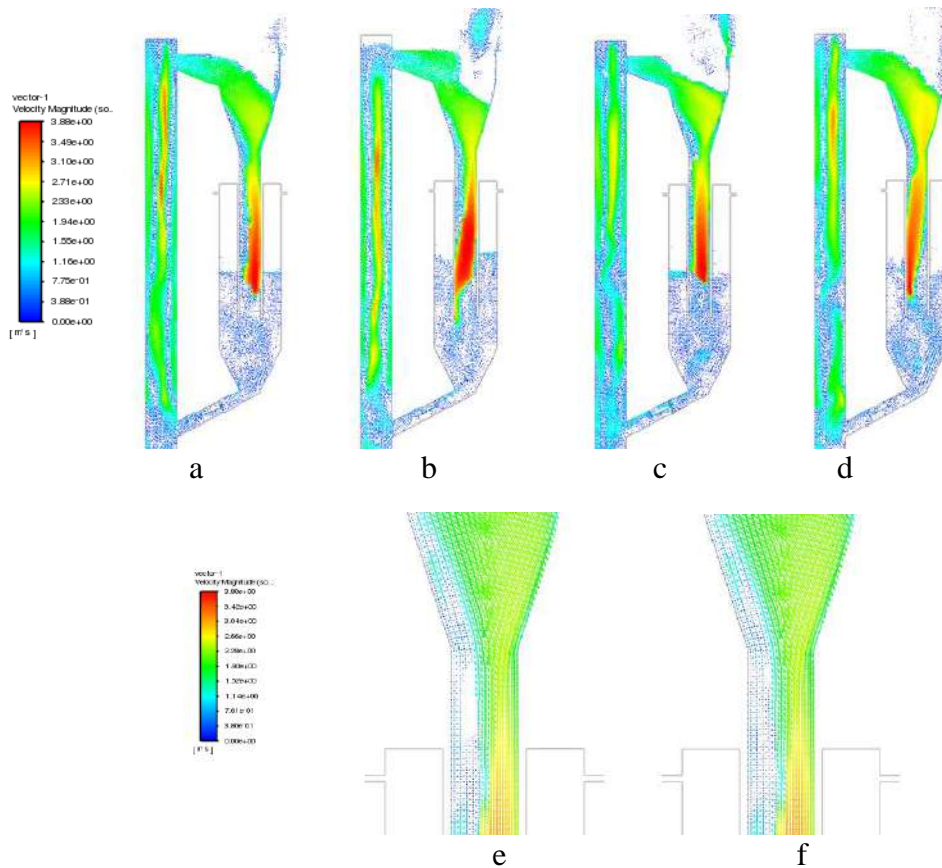


Figure 5 The flow of solids inside the downer

Now, there are two drag models in the system, one for the riser for which the Gidaspow was selected. The other model for the downer is one of the four models mentioned above. Figures 5 a-d are the hydrodynamic contours when the drag models in the riser and downer are (a) Gidaspow-Gidaspow (b) Gidaspow-Wen&Yu (c) Gidaspow-Syamlal-O'Brien (d) Gidaspow-EMMS. With different drag models were used for predicting hydrodynamics in the downer, at 40 seconds, every model showed the solid flow falling to the bottom of the downer, due to gravity. The system, which was modeled by the Gidaspow-Gidaspow drag model (Figure 5a) and by Gidaspow-EMMS drag model (Figure 5d), shows a similar solid flow pattern in the downer. That is, it was found the solids were dense on the wall of the downer and fell to the bottom according to the gravity force. Furthermore, it was found that at the wall of the downer of the reactor, the solid was circulated upwards to the top of the reactor due to the distribution of solids fully filled across the width of the downer. The space for solids to flow down became narrower. The solid collided with each other and caused the increase in solid flow resistance downward. Then, the solid flow changes its direction and speed in the opposite direction.

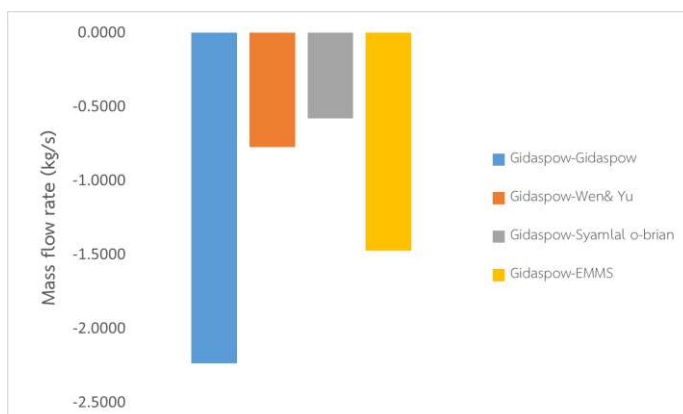


Figure 6 The mass flow rate of the adsorbent at a height of 1 m

Figure 6 shows the mass flow rate of the adsorbent at a height of 1 m, with the minus sign showing the downward direction of the adsorbent. The Gidaspow drag model and the EMMS drag model predict close values to each other, while the Wen & Yu drag model and Syamlal O'brien values are close to among the latter. However, the Gidaspow drag model provides the proper solid circulation rate as mentioned above. Figure 5b shows the model with the Gidaspow - Wen & Yu drag models. It was found that the solid density on the side wall in this model is lower than in other models. It also shows that the solids are moving backward to the top of the downer. The solids are dense on one side of the reactor, resulting in combining solids into a cluster in the downer. (Figure 5e, 5f) Moreover, the agglomeration of solid particles is formed in the lower part of the downer and forms a large gap in the bed. This phenomenon was also observed when using the Gidaspow-Syamlal O'Brien drag model as shown in Figure 5c.

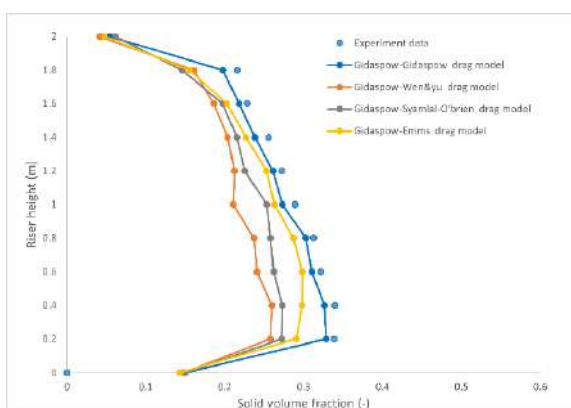


Figure 7 Solid volume fraction along height after change drag model

Because the solids in the system are circulating between the riser and the downer, when the system is at a pseudo-steady state, the solid volume fraction of the riser can be used as a reference condition for validating the model. From Figure 7, it is found that the distribution of solids according to the height of each model is different. Typically, the solids will circulate between the riser and downer due to the pressure difference in both reactors. The simulation results using the Gidaspow and the EMMS drag models in the downer provide the solid volume fraction distribution along the riser similar to the experiment. However, the Gidaspow provides

better results. On the contrary, the model with Wen & Yu drag model and that with Syamlal O'Brien drag model show a large bubble gap in the downer preventing the return flow of the solids to the riser. Thus, the solid distribution is uneven. Thus, the drag model used in the riser and downer of the CFB system will be the Gidaspow-Gidaspow drag model.

### 3.2 Carbon dioxide adsorption and regeneration

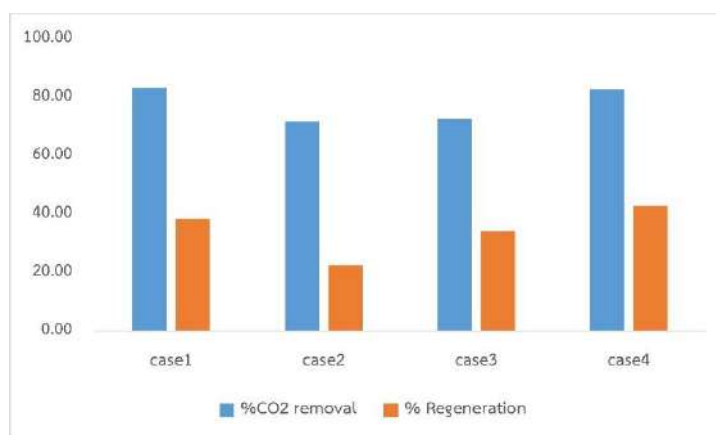


Figure 8 The carbon dioxide gas capture performance.

Figure 8 shows the CO<sub>2</sub> performance in the riser with different drag models for the cases (1) Gidaspow-Gidaspow (2) Gidaspow-Wen&Yu (3) Gidaspow-Syamlal-O'Brien (4) Gidaspow-EMMS. The simulation results show different CO<sub>2</sub> capture and regeneration performances. In this study, the Gidaspow-Gidaspow drag model shows the highest CO<sub>2</sub> removal. The reason is that this model shows the adsorbent well distributed throughout the height of the riser. The sorbent, in this case, potassium carbonate, has become well contact between gas and sorbent and can thoroughly react with carbon dioxide in the system to produce potassium bicarbonate. A large amount of carbon dioxide gas was captured. In the simulation with the Wen&Yu drag model and the Syamlal O'Brien drag model, the solid distribution in the riser side is uneven, resulting in less CO<sub>2</sub> capture performance. Furthermore, a few adsorbents are falling into the downer, resulting in less sorbent to be regenerated. Consequently, the regeneration efficiency is reduced. Thus, proper hydrodynamic prediction is very crucial to predict the adsorption and regeneration performance of the CO<sub>2</sub> capture system.

### 4. Conclusion

The manuscript was to determine the proper drag models to represent the hydrodynamics inside the CFB system for CO<sub>2</sub> capture. Several drag models were used for simulating the gas-solid flow in the downer. It was found that the Gidaspow-Gidaspow drag model for the riser and downer shows the most consistent behavior with the experimental result. The Gidaspow model reduces the buoyancy of solids moving backward in the downer. It can imitate the actual hydrodynamic behavior in the downer. Further, the simulation results also showed that the proper drag model is important not only for the hydrodynamics behavior but also for predicting the CO<sub>2</sub> capture performance.

## References

- [1] Kongkitisupchai, S., & Gidaspow, D. (2013). Carbon dioxide capture using solid sorbents in a fluidized bed with reduced pressure regeneration in a downer. *AIChE Journal*, 59(12), 4519-4537.
- [2] Jaiboon, O. A., Chalermssinsuwan, B., Mekasut, L., & Piumsomboon, P. (2015). Effect of regeneration temperature on the composition and carbon dioxide sorption ability of a K<sub>2</sub>CO<sub>3</sub>/Al<sub>2</sub>O<sub>3</sub> solid sorbent in a bubbling fluidized bed reactor. *Chemical Engineering Communications*, 202(3), 361-365.
- [3] Chaiwang, P., Chalermssinsuwan, B., & Piumsomboon, P. (2017). Two-dimensional CFD simulation of reducing operating pressure effect on the system hydrodynamics in a downer reactor. *Engineering Journal*, 21(2), 133-149.
- [4] Chaiwang, P., Chalermssinsuwan, B., & Piumsomboon, P. (2019). Carbon Dioxide Capture from Flue Gas Using a Potassium-Based Sorbent in a Circulating-Turbulent Fluidized Bed. *Engineering Journal*, 23(5), 13-27.
- [5] Boonprasop, S., Chalermssinsuwan, B., & Piumsomboon, P. (2019). CO<sub>2</sub> sorption and sorbent depressurized regeneration in circulating-turbulent fluidized bed regime. *Journal of Environmental Chemical Engineering*, 7(1), 102928.
- [6] Won, Y., Kim, J. Y., Park, Y. C., Yi, C. K., Nam, H., Woo, J. M., ... & Jo, S. H. (2020). Post-combustion CO<sub>2</sub> capture process in a circulated fluidized bed reactor using 200 kg potassium-based sorbent: The optimization of regeneration condition. *Energy*, 208, 118188.

## Removal of iodine compounds in periodate oxidation of water-soluble carbohydrates

Yingrak Chinkamonthong<sup>1</sup>, Thanawadee Leejarkpai<sup>2</sup>, and Suchata Kirdponpattara<sup>1,\*</sup>

<sup>1</sup> Department of Chemical Engineering, Faculty of Engineering, King Mongkut's University of Technology North Bangkok, Bangkok, Thailand

<sup>2</sup> National Metal and Materials Technology Center (MTEC), National Sciences and Technology Development Agency (NSTDA), Thailand Science Park, Pathum Thani, Thailand  
E-mail: \*suchata.k@eng.kmutnb.ac.th

### Abstract

Periodate oxidation is extensively used to functionalize carbohydrates because of its high efficiency. Free vicinal hydroxyl groups are specifically cleaved and formed aldehyde groups by periodate. However, a crucial issue arises due to the residual iodine compounds (periodate and iodate) in treated carbohydrates, especially for water-soluble carbohydrates (i.e., glucose and starch). To address this issue, two popular techniques have been developed for removing iodine compounds: ethylene glycol (EG) addition and dialysis. This research aims to compare the efficiency of these techniques in removing iodine compounds from tamarind kernel powder (TKP), which is used as a representative of water-soluble carbohydrate polymers. The concentration of residual iodate compounds in oxidized TKP (O-TKP) was measured. Moreover, O-TKP was analyzed using X-ray Diffraction (XRD) and a colorimeter. Results revealed that the effective method for removing iodine compounds was dialysis. Most of the iodine compounds, nearly 95%, were eliminated. Moreover, the color of the final product was light yellow, which was an insignificant change compared with TKP. Dialysis is a potential method to remove the iodine compound residue in the periodate oxidation of water-soluble carbohydrates.

**Keywords:** Carbohydrate; Dialysis; Ethylene glycol; Iodate; Periodate oxidation

### 1. Introduction

Periodate oxidation has been one of the extensive functional modification techniques for beneficial properties and value-added biopolymers. For example, cellulose was modified to dialdehyde cellulose for use as food packaging [2] and biomedical material [3]. Starch was modified to dialdehyde starch to combine with other polymers to produce bioplastic [4]. Dialdehyde chitosan was synthesized by sodium periodate ( $\text{NaIO}_4$ ) oxidation for use as a crosslinking agent in biomedical applications [5]. Sodium alginate was prepared to dialdehyde sodium alginate to bond with dicyandiamide for formaldehyde-free leather [6].

The periodate oxidation reaction involves oxidative cleavage of vicinal diols (-OH) and formation of aldehydes (-COH) or ketones (-COC-) through strong oxidizing agents like  $\text{NaIO}_4$  under low temperatures in an aqueous system [7]. The main product of this reaction is dialdehyde polymers, with iodate ( $\text{IO}_3^-$ ) and excess periodate ( $\text{IO}_4^-$ ) as by-products [8]. Residual iodine compounds can lead to various undesirable reactions, causing contamination of the final product, especially for water-soluble carbohydrates, or appearance change, such as color [9].

Two popular methods, 1) ethylene glycol addition [10-15] and 2) dialysis [16-17], have been widely used to remove the iodine compounds after the reaction. It was claimed that adding ethylene glycol after the functional modification could prevent side reactions and aid in



eliminating residual periodate and formed iodate and formaldehyde [9]. On the other hand, dialysis removes periodate and iodate compounds by transferring the undesired substance molecules through a dialysis tube in a water medium, maintaining the only desired molecule.

Due to the current need for clarity on the best removal method, this research aims to compare the efficiency of two methods - ethylene glycol addition and dialysis - in removing iodine compounds from the periodate oxidation of water-soluble carbohydrates to obtain an aldehyde product-free impurity. Tamarind kernel powder (TKP) was used as a representative of a water-soluble carbohydrate polymer. Oxidized TKP (O-TKP) was obtained after oxidizing with NaIO<sub>4</sub>. The residual iodine compounds in O-TKP, O-TKP added ethylene glycol, and dialyzed O-TKP were qualitatively analyzed by X-ray Diffraction (XRD) and quantitatively measured by titration. Additionally, the color of the final products was characterized.

## 2. Materials and Methods

### 2.1. Materials

Tamarind kernel powder (TKP) was purchased from Freshy Thai Co., Ltd., Thailand. Sodium periodate was purchased from Kemaus (Australia). 99% ethylene glycol and 95% sulfuric acid were purchased from J.T. Baker (US). Sodium iodide was purchased from Ajax Finechem (Australia). Potato starch was purchased from McGarrett (Thailand). Sodium thiosulfate pentahydrate was purchased from Qrec (New Zealand).

### 2.2. Preparation of oxidized-TKP (O-TKP)

A 5 % w/w TKP solution was prepared by slowly dissolving TKP in distilled water at 45 °C, 500 rpm for 60 min. Then, the solution was centrifuged at 5000 rpm for 15 min to remove insoluble solids. Next, the supernatant was reacted with NaIO<sub>4</sub> solution (3.6 g NaIO<sub>4</sub> and 35 g water) at room temperature (RT) in darkness for 2 h [18]. Finally, an O-TKP solution was obtained.

### 2.3. Residual iodine compound removal

For the first method, the O-TKP solution was mixed with 2.5 mL of ethylene glycol at RT, 500 rpm for 30 min. After that, the solution was dried in an oven at 60°C for 24 h to obtain O-TKP(EG). For another method, the O-TKP solution was dialyzed against distilled water using a dialysis tube with MWCO 8000-14000 Da at RT for 3 days. Finally, O-TKP(DL) was obtained after the solution was dried with the same conditions.

### 2.4. Characterization of O-TKP

#### 2.4.1. Determination of residual iodine.

Following the published procedure [9], a 20 g/L sample was mixed with 5 wt% NaI and 1 M H<sub>2</sub>SO<sub>4</sub> in a 250 mL Erlenmeyer flask. Then, a 1 wt% potato starch solution was added to the flask, turning the mixture dark purple. After that, the mixture was diluted with 50 mL water. The mixture was titrated with Na<sub>2</sub>S<sub>2</sub>O<sub>3</sub> until the purple color disappeared. The amount of residual iodate can be calculated using Eq. (1).

$$\text{Residual iodine [g/L]} = \frac{C_{Na_2S_2O_3} \times V_{Na_2S_2O_3} \times MW_{NaIO_3}}{6 \times V_{suspension}} \quad (1)$$

$C_{\text{Na}_2\text{S}_2\text{O}_3}$  and  $V_{\text{Na}_2\text{S}_2\text{O}_3}$  denote the concentration and volume of  $\text{Na}_2\text{S}_2\text{O}_3$  used for titration.  $V_{\text{suspension}}$  represents the volume of suspension.

#### 2.4.2. X-ray Diffraction (XRD).

The samples were analyzed using XRD to identify the types of each substance. The analysis was conducted using the Smart Lab Studio II (Rigaku, US) in the  $2\theta$  ranges from  $5^\circ$  to  $60^\circ$  under 40 kV and 100 mA. The solid prepared from the drying supernatant of the TKP solution was used as a control.

#### 2.4.3. Color.

The color of the sample was tested by a Color Quest Spectrophotometer (HunterLab, US) in  $L^*$  for lightness,  $a^*$  for redness, and  $b^*$  for yellowness. The overall color difference ( $\Delta E$ ) value can be calculated from Eq. (2).

$$\Delta E = \sqrt{(L^*_1 - L^*_2)^2 + (a^*_1 - a^*_2)^2 + (b^*_1 - b^*_2)^2} \quad (2)$$

### 3. Results and Discussion

#### 3.1. Residual iodine compound

The residual iodine compound was quantitatively determined by titration. For the chemical reaction of titration,  $\text{IO}_3^-$  and  $\text{IO}_4^-$  in the sample reacted with  $\text{I}^-$  of NaI to form  $\text{I}_2$ . Then, the mixture color became dark purple after adding starch solution.  $\text{I}_2$  reduction occurred during titration of the mixture by  $\text{Na}_2\text{S}_2\text{O}_3$  solution. Thiosulfate ( $\text{S}_2\text{O}_3^{2-}$ ) reduced  $\text{I}_2$  to  $\text{I}^-$ , resulting in the disappearance of the purple color. Concentrations of iodine compound in the sample are summarized in Table 1. The result demonstrated that high residual iodine concentration in O-TKP confirmed that  $\text{IO}_3^-$  was generated as a by-product and  $\text{IO}_4^-$  might be excess and remain in the final product. For O-TKP added ethylene glycol, the iodine compounds of O-TKP(EG) were a bit lower than O-TKP. Wu et al. (1985) [19] reported that periodate could oxidize ethylene glycol to form iodate and formaldehyde. Consequently, adding ethylene glycol was unable to remove residual iodine compounds because ethylene glycol only utilized the excess periodate and generated more iodate. Moreover, O-TKP(EG) was contaminated with formaldehyde. In contrast, the iodine compounds were potentially removed by the dialysis technique.

Table 1. Residual iodine compound.

Sample	Iodine compounds (g/L)
O-TKP	$7.60 \pm 0.13$
O-TKP(EG)	$7.24 \pm 0.43$
O-TKP(DL)	$0.40 \pm 0.01$

#### 3.2. X-ray diffraction (XRD)

From the XRD analysis (Fig. 1), it was shown that the XRD pattern of the control presenting a typical peak of approximately 2 at  $20^\circ$  was similar to those found in galactoxyloglucan extracted from tamarind seed [20] and xyloglucan extracted from *Hymenaea*

*courbaril* var. *courbaril* seeds [21]. The compositions of TKP are 65-72% xyloglucan, 11-23% moisture, 15-21% protein, 4-16% fat/oil, 3-8% crude fiber, and 2-4% total ash [22]., which only xyloglucan is water soluble. Therefore, the main composition in the control was xyloglucan. O-TKP(DL) illustrated the XRD pattern similar to that of the control, which was consistent with the concentration of iodine compounds. The diols cleavage and aldehydes formation in the xyloglucan polymer chain did not affect the XRD pattern. It was well agreed with the finding of Wannous et al. (2022) [23] that starch and dialdehyde starch had the same XRD patterns. All peaks marked with triangles of O-TKP could be attributed to iodate, according to [24]. The XRD pattern of O-TKP(EG) presented all the peaks of O-TKP with lower intensity. It could be concluded that adding ethylene glycol could not eliminate iodine compounds out of O-TKP.

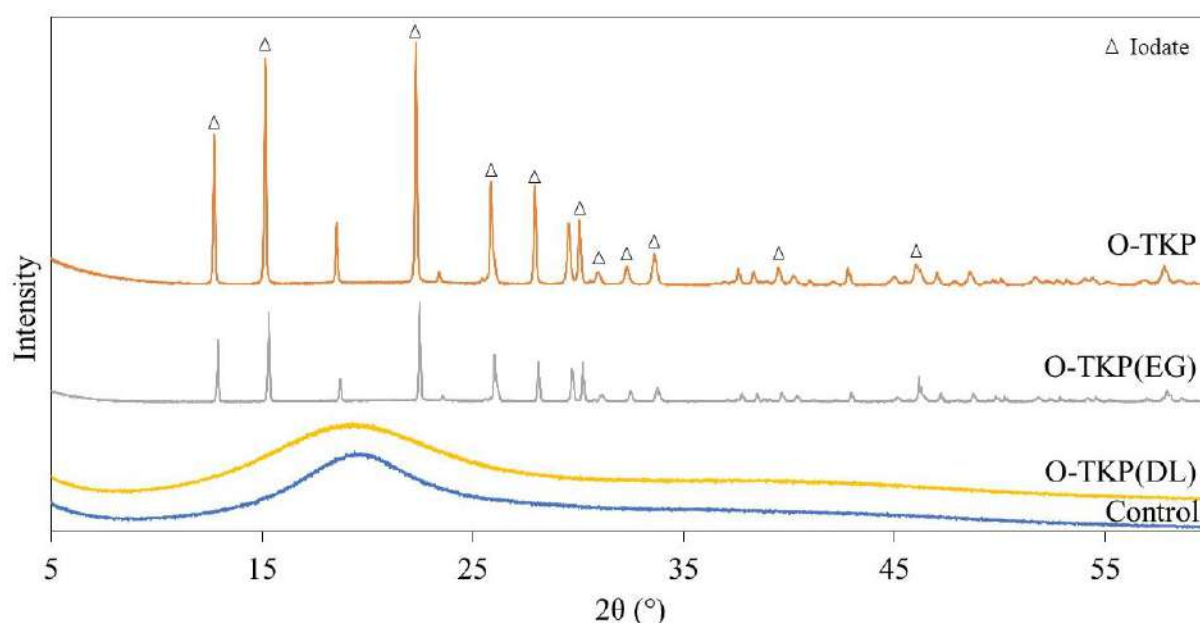


Fig. 1 XRD patterns of the control, O-TKP, O-TKP(EG), and O-TKP(DL).

### 3.3. Color

Images of the samples are shown in Fig. 2. TKP originally was off-white like other seed starch powder. After TKP was oxidized with NaIO<sub>4</sub>, O-TKP demonstrated yellowish. By adding ethylene glycol, O-TKP(EG) was yellowish-brown. A light yellow color was observed in O-TKP(DL). After the samples were stored in a desiccator for about 30 days, it was noticed that the color of O-TKP and O-TKP(EG) changed to brighter yellow and dark brown, respectively. Impurities such as iodate and periodate could induce side reactions during storage. Especially for O-TKP(EG), as mentioned before, ethylene glycol was oxidized by the excess periodate to generate formaldehyde [25], which might cause the yellowish-brown color to turn dark brown.

Moreover, the color of the sample was measured and presented in the CIELAB system (Table 2). The L\* value indicated that O-TKP had the most lightness, which was opposed to the images in Fig. 2. It might be because the transparency presented in O-TKP(DL) only affected the measurement. However, the CIELAB results of TKP, O-TKP, and O-TKP(EG) were reliable. Since the  $\Delta E$  value was calculated using TKP as a control, the value represented the color change of the sample against TKP. The  $\Delta E$  values were well consistent with the

images (excepting that of O-TKP(DL)) that O-TKP(EG) had the most significant color change compared to that of TKP.



Fig. 2 Images of the samples after drying at 60° C and storing for 30 days (small circle images).

Table 2. Colorimetric results.

Sample	L*	a*	b*	ΔE
TKP	71.0 ± 0.9	4.3 ± 0.3	21.1 ± 0.3	0
O-TKP	74.6 ± 0.1	4.0 ± 0.1	24.7 ± 0.2	5.0 ± 0.4
O-TKP(EG)	64.4 ± 0.1	8.3 ± 0.1	43.8 ± 0.1	24.0 ± 0.6
O-TKP(DL)	29.4 ± 1.3	-0.8 ± 0.1	4.6 ± 0.3	45.1 ± 2.0

#### 4. Conclusions

Upon removal of the residual iodine compounds from O-TKP, dialysis was the potential method. Most iodine compounds were removed without affecting the color of the final product. Formaldehyde might be the main reason for color change in O-TKP(EG). The qualitative iodine compound was well agreed with that quantitative analysis. It is still challenging to eliminate all impurities from oxidized water-soluble carbohydrates with a shorter period.

#### 5. References

- [1] Kristiansen, K. A., Potthast, A., and Christensen, B. E. (2010). Periodate oxidation of polysaccharides for modification of chemical and physical properties. *Carbohydrate Research*, 1264–1271.
- [2] Plappert, S. F., Quraishi, S., Pircher, N., Mikkonen, K. S., Veigel, S., Klinger, K. M., Potthast, A., Rosenau, T., and Liebner, F. W. (2018). Transparent, Flexible, and Strong 2,3- Dialdehyde Cellulose Films with High Oxygen Barrier Properties. *Biomacromolecules*, 2969-2978.
- [3] Zhang, L., Ge, H., Xu, M., Cao, J., and Dai, Y. (2017). Physicochemical properties, antioxidant and antibacterial activities of dialdehyde microcrystalline cellulose. *Cellulose*, 2287-2298.

- [4] Zhang, H., Su, Z., and Wang, X. (2022). Starch-Based Rehealable and Degradable Bioplastic Enabled by Dynamic Imine Chemistry. *ACS Sustainable Chemistry & Engineering*, 8650-8657.
- [5] Wegrzynowska-Drzymalska, K., Grebicka, P., Mlynarczyk, D. T., Chelminiak-Dudkiewicz, D., Kaczmarek, H., Goslinski, T., and Ziegler-Borowska, M. (2020). Crosslinking of Chitosan with Dialdehyde Chitosan as a New Approach for Biomedical Applications. *Materials*.
- [6] Ding, W., Wang, Y., Sun, J., Bao, L., and Pang, X. (2020). Dialdehyde sodium alginate bonded dicyandiamide for formaldehyde-free leather production with enhanced properties. *Carbohydrate Polymers*.
- [7] Pandeirada, C. O., Achterweust, M., Janssen, H.-G., Schols, H. A., and Westphal, Y. (2022). Periodate oxidation of plant polysaccharides provides polysaccharide-specific oligosaccharides. *Carbohydrate Polymers*.
- [8] Kara, H. T., Anshebo, S. T., Sabir, F. K., and Workineh, G. A. (2021). Removal of Methylene Blue Dye from Wastewater Using Periodiated Modified Nanocellulose. *International Journal of Chemical Engineering*.
- [9] Simon, J., Fliri, L., Drexler, F., Bacher, M., Sapkota, J., Ristolainen, M., Hummel, M., Potthast, A., and Rosenau, T. (2023). Debugging periodate oxidation of cellulose: Why following the common protocol of quenching excess periodate with glycol is a bad idea. *Carbohydrate Polymers*.
- [10] Palasingh, C., Nakayama, K., Abik, F., Mikkonen, K. S., Evenas, L., Strom, A., and Nypelo, T. (2022). Modification of xylan via an oxidation-reduction reaction. *Carbohydrate Polymers*.
- [11] Brabham, R. L., Keenan, T., Husken, A., Bilsborrow, J., McBerney, R., Kumar, V., Turnbull, W. B., and Fascione, M. A. (2020). Rapid sodium periodate cleavage of an unnatural amino acid enables unmasking of a highly reactive  $\alpha$ -oxo aldehyde for protein bioconjugation. *Organic & Biomolecular Chemistry*.
- [12] Rafiee, F., Abbaspour, M., and Ziarani, G. M. (2022). Immobilization of vitamin B1 on the magnetic dialdehyde starch as an efficient carbene-type support for the copper complexation and its catalytic activity examination. *Reactive and Functional Polymers*.
- [13] Kristiansen, K. A., Dalheim, M. Ø., and Christensen, B. E. (2013). Periodate oxidation and macromolecular compaction of hyaluronan. *Pure and Applied Chemistry*, 1893-1900.
- [14] Sickinga, M. C., Kline, T., Whitehead, M. A., and Ven, T. G. (2022). One-pot eco-friendly oxidative synthesis of imine carboxymethyl dialdehyde cellulosic fibers. *Cellulose*, 799-815.
- [15] Vold, I. M., and Christensen, B. E. (2005). Periodate oxidation of chitosans with different chemical compositions. *Carbohydrate Research*, 679-684.
- [16] Amer, H., Nypelö, T., Sulaeva, I., Bacher, M., Henniges, U., Potthast, A., and Rosenau, T. (2016). Synthesis and Characterization of Periodate-Oxidized Polysaccharides: Dialdehyde Xylan (DAX). *Biomacromolecules*, 2972-2980.
- [17] Siebe, H. S., Sardjan, A. S., Maßmann, S. C., Flapper, J., Berg, K. J., Eisink, N. N., Kentgens, A. P. M., Feringa, B. L., Kumar, A., and Browne, W. R. (2023). Formation of substituted dioxanes in the oxidation of gum arabic with periodate. *Green Chemistry*, 4058-4066.

- [18] Kochumalayil, J. J., Zhou, Q., Kasai, W., and Berglund, L. A. (2013). Regioselective modification of a xyloglucan hemicellulose for high-performance biopolymer barrier films. *Carbohydrate Polymers* 93, 466-472.
- [19] Wu, Y.-P., Miller, L. G., and Danielson, N. D. (1985). Determination of Ethylene Glycol Using Periodate Oxidation and Liquid Chromatography. *The Analyst*.
- [20] Kaur, H., Yadav, S., Ahuja, M., and Dilbaghi, N. (2012). Synthesis, characterization and evaluation of thiolated tamarind seed polysaccharide as a mucoadhesive polymer. *Carbohydrate Polymers*, 1543-1549.
- [21] Arruda, I. R., Albuquerque, P. B., Santos, G. R., Silva, A. G., Mourão, P. A., Correia, M. T., Vicente, A. A., and Carneiro-da-Cunha, M. G. (2015). Structure and rheological properties of a xyloglucan extracted from *Hymenaea courbaril* var. *courbaril* seeds. *International Journal of Biological Macromolecules*, 31-38.
- [22] Kumar, C. S., and Bhattacharya, S. (2008). Tamarind Seed: Properties, Processing and Utilization. *Critical Reviews in Food Science and Nutrition*, 1-20.
- [23] Wannous, A., Milaneh, S., Said, M., and Atassi, Y. (2022). New approach for starch dialdehyde preparation using microwave irradiation for removal of heavy metal ions from water. *SN Applied Sciences*.
- [24] Zanoletti, A., Vassura, I., Venturini, E., Monai, M., Montini, T., Federici, S., Zacco, A., Treccani, L., and Bontempi, E. (2018). A New Porous Hybrid Material Derived From Silica Fume and Alginate for Sustainable Pollutants Reduction. *Frontiers in Chemistry*.
- [25] Rajagopal, G., and Ramakrishnan, S. (1975). A New Method for Estimation of Ethylene Glycol in Biological Material. *ANALYTICAL BIOCHEMISTRY*, 132-136.

## Performance Analysis and Optimization of Sorption-Enhanced Chemical Looping Oxidative Steam Reforming of Methanol for High-Temperature Proton Exchange Membrane Fuel Cell

Supawat Taweekayujan, Phuett Prasertcharoensuk, and Amornchai Arpornwichanop\*

Center of Excellence in Process and Energy Systems Engineering, Department of Chemical Engineering,  
Faculty of Engineering, Chulalongkorn University, Bangkok 10330, Thailand  
E-mail: Amornchai.a@chula.ac.th

### Abstract

Hydrogen is widely regarded as a promising energy carrier for sustainable energy systems, particularly in achieving high efficiency through fuel cell applications. However, the storage of hydrogen poses significant challenges in the development of a hydrogen-based economy. Alternatively, due to its distinctive properties, methanol emerges as an attractive hydrogen carrier. This study explores an integrated system that combines sorption-enhanced chemical-looping oxidative steam methanol-reforming (SECL-OSRM), utilizing CuO-MgO as a bi-functional material, with a high-temperature proton exchange membrane fuel cell (HT-PEMFC). The integrated process simulation employs a thermodynamic model in Aspen Plus. A comprehensive parametric analysis of the proposed system is conducted to gain insights into the impact of the mole ratio of CuO/CH<sub>3</sub>OH, MgO/CH<sub>3</sub>OH on SECL-OSRM performance parameters including methanol conversion, hydrogen production concentration, carbon monoxide concentration, and hydrogen production rate. Additionally, the effects of operating temperature and current density are considered to assess the performance of the HT-PEMFC. The findings indicate that the SECL-OSRM system enhances the production of high-purity hydrogen, achieves low CO concentrations at lower than 0.3 vol.%, and high production flowrate at 0.5, 0.5 mole ratio of the CuO/CH<sub>3</sub>OH, MgO/CH<sub>3</sub>OH, which is suitable for HT-PEMFC operation. Furthermore, SECL-OSRM has the capability to achieve auto-thermal operation and can be enhanced by harnessing waste heat from the fuel cell. The increment of fuel cell temperature and current density are favorable for improving net power output. The proposed system presents a maximum system total efficiency at 41.5%.

**Keywords:** Sorption-enhanced chemical looping reforming; Methanol; High-temperature proton exchange membrane fuel cell; Performance optimization; Exergy analysis

### 1. Introduction

As fossil fuel reserves diminish and environmental degradation becomes more pronounced, global interest is growing in harnessing renewable energy sources. Hydrogen is commonly seen as a prospective energy carrier for sustainable energy due to its capacity to be generated from diverse sources and its versatile applications, particularly in fuel cell technology (Li et al., 2023). However, the need for elevated pressure in compressed hydrogen storage, involving costly materials, and extremely low temperatures for liquefaction has posed challenges for secure storage, expenses, and transportation (Herdem et al., 2019; Sun & Sun, 2020). Therefore, alternative fuels (natural gas, alcohol, etc.) are attractive to use in fuel reforming (Li et al., 2023).

Methanol emerges as an attractive hydrogen carrier because it has several advantages. It exists in a liquid phase under standard atmospheric pressure and temperature, exhibiting a higher volumetric energy density. Its elevated H/C ratio allows for a greater hydrogen content in the reformat gas, enabling the use of lower reforming temperatures due to the absence of a robust C-C bond. The resulting reformat gas contains minimal sulfur and low CO content. Additionally, methanol can be derived from both renewable and non-renewable sources. (Herdem et al., 2019; Li et al., 2021; Li et al., 2023). Main approaches for hydrogen production from methanol are steam reforming of methanol (SRM), partial oxidation of methanol (POM), oxidative steam reforming of methanol (OSRM), sorption enhanced steam methanol reforming (SE-SRM), and sorption-enhanced chemical-looping oxidative steam methanol reforming (SECL-OSRM) (Liu et al., 2020; Sun & Sun, 2020). The SRM method is extensively researched as it offers relatively high hydrogen concentration and operates at a lower reforming temperature. Nevertheless, CO production is a concern during SRM, and even minimal concentrations of CO can lead to catalyst deactivation at the anode fuel cell. Additionally, SRM requires external heat to occur the reaction. Therefore, SECL-SRM combined a suitable proportion of endothermic SRM reaction and exothermic POM reaction which could make the auto-thermal condition (no external heat) (Sun & Sun, 2020). Furthermore, SECL-SEM has absorbent which can promote the equilibrium of forward water-gas shift reaction by absorbing carbon dioxide. SE-SEM achieves low CO concentrations, which is suitable for high-temperature proton exchange membrane fuel cell (HT-PEMFC) without external purify system.

Additionally, fuel cells generally operate at about 40-60% electrical efficiency in continuous operation, and nearly half of the chemical energy is lost as heat to the environment. It has increasingly become a focus of attention to improve the thermal efficiency of fuel cells through waste heat recovery, which can be used for self-serving to increasing the feasible region operating. Therefore, our research aims to simulate an integrated system that combines sorption-enhanced chemical-looping oxidative steam methanol-reforming (SECL-OSRM) with a high-temperature proton exchange membrane fuel cell (HT-PEMFC) in Aspen Plus. This integration aims to address challenges in hydrogen storage by utilizing methanol as a hydrogen carrier and improve the total efficiency. For the first section, the impact of the CuO/CH<sub>3</sub>OH, MgO/CH<sub>3</sub>OH ratio on SECL-OSRM performance parameters including methanol conversion, hydrogen concentration, and carbon monoxide concentration, hydrogen production rate, and heat balance of fuel reactor and regeneration to find the optimal region for operating. Furthermore, the effects of operating temperature and current density are considered to define the system performance.

## 2. Methodology

### 2.1 System Modules

#### 2.1.1 SECL-OSRM Subsystem

This section is composed of two main reactors, which are fuel reactor and regeneration reactor, for supply rich-hydrogen reformat gas to HT-PEMFC by methanol reforming. The SECL-OSRM reaction is simulated by utilizing Gibb free energy minimization method in RGIBBS unit. The reaction in a fuel reactor can be defined as steam reforming ( $CH_3OH + H_2O \rightarrow CO_2 + 3H_2$ ), partial oxidation ( $CH_3OH + CuO \rightarrow CO_2 + 2H_2 + 3Cu$ ), complete oxidation ( $CH_3OH + 3CuO \rightarrow CO_2 + 2H_2O + 3Cu$ ), decomposition of methanol



( $CH_3OH \rightarrow CO + 2H_2$ ), water-gas shift ( $CO + H_2O \rightarrow CO_2 + H_2$ ), copper oxide reduction ( $CuO + H_2 \rightarrow Cu + H_2O$ ), copper oxide oxidation ( $CO + CuO \rightarrow CO_2 + Cu$ ),  $CO_2$  sorption ( $MgO + CO_2 \rightarrow MgCO_3$ ). Furthermore, other reactions including dehydration ( $2CH_3OH \rightarrow CH_3OCH_3 + H_2O$  and  $3CH_3OH \rightarrow CH_3OCH_3 + CO_2 + 3H_2$ ), dehydrogenation ( $2CH_3OH \rightarrow HCOOCH_3 + 2H_2$ ), formaldehyde synthesis ( $CH_3OH \rightarrow HCHO + H_2$ ). For the regeneration reactor, the reactions include Copper oxidation ( $2Cu + O_2 \rightarrow 2CuO$ ) and  $CO_2$  desorption ( $MgCO_3 \rightarrow MgO + CO_2$ ).

### 2.1.2 HT-PEMFC Subsystem

HT-PEMFC generates electricity by electrochemical reactions using hydrogen and oxygen in the anode and cathode catalyst layers. The model is simulated in Aspen Plus with the assumption that fuel cell is operated under steady state, isothermal, and isobaric conditions. The main components are composed of an anode side and cathode side. The anode side was modeled by a spilt block which defines the amount of utilizing hydrogen. The remaining hydrogen enters the cathode to react with oxygen from air. For the cathode side, RSTOIC reactor is used to simulate the reaction. The products from the HT-PEMFC are electricity, heat, and steam. Furthermore, the calculation block is used to calculate the electricity properties by Fortran that including cell voltage, reversible cell voltage, the activation loss, ohmic loss, temperature dependence of exchange current density and membrane conductivity, concentration loss, and limiting current density calculation. The operation conditions and parameters of the model were developed by Shamardina et. al. (Shamardina et al., 2010).

## 2.2 System Description

The flowsheet of the integrated system developed in ASPEN plus by Peng-Robinson method as shown in Fig. 1. The configuration of network heat exchanger is developed from sorption-enhanced steam methane reforming design (Collins-Martinez et al., 2020). Firstly, the feed (L), including mixture of methanol and water, enters preheated section with heat exchanger HX-1 and HX-2 by heat of gaseous out. Both of heat exchangers are fixed the hot outlet temperature at 80 °C. The preheated feed is finally evaporated in EVAP by additional heat generation from fuel cell. For fuel reactors (FR), the CuO, MgO, and feed are entered to produce  $H_2$ -rich gas with low CO at 220 °C temperature. The solids in gaseous product are separated by cyclone (CYC1). The consumed solid is regenerated in regeneration reactor with air at 410 °C by preheated air. The fresh air, including reacted air in regeneration reactor and reacted air in cathode side, are preheated in heat exchanger HX-3 and HX-4 with gaseous out from both cyclone to 400 °C. The  $H_2$ -rich gas is fed to fuel cell for electricity generation. For HT-PEMFC section,  $H_2$ -rich gas and spilt air enter to compressor and heater for adjust condition to the operating pressure and temperature (1.2 atm and 140-180°C) before it is fed to the ANODE and CATHODE site respectively. The consumed  $H_2$  is separated from anode proportionally with operating current density to cathode side to occur electrochemical reaction. Unutilized  $H_2$  is recycled to the anode through a controlled, constant feeding of fresh feed and recycled feed.

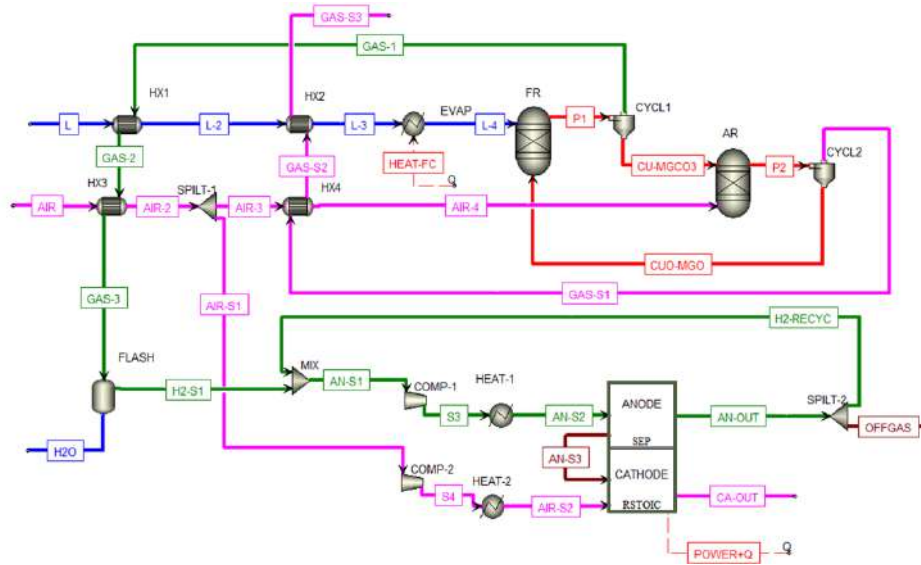


Fig. 1 The simulation flowsheet of the integrated system.

### 2.3 Performance characteristics

Fuel cell efficiency, total system efficiency are considered during the simulation, which are given in Eq. (1) and (2).

$$\text{Fuel cell efficiency: } \eta_{fuel-cell} = \frac{W_{electrical}}{F_{H_2,utilized} \cdot LHV_{H_2}} \times 100\% \quad (1)$$

$$\text{Total system efficiency: } \eta_{system} = \frac{W_{net} + Q_{recovery}}{F_{fuel} \cdot LHV_{fuel}} \times 100\% \quad (2)$$

where  $W_{electrical}$  is the stack power generation from fuel cell,  $F_{H_2,utilized}$  is flowrate of utilized hydrogen,  $LHV_{H_2}$  is the lower heating value of hydrogen,  $W_{net}$  is net output power of the system,  $Q_{recovery}$  is the recoverable heat from fuel cell to evaporator,  $F_{fuel}$  is the flowrate of the methanol,  $LHV_{fuel}$  is the lower heating value of the methanol.

## 3. Results & Discussion

### 3.1 Model Validation

The SECL-OSRM module can be validated by Li et al. research (Li et al., 2020), which proposed Cu-MgO/Al<sub>2</sub>O<sub>3</sub> bifunctional catalyst as enhanced sorption capacity and reaction activity. The results showed that 8 wt% Cu-MgO/Al<sub>2</sub>O<sub>3</sub> is the superior performance at 99.3% of H<sub>2</sub> selectivity and less than 0.15% of CO selectivity over 10 repeated cycles, the validation is shown in Fig. 2(a). And for HT-PEMFC model, it has been validated with experiment data by Shamardina et. al. (Shamardina et al., 2010). Their experiment used 0.04 cm of the gas diffusion layer thickness, 0.006 cm of membrane thickness, and they operated at 120-180 °C and 1 atm. The model prediction is good agreement with experiment data as shown in the polarization curve in Fig. 2(b)

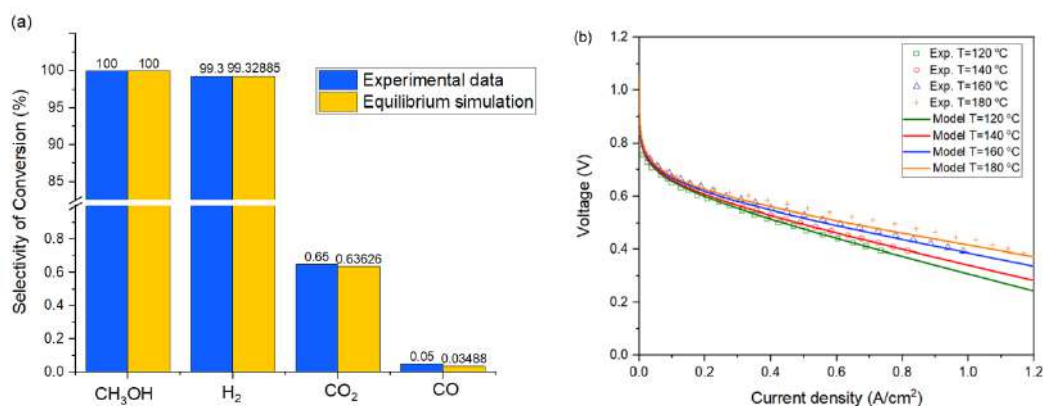


Fig. 2 (a) Comparison between predictions and experiment results of (a) SECL-OSRM (at steam to methanol ratio = 1.3, reforming temperature = 220 °C); (b) HT-PEMFC model.

### 3.2 Effect of CuO/CH<sub>3</sub>OH and MgO/CH<sub>3</sub>OH mole ratio

The effect of CuO/CH<sub>3</sub>OH and MgO/CH<sub>3</sub>OH mole ratio on CH<sub>3</sub>OH conversion, H<sub>2</sub> concentration, CO concentration, heat duty of fuel reactor, heat duty of regeneration reactor are shown in Fig. 3. As Fig. 3(a), the result show that the complete conversion of CH<sub>3</sub>OH (>0.999). As Fig 3(b), the H<sub>2</sub> concentration is higher when increasing mole ratio of MgO/CH<sub>3</sub>OH. However, H<sub>2</sub> concentration decrease is found when CuO/CH<sub>3</sub>OH mole ratio increases. It might be because of the increase in copper oxide oxidation reaction, which consumes the amount of H<sub>2</sub>. For the normal operation of HT-PEMFC the H<sub>2</sub> concentration should be higher than 50 vol.%. So that the left side of the green line displays the appropriate ranges of concentration (higher than 60 vol.%). These ranges ensure that after passing through the flash drum unit to remove impurities or unreacted substances, the resulting volume reaches 95 vol.% (free-unreacted substances).

Furthermore, due to the poisoning of CO on fuel cell platinum-based catalyst. Therefore, the CO concentration must be controlled at lower than 0.3 vol.% (Liu et al., 2020). As shown in Fig. 3(c), higher mole ratio of MgO/CH<sub>3</sub>OH in system can reduce the CO concentration because MgO can adsorb the CO<sub>2</sub> in system, which increase shift forward of water-gas shift equilibrium. Therefore, feasible mole ratio of CuO/CH<sub>3</sub>OH and MgO/CH<sub>3</sub>OH to avoid deactivation of fuel cell catalyst are shown in the right-side area of the green line.

Autothermal operation requires the overall process to be able to operate without the external heat input. This condition occurs when heat duty is negative. In other words, when heat generation of reaction is higher than heat require. Therefore, Fig. 3(d-e) shows the heat duty of fuel reactor (Q1) and regeneration reactor (Q2) in various mole ratio of CuO/CH<sub>3</sub>OH and MgO/CH<sub>3</sub>OH. The results show that the recovery heat from fuel cell to evaporator is sufficient to make fuel reactor an exothermic condition (autothermal condition) in all operating conditions. In addition, the duty of fuel reactor is more negative when the mole ratio of CuO/CH<sub>3</sub>OH and MgO/CH<sub>3</sub>OH increases because of the higher amount of heat generation from exothermic reaction, which are partial oxidation, complete oxidation, and CO<sub>2</sub> adsorption. For the duty of regeneration reactor, the negative heat duty is increasing when increase the mole ratio of CuO/CH<sub>3</sub>OH because the copper oxidation with air is an exothermic reaction. In other

hand, the higher MgO/CH<sub>3</sub>OH mole ratio makes the positive heat duty because the CO<sub>2</sub> desorption in air reactor is the endothermic reaction.

After comprehensive consideration of the requirement of each parameter, the feasible area is illustrated in terms of H<sub>2</sub> production flowrate in Fig. 3(f). It can be concluded that the suitable operating conditions are inside the green line. The selected point is 0.5, 0.5 CuO/CH<sub>3</sub>OH and MgO/CH<sub>3</sub>OH mole ratio, which give the high H<sub>2</sub> production flowrate, high H<sub>2</sub> concentration, low CO concentration, and auto-thermal conditions.

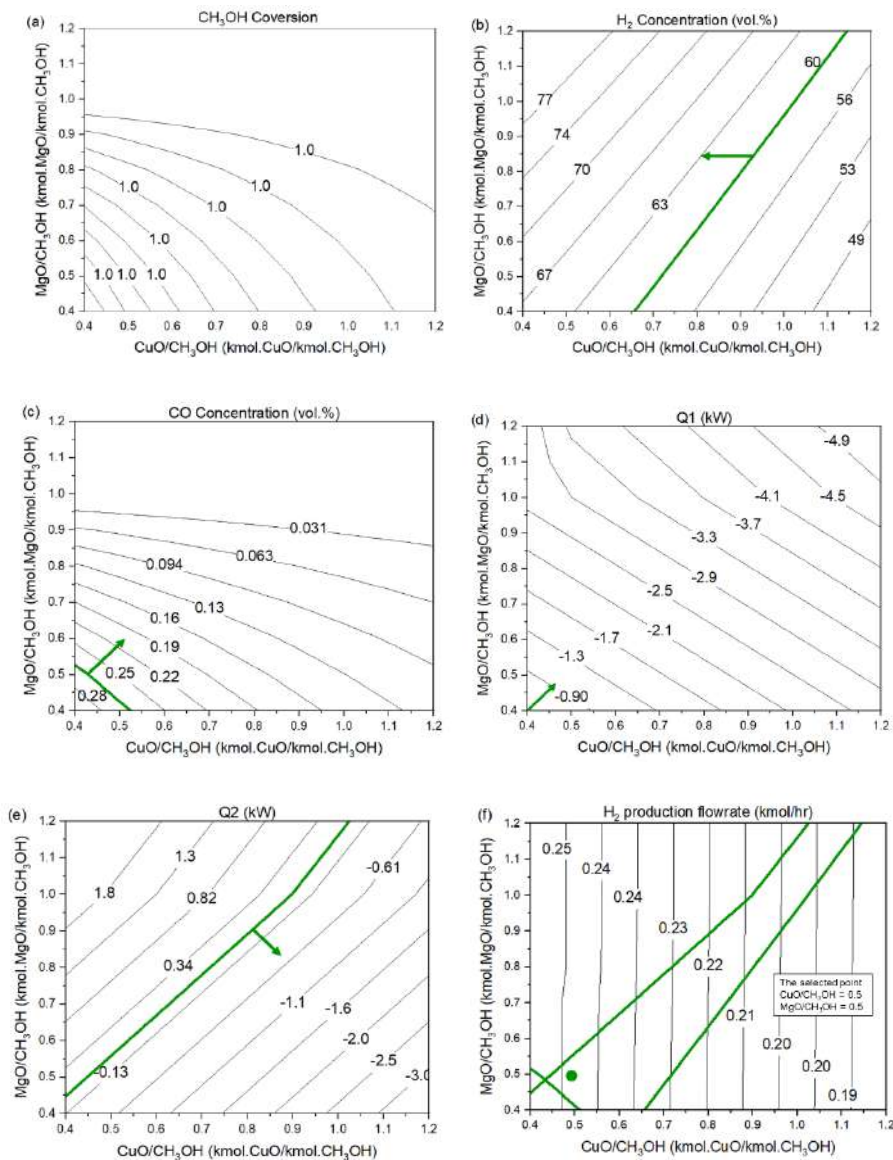


Fig. 3 Effect of CuO/CH<sub>3</sub>OH and MgO/CH<sub>3</sub>OH mole ratio on (a) CH<sub>3</sub>OH conversion; (b) H<sub>2</sub> concentration; (c) CO concentration; (d) heat balance of fuel reactor; (e) heat balance of regeneration reactor; (f) feasible area and the selected operating point (CH<sub>3</sub>OH feed rate = 0.1 kmol/h, FR temperature = 220 °C, AR temperature = 410 °C, H<sub>2</sub>O/CH<sub>3</sub>OH mole ratio = 1.3).

### 3.3 Effect of H<sub>2</sub>O/CH<sub>3</sub>OH and reforming temperature

The effect of H<sub>2</sub>O/CH<sub>3</sub>OH and reforming temperature on mole ratio on H<sub>2</sub> concentration, CO concentration, heat duty of fuel reactor, and H<sub>2</sub> production flowrate are shown in Fig. 4. The results show that higher mole ratio of H<sub>2</sub>O/CH<sub>3</sub>OH decreases the H<sub>2</sub> concentration as shown in Fig. 4(a) because the unreacted water with methanol is more remain in the gas production. Furthermore, the rising of H<sub>2</sub>O/CH<sub>3</sub>OH will increase the energy evaporation in fuel reactors (less negative), which is presented in Fig. 4(c). Therefore, the suitable mole ratio of H<sub>2</sub>O/CH<sub>3</sub>OH should be below 1.5. In terms of reforming temperature, increasing fuel reactor temperature will increase the CO concentration from higher methanol decomposition in fuel reactor as depicted in Fig. 4(b). However, raising reforming temperature will make higher exothermic conditions for regeneration reactor as shown in Fig 4(c). Finally, feasible operating conditions are shown in the green area in Fig. 4(d), and the selected point is 1.3 of H<sub>2</sub>O/CH<sub>3</sub>OH mole ratio and 220°C reforming temperature.

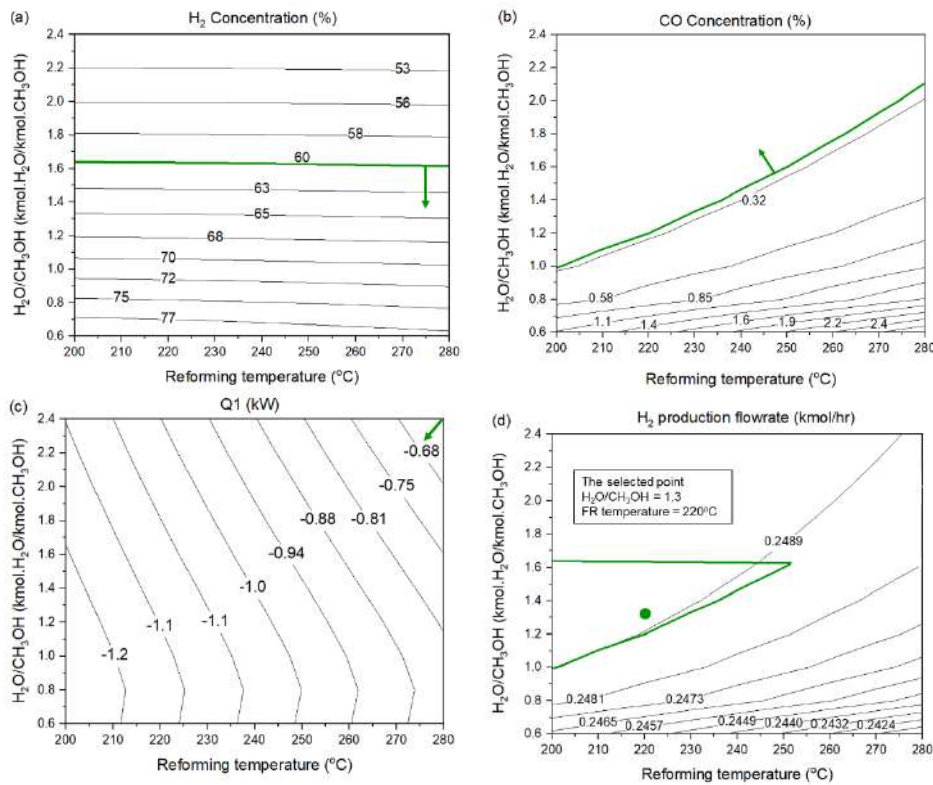


Fig. 4 Effect of H<sub>2</sub>O/CH<sub>3</sub>OH and Temperature on (a) H<sub>2</sub> concentration; (b) CO concentration; (c) heat balance of fuel reactor; (f) feasible area and the selected operating point (CH<sub>3</sub>OH feed rate = 0.1 kmol/h, AR temperature = 410 °C, CuO/CH<sub>3</sub>OH = 0.5, and MgO/CH<sub>3</sub>OH = 0.5).

### 3.4 Performance of HT-PEMFC at different conditions

Figure 5 illustrates the impact of fuel cell temperature and current density. The model operates with a stack consisting of 45 fuel cells, each having a 300 cm<sup>2</sup> active area. Hydrogen (H<sub>2</sub>) consumption is determined proportionally to the current density, and specific CuO/CH<sub>3</sub>OH and MgO/CH<sub>3</sub>OH mole ratios are utilized at selected points within the system.

For a fixed current density, the system output power and fuel cell efficiency increased slightly with an increase in the operating temperature as shown in Fig. 4(a,c). This was caused by reducing the ohmic overvoltage loss, and enhancing the exchange current density, consequently decreasing the activation overpotential. The increasing current density could significantly increase both of stack power and heat generation as depicted in Fig 4(a-b), but the fuel cell efficiency decreased. This phenomenon occurs because higher levels of current density necessitate greater utilization of H<sub>2</sub>. However, the increase in power generation is not directly proportional to the increase in H<sub>2</sub> usage according to Eq. (1). This discrepancy stems from energy dissipation in the form of ohmic loss and concentration loss within the fuel cell, evident in the increment of heat generation illustrated in Fig. 4(b). For system total efficiency, the increment of temperature and current density increase the system total efficiency according to Eq. (2). Therefore, The maximum system total efficiency of 41.5% was achieved for the proposed system at high current density (above 0.9 A/cm<sup>2</sup>) and high temperature (above 170 °C).

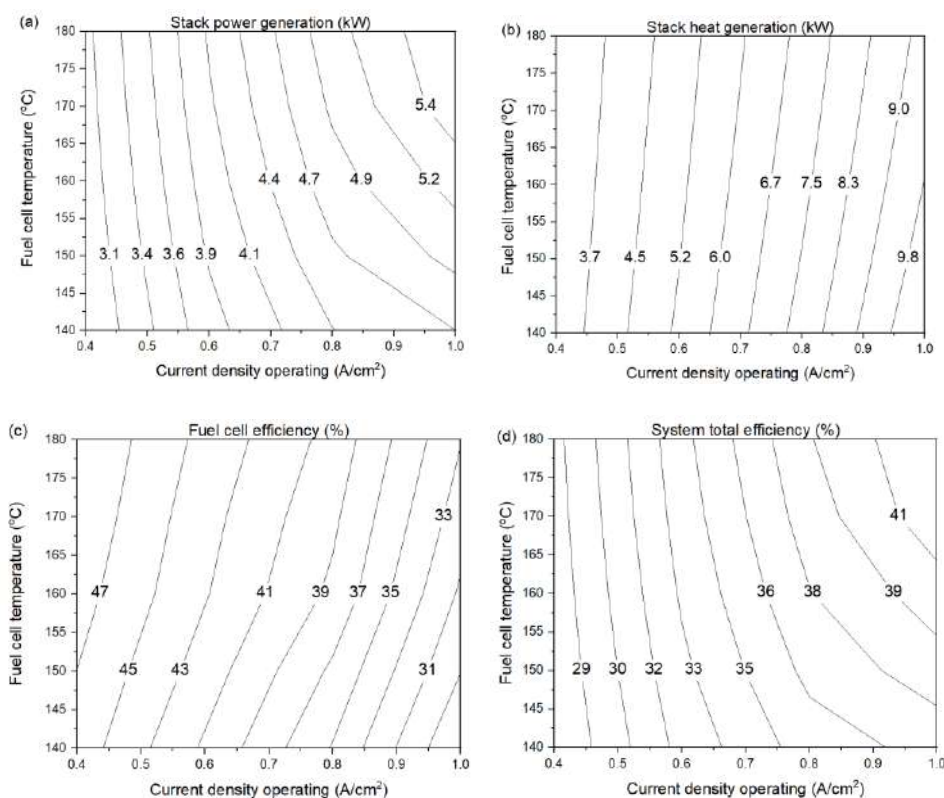


Fig. 5 Fuel cell temperature and current density on (a) stack power generation; (b) stack heat generation; (c) fuel cell efficiency; and (d) system total efficiency.

#### 4. Conclusion

This study involves the development of a HT-PEMFC system integrated with sorption-enhanced chemical-looping oxidative steam methanol-reforming (SECL-OSRM). An analysis of the model was performed to explore the system's operational performance across different input parameters. The suitable operating of SECL-OSRM system is mole ratio of CuO/CH<sub>3</sub>OH and MgO/CH<sub>3</sub>OH at 0.5, 0.5 respectively. The results show the high methanol conversion above

99%, with low CO content below 0.3 vol.%, H<sub>2</sub> concentration higher than 95 vol.% (free unreacted substances), and it can be operated with auto-thermal condition. The maximum system total efficiency of 41.5% was achieved for the proposed system at high current density (above 0.9 A/cm<sup>2</sup>) and high temperature (above 170 °C).

## References

- [1] Collins-Martinez, V. H., Cazares-Marroquin, J. F., Salinas-Gutierrez, J. M., Pantoja-Espinoza, J. C., Lopez-Ortiz, A., & Melendez-Zaragoza, M. J. (2020). The thermodynamic evaluation and process simulation of the chemical looping steam methane reforming of mixed iron oxides. *RSC Adv*, *11*(2), 684-699. <https://doi.org/10.1039/d0ra08610j>
- [2] Herdem, M. S., Sinaki, M. Y., Farhad, S., & Hamdullahpur, F. (2019). An overview of the methanol reforming process: Comparison of fuels, catalysts, reformers, and systems. *International Journal of Energy Research*, *43*(10), 5076-5105. <https://doi.org/10.1002/er.4440>
- [3] Li, H., Ma, C., Zou, X., Li, A., Huang, Z., & Zhu, L. (2021). On-board methanol catalytic reforming for hydrogen Production-A review. *International Journal of Hydrogen Energy*, *46*(43), 22303-22327. <https://doi.org/10.1016/j.ijhydene.2021.04.062>
- [4] Li, H., Tian, H., Chen, S., Sun, Z., Liu, T., Liu, R., Assabumrungrat, S., Saupsor, J., Mu, R., Pei, C., & Gong, J. (2020). Sorption enhanced steam reforming of methanol for high-purity hydrogen production over Cu-MgO/Al<sub>2</sub>O<sub>3</sub> bifunctional catalysts. *Applied Catalysis B: Environmental*, *276*. <https://doi.org/10.1016/j.apcatb.2020.119052>
- [5] Li, N., Cui, X., Zhu, J., Zhou, M., Liso, V., Cinti, G., Sahlin, S. L., & Araya, S. S. (2023). A review of reformed methanol-high temperature proton exchange membrane fuel cell systems. *Renewable and Sustainable Energy Reviews*, *182*. <https://doi.org/10.1016/j.rser.2023.113395>
- [6] Liu, J., Zhou, Z., Yue, B., Sun, Z., & Sun, Z. (2020). Chemical looping induced CH<sub>3</sub>OH-H<sub>2</sub>-PEMFC scheme for fuel cell vehicle: Parameter optimization and feasibility analysis. *Journal of Power Sources*, *479*. <https://doi.org/10.1016/j.jpowsour.2020.228790>
- [7] Shamardina, O., Chertovich, A., Kulikovskiy, A. A., & Khokhlov, A. R. (2010). A simple model of a high temperature PEM fuel cell. *International Journal of Hydrogen Energy*, *35*(18), 9954-9962. <https://doi.org/10.1016/j.ijhydene.2009.11.012>
- [8] Sun, Z., & Sun, Z.-q. (2020). Hydrogen generation from methanol reforming for fuel cell applications: A review. *Journal of Central South University*, *27*(4), 1074-1103. <https://doi.org/10.1007/s11771-020-4352-8>

## Study the parameters for acetylation over glycerol and acetic acid involving exploring Indion 225-H as alternative ion-exchange resin.

Pakin\_Sopolapikul<sup>1, a</sup>, Apiluck eiad-ua<sup>2</sup>, Kanokwan Ngaosuwan<sup>3</sup>, Weerinda Mens<sup>4</sup>,  
Doonyapong Wongsawaeng<sup>5</sup>, Worapon Kiatkittipong<sup>6</sup>, Armando T. Quitain<sup>7</sup>,  
Tetsuya Kida<sup>8</sup>, Santi Cheutor<sup>9</sup>, Suttichai Assabumrungrat<sup>1,9, b\*</sup>

<sup>1</sup>Center of Excellence in Catalysis and Catalytic Reaction Engineering, Department of Chemical Engineering, Faculty of Engineering, Chulalongkorn University, Bangkok 10330, Thailand

<sup>2</sup>King Mongkut Institute of technology Langkrabang (KMITL), Faculty of Engineering, 1 Chalong Krung 1 Alley, Lat Krabang, Bangkok 10520, Thailand

<sup>3</sup>Chemical Engineering Division, Faculty of Engineering, Rajamangala University of Technology Krungthep, Bangkok 10120, Thailand

<sup>4</sup>Department of Chemical and Materials Engineering, Faculty of Engineering, Rajamangala University of Technology Thanyaburi, Pathum Than 12110, Thailand

<sup>5</sup>Research Unit on Plasma Technology for High-Performance Materials Development, Department of Nuclear Engineering, Faculty of Engineering, Chulalongkorn University, Bangkok 10330, Thailand

<sup>6</sup>Department of Chemical Engineering, Faculty of Engineering and Industrial Technology, Silpakorn University, Nakhon Pathom 73000, Thailand

<sup>7</sup>Center for International Education, Kumamoto University, 2-39-1 Kurokami, Chuo-ku, Kumamoto 860-8555, Japan Research Organization for Advanced Science and Technology (IROAST), Kumamoto University, 2-39-1 Kurokami, Chuo-ku, Kumamoto 860-8555, Japan

<sup>8</sup>Faculty of Advanced Science and Technology, Kumamoto University, 2-39-1 Kurokami, Chuo-ku, Kumamoto 860-8555, Japan

<sup>9</sup>King Mongkut University of Technology North Bangkok (KMUTNB), Faculty of Engineering, 1 Bangsue, Bangkok 10800, Thailand

<sup>10</sup>Bio-Circular-Green-economy Technology & Engineering Center (BCGeTEC), Faculty of Engineering, Chulalongkorn University, Bangkok 10330, Thailand

E-mail: \*apiluck.ei@kmitl.ac.th

### Abstract

Acetylation optimizing the glycerol-esterification process with acetic acid to produce bio-additive fuel compounds monoacetin (MA), diacetin (DA), and triacetin (TA). Employing a modified Indion 225-H resin catalyst. The acetylation study meticulously controls the reaction parameters including temperature, molar ratio and catalyst loading range about 7 wt.%, and the attain reaction exceeds 90% glycerol conversion within 4 hours. The Optimization study various factors within temperature, catalyst loading, reaction time and reactant mixing ratio under consist stirred speed of rotates. The 5% loading catalyst (molar ratio 9:1 115°C). The optimization condition was reached highest toward selectivity at 3.43%, 52.95 and 43.62 toward MAG, DA and TAG respectively 4h reaction time.

**Keywords:** Glycerol-esterification; Monoacetin (MA); Diacetin (DAG; Triacetin (TAG); Indion 225-H resin; etc.



## Introduction

At present, biodiesel has slightly increased its refinement as a bio-resource fuel. Biodiesel produced highly methyl ester of long chain fatty acid via transesterification with triglyceride and methanol. The implement of biodiesel production emits crude glycerol as by-product. In 2020 global biodiesel production has been slightly increased from 22.7 million metric tons in 2012 to 36.9 million metric tons. The value of product and by-product demanded attention, leading to a surge in the trending over the years cause impacting the environment and resource dependency in each country [1-2]. Crude glycerol widely increased as low value by-product from biodiesel production and is not available in global markets for economical purposes. In market biodiesel is related with highly by-production emitting low-cost value with highly capacity to contain substances such as crude glycerine and crude glycerol, which can be alter chemical vaporization to more value product [3-4]. Crude glycerol can be converted into pure glycerol were uses widely commercial and industries such as cosmetics, plasticizer, food production and precursor convert to highly value chemical product by abundant various chemical reaction and catalytic implement uses servals universally commercial trade, for example glycidol, epicholhydrine, acetin, propanediol, acroleine, glycerol carbonate, Isopropylidenglycerol and glycidol. Acetin was particulary in value market demand globally in 2020 [5-6]. Hence, Acetylation in glycerol with carboxyl group like carboxylic acid, acetic acid and acetic anhydride has been considered a participant in esterification reactions, resulting in the formation of ester product occur continuous reaction three-step reaction, lead to glyceride acetates class like monoacetyl glycerol (MAG, monoacetin), diacetyl glycerol (DAG, diacetin) and Triacetyl glycerol (TAG, Triacetin). Mono- and diacetin occur as first-two step reaction which is presenting a symmetric difference isomer [7]. Consequently, Mono- and diacetin feature two discernible isomers, with monoacetin encompassing 1-monoacetin and 2-monoacetin, meanwhile diacetin exist as a pair of isomers namely 1,2 diacetin and 1,3 diacetin. Both compounds have widespread applications in food industry and biodegradable polymers, while TAG attend larger applications. TAG is reputation as bio-additive fuel and bio-plasticizer [8]. To perform acetylation, Strong acid and Bronsted acid has been interested using homogenous catalysts based on sulfuric acid as functional groups. However, The esterification required to develop new types of solid catalysts to replace homogeneous catalysts. Additionally, role of catalysts some solid catalysts, e.g. modified clay, zeolite (HZSM-5), heteropolyacids, carbon functional based, Nobel metal, zirconia-based metal including ion-exchange resins [9]. According to these catalyst, cation-exchange ion showed excellent glycerol conversions towards higher selectivity acetin product. Amberlyst particularly ion-exchange resin that highest embed sulfonic group functional and physical properties with excellent toward equilibrium for reaching triacetin under 1 h. For study parameters influences were achieved highly selectively destined triacetin nearly 60% and 40% selectively of diacetin under high reactant molar ratio with glycerol/acetic acid (1:24) and high pressure (200 bar) lead temperature to 110°C for 25 h [10]. Despite, the impracticality of the high molar industries process and the high costly catalyst like amberlyst not applicate for implements. In this work, study influences acetylation condition over alternative resin namely indion-225H, due to its more price related to economize with similar properties [11]. The impact parameter of reaction was analytic with acetic acid/glycerol molar ratio and catalyst loading under difference temperature was investigated for optimization in term of glycerol conversion and approaching triacetin selectivity. Acetic acid and glycerol high purity grade were of prepared for experiment.

## Materials

Acetic acid and glycerol of high purity (> 99.95%) were of analytical grade purchased from (Sigma-Aldrich) and isopropyl acetate (Sigma-Aldrich) were considered uses as solvent for investigate products (MAG, DAG and TAG) for analysed selectivity product. The commercial strong sulfonic acid functional ion-exchange resin (indion-225H) were used as esterification catalysts.

Table 1. Commercial Properties of Indion 225-H (an acidic ion-exchange resins) catalyst [12]

<b>Physical properties</b>	
Color	Golden yellow bead
Functional group	Sulphonic
Bulk density, kg/m <sup>3</sup>	780
Ionic form as supplied	Hydrogen, H <sup>+</sup>
Particle size	0.3 to 1.2 mm
Average bead size, m	0.0048
Porosity, %	52.0
Total ion-exchange capacity, meq H <sup>+</sup> /g	5.5 (1.8 meq/ml, minimum)
Specific surface area, m <sup>2</sup> /g	18-20
Effective operating pH	0-14
Temperature stability	120
Moisture holding capacity	49-55%

## Methods

Gas chromatography analyses were performed every 75 min, using a GC-FID (Shimadzu GC-FID 2010) with ZB-5HT (5% phenyl 95% Dimethylsiloxane) fused silica capillary column (30m x 0.25mm, film thickness 0.25 μm); carrier gas Helium (0.7 ml min<sup>-1</sup>) temperature injector and detector 250°C, column oven 70°C hold for 5 min then increase to 130°C at 10 min<sup>-1</sup>, FID 250°C). For analysis, Product 20 mg from reaction dissolve with isopropyl acetate 10 ml, Detector were indicated product exhibiting the retention time at (glycerol), 11.5 min, 19 min (monoacetin), 38 min (diacetin) and 48 min (triacetin). These times were compared with standard mono-, di and triacetin compound with high purity (Sigma - Aldrich). The glycerol conversion ( $X_G$ ) and the selectivity to the product ( $S_i$ ) could be defined as the following expression equation (1)-(2).

$$X_G (\%) = \left( 1 - \frac{[C_{i, glycerol}(time\ at\ interested)]}{[C_{0, glycerol}(intial)]} \right) \times 100 \quad (1)$$

$$S_i (\%) = \left( 1 - \frac{concentration\ interested\ time}{concentrate\ of\ initital\ glycerol} \right) \times 100 \quad (2)$$

## Acetylation reactions in batch system

All reactions were carried out in batch system. Glycerol (10g; 0.1 mol.), acetic acid (39g; 0.64 mol.) and resin catalyst prepared weight as 1%, 3%, 5% and 7% weight of glycerol as catalyst percentage loading, were employed the reaction. The reaction was heating separate container each reactant (glycerol and acetic acid) until reaching the desired temperature and then mixing in a three-neck round. Bottom flasks were adapted to batch-system under vigorously stirred for miscibility in an aqueous, the system was equipped with graham helix coil-condenser was being apart and thermocouple inside the flask. After reaching the desired temperature for reactant mixture then catalyst resin was added with a loading percentage based on weight of glycerol. Experimental data under these conditions, with time a variable, were collected as study experiment data.

## Results and Discussion

### Effect of the weight catalytic loading

Glycerol acetylation is a complicate of acid resin catalysed reaction with 3 step formation of mono- (MAG), di- (DAG) and triacetin (TAG). Among of the product is reactive reaction currently the following as consecutive reaction. The most desired product concern DAG and TAG are more value market in acetin productions. The esterification of glycerol with acetic acid mechanism of reaction was shown in figure 1.

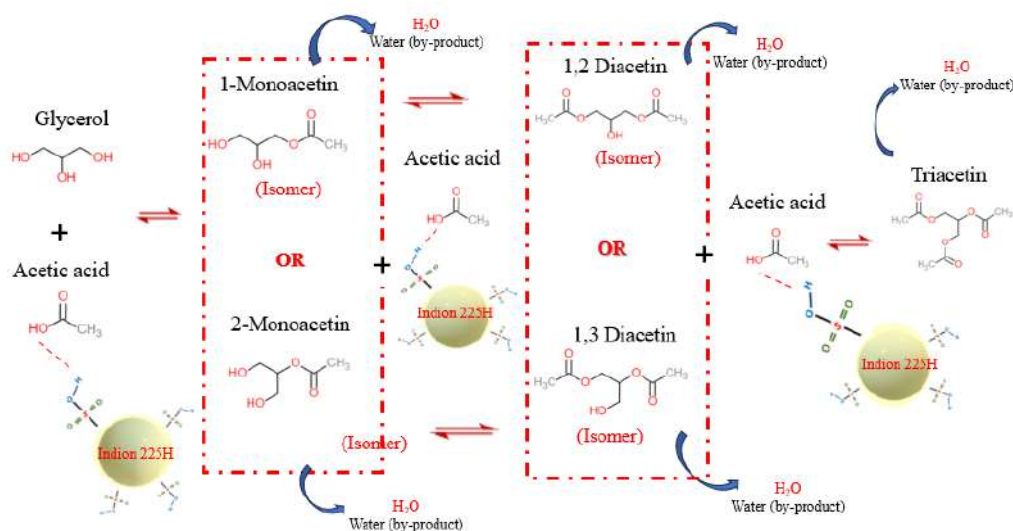


Fig 1. Catalytic reaction with indion 225-H resin (ion-exchange resin)

The comparison of glycerol acetylation over different weight loading was indicated in Table 2, it could be seen that Indion 225-H shown highest activity as well DAG and TAG selectivity at 5% loading to compare with another percentage weight both temperature 115°C and 105°C. DAG was the major product with a selectivity of 64.03% were detected but not distinguish isomer product and excess DAG to second major product (TAG) with 26.04% selectivity. contrarily, the more catalyst weight than 5% its resulting loading 7-9% range give approaching

complete glycerol conversion about 99.89% but lower reaching toward equilibrium for synthetic triacetin cause the mass transfer limiting where limited transport efficiently hinder rapid exchange acidity group to reactant for toward kinetics [13]. It is well known that the acid strength of catalyst has a significant impact on the catalytic activity and reach destined product like triacetin. Theoretically, we can assume a Fischer esterification mechanism begin participant of this reactions by exchange proton to carboxyl group emitting water as by-product after operating, facilitating nucleophile attack of hydroxide in acetic acid from product formatted MAG, DAG and TAG and leave water as by-product [14]. In the result indicated that the higher conversion is not necessary accompanied by higher selectivity from temperature reaction profiles with each catalyst.

Table 2. Performance of Indion 225-H resin in glycerol acetylation molar ratio (1:6) under 4h with different weight loading catalyst.

Run number	Reaction parameter		Conversion $X_G$ (%)	Selectivity (%)		
	Temperature (°C)	Wt.% Catalyst loading		$S_{MAG}$ (%)	$S_{DAG}$ (%)	$S_{TAG}$ (%)
1	115	1	98.94	26.15	60.16	13.68
2	115	3	98.26	19.70	59.34	20.94
3	115	5	99.21	9.92	64.03	26.04
4	115	7	99.20	19.70	59.34	20.94
5	115	9	99.30	20.13	60.17	19.67
6	115	No cat.	24.00	100	0	0

### The influences temperature of acetylation reactions

The resulting temperature profile for esterification over Indion 225-H resin catalyst and different temperatures between 115°C, 105°C and 95°C shown Table 3. Impact of temperature were exceeding the chemical equilibrium shift toward the product. Furthermore, an excess of acetic acid with temperature also slightly increases TAG selectivity, as the temperature close boiling point acetic acid (117.9°C) and related to emulsifier properties lead to miscible with glycerol for homogeneous phase of reaction. The complete reaction were increasing temperature to enhance the selectivity toward DAG and TAG selectivity with a simultaneous decrease of MAG and glycerol for conversion. The selectivity of DAG and TAG is prominent at 115°C depicted highest destination selectivity of reaction. The superior reaction at each weight loading of glycerol weight preferred higher temperature that influences more glycerol conversion and desired product compare with 105°C conditions. For optimizing condition reaching to 17.21% selectivity, 64.03% and 26.04% selectivity of MAG, DAG and TAG respectively. The Fischer esterification also dedicated commonly vary temperature between 100°C and 150°C [15]. Elevated temperatures are favored to increase reaction rate in esterification reactions and achieve earlier rate into equilibrium [16].

Table 3. Performance of Indion 225-H resin in glycerol acetylation (molar ratio 1:6 glycerol with acetic acid under 4h with different temperature profile.)

Run number	Reaction parameter		Conversion ( $X_G$ %)	Selectivity (%)		
	Temperature (°C)	Wt.% Catalyst loading		$S_{MAG}$ (%)	$S_{Di}$ (%)	$S_{Tri}$ (%)
1	115	1	98.94	18.34	65.80	15.86
2	105	1	98.04	19.67	69.20	11.13
3	115	3	98.26	17.21	63.60	19.19
4	105	3	99.16	18.34	65.80	15.86
5	115	5	99.21	9.92	64.03	26.05
6	105	5	99.45	11.96	63.64	24.40
7	115	7	99.20	19.70	59.34	20.96
8	105	7	99.75	17.62	63.13	19.25
9	95	5	98.30	13.49	68.40	18.11

### The impact of reaction time

The impact of reaction time on the glycerol acetylation was studied with different loading catalyst and temperature surrounding 1-3 h for appropriate different percent loading catalyst the similar pattern for reaction time consumes the time reaction require further glycerol conversion. MAG as primarily product was consumed with acetic acid to covert consecutive product (DAG and TAG) could be confirmed from the product that after reaching to DAG passed to highest selectivity there some decrease to triacetin steadily. While TAG occurring through reaction as final product. A relatively small latter fraction DAG is increase. Shown in Table 4. Performance of reaction with 4 different gap time for exhibited that reaction time were determined glycerol conversion and capability equilibrium shift toward that required low produced desired product, when shorter time in case meaning kinetic rate were not accomplished to DAG and TAG as major product based on Arrhenius equation outcoming to esterification, which mean rate of reaction for DAG is sloppy increase in the of reaction before 1 h reactions related equilibrium after that, 15 mins after reaction MAG also rapid increases rate after drastically decrease for formation as DAG after 30 mins. The distinctive rate for two different temperature profile (115°C and 105°C under 15 min at loading catalyst 0.05g) [17]. The optimum conditions were faster rate of reaction at lower MAG than 105°C (64.30% selectivity; 115°C and 95.36% selectivity; 105°C). However, 105°C, there was a lower occurrence of DAG and TAG product compared to the optimum conditions. TAG was significantly decidedly increase in both temperatures (Figure 2), with a smaller different competition at 4 h reaction time. (26.05% selectivity at 115°C and 24.40% selectivity at 105°C). This occurred because both reactions were reaching equilibrium around 30 mins. There was capable observed the curve after at 30 mins for glycerol conversion becoming to steadily result and DAG were lower consumption of TAG as subsequent final products. Form mathematics chemical mole balanced calculation, acetic acid was not totally consumed after a molar ratio of more than between 1:3 molar ratio between glycerol and acetic acid, respectively.

Table 4. Performance of Indion 225-H resin in glycerol acetylation

Run number	Reaction parameter			Conversion ( $X_G$ %)	Selectivity (%)		
	%Cat loading	Temperature (°C)	Time (min)		$S_{MAG}$ (%)	$S_{DAG}$ (%)	$S_{TAG}$ (%)
1	1	115	60	98.06	41.91	52.64	5.45
2	1	115	120	98.89	39.14	53.36	7.50
3	1	115	180	98.94	29.84	58.78	11.38
4	1	115	240	98.94	18.34	65.80	15.86
5	3	115	60	97.87	41.75	50.76	7.49
6	3	115	120	97.31	27.83	60.34	11.83
7	3	115	180	97.53	25.09	61.86	13.05
8	3	115	240	98.26	17.21	63.60	19.19
9	5	115	60	98.31	29.77	59.74	10.49
10	5	115	120	98.56	20.04	62.59	17.37
11	5	115	180	98.67	16.02	62.02	21.96
12	5	115	240	99.21	9.92	64.03	26.05
13	7	115	60	99.37	31.13	58.98	9.89
14	7	115	120	99.89	22.97	61.45	15.58
15	7	115	180	99.93	21.82	60.07	18.11
16	7	115	240	99.20	19.70	59.34	20.96
17	1	105	60	96.68	49.53	45.08	5.39
18	1	105	120	98.04	34.37	56.85	8.78
19	1	105	180	98.12	30.16	59.35	10.40
20	1	105	240	98.04	19.67	69.20	11.13
21	3	105	60	96.40	49.40	44.80	5.82
22	3	105	120	98.51	33.82	56.67	9.60
23	3	105	180	99.28	25.09	61.86	13.05
24	3	105	240	99.16	18.34	65.80	15.86
25	5	105	60	96.64	31.65	57.05	11.30
26	5	105	120	98.18	17.92	66.93	15.15
27	5	105	180	99.89	13.89	65.87	20.24
28	5	105	240	99.45	11.96	63.64	24.40
29	7	105	60	98.56	44.84	50.02	5.14
30	7	105	120	98.26	27.96	58.50	13.54
31	7	105	180	98.93	19.83	65.18	14.99
32	7	105	240	99.75	17.62	63.13	19.25

The reaction was studied molar ratio 1:6 (glycerol 10 g with acetic acid 39.16 g); under 1-3h with different time reaction and varying 1-7 percentage loading catalyst range.

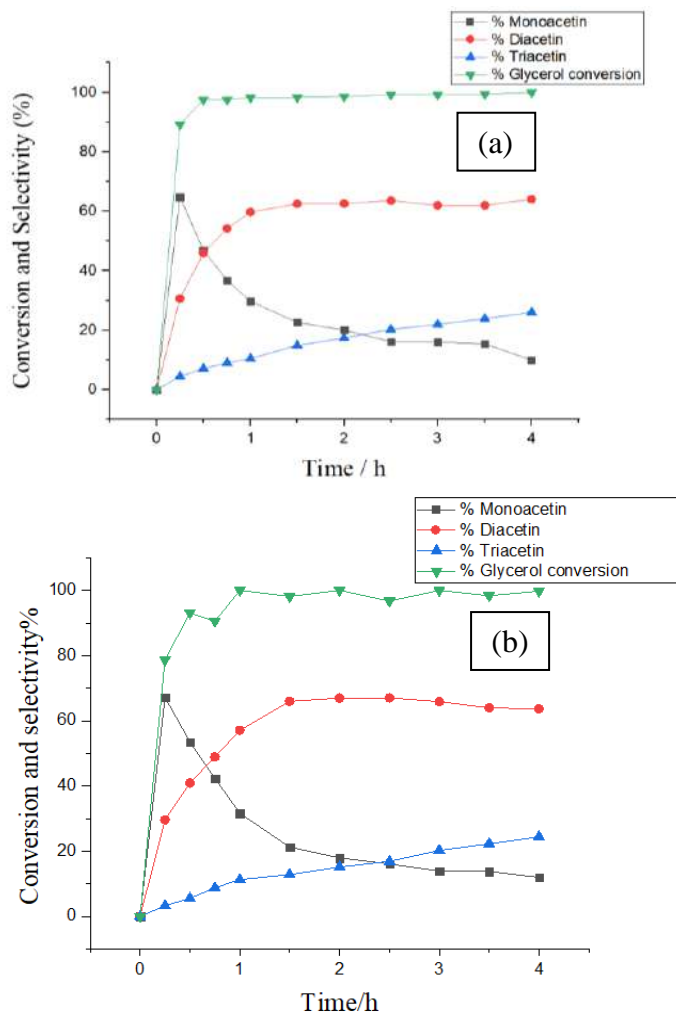


Fig 2. Influence of the different temperature on periodic reaction (a) 115°C; (b) 105°C on the rate of reaction of glycerol acetylation (Catalyst loading with 0.05 g; the glycerol to acetic acid molar ratio=1:6).

The lower temperature made less stability glycerol conversion, we can assume reversible of acetylation reaction, which is product interact hydrolysis with water that leading to reverse reaction through glycerol conversion decline in the system, Resulting were shown instability in reaction rate.

### The acetic molar ratio

The comparison of glycerol acetylation over different weight loading was indicated in Table 2, it could be seen that Indion-225H shown highest activity as well DAG and TAG selectivity at both constant 5% loading weight catalyst and temperature at 115°C to compare the resulting data. The optimum reaction was studied controlled with initial glycerol and acetic acid molar for catalytic reaction by varying between 1:3 and 1:9. The result is shown in Table 5.

Table 5. Influence of molar ratio under 5% loading catalyst and temperature at 115°C

Run number	Reaction parameter		Conversion ( $X_G\%$ )	Selectivity (%)		
	Molar ratio	Wt.%		MAG	DAG	TAG
	Gly : AcOH	Catalyst loading		$S_i$ (%)	$S_i$ (%)	$S_i$ (%)
1	1:3	5	99.01	36.97	53.05	9.96
5	1:6	5	98.26	9.92	64.03	26.04
3	1:9	5	99.85	3.43	52.95	43.62

1:3 molar ratio (13.5 g acetic acid and 10 g of glycerol); 1:6 molar ratio (39.16 g acetic and 10 g); 1:9 (58.9 g acetic acid and 10 g with 0.5 g) with loading catalyst weight of 0.5 g; reaction 4 h; Gly = Glycerol; AcOH = acetic acid

The resulting impact of acetic molar ratio with optimum condition higher ratio molar relatively led to higher conversion and equilibrium shifting toward to desired product in experimental shown 1:9 highest triacetin selectivity (43.61%) for consumption based on Le Chatelier's principle theoretical [18]. Both product DAG and TAG increase product distribution case interact molecule between acetic acid and glycerol were more occasionally formation and better transport for and decrease viscosity from acetic acid of homogenous phase under vigorously stirred.

## Conclusion

Parameter was studied over acidic ion-exchange resins Indion-225H, the catalysts showed best performance with selectivity to triacetin of more than 43.61% at complete conversion of glycerol (99.85% of glycerol conversion). This could be explained in terms of both the strong Brønsted acid sites of these catalysts and physical properties. In addition, selective product possible inhibiting effect of transport limiting, and entire reaction system (equilibrium limitation) might be constrained. The total number of acid sites effect the reaction However, Properties of specific surface area does not begin participating. The acetylation reaction also impacts on several parameter such temperature, molar ratio and reaction time as mainly factor for experiment. The rate of product selectivity was observed in different time reaction and two temperatures (115°C and 105°C), potentially formed by reforming of diacetin through at 30 mins were covert to triacetin as desired product. By-product was not being detected at low water content after reaction. Influence of glycerol conversion, which can be explained first by the weight loading catalyst and temperature direct variations for increasing, but its lower selective triacetin as required product, Consequently the chemical equilibrium controls were observed product distribution, the result shows indion-225H could not attended 100% selectivity of triacetin by 1:9 moral ratios at highest temperature in experiment. Indion-225 H were deactivated beyond temperature stability, it probably cracks of structural effect by temperature that made catalytic reaction ineffective reaction. This study demonstrates the practical of an alternative acidity-resin catalyst for using into acetylation reaction that cause more economical process for producing diacetin and triacetins.



## Reference

- [1] Benjamin Katryniok., Sebastian Paul, F. (2013). Recent Developments in the Field of Catalytic Dehydration of Glycerol to Acrolein. *ACS Catal*, 3, 8, 1819-1834.
- [2] Sujata Brahma., Biswajit Nath., B. (2022). Biodiesel production from mixed oils: A sustainable approach towards industrial biofuel production. *Chemical Engineering Journal Advances* 10, (4):100284.
- [3] Rosamond L. Naylor., Matthew M. Higgins. (2017). The political economy of biodiesel in an era of low oil prices. *Renewable and Sustainable Energy Reviews*, 77, 695-705.
- [4] Km Abida., Amjad Ali. (2022). A review on catalytic role of heterogeneous acidic catalysts during glycerol acetylation to yield acetins. *Journal of the Indian Chemical Society*, 99(6), 100459.
- [5] Nda-Umar, U. I., Ramli, I., Muhamad, E. N., Azri, N., Amadi, U. F., & Taufiq-Yap, Y. H. (2020). Influence of heterogeneous catalysts and reaction parameters on the acetylation of glycerol to acetin: a review. *Applied Sciences*, 10(20), 7155.
- [6] Oliveira, G. N., Barbosa, N. C., Araújo, F. C., Souza, P. H. G., Soares, A. V., Peixoto, F. C., Carneiro, J. W. M., & Passos, F. B. (2019). Conversion of Glycerine into 1,2-Propanediol for Industrial Applications. In *Springer eBooks* (pp. 383–414).
- [7] Tasuna, N., Hidayatillah, K. H., Marwan, M., & Zuhra. (2021). Selective esterification of glycerol diacetin and triacetin over rice husk biosilica catalyst with microwave heating. *IOP Conference Series: Materials Science and Engineering*, 1087(1), 012063.
- [8] Lacerda, C. V., Carvalho, M. J. S., Ratton, A. R., Soares, I. P., & Borges, L. E. P. (2015). Synthesis of triacetin and evaluation on motor. *Journal of the Brazilian Chemical Society*.
- [9] Farisya, M. R. S., Ramli, I., Shafizah, I. N., Taufiq-Yap, Y. H., Muhamad, E. N., Lee, S. L., & Salamun, N. (2021). Assessment on the Effect of Sulfuric Acid Concentration on Physicochemical Properties of Sulfated-Titania Catalyst and Glycerol Acetylation Performance. *Catalysts*, 11(12), 1542.
- [10] Liao, X., Zhu, Y., Wang, S., Chen, H., & Li, Y. (2010). Theoretical elucidation of acetylating glycerol with acetic acid and acetic anhydride. *Applied Catalysis B: Environmental*, 94(1–2),
- [11] Rambhia, D. A., Veluturla, S., & Narula, A. (2022). Parametric and kinetic study of solvent-free synthesis of solketal using ion exchange resin. *Turkish Journal of Chemistry*, 46(3), 881–889.
- [12] Hajra, B., Pathak, A. K., & Guria, C. (2014). Optimal synthesis of methyl ester of Sal oil (*Shorea robusta*) using ion-exchange resin catalyst. *International Journal of Industrial Chemistry*, 5(3–4), 95–106.

- [13] Caballero, K. V., Guerrero-Amaya, H., & Baldovino-Medrano, V. G. (2019). Revisiting glycerol esterification with acetic acid over Amberlyst-35 via statistically designed experiments: Overcoming transport limitations. *Chemical Engineering Science*, 207, 91–104.
- [14] Kale, S. S., Umbarkar, S. B., Dongare, M. K., Eckelt, R., Armbruster, U., & Martin, A. (2015). Selective formation of triacetin by glycerol acetylation using acidic ion-exchange resins as catalyst and toluene as an entrainer. *Applied Catalysis A: General*, 490, 10–16.
- [15] Shafiei, A., Rastegari, H., Ghaziaskar, H. S., & Yalpani, M. (2017). Glycerol transesterification with ethyl acetate to synthesize acetins using ethyl acetate as reactant and entrainer. *Biofuel Research Journal*, 4(1), 565–570
- [16] Khan, Z., Javed, F., Shamair, Z., Hafeez, A., Fazal, T., Aslam, A., Zimmerman, W. B., & Rehman, F. (2021). Current developments in esterification reaction: A review on process and parameters. *Journal of Industrial and Engineering Chemistry*, 103, 80–101.
- [17] Meireles, B. A., & Pereira, V. L. P. (2013). Synthesis of bio-additives: transesterification of ethyl acetate with glycerol using homogeneous or heterogeneous acid catalysts. *Journal of the Brazilian Chemical Society*, 24(1), 17–57.
- [18] Khan, Z., Javed, F., Shamair, Z., Hafeez, A., Fazal, T., Aslam, A., Zimmerman, W. B., & Rehman, F. (2021b). Current developments in esterification reaction: A review on process and parameters. *Journal of Industrial and Engineering Chemistry*, 103, 80–101.

## Preparation of sulfonated activated carbon from plastic waste for fructose dehydration

**Siriboon Supajaruwong<sup>1,2</sup>, Babasaheb M. Matsagar<sup>2</sup>, Kevin C.-W. Wu<sup>2</sup>, and Artiwan Shotipruk<sup>1,\*</sup>**

<sup>1</sup> Bio-Circular-Green-economy Technology & Engineering Center, BCGeTEC, Department of Chemical Engineering, Faculty of Engineering, Chulalongkorn University, Phayathai Road, Patumwan, Bangkok 10330, Thailand.

<sup>2</sup> Department of Chemical Engineering, Faculty of Engineering, National Taiwan University, Taipei 10617, Taiwan.

E-mail: \*Artiwan.Sh@chula.ac.th

### Abstract

Conversion of plastic waste (PW) from industry to valuable products such as activated carbon (AC) is an interesting and sustainable pathway. This research aims to investigate the preparation of AC from PW, focusing on the effects of one-step and two-step through potassium hydroxide (KOH) activation on the characteristics of AC. Via one-step and two-step KOH activation at 800°C in N<sub>2</sub>, respectively, activated PW (A) and activated pyrolyzed PW (P/A) were synthesized. The most suitable AC will be used for catalytic application and the results will be presented further.

**Keywords:** Activated carbon; plastic waste; activation; pyrolysis

### Introduction

Plastic waste (PW) has experienced a significant increase worldwide [1]. Examples of plastic waste include polyurethane (PU), polyvinylchloride (PVC), and polyethylene terephthalate (PET), and recycling of these plastic wastes is of paramount importance. The current method of PW recycling widely adopted in many countries, involves mechanical grinding, melting, and forming plastic materials. Alternatively, chemical recycling aims at recovering monomers and reassemble them into new plastics or chemicals. The application of these process, however, can be limited with mixed or heavily contaminated PW. Recently, PW has drawn considerable attention due to its high carbon content, leading to its recognition as an effective carbon source. This has sparked interest in converting PW into carbon-based materials such as activated carbon (AC). AC can be used for catalytic reaction because high surface area, functional group and high stability. For example, AC can be modified with Brønsted acid such as sulfonic group and etc. This Brønsted acid acted active site for sugar dehydration, cellulose hydrolysis, and esterification. Gupta Vipul and coworkers (2021)[2] successfully prepared AC from mixed plastic waste, and demonstrated promising results for its use as an adsorbent to remove chlorophenolic compounds from wastewater.

Originally, a two-step activation process was used to synthesize AC. The process involves pyrolysis to convert carbonaceous materials such as biomass or plastic into carbon, followed

by activation with either an acid (e.g.,  $\text{H}_3\text{PO}_4$ ,  $\text{H}_2\text{SO}_4$ , etc.) or a base (e.g.,  $\text{KOH}$ ,  $\text{ZnCl}_2$ ,  $\text{K}_2\text{CO}_3$ , etc.) to transform it into AC. This method however suffered from high energy consumption and involves multiple preparation steps. Interest has grown in the production of AC using a one-step activation process. In a previous study, Nan Yao et al.(2023)[3] successfully investigated the preparation of AC from PVC using one-step activation varying the ratios of  $\text{KOH}$ . They also compared of characteristics of AC produced using one-step and two-step  $\text{KOH}$  activation with same ratio of  $\text{KOH}$ . The result revealed that AC produced through two-step  $\text{KOH}$  activation exhibited lower specific surface area, with few pores and cracks. The advantages of one step  $\text{KOH}$  activation were obtained AC which high specific surface area. This study therefore aims to investigate the effects of the activation step on the characteristics of AC from PW and ensure that activated carbon was stable for fructose dehydration.

## 1. Materials and Methods

### 1.1. Prepare activated carbon from waste

Activated carbon was prepared using a tubular reactor, comprising a quartz tube, an electric heater, and a temperature controller. In the one step method, 1 g of PW and  $\text{KOH}$  as the activator were mixed at mass ratio 1-3 and activated in the tube furnace at  $800^\circ\text{C}$  for 2 h with ramp rate  $13^\circ\text{C}/\text{min}$ , under a flow of nitrogen. The tubular reactor was connected to an Erlenmeyer flask containing the water to trap toxic gas. After cooling to room temperature, the resulting activated carbons were washed and filtered through a Whatman filter paper (1) initially with DI water, followed by 10 mmol  $\text{HCl}$  until pH was neutral. Subsequently, the sample was washed by DI water to remove  $\text{KCl}$ ,  $\text{K}_2\text{O}$ , and  $\text{K}$  until the pH of the wash water remained constant. The resulting activated carbon was then dried in an oven at  $110^\circ\text{C}$  overnight. The prepared sample was denoted as "A".

In the two-step method, PW was initially heated at  $800^\circ\text{C}$  with ramp rate  $13^\circ\text{C}/\text{min}$  for 1 hour under nitrogen gas. The reactor was subsequently cooled to room temperature, and then 1 g of pyrolyzed PW and  $\text{KOH}$  as activator were mixed at a mass ratio 1:3. The two-step method was carried out under the same conditions (temperature and time) as the one-step method. The prepared sample was denoted as "P/A".

### 1.2. Characterizations

Various analyses were conducted to evaluate the properties of the activated carbon. The Brunauer-Emmett-Teller (BET) method with  $\text{N}_2$  adsorption was employed to determine specific surface area and porosity. Elemental composition, including carbon (C), hydrogen (H), and nitrogen (N), was analyzed using an element analyzer. Fourier transform infrared (FTIR) spectroscopy was utilized to identify functional groups present on the activated carbon. Thermal stability was assessed through thermal gravimetric analysis (TGA) under air and nitrogen gas as medium, with a ramping rate of  $10^\circ\text{C}/\text{min}$ . Additionally, X-ray crystallography (XRD) was employed to investigate the degree of amorphousness in the activated carbon samples.

## 2. Results and discussion

Following the synthesis of AC from KOH through both the two-step and the one-step activation methods, two types of AC were obtained: P/A and A. The XRD analysis revealed the degree of amorphous of AC at 22°. Upon activation, degree of amorphousness increased for both P/A and A, as shown in Fig. 1.

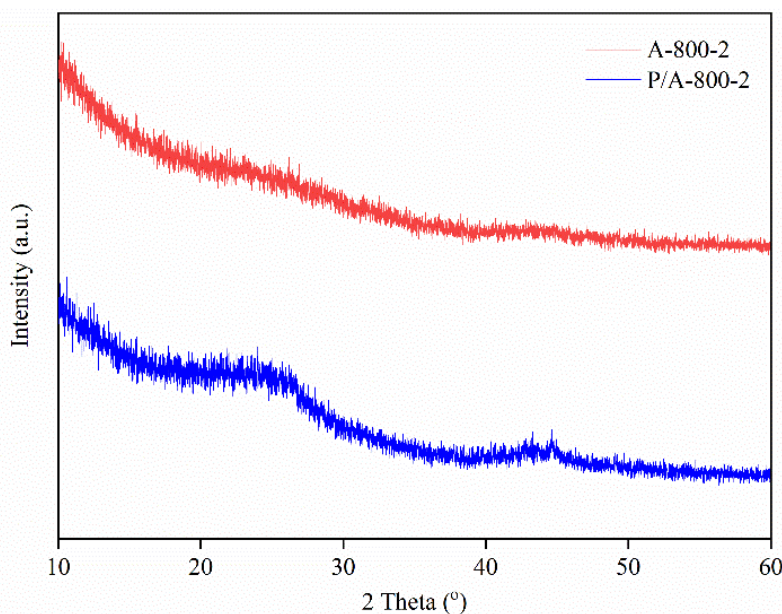


Fig. 1 XRD of A and P/A

From the elemental analysis results for percentage of carbon (C%), hydrogen (H%), and nitrogen (N%) summarized in Table 1. Composition of P/A and A contained carbon content around 90%. Comparing P/A and A with the original waste, C% increased by approximately 20%. In contrast, N% decreased by around 9% due to the reaction nitrogen with  $K_2CO_3$  during the PW activation process [4]. This result can be attributed to this AC from two methods was dominantly stable because of high carbon content. Following activation, specific surface area of A and P/A increased from PW and P, respectively. The specific surface area of A at 2860  $m^2/g$  exceeded that of P/A, at 1460  $m^2/g$ . The reason might be attributed to the reaction between the chemical composition of PW and KOH[5]. From the literature, Oluwatosin Oginni et al.[5] demonstrated that the KOH activation step influenced to characteristics of activated carbon from herbaceous biomass. Some chemical compositions of biomass can be easily reacted with KOH during activation, leading to increased formation of porous. As depicted in Fig. 2, both P/A and A Exhibited Type 1 isotherm characteristic.

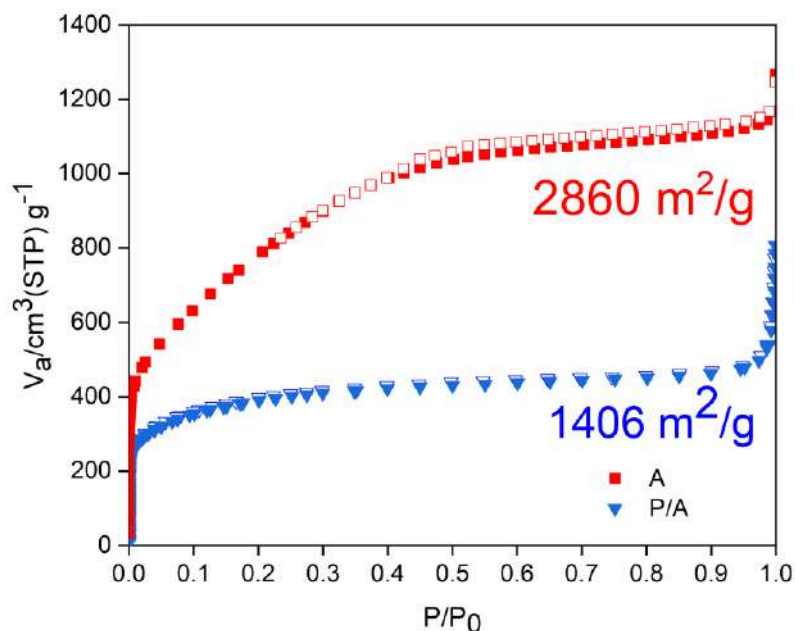


Fig. 2 N<sub>2</sub> adsorption-desorption of A and P/A

Table 1. Elemental composition and specific surface area of PW, P/A, and A.

Sample	Elemental composition			Specific surface area (m <sup>2</sup> /g)	Yield (%)
	C%	H%	N%		
PW	72.44	2.97	9.56	7	-
P	81.66	1.17	9.42	2	83.55
P/A	91.42	0.72	0.55	1406	43.25
A	90.21	0.86	0.36	2860	37.18

The thermal stability analysis results shown in Fig. 2. revealed that both P/A and A have two decomposition zones. The small weight loss was observed at 100°C was attributed to water loss. The rapid weight loss observed at 400°C was a result of the decomposition of volatile compound present in the AC. Therefore, both P/A and A demonstrated stability up to 400°C.

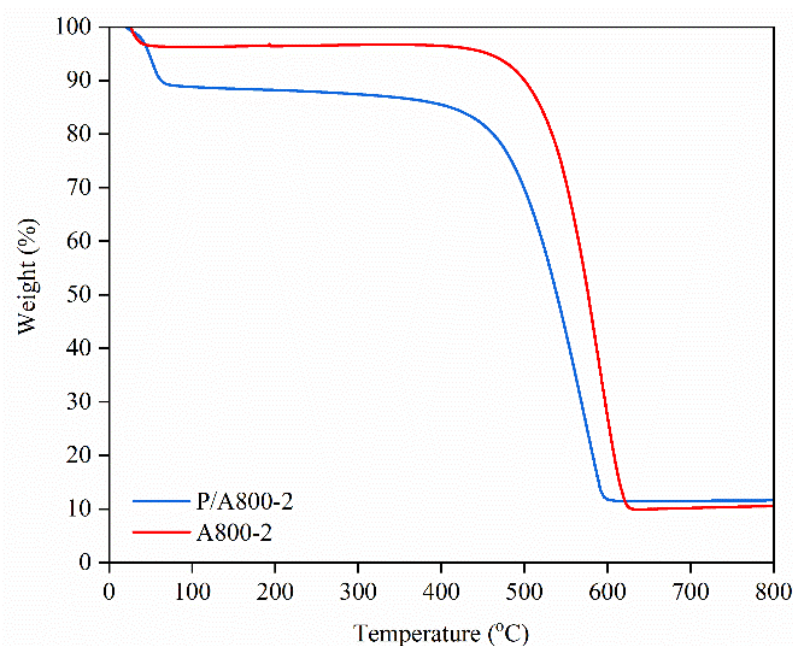


Fig. 2 TGA of A and P/A

Fig. 3 displays the FTIR of the waste, A, and P/A. The adsorption bands corresponding to O-H and C-H functionalities were observed at around 3400 and 2700-3000  $\text{cm}^{-1}$ , respectively. Additionally, peaks attributed to the C=O and C=C conjugated with aromatic groups were identified at 1600  $\text{cm}^{-1}$ . The vibrations associated with C=O (referring to carboxyl group) and C-O bonds were observed at approximately at 1400 and 1100  $\text{cm}^{-1}$ , respectively.

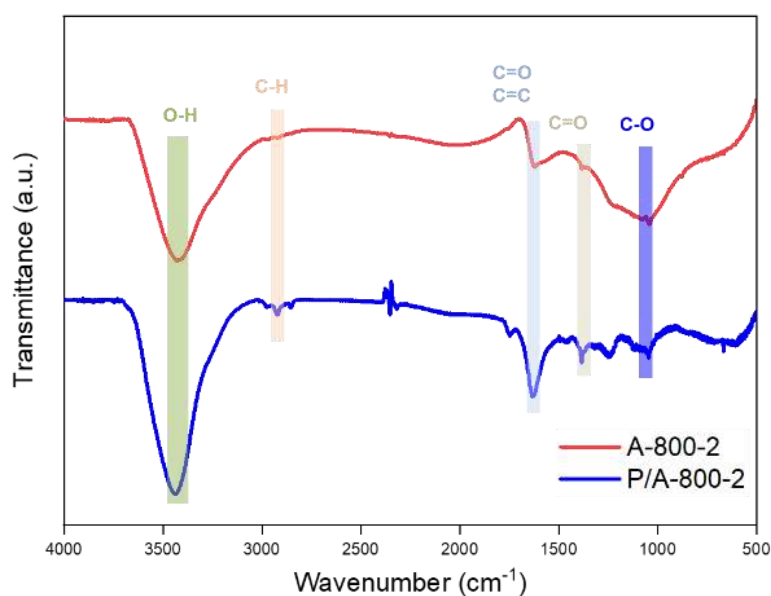


Fig. 3 FTIR of A and P/A

The characterizations of AC containing high specific surface area, stability, and functional groups of AC (e.g., -OH or C-H) were suitable for catalytic application. Previously, commercial AC with specific surface area at 800 m<sup>2</sup>/g was used for functionalization. Acid and organosulfur compound were used that reacted with the functional groups of AC. Therefore, the synthesis of AC from PW can effectively utilize one-step KOH activation can be used as supporter for catalytic application.

### 3. Conclusions

AC can be synthesized using one-step KOH activation methods. The properties of AC contain a high specific surface area, high stability, and various functional groups. Therefore, the one-step KOH activation method proves to be suitable for the preparation of stable AC as a supporter.

### 4. References

1. Plastics – the Facts 2022. 2022.
2. Vipul G, Kant BN, Kumar RR. Remediation of Chlorophenolic Compounds from Paper Mill Effluent Using High-Quality Activated Carbon from Mixed Plastic Waste. *Water, Air, & Soil Pollution*. 2021;232(8):326.
3. Yao N, Wang X, Yang Z, Zhao P, Meng X. Characterization of solid and liquid carbonization products of polyvinyl chloride (PVC) and investigation of the PVC-derived adsorbent for the removal of organic compounds from water. *Journal of Hazardous Materials*. 2023;456:131687.
4. Wabo SG, Klepel O. Nitrogen release and pore formation through KOH activation of nitrogen-doped carbon materials: an evaluation of the literature. *Carbon Letters*. 2021;31(4):581-92.
5. Oginni O, Singh K, Oporto G, Dawson-Andoh B, McDonald L, Sabolsky E. Influence of one-step and two-step KOH activation on activated carbon characteristics. *Bioresource Technology Reports*. 2019;7:100266.



## **A Pouch-Type Liquid-to-Gas Phase Transition Actuator: Performance Tests and Cost Analysis**

**Julamane Wachiradecha<sup>1</sup>, Sira Srinives<sup>2</sup>, and Yodchanan Wongsawat<sup>1,\*</sup>**

<sup>1</sup> Department of Biomedical Engineering, Faculty of Engineering, Mahidol University, Nakhon Pathom, 73170, Thailand, <sup>2</sup> Department of Chemical Engineering, Faculty of Engineering, Mahidol University, Nakhon Pathom, 73170, Thailand

E-mail: \* yodchanan.won@mahidol.ac.th

### **Abstract**

Electric-driven liquid-to-vapor phase transition actuators are a group of outstanding actuators with advantages in design and functionalities, such as high power density, high adaptability to environments, ease of processing, and high precision in device operation. The advantages make the actuators well-suited to be implemented in industrial and electronic devices, vehicles, and robots. In this work, we fabricated 20 x 20 mm pouch-type actuators relying on laminated aluminum films as the structural material and Dichloromethane as the phase transition fluid. The conductive carbon coat was applied to the aluminum pouch's surface as a heat source for phase transition. The transition drives volumetric increase inside the pouch and causes mechanical deformation in the actuator. The actuators were tested and analyzed for thermal and mechanical responses. The fabrication cost, durability, and thermodynamic correlations between deformation, force, temperature, and operating time were determined. Our best device realized a maximum vertical displacement of 10.82 mm (7.98 times the initial value), yielding 75% displacement within 30 s. The fabrication cost was determined to be 0.53 USD/device at a total weight of 0.35 to 0.42 g/device. The actuator was tested to be cost-effective and high-performance.

**Keywords:** Liquid-to-vapor phase transition actuator; phase transition actuators; pouch motor

### **1. Introduction**

A liquid-to-vapor phase change actuator converts thermal energy into mechanical work by exploiting a volume change of a working fluid during phase transition. Recently, liquid-to-vapor phase change actuator types were developed and have progressed dramatically with various designs based on different materials. The progress provides several features, varying from tubular steel actuators operating at elevated temperatures [1] to silicone elastomer actuators offering flexibility and biocompatibility [2,3].

The film-shaped design is popular in phase transition actuators due to its lightweight, versatility, and ease of implementation [4,5]. A film-shaped actuator was fabricated using several fabrication techniques, including a simple pouch shape using an average thermal compressor and a complex structure that requires precise cutting and assembly tools. Such devices benefited a broad spectrum of applications, such as robotics, medical technologies, and soft electronics, owing to their ability to achieve complex motions and deformations with minimal energy input [6,7].

There has recently been a growing interest in exploring the potential of liquid-to-vapor phase change actuators for diverse applications. However, challenges remain in optimizing their performance and functionality, particularly regarding selecting and managing the working fluid [8]. In this regard, Dichloromethane has emerged as a promising candidate for such

actuators due to its favorable properties, including a low boiling point at 40°C, high vapor pressure, and compatibility with standard materials. By varying the amount of Dichloromethane within the actuator pouches, it is possible to tailor the performance characteristics of the actuators to suit specific application requirements.

This paper presents a study on the behavior of electric-driven liquid-to-vapor phase change actuators that use Dichloromethane as the phase change fluid. The actuators consist of pouches made of laminated aluminum films with a conductive carbon coat that serves as a heating element. The amount of Dichloromethane in the pouches was varied to investigate its effect on the actuator performance. The study aimed to evaluate the thermal and mechanical responses of the actuators, such as deformation, force, temperature, and operating time. The study also analyzed the actuators' fabrication cost, durability, and thermodynamic correlations.

## 2. Materials and Methods

### 2.1. Materials

The aluminum laminated film (100  $\mu\text{m}$  thick) was purchased from TSC Intertrade Group Co., Ltd. and served as an actuator structure. The film consists of laminated polyester, aluminum, and polyethylene layers. The conductive carbon paste (JELCON-18) from Jujo Chemical Co., Ltd. and Dichloromethane (99.8%, AR grade) from RCI Labscan Co., Ltd. were used as the heater and phase transition fluid, respectively.

### 2.2. Actuator fabrication

Two laminated films were cut (30x50 mm in size). One film was attached with a 3M™ scotch tape (0.0625 mm), creating a heater frame. The conductive carbon paste was screened on films using the doctor blade technique and blown dry with hot air at 120 °C. After removing the template tape, the screened heater sheet was obtained. The actuator pouch was fabricated by sealing the screened and plain films together using a thermo-compressor (PFS-100, OKURA), placing the coated film facing outward. The films were sealed according to an actuator design, leaving an area of 20 x 20 mm as the pouch storing the working fluid. One side of the pouch was left open for injecting the fluid. Dichloromethane was injected into the pouch in amounts of 30, 40, and 50  $\mu\text{L}$ , and the samples were labeled as C30, C40, and C50, respectively. After injection, the remaining side of the actuator was sealed. A schematic diagram of the actuator's design is presented in Fig. 1.

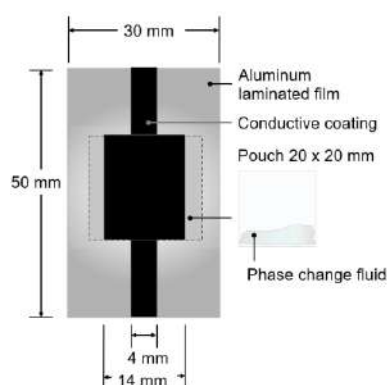


Fig. 1 A schematic diagram showing a liquid-to-vapor phase change actuator's design.

### 2.3 Working mechanism

The actuator relied on pressure change during the transition between the liquid and vapor phases. When electricity is applied, the heat generated from the conductive coating increases the actuator's temperature and causes the pouch's working fluid to vaporize. The increased pressure from the phase transition process causes the actuator to expand and produces force due to the vertical growth of the pouch. On the other hand, the pouch can revert to its original shape as the vapor condenses into a liquid phase following a temperature decrease during a power outage.

### 2.4 Deformation evaluation of the actuator with different fluid content

We evaluated the deformation of the actuator by examining the vertical displacement change, response time, and temperature. Actuators with varied Dichloromethane volumes were studied at 25V and 0.4A for 60 s. An actuator setup station was designed to hold the sample securely in place and prevent actuator damage during the experiment. This setup includes a built-in scale and a conductive surface connected to a power supply (Keysight EDU36311A) for transferring electricity to the actuators. Additionally, a thermal camera (UTi120Mobile) and a video camera (Panasonic HC-V520) were used to gather data from the experiment. A computer was employed to control the electrical input power and duration precisely.

### 2.5 Output force measurement of the actuator

An actuator was placed 5 mm below a measuring probe of a force gauge (IMADA DS2-1000N) and subjected to 25V and 0.4A for 60 s to measure the vertical expansion force of the actuator.

### 2.6 Cost, durability, and power consumption evaluation

A comprehensive evaluation was analyzed using three primary criteria—cost, durability, and power consumption. Both fabrication and material costs were analyzed to estimate the total expenses. The durability of the actuators was tested by subjecting them to repeated operations until operational failure occurred. Information concerning the average power consumption exhibited by the actuators was provided.

## 3. Results

### 3.1 The correlation between vertical displacement, temperature, and time of varying amounts of phase change fluid actuators

The vertical displacement, temperature, and time correlations of different amounts of phase change fluid actuators are shown in Fig. 2.

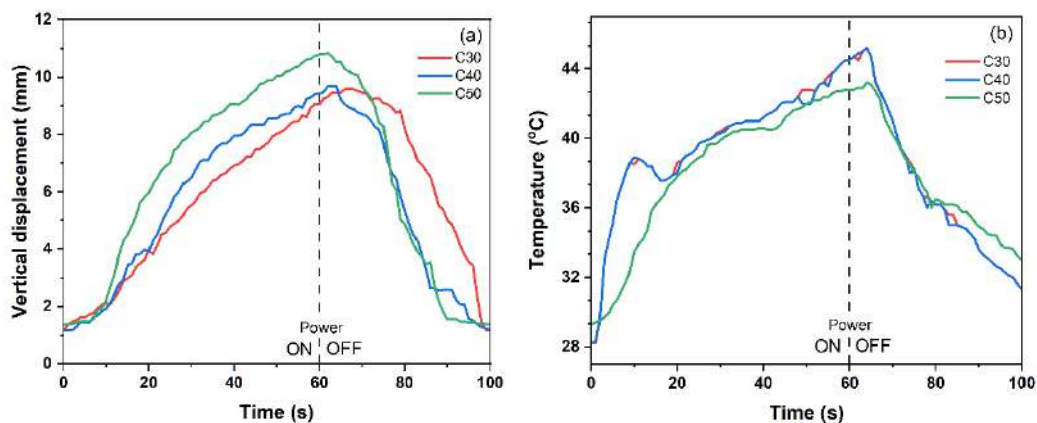


Fig. 2 Deformation evaluation results of the actuators in different relationships: (a) the relationship between the vertical displacement and time, and (b) the relationship between the pouch surface temperature and time.

For the vertical displacement experiment, an actuator's pouch expanded at 10 s. The displacement increased sharply until the electric power stopped at 60 s. For C40 and C50, pouch size increased for 2-5 s after a power outage, which promptly decreased and stabilized at 85 (C40) and 90 (C50) s. For C30, the pouch continued to expand and remained stable in its high displacement state for 20 s before decreasing to its original size.

The temperature of the C50 sample increased significantly within the first 30 s of operation, while the other two samples experienced a temporary drop in temperature during 13-20 s of operating time. However, the temperature of all actuators gradually increased and surprisingly reached their peak at the same time of 64 s, which is a few s after the electricity was switched off before the temperature dropped.

The highest vertical displacement and lowest maximum temperature were detected in the C50 sample, which contains the highest amount of Dichloromethane in all the samples. Detailed information of each liquid volume actuator on the vertical displacement ( $D_{60}$ ) and temperature ( $T_{60}$ ) at the 60-second mark, along with the maximum values of displacement ( $D_{max}$ ) and temperature ( $T_{max}$ ) detected from the whole experiment time, are shown in Table 1.

Table 1. The vertical displacements and temperatures of the actuators at different detected times.

Sample	$D_{60}$ (mm)	$T_{60}$ (°C)	$D_{max}$ (mm)	Time at $D_{max}$ (s)	$T_{max}$ (°C)	Time at $T_{max}$ (s)
C30	9.04	44.5	9.57	66	45.2	64
C40	9.43	44.5	9.68	63	45.2	64
C50	10.78	42.8	10.82	62	43.2	64

### 3.2 Output force

Due to the force gauge's limited resolution, we can only receive information when the force changes by 1 N. C50 was the only device that produced the maximum output force of 2 N at 62 s, while the other samples could not achieve the force of 2 N. C30, C40, and C50 reached the output force of 1 N at 54, 50, and 46 s, respectively.

### 3.3 Cost, durability, and power consumption evaluation

#### 3.3.1 Cost

The cost for the fabrication of an actuator was determined based on a small-scale production in the laboratory. The production rate was estimated at 5 samples per hour per worker or 40 devices per day per worker. The total fabrication cost was determined to be 0.53 USD per device. Figure 3 displays the estimated expenses for the entire process over a year, including material costs, fabrication and testing equipment, facility, and labor at 4.2%, 4.9%, 37.7%, and 53.2%, respectively.

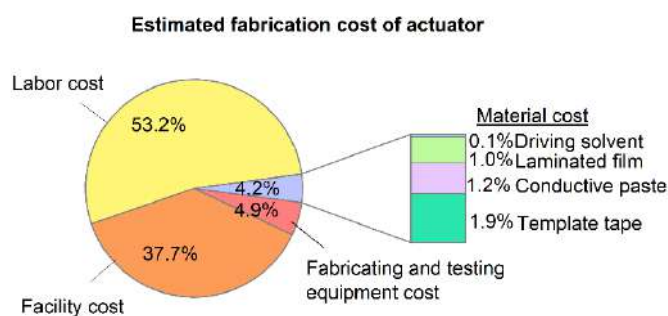


Fig. 3 The estimated fabrication expense of actuators with the details in material costs.

The material cost of the liquid-to-vapor phase change actuator consists of the expenses of the conductive carbon paste, driving solvent (dichloromethane), laminated film, and template tape. The material costs of fabricating one actuator are around 0.023 USD. Although the conductive paste has the highest unit cost at 63.26 USD per 1000g, much higher than the unit cost of template tape, it is more cost-effective than the template tape due to the larger supply size and the minimal amount of 0.1g required per sample. This results in the lower cost of the conductive coating in percentage, which is around 0.0038 USD per device.

To calculate the yearly cost of producing and testing equipment, we considered the initial cost of the devices, their lifespan, and maintenance expenses. The facility cost was also calculated by considering the cost of utilities and rent for one year. The facilities and labor costs were calculated using the prevailing rates in Thailand for the year 2023.

#### 3.3.2 Durability

The study found that the durability of actuators was not significantly affected by the different liquid volume conditions. The actuators can perform  $10 \pm 2$  cycles before they stop functioning further when applied with testing cycles of a 60-s power loop by waiting for the actuator to return to its original form before starting the next cycle. However, the actuator performed better when subjected to a different heating program. This program included a pre-heating phase lasting 30 s before initiating cycles, which consisted of 10 s of power-off followed by 5 s of power-on. The actuator achieved more repeating cycles of  $30 \pm 2$  cycles under this program.

#### 3.3.3 Power consumption

The average electrical power consumption of the C30, C40, and C50 actuators ranges from  $1.261 \pm 0.049$ ,  $1.176 \pm 0.038$ , and  $1.244 \pm 0.031$  Watts, respectively.

#### 4. Discussion

As we observed a decrease in the maximum displacement value with decreasing solvent volume, this phenomenon is directly linked to the amount of solvent present in the actuators. Assuming complete vaporization of the liquid solvent in the expanded state, we adapted a simple model from the ideal gas law as shown in Eq. (1):

$$V_{pouch} = \frac{V_{liq} \rho RT}{MP} \quad (1)$$

, in which  $V_{pouch}$  represents the pouch volume,  $V_{liq}$  is the liquid volume,  $\rho$  is the density of the driving solvent,  $M$  is the molar mass of the liquid,  $R$  is the gas constant,  $P$  is the pressure inside the actuator pouch, and  $T$  is the temperature of the liquid.

When testing actuators with different liquid volumes under identical environmental and temperature conditions, the pressure inside the pouch cannot surpass the solvent's vapor pressure at the given temperature. This is the equilibrium condition for evaporation. Therefore, we can assume that the pressure inside the pouch will remain the same as the solvent's vapor pressure at a specific temperature. As a result, the actuator with a higher liquid volume has the capability to create a larger volume of gas inside the pouch, which leads to an increase in the maximum vertical displacement. In addition, the higher pressure inside the actuator pouch generates a more expansive force. This is why the C50, which has the highest vertical displacement, also achieves the most detected output force.

On the other hand, the larger liquid volume also increased the heat capacity, which makes the actuator require more energy to heat up, as indicated in Eq. (2):

$$Q = C\Delta T = mc\Delta T \quad (2)$$

, where  $Q$  is the amount of absorbed heat energy,  $C$  is the heat capacity,  $m$  is the mass of the substance,  $c$  is the specific heat capacity, and  $\Delta T$  is the corresponding temperature change.

When we apply the same amount of electricity or heat energy to two different actuators, the one with higher liquid content (more mass volume) will increase in temperature at a slower heating rate than the one with lower liquid content. This means that at the same operating time, the actuator with higher liquid content will have a lower temperature compared to the one with lower liquid content. For example, in the case of C50, the heating rate is around 0.225 °C/s, whereas in the case of C30, it is around 0.272 °C/s.

Regarding the relationship between vertical displacement and temperature, it should be noted that the highest temperature does not necessarily lead to the highest deformation. Additionally, similar temperature gradients do not always result in similar displacement values. For example, the C30 and C40 samples exhibit a similar temperature trend but differ in their vertical displacement values. Therefore, we are unable to determine the effect of temperature on actuator deformation at this time due to a limited number of samples. However, collecting additional data will provide us with the necessary information to make informed decisions and improve our understanding of this critical issue.

In our pursuit of developing actuators that offer optimal performance at a low fabrication cost, we selected Dichloromethane as an attractive phase change fluid for actuators that operate at room temperature after considering other working fluids in this research field. The properties of working fluids used in the liquid-to-vapor phase change actuators are shown in Table 2.

Table 2. The properties of phase change fluids at 1 atm in liquid-to-vapor transition actuator research

Fluids	Boiling temperature (°C)	Latent heat of vaporization (cal/g)	Flammability at room temperature	Ref
Dichloromethane	40	78.7	No	This work
Novec <sup>TM</sup> 7000	34	33.9	No	[4-8]
Acetone	56	122	Yes	[4,8]
Ethanol	78	220	Yes	[2,3,8]
Water	100	540	No	[1]

The performance of actuators can be predicted by considering factors such as boiling temperature and latent heat of vaporization of phase change fluids. Fluids with a smaller differential in boiling point compared to room temperature, as well as lower latent heat of vaporization, may result in a faster shape-changing response of the actuator when exposed to the same amount of energy under equal conditions. For instance, Narumi and colleagues [5] demonstrated this with their Novec<sup>TM</sup> 7000-filled actuator, which expanded a rectangle-shaped actuator measuring 25 x 15 mm in just 35 s. While their performance surpasses that of our actuator, direct comparison is still challenging due to differences in design and experimental conditions. However, our work demonstrated an easy and low-cost fabrication procedure, resulting in a lower fabrication cost per actuator (0.53 USD) compared to Narumi's work (1 USD).

Although Dichloromethane is not the best candidate in terms of performance when compared with Novec<sup>TM</sup> 7000 with the above factors, it presents better advantages in terms of cost, ease of supplementation, use, and storage. Dichloromethane costs 32 times less than Novec<sup>TM</sup>, priced at around 11.33 USD/L compared to Novec<sup>TM</sup> 7000's 363.62 USD/L. Additionally, it offers more options for supplementation from various manufacturers, fostering price competition, unlike Novec<sup>TM</sup> 7000, which is exclusively produced by 3M<sup>TM</sup> Company and requires an import process for use in our laboratory based in Thailand. Moreover, with a higher boiling point, an actuator filled with Dichloromethane can ensure that it does not expand on its own due to rising environmental temperatures on hot days ( $\geq 35^{\circ}\text{C}$ ), as indicated by the Thai Meteorological Department [9]. This feature results in ease of storage compared to Novec<sup>TM</sup> 7000. Additionally, Dichloromethane also inflammable in the operate condition which is enhance the user safety compared to the flammable fluids.

## 5. Conclusions

We introduced a low-cost and easy-to-fabricate liquid-to-vapor phase change actuator. The proposed electric-driven actuator provided a lightweight and low-power consumption design. Through rigorous testing and analysis, our study demonstrates the efficacy and cost-effectiveness of the developed actuators. The best-performing device achieved a substantial maximum vertical displacement of 10.82 mm, showcasing impressive dynamic capabilities with 75% displacement within 30 s of the operation. The fabrication cost was found to be economically viable, further highlighting the feasibility and potential of these actuators for practical deployment.

## References

- [1] Matsuoka, H., Suzumori, K., & Kanda, T. (2016). Development of a gas/liquid phase change actuator for high temperatures. *Robomech Journal*, 3(1), 1-7.
- [2] Miriyev, A., Stack, K., & Lipson, H. (2017). Soft material for soft actuators. *Nature communications*, 8(1), 596.
- [3] Xia, B., Miriyev, A., Trujillo, C., Chen, N., Cartolano, M., Vartak, S., & Lipson, H. (2020). Improving the actuation speed and multi-cyclic actuation characteristics of silicone/ethanol soft actuators. *Actuators*, 9(3), 62.
- [4] Hiraki, T., Nakahara, K., Narumi, K., Niiyama, R., Kida, N., Takamura, N., Okamoto, H., & Kawahara, Y. (2020). Laser pouch motors: Selective and wireless activation of soft actuators by laser-powered liquid-to-gas phase change. *IEEE Robotics and Automation Letters*, 5(3), 4180-4187.
- [5] Narumi, K., Sato, H., Nakahara, K., ah Seong, Y., Morinaga, K., Kakehi, Y., Niiyama, R., & Kawahara, Y. (2020). Liquid pouch motors: printable planar actuators driven by liquid-to-gas phase change for shape-changing interfaces. *IEEE Robotics and Automation Letters*, 5(3), 3915-3922.
- [6] Uramune, R., Ishizuka, H., Hiraki, T., Kawahara, Y., Ikeda, S., & Oshiro, O. (2022). HaPouch: a miniaturized, soft, and wearable haptic display device using a liquid-to-gas phase change actuator. *IEEE Access*, 10, 16830-16842.
- [7] Usui, T., Ishizuka, H., Hiraki, T., Kawahara, Y., Ikeda, S., & Oshiro, O. (2021). Fully flexible liquid-to-gas phase change actuators with integrated liquid metal heaters. *Japanese Journal of Applied Physics*, 60(SC), SCCL11.
- [8] Decroly, G., Raffoul, R., Deslypere, C., Leroy, P., Van Hove, L., Delchambre, A., & Lambert, P. (2021). Optimization of phase-change material–elastomer composite and integration in kirigami-inspired voxel-based actuators. *Frontiers in Robotics and AI*, 8, 672934.
- [9] Thai Meteorological Department. (2022, August 19). Weather criteria. Thai Meteorological Department. <https://tmd.go.th/info/%E0%B9%80%E0%B8%81%E0%B8%93%E0%B8%91%E0%B8%AD%E0%B8%B2%E0%B8%81%E0%B8%B2%E0%B8%A8>



## Synergistic Effects of Plastic Wastes and Sludge for Producing Fuel via Co-pyrolysis in a Batch Reactor

Tosporn Phetyim<sup>1</sup>, Tanawat Artyota<sup>2</sup>, Natthawan Prasongthum<sup>1</sup>, Pathumrat Butniam<sup>1</sup>,  
Wanchana Sisuthog<sup>1</sup>, Amornrat Suemanotham<sup>1</sup>, Yoothana Thanmongkhon<sup>1</sup>,  
Apichat Junsod<sup>1</sup>, and Lalita Attanatho<sup>1,\*</sup>

<sup>1</sup> Expert Centre of Innovative Clean Energy and Environment, Thailand Institute of Scientific and Technological Research (TISTR), Khlong Ha, Khlong Luang, Pathum Thani 12120, Thailand

<sup>2</sup> Department of Chemical Engineering, College of Engineering, Rangsit University, Lak-Hok, Muang, Pathum Thani 12000, Thailand

E-mail: \* lalita@tistr.or.th

### Abstract

Municipal Solid Waste (MSW) management, particularly disposal as open dumps are nationwide crisis resulting into the global warming and climate change issues. Plastic wastes are certainly crucial problem, on contrary, considered as sustainable sources of energy. Plastics co-mingled with other wastes, i.e., biomass and sludge, is an interesting research trended in enhancing the yield and property of oil products toward taking advantage of flexible resources and sustainable fuel development. This study aims to investigate the influences of dried sludge acquired from wastewater treatment plant co-pyrolyzed with mixed plastics (polyethylene; PE, mixed with polypropylene; PP) using a fixed-bed reactor. The products yields and compositions were determined via the individual pyrolysis process of plastics and sludge at temperature of 500 °C, and their synergistic effects (25, 50 and 75 %wt of sludge in plastic wastes) were also explored under the inert atmosphere, 100 ml/min of nitrogen, with 60 min of reaction time. The experimental results revealed that decomposition of plastic pyrolysis was significantly improved when the mixing ratio of sludge was increased. However, the oil yield of plastic co-pyrolyzed with 25 %wt of sludge was reportedly achieved about 51 %wt which rose up to about 20% from the pure plastics used as feed. Moreover, the higher mixing ratios, the lower oil yields were obtained.

**Keywords:** Plastic wastes; Sludge; Synergistic effects; Pyrolysis, Fuel

### 1. Introduction

Municipal solid waste (MSW) is a combination of diverse solid waste materials that result from human activities. These wastes consist of a wide range of substances such as food waste, paper, biomass, glass, metals, plastics, rubbers, and textiles. MSW management presently involves landfill, composting, and incineration, etc. In term of energy aspects, liquid fuel converted from MSW via thermo-chemical processes has played an important role as value creation of wastes. Apart from conventional biofuel production through chemical or biological pathways, liquid fuel derived from solid wastes has been getting a high attention [1].

Pyrolysis is a thermal process applied to decompose the organic materials in oxygen-free atmosphere, resulting in the production of gaseous, liquid, and solid products. The amount and composition of those are depended on the pyrolysis conditions, i.e., types of the reactor, characteristics of material, heating rate, reaction time, temperature, pressure and, also, the presence of catalysts [2]. Liquid product obtained from the process, can be directly utilized as

an alternative fuel or incorporated with petroleum refinery [3]. Solid product, called char, leftover from the pyrolysis has several applications, i.e., the sources of activated carbon, catalysts, etc. Gas produced during pyrolysis also holds potential as a gaseous fuel.

In this study, the production of pyrolysis oil using a laboratory scale setup of fixed-bed reactor was investigated. The product yields and chemical properties were determined and compared at different residence time and ratios of sewage sludge to assess its characteristics.

## 2. Materials and Methods

### 2.1 Materials

The plastic wastes were collected from TISTR's Municipal Solid Waste Management, Tan Diao Model, Tan Diao sub-district, Kaeng Khoi district, Saraburi province, in Thailand. The sample of plastic wastes consisted of 90% polyethylene (PE) and 10% polypropylene (PP) by mass with crushed particles ranging of 1 - 5 mm, approximately. The dried sludge waste was received from the waste water treatment facilities of an ice cream factory.

### 2.2 Methods

#### 2.2.1 Batch pyrolyzer

The mixed plastic waste feedstock was subjected to pyrolysis using a fixed-bed stainless steel reactor with an externally heated electrical furnace. The reactor had a volume of 600 ml and an internal diameter of 47 mm. The configuration of the fixed bed pyrolysis system can be observed in Fig. 1. A weighed sample of 20 grams, along with glass balls and glass wool as the media, was introduced into the reactor. The pyrolysis process was carried out by gradually increasing the temperature from room temperature to a final temperature of 500 °C [2,4], while maintaining different residence time of 60, 90 and 120 min. The system was thoroughly purged by N<sub>2</sub> gas with a flow rate of 100 ml/min. The liquid product was condensed in a series of tar trap cooled in a water bath at 0 °C meanwhile the non-condensable gas was sampled by a gas bag for analysis. In Fig.2, the oil phase apparently separated from aqueous solution was then simply taken using a separation funnel. The solid portion was determined by measuring the overall weight loss of reactor. Yields of each product were calculated using equation (1) and gas fraction was determined by difference.

$$Product\ yield = \frac{W_i \times 100}{W_{raw\ material}}, \quad i = oil, aqueous, solid \quad (1)$$

#### 2.2.2 Characterization of liquid products

The oil product derived from the pyrolysis process underwent characterization using gas chromatography-mass spectrometry (GC-MS). The analysis was conducted using a 7820A model GC with a 5975-mass selective detector. A DB-5HT column measuring 60 m x 0.25 mm (I.D) x 0.10 μm was utilized and helium was employed as the carrier gas at a constant flow rate of 1 ml/min. The initial oven temperature was set at 40 °C and subsequently increased to 100 °C at a heating rate of 3 °C/min. It was then further raised to 370 °C at a heating rate of 5 °C/min and maintained at that temperature for 25 minutes. A split ratio of 20:1 injection was applied at 280 °C. The ion source and transfer line temperature were maintained at 230 °C and 320 °C, respectively. Data acquisition was performed in the full-scan mode within the m/z range of 20 to 800. Chromatographic peaks were identified by

referring to the NIST mass spectral data library. The percentages of the peaks were calculated based on the peak area of the total ion chromatogram (TIC).

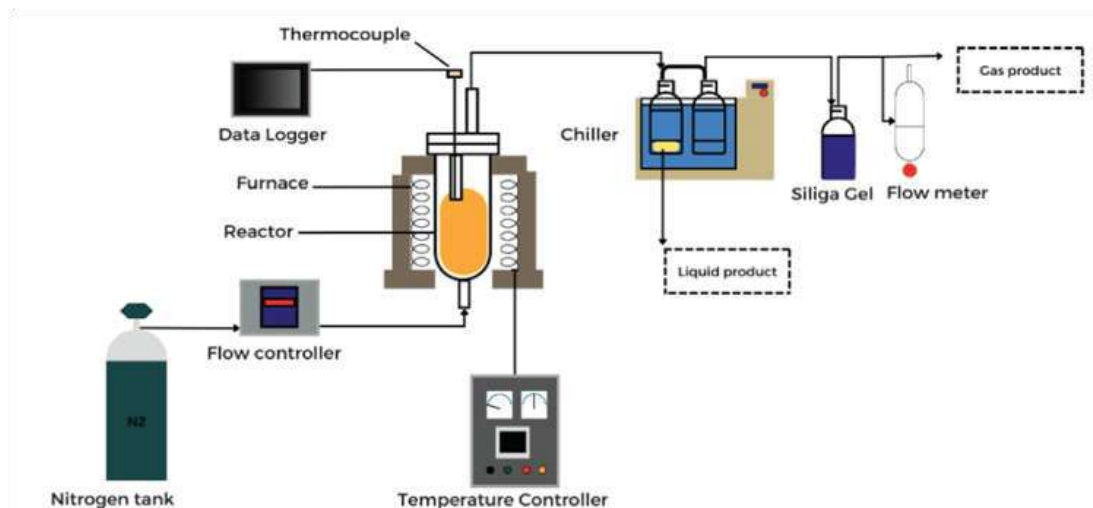


Fig. 1 Schematic diagram of a fixed-bed reactor for pyrolysis process

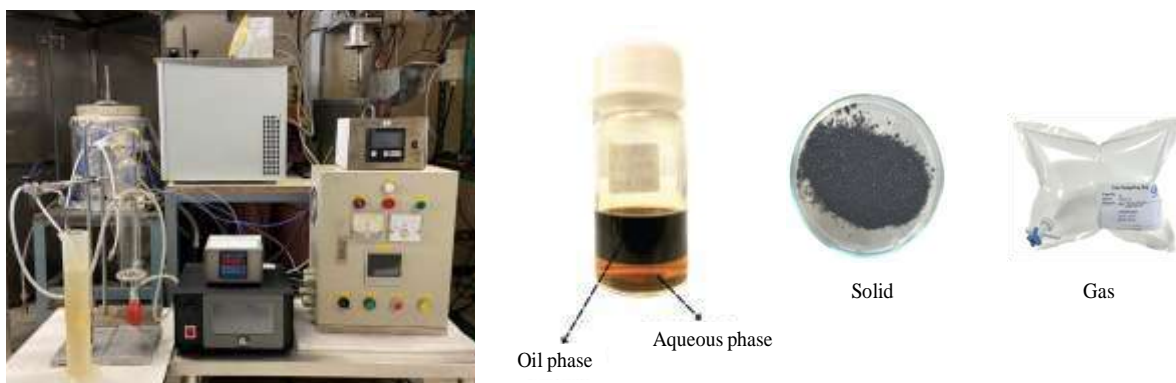


Fig. 2 The laboratory scale setup of pyrolysis process and the obtained products

### 2.2.3 Characterization of gas products

The non-condensed gas products were subjected to analysis using an Agilent GC 7890B gas chromatograph. This instrument was equipped with two detectors, namely a thermal conductivity detector (TCD) and a flame ionization detector (FID), and employed four chromatography columns: Porapak Q, Molsieve 13X, HP-AL/S, and GS-Oxyplot. Helium was utilized as the carrier gas throughout the analysis. The temperature of the columns was programmed to follow a specific sequence: initially maintained at 45 °C for 2 minutes, then increased to 120 °C at a rate of 15 °C/min, further raised to 180 °C at a rate of 12 °C/min, and finally held at the last temperature for a duration of 26 minutes.

## 3. Results and Discussion

### 3.1. Properties of feedstock

The mixed plastic wastes and sewage sludge used in this study are given in Table 1.

Table 1 Characterization of raw material

Properties	Mixed plastic wastes	Sewage sludge
Proximate analysis (% wt, dry basis)		
Moisture	0.46	9.76
Volatile matter	97.61	84.03
Fixed carbon	0.01	7.29
Ash	2.38	8.68
Ultimate analysis (% wt, dry basis)		
Carbon	83.61	48.91
Hydrogen	14.14	7.70
Nitrogen	0.20	6.38
Sulfur	0.02	1.07
Oxygen *	N/A	27.26
High heating value (MJ/kg)	43.16	21.65
Low heating value (MJ/kg)	40.15	19.77

\* By difference

### 3.2. Effects of residence time

The products obtained from the pyrolysis of plastic waste are oil, char, and gas operated at temperature of 500 °C. Each product yield was determined in percentage by weight (%wt) shown in Fig. 3. The liquid yields were about 23.6, 30.9, and 36.1 %wt within residence time of 60, 90, and 120 min, respectively. The increase of reaction time promoted the fractions of liquid and gas, though the solid decreased. The liquid yield possibly decreased in longer residence because the decomposition effect of small HCs into gas was occurred [5]. The oil fraction, however, is resulted from the performance of liquid condensers as well.

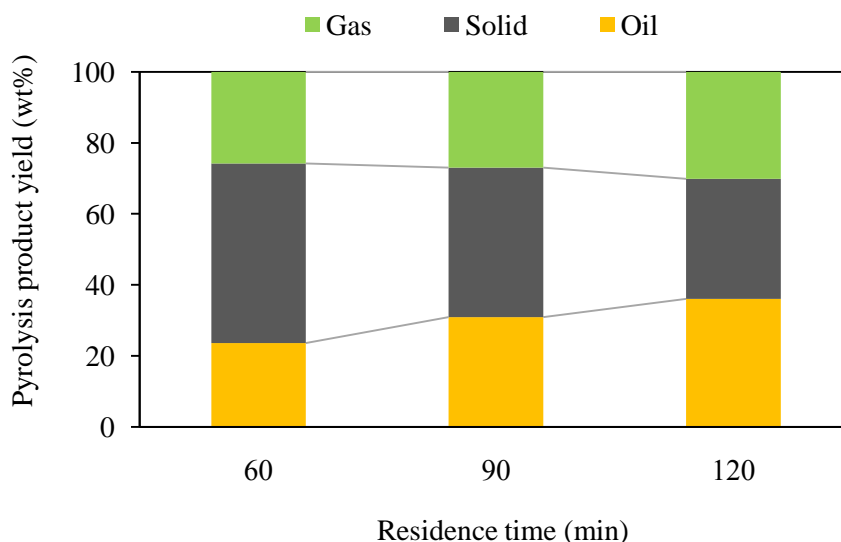


Fig. 3 Product yields obtained from pyrolysis of plastic waste at different time (500 °C)

A shorter retention time is aided the creation of primary products, i.e., monomers, while the creation of more thermodynamically stable products, i.e., H<sub>2</sub>, CH<sub>4</sub> and aromatics, are linked to longer time. Slow pyrolysis (and batch process), which is the conventional pyrolysis, presents residence time as the duration when the waste plastic begins heat up to that when the products are attained [4]. With a longer time, a further conversion of the primary products

into secondary ones (such as light molecular hydrocarbons and non-condensable gases), which are more thermally stable, is achievable [6]. Miller studied a pyrolysis process for conversion of plastic to lubricating oil obtained the oil yields in range of 37-57 %wt above temperature of 385 °C [7].

### 3.3. Effects of sludge mixed in plastic waste for pyrolysis

The pyrolysis of plastic waste (PW) mixed with sewage sludge (SS), at temperature of 500 °C and time of 60 min, at several ratios, i.e., 100:0, 75:25, 50:50 25:75 and 0:100 by weight. The results found that liquid products obtained from the co-pyrolysis of plastic and sludge, ratio of 25-100 %wt, had physical appearances into 2 phases, usually named oil and aqueous phases. The portion of aqueous product was higher when increasing the amount of sludge. Fig. 4 presents that oil fraction increased from 23.6 to 54.2 %wt when adding the amount of sludge to 25 %wt. However, the oil products were lowered when increasing the amount of sludge to 50-100 %wt. Meanwhile the solid parts decreased from 50.6 to 13.1 %wt when the sludge was added about 25 %wt. On the other hand, the amount of solid char was more leftover when the sludge was increased to 50-100 %wt, as shown in Fig. 4.

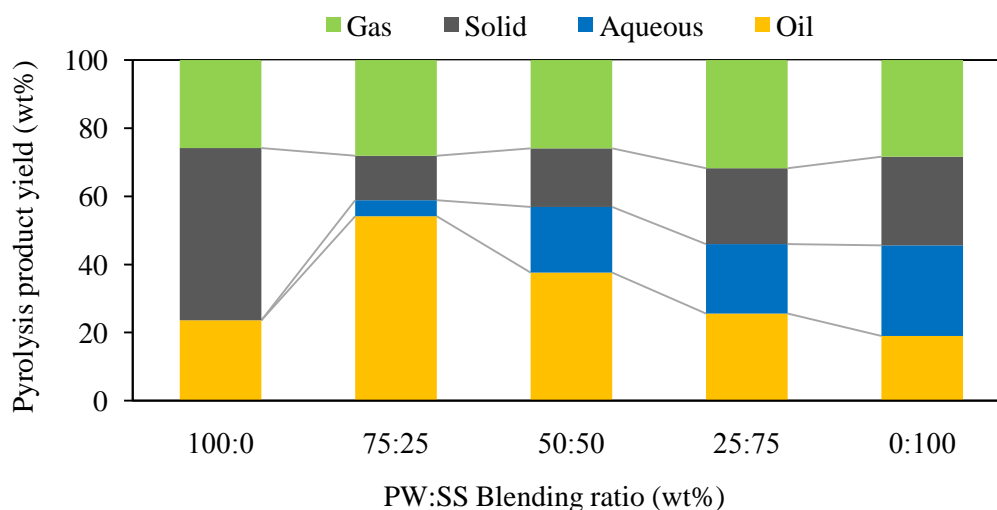


Fig. 4 Product yields obtained from co-pyrolysis of plastic waste and sludge at different ratio (500 °C and 60 min)

As results, the process of plastic co-pyrolyzed with 25 %wt of sludge was the optimal ratio in term of oil yield. Because the minerals and oxygen-contained substances existed in the sludge, listed in Table 2, could probably enhance the de-polymerization of plastic feedstock during the process. The results also show a trend of further reactivity to produce more gaseous products when the portion of sludge was increased. The characterization of oil samples obtained from the investigation compared between plastic pyrolysis and co-pyrolysis of plastic with 25%wt of sludge is given in Table 3. The calorific values of oil produced from the feedstock are 45.67 and 44.29 MJ/kg, respectively.

Table 2 Components of mineral oxides in the sludge

Composition	CaO	Al <sub>2</sub> O <sub>3</sub>	SO <sub>3</sub>	P <sub>2</sub> O <sub>5</sub>	SiO <sub>2</sub>	Na <sub>2</sub> O	Fe <sub>2</sub> O <sub>3</sub>	MgO	Cl
%wt	33.2	20.4	15.3	13.0	10.2	2.54	2.18	1.01	1.00

Table 3 Properties of oil product obtained from the pyrolysis process

Type of oil products	Elemental composition (% wt)					High heating value (MJ/kg)	Low heating value (MJ/kg)
	C	H	N	S	O*		
Plastic wastes	86.54	13.32	0	0.09	0.05	45.67	42.77
Plastic wastes + Sewage sludge (75:25)	79.47	13.15	0.12	0.03	7.22	44.29	41.51

\* By difference

### 3.4. Characterization of py-oil and py-gas products

The pyrolytic oil composition was characterized using GC-MS. The distribution of hydrocarbon components in oil was determined using a semi-quantitative study by means of the percentage area of the chromatographic peaks. Fig. 5 illustrates the chemical-based components of pyrolysis oil operated at reaction temperature of 500 °C and residence time of 60 min. The most important point in investigating the similarity of oil as a fuel is the aliphatic compounds, i.e., alkanes and alkenes. As GC-MS results, the oil obtained from the plastic waste has substances of carbon distribution in range of C5-C26 which is more gasoline-like hydrocarbons. Furthermore, Al-Salem found that most (> 96%) of pyrolysis oil formed by pyrolyzing HDPE in temperature range of 500–800 °C was aliphatic C8-C12, and C13+ could be found when increasing temperatures [8].

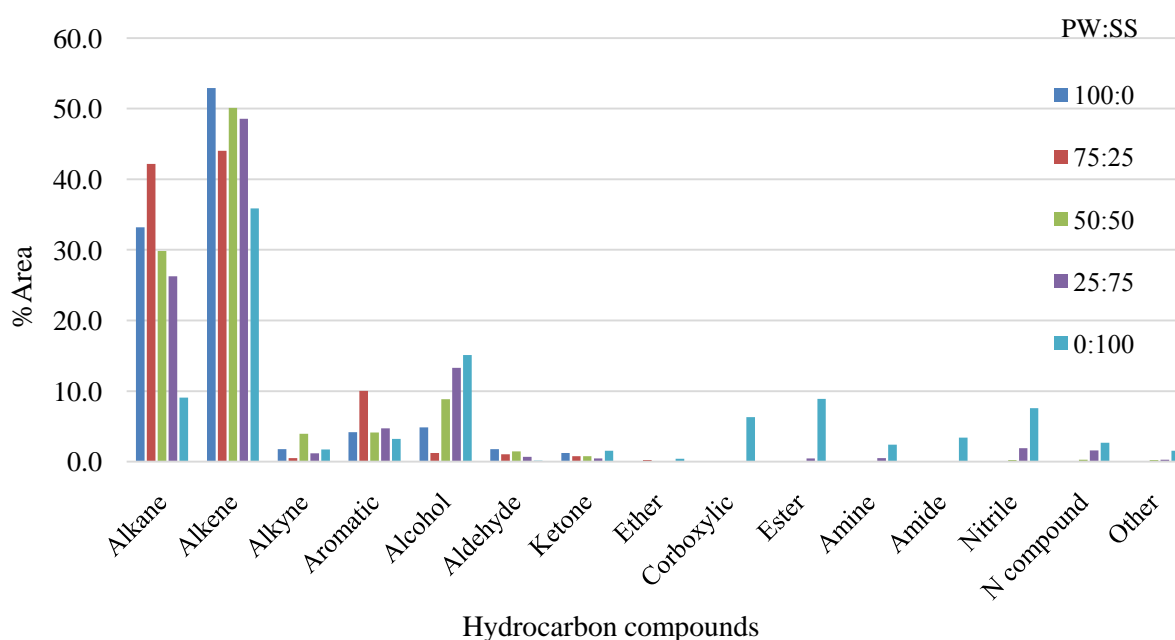


Fig. 5 Hydrocarbon distribution of py-oil obtained from co-pyrolysis of plastic waste and sludge at different ratio (500 °C and 60 min)

In Fig. 6, the oil product derived from the plastic waste is presented acidic property. The pH value is around 4. On contrary, the oil produced from the sludge pyrolysis is alkaline basis, pH value of 9-10. The elemental composition of the sludge shows that the amount of C, H, N, S and O were 48.91, 7.70, 6.38, 1.07 and 27.26 %wt, respectively, and its oxide components are apparently alkali dominated. Therefore, the oil received from the co-pyrolysis

of plastic and sludge have pH values in the ranges of 6-8, indicating that the utilization of sewage sludge in pyrolysis process could appropriately improve the oil portion and its acidity. However, the py-gas analyses are exhibited slightly different in each fraction of hydrocarbon gas distribution as seen in Fig. 7.

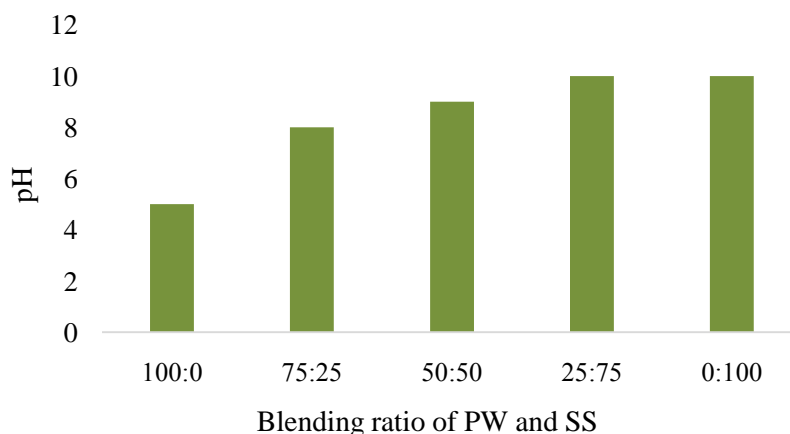


Fig. 6 pH of py-oil obtained from co-pyrolysis of plastic waste and sludge at different ratio (500 °C and 60 min)

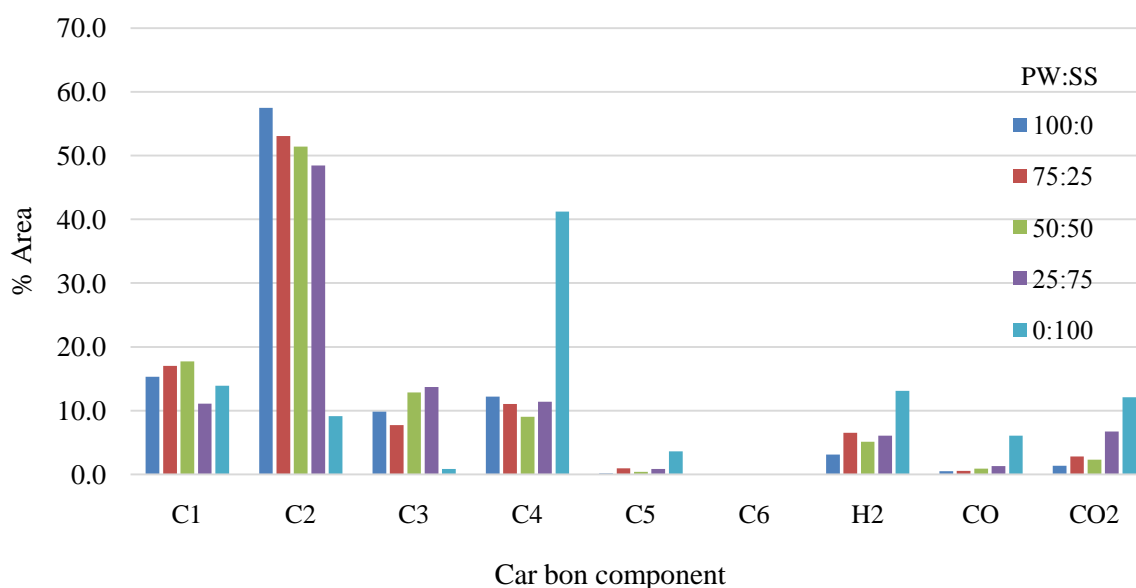


Fig. 7 Carbon distribution of py-gas obtained from co-pyrolysis of plastic waste and sludge at different ratio (500 °C and 60 min)

#### 4. Conclusions

This study carried out the plastic pyrolysis and synergistic effects of sludge co-pyrolyzed with plastic waste collected from Tan Diaio community's municipal solid waste management. The oil product was achieved approximately 54 %wt increasing from 24 %wt, only plastic as feed, when the plastic mixed with 25 %wt of sewage sludge. The oil was characterized by GC-MS and the results were determined as gasoline-liked oil with the major proportion of



alkanes and alkenes. The optimal mixing ratio of plastic and sludge, 25 %wt, for pyrolysis showed the highest yield and the pH value of 6-8, which is nearly neutral and potentially applied in the agricultural machines.

## 5. Acknowledgements

The authors are very grateful for the financial support to Thailand Science Research and Innovation (TSRI) and the raw material are kindly provided from TISTR's Municipal Solid Waste Management, Tan Diao Model at Saraburi, facilitated by Dr. Rewadee Anuwattana.

## References

- [1] Islam, M. N., Islam, M. N., Beg, M. R. A. and Islam, M. R. 2005. Pyrolytic Oil from Fixed Bed Pyrolysis of Municipal Solid Waste and Its Characterization. *Renewable Energy* 30(3): 413–420.
- [2] Velghe, I., Carleer, R., Yperman, J. and Schreurs, S. 2011. Study of the Pyrolysis of Municipal Solid Waste for the Production of Valuable Products. *Journal of Analytical and Applied Pyrolysis* 92(2): 366–375.
- [3] Bridgwater, A V. 2012. Review of fast pyrolysis of biomass and product upgrading. *Biomass and Bioenergy* 38: 68-94.
- [4] Yansaneh, O. Y. and Zein, S. H. 2022. Recent Advances on Waste Plastic Thermal Pyrolysis: A Critical Overview. *Processes* 10(2): 332.
- [5] Chaiya, C., Pankumpet, N., Buapibal, B., Chalermssinsuwan, B. 2020. Alternative liquid fuel from pyrolysis of polyethylene wax. *Energy Reports* 6: 1262-1267.
- [6] Aguado, J., Serrano, D. P., Vicente, G. and Sánchez, N. 2007. Enhanced Production of  $\alpha$ -Olefins by Thermal Degradation of High-Density Polyethylene (HDPE) in Decalin Solvent: Effect of the Reaction Time and Temperature, *Industrial and Engineering Chemistry Research* 46(11): 3497–3504.
- [7] Miller, S. J., Shah, N. and Huffman, G.P. 2005. Conversion of Waste Plastic to Lubricating Base Oil. *Energy and Fuels* 19(4): 1580–1586.
- [8] Al-Salem, S. M. 2019. Thermal Pyrolysis of High Density Polyethylene (HDPE) in a Novel Fixed Bed Reactor System for the Production of High Value Gasoline Range Hydrocarbons (HC), *Process Safety and Environmental Protection* 127: 171–179.



## Enhancement of Porous Carbon from Oil Palm Empty Fruit Bunch and CO<sub>2</sub> Capture Application

Wanchana Sisuthog<sup>1</sup>, Natthawan Prasongthum<sup>2</sup>, Amornrat Suemanotham<sup>2</sup>, Yoothana Thanmongkhon<sup>2</sup>, Lalita Attanatho<sup>2</sup>, Sasiradee Jantasee<sup>1</sup>, Weerinda Mens<sup>1</sup> and Chaiyan Chaiya<sup>1\*</sup>

<sup>1</sup>*Department of Chemical and Materials Engineering, Faculty of Engineering,*

*Rajamangala University of Technology Thanyaburi, Pathum Thani, 12110, Thailand*

<sup>2</sup>*Expert Centre of Innovative Clean Energy and Environment, Thailand Institute of Scientific and Technological Research (TISTR), Pathum Thani, 12120, Thailand*

E-mail: \*Chaiyan\_c@rmutt.ac.th

### Abstract

Two hydrochars were produced from palm oil empty fruit bunch (EFBs) using hydrothermal carbonization (HTC) at a temperature of 240 °C for 2 hour. These hydrochars, namely conventional hydrochar (CH) and H<sub>2</sub>SO<sub>4</sub>-assisted hydrochar (A-CH). They also were developed to enhance higher porosity by KOH chemical activation using appropriate conditions, including a weight ratio of 1:1 between hydrochar and KOH, an activation temperature of 800 °C, and a duration of 1 hour, namely CH-K and A-CH-K. The results showed H<sub>2</sub>SO<sub>4</sub>-assisted HTC plus KOH activation (A-CH-K) produced the excellent properties porous carbon that contained surface area 1,348 m<sup>2</sup>/g, pore volume 0.83 cm<sup>3</sup>/g and proper pore size in mesoporous range 2.47 nm. CH and A-CH provided the same chemical functional groups such as C-H, C-O and C=O, but all disappeared after the KOH activation. A-CH-K showed the highest amount CO<sub>2</sub> capture as 1.002 mmol CO<sub>2</sub>/g.

**Keywords:** Palm oil; Empty fruit bunch; Porous carbon; Chemical activation; CO<sub>2</sub> capture.

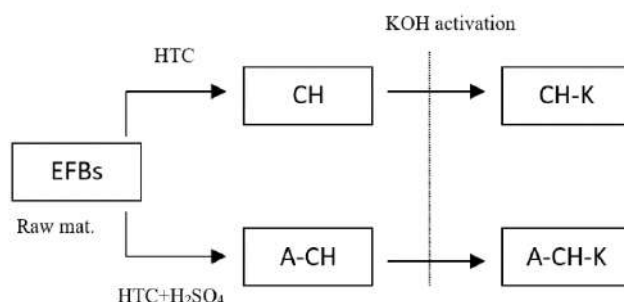
## 1. Introduction

During the palm oil extraction process, an enormous amount of empty fruit branches (EFBs) is wasted. This waste was processed in a variety of ways, including landfill disposal and use as boiler fuel and fertilizer. It has undergone thermochemical conversion to carbon-based products such as pyrolysis, carbonization, activation, gasification, and hydrothermal carbonization (HTC). These reactions produce carbon-based compounds in gaseous, liquid, and solid phases. The hydrothermal technique was chosen for this study because the reaction requires water as a precursor and the high moisture raw material, which were EFBs abandoned from a palm oil processing factory in Thailand. HTC typically creates "hydrochar" a solid carbon with several functional groups (Śliz & Wilk, 2020). Hydrochar benefits from low energy consumption and high production rate; nevertheless, both pore volume and specific surface area are low (Sun et al., 2014), which may require a more modified procedure for various applications such as adsorption, catalyst support, and solid fuel. Because of the many functional groups of hydrochar, the application of adsorption was investigated, particularly for adsorbates that are inert or difficult to make chemical bonds, such as CO<sub>2</sub>. Previous research has shown that hydrochar can be a dominant adsorbent in a variety of processes. (Zhang et al., 2022) used HTC to transform Chinese medicine industrial waste into hydrochar, which showed high methylene blue adsorption efficiency. (Huang et al., 2019) created the adsorbent from garlic peel using HTC and KOH activation. It was discovered that it has the highest CO<sub>2</sub> uptake of up to 4.22 mmol/g at 25 °C and 1 bar due to its increased microporosity of up to 98% and many narrow micropores. (Zhang et al., 2020) improved the surface area of pristine hydrochar by activating it with CO<sub>2</sub> for acetone and cyclohexane adsorption. As a result, the pristine hydrochars had lower VOC adsorption (13.24-24.64 mg/g) than the activated hydrochars (39.42-121.74 mg/g). (Benedetti et al., 2019) transformed biomass from gasification procedures into char before activating it with KOH and ZnCl<sub>2</sub> to produce activated carbon. It was evaluated the CO<sub>2</sub> adsorption efficiency by using thermogravimetric analysis and found that the material showed the CO<sub>2</sub> adsorption efficiency at 3.7 % uptake. However, several research have reported that the strong basic such as KOH effect destroys the cellulose structure and increases the biomass porosity. This study looked into the feasibility of using hydrothermal carbonization to produce hydrochar from moisture-rich EFBs abandoned by the palm oil industry. However, adding an activator to HTC accelerated the hydrolysis and dehydration processes that may take place at lower temperatures, as well as the formation of chemical functional groups and porosity (Sarwono & Kurniawan, 2017). The use of an acidic H<sub>2</sub>SO<sub>4</sub> activator in the HTC process appears to result in uniformly porous hydrochar. Whereas using H<sub>2</sub>O<sub>2</sub> as an activator boosted both the oxygenated functional groups and the porosity of hydrochar (Jain et al., 2015).

This study focuses on the conversion of palm oil EFBs into value-added products for CO<sub>2</sub> capture. Four materials were investigated: conventional hydrochar (CH), conventional hydrochar-assisted H<sub>2</sub>SO<sub>4</sub> (A-CH), conventional hydrochar-activated KOH (CH-K), and conventional hydrochar-assisted H<sub>2</sub>SO<sub>4</sub>-activated KOH (A-CH-K). The resultant biochars were evaluated for physical characteristics like surface area and morphology, as well as chemical functional groups. Finally, it was evaluated the CO<sub>2</sub> adsorption efficiency via thermal-gravimetric analysis.

## 2. Materials and Methods

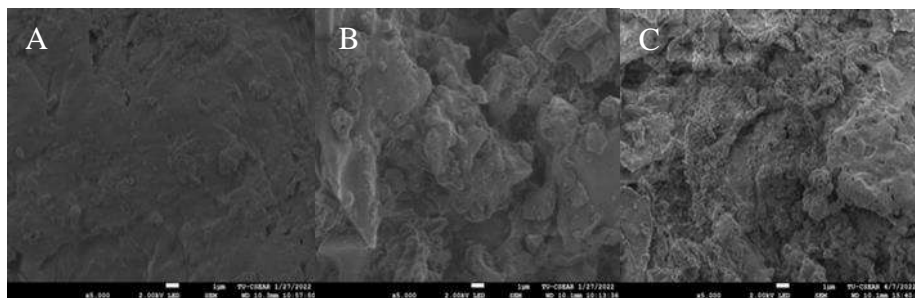
This study used EFBs obtained from the oil palm industry in Thailand as raw material. The EFBs were dried in the oven overnight at 105 °C before being crushed into small pieces with the crusher machine. The EFBs were sieved with a mechanical sieve with a maximum size of 2 cm. The hydrothermal carbonization (HTC) was carried out in a 4.5 L hydrothermal reactor. EFBs and water were weighed at a constant ratio of 1:10. EFBs and water were used in the reaction at a constant weight ratio of 1:10. Temperature was constant 240 °C, and operating times 2 hour under the N<sub>2</sub> atmosphere throughout the entire operating time. This product obtained was called conventional hydrochar or “CH”. Replacing hydrolytic solutions of 0.1 M H<sub>2</sub>SO<sub>4</sub> with pure water would obtain conventional hydrochar-assisted H<sub>2</sub>SO<sub>4</sub> or “A-CH”. Both CH and A-CH were activated by KOH by varying weight ration 1:1 under 800 °C for 1 hour, then “CH-K” and “A-CH-K” were produced (Fig.1). An automated gas adsorption analyzer from Quanta Chrome AUTOSORB IQ station 1 was used to characterize surface area, pore size, and pore volume. The morphology was captured using a JEOL JSM 7800F scanning electron microscope (SEM). The chemical functional groups (CFG) in the biochars were identified using Shimadzu model IRresting-21 Fourier Transform Infrared spectroscopy (FTIR). Finally, four materials were evaluated the CO<sub>2</sub> adsorption efficiency by using thermogravimetric analysis. 40%vt of CO<sub>2</sub> was fed in the chamber of TGA under 20 ml/min and isothermal conditions. The weight change of sample from 0 to 105 min was collected and evaluated the % adsorption of CO<sub>2</sub>.



**Fig.1.** Product preparations

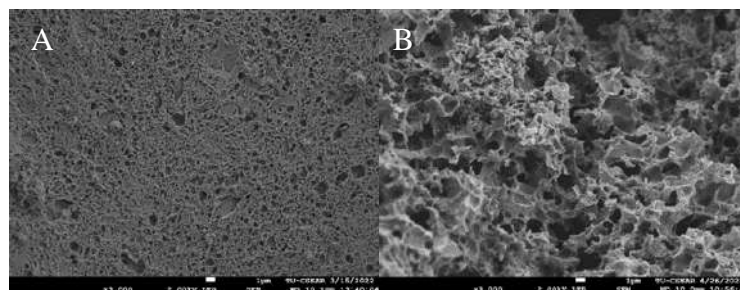
## 3. Results and Discussion

Figure 2 shows SEM pictures comparing the surface appearance and physical attributes of EFB and hydrochar. As expected, a significant difference was seen. Fig. 2A shows that raw EFB has a cellular structure similar to lignocellulosic biomass and has many holes. The HTC process caused the lignocellulosic structure to burst into fragments. Gas release from volatile matter resulted in the formation of tiny pores in CH (Fig. 2B). Samples produced with sulphuric acid (A-CH) showed more tiny porous structures. The surface appears to have a more rectangular shape. H<sub>2</sub>SO<sub>4</sub> is a strong dehydrating agent, which may stimulate the creation of these types of structures (Fig. 2C).



**Fig.2.** Materials from HTC (A) EFBs (B) CH (C) A-CH

After KOH activation, there were the different morphology of CH-K and A-CH-K in Fig. 3. The SEM photo of CH-K showed in Fig. 3B that a uniformly tiny porous was developed, and many pores were developed by the KOH's reaction. While A-CH-K showed that the external surfaces for are full of cavities and quite large irregular because of KOH activation. Activation at 800 °C with KOH resulted in the creation of more pores and substantial removal of volatiles. It seems that the usage of H<sub>2</sub>SO<sub>4</sub> as an activator on the HTC process (A-CH), affecting the weakened EFBs structure. Then KOH reaction in activation process made the A-CH-K surface seems larger than CH-K.



**Fig.3.** Materials from KOH activation (A) CH-K (B) A-CH-K

Table 2 showed the specific surface area (BET) of four materials. It seems that CH from conventional HTC contained slightly low surface area with the large pore. Although, the usage of H<sub>2</sub>SO<sub>4</sub> in HTC process (A-CH) created the higher surface area and decreased the pore diameter as 4.32 nm which was the useful pore size for adsorption than 10.89 nm, A-CH contained the shallow volume which may lead the low efficiency adsorption. The results of surface area of CH-K and A-CH-K confirmed the SEM photo because their surface area rise higher than 10 times. CH-K surface area was 931.00 m<sup>2</sup>/g, while the CH pre-modified with H<sub>2</sub>SO<sub>4</sub> showed the surprising surface area as 1348 m<sup>2</sup>/g. Additional, the pore diameter of CH-K and A-CH-K were in range of lower mesoporous (2.00 ≤) which was the benefit for adsorption process because it is compatible with several type of adsorbate molecules and effect the high mass transfer rate into the pore structure.

**Table 1.** Physical properties of samples

Materials	surface area (m <sup>2</sup> /g)	pores volume (cm <sup>3</sup> /g)	Average pores diameter (nm)
CH	11.91	0.03	10.89
A-CH	84.31	0.03	4.32
CH-K	931.00	0.47	2.70
A-CH-K	1,348.00	0.83	2.47

Figure 4 shows the FTIR spectra of the chemical functional groups (CFG) of EFBs with O-H stretching (hydroxyl group 3,200-3,500 cm<sup>-1</sup>), C-H stretching (aliphatic groups 2,840-3,000 cm<sup>-1</sup>), C=O stretching (carbonyl group 1,705-1,725 cm<sup>-1</sup>), and C-O. They were stretching bands made of lignocellulosic material. After HTC at 240 °C or sample CH, the bands of hydroxyl O-H stretching at 3,200-3,500 cm<sup>-1</sup> disappeared, whereas the peak of C-H stretching at wavenumber at 2,840-3,000 cm<sup>-1</sup> was reduced. The ketone C=O groups at 1,705-1,725 cm<sup>-1</sup> and C-O remained stable during the HTC process. There was no change in CFG when HTC added H<sub>2</sub>SO<sub>4</sub> as an activator (A-CH), which was similar to CH. For CH-K and A-CH-K, which were activated by KOH at 800 °C, it was found that all CFG were dispersed due to the high-temperature impact.

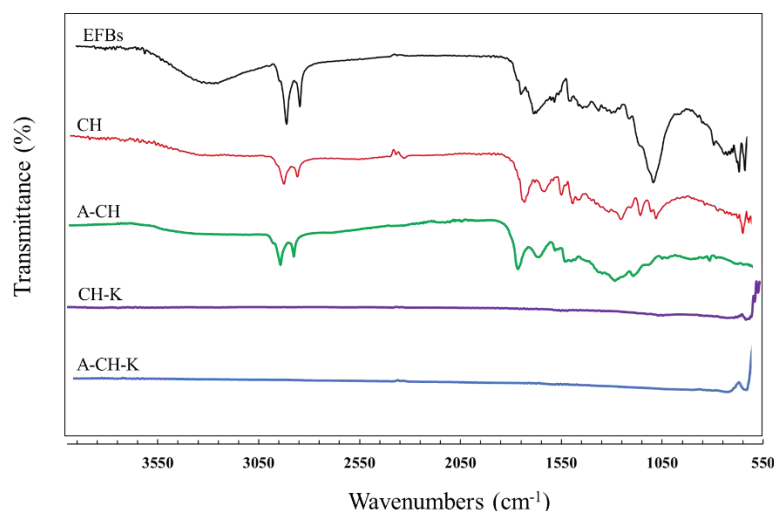
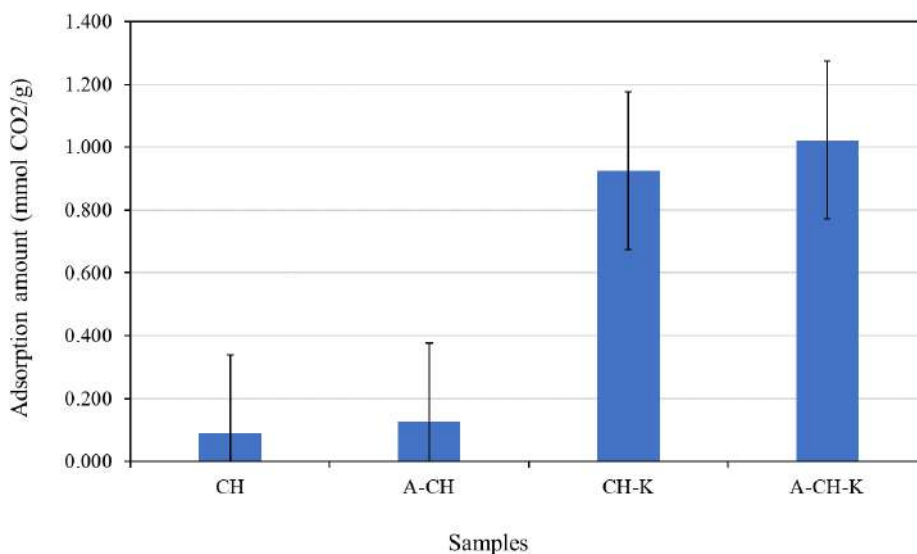
**Fig.4.** FT-IR spectra of various samples

Figure 5 demonstrates that the adsorption of CO<sub>2</sub> is significantly affected by the surface area of the sample, suggesting that A-CH-K presented the highest CO<sub>2</sub> capture at an amount of 1.002 mmol CO<sub>2</sub>/g. Based on the prior FTIR analysis, it was determined that A-CH-K no longer contains any CFG. This CO<sub>2</sub> adsorption is mainly a result of physical adsorption. However, the porous volume is highly efficient. An analysis of the adsorption properties of CH and A-CH revealed that their CO<sub>2</sub> adsorption capacities are highly similar. Both samples had an equal amount of porous volume while having surface areas that differ by over 8 times. It showed that the CO<sub>2</sub> molecules could only diffuse into the external surface.



**Fig.5.** CO<sub>2</sub> adsorption of various samples

#### 4. Conclusion

The sample from H<sub>2</sub>SO<sub>4</sub> assisted HTC (A-CH) effect the increasing of external surface area from 11.91 to 84.31 m<sup>2</sup>/g but does not change the pore volume of CH. However, A-CH and CH samples contained the same chemical functional groups. The modified sample with KOH activation (CH-K and A-CH-K) developed the large amount of surface area and pore volume and also the proper pore diameter for adsorption mechanism. The CO<sub>2</sub> capture results showed that its efficiency mainly depended on surface area than chemical functional groups and A-CH-K showed the highest amount capture as 1.002 mmol CO<sub>2</sub>/g.

#### Acknowledgement

This research was supported by Thailand Science Research and Innovation Promotion Funding (TSRI) (Grant no. FRB650070/0168). This research block grants were managed under Rajamangala University of Technology Thanyaburi (FRB65E0711), and Thailand Institute of Scientific and Technological Research (TISTR) are gratefully acknowledged.

#### References

- Benedetti, V., Cordioli, E., Patuzzi, F., & Baratieri, M. (2019). CO<sub>2</sub> Adsorption study on pure and chemically activated chars derived from commercial biomass gasifiers. *Journal of CO<sub>2</sub> Utilization*, 33(May), 46–54. <https://doi.org/10.1016/j.jcou.2019.05.008>
- Huang, G., Liu, Y., Wu, X., & Cai, J. (2019). Activated carbons prepared by the KOH activation of a hydrochar from garlic peel and their CO<sub>2</sub> adsorption performance. *New Carbon Materials*, 34(3), 247–257.

- Jain, A., Balasubramanian, R., & Srinivasan, M. P. (2015). Production of high surface area mesoporous activated carbons from waste biomass using hydrogen peroxide-mediated hydrothermal treatment for adsorption applications. *Chemical Engineering Journal*, 273, 622–629.
- Sarwono, R., & Kurniawan, H. H. (2017). The influenced of reaction time on the degradation of palm oil empty fruit bunch (EFB) in hydrothermal carbonization. *AIP Conference Proceedings*, 1904. <https://doi.org/10.1063/1.5011897>
- Śliz, M., & Wilk, M. (2020). A comprehensive investigation of hydrothermal carbonization: Energy potential of hydrochar derived from Virginia mallow. *Renewable Energy*, 156, 942–950. <https://doi.org/https://doi.org/10.1016/j.renene.2020.04.124>
- Sun, Y., Gao, B., Yao, Y., Fang, J., Zhang, M., Zhou, Y., Chen, H., & Yang, L. (2014). Effects of feedstock type, production method, and pyrolysis temperature on biochar and hydrochar properties. *Chemical Engineering Journal*, 240, 574–578.
- Zhang, X., Liu, S., Wang, M., Ma, X., Sun, X., Liu, X., Wang, L., & Wang, W. (2022). Hydrochar magnetic adsorbent derived from Chinese medicine industry waste via one-step hydrothermal route: Mechanism analyses of magnetism and adsorption. *Fuel*, 326, 125110. <https://doi.org/https://doi.org/10.1016/j.fuel.2022.125110>
- Zhang, X., Xiang, W., Wang, B., Fang, J., Zou, W., He, F., Li, Y., Tsang, D. C. W., Ok, Y. S., & Gao, B. (2020). Adsorption of acetone and cyclohexane onto CO<sub>2</sub> activated hydrochars. *Chemosphere*, 245, 125664.

## Chemical Recycling of Waste PET into Terephthalic Acid by Alkaline Hydrolysis

Natthawan Prasongthum<sup>1,\*</sup>, Nattarika Khoduangklang<sup>1,2</sup>, Kritakorn Janna<sup>3</sup>,  
Amornrat Suemanotham<sup>1</sup>, Lalita Attanatho<sup>1</sup>, Prasert Reubroycharoen<sup>2</sup>,  
Suda Ittisupornrat<sup>4</sup> and Yoothana Thanmongkhon<sup>1</sup>

<sup>1</sup> Expert Centre of Innovative Clean Energy and Environment, Thailand Institute of Scientific and Technological Research (TISTR), Khlong Ha, Khlong Luang, Pathum Thani 12120, Thailand

<sup>2</sup> Department of Chemical Technology, Faculty of Science, Chulalongkorn University, Bangkok 10330, Thailand

<sup>3</sup> Department of Chemistry, Faculty of Science and Technology, Thammasat University, Pathum Thani 12120, Thailand

<sup>4</sup> Environmental Research and Training Center (ERTC), Department of Environmental Quality Promotion, Khlong 5, Khlong Luang, Pathumthani 12120, Thailand

E-mail: \* natthawan@tistr.or.th.

### Abstract

The intensifying issue of plastic waste and widespread use of petrochemical resources for single-use plastics has become a global concern that requires urgent attention. Polyethylene terephthalate (PET) is one of the most widely produced single-use polymers globally. Although mechanical recycling is widely used for recycling PET, this process presents challenges due to the loss of mechanical and chemical properties during reprocessing. Chemical recycling such as hydrothermal depolymerization is a potential alternative pathway to recover terephthalic acid (TPA) monomers from PET waste. In this work, waste PET bottles were completely depolymerized using alkaline hydrolysis. Effects of experimental parameters, such as NaOH concentration, hydrolysis time and ethanol concentration on TPA yield, were investigated. The results revealed that adding ethanol in alkaline hydrolysis not only accelerated depolymerization of PET but also aided in separation of TPA product, enhancing overall efficiency of the process. In the presence of ethanol as a co-solvent, the highest TPA yield of 96% was achieved at reaction of 3 h with ethanol of 75 vol%. In contrast, when using an aqueous system without ethanol, it required a reaction time of 6 h to achieve 100% conversion of PET, with a resulting TPA yield of 90%. In addition, the structure of the obtained TPA was confirmed by FTIR and NMR spectroscopy. These results provided a promising approach for degradation of PET to obtain TPA, which can be potentially used as a crucial precursor to produce various products such as new PET polymers, biodegradable plastics, and metal-organic frameworks.

**Keywords:** Polyethylene terephthalate; Terephthalic acid; Hydrolysis; Depolymerization

### 1. Introduction

Over the last few decades, the widespread manufacturing and usage of polyethylene terephthalate (PET) has caused environmental concerns, primarily associated with the aggregation of post-consumer PET in the environment. In this regard, recycling PET plastics is considered as an effective strategy to address the environmental impact of PET [1]. Currently, mechanical recycling is the most common method to recycle waste PET. This method includes techniques such as grinding and melting to obtain recycled PET particles. However, these processes face challenges related to the potential loss of quality in recycled products due to the



varying degrees of polymer degradation. Chemical recycling, notably through hydrothermal depolymerization, presents a promising alternative to the conventional mechanical recycling of PET waste. This method enables the recovery of terephthalic acid (TPA) monomers from PET waste, facilitating their utilization in closed-loop applications subsequent to depolymerization [2]. TPA is recognized as a crucial chemical in the synthesis of PET and other valuable chemicals. Its global annual production has reached a substantial 107.66 million tons as of 2030, exhibiting a noteworthy annual growth rate of 5.5% [3]. Chemical recycling processes can be classified into different pathways based on the specific reagents used and desired products including hydrolysis, alcoholysis and aminolysis. Among the chemical pathways, hydrolysis is an extensively employed technique for the depolymerization of PET due to its ability to yield TPA monomers with higher purity and efficiency. Different types of hydrolysis have been reported in literature including neutral, acidic and alkaline hydrolysis. Acidic hydrolysis is noted for its ability to obtain high TPA yields, but the use of high amounts of acids contributes to the overall expenses of this process, making it very costly. Neutral hydrolysis is acknowledged for its environmental friendliness. However, the problem is that any impurities in the polymer might remain in the TPA, thereby impacting its quality. Consequently, alkaline hydrolysis of PET has been explored as an alternative to both acid and neutral hydrolysis methods. Nevertheless, one of the biggest issues for hydrolysis is the incompatibility between the liquid phase and the polymer, leading to low reaction efficiency [4]. In recent years, numerous studies focused on incorporating co-solvents to enhance the mass transfer of reaction reagents [5].

In this present work, ethanol was used as a co-solvent to increase the interaction between alcohol-water and PET. The effects of experimental parameters, such as NaOH concentration, hydrolysis time and the amount of ethanol cosolvent on the yield of TPA, were investigated. Analytical methods, specifically Fourier transform-infrared spectroscopy (FT-IR) and nuclear magnetic resonance (NMR) were employed to assess the quality of TPA obtained from PET bottles.

## 2. Materials and methods

### 2.1. Materials

Post-consumer PET water bottles were used as feedstock in the hydrolysis process. Prior to the experiment, the PET was cleansed with soap and dried to remove residual moisture. It was then cut into small pieces, about 2.5-3 mm in size. Hydrochloric acid (HCl 37 %), sodium hydroxide (NaOH) and ethanol (99.9%) were purchased from Sigma Aldrich. These chemical compounds used were reagent grade. TPA (99%) obtained from Sigma-Aldrich was used as a reference material.

### 2.2. PET hydrolysis

Experimental setup for PET hydrolysis is shown in Scheme 1. In this study, 1.5 g of polyethylene terephthalate (PET) underwent hydrolysis with 50 ml of water and NaOH concentrations ranging from 2.5 to 20 wt.% in a hydrothermal reactor at 200 °C for 6 h. After the completion of the reaction, a sludge comprising unhydrolyzed PET and Terephthalic Acid (TPA) was obtained and left to cool to room temperature. Subsequently, unhydrolyzed PET was separated through filtration, and the resulting filtrate was supplementary with 150 ml of 2M HCl for TPA precipitation. Then, the precipitate underwent additional filtration, washing until achieving a pH of 7, and drying to remove moisture. Weights of both the non-hydrolyzed

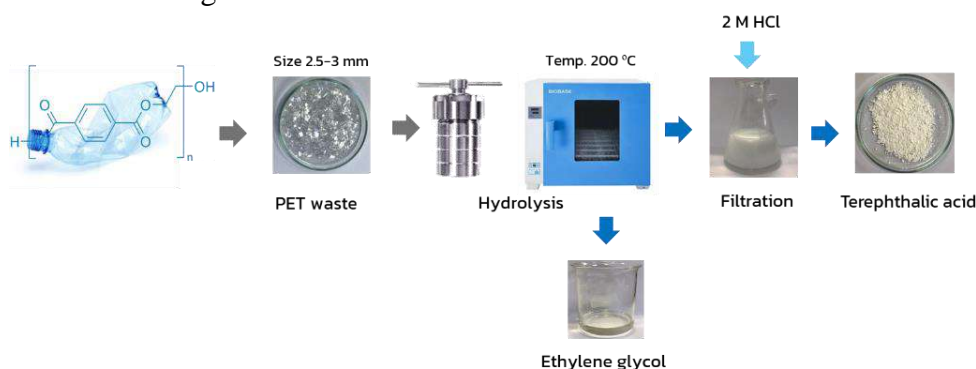
PET and the precipitated TPA were measured to calculate the change from PET to TPA. The effect of time on the hydrolysis process was investigated at two different durations: 3 h and 6 h. The study also evaluated the impact of ethanol concentration on the hydrolysis process, and its concentration varied at three different levels: 25, 50, and 75 vol%. All experimental conditions are shown in Table 1.

The obtained product was characterized by nuclear magnetic resonance (NMR) and Fourier transform infrared (FT-IR). PET conversion and TPA yield were calculated using equations (1) and (2), respectively.

$$PET\ conversion = \frac{(W_0 - W_1) \times 100}{W_0} \quad (1)$$

$$TPA\ yield = \frac{W_2 \times 100}{W_0 \times 0.874} \quad (2)$$

where  $w_0$ ,  $w_1$ , and  $w_2$  are the weight of initial PET, residual PET and TPA obtained after the reaction, respectively. The 0.874 coefficient corresponds to the ratio of molecular weight of TPA and molecular weight of PET.



Scheme 1. Experimental setup for PET hydrolysis

Table 1. PET conversion and TPA yield obtained after hydrolysis under different conditions.

Entry	T (°C)	NaOH (wt.%)	Time (h)	H <sub>2</sub> O (vol%)	EtOH (vol.%)	PET conversion (%)	TPA yield (%)
1	200	2.5	6	100	0	68 ± 0.62	67 ± 1.93
2	200	5	6	100	0	100 ± 0.00	90 ± 2.03
3	200	10	6	100	0	80 ± 1.12	64 ± 8.10
4	200	15	6	100	0	59 ± 1.87	58 ± 6.43
5	200	20	6	100	0	44 ± 2.03	38 ± 5.35
7	200	5	3	100	0	38 ± 2.17	32 ± 4.13
8	200	5	3	75	25	53 ± 3.97	47 ± 1.39
9	200	5	3	50	50	100 ± 0.00	69 ± 1.62
10	200	5	3	25	75	100 ± 0.00	96 ± 2.14

### 3. Results and discussion

To explore the optimal degradation conditions, the effects of NaOH concentration, time, and ethanol concentration were investigated. The optimization of degradation conditions is

detailed in Table 1. The effect of NaOH concentration was investigated at 200 °C for 6 h (Table 1, Entries 1-3). With the increasing of concentration from 2.5 to 5 wt.%, the PET conversion and TPA yield increased significantly from 76 to 100% and 66 to 90%, respectively. Increasing the concentration of base resulted in higher reaction speeds and the achievement of the highest conversions [4]. However, further increase in NaOH concentration, a decline in both PET conversion and TPA yield was observed. This phenomenon could be attributed to the potential deposition of excess NaOH on the surface of the PET sample, hindering the accessibility of hydroxide ions to new carbonyl carbons in unreacted PET. Consequently, this may lead to a reduction in the efficiency of the hydrolysis reaction [4]. Furthermore, Table 1 shows the effect of reaction time on PET conversion and TPA yield. The results show that the decrease in reaction time from 6 to 3 h led to a decrease in both PET conversion and TPA yield. However, at a reaction time of 3 h, when ethanol was introduced as a co-solvent at 25% vol., there was an increase in both PET conversion and TPA yield, reaching 53% and 47%, respectively. Further enhancement was observed, with PET conversion reaching 100% at an ethanol volume of 75%, and TPA yield reaching 96%. These results indicated that the co-solvent could impact the reaction pathways during degradation. Ethanol served as a phase transfer catalyst in the aqueous phase, playing a crucial role in transporting the nucleophile ( $\text{RO}^-$ ) to the surface of the PET, thereby facilitating the reaction. This was attributed to the opposing polarity between the hydrophilic nucleophile ( $\text{RO}^-$ ) and the hydrophobic PET material. The addition of ethanol can minimize this polarity difference and assist in the transfer of the nucleophile to the PET surface, where the reaction took place efficiently. More importantly, in alkaline conditions, ethanol can undergo deprotonation to form ethoxide ions ( $\text{EtO}^-$ ), which are highly reactive species capable of carrying out attack on PET reactants more efficiently, leading to faster and more efficient conversion of the reactants [5]. The possible depolymerization mechanism of PET in ethanol is shown in Fig.1. In addition, the presence of alcohol in the reaction system has another important benefit, it facilitated the isolation of the TPA product from the reaction solution due to its insolubility in alcohol, making it easier to separate and purify from the reaction mixture. Thus, alcohol not only facilitated the reaction but also assisted in the separation and isolation of the TPA product, enhancing the overall efficiency of the process.

The obtained TPA via PET hydrolysis with 5%wt NaOH, 100%vol  $\text{H}_2\text{O}$ , 200 °C for 6 h was analyzed by FTIR spectroscopy. The peaks between 2819 and 2563  $\text{cm}^{-1}$  are referred to the -OH group of carboxylic acid. The strong peak at 1675 and 1278  $\text{cm}^{-1}$  are referred to as the C=O and C-O groups of carboxylic acid. The characteristic peaks at 1570, 1510 and 1417  $\text{cm}^{-1}$  are due to C=C bonds of benzene ring of TPA. The peaks found between 725 and 875  $\text{cm}^{-1}$  are characteristic of para-substituted arene group of TPA [6]. The FTIR characteristic peaks of the obtained TPA were consistent with those in commercial TPA.

The obtained TPA was further analyzed via NMR spectroscopy and  $^1\text{H}$ -NMR and  $^{13}\text{C}$ -NMR spectroscopy are shown in Fig. 3(a) and (b), respectively.  $^1\text{H}$  NMR spectra revealed a chemical shift of 13.29 ppm in the hydroxyl protons of TPA (denoted as H1), while non-substituted H in the benzene ring exhibited chemical shifts of 8.03 ppm (denoted as H1). Similarly, in the  $^{13}\text{C}$  NMR spectra, three peaks at 130.1, 135.0, and 167.1 ppm were assigned to the aromatic (labeled as C1), quaternary aromatic (labeled as C2), and carbonyl (labeled as C3) carbon atoms of TPA [5]. According to NMR spectra of commercial TPA as shown in Fig. 4, the TPA produced from PET hydrolysis in this work had a consistent structure with that of commercial TPA.

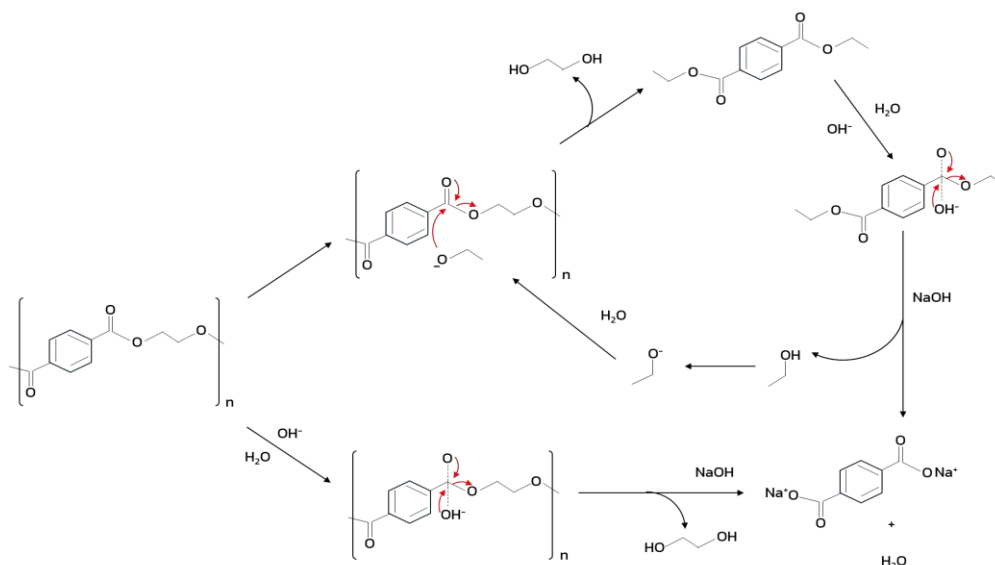


Fig. 1. The possible depolymerization mechanism of PET in ethanol

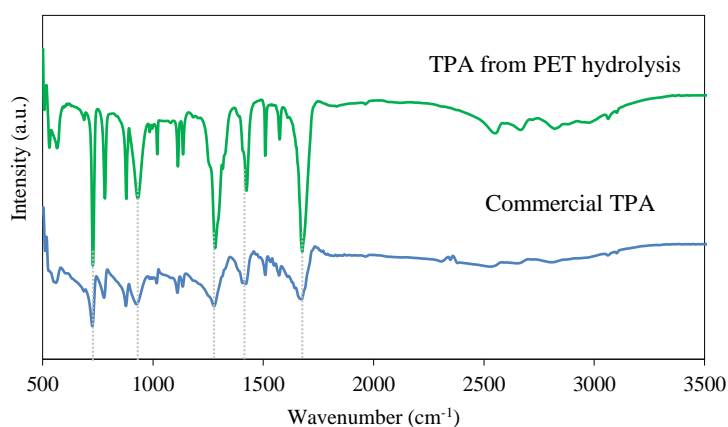


Fig. 2. FTIR spectra of TPAs obtained from hydrolysis of waste PET

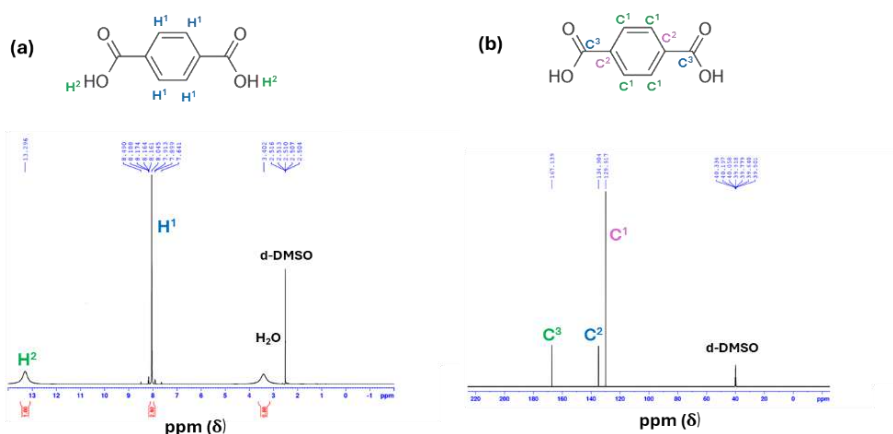


Fig. 3. (a) <sup>1</sup>H NMR and (b) <sup>13</sup>C NMR spectrum of TPA produced from PET hydrolysis

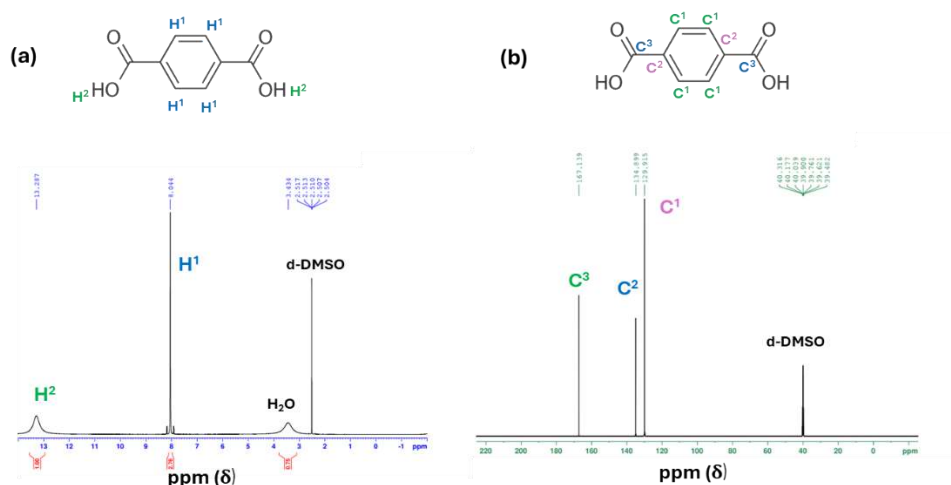


Fig. 4. (a)  $^1\text{H}$  NMR and (b)  $^{13}\text{C}$  NMR spectrum of commercial TPA.

#### 4. Conclusions

This work studied the conversion of waste PET bottles to TPA using alkaline hydrolysis in a mixed solvent of water and ethanol. The effect of NaOH concentration, reaction time and ethanol concentration were investigated. Without adding ethanol, the conversion of PET and TPA yield reached 100% and 90%, respectively, when NaOH concentration and reaction time were 5 wt.% and 6 h, respectively. However, adding ethanol helped accelerate the reaction, reducing the time needed from 6 h to 3 h while maintaining the same conversion yields for PET and TPA. The presence of ethanol in the reaction also aided in the separation between TPA product and reaction solution due to its insolubility in alcohol. The results from this study revealed a promising environmentally friendly and efficient method for converting PET plastic waste into valuable TPA product, which can serve as a crucial raw material for various applications, including the production of new PET polymers, synthesis of biodegradable plastics, and creation of metal-organic frameworks.

#### Acknowledgement

The authors would like to thank Thailand Science Research and Innovation (TSRI) for financial support and, also, raw material kindly provided from TISTR's Municipal Solid Waste Management, Tan Diao Model at Saraburi, facilitated by Dr. Rewadee Anuwattana.

#### References

- [1] Yang, W., Liu, R., Li, C., Song, Y. and Hu, C. (2021). Hydrolysis of waste polyethylene terephthalate catalyzed by easily recyclable terephthalic acid. *Waste Management*, 135, 267–274.
- [2] Arias, J.J.R. and Thielemans, W. (2021). Instantaneous hydrolysis of PET bottles: an efficient pathway for the chemical recycling of condensation polymers. *Green Chemistry*, 23, 9945–9956.
- [3] Market volume of purified terephthalic acid worldwide from 2015 to 2022, with a forecast for 2023 to 2030. <https://www.statista.com/statistics/1245249/purified-terephthalic-acid-market-volume-worldwide/>



- [4] Ügdüler, S., Geem, K.M.V., Denolf, R., Roosen, M., Mys, N., Ragaert, K. and Meester S.D. (2020). Towards closed-loop recycling of multilayer and coloured PET plastic waste by alkaline hydrolysis. *Green Chemistry*, 22, 5376–5394.
- [5] Wang, X., An, W., Du, R., Tian, F., Yang, Y., Zhao, X., Xu, S. and Wang, Y. (2023). Rapid hydrolysis of PET in high-concentration alcohol aqueous solution by pore formation and spontaneous separation of terephthalate, *Journal of Environmental Chemical Engineering*, 11, 109434.
- [6] Wang, Y., Zhang, Y., Song, H., Wang, Y., Deng, T. and Hou, X. (2019). Zinc-catalyzed ester bond cleavage: Chemical degradation of polyethylene terephthalate, *Journal of Cleaner Production*, 208, 1469-1475.

## Coaching for Research and Development in Chemical Engineering Senior Projects

**Thirawat Mueansichai<sup>1,\*</sup>, and Terdtoon Thaisriwichai<sup>2</sup>**

<sup>1</sup>Department of Chemical and Materials Engineering, Faculty of Engineering, Rajamangala University of Technology Thanyaburi, Pathum Thani, Thailand 12110

<sup>2</sup>Thailand Coaching Institute, Tha Raeng, Bang Khen, Bangkok, Thailand 10230

E-mail: \*thirawat.m@en.rmutt.ac.th

### Abstract

This research investigates the application of coaching methodologies to enhance the research and development (R&D) aspects of chemical engineering senior projects. The objective is to assess how coaching can effectively guide students in formulating, executing, and presenting research within the senior design project context. The study develops a personalized coaching framework tailored to individual project requirements, emphasizing skill development, problem-solving, and fostering continuous improvement. Employing a GROW model approach, the research evaluates the impact of coaching on student performance in R&D activities, with a focus on indicators such as research design quality, data interpretation effectiveness, and project innovation. The findings of the research demonstrate how well students enhance their problem-solving and skill-building abilities when they receive coaching for project-based learning. In order to better prepare students for the dynamic and innovative world of chemical engineering research and development, the report's suggestions propose for the curriculum to incorporate coaching techniques.

**Keywords:** Coaching; Chemical Engineering; Senior Project; Problem-solving; Continuous improvement

### 1. Introduction

The value of project-based learning approaches in helping students build their competences and skills is becoming increasingly apparent in the field of chemical engineering education [1]. Witt et al. (2002) conducted research that highlights the value of project-based cooperative learning in developing students' coaching competences. The study also shows how these techniques can improve students' problem-solving and collaboration skills. Additionally, it has been demonstrated that interdisciplinary project-based learning helps students develop their problem-solving skills [2]. Through multidisciplinary projects, Ling et al. (2024) showed how middle school students' problem-solving skills might be developed. This suggests that project-based learning approaches can be applied more broadly across educational levels.

Additionally, initiatives aimed at improving chemical engineering education have emphasized the significance of enhancing one's skill set in order to handle societal issues [3]. An institutional modernization initiative in Brazil that emphasized the development of abilities beyond technical skills was emphasized by Ramos et al. (2023), highlighting the necessity of a comprehensive approach to education. In the same way, initiatives like "From Laboratory to Industry" have helped students studying biotechnology develop their technical abilities [4]. The benefit of innovation projects in bridging the knowledge gap between



academia and industry practices was demonstrated by Ripoll et al. (2023), highlighting the importance of project-based learning strategies for skill development.

Furthermore, it has been demonstrated that incorporating project-based learning into lab environments improves students' engineering design abilities [5]. Gomez-del Rio and Rodriguez (2022) emphasized the planning and evaluation of project-based learning programmes in lab environments, demonstrating how they can help students integrate knowledge and develop their engineering design skills.

In addition, new research has demonstrated the function of coaching in improving project-based learning strategies and encouraging students to study independently [6-8]. In their investigation of practice-based coaching for project-based learning, Kavanagh et al. (2023) emphasized the connections between coaching and teaching practices. In higher education settings, the empowerment of students through coaching methodologies to assist learning, personal development, and action research was studied by Gurbutt and Gurbutt (2015) and Othman and Yee (2015).

This study explores the use of coaching approaches to improve the R&D component of senior projects in chemical engineering in light of recent studies. Using the knowledge gained from earlier studies on competency development and project-based learning, the purpose of this research is to evaluate the ways in which coaching might assist students in planning, carrying out, and presenting their research projects in the context of senior design projects.

## 2. Methodology

The basic research for creating and refining coaching systems to improve student performance in senior chemical engineering projects is represented by this study. It emphasizes how the coaching framework incorporates concepts of continual improvement, problem-solving techniques, and skill development. The three separate phases that make up the research process are as follows:

### 2.1 Development of Coaching Framework

Preparing the coaching system involves studying, researching, and gathering fundamental information about coaches and the GROW Model. This phase includes crafting a research outline, assembling a sample group of students and devising a coaching plan. The GROW Model is employed to prepare the framework for coaching sessions.

### 2.2 Coaching Operations

The coaching operations commence with scheduling a meeting between the teacher (coach) and student (coachee) to establish rapport, discuss objectives, and set joint plans and goals. Throughout the process, supervision, coordination, and ongoing collaboration with coaches are maintained. Coaching sessions are conducted online via MS Teams, with two groups of students, each working on different projects, comprising three students per group. Sessions are held once a week and follow the GROW model. Coaches are tasked with addressing questions and exploring alternative solutions to emerging challenges. Questions are tailored to facilitate understanding, acceptance, and assessment of outcomes. The design choices are aligned with the coachees' projects, and coaches evaluate the design outcomes accordingly.



### 2.3 The evaluation of the coach system

The evaluation of the coach system involves collecting recording forms and observing the methods employed by the coaches across various groups. Coaches evaluate research projects to solicit support and seek opinions from coaches to enhance students' research design using the GROW model coaching system. Additionally, coaches' satisfaction with each coach is assessed. Coachees also self-evaluate their progress and experiences within the coaching system.

### 3. Results and Discussion

The outcomes of developing a coaching system utilizing the GROW model to enhance students' competency in designing research work are as follows:

1. Results of implementing the coaching system: evaluation of the coaching system's implementation reveals improvements in students' ability to design research projects. Utilizing the GROW model facilitated goal-setting and guided students through the research process effectively.

2. Results of coaching methods study: analysis of coaching methods employed within the GROW model framework elucidates effective strategies utilized by coaches. These findings contribute to refining coaching approaches for optimal student support.

3. Results of the study on student effectiveness: the study acknowledges the effectiveness of students in undertaking senior projects with the assistance of coaches. This recognition underscores the positive impact of the developed coaching system on student performance.

These results collectively demonstrate the efficacy of the coaching system developed with the GROW model in enhancing student performance. The high-quality research design validates the practical utility of the proposed coaching approach, positioning it as a valuable resource for improving student outcomes in senior project endeavors.

#### 3.1. Implementing a coaching system utilizing the GROW model

Based on the outcomes of coaching operations employing the GROW model coaching system, researchers analyzed the coaching methods and processes, culminating in the development of a coding model. Beginning with the "G" for Goal, the coaching process involves identifying the coach's objectives, thereby enabling coaches to establish clear goals. The coaching operation system was then structured into four steps:

Step 1: Establishing a positive atmosphere: begin coaching sessions with warm greetings, fostering a friendly rapport between the coach and coachees. Utilize questioning techniques to elucidate clear coaching goals.

Step 2: Building rapport: cultivate a strong rapport between coaches and coachees to instill trust and confidence. Employ strategies to connect on a personal level and nurture a positive relationship.

Step 3: Defining coaches' goals: guide coachees through reflective questioning to identify pertinent topics and desired outcomes, including research goals. Coaches can also define their own objectives during this stage.



Step 4: Setting SMART goals: utilize questioning strategies to establish goals that are Specific, Measurable, Achievable, Relevant, and Time-bound (SMART). Ensure coachees feel motivated and satisfied with the defined goals.

R - Reality: this phase of coaching is focused on uncovering the genuine issues faced by the coachee. It involves the following steps:

Step 1: Establishing a positive atmosphere: begin by fostering a positive environment where the coach and coachee feel comfortable and connected. Greetings are exchanged to cultivate familiarity and friendliness, allowing the coachee to feel at ease and open to answering questions.

Step 2: Building rapport: develop rapport with the coachee to foster relaxation and confidence. The coach creates an environment where the coachee feels supported, understood, and encouraged to share without fear of judgment. Listening attentively to their stories without offering advice or suggestions helps build trust and rapport.

Step 3: Reflecting on goals: guide the coachee through reflective questioning until they identify a suitable topic. Encourage the coachee to delve deeper into their research goals and uncover the underlying truths.

Step 4: Goal setting: assist the coachee in identifying and articulating the real problems they are facing. This step is crucial for the coachee to gain clarity on their current situation and understand the challenges they need to address.

O - Options: coaching is geared towards helping coachees explore alternative solutions to their problems. This process unfolds through four sequential steps:

Step 1: Establishing a positive atmosphere: initiate sessions with warm greetings, fostering a friendly ambiance. Discuss research principles by students and use questioning to prompt coachees to consider various alternatives. Emphasize commitment to problem-solving, instilling trust and confidence in the coaching process.

Step 2: Building rapport: cultivate rapport with coachees, fostering an environment of trust and open communication. Motivate and remind coachees to navigate challenges and explore alternative solutions. Keep the focus on finding effective ways to address issues.

Step 3: Defining coachees' goals: guide coachees in articulating ways to achieve their objectives and explore options for problem-solving. Encourage research endeavors aligned with their goals and inquire about their vision of success.

Step 4: Reflecting coachees' options: evaluate methods or alternatives aligning with coachees' objectives. Discuss strategies for achieving goals and assess coachees' feelings regarding success. Encourage confidence in writing a research outline and express appreciation for their efforts.

W – Way forward: this part of coaching involves empowering coachees to make decisions and take action. It consists of four steps:

Step 1: Establishing a positive atmosphere: initiate the session with warm greetings, fostering a positive connection between the coach and coachee. Utilize questioning to explore alternative problem-solving methods, instilling confidence in coachees.

Step 2: Building rapport: foster rapport with coachees, creating an environment where they feel relaxed and comfortable. Engage in dialogue, ask questions, and express genuine concern. Motivate and remind coachees to overcome challenges and crises.



Step 3: Defining coachees' goals: utilize questioning techniques to guide coachees in evaluating their research outline according to the university model. Offer advice and recommendations for implementation in their field if necessary. Inquire about factors contributing to the completion of the research outline.

Step 4: Setting way forward and plan from options: discuss and congratulate coachees on their ability to design research work and write research outlines to achieve their goals. Provide encouragement and instill confidence to propel coachees forward in completing their research work. Express gratitude for their participation in coaching and readiness to collaborate in future sessions.

### 3.2. Results of coaching methods study

In investigating coaching methods employed by coaches to enhance student performance in research design, the researcher compiled observations of coaching sessions involving coaches and coachees from diverse groups for analysis. These coaching methods align with the GROW Model framework. The researchers propose presenting research findings on four key issues utilizing descriptive statistics derived from the study.

3.2.1 In examining the coach's approach to identifying research topics, defining problems, objectives, and the scope of the coachee's research, this topic is structured around the coaching process aimed at elucidating the coachee's goals. The coach and coachee engage in online meetings via MS Teams, with each session lasting one hour. The session commences with introductions and discussions regarding the purpose of the activities, research goals, and anticipated challenges. During this phase, the coach and coachee collaborate to formulate a coaching plan, document agreements, and commence the session. Through instant coaching, the coachee elucidates the problem, work, and research topic under consideration, while the coach attentively listens and seeks to understand the proposed research topics. Once clarity is achieved, the coachee is tasked with studying and designing research within an agreed-upon framework, adhering to specified time constraints. Throughout this process, the coach provides ongoing support, follows up on research progress, and ensures alignment with the established objectives.

3.2.2 This topic focuses on studying how the coachee designs methods and conducts research within the coaching process aimed at identifying emerging issues. When the scheduled date arrives as per the plan, the coach and coachee convene to address the reality of the coachee's progress. Each group of coachees undergoes research review during this phase, where their understanding of research outlines is assessed. It is observed that certain areas still require development among the coachees. Therefore, coaching involves dialogue, questioning, explanations, and presentations to facilitate growth. Throughout the coaching process, the coach ensures a relaxed atmosphere and encourages the coachee to work towards the established goals outlined in the plan.

3.2.3 This topic delves into the literature review of the coach's methods and is integrated into the coaching process aimed at exploring options to address coaches' challenges. During this coaching session, the focus is on understanding the methods employed by the coach. The results from the initial coaching session are considered alongside those from subsequent sessions to assess their impact on research design and writing research outlines. If errors are identified, the coach takes corrective action to guide the coachee accordingly. Discussions and inquiries are then facilitated to help coaches identify suitable options for resolving any emerging issues. Additionally, discussions and inquiries about the literature review are conducted to enhance understanding and address any related concerns.

3.2.4 From examining the coach's methods for drafting research outlines, this topic is incorporated into the coaching process where coaches demonstrate their willingness to execute the outlined plan (will). As this coaching session marks the final one, coaches primarily rely on scrutinizing the documents detailing research design and outlines. Upon completion of all research topics, coaches deliberate and assess the research framework, engaging in discussions regarding the intricacies of research design and outline composition until successful outcomes are achieved. Mutual commendation ensues, with coaches expressing satisfaction at having each other as partners in the coaching journey, while coachees reciprocate gratitude for the invaluable guidance received. Reflecting on the knowledge gained from coaching, coachees express excitement and confidence in their abilities, affirming their readiness to proceed. The coach evaluates the research outline, offering advice and corrections where necessary, and then seeks approval from the teacher acting as the coach by presenting a signed copy of the document. Additionally, a request for further research is proposed as part of the concluding phase of the coaching process.

The results of the coaching intervention demonstrated significant improvements in various dimensions of student performance within the context of chemical engineering senior projects. Participants exhibited enhanced proficiency in conducting literature reviews, identifying research gaps, and formulating research hypotheses relevant to their respective subfields. Moreover, students demonstrated greater confidence and competence in experimental design, data collection, and analysis, leading to more robust research outcomes. Qualitative feedback from both students and coaches highlighted the value of personalized mentorship and guidance in navigating the complexities of senior projects in chemical engineering. Furthermore, the incorporation of relevant examples, case studies, and practical exercises enriched the learning experience and facilitated deeper understanding of key concepts. Table 1 illustrates the evolution of student performance and the influence of coaching interventions, offering valuable insights into the efficacy of the coaching methodology. Overall, the findings underscored the transformative potential of coaching methodologies in enhancing student outcomes and preparing them for successful careers in chemical engineering.

Table 1. The performance of senior project students.

<b>Student group</b>	<b>Pass rate</b>	<b>Mean</b>	<b>S.D.</b>
Group A	100%	70	14.14
Group B	100%	80	7.64

### 3.3. Results of the study on student effectiveness

Throughout the coaching process employing the GROW Model between the coach (teacher) and the coachee (student), systematic steps were followed. Coaching sessions were conducted once a week for a total of 15 sessions. Additionally, the coach actively participated in the coaching sessions, utilizing audio recordings, photographs, and video recordings. These

materials were then analyzed using the coaching observation model developed by the researchers.

Following coaching sessions focused on research design, coachee satisfaction was evaluated, and coachees were encouraged to self-assess their research outcomes. It was found that both groups of coachees successfully accomplished the goal of designing research and writing research outlines with precision and accordance with the coaching plan objectives.

Upon investigating the perspectives of coachees regarding their development in research design through the GROW model coaching system, it was evident that both groups shared unanimous opinions. Coachees from all 2 groups expressed the highest levels of development in various aspects, including:

1. Enhanced self-confidence and willingness to tackle challenging research problems.
2. Demonstrated determination, enthusiasm, and readiness to engage in coaching sessions as per the established plan.
3. Consistent adherence to the coaching plan and goals.
4. Successful achievement of research components such as title setting, problem definition, objectives delineation, and research scope.
5. Utilization of innovative ideas to address problems and apply them to their work.
6. Punctual attendance and active participation in coaching sessions.
7. Recognition of the meticulous consideration and relevance of their research work across various domains, indicating its potential applicability and importance.

These findings underscore the effectiveness of the GROW model coaching system in fostering comprehensive development among coachees, thereby positioning them favorably for further research endeavors.

#### 4. Conclusions

In conclusion, this research has provided valuable insights into the application of coaching methodologies to enhance the performance of students in chemical engineering senior projects. Through the implementation of a personalized coaching framework, tailored to individual project requirements, significant improvements have been observed in skill development, problem-solving abilities, and overall project outcomes. The adoption of the GROW model approach has facilitated effective guidance for students in formulating, executing, and presenting their research within the senior design project context.

The results of this study underscore the importance of integrating coaching strategies into the curriculum to better prepare students for the dynamic and innovative landscape of chemical engineering research and development. By fostering a supportive coaching environment, students have been empowered to tackle challenges, innovate, and achieve success in their senior projects.

Moving forward, it is recommended to further refine and expand upon the coaching methodologies employed in this research, ensuring continuous improvement and adaptation to evolving educational needs. Additionally, future studies could explore the long-term impact of coaching on students' professional development and career trajectories in the field of chemical engineering. Overall, this research contributes to the body of knowledge in educational coaching and underscores its potential as a transformative tool for enhancing student learning and performance in engineering disciplines.



## 5. Acknowledgements

We are truly appreciative of the Thailand Coaching Institute's generous scholarship for 2022 given out as part of the Thai Higher Education Teachers with Hearts of Coaches initiative. This priceless support has made a substantial contribution to our professional development and advancement as instructors. We also like to sincerely thank Rajamangala University of Technology Thanyaburi's Faculty of Engineering for their unreserved support during this journey. Their support and direction have been crucial to our academic endeavours and successes. We sincerely appreciate the opportunities that the Thailand Coaching Institute and the Faculty of Engineering have given us, as they have enabled us to achieve success in our capacities as researchers and teachers.

## References

- [1] Witt, H. J., Alabart, J. R., Giralt, F., Herrero, J., Medir, M., & Fabregat, A. (2002). Development of coaching competencies in students through a project-based cooperative learning approach. In 32nd Annual Frontiers in Education (Vol. 2, pp. F2A-F2A). IEEE.
- [2] Ling, Y., Zhou, L., Zhang, B., & Ren, H. (2024). Developing middle school students' problem-solving ability through interdisciplinary project-based learning. *Education for Chemical Engineers*, 46, 43-53.
- [3] Ramos, B., dos Santos, M. T., Vianna Jr, A. S., & Kulay, L. (2023). An institutional modernization project in chemical engineering education in Brazil: Developing broader competencies for societal challenges. *Education for Chemical Engineers*, 44, 35-44.
- [4] Ripoll, V., Godino-Ojer, M., & Calzada, J. (2023). Development of engineering skills in students of biotechnology: Innovation project "From laboratory to industry". *Education for Chemical Engineers*, 43, 37-49.
- [5] Gomez-del Rio, T., & Rodriguez, J. (2022). Design and assessment of a project-based learning in a laboratory for integrating knowledge and improving engineering design skills. *Education for Chemical Engineers*, 40, 17-28.
- [6] Kavanagh, S. S., Gotwalt, E. S., & Farrow, J. (2023). Practice-based coaching for project-based teaching: Understanding relationships between coaching practice and teaching practice. *Teaching and Teacher Education*, 132, 104255.
- [7] Gurbutt, D., & Gurbutt, R. (2015). Empowering students to promote independent learning: A project utilising coaching approaches to support learning and personal development. *Journal of Learning Development in Higher Education*, 8.
- [8] Othman, N., & Yee, C. S. (2015). Empowering teaching, learning, and supervision through coaching in action research. *Journal of Management Research*, 7(2), 98-108.

## **Ethanol Purification Comparison Between Adsorption and Azeotropic Distillation: A Rough Simulation and Economic Analysis Using Aspen Plus V.11**

**Thirawat Mueansichai<sup>1,\*</sup>, Tipkamon Pukang<sup>1</sup>, Pattamanuch Yodkhammee<sup>1</sup>, Supatsorn Thumrongsombat<sup>1</sup>, Chaiyapop Siraworakun<sup>1</sup>, Sarawut Jitpinit<sup>1</sup>, Weerinda Appamana<sup>1</sup>, and Suttichai Assabumrungrat<sup>2,3</sup>**

<sup>1</sup> Department of Chemical and Materials Engineering, Faculty of Engineering, Rajamangala University of Technology Thanyaburi, Pathum Thani 12110, Thailand

<sup>2</sup> Center of Excellence in Catalysis and Catalytic Reaction Engineering, Department of Chemical Engineering, Faculty of Engineering, Chulalongkorn University, Bangkok 10330, Thailand

<sup>3</sup> Bio-Circular-Green-economy Technology & Engineering Center, BCGeTEC, Department of Chemical Engineering, Faculty of Engineering, Chulalongkorn University, Bangkok 10330, Thailand

E-mail: \* thirawat.m@en.rmutt.ac.th

### **Abstract**

This study explores the production of bioethanol from Napier grass through process simulation using Aspen Plus V.11 software. The research delves into the simulation of bioethanol production, examining the evolution of bioethanol production from the prototype process. Additionally, it conducts a comparative economic analysis of two processes: the pure ethanol production process utilizing the absorption method and the distillation process employing azeotropic distillation. The optimization of the azeotropic distillation simulation encompasses key variables such as the mass ratio of ethanol to hexane fed into the distillation column, the product flow rate entering the column's bottom, the number of trays, and the positions for introducing ethanol and hexane. Employing Aspen Plus V.11, optimal conditions were identified, including a mass ratio of ethanol to hexane at 1.5:1, a product flow rate at 102 kg/h entering the bottom of the distillation column, 12 trays, and specific feed positions for ethanol and hexane. Comparative analyses revealed that the original process achieved ethanol separation with a concentration of 99.9%, while the modified process achieved a separation of 99.5%. The economic assessment favored the absorption process, deeming it the most suitable, with a total production cost estimated at \$6,694,964. This research provides insights into process optimization and economic considerations for bioethanol production, offering valuable implications for sustainable biofuel development.

**Keywords:** Bioethanol Production; Process Simulation; Azeotropic Distillation; Economic Analysis

### **1. Introduction**

A lot of research has been done on the production of bioethanol from Napier grass as an environmentally friendly alternative for fossil fuels. Pre-treatment and fermentation techniques as well as optimisation strategies for higher ethanol yields have all been studied. Delimanto compared pre-treatment and fermentation techniques for Napier grass bioethanol production, and Mueansichai et al. looked into lignocellulosic bioethanol production using co-culture fermentation of *Saccharomyces cerevisiae* and *Trichoderma reesei* [1-2].



In addition, Kongkeitkajorn et al. assessed various fermentation techniques in order to determine the best processes for batch bioethanol production from Napier grass. In order to produce bioethanol, Panakkal et al. optimised the deep eutectic solvent pretreatment, highlighting the significance of effective pre-treatment procedures. Pensri et al. investigated the feasibility of using Napier grass residue as a feedstock for bioethanol production and demonstrated the possibility of producing fermentable sugar from it [3-5].

Moreover, Ko et al. investigated bioethanol production from recovered Napier grass contaminated with heavy metals, emphasizing the importance of addressing environmental concerns in biomass utilization. Additionally, Liu et al. focused on simultaneous saccharification and co-fermentation processes for bioethanol production from Napier grass, demonstrating innovative approaches to enhance ethanol yields [6-7].

In this context, the present study contributes to the existing body of knowledge by exploring bioethanol production from Napier grass through process simulation using Aspen Plus V.11 software. Building upon previous research, this study delves into the simulation of bioethanol production processes, including a comparative economic analysis of different production methods. By optimizing azeotropic distillation parameters, the study identifies optimal conditions for bioethanol separation, shedding light on both technical and economic aspects of Napier grass bioethanol production.

Through a comprehensive analysis encompassing process simulation and economic evaluation, this research aims to provide valuable insights into process optimization and economic considerations for sustainable bioethanol production. Ultimately, this study seeks to contribute to the advancement of renewable energy technologies and the promotion of environmentally sustainable fuel alternatives.

## 2. Materials and Methods

The bioethanol production process was simulated using Aspen Plus V.11 software. The simulation model was developed based on the known chemical reactions and process parameters involved in each step of the production process. Thermodynamic models and property methods suitable for the components involved were selected, ensuring accurate representation of the system [8].

An adsorption process for ethanol purification was simulated using Aspen Plus V.11 software for comparison with azeotropic distillation. The simulation involved modeling the adsorption of ethanol onto a solid adsorbent material, followed by desorption to recover purified ethanol.

Azeotropic distillation was employed for ethanol separation, and the process was optimized using Aspen Plus V.11. Key variables such as the mass ratio of ethanol to hexane fed into the distillation column, product flow rate entering the column's bottom, number of trays, and feed positions for ethanol and hexane were systematically varied to identify optimal conditions.

A comparative economic analysis was conducted to assess the production costs associated with the two bioethanol production processes: absorption method and azeotropic distillation. Costs including raw materials, equipment, energy consumption, and labor were considered to determine the total production cost for each process configuration.

The bioethanol production process, simulated using Aspen Plus V.11 software, involves several steps aimed at converting raw materials into purified ethanol. Here's a breakdown of the process and simulation methodology:



## 2.1 Simulation Model Development

- The simulation model is constructed based on known chemical reactions and process parameters involved in each step of the production process. This includes reactions such as fermentation of sugars to ethanol and subsequent purification steps.

- Thermodynamic models and property methods suitable for the components involved in the process are selected to ensure accurate representation of the system. These models help in predicting phase equilibria, thermodynamic properties, and chemical reaction kinetics.

## 2.2 Adsorption Process Simulation

- An adsorption process for ethanol purification is simulated using Aspen Plus V.11 software. This involves modeling the adsorption of ethanol onto a solid adsorbent material, followed by desorption to recover purified ethanol.

- The simulation considers parameters such as adsorbent material properties, temperature, pressure, and flow rates to accurately model the adsorption-desorption process.

## 2.3 Azeotropic Distillation Simulation

- Azeotropic distillation is employed for ethanol separation, and the process is optimized using Aspen Plus V.11.

- Key variables such as the mass ratio of ethanol to hexane fed into the distillation column, product flow rate entering the column's bottom, number of trays, and feed positions for ethanol and hexane are systematically varied to identify optimal conditions.

- The simulation considers thermodynamic properties, column configurations, and operating conditions to optimize the distillation process for ethanol purification.

## 2.4 Comparative Economic Analysis

- A comparative economic analysis is conducted to assess the production costs associated with the two bioethanol production processes: absorption method and azeotropic distillation.

- Costs including raw materials (such as feedstock for fermentation), equipment (such as reactors, distillation columns, and adsorption units), energy consumption (for heating, cooling, and operation), and labor (for operation and maintenance) are considered.

- Total production costs for each process configuration are determined by summing up all relevant costs, including capital and operating expenses.

In summary, the simulation of the bioethanol production process using Aspen Plus V.11 software involves modeling chemical reactions, thermodynamic properties, and process parameters to optimize ethanol purification methods. The comparative economic analysis helps in evaluating the cost-effectiveness of different production processes, aiding decision-making for industrial-scale bioethanol production.

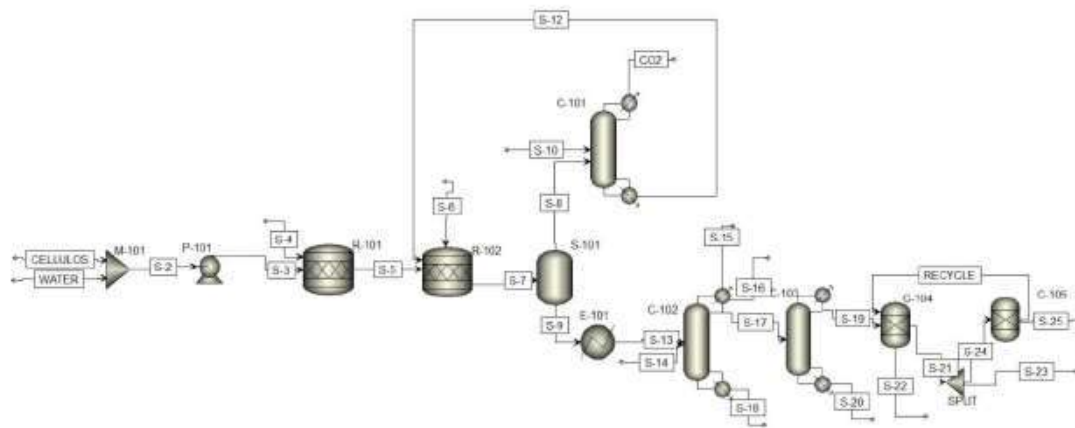


Fig. 1 The simulation of the bioethanol production process and its purification using an adsorption process.

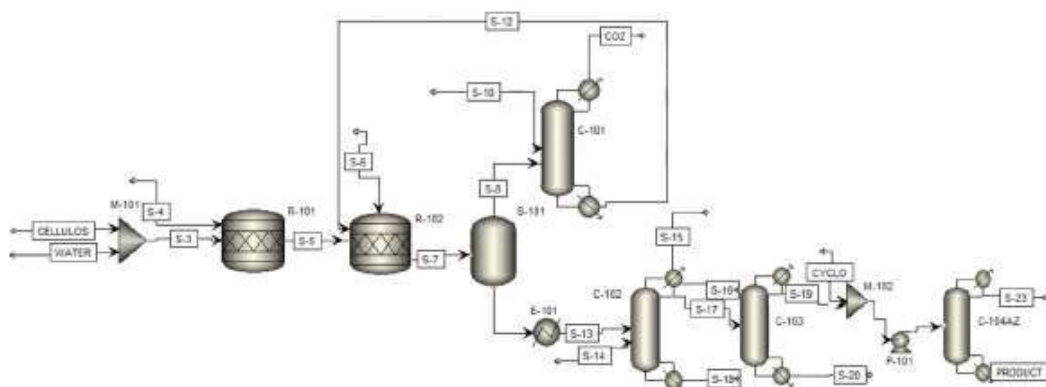


Fig. 2 The simulation of the bioethanol production process and its purification using an azeotropic distillation process.

### 3. Results and Discussion

#### 3.1. Purity of products obtained from bioethanol production simulations

The simulation of the bioethanol production process yielded promising results regarding the purity of the final product. Across all simulations, it was determined that the ethanol product obtained had a purity of not less than 99 percent, meeting the stringent quality standards required for commercial bioethanol applications. Table 1 presents the detailed results obtained from the simulations.

Comparison between the purification methods, azeotropic distillation and adsorption process, revealed notable differences in ethanol purity. The azeotropic distillation method achieved a purity level of 99.5 percent, while the adsorption process surpassed this with a remarkably high purity of 99.91 percent.

These results highlight the efficiency and effectiveness of both purification methods in isolating ethanol from the fermentation broth. The slight difference in purity levels could be

attributed to the varying mechanisms and operating conditions inherent in each purification process.

The exceptional purity achieved through the adsorption process underscores its potential as a superior purification method for bioethanol production. This method not only surpasses the industry standard but also offers promising opportunities for further optimization to enhance purity levels and overall process efficiency.

In conclusion, the simulations confirm the capability of both azeotropic distillation and adsorption processes to consistently produce bioethanol of exceptional purity. These findings provide valuable insights into the selection of purification methods, facilitating the optimization of bioethanol production processes for enhanced performance and commercial viability.

Table 1. Purity of bioethanol product.

Product	Adsorption	Adsorption	Azeotropic distillation	Azeotropic distillation
	Input (%)	Output (%)	Input (%)	Output (%)
Ethanol	94.00	99.91	94.00	99.50
Water	5.00	0.09	5.00	0.11
Other	1.00	0.00	1.00	0.39

### 3.2. Production of bioethanol and its purification using an adsorption process

The adsorption process diagram outlines the sequential steps involved in purifying ethanol from cellulose and water feed stocks. Initially, cellulose, at a rate of 200 tons per day, and water, at 20.1 tons per day, are introduced into a pump to regulate pressure before entering the first reactor. The operating conditions are maintained at 25 degrees Celsius and 1 atm in the reactor to facilitate the balanced reaction between the feed stocks. Once the reaction is completed, the mixture is transferred to a second reactor, where the temperature is increased to 30 degrees Celsius while maintaining a pressure of 1 atm.

Subsequently, the mixture enters a flash tank to separate carbon dioxide from ethanol. The separated carbon dioxide is recycled and reused in the second reactor. The remaining mixture is then divided into two streams: an upper stream, which enters the first distillation tower (C-101), and a bottom stream, which undergoes heating to 60 degrees Celsius and 5 atm before entering the second distillation tower (C-102).

In the first distillation tower (C-101), which comprises 35 levels and operates at 1 atm, carbon dioxide is further separated from the by-products. The bottom stream from this tower then proceeds to the second distillation tower (C-102), which also consists of 35 levels but operates at 5 atm. In this tower, water, carbon dioxide, and remaining by-products are separated from ethanol.

Finally, the ethanol, with a purity of 95%, is directed to the third distillation tower (C-103). This tower, containing 30 levels and operating at 1.5 atm, serves to further purify the ethanol, increasing its purity to 99.9%. The purified ethanol is then sent to the Separator (C-104, C-105), where any remaining impurities are removed, resulting in a final product of high-quality ethanol with a concentration of 99.9%.



### 3.3. Bioethanol production and purification using azeotropic distillation process

Figure 2 illustrates the schematic diagram of the adsorption process, delineating the series of steps involved in purifying ethanol from cellulose and water feed stocks. Initially, cellulose is fed into the system at a rate of 200 tons per day, alongside water at 20.1 tons per day, both maintained at 25 degrees Celsius and 1 atmosphere pressure. These feed stocks enter a pump to regulate pressure before entering the first reactor, where the temperature and pressure remain constant at 25 degrees Celsius and 1 atmosphere, respectively, to facilitate the reaction.

Upon completion of the reaction, the mixture proceeds to a second reactor, where the temperature is adjusted to 30 degrees Celsius, maintaining a pressure of 1 atmosphere. The resultant mixture is then directed to a flash tank to separate carbon dioxide from ethanol. The upper stream, containing ethanol, enters a tower.

The first distillation chamber (C-101) comprises 35 levels and operates at 1 atm, facilitating the separation of carbon dioxide from the by-product, which is recycled and reused in the second reactor. Meanwhile, the bottom stream undergoes heating to 60 degrees Celsius and 5 atm before entering the second distillation tower (C-102). This tower, also consisting of 35 levels and operating at 5 atm, further separates water, carbon dioxide, and remaining by-products from ethanol.

The purified ethanol, with a purity of 95%, is directed to the third distillation tower (C-103), consisting of 30 levels and operating at 1.5 atm. Here, the ethanol's purity is increased to 95%, and it is subsequently mixed with cyclohexane, fed into the mixer at a rate of 16.5 tons per day, maintained at 25 degrees Celsius and 2 atm. This mixture, containing ethanol with a concentration of 37.6%, is then sent to the azeotrope distillation tower (C-104AZ). With 12 levels and operating at 2 atm, this tower further purifies the ethanol, resulting in a final concentration of 99.5%.

After analyzing the experimental results to optimize the simulation parameters, it was determined that an azeotropic distillation tower utilizing cyclohexane as the distillation aid yielded the most favorable outcomes. Specifically, the optimal ratio of cyclohexane to ethanol was found to be 1.5:1.0. It was observed that surpassing this optimum ratio led to a decline in ethanol product concentration.

Furthermore, for each ratio of cyclohexane to ethanol, a corresponding value for the product flow rate to the bottom of the distillation tower was identified. The most optimal performance was achieved at the ratio of 1.5:1.0, where the product flow rate to the bottom of the distillation tower was determined to be 102 kg/hr. Additionally, the optimal number of layers in the distillation tower was found to be 12, further confirming the effectiveness of this configuration in maximizing ethanol concentration. Results of economic analysis

### 3.4. Results of economic analysis

In selecting a purification process, the adsorption process emerged as the optimal choice, primarily due to its superior economic performance. The economic evaluation was based on comprehensive considerations of production costs, encompassing fixed costs, direct costs, and general costs.

The adsorption process demonstrated a compelling economic advantage, characterized by fixed costs amounting to \$1,002,004. These fixed costs represent the initial investment required for equipment, infrastructure, and other capital expenditures associated with setting up the purification process.



Furthermore, the direct costs associated with the adsorption process were evaluated at \$4,570,994. These direct costs include expenses directly incurred during the operation of the process, such as raw materials, labor, utilities, and maintenance.

In addition to fixed and direct costs, general costs totaling \$1,269,844 were accounted for in the economic analysis of the adsorption process. These general costs encompass various overhead expenses, administrative costs, and other miscellaneous expenditures essential for sustaining the operation of the purification process.

Collectively, the total manufacturing costs for implementing the adsorption process were calculated at \$6,842,842. This comprehensive evaluation underscores the economic viability and competitiveness of the adsorption process as the preferred purification method.

The selection of the adsorption process based on its favorable economic return highlights the importance of considering cost-effectiveness and efficiency in decision-making processes related to bioethanol production. By prioritizing economic considerations, stakeholders can make informed decisions that optimize resource utilization and enhance the overall profitability and sustainability of biofuel production operations.

#### 4. Conclusions

This research endeavors to explore and optimize the bioethanol production process from Napier grass, focusing on process simulation, economic analysis, and purification methods. Through rigorous experimentation and simulation using Aspen Plus V.11 software, valuable insights have been gained into the feasibility and efficiency of various production and purification techniques.

The study highlights the potential of the adsorption process as the optimal purification method, demonstrating superior economic returns compared to alternative techniques. The adsorption process, with fixed costs totaling \$1,002,004, direct costs amounting to \$4,570,994, and general costs accounting for \$1,269,844, yielded a total manufacturing cost of \$6,842,842. This economic evaluation underscores the economic viability and competitiveness of the adsorption process for bioethanol purification.

Furthermore, the research provides valuable implications for process optimization and economic considerations in bioethanol production. Through the optimization of azeotropic distillation parameters and comparative economic analysis, significant advancements have been made in enhancing process efficiency and reducing production costs.

In conclusion, this study contributes to the advancement of sustainable biofuel technologies by providing valuable insights into process optimization, economic considerations, and purification methods for bioethanol production from renewable feed stocks like Napier grass. By implementing the findings and recommendations outlined in this research, stakeholders in the bioethanol industry can make informed decisions that optimize resource utilization, enhance economic viability, and contribute to the broader goal of transitioning towards a more sustainable and environmentally friendly energy future.

#### 5. Acknowledgements

We would like to express our sincere gratitude to the Faculty of Engineering, Rajamangala University of Technology Thanyaburi, for their invaluable support throughout this research endeavor. Their unwavering support and encouragement have been instrumental in the successful completion of this study. We extend our heartfelt appreciation to the faculty members, researchers, and staff for their guidance, expertise, and resources provided, which



have greatly contributed to the advancement of our research efforts. We are truly grateful for the opportunities and resources afforded to us by the Faculty of Engineering, Rajamangala University of Technology Thanyaburi, and we look forward to continued collaboration and partnership in future endeavors.

## References

- [1] Delimanto, W. O. (2020). Production of Bioethanol from Napier grass: Comparison in Pre-treatment and Fermentation Methods. In IOP Conference Series: Earth and Environmental Science (Vol. 520, No. 1, p. 012005). IOP Publishing.
- [2] Mueansichai, T., Rangseesuriyachai, T., Thongchul, N., & Assabumrungrat, S. (2022). Lignocellulosic bioethanol production of Napier grass using *Trichoderma reesei* and *Saccharomyces cerevisiae* co-culture fermentation. *International Journal of Renewable Energy Development*, 11(2), 423-433.
- [3] Kongkeitkajorn, M. B., Yaemdeeka, R., Chaiyota, I., Hamsupo, K., Oraintara, A., & Reungsang, A. (2021). Bioethanol from Napier grass employing different fermentation strategies to evaluate a suitable operation for batch bioethanol production. *Energy Conversion and Management: X*, 12, 100143.
- [4] Panakkal, E. J., Cheenkachorn, K., Chuetor, S., Tantayotai, P., Raina, N., Cheng, Y. S., & Sriariyanun, M. (2022). Optimization of deep eutectic solvent pretreatment for bioethanol production from Napier grass. *Sustainable Energy Technologies and Assessments*, 54, 102856.
- [5] Pensri, B., Aggarangsi, P., Chaiyaso, T., & Chandet, N. (2016). Potential of fermentable sugar production from Napier cv. Pakchong 1 grass residue as a substrate to produce bioethanol. *Energy Procedia*, 89, 428-436.
- [6] Ko, C. H., Yu, F. C., Chang, F. C., Yang, B. Y., Chen, W. H., Hwang, W. S., & Tu, T. C. (2017). Bioethanol production from recovered napier grass with heavy metals. *Journal of environmental management*, 203, 1005-1010.
- [7] Liu, Y. K., Chen, W. C., Huang, Y. C., Chang, Y. K., Chu, I. M., Tsai, S. L., & Wei, Y. H. (2017). Production of bioethanol from Napier grass via simultaneous saccharification and co-fermentation in a modified bioreactor. *Journal of bioscience and bioengineering*, 124(2), 184-188.
- [8] Qamar, R. A., Mushtaq, A., Ullah, A., & Ali, Z. U. (2019). Production of fuel grade ethanol from cellulose using Aspen plus simulation. *Science International (Lahore)*, 31(5), 683-694.

## Adsorption of Uremic Toxins in Hemodialysis using Bio-based Hybrid Granular Activated Carbon for Dialysate Regeneration

Nuttawan Arpasopana<sup>1</sup>, Tissawan Rasmee<sup>2</sup>, Pensiri Prachakitikul<sup>2</sup>,  
Sutthira Sutthasupa<sup>3</sup>, Nakorn Worasuwannarak<sup>4</sup>, Wanida Koo-amornpattana<sup>5</sup>,  
Suwana Kitpati Boontanon<sup>1</sup>, and Weerawut Chaiwat<sup>5,\*</sup>

<sup>1</sup>Department of Civil and Environmental Engineering, Mahidol University, Nakhon Pathom, Thailand

<sup>2</sup>Department of Environmental Engineering and Disaster Management, Mahidol University Kanchanaburi Campus, Kanchanaburi, Thailand

<sup>3</sup>Department of Science Program in Packaging Technology, Chiang Mai University, Thailand.

<sup>4</sup>The Joint Graduate School of Energy and Environment, King Mongkut's University of Technology Thonburi, Thailand.

<sup>5</sup>Department of Chemical Engineering, Mahidol University, Nakhon Pathom, Thailand.

E-mails: \*weerawut.cha@mahidol.edu

### Abstract

In kidney hemodialysis system, adsorption has been investigated as a beneficial physical treatment to reuse spent dialysate containing uremic toxins such as creatinine and uric acid. This could minimize the required quantity of new dialysate. In this study, sugarcane bagasse (SCB) and sugarcane bagasse ash (SCBA) were utilized as main raw materials to produce granular activated carbon (GAC) hybridized with alginate as a bio-based polymer matrix via gelation method. SCB activated carbon (SCB AC) was firstly prepared from raw SCB by carbonization at 500 °C for 1 h and steam activation at 900 °C for 1 h. The strength and stability of the hybrid GAC could be improved by adding SCBA-derived mesoporous silica (SCB MPS) at different mixing ratios. Swelling degree was primarily investigated by comparing commercial GAC and SCB GAC at different ratios of SCB AC and SCB MPS. It was observed that SCB GAC mostly exhibited better swelling degrees than those of commercial GAC. The higher swelling degree was possibly anticipated to enhance adsorption efficiency of uric acid and creatinine in dialysate solution. The weight ratio of SCB AC to SCB MPS at 1:2 and 1:1 in the GAC seems to be the optimum ratio to achieve relatively high swelling degree and adsorption efficiency due to their less structural deformation. Briefly, SCB-derived hybrid GAC could be potentially considered as a competitive adsorbent for uremic toxin removal in terms of economics due to its zero cost in raw materials and steam, which could be self-produced in the sugar mill.

**Keywords:** Sugarcane bagasse; Granular activated carbon; Adsorption; Dialysate; Uremic toxins

### 1. Introduction

For individuals suffering from end-stage chronic renal disease, kidney dialysis serves as a vital treatment option. This treatment aims to assist those with kidney dysfunction, wherein the kidneys fail to effectively filter waste from the body, by employing two primary types of dialysis: 1) hemodialysis, involving extracting blood from the body for purification and 2) peritoneal dialysis (PD), involving the patient introducing a solution into the abdomen for a minimum of 4–6 h, facilitating the removal of waste. In hemodialysis, uremic toxins within the blood are exchanged with the dialysate solution, allowing for the elimination of these

uremic toxins. Key components requiring removal from the dialysate include uric acid and creatinine, which are toxic in the body [1]. However, the substantial volume of dialysate required, ranging from 240 to 1440 liters per person per month for most patients, poses a significant issue of waste in medical treatment. Consequently, recycling the spent dialysate for regeneration emerges as an alternative approach to mitigate this waste. Recently, there have been research studies on the use of activated carbon derived from biomass, used to adsorb uric acid and creatinine [2]. Furthermore, there have been attempts to derive silica particles by synthesizing sodium silicate from sugarcane bagasse ash (SCBA) [3]. The additional SCBA in the hybrid granular adsorbent materials could possibly enhance mechanical properties and a relatively inert chemical composition, making it suitable for applications such as adsorption [4]. Consequently, this study utilized sugarcane bagasse (SCB) and sugarcane bagasse ash (SCBA) wastes as primary ingredients to produce hybrid granular activated carbon (GAC) combined with alginate, as a bio-based polymer matrix, via the gelation method. The main objective of this research is to assess the batch adsorption efficiency and capacity of uremic toxins, such as uric acid and creatinine, in dialysate solution using the developed SCB-derived hybrid GAC compared with the commercial hybrid GAC (C GAC).

## 2. Materials and Methods

### 2.1. Preparation of SCB-derived activated carbon via carbonization and steam activation

Raw sugarcane bagasse (SCB) sieved with a size range of 500 microns to 3 mm was classified and dried at 110 °C for 24 h prior to use. 300 g of dried SCB was then introduced into a stainless-steel tube reactor with an internal diameter of 15.4 cm. The carbonization was conducted under nitrogen gas flow with a heating rate of 5 °C/min from room temperature to 500 °C and held for 1 h. After cooling down the reactor, biochar product is then obtained and weighed to determine the yield.

40 g of biochar was dried at 105 °C for 3 h for moisture removal before being weighed and placed in the tray inside the same tube reactor connected with an injection valve from a steam generator. The steam activation was then performed at 900 °C for 1 h to obtain SCB-derived activated carbon, SCB AC). Physicochemical properties such as product yield, proximate analysis, elemental analysis, iodine absorption test were characterized prior to develop a hybrid granular activated carbon with SCB-derived mesoporous silica and alginate via gelation.

### 2.2. Preparation of SCB-derived mesoporous silica via acid leaching and extraction

For acid leaching, 20 g of raw SCBA was firstly washed by adding 200 mL of 1 M hydrochloric acid (HCl) at 90 °C for 1 h to remove some inorganic impurities, then was filtered and rinsed with DI water till pH closed to 5-6 and then dried in a hot air oven at 110 °C for 24 h. The dried leached ash was then calcined under air atmosphere in a muffle furnace at 800 °C for 2 h to completely remove unburnt carbon residues in raw SCBA.



To produce SCB-derived mesoporous silica, 15 g of acid-leached ash was then extracted with 150 mL of 1 M sodium hydroxide (NaOH) solution at 90 °C for 1 h to form sodium silicate. The intermediate sodium silicate solution was then reacted with 1 M HCl till the pH is equal to 7 using vacuum filter. The filtrate solution was then left for 18 h to form SCB-derived mesoporous silica gel, while the remaining ash was called as an SCB-derived extracted ash. The MPS gel was separated using centrifuge and then dried at 110 °C overnight to obtain SCB-derived mesoporous silica (SCB MPS) as a product. Inorganic composition in all types of the ash were then characterized by X-ray fluorescence (XRF).

### 2.3. Granulation of hybrid GAC via gelation with bio-based polymer

1% (w/v) sodium alginate solution, i.e., 1 g of alginate as a bio-based polymer in 100 mL of DI water was prepared prior to mix dried mesoporous silica with dried activated carbon powder at a ratio of SCBA MPS to SCB AC (S:C) at 0:1, 1:2, 1:1, 2:1, and 1:0. It is dissolved and stirred at 60 °C till the mixture solution was homogeneous. The suspended alginate solution was then added into a 1% (w/v) calcium chloride dihydrate solution (1 g of calcium chloride dihydrate in 100 mg of DI water) using a 2-mm diameter syringe pump at the flow rate of 3 mL/min, then left the hybrid alginate beads in calcium chloride solution for 24 h. After that the beads (hybrid granular activated carbon, GAC) were rinsed with DI water. Finally, the hybrid GAC was dried at 60 °C to remove moisture for 24 h prior to use in batch adsorption test.

### 2.4. Batch adsorption test of uremic toxins using hybrid GAC

The dried hybrid GAC was weighed at 0.05 g as a fixed sample dose in the flasks to test the batch adsorption in 50 mL of 100-ppm uric acid and creatinine as two major uremic toxins in dialysate solution. The dialysate solution was prepared by mixing Heamo A reagent solution (containing NaCl, KCl, CaCl<sub>2</sub>, MgCl<sub>2</sub>, CH<sub>3</sub>COOH and d-glucose), Heamo B reagent solution (containing NaHCO<sub>3</sub>) in DI water with the volume ratio of 1: 1.225: 32.775 (the total volume of 50 mL). The flasks were placed in a shaker using a speed of 120 rpm for 24 h at a constant temperature of 25 °C. UV-spectrophotometer was used to examine the wavelengths of 233 and 290 nm for creatinine and uric acid, respectively, before and after 24-h batch adsorption test. The adsorption efficiency (%) and adsorption capacity ( $q_e$ , mg/g) were then determined. The hybrid GAC prepared from commercial power activated carbon and commercial mesoporous silica was also tested for comparison with the SCB GAC.

## 3. Results and Discussion

### 3.1 As-synthesized activated carbon by sugarcane bagasse (SCB AC)

Table 1 shows that the biochar yield from carbonization of raw SCB was 31.39%, while the yield of activated carbon through steam activation was achieved at 48.53%. The results could be comparable to those reported in our previous study [5]. Proximate analysis showed a significant increase in a fixed-carbon content to 78.7% in SCB-biochar because volatile matter decomposed at 300-500 °C during the carbonization, while a decrease in the fixed-carbon content to 48.1% in SCB AC was observed due to the gasification of biochar destroying carbons and developing pores in its structure. This led to an enhancement in carbon porosity and specific surface area of the SCB AC powder.

Table 2 shows the ultimate analysis to determine carbon (C), hydrogen (H), oxygen (O), and nitrogen (N)—in raw SCB, SCB-biochar, SCB AC, and raw SCBA. It was observed that activated carbon exhibited a slightly lower carbon content of 83.03% with higher oxygen content of 11.97% due to the reaction of carbon with steam, leading to some carbon loss. The iodine number of SCB AC was found at 687.11 mg/g. Although this value was still lower than that of commercial activated carbon, it was comparable with other biomass-derived activated carbon reported elsewhere [5].

**Table 1.** Yields and proximate analysis of raw SCB, SCB-biochar, SCBAC and raw SCBA.

Samples	Yield (wt%)		Proximate analysis (wt%, dry basis)		
	Sample basis	Raw basis	Volatile matter	Fixed carbon	Ash
Raw SCB	-	-	82.8	15.5	1.8
SCB-biochar	31.39 ± 0.74	-	11.0	78.7	10.3
SCBAC	48.53	17.36	9.3	48.11	42.56
Raw SCBA	-	-	2.29	1.68	96.03

**Table 2.** Ultimate analyses of raw SCB, SCB-biochar, SCBAC and raw SCBA.

Sample	[wt%, dry ash-free basis] (average)			
	C	H	O	N
Raw SCB	47.12±1.15	7.16±0.29	45.20±1.54	0.52±0.09
SCB-biochar	85.76±0.56	3.98±0.00	9.31±0.52	0.95±0.03
SCB AC-900	83.03±0.83	4.28±0.67	11.97±1.73	0.72±0.25
Raw SCBA	71.90±2.94	10.85±2.05	15.52±5.76	1.72±0.77

### 3.2 As-synthesized mesoporous silica by sugarcane bagasse ash (SCBA MPS)

Physical appearances raw SCBA, SCBA-derived leached ash, SCBA-derived extracted ash and SCBA-derived mesoporous silica (SCBA MPS) were shown in Fig. 1. The SCBA MPS was clearly white as the color of commercial silica (CS). Table 4 demonstrates inorganic matter composition by XRF analysis. Silica content in SCBA MPS could be achieved up to >95% , which was comparable with the CS at >98%. Consequently, SCBA MPS with high purity of silica was used to boost the sorbent's strength in the hybrid SCB GAC.



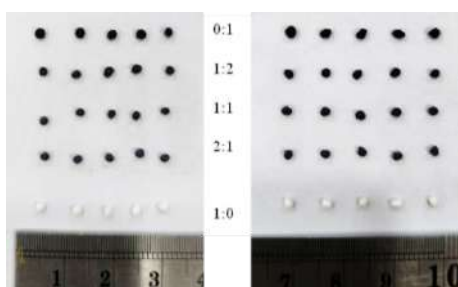
**Fig. 1.** Physical appearances of a. raw SCBA, b. SCBA-derived leached ash, c. SCBA-derived extracted ash and d. SCBA-derived mesoporous silica (SCBA MPS).

**Table 3.** Inorganic matter composition of raw SCBA, SCBA-derived leached ash, extracted ash, and mesoporous silica compared with commercial silica (CS) by XRF analysis.

Samples (wt%, d.b.)	SiO <sub>2</sub>	Al <sub>2</sub> O <sub>3</sub>	Fe <sub>2</sub> O <sub>3</sub>	Others
Raw SCBA	66.46	4.93	7.37	21.24
SCBA-derived leached ash	83.44	3.59	3.22	9.75
SCBA-derived extracted ash	81.07	4.04	4.57	10.32
SCBA-derived mesoporous silica (SCBA MPS)	95.55	3.80	0.38	0.27
Commercial silica (CS)	98.92	1.08	-	-

### 3.3 Granulation of hybrid GAC via gelation

Physical appearances of commercial beads (C GAC) and SCB-derived beads (SCB GAC) developed with various weight ratios of silica and carbon (0:1, 1:2, 1:1, 2:1, 1:0) were demonstrated in Fig. 2. Average diameter of both beads was measured at least 20 replicates per sample using a digital vernier. The results in Table 3 revealed that the diameter of the beads decreased from 1.64–1.78 mm to 1.41–1.53 mm when adding more amount of silica into the bead's structure. SCB GAC samples were slightly smaller than C GAC.

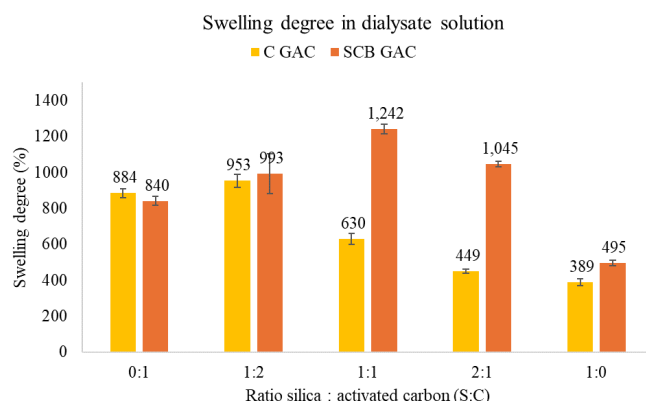


a. C GAC      b. SCB GAC

**Fig. 2.** Physical appearances of (a) C GAC and (b) SCB GAC developed with various weight ratios of silica and carbon (0:1, 1:2, 1:1, 2:1, 1:0).

**Table 4.** Average diameter of C GAC and SCB GAC developed with various weight ratios of silica and carbon (S:C).

Silica : Carbon (w/w)	Average diameter (mm)	
	C GAC	SCB GAC
0:1	1.78 ± 0.08	1.64±0.14
1:2	1.60 ± 0.10	1.61±0.09
1:1	1.57 ± 0.10	1.56±0.09
2:1	1.55 ± 0.06	1.53±0.08
1:0	1.53 ± 0.10	1.41±0.15



**Fig. 3.** Swelling degree in dialysate solution of the hybrid C GAC and SCB GAC developed with various weight ratios of silica and carbon, S:C=0:1. 1:2. 1:1. 2:1. 1:0).

Swelling degree in dialysate solution of the hybrid C GAC and SCB GAC developed with various weight ratios of silica and carbon was determined in triplicates and expressed in Fig. 3. For both C GAC and SCB GAC, the optimum swelling degrees were found at the weight mixing ratio of silica and carbon at 1:2 and 1:1, respectively. The maximum swelling degree in dialysate could be enhanced up to 1242% for the SCB GAC with S:C=1:1, while it showed 953% for the C GAC with S:C=1:2. Further adding silica in the bead's structure reduced the swelling degree lower than 500%, particularly the samples without AC (S:C=1:0). For batch adsorption test of uremic toxins, the mixing ratios of silica and carbon at 1:2 and 1:1 in the hybrid GAC were then selected to optimize both adsorption efficiency and the bead's strength.

### 3.4 Batch adsorption test of uremic toxins using hybrid GAC

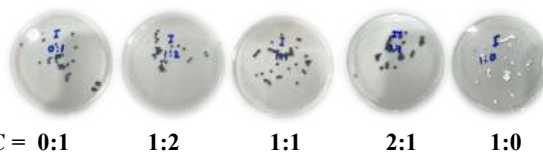
Fig. 4 shows physical appearances of the developed hybrid C GAC and SCB GAC with various weight ratios of silica and carbon (S:C=0:1. 1:2. 1:1. 2:1. 1:0) during batch adsorption test of uremic toxins in dialysate solution and after 24-h adsorption and drying. The one without silica (S:C=0:1) rather deformed and AC powder could be released out of its granule's structure, while other samples containing silica could remain their structures with much less release of AC powder. This indicates that silica in the bead's structure could improve granular strength.

**(a) During batch adsorption in dialysate solution**



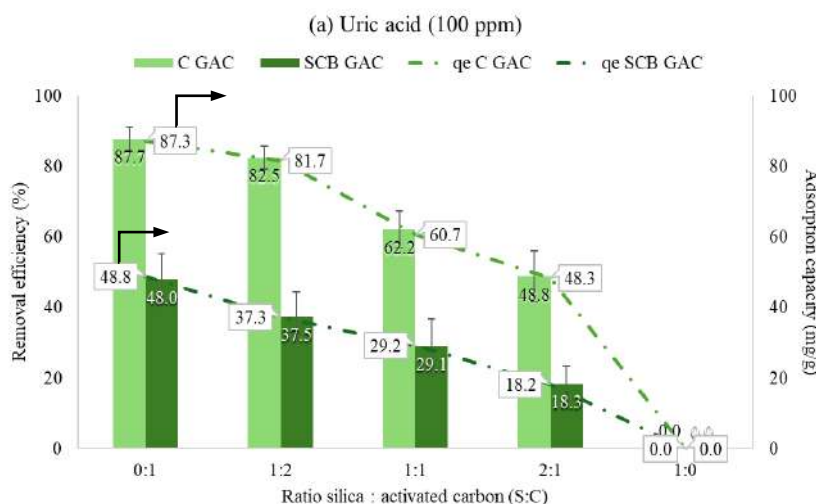
S:C = 0:1      1:2      1:1      2:1      1:0

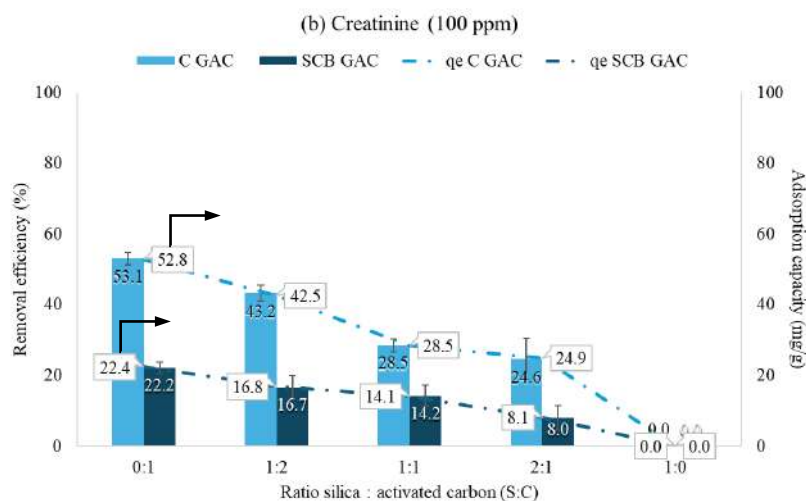
**(b) After 24-h adsorption and drying**



**Fig. 4.** Physical appearances of the developed hybrid C GAC and SCB GAC with various weight ratios of silica and carbon, S:C=0:1. 1:2. 1:1. 2:1. 1:0) (a) during batch adsorption test in dialysate solution and (b) after 24-h adsorption and drying.

Fig. 5 shows the comparison of the batch adsorption tests for uric acid and creatinine as two of major composition in uremic toxins using C GAC and SCB GAC. It reveals that C GAC demonstrated higher adsorption efficiencies and capacities than CB GAC because of its larger specific surface area. The maximum adsorption efficiencies of C GAC with S:C=0:1 were observed at 87.7% and 53.1% for uric acid and creatinine, respectively, while they were decreased to 48.0% and 22.2% for uric acid and creatinine, respectively, for SCB GAC with S:C=0:1. Once silica was added into the granule, adsorption efficiencies of both uric acid and creatinine were gradually decreased for C GAC and SCB GAC. Since the granules without added silica could be deformed after the adsorption as mentioned before, the GAC with S:C equal to 1:2 and 1:1 by weight would be selected and used for further studies in adsorption kinetics, equilibrium isotherms, and regeneration with substantial performance with adsorption capacities of uric acid and creatinine at 60.7–81.7 mg/g and 28.5–42.5 mg/g using C GAC, and 29.1–37.5 mg/g and 14.2–16.7 mg/g using SCB GAC. This also responded to the optimum swelling degree in dialysate for the GAC with S:C ratios at 1:2 and 1:1 by weight.





**Fig. 5.** Adsorption efficiency and adsorption capacity ( $q_e$ ) of (a) uric acid and (b) creatinine with a concentration of 100 ppm in dialysate solution using the developed hybrid C GAC and SCB GAC with various weight ratios of silica and carbon, S:C=0:1. 1:2. 1:1. 2:1. 1:0).

## Conclusion

In this study, granular activated carbon (GAC) was developed from sugarcane bagasse-derived activated carbon (SCB AC) and sugarcane bagasse ash-derived mesoporous silica (SCBA MPS) hybridized with sodium alginate as a bio-based polymer for use in kidney dialysis system to adsorb selected uremic toxins and reuse the spent dialysate. The commercial GAC (C GAC) was investigated to compare with the SCB GAC. Even though the C GAC clearly showed better efficiencies in adsorbing uremic toxins for both uric acid and creatinine due to their relatively larger surface area, the SCB GAC could also potentially adsorb a substantial amount of uremic toxins in dialysate solution. The adsorption showed their maximized performance when only AC was added into the structure of the granules (S:C=0:1) for all samples, while their adsorption efficiencies were gradually dropped once silica was added into the samples. However, the SCB GAC samples with S:C = 1:2 or 1:1 were selected for further studies in adsorption kinetics, equilibrium isotherms, and regeneration due to its higher strength of the beads with much less deformation and small release of AC powder into the dialysate solution. Briefly, in terms of economics, with zero cost on sugarcane bagasse and its ash as raw materials including steam as the gasifying agent, which could be self-produced in the sugar mill, in the production of activated carbon, it could be potentially considered as one of a competitive adsorbent for use in uremic toxin removal. Cost analysis by comparing with the commercial granular activated carbons will be further studied in the future.

## Acknowledgements

This work was financially supported by the Mahidol University Partnering Initiative under the MU-KMUTT Biomedical Engineering & Biomaterials Research Consortium. The authors also gratefully acknowledge the Water Quality Research Lab of the Civil and Environmental Engineering Department and Chemical Engineering Department, Faculty of Engineering, Mahidol University, for the support of experimental facilities and equipment. The authors

would also like to gratefully thank Ms. Pimonpan Inthapat and Ms. Nadiya Abdulroman for their kind assistance and suggestions in experiments.

## References

- [1] Clark, W. R., Dehghani, N. L., Narsimhan, V., & Ronco, C. (2019). Uremic Toxins and their Relation to Dialysis Efficacy. *Blood Purif*, 48( 4) , 299-314. <https://doi.org/10.1159/000502331>
- [2] Wang, W., Wang, Z., Li, K., Liu, Y., Xie, D., Shan, S., He, L., & Mei, Y. (2021). Adsorption of uremic toxins using biochar for dialysate regeneration. *Biomass Convers Biorefin*, 1-13. <https://doi.org/10.1007/s13399-021-01946-4>
- [3] Sarkar, J., Mridha, D., Sarkar, J., Orasugh, J. T., Gangopadhyay, B., Chattopadhyay, D., Roychowdhury, T., & Acharya, K. (2021). Synthesis of nanosilica from agricultural wastes and its multifaceted applications: A review. *Biocatalysis and Agricultural Biotechnology*, 37. <https://doi.org/10.1016/j.bcab.2021.102175>
- [4] Xu, S., Zhou, C., Fang, H., Zhu, W., Shi, J., & Liu, G. (2023). Synthesis of ordered mesoporous silica from biomass ash and its application in CO<sub>2</sub> adsorption. *Environ Res*, 231(Pt 1), 116070. <https://doi.org/10.1016/j.envres.2023.116070>
- [5] Sutthasupa, S., Koo-Amornpattana, W., Worasuwanarak, N., Prachakittikul, P., Teachawachirasiri, P., Wanthong, W., Thungthong, T., Inthapat, P., Chanamarn, W., Thawonbudit, C., Srifa, A., Ratchahat, S., & Chaiwat, W. (2023). Sugarcane bagasse-derived granular activated carbon hybridized with ash in bio-based alginate/gelatin polymer matrix for methylene blue adsorption. *Int J Biol Macromol*, 253(Pt 7), 127464. <https://doi.org/10.1016/j.ijbiomac.2023.127464>

## UV-vulcanized Natural Rubber Grafted with Methyl Methacrylate for Production of Ultrafine Powder as Toughening Fillers in Polylactic Acid

**Torntawat Kiratiphongwut, Krittapas Charoensuk, and Sarawut Rimdusit**\*

Center of Excellence in Polymeric Materials for Medical Practice Devices, Department of Chemical Engineering, Faculty of Engineering, Chulalongkorn University, Bangkok 10330, Thailand  
E-mail: \* Sarawut.r@chula.ac.th

### Abstract

This research focuses on the development of UV-vulcanized natural rubber grafted with methyl methacrylate (MMA) as a promising toughening filler for polylactic acid (PLA). To enhance compatibility with PLA, deproteinized natural rubbers (DPNRs) were endowed with hydrophilic functions through grafting copolymerization with MMA monomer. UV vulcanization was employed to enhance crosslinking in the resulting grafted DPNR. The study integrates an assessment of the efficacy of grafting process of the DPNR-g-PMMA in terms of monomer conversion and grafting efficiency with the highest values achieved at 20 phr MMA content, reaching 84.6% and 89.0%, respectively. Compatibility between the obtained DPNR-g-PMMA and PLA film was assessed based on water contact angle (WCA), revealing optimal grafting at 10 phr MMA content with a WCA value of 57 °. Additionally, swell testing was incorporated to evaluate the swelling ratio and crosslink density of the UV-vulcanized DPNR-g-PMMA, with the lowest swelling ratio and highest crosslink density observed at 10 phr MMA content. This study highlights the potential of UV-vulcanized natural rubber grafted with MMA as an effective toughening filler, offering a sustainable solution for enhancing the mechanical performance of environmentally friendly PLA-based materials in various applications.

**Keywords:** UV vulcanization; Grafted copolymerization; Natural rubber; Methyl methacrylate; Polylactic acid.

### 1. Introduction

In recent years, natural rubber (NR), notably sourced from *Hevea brasiliensis*, has become a significant component of our daily routines, finding use not only in the tire sector. Examples of potential applications include such as gloves, mattresses, condoms, as well as medical tubing, and artificial tissues and organs for applications in bioengineering [1]. NR is often utilized as an additive in polymer matrices owing to its impressive impact strength and ductility [2].

Initially, NR possesses stickiness and lacks elasticity. To enhance its properties for various uses, vulcanization is utilized to crosslink NR molecules, resulting in increased heat stability and elasticity. Vulcanization of NR can be accomplished through sulfur, peroxide, or radiation methods [3]. One type of radiation technique, UV radiation vulcanized natural rubber latex (UVNRL) has been created to manufacture NR latex devoid of accelerated sulfur chemicals. UVNRL exhibits excellent biocompatibility, poses fewer safety risks during operation compared to ionizing radiation vulcanization, eliminates the need for expensive shielding against ionizing radiation, and requires low energy consumption [4]. UV light can be used for vulcanizing NR latex without accelerators. Photoinitiators typically employed in UV-based



curing processes include 2,2-dimethoxy-2-phenyl acetophenone, often in conjunction with an acrylate coagent. This method offers a safer and more efficient alternative to traditional vulcanization techniques [5].

Chemical modification through graft copolymerization stands out as a particularly appealing method. The molecular composition of NR, featuring cis-1,4-polyisoprene with a methyl group that donates electrons bonded to the carbon-carbon double bond in its primary chain, enables it to readily react with additional vinyl monomers and become covalently bonded to the NR backbone [6]. For instance, a vinyl monomer with desirable properties, such as methyl methacrylate (MMA) [7], was grafted onto a polyisoprene backbone to enhance the solvent resistance, thermal stability, mechanical properties, and compatibility of NR [8].

Poly(lactic acid) (PLA) is a biodegradable and bio-based polymer, derived from renewable resources. Commercial PLA has high modulus and strength. However, it is brittle. One technique that can improve the toughness of PLA is blending with elastomers. NR is a bio-based elastomer that is derived from sustainable resources. Since NR can be blended with PLA directly [9], however due to immiscibility of NR and PLA, compatibilization techniques are necessary. Grafting MMA onto NR can improve the compatibility, the dispersion of NR in PLA.

The focus of this study is the modification of UVNRL to enhance compatibility with PLA through graft-copolymerization with MMA monomers onto DPNR latex. This process utilizes tert-butyl hydroperoxide (TBHPO) and tetraethylenepentamine (TEPA) as a redox initiator [6]. The study investigates the impact of monomer content on monomer conversion, grafting efficiency, and water contact angle. Additionally, swell testing was conducted to investigate the impact of radiation time on the swelling ratio and crosslink density of the UFPNR-g-(PMMA). To enter the spray dry process for producing Ultrafine Fully Vulcanized Natural Rubber Powder (UFPNR) in the future.

## 2. Materials and Methods

### 2.1 Materials

DPNR latex (60 wt% of dry rubber content) was purchased from the Unimac Rubber Co., Ltd. (Trang, Thailand), sodium dodecyl sulfate (SDS; 99%, Merck), tert-butyl hydroperoxide (TBHPO; 70% in water), tetra ethylene pentaamine (TEPA; 94% in water), methyl methacrylate (99.8%), Toluene (95%), Magnesium-sulfate heptahydrate ( $\text{MgSO}_4 \cdot 7\text{H}_2\text{O}$ ), 2-hydroxy-2-methyl-1-phenylpropanone (96%) and 1,6-nonanedioldiacrylate (85%) were purchased from Chemical Express Co., Ltd. (Thailand). 37% Potassium Laurate solution were prepared in a laboratory.

### 2.2 Methods

#### 2.2.1 Preparation of DPNR latex and purification of MMA monomers

DPNR latex was diluted to 30% of dry rubber content with de-ionized water [10] and stabilized with SDS (0.8 wt%) The mixture was stirred with a nitrogen atmosphere at 400 rpm and 30 °C for 1 hour to remove oxygen concentration. The MMA monomer was purified by

extracting it with a 10% sodium hydroxide solution, then washed with deionized water until neutral. Finally, it was dried using  $\text{MgSO}_4 \cdot 7\text{H}_2\text{O}$  to remove any inhibitors [11].

### 2.2.2 Graft copolymerization of DPNR with MMA

TEPA and TBHPO initiators were added dropwise onto DPNR latex at a rate of  $5.5 \times 10^{-5}$  mol per gram of dry rubber [12], followed by the addition of MMA monomer at different concentrations of 5, 10, 15, and 20 parts per one hundred rubbers (phr). The latex mixture was then continuously stirred at 400 rpm and 40 °C for 3 hours. The residual MMA was eliminated through evaporation using a rotary evaporator under reduced pressure. The resulting product was then placed in a glass Petri dish and dried in a vacuum oven at 50°C for a week. The conversion of MMA (degree of polymerization) and grafting efficiency (GE, degree of grafting) were assessed using a gravimetric method, as outlined in the following expressions [13].

$$\text{Monomer conversion (\%)} = \frac{\text{weight of polymer in gross copolymer}}{\text{weight of monomer}} \times 100 \quad (1)$$

$$\text{Grafting efficiency (\%)} = \frac{\text{weight of polymer linked to natural rubber}}{\text{weight of polymer in gross copolymer}} \times 100 \quad (2)$$

### 2.2.3 Preparation of mixture and UV radiation

The coagent (1,6-nonanedioldiacrylate), the photoinitiator (2-hydroxy-2-methyl-1-phenylpropanone) and potassium laurate solution were added dropwise onto DPNR-g-PMMA in 500 cm<sup>3</sup> beaker. The total quantity of the coagent and photoinitiator was always 4 phr [5] Potassium laurate solution was used 0.5 phr. After that, stir for 10 minutes in the dark. The UV-vulcanization process took place while continuously mixing the components under standard air conditions in a dark room at 28°C [14]. The mixtures were radiated by two UV lamps (250–350 nm wavelength, 18 W) with various times of 40, 80 and 120 minutes.

### 2.2.4 Characterizations

The swelling behaviors of UV-vulcanized NR grafted with MMA (UVNR-g-PMMA) were analyzed by dissolving approximately 0.01 g of the sample in 20 mL of toluene at room temperature for 24 hours [10]. After recording the dried weight of the UFPNR sample ( $W_1$ ), it was immersed in toluene ( $\rho_s = 0.87 \text{ g/cm}^3$ ,  $V_1 = 106.5 \text{ cm}^3/\text{mol}$ ) for another 24 hours. The weight of the swollen UFPNR sample ( $W_2$ ) was then recorded, followed by drying the sample in a vacuum oven at 70 °C for 24 hours. The final weight of the sample ( $W_3$ ) was recorded after drying. The swelling ratio ( $Q$ ), gel fraction, molecular weight between crosslinks ( $M_c$ ), and crosslinking density (CLD) were calculated using following Eq. (3)-(6), respectively [15-16]. The rubber density ( $\rho_r$ ) is 0.91 g/cm<sup>3</sup>.  $\phi_r$  represents the volume fraction of the polymer in the swollen stage, and  $\chi_{12}$  denotes the polymer–solvent interaction.

$$Q = \frac{(W_2 - W_1)/\rho_s}{W_1/\rho_s} \quad (3)$$

$$\text{Gel fraction} = \frac{W_3}{W_1} \quad (4)$$

$$M_c = \frac{-\rho_r V_1 (\varphi_r^{1/3} - \frac{\varphi_r}{2})}{\ln(1-\varphi_r) + \varphi_r + \chi_{12} \varphi_r^2} \quad : \text{ where } \varphi_r = \frac{1}{1+Q} \quad (5)$$

$$\text{CLD} = \frac{\rho_r N}{M_c} \quad (6)$$

The molecular structure of DPNR-g-PMMA was analyzed to confirm the existing grafted PMMA on rubber structures by using a Fourier-transform infrared (FT-IR) spectrometer (Spectrum GX, Perkin Elmer) equipped with an attenuated total reflection (ATR) (Waltham, Massachusetts, United States). The analysis employed a scan range of 4000–400 cm<sup>-1</sup>, with a total of 32 scans and a resolution of 4 cm<sup>-1</sup> [3].

Following UV radiation, the DPNR-g-PMMA obtained was directly applied onto a glass slide and then dried in an oven at 80 °C until a constant weight was achieved to produce films. Then, PLA was formed by compression molding. The polarity of the UVNR-g-PMMA films and PLA were estimated in terms of the contact angle of a 0.1 µL water droplet on surfaces.

### 3. Results and Discussion

#### 3.1 Effects of Monomer Contents on Monomer Conversion and Grafting Efficiency of Grafted DPNR.

The percentage of monomer molecules that convert to copolymer on the polyisoprene chain, along with any residual monomer in its homopolymer form in the aqueous phase, was calculated by using Eq. (1). Grafting efficiency indicates the percentage of monomer successfully bonded to the polyisoprene backbone, was calculated by using Eq. (2), and the results are summarized in Table 1.

The monomer conversion and the grafting efficiency of DPNR grafting with MAA at monomer contents of 5, 10, 15 and 20 phr were found to be 75.4%, 77.7%, 81.5% and 84.6%, 79.3%, 84.1%, 87.2% and 89%, respectively. From the results, it can be observed that an increasing the monomer content resulted in greater monomer conversion, due to the higher opportunity of monomer molecules to frequently copolymerized on the polyisoprene backbone.

Table 1. Monomers conversion and grafting efficiency of the DPNR-g-PMMA with various monomer contents.

Monomer content (phr)	Monomer conversion (%)	Grafting efficiency (%)
5	75.4	79.3
10	77.7	84.1
15	81.5	87.2
20	84.6	89.0

#### 3.2 Molecular Structural Characterization of the DPNR-g-PMMA.

Figure 1(a) shows characteristic absorption bands of DPNR, including the C-H stretching vibration at  $2961\text{ cm}^{-1}$ , the C=C bending vibration at  $842\text{ cm}^{-1}$ , and the C-H stretching vibration at  $1452\text{ cm}^{-1}$ . Additionally, figure 1(b) indicates new peaks of carbonyl groups which are C=O stretching and C-O-C stretching in  $1730$  and  $1145\text{ cm}^{-1}$ , respectively. These results evidence the presence of PMMA structure that successfully grafted onto the natural rubber backbone [12, 16].

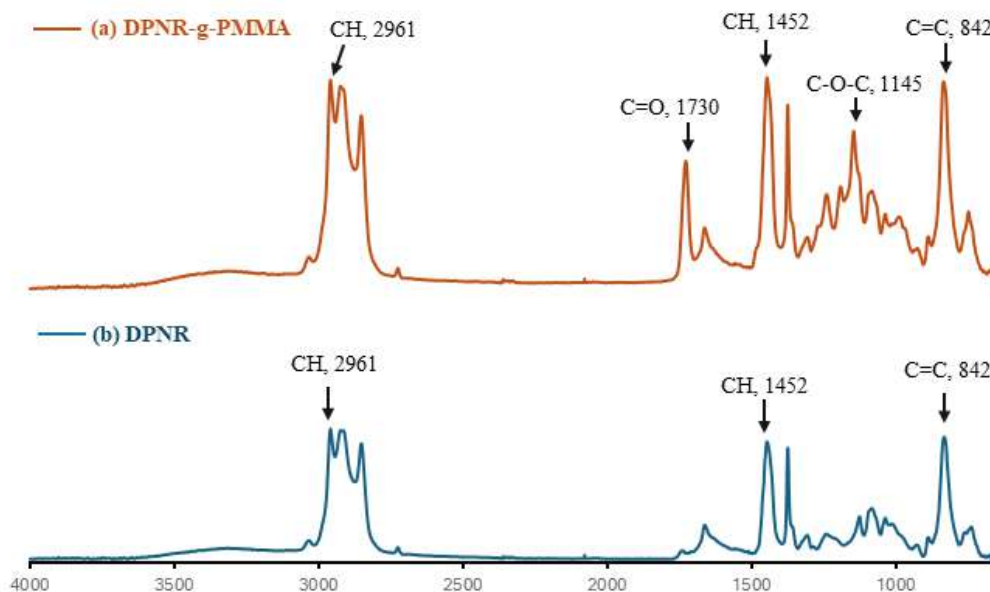


Fig. 1 The FTIR spectra of (a) DPNR-g-PMMA 20 phr and (b) DPNR.

### 3.3 Effects of Monomer Contents and UV-Radiation Times on Swelling Behavior and Gel fraction of DPNR-g-PMMA.

The swelling ratios, gel fractions, and crosslink densities (CLD) of DPNR-g-PMMA were determined using Eq. (3-6), with the summarized results presented in Table. 2. It was found that as the UV-radiation time increased, the gel fractions increased while the swelling ratios decreased systematically. This can be attributed to the longer reaction time, leading to a higher formation of the crosslinked structure of polyisoprene. These findings align with the CLD results, which also showed an increase with longer reaction times. Furthermore, the results suggest that UV radiation vulcanization is suitable for our system, as no devulcanization behaviors were observed during the vulcanization process. Additionally, it was noted that gel fraction and crosslink density of DPNR-g-PMMA at monomer contents of 15 and 20 phr tended to decrease with increasing exposure times compared to those at monomer contents of 5 and 10 phr. This trend can be attributed to hindered crosslinking of excess monomers, as the surplus MMA monomer may occupy most active sites of the isoprene backbone, such as the double bond (C=C) and the allylic carbon [5, 17]. Consequently, fewer remaining active sites of isoprene result in a reduction of crosslinking formation.

Table 2. Effects of monomer content and UV-radiation time on swelling ratio, gel fraction and crosslink density of DPNR-g-PMMA.

Monomer content (phr)	UV-radiation time (minute)	Swelling ratio (Q)	Gel fraction	CLD $\times 10^{18}$ (mol/cm <sup>3</sup> )
5	40	27.3 $\pm$ 1.88	0.66 $\pm$ 0.01	2.73 $\pm$ 0.32
	80	20.7 $\pm$ 0.42	0.76 $\pm$ 0.01	4.41 $\pm$ 0.16
	120	18.1 $\pm$ 0.16	0.80 $\pm$ 0.01	5.59 $\pm$ 0.09
10	40	22.7 $\pm$ 0.91	0.72 $\pm$ 0.01	3.72 $\pm$ 0.26
	80	20.1 $\pm$ 1.11	0.74 $\pm$ 0.02	4.65 $\pm$ 0.45
	120	17.8 $\pm$ 0.15	0.80 $\pm$ 0.02	5.73 $\pm$ 0.09
15	40	24.1 $\pm$ 2.80	0.61 $\pm$ 0.14	3.41 $\pm$ 0.69
	80	22.9 $\pm$ 0.82	0.63 $\pm$ 0.03	3.69 $\pm$ 0.23
	120	20.2 $\pm$ 0.37	0.71 $\pm$ 0.02	4.61 $\pm$ 0.15
20	40	33.1 $\pm$ 0.92	0.54 $\pm$ 0.06	1.94 $\pm$ 0.09
	80	30.9 $\pm$ 1.06	0.57 $\pm$ 0.01	2.26 $\pm$ 0.11
	120	29.0 $\pm$ 2.91	0.63 $\pm$ 0.07	2.47 $\pm$ 0.43

### 3.4 Effects of monomer contents on surface property of DPNR-g-PMMA.

The compatibility between filler and polymer matrix is vital for composite properties, often assessed by comparing their polarities. Contact angle measurements determine the angle between a liquid droplet and a polymer surface, offering insights into surface properties and the interaction between the liquid and the polymer [18].

Following the UV-radiation process, the resulting latex was oven-dried to form a film. Subsequently, water contact angle (WCA) measurement was conducted by dropping 1.0  $\mu$ L of water onto the film. The results are shown in Fig. 2 and the numerical data are tabulated in Table 3. It was found that increasing MMA monomer content led to enhanced hydrophilic behaviors of the grafted DPNR, as evidenced by decreasing WCA values. Specifically, at a monomer content of 10 phr, the water contact angle measured 57.8 $^{\circ}$  $\pm$ 2.6 $^{\circ}$ , which is close to that of neat PLA, which has a value of 54.2 $^{\circ}$  $\pm$ 1.6 $^{\circ}$ . This indicates that grafting MMA monomer content at 10 phr might offer the greatest compatibility with PLA when used as a toughening filler.

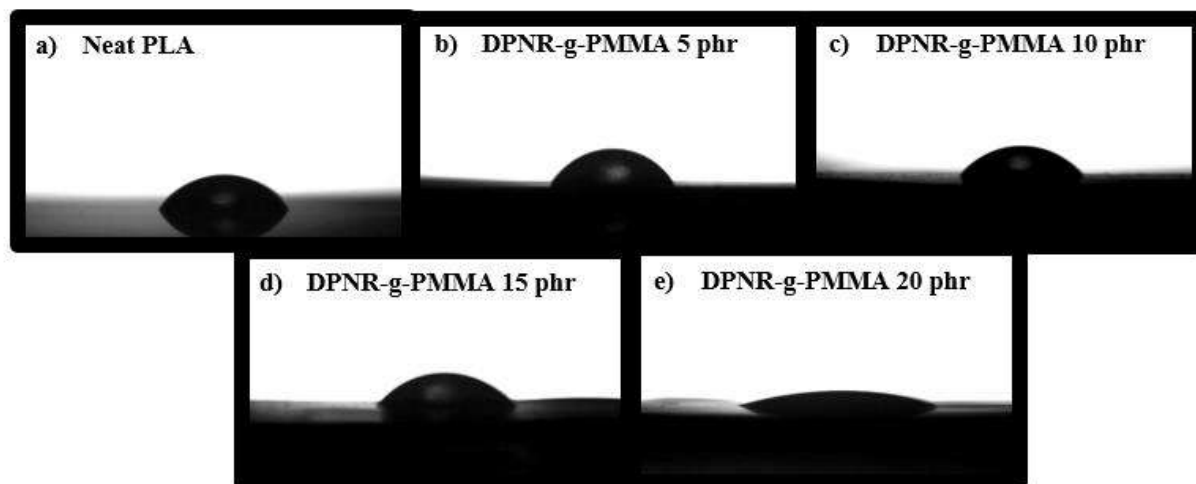


Fig. 2 Contact angle measurements of a 1.0  $\mu\text{L}$  water droplet on surfaces: (a) Neat PLA, (b) DPNR-g-PMMA 5 phr, (c) DPNR-g-PMMA 10 phr, (d) DPNR-g-PMMA 15 phr, and (e) DPNR-g-PMMA 20 phr

Table 3 Water contact angles of water droplet on PLA film and DPNR-g-PMMA film (UV-radiation time 120 minutes)

Samples	Monomer content (phr)	Water contact angle, $\theta$ ( $^{\circ}$ )
Neat PLA	-	$54.2 \pm 1.6$
DPNR-g-PMMA	5	$65.8 \pm 2.9$
DPNR-g-PMMA	10	$57.8 \pm 2.6$
DPNR-g-PMMA	15	$48.3 \pm 0.6$
DPNR-g-PMMA	20	$15.7 \pm 0.9$

#### 4. Conclusions

In this work, the modified NR latex, DPNR-g-PMMA was successfully prepared through graft copolymerization of MMA monomer onto DPNR latex, confirmed by FTIR spectra. The highest monomer conversion (84.6%) and grafting efficiency (89%) were achieved with 20 phr MMA monomer content. Structural modification of NR via UV-radiation was also successful, with DPNR-g-PMMA containing 5 and 10 phr of MMA monomer facilitating the formation of high crosslinks density and gel fraction. Additionally, the compatibility between PLA and DPNR-g-PMMA was assessed via water contact angle, revealing that DPNR-g-PMMA with 10 phr MMA content, irradiated with UV for 120 minutes, exhibited a water contact angle closest to that of PLA, with a value of  $57.8^{\circ} \pm 2.6^{\circ}$  and  $54.2^{\circ} \pm 1.6^{\circ}$ , respectively. Therefore, the UV-vulcanized DPNR-g-PMMA with 10 phr MMA content emerges as the most promising candidate for toughening filler production in PLA.

#### Acknowledgements

This project is funded by National Research Council of Thailand (NRCT) and Chulalongkorn University (N42A660910) and Thailand Science Research and Innovation Fund Chulalongkorn University (No. 6641/2566).

## References

- [1] Sriring, M., Nimpaiboon, A., Kumarn, S., Takahara, A., & Sakdapipanich, J. (2020). Enhancing viscoelastic and mechanical performances of natural rubber through variation of large and small rubber particle combinations. *Polymer Testing*, *81*, 106225
- [2] Sangthongyingdee, N., Low, D. Y. S., Rahim, A. H. B. A., Boonvisood, I., Tang, S. Y., & Soottitantawat, A. (2021). Spray drying preparation of polymethyl methacrylate-grafted natural rubber composite powders and its impact reinforcement effect. *Drying Technology*, *40*(13), 2770–2782.
- [3] Wongkumchai, R., Amornkitbamrung, L., Mora, P., Jubsilp, C., & Rimdusit, S. (2021). Effects of coagent incorporation on properties of ultrafine fully vulcanized powdered natural rubber prepared as toughening filler in polybenzoxazine. *SPE Polymers*, *2*(3), 191–198.
- [4] Noorwadi, M., et al. (2021) The Effects of HDDA and n-BA & TMPTMA on the Physical and Thermal Properties of UV Irradiation Vulcanization Natural Rubber Latex. *International Transaction Journal of Engineering, Management, & Applied Sciences & Technologies*, vol. 12, no. 9, pp. 1–10.
- [5] Hansupalak, N., Srisuk, S., Wiroonpochit, P., & Chisti, Y. (2016). Sulfur-Free pre vulcanization of natural rubber latex by ultraviolet irradiation. *Industrial & Engineering Chemistry Research*, *55*(14), 3974–3981
- [6] Longsiri, K., Mora, P., Peeksumtiye, W., Jubsilp, C., Hemvichian, K., Karagiannidis, P., & Rimdusit, S. (2022). Ultrafine fully vulcanized natural rubber modified by graft-copolymerization with styrene and acrylonitrile monomers. *Bioresources and Bioprocessing*, *9*(1).
- [7] Nhan, N.T.; Dung, T.A.; Khanh, P.D.; Thuong, N.T.; Tung, N.H.; Nghia, P.T.; Thuy, T.T. (2016). Investigation of cure and mechanical properties of deproteinized natural rubber-g-poly methyl methacrylate. *Vietnam J. Chem.*, pp. 520–523.
- [8] Rimdusit, N., Jubsilp, C., Mora, P., Hemvichian, K., Thi, T. T., Karagiannidis, P., & Rimdusit, S. (2021). Radiation Graft-Copolymerization of ultrafine fully vulcanized powdered natural rubber: Effects of styrene and acrylonitrile contents on thermal stability. *Polymers*, *13*(19), 3447.
- [9] Patcharaporn, S. (2009). *Natural Rubber Toughened Polylactic acid* [Unpublished doctoral or master's thesis]. Suranaree University of Technology.
- [10] Lin, Y., Amornkitbamrung, L., Mora, P., Jubsilp, C., Hemvichian, K., Soottitantawat, A., Ekgasit, S., & Rimdusit, S. (2021). Effects of coagent functionalities on properties of ultrafine fully vulcanized powdered natural rubber prepared as toughening filler in rigid PVC. *Polymers*, *13*(2), 289.
- [11] Pisuttisap, A. (2011) Modified Natural Rubber Latex by Graft Copolymerization with Styrene and Diimide Hydrogenation. Master's Thesis, Chulalongkorn University.
- [12] Nguyễn, T. N., Duy, H. N., Anh, D. T., Thi, T. N., Van, N. N., Quang, T. T., & Huy, T. N. (2020). Improvement of Thermal and Mechanical Properties of Vietnam

- Deproteinized Natural Rubber via Graft Copolymerization with Methyl Methacrylate. *International Journal of Polymer Science*, 2020, 1–11.
- [13] Dung, T. A., Nàh, N. T. T., Thung, N. T., Nghia, P. T., Yamamoto, Y., Kosugi, K., Kawahara, S., & Thi, T. T. (2016). Modification of Vietnam Natural Rubber via Graft Copolymerization with Styrene. *Journal of the Brazilian Chemical Society*.
- [14] Wiroonpochit, P., Ultra, K., Jantawatchai, K., Hansupalak, N., & Chisti, Y. (2017). Sulfur-Free prevulcanization of natural rubber latex by ultraviolet irradiation in the presence of diacrylates. *Industrial & Engineering Chemistry Research*, 56(25), 7217–7223.
- [15] Flory, P.J.; Rehner (1943). *J. Statistical mechanics of cross-linked polymer networks I. Rubberlike elasticity*. *J. Chem. Phys.*, pp. 512–520.
- [16] Kochthongrasamee, T., Prasassarakich, P., & Kiatkamjornwong, S. (2006). Effects of redox initiator on graft copolymerization of methyl methacrylate onto natural rubber. *Journal of Applied Polymer Science*, 101(4), 2587–2601.
- [17] Chueangchayaphan, W., Tanrattanakul, V., Chueangchayaphan, N., Muangsap, S., & Borapak, W. (2017). Synthesis and thermal properties of natural rubber grafted with poly(2-hydroxyethyl acrylate). *Journal of Polymer Research*, 24(7).
- [18] Ramesh, M., Rajeshkumar, L., Srinivasan, N., Kumar, D. V., & Balaji, D. (2022). Influence of filler material on properties of fiber-reinforced polymer composites: A review. *E-polymers*, 22(1), 898–916.



## The Assessment of Greenhouse Gases for Lerdsin Hospital

Suthasinee Pengnarapat<sup>1,\*</sup>, Tanapat Sukthummawat<sup>2</sup> and Pattamaporn Surawongsin<sup>1</sup>

<sup>1</sup> Research and Technology Assessment Department, Lerdsin Hospital, Department of Medical Services, Bangkok, Thailand

<sup>2</sup> General Administration Department, Lerdsin Hospital, Department of Medical Services, Bangkok, Thailand  
E-mail: \*suthasineefon8@gmail.com

### Abstract

This research aimed to study an evaluation of greenhouse gases (GHG) emissions from activities of Lerdsin Hospital. The emissions were evaluated by calculating the carbon footprint as kilogram carbon dioxide equivalent (kgCO<sub>2e</sub>). The GHG emissions were divided into 3 categories based on activities of the hospital as follows: Scope 1 was comprised direct GHG emissions from sources that were owned or controlled by hospital such as stationary combustion, mobile combustion, refrigerants, CH<sub>4</sub> emission from septic tank & wastewater and LPG consumption. Scope 2 was composed of indirect GHG emissions from purchased electricity by hospital. Scope 3 was consisted of all other indirect emissions e.g., water supply, amount of paper used and municipal solid waste. The results of GHG emissions were evaluated using Thailand Greenhouse Gas Management Organization (TGO) from January to December 2023. It was revealed that the total GHG emission was 7,060,841 kgCO<sub>2e</sub>. Scope 1 had GHG emissions of 288,956 kgCO<sub>2e</sub> (providing to 4.09%). The use of electricity (Emission Scope 2) contributed most greenhouse gas emission which emitted 5,691,900 kgCO<sub>2e</sub> (accounting of 80.61%). Finally, the GHG emissions from Scope 3 were the second rank with the value of 1,079,984 kgCO<sub>2e</sub> which shared 15.3% of the total emission. The present result was in agreement with GHG emissions and share (%) in 2021 and 2022.

**Keywords:** Greenhouse Gases; Carbon Footprint for Organization; Global Warming; Climate Change

### 1. Introduction

Nowadays, all sectors in Thailand are beginning to realize more problems caused by greenhouse gases. One of the important organizations is the Thailand Greenhouse Gas Management Organization (Public Organization: TGO), which is an agency that supports assessment of greenhouse gas emission reduction and its impacts. Promote and develop potential as well as providing advice to government agencies and the private sector on greenhouse gas management. Including having a nationally recognized and reliable database for assessing greenhouse gas emissions in various industrial groups [1].

Climate change is posing threats to human health, for instance, through increased mortality in extreme weather events or by decreasing agricultural yields and rising sea levels, endangering human livelihoods. However, in the climate change discourse, health and the health sector have more nuanced roles than that. The health sector, including all organizations, institutions and resources devoted to producing health actions, will not only be impacted by climate change, but will also be key in adapting to climate change and to motivate climate-friendly behaviors. At the same time, the health sector is also a relevant contributor to rising levels of GHG emissions and thereby to climate change [2].

According to the Kyoto Protocol, the six greenhouse gases (GHG) are carbon dioxide (CO<sub>2</sub>), methane (CH<sub>4</sub>), nitrous oxide (N<sub>2</sub>O), hydrofluorocarbons (HFCs), perfluorocarbons (PFCs) and sulfur hexafluoride (SF<sub>6</sub>). Emissions of these six gases are taken into account for the calculation of the carbon footprint indicator of products, which counts the total emission of GHG in CO<sub>2</sub> equivalents (CO<sub>2</sub>e). Such emissions may be caused directly or indirectly by persons, organizations, events or products [3].

Greenhouse gases (GHG) emissions can be calculated by using the life cycle assessment (LCA), which is the international standard ISO 14040, 14044, used for the assessment of environmental impact throughout the life cycle. It can be calculated from the formula: CO<sub>2</sub> equivalent of each process = Amount of activity x CO<sub>2</sub> emission intensity. Total amount of every type of greenhouse gas from all activities, which were converted into units of carbon dioxide equivalents by multiply total emissions of each type of greenhouse gas with its global warming potential (GWP), is the Carbon Footprint of the organization [4].

This research aims to study an evaluation of GHG emissions from activities of Lerdsin Hospital. The emissions were evaluated by calculating the carbon footprint as kilogram carbon dioxide equivalent (kgCO<sub>2</sub>e). The emissions of GHG were divided into 3 categories based on activities of the hospital as follows: 1) Direct GHG emissions and removals from the hospital's activities (Scope 1), 2) Indirect GHG emissions from imported energy of the hospital (Scope 2), and 3) Indirect GHG emissions from other sources (Scope 3).

## 2. Materials and Methods

### 2.1. Setting Organization Boundaries

Lerdsin Hospital, 190 Si Lom, Silom, Bang Rak, Bangkok 10500, consists of three buildings as follows: Kanrchanapisek building, Promoting Services building, and Supporting Services building.

### 2.2. Setting Operational Boundaries

The GHG protocol was a well-established and widely used standard for GHG emissions reporting in many sectors, including the health sector. The GHG protocol distinguished three Scopes as follows:

- Scope 1 was comprised direct GHG emissions from sources that were owned or controlled by hospital such as stationary combustion, mobile combustion, refrigerants, CH<sub>4</sub> emission from septic tank & wastewater and LPG consumption.
- Scope 2 was composed of indirect GHG emissions from purchased electricity by hospital.
- Scope 3 was consisted of all other indirect emissions e.g., water supply, amount of paper used and municipal solid waste.

### 2.3. Data Inventory

The data were the collected relevant documents of both primary data (municipal solid waste occurred) and secondary data (electricity and water supply, quantity and quality of the wastewater, stationary combustion, mobile combustion and paper consumption).

## 2.4. Calculation of GHG Emission

GHGs can be calculated by multiplying with the emission factor, which is commonly used internationally, and in accordance with the guidelines of the Intergovernmental Panel on Climate Change (IPCC) or from a national database of each country, and so on. The example of emission factors that are used in the study are shown in Table 1. Therefore, the amount of GHG emissions from Lerdsin Hospital was calculated by Equation (1).

$$\text{GHG emissions} = \text{Activity data} \times \text{Emission factor} \quad (1)$$

Where GHG emissions = amount of greenhouse gases (kgCO<sub>2</sub>e)

Activity data = Activity data (value in liter/kg/kWh/m<sup>3</sup>)

Emission factor = greenhouse gas emission coefficient (kgCO<sub>2</sub>e/unit of activity data)

Table 1. GHG sources and emission factor [5].

GHG Sources	Unit	Emission Factor (kgCO <sub>2</sub> e)
Stationary Combustion		
-Diesel Oil of Generator & Fire Pump	liter	2.7078
Mobile Combustion		
-Diesel Oil	liter	2.7406
Refrigerants (R-32)	kg	677
CH <sub>4</sub> emission from septic tank	kgCH <sub>4</sub>	-
CH <sub>4</sub> emission from wastewater	kgCH <sub>4</sub>	-
LPG consumption	kg	3.1134
Electricity consumption	kWh	0.4999
Water supply	m <sup>3</sup>	0.7948
Amount of paper used	kg	2.1639
Municipal solid waste		
-Landfill	kg	0.7933
-Incineration	kg	2.3200
-Organic waste	kg	2.5300

## 3. Results and Discussion

Resource consumption and waste generated by Lerdsin hospital in the year 2021-2023 and the emission factors were used to calculate the amount of each greenhouse gas sources are presented in Table 2. Scope 1, Direct GHG emissions from hospital's activities were generated by stationary combustion, mobile combustion, refrigerants, CH<sub>4</sub> emission from septic tank & wastewater and LPG consumption. Scope 2, Indirect GHG emissions which arose from energy imports and the purchase of electricity. Scope 3 was consisted of the water supply, amount of paper used and municipal solid waste were calculated for indirect GHG emissions.

The movement of Lerdsin hospital's activities in 2023 was the main emission source category (5,691,900 kgCO<sub>2</sub>e of electricity), followed by the municipal solid waste with 821,205 kgCO<sub>2</sub>e. Amount of paper used, water supply and CH<sub>4</sub> emission from wastewater were 130,066 kgCO<sub>2</sub>e, 128,714 kgCO<sub>2</sub>e and 121,539 kgCO<sub>2</sub>e, respectively. Next LPG consumption, CH<sub>4</sub> emission from septic tank, mobile combustion and stationary combustion were 74,123 kgCO<sub>2</sub>e,

46,399 kgCO<sub>2</sub>e, 44,317 kgCO<sub>2</sub>e and 2,578 kgCO<sub>2</sub>e, respectively, while the share of refrigerants was limited to 0 kgCO<sub>2</sub>e. As a consequence, it was consistently with GHG emissions in 2021 and 2022.

Table 2. The amount of GHG emissions that result from the activities of Lerdsin Hospital.

GHG Sources	GHG emissions (kgCO <sub>2</sub> e)		
	2021	2022	2023
<b>Scope 1</b>			
Stationary Combustion	2,315	2,315	2,578
Mobile Combustion	56,220	41,573	44,317
Refrigerants	0	0	0
CH <sub>4</sub> emission from septic tank	44,415	45,932	46,399
CH <sub>4</sub> emission from wastewater	110,760	120,191	121,539
LPG consumption	69,939	65,755	74,123
<b>Scope 2</b>			
Electricity consumption	4,658,635	5,082,483	5,691,900
<b>Scope 3</b>			
Water Supply	124,036	125,907	128,714
Amount of paper used	134,099	130,233	130,066
Municipal solid waste	767,433	712,556	821,205

The Scope 1, 2 and 3 of GHG emissions and share (%) in 2021-2023 as shown in Table 3. The results of GHG emissions were evaluated using Thailand Greenhouse Gas Management Organization (TGO) from January to December 2023. It was revealed that the total GHG emission was 7,060,841 kgCO<sub>2</sub>e. Scope 1 had GHG emissions of 288,956 kgCO<sub>2</sub>e (providing to 4.09%). The use of electricity (Emission Scope 2) contributed most greenhouse gas emission which emitted 5,691,900 kgCO<sub>2</sub>e (accounting of 80.61%). Finally, the GHG emissions from Scope 3 were the second rank with the value of 1,079,984 kgCO<sub>2</sub>e which shared 15.3% of the total emission. The present result was in agreement with GHG emissions and share (%) in 2021 and 2022 were seen in Fig. 1.

Table 3. Scope 1, 2 and 3 of GHG emissions and share (%) in 2021-2023.

Category	GHG emissions (kgCO <sub>2</sub> e)					
	2021	Share (%)	2022	Share (%)	2023	Share (%)
Scope 1	283,650	4.75	275,765	4.36	288,956	4.09
Scope 2	4,658,635	78.06	5,082,483	80.33	5,691,900	80.61
Scope 3	1,025,568	17.18	968,696	15.31	1,079,984	15.30
Total	5,967,852	100.0	6,326,944	100.0	7,060,841	100.0

When compared to GHG emissions estimated using life cycle assessment principles. It was found that the values differ due to the limitations of the data in different parts, including the differences in the included sectors, completeness of information and data collection period.

It was found that the values of GHG emissions by both calculation methods were different due to the limitations of data in several parts. If more data of GHG emissions in other sectors had been added besides fuel combustion, i.e., evacuation fire drill, using of N<sub>2</sub>O anesthesia and CO<sub>2</sub> for Laparoscopic Surgery to be more consistent will make the study results come out similar

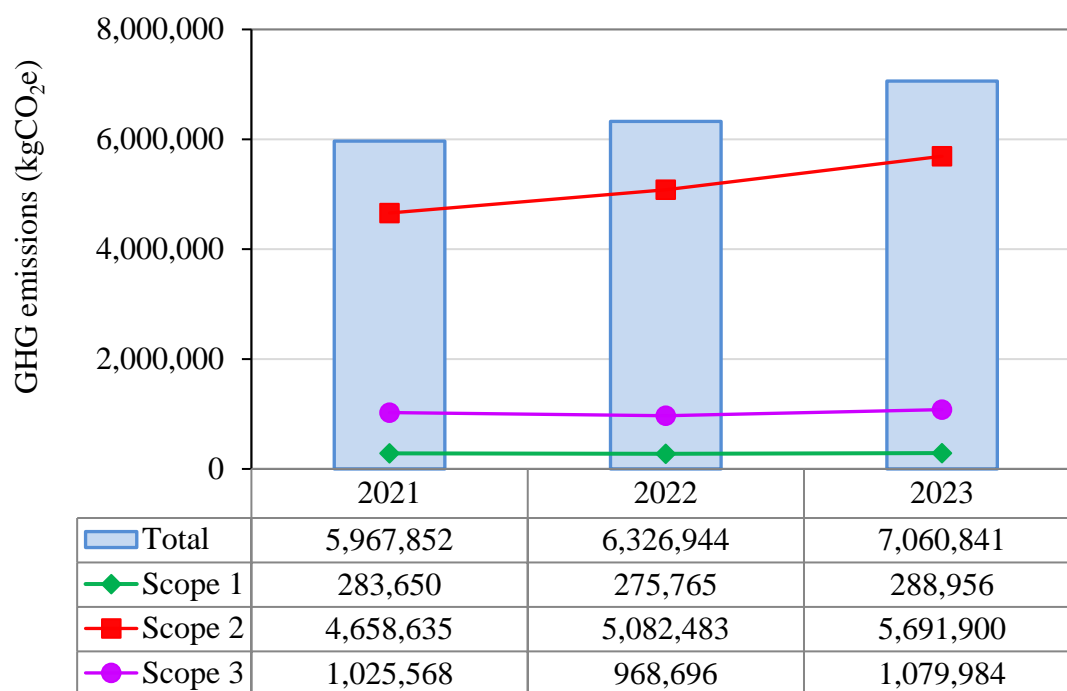


Fig. 1 Scope 1, 2 and 3 of GHG emissions and share (%) in 2021-2023.

The total of the GHG emissions 2021 to 2023 were 5,967,852 kgCO<sub>2</sub>e, 6,326,944 kgCO<sub>2</sub>e and 7,060,841 kgCO<sub>2</sub>e, respectively. It was revealed that significantly increased because Supporting Services building at Lerdsin Hospital was firstly opened in 2023.

The source of GHG emissions that had the highest emissions is electricity consumption, followed by the municipal solid waste. The source with the minimal release was refrigerants. Lerdsin Hospital, 190 Si Lom, Silom, Bang Rak, Bangkok 10500, consists of three buildings as follows: Kanrchanapisek building, Promoting Services building, and Supporting Services building.

It is a medical organization that has consumption of electricity, water supply, and waste from patient and medical staff, which have activities related to healthcare institution providing patient treatment the area of the hospital. The best-known type of hospital is the general hospital, which typically has an emergency department to treat urgent health problems ranging from fire and accident victims to a sudden illness. Moreover, the best-known type of hospital is the general hospital, which typically has an emergency department to treat urgent health problems ranging from fire and accident victims to a sudden illness that causes the amount of greenhouse gases from waste to increase as well.

#### 4. Conclusions

The GHG emissions were divided into 3 categories based on activities of the Lerdsin hospital as follows: Scope 1 was comprised direct GHG emissions from sources that were owned or controlled by hospital such as stationary combustion, mobile combustion, refrigerants, CH<sub>4</sub> emission from septic tank & wastewater and LPG consumption. Scope 2 was composed of indirect GHG emissions from purchased electricity by hospital. Scope 3 was consisted of all other indirect emissions e.g., water supply, amount of paper used and municipal solid waste. The results of GHG emissions were evaluated using Thailand Greenhouse Gas Management Organization (TGO) from January to December 2023. It was revealed that the total GHG emission was 7,060,841 kgCO<sub>2e</sub>. Scope 1 had GHG emissions of 288,956 kgCO<sub>2e</sub> (providing to 4.09%). The use of electricity (Emission Scope 2) contributed most greenhouse gas emission which emitted 5,691,900 kgCO<sub>2e</sub> (accounting of 80.61%). Finally, the GHG emissions from Scope 3 were the second rank with the value of 1,079,984 kgCO<sub>2e</sub> which shared 15.3% of the total emission. The present result was in agreement with GHG emissions and share (%) in 2021 and 2022.

#### 5. Acknowledgement

I would like to thank my deep gratitude to Prof. Dr. Tharapong Vitidsant, Department of Chemical Technology, Faculty of Science, Chulalongkorn University, for his great advice and support all the way through. My sincere appreciation also goes to Research and Technology Assessment, General Administration, Supplies and Maintenance Human Resources, Lerdsin Hospital, Department of Medical Services, Ministry of Health, and Greenhouse Gas Management Organization (TGO) Ministry of Energy, for all useful data.

#### References

- [1] Bozoudis, V., Sebos I., and Tsakanikas, A. (2022). Action plan for the mitigation of greenhouse gas emissions in the hospital-based health care of the Hellenic Army. *Environmental Monitoring and Assessment*, 194(221), 1-13.
- [2] Xiang, Z., Klaus A., Rosenthal, H., Rogowski, S., Wolf, H. (2022). Carbon footprinting for hospital care pathways based on routine diagnosis-related group (DRG) accounting data in Germany: an application to acute decompensated heart failure. *Journal of Industrial Ecology* 26(4), 1528-1542.
- [3] Keil, M. (2023). The greenhouse gas emissions of a German hospital - A case study of an easy-to-use approach based on financial data. *Cleaner Environmental Systems Cleaner Environmental Systems*, 11(100140). 1-9.
- [4] Karoonwattana, K., Phungrassami H., and Usubharatana P. (2023). Greenhouse Gas Emissions from Fossil Fuels Combustion for Paper Products in Thailand based on Input-Output Model. In *Proceedings of the 32nd Thai Institute of Chemical Engineering and Applied Chemistry Conference*, pp. 1-10. Nakhon Pathom, Thailand.
- [5] Thailand Greenhouse Gas Management Organization (Public Organization: TGO). (2022). EF CFP (Jul 2022). Available: [http://thaicarbonlabel.tgo.or.th/admin/uploadfiles/emission/ts\\_af09c20f4f.pdf](http://thaicarbonlabel.tgo.or.th/admin/uploadfiles/emission/ts_af09c20f4f.pdf) [Accessed: 15 November 2022]

## Rice Bran Wax as a Renewable Resource for Biolubricant Formulation

Phee Petchruarn, Kantharakorn Macharoen\*, and Jindarat Pimsamarn

Department of Chemical Engineering, Faculty of Engineering, King Mongkut's University of Technology Thonburi, 126 Pracha Uthit Rd., Bang Mod, Thung Khru, Bangkok, 10140, Thailand  
E-mail: kantharakorn.mac@kmutt.ac.th

### Abstract

Rice bran wax (RBW) is the major byproduct of rice bran oil production, which can be directly used in several applications such as cosmetics, personal care products, and pharmaceuticals. The wax esters in RBW, containing long-chain fatty acids and fatty alcohols, could be used in biolubricant preparation. In this study, a saponification reaction was initially performed by treating RBW with 30% potassium hydroxide in isopropanol to obtain fatty acid potassium salt. Subsequently, this salt was treated with 30% HCl to obtain fatty acids via a substitution reaction, while fatty alcohols from the initial reaction were discarded. Following this, the obtained crude fatty acids were treated with 5% methanol in the presence of sulfuric acid as a catalyst to produce crude fatty acid methyl esters (FAME). Fourier-transform infrared spectroscopy (FTIR) confirms the presence of fatty acids in the RBW and the crude fatty acids obtained after the saponification and substitution reactions. FTIR was also used to characterize the crude FAMEs. In the future, a transesterification process could be then performed using the crude FAME and trimethylolpropane (TMP) to obtain TMP-esters, which can be utilized as a biolubricant precursor.

**Keywords:** Biolubricant, Fatty acid methyl ester, Rice bran wax, Saponification, Transesterification

### 1. Introduction

The term lubricant means a substance used to facilitate movement between surfaces, widely used to reduce friction corrosion and improve the efficiency in the vehicle and a variety of machines. The lubricant is produced from mineral base oil and chemical additives to modify and enhance their tribology properties, which are petroleum-based chemicals containing paraffin, olefin, aromatic hydrocarbon, and other toxic chemicals [1,2], which can cause significant problems to the environment, such as toxicity, microbiology decontamination, and poor biodegradability [3]. Biolubricants can serve as renewable raw materials, which have the potential to make significant contributions to sustainable development [4], as they are biodegradable, environmentally friendly, and less toxic than petroleum-based lubricants. Many biomaterials have been used to synthesize biolubricant. For example, vegetable oil was found to be suitable for biolubricant production as it was 95% biodegradable and 30 – 50% faster degraded than petroleum-based lubricants [5]. Vegetable oil containing fatty acids plays an essential role in biolubricant synthesizing because they are biodegradable, low in ecotoxicity, and do not contribute to emissions of volatile organic compounds [6]. In addition, some chemical modifications, such as trimethylolpropane, can enhance the lubrication properties [7-9]. Rice bran oil constitutes one of the primary commodities in Thailand's export

portfolio due to the country's agricultural nature [10]. However, a byproduct known as rice bran wax (RBW) is generated during the winterization process, finding extensive utilization across the cosmetic, pharmaceutical, food, polymer, and leather industries. Scholarly research, as evidenced by numerous patents and publications, has explored RBW's application in various cosmetic formulations, including cold creams, pharmaceutical formulations, and hair-conditioning products [11]. The wax ester within RBW, comprising a fusion of long-chain fatty acids and fatty alcohols, holds promise for the potential synthesis of biolubricants. The objective of this study is to isolate and recover long-chain fatty acids from RBW and synthesize them into fatty acid methyl esters (FAMES), serving as a biolubricant precursor.

## 2. Methodology

### 2.1. Material

Cosmetic-grade rice bran wax (RBW SK-80) was obtained from Thai Edible Oil Co., Ltd. The RBW is the byproduct of rice bran oil production without using any solvent for extraction. The physical properties can be seen in Table 1. The majority content of RBW SK-80 is wax esters.

Table 1. Physical Property of RBW SK-80

Property	SK-80	Test method
Melting point (°C)	75-76	AOCS Cc 1-25
Color	Off-White	Visual
Oil content (%)	30-50	N/A
Wax content (%)	50-70	N/A

### 2.2. Saponification of RBW

In this step, RBW SK-80 of 20 grams was mixed with 25 mL of 30% KOH in isopropanol in a round flask. The mixture was refluxed for 4 hours, utilizing an oil bath heated to 100°C as the heat source [11]. After that, the isopropanol was removed through a rotary vacuum evaporator until the residue was dry. Subsequently, ethyl acetate of 50 mL was introduced to the dry residue, and the mixture was stirred using a magnetic stirrer at a temperature of 50°C for 2 hours. The resulting mixture was vacuum filtered with Whatman No.42 to separate fatty alcohols dissolving in the filtrate and to recover solid residue containing fatty acid potassium salt. To ensure the removal of any residual fatty alcohols from the solid residue, a washing step with ethyl acetate was performed. The collected filtrates were subsequently subjected to drying over anhydrous sodium sulfate. Following the filtration, the solid portion was acidified with 30 mL of 30% HCl for 1 hour at a temperature of 50°C. After acidification, 20 mL of distilled water is added to the acidified mixture to neutralized the pH of the mixture. Ethyl acetate of 20 mL was then added to extract fatty acids from the mixture thrice. The combined ethyl acetate extract was further washed with water until it had a neutral pH. The ethyl acetate layer was separated and dried over anhydrous sodium sulfate. Lastly, the crude fatty acids in the liquid



phase were recovered in a vacuum rotary evaporator. The saponification of RBW was performed for four batches, and the overall mass balance was determined and shown in Table 1.

### 2.3. Synthesis of fatty acid methyl ester (FAMES)

The obtained crude fatty acids from the previous section were reacted with methanol with sulfuric acid as a catalyst (methanolic sulfuric acid) via an esterification reaction to acquire FAMES. The amount of crude fatty acids and methanolic sulfuric acid was varied as shown in Table 2. After the reaction was complete, the mixture was vacuum filtered with Whatman No.42. The filtrate was then put into a 1000 mL separatory funnel and washed with deionized water. After that, the FAME was extracted from the mixture with 100 mL of isooctane thrice. The mixture of FAME and isooctane was then put into a centrifuge at 8,000 rpm at 25°C to remove small solid particles that are potentially the remaining wax ester and other waxy contaminants. The supernatant containing isooctane and FAME was transferred into a rotary vacuum evaporator to evaporate isooctane. Lastly, the crude FAMES were put in another centrifuge at 14,000 rpm at 25°C for 30 min to remove suspended particles. Finally, FAME was analyzed with gas chromatography with mass spectroscopy to inspect the composition and the impurities before proceeding to the following procedure.

### 2.4. Characterization of RBW, crude fatty acids, and crude FAMES

Fourier-transform infrared spectroscopy (FTIR; Nicolet 6700, Thermofisher, USA) was used to analyze the functional group of crude RBW SK-80 (CRBW), crude fatty acid, and crude FAME. Gas chromatography-mass spectrophotometry (GC-MS; 5977B GC/MSD, Agilent Technology, USA) equipped with a capillary column (MEGA-5HT 1.80  $\mu$ m, 30 m  $\times$  0.32 mm) was used to analyze crude FAMES to indicate the species of fatty acid in the RBW SK-80.

## 3. Results and discussion

### 3.1. Crude fatty acids from RBW

During the saponification of RBW, the mass balance of the experiment was recorded and shown in Table 2. The wax ester in RBW was estimated at 70% w/w corresponding to 14 g when 20 g of RBW was used.

Table 2. Mass of each component during the saponification of RBW.

Batch No.	RBW (g)	30%w/v KOH in IPA (mL)	Crude fatty acid potassium salt (g)	Crude fatty acid (g)
1	20	25	29.72	19.14
2	20	25	27.51	16.27
3	20	25	27.53	18.25
4	20	25	28.66	20.67

From Table 2, it could be said that the amount of crude fatty acid potassium salts and crude fatty acids are quite consistent among the four batches ranging from 27.5-29.7 g of crude fatty acid potassium salts and 16.3-20.7 g of crude fatty acids. By starting with 20 g of RBW, corresponding to roughly 14 g of wax esters, the amount of fatty acids obtained from the saponification of wax esters should be theoretically less than 14 g. Our result suggests that crude fatty acids are likely from the saponification of triglycerides in the RBW as well. In addition, the remnant of unreacted wax esters, fatty alcohols, and resinous matter might be responsible for the overestimated amount of crude fatty acids.

### 3.2. Crude FAMES from crude fatty acids

The crude fatty acids were prepared at 10, 20, 30, 40, and 50 g and were reacted with 5% v/v methanolic sulfuric acid with a ratio of 1 to 10 as seen in Table 3. The mixture was refluxed for 2 hours at 75°C, and methanol was then removed. The esterification reaction results in FAMES and H<sub>2</sub>O. As mentioned earlier, the crude fatty acids from RBW SK-80 contained some impurities that are carried to the esterification. In other words, crude FAMES still contain these impurities.

Table 3. Mass of each component during the esterification of crude fatty acids with methanolic sulfuric acid.

Crude fatty acids (g)	5%v/v MeOH-H <sub>2</sub> SO <sub>4</sub> (mL)	Crude FAMES (mL)	Crude FAMES (g)	H <sub>2</sub> O (mL)
10	100	14	12.6	3
20	200	22	19.8	5
30	300	32	28.8	9
40	400	41	36.9	7
50	500	60	54.0	13

From Table 3, assuming a FAME density of 0.9 g/cm<sup>3</sup> [12], it can be observed that the amount of crude FAMES is comparable to the initial mass of crude fatty acids used, possibly due to impurities carried over from the crude fatty acids to the crude FAMES. The amount of crude FAMES also increases as the reaction scale increases, as expected. The color of the crude FAMES in this study was dark brown (data not shown) compared with FAMES derived from vegetable oil from other studies [13], indicating that different sources of fatty acids could lead to different properties of FAMES.

### 3.3. FTIR analysis of RBW and fatty acids

Fourier-transform infrared spectroscopy (FTIR) was used to analyze the functional groups of crude (or untreated) RBW SK-80 and crude fatty acids. The presence of fatty acids and fatty alcohols in the RBW was confirmed as shown in Fig.1

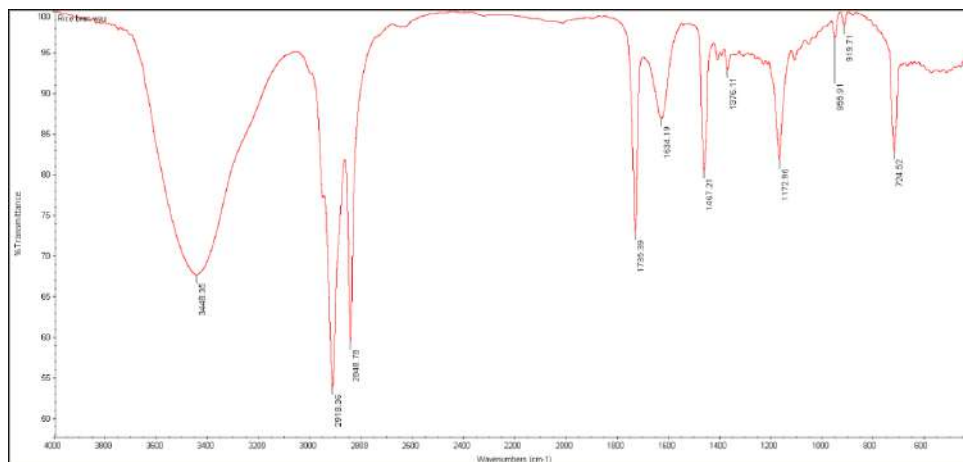


Fig. 1. FTIR spectrum of RBW SK-80.

From Fig. 1, the O-H stretch for carboxylic acids and alcohol appears broad and strong at  $3448.35\text{ cm}^{-1}$ . Peaks at  $2918.36\text{ cm}^{-1}$  and  $2848.78\text{ cm}^{-1}$  indicate the presence of methylene groups [14]. The peak at  $1735.39\text{ cm}^{-1}$  corresponds to C=O and could indicate the presence of aldehydes, ketones, ester groups, or carboxylic acids [15]. Additional peaks at  $1634.19$ ,  $1467.21$ , and  $1376.11\text{ cm}^{-1}$  suggest the presence of alkene, CH<sub>3</sub> group, and bending vibration of the CH<sub>3</sub> group, respectively [16]. The peak at  $1172.96\text{ cm}^{-1}$  is assigned to (C-O-C) stretching of saturated ester functionalities [17], while the peaks at  $955.91\text{ cm}^{-1}$  and  $919.71\text{ cm}^{-1}$  indicate O-H bending, and the peak at  $724.62\text{ cm}^{-1}$  is attributed to C-H bending.

After removing oil content (Defatted RBW) with hexane and isopropanol and other compounds, which were the short-chain free fatty acid and alcohol, polar lipid, triglycerides, and resinous matter with 10% NaBH<sub>4</sub> (Bleached RBW), each sample of rice bran wax was analyzed with FTIR to confirm that the undesired component was removed. The FTIR spectra of crude, defatted, and bleached RBW are shown in Fig. 2. From the comparison among the FTIR spectrum of crude, defatted, and bleached RBW, the spectra seem to be the same for all the RBW samples. The only difference that can be seen is that the spectrum was smoother after passing through the treatment process.

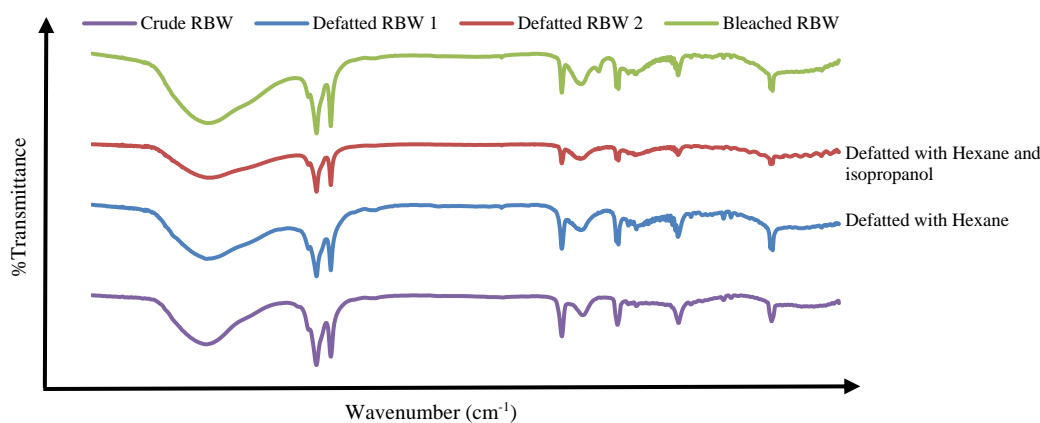


Fig.2 Comparison of FTIR spectrum of crude, defatted, and bleached RBW.

Figure 3 shows the FTIR spectrum of crude fatty acids. The peak of about 2915  $\text{cm}^{-1}$  shows the presence of C-H stretching, representing the unsaturated fatty acid content in the crude fatty acids, which were oleic and linoleic acid [18]. The peak at 1738.40  $\text{cm}^{-1}$  corresponds to C=O and could indicate the presence of aldehydes, ketones, ester groups, or carboxylic acids [16]. The peaks at 955.91  $\text{cm}^{-1}$  and 919.71  $\text{cm}^{-1}$  indicate O-H bending. With these three peaks, it can be identified the presence of fatty acid. Another minor peak is the footprint of the impurity contained in crude rice bran wax.

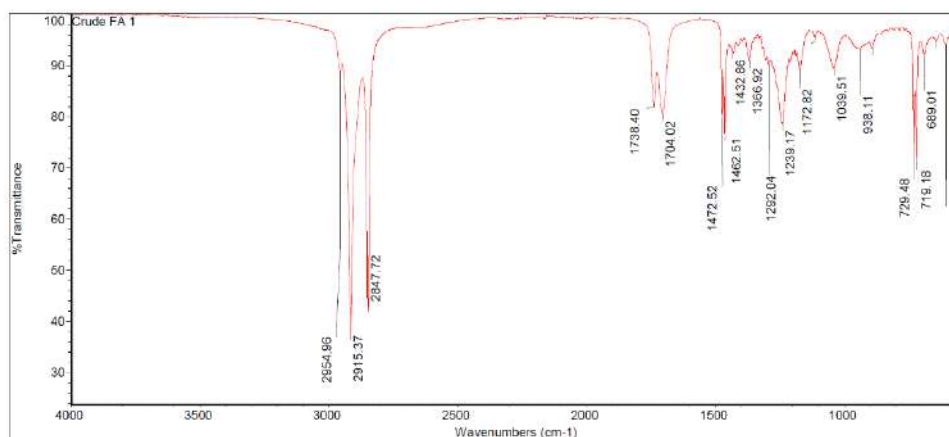


Fig. 3. FTIR spectrum of crude fatty acid from RBW saponification.

### 3.4. GC-MS analysis of crude FAMES

Crude FAMES derived from RBW were injected into the GC/MS system with the following conditions. The temperature of the column was set to 50°C, held for 3 min, then ramped to 300°C at 5°C/min and held for 3 min. The chromatogram is shown in Fig. 4.

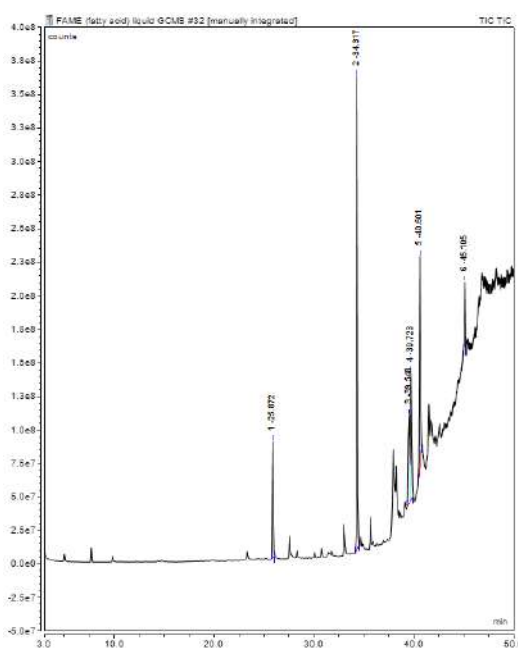


Fig. 4. The GC-MS chromatogram of crude FAME sample derived from RBW.

Figure 4 shows that six major peaks were found and matched with the mass spectroscopy library, and only one fatty acid species, palmitic acid ( $C_{16}H_{32}O_2$ ), was found at a retention time of 34.32 minutes. According to the certificate of analysis of the RBW from Thai Edible Oil, Co., Ltd., eight species of fatty acids were expected to be found, which were  $C_{16}$ ,  $C_{18}$ ,  $C_{18:1}$ ,  $C_{18:2}$ ,  $C_{20}$ ,  $C_{22}$ ,  $C_{24}$ , and  $C_{26}$ . It could be said that palmitic acid is the majority of fatty acid in the crude FAMES, while other fatty acids may be lost during the saponification and esterification steps.

#### 4. Conclusions

The extraction of crude fatty acid was accomplished through saponification of RBW SK-80 using potassium hydroxide, followed by a subsequent treatment to eliminate fatty alcohol. The crude fatty acid underwent methanolysis, resulting in the formation of crude FAMES, a biolubricant precursor. Lastly, the crude rice bran wax and fatty acid samples were subjected to FTIR analysis, while the crude FAME underwent analysis through GC-MS. The findings obtained from the FTIR analysis revealed the presence of fatty acids in the crude RBW, while the crude fatty acids were found to be devoid of fatty alcohols. However, upon examining the chromatogram of the FAME, only palmitic acid was observed in the sample. Improvement in each process is necessary to improve the quantity, quality, and purity of FAMES. The future work may focus on the synthesis of trimethylolpropane (TMP)-ester, a biolubricant, from FAME and TMP.

#### 5. Acknowledgment

This study was financially supported by the Research Strengthening Project of the Faculty of Engineering, King Mongkut's University of Technology Thonburi (KMUTT), and the crude rice bran wax was provided by Thai Edible Oil Co., Ltd. The characterization and analysis were carried out with the aid of chemical engineering laboratory staff at KMUTT. Phee Petchruam's tuition fee was partially supported by the Department of Chemical Engineering, KMUTT. The authors express their gratitude to the staff who provided valuable suggestions for this research.

#### References

- [1] Cecilia, J.A., Ballesteros Plata, D., Alves Saboya, R.M., Tavares de Luna, F.M., Cavalcante, C.L. and Rodríguez-Castellón, E., (2020), An Overview of the Biolubricant Production Process: Challenges and Future Perspectives, *Processes*, 8(3), 257.
- [2] Bart, C.J., Gucciardi, E., Cavallaro, S., (2013), Renewable lubricants, In Woodhead Publishing Series in Energy, Biolubricants, Woodhead Publishing, UK, 1-9.
- [3] Battersby, N.S., (2000), The biodegradability and microbial toxicity testing of lubricants – some recommendations, *Chemosphere*, 41(7), 1011-1027.
- [4] Salimon, J., Salih, N. and Yousif, E., (2012), Biolubricant Basestocks from Chemically Modified Ricinoleic Acid, *Journal of King Saud University - Science*, 24, 11-17.

- [5] Panchal, T.M., Patel, A., Chauhan, D.D., Thomas, M. and Patel, J.V., (2017), A Methodological Review on Bio-Lubricants from Vegetable Oil Based Resources", *Renewable and Sustainable Energy Reviews*, 70, 65-70.
- [6] Arbain, N. and Salimon, J., (2010), Synthesis And Characterization of Ester Trimethylolpropane Based Jatropha Curcas Oil as Biolubricant Base Stocks, *J Sci Technol.* 2, 47-58.
- [7] Jeevan, T.P. and Jayaram, S.R., (2018), Performance Evaluation of Jatropha and Pongamia Oil Based Environmentally Friendly Cutting Fluids for Turning Aa 6061, *Advances in Tribology*, 2018, 1-9.
- [8] Schneider, M.P., (2006), Plant-Oil-Based Lubricants and Hydraulic Fluids, *Journal of the Science of Food and Agriculture*, 86(2), 1769-1780.
- [9] Encinar, J.M., Nogales, S. and González, J.F., (2020), Biodiesel and Biolubricant Production from Different Vegetable Oils through Transesterification", *Engineering Reports*, 2(12).
- [10] F. T. Orthoefer, (2005), Rice bran oil, *Bailey's Industrial Oil and Fat Products*.
- [11] Vali, S.R., Ju, YH., Kaimal, TNB., (2005), A process for the preparation of food-grade rice bran wax and the determination of its composition, *J Amer Oil Chem Soc*, 82, 57-64
- [12] Dhandapani, S., and Thangavel, K., (2022), Fuel Properties of Fatty Acid Methyl Esters (FAME) Produced with Fats of Gamma - Irradiated Mutants of Oleaginous Microalga - *Chlorella sp. KM504965*, *Madras Agruc. J.*, 29-35.
- [13] Panchal, T.M., Patel, A., Chauhan, D.D., Thomas, M., and Patel, J.V., (2017), A Methodological Review on Bio-Lubricants from Vegetable Oil Based Resources, *Renewable and Sustainable Energy Reviews*, 70, 65-70.
- [14] Numthongkum, P., Aryusuk, K., Krisnangkura, K., (2009), The 6th KU-KPS Conference, Preparation of Fatty Acid Ethyl Ester from Crude Rice Bran Wax, 317-324.
- [15] Gomez, N. A., Abonia, R., Cadavid, H., and Vargas, I. H., (2011), Chemical and spectroscopic characterization of a vegetable oil used as dielectric coolant in distribution transformers, *Journal of the Brazilian Chemical Society*, 22(12), 2292-2303.
- [16] Silverstein, R.M, Webster, F.X, Kiemle, D.J, (2015), Spectrometri identification of organic compound, *JohnWiley & Sons*, 149-150
- [17] Ghazani, S. M., Marangoni, A. G., (2005), Healthy Fats and oils, *Encyclopedia of Food Grains*, 257-267.
- [18] Febri, N., and Juminaa, Dwi, S., Sholikhah, E., (2015), Reaction path synthesis of monoacylglycerol from fat and oils, *Int. J. Pharm. Sci*, 35, 126-136.

## **Influence of chitosan content on antibacterial property of chitosan/polyvinyl alcohol composites**

**Saranporn Kreerojanee<sup>1</sup>, Chompunuch Manee<sup>1</sup>, Jinnapat Patthasan<sup>1</sup>, Suchada chankongchuai<sup>1</sup>, Monthai Dankamon<sup>1</sup>, Chayanoot Kositanont<sup>2</sup>, Preeyawis Na Ubol<sup>2</sup>, Chalanan Pengsuk<sup>3</sup>, Weraporn Pivsa-Art<sup>1</sup>, Rinlada Sirisangsawang<sup>1</sup>, and Sasiradee Jantasee<sup>1,\*</sup>**

<sup>1</sup> Department of Chemical and Materials Engineering, Faculty of Engineering, Rajamangala University of Technology Thanyaburi, Pathum Thani 12110, Thailand

<sup>2</sup> National Metal and Materials Technology Center (MTEC), National Science and Technology Development Agency (NSTDA), Pathum Thani, 12120, Thailand

<sup>3</sup> Division of Biotechnology Technology and Agricultural Products, Faculty of Agricultural Product Innovation and Technology, Srinakharinwirot University, Ongkarak, Nakhon Nayok 26120, Thailand

\*E-mail: sasiradee\_j@rmutt.ac.th

### **Abstract**

In this study, the objectives were to determine the effects of chitosan concentration and the method of chitosan incorporation into PVA film on composite material properties. The results showed that, for chitosan/polyvinyl alcohol (PVA) composites, increasing the amount of chitosan decreased the transparency of the materials. Films were prepared using powdered chitosan and a chitosan solution. Films using chitosan powder exhibited clear agglomeration on the surface, whereas those using a chitosan solution showed a uniform distribution on the film surface, demonstrating an effective combination with the PVA solution. Additionally, various concentrations of chitosan solution and chitosan/PVA composite material were tested for antibacterial activity against *Escherichia coli* (*E. coli*) and *Staphylococcus aureus* (*S. aureus*). The results indicated that the chitosan solution exhibited antibacterial properties, with increased antibacterial activity as the chitosan concentration increased. However, when molded into a composite material, it was unable to resist bacteria.

**Keywords:** Chitosan; polyvinyl alcohol; composite materials; antibacterial.

### **1. Introduction**

Bacteria present on the skin and in the surrounding environment are often the culprits behind unpleasant odors. The proliferation of bacteria thrives in humid conditions (Natsch et al., 2006). To combat these undesirable scents, three main approaches have been employed: malodor-masking deodorants (Gautschi et al., 2007), malodor-neutralizing deodorants (Ballarin et al., 2015), and antimicrobial deodorants (Nakashima et al., 2001). Various substances are utilized to inhibit bacterial growth, each with distinct mechanisms of action.

Currently, there is a global effort to develop environmentally friendly polymer materials and biodegradable substances sourced from natural, renewable resources. This is driven by the adverse environmental impact of non-degradable polymer materials derived from petroleum

(F. Liu et al., 2023). Therefore, researchers are trying to create new functional biofilm materials with enhanced film-forming properties and strong antimicrobial properties. Polyvinyl alcohol (PVA) is a water-soluble polymer known for its biodegradability, film-forming ability, and tensile strength properties (Y. Liu et al., 2018). However, pure PVA film lacks antibacterial properties. To address this limitation, chitosan (CS) was selected to combine with PVA due to its antibacterial properties, and its hydroxyl and amine groups which enable the formation of hydrogen bonds with PVA. As a result, CS/PVA composite films have garnered significant attention for their excellent biodegradability and biocompatibility (Rafique et al., 2016). Chitosan, a straight-chain polysaccharide and the second most abundant biopolymer after cellulose, exhibits broad-spectrum antimicrobial properties and excellent biocompatibility (Anitha et al., 2014). Consequently, it presents an appealing option for combatting bacteria responsible for musty odors. For instance, Zhen Wang et al. demonstrated that customized antibacterial and environmentally friendly CS/PVA blended membranes exhibited high air filtration efficiency and antibacterial activity due to the successful blending of CS and PVA (Wang et al., 2018). Similarly, Suyoung Lee et al. found that chitosan particle size plays a significant role in antimicrobial activity against various fungi and bacteria, including both Gram-positive and Gram-negative strains (Lee et al., 2023)(Yanat et al., 2021). This suggests that chitosan particle size may contribute to its ability to combat odor-causing bacteria.

The objectives of this study were to explore the impact of chitosan content and the method of chitosan incorporation into PVA film preparation on antibacterial performance and the resulting properties. The aim is to gain insights that can guide the further development of antibacterial materials for film packaging applications.

## 2. Experimental

### 2.1 Materials

All chemicals in this work were commercially available. Chitosan from different sources were employed: chitosan A (powder form with low molecular weight, Deacetylation over 75%) from Sigma-Aldrich (Thailand) Co. Ltd., and chitosan B (powder form, Deacetylation 99%) obtained from Sisco Research Laboratories Pvt. Ltd and used as received. Additionally, acetic acid (Glacial) 99.8% was procured from M&P Impex Ltd.

### 2.2. Preparation of CS/PVA films using chitosan solution

The composite films were prepared by first weighing chitosan particles of 0.008, 0.28, and 0.42 g and then chitosan was added into 25 ml of a 2% v/v acetic acid solution and stirred at room temperature for 6 hours. PVA amounts of 1.14, 1.30, and 1.62 g were separately dissolved in acetic acid solution at 90 °C for 3 hours and cooled to room temperature. The chitosan and PVA solutions were mixed in equal volumes, ensuring homogeneity and removal of air bubbles. The resulting solution was poured into a glass petri dish and left at room temperature for 2 days until dry (Sukthawon et al., 2020). Subsequently, the film was peeled off and subjected to antibacterial testing.



## 2.3 Preparation of CS/PVA films using chitosan powder

Similarly, composite films were prepared by weighing chitosan particles of 0.008, 0.28, and 0.42 g. PVA pellets were dissolved in the acetic acid solution at 90 °C for 3 hours, followed by cooling to room temperature. Chitosan particles were mixed with the PVA solution at room temperature until homogeneity was achieved. After removing air bubbles, the mixture was poured into a glass Petri dish and left to dry for 2 days at room temperature. The resulting film was then peeled off and subjected to antibacterial testing.

## 2.4 Antimicrobial testing

Bacterial cultures were grown in nutrient broth and incubated at 37 °C for 18–24 hours to assess growth. A clear turbidity indicated bacterial growth. Subsequently, the starter culture was spread onto nutrient agar plates using the Swab Plate Technique. A hole was drilled into the agar, and the composite material was placed into it. The formation of a clear zone around the hole was observed, and the diameter of this zone was measured, indicating antibacterial activity (Selim et al., 2022).

## 3. Results and Discussion

### 3.1 Chitosan particle characteristics

In this research, two distinct sources of chitosan particles, labeled as chitosan A and chitosan B, were used. Utilizing a Particle Size Analyzer, an assessment of both particle sizes range was conducted. The results revealed that chitosan A exhibited an average particle size ranging from 102 to 186  $\mu\text{m}$ , while chitosan B displayed an average particle size ranging from 89 to 179  $\mu\text{m}$ , as depicted in Fig. 1. Notably, it was observed that the chitosan A appeared slightly larger particle size compared to chitosan B.

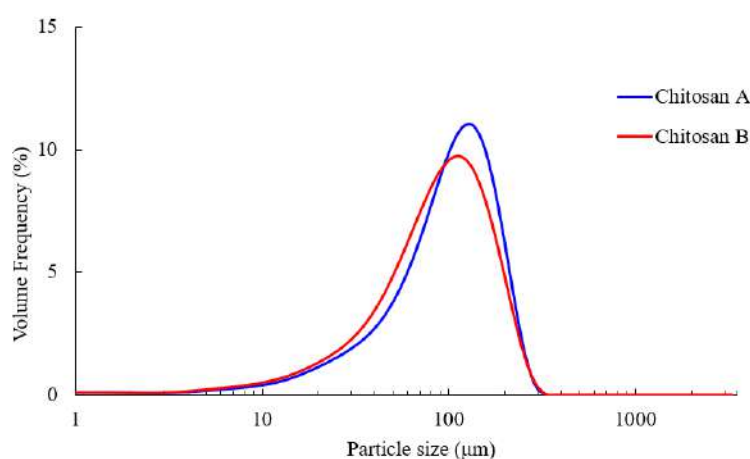


Fig. 1 Particle size distribution of chitosan particles.

Further examination of the morphology and distribution of these chitosan particles was performed using Scanning Electron Microscopy (SEM), as illustrated in Fig. 2. The SEM

images revealed the rugged surfaces of commercial-grade chitosan A and B. Both types of chitosan particles exhibited irregular shapes and non-uniform morphology.

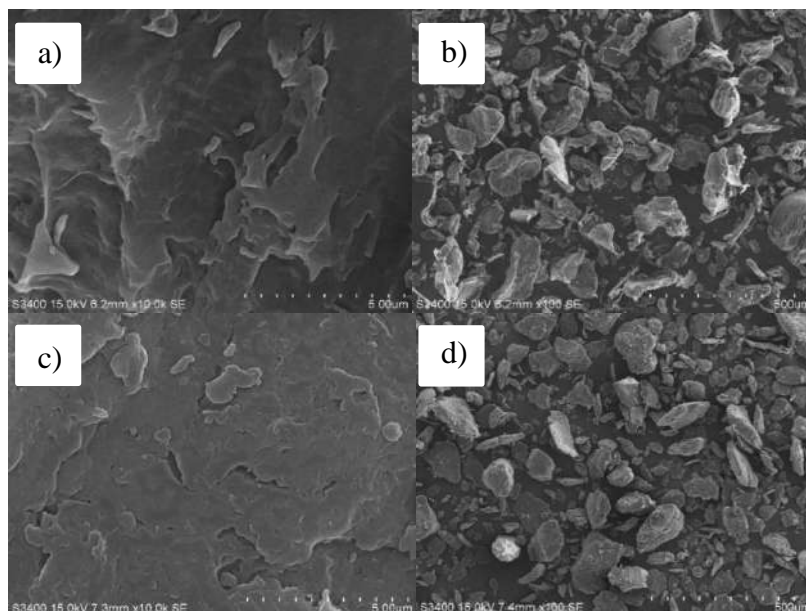


Fig. 2 SEM images of: (a, b) chitosan A, (c, d) chitosan B.

### 3.2 CS/PVA films characteristics

Table 1. Film thickness size.

Order	Film name	Thickness(mm)
1	A-0.008P	0.10
2	A-0.28P	0.11
3	A-0.42P	0.13
4	B-0.28P	0.09
5	A-0.28S	-
6	B-0.28S	-
7	pure PVA	0.12

Note \* – Digital thermoplastic vernier cannot be used for measurement.

– P, S = chitosan powder and chitosan solution

– A, B = chitosan particle size A and chitosan particle size B

The characteristics of CS/PVA films were assessed by measuring their thickness using a Vernier caliper. These molded films, comprising PVA and chitosan powder or chitosan solution, were found to possess similar dimensions, as they were fabricated using consistent solution volumes and petri dish sizes. Consequently, the thickness measurements fell within a comparable range of 0.9-0.12 mm (Table 1).

The transparency of the PVA film was apparent (see Fig. 3(g)). Films containing chitosan A in powder form and varying ratios of PVA exhibited distinct properties. When 0.008 g of

chitosan A was mixed with PVA, a uniform distribution was achieved, resulting in a transparent film akin to pure PVA (Fig. 3(a)). However, as the amount of chitosan A in solution increased, the films displayed a yellowish hue due to the dispersed chitosan particles throughout (Fig. 3(b) and 3(c)). Fig. 3(c) appeared notably more yellowish than Fig. 3(b) due to the higher chitosan concentration. Moreover, clumps were evident in areas of the film, attributed to chitosan particle agglomeration within the PVA solution, particularly pronounced at higher concentrations.

Comparatively, films prepared from chitosan A and B powder at a ratio of 0.28 g demonstrated distinct characteristics (Fig. 3(b) and 3(d)). Chitosan B exhibited poor homogeneity with PVA, resulting in clumps formation. This was attributed to its smaller particle size, leading to increased agglomeration in the PVA solution. Conversely, films utilizing chitosan A and B in solution form (Fig. 3(e) and 3(f)) exhibited a more uniform distribution of chitosan over the film surface, indicating effective integration with the PVA solution.

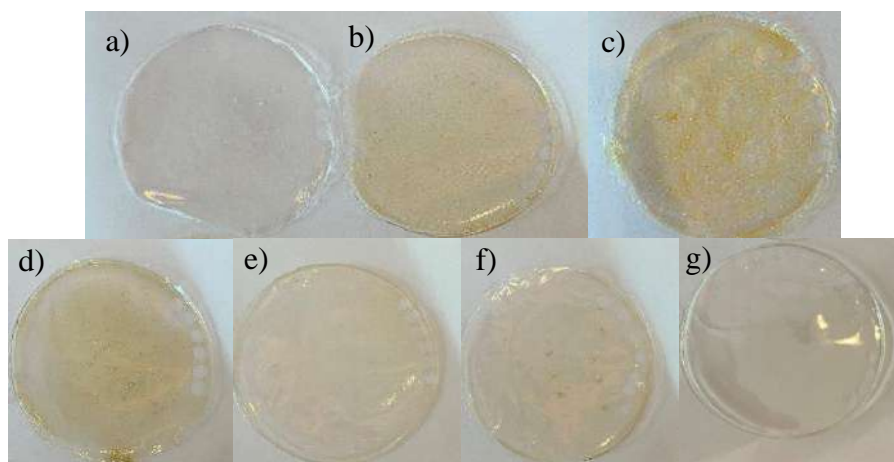


Fig. 3 The CS/PVA films: (a) A-0.008P, (b) A-0.28P, (c) A-0.42P, (d) B-0.28P, (e) A-0.28S, (f) B-0.28S, and (g) pure PVA.

### 3.3 Transparency of the films

The transparency of CS/PVA films was assessed through photographic analysis, as depicted in Fig. 4. It was observed that varying the chitosan content had a noticeable impact on the transparency of the resulting films. For instance, the film composed of PVA and 0.008 g of chitosan A powder (Fig. 4(a)) exhibited a clear, transparent appearance akin to pure PVA film (Fig. 4(g)). However, increasing the chitosan A powder content altered the color and transparency of the film (Fig. 4(a)-4(c)). Higher concentrations of chitosan powder resulted in a yellowish hue, corresponding to the color of the chitosan particles, and decreased transparency. However, the addition of chitosan in solution form (Fig. 4(e)-4(f)) had a lesser impact on film transparency compared to chitosan powder.

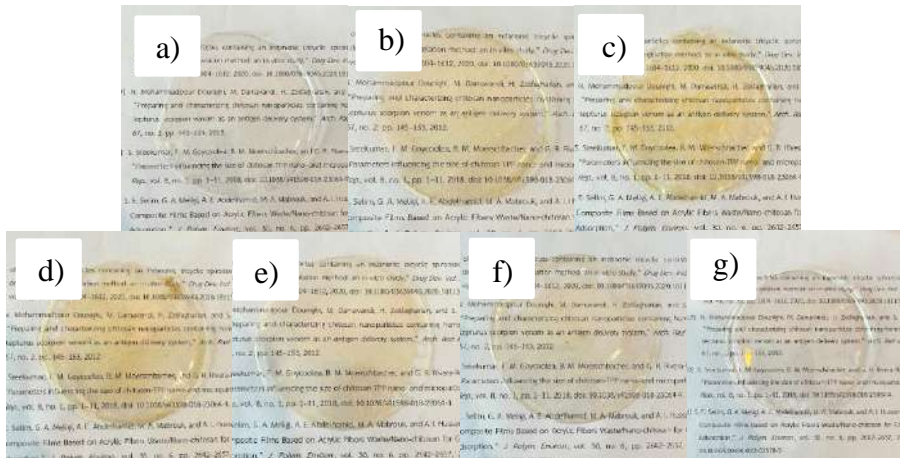


Fig. 4 Transparency test of the CS/PVA films: (a) A-0.008P, (b) A-0.28P, (c) A-0.42P, (d) B-0.28P, (e) A-0.28S, (f) B-0.28S, and (g) pure PVA.

### 3.4 Antimicrobial test

The antibacterial efficacy of chitosan solution was evaluated by testing its ability to inhibit two bacterial strains, *Escherichia coli* and *Staphylococcus aureus*, using varying concentrations of chitosan (0.008, 0.28, and 0.42 g) in acetic acid, as illustrated in Fig. 5. Against *Escherichia coli*, chitosan A solution at 0.42 g formed a clear zone of 1.4 cm, while chitosan B solution at the same concentration resulted in a clear zone of 1.6 cm. At 0.28 g, chitosan A solution formed a clear zone of 1.2 cm, and chitosan B solution produced a clear zone of 1.5 cm. Similarly, when tested against *Staphylococcus aureus*, chitosan A solution at 0.42 g resulted in a clear zone of 1.8 cm, and chitosan B solution produced a clear zone of 1.7 cm. At 0.28 g, chitosan A solution formed a clear zone of 1.5 cm, while chitosan B solution resulted in a clear zone of 1.3 cm. Notably, even at a concentration of 0.008, a clear zone was observed, although some bacteria remained within the cleared area. These results indicate that higher concentrations of chitosan are more effective in inhibiting bacterial growth, as evidenced by the formation of wider clear zones. Therefore, it can be inferred that the width of the clear zone correlates with the efficiency of bacterial inhibition (Yang et al., 2018).

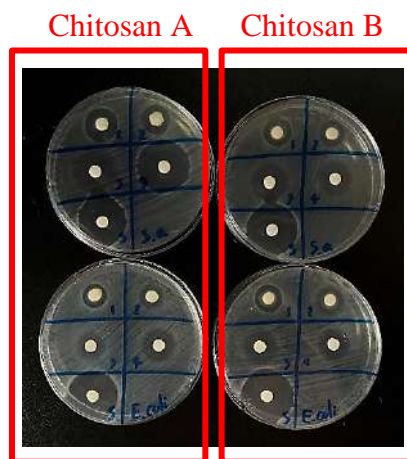


Fig. 5 Antibacterial activity of chitosan A and chitosan B solutions.

The antibacterial efficacy of CS/PVA films was assessed by testing their ability to inhibit two bacterial strains, *Escherichia coli* and *Staphylococcus aureus*. The results are presented in Fig. 6. Films were fabricated using powdered chitosan particles and PVA solution, as depicted in Fig. 6(a). However, no antibacterial activity was observed against either bacterial strain, indicated by the absence of a clear zone. Similarly, films fabricated from chitosan solution, shown in Fig. 6(b), displayed no antibacterial activity against *Escherichia coli* and *Staphylococcus aureus*, as evidenced by the absence of clear zones. Despite chitosan being inherently antibacterial, it did not leach from the film but remained well-contained within the film structure. Consequently, the outer surface of the film lacked antibacterial resistance. It can be concluded that neither type of film exhibited antibacterial properties under the tested conditions.

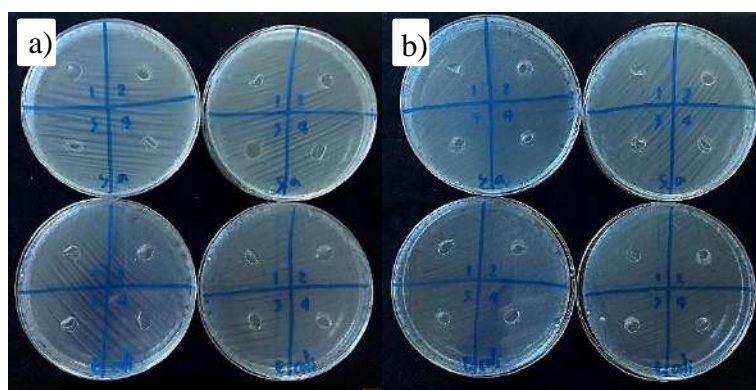


Fig. 6 Antibacterial activity of CS/PVA films: a) Chitosan powder, b) Chitosan solution.

#### 4. Conclusion

A composite film of chitosan/polyvinyl alcohol film was fabricated to explore the impact of chitosan content and the method of chitosan incorporation into PVA film on antibacterial efficacy. Antibacterial tests were conducted using chitosan solution against *Escherichia coli* and *Staphylococcus aureus*. Interestingly, clear zones were observed in every solution, indicating antibacterial activity. However, when examining films made with chitosan both in powder form and solution form, no clear zones were evident. Furthermore, the influence of chitosan concentration on composite material properties was investigated. Increasing chitosan content affected the homogeneity and transparency of CS/PVA composite.

#### References

- Anitha, A., Sowmya, S., Kumar, P. T. S., Deepthi, S., Chennazhi, K. P., Ehrlich, H., Tsurkan, M., & Jayakumar, R. (2014). Chitin and chitosan in selected biomedical applications. In *Progress in Polymer Science* (Vol. 39, Issue 9, pp. 1644–1667). Elsevier Ltd. doi: 10.1016/j.progpolymsci.2014.02.008

- Ballarin, B., Mignani, A., Mogavero, F., Gabbanini, S., & Morigi, M. (2015). Hybrid material based on ZnAl hydrotalcite and silver nanoparticles for deodorant formulation. *Applied Clay Science*, *114*, 303–308. doi: 10.1016/j.clay.2015.06.014
- Gautschi, M., Natsch, A., & Schröder, F. (2007). Biochemistry of human axilla malodor and chemistry of deodorant ingredients. *Chimia*, *61*(1–2), 27–32. doi: 10.2533/chimia.2007.27
- Lee, S., Hao, L. T., Park, J., Oh, D. X., & Hwang, D. S. (2023). Nanochitin and Nanochitosan: Chitin Nanostructure Engineering with Multiscale Properties for Biomedical and Environmental Applications. In *Advanced Materials* (Vol. 35, Issue 4). John Wiley and Sons Inc. doi: 10.1002/adma.202203325
- Liu, F., Zhang, X., Xiao, X., Duan, Q., Bai, H., Cao, Y., Zhang, Y., Alee, M., & Yu, L. (2023). Improved hydrophobicity, antibacterial and mechanical properties of polyvinyl alcohol/quaternary chitosan composite films for antibacterial packaging. *Carbohydrate Polymers*, *312*. doi: 10.1016/j.carbpol.2023.120755
- Liu, Y., Wang, S., & Lan, W. (2018). Fabrication of antibacterial chitosan-PVA blended film using electrospray technique for food packaging applications. *International Journal of Biological Macromolecules*, *107*(PartA), 848–854. doi: 10.1016/j.ijbiomac.2017.09.044
- Nakashima, T., & Matsuo, M. (2001). Relationship between Antimicrobial Activity and Deodorant Efficacy for Cotton Socks Treated with Metal. In *Biocontrol Science* (Vol. 6, Issue 1).
- Natsch, A., Derrer, S., Flachsmann, F., & Schmid, J. (2006). *A Broad Diversity of Volatile Carboxylic Acids, Released by a Bacterial Aminoacylase from Axilla Secretions, as Candidate Molecules for the Determination of Human-Body Odor Type.*
- Rafique, A., Mahmood Zia, K., Zuber, M., Tabasum, S., & Rehman, S. (2016). Chitosan functionalized poly(vinyl alcohol) for prospects biomedical and industrial applications: A review. In *International Journal of Biological Macromolecules* (Vol. 87, pp. 141–154). Elsevier B.V. doi: 10.1016/j.ijbiomac.2016.02.035
- Selim, S. E., Meligi, G. A., Abdelhamid, A. E., Mabrouk, M. A., & Hussain, A. I. (2022). Novel Composite Films Based on Acrylic Fibers Waste/ Nano- chitosan for Congo Red Adsorption. *Journal of Polymers and the Environment*, *30*( 6 ), 2642– 2657. doi: 10.1007/s10924-022-02378-5
- Sukthawon, C., Dittanet, P., Saeoui, P., Loykulnant, S., & Prapainainar, P. (2020). Electron beam irradiation crosslinked chitosan/ natural rubber - latex film: Preparation and characterization. *Radiation Physics and Chemistry*, *177*. doi: 10.1016/j.radphyschem.2020.109159

- Wang, Z., Yan, F., Pei, H., Li, J., Cui, Z., & He, B. (2018). Antibacterial and environmentally friendly chitosan/polyvinyl alcohol blend membranes for air filtration. *Carbohydrate Polymers*, *198*, 241–248. doi: 10.1016/j.carbpol.2018.06.090
- Yanat, M. , & Schroën, K. (2021). Preparation methods and applications of chitosan nanoparticles; with an outlook toward reinforcement of biodegradable packaging. *Reactive and Functional Polymers*, *161*. doi: 10.1016/j.reactfunctpolym.2021.104849
- Yang, S., Lei, P., Shan, Y., & Zhang, D. (2018). Preparation and characterization of antibacterial electrospun chitosan/ poly ( vinyl alcohol) / graphene oxide composite nanofibrous membrane. *Applied Surface Science*, *435*, 832–840. doi: 10.1016/j.apsusc.2017.11.191

## Conversion of furfuryl alcohol to butyl levulinate using alumina-supported tungsten catalysts

**Yanisa Saisema<sup>1</sup>, Saranporn Kreerojane<sup>1</sup>, Kritamate Prakrongjai<sup>1</sup>,  
Ratwachirawit Bunchom<sup>1</sup>, Pansatorn Titasiriratchata<sup>1</sup>,  
and Sasiradee Jantasee<sup>1,\*</sup>**

<sup>1</sup> Department of Chemical and Materials Engineering, Faculty of Engineering, Rajamangala University of Technology Thanyaburi, Pathum Thani 12110, Thailand  
\*E-mail: sasiradee\_j@rmutt.ac.th

### Abstract

Butyl levulinate (BL) is an attractive alternative as a biofuel additive. This research was studied conversion of furfuryl alcohol to butyl levulinate using an alumina-supported tungsten catalyst. The effect of different tungsten precursors, including ammonium metatungstate (ANW), phosphotungstic acid (PWA), silicotungstic acid (SWA), amount of tungsten and reaction time on furfuryl alcohol conversion and product yield were investigated. The catalysts were prepared by an incipient wetness impregnation, and they were tested in the reaction between furfuryl alcohol and butyl alcohol. The results from the reaction test showed that the catalyst with the best results was the SWA/Al<sub>2</sub>O<sub>3</sub> catalyst. It presented the highest furfuryl alcohol and BL yield. An increasing the amount of tungsten on the SWA/Al<sub>2</sub>O<sub>3</sub> catalyst from 10 to 30 wt% resulted in improving BL yield due to the large amount active site making it highly reactive. By changing the reaction time, it was found that the increase of reaction time from 3 to 6 hours can enhance BL yield. The appropriate conditions for converting furfuryl alcohol to butyl levulinate using the alumina-supported tungsten catalyst in this study were using 30 wt% of SWA on Al<sub>2</sub>O<sub>3</sub> catalyst, furfuryl alcohol to butyl alcohol ratio of 1:20 at 120°C for 6 hr.

**Keywords:** Furfuryl alcohol, butyl levulinate, tungsten, alumina

### 1. Introduction

The widespread use of petroleum fuels worldwide has led to a significant escalation in air pollutant emissions, stemming from fossil-based sources like gasoline and diesel. This poses substantial environmental and health concerns, exacerbated by the increasing demand for petroleum fuels amid dwindling fossil fuel reserves. Consequently, numerous countries are actively seeking alternatives to fossil energy, turning to renewable energy sources for sustainability. Biomass energy, as a renewable and environmentally benign energy source, has garnered significant attention in this pursuit of greener energy solutions. Leveraging biomass resources aligns with the principles of sustainable development and green economic growth, offering promising avenues for biofuel and biochemical production. For instance, cellulose and lignocellulose biomass can be directly converted into bioethanol or transformed into furfuryl alcohol, which can then be further processed into liquid ester compounds, such as butyl



levulinate, presenting an attractive alternative to conventional fuel additives like methyl butyl ether or MTBE (Zhou et al., 2022).

Reaction conditions and catalysts play pivotal roles in determining the yield of butyl levulinate. Numerous studies have explored various catalysts and reaction conditions to enhance butyl levulinate production under mild conditions. For example, Thuppati et al. investigated the conversion of furfuryl alcohol to butyl levulinate using tungsten state zirconia and a carbon sulfonate catalyst, achieving a high yield of 80% (Thuppati et al., 2021). Similarly, Rao et al. explored the conversion using zinc exchanged heteropoly tungstate supported on niobia catalysts, achieving an impressive yield of 94% (Rao et al., 2017). Additionally, Zhang et al. studied furfuryl alcohol conversion to butyl levulinate using solid catalysts composed of organic and inorganic acids, with yields reaching up to 93% (Zhang et al., 2011).

This study focuses on the production of butyl levulinate through the conversion of furfuryl alcohol and butanol using various tungsten-modified alumina catalyst. Alumina exhibits several advantageous properties, including high acidity, high surface area and high thermal stability. Three tungsten precursors including phosphotungstic acid, silicotungstic acid, and ammonium metatungstate, known for their superior catalytic properties and high acidity, was employed. These tungsten precursors catalysts are environmentally friendly and stable, qualifying them as green catalysts. Consequently, there is an intriguing prospect of modifying alumina with these catalysts.

## 2. Experimental

### 2.1 Chemicals

Furfuryl alcohol (98%) was purchased from Sigma-Aldrich. Alfa Aesar supplied reagent-grade tungstosilicic acid hydrate, ammonium metatungstate hydrate, 12-tungstophosphate hydrate, and gamma-phase aluminum oxide. 1-Butanol (analytical reagent grade) was obtained from Quality Reagent Chemical Product (QREC Asia). All reagents were used as received without further purification.

### 2.2 Catalyst preparation

Tungsten catalysts supported on alumina were prepared using the incipient wetness impregnation method. Gamma-alumina served as the supporting material. Each tungsten precursor was dissolved in deionized water to achieve the desired concentration. Subsequently, the solution was dropped to the alumina support and thoroughly grinded. After drying at 110°C for 24 hours, the catalysts were calcined at 500 °C for 3 hours, resulting in the formation of PWA/Al<sub>2</sub>O<sub>3</sub>, SWA/Al<sub>2</sub>O<sub>3</sub>, and ANW/Al<sub>2</sub>O<sub>3</sub> catalysts.

### 2.3 Characterizations of catalysts

The catalysts' properties were analyzed through various analytical techniques. The structure and crystal characteristics were examined using an X-ray Diffractometer (XRD) on Bruker AXS Model D8 Discover with CuK<sub>α</sub> radiation from 20°-80°. The morphology of the catalysts and the distribution of tungsten on the catalyst surface were analyzed using a Scanning Electron Microscope with Energy Dispersive X-Ray Analysis (SEM-EDX). The JEOL mode JSM-6400 SEM was used. The programme Link Isis series 300 was applied for the EDX. Additionally, the acidity of the catalyst was determined using the potentiometric titration method.

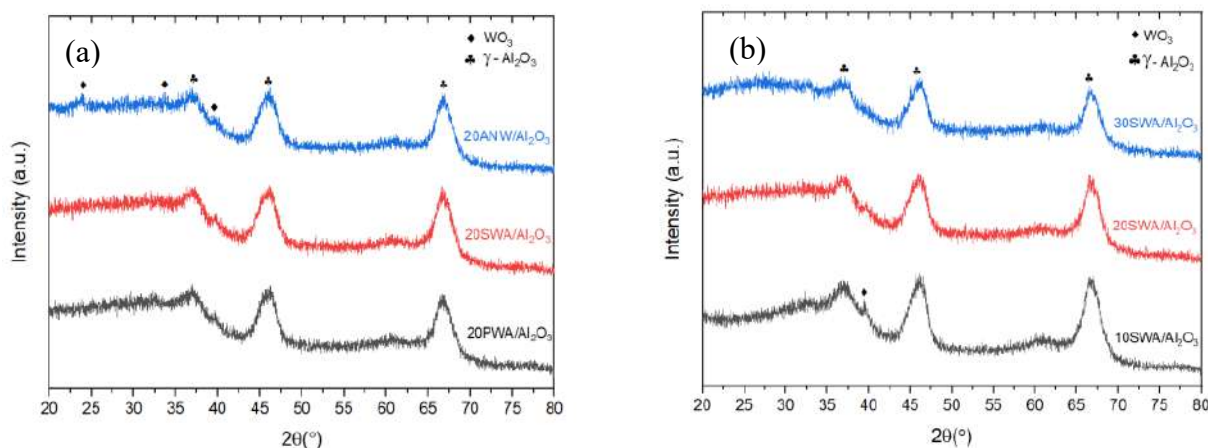
## 2.4 Reaction Test

The catalytic activity of alumina-supported tungsten catalysts was examined through the alcoholysis of furfuryl alcohol and n-butanol. The catalyst and reactants were introduced into a reactor, after which the air inside the reactor was evacuated and replaced with nitrogen to reach a pressure of 1 bar. The reactor was then heated to 120 °C and maintained at this temperature for varying durations. Following the reaction, the reactor was rapidly cooled in a cooling bath, and the catalyst was separated from the solution. Gas chromatograph with flame ionization detector (GC-FID) and DB-5 capillary column was employed at a detector temperature of 250 °C to determine the concentrations of remaining reactants and occurring products. These concentrations were used to calculate the conversion and selectivity of the reaction.

## 3. Result and discussion

### 3.1 Catalysts characteristics

XRD analysis was conducted to examine the crystallinity of the alumina-supported tungsten catalysts. In Fig. 1(a)-1(b), peaks corresponding to Al<sub>2</sub>O<sub>3</sub> were observed in all catalysts at 37°, 45°, and 66° (Samruddhi et al., 2022). WO<sub>3</sub> peaks were only detected in the ANW/Al<sub>2</sub>O<sub>3</sub> catalyst, presenting as minor peaks at 23°, 33°, and 39° (Mengesha et al., 2020). The absence of WO<sub>3</sub> peaks in the SWA/Al<sub>2</sub>O<sub>3</sub> and PWA/Al<sub>2</sub>O<sub>3</sub> catalysts suggests that tungsten oxide was well dispersed on the Al<sub>2</sub>O<sub>3</sub> support. Despite the increased tungsten content to 30 wt% in the SWA/Al<sub>2</sub>O<sub>3</sub> catalyst, WO<sub>3</sub> peaks remained absent.



**Fig. 1** XRD patterns of alumina-supported tungsten catalysts: a) with different tungsten precursors, b) with different amount of SWA.

The SEM technique was employed to analyze the morphology and distribution of various tungsten precursor types on the Al<sub>2</sub>O<sub>3</sub> support. As depicted in Fig. 2, the particle sizes of the catalysts were relatively uniform and irregular shape, ranging from 50 to 95 μm across all catalysts due to the utilization of the same alumina support. Moreover, the SEM images displayed a similar rough surface texture. The elemental composition of the catalyst, featuring different types of tungsten precursors on an alumina support, was analyzed using the EDX technique. The analysis depicted the presence of oxygen (O), alumina (Al), and tungsten (W), as illustrated in Fig. 3. Each element was visually represented by green, red, and blue dots, respectively. Tungsten exhibited a uniform distribution on the alumina surface.

Among the different tungsten precursors, 20% SWA/ $\text{Al}_2\text{O}_3$  appeared to possess the highest density of tungsten on the surface compared to 20% PWA/ $\text{Al}_2\text{O}_3$  and 20%ANW/ $\text{Al}_2\text{O}_3$ , while 20%ANW/ $\text{Al}_2\text{O}_3$  exhibited the lowest density of tungsten on the surface. Furthermore, the surface composition of tungsten in 30% SWA/ $\text{Al}_2\text{O}_3$  had a higher amount compared to 20% SWA/ $\text{Al}_2\text{O}_3$ .

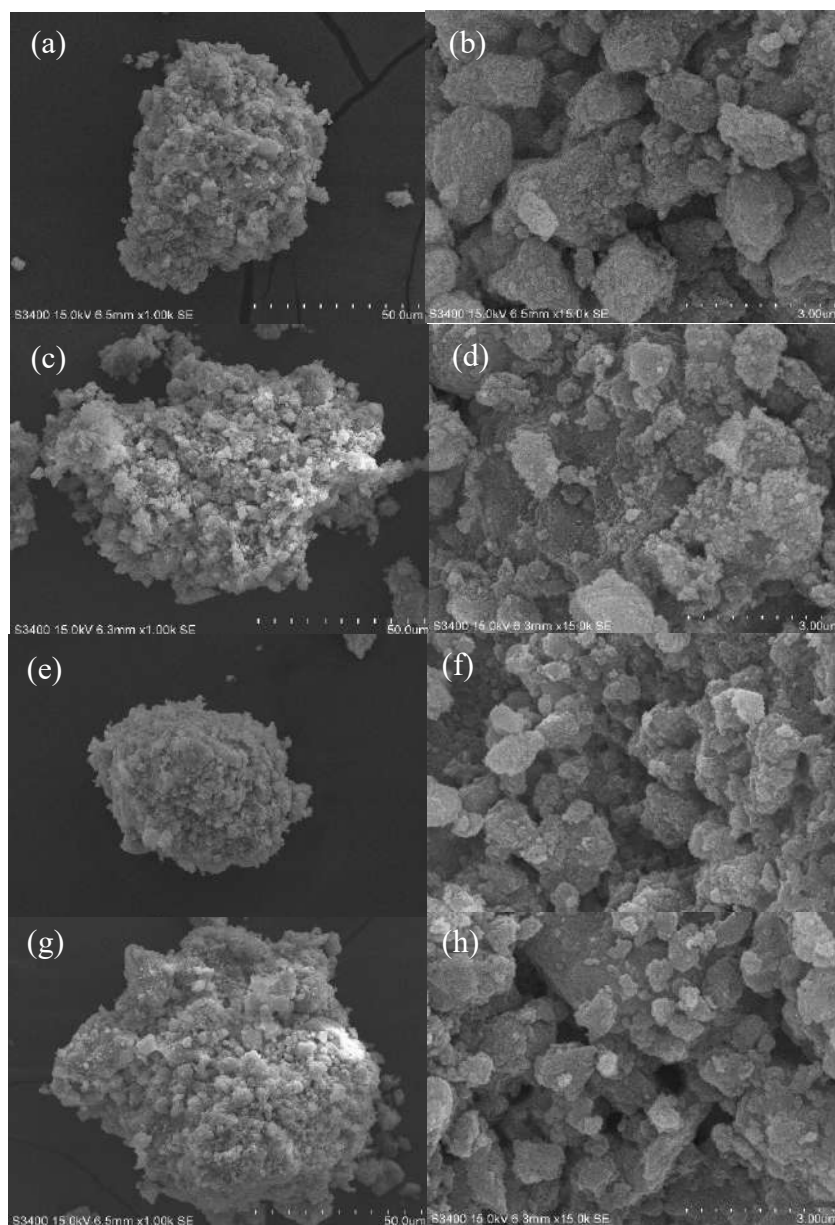


Fig. 2 SEM images of the catalysts: (a, b) 20%ANW/ $\text{Al}_2\text{O}_3$ , (c, d) 20%PWA/ $\text{Al}_2\text{O}_3$ , (e, f) 20%SWA/ $\text{Al}_2\text{O}_3$ , (g, h) 30%SWA/ $\text{Al}_2\text{O}_3$ .

Based on Fig. 4, the acidity was evaluated by the back titration (Rao et al., 2006). From the initial electric potential readings, it was observed that the 20%SWA/ $\text{Al}_2\text{O}_3$  exhibited the highest acidity at 87.4 mV, followed by 20%PWA/ $\text{Al}_2\text{O}_3$  at 85.1 mV, and 20%ANW/ $\text{Al}_2\text{O}_3$  showed the lowest acidity strength at 80.2 mV. All three catalysts displayed electric potentials within the strong site range (Rao et al., 2006). Further analysis of the acidity levels revealed that 20%SWA/ $\text{Al}_2\text{O}_3$  demonstrated the highest acidity amount, indicated by the length of the

curve before reaching equilibrium. A longer curve suggests the utilization of more base, hence indicating higher acidity. Consequently, 20%PWA/ $\text{Al}_2\text{O}_3$  displayed the next highest acidity level, while 20%ANW/ $\text{Al}_2\text{O}_3$  exhibited the lowest acidity content.

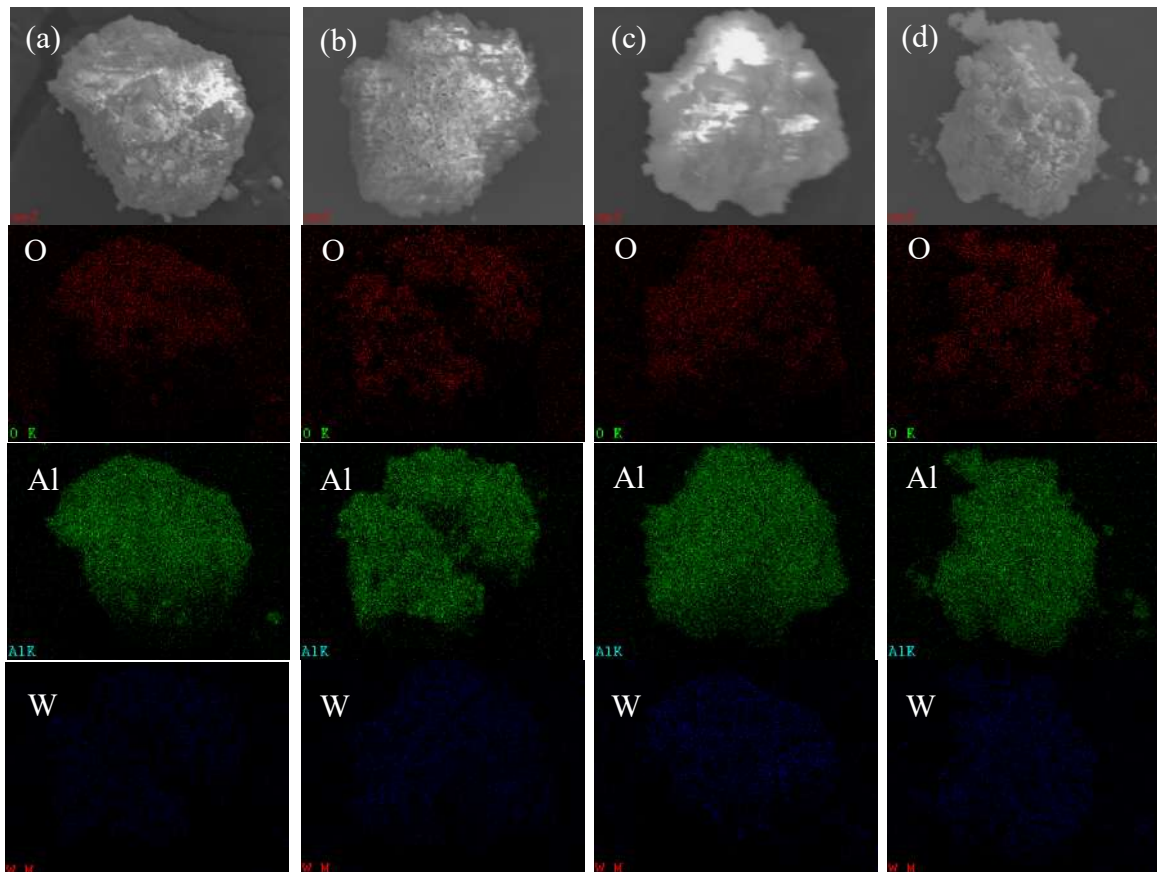


Fig. 3 EDX mappings of the catalysts: (a) 20%ANW/ $\text{Al}_2\text{O}_3$ , (b) 20%PWA/ $\text{Al}_2\text{O}_3$ , (c) 20%SWA/ $\text{Al}_2\text{O}_3$ , (d) 30%SWA/ $\text{Al}_2\text{O}_3$

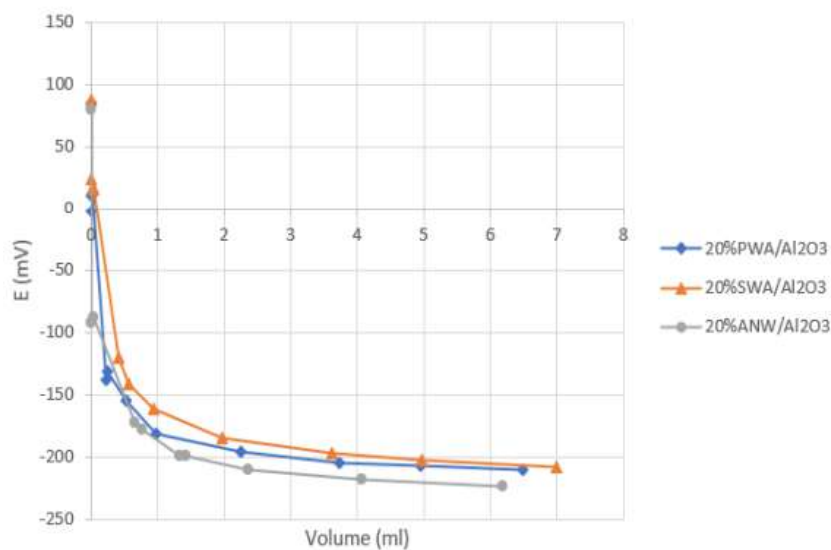


Fig. 4 Relationship between the electric potential value and the amount of base.

### 3.2 Reaction test

Table 1 displays the furfuryl alcohol conversion, product selectivity, and yield, presenting the impact of various tungsten precursors on alumina supports. Among the different tungsten precursor types, the 20% SWA/ SWA/Al<sub>2</sub>O<sub>3</sub> catalyst demonstrated the highest furfuryl alcohol conversion and butyl levulinate yield, consistent with the acidity analysis findings. This underscores the pivotal role of acidity in catalyst performance, facilitating rapid reaction rates (Mohammadbagheri et al., 2018) and thereby influencing furfuryl alcohol conversion and butyl levulinate yield during product formation. Additionally, an increase in tungsten content on the alumina support correlated with higher furfuryl alcohol conversion (Siva Sankar et al., 2017). For instance, the 30%SWA/Al<sub>2</sub>O<sub>3</sub> catalyst achieved a furfuryl alcohol conversion of 73.7% in 1 hour and 77.8% in 3 hours, with the highest butyl levulinate yield of 88.7% observed after 6 hours of reaction time. However, despite the high yield, the selectivity of butyl levulinate remained low, with 2-butyl furan exhibiting the highest selectivity among all catalysts used. Examining the effect of tungsten precursor amount on Al<sub>2</sub>O<sub>3</sub>-supported reactions revealed that a tungsten content exceeding 10 wt% is necessary for butyl levulinate production through furfuryl alcohol conversion using the SWA/Al<sub>2</sub>O<sub>3</sub> catalyst. It can conclude that the 30% SWA/Al<sub>2</sub>O<sub>3</sub> catalyst exhibited superior reactivity in this study, resulting in the highest conversion and butyl levulinate selectivity.

Table 1 Catalytic performance of the catalysts.

Catalysts	Time (hr)	FA Conversion (%)	% Selectivity			% Yield		
			2-Butyl Furan	Butyl Levulinate	Others	2-Butyl Furan	Butyl Levulinate	Others
20%ANW/Al <sub>2</sub> O <sub>3</sub>	3	22.6	71.3	20.7	8.0	16.1	4.7	1.8
20% PWA/Al <sub>2</sub> O <sub>3</sub>	3	50.6	100	0.0	0.0	50.7	0.0	0.0
20% SWA/Al <sub>2</sub> O <sub>3</sub>	3	57.4	82.0	18.0	0.0	47.1	10.3	0.0
10% SWA/Al <sub>2</sub> O <sub>3</sub>	3	26.3	100	0.0	0.0	26.3	0.0	0.0
30% SWA/Al <sub>2</sub> O <sub>3</sub>	3	77.8	67.9	17.5	14.6	52.8	13.6	11.4
30% SWA/Al <sub>2</sub> O <sub>3</sub>	1	73.7	73.7	13.5	12.9	54.3	9.9	9.5
30% SWA/Al <sub>2</sub> O <sub>3</sub>	6	88.7	73.7	19.4	7.2	65.1	17.2	6.4

### 4. Conclusion

This study focused on the conversion of furfuryl alcohol to butyl levulinate utilizing an alumina-supported tungsten catalyst. Various tungsten precursors, including ANW, PWA, and SWA, along with different amounts of tungsten and reaction times, were investigated to assess their impact on furfuryl alcohol conversion and product yield. The SWA/Al<sub>2</sub>O<sub>3</sub> emerges as a particularly suitable catalyst for converting furfuryl alcohol to butyl levulinate. Further investigation into the impact of tungsten precursor quantity on alumina support during the reaction revealed promising results with increased SWA content. A tungsten content in the SWA/Al<sub>2</sub>O<sub>3</sub> exceeding 10wt% is necessary to achieve significant butyl levulinate production. Prolonged reaction times, particularly observed with 30%SWA/Al<sub>2</sub>O<sub>3</sub> at 6 hours, yielded highest conversion and product selectivity.

### Acknowledgement

The financial supports from Thailand Science Research and Innovation (TSRI) managed by Rajamangala University of Technology Thanyaburi (FRB66E0708E.3). The National Research Council of Thailand (NRCT) are also gratefully acknowledged.

### References

- Mengesha, G. A., Chu, J. P., Lou, B. S., & Lee, J. W. (2020). Corrosion performance of plasma electrolytic oxidation grown oxide coating on pure aluminum: effect of borax concentration. *Journal of Materials Research and Technology*, 9(4), 8766–8779. doi: 10.1016/j.jmrt.2020.06.020
- Mohammadbagheri, Z., & Najafi Chermahini, A. (2018). KCC-1/Pr-SO<sub>3</sub>H as an efficient heterogeneous catalyst for production of n-butyl levulinate from furfuryl alcohol. *Journal of Industrial and Engineering Chemistry*, 62, 401–408. doi: 10.1016/j.jiec.2018.01.020
- Rao, B. S., Kumari, P. K., Dhanalakshmi, D., & Lingaiah, N. (2017). Selective conversion of furfuryl alcohol into butyl levulinate over zinc exchanged heteropoly tungstate supported on niobia catalysts. *Molecular Catalysis*, 427, 80–86. doi: 10.1016/j.molcata.2016.11.032
- Rao, K. N., Reddy, K. M., Lingaiah, N., Suryanarayana, I., & Prasad, P. S. S. (2006). Structure and reactivity of zirconium oxide-supported ammonium salt of 12-molybdophosphoric acid catalysts. *Applied Catalysis A: General*, 300( 2) , 139– 146. doi: 10.1016/j.apcata.2005.10.051
- Samruddhi, M., Bhatkar, A., Prabu, M., Mekala, S. P., Gogoi, P., Mohapatra, G., & Thirumalaiswamy, R. (2022). Selective O-alkylation of Phenol Using Dimethyl Ether. *Reactions*, 3(4), 602–614. doi: 10.3390/reactions3040040
- Siva Sankar, E., Saidulu Reddy, K., Jyothi, Y., David Raju, B., & Rama Rao, K. S. (2017). Alcoholysis of Furfuryl Alcohol into n- Butyl Levulinate Over SBA-16 Supported Heteropoly Acid Catalyst. *Catalysis Letters*, 147(11), 2807–2816. doi: 10.1007/s10562-017-2155-9
- Thuppati, U. R., Choi, C., Machida, H., & Norinaga, K. (2021). A comprehensive study on butanolysis of furfuryl alcohol to butyl levulinate using tungstated zirconia and sulfonated carbon catalysts. *Carbon Resources Conversion*, 4, 111– 121. doi: 10.1016/j.crcon.2021.03.003
- Tiwari, M. S., Dicks, J. S., Keogh, J., Ranade, V. V., & Manyar, H. G. (2020). Direct conversion of furfuryl alcohol to butyl levulinate using tin exchanged tungstophosphoric acid catalysts. *Molecular Catalysis*, 488. doi: 10.1016/j.mcat.2020.110918
- Zhang, Z., Dong, K., & Zhao, Z. (2011). Efficient conversion of furfuryl alcohol into alkyl levulinates catalyzed by an organic-inorganic hybrid solid acid catalyst. *ChemSusChem*, 4(1), 112–118. doi: 10.1002/cssc.201000231



The 33<sup>rd</sup> Thai Institute of Chemical Engineering and Applied Chemistry  
International Conference TIChE2024, Phra Nakhon Si Ayutthaya, Thailand,  
March 7-8, 2024



Zhou, S., Lai, J., Liu, X., Huang, G., You, G., Xu, Q., & Yin, D. (2022). Selective conversion of biomass-derived furfuryl alcohol into n-butyl levulinate over sulfonic acid functionalized TiO<sub>2</sub> nanotubes. *Green Energy and Environment*, 7(2) , 257– 265. doi: 10.1016/j.gee.2020.09.009

## The Development of Metal/Carbon Quantum Dots/Cellulose Nanocomposites for Glucose Sensing by Fluorimetric and Colorimetric Detection

Nichapat Juntree<sup>1,#</sup>, Athapon Srifa<sup>1</sup>, Pattaraporn Posoknistakul<sup>1</sup>  
Pisut Pongchaikul<sup>2</sup>, Pariyapat Arjfuk<sup>2</sup>, Wanwitoo Wanmolee<sup>3</sup>,  
Pongtanawat Khemthong<sup>3</sup>, and Chularat Sakdaronnarong<sup>1,\*</sup>

<sup>1</sup> Department of Chemical Engineering, Faculty of Engineering, Mahidol University, Nakhon Pathom, 73170, Thailand

<sup>2</sup> Chakri Naruebodindra Medical Institute, Faculty of Medicine Ramathibodi Hospital, Mahidol University, Samut Prakarn, 10540 Thailand

<sup>3</sup> National Nanotechnology Center (NANOTEC), National Science and Technology Development Agency (NSTDA), Pathum Thani 12120, Thailand

E-mail: # nichapat.jut@student.mahidol.edu, \* chularat.sak@mahidol.ac.th (Corresponding author)

### Abstract

Diabetes is concerned as one of the principal chronic diseases which is indicated by the high glucose level in human blood stream. In clinical diagnosis, high glucose concentration in blood can cause fast coagulation, while intensive biomolecule components lead to analytical problems. Therefore, noninvasive and accurate glucose detection is preferred. In this work, synthesis of carbon quantum dots using lignin as a carbon source (LCDs) via a simple and eco-friendly hydrothermal method in an aqueous solution was developed. The influence of mono- and bi-metallic dopants (Pt and Ru) onto LCDs structure on enhanced catalytic activity for low glucose concentration detection was investigated. The results exhibited that PtRu/LCDs-water was the best nanozyme that showed best performance on catalyzing H<sub>2</sub>O<sub>2</sub> dissociation and thus promisingly facilitated both colorimetric and fluorimetric glucose detection with high accuracy. Successful colorimetric glucose detection using PtRu/LCDs nanozyme at the range of glucose between 0.01 mM and 1 mM at limit of detection of 0.01 mM covered the glucose blood level range of both healthy persons and ones with diabetes. The color changes of PtRu/LCDs-water/cellulose nanocomposites were virtually observed at the different concentrations of H<sub>2</sub>O<sub>2</sub>. PtRu/LCDs-water/cellulose nanocomposites have potential to utilize as paper-based H<sub>2</sub>O<sub>2</sub> and glucose sensing application.

**Keywords:** carbon dots; metal/cellulose nanocomposite; fluorescence assay; colorimetric assay; glucose detection.

### 1. Introduction

According to the World Health Organization (WHO) database of adult's diabetes risk currently, the number of patients has been rising over 8.8% of the world's population and it is believed that the continuous increase will continue up to 9.9% in 2045 (Standl et al., 2019). The most common glucose detection method for diabetes's clinical diagnosis is carried on by using blood glucose measurement, but in detail, high concentration of glucose and intensive biomolecule components in blood stream lead to considerable problems for analytical procedure (Boselli et al., 2021). It was reported that the fasting blood glucose level of healthy people is in the range of 0.05-0.55 mM (Boselli et al., 2021) and that of people with diabetes is in the range of 0.55-1.77 mM (Lee et al., 2017). Therefore, the development of rapid, accurate



and sensitive glucose detection assays for both ranges aforementioned from nanomolar to millimolar level have been extensively investigated.

Colorimetric and fluorimetric assays for glucose detection with high sensitivity have been widely disclosed due to their simplicity and rapid process. One of interesting procedures is using nanozymes or nanomaterials that could effectively catalyze the reaction with glucose substrate at room temperature to generate color or fluorescent emission of compounds. In general, the oxidation of glucose catalyzed by glucose oxidase (GOx) enzyme produces gluconic acid and hydrogen peroxide ( $H_2O_2$ ) as the products. Thus, generated  $H_2O_2$  is a key substrate in an optical or fluorimetric detection. Horseradish peroxidase (HRP) is a selective enzyme to catalyze not only the decomposition of  $H_2O_2$  into  $H_2O$  and  $O_2$ , but also the production of OH radicals ( $\cdot OH$ ). In the colorimetric method, 3,3',5,5'-tetramethylbenzidine (TMB) is widely used as a substrate that could be oxidized by  $\cdot OH$ . The oxidized TMB generates a blue-colored compound having absorbance at 652 nm (Wang et al., 2023), and thus it can be detected under UV-vis spectroscopic analysis. In case of fluorimetric assay, it was reported that carbon nanodots doped silver nanoparticles showed an outstanding fluorescence property as a nanozyme. The changes of fluorescent intensity during the reaction can be nicely correlated with the concentration of  $H_2O_2$  and glucose. The fluorescence quenching occurred when the mimetic nanozyme is covered by the metal on the surface, after the oxidation of glucose, it causes the fluorescence turn on. This turn-on/turn-off fluorescence property of the nanomaterials can be detected under spectrofluorimetric analysis (Ma et al., 2016). It was additionally revealed that nitrogen and/or sulfur doped carbon dots (NS-CDs) and metal CDs hybrid structures were nanozymes that exhibited peroxidase-like activity, therefore they have potential for colorimetric and fluorimetric  $H_2O_2$  (Saengsrichan et al., 2022) and glucose sensing (Ngo et al., 2021).

In this work, carbon quantum dots derived from lignin (LCDs) was prepared in aqueous solution via hydrothermal process. The influence of mono-metallic and bi-metallic dopants including Pt, Ru, and PtRu, on an increase of the catalytic peroxidase-like activity of LCDs was investigated in comparison with native LCDs. Firstly, the study on their performance on catalyzing peroxidase-like reaction in the presence of  $H_2O_2$  at room temperature was conducted. Secondly, the best nanozyme with highest peroxidase-like reactivity was employed for glucose sensing for both colorimetric and fluorimetric detection assays. Limit of detection (LOD) and linearity range of both glucose detection methods were reported herein.

## 2. Materials and Methods

### 2.1. Materials

Alkali lignin (AL) with low sulfonate content, chloroplatinic acid ( $H_2PtCl_6 \cdot xH_2O$ ), ruthenium (III) chloride hydrate ( $RuCl_3 \cdot xH_2O$ ), sodium borohydride ( $NaBH_4$ ) ( $\geq 99.98\%$  trace metals basis) were purchased from Sigma-Aldrich, USA. Hydrogen peroxide ( $H_2O_2$ ) 3 wt.% solution, D-(+)-Glucose ( $C_6H_{12}O_6$ ), glucose oxidase (GOx) from *Aspergillus niger*, 3,3',5,5'-Tetramethylbenzidine (TMB), and filter papers (Whatman No. 4) were purchased from Sigma-Aldrich, USA. Sodium acetate, acetic acid, potassium dihydrogen phosphate, and sodium hydroxide were supplied from Ajax Finechem, USA.

### 2.2. Synthesis of lignin derived carbon quantum dots (LCDs) and metal doped LCDs

LCDs was synthesized via 220°C hydrothermal process for 6 h. To obtain LCDs, lignin was hydrothermally reacted with ultrapure water in a pressurized reactor and after the reaction

it was cooled down naturally. LCDs solution was first centrifuged to separate large particle of residual lignin and then filtered via microfiltration at 0.22  $\mu\text{m}$ . LCDs solution was afterward dialyzed in dialysis membrane to remove unwanted intermediate chemicals generated.

For the synthesis of mono-metallic/LCDs, 20 mmol of  $\text{H}_2\text{PtCl}_6 \cdot x\text{H}_2\text{O}$  or 20 mmol of  $\text{RuCl}_3 \cdot x\text{H}_2\text{O}$  was added in 48 mg LCDs sample, the obtained products were named as Pt/LCDs-water and Ru/LCDs-water, respectively. For the bi-metallic/LCDs, 20 mmol of  $\text{H}_2\text{PtCl}_6 \cdot x\text{H}_2\text{O}$  and 20 mmol of  $\text{RuCl}_3 \cdot x\text{H}_2\text{O}$  were added in 48 mg LCDs sample, the obtained product was named as PtRu/LCDs-water.

### 2.3. Peroxidase-like activity of hydrogen peroxide ( $\text{H}_2\text{O}_2$ ) and glucose detection by colorimetric and fluorimetric methods

For peroxidase-like activity study, various concentrations of  $\text{H}_2\text{O}_2$  solution were prepared and added into a mixture of metal doped LCDs, or native LCDs containing TMB dissolved in Na-acetate buffer pH 4.0. UV-vis spectroscopy at 652 nm was conducted to quantify amount of oxidized TMB in the case of colorimetric analysis from 0 min to 30 min at room temperature (25  $^\circ\text{C}$ ). While fluorometry was conducted at excitation wavelength of 280 nm from 0 min to 30 min at room temperature (25  $^\circ\text{C}$ ) in the case of fluorimetric detection of  $\text{H}_2\text{O}_2$ .

For glucose detection, D-(+)-glucose stock solution was diluted to various concentrations and thus mixed with glucose oxidase (GOx) dissolved in 0.1 M phosphate buffer solution (PBS) pH 7.4. Then, the mixture was incubated at 37 $^\circ\text{C}$  for 30 min to fully produce  $\text{H}_2\text{O}_2$  as a product. The peroxidase-like reaction was again carried on similar to the aforementioned procedures of both colorimetric and fluorimetric detection.

### 2.4. Fabrication of metal/LCDs/cellulose nanocomposites

The filter paper (Whatman No. 4) was used as a cellulose matrix for the fabrication of metal/LCDs/cellulose nanocomposites. For  $\text{H}_2\text{O}_2$  detection in the solid-state form, the filter paper strip was soaked in the mixture of LCDs, TMB, and Na-acetate buffer pH 4.0. The nanocomposite was subsequently dried at 50 $^\circ\text{C}$  for 1 h, dipped into the different concentrations of  $\text{H}_2\text{O}_2$  and waited for 60 min. The color developed was finally observed.

## 3. Results and Discussion

### 3.1. Characterization of LCDs and metal doped LCDs

Carbon quantum dots derived from lignin (LCDs) was synthesized through hydrothermal treatment, then the obtained LCDs solution was doped with metals. The crystalline structure of LCDs-water and PtRu/LCDs-water was investigated using Raman spectroscopy as shown in Fig. 1(A) and Fig. 1(B), respectively. The Raman spectrum of LCDs-water and PtRu/LCDs-water showed the peak at 1,358 and 1,374  $\text{cm}^{-1}$  representing  $I_D$  band of amorphous carbon, and that at 1,581 and 1,578  $\text{cm}^{-1}$  representing  $I_G$  band of crystallinity of carbon quantum dots, respectively (Niu et al., 2017). Low  $I_D/I_G$  ratio obtained from pristine LCDs confirms their high-quality of graphitic structure of carbon. After doping PtRu onto LCDs,  $I_D/I_G$  ratio slightly decreased. This meant that Pt and Ru did not make any more defects to LCDs structure of PtRu/LCDs-water. From Fig. 1(C), PtRu/LCDs-water contained both sulfur (S) which presumably contaminants in lignin precursor from sulfite pulping process resulting in lignosulfonate (Fabbri et al., 2023) while chlorine (Cl) found in the sample came from Pt precursor. Pt and Ru were found in substantial amount from doping reaction onto LCDs surface

as shown in Fig. 1(D). Pt was successfully doped onto LCDs at 25.69 wt% and in the presence of Ru was ~10.78 wt%.

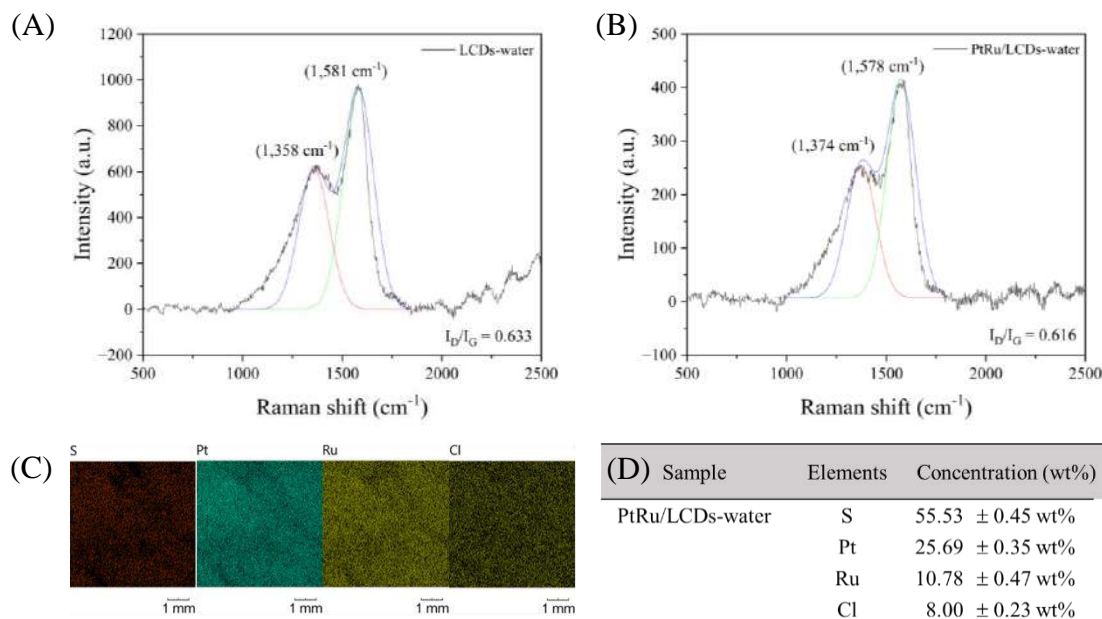


Fig. 1 Raman spectroscopy of (A) LCDs-water and (B) PtRu/LCDs-water, (C) XRF of PtRu/LCDs-water, and (D) The elemental composition of PtRu/LCDs-water.

### 3.2. Colorimetric H<sub>2</sub>O<sub>2</sub> and glucose detection of LCDs and metal doped LCDs

From the colorimetric assay for H<sub>2</sub>O<sub>2</sub> detection, the color of oxidized TMB (ox-TMB) at 1 mM H<sub>2</sub>O<sub>2</sub> from different nanozymes namely LCDs, Pt/LCDs, Ru/LCDs, PtRu/LCDs and the control without nanozyme was demonstrated in Fig. 2(A). TMB was oxidized and its color was changed from colorless to blue color indicating higher amount of ox-TMB. Among all metal doped LCDs, PtRu/LCDs exhibited the highest reactivity on catalyzing TMB oxidation and produced strongest blue color of the reaction mixture within 30 min at room temperature (Fig. 2(B)) due to the high catalytic property of bi-metallic nanostructure (Sergeev et al., 2014). The highest UV-vis absorbance of PtRu/LCDs with time-dependent peroxidase-like activity was achieved compared with the control. The lower absorbance intensity was found for Ru/LCDs, Pt/LCDs and native LCDs, respectively.

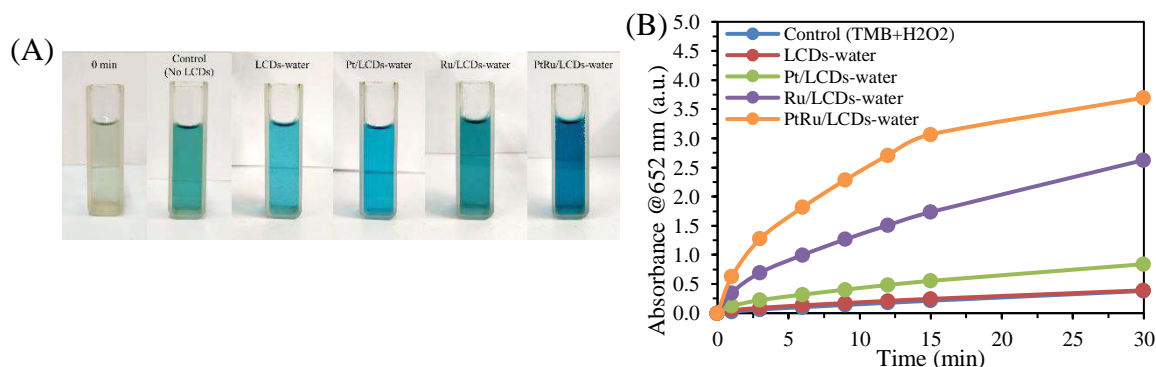


Fig. 2 (A) The color developed of reaction mixture at 30 min, and (B) UV-vis absorption of ox-TMB observed at 652 nm from 0-30 min at room temperature (25 °C).

As illustrated in Fig. 3(A), a good correlation of glucose concentration from 0.01 mM to 10 mM and the UV-vis absorbance of ox-TMB at 652 nm was obtained when the reaction was catalyzed by PtRu/LCDs. With an increase of glucose concentration in the reaction mixture, the more H<sub>2</sub>O<sub>2</sub> was produced and the higher absorbance of oxidized TMB was obtained. The amount of ox-TMB can be calculated using the absorbance at wavelength 652 nm with the molar extinction coefficient (39,000 M<sup>-1</sup> cm<sup>-1</sup>) (Bresoli-Obach et al., 2020). The very high correlation between amount of ox-TMB and glucose concentration was depicted in Fig. 3(B). The linear regression result provided the coefficient of determination (R-square) of 0.9923 for the linear range of 0.01-10 mM glucose. Therefore, the indirect colorimetric glucose detection assay using peroxidase mimetic nanozyme (PtRu/LCDs) could be efficiently used for glucose sensing with high accuracy. The finding demonstrated that using PtRu/LCDs as a nanozyme, the greatest length of linearity from 0.01 mM to 10.0 mM was achieved with high sensitivity at very low limit of detection (LOD) of 0.01 mM of glucose.

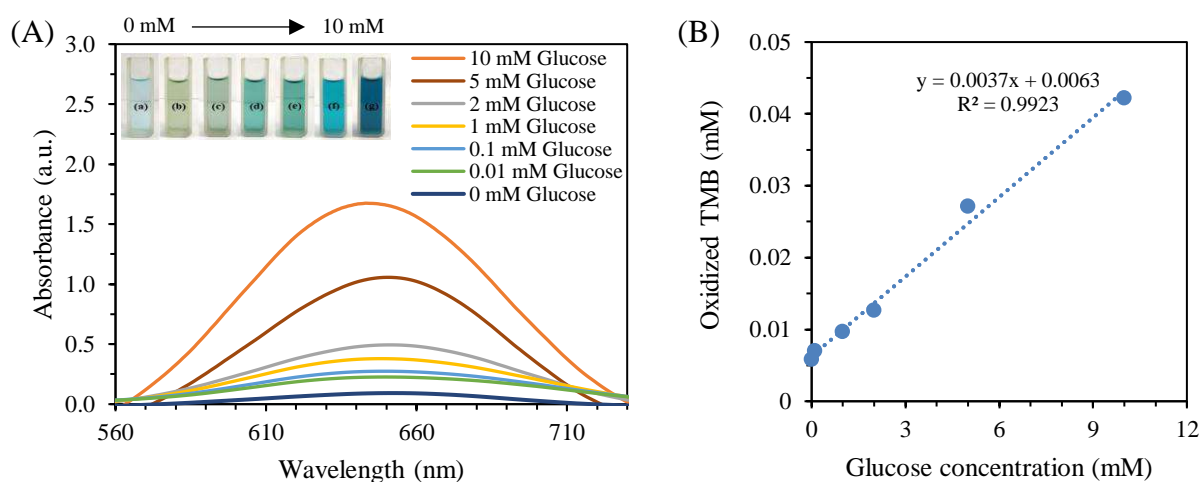


Fig. 3 (A) The UV-vis absorption spectra from PtRu/LCDs-water; the inset, the color of buffer+TMB+PtRu/LCDs-water solution at different glucose concentrations at 60 min; (a)-(g) is 0, 0.01, 0.1, 1, 2, 5, and 10 mM and (B) The linear correlation of oxidized TMB catalyzed by PtRu/LCDs-water at 60 min at different glucose concentrations from 0.01-10.0 mM.

### 3.3. Fluorimetric glucose detection of LCDs and metal doped LCDs

As demonstrated in Fig. 4(A), the fluorescence emissive intensities of ox-TMB at different glucose concentrations from 0.1-10 mM catalyzed by PtRu/LCDs-water were compared with control in the absence of PtRu/LCDs-water nanozyme. At the excitation wavelength ( $\lambda_{Ex}$ ) of 280 nm, the maximum fluorescent emissive intensity was found at wavelength ( $\lambda_{Em}$ ) of 410 nm. The results confirm the effect of PtRu/LCDs-water as a nanozyme for catalyzing the dissociation of H<sub>2</sub>O<sub>2</sub> to generate the ·OH radicals which further ox-TMB molecule. The inset of Fig. 4(A) shows the photographs of the solution mixture of 0.1 mM glucose in the presence of TMB after the reaction with PtRu/LCDs for 60 min under visible light and UV irradiation at 254 nm. The emissive fluorescent color of the reaction mixture under UV irradiation was violet which corresponded to the  $\lambda_{Em}$  at 410 nm of electromagnetic radiation wave.

For quantitative analysis, a good correlation between fluorescence quenching (log  $\Delta FL$ ) after 60 min and the glucose concentration was obtained as shown in Fig. 4(B). The linear range of the fluorimetric glucose detection by PtRu/LCDs nanozyme was achieved between 1 mM

and 10 mM with the LOD of 0.1 mM. It can be concluded that the fluorimetric glucose sensing assay was achieved when using PtRu/LCDs as the nanozyme that is virtually covered blood glucose concentration of patients with diabetes. The reactivity of PtRu/LCDs-water is the key parameter in the peroxidase-like reaction which leads to an enhanced glucose sensing sensitivity, accuracy and precision. To lower the LOD of fluorimetric detection of glucose, further optimization study as such metal loading for PtRu/LCDs synthesis, nanozyme dosage in the reaction, and kinetic study could be rigorously performed.

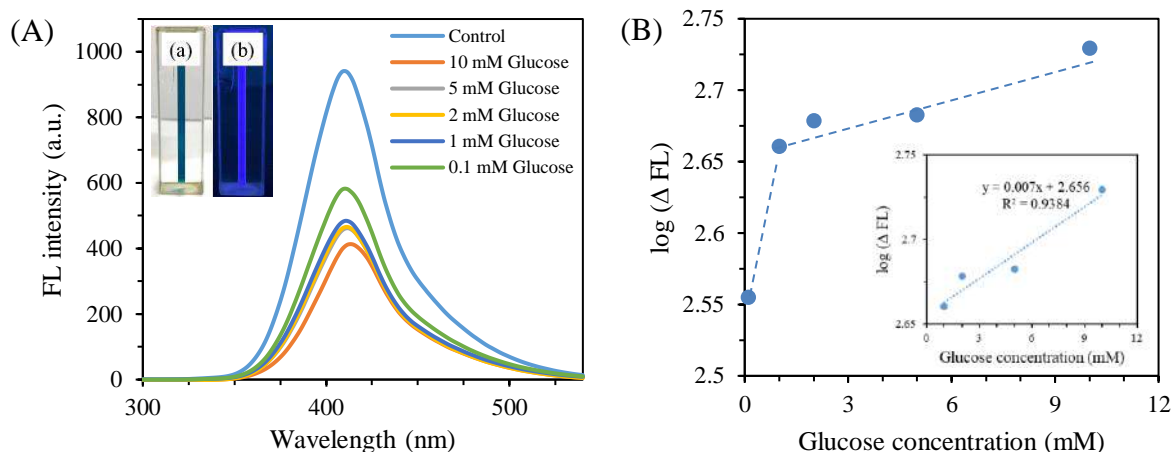


Fig. 4 (A) The fluorescence intensity of the glucose sensing by PtRu/LCDs-water at different glucose concentration at  $\lambda_{Ex} = 280$  nm; the inset is the solution of buffer+TMB+PtRu/LCDs-water at 0.1 mM glucose after 60 min under (a) visible light and (b) UV light @254 nm; (B) The plot of  $\log \Delta FL$  versus glucose concentration (0.1-10 mM) catalyzed by PtRu/LCDs-water at 60 min; inset showed the linear range between 1-10 mM of glucose concentration.

The PtRu/LCDs-water/cellulose nanocomposites was tested in the peroxidase-like reaction in the presence of different concentration of  $H_2O_2$  from 0.1-1 mM. The color was intense when the  $H_2O_2$  concentration was increased and it can be observed easily with naked eyes (Fig. 5). This can be concluded that PtRu/LCDs-water/cellulose nanocomposites have potential to utilize as paper-based  $H_2O_2$  and glucose sensing application. The accuracy and sensitivity of this technique will be continually proved.

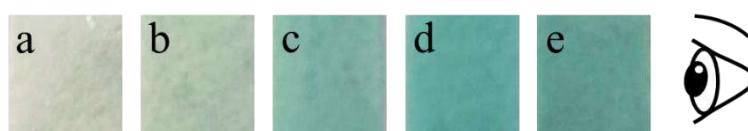


Fig. 5 Colorimetric  $H_2O_2$  detection by PtRu/LCDs-water/cellulose nanocomposites from 0.1-1 mM at 60 min; (a) control (buffer+TMB+ $H_2O_2$ ), and PtRu/LCDs-water sensing at (b) 0 mM, (c) 0.1 mM, (d) 0.5 mM, and (e) 1 mM of  $H_2O_2$ .

#### 4. Conclusions

Lignin derived carbon quantum dots (LCDs) was magnificently synthesized via hydrothermal process. Among all conjugated metals onto LCDs, the bi-metallic PtRu/LCDs-water was the best nanozyme that exhibited best performance on catalyzing  $H_2O_2$  dissociation

and thus could provide both colorimetric and fluorimetric glucose detection with high accuracy. Effective colorimetric glucose detection using PtRu/LCDs nanozyme resulted in high sensitivity at lengthy range of glucose between 0.01 mM and 1 mM which covers the glucose blood level range of both healthy persons and diabetic patients. PtRu/LCDs-water/cellulose nanocomposites fruitfully catalyzed color developed reaction with well correlation for the different concentrations of H<sub>2</sub>O<sub>2</sub>. PtRu/LCDs-water/cellulose nanocomposites have potential to utilize as paper-based H<sub>2</sub>O<sub>2</sub> and glucose sensing application.

### Acknowledgement

This work was supported by Mahidol University, Specific League Funds 2023, World University Ranking by Subject. Partial support was from National Research Council of Thailand (NRCT), Research Grant for Talented Mid-Career Researchers (N42A650248), and the Scholarship to Promote Master and Doctoral Students' Competency for Academic Presentations from the Faculty of Graduate Studies, Mahidol University. The authors are thankful to Mahidol University-Frontier Research Facility (MU-FRF) for instrument supports and additionally, scientists of MU-FRF, Dr. Suwilai Chaveanghong for generous support on X-ray fluorescence (XRF) and Raman spectroscopy and Dr. Aphiwat Pankeaw for kindly support on Spectrofluorometer.

### References

- [1] Boselli, L., Pomili, T., Donati, P., and Pompa, P. P. (2021). Nanosensors for Visual Detection of Glucose in Biofluids: Are We Ready for Instrument-Free Home-Testing?. *Materials*, 14(8), 1978.
- [2] Bresoli-Obach, R., Frattini, M., Abbruzzetti, S., Viappiani, C., Agut, M., and Nonell, S. (2020). Tetramethylbenzidine: An Acoustogenic Photoacoustic Probe for Reactive Oxygen Species Detection. *Sensors*, 20(20), 5952.
- [3] Fabbri, F., Bischof, S., Mayr, S., Gritsch, S., Jimenez Bartolome, M., Schwaiger, N., Guebitz, G. M., and Weiss, R. (2023). The Biomodified Lignin Platform: A Review. *Polymers*, 15(7), 1694.
- [4] Lee, H., Song, C., Hong, Y. S., Kim, M., Cho, H. R., Kang, T., Shin, K., Choi, S. H., Hyeon, T., and Kim, D. H. (2017). Wearable/disposable sweat-based glucose monitoring device with multistage transdermal drug delivery module. *Science Advances*, 3(3), e1601314.
- [5] Ma, J.-L., Yin, B.-C., Wu, X., and Ye, B.-C. (2016). Simple and Cost-Effective Glucose Detection Based on Carbon Nanodots Supported on Silver Nanoparticles. *Analytical Chemistry*, 89(2), 1323-1328.
- [6] Ngo, Y.-L. T., Nguyen, P. L., Jana, J., Choi, W. M., Chung, J. S., and Hur, S. H. (2021). Simple paper-based colorimetric and fluorescent glucose sensor using N-doped carbon dots and metal oxide hybrid structures. *Analytica Chimica Acta*, 1147, 187-198.
- [7] Niu, N., Ma, Z., He, F., Li, S., Li, J., Liu, S., and Yang, P. (2017). Preparation of Carbon Dots for Cellular Imaging by the Molecular Aggregation of Cellulolytic Enzyme Lignin. *Langmuir*, 33(23), 5786-5795.
- [8] Saengsrirachan, A., Khemthong, P., Wanmolee, W., Youngjan, S., Phanthasri, J., Arjfuak, P., Pongchaikul, P., Ratchahat, S., Posoknistakul, P., Laosiripojana, N., Wu, K. C. W., and Sakdaronnarong, C. (2022). Platinum/carbon dots nanocomposites from palm bunch hydrothermal synthesis as highly efficient peroxidase mimics for ultra-low H<sub>2</sub>O<sub>2</sub>

- sensing platform through dual mode of colorimetric and fluorescent detection. *Analytica Chimica Acta*, 1230, 340368.
- [9] Sergeev, M. O., Revina, A. A., Busev, S. A., Zolotarevskiy, V. I., Zhavoronkova, K. N., and Boeva, O. A. (2014). Catalytic properties of monometallic and bimetallic palladium and rhodium nanoparticles obtained in reverse micellar systems. *Nanotechnology Reviews*, 3(5), 515-525.
- [10] Standl, E., Khunti, K., Hansen, T. B., and Schnell, O. (2019). The global epidemics of diabetes in the 21st century: Current situation and perspectives. *European Journal of Preventive Cardiology*, 26(2S), 7-14.
- [11] Wang, F., Liao, L., Liu, X., Zhang, J., and Wu, F. (2023). Porphyrin-based porous organic frameworks as efficient peroxidase mimics for selective detection of hydrogen peroxide and glucose. *Inorganic Chemistry Communications*, 155, 111011.

## Assessing Sustainability Performance of Thailand Provinces via Super-efficiency Data Envelopment Analysis

Narawit Yingyong<sup>1</sup>, Satawat Thumwong<sup>1</sup>, and Phantisa Limleamthong<sup>1,\*</sup>

<sup>1</sup> Department of Chemical Engineering, Faculty of Engineering, Kasetsart University, Bangkok 10900, Thailand  
E-mail: \*phantisa.l@ku.th

### Abstract

Sustainable development at the provincial level involves striving for economic and social growth while minimizing adverse impacts on the environment. Assessing the sustainability performance of provinces not only provides a measure of their sustainability but also highlights areas that require immediate attention. This assessment can lead to suggestions for improvement methods to move towards sustainable development. This research aims to evaluate the sustainability performance of 77 Thailand provinces in 2022 using Super-efficiency Data Envelopment Analysis (DEA) model, considering various sustainability indicators that cover all three key elements: social, economic, and environmental. The chosen social indicator is the unemployed rate, the economic indicator is provincial gross product, and the environmental indicators include electricity consumption, water consumption, the amount of waste generated, and the amount of waste that can be recycled. The results indicated that approximately 28.6 percent of the provinces are efficient, while the remaining 71.4 percent are considered inefficient. The inefficient provinces have the potential to improve their efficiency by learning from the efficient ones. Notably, Sisaket is frequently referenced by the inefficient provinces for improvements, with the most significant area for enhancement being the recycling of waste, followed by water consumption. Additionally, the analysis revealed that Yasothon as the most efficient province, obtained an impressive score of 4.95. This suggests that Yasothon excels in waste resource management while efficiently utilizing other resources.

**Keywords:** Sustainability Assessment; Thailand Provinces; Data Envelopment Analysis; Super-efficiency; Sustainability Indicators

### 1. Introduction

The province operates as an economic system driven by the efficient flow of materials and energy [1]. This involves utilizing resources such as water and electrical energy to manufacture goods and deliver services that meet consumer demands. Concurrently, the province plays a pivotal role in fostering economic prosperity and generating social benefits for the local population, encompassing education, culture, and livelihood opportunities, including increased employment prospects [2]. However, resource utilization has led to unavoidable environmental consequences, manifesting as global warming, diminished resource availability, air pollution, and a substantial increase in waste production [3]. To ensure sustainable development, encompassing economic and social advancement while remaining environmentally responsible, it becomes imperative to evaluate sustainability performance at the provincial level. This assessment serves as a gauge of the province's overall performance, shedding light on critical areas that demand attention. Ultimately, it paves the way for recommendations and strategies aimed at refining the province's approach to sustainable development.



Sustainable development practices have been implemented across various provinces in Thailand with the aim of fostering economic and societal progress while mitigating environmental impacts. The sustainability performance assessment involves considering economic, social, and environmental indicators, acknowledging their interconnected but often conflicting nature. Achieving optimal goals in all three elements simultaneously can be challenging [4]. Traditional multi-criteria decision-making tools (MDCM) are the most common techniques to serve this task; however, they rely on manually set weight values, leading to diverse results based on user preferences [5]. In contrast, this research utilizes DEA, as it calculates the efficiency score of decision-making units without having to manually assign the weights. DEA utilizes linear programming to determine optimal weights, allowing for clear identification of inefficient and effective decision-making units [6]. Additionally, DEA provides insights into improving and developing each indicator for every decision-making unit, enhancing the overall assessment process.

This research aims to assess the sustainability performance of all 77 provinces in Thailand by examining social, economic, and environmental indicators consisting of employment rate, electrical consumption, water consumption, waste generation, recycled waste, and gross provincial product (GPP). DEA was employed to identify the sustainably efficient provinces, which will serve as benchmarks for improving indicators in less efficient provinces. This approach is designed to reduce resource consumption, minimize waste, and increase waste recycling, while enhancing economic returns. The continuous development of sustainable efficiency of the provinces can significantly impact the society, the economy, and the environment in Thailand. Consequently, this assessment sheds light on resource and waste management efficiency in each province and identifies essential factors influencing sustainability performance.

## 2. Methods

This section provides information regarding the mathematical tools used in this study.

### 2.1 Data Envelopment Analysis

Data Envelopment Analysis or DEA is a mathematical method used to assess the efficiency of a set of decision-making units (DMUs) through a mathematical process known as linear programming [7]. It establishes efficiency boundaries from specified data, creating an efficient frontier that illustrates the relationship between output and input data. The efficient frontier serves as a benchmark for measuring the efficiency scores of other DMUs. The efficiency scores are determined by calculating the ratio of weighted-sum outputs to weighted-sum inputs without requiring the knowledge of input-output relationships. DEA seeks to find the maximum relative efficiency score for each DMU when compared to the scores of the others. It is also essential to standardize the data for reasonable comparison, ensuring that all data are fairly treated on the same basis. This standardization allows for accurate and reliable assessments.

### 2.2 Super-efficiency dual DEA Model

The super-efficiency dual DEA is a model that can further assess the efficiency scores of DMUs beyond the efficient frontier [8]. In this model, the efficiency scores can exceed 1. This model excludes the assessed DMU from the reference set. Generally, the model measures how much the assessed DMU exceeds the boundary of the efficient frontier. However, the super-efficiency dual DEA model may encounter infeasibility issues when assumptions of Variable Returns to Scale (VRS) occur. In general, infeasibility usually occurs when it is

impossible to find a solution that satisfies the constraints of a particular problem. In the context of super-efficiency dual DEA with VRS, the infeasibility of model may arise due to the fact that the assessed DMU does not display input saving but only demonstrating output surplus [9].

Therefore, the current research has adopted the super-efficiency dual DEA model proposed by Lee et al. [9], which can address the infeasibility problem in the original model by seeking to determine potential surpluses in individual outputs, as illustrated in Eq. (1) below.

$$\begin{aligned} \min_{\lambda_j, S_r} \quad & \sum_{r=1}^s S_r & (1) \\ \text{Subjected to :} \quad & \sum_{j=1, j \neq o}^n \lambda_j y_{rj} + S_r y_{ro} \geq y_{ro} ; \forall r \\ & \sum_{r=1}^s \lambda_j = 1 \end{aligned}$$

Eq. (1) is calculated for each DMU<sub>o</sub>. Give a symbol ‘\*’ refers to the optimal decision variable or the output surplus ( $S_r^*$ ) obtained from Eq. (1) and it will be further used in Eq. (2).

$$\begin{aligned} \min_{\lambda_j} \quad & \hat{\theta}_o & (2) \\ \text{Subjected to :} \quad & \sum_{j=1, j \neq o}^n \lambda_j x_{ij} \leq \hat{\theta}_o x_{io} ; \forall i \\ & \sum_{j=1, j \neq o}^n \lambda_j y_{rj} + S_r^* y_{ro} \geq y_{ro} ; \forall r \\ & \sum_{j=1}^n \lambda_j = 1 \\ & \lambda_j \geq 0, i = 1, \dots, m, r = 1, \dots, s \end{aligned}$$

where n refers to the number of DMUs included in the assessment; o serves as an index for the assessed DMU for o = 1, ..., n; j serves as an index for other DMUs for j = 1, ..., n; m is the number of inputs consumed by DMU<sub>j</sub>; x<sub>ij</sub> is the amount of input i (for i = 1, ..., m) consumed by DMU<sub>j</sub>; s is the number of outputs generated by DMU<sub>j</sub>; and y<sub>rj</sub> is the amount of output r (for r = 1, ..., s) generated by DMU<sub>j</sub>. The optimal decision variables of Eq. (2) are as follows:  $\hat{\theta}_o$  is the super-efficiency score of DMU<sub>o</sub>; and  $\lambda_j$  is a linear weight attached to every DMU<sub>j</sub> (for j = 1, ..., n).

The super-efficiency dual DEA model score ( $\theta_o^{SE}$ ) can be calculated from Eq. (3)

$$\theta_o^{SE} = 1 = \begin{cases} \frac{\sum_{r \in R} \left( \frac{y_{ro}}{y_{ro} - S_r^* y_{ro}} \right)}{|R|} + \hat{\theta}_o^*, & \text{if } R \neq \emptyset \\ \hat{\theta}_o^*, & \text{if } R = \emptyset \end{cases} \quad (3)$$

where  $R = \{r | S_r^* > 0\}$

In addition, the super-efficiency dual DEA model can suggest the improvement pathway of every inefficient DMU through its projection onto the efficient frontier [10]. The development targets are determined by referencing the benchmark efficiency scores of the efficient provinces, and the calculation involves multiplying indicator data by the corresponding linear weights, as shown in Eq. (4) and (5) for input and output data targets, respectively.

$$T_{io}^* = \sum_{j=1}^n \lambda_j^* x_{ij} \quad (4)$$

$$T_{ro}^* = \sum_{j=1}^n \lambda_j^* y_{rj} \quad (5)$$

where  $T_{io}^*$  is a target of input  $i$  for DMU $_o$ ;  $T_{ro}^*$  is a target of output  $r$ ; and  $\lambda_j^*$  is a linear weight attached to DMU $_j$  which is obtained by solving Eq. (2).

It is worth pointing out that the target for input is always less than the original input data. On the other hand, the target for output is typically greater than the original output data. Subsequently, the improvement percentage for the inefficient provinces having the efficiency scores less than 1, is calculated on the basis of the projecting distance from the inefficient DMU $_o$  [11] onto the efficient frontier as shown in Eq. (6) and (7) of input and output data, respectively.

$$\%IMP_i^* = \frac{\left(\sum_{j=1}^n \lambda^* x_{ij}\right) - x_{io}}{x_{ij}} \times 100 \quad (6)$$

$$\%IMP_r^* = \frac{y_{ro} - \left(\sum_{j=1}^n \lambda^* y_{rj}\right)}{y_{ro}} \times 100 \quad (7)$$

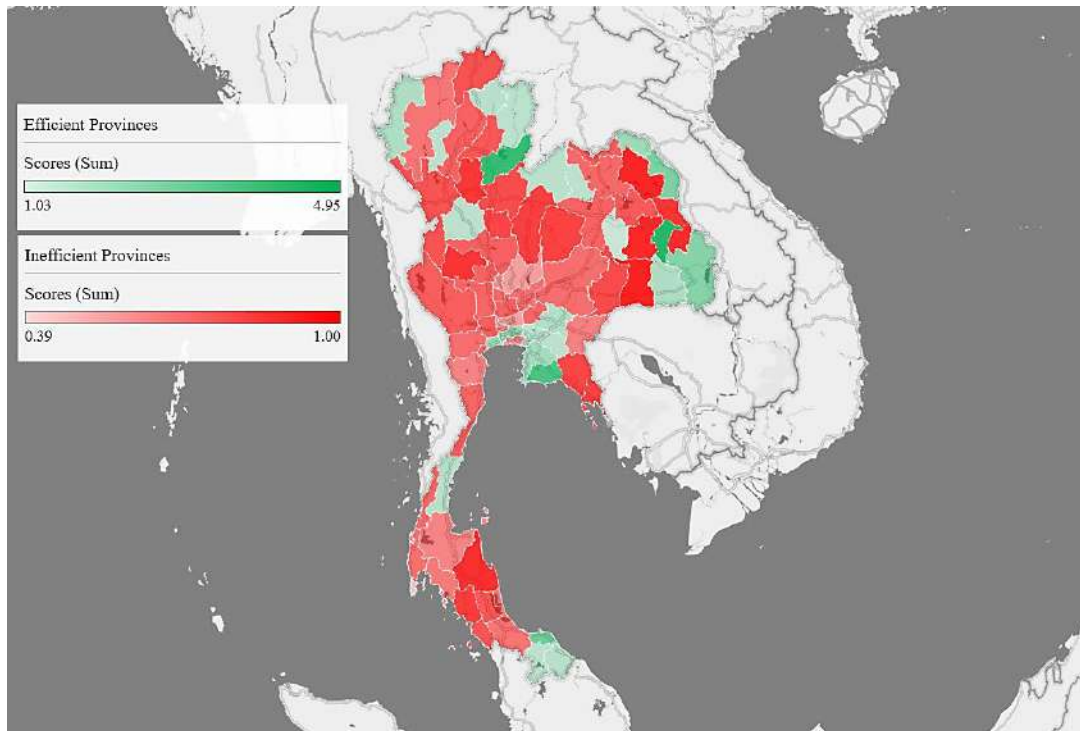
### 3. Results and discussion

#### 3.1 Efficiency score

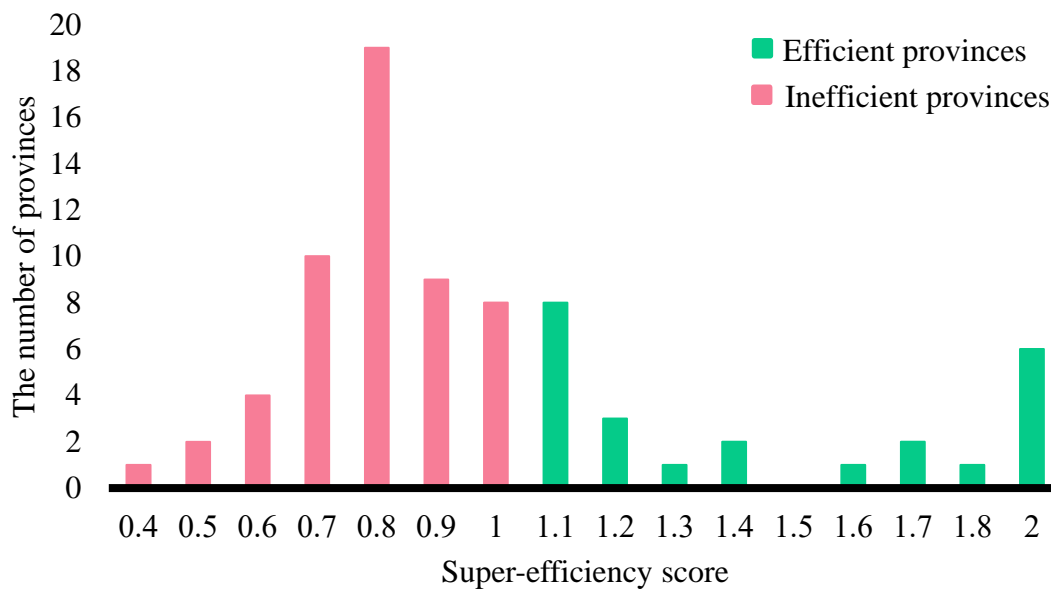
The efficiency scores of each province were assessed through Data Envelopment Analysis, considering six sustainability indicators categorized into an input category (indicators to be minimized) and an output category (indicators to be maximized). Four inputs include Water Consumption, Electrical Consumption, Waste Generation, and Unemployment Rate, and two outputs include GPP and Waste Recycle. The analysis revealed 53 inefficient provinces, constituting 71.4 percent, exhibited efficiency scores lower than 1. In Fig. 1, the inefficient provinces are highlighted in red, with varying shades to denote the degree of inefficiency. Light red indicates extreme inefficiency, while dark red indicates increasing inefficiency closer to 1. These inefficient provinces present opportunities for development to enhance the efficiency. On the other hand, 24 efficient provinces, comprising 28.6 percent of the total, demonstrated efficiency scores greater than 1. In Fig. 1, these efficient provinces are depicted in green, with dark green indicating higher efficiency scores. Notably, the efficient provinces were distributed across various regions. Overall, the rural provinces were sustainably efficient as they could efficiently manage their resources with less constraints relevant to tourism or industry.

Figure 2 shows a histogram of the efficiency scores of Thailand's provinces in 2022. Each bar on the graph represents the number of provinces having the efficiency score within a specific range. For instance, the 0.5 bar corresponds to provinces with an efficiency score ranging from 0.4 to 0.5. The green color denotes the efficient provinces, and the red color signifies the inefficient provinces. The histogram shows a right-skewed pattern with the median of the efficiency score of 0.839, which falls within the 0.9 bar. Furthermore, the majority of provinces are clustered within the 0.7 to 0.8 scores range, indicating that most provinces still exhibit an unsustainability and inefficiency. This observation is supported by the presence of a score range below 1 in the majority of Thailand's provinces, suggesting ineffective resource management. Therefore, there appears to be a need for further development efforts.

The efficiency scores of each province are contingent upon the values of sustainability indicators. A lower value of the input indicators corresponds to a higher score, while conversely, a higher value of the output indicators correlates with a higher score. Phuket performed worst in terms of sustainability with a score of 0.39. Despite being a popular tourist destination, Phuket faced inefficiencies due to several factors. The small size of the province



**Fig. 1** Spatial heatmap of Thailand's provinces super-efficiency scores in 2022.



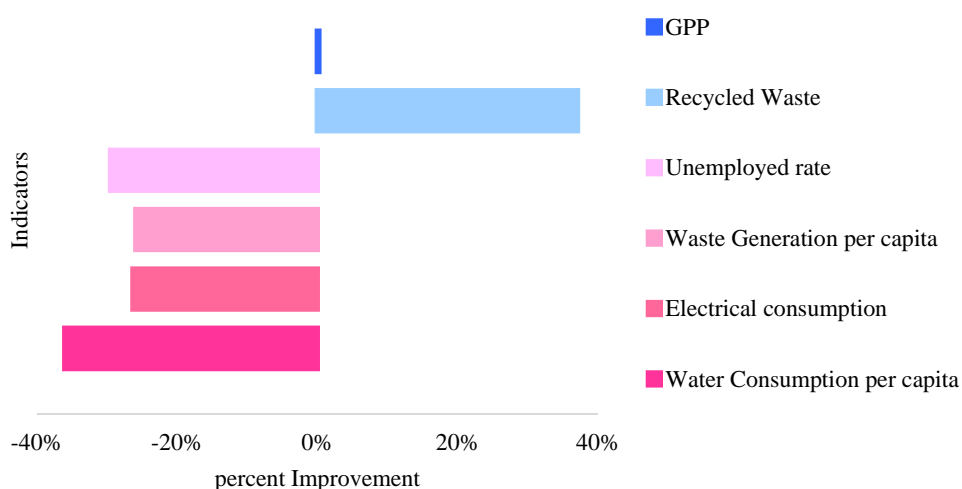
**Fig. 2** The histogram of Thailand's provinces super-efficiency scores in 2022.

coupled with high tourism levels can lead to challenges in waste management. The influx of tourists may contribute to increased waste generation. The substantial electricity usage, paired with a relatively low GPP, suggests an imbalance in resource utilization. Furthermore, difficulties in proper waste recycling contribute to Phuket Province's lower efficiency score. Conversely, Yasothon stood out as the most efficient province with a score of 4.95. Its success can be attributed to minimal resource usage, particularly in terms of electricity and water

consumption per capita. The low unemployment rate, with over 99 percent of the population in appropriate employment, reflects a well-managed labor market. Yasothon also excels in waste recycling, ranking third in the country for reusing waste to produce valuable products. Notable waste management projects, such as the "Sorting and Separating (Waste) for Merit" initiative, further contribute to Yasothon's efficiency. Despite a modest GPP value, effective resource management positions Yasothon Province as a model for efficiency and sustainability.

### 3.2 Improving the inefficient provinces

Figure 3 illustrates the average improvement percentage for each indicator across the inefficient provinces. It is evident that the input indicators, including Water Consumption, Electrical Consumption, Waste Generation, and Unemployment Rate, should undergo reduction. Conversely, the output indicators, encompassing the Rate of Recycled Waste and Gross Provincial Product, should be increased. This adjustment aims to propel a province towards sustainability efficiency or an efficiency score of 1. Overall, the inefficient provinces should prioritize their improvement strategies towards maximizing the recycling rate, as it demonstrates the highest average percentage improvement at 37 percent. Subsequently, an emphasis should be placed on reducing water consumption, with an average percentage improvement as high as 36 percent, followed by an unemployment rate. Additionally, if waste generation and electricity consumption can be curtailed by comparable values, it will contribute to achieving sustainable efficiency. As for the provincial gross product, no additional adjustments are deemed necessary, as the value is already deemed appropriate.



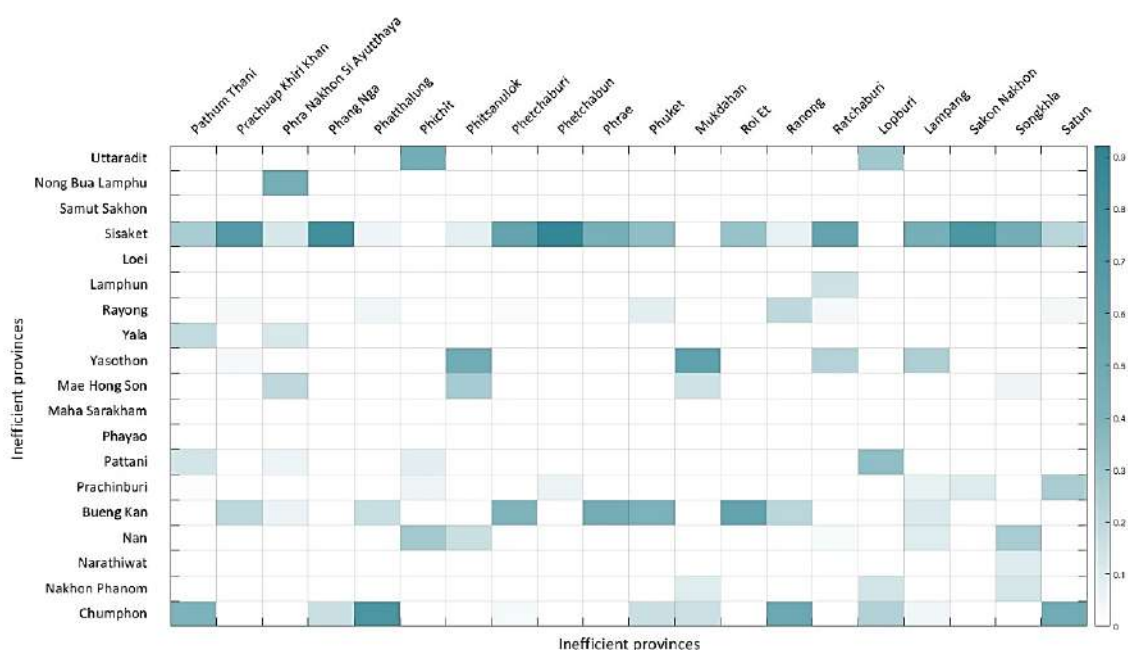
**Fig. 3** Average improvement percentage for each sustainability indicator of the inefficient provinces.

Furthermore, the province has undertaken additional development initiatives by creatively utilizing leftovers to add more value. Unsellable items, such as milk cartons, are transformed through innovation into aesthetically pleasing and functional products. This not only contributes to waste reduction but also encourages local people to use their free time in a meaningful way by adding significant value to the discarded materials. These practices not only address environmental concerns but also foster a sense of community engagement and resourcefulness.

### 3.3 Exemplary Provinces

To enhance the efficiency of the provinces with efficiency scores less than 1, a viable approach is to refer to the lambda derived from the benchmarking against the efficiency frontier that is constructed from those efficient provinces. The lambda of the efficient provinces that were referenced by the inefficient provinces can be visualized as a heatmap in Fig. 4. The stronger green color denotes the higher value of lambda, reflecting the greater contribution of the efficient province that was used as a reference by the inefficient one.

Sisaket stood out among the efficient provinces as a prominent reference, having a summation of lambda values of 19.26 and has an efficiency score of 1.33. Sisaket's efficiency score was not the highest, yet it remained the most frequent reference for improvements by the other inefficient provinces. This prominence is attributed to its wealth of pertinent indicators. Sisaket occupies a favorable position on the efficient frontier, while many inefficient provinces are dispersed outside the frontier and projected through the frontier closely aligns with Sisaket, thereby solidifying it as a prominent reference point [12].



**Fig. 4** Heat map of lambda for non-performing provinces that use the efficient provinces as references.

### 4. Conclusion

This research assessed the sustainability performance of 77 Thailand provinces in 2022, covering three dimensions of sustainability: economic, social, and environmental. The super-efficiency DEA model was employed as the assessment tool which suggests that 24 out of 77 provinces, 31 percent demonstrated overall sustainability efficiency, while the other 53 provinces (69 percent) were found to be inefficient. The provinces identified as inefficient can enhance their sustainability by referencing the weighted values of the efficient provinces. The province with the highest reference weight was Sisaket, followed by Bung Kan. Subsequently, these weights were used to determine the targets and percentage improvement for each indicator. Overall, the inefficient provinces should prioritize their improvements on the recycling rate, with an average percentage improvement of 37 percent, followed by water consumption per capita with an average percentage improvement of 36 percent.

The analysis suggests that enhancing sustainability efficiency involves increasing input values and decreasing output values. Additionally, the use of the super-efficiency dual DEA model not only provides insightful results for the inefficient provinces but also allowed for measuring efficiency scores exceeding 1. This further facilitates the ranking of provinces based on their efficiency scores. The province with the highest efficiency score among all 77 provinces was Yasothon, with a score of 4.95, while the province with the lowest efficiency score was Phuket, with a score of 0.39.

## References

- [1] González-Garay, A., Pozo, C., Galán-Martín, Á., Brechtelsbauer, C., Chachuat, B., Chadha, D., Hale, C., Hellgardt, K., Kogelbauer, A., Matar, O. K., McDowell, N., Shah, N., & Guillén-Gosálbez, G. (2019). Assessing the performance of UK universities in the field of chemical engineering using data envelopment analysis. *Education for Chemical Engineers*, 29, 29–41. <https://doi.org/10.1016/j.ece.2019.06.003>
- [2] Bettencourt, L., & West, G. (n.d.). *467912a (1)*. 9–10.
- [3] Huesemann, M. H. (2001). Can pollution problems be effectively solved by environmental science and technology? An analysis of critical limitations. *Ecological Economics*, 37(2), 271–287. [https://doi.org/10.1016/S0921-8009\(00\)00283-4](https://doi.org/10.1016/S0921-8009(00)00283-4)
- [4] Janoušková, S., Hák, T., & Moldan, B. (2018). Global SDGs assessments: Helping or confusing indicators? *Sustainability (Switzerland)*, 10(5), 1–14. <https://doi.org/10.3390/su10051540>
- [5] Taherdoost, H., & Madanchian, M. (2023). Multi-Criteria Decision Making (MCDM) Methods and Concepts. *Encyclopedia*, 3(1), 77–87. <https://doi.org/10.3390/encyclopedia3010006>
- [6] Dinc, M., Haynes, K. E., & Tarimcilar, M. (2003). Integrating models for regional development decisions: A policy perspective. *Annals of Regional Science*, 37(1), 31–53. <https://doi.org/10.1007/s001680200093>
- [7] Cook, W. D., & Seiford, L. M. (2009). Data envelopment analysis (DEA) - Thirty years on. *European Journal of Operational Research*, 192(1), 1–17. <https://doi.org/10.1016/j.ejor.2008.01.032>
- [8] Hosseinzadeh Lotfi, F., Allahviranloo, T., Shafiee, M., & Saleh, H. (2023). Data Envelopment Analysis. *Studies in Big Data*, 122, 179–241. [https://doi.org/10.1007/978-3-031-28247-8\\_6](https://doi.org/10.1007/978-3-031-28247-8_6)
- [9] Lee, H. S., Chu, C. W., & Zhu, J. (2011). Super-efficiency DEA in the presence of infeasibility. *European Journal of Operational Research*, 212(1), 141–147. <https://doi.org/10.1016/j.ejor.2011.01.022>
- [10] Lozano, S., Soltani, N., & Dehnohalaji, A. (2020). A compromise programming approach for target setting in DEA. *Annals of Operations Research*, 288(1), 363–390. <https://doi.org/10.1007/s10479-019-03486-7>
- [11] Wu, J., Chu, J., Sun, J., & Zhu, Q. (2016). DEA cross-efficiency evaluation based on Pareto improvement. *European Journal of Operational Research*, 248(2), 571–579. <https://doi.org/10.1016/J.EJOR.2015.07.042>
- [12] Jiang, S., & Yang, S. (2017). A strength pareto evolutionary algorithm based on reference direction for multiobjective and many-objective optimization. *IEEE Transactions on Evolutionary Computation*, 21(3), 329–346. <https://doi.org/10.1109/TEVC.2016.2592479>

## Machine Learning for Predictive Modelling of Hydrogen Production from Biomass Gasification

**Kitti Kamolram<sup>1</sup>, Kanawat Tariyo<sup>1</sup>, and Phantisa Limleamthong<sup>1,\*</sup>**

<sup>1</sup> Department of Chemical Engineering, Faculty of Engineering, Kasetsart University, Bangkok 10900, Thailand  
E-mail: \*phantisa.l@ku.th

### Abstract

Biomass gasification has been studied widely as one of the most suitable approaches to recover energy from biomass feedstocks. However, the process typically relies on a complex mix of interacting variables, traditional models such as thermodynamic equilibrium and kinetics often struggle to achieve an accurate prediction. This research, therefore, focuses on a more powerful alternative that can handle complex input-output relationships, i.e., machine learning techniques, to develop predictive models of syngas from biomass gasification, including Hydrogen. The inputs of machine learning models include different key variables affecting product yield which cover different feedstocks and operating conditions, while the effect of cross-validation was also explored. The results showed that the most accurate model for hydrogen prediction was the Gradient Boosting Regressor, having the coefficient of determination or an R-squared of 0.9576 with 10-fold cross-validation. It can be observed that the model with cross-validation exhibited a lower performance than the model without cross-validation. This could be attributed to the step of hyperparameter tuning with cross-validation which gives a more generalized set of hyperparameters that leads to a slightly less accurate model but could be more reliable to handle unseen data. SHapley Additive exPlanations analysis was implemented to the highest performance model to determine the important factors influencing the gasification process. It was found that gasifying agents are the most influential factor for hydrogen production. This information can be used as a valuable guideline for further process optimization.

**Keywords:** Biomass gasification; Hydrogen; Machine learning; K-fold cross-validation; SHapley Additive exPlanation analysis

### 1. Introduction

The world is actively seeking renewable energy alternatives due to the eventual depletion of non-renewable sources like oil, gas, coal, and nuclear energy. Renewable energy, including hydroelectricity, wind, solar, geothermal, biomass, and others, is favored for its environmentally friendly nature, aiming to reduce greenhouse gas emissions and combat climate change. Biomass, derived from organic materials like plants or animal waste, serves as a renewable energy source, contributing to sustainable development by allowing the growth of new biomass.

Thailand, with a strong agricultural sector, possesses substantial biomass resources that can be utilized for energy production. The extensive agricultural land, around 40% of the country's area, provides a significant platform for biomass production [1]. As the population grows, there has been a rising demand for agricultural land, emphasizing the importance of sustainable practices.



Converting biomass into energy can be achieved through various technologies. Gasification is one of the most common thermochemical processes, which transforms biomass into usable fuels or chemicals, with H<sub>2</sub> being a significant product. H<sub>2</sub>, a green fuel with high heating value, is environmentally friendly and holds potential for transportation and electricity generation. The accurate prediction of H<sub>2</sub> production from biomass gasification is crucial for effective utilization.

The prediction of syngas products from biomass gasification involves complex tasks influenced by multiple variables. Traditional models, such as thermodynamic equilibrium and kinetic models, have been complemented by modern alternatives like machine learning. Ascher et al. [2] have developed a high-performance predictive model of H<sub>2</sub> from biomass gasification using an Artificial Neural Network (ANN). However, besides the neural-network-based model, other different types of machine learning algorithms, e.g., Extra Trees, Multi-layer Perceptron, Gradient Boosting, and K-nearest neighbors, have not yet been explored particularly for this application.

Thus, this study aims to seek the highly accurate machine learning model for predicting H<sub>2</sub> production from biomass gasification by investigating various forementioned machine learning techniques. Here, we also studied the effect of K-fold Cross-validation on the models' performance. Using various types of feedstocks and operating conditions, the models consider other important factors such as particle size, proximate and ultimate analysis components, temperature, and steam-to-biomass ratio. SHAP analysis was employed to illustrate the relationships among various variables and observe how these variables affect the generation of H<sub>2</sub> gas. This analysis helps to visualize the impact of different variables on the occurrence of H<sub>2</sub> gas and understand their contributions.

## 2. Materials and Methods

### 2.1 Data collection and description of dataset

A dataset of 408 samples involving different types of biomass feedstocks and reactor conditions was collected from various literatures, i.e., plastic with bubbling fluidized-bed reactor [3], different types of biomass feedstocks (including woody biomass, herbaceous biomass, sewage sludge, municipal solid waste, plastics, etc.) with downdraft and fluidized-bed reactor [4-6], municipal solid waste with horizontal reactor [7]. The input variables include the information of raw materials, covering the ultimate analysis, i.e., carbon, hydrogen, nitrogen, sulfur, and oxygen, and the proximate analysis, i.e., volatile matter, moisture, ash, and fixed carbon. Data on other operational parameters include those related to the characters of feedstock, i.e., feed type), feed shapes, particle sizes, low heating values, as well as the operating conditions, i.e., temperature, pressure, residence time, steam/biomass ratio, equivalency ratio, gasifying agent, reactor types, bed material, catalyst, and scale of operation. The output variables consist of the percent volume of syngas produced, i.e., H<sub>2</sub> and CO<sub>2</sub>.

### 2.2 Data pre-treatment

In the machine learning procedure, data pre-treatment is the most time-consuming process in order to meticulously prepare a completed and high-quality dataset for model development. There are various steps needed to conduct as follows:

### 2.2.1 Dealing with missing data

The data collected from various literature may suffer from incompleteness or missing data. Before using the data for training and testing purposes, data replacement must be completed to fill in the missing information to prepare a completed dataset for all selected variables. In this research, missing data was replaced with the median value since the collected data does not follow a normal distribution. Therefore, substituting with the median is an appropriate approach to fill in missing information without causing substantial changes to the overall data distribution.

### 2.2.2 One-hot encoding

When there are categorical variables involved in the machine learning models, there is a clear need to convert these variables numerically to improve the prediction accuracy of the models. One-hot encoding is often used to serve this task by creating a binary column for each category and assigning the values of 1 or 0 to each column representing the selection and no selection for each category, respectively.

### 2.2.3 Data normalization

The order of magnitude in the numeric values of some variables usually have significant variability, the data normalization is, therefore, an essential step to standardize the scale of these numerical features, ensuring consistency of the model's weights and biases. This step also accelerates the learning process by facilitating faster convergence of machine learning algorithms and enhancing model performance and training stability. In this study, Min-Max scaling was employed to normalize the data, bringing all variables within the range of 0 and 1.

## 2.3 Exploratory Data Analysis (EDA)

To facilitate the understanding of the underlying relationship among various input variables, the Pearson correlation coefficient (PCC) was utilized to assess the linear relationship between two variables. It is a normalized measure, ranging from -1 to 1, calculated as the ratio of their covariance to the product of their standard deviations. However, it solely captures linear correlations and overlooks other relationship types.

## 2.4 Model development

Multiple machine learning models, including Extra Trees, Gradient Boosting Regressor, Multilayer Perceptron, and K-Nearest Neighbors, were studied and developed to predict H<sub>2</sub> and CO<sub>2</sub> production. To begin with, the dataset was split into two separate sets with a ratio of 70:30 for a training set and a testing set (unseen data), respectively. The training dataset was divided into K-fold corresponding to 5-fold and 10-fold cross-validation cases, before passing through the model training step which involves the tuning of the model's hyperparameter through Bayesian algorithm. Then, the trained models were tested against the unseen data (test dataset) to assess their predictive performance, through the use of different performance metrics, i.e., the coefficient of determination (R<sup>2</sup>), mean absolute error (MAE), and mean squared error (MSE). The objective was to find the most suitable and accurate model for predicting the H<sub>2</sub> and CO<sub>2</sub> production. The selected prediction model will go through SHAP value analysis to analyze important factors affecting H<sub>2</sub> and CO<sub>2</sub> production.

The following machine learning procedure was carried out in the Python programming language version 3.11.

### 3. Results and Discussion

Before the collection of datasets was used for model development, it was pre-treated by filling in the missing data in some variables as mentioned earlier. The data has been categorized into numerical and categorical types. Using a one-hot encoder, categorical variables were transformed into numerical variables, which are more usable by the models. On the other hand, numerical variables were normalized to be within the same range, between 0 and 1. The step of EDA was done afterward to understand linear relationships between each numerical input variable through the creation of a Pearson correlation matrix. This matrix helps in eliminating variables with high correlations. The remaining variables are used to build a predictive model for further analysis. The Pearson correlation matrix for each pair of input variables was calculated and illustrated in Fig. 1.

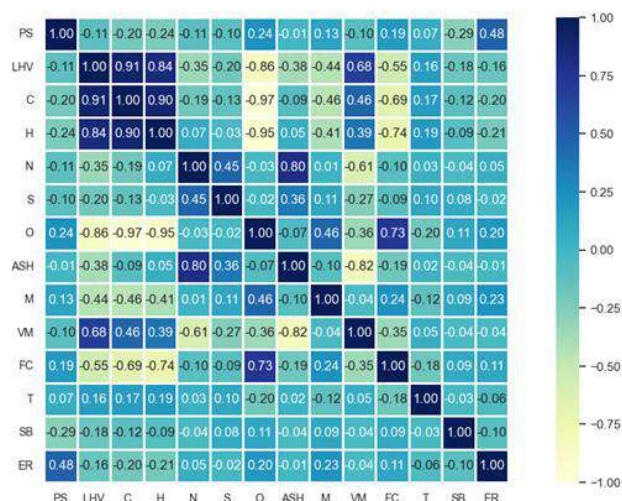


Fig. 1 Correlation matrix for the following continuous input variables: Particle size (PS), Lower heating value (LHV), Carbon (C), Hydrogen (H), Nitrogen (N), Sulphur (S), Oxygen (O), Ash (ASH), Moisture (M), Volatile matter (VM), Fixed carbon (FC), Temperature (T), Steam-to-biomass ratio (SB), Equivalence Ratio (ER)

The Pearson correlation coefficient ( $r$ ) assesses the strength and direction of a linear relationship between two variables. In technical terms, a positive  $r$  (close to 1) indicates a strong positive relationship, meaning that as one variable increases, the other tends to increase. Conversely, a negative  $r$  (close to -1) indicates a strong negative relationship, where an increase in one variable is associated with a decrease in the other. When  $r$  is close to 0, there is little to no linear relationship. In this experiment, variables with correlation coefficients greater than 0.6 or less than -0.6 will be excluded. This exclusion applies to variables such as LHV, N, O, FC, and VM, which exhibit a strong relationship in the same direction as other important variables. The goal is to improve the efficiency and accuracy of the model while reducing complexity in prediction.

Subsequently, the remaining variables are used to create models, including Extra Trees, Gradient Boosting, K-nearest neighbors (KNN), 1-hidden-layer MLP, and 2-hidden-layer MLP,

with both cross-validation and no cross-validation. The performance of these models is compared based on various performance indicators such as  $R^2$ , MSE, MAE, and the runtime for each model. The results are presented in Table 1 and Table 2.

Table 1. Summary of performance evaluation of a test set of Extra trees and Gradient boosting model for syngas  $H_2$

Indicator	Extra trees			Gradient Boosting		
	No CV	5-fold CV	10-fold CV	No CV	5-fold CV	10-fold CV
$R^2$	0.9597	0.9583	0.9536	0.9687	0.9534	0.9576
MSE	0.0019	0.002	0.0022	0.0015	0.0022	0.0021
MAE	0.0259	0.0273	0.0294	0.242	0.0294	0.028
Time (s)	85.29	137.03	232.67	86.06	92.34	100.78

Table 2. Summary of performance evaluation of a test set of KNN and MLP model for syngas  $H_2$

Indicator	KNN			1-hidden-layer MLP			2-hidden-layer MLP		
	No CV	5-fold CV	10-fold CV	No CV	5-fold CV	10-fold CV	No CV	5-fold CV	10-fold CV
$R^2$	0.9486	0.942	0.9486	0.8767	0.8752	0.8421	0.8852	0.8778	0.8542
MSE	0.0025	0.0028	0.0025	0.0059	0.006	0.0075	0.0055	0.0058	0.007
MAE	0.0304	0.0386	0.0304	0.0593	0.0586	0.0668	0.056	0.0594	0.066
Time (s)	45.45	85.49	121.7	51.68	104.2	162.7	76.13	66.7	74.34

Given the necessity of utilizing the model for predicting unseen data, employing cross-validation becomes crucial. A model with cross-validation is adept at handling external data the model has not encountered before. Comparing the results in Tables 1 and Table 2, the 10-fold cross-validation model displayed  $R^2$  values different from both the 5-fold and no cross-validation models, though by a very small difference. Therefore, for the purpose of deploying the model to predict unseen data, the decision was to favor the 10-fold cross-validation model due to its slightly superior performance.

After evaluating and comparing the performance of all five machine learning models with 10-fold cross-validation, it is evident that the gradient-boosting model exhibits the best performance. This is reflected in its  $R^2$  value of 0.9576, MAE of 0.028, and MSE of 0.0021. In comparison to the other models (Extra trees, K-nearest neighbors, 1-hidden-layer Multi-layer Perceptron, 2-hidden-layer Multi-layer Perceptron), which have  $R^2$  values of 0.9486, 0.8421, 0.8542, and the MAE values are 0.0294, 0.0304, 0.0668, 0.066, while the MSE values are 0.0022, 0.0025, 0.0075, 0.007, respectively. Therefore, Gradient Boosting outperforms the other models in terms of predictive accuracy.

The overall process is more time-consuming when using cross-validation, as observed in Table 1. and Table 2. This occurs because the model consistently divides the data into smaller groups more frequently during testing, leading to increased processing time and a reduction in the  $R^2$  value. However, a model with cross-validation is better at handling new, unseen data, even though it requires more time for each run.

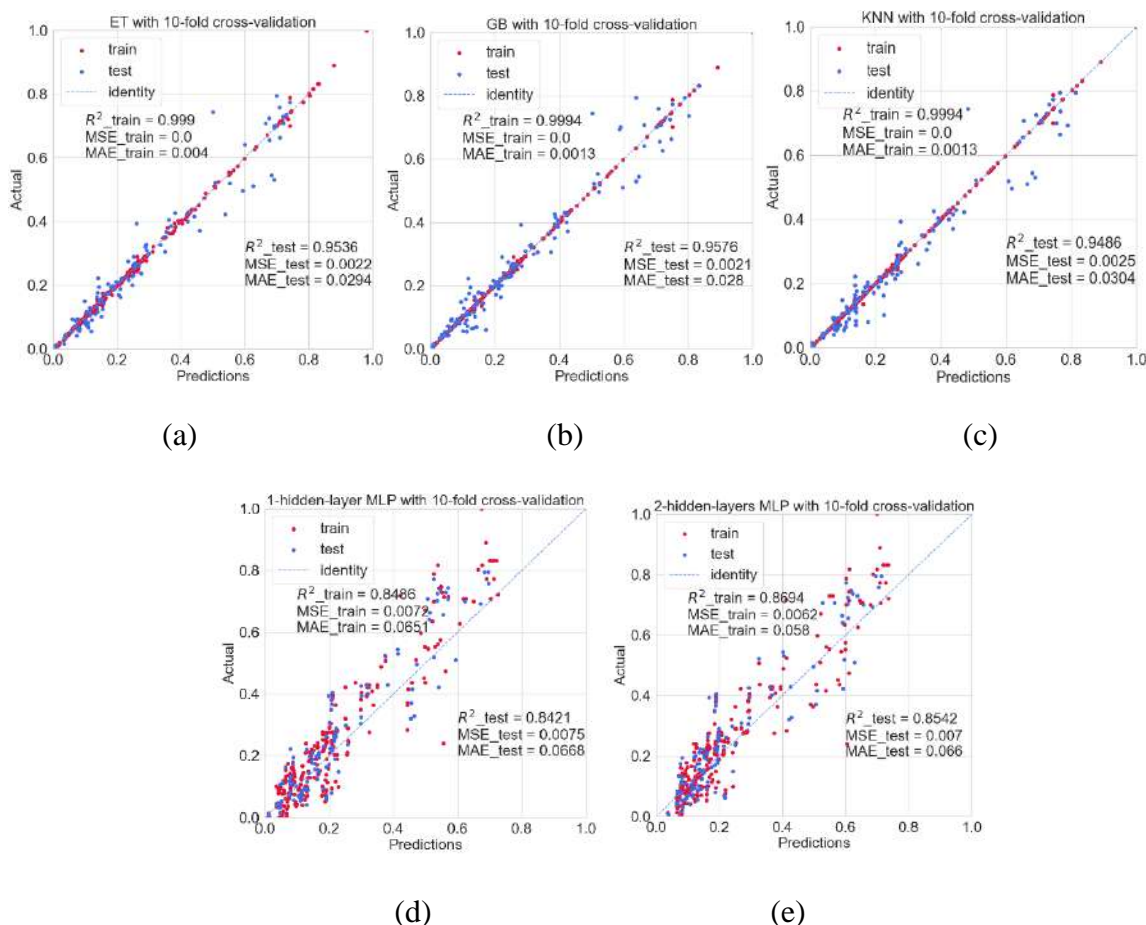


Fig 2. Distribution of predictions of difference models: (a) Extra trees (b) Gradient boosting (c) K-nearest neighbors (KNN) (d) 1-hidden-layer Multi-layer perceptron (e) 2-hidden-layer Multi-layer perceptron with 10-fold cross-validation for  $H_2$  prediction.

In summary, training the model, one can observe that the  $R^2$  of 3 models are closely comparable, including Extra tree, Gradient Boosting, and K-nearest neighbors. However, the performance of the model Multi-layer perceptron 1 and 2 hidden-layer significantly declines, as illustrated in Fig2(a), Fig2(b), Fig2(c), Fig2(d), and Fig2(e). This is attributed to the fact that Model Multi-layer perceptron requires careful selection of hidden layer values to ensure an appropriate fit for the model. So, the chosen prediction model with the highest accuracy is Gradient Boosting with 10-fold cross-validation, featuring the highest  $R^2$  value (0.9576), as illustrated in Fig. 2(a), when comparing the performance of the five different types of models, which can be observed for graphs comparison in Fig. 2(b), Fig. 2(c), Fig. 2(d), and Fig. 2(e). Despite not being the fastest in terms of runtime due to its higher precision, this model demonstrates superior efficiency. The optimal balance between a high  $R^2$  and a runtime that, while not the lowest, is reasonable, positions the Gradient Boosting model as the most effective

choice, considering both high precision and operational efficiency, for use in predicting H<sub>2</sub> and CO<sub>2</sub> emissions.

The analysis utilized the Gradient Boosting model, identified as the best-performing, and applied SHAP analysis to understand the relationship between input variables and model predictions. This exploration aimed to reveal the significance and impact of each input feature on the model's predictions. The outcomes depicted in Fig. 3(a) for H<sub>2</sub> prediction models offer valuable insights for further research on process optimization. From Fig. 3(a), Steam is the most influential feature for H<sub>2</sub> prediction. Since steam is a gasifying agent in the process that consists of a high ratio of Hydrogen, it seems reasonable that the steam feature can be influential to the model. The second-rank feature was Hydrogen content, which is indeed the main component for a syngas H<sub>2</sub> to be produced, followed by Sulphur which may seem to be unexpected. Low Sulphur content does not directly increase H<sub>2</sub> production. However, it may increase the composition of H<sub>2</sub>, which directly increases H<sub>2</sub> production. On the other hand, the high Sulphur composition can increase the chance for Sulphur compounds, such as H<sub>2</sub>S, to be formed and reduce syngas production, or even cause catalyst poisoning. Air and temperature can also be influential to H<sub>2</sub> production since air is also a gasifying agent like steam, and temperature is crucial as gasification needs to be operated within a specific range of temperature that affects the reaction between biomass and gasifying agent.

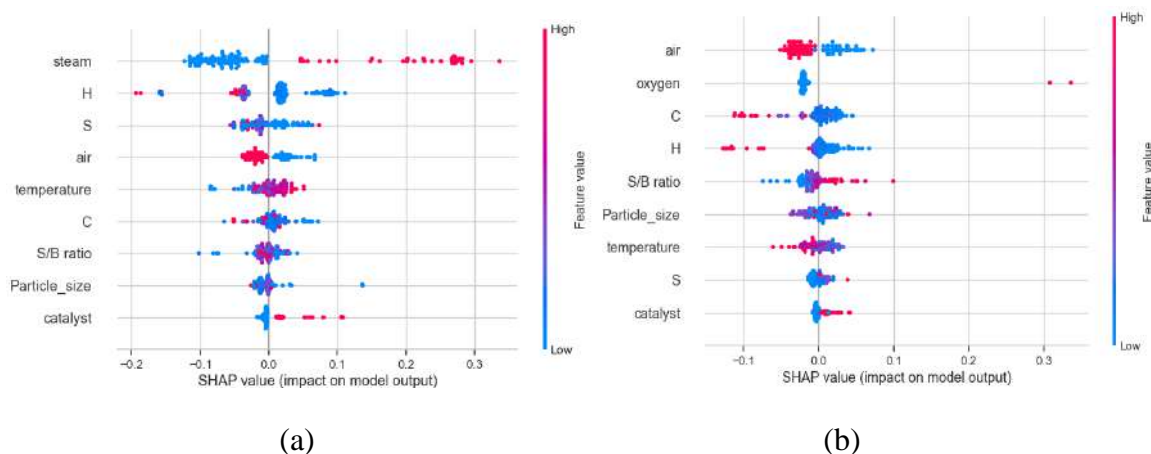


Fig 3. (a) The results of SHAP analysis of H<sub>2</sub> prediction model, (b) The results of SHAP analysis of CO<sub>2</sub> prediction model

Figure 3(b) suggests that Air as a gasifying agent influences the output of the CO<sub>2</sub> prediction model the most. Not only does it lead to the occurrence of a gasification reaction, but also, consists of some portion of CO<sub>2</sub>, thereby increasing the composition of CO<sub>2</sub> directly. This is followed by Oxygen as a gasifying agent and composition of Carbon in biomass which can promote the formation of CO<sub>2</sub> in the process.

#### 4. Conclusion

Various machine-learning methods, namely, Extra Trees, Gradient Boosting, K-nearest neighbors, and Multi-layer perceptron, were studied for predicting syngas H<sub>2</sub> and CO<sub>2</sub> production from biomass gasification. For the H<sub>2</sub> model, with 10-fold cross-validations, Gradient Boosting had the highest R<sup>2</sup> (0.9576), followed by Extra Trees (0.9536), K-nearest

neighbors (0.9486), and Multilayer perceptron with 1 and 2 hidden layers ( $R^2 = 0.8421$  and  $0.8542$ ). Results can be attributed to cross-validated hyperparameter tuning, providing a more generalized set. Although accuracy slightly decreased, the model became more reliable for unseen data. Our best model shows even better accuracy than the existing literature [8], which utilized the ANN model to predict hydrogen generation from biomass and waste gasification processes with the  $R^2$  of 0.9310. In the case of the  $CO_2$  prediction model, the model using Gradient Boosting with 10-fold cross-validation achieved an  $R^2$  of 0.899. SHAP value analysis identified steam as the most influential factor for  $H_2$  production, followed by Hydrogen composition in the feedstock. For the  $CO_2$  model, the air gasifying agent ranked highest, followed by the oxygen gasifying agent carbon content in biomass. In summary, the machine learning models developed in this research work are highly accurate in predicting  $H_2$  and  $CO_2$  production from biomass gasification. These models can be further integrated with multi-objective optimization to find the optimal operating conditions aiming toward maximizing  $H_2$  and minimizing  $CO_2$  yield for biomass gasification processes.

## 5. References

- [1] Sajjakulnukit, B., & Verapong, P. (2003). Sustainable biomass production for energy in Thailand. *Biomass and Bioenergy*, 25(5), 557–570. [https://doi.org/10.1016/S0961-9534\(03\)00091-6](https://doi.org/10.1016/S0961-9534(03)00091-6)
- [2] Ascher, S., Sloan, W., Watson, I., & You, S. (2022). A comprehensive artificial neural network model for gasification process prediction. *Applied Energy*, 320(April). <https://doi.org/10.1016/j.apenergy.2022.119289>
- [3] Arena, U., Zaccariello, L., & Mastellone, M. L. (2009). Tar removal during the fluidized bed gasification of plastic waste. *Waste Management*, 29(2), 783–791. <https://doi.org/10.1016/j.wasman.2008.05.010>
- [4] Channiwala, S. A., & Parikh, P. P. (2002). A unified correlation for estimating HHV of solid, liquid and gaseous fuels. *Fuel*, 81(8), 1051–1063. [https://doi.org/10.1016/S0016-2361\(01\)00131-4](https://doi.org/10.1016/S0016-2361(01)00131-4)
- [5] Demirbaş, A. (1997). Calculation of higher heating values of biomass fuels. *Fuel*, 76(5), 431–434. [https://doi.org/10.1016/S0016-2361\(97\)85520-2](https://doi.org/10.1016/S0016-2361(97)85520-2)
- [6] Jenkins, B. M., Baxter, L. L., Miles, T. R., & Miles, T. R. (1998). Combustion properties of biomass. *Fuel Processing Technology*, 54(1–3), 17–46. [https://doi.org/10.1016/S0378-3820\(97\)00059-3](https://doi.org/10.1016/S0378-3820(97)00059-3)
- [7] Jamro, I. A., Raheem, A., Khoso, S., Baloch, H. A., Kumar, A., Chen, G., Bhagat, W. A., Wenga, T., & Ma, W. (2023). Investigation of enhanced  $H_2$  production from municipal solid waste gasification via artificial neural network with data on tar compounds. *Journal of Environmental Management*, 328(August 2022). <https://doi.org/10.1016/j.jenvman.2022.117014>
- [8] Ascher, S., Sloan, W., Watson, I., & You, S. (2022). A comprehensive artificial neural network model for gasification process prediction (p. 7). *Applied Energy*, 5, 320(April).

## Transdermal Drug Delivery System of Hesperidin-Loaded Cubosomes for Anti-Aging

**Thiyada Chankhiao and Somnuk Jarudilokkul\***

Department of Chemical Engineering, King Mongkut's University of Technology Thonburi  
E-mail: \* somnuk.jar@kmutt.ac.th

### Abstract

Skin, being the largest external organ of humans, is constantly exposed to the external environment. Consequently, it is highly susceptible to damage from external factors. Such damage affects the skin at the molecular level, causing signs of aging, leading to diseases, and resulting in premature skin aging. To combat this phenomenon, researchers have explored the potential of hesperidin as an antioxidant agent. Hesperidin is distinguished by its high capacity to effectively scavenge reactive oxygen species, its safety for the skin, and its affordability. However, hesperidin faces certain challenges that can be overcome with the use of an efficient carrier system like Cubosomes. These self-assembled inverted bicontinuous cubic nanoparticles, ranging from 100 to 500 nm in size, offer an ideal solution. This study aimed to determine the optimal formulation ratio of GMO (Glyceryl Monooleate) and Poloxamer 407 for loading the maximum amount of hesperidin, thereby maximizing its anti-aging effect on the skin. The study revealed that a compromise ratio of 4.5% GMO to 0.5% Poloxamer 407 achieved the highest encapsulation of hesperidin, with an impressive entrapment efficiency rate of 94% and a particle size of 207.4 nm. The formulation also demonstrated the highest drug release of 88.98%, along with 30% antioxidant activity.

**Keywords:** Cubosomes; Hesperidin; Transdermal Drug Delivery; Skin; Anti-aging

### 1. Introduction

Skin is the largest organ and serves as an excellent model for studying aging, as it is affected by both intrinsic and extrinsic environmental factors. These aging factors stimulate the production of reactive oxygen species (ROS), which are at the root of various diseases. Therefore, to minimize skin damage, choosing natural antioxidants is considered a safe approach to protect the skin from aging conditions. Hesperidin, a natural flavonoid found abundantly in the peel of citrus fruits, has the potential to scavenge free radicals and ROS, which are associated with cell damage and aging [1-3]. Due to its low cost, wide availability, and exceptional safety, hesperidin is considered for use against a variety of diseases, including skin cancer, wound healing, anti-inflammatory conditions, UV protection, and anti-microbial applications. However, the limited water solubility, poor bioavailability, and environmental sensitivity of hesperidin are bottlenecks for its use in transdermal drug delivery systems [3].

In recent years, the approaches to drug delivery systems utilizing nanoparticles include liposomes, ethosomes, and transethosomes [4]. There are, however, very few works using cubosomes. Cubosomes have emerged as a prominent biocompatible nanocarrier for drug delivery. The bicontinuous lipid nanostructure and large surface area of cubosomes allow them to load substantial quantities of hydrophilic, hydrophobic, and amphiphilic drugs. Additionally, the process to form cubosomes is straightforward; it requires only the mixing of



lipid, stabilizer, and hydrotrope with either high or low energy input. Cubosomes offer many advantages, including being non-toxic, biocompatible, possessing excellent bioadhesive properties, thermodynamic stability, targeted release, and controlled release capabilities. Moreover, due to their inner structure's similarity to the stratum corneum, cubosomes facilitate the entry of medications through the skin epidermis. Therefore, cubosomes represent a promising nanocarrier in this study for delivering hesperidin through the skin. This study aims to determine the optimal ratio of lipid and stabilizer to maximize the loading of hesperidin in cubosomes, to study the release of hesperidin, and to evaluate the activity of the released hesperidin.

## 2. Materials and Methods

Glyceryl monooleate (GMO) was received as a gift sample from Kao Industrial (Thailand) Co., Ltd (Bangkok, Thailand). Hesperidin was purchased from Thermo Fisher Scientific (Thailand) Co., Ltd (Bangkok, Thailand). Poloxamer 407 was procured from Sigma-Aldrich (St. Louis, MO, USA). All the chemicals and reagents used in this study were of analytical grade.

### 2.1 Preparation of Cubosomes

The emulsification method adopted to prepare cubosomes, as reported by Khan et al. [5], is briefly described as follows: GMO and Poloxamer 407 are mixed and melted in a water bath at 60°C. Forty-five µM of hesperidin is added to this mixture and stirred at 1400-1500 rpm until completely dissolved. Preheated distilled water (70°C) is then gradually added while stirring. The solution is allowed to equilibrate for a day at room temperature. To disturb the system, the solution is stirred at 1400-1500 rpm for 2 hours at room temperature. The cubosomes are obtained by homogenizing at 3200 rpm at 60°C for 1 minute. The composition of various batches of hesperidin-loaded cubosomes is presented in Table 2.1.

Table 2.1 Composition of hesperidin-loaded cubosomes

No	GMO (%)	Poloxamer 407 (%)	Ratio
1	2.5	0.5	5 : 1
2	3.5	0.5	7 : 1
3	4.5	0.5	9 : 1
4	2.5	1.0	2.5 : 1
5	3.5	1.0	3.5 : 1
6	4.5	1.0	4.5 : 1
7	2.5	1.5	1.7 : 1
8	3.5	1.5	2.3 : 1
9	4.5	1.5	3 : 1

## 2.2 Characterization of Cubosomes

Characterization of cubosomes is assessed via drug entrapment efficiency, particle size analysis, polydispersity index, FTIR, and drug release study.

## 2.3 Drug entrapment efficiency

The entrapment efficiency (%EE) of the prepared cubosomal formulation was determined using the centrifugation method [6]. Cubosomes were centrifuged at 1,400 rpm for 30 minutes at 4°C. The upper phase, obtained as the supernatant containing untrapped hesperidin, was separated and measured by a UV spectrophotometer at 284.5 nm against a phosphate buffer (pH 6.4). The amount of hesperidin entrapped in the cubosomes was determined by calculating the entrapment efficiency using Equation (1).

$$\%EE = \frac{[\text{Amount of added drug}] - [\text{Amount of un-entrapped drug}]}{[\text{Amount of added drug}]} \times 100 \quad (1)$$

## 2.4 Particle size analysis and polydispersity index

The average particle size and polydispersity index (PDI) were measured using a Malvern Zetasizer at 25°C. The sample was placed in a polystyrene cuvette, and the readings were taken at an angle of 90 degrees.

## 2.5 Characteristics of hesperidin

The determination of hesperidin in hesperidin-loaded cubosomes was carried out using FTIR, focusing on the middle infrared region from 400 to 4000 cm<sup>-1</sup>. The results were then compared to the peaks of pure hesperidin and blank cubosomes.

## 2.6 In vitro drug release study

The release studies of hesperidin-loaded cubosomes were performed by adding 1 mL of the cubosomes into 50 mL of phosphate-buffered saline (PBS) at pH 7.4 containing 1% Tween 80. The buffer solution containing the sample was maintained at 37°C and stirred at 50 rpm using a magnetic stirrer. One mL of the buffer solution was withdrawn and replaced with an equal amount of fresh dissolution medium at intervals of 5, 10, 15, 20, 25, 30, 45, 60, 120, and 180 minutes. The hesperidin in the buffer samples could be quantified using UV-vis spectroscopy at 284.5 nm.

# 3. Results and Discussion

## 3.1 Particle size analysis, PDI, and Zeta potential

Dynamic light scattering was used for the particle size analysis. According to Table 3.1, the mean particle size ranged from 200 nm to 227 nm. The results showed that as the percentage of GMO and Poloxamer ratio increased from 3.5 to 9, with an increase in the concentration of GMO, the particle size also increased. This increase in particle size might be due to the larger viscosity of GMO obstructing the emulsification of hesperidin-loaded cubosomes. Furthermore, a direct correlation between the effect of Poloxamer 407 on particle size and PDI was observed. The particle size decreased with an increase in the concentration (%) of Poloxamer 407. This is attributed to the stabilizer's ability, where adding a higher amount of Poloxamer 407 resulted in a smaller size of hesperidin-loaded cubosomes since the surface tension was reduced during the emulsification process. Nonetheless, the particle size (< 500

nm) and PDI (< 1.00) values of all batches of hesperidin-loaded cubosomes were within acceptable ranges and can be used for transdermal applications without concern of any aggregation.

The zeta potential is important for confirming stability against aggregation over time. The zeta potential results for all batches were displayed in Table 3.1. The data showed that the zeta potential of all batches had values lower than -30 mV, which indicates that the particles are stable against aggregation.

Table 3.1 Composition and characteristics of hesperidin-loaded in cubosomes.

No.	GMO (%)	Poloxamer 407 (%)	Ratio	Particle size (nm)	Polydispersity Index	Zeta potential (mV)	EE (%)
1	2.5	0.5	5 : 1	207 ± 7.95	0.27 ± 0.09	-51.03 ± 0.19	91.33 ± 2.32
2	3.5	0.5	7 : 1	211.1 ± 8.57	0.15 ± 0.15	-53.76 ± 0.34	91.66 ± 0.80
3	4.5	0.5	9 : 1	227.4 ± 10.78	0.26 ± 0.03	-49.76 ± 0.28	94.03 ± 1.36
4	2.5	1	2.5 : 1	200.1 ± 7.59	0.52 ± 0.07	-37.20 ± 0.44	90.41 ± 0.98
5	3.5	1	3.5 : 1	213.8 ± 2.90	0.17 ± 0.19	-39.40 ± 0.12	91.94 ± 1.65
6	4.5	1	4.5 : 1	229.0 ± 2.40	0.27 ± 0.17	-44.36 ± 0.26	92.62 ± 3.48
7	2.5	1.5	1.7 : 1	200.6 ± 3.15	0.34 ± 0.21	-33.56 ± 0.28	90.88 ± 0.63
8	3.5	1.5	2.3 : 1	215.9 ± 7.21	0.34 ± 0.01	-39.56 ± 0.22	91.70 ± 3.21
9	4.5	1.5	3 : 1	218.2 ± 7.41	0.29 ± 0.26	-38.76 ± 0.26	92.66 ± 0.72

### 3.2 Drug Entrapment Efficiency

The entrapment efficiency of hesperidin-loaded cubosomes was found to be in the range of 90.41% to 94.03%, as shown in Table 3.1. It was clearly observed that sample no.3 exhibited the highest %EE, along with a small particle size and PDI value. Moreover, every batch provided an %EE of more than 90%, which is considered a high percentage. It is not necessary to achieve an extremely high %EE; in other words, the presence of free drug could also enhance the penetration of the drug through the skin [7-8]. In comparison, the hesperidin-loaded transethosomes formulation, which has a spherical shape, exhibited a vesicle size of 178.98 nm, a PDI of 0.259, a zeta potential of -31.14 mV, and an entrapment efficiency (%EE) of 89.51%. [9]

### 3.3 Characteristics of Hesperidin

The FTIR spectra of pure hesperidin, blank cubosomes, and hesperidin-loaded cubosomes are presented in Figure 3.1. The FTIR spectra of pure hesperidin exhibited characteristic bands due to the presence of different functional groups; for instance, 3325.64, 2946.70, 1656.55,

1452.14, 1023.05  $\text{cm}^{-1}$ , which could be attributed to O-H stretching vibration, C-H stretching, C=O stretching, C=C stretching, and C-O stretching, respectively. The absorbance band at 3323.71  $\text{cm}^{-1}$  is due to the hydroxyl group O-H stretching vibration. The band at 1642.09  $\text{cm}^{-1}$  corresponds to carbonyl C=O stretching. The band at 1459.85  $\text{cm}^{-1}$  is attributed to the aromatic C=C stretch, and the aromatic C-O stretch at 1024.98  $\text{cm}^{-1}$ . The differing characteristic peaks between hesperidin-loaded cubosomes and pure hesperidin are due to the chemical interaction between pure hesperidin and the cubosome matrix. Moreover, the characteristic band of the hydroxyl group at 3500 – 3700  $\text{cm}^{-1}$  in the blank cubosomes confirmed the successful conjugation in hesperidin-loaded cubosomes.

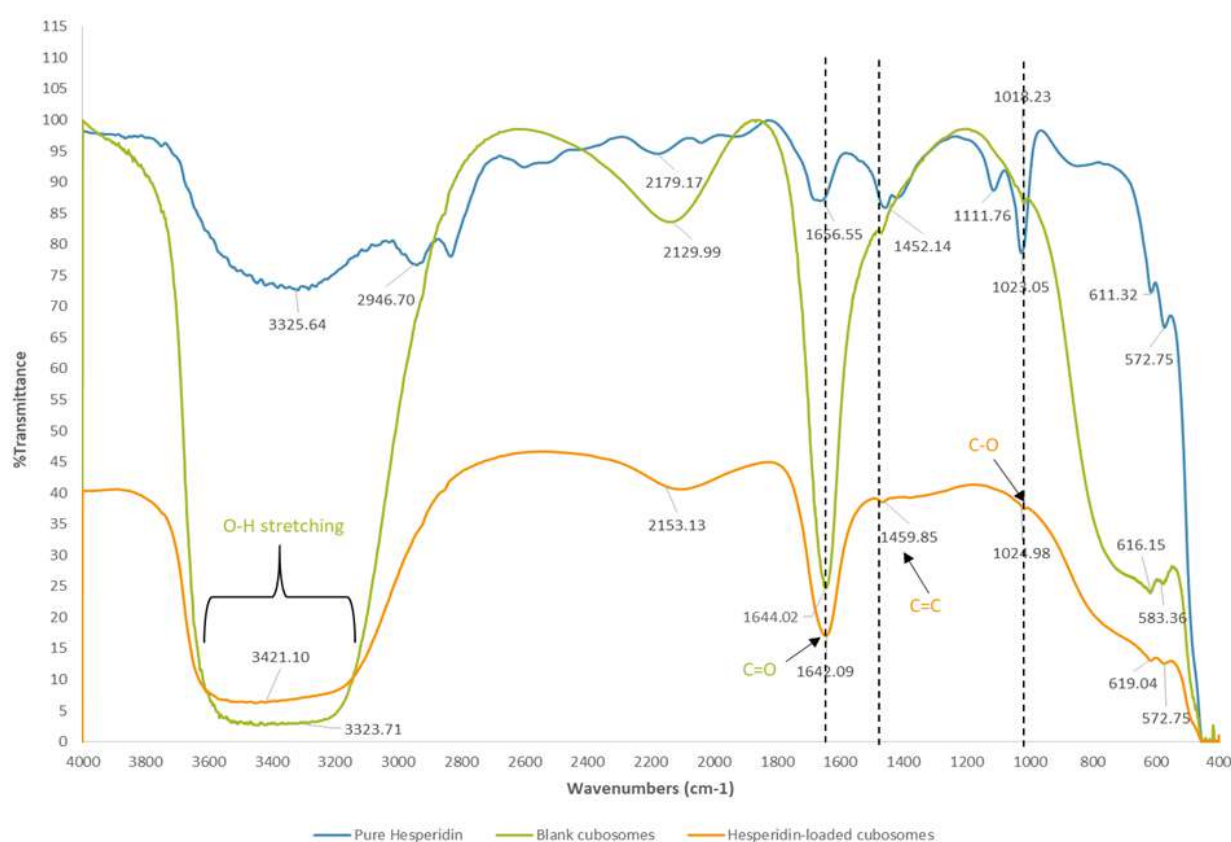


Figure 3.1 FTIR spectra of pure hesperidin, blank cubosomes, and hesperidin-loaded cubosomes.

### 3.4 In vitro drug release study

The study of drug release in vitro using Hesperidin loaded in cubosomes employs Phosphate Buffered Saline (PBS) with a pH value of 7.4 as the medium. This pH value is representative of the human body's overall pH as well as the pH of skin cells [10]. The study utilizes a

proportion acknowledged for having small particles and high efficacy in drug encapsulation. The release behavior of Hesperidin encapsulated within cubosomes is demonstrated in Figure 3.2, over a study duration of 3 hours, with sample collection at times 0, 5, 10, 15, 20, 25, 30, 45, 60, 120, and 180 minutes. Due to the structure of cubosomes, which includes hydrophobic regions (between the two layers' walls) and hydrophilic regions (the outer and inner walls), there is no initial drug release from the nano particles within the first 10 minutes because the dual-layered walls are relatively difficult to break down. After 15 minutes, the nano particles begin to release the drug more rapidly as the double-layered walls break down, allowing the large quantity of Hesperidin contained within the innermost part of the nanoparticles to be released quickly. Between 30 to 45 minutes, the drug release slows down gradually through diffusion, as the amount of Hesperidin begins to deplete, although some of the drug still remains adhered within the nanoparticles, allowing for a maximum release of 88.98%. This indicates that the cubosomes developed here are effective in slowly releasing Hesperidin from PBS with pH 7.4, ensuring that the skin receives a sufficiently concentrated dose of the drug. Therefore, the continuous drug delivery system of Hesperidin released is an efficient method for skin application, aligning with the study findings of Rajendra Jangde et al. [11].

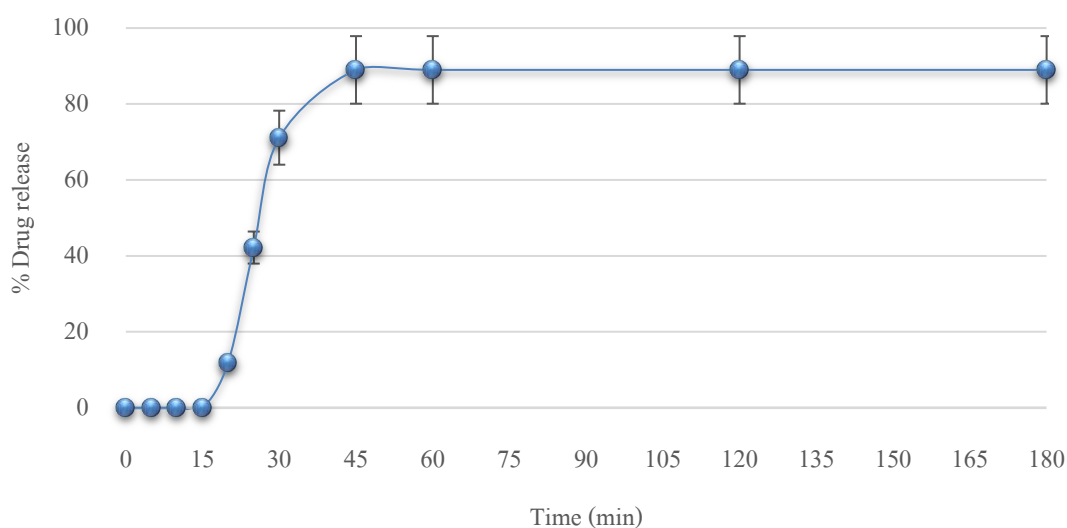


Figure 3.2 In vitro drug release profile of hesperidin-loaded cubosomes.

### 3.5 The ability to counteract free radicals

From the release study, the sample was then determined the DPPH activity. It was found that it can inhibit free radicals by 30%. This is due to the oxidants or free radicals in the body, known as reactive oxygen species (ROS), which can cause cellular damage. Conversely, ROS can also be beneficial to the body, especially playing an important role in the development of the response in wound healing. Therefore, it is crucial to maintain an appropriate balance between low and high levels of ROS. Having ROS at the lowest possible level can be beneficial in protecting tissues from infection and helping to heal wounds better. When ROS accumulates at higher levels, it can cause oxidation reactions in cells, leading to cell damage. Antioxidants are therefore essential to maintain the balance of ROS without necessarily eliminating the most ROS. Antioxidants are becoming popular for targeted use, as they help target the upper layers of the skin [12-14]. Therefore, Hesperidin in nanocubosome particles, with a 30% ability to inhibit free radicals, is suitable for use on the body's skin to reduce the accumulation of ROS.

### Conclusions

Hesperidin-loaded cubosomes achieved a high drug entrapment efficiency of 94%, and a particle size of 207.4 nm at a ratio of 9:1, %GMO:%Poloxamer 407. The PDI of the particles was less than 1 in every batch, showing the uniform dispersion of cubosomes in the solution. The FTIR results revealed the successful encapsulation and formation of hesperidin-loaded cubosomes. Finally, the release profile of hesperidin from the cubosomes displayed a burst release of 88.98% and an activity of 30%.

### References

- [1] Wilmsen, P.K., Spada, D.S., and Salvador, M. (2005) Antioxidant activity of the flavonoid hesperidin in chemical and biological systems, *J Agric Food Chem*, 53(12), 4757-61.
- [2] Sun, K., Xiang, L., Ishihara, S., Matsuura, A., Sakagami, Y. and Qi, J. (2012) Anti-aging effects of hesperidin on *Saccharomyces cerevisiae* via inhibition of reactive oxygen species and UTH1 gene expression, *Biosci Biotechnol Biochem*, 76(4): 640-645.
- [3] Ali, S.H., Sulaiman, G.M., Al-Halbosiy, M.M.F., Jabir, M.S., and Hameed A.H. (2019) Fabrication of hesperidin nanoparticles loaded by poly lactic co-Glycolic acid for improved therapeutic efficiency and cytotoxicity, *Artif Cells Nanomed Biotechnol*, 47(1): 378-394.
- [4] Abdallah, M.H.; Elghamry, H.A.; Khalifa, N.E.; Khojali, W.M.; Khafagy, E.S.; Shawky, S.; El-Horany, H.E.S.; El-Housiny, S. (2023) Development and Optimization of Erythromycin Loaded Transethosomes Cinnamon Oil Based Emulgel for Antimicrobial Efficiency. *Gels*, 9, 137-156.

- [5] Khan, S., Jain, P., Jain, S., Jain, R., Bhargava, S., and Jain, A. (2018) Topical Delivery of Erythromycin Through Cubosomes for Acne, *Pharm Nanotechnol*, 6(1), 38-47.
- [6] Sharma, R., Kaur, G., and Kapoor, D. (2015) Fluconazole Loaded Cubosomal Vesicles for Topical Delivery, *International Journal of Drug Development and Research*, 7(3), 32-41.
- [7] Rattanapak T., Young K., Rades T., and Hook S. (2012) Comparative study of liposomes, transfersomes, ethosomes and cubosomes for transcutaneous immunisation: characterization and in vitro skin penetration, *J. Pharm. Pharmacol.* 64, 1560–1569.
- [8] Verma D.D., Verma S., and Blume G. (2003) Liposomes increase skin penetration of entrapped and non-entrapped hydrophilic substances into human skin: a skin penetration and confocal laser scanning microscopy study, *Eur. J. Pharm. Biopharm.* 55, 271–277.
- [9] Perwez A., Mohd I., Samreen J., Ali A., and Zafrul H. (2023) Formulation and Characterization of Hesperidin-Loaded Transethosomal Gel for Dermal Delivery to Enhance Antibacterial Activity: Comprehension of In Vitro, Ex Vivo, and Dermatokinetic Analysis, *Gel*, 9, 791-814.
- [10] Gaohua L., Miao X. and Dou L. (2021) Crosstalk of physiological pH and chemical pKa under the umbrella of physiologically based pharmacokinetic modeling of drug absorption, distribution, metabolism, excretion, and toxicity, *Expert Opinion on Drug Metabolism & Toxicology*, 17(9), 1103-1124.
- [11] Rajendra J., Gamal O. E., Sulekha K., and Ram K.S. (2022), Hesperidin-Loaded Lipid Polymer Hybrid Nanoparticles for Topical Delivery of Bioactive Drugs, *Pharmaceuticals*, 15(2), 211.
- [12] Comino-Sanz, I.M., López-Franco, M.D., Castro, B., and Pancorbo-Hidalgo, P.L. (2021) The Role of Antioxidants on Wound Healing: A Review of the Current Evidence., *J. Clin. Med.*, 10(16), 3558.,
- [13] Zhao, R.Z., Jiang, S. Zhang, L., and Yu. Z.B. (2019) Mitochondrial electron transport chain, ROS generation and uncoupling (Review)., *Int. J. Mol. Med.*, 44, 3–15.
- [14] Cano, S.M., Lancel, S., Boulanger, E., and Nevier, R. (2018) Targeting Oxidative Stress and Mitochondrial Dysfunction in the Treatment of Impaired Wound Healing: A Systematic Review. *Antioxidants*, 7(8), 98.

## Travelling Salesman Problem Considering Traffic Data and IoTs for Smart Waste Collection System: Case Study of a University

<sup>1</sup>Hnin Sandar Lwin, <sup>2</sup>Saowanit Lekhavat, <sup>3</sup>Phantisa Limleamthong\*

<sup>1</sup>Master of Engineering Program in Sustainable Energy and Resources Engineering, Faculty of Engineering, Kasetsart University, Bangkok, 10900, Thailand

<sup>2</sup>School of Integrated Science, Kasetsart University, Bangkok, 10900, Thailand

<sup>3</sup>Department of Chemical Engineering, Faculty of Engineering, Kasetsart University, Bangkok, 10900, Thailand

E-mail: \*Phantisa.l@ku.th

### Abstract

The crucial way to protect the environment from bad smells and unsightly views from waste bins is collecting full waste bins in time as an efficient waste collection system. This research aims at developing a decision-support tool for smart waste collection system using real-time bin information from Internet of things (IoT) and suggesting the shortest route for waste collection vehicles at a university. Historical traffic data collected from Google Traffic Maps was used to define a rush hour period when the launching of collecting vehicles should be avoided. Geographic Information System – GIS and Travelling Salesman Problem were used to find the shortest path and a route sequence for different scenarios considering possible combination of locations to be collected. The result indicates that there were two rush hour periods consisting of around 1-2 hours during the morning work hours and 1-2 hours during the evening off-duty hours for the university closing and opening periods. The graduation ceremony event took much longer rush hour period covering almost the whole day except 3-4 PM for the commencement day. The results of the optimal route for collecting scenarios were grouped as they shared the same route pattern; however, the collecting sequences were different. This research provides useful pieces of information for further development of a decision-support tool for smart waste collection system.

**Keywords:** Geographic Information System; Travelling Salesman Problem; Vehicle Routing problem; waste collection system.

### 1. Introduction

Waste collection is a crucial part in waste management systems. In terms of regional data, waste collection rate of South Asia and the East Asia and Pacific were 44% and 71%, respectively according to the waste generation statistical data in 2016 [1]. Even though the expenditure on the waste collection and transportation were very high, the municipal authorities have still been facing the challenges to provide sufficient waste management service [2]. The integration of Internet of things (IoT) into the waste collection system will assist in monitoring the real-time conditions of smart bins which will foster the effectiveness of the waste management systems [3].

Ineffective and delayed waste collection system can lead to overflowing waste bins, which impact the environment. Improvement of waste collection system is a crucial process to minimize the resulting pollution for being clean environment and improve human health [1]. Previous researchers studied how to improve waste collection systems with different



approaches. The optimized dynamic collection routes were defined considering IoTs and the prioritization of bins using mathematical model were solved by different heuristic approaches [4, 5]. Ant colony optimization (VNS-ACO) algorithm and Travelling Salesman Problem were applied to examine optimal path exclusive of traffic condition [3]. Geographic Information System (GIS) approaches was used to designate the route sequence with minimum distance including traffic condition in [6] and the most cost-effective waste collection system without considering traffic condition was examined in [7, 8].

To the best of our knowledge, there is no research studying how to define rush hour to avoid traffic congestion and suggest the shortest route for waste collection trucks in the case of a university. The characteristics of waste collection system in a university is distinct from urban community areas, especially in terms of the scale of collection area, collection methods, types of waste and waste management system. Moreover, the community areas produce a significant amount of waste depending on large population density and complicated road patterns, and traffic conditions than the university. Therefore, the university area is an appropriate specific area worth an extensive investigation of the traffic pattern and the improvement of IoTs based waste collection system model.

This research, therefore, proposes a smart waste collection system based on the real-time data of waste bins level through IoTs by avoiding rush hour during collection periods. In addition, the shortest routes for the waste collection vehicles were suggested for various collecting scenarios to reduce the operating expenditure of solid waste management systems. Here, a university in Bangkok, Thailand, was used as a case study through the realistic implementation of geographical information and the practical availability of roads inside the university for different cases of the university activities.

## 2. Methodology

### 2.1 Designated process of waste collection system for smart waste bins

The proposed smart waste collection system for a university was originally designed as three main parts: 1) Defining rush hour and truck launching conditions, 2) Identification of the waste bins for collection and 3) Generating different collecting scenarios and calculating the appropriate shortest paths for each scenario.

First, the level of waste bins is checked using the data from the IoTs and the information is transferred to the decision support system. If the level of waste bin was over 80%, it was defined as a full waste bin. After that, the instant time is checked whether it is a rush hour or not in order to avoid the traffic congestion which will lead to longer waste collection periods and will intensify more traffic congestion to the community. When the time is a normal hour, the truck status will be set as “ready for launching” to collect the waste bins. After that, the number of collected waste bins and their locations are examined. The shortest route pattern and the route sequence are generated according to different collecting scenarios which consider every possible combination of locations to be collected. The workflow diagram of the decision support system is illustrated in Fig. 1.

### 2.2 Defining rush hour for truck launching conditions

Traffic conditions for the university are quite unique and have specific patterns depending on the activities organized within the university. Here, we categorized the university activities into normal days and special events which can be observed as an annual routine schedule.

Normal days include the university opening and closing periods, while the special events can be an annual event like Graduation ceremony or a university fair. To define the rush hour period, the historical traffic data were collected from Google maps by using traffic layer. The traffic level was defined from 0 to 4 based on the traffic color on the Map, which shows the speed of traffic on each road. Google Maps displays real-time traffic conditions and visualizes them by using four different colors, i.e., green, orange, red, and darker red, representing no traffic delays, medium amount of traffic, traffic delays, and the slower speed of traffic, respectively. Another color is grey, meaning that there is insufficient data from passing vehicles.

The collection of traffic data was performed every hour from 6 am to 6 pm on a daily basis. For both university opening and closing periods, the data was continuously collected for four weeks, so that there were four samples for each time instant for each day of the week. Therefore, the historical traffic patterns for these cases were generated on a weekly basis considering both weekdays and weekend. The traffic data for the graduation period was collected during the 2023 graduation ceremony which was held from 4th to 7th October 2023 as the rehearsal days and from 9th to 12th October as the commencement days.

The traffic value was averaged across the same day of the week and was used as the representative of the day, which will be further used to define the lower bound of the traffic values for the rush hour period. However, the Graduation ceremony events show distinct traffic patterns, typically based on the intensity of the activity, i.e., whether it is the rehearsal day or the commencement day.

To avoid the differences in the distribution of traffic values for each case, the mode for each university activity, namely, the university opening and closing periods, and the graduation ceremony, was utilized as the representative and multiplied by 1.05, which was assumed as a factor to define the lower bound of the traffic level for the rush hour period. This factor was exhaustively examined by a trial-and-error method, and the obtained value also corresponds to the Pareto rule [9, 10].

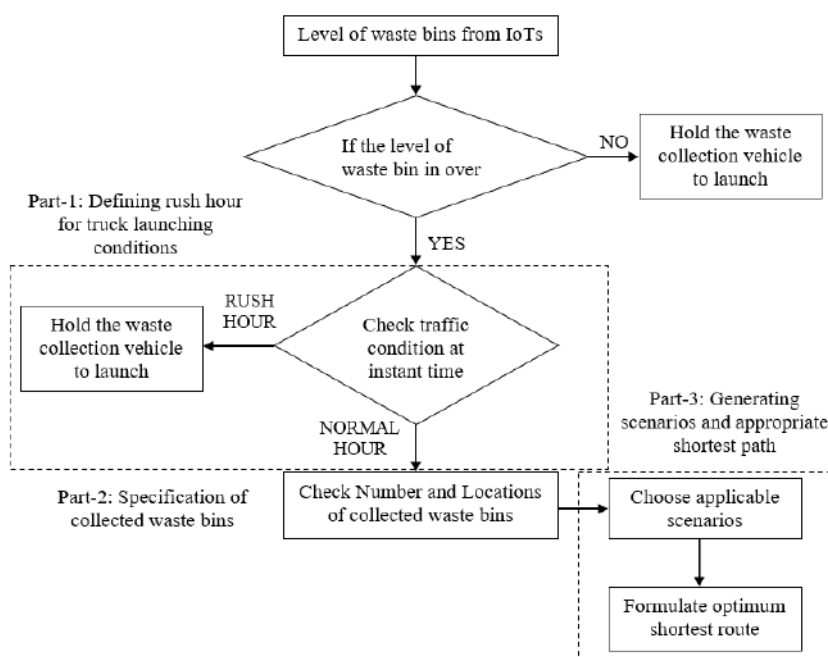


Fig. 1 The workflow diagram of a decision-support tool for waste collection system

### 2.3 Establishing the possible scenarios of waste collection locations

Smart waste bins were installed at five different locations on the University campus. The possible collection scenarios were generated based on the number of collecting locations, which was derived from whether there is any full waste bin in each location or not. These scenarios were exhaustively examined using the combination for choosing the  $r$  number of objects from the total  $n$  objects. The equation to calculate the probability for possible combination of full locations out of five is displayed in [11].

$${}^n P_r = \frac{n!}{r!(n-r)!} \quad (1)$$

where,  $P$  is the probability of full waste bin's location,  $n$  is the total number of locations, and  $r$  is the number of locations containing any full waste bin.

A total of 31 possible collecting scenarios were generated and can be categorized into five groups according to the number of collecting points. Group 1 contains scenarios where any one out of five locations is visited. Similarly, Group 2 contains scenarios where any two out of five locations are visited, and so on. The optimized routes for the waste collection trucks were calculated corresponding to these 31 scenarios. However, the trucks did not necessarily collect the waste from the bins having the waste level lower than 80%.

### 2.4 Calculation of shortest path between each location

After the collecting locations is defined, the next step is to find the shortest path between each location. QGIS Network Analyst was used to find the shortest path from point to point providing Dijkstra's algorithm [12]. Two functional routes with shortest and fastest functions can be computed given start point and end point in QGIS [13].

To calculate the shortest path for each scenario in QGIS, the waste collecting points (i.e., waste bin locations), the starting point (i.e., truck launching location), and the ending points (i.e., waste offloading locations) should be specified. Five collecting locations were designated as waste bins' locations and called Location 1, 2, 3, 4, and 5 in this research. Shortest paths were computed for each possible pair of six locations including Garbage Dump (GD), which was assigned as the starting and the ending points of waste collection truck, and finally the distance matrix between each location was created.

Road network availability is also the most fundamental input in QGIS, which significantly affects the results of the shortest path. The road network availability might vary according to different activities in the university; for example, some roads are closed during an annual fair because food stalls and various shops are opened on the campus. The normal school days and the Graduation ceremony shared the same road network pattern; however, the different road network has to be created based on the road availability during the annual fair. Consequently, in the case of the annual fair, the waste collection points for Location 2 and 4 were temporarily moved because the roads next to the original location were closed. Fig. 2 and Fig. 3 illustrate the location of waste collection points and the garbage dump for the normal conditions and the annual fair, respectively.

The open-source Geographic Information System software, QGIS, can be used to digitize the road networks and compute the shortest path. QGIS was set up with WGS 1984 UTM Zone 47N projection for Thailand to create the road network of the university. The road information for each instance direction and the number of lanes were added according to Google Earth. The distance matrix was, therefore, generated for the normal school days and the annual fair conditions by using the shortest path calculation from the point-to-point function in QGIS.



Fig. 2 Location of waste collection points during the normal condition



Fig. 3 Location of waste collection points during the annual fair

## 2.5 Calculation of route sequence by Travelling Salesman Problem

This research determined the route sequence with the minimum total distance by applying Branch and Bound Algorithm to solve Travelling Salesman problem. Travelling Salesman Problem means that a person visits each city, i.e., node, exactly once and then returns to the initial starting point. The constraints involve that every single node is visited only one time and subtours are eliminated [12]. The minimum distance of the total distance travelled is determined using the Eq. (2).

$$\min \sum_{i=1}^n \sum_{j \neq i, j=1}^n d_{ij} X_{ij} \quad (2)$$

$$\text{Subject to } \sum_{j=1}^n X_{ij} = 1 \text{ for } \forall i \quad (3)$$

$$\sum_{i=1}^n X_{ij} = 1 \text{ for } \forall j \quad (4)$$

where,  $d_{ij}$  is the distance from node  $i$  to node  $j$ , and  $X_{ij}$  is a binary variable where the value is 1 if there is the selection of the path goes from node  $i$  to node  $j$ , and 0 if otherwise [12].

An effective Branch and Bound minimization process necessitates a good lower bound as a fundamental requirement [14]. The trip must travel to all nodes and the lower bound means the minimum distance of travel by going to each node. The first node that has the smallest value of lower bound branches to its child nodes until the algorithm is terminated. The minimum route sequence can then be determined using Branch and Bound Tree Diagram [12].

In this research, the shortest route sequence was defined by Traveling salesman problem based on Branch and Bound algorithm in MS Excel solver. According to Travelling Salesman Problem, the truck will be launched from the garbage dump as a starting point and back to the garbage dump. Therefore, the optimum route sequence with minimum distance for each scenario was resulted in a circular manner.

## 3. RESULTS AND DISCUSSION

### 3.1 Rush hour for different university activities

The lower bound of the traffic level to define the rush hour period for different university activities were determined as 1.84, 1.79, and 2.1 for the case of the university opening and closing periods, and the graduation ceremony, respectively. During the university opening and closing periods, it is common to experience traffic congestion at the time upon arrival and

departure from the university on weekdays. There was no traffic on weekends at the campus. During the graduation period, the traffic value was relatively high for most of the working hours. The situation of rehearsal days and the final commencement days for all departments in the university were also considered. The results show that traffic congestion occurred at almost all times of the day during the final graduation days. The rush hours for the university opening and closing periods were presented as a weekly basis as shown in Fig. 4 and 5, respectively. The rush hours for the graduation ceremony period were presented as the pattern of the rehearsal day and the commencement day as shown in Fig. 6. Green color represents the normal hours and red color represents the rush hours.

	6:00 AM	7:00 AM	8:00 AM	9:00 AM	10:00 AM	11:00 AM	12:00 PM	1:00 PM	2:00 PM	3:00 PM	4:00 PM	5:00 PM	6:00 PM
Sunday	Green	Green	Green	Green	Green	Green	Green	Green	Green	Green	Green	Green	Green
Monday	Green	Green	Red	Green	Green	Green	Green	Green	Green	Green	Red	Red	Green
Tuesday	Green	Green	Red	Red	Green	Green	Green	Red	Green	Green	Green	Green	Green
Wednesday	Green	Green	Red	Red	Green	Green	Green	Green	Green	Green	Red	Red	Green
Thursday	Green	Green	Red	Red	Green	Green	Green	Green	Green	Green	Red	Red	Green
Friday	Green	Green	Red	Red	Green	Green	Green	Green	Green	Green	Red	Red	Green
Saturday	Green	Green	Green	Green	Green	Green	Green	Green	Green	Green	Green	Green	Green

Fig. 4 Rush hours for the university opening period

	6:00 AM	7:00 AM	8:00 AM	9:00 AM	10:00 AM	11:00 AM	12:00 PM	1:00 PM	2:00 PM	3:00 PM	4:00 PM	5:00 PM	6:00 PM
Sunday	Green	Green	Green	Green	Green	Green	Green	Green	Green	Green	Green	Green	Green
Monday	Green	Green	Red	Red	Green	Green	Green	Green	Green	Green	Green	Red	Red
Tuesday	Green	Green	Red	Red	Green	Green	Green	Green	Green	Green	Green	Red	Red
Wednesday	Green	Green	Red	Red	Green	Green	Green	Green	Green	Green	Green	Red	Red
Thursday	Green	Green	Red	Red	Green	Green	Green	Green	Green	Green	Green	Red	Red
Friday	Green	Green	Red	Red	Green	Green	Green	Green	Green	Green	Green	Red	Red
Saturday	Green	Green	Green	Green	Green	Green	Green	Green	Green	Green	Green	Green	Green

Fig. 5 Rush hours for the university closing period

	6:00 AM	7:00 AM	8:00 AM	9:00 AM	10:00 AM	11:00 AM	12:00 PM	1:00 PM	2:00 PM	3:00 PM	4:00 PM	5:00 PM	6:00 PM
Rehearsal Day	Green	Red	Red	Red	Red	Red	Red	Red	Red	Red	Red	Red	Red
Commencement Day	Green	Red	Red	Red	Red	Red	Red	Red	Red	Red	Red	Red	Red

Fig. 6 Rush hours for the graduation period

### 3.2 Shortest route patterns and sequences for the normal and the annual fair conditions

If any waste bin location exists along the designated route, the truck will pass through even if there are no full waste bins at that location. Therefore, some collection scenarios may share the same route patterns so that they can be grouped together. For the normal conditions, all of route patterns in the same group have the same route sequence as shown in Table. 1. The typical route sequence started from garbage dump (GD) to location 4 (L4), location 1 (L1), location 2 (L2), location 3 (L3), location 5 (L5) and ended at the starting point. The route sequence of scenario-14 which has an individual route pattern is about 24-m shorter than the typical route sequence. Route Pattern J and D cover all five locations of waste collection points for the normal and the annual fair conditions, respectively as shown in Fig. 7 and Fig. 8. The route sequence for the annual fair condition is the same as the normal condition except scenario-4, scenario-5, and scenario-15. The route sequence of scenario-15 can shorten the distance approximately 469 m than the typical sequence.

## 4. CONCLUSION

This research proposes an innovative approach to enhance the smart waste collection system in the university with the integration of IoTs, traffic conditions and GIS software. The research work particularly addresses two research questions: “How does the waste collection vehicle avoid the traffic congestion?” and “What are the optimal route pattern and route sequence with the minimum distance for different conditions?”. For the first question, rush hour was



Fig. 7 Route pattern J for normal condition Fig. 8 Route pattern D for the university fair

Table. 1 Grouping for similar route pattern in normal condition

Scenario No.	Minimum Distance (m)	Route Pattern	Scenario No.	Minimum Distance (m)	Route Pattern
<b>Route Pattern A</b>			<b>Route Pattern G</b>		
1	3,227	GD - L1 - GD	12	4,931	GD - L5 - L2 - GD
7		GD - L1 - L3 - GD	23		GD - L5 - L2 - L3 - GD
<b>Route Pattern B</b>			<b>Route Pattern H</b>		
2	3,400	GD - L2 - GD	15	5,440	GD - L4 - L5 - GD
10		GD - L2 - L3 - GD	21		GD - L4 - L1 - L5 - GD
<b>Route Pattern C</b>			25		GD - L4 - L3 - L5 - GD
4	3,885	GD - L4 - GD	29		GD - L4 - L1 - L3 - L5 - GD
8		GD - L4 - L1 - GD	<b>Route Pattern I</b>		
13		GD - L4 - L3 - GD	18	GD - L1 - L2 - L5 - GD	
19		GD - L4 - L1 - L3 - GD	27	GD - L1 - L2 - L3 - L5 - GD	
<b>Route Pattern D</b>			<b>Route Pattern J</b>		
6	3,758	GD - L1 - L2 - GD	24	5,971	GD - L4 - L2 - L5 - GD
16		GD - L1 - L2 - L3 - GD	28		GD - L4 - L1 - L2 - L5 - GD
<b>Route Pattern E</b>			30		GD - L4 - L2 - L3 - L5 - GD
9	4,781	GD - L1 - L5 - GD	31		GD - L4 - L1 - L2 - L3 - L5 - GD
20		GD - L1 - L3 - L5 - GD	<b>Route Pattern for individual scenario</b>		
<b>Route Pattern F</b>			<b>Route Pattern K</b>		
11	4,417	GD - L4 - L2 - GD	3	2,788	GD - L3 - GD
17		GD - L4 - L1 - L2 - GD	<b>Route Pattern L</b>		
22		GD - L4 - L2 - L3 - GD	5	3,450	GD - L5 - GD
26		GD - L4 - L1 - L2 - L3 - GD	<b>Route Pattern M</b>		
			14	4,319	GD - L5 - L3 - GD

designated to identify the traffic congestion in the university and the truck was planned to launch beyond rush hour. Second, the optimal route pattern and route sequence were determined by using QGIS and travelling salesman problem. The road conditions based on various campus events, bin locations and collection scenarios were considered as variables. The smart waste

collection system at a university will become a more efficient and effective system by applying the proposed decision support process.

## 5. ACKNOWLEDGEMENT

The author acknowledges the scholarship under Thailand Advanced Institute of Science and Technology and Tokyo Institute of Technology (TAIST-Tokyo Tech) program, funded by the National Research Council of Thailand (NRCT). This research received funding from Program Management Unit for Competitiveness (PMUC) of the Office of National Higher Education Science Research and Innovation Policy Council in collaboration with Magnolia Quality Development Corporation Limited and Dolphin Industries Company Limited.

## 6. REFERENCES

- [1] Kaza, S., et al.,(2018). What a waste 2.0: a global snapshot of solid waste management to 2050. World Bank Publications.
- [2] Kouloughli, S. and S. Kanfoud, (2017). Municipal solid waste management in Constantine, Algeria. *Journal of Geoscience and Environment Protection*, 5(1), p. 85-93.
- [3] Roy, A., et al., (2022). IoT-based smart bin allocation and vehicle routing in solid waste management: A case study in South Korea. *Computers & Industrial Engineering*, 171.
- [4] Ramos, T.R.P., C.S. de Moraes, and A.P. Barbosa-Povoa, (2018). The smart waste collection routing problem: Alternative operational management approaches. *Expert Systems with Applications*, 103: p. 146-158.
- [5] Kim, J., et al., (2023). Clustered vehicle routing problem for waste collection with smart operational management approaches. *International Transactions in Operational Research*.
- [6] Shafik, A., et al., (2022). Environmental Impacts of MSW Collection Route Optimization Using Gis: A Case Study Of 10th Of Ramadan City, Egypt.
- [7] Singh, M. and A. Gupta, (2022). Optimizing and Analyzing the Cost of Collection and Transportation of Solid Waste Using GIS. *International Journal for Research in Applied Science & Engineering Technology*.
- [8] Apaydin, O. and M. Gonullu, (2007). Route optimization for solid waste collection: Trabzon (Turkey) case study. *Global NEST Journal*, 9(1): p. 6-11.
- [9] Nicholas, J., (1990) Introduction to descriptive statistics, Mathematics Learning Centre, University of Sydney.
- [10] Pareto, V., (1896) *Cours conomie Politique* Profess a l'Universit de Lausanne, Vol. I.
- [11] Croarkin, C. and P. Tobías, (2012). *Engineering Statistics Handbook*, NIST/SEMAECH. [Online URL: <https://www.itl.nist.gov/div898/handbook, 2012>] accessed on December 23, 2023.
- [12] Srinivasan, G., (2010). *Operations Research: principles and applications*, 2<sup>nd</sup> Edition: PHI Learning Pvt. Ltd.
- [13] QGIS Documentation (2023, December 23). *PyQGIS Developer Cookbook : Network analysis library*. [https://docs.qgis.org/3.28/en/docs/pyqgis\\_developer\\_cookbook/network\\_analysis.html#finding-shortest-paths](https://docs.qgis.org/3.28/en/docs/pyqgis_developer_cookbook/network_analysis.html#finding-shortest-paths).
- [14] Toffolo, T.A., et al., (2016) Branch-and-bound with decomposition-based lower bounds for the traveling umpire problem. *European Journal of Operational Research*, 250(3): p. 737-744.

## Zinc-Organic Framework and Titanium Dioxide Nanocomposite for Use as Photocatalyst for Dye Wastewater Treatment

Pemika Chaichana<sup>1</sup>, Saranphong Yimklan<sup>2</sup>, Yothin Chimupala<sup>3,\*</sup>

<sup>1</sup> Department of Industrial Chemistry and Master's Degree Program in Industrial Chemistry, Faculty of Science Chiang Mai University, Thailand

<sup>2</sup> Department of Chemistry, Center of Excellence in Materials Science and Technology, and Materials Science Research Center, Faculty of Science, Chiang Mai University, Thailand

<sup>3</sup> Department of Industrial Chemistry, Center of Excellence in Materials Science and Technology, and Materials Science Research Center, Faculty of Science, Chiang Mai University, Thailand

\*Corresponding Author's E-mail: yothin.chimupala@cmu.ac.th

### Abstract

The objective of this research is to create novel composite photocatalyst materials that combine a new zinc-based metal-organic framework (Zn-MOF) and Titanium dioxide (TiO<sub>2</sub>) nanoparticles. The first step, a Zn-MOF was synthesized using microwave technique. The [Zn(4,4'-bipy)<sub>2</sub>(Suc)]<sub>n</sub>, contains a central zinc(II) ion which was coordinated by two molecules of 4,4'-bipyridine ligands and two molecules of succinic acid ligands. In the second step, the surface of [Zn(4,4'-bipy)<sub>2</sub>(Suc)]<sub>n</sub> microcrystals was coated with TiO<sub>2</sub> nanorods (P25 and anatase TiO<sub>2</sub>) by co-precipitation method. The chemical structure of a Zn-MOF crystal was studied using the Single-crystalline X-ray diffraction technique. Both bulk samples of [Zn(4,4'-bipy)<sub>2</sub>(Suc)]<sub>n</sub> and composited materials were confirmed their crystal structures by powder XRD diffraction technique. The powder XRD peaks indicated that the composite materials comprised a small amount of TiO<sub>2</sub> anatase and TiO<sub>2</sub> rutile and the majority phase of Zn-MOF. In addition, the location of TiO<sub>2</sub> particles were characterized by SEM images to confirm that TiO<sub>2</sub> nanoparticles were well deposited on the entire MOF surface. Finally, the as-synthesized materials were studied for the photocatalytic performance for methyl orange degradation using 2.5 mg/L of catalysts. The best results from nanocomposite sample showed that the degradation efficiency reached 48.76% within 300 min under UV-C irradiation which higher than solely MOF (24.56%).

**Keywords:** Metal-Organic framework; Composite material; Titanium dioxide; Photocatalyst; Dye degradation

### 1. Introduction

Technology and science developed quickly after the industrial revolution. The textile industry is one example of how small manufacturing units developed into industries and started producing things on a huge scale for export to other nations. The textile industry uses a lot of water and chemicals as a precursor and releases a huge amount of dye wastewater, particularly during dyeing, which has a significant environmental impact. Wastewater often contains toxic organic pollutants that can adversely affect human health and aquatic life upon exposure. Therefore, wastewater management is at the heart of environmental protection. Large manufacturers utilize several methods to remove organic colors from wastewater, such as



chemical coagulation and membrane filtering. However, these treatment methods require a lot of money and area to install the treatment systems.

As a result, photocatalysis appears to be an intriguing treatment method for water purification, with the potential to use sunlight as a sustainable and renewable energy source. This technology is based on the usage of a semi-conductor that can be activated by light with energy greater than its band gap, resulting in the generation of energy-rich electron-hole pairs that can participate in redox reactions [3]. TiO<sub>2</sub> is commonly employed for photocatalytic processes because of its high conductivity, outstanding optical or electronic characteristics, and non-toxicity [4].

Several investigations have revealed that photocatalytic activity depends on light absorption and charge carrier separation. One of the key strategies for addressing charge carrier recombination in photocatalysts is the construction of heterostructures through coupling with other semiconductors [7]. The creation of heterojunctions between photocatalysts with acceptable band edge potentials considerably improves photocatalytic degradation performance [3]. Unlike TiO<sub>2</sub>-based inorganic photocatalysts, MOFs are porous crystalline materials formed by coordination bonding between organic ligands and metal clusters as nodes [1]. MOFs have received attention as heterogeneous catalysts due to their ultra-high surface area, persistent porosity, and customizable functionality or structural diversity [2]. Meanwhile, MOFs illustrate their potential applications in photocatalysts. Thus, Chimupala and et al. reported a microwave-heating synthesis of a new 3D zinc(II) cationic metal-organic framework using the rigid rodlike *exo*-bidentate ligand 4,4'-bipy and the flexible chainlike glu<sup>2-</sup> as co-organic linkers with an encapsulated perchlorate counter anion, {[Zn<sub>3</sub>(4,4'-bipy)<sub>4</sub>(glu)<sub>2</sub>](ClO<sub>4</sub>)<sub>2</sub>]<sub>n</sub> for use as photocatalyst. [5]. And then Kaeosamut and et al. present new solvent-responsive isostructural two-dimensional cationic metal-organic frameworks (MOFs) of Mn(II) and Zn(II) by microwave-heating method [6], were reported as photocatalysts for an anionic dye (methyl orange (MO)) degradation and MOFs Zn(II) showed high performance for MO degradation at 94.27%.

This research used novel composite photocatalyst materials for heterojunction photocatalyst that combine a Zn-MOF and titanium dioxide nanoparticles to study the photodegradation of the methyl orange (MO) dye.

## 2. Materials and Methods

### 2.1. Materials

All of the ligands, zinc salt and titanium dioxide (P25) were purchased from Sigma-Aldrich and utilized without additional purification including, 4,4'-bipy (C<sub>10</sub>H<sub>8</sub>N<sub>2</sub>, 98%), succinic acid (C<sub>4</sub>H<sub>6</sub>O<sub>4</sub>, 99%), P25 (TiO<sub>2</sub>, 99%) and zinc acetate dihydrate (Zn(CH<sub>3</sub>COO)<sub>2</sub>·2H<sub>2</sub>O, 99%) was a source of zinc salt. Methyl orange (C<sub>14</sub>H<sub>14</sub>N<sub>3</sub>SO<sub>3</sub>Na, MO) was purchased from ACI Labscan. Deionized water (DI water) was used to prepare all chemical solutions. TiO<sub>2</sub> nanorods were synthesized by hydrothermal technique and calcination.

### 2.2. Physical measurements

The chemical structure of MOF was confirmed by the Single-crystalline X-ray diffraction technique (SC X-ray, Rigaku-Oxford XtalLab Supernova diffractometer). The morphologies of P25 and TiO<sub>2</sub> nanoparticles on MOF surfaces were studied by a scanning

electron microscope (SEM, JSM-IT300) with energy dispersive spectroscopy (EDS). Powder X-ray diffraction (PXRD) ( $2\theta = 5-55^\circ$ ) was used to analyze the structure and properties of P25 and TiO<sub>2</sub> composite materials in Rigaku SmartLab. The BET surface area and pore size were determined by a Quantachrome Autosorb analyzer. The concentration of the MO dye was determined at 464 nm Lambda max ( $\lambda_{\max}$ ) absorbance using a UV-Vis spectrophotometer (Thermo Scientific, Genesys 10S UV-Vis). Thermal stability was investigated by Thermoplus EVO2 thermogravimetry (TG) and derivative thermogravimetry (DTG) in an air atmosphere.

### 2.3. Synthesis of [Zn(4,4'-bipy)<sub>2</sub>(Suc)]<sub>n</sub> (MOF) by Microwave-heating Techniques.

Firstly, a solution of Zn(CH<sub>3</sub>COO)<sub>2</sub>·2H<sub>2</sub>O (0.219 g, 1.00 mmol), 4,4'-bipy (0.156 g, 1.00 mmol), and succinic acid (H<sub>2</sub>Suc, C<sub>4</sub>H<sub>6</sub>O<sub>4</sub>, 0.118 g, 1.00 mmol) were prepared in deionized (DI) water (40.00 mL). The mixed solution was transferred into an open 50 mL glass reactor, and then heated with an 800 W microwave for 10 min and cooled to room temperature.

### 2.4. Synthesis of [Zn(4,4'-bipy)<sub>2</sub>(Suc)]<sub>n</sub> composite with TiO<sub>2</sub> nanoparticles (P25 and anatase TiO<sub>2</sub>) by microwave-heating and co-precipitating method.

The composite materials were synthesized by formulating TiO<sub>2</sub> nanoparticles (P25 and anatase TiO<sub>2</sub>) on the surface of MOF crystals with the precipitating method. MOF was synthesized by microwave-assisted 800W for 10 min. The mixed solution of MOF and TiO<sub>2</sub> nanoparticles powder were stirring for 5 min and cooled to room temperature. P25 and TiO<sub>2</sub> nanoparticles on MOF were named MOF\_P25 and MOF\_TiO<sub>2</sub>, respectively.

### 2.5. Photodegradation process

The photocatalytic activity of the sample was determined by the decomposition of methyl orange (MO). A 100 mg amount of catalyst (as-synthesized MOF and composite materials) was mixed with 100 mL the dye solution (2.5 ppm). The suspension was sonicated in an ultrasonic bath (120 W, 40 kHz) for 1 min and kept in the dark for 30 min to obtain an adsorption equilibrium. The mixture was then stirred continuously under UV-C irradiation (265 nm) with an intensity of 940 mW cm<sup>-2</sup> for 5 h. In order to evaluate the decomposition of methyl orange, 5 mL aliquots were collected at certain intervals and then centrifuged at 4000 rpm for 10 min to separate the catalyst before UV-vis measurement of supernatants (at  $\lambda_{\max} = 464$  nm). The amount of methyl orange in the solution was calculated by considering the ratio  $(C_0 - C_t)/C_0$ , where  $C_0$  is the initial concentration of methyl orange and  $C_t$  is the residual concentration after an UV irradiation time  $t$ .

## 3. Results and Discussions

### 3.1. Characterization of [Zn(4,4'-bipy)<sub>2</sub>(Suc)]<sub>n</sub> (MOF) structural description

The crystal structure of MOF was determined by Single-crystal X-ray diffraction technique. The single-crystal X-ray diffraction analysis reveals the asymmetric unit central atom of one Zn(II) was coordinated by two molecules of 4,4'-bipyridine ligands and two succinato (Suc<sup>2-</sup>) ligands that crosslinked the Zn(II) and extended the structure into an infinite ladder-like structure, as shown in Fig. 1.

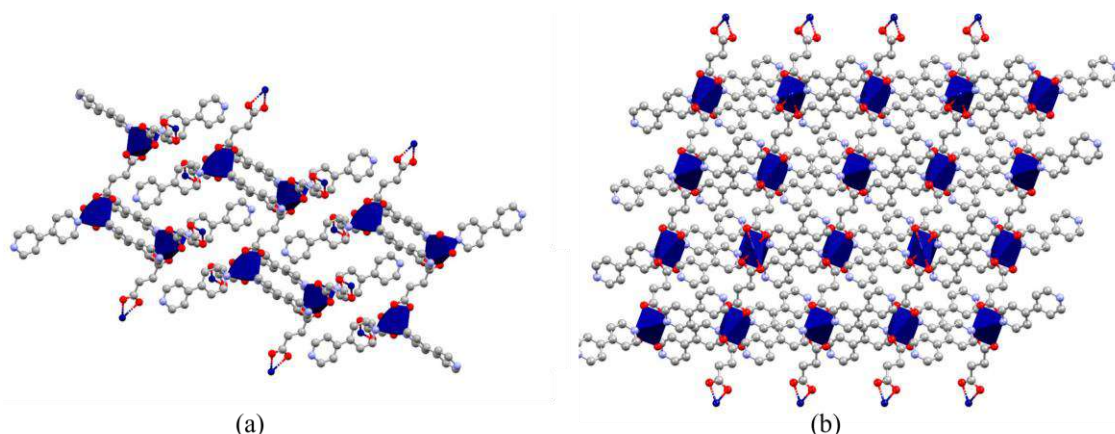


Fig. 1 Crystal structure of MOF: (a) the infinite ladder-like structure and (b) the supramolecular packing of the coordination network.

### 3.2. Characterization of $[Zn(4,4'-bipy)_2(Suc)]_n$ composite with $TiO_2$ nanoparticles (P25 and anatase $TiO_2$ )

The characterization of the Zn-MOF and composite materials: SEM, EDS, XRD, TGA and BET were studied, starting from the morphological was analyzed by the SEM results. The average diameter of P25 and anatase  $TiO_2$  nanoparticles are 30 and 130 nm, respectively. The effect of  $TiO_2$  nanoparticles precursor on the Zn-MOF surface was studied. The composite materials were found that small P25 spherical nanoparticles (MOF\_P25) and anatase  $TiO_2$  nanorods (MOF\_ $TiO_2$ ) are homogeneously immobilized on the dispersed MOF rods. It was appeared that P25 was sphere nanoparticles and slightly coated on MOF surface (MOF\_P25), as seen in Fig. 2(b). From Fig. 2(c), it was found the  $TiO_2$  nanorods was well distributed onto the Zn-MOF surface (MOF\_ $TiO_2$ ).

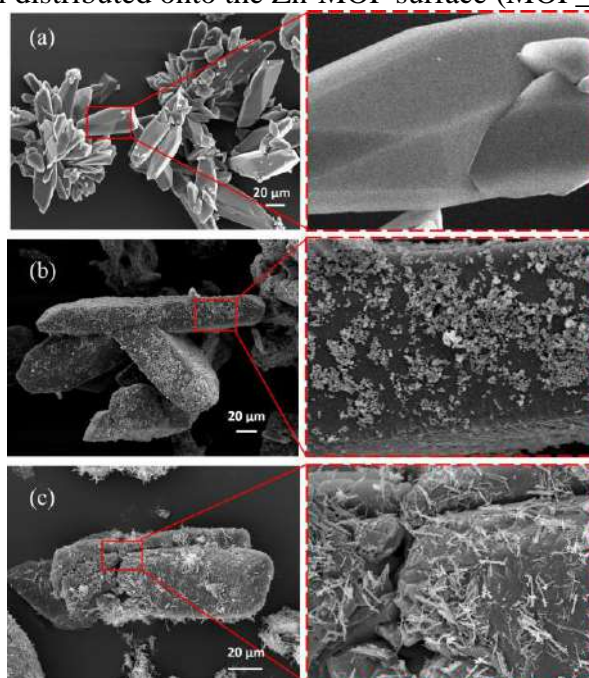


Fig. 2 SEM images of the surface of MOF and  $TiO_2$  nanoparticles on MOF surface: (a) MOF, (b) MOF\_P25 and (c) MOF\_ $TiO_2$ .

After that, the EDS technique was studied to confirm the presence of TiO<sub>2</sub> onto the surface of Zn-MOF. Small white particles can be observed at the surface from the particle surface image. The result showed the small particle composed of Ti and O elemental composition, indicating the TiO<sub>2</sub> nanoparticles on Zn-MOF surface (MOF\_TiO<sub>2</sub>). The results can be verified from the EDS images, as shown in Fig. 3. The weight percent of carbon, zinc, titanium, and oxygen is 59.11, 12.16, 10.72 and 18.01 respectively.

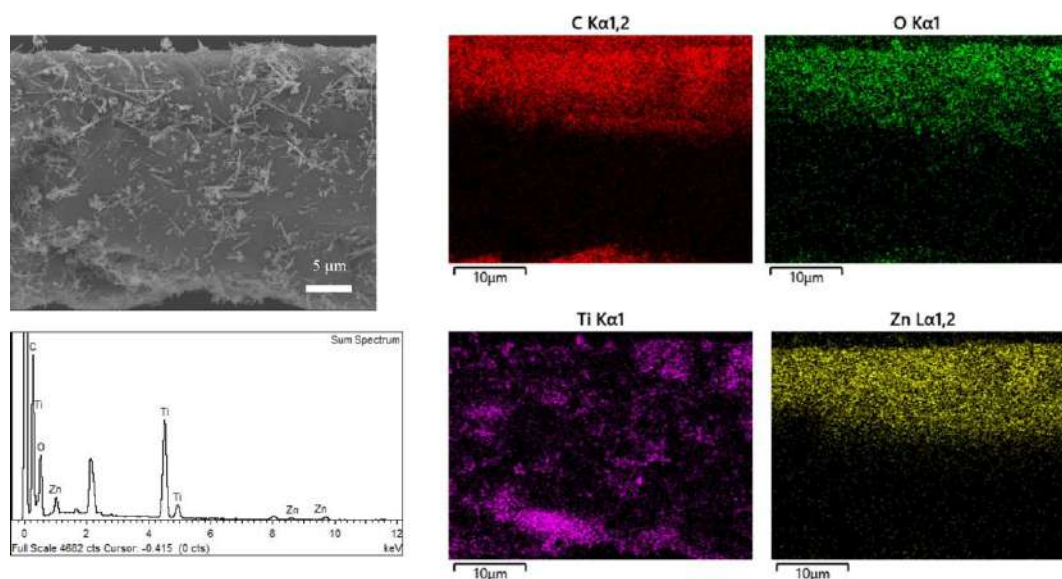


Fig. 3 EDS images of MOF\_TiO<sub>2</sub>

The indexed PXRD pattern (see Fig. 4) demonstrated the high purity of the crystalline phase. PXRD analysis was studied to observe the crystal structure of Zn-MOF and composite material, which are immobilized at different TiO<sub>2</sub> precursors. as shown in Fig. 4. It was found that the XRD pattern of MOF\_TiO<sub>2</sub> seems to match well with Zn-MOF crystalline and TiO<sub>2</sub> anatase. Meanwhile, MOF\_P25 comprised a small amount of TiO<sub>2</sub> anatase and TiO<sub>2</sub> rutile and the majority phase of MOF crystal.

Thermogravimetric analysis (TGA) and differential thermal analysis (DTA) were used to investigate the thermal stability and chemical composition of composite materials, particularly for estimating the amount of water crystallization in the MOF. Figure 5 displays the TGA and DTA thermograms of Zn-MOF and composite materials observed during flow. The MOF net weight loss of 80.12%, which happened at 45, 151, 249, 294, 320 and 430 °C, corresponds to the chemical formula of [Zn(4,4'-bipy)<sub>2</sub>(Suc)]<sub>n</sub>. Three endothermic (45, 151, 249 and 294 °C) peaks and one exothermic (320 and 430 °C) peak appeared in the DTA. These transformations are due to the removal of both crystalline and coordinated waters, acetate, and gaseous products of the combustion of organic moieties. It is known that H<sub>2</sub>O, CO, CO<sub>2</sub>, and NO<sub>x</sub> were lost during the TGA experiment, as the 19.88% residue is ZnO (confirmed by PXRD, 19.88%). Moreover, P25 and TiO<sub>2</sub> net weight on MOF surface were determined by TGA result, which calculated from ZnO residue and Zn-MOF loss weight. The composite materials showed P25 and TiO<sub>2</sub> residue as 12.01 and 12.89 %, respectively (see Fig. 5(b)).

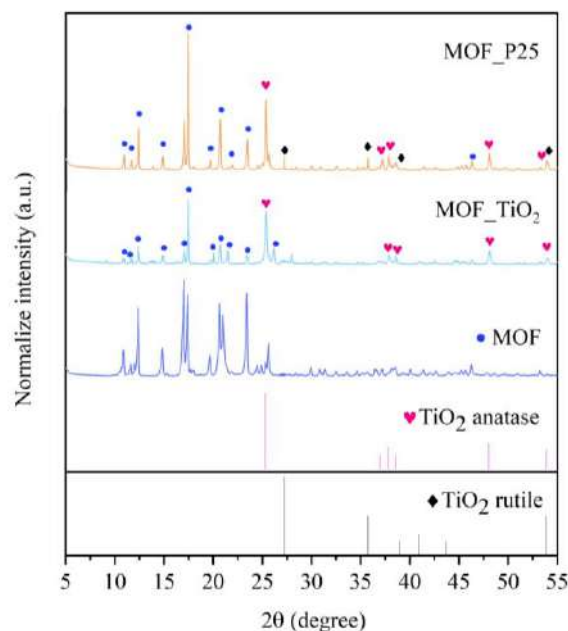


Fig. 4 PXRD of MOF and composite materials

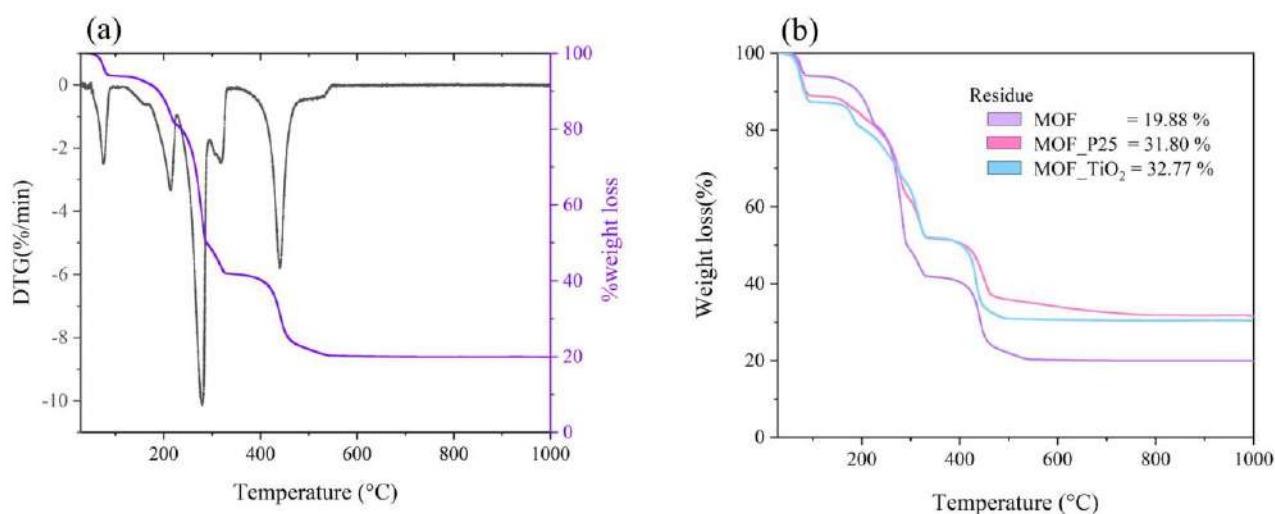


Fig. 5 Thermogravimetric analysis (a) TGA and DTA thermograms of MOF and (b) Percent loss weight and residue

The surface area and pore volume of the MOF and composite materials were determined using nitrogen adsorption-desorption isotherms at 77K. According to the results, MOF\_P25 and MOF\_TiO<sub>2</sub> exhibit a mixture of adsorption isotherms classified as type-II and type IV indicating the existence of mesopore structure. The specific surface areas of MOF, MOF\_P25, and MOF\_TiO<sub>2</sub> were measured to be 47.40, 34.51, and 59.54 m<sup>2</sup>/g, respectively. Furthermore, the pore volumes for the Zn-MOF, MOF\_P25 and MOF\_TiO<sub>2</sub> were 0.1004, 0.1002, and 0.1870 cc/g, respectively. As can be observed, MOF\_TiO<sub>2</sub> has the largest surface area and pore volume of micropores. The BJH model calculated the micropore

volume of MOF, MOF\_P25, and MOF\_TiO<sub>2</sub>, which showed 0.0862, 0.0956, and 0.1499 cm<sup>3</sup>/g, respectively.

### 3.3. Degradation of methyl orange (MO) dye wastewater treatment

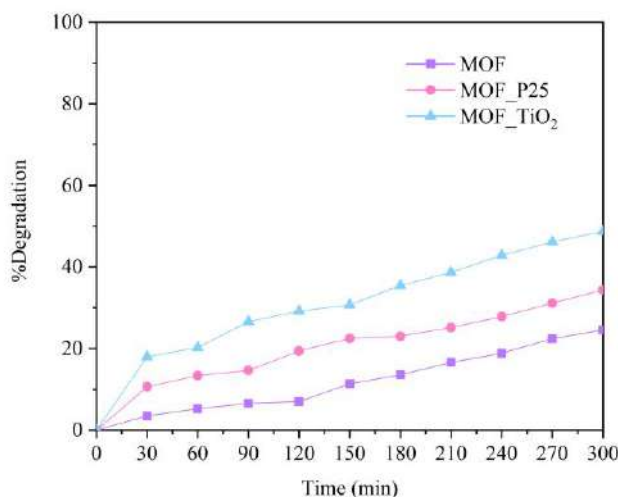


Fig. 6 Methyl orange (MO) degradation efficiency

The photocatalytic activity of the catalysts was determined by the decomposition of methyl orange (see Fig.6). Methyl orange (MO) was used as the model anionic pollutant. Figure 6 shows that 100 mg of the MOF\_P25 and MOF\_TiO<sub>2</sub> have a degrading efficiency of 34.34 and 48.76%, respectively at 300 mins, which is higher than MOF (24.56%). The influence of the co-precipitation upon the photocatalytic performance is clearly observed as the degradation efficiency increased almost 1.5 times for the well-dispersed catalyst (MOF\_TiO<sub>2</sub>) compared to the MOF\_P25. This phenomenon is due to the increase of active surface area. Moreover, MOF\_P25 showed higher degradation efficiency than MOF due to the heterojunction structure between MOF and P25 with acceptable band edge potentials considerably improving photocatalytic degradation performance.

The aromatic ring in 4,4'-bipy of the Zn-MOF might absorb UV-C light as a light-harvesting unit before transferring the energy to the nearby Zn clusters. The Zn clusters produced excited electrons (e<sup>-</sup>) in the conduction band (CB) and holes (h<sup>+</sup>) in the valence band (VB). The reactive species were employed to generate a reactive hydroxyl radical (•OH), which quickly reacts with the MO on the catalyst's surface. The MO was subsequently broken into smaller molecules, such as CO<sub>2</sub> and H<sub>2</sub>O. Meanwhile, composite materials showed higher degradation efficiency than MOF due to higher specific surface area, which agreed with the characterization results. Moreover, the structure of composite materials includes a heterojunction energy band. The Kubelka-Munk function determined the energy band gap of MOF and MOF\_TiO<sub>2</sub> as shown 2.26 and 2.81 eV, respectively. Heterojunction catalysts frequently exhibit higher electrolytic water activity than single component catalysts, and charge transfer or complementing redox properties between the components in heterojunction catalysts can enhance activity and efficiency in photocatalytic process [2]. In this research, composite materials were synthesized to treat wastewater for environmental protection. There are proposals to improve the photocatalytic degradation of composite materials.

#### 4. Conclusion

The new-zinc organic frameworks were synthesized by microwave-heating technique and used for photocatalyst. The synthesis of TiO<sub>2</sub> nanoparticles on zinc organic frameworks indicates that small P25 and TiO<sub>2</sub> nanoparticles are homogeneously immobilized on the Zn-MOF surface. MOF-TiO<sub>2</sub> had the highest specific surface area and porous volume, which corresponded to the highest degradation efficiency (48.76%). While the photocatalytic response correlates to the TiO<sub>2</sub> morphology. The TiO<sub>2</sub> nanorods were thoroughly covered, which accelerated photocatalytic degradation. The degradation mechanism via heterojunction band energy, involving the role of a charged recombination on enhancing dye degradation efficiency, was proposed.

#### Acknowledgement

This work was supported by the Department of Industrial Chemistry and TA/RA scholarship from the Graduate School, Chiang Mai University and the author would like to thank the Research Laboratory of Pollution Treatment and Environmental Materials (PTM) Laboratory.

#### References

- [1]. Bathla, A., Lee, J., Younis, S. A., and Kim, K.-H. (2022). Recent advances in photocatalytic reduction of CO<sub>2</sub> by TiO<sub>2</sub>- and MOF-based nanocomposites impregnated with metal nanoparticles. *Materials Today Chemistry*, 24, 100870.
- [2]. Bavykina, A., Kolobov, N., Khan, I. S., Bau, J. A., Ramirez, A., and Gascon, J. (2020). Metal-Organic Frameworks in Heterogeneous Catalysis: Recent Progress, New Trends, and Future Perspectives. *Chemical Reviews*, 120(16), 8468–8535.
- [3]. Belder, C., Bedia, J., Rodriguez, J. J., Gómez-Avilés, A., and Peñas-Garzón, M. (2019). Semiconductor Photocatalysis for Water Purification. *Nanoscale Materials in Water Purification*.
- [4]. Chimupala, Y., Hyett, G., Simpson, R., Mitchell, R., Douthwaite, R., Milne, S. J., and Brydson, R. D. (2014d). Synthesis and characterization of mixed phase anatase TiO<sub>2</sub> and sodium-doped TiO<sub>2</sub>(B) thin films by low pressure chemical vapour deposition (LPCVD). *RSC Advances*, 4(89), 48507–48517.
- [5]. Chimupala, Y., Kaeosamut, N., and Yimklan, S. (2021). Octahedral to Tetrahedral Conversion upon a Ligand-Substitution-Induced Single-Crystal to Single-Crystal Transformation in a Rectangular Zn(II) Metal-Organic Framework and Its Photocatalysis. *Crystal Growth and Design*, 21(9), 5373–5382.
- [6]. Kaeosamut, N., Chaichana, P., Watwiangkham, A., Suthirakun, S., Wannapaiboon, S., Sammawipawekul, N., Chimupala, Y., and Yimklan, S. (2023). Synergistic Induction of Solvent and Ligand-Substitution in Single-Crystal to Single-Crystal Transformations toward a MOF with Photocatalytic Dye Degradation. *Inorganic Chemistry*, 62(49), 19908–19921.
- [7]. Ma, J., Miao, T. J., and Tang, J. (2022). Charge carrier dynamics and reaction intermediates in heterogeneous photocatalysis by time-resolved spectroscopies. *Chemical Society Reviews*, 51(14), 5777–5794.

## Bioethanol Production from Rice Straw Using Simultaneous Saccharification and Fermentation Process

**Chitsanupong Uengudornbhakdee<sup>1</sup>, Supatcha Suankhem<sup>1</sup> and Pornchai Bumroongsri<sup>1,\*</sup>**

<sup>1</sup> Department of Chemical Engineering, Faculty of Engineering, Mahidol University  
E-mail: chitsanupong.ueg@student.mahidol.ac.th, supatcha.sua@student.mahidol.edu and  
pornchai.bum@mahidol.ac.th\*

### Abstract

Rice straw is one of the biomaterials with potential to reduce the dependency of Thailand on fossil fuel. In this paper, rice straw is converted to bioethanol using the simultaneous saccharification and fermentation (SSF) process. Different types of microorganisms are used in the experiments including *Zymomonas mobilis*, *Saccharomyces cerevisiae* and *Pichia stipitis*. The results show that the SSF process can give the highest amount of bioethanol using *Zymomonas mobilis* in combination with *Pichia stipitis* via the pre-hydrolysis step at 50°C for 1 hour followed by the SSF process at 30°C for 48 hours. The yield of bioethanol is 0.23 g/g reduced sugar. The highest amount of bioethanol that can be produced is 1.34 g/L. In addition, the developed SSF process gives higher yield in bioethanol production than the current separate hydrolysis and fermentation (SHF) process.

**Keywords:** rice straw; bioethanol; microorganisms; simultaneous saccharification and fermentation; separate hydrolysis and fermentation

### 1. Introduction

Bioethanol holds significant importance in today's context as a renewable energy source derived from agricultural residues. Among the abundant agricultural byproducts, rice straw stands out as a viable raw material. In an effort to maximize the benefits of rice production, researchers have successfully converted waste rice straw into bioethanol. This bioethanol can be blended with gasoline to create a fuel suitable for combustion in engines, commonly referred to as gasohol [1]. Bioethanol can be synthesized through biological processes involving the fermentation of plants in which starch is converted into sugar. Sugar is then transformed into alcohol with the aid of specific enzymes or chemicals to facilitate digestion. The purification of alcohol involves distillation and the separation of water. The most cost-effective method involves pretreating biomass with alkali which is highly efficient in extracting a significant amount of lignin from the biomass. This process facilitates the separation of a substantial quantity of cellulose for bioethanol production process. Additionally, this method ensures the retention of essential properties [2].

Another essential step involves the hydrolysis process where cellulose is transformed into sugar for fermentation in the subsequent phase. Although hydrolysis can be achieved through various methods, the use of acid poses challenges due to its microbial toxicity. A more effective and environmentally friendly approach involves employing the cellulase enzyme which facilitates the breakdown of cellulose crystals and results in the production of fermentable sugar [3]. The fermentation of bioethanol necessitates precise conditions such as pH and fermentation temperature in order to ensure optimal outcomes. Bacteria survival during fermentation is critical. There are two primary methods employed for this purpose. The first one is separate hydrolysis and fermentation (SHF) in which the cellulose degradation is entirely



separated from the fermentation process. Another one is simultaneous saccharification fermentation (SSF) in which the cellulose degradation and fermentation are integrated within the same system [4]. Apart from investigating the outcomes of different fermentation types, this work also studies the impact of various microorganisms on bioethanol production.

Bioethanol production from rice straw involves crucial choices in processing methodologies between separate hydrolysis and fermentation (SHF) and simultaneous saccharification and fermentation (SSF). SHF consists of two stages: enzymatic hydrolysis to break down biomass into sugars followed by fermentation to produce ethanol. In contrast, SSF integrates both saccharification and fermentation to offer higher efficiency and faster processing. The decision to employ SSF in this study is motivated by efficient approach to bioethanol production from rice straw.

## 2. Materials and Methods

### 2.1 Materials

Rice straw was picked up from the Khlong Yong community, Nakhon Pathom, Thailand. Sodium hydroxide, ferrous sulfate, sodium potassium tartrate and glucose was purchased from KemAus (Australia). Potassium dichromate was purchased from KC (Thailand). Ferrous ammonium sulfate was purchased from QReC (New Zealand). Sulfuric acid, 1,10-phenanthroline monohydrate, citric acid, sodium citrate, and hydrochloric acid was purchased from Labscan (Ireland). Yeast extract and Malt extract was purchased from Himedia (India). *Zymomonas mobilis*, *Pichia stipitis* and *Saccharomyces cerevisiae* were purchased from the National Science and Technology Development Agency (Thailand).

### 2.2 Rice Straw Preparation

Rice straw was placed and dried in an oven at 60 °C for 24 hours to maintain humidity below 10% following the TAPPI (2001) protocol. Subsequently, the dried straw was finely ground using a grinder and sifted through a sieve to achieve a size smaller than 0.25 mm. Finally, the processed material was analyzed to quantify biomass components such as cellulose, hemicellulose and lignin by employing the TAPPI T203 om-88 method for this comprehensive analysis.

### 2.3 Pretreatment of Rice Straw for Cellulose Extraction

The pretreatment of rice straw with sodium hydroxide solution was explored to determine optimal conditions for cellulose extraction while minimizing lignin content and maximizing hemicellulose yield. The prepared rice straw was obtained through crushing and size sorting in Step 2.2 of the rice straw preparation process. The rice straw was immersed in a 2% sodium hydroxide solution at room temperature for 24 hours. Following this pretreatment, the rice straw was filtrated to separate the sodium hydroxide solution, and subsequent rinsing with tap water and distilled water until achieving a neutral pH value of 7. The treated rice straw was then dried at 60 °C. The efficacy of the pretreatment was assessed by analyzing cellulose, lignin, and hemicellulose content using the TAPPTI T203 om-88 method. Adjustments in pretreatment conditions were made based on the rice straw prepared in Section 2.2, taking into consideration various factors.

### 2.4 Hydrolysis

In investigating optimal conditions for cellulose degradation using cellulase enzyme, experiments were conducted to determine the most effective temperature and default pH

conditions leading to the highest yield of recycled sugar during the decomposition of pre-treated biomass. The biomass was treated according to the appropriate conditions outlined in Section 2.1, based on the initial pH values. The experiment followed the optimal conditions for cellulase enzyme activity at a concentration of 15 FPU/g. Initial pH values were set at 4.5, 5, 5.5, and 6.5, while temperatures varied between 40, 50, and 60 °C for 1 hour.

#### **2.4.1 pH Impact on Reducing Sugar Production**

To study the impact of pH on reducing sugar production efficiency, 50 mg of pretreated biomass sludge was weighed and placed in a test tube. A 0.05 M concentrated citrate buffer solution was added with varied pH of 4.5, 5, 5.5, and 6.5. Cellulase enzyme was introduced at concentration of 15 FPU/g, and the reaction was conducted in a temperature-controlled bath at 50 °C. Samples were collected from each tube to analyze the amount of reducing sugar produced using the DNS Method.

#### **2.4.2 Temperature Effects on Reducing Sugar Production**

In investigating the suitable starting temperature for reducing sugar production efficiency, 50 mg of pretreated biomass sludge was weighed and placed in a test tube. A 0.05 M citrate buffer solution was added, adjusting the pH according to the values obtained from Section 2.3.1. Cellulase enzyme at concentration of 15 FPU/g was added, and the reaction occurred in a temperature-controlled bath with temperature 30, 40, and 50 °C for 1 hour. Samples were collected from each tube to analyze the amount of reducing sugar produced using the DNS Method.

### **2.5 Optimization of Ethanol Fermentation Conditions**

To determine optimal conditions for ethanol fermentation, various acidity levels and initial temperature conducive to the highest ethanol yield were investigated using preconditioned biomass. This involved enzymatic digestion and exposure to different microorganisms.

#### **2.5.1 Microorganism Growth Study**

Prepare a 15 ml liquid culture medium in a test tube and a 50 ml liquid medium in a bottle for sterilization. Once cooled, extract a culture loop from the agar slant and introduce it into the test tube. Incubate the culture at 30 °C for 48 hours, measuring the absorbance at 600 nm, which was recorded as 0.4. Subsequently, transfer 5 mL of the culture into a vial with sterilized culture media. Periodically measure the absorbance at 600 nm every 3 hours to construct a growth curve.

#### **2.5.2 Microorganism Effect Study in Biomass Fermentation**

In the experiment aimed at assessing the impacts of various microorganisms on biomass fermentation, the solution containing reducing sugar derived from biomass digestion was prepared at concentration of 5 grams per liter. Following this, 5 ml of the initial culture was introduced into the sterilized liquid medium containing the reducing sugar solution. The objective was to identify microorganisms suitable for fermentation. The solution, adjusted to a pH of 5 using hydrochloric acid and sodium hydroxide, was transferred into 50 ml bottle, sterilized at 121 °C for 15 minutes, and cooled to room temperature. Subsequently, 5 ml of the initial culture was transferred into the sterilized liquid medium containing the reducing sugar solution as shown in Table 1, incubated at 30 °C, and shaken with a shaker at a speed of 150 rpm for 48 hours. This process aimed to identify suitable microorganisms for fermentation and

analyze the reduced sugar amount using the DNS method. The bioethanol yield was analyzed by Gas Chromatography.

**Table 1** Type of microorganisms for fermentation.

Sample	<i>Zymomonas m.</i> (ml)	<i>Saccharomyces c.</i> (ml)	<i>Pichia s.</i> (ml)	Type of medium
1	5	0	0	Bacteria.
2	0	5	0	Yeast.
3	0	0	5	Yeast.
4	2.5	0	2.5	Yeast.
5	0	2.5	2.5	Yeast.
6	5	0	2.5	Yeast.

Two distinct processes for ethanol production were investigated in this study. The first one was separate hydrolysis and fermentation (SHF), a method that fully isolated cellulose degradation from the fermentation process. The second one was simultaneous saccharification fermentation (SSF) that integrated cellulose degradation and fermentation within a same system. The conditions of these processes are outlined in Table 2.

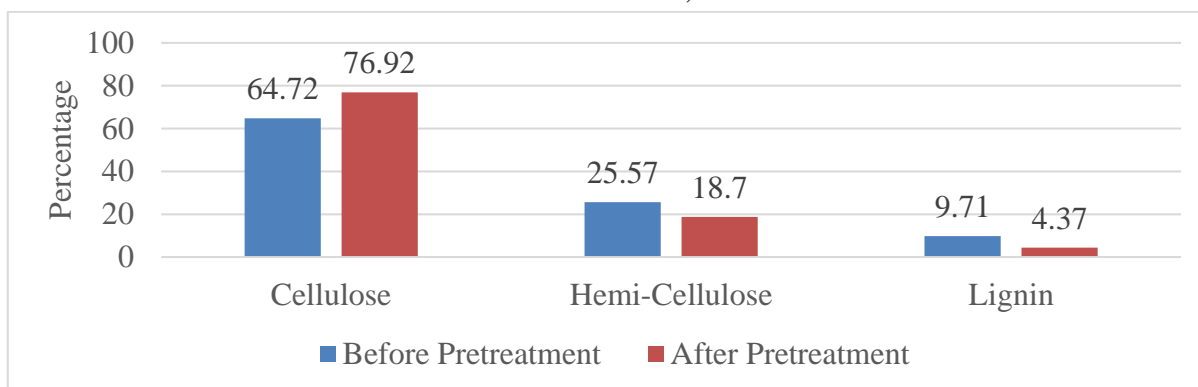
**Table 2** Types of bioreactors for fermentation.

Sample	Type of Process	Condition
1	SHF	Decomposition process at 50 °C, duration 1 hour, followed by fermentation process at 30 °C, duration 48 hours.
2	SSF	Primary degradation process at 50 °C, duration 1 hour, followed by simultaneous degradation and fermentation processes at 30°C, duration 48 hours.
3	SSF	Simultaneous degradation and fermentation process at 50 °C, duration 1 hour, followed by simultaneous degradation and fermentation process at 30 °C , duration 48 hours.
4	SSF	Simultaneous degradation and fermentation process at 50 °C, duration 49 hours.

### 3. Results and Discussion

#### 3.1 Impact of Sodium Hydroxide Pretreatment on the Composition of Rice Straw

To investigate the composition changes in rice straw before and after pretreatment, the samples were prepared by sequentially drying, baking, grinding, sizing, and treatment with 2% sodium hydroxide solution for 24 hours. Subsequently, the composition analysis was performed using the TAPPI T203 om-88 method, which quantifies cellulose, hemicellulose, and lignin content by comparing the results with untreated rice straw. The obtained composition of rice straw before and after pretreatment is illustrated in Figure 1. Specifically, cellulose content in rice straw increased from 64.72% to 76.92%, hemicellulose content decreased from 25.57% to 18.70%, and lignin content decreased from 9.71% to 4.37% after pretreatment was consistent with Department of Alternative Energy Development and Efficiency [6].



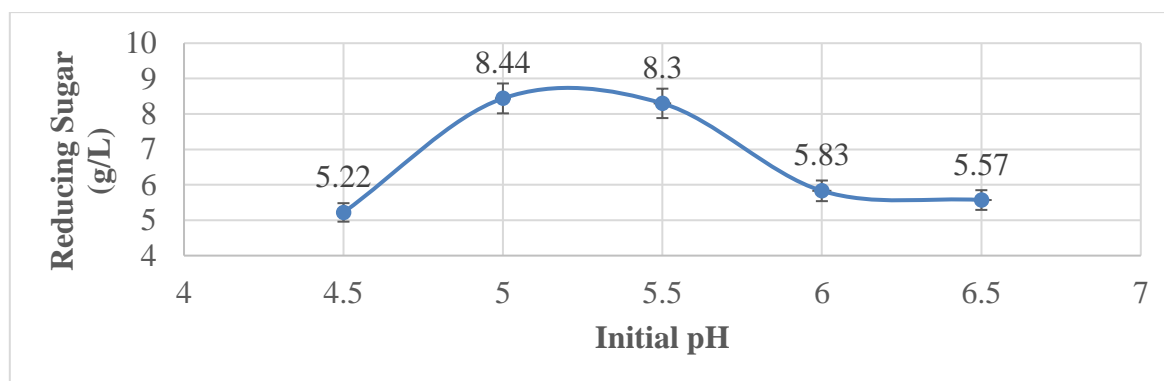
**Figure 1** Composition of rice straw before and after pretreatment.

### 3.2 Investigation of Optimal Conditions for Cellulose Degradation Using Cellulase Enzyme

The main enzyme used to degrade cellulose was cellulase. In cellulose degradation, various important factors affect the amount of reduced sugar produced. An optimal enzyme concentration of 15 FPU/g was identified for cellulose degradation in rice straw. The enzyme's performance under varying pH values and the temperature conditions for cellulose decomposition, along with different cellulose degradation processes were subsequently investigated as detailed in the following sections.

#### 3.2.1 pH Impact on Reducing Sugar Production

To assess the efficacy of cellulose degradation in rice straw, pretreated samples from the previous step were combined with cellulase enzyme at a concentration of 15 FPU/g in a citrate buffer solution. The pH value was adjusted within the range of 4.5 to 6.5. The reaction occurred in a temperature-controlled bath set at 50°C for 1 hour. After that, samples were collected and analyzed to determine the amount of reducing sugar produced as shown in Figure 2.



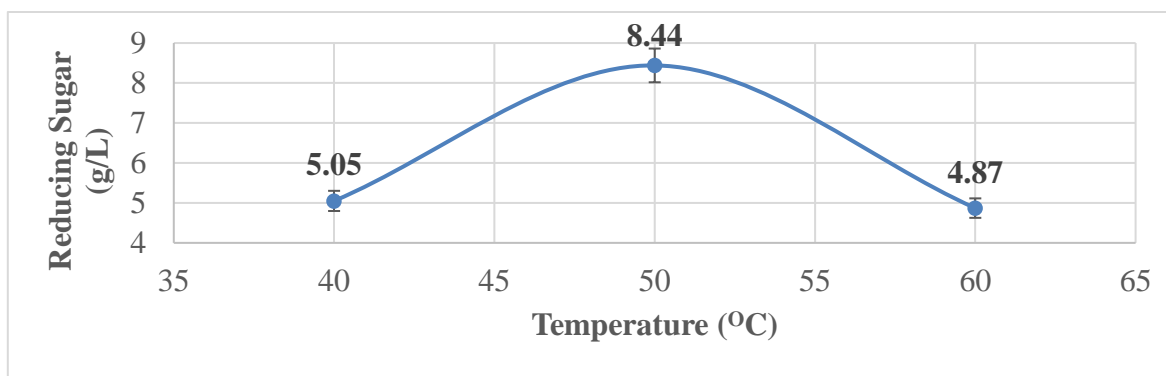
**Figure 2** Amount of reducing sugar produced from the degradation of cellulose from rice straw at different pH conditions.

The experimental findings revealed that cellulose extracted from rice straw underwent degradation by cellulase enzyme, achieving optimal results at a concentration of 15 FPU/g. This process occurred at a temperature of 50 °C for 1 hour, with pH variations tested across the range of 4.5 to 6.5. Notably, the highest yield of reducing sugar, measuring 8.44 g/L, occurred during cellulose degradation at a pH value of 5. Sequentially, cellulose degradation at pH values of 5.5, 6, and 6.5 resulted in reducing sugar quantities of 8.30, 5.83, and 5.57 g/L, respectively.

Cellulose degradation at a pH of 4.5 yielded the lowest reducing sugar production, measuring 5.22 g/L. The experiment revealed that at elevated pH levels or when enzyme activity was significantly low, there was a decrease in both enzyme activity and enzyme stability. This reduction might be the result of structural damage to the enzyme. Additionally, there could be alterations in the protein charge, rendering it unsuitable for effective interaction with the reactant [5].

### 3.2.2 Temperature Effects on Reducing Sugar Production

The pretreated rice straw samples were mixed with cellulase enzyme at concentration of 15 FPU/g in citrate buffer solution with a pH value of 5.5. The reaction was carried out in a temperature-controlled bath at different temperatures from 40, 50, and 60 °C for 1 hour. After that, samples were collected and analyzed to determine the water content. The reduced sugar produced is shown in Figure 3



**Figure 3** Amount of reducing sugar produced from cellulose decomposition from rice straw at different temperature

Specifically, cellulose degradation at 50 °C yielded the highest production of reducing sugar at 8.44 grams per liter, followed by cellulose degradation at 40 °C which exhibited the reducing sugar content at 5.05 grams per liter. Cellulose degradation at 60 °C resulted in the least amount of reducing sugar, measured at 4.87 g/l. The investigation into cellulase enzyme activity across temperatures ranging from 40 to 60 °C revealed an optimal temperature for enhancing enzyme efficiency in sugar production, approximately at 50 °C, resulting in a yield of approximately 8.44 g/l. However, the enzyme stability decreased at higher temperature [5].

## 3.3 Study of Suitable Conditions for Ethanol Fermentation

### 3.3.1 Growth of Microorganisms

This research investigated three distinct types of microorganisms designated for applications in the fermentation process. These microorganisms were identified as follows: (i) *Zymomonas m.*, a species that thrives at temperature of 30°C when utilizing the *Zymomonas* medium formula; (ii) *Saccharomyces c.*, a microorganism demonstrating optimal growth at temperature of 30°C with the yeast malt medium formula; and (ii) *Pichia s.*, a microorganism exhibiting elevated growth at 30°C using the yeast malt medium formula. The investigation of microbial growth patterns in the fermentation process involved transferring a single loop of culture into a 125 ml apple-shaped bottle, each pre-prepared with a specific food formula of 50 ml volume. The outcomes of microbial growth are visually depicted in Figure 4. Analyzing the growth dynamics of each microorganism type revealed an initial rapid growth phase. Specifically, *Pichia s.* exhibited growth within the first 9 hours, *Zymomonas m.* within the initial

16 hours, and *Saccharomyces cerevisiae* within the initial 21 hours. After 30 hours, all three microorganism types entered a steady-state growth phase. It was decided to advance the fermentation process, selecting a time point beyond 48 hours for further investigation.

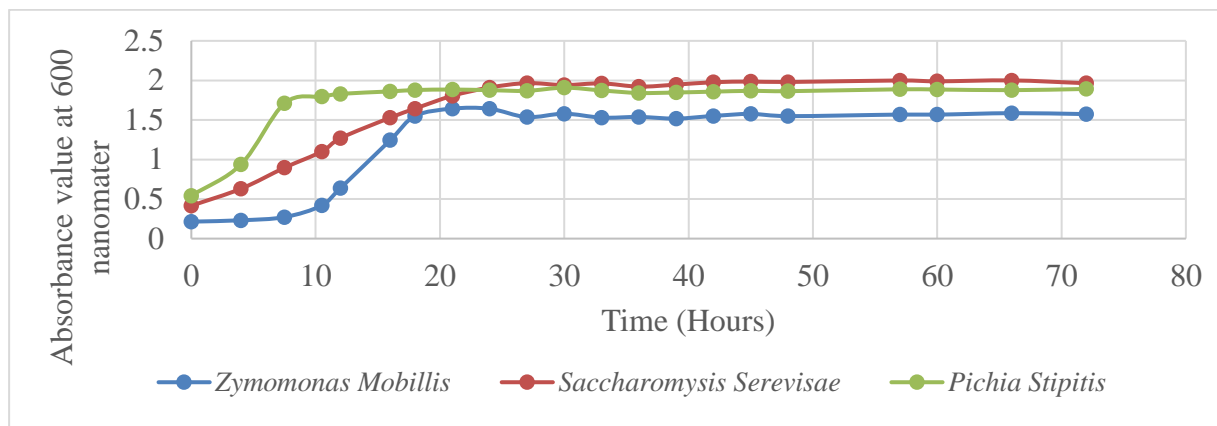


Figure 4 Growth of each type of microorganism

### 3.3.2 Effects of Using Different Types of Microorganisms in Biomass Fermentation

From Fig. 5, the combination of 5 ml of *Zymomonas m.* with 2.5 ml of *Pichia s.* yields the highest ethanol amount, reaching 1.34 g/L. This is because *Zymomonas m.* utilized a source other than glucose when co-cultured with *Pichia stipitis*. In contrast, the microorganism resulting in the lowest ethanol production is *Pichia stipitis* in the separate hydrolysis and fermentation process with ethanol yield of 1.15 g/L. As compare with Goncalves et al. [7], the ethanol yield was 0.23 g/(Lh).

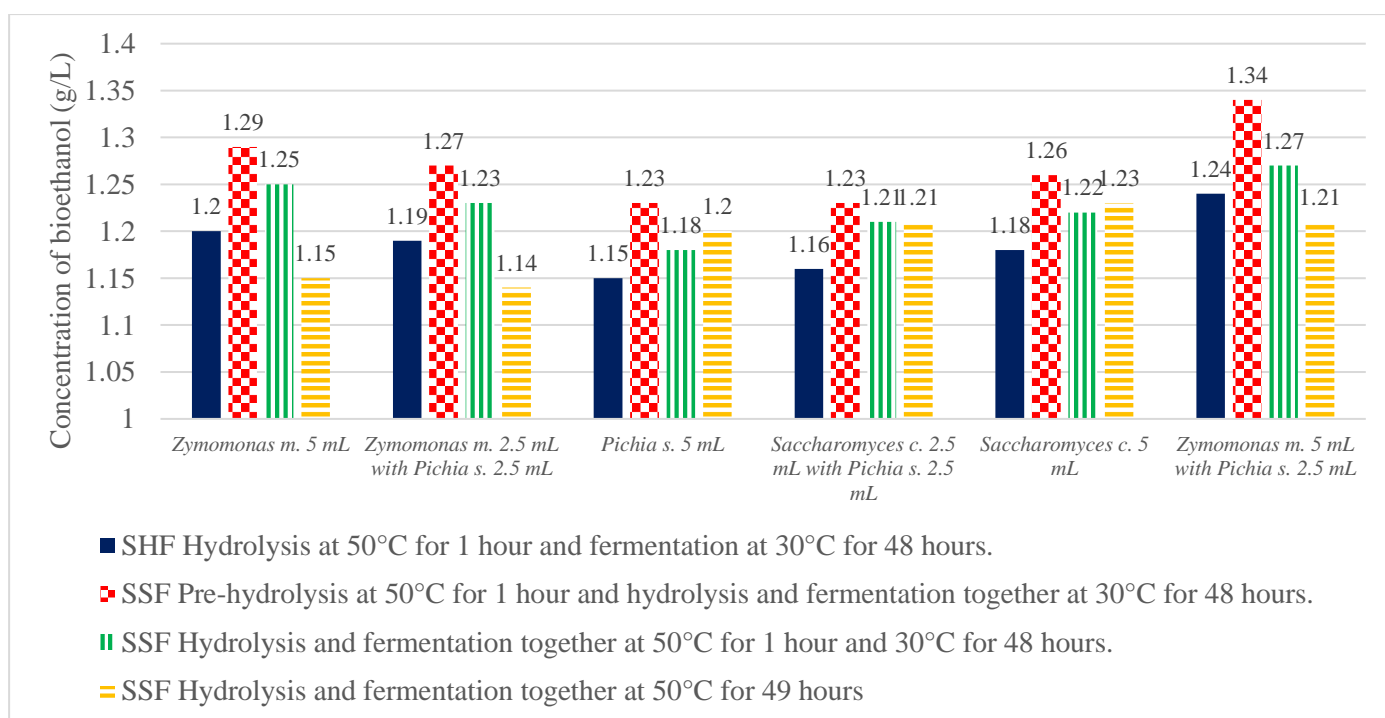


Figure 5 Concentration of ethanol produced from different processes

#### 4. Conclusions

The investigation of bioethanol fermentation from rice straw revealed the significance of pretreatment to separate cellulose for hydrolysis which yields reducing sugar. The determination of sugar content identified the optimal pH and temperature for hydrolysis at 5.5 and 50°C, respectively. Subsequently, the reduced sugar obtained from hydrolysis was utilized for bioethanol fermentation. The study revealed that the most favorable condition for bioethanol production was achieved by employing 5 ml of *Zymomonas mobilis* with 2.5 ml of *Pichia stipitis*. This combination yielded the highest amount of bioethanol. It was found that the most efficient method occurred for the pre-hydrolysis at 50°C for 1 hour, followed by the hydrolysis and fermentation together at 30°C for 48 hours. These findings underscore the importance of precise conditions and microorganism selection in optimizing the bioethanol production process from rice straw that provides valuable insights for future advancements in sustainable energy production.

#### Acknowledgements

This research paper is supported by Specific League Funds from Mahidol University. This research project is supported by Mahidol University (Fundamental Fund: fiscal year 2023 by National Science Research and Innovation Fund (NSRF)).

#### References

- [1] Novia N., Hasanudin H., Hermansyah H., Ahmad F., Vishnu K. P. (2023). Recent advances in CFD modeling of bioethanol production processes. *Renewable and Sustainable Energy Reviews* 183 (2023) 113522
- [2] Shahabazuddin M., Chandraa T.S., Meenac S., Sukumaranc R.K., Shettya N.P., Mudliar S.N. (2018). Thermal assisted alkaline pretreatment of rice husk for enhanced biomass deconstruction and enzymatic saccharification: Physico-chemical and structural characterization. *Bioresource Technology* 263 (2018) 199-206
- [3] Zabeda H., Sahuc J.N., Suelya A., Boycea A.N., Faruqf. G. (2017). Bioethanol production from renewable sources: Current perspectives and technological progress. *Renewable and Sustainable Energy Reviews* 71 (2017) 475–501
- [4] Pratto B., Santos-Rochab M.S.R., Longatic A.A., Júniora R.S., Gonçalves C.A.J. (2020) Experimental optimization and techno-economic analysis of bioethanol production by simultaneous saccharification and fermentation process using sugarcane straw. *Bioresource Technology* 297 (2020) 12244
- [5] Kalawong R., Anantalabhochai S., Wagayama M. (2014). Purification and Characterization of Bacterial Cellulase from Cow's Rumen. Graduated Research Conference Khon Kaen University.
- [6] Department of Alternative Energy Development and Efficiency, Ministry of Energy. (2013) Study project in commercial production of ethanol from cellulose
- [7] Gonçalves F.A., Ruiz H.A., Santos E.S., Teixeira J.A., Macedo G.R. (2016). Bioethanol production by *Saccharomyces cerevisiae*, *Pichia stipitis* and *Zymomonas mobilis* from delignified coconut fibre mature and lignin extraction according to biorefinery concept. *Renewable Energy* 94 (2016) 353-365

## Effect of Enantiomeric Configuration of Chiral Coformer in Chiral Resolution by Cocrystallization

Sarita Songsermsawad<sup>1</sup>, Oleksii Shemchuk<sup>2</sup>, Tom Leysens<sup>2,\*</sup>, and Adrian Flood<sup>1,\*\*</sup>

<sup>1</sup> School of Energy Science and Engineering, VISTEC, 555 Moo 1, Payupnai, Wang Chan, 21210, Rayong, Thailand.

<sup>2</sup> Institute of Condensed Matter and Nanosciences, Université catholique de Louvain, Louvain-La-Neuve, Belgium.

E-mail: \*tom.leysens@uclouvain.be

E-mail: \*\*adrian.flood@vistec.ac.th

### Abstract

Chiral separation is crucial in the pharmaceutical industry due to the increasing demand in obtaining enantiopure products. Enantiomers of a species have different biological activities. Therefore, the enantiomer with the higher activity or lower toxicity is desired. However, due to the identical physical properties between enantiomers, advanced techniques have to be employed. One of the techniques, cocrystallization with a chiral coformer, was selected to study. The separation process is started by combining a racemic mixture of an active pharmaceutical ingredient (API) with a chiral coformer to form cocrystal(s). In the case of an enantiopure coformer, the product can be either an enantiospecific or a diastereomeric system if the coformer forms cocrystal with one enantiomer of the API or both, respectively. If a racemic coformer is used, it is hoped that a conglomerate cocrystal will form which leads to simultaneously resolution of both enantiomers of the API. Regarding the different outcomes from cocrystallization, we studied the effect of changing the configuration of formerly known chiral-chiral cocrystal systems. We found that the system that can be resolved by forming enantiospecific or diastereomeric cocrystals when combining an API with an enantiopure coformer (*RS*-API + enantiopure coformer) was not always able to separate the enantiomers of the coformer; *i.e.* *RS*-coformer + enantiopure API did not result in separation of the enantiomers of the coformer.

**Keywords:** chiral resolution; cocrystallization; chiral coformer

### 1. Introduction

Most active pharmaceutical ingredients (APIs) in drugs are chiral compounds, compounds that have stereoisomers which cannot be superimposed on their mirror images. [1] A pair of molecules that are mirror-image stereoisomers are called enantiomers. Each enantiomer has similar physical properties, such as solubility and melting point, but their biological activity differs. [2] Therefore, the one having a higher activity or being non-toxic is desired. [3]

Racemic mixtures, an equimolar mixture of each enantiomer, crystallize into three modes: racemic compound, conglomerate, and solid solution. [4] Most chiral compounds are crystallized into racemic compounds in which the crystal lattice contains an equimolar amount of both enantiomers, while the rest are mostly crystallized as a conglomerate (an equimolar mixture of enantiomers). Lastly, solid solutions (crystals with a random arrangement of the two enantiomers) are rarely found. [4]

In achieving a pure enantiomer, resolution from a racemic mixture is preferred rather than asymmetric synthesis. [5] Among many processes [6], crystallization-based methods are



preferred since they are commonly practical in industrial processes with low cost and high yield. Different crystallization approaches have been used depending on the nature of the target compound. Preferential crystallization is a technique that can recover enantiopure product but it is limited to only cases where the target compound is crystallized as a conglomerate. [7] Therefore, to tackle racemic compounds, a more advanced approach is required. This study focuses on cocrystal-based separation with a chiral cofomer. [8]

Cocrystals are a type of multicomponent crystal where one unit cell contains two or more compounds with a specific stoichiometric ratio between the constituents. [9] The components in a cocrystal are connected by non-covalent bonds, which are mainly hydrogen bonds and other weak interactions. The main feature of cocrystals is that they can alter the physical properties of compounds without changing the chemical molecular moiety of the parent compounds. [10]

The cocrystal-based separation process is started by combining the racemic compound with a chiral cofomer to form cocrystal(s) as shown in Fig. 1. The product of cocrystallization depends on each chiral cofomer and/or the enantiomeric configuration of the chiral cofomer. In the case of an enantiopure cofomer (top row), the product can be either an enantiospecific [11] or a diastereomeric [12] system if the cofomer forms cocrystal with one enantiomer or both, respectively. Other than these products, the racemic compound is impossible to resolve; for example, if a racemic cocrystal is formed, the two enantiomers of the compound still stay in the same crystal form in which enantiomers cannot be separated. [13] If a racemic cofomer is used (bottom row), the preferred outcome that is able to separate the enantiomers of the API is where a conglomerate is formed. [14] In the case of conglomerate of enantiospecific cocrystal formation, enantiomers of both API and cofomer can be simultaneously resolved by preferential crystallization.

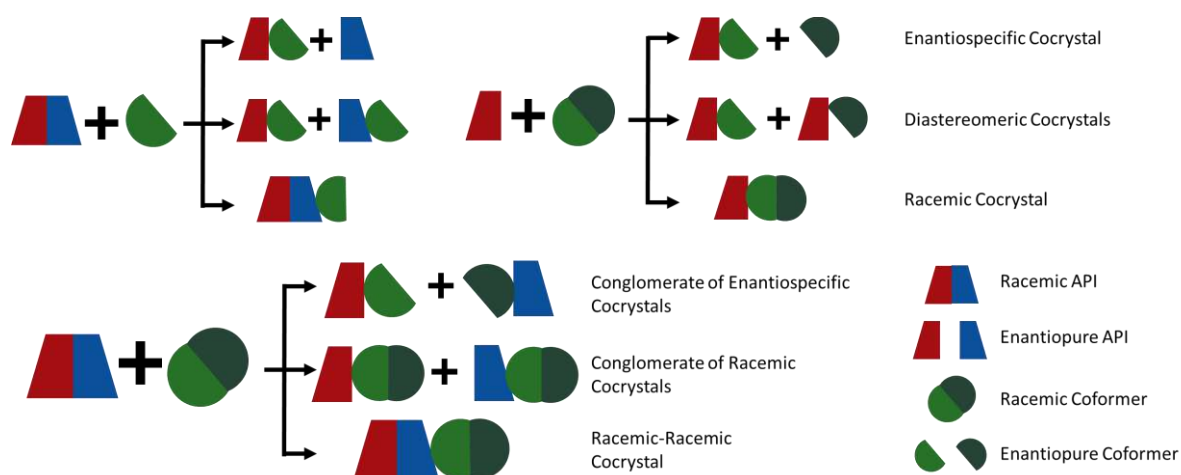


Fig. 1 Schematic diagram of common possible outcomes of combining two chiral compounds in different enantiomeric configuration combinations.

In this contribution, we searched through the literature for reported chiral-chiral cocrystals. Six cocrystal systems were selected to study as shown in Table 1. They were initially reported as enantiospecific or diastereomeric systems by combining a racemic mixture of the first compound (denoted as 1) with the second compound (2) being enantiopure. The possibility to separate enantiomers by forming cocrystal was investigated by grinding two compounds while varying five different enantiomeric configuration combinations between components [15]. Even though the products of the combinations for some systems were already reported, nonetheless, they were repeated in this study to confirm the results.

Table 1. List of selected formerly known cocrystal systems

Ref No.	System	Type of system	Cocrystal	CCDC refcode
[11,16,17]	(1) etiracetam (2) mandelic acid	Enantiospecific system	S1:S2	YASGIK
[14,16]	(1) etiracetam (2) tartaric acid	Enantiospecific system	S1:S2	YASGEG
[14,18]	(1) etiracetam (2) ibuprofen	Enantiospecific system	S1:S2	ROQMAN
[12,19]	(1) malic acid (2) tartaric acid	Diastereomeric system	S1:S2 S1:R2	WENLOT NIVYOG
[20,21]	(1) praziquantel (2) malic acid	Diastereomeric system	S1:S2 R1:S2	CUZPEU CUZPIY
[22]	(1) baclofen (2) mandelic acid	Diastereomeric system	S1:S2 R1:S2	- BAWNUM

## 2. Materials and Methods

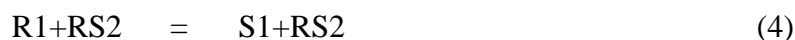
### 2.1. Reactants

*R*-malic acid, *S*-malic acid, *RS*-tartaric acid, and *S*-tartaric acid were purchased from Acros Organics. *RS*-praziquantel and *RS*-malic acid were purchased from Alfa Aesar. *RS*-methylsuccinic acid and *R*-tartaric acid were purchased from Sigma-Aldrich. *RS*-baclofen, *R*-methylsuccinic acid, *RS*-ibuprofen, *RS*-mandelic acid, *R*-mandelic acid, and *S*-mandelic acid were purchased from TCI. *S*-etiracetam, *R*-ibuprofen, *S*-ibuprofen, and *S*-methylsuccinic acid were purchased from Xiamen Top Health Biochem Tech, BLDPharm, CarboSynth, and VWR, respectively. *RS*-etiracetam was racemized from *S*-etiracetam by adding 10 g of *S*-etiracetam and a catalytic amount (0.05 eq) of sodium methoxide to 10 mL of methanol. The solution was kept at reflux under continuous stirring for 24 h and then cooled to room temperature. The compound crystallizes spontaneously. After filtration, the compound was washed twice with methanol. 95% enantiomeric excess (ee) of *S*-praziquantel was resolved from *RS*-praziquantel by *S*-malic acid following a previously reported method [20]. 95% ee *R*-baclofen was resolved from *RS*-baclofen by *S*-mandelic acid following a previously reported method [22].

### 2.2. Liquid-Assisted Grinding (LAG)

LAG is a nearly solvent-free synthesis method of cocrystal formation that frequently used for screening due to its fast and convenient preparation. Typically, a small amount of solvent (0-2  $\mu$ L solvent/ mg solid powder) is sufficient to add to mixture prior grinding. [23] LAG was performed by a RETSCH Mixer Mill (MM400) in a 2mL-plastic tube with 3 stainless steel-balls. A mixture between the two compounds of each system was prepared in a 1:1 stoichiometric ratio, as cocrystals are composed of 1:1 stoichiometric ratio between API and cofomer in all system (Table 1). 150 mg mixture of each system was added along with 10  $\mu$ L of methanol solvent, which is commonly used in LAG (0.067  $\mu$ L solvent/ mg solid powder) before grinding for 1.5 h with a frequency of 30 Hz. The grinding time and frequency are the maximum values allowed for the MM400. Each pair of cocrystal components were ground in

5 experiments with 5 different combinations. All of the enantiomeric configuration combinations between two chiral compounds (1 and 2) are shown in Eq. (1)-(5). R and S refer to enantiopure *R* and *S* configurations of that compound while RS refers to the racemic compound. Equations (1) and (2) are diastereomer pairs, which refer to cocrystal formation between enantiopure components of the two compounds. Equations (3)-(5) are tested to explore the potential of enantiospecific or diastereomeric cocrystal chiral resolution of either the API (3) and the coformer (4), and the potential to find a conglomerate cocrystal (5), as shown in Fig. 1. The two sides of each equation show the true stereoisomers that have identical stability. Therefore, grinding only one of the two identical combinations from Eq. (1)-(4) was sufficient. After grinding, the samples were dried for 24 h and then were characterized by XRPD.



### 2.3. Powder X-Ray Diffraction (XRPD)

XRPD patterns of the samples were measured on a Bruker D8 Advance powder X-ray diffractometer equipped with a Cu-K $\alpha$  X-ray source ( $\lambda = 1.5406 \text{ \AA}$ ) operating at 40 kV and 30 mA. The data were collected within  $2\theta$  values from 6 to 35° at a scan rate of 12°/min. The XRPD patterns of the samples were compared to reactants and simulated patterns of reported cocrystals from CCDC. If the patterns were different from their reactants and contained an enantiospecific or a diastereomeric cocrystal phase, it was defined as a separable process. Otherwise, it was considered as a process with no separation even though a new phase was formed (as it could be a racemic cocrystal which is not suitable for the resolution process).

### 3. Results and Discussion

XRPD results of LAG samples are shown in Fig. 2; Figures 2a-c represent the results of chosen enantiospecific systems while Figs. 2d-f show XRPD patterns of diastereomeric systems. By repeating the combinations related to only enantiopure components (Eq. (1) and/or (2)) from all selected systems to confirm the results, all reported cocrystals were successfully formed by grinding, as XRPD patterns of ground samples match the simulated patterns of cocrystals from CCDC. In the case of an enantiospecific system, only the combination of Eq. (1) forms cocrystal (black lines, Fig. 2). LAG of Eq. (2) gave a mixture of the enantiomers of the reactants. For a diastereomeric system, cocrystals are formed from both Eq. (1) and (2) (black and red lines, respectively). Excepting for one of the diastereomers of the baclofen-mandelic acid system (Fig. 2f), R1+R2 (or S1+S2) sample was compared to the pattern in the publication [22] instead due to absence of reported structure of S1:S2 cocrystal. The pattern of that combination matched the literature and suggested the cocrystal formation.

The combinations from Eq. (3) of all systems gave results according to the literature results that RS1+R2 resulted in cocrystal formation (green lines, Fig. 2). The enantiopure coformer can be used to form a cocrystal by mixing it with racemic API and, hence, can separate the

enantiomers of the API. Interestingly, we found that LAG of combinations in Eq. (4) and (5) led to different outcomes in each cocrystal system.

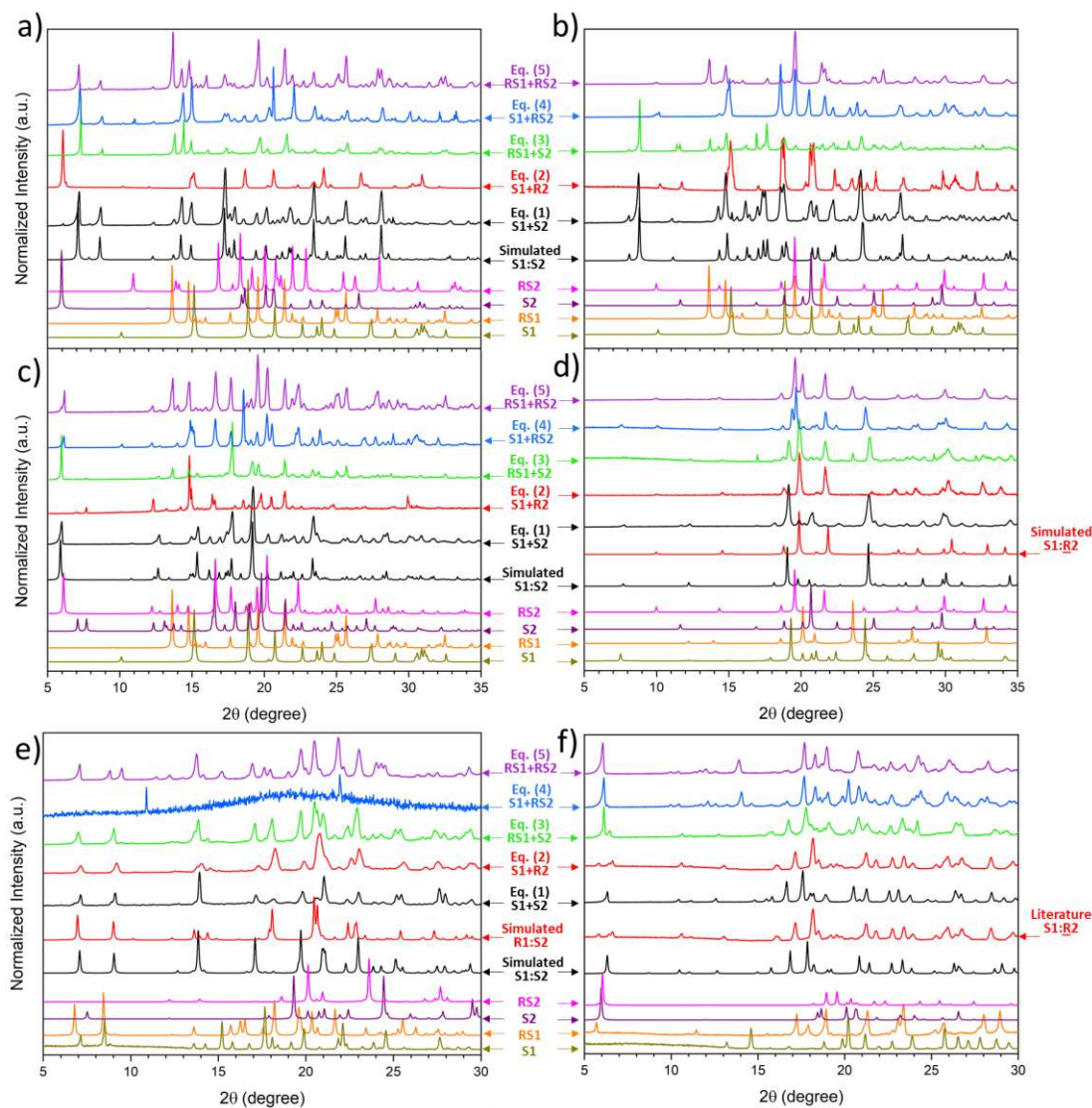


Fig. 2 XRPD patterns of ground samples between two chiral compounds of a) etiracetam (1) and mandelic acid (2), b) etiracetam (1) and tartaric acid (2), c) etiracetam (1) and ibuprofen (2), d) malic acid (1) and tartaric acid (2), e) praziquantel (1) and malic acid (2), and f) baclofen (1) and mandelic acid (2). Enantiomeric configuration of each pair was varied from R1-R2, R1-S2, RS1-R2, R1-RS2, and RS1-RS2.

The XRPD pattern of LAG in Eq. (4) of the etiracetam-mandelic acid system (blue line, Fig. 2a) shows the same patterns of cocrystal formation as in Eq. (1) and (3). As the combination R1+RS2 (Eq. (4)) gave cocrystal, therefore, not only enantiopure mandelic acid cofomer can be utilized to resolve *RS*-etiracetam but enantiopure etiracetam also can be applied to resolve *RS*-mandelic acid. The etiracetam-mandelic acid system was previously investigated in Eq. (5) by mixing racemic compounds. [14] Zhou *et al.* discovered conglomerate formation when combining racemates of both components and proposed the resolution process where two racemic compounds were simultaneously resolved by preferential crystallization. [17] We

obtained the same result from Eq. (5); the cocrystal was formed, suggesting the conglomerate cocrystal formation (purple line, Fig. 2a).

Etiracetam-tartaric acid and etiracetam-ibuprofen exhibited similar behavior, as only mixtures of the reactants were present in XRPD patterns of Eq. (4) (blue lines, Fig. 2b-c). As well as Eq. (5), no cocrystal formation was indicated for either system (purple lines, Fig. 2b-c).

New patterns occur in LAG with both Eq. (4) and (5) in the malic acid-tartaric acid systems (blue and purple lines, Fig. 2d). It could imply the new phase formations which were revealed by Cruz-Cabeza *et al.* to be solid solution cocrystals. [19] Solid solution cocrystals cannot be employed for chiral separation. Similar to praziquantel-malic acid (Fig. 2e), the new XRPD pattern of LAG in Eq. (5) was also shown by Cappuccino *et al.* to be a solid solution cocrystal. [21] LAG of Eq. (4) in the praziquantel-malic acid system resulted in an amorphous phase which could be due to the instability of the phase formation.

For the baclofen-mandelic acid system, the same phases were obtained from Eq. (4) and (5). This phase did not correspond to any diastereomeric cocrystals of baclofen-mandelic acid. Therefore, the new phase from grinding R1+RS2 of Eq. (4) could be racemic cocrystal R1:RS2. The result from RS1+RS2 of Eq. (5) could be either a conglomerate of R1:RS2 and S1:RS2 or a fully racemic cocrystal RS1:RS2 that is isostructural to R1:RS2. A conglomerate of racemic cocrystals can be utilized to achieve enantiopure of one compound, while a formation of a fully racemic cocrystal is not useful for chiral separation (see Fig. 1). Nevertheless, the results need to be confirmed further.

All the results are summarized in Table 2. If the LAG of the combinations in Eq. (3)-(5) resulted in the cocrystal formation of Eq. (1) or/and (2), that combination was defined as separable (denoted with Y). Even though the new phase formations from Eq. (4)-(5) in all of diastereomeric systems required further confirmation, the results were described as no separation potential due to the complexity.

Table 2. Summary of the LAG results from XRPD of combining selected two chiral compounds in different enantiomeric combinations<sup>a,b</sup>

System	Eq. (1) R1+R2 S1+S2	Eq. (2) R1+S2 S1+R2	Eq. (3) RS1+R2 RS1+S2	Eq. (4) R1+RS2 S1+RS2	Eq. (5) RS1+RS2
etiracetam-mandelic acid	Y	M	Y, S	Y, S	Y, S
etiracetam-tartaric acid	Y	M	Y, S	M	M
etiracetam-ibuprofen	Y	M	Y, S	M	M
malic acid-tartaric acid	Y	Y	Y, S	Y, N	Y, N
praziquantel-malic acid	Y	Y	Y, S	N	Y, N
baclofen-mandelic acid	Y	Y	Y, S	Y, N	Y, N

<sup>a</sup> Y = cocrystal formation; S = separable process; M = mixture of reactants; N = no separation potential.

<sup>b</sup> Green color is applied to combinations in which the enantiospecific/diastereomeric cocrystal phase(s) as Eq. (1) or/and (2) is/are obtained, leading to chiral resolution. Yellow color is used for the combination that results in the cocrystal formation of a phase other than the first two equations, but usually a racemic cocrystal which is not suitable for the separation process. Red color shows combinations where there is no cocrystal formation.

From all six cases, only the etiracetam-mandelic acid system formed a conglomerate when combining two racemic compounds and it is also the one that is possible to resolve either

racemic API or racemic coformer by using an enantiopure compound of the other species by forming a cocrystal. Whereas in other systems, they formed cocrystals that are only possible to resolve enantiopure API when mixing racemic API with enantiopure coformer but show no separation potential in other combinations. These are the study cases to demonstrate the possibility in finding conglomerate cocrystal formation and highlight the behavior of combining two chiral compounds.

#### 4. Conclusions

We want to highlight the effect of enantiomeric configuration combinations between two chiral compounds in chiral resolution by cocrystallization. The six selected systems exhibit different outcomes in each combination. All the systems can be resolved by forming enantiospecific or diastereomeric cocrystals when combining a racemic API with an enantiopure coformer (Eq. (3), *RS*-API + enantiopure coformer). However, five out of six systems were not able to separate the enantiomers of the coformer in the opposite way (Eq. (4)). *RS*-coformer + enantiopure API did not result in separation of the enantiomers of the coformer. Moreover, only one of the six systems has a conglomerate formation when mixing racemic mixtures of both components (Eq. (5)).

#### References

- [1] Nguyen, L. A., He, H., and Pham-Huy, C. (2006). Chiral drugs: an overview. *International Journal of Biomedical Science*, 2(2), 85-100.
- [2] Smith, S. W. (2009). Chiral toxicology: It's the same thing...only different. *Toxicological Science*, 110(1), 4.
- [3] Calcaterra, A., and D'Acquarica, I. (2018). The market of chiral drugs: Chiral switches versus de novo enantiomerically pure compounds. *Journal of Pharmaceutical and Biomedical Analysis*, 147, 323-340.
- [4] Jacques, J., Collet, A., and Wilen, S. H. (1981). *Enantiomers, racemates, and resolutions*: Wiley.
- [5] Hawkins, J. M., and Watson, T. J. N. (2004). Asymmetric catalysis in the pharmaceutical industry. *Angewandte Chemie International Edition*, 43(25), 3224-3228.
- [6] Teng, Y., Gu, C., Chen, Z., Jiang, H., Xiong, Y., Liu, D., and Xiao, D. (2022). Advances and applications of chiral resolution in pharmaceutical field. *Chirality*, 34(8), 1094-1119.
- [7] Coquerel, G. (2006). Preferential crystallization. In *The Novel Optical Resolution Technologies* (Sakai, K., Hirayama, N., and Tamura, R., Eds.), pp. 1-51. Heidelberg, Berlin: Springer.
- [8] Kaviani, R., Jouyban, A., and Shayanfar, A. (2023). Chiral resolution methods for racemic pharmaceuticals based on cocrystal formation. *CrystEngComm*, 25(44), 6120-6131.
- [9] Aitipamula, S., Banerjee, R., Bansal, A. K., Biradha, K., Cheney, M. L., Choudhury, A. R., Desiraju, G. R., Dikundwar, A. G., Dubey, R., Duggirala, N., Ghogale, P. P., Ghosh, S., Goswami, P. K., Goud, N. R., Jetti, R. R. K. R., Karpinski, P., Kaushik, P., Kumar, D., Kumar, V., Moulton, B., Mukherjee, A., Mukherjee, G., Myerson, A. S., Puri, V., Ramanan, A., Rajamannar, T., Reddy, C. M., Rodriguez-Hornedo, N., Rogers, R. D., Row, T. N. G., Sanphui, P., Shan, N., Shete, G., Singh, A., Sun, C. C., Swift, J. A., Thaimattam, R., Thakur, T. S., Kumar Thaper, R., Thomas, S. P., Tothadi, S., Vangala, V. R., Variankaval, N., Vishweshwar, P., Weyna, D. R., and Zaworotko, M. J. (2012).

- Polymorphs, Salts, and Cocrystals: What's in a Name? *Crystal Growth & Design*, 12(5), 2147-2152.
- [10] Karagianni, A., Malamatari, M., and Kachrimanis, K. (2018). Pharmaceutical cocrystals: New solid phase modification approaches for the formulation of APIs. *Pharmaceutics*, 10(1), 18.
- [11] Springuel, G., and Leysens, T. (2012). Innovative chiral resolution using enantiospecific co-crystallization in solution. *Crystal Growth & Design*, 12(7), 3374-3378.
- [12] Eddleston, M. D., Arhangelskis, M., Frišćić, T., and Jones, W. (2012). Solid state grinding as a tool to aid enantiomeric resolution by cocrystallisation. *Chemical Communications*, 48(92), 11340-11342.
- [13] Li, W., de Groen, M., Kramer, H. J. M., de Gelder, R., Tinnemans, P., Meekes, H., and ter Horst, J. H. (2021). Screening approach for identifying cocrystal types and resolution opportunities in complex chiral multicomponent systems. *Crystal Growth & Design*, 21(1), 112-124.
- [14] Zhou, F., Body, C., Robeyns, K., Leysens, T., and Shemchuk, O. (2023). On the pairwise cocrystallization of racemic compounds. *CrystEngComm*, 25(20), 3060-3065.
- [15] Tumanova, N., Tumanov, N., Fischer, F., Morelle, F., Ban, V., Robeyns, K., Filinchuk, Y., Wouters, J., Emmerling, F., and Leysens, T. (2018). Exploring polymorphism and stoichiometric diversity in naproxen/proline cocrystals. *CrystEngComm*, 20(45), 7308-7321.
- [16] Springuel, G., Norberg, B., Robeyns, K., Wouters, J., and Leysens, T. (2012). Advances in pharmaceutical co-crystal screening: Effective co-crystal screening through structural resemblance. *Crystal Growth & Design*, 12(1), 475-484.
- [17] Zhou, F., Shemchuk, O., Charpentier, M. D., Matheys, C., Collard, L., ter Horst, J. H., and Leysens, T. (2021). Simultaneous chiral resolution of two racemic compounds by preferential cocrystallization. *Angewandte Chemie International Edition*, 60(37), 20264-20268.
- [18] Harmsen, B., and Leysens, T. (2018). Dual-drug chiral resolution: Enantiospecific cocrystallization of (*S*)-ibuprofen using levetiracetam. *Crystal Growth & Design*, 18(1), 441-448.
- [19] Cruz-Cabeza, A. J., Lestari, M., and Lusi, M. (2018). Cocrystals help break the "Rules" of isostructurality: Solid solutions and polymorphism in the malic/tartaric acid system. *Crystal Growth & Design*, 18(2), 855-863.
- [20] Sánchez-Guadarrama, O., Mendoza-Navarro, F., Cedillo-Cruz, A., Jung-Cook, H., Arenas-García, J. I., Delgado-Díaz, A., Herrera-Ruiz, D., Morales-Rojas, H., and Höpfl, H. (2016). Chiral resolution of *RS*-praziquantel via diastereomeric co-crystal pair formation with *L*-malic acid. *Crystal Growth & Design*, 16(1), 307-314.
- [21] Cappuccino, C., Spoletti, E., Renni, F., Muntoni, E., Keiser, J., Voinovich, D., Perissutti, B., and Lusi, M. (2023). Co-crystalline solid solution affords a high-soluble and fast-absorbing form of praziquantel. *Molecular Pharmaceutics*, 20(4), 2009-2016.
- [22] Songsermsawad, S., Nalaoh, P., Promarak, V., and Flood, A. E. (2022). Chiral resolution of *RS*-baclofen via a novel chiral cocrystal of *R*-baclofen and *L*-mandelic acid. *Crystal Growth & Design*, 22(4), 2441-2451.
- [23] Ying, P., Yu, J., Su, W. (2021). Liquid-Assisted Grinding Mechanochemistry in the Synthesis of Pharmaceuticals. *Advance Synthesis & Catalysis*, 363(5), 1246-1271.

## Inhibitory Effects of *Schinus terebinthifolia* Leave Extract on Polyphenol Oxidase Activity and Enzymatic Browning

Supatcha Suankhem<sup>1</sup>, Suthida Boonsith<sup>1,\*</sup>, and Warangkana Pornputtapitak<sup>1</sup>

<sup>1</sup>Department of Chemical Engineering, Faculty of Engineering, Mahidol University, Nakhon Pathom 73170, Thailand

E-mail: supatcha.sua@student.mahidol.edu, \*suthida.bos@mahidol.edu (Corresponding author)

### Abstract

In response to the significant challenge posed by polyphenol oxidase (PPO)-induced enzymatic browning in food products, this study aimed to assess the effectiveness of natural anti-browning agents in preserving the quality and visual appeal of *Musa acuminata* banana peels. Specifically, the study focused on the high-antioxidant extract derived from *Schinus terebinthifolia* leaves. The antioxidant properties of the extract were evaluated through DPPH and FRAP assays, revealing an impressive 99% inhibition of PPO activity, comparable to sodium metabisulphite. Further analysis identified phenolic and flavonoid compounds in the extract as crucial contributors to its PPO inhibitory activity. Additionally, the study explored the practical application of the *Schinus terebinthifolia* leave extract in combination with a coating agent (Chitosan/Polyvinyl Alcohol) to reduce the browning index of banana peels. Results demonstrated a substantial reduction in the browning index, highlighting the extract's efficacy in minimizing enzymatic browning. The findings not only offer a natural and sustainable alternative to synthetic inhibitors but also underscore the potential of *Schinus terebinthifolia* leave extract in enhancing the shelf life and visual appeal of fruits. This research contributes to the advancement of eco-friendly approaches in the food industry, providing valuable insights into the application of natural anti-browning agents for improved food preservation.

**Keywords:** Enzymatic browning; Polyphenol Oxidase Inhibitor; Banana peel; Browning index

### 1. Introduction

The degradation of food quality due to the undesirable process of browning, catalyzed by polyphenol oxidase (PPO), poses a considerable challenge in the preservation and visual appeal of various food products. Browning not only affects the sensory attributes of food but also signifies the loss of nutritional value. Understanding and mitigating this phenomenon are crucial for maintaining the overall quality of food. Polyphenol oxidase, a key enzyme involved in the browning process, has been a focal point in research aimed at preserving the visual and nutritional qualities of food items. This study delves into the potential of natural anti-browning agents as effective inhibitors of PPO-induced browning [1].

*Schinus terebinthifolia* Raddi, commonly known as Brazilian Pepper, belongs to the cashew family. Thais have a preference for consuming fresh leaves with chili paste. It is not only rich in fiber, promoting healthy digestion but it is also very high in antioxidants. These leaves play a role in traditional medicine, with various applications such as brewing them into tea to alleviate joint pain [2]. However, there has been no report of its ability to inhibit browning.

Specifically, we focus on the high-antioxidant extract derived from *Schinus terebinthifolia* leaves and its impact on *Musa acuminata* banana peels. The choice of banana peels as the



experimental substrate is significant, considering their susceptibility to rapid browning and the importance of bananas as a widely consumed fruit. Previous studies have highlighted the effectiveness of synthetic anti-browning agents, such as sodium metabisulphite, but the exploration of natural alternatives remains a promising avenue. In this context, our research aims to contribute to the understanding of the inhibitory effects of the *Schinus terebinthifolia* extract on PPO, comparing its efficacy with established synthetic inhibitors. Furthermore, the practical applications of these findings are explored through the combination of the *Schinus terebinthifolia* extract with an edible film coating, presenting a potential solution for preventing browning and preserving banana peels in a natural and sustainable manner.

## 2. Materials and Methods

### 2.1. Preparing the *Schinus terebinthifolia* leave extract

The leaves of *Schinus terebinthifolia* were dried in a hot air oven at 60 °C for 24 hours, and grinded to a fine powder using a Philips ProBlend 4 grinder. After measuring 10 g of dried leaf powder, it was loaded into a Soxhlet extractor thimble and subjected to reflux with 200 mL of ethanol for 3 hours. The resulting solution was then cooled, filtered, and concentrated under reduced pressure using a rotary evaporator. The extract was either used immediately or stored at 4 °C for up to two weeks, retaining its efficacy.

### 2.2. Antioxidant power

The extract was tested for antioxidant activity by different mechanisms via DPPH and FRAP assay.

**DPPH assay.** To evaluate the extract's ability to scavenge DPPH<sup>•</sup> and reduce it to hydrazine, a modified 2,2-diphenyl-1-picrylhydrazyl (DPPH) scavenging assay was conducted [3]. In a 96-well microplate, 200 μL of the extract (200 μg/mL) and 400 μL of ethanolic DPPH solution (250 μM) were mixed and incubated in darkness for 30 minutes. Absorbance at 517 nm was measured using a Microplate Reader (Thermo: Varioskan Flash), and compared to a control (lacking the extract), with %DPPH<sup>•</sup> scavenging calculated based on three measurements.

**FRAP assay.** Slight modifications were introduced to the Ferric-reducing antioxidant power (FRAP) procedure, a method reliant on the conversion of the colorless Fe<sup>3+</sup>-2,4,6-Tris(2-pyridyl)-s-triazine complex to the blue-colored Fe<sup>2+</sup>-tripyridyl triazine complex. This conversion occurs in the presence of electron-donating antioxidants at a pH of 3.6 [3]. The FRAP reagent was formulated by combining 300 mM acetate buffer with a TPTZ solution (10 mM TPTZ in 40 mM HCl) and 20 mM FeCl<sub>3</sub>·6H<sub>2</sub>O in a ratio of 10:1:1 (v/v/v). Following this, the mixture was incubated at 37 °C for 30 minutes. Subsequently, a thoroughly mixed solution of 10 μL of the diluted extract and 300 μL of FRAP reagent was prepared. The reduction of the Fe<sup>3+</sup>TPTZ complex to the Fe<sup>2+</sup> form led to the development of an intense blue-colored complex, and the absorbance at 593 nm was measured using a Microplate Reader. This entire process was performed in triplicate, and the FRAP values were expressed as equivalent mmol of Fe<sup>2+</sup>/g of dried extract.

### 2.3. Total Phenolic Content of the extract

The Total Phenolic Content (TPC) of the extract was assessed using the Folin-Ciocalteu reagent method [3]. The extract (1 mL, 1 mg/mL) was mixed with Folin-Ciocalteu reagent (200

$\mu\text{L}$ , 10% v/v) and  $\text{Na}_2\text{CO}_3$  solution (2 mL, 7.5% w/v) for 3 minutes. After incubation in the dark for 90 minutes, absorbance was measured at 765 nm using a UV/Vis Microplate Reader. TPC was determined using a gallic acid standard calibration curve, expressed as mg GAE/g of dried leaf extract. This procedure was repeated three times, and the mean  $\pm$  S.D. was documented.

#### 2.4. Total Flavonoid Content of the extract

The quantitative determination of total flavonoid content (TFC) in the extracts of vegetable leaves utilized the aluminum chloride colorimetric method [4]. In this procedure, 0.6 mL of the extract solution (1 mg/mL) was thoroughly mixed with 0.6 mL of a 2% (w/v)  $\text{AlCl}_3$  solution. The resulting mixture was allowed to stand for 60 minutes at room temperature. Subsequently, the absorbance of the resulting supernatant was measured at 420 nm using a 96-well UV/Vis Microplate Reader. The concentration of TFC in the extract was then determined from the quercetin standard calibration curve. The outcomes were expressed as quercetin equivalents, denoted in milligrams per gram of dried extract (mg QE/g). This analytical procedure was replicated three times, and the mean  $\pm$  standard deviation (S.D.) was documented.

#### 2.5. PPO inhibition study

*Musa acuminata* banana peel served as the primary material for PPO source. The bananas were washed, peeled, and subsequently frozen at  $-40\text{ }^\circ\text{C}$  in a Thermo Fisher Scientific-729 freezer. After freezing, the peels underwent a 72-hour freeze-drying process in a Labconco Freezone 6 Plus freeze dryer. The resultant freeze-dried peels were then ground into flour using a Philips ProBlend4 blender for 60 seconds. The obtained flour was stored at  $-20\text{ }^\circ\text{C}$  until the PPO extraction process. In the extraction process, 1 g of banana peel flour was homogenized (Heidolph: SilentCrusher M) at 3500 rpm on ice for 30 seconds with a chilled McIlvaine buffer (pH 6.8,  $4\text{ }^\circ\text{C}$ ). The buffer contained 0.2 M disodium phosphate and 0.1 M citric acid, maintaining a liquid-to-solid ratio of 30:1. Additionally, it included 0.5 g/g sample of filter aid polyvinylpyrrolidone (PVP) and 0.5% (v/v) Triton X-100. Following homogenization, the mixtures underwent centrifugation for 20 minutes ( $4\text{ }^\circ\text{C}$ ) at  $10,000\times g$  (Eppendorf Centrifuge 5810R). The resulting supernatant, after filtration through Whatman No.1 filter paper, was collected and stored at  $-20\text{ }^\circ\text{C}$  for up to two weeks for subsequent enzyme activity determination and inhibition assays.

The spectrophotometric assessment of PPO activity was conducted in this study. Sodium metabisulphite acted as the chemical inhibitor, while the extract from *Schinus terebinthifolia* leaves served as a natural inhibitor. PPO activities were assayed with inhibitors at three different concentrations (0.5, 1.0, and 4.0 mg/mL) using L-DOPA as the substrate. The reaction mixture, comprising 100  $\mu\text{L}$  crude PPO and 100  $\mu\text{L}$  inhibitor, underwent a 30-minute incubation at room temperature. To initiate the formation of a pink reaction product, 600  $\mu\text{L}$  of pre-incubated 15 mM L-DOPA in assay buffer was added, and the mixture was further incubated at  $45\text{ }^\circ\text{C}$ . PPO activity was monitored by measuring the increase in absorbance at 475 nm using a UV-vis spectrophotometer (SHIMAD-ZU/UV-1800) every 15 seconds for 4 minutes. The PPO activity was quantified by analyzing the linear increase in absorption over the initial 60 seconds. One unit of PPO activity was defined as an increase in absorbance by 0.001 per min/mL, expressed as U/mL $\cdot$ min. Percentage inhibition values for each inhibitor were calculated using the initial PPO activity without an inhibitor as a reference. The percent inhibition was determined using the formula presented in Equation (1):

$$\%PPO \text{ inhibition} = \frac{A-B}{A} \times 100 \quad (1)$$

where A represents Initial PPO activity (use deionized water instead of inhibitor), B represents PPO activity in the presence of natural inhibitor. All determinations were performed in triplicate.

The study investigated the Michaelis-Menten constant ( $K_m$ ), maximum velocity ( $V_{max}$ ), and  $K_m/V_{max}$  values by employing L-DOPA as a substrate in the 1-35 mM range under standard conditions, with absorbance monitored at 475 nm. Analysis was conducted using  $1/V$  and  $1/[S]$  plots, following the approach described by Lineweaver and Burk (1934) [5]. This experiment aimed to assess the influence of inhibitors on polyphenol oxidase activity in banana peel.

## 2.6. Browning index

To explore the anti-browning effects, a solution of exogenous Chitosan/Polyvinyl Alcohol (CS/PVA) blended with an inhibitor at concentrations of 0.5 mg/mL was applied to banana coating agents, aiming to reduce fruit peel browning during shelf life. The coating agents were prepared by incorporating the inhibitor into a polymer CS/PVA solution and mixed in a 1,000 mL solution under magnetic stirring for 4 hours at 27 °C. Bananas (10 hands from the same bunch) were chosen for uniformity in size and color at stage 3 [6]. The bananas underwent a 10-minute immersion in the coating agent under ambient air conditions and were subsequently stored at room temperature (27 °C ± 1 and RH 38 ± 2) for 14 days. In browning index measurement, fresh banana peel (1 g) was homogenized in 15 mL of 10% trichloroacetic acid. The mixture was incubated at 35 °C for 2 hours before being subjected to centrifugation at 11,000×g for 15 minutes at 25 °C. The resulting supernatants were analyzed for absorbance at 420 nm using a spectrophotometer, with findings reported as the absorbance at 420 nm.

## 2.7. Statistical analysis

Statistical analysis of all assays and inhibition studies were performed in triplicate and mean value and standard deviation were calculated.

## 3. Results and Discussion

### 3.1. Antioxidant properties of *Schinus terebinthifolia* leave extract

The antioxidant properties of the *Schinus terebinthifolia* leave extract were assessed using both the DPPH and FRAP assays as shown in Table 1. The DPPH assay demonstrated an 85% scavenging activity, highlighting the extract's robust ability to neutralize free radicals. Soxhlet extraction with ethanol as the solvent yielded high antioxidant activity in *Schinus terebinthifolia* leave extract, corroborating findings from Russo et al. (2017) and Andrade et al. (2017) [7, 8]. The FRAP assay revealed a reducing antioxidant power of 211 mmol of  $Fe^{2+}$ /g of dried extract, emphasizing the extract's capacity to reduce ferric ions. The results from both the DPPH and FRAP assays collectively underscore the remarkable antioxidant potential of the extract. This reducing power is crucial for mitigating the oxidative reactions catalyzed by polyphenol oxidase, thus inhibiting the enzymatic browning process [9].

Table 1. Antioxidant properties and bioactive composition of *Schinus terebinthifolia* leave extract.

Extract	DPPH (%)	FRAP (mmol Fe <sup>2+</sup> /g)	TPC (mgGAE/g)	TFC (mgQE/g)
<i>S. terebinthifolia</i> leaves	84.66 ± 0.61	211.20 ± 9.40	712.19 ± 12.22	45.70 ± 1.12

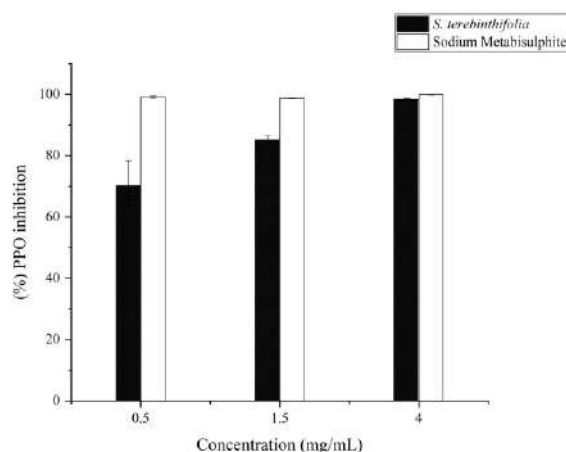
Results are expressed as means ± standard deviation.

TPC and TFC of the extract was determined to gain insights into the amount of bioactive compounds as shown in Table 1. The results indicated a TPC of 712 mg GAE/g which was consistent with Russo et al. (2017). TFC in the extract was revealed a TFC of 46 mg QE/g. The leaf extract has a slightly higher flavonoid content than the *Schinus terebinthifolius Raddi* fruit extract, which was previously reported by de Oliveira et al. (2020) [10]. TPC and TFC with FRAP and DPPH reflect that these phenolic and flavonoid compounds play a major role in the antioxidant activity of vegetable extracts. Phenolic compounds, namely Gallic acid amide, ethyl digallate and Syringic acid, were detected in the leave extract of *Schinus terebinthifolia*, along with flavonoid constituents including Myricetin, Myricitrin (Quercetin-3-D-glucoside), Reynoutrin (Quercetin 3-O-beta-D-glucopyranoside), and Quercetin. These compounds exhibit antioxidative properties [11-13].

### 3.2. PPO inhibition study

#### 3.2.1. Effect of the extract on the inhibition of PPO

In the absence of an inhibitor, PPO acts as a catalyst in the oxidation of the substrate (L-DOPA), leading to the formation of DOPA-quinone. Subsequently, this DOPA-quinone compound undergoes polymerization, resulting in the formation of melanin. The presence of antioxidants in the extract influences PPO inhibition by engaging in reactions with oxygen, thereby impeding the initiation of browning. Furthermore, these antioxidants can interact with intermediate products, disrupting the chain reaction and effectively inhibiting melanin formation [14]. The PPO inhibitory activity of the extract at different concentrations (0.5, 1.5, and 4.0 mg/mL) is expressed as a percentage of inhibition of PPO, as illustrated in Fig. 1, with inhibition percentages ranging approximately from 70% to 99%. The extract exhibits significant inhibitory activity against PPO, comparable to the effectiveness of sodium metabisulphite, a chemical inhibitor, at the same concentration and extraction medium. The extract's PPO inhibitory activity shows a concentration-dependent pattern due to the antioxidant activity of the extracts. The result was in agreement with Lim et al. (2019) said that increasing the concentration of natural inhibitors increases the ability to inhibit PPO [15]. Besides antioxidants, certain crucial compounds in the extract may contribute to PPO inhibition. The application of heat during the Soxhlet extraction process results in an elevation of flavonoids and phenolic content in the extract, enhancing its antioxidant capability and leading to a higher inhibition percentage [16]. Phenolic compounds may inhibit PPO activity by interacting with the enzyme's active site, acting as chelating agents for Cu<sup>2+</sup>, essential for PPO activity [17]. This inhibition can occur through the formation of bonds, electron donation, cross-linking with PPO via hydrogen bonding, or competitive inhibition of tyrosinase by mimicking its substrate [18].



**Fig. 1** Percent inhibition towards banana peel PPO of the *Schinus terebinthifolia* leave extract and sodium metabisulphite. Vertical represents standard errors of means, n=3.

### 3.2.2. Enzyme Kinetics Parameters

*Musa acuminata* banana peel PPO activity determined in this study was 1.027 U/min·mL for L-DOPA.  $K_m$ ,  $V_{max}$ , and  $K_m/V_{max}$  values of PPO with L-DOPA and no inhibitor from the Lineweaver-Burk plots were shown in Table 2. The values were in the range of those reported by Wohlt et al. (2021) [19]. To investigate the inhibitory effects of the examined extracts on PPO activities, kinetic studies were conducted using the Lineweaver-Burk method. Analysis of the kinetic parameters, it was determined that the inhibition patterns of the inhibitors differ. When treated with the extract, the enzyme exhibited mixed noncompetitive inhibition, characterized by altered higher  $K_m$  and lower  $V_{max}$  values and distinct patterns suggested varying modes of interaction between the inhibitors and the PPO enzyme. In contrast to Sukhonthara et al. (2012) study, where rice bran extract was employed to inhibit banana polyphenol oxidase, our current investigation revealed that the *Schinus terebinthifolia* extract exhibited a superior PPO inhibitory capacity when compared to rice bran extract [20].

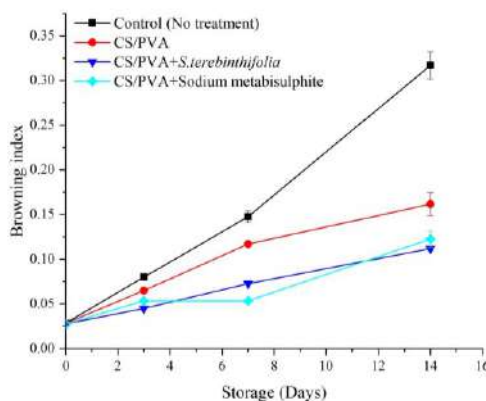
Table 2. Kinetic parameters of the PPO enzyme after the inhibitor inserted.

Inhibitor	$K_m$	$V_{max}$	$K_m/V_{max}$	Type
No Inhibitor	8.76	1.88	4.67	-
<i>S. terebinthifolia</i>	23.76	1.22	19.45	Mixed noncompetitive
Sodium Metabisulphite	40.94	1.70	24.04	Competitive

### 3.3. Browning index

From the study of the antioxidant properties and PPO inhibitory effect of the extract, in order to prolong the browning life of bananas, the extract and sodium metabisulphite in the examined concentration 0.5 mg/mL were assessed for application by applying a load-in coating agent (CS/PVA). Figure 3 shows browning index recorded with the absorbance at 420 nm. The extract and sodium metabisulphite effectively reduced the browning index of bananas, whereas the browning index of untreated bananas was constantly increasing. Coating bananas with a polymer solution proves effective in reducing browning by minimizing oxygen exposure. However, when combined with either the extract or sodium metabisulphite, the results are

further enhanced, providing even better outcomes. Enzymatic browning can decrease as a result of PPO inhibition.



**Fig. 3** Browning index in untreated and treated bananas over the storage period of 14 days. Vertical represents standard errors of means, n=3.

#### 4. Conclusions

In conclusion, the *Schinus terebinthifolia* leaf extract exhibited remarkable antioxidant properties, as evidenced by its significant scavenging activity in the DPPH assay and substantial reducing antioxidant power in the FRAP assay. These findings position the extract as a potent natural antioxidant with the potential to counteract oxidative stress and enzymatic browning in food products. TPC and TFC of further underscore the extract's rich composition of bioactive compounds. Additionally, the extract demonstrated significant inhibitory activity against the PPO enzyme with %PPO inhibition which was as high as sodium metabisulphite in a mixed noncompetitive way. Overall, these findings suggest the *Schinus terebinthifolia* leaf extract as a promising natural source of antioxidants and PPO inhibitors, highlighting its potential applications in the food industry for enhancing shelf life and preserving the visual appeal of perishable fruit products.

#### Acknowledgment

This research project received research funding for graduate studies in agriculture and agricultural industry from the Office of Agricultural Research Development (Public Organization) for the fiscal year 2022.

#### References

- [1] Sui, X., Meng, Z., Dong, T., Fan, X., & Wang, Q. (2023). Enzymatic browning and polyphenol oxidase control strategies. *Current Opinion in Biotechnology*, 81, 102921.
- [2] Patocka, J., & de Almeida, J. D. (2017). Brazilian pepper tree: Review of pharmacology. *Mil. Med. Sci. Lett*, 86, 32-41.
- [3] Alara, O. R., Abdurahman, N. H., & Ukaegbu, C. I. (2018). Soxhlet extraction of phenolic compounds from *Vernonia cinerea* leaves and its antioxidant activity. *Journal of Applied Research on Medicinal and Aromatic Plants*, 11, 12-17.
- [4] Singh, R., & Kumar, S. (2021). Study on correlation of Antioxidant activities with presence of phenolic and Flavanoid contents in *Embllica officinalis* and *Terminalia chebula*. *Journal of Drug Delivery and Therapeutics*, 11(1), 32-35.

- [5] Lineweaver, H., & Burk, D. (1934). The determination of enzyme dissociation constants. *Journal of the American chemical society*, 56(3), 658-666.
- [6] Soltani, M., Alimardani, R., & Omid, M. (2010). Comparison of some chromatic, mechanical and chemical properties of banana fruit at different stages of ripeness. *Modern Applied Science*, 4(7), 34.
- [7] Russo, D., Balistreri, C., Tapanes-Castillo, A., & Pina, M. (2017). Preliminary Antioxidant Activity Analysis of Brazilian Pepper Tree (*Schinus terebinthifolius*) Extracts via TLC, FRAP, and DPPH. In International Conference Series on Multidisciplinary Sciences (Vol. 1, pp. 1-3).
- [8] Andrade, K. S., Poncelet, D., & Ferreira, S. R. (2017). Sustainable extraction and encapsulation of pink pepper oil. *Journal of Food Engineering*, 204, 38-45.
- [9] Rho, S.-J., Mun, S., Park, J., & Kim, Y.-R. (2021). Retarding oxidative and enzymatic degradation of phenolic compounds using large-ring cycloamylose. *Foods*, 10(7), 1457.
- [10] de Oliveira, V. S., Augusta, I. M., da Conceição Braz, M. V., Riger, C. J., Prudêncio, E. R., Sawaya, A. C. H. F., Sampaio, G. R., da Silva Torres, E. A. F., & Saldanha, T. (2020). Aroeira fruit (*Schinus terebinthifolius* Raddi) as a natural antioxidant: Chemical constituents, bioactive compounds and in vitro and in vivo antioxidant capacity. *Food chemistry*, 315, 126274.
- [11] Jeong, Sook, Noh. (2023). Antioxidant Function of Plant Food Ingredients. 2(1):53-63.
- [12] Alqathama, A., Abdelhady, M. I., Al-Omar, M. S., Barghash, M. F., & Shallan, A. I. (2023). Antioxidant, Anti-inflammatory and Cytotoxic Activity of *Schinus terebinthifolia* Fruit and Isolation of a New Immunomodulatory Polyphenolic Compound. *Pharmacognosy Magazine*, 19(1), 13-22.
- [13] Farag, S. F. (2008). Polyphenolic compounds from the leaves of *Schinus terebinthifolius* Raddi. *Bulletin of Pharmaceutical Sciences. Assiut*, 31(2), 319-329.
- [14] Fu, W., Wu, Z., Zheng, R., Yin, N., Han, F., Zhao, Z., Dai, M., Han, D., Wang, W., & Niu, L. (2022). Inhibition mechanism of melanin formation based on antioxidant scavenging of reactive oxygen species. *Analyst*, 147(12), 2703-2711.
- [15] Lim, W. Y., Cheun, C. F., & Wong, C. W. (2019). Inhibition of enzymatic browning in sweet potato (*Ipomoea batatas* (L.)) with chemical and natural anti-browning agents. *Journal of Food Processing and Preservation*, 43(11), e14195.
- [16] Lim, W. Y., & Wong, C. W. (2018). Inhibitory effect of chemical and natural anti-browning agents on polyphenol oxidase from ginger (*Zingiber officinale* Roscoe). *Journal of food science and technology*, 55, 3001-3007.
- [17] Bobo, G., Arroqui, C., & Virseda, P. (2022). Natural plant extracts as inhibitors of potato polyphenol oxidase: The green tea case study. *LWT*, 153, 112467.
- [18] Sai-Ut, S., Noknoi, N., & Nakjai, N. (2020). Effect of mango seed kernel extract on polyphenol oxidase inhibition and shelf life of shrimp during iced storage. *Agriculture and Natural Resources*, 54(6), 641-648-641-648.
- [19] Wohlt, D., Schwarz, E., Schieber, A., & Bader-Mittermaier, S. (2021). Effects of extraction conditions on banana peel polyphenol oxidase activity and insights into inactivation kinetics using thermal and cold plasma treatment. *Foods*, 10(5), 1022.
- [20] Sukhonthara, S., & Theerakulkait, C. (2012). Inhibitory effect of rice bran extract on polyphenol oxidase of potato and banana. *International Journal of Food Science & Technology*, 47(3), 482-487.

## Catalytic conversion of refined palm oil to bio-hydrogenated diesel over monometallic and bimetallic supported on ZSM-5

Natnicha Ritmun<sup>1</sup>, Apiluck Eiad-ua<sup>2\*</sup>, Atthapon Srifa<sup>3</sup>, Worapon Kiatkittipong<sup>4</sup>,  
Suttichai Assabumrungrat<sup>1,5</sup>

<sup>1</sup> Center of Excellence on Catalysis and Catalytic Reaction Engineering, Department of Chemical Engineering, Faculty of Engineering, Chulalongkorn University, Bangkok 10330, Thailand,

<sup>2</sup> College of Materials Innovation and Technology, King Mongkut's Institute of Technology Ladkrabang, Bangkok 10520, Thailand,

<sup>3</sup> Department of Chemical Engineering, Faculty of Engineering, Mahidol University, Nakhon Pathom 73170, Thailand

<sup>4</sup> Department of Chemical Engineering, Faculty of Engineering and Industrial Technology, Silpakorn University, Nakhon Pathom 73000, Thailand

<sup>5</sup> Bio-Circular-Green Economy Technology and Engineering Center (BCGeTEC), Department of Chemical Engineering, Faculty of Engineering, Mahidol University, Nakhon Pathom 73170, Thailand

E-mail: \* Corresponding [Apiluck.ei@kmitl.ac.th](mailto:Apiluck.ei@kmitl.ac.th)

### Abstract

The deoxygenation of Refined Palm oil to bio-hydrogenated diesel (BHD) via hydrotreating process over the ZSM-5 zeolite supported catalysts prepared monometallic and bimetallic catalyst by the wet-impregnation method was conducted into high-pressure autoclave reactor (fixed bed reactor system) under a hydrogen pressure of 30 bar, the reaction time of 3 hours and operating temperature is 360 °C. These studies were divided into 2 parts. Firstly, the effect of monometallic and bimetallic catalysts (Ni, NiCu, NiMo). Secondly, the comparison of SiO<sub>2</sub>/Al<sub>2</sub>O<sub>3</sub> molar ratios in ZSM-5 Zeolite (molar ratio of 23 and 40), respectively. The catalyst was investigated by X-ray diffraction (XRD), Scanning electron microscope and energy dispersion X-ray (SEM-EDX) converting of refining palm oil occurred mainly via decarboxylation/decarbonylation pathways accompanied by cracking reaction to lighter hydrocarbon. Overall, this work showcases a promising route to produce biofuels using metallic-doped ZSM-5 catalysts. The 12.5Ni2.5Cu on the ZSM-5 with SiO<sub>2</sub>/Al<sub>2</sub>O<sub>3</sub> molar ratios of 40 catalysts provided the highest conversion, jet fuel yield, and diesel yield of 96.85%, 42.33 %, and 30.15 %, respectively.

**Keywords:** Monometallic; Bimetallic; ZSM-5; Hydro process; Bio-hydrogenated diesel.

### Introduction

Fossil fuel consumption has been consistently increasing, with 33 quadrillion British thermal units (Btu) used in May 2022 and 76 quadrillion Btu used in 2021. [1] By 2050, it is predicted that global fossil fuel use will surpass 800 quadrillion Btu, with the industrial sector accounting for 50.9% of that total and transportation accounting for the remaining 27.9%. This increased use of fossil fuels not only harms the environment but also depletes petroleum storage. [2] There is an increasing demand for renewable energy sources to address the issues linked with fossil fuels. This is especially important for the transport sector, which accounts for approximately 40% of energy consumption.[3] The development of renewable alternative



fuels like bioethanol, biodiesel, bio-jet, and bio-hydrogenated diesel or green diesel is enabled by eco-friendly processes and sustainable resources.[4]

Bio-hydrogenated diesel can be produced through several reactions, including hydrodeoxygenation (HDO), decarboxylation (DCO<sub>2</sub>), and decarbonylation (DCO). Hydrodeoxygenation removes oxygen by introducing hydrogen, which results in the production of water and hydrocarbons with the same number of carbon atoms as the original feedstock. On the other hand, in the decarboxylation pathway, the discharge of CO<sub>2</sub> releases oxygen, resulting in hydrocarbons with one less carbon atom. Meanwhile, decarbonylation removes oxygen from fatty acids and produces CO in the presence of hydrogen. The extent to which these three pathways are involved is greatly influenced by the catalyst, pressure, and temperature, which ultimately leads to excellent fuel properties. In this research study, a dual metal catalyst made up of Copper (Cu) and Molybdenum (Mo) has been developed and supported by ZSM-5 zeolite. The catalyst has been designed for potential use in catalyst-cracking processes, and to investigate the product yield of bio jet (C8-C14) and diesel range (C15-C20) production synthesis.

## Materials and Methods

### 2.1 Catalyst Preparation

The ZSM-5 zeolite supported catalysts are calcined at 500°C for 5 hours at a heating rate of 5°C/min to remove impurities and change the phase of NH<sub>4</sub><sup>+</sup> to H<sup>+</sup> before loading monometallic of 15Ni wt.%, bimetallic 12.5Ni2.5Cu wt.%, and 12.5Ni2.5Mo wt.% catalyst solution that dissolved the Nickel (II) nitrate hexahydrate (QReC, 97%), Copper (II) nitrate hexahydrate (Dae Jung, 99%), and Ammonium molybdate (Univar, 83%) with deionized water on zeolite support powder, which is prepared by a sequential wetness impregnation.

The mixture was progressively dried in an oven at 110°C to eliminate surplus water for 12 hours. Then calcined at 550°C for 5 hours at a heating rate of 10°C/min to assess performance in the deoxygenation reaction.

### 2.2 Catalyst Characterization

The measurement of the morphology and elemental composition of the catalysts were analyzed using a scanning electron microscope equipped with the Hitachi model S3400N and energy dispersion X-ray spectroscopy model Apollo (SEM-EDX). To analyze the X-ray diffraction (XRD) patterns, the Bruker D8 Advance was used, which was equipped with Cu-K $\alpha$  radiation, operated at 30 kV and 10 mA in 2 $\theta$  range of 5–80° step time of 0.5 s.

### 2.3 Catalyst hydroprocessing

The catalysts were pre-reduced for 3 hours at a temperature of 500°C, with a flow rate of 30 ml/min of hydrogen, before running the high-pressure batch reactor shown in Figure 1. The deoxygenation process was performed in a 100 ml batch reactor with an internal diameter of 40 mm and a mechanical stirrer. The reactor was designed to operate at 600°C and 100 bar pressure. For this research, refined palm oil was used as a bio-based feedstock, with fatty acid compositions (wt.%) obtained from the transesterification of triglycerides with an excess amount of methanol to fatty acid methyl esters (FAMES) using a base catalyst, as summarized in Table 1. Initially, the pressure of hydrogen gas was 30 bar. The reaction was carried out at 360°C for 3 hours while stirring at 400 rpm. Finally, the liquid products were collected and analyzed.

Table 1. Fatty acid compositions of refined palm olein as a feedstock

Fatty acid	Formula	Composition(%wt.)
Lauric acid	C <sub>12</sub> H <sub>24</sub> O <sub>2</sub>	0.4
Myristic acid	C <sub>14</sub> H <sub>28</sub> O <sub>2</sub>	0.8
Palmitic acid	C <sub>16</sub> H <sub>32</sub> O <sub>2</sub>	37.4
Palmitoleic acid	C <sub>16</sub> H <sub>30</sub> O <sub>2</sub>	0.2
Stearic acid	C <sub>18</sub> H <sub>36</sub> O <sub>2</sub>	3.6
Oleic acid	C <sub>18</sub> H <sub>34</sub> O <sub>2</sub>	45.8
Linolenic acid	C <sub>18</sub> H <sub>32</sub> O <sub>2</sub>	11.1
Linolemic acid	C <sub>18</sub> H <sub>30</sub> O <sub>2</sub>	0.3
Arachidic acid	C <sub>20</sub> H <sub>40</sub> O <sub>2</sub>	0.3
Eicosenoic acid	C <sub>20</sub> H <sub>38</sub> O <sub>2</sub>	0.1

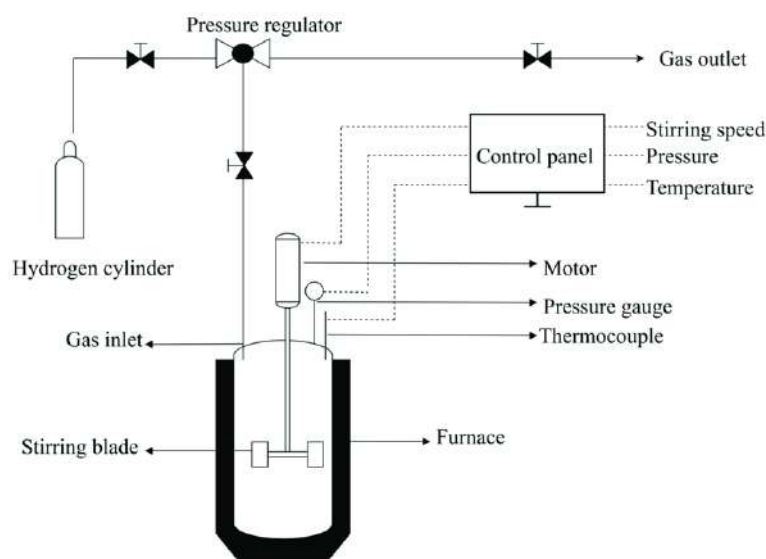


Fig. 1 Schematic diagram of a high-pressure autoclaved batch reactor.[8]

## 2.4 Liquid Product Analysis

The water phase has been eliminated by separating the liquid product. After diluting the oil phase with hexane, gas chromatography was used to evaluate it using a flame ionization detector (GC-FID, GC Shimadzu 2014). The content of n-alkanes (n-C<sub>8</sub> to n-C<sub>20</sub>) in the liquid products was ascertained using a calibration curve of standards. To accomplish this, 0.001 cm<sup>3</sup> of the sample was injected into a Gas Chromatography (GC) with a split ratio of 100 after 50 mg of the sample had been combined with 1 cm<sup>3</sup> of hexane without chemical derivatization, triglycerides could be directly analyzed using high injection and column temperatures. The temperatures of the injection and detector were adjusted to 340 and 370 °C, respectively. The mole balance of the liquid products was used to determine the conversion and total liquid yields, jet yield, and diesel yield were calculated using the following equations (1), equations (2), equations (3), and equations (4) respectively.

$$\text{Conversion (\%)} = \frac{\text{weight of TG in feedstock} - \text{weight of TG in product}}{\text{Total weight of feedstock}} \times 100 \quad (1)$$

$$\text{Total liquid yield (\%)} = \frac{\text{Total weight of product}}{\text{Total weight of feedstock}} \times 100 \quad (2)$$

$$\text{Jet yield (\%)} = \frac{\text{weight of C8 to C14 in product}}{\text{Total weight of feedstock}} \times 100 \quad (3)$$

$$\text{Diesel yield (\%)} = \frac{\text{weight of C15 to C18 in product}}{\text{Total weight of feedstock}} \times 100 \quad (4)$$

## Results and Discussion

### 3.1 Catalyst characterizations

The study aimed to examine the textural properties of the calcined ZSM-5 zeolite support material that has mesopore structures, using N<sub>2</sub> sorption. As per Table 2, the ZSM-5 zeolite support has a higher BET surface area and total pore volume than ZSM-5 zeolite with a SiO<sub>2</sub>/Al<sub>2</sub>O<sub>3</sub> molar ratio of 30. Mesoporous structure helps the entry of triglycerides into active sites situated within the interior pore, as per the literature. The BET surface area and total pore volume of the bimetallic NiCu and NiMo catalysts were lower than those of the monometallic Ni catalysts due to the increase in total metal loading.[13] Nonetheless, 12.5Ni2.5Cu/ZSM-5 (Si/Al=40) had the highest BET surface area compared to the other bimetallic catalysts. When the metal species were loaded into the ZSM-5 Zeolite support, the amount of small and large pores decreased. This was due to the blockage of pores by metal species and/or the collapse of pores by water during the impregnation step.[14]

Table 2. The physical properties of the different catalysts.

Catalyst	S <sub>BET</sub> <sup>a</sup> (m <sup>2</sup> /g)	V <sub>p</sub> <sup>b</sup> (cm <sup>3</sup> /g)	D <sub>p</sub> <sup>c</sup> (Å)
15Ni/ZSM-5 (Si/Al=23)	217.170	0.157	28.934
15Ni/ZSM-5 (Si/Al=40)	232.356	0.124	21.298
12.5Ni2.5Cu/ZSM-5 (Si/Al=23)	167.354	0.138	32.693
12.5Ni2.5Cu/ZSM-5(Si/Al=40)	180.243	0.110	24.374
12.5Ni2.5Mo/ZSM-5(Si/Al=23)	169.672	0.135	31.887
12.5Ni2.5Mo/ZSM-5(Si/Al=40)	176.217	0.105	23.977

<sup>a</sup> S<sub>BET</sub> determined from the adsorption branch of the N<sub>2</sub> isotherm.

<sup>b</sup> V<sub>p</sub> total pore volume determined from the N<sub>2</sub> adsorption at a relative pressure of 0.99

<sup>c</sup> D<sub>p</sub> means pore diameter determined from N<sub>2</sub> adsorption.

The X-ray diffraction (XRD) analysis of the catalysts revealed their phase identity and crystallinity. Figure 2 shows the diffraction peaks at  $2\theta = 7.9^\circ, 8.8^\circ, 9.0^\circ, 23.0^\circ, 23.3^\circ, 23.7^\circ, 23.9^\circ,$  and  $24.3^\circ$ , which are typical of the MFI structure of HZSM-5 zeolite. [5, 6] The X-ray diffraction (XRD) analysis showed that the peaks of typical nickel oxides (NiO and Ni<sub>2</sub>O<sub>3</sub>) were identified at  $37.2^\circ, 43.3^\circ,$  and  $62.9^\circ$ . [9] The X-ray diffraction (XRD) pattern revealed that the nanoparticles of Ni, Cu, and Mo embedded in the zeolite support exhibited weak peaks, indicating that these metal particles were dispersed in the nano-size range, with the presence of a small broad peak at  $27^\circ$  specifically attributed to MoO<sub>3</sub>, [10] suggesting a shift in the NiO-CuO particle size towards a smaller dimension.

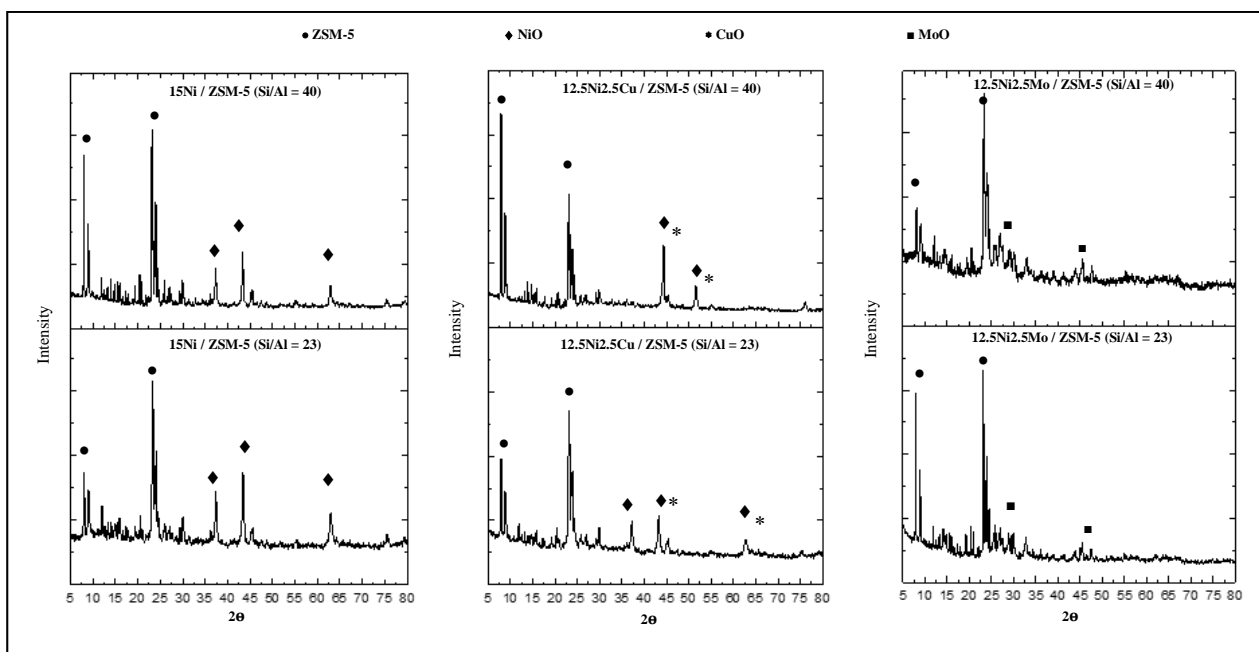


Fig. 2 X-ray diffraction (XRD) pattern of Ni/ZSM-5, NiCu/ZSM-5, and NiMo/ZSM-5

The surface morphology of the ZSM-5 zeolite catalyst was studied using a scanning electron microscope, as shown in Figure 2(a-f). a) 15Ni/ZSM-5 (Si/Al =23), b) 15Ni/ZSM-5 (Si/Al =40), c) 12.5Ni2.5Cu (Si/Al = 23), d) 12.5Ni2.5Cu (Si/Al = 40), e) 12.5Ni2.5Mo (Si/Al = 23),f) 12.5Ni2.5Mo (Si/Al = 23) The catalyst has a similar morphological shape to a hexagonal crystal. The catalyst was prepared using the sequential wetness impregnation method and doped with monometallic (Ni) and bimetallic (NiCu and NiMo) on a zeolite support. The metal in each catalyst was well dispersed on ZSM-5, which confirmed that there was no aggregation of metal in any of the catalysts. The presence of Ni, NiCu, and NiMo on ZSM-5 was confirmed by energy dispersive X-ray spectroscopy (EDX).

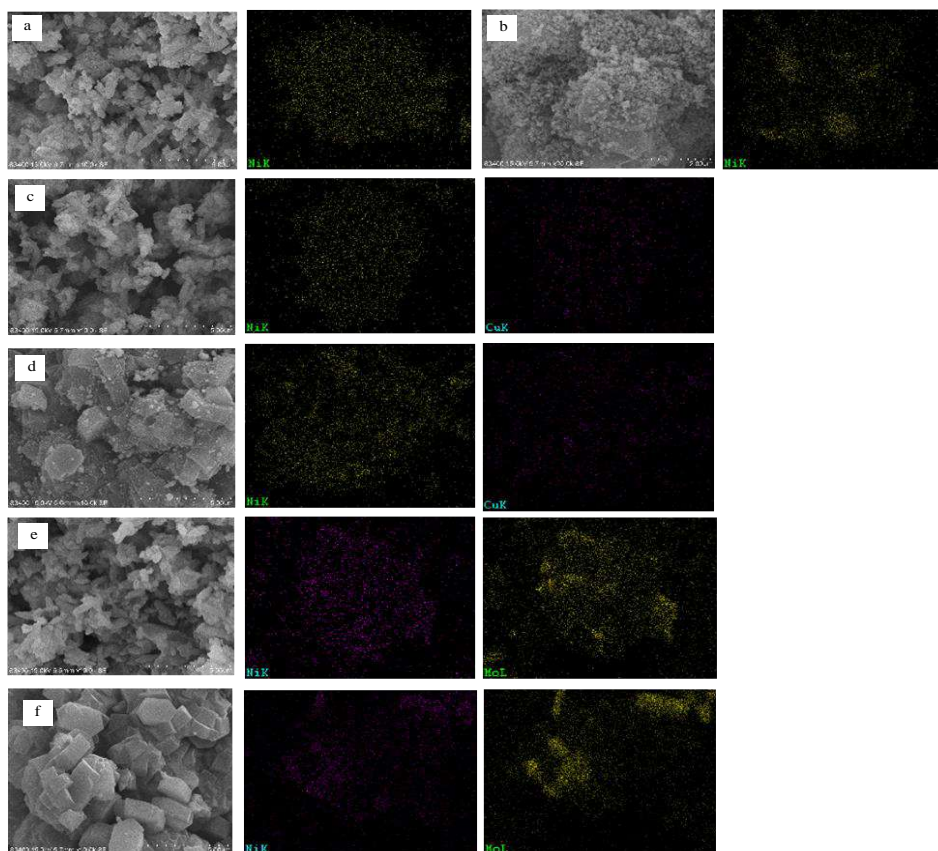


Fig. 3 Scanning electron microscope and energy dispersion X-ray spectroscopy (SEM-EDX) of catalyst: a) 15Ni/ZSM-5 (Si/Al =23), b) 15Ni/ZSM-5 (Si/Al =40), c) 12.5Ni2.5Cu (Si/Al = 23), d) 12.5Ni2.5Cu (Si/Al = 40), e) 12.5Ni2.5Mo (Si/Al = 23), f) 12.5Ni2.5Mo (Si/Al = 23)

### 3.2 Catalytic hydroprocessing

A recent study investigated the effectiveness of monometallic and bimetallic catalysts (Ni, NiCu, NiMo) loaded on ZSM-5 zeolite support. The study found that the 12.5Ni2.5Cu catalyst was the most efficient in terms of conversion and product yield, followed by 12.5Ni2.5Mo and 15Ni (as shown in Figure 4). The presence of Ni improved efficiency by promoting the cracking of Ni-H<sub>2</sub> bond activity. The addition of 2.5wt.%Cu on ZSM-5 also improved the activity of Ni due to H<sub>2</sub> spillover. However, the addition of 2.5wt.% Mo replaced Cu, which resulted in a slight decrease in conversion and product yield due to the reduction in Mo activity. This is because Mo isn't a good working catalyst and blocks active sites. The 12.5Ni2.5Cu/ZSM-5 catalyst provided the highest conversion, jet fuel yield, and diesel yield of 96.85%, 42.33 %, and 30.15 %, Meanwhile, 12.5Ni2.5Mo/ZSM-5 had lower conversion, jet fuel yield, and diesel yield of 90.17%, 33.99%, and 40.51%, respectively. It was noted that hydrogen molecules could more easily absorb Ni surfaces than Cu surfaces because Cu had higher binding energies of hydrogen bonds than Ni. The spillover of hydrogen from Ni to Cu was energetically unpreferred due to the large difference in the binding energies of hydrogen bound to Ni and Cu [7]. The study showed that monometallic and bimetallic catalysts loaded on ZSM-5 zeolite support show better efficiency with SiO<sub>2</sub>/Al<sub>2</sub>O<sub>3</sub> molar ratios of 40 compared to 30.

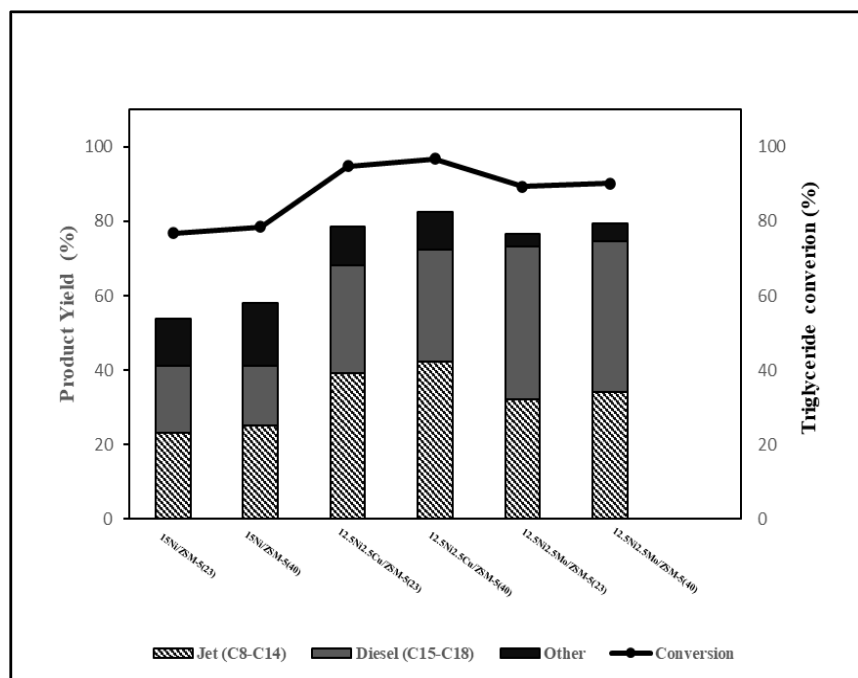


Fig. 4 shows the comparison in terms of product yields in jet and diesel range hydrocarbons obtained from triglyceride conversion over monometallic and bimetallic catalysts (Ni, NiCu, NiMo) loaded on ZSM-5 zeolite support of different molar ratios (23 and 40).

Table 3. The physical properties of the different catalysts.

Feedstock	Catalyst	Reactor	Condition	Performance	Ref.
Palm oil	Ni-Mo-W/ $\gamma$ Al <sub>2</sub> O <sub>3</sub> -ZSM5 (pre-sulfided)	Fixed-bed reactor	360°C, 50bar of H <sub>2</sub> , 1 h <sup>-1</sup> of LSHV, 1000 of H <sub>2</sub> /oil	nC8-nC14 = 6% nC15-nC18 = 82.9 % iC15-iC18 = 6 %	[15]
Palm oil	Ni-Mo/ $\gamma$ Al <sub>2</sub> O <sub>3</sub> (pre-sulfide)	Fixed-bed reactor	360°C, 60bar of H <sub>2</sub> , 1 h <sup>-1</sup> of WHSV, 1000 of H <sub>2</sub> /oil	nC8-nC18 = 88.9 % iC8-iC18 = 10 %	[16]
Soybean oil	Ni/SiO <sub>2</sub> - Al <sub>2</sub> O <sub>3</sub> NiMo/ $\gamma$ Al <sub>2</sub> O <sub>3</sub> CoMo/ $\gamma$ Al <sub>2</sub> O <sub>3</sub>	Trickle-bed reactor	400°C, 60bar of H <sub>2</sub> , 1h.	nC15-nC18 = 91.0 % nC15-nC18 = 39.3 % nC15-nC18 = 67.1 %	[17]
FAME	Ni/ZSM-5	Trickle-bed reactor	280°C, 8bar of H <sub>2</sub> , 4 h <sup>-1</sup> of LSHV	≤ nC7 = 6.8 % nC8-nC14 = 27.7% nC15-nC18 = 40.6 %	[18]
PFAD	10Ni5Cu/HZSM-5	Fixed-bed reactor	375°C, 50bar of H <sub>2</sub> , 3h.	≤ nC7 = 8.75 % nC8-nC14 = 26.24% nC15-nC18 = 23.38 %	[19]

Therefore, the various literature studies using different catalysts and experimental conditions for the hydro-conversion of vegetable oil into renewable diesel fuel production compared to this study were demonstrated in Table 3. Metal sulfide catalysts are efficient in improving catalytic activity. However, the formation of sulfur-containing byproducts during the reaction process can lead to the release of toxic sulfur agents. [20] Therefore, there is a

growing interest in the use of sulfur-free metal catalysts, such as metal oxides, which have shown a high yield of biojet fuel and green diesel-like metal sulfide catalysts. Metal oxides are preferred due to their lower cost when compared to noble metals and their excellent catalytic activity in biofuel production. [21]

## Conclusions

In this study, we prepared monometallic and bimetallic catalysts through sequential wetness impregnation. We analyzed the physicochemical properties of the catalysts using XRD and SEM-EDX. We tested different loadings of monometallic and bimetallic catalysts in a batch reactor to identify the best catalyst. Our results showed that using ZSM-5 with SiO<sub>2</sub>/Al<sub>2</sub>O<sub>3</sub> molar ratios of 40, at an operating temperature of 360°C, initial H<sub>2</sub> pressure of 30 bar, and reaction time of 3 hours, yields better results than SiO<sub>2</sub>/Al<sub>2</sub>O<sub>3</sub> molar ratios of 30. The conversion, jet fuel yield, and diesel yield of metallic-doped were 12.5Ni2.5Cu > 12.5Ni2.5Mo > 15Ni, respectively.

## References

- [1] D. R. Dunn, J. Zaidi, M. Kopalek, G. Long, R. Berry G. McGrath, T. Shear, M. Klein, A. Gorski, E. Harrison, L. Jamison and K. Nakolan, *Monthly Energy Review*- August 2022, Energy Information Administration, United States, 2022
- [2] F. Millo, T. Vlachos and A. Piano, *Fuel*, 2021, 285, 119092.
- [3] Dinesh Mohan CUPJ, and Philip H. Steele. *Pyrolysis of Wood/Biomass for Bio-oil: A Critical Review. Energy & Fuels*. 2006;20(3):848-89.
- [4] J. K. Lin, C. P. Lee, H. P. Lin, E. Halim, W. C. Wang, *Int. J. Energy Res.*2021,45, 19043–19061
- [5] Tiwari. S. Rana, R. Kumar, D. Verma, R. Kumar, R. K. Joshi, M. O. Garg, A. K. Sinha, *Catal. Commun.*2011,12,559–562;d), *Renewable Sustainable Energy Rev.*2020,132,110109;e),
- [6] A. Srifa, W. Chaiwat, P. Pitakjakpipop, W. Anutrasakda, K. Faungnawakij, *Sustain Bioenergy*, 2019, pp. 167 – 198
- [7] He, M., Ali, M.-F., Song, Y.-Q., Zhou, X.-L., Wang, J. A.; Nie, X.-Y.; Wang, Z. Study on the deactivation mechanism of HZSM-5 in the process of catalytic cracking of n-hexane. *Chemical Engineering Journal* 2023, 451. DOI: 10.1016/j.cej.2022.138793.
- [8] Chen, B. H., Chao, Z. S., He, H.; Huang, C.; Liu, Y. J.; Yi, W. J.; Wei, X. L., An, J. F. Towards a full understanding of the nature of Ni(II) species and hydroxyl groups over highly siliceous HZSM-5 zeolite supported nickel catalysts prepared by a deposition-precipitation method. *Dalton Trans* 2016, 45 (6), 2720-2739. DOI: 10.1039/c4dt00399c.
- [9] Yao, Y. and Goodman, D.W. Direct evidence of hydrogen spillover from Ni to Cu on Ni–Cu bimetallic catalysts. *Journal of Molecular Catalysis A: Chemical* 383 (2014): 239-242
- [10] M. Papananee, W. James, and K. Pakawadee, *Biojet Fuel Production from Waste of Palm Oil Mill Effluent through Enzymatic Hydrolysis and Decarboxylation. Catalysts* 2021, 11, 78.: 2-10
- [11] Z. Wei, H. Qiaoc, H. Yanga, C. Zhanga, and X. Yan. Characterization of NiO nanoparticles by an anodic arc plasma method. *journal of Alloys and Compounds* 479 (2009) 855–858

- [12] D. Wu<sup>1</sup>, R. Shen<sup>1</sup>, R. Yang, W. Ji<sup>1</sup>, M. Jiang, W. Ding, and L. Peng. Mixed Molybdenum Oxides with Superior Performances as an Advanced Anode Material for Lithium-Ion Batteries. *Scientific report*.7:44697 (2017)
- [13] Lyu Y, Liu Y, Xu L, Zhao X, Liu Z, Liu X, Yan Z. Effect of ethanol on the surface properties and n-heptane isomerization performance of Ni/SAPO-11. *Applied Surface Science*. 2017; 401:57-64
- [14] J. Chuseang, V. Itthibenchapong, A. Srifa, B. Rungtaweavoranit, W. Klysubun, A. Eiadua, W. Kiatkittipong, S. Assabumrungrat, Production of Low-Cold Flow Diesel by Combination of Hydro-Deoxygenation and Isomerization Over Bimetallic NiRe Supported Sapo-11 Catalyst. *SSRN Electronic Journal*. (2022) DOI - 10.2139/ssrn.4217548
- [15] Wang H-Y, Jiao T-T, Li Z-X, Li C-S, Zhang S-J, Zhang J-L. Study on palm oil hydrogenation for clean fuel over Ni-Mo-W/ $\gamma$ -Al<sub>2</sub>O<sub>3</sub>-ZSM-5 catalyst. *Fuel Processing Technology*. 2015;139:91-9.
- [16] Lin JK, Lee CP, Lin HP, Halim E, Wang WC. The production of hydro-processed renewable diesel over the nonsulfide catalyst. *International Journal of Energy Research*. 2021;45(13):19043-61.
- [17] Zheng, X., Chang, J., and Fu, Y. One-pot catalytic hydrocracking of diesel distillate and residual oil fractions obtained from bio-oil to gasoline-range hydrocarbon fuel. *Fuel* 157 (2015): 107-114
- [18] Chen, L., Li, H., Fu, J., Miao, C., Lv, P., and Yuan, Z. Catalytic hydroprocessing of fatty acid methyl esters to renewable alkane fuels over Ni/HZSM-5 catalyst. *Catalysis Today* 259 (2016): 266-276.
- [19] P. Wirikulcharoen, W. Kiatkittipong, K. Ngaosuwan, S. Assabumrungrat, Bimetallic NiCu/HZSM-5 Catalyst in hydroprocessing of palm fatty acid distillate for green fuel production. *Pure and Applied Chemistry International Conference Proceeding 2017; IC-P-006*
- [20] Zheng, X., Chang, J., and Fu, Y. One-pot catalytic hydrocracking of diesel distillate and residual oil fractions obtained from bio-oil to gasoline-range hydrocarbon fuel. *Fuel* 157 (2015): 107-114
- [21] Zhang, Y.; Bi, P.; Wang, J.; Jiang, P.; Wu, X.; Xue, H.; Liu, J.; Zhou, X.; Li, Q. Production of jet and diesel biofuels from renewable lignocellulosic biomass. *Applied Energy* 2015, 150, 128-137. DOI: 10.1016/j.apenergy.2015.04.023.



## Enhancing Polycaprolactone (PCL) by Incorporating Lignin to Improve Properties

Nichapa Lertnimitthum<sup>a\*</sup>, Chayanon Chotirotsukhon<sup>b</sup>, Suchat Pongchaiphol<sup>b</sup>, Marisa Raita<sup>b</sup>, Sorachapat Sutikulsoombat<sup>c</sup>, Khaow Tonsomboon<sup>c</sup>, Navadol Laosiripojana<sup>a</sup>, Verawat Champreda<sup>b</sup>

<sup>a</sup>The Joint Graduate School of Energy and Environment, King Mongkut's University of Technology Thonburi, Tungkru, Bangkok, 10140, Thailand

<sup>b</sup>BIOTEC\_JGSEE Integrative Biorefinery Laboratory, Biorefinery and Bioproduct Technology Research Group, National Center for Genetic Engineering and Biotechnology, Khlong Luang, Patum Thani 12120, Thailand

<sup>c</sup>Biosensing and Bioprospecting Technology Research Group, National Center for Genetic Engineering and Biotechnology, Khlong Luang, Patum Thani 12120, Thailand

E-mail: \* nat\_nichapa@hotmail.com

### Abstract

This study investigates the development of polycaprolactone (PCL) properties, focusing on UV protection and antibacterial activity, through the incorporation of lignin extracted from biomass. Lignin, a natural biological polymer renowned for its exceptional UV and antibacterial properties, holds promise as a suitable additive for PCL, particularly in biomedical applications. The lignin used in this study was extracted into ethanol organosolv lignin (EOL). Different ratios of PCL and lignin were 10:0, 9:1, 8:2, 7:3, and 6:4 were introduced and processed through electrospinning under optimal conditions. The fiber size in PCL/lignin films decreased proportionally with an increasing lignin ratio, ranging from 170 to 250 nm, indicating a finer fiber structure. Concurrently, enhanced fiber distribution was observed with escalating lignin ratios. Despite the absence of antibacterial efficacy against Gram-negative bacteria, further evaluation for resistance to Gram-positive bacteria is recommended. UV and visible light transmittance tests revealed a reduction as the lignin ratio increased, particularly in the UVB and visible light wavelength ranges. Mechanical properties demonstrated favorable compatibility between PCL and lignin when the lignin ratio remained below 20%. This research contributes valuable insights into the potential applications of lignin as an effective additive for enhancing PCL properties, specifically in the realms of UV protection and antibacterial activity.

**Keywords:** Lignin, Composite, Functional additive, Organosolv lignin, Polycaprolactone, Electrospinning

### 1. Introduction

Most of the agricultural industrial waste products that are discarded are lignocellulosic biomass. Although plant biomass is commonly utilized for energy production, substantial quantities of these potent by-products remain unused, contributing to waste generation. Lignin is one of the least exploited main components of lignocellulose. It is a natural amorphous highly branched polyphenolic heteropolymer with high molecular weight [1,2]. It has inherent properties, including antibacterial and UV protection [3], along with its reported compatibility with various synthetic polymers. [4,5,6]

Polycaprolactone (PCL) is a semi-crystalline hydrophobic biodegradable polyester that is commonly utilized in biomedical and healthcare applications [7,8,9] It is strong, lightweight, and non-toxic. Given these characteristics, the incorporation of lignin into PCL using the electrospinning technique is an inexpensive method of manufacturing. Furthermore, the

workpiece is a thin film, making it easy to test the properties. This research has focused on the addition of lignin to different polymers because it can improve their ability to absorb UV light and their antibacterial activity.

## 2. Material and Method

### 2.1. Material Preparation

Polycaprolactone (PCL) pellet (Mn: 80,000, Sigma Aldrich Co., USA) and Ethanol Organosolv Lignin (EOL) powder (Mw: 2800) were dissolved in Dichloromethane (99.8%, RCI Labscan, Thailand) and Acetone ( $\geq 99.8\%$  Mw: 58.08, Fisher Chemical, Finland) in a 2:1 ratio to prepare a 10% w/v solution. The composite samples were prepared samples with PCL to lignin ratios of 10:0, 9:1, 8:2, 7:3, and 6:4, respectively. The mixture was stirred at room temperature for 1 hour. Ten-milliliter solution was loaded into a 20 mL syringe fitted with a 20-ga needle tip and connected to an automatic pump with a flow rate of 1.8 ml/hr. The working distance from the power supply was 10 cm with a voltage of 15 kV. Each sample took 1 hour to spin at room temperature.

### 2.2. Surface Morphology and Fiber Diameter

A Field Emission Scanning Electron Microscope (FE-SEM) model SU5000 was used to examine the surface morphology of the PCL/lignin films at a magnification of 1000x. Prior to examination, the samples were gold-coated to increase electron conductivity. The average diameter and uniformity of fibers were estimated from 40 measurements via a line drawn at 5000x magnification on the SEM.

### 2.3. Antibacterial Properties

The antimicrobial properties of the PCL/lignin films following ISO 22196, a standard method for quantifying antibacterial activity on impermeable surfaces, including plastics. *Escherichia coli* was used in this study as a representative of gram-negative bacteria. The experimental procedure entailed the preparation of a cell suspension at a concentration of  $10^5$  CFU/ml, which was then inoculated onto 5x5 cm sample films covered with 4x4 cm polyethylene film, followed by a 24-hour incubation period. Subsequently, 10 ml of Luria-Bertani (LB) broth was introduced as a neutralizer. After incubation, 10 ml of LB broth was introduced as a neutralizer. A 10-fold serial dilution of the suspension was plated on Plate Count Agar (PCA) and subjected to overnight incubation at 37°C, after which the resulting bacterial colonies were counted. Each different ratio of PCL/lignin films was tested in triplicate.

### 2.4. UV-Transmission Properties

A UV-vis absorption spectrometer was used to measure the transmittance data of the PCL/lignin films. The wavelength range of visible light and ultraviolet radiation was observed between 200 and 700 nm with a wavelength range at intervals of 2 nm. The film sample was inserted in a quartz cuvette, with an empty cuvette serving as a control sample. The PCL/Lignin film samples with a 0.08-0.09 mm thickness were prepared for testing, and each sample was tested in triplicate.

## 2.5. Mechanical Properties

The mechanical properties, encompassing tensile strength (MPa) and percentage of elongation at break, were systematically evaluated following the standard procedure outlined in ASTM D882. Using a tensile testing machine (Instron 5943 Single Column Tabletop Testing System) with a 100 N load cell capacity, tests were conducted at a cross-head speed of 10 mm/min with an attached sample at a gauge length of 20 mm. A minimum of three specimens for consistency, each featuring a cross-sectional dimension of 0.09 mm x 10 mm.

## 3. Result and Discussion

### 3.1. Surface Morphology and Fiber Diameter

The PCL/Lignin film surface was examined via scanning electron microscopy (SEM) at 1000 $\times$  magnification and fiber size measurements were conducted at 5000 $\times$  magnification. The results indicated the presence of beads interspersed with fibers, particularly in samples without lignin (PCL/lignin 10:0). An increase in the lignin ratio led to a reduction in bead volume, accompanied by better fiber dispersion as illustrated in Fig. 1. On the other hand, the PCL/Lignin film with a PCL to lignin ratio of 6:4 exhibited tangled fibers, a non-uniform arrangement, and an increased amount of beads.

Figure 2 illustrates the average measurement of the fiber diameter of each PCL/lignin film sample at all 40 points measured. The results showed a decreasing trend in fiber diameter with increased lignin content. As reported by Greiner et al., the viscosity of the solution affects the diameter of the fibers spun through the electrospinning machine, wherein a decrease in solution viscosity results in a reduction in fiber diameter. [10] Consequently, films with lower PCL ratios exhibit concomitantly diminished fiber diameters.

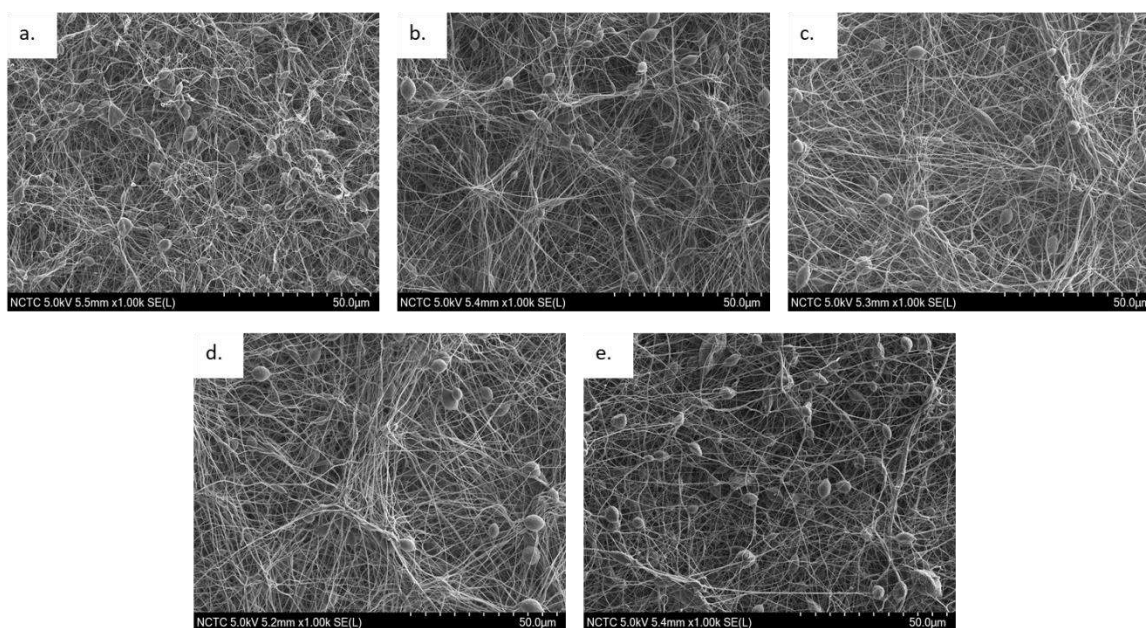


Fig. 1. SEM image of PCL/Lignin ratios of 6:4 (a.), 7:3 (b.), 8:2 (c.), 9:1 (d.), and 10:0 (e.)

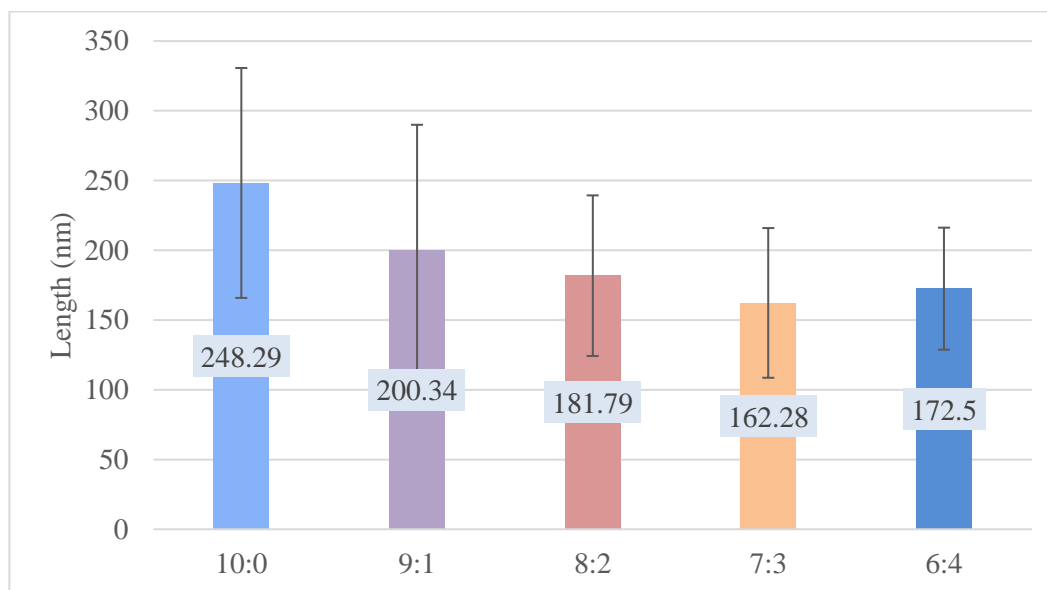


Fig. 2. Fiber diameter of PCL/Lignin samples

### 3.2. Antimicrobial Properties

In the antibacterial test for PCL/lignin film samples, *E. coli* is used as a representative for Gram-negative bacteria. After incubating the test specimen for 24 hours, the results showed that the percentage of bacteria decreased by less than 2% for the film sample without lignin, which did not show any difference from the number of bacteria at 0 hours. With an increase in lignin to a PCL/lignin ratio of 9:1, there was a 7.26% decrease in bacterial percentage. In contrast, at PCL/lignin ratios of 8:2, 7:3, and 6:4, the bacterial percentage decreased by approximately 9% of *E. coli* bacteria (Fig. 3 and Table 1). Despite the seeming reduction in bacteria, the antimicrobial activity (R) value is less than 2, meaning that there is no antimicrobial effectiveness, and there is a chance that bacteria could be recovered from the surfaces. [11] Moreover, Gram-positive bacteria should also be examined for antibacterial activity against PCL/lignin films.

Table 1. Antimicrobial activity of *Escherichia coli* of PCL/lignin films

Sample	% Reduction	R
10:0	1.60	0.11
9:1	7.26	0.49
8:2	9.96	0.67
7:3	9.61	0.65
6:4	9.19	0.62

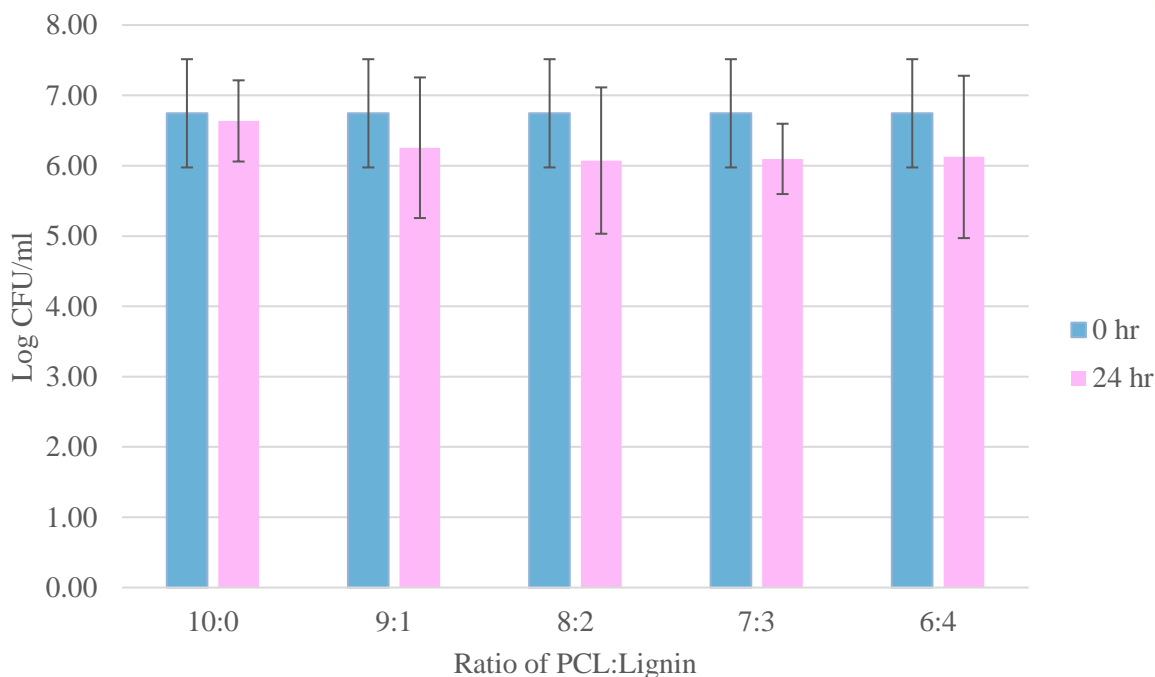


Fig 3. The logarithm of the population of *E. coli* bacteria at 0 hr. and 24 hr. of PCL/Lignin films testing.

### 3.3. UV-Transmission Properties

The measurement of UV-vis absorption spectra was used to evaluate light transmission across different wavelengths. In the PCL/lignin film samples, the results revealed an obvious reduction in transmittance with an increasing lignin ratio. Notably, variations in transmittance were observed in the wavelength range of 300 to 700 nm, which is the wavelength range of UVA and visible light [12]. Specifically, within the range of 315 to 400 nm, corresponding to UVA rays, and the range of 400 to 700 nm, encompassing visible light perceptible to humans, the film samples featuring PCL/lignin ratios of 7:3 and 6:4 exhibited remarkable UV protection, surpassing 99.9%, highlighting their potential efficacy in shielding against the adverse effects of UVA rays and visible light on skin and wound healing.

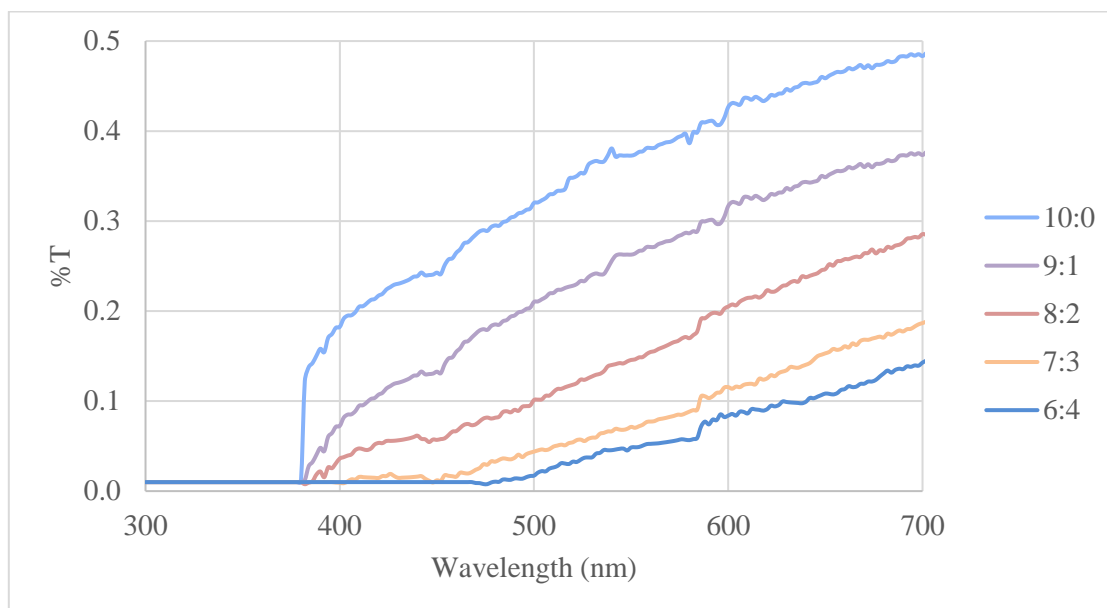


Fig 4. UV-vis absorption spectra of PCL/Lignin film samples

### 3.4. Mechanical Properties

The mechanical test results for the PCL/lignin film samples present the mean tensile strength (Fig. 5) and percentage of elongation at break values (Fig. 6) derived from three measurements, with the error bars indicating the standard deviation corresponding to each PCL: lignin ratio. Furthermore, it was found that the tensile strength and percentage elongation at break values of the films containing PCL/Lignin ratios of 9:1 and 8:2 were not different from those of the films without lignin after lignin was added. For this reason, it exhibited good compatibility with the mechanical properties of the film when applied in appropriate amounts of lignin. On the other hand, the addition of lignin resulted in a decrease in the material's tensile strength and percentage of elongation at break values. to 0.293 mPa and 28.70%, respectively, for the film with a PCL/lignin ratio of 7:3 and to 0.190 mPa and 19.17% for the film with a PCL/lignin ratio of 6:4, indicating that adding more than 20% of lignin reduced the tensile strength and elongation ability.

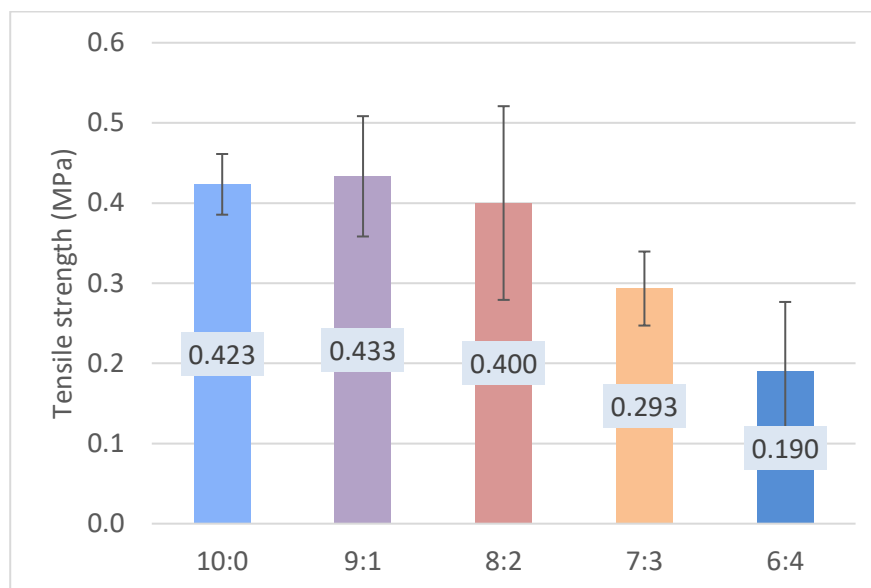


Fig 5. Tensile strength of PCL/Lignin film samples

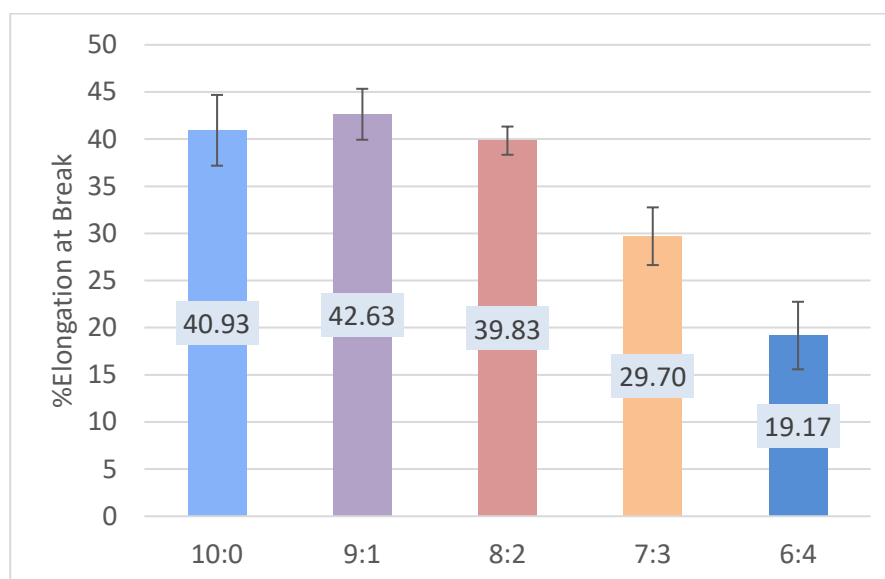


Fig 6. Percentage of elongation at break of PCL/Lignin film samples

#### 4. Conclusion

This study investigated the effects through a multifaceted analysis of the incorporation of organosolv lignin into PCL using an electrospinning method under appropriate conditions. Surface morphology assessments, utilizing SEM, unveiled intricate fiber structures, highlighting the influence of lignin on bead volume and fiber dispersion. While an increase in the PCL/lignin ratio generally led to improved dispersion, a 6:4 ratio resulted in tangled fibers and increased bead content. The antimicrobial properties show a minimal reduction in the number of gram-negative bacteria. However, the antimicrobial activity (R) value remained below 2, indicating limited effectiveness. UV-vis absorption spectra analyses revealed a

reduction in transmittance with escalating lignin ratios, with films at 7:3 and 6:4 ratios displaying exceptional UV protection. Mechanical testing demonstrated good compatibility between lignin and the mechanical properties of PCL films at appropriate ratios, yet exceeding 20% lignin led to a decline in tensile strength and elongation ability. In conclusion, the findings from the antibacterial, UV protection, and mechanical properties analyses affirm that PCL/lignin films have the potential to impart distinctive properties to lignin, thereby enhancing the overall performance of PCL polymers.

## References

- [1] Yousuf, A., Pirozzi, D., & Sannino, F. (2020). Fundamentals of lignocellulosic biomass. In *Lignocellulosic biomass to liquid biofuels* (pp. 1-15). Academic Press.
- [2] Saldarriaga-Hernández, S., Velasco-Ayala, C., Flores, P. L. I., de Jesús Rostro-Alanis, M., Parra-Saldivar, R., Iqbal, H. M., & Carrillo-Nieves, D. (2020). Biotransformation of lignocellulosic biomass into industrially relevant products with the aid of fungi-derived lignocellulolytic enzymes. *International journal of biological macromolecules*, 161, 1099-1116.
- [3] Morena, A. G., & Tzanov, T. (2022). Antibacterial lignin-based nanoparticles and their use in composite materials. *Nanoscale advances*, 4(21), 4447-4469.
- [4] Lazzari, L., Domingos, E., Silva, L., Kuznetsov, A., Romão, W., & Araujo, J. (2020). Kraft lignin and polyethylene terephthalate blends: effect on thermal and mechanical properties. *Polímeros*, 29.
- [5] Lee, E., Song, Y., & Lee, S. (2019). Crosslinking of lignin/poly (vinyl alcohol) nanocomposite fiber webs and their antimicrobial and ultraviolet-protective properties. *Textile Research Journal*, 89(1), 3-12.
- [6] Salami, M. A., Kaveian, F., Rafienia, M., Saber-Samandari, S., Khandan, A., & Naeimi, M. (2017). Electrospun polycaprolactone/lignin-based nanocomposite as a novel tissue scaffold for biomedical applications. *Journal of medical signals and sensors*, 7(4), 228.
- [7] Malikmammadov, E., Tanir, T. E., Kiziltay, A., Hasirci, V., & Hasirci, N. (2018). PCL and PCL-based materials in biomedical applications. *Journal of Biomaterials science, Polymer edition*, 29(7-9), 863-893.
- [8] Raina, N., Pahwa, R., Khosla, J. K., Gupta, P. N., & Gupta, M. (2021). Polycaprolactone-based materials in wound healing applications. *Polymer Bulletin*, 1-23.
- [9] Lyu, J. S., Lee, J. S., & Han, J. (2019). Development of a biodegradable polycaprolactone film incorporated with an antimicrobial agent via an extrusion process. *Scientific Reports*, 9(1), 20236.
- [10] Greiner, A., & Wendorff, J. H. (2007). Electrospinning: a fascinating method for the preparation of ultrathin fibers. *Angewandte Chemie International Edition*, 46(30), 5670-5703.
- [11] Fontecha-Umaña, F., Ríos-Castillo, A. G., Ripolles-Avila, C., & Rodríguez-Jerez, J. J. (2020). Antimicrobial activity and prevention of bacterial biofilm formation of silver and zinc oxide nanoparticle-containing polyester surfaces at various concentrations for use. *Foods*, 9(4), 442.
- [12] Matsumura, Y., & Ananthaswamy, H. N. (2004). Toxic effects of ultraviolet radiation on the skin. *Toxicology and applied pharmacology*, 195(3), 298-308.



## Data Augmentation Enhanced Multilayer Perceptron Neural Network Model for Catalytic CO<sub>2</sub> Methanation

**Kittithat Kongtaworn<sup>1,a</sup>, Panyanat Aonpong<sup>2,b</sup>, and Nutchapon Chotigkrai<sup>1,c,\*</sup>**

<sup>1</sup> Department of Chemical Engineering, Faculty of Engineering and Industrial Technology, Silpakorn University, Nakhon Pathom 73000, Thailand

<sup>2</sup> Department of Computing, Faculty of Science, Silpakorn University, Nakhon Pathom 73000, Thailand  
E-mail: <sup>a</sup> [kongtaworn\\_k@silpakorn.edu](mailto:kongtaworn_k@silpakorn.edu), <sup>b</sup> [aonpong\\_p@silpakorn.edu](mailto:aonpong_p@silpakorn.edu), <sup>c,\*</sup> [chotigkrai\\_n@silpakorn.edu](mailto:chotigkrai_n@silpakorn.edu)

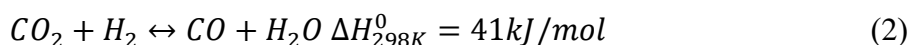
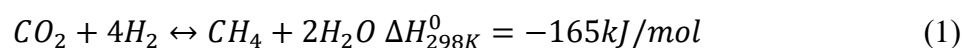
### Abstract

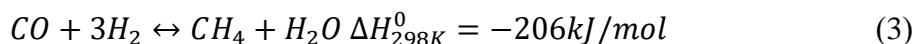
CO<sub>2</sub> methanation is beneficial not only for green-house gas abatement but also energy demand support. Various catalysts and reaction conditions have been studied and its experimental data were accumulated for decades. Machine learning is received wide attention due to the ability to reveal insight from literature data. However, the size of experimental data is limited and considerably small even accumulated for decades, affecting the accuracy and robustness of the model. In this work, we used data augmentation technique to increase the size of dataset to 5 and 10 times for training multilayer perceptron neural network model. For default model parameters, R<sup>2</sup> and RMSE for predicting CO<sub>2</sub> conversion were increased from (0.89, 10.5) to (0.91, 9.7) and (0.92, 9.5) for 5 and 10 times training set, respectively. The best R<sup>2</sup> and RMSE of 0.94 and 7.6 were obtained by tuning hidden layer and maximum iteration. This work demonstrates the advantage of applying data processing technique to improve the accuracy and robustness of the model in catalyst domain.

**Keywords:** Machine learning; multilayer perceptron; data augmentation; CO<sub>2</sub> methanation.

### 1. Introduction

Nowadays, natural disasters are becoming more serious. Many countries around the world are experiencing climate change and rising temperatures. This is a result of global warming caused by human activities that increase carbon dioxide in the atmosphere. In 2021, Thailand recorded its highest CO<sub>2</sub> emissions in the industrial sector, reaching 76.5 million tons, marking a 9.9% increase compared to the previous year. This surge aligns with the expansion of industrial production in 2021, particularly within key sectors such as the automotive and steel industries. The capture and catalytic conversion of CO<sub>2</sub> to fuels or commodity chemicals, as an effective approach, have been extensively studied. Among the numerous target products, methane is a promising one as it is in great demand and feasible for cost-effective distributions. The CO<sub>2</sub> methanation has also stimulated great research interest. This is because it has the potential to be used in renewable power-to-gas (P2G) systems [1]. Specifically, in P2G technology, H<sub>2</sub> produced from renewable sources reacts with CO<sub>2</sub> (produced from industrial processes) and can be chemically converted into synthetic natural gas [2]. The CO<sub>2</sub> methanation is a reaction that is strongly exothermic. It was first discovered by Paul Sabatier and Jean-Batiste Senderens in 1897 and is described by the following equation scheme (Eqs. 1-3):





The general consensus in the literature is that CO<sub>2</sub> methanation (Eq. (1)) proceeds via the production of carbon monoxide through the reaction of reverse water gas shift (RWGS, Eq. (2)) as an intermediate step, and then CO hydrogenation to CH<sub>4</sub> [3]. However, CO<sub>2</sub> is a highly stable molecule that requires high temperatures to be activated [4]. Consequently, CO<sub>2</sub> methanation is a challenging process that requires optimum operating conditions and appropriate catalysts for high yield and selectivity for methane. As the result of these efforts, a large amount of data has been accumulated in literature over year; these data can be collected and analyzed using machine learning (ML) to extract the knowledge distributed over the entire methanation literature [5]. The multilayer perceptron (MLP), a prominent type of artificial neural network (ANN), finds widespread applications in machine learning and pattern recognition. Comprising an input layer, multiple hidden layers, and an output layer, an MLP processes information through these layers. Each node within the network calculates a weighted sum of its inputs, and this sum undergoes a nonlinear activation function, facilitating the generation of an output. Renowned for their ability to grasp intricate relationships between inputs and outputs, MLPs can be trained using various algorithms, such as backpropagation. The backpropagation algorithm adjusts the network's weights to minimize the error between predicted and actual outputs during the training process [6]. B Yilmaz study machine learning while using random forest (RF) model for analysis of catalytic CO<sub>2</sub> methanation, achieved in predict CO<sub>2</sub> conversion with root mean square error (RMSE) of 6.4 and 12.7 respectively and R-square (R<sup>2</sup>) was 0.97 for training set while it was 0.85 for testing set [5]. S. Wei et al. used data augmentation algorithms such as variational auto-encoder (VAE) and generative adversarial network (GAN) for the bio-polymerization process, achieved the highest for VAE at 0.85 R<sup>2</sup> and GAN at 0.74 R<sup>2</sup> in testing set [7].

In this work, we used data augmentation techniques to create 5 and 10 times augmented data for training multilayer perceptron neural network model.

## 2. Materials and Methods

### 2.1 Dataset

The original dataset used in this work was collected by R. Yildirim's group and the details were described elsewhere [5]. In summary, 4,051 data points were manually extracted from 100 published experimental papers using "CO<sub>2</sub> methanation" and "catalytic CO<sub>2</sub> hydrogenation as keywords in web of science. The input parameters (features) and output parameter (target) were summarized in Table 1, shows the features used in the experiment.

Table 1. Input-output features used in the dataset.

Input		Output	
Catalyst properties	Synthesis conditions	Reaction conditions	Catalytic performance
Base	Catalyst preparation	Reduction temperature	CO <sub>2</sub> conversion %
Base wt. %	method	(°C)	
Base 2 (co metal)	Calcination	Reduction pressure	
Base 2 wt. %	temperature (°C)	(bar)	
Support	Calcination time (h)	Reduction time (h)	

---

Support wt. %	Reduction H <sub>2</sub> %
Support 2 (co support)	Temperature (°C)
	Pressure (bar)
	W/F (mgcat/minml)
	Time on stream (h)
	CO% in feed
	Inert% in feed
	CH <sub>4</sub> % in feed
	H <sub>2</sub> O% in feed
	H <sub>2</sub> /CO <sub>2</sub> in feed

---

## 2.2 Data Preparation

### 2.2.1. One-Hot Encoding

Categorical features including Base, Base 2, Support, Support 2, and Catalyst preparation method were converted to numbers [0, 1] using the command `pandas.get_dummies()` before analysis because MLP works well on numbers.

### 2.2.2. Missing Values

Missing values were filled with average values, as defined in Eq. (4).

$$Mean(\bar{x}) = \frac{\sum x}{n} \quad (4)$$

### 2.2.3. Data Partition

4,051 points of the dataset were divided into 80 and 20% as training and testing datasets, respectively. When learning a model, it is essential to organize a dataset into subsets. The original dataset can be divided into two sub-sets: the training set, and the testing set. The training set directly participates in the training process, which is used to learning the model and modify its parameters. A test set is used to evaluate the performance and robustness of the model [8].

### 2.2.4. Data Augmentation

Data augmentation was used to increase the diversity of a dataset by applying various transformations or modifications to the existing data. The goal is to enhance the performance and robustness of machine learning models. To enhance model performance through data augmentation techniques, one must be mindful of certain limitations. Firstly, it is crucial that models employing these techniques should be neural networks. Secondly, the dataset's magnitude should significantly surpass the number of inputs. Lastly, before applying data augmentation techniques, it is imperative to initially construct a model that exhibits commendable performance on the existing datasets.

In this study, data augmentation generated training set of the original dataset 3,240 data points, increasing to 16,200 data points (5 times) and 32,400 data points (10 times). The data was generated by adding noise that is randomly drawn from a normal distribution with mean equal to 0 and standard deviation equal to 1 as defined in Eq. (5).

$$\text{output}[i] = \text{input}[i] + \text{noise} \times \text{beta} \quad (5)$$

Where  $\text{output}[i]$  represent the value obtained after adding noise in  $i$  loop,  $\text{input}[i]$  represent the original data value at  $i$  in loop,  $\text{noise}$  represent random values are obtained from the normal distribution, and  $\text{beta}$  represent the size adjuster noise.

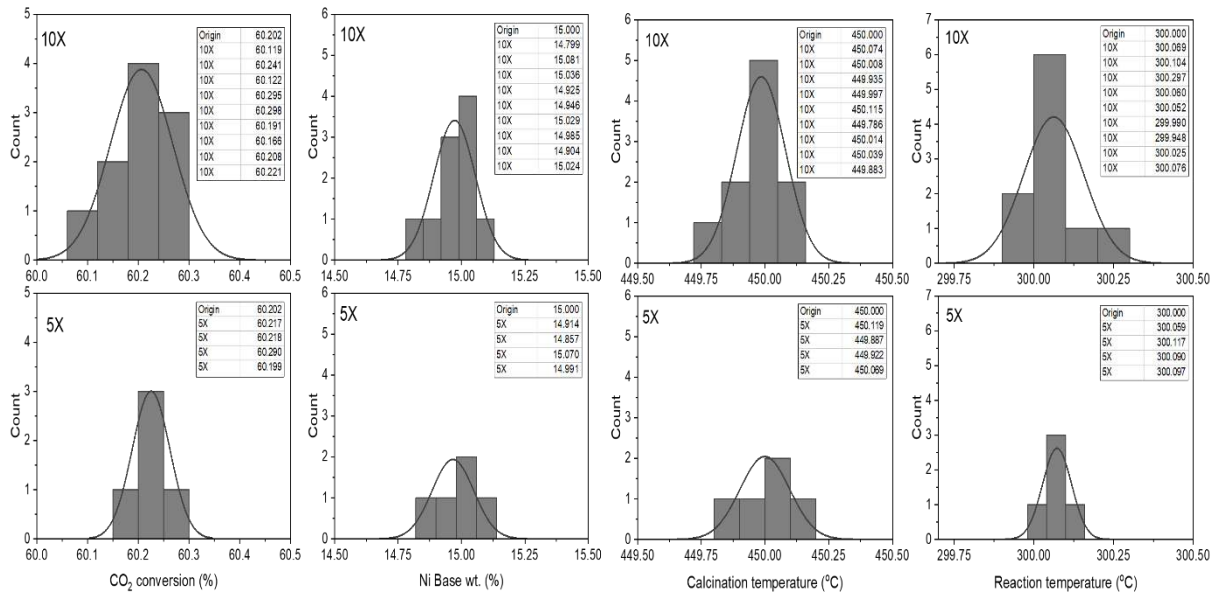


Fig. 1 Example of distribution for 5X (Lower) and 10X (Upper) data points.

### 2.2.5. Data Normalization

Data normalization was performed to standardize the scale of features in datasets, ensuring fair comparison, faster convergence in machine learning models, equal importance of features, improved interpretability, and mitigation of the impact of outliers. The standardized Z-score was adopted, as defined in Eq. (6).

$$Z = \frac{X - \mu}{\sigma} \quad (6)$$

Where  $X$  represents the individual data point, and  $\mu$  and  $\sigma$  represent the mean and standard deviation of the dataset, respectively.

### 2.3 Model Evaluation

Quantifying the quality of the model can be calculated using root mean square error (RMSE), as defined in Eq. (7) and the reliability of the model are obtained from  $R^2$  score.

$$RMSE = \sqrt{\frac{1}{N} \sum_{i=1}^N (y_i - \hat{y}_i)^2} \quad (7)$$

$$R^2 = 1 - \frac{\sum_{i=1}^n (y_i - \hat{y}_i)^2}{\sum_{i=1}^n (y_i - \bar{y})^2} \quad (8)$$

## 2.4 Multi-layer Perceptron regressor

Multilayer Perceptron (MLP), offers effective solutions for complex problems, showcases deep learning capabilities, and automatically adjusts weights during training, providing flexibility for various tasks and accurate predictions when appropriately configured.

In this study, Multilayer Perceptron (MLP) was used to learn with original data and training data with 5 and 10 times. In the model learning step, the hyperparameter set value is default first to compare results, then hyperparameter modification (hidden layer sizes and max number of iteration) was performed to find the best hyperparameter that gave the lowest RMSE score and the highest  $R^2$  score.

## 3. Results and Discussion

### 3.1. Effect of Augmented Data Size

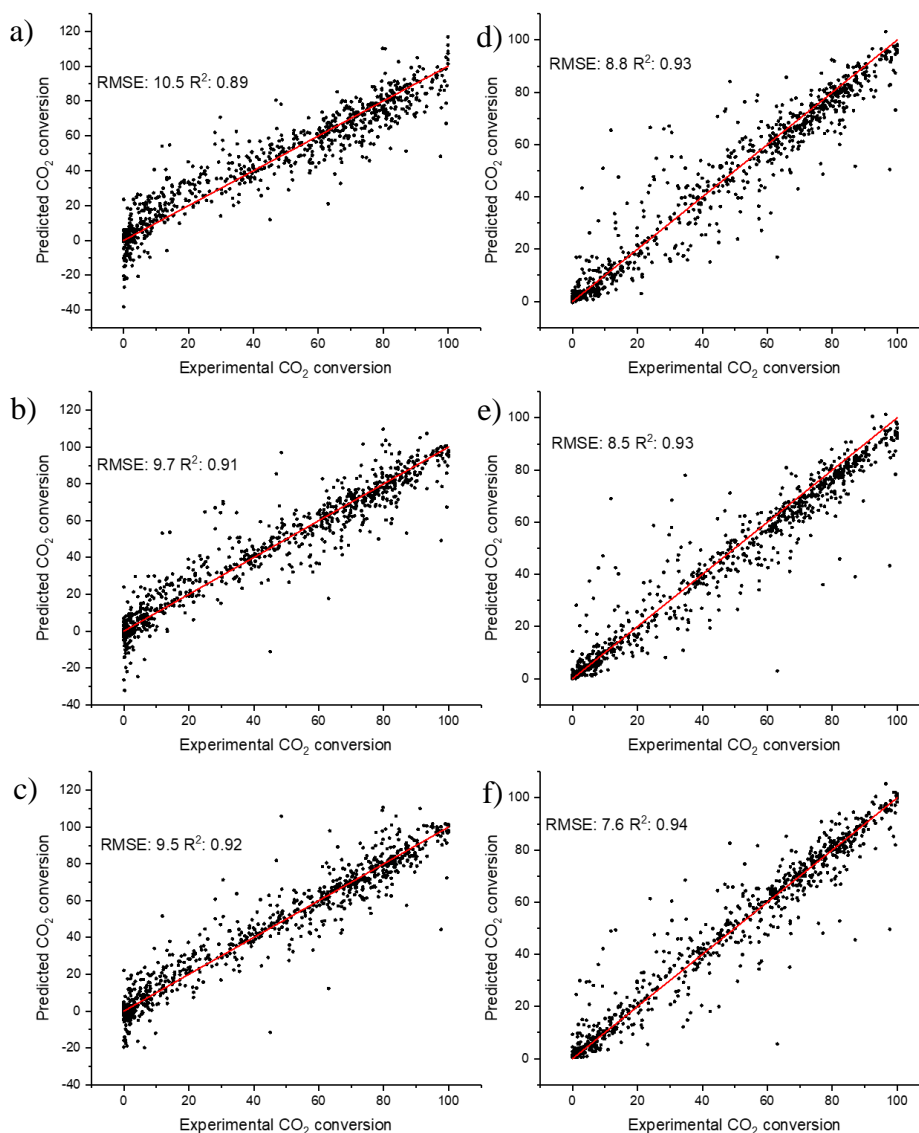


Fig. 2 Comparison of predicted and experimental CO<sub>2</sub> conversion for testing dataset, a) original (default), b) 5X (default), c) 10X (default), d) original (best), e) 5X (best), and 10X (best).

A predictive model for CO<sub>2</sub> conversion% was developed using MLP algorithm; the predictions for origin training, augment 5 time and augment 10 time of training with testing sets are given in Table 2, respectively, for the default model (with hidden layer size of (100) and max iter of 100000). The R<sup>2</sup> score are 0.98 and 0.92 for augment 10 time of training and testing set, respectively, is the highest R<sup>2</sup> score. while R<sup>2</sup> score original training and testing set are the lowest at 0.95 and 0.89, respectively. because the addition of learning data increases the complexity of the model, potentially enhancing its ability to predict CO<sub>2</sub> conversion% more accurately and reliably. However, the Fig. 2(a-c) reveals limitations, particularly in predicting CO<sub>2</sub> conversion% values near 0 and 100. Adjustments to the model parameters were made to address this issue, and further explanations will be provided in the next section.

### 3.2. Tuning of MLP parameters

In Table 2 shown the predictions for origin training, augment 5 time and augment 10 time of training with testing sets, respectively, for the best model (with hidden layer size of (136,136,136,136,136,136) for origin training, (136,136,136,136,136,136,136) for augment 5 time and 10 time and max iter of 100000). The R<sup>2</sup> score are 0.99 and 0.94 for augment 10 time of training and testing set, respectively, is the highest R<sup>2</sup> score. while R<sup>2</sup> score origin training and testing set are the lowest at 0.98 and 0.93, respectively. The observed improvement in predictive capabilities is attributed to modifications in the neural network, specifically by increasing the number of hidden layers. This structural adjustment enhances the model's capacity to comprehend and learn from the additional data. The augmented training data, increase of 5 and 10 time, contributes to increased efficiency in both the original and augmented datasets. Notably, the augmentation 10 time yields the best results due to the augmented data's heightened complexity compared to the original dataset. This complexity allows the learning model to explore a broader spectrum of data behavior than the original training data. The Fig. 2(d-f) illustrates those predictions for CO<sub>2</sub> conversion% values near 0 and 100 are notably improved, indicating a more robust predictive capability in these critical ranges.

Root Mean Square Error (RMSE) is a performance metric that quantifies the difference between predicted values from a model and the actual values in a test dataset. A lower RMSE indicates closer agreement between predictions and actual values, while a higher RMSE suggests a larger deviation. The formula used to compute RMSE is given in Eq. 7.

Table 2. R<sup>2</sup> and RMSE of various datasets.

Dataset	Default				Best			
	Train		Test		Train		Test	
	R <sup>2</sup>	RMSE	R <sup>2</sup>	RMSE	R <sup>2</sup>	RMSE	R <sup>2</sup>	RMSE
Yilmaz's work	-	-	-	-	0.97	6.4	0.85	12.7
Original	0.95	7.6	0.89	10.5	0.98	5.1	0.93	8.8
5X	0.98	4.6	0.91	9.7	0.98	4.5	0.93	8.5
10X	0.98	4.1	0.92	9.5	0.99	2.7	0.94	7.6

In Yilmaz's work used data carbon dioxide methanation in their study. A random forest model was used to analyze the data. The results showed that the training set had R<sup>2</sup> and RMSE values of 0.97 and 6.4, respectively, while the test set had values of 0.85 and 12.7, respectively.

To improve the performance of the model, a neural network or multilayer perceptron algorithm was used to learning with the original data set. The experimental results are shown in Table 2. This model achieves results when trained on the original training dataset, showing  $R^2$  and RMSE values of 0.98 and 5.1 for the training set, and 0.93 and 8.8 for the testing set, respectively.

To improve the performance of neural network models or multilayer perceptron algorithm, data augmentation techniques were employed to enhance the performance of model. The experimental findings are summarized in Table 2. The results indicate that utilizing the data augmentation technique, with 5 times increase in the training dataset, it was found that the performance values such as  $R^2$  and RMSE at 0.98 and 4.5 for the training dataset, and 0.93 and 8.5 for the test dataset, respectively. Further augmenting the training dataset 10 times resulted in improved, with  $R^2$  and RMSE values reaching 0.99 and 2.7 for the training set, and 0.94 and 7.6 for the testing set. A comparative analysis with the original training dataset results revealed that 10 times increase in the training dataset proved to be more efficient and reliable in improving model performance. Increasing the dataset size in training promotes diverse learning, allowing the model to adapt to a wider range of data, while hyperparameter tuning enhances the model's ability to comprehend and learn from the data. This leads to improved performance and reliability of the model.

#### 4. Conclusions

In this study, a data augmentation technique was employed to enhance the analysis of catalytic CO<sub>2</sub> methanation using machine learning tools. The investigation revealed that the performance and reliability of the model are significantly influenced by the size of the training dataset. When the training dataset was augmented by a factor of 10 and an MLP (Multi-Layer Perceptron) was utilized, the model exhibited an RMSE value of 9.4 and an  $R^2$  score of 0.92. This outperformed the model trained with an augmented dataset five times and the original training dataset, indicating that the augmented training dataset 10 time was more efficient and reliable. Further improvement was achieved by adjusting hyperparameters, such as the hidden layer. With these adjustments, the RMSE value decreased to 7.6, and the  $R^2$  score increased to 0.94 when using the augmented training dataset 10 time. Notably, this improvement extended the predictive capability to critical ranges, demonstrating the effectiveness of increasing the training data. The augmentation facilitated a broader exploration of information, enabling the MLP model to learn diverse data behaviors akin to the complexity of the human body's neural network system.

#### 5. Acknowledgements

The authors would like to thank Department of Chemical Engineering, Faculty of Engineering and Industrial Technology, Silpakorn University for financial support.

#### References

1. Vogt, C., et al., The renaissance of the Sabatier reaction and its applications on Earth and in space. *Nature catalysis*, 2019. **2**(3): p. 188-197.
2. Vita, A., et al., Activity and stability of powder and monolith-coated Ni/GDC catalysts for CO<sub>2</sub> methanation. *Applied Catalysis B: Environmental*, 2018. **226**: p. 384-395.

3. Siakavelas, G.I., et al., Highly selective and stable Ni/La-M (M= Sm, Pr, and Mg)-CeO<sub>2</sub> catalysts for CO<sub>2</sub> methanation. *Journal of CO<sub>2</sub> Utilization*, 2021. **51**: p. 101618.
4. Hu, F., et al., Structure–activity relationship of Ni-based catalysts toward CO<sub>2</sub> methanation: Recent advances and future perspectives. *Energy & Fuels*, 2021. **36**(1): p. 156-169.
5. Yılmaz, B., B. Oral, and R. Yıldırım, Machine learning analysis of catalytic CO<sub>2</sub> methanation. *International Journal of Hydrogen Energy*, 2023.
6. Venkatesan, P. and S. Anitha, Application of a radial basis function neural network for diagnosis of diabetes mellitus. *current science*, 2006. **91**(9): p. 1195-1199.
7. Wei, S., et al., Data augmentation and machine learning techniques for control strategy development in bio-polymerization process. *Environmental Science and Ecotechnology*, 2022. **11**: p. 100172.
8. Liaw, A. and M. Wiener, Classification and regression by randomForest. *R news*, 2002. **2**(3): p. 18-22.



## Development of Convolutional Neural Network for Leaked Gas Detection and Classification in Chemical Processes

**Satrio Yudanto<sup>1</sup>, Poomiwat Phadungbut<sup>1</sup>, and Pornchai Bumroongsri<sup>1,\*</sup>**

<sup>1</sup> Department of Chemical Engineering, Faculty of Engineering, Mahidol University, Nakhon Pathom, Thailand, 73170

E-mail: satrioyudanto@gmail.com, poomiwat.pha@mahidol.edu, pornchai.bum@mahidol.ac.th\*

### Abstract

In recent years, the advancement of machine learning stands out as a significant technological breakthrough. Numerous of machine learning algorithms have emerged to address complex real-world challenges across various domains such as bioinformatics, medical data processing, cybersecurity, and gas classification. Gas detection holds important role in ensuring health and safety within the chemical industry. Accurate classification of gases is vital for determining optimal treatment strategies, particularly in scenarios involving minor pipeline leakages. Machine learning techniques offer a promising approach to gas classification, with convolutional neural networks (CNNs) being among the most widely adopted algorithms. CNNs are favored for their ability to autonomously identify salient features without human intervention and their superior generalization capabilities. In this study, we propose a CNN architecture specifically tailored for gas classification tasks. The model will be trained and validated using diverse datasets encompassing five gas types: pure methane, pure ethylene, pure CO, CO-ethylene mixture, and methane-ethylene mixture. The CNN architecture's performance will be evaluated based on its accuracy, with the highest achieved accuracy serving as the benchmark for identifying the most effective model.

**Keywords:** Deep learning; convolutional neural network; gas detection; classification

### 1. Introduction

There are several types of oil spills and gas leaks especially in the field of chemical industry. For instance, gas leaks and oil spills can be happened by drilling blowouts, daily spills (small spills), transportation leaks, and many others [1]. In April 20th, 2010 known as "The Deepwater Horizon", the worst oil spill happened in United States which killed 11 peoples. It was estimated 3.19 million barrels of oil had leaked into the gulf [2].

Various types of method for detecting gas leakage or oil spills had been introduced among researchers to help for detecting the leakage. For instance, Jiang et al. [3] used a hyperspectral imaging approach for detecting a single point of natural gas leakage. By using hyperspectral images of bean, corn crops, and grasslands, the experiment can detect natural gas leaks. With the accuracies of the detection results based on the vegetation indices and color index were 53% and 56%, respectively. Furthermore, Li et al. [4] used the combination of noise and pressure interaction model for detecting the leakage on gas pipeline. The technique demonstrated enhanced suitability for industrial applications. With ongoing advancements, machine learning has emerged as a viable approach for detecting leakages within the chemical industry.

In recent years, there has been a big interest of implementing machine learning for leakage detection especially in chemical industry. The integration of machine learning often complements other tools or devices, such as unmanned aerial vehicles (UAVs) or gas sensors. Furthermore, leveraging machine learning for leakage detection offers the advantage of robust gas concentration classification capabilities. It is beneficial to enhance the leakage detection on pipelines [5]. For this purpose, it is necessary to choose the best pattern recognition algorithm with good performance in terms of classification accuracy and acceptable network architecture with deep consideration of existing conditions [6].

Industrial accidents caused by gas leakage especially in chemical industry have been increased within the past few years. One of the primary sources of leakage originates from pipelines. Failure to detect such leaks promptly can pose significant risks to both the environment and individuals in the vicinity. Pipelines are considered as one of the best ways and effectively to transport oil and gas products in chemical industry. This system usually comes up with hundreds of kilometers long. Therefore, it is important to all gas companies worldwide to develop efficient method of leakage detection as well as establish an effective monitoring system across the pipelines [7].

Given the myriad challenges faced by industries, the occurrence of gas or oil leaks is practically unavoidable. Thus, it becomes imperative for companies to adopt preventive measures and swiftly detect any leaks. This study introduces CNN to analyze several gases typically encountered in industries, notably CO and methane. Subsequently, CNN will be employed to classify these gases, leveraging the dataset comprising the five gas types investigated in this study. The ultimate goal is to initiate the integration of CNN with diverse instruments, such as drones, to enhance the detection of pipeline leaks.

## 2. Materials and Methods

In this research, the experiment will be focused on classifying the gas based on the developed convolutional neural network (CNN). The procedures in this research are shown in Fig. 1. Firstly, the raw data will be collected by experiment. The data that had been collected then will be augmented automatically and manually for further use in study.

Furthermore, in this research, the datasets will be divided into four different types, namely Dataset 1, Dataset 2, Dataset 3, and Dataset 4. After completing the pre-processing with dataset, convolutional neural network architecture will be developed. Training and validation processes are necessary to validate if the CNN model could achieve the best result. However, unsatisfying result shown by the CNN model indicates that the architecture needs to be re-designed or adjusted for hyperparameters.

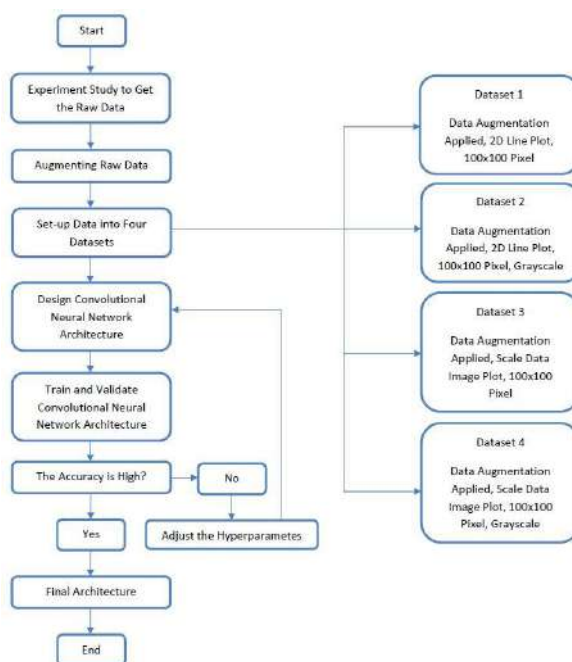


Fig. 1 Experimental procedure

## 2.1. Dataset

The background of the experiment was designed to test the gas sensor in realistic environment. In [8], a wind tunnel equipped with two distinct gas sources, labeled Source 1 and Source 2, was constructed to generate two separate gas plumes. Furthermore, the plumes will naturally get mixed along with a turbulent flow and reproduce the gas concentration that can be observed similar in natural environment. Thus, the gas sensor will capture some information contained in the gas plumes.

In the experiment [8], there are 30 kinds of mixture which are composed by 15 kinds of a mixture of CO and ethylene, 15 kinds of mixture of ethylene and methane. Each configuration was repeated six times with the total of 180 sets of data. The main goal of this experiment is to detect five kinds of gases, which are pure CO, pure ethylene, pure methane, CO-ethylene mixture, and methane-ethylene mixture.

The total duration in the experiment was separated into three parts with total of 300 s for each measurement. In the first 60 s, no gas was released in the tunnel. After 60 s, the gas was released in the tunnel from both sources for 180 s long. Furthermore, in the last 60 s, the system acquired the recovery phase. Throughout the experiment, the sensors signals were obtained in every 20 s intervals. In addition, 8 time series that indicate the gas condition in the experiment were obtained [8].

Additionally, the goal of this research is by using the raw data that captured by the sensors without any changes from the data, so that hopefully the CNN can extract the features comprehensively. Therefore, the size of 2,970 x 8 matrix was used without any interference.

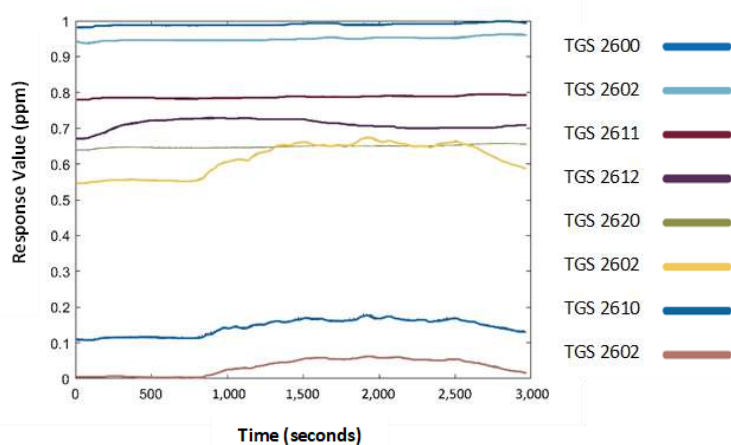


Fig. 2 Line plots of data from 8 sensors.

Figure 2 shows line plots that are used in this research as an input fed to the CNN. The different colors in the image indicate the 8 sensors employed in the experiment. As shown in Fig 2 the upward and downward signal represent the sensors activity that records the gas in the tunnel. In the figure, horizontal axis represents the time in seconds multiplied by 10, while the vertical axis represents the response value of the sensor.

As mentioned before, the three parts of the measurement can be seen from the Fig 2 from 0 s to 60 s is called as preparation time, it can be seen from the Fig 2 that the line is in baseline value. In the preparation time, air is remained as the input. In 60 s to 240 s, the two gas sources are began to release the gas into the tunnel shown by the changing of the line that is gradually increased. Finally in 240 s to 300 s is a recovery time for the sensors, as shown in the figure that the line is gradually decreasing back to the baseline.

## 2.2. Convolutional Neural Network Architecture

In this research, developed convolutional neural network with shortcut connection was applied. Inspired by [9], residual network was built to tackle degradation problem that exposed in plain network. The idea came from the fact that deep neural networks are more difficult to train than traditional neural network. Following by the increasing of the network depth, the accuracy gets saturated and will degrades rapidly.

In this research, a new CNN architecture is developed. The developed CNN architecture is inspired by ResNet18 [9]. By using shortcut connection in the architecture, the layers were made with the total of 53 layers. The method used in determining the number of layers is by trial and error. In the proposed model, two new methods are introduced.

Shortcut connection in skipping 1 convolutional block followed by 2 convolutional blocks, repeated. Commonly in the application of shortcut connection, skipping one or two convolutional block is applied. So far in terms of gas prediction, this unique method is the first time that has been used. The method can help reduce the total number of layers and parameters compared to the original residual network like ResNet.

Additionally, with a total of 53 layers, a lesser number of layers is applied. The network has been proven to effectively handle various types of images as inputs. Despite differences in complexity within the dataset, the model can be easily trained and accurately predict each

dataset. Furthermore, the number with 53 layers is the most appropriate number. As is known, the number of layers will greatly affect the value of the loss and accuracy of a model. Moreover, in this experiment the number of layers more than 53 will result in overfitting of the model. This will be seen later in the experiments conducted by model ConvsNet and SkipCNN. The similar thing also happens when the number of layers is less than 53. The model will not be able to recognize an object properly and will result in overfitting of the model.

Furthermore, the proposed CNN model used in this research is constructed with shortcut connection or skip connection. Shortcut connection is a well-known method to help tackle the degradation problem for deep learning model.

### 3. Results and Discussion

In this research, three CNN architectures are compared to point the best model that will be used in the experiment. As shown in Table 1, three CNN architectures are applied in the experiment.

Table 1. Model of CNN architecture in this research.

Name of Architecture	Network Type	Number of Layer
ConvsNet	Plain Network	69
SkipCNN	Residual Network	66
ShortcutNet (Proposed Model)	Residual Network	53

From Table 1, the model of architecture in this research not only used the residual network (SkipCNN, ShortcutNet) but also the plain network (ConvsNet) of CNN. Furthermore, the total number of layers for each architecture differed. These three CNN architectures will be trained with one of four datasets. As mentioned in research methodology, different type of concentration level of each gas will be applied for the CNN model to feed the CNN with different input. Zero ppm for pure concentration between CO, methane, and ethylene, low concentration, medium concentration, and high concentration.

Developed convolutional neural network for gas classification has been applied in this experiment. Five types of gases (pure CO, pure ethylene, pure methane, mixture of ethylene-CO, and mixture of methane-ethylene) are applied to test and validate the developed convolutional neural network, along with the other model comparison. As mentioned in the previous chapter, trial and error method is applied to Dataset 1 for each network to choose the best network to be implemented for Dataset 2, Dataset 3, and Dataset 4. Table 2 shows the final accuracy from each network using Dataset 1. From Table 2, we can conclude that the proposed model gives the best result and outperforms other networks as can be observed from the highest final accuracy with the least number of layers.

Table 2. Final training accuracy for model comparison with Dataset 1.

Network Name	Type of Network	Total Layer	Final Accuracy
ConvsNet	Plain Network	69	56.82%
SkipCNN	Residual Network	66	60.84%
ShorcutNet (Proposed Model)	Residual Network	53	95.30%

After the network is determined, the proposed network is applied to the rest of dataset. Table 3 shows the final accuracy from the proposed model using Dataset 2, Dataset 3, and Dataset 4. With the proper hyperparameter adjustments, the proposed network shows tremendous result with Dataset 2 final accuracy at 94.67%, Dataset 3 with 98.06% accuracy, and Dataset 4 with 97.50% accuracy. The average final accuracy is 96.74%. From Table 3, the highest final accuracy can be achieved from Dataset 3 with 98.06% accuracy. Various factors can affect the final accuracy. For instance, the total amount of data used, the complexity of the image and the hyperparameters in the model.

Table 3. Final validation accuracy of proposed model.

Network Name	Dataset Group	Final Accuracy
ShortcutNet (Proposed Model)	Dataset 2	94.67%
	Dataset 3	98.06%
	Dataset 4	97.50%

#### 4. Conclusions

In this study, residual convolutional neural network (CNN) with shortcut connection is developed. In addition, residual learning is applied to tackle degradation problem when layer is stacked. The model is proposed to classify five types of gases, which are pure methane, pure ethylene, pure CO, methane-ethylene mixture, and CO-ethylene mixture. Furthermore, four types of different datasets are applied in the experiment to train and validate the proposed model performance. The results show that the proposed model can achieved 96.74% on average accuracy between four types of datasets. The advantage of the proposed model is although the less layer is applied to different types of datasets, the proposed model can still obtain superfine accuracy score.

#### Acknowledgements

This research paper is supported by Specific League Funds from Mahidol University. This research project is supported by Mahidol University (Fundamental Fund: fiscal year 2023 by National Science Research and Innovation Fund (NSRF)).

#### References

- [1] Library of Congress. (2021, December 6). "Oil and Gas Industry: A Research Guide." [Online]. Available: <https://guides.loc.gov/oil-and-gas-industry/controversies/oil-spills>.
- [2] National Museum of Natural History. (2021, December 6). "Gulf Oil Spill," *Smithsonian Ocean*, 2018. [Online]. Available: <https://ocean.si.edu/conservation/pollution/gulf-oil-spill>.
- [3] Jiang, J., Ran, W., Xiong, K., and Pan, Y. "A spectral-spatial approach for detection of single-point natural gas leakage using hyperspectral imaging," *Int. J. Greenh. Gas Control*, vol. 103, no. 11, p. 103181, 2020.
- [4] Li, F., Zhang, L., Dong, S., Zhang, H., Wang, W., and You, Y. "Noise-Pressure interaction model for gas pipeline leakage detection and location," *Measurement*, vol. 184, no. April, p. 109906, 2021.
- [5] Zhang, J., Xue, Y., Sun, Q., Zhang, T., Chen, Y., Yu, W., Xiong, Y., Wei, X., Yu, G., Wan, H., Wang, P. "A miniaturized electronic nose with artificial neural network for anti-interference detection of mixed indoor hazardous gases," *Sensors Actuators, B Chem.*, vol. 326, no. September 2020, 2021.



- [6] Attari, M., Biuhedda, M., and Benrekia, F. “Gas Sensors Characterization and Multilayer Perceptron (MLP) Hardware Implementation for Gas Identification Using a Field Programmable Gate Array (FPGA),” *sensors*, vol. 13, pp. 2967–2985, 2013.
- [7] Gupta, P., Wang, M., Dauwels, J., Thein Zan, T. T., and Ukil, A. “Leak detection in low-pressure gas distribution networks by probabilistic,” vol. 58, no. April, pp. 69–79, 2018.
- [8] Fonollosa, K., Rodriguez-Lujan, I., Trincavelli, M., Vergara, A., and Huerta, R. “Chemical Discrimination in Turbulent Gas Mixtures with MOX Sensors Validated by Gas Chromatography-Mass Spectrometry,” *Sensors*, vol. 14, pp. 19336–19353, 2014.
- [9] He, K., Zhang, X., Ren, S., and Sun, J. “Deep Residual Learning for Image Recognition,” *Microsoft Res.*, vol. 45, no. 8, pp. 770–778, 2015.

## **A STUDY OF PIG FARM WASTE TO PROMOTE THE CIRCULAR ECONOMY CONCEPT**

**Suparat Eiamtako<sup>1</sup>, Trakarn Prapasongsa<sup>1</sup>, Romanee Thongdara<sup>1</sup>  
and Nawatch Surinkul<sup>1\*</sup>**

<sup>1</sup>Department of Civil and Environmental Engineering, Mahidol University, Nakhon Pathom, Thailand  
E-mails: \*nawatch.sur@mahidol.ac.th

### **Abstract**

Wastewater pollution from pig farming activities is the main source of contamination in the lower Tha Chin River Basin, particularly in Nakhon Pathom province. This pollution occurs from various activities within pig farming such as the improper treatment of wastewater. Despite the prevalent use of biogas production systems, current wastewater management practices remain inadequate in addressing this issue effectively. This study aims to estimate the pollution loads from pig farms in Nakhon Pathom province discharging into the Tha Chin River Basin and proposes waste management strategies under the circular economy principle. Through Material Flow Diagram analysis, it was found that improving the wastewater treatment system could significantly reduce pollution by 0.0015 kg BOD/day per pig. Therefore, enhancing wastewater treatment efficiency and promoting reuse within farms are imperative steps to meet Thailand's water quality standards and mitigate the environmental impact of pig farming in the region.

**Keywords:** Pollution load; Waste management model; Pig farm; Circular economy concept.

### **1. Introduction**

The problem with pig farms in Thailand is the quality of the wastewater released from the farms, which has an impact on the environment. Poor quality wastewater is exported to rivers or nearby water bodies from various activities. up within the pig farm, such as raising and cleaning the barns, cause pollution to the surrounding environment. To solve this problem, pollution control agencies operate from within the pig farm to the outside environment. This is because there is a problem of deterioration of water sources in the country, which is the main cause. Wastewater treatment systems recommended by government agencies in Thailand include: Anaerobic tank system and static adjustment pond but at present, biogas treatment systems are of interest to the agricultural sector [2] by managing wastewater generated from pig farms. By collecting wastewater and processing it into electrical energy for use in farm activities. Although this system requires a large investment of resources, it can be cost-effective in the case of such large pig farms. Currently, the water quality in the Tha Chin River is deteriorating due to many contaminants. Due to the use and release of untreated water into the Tha Chin River. There are many factors that cause water quality to decrease. One of them is the release of wastewater from a pig farm into the Tha Chin River without treatment or with insufficient treatment, according to a 2021 report by the Pollution Control Department focusing on the Chedi Bucha Canal issue, which flows through Mueang Nakhon Pathom District and Nakhon Chai Si District. In an area with a high density of pig farms, it was found that 91% of pig farms regularly used wastewater treatment systems, while 9 % did not use them [2]. Pollution Control



Department officials gave recommendations for improving the system, with an emphasis on increasing efficiency. Wastewater treatment increase pond capacity and prevent water from leaking out of the farm [3]. Wastewater management systems on pig farms represent an investment in environmental awareness rather than a profit for the operator. Its value lies primarily in the environmental awareness of entrepreneurs. Therefore, it is of utmost importance to consider selecting a treatment system that matches the amount of wastewater generated on the farm. [4]. The concept of circular economy aims to create a sustainable cycle. Where economic activity is renewed, rebuilt, and designed with long-term impacts in mind. All economic activities are created and circulated within the entire system in such a way that they are produced, used, and reproduced. In Thailand, this is driven by the industrial sector due to concerns about the shortage of energy and key production resources. The government has issued a policy for the public and private sectors to adjust the system appropriately and apply this concept to the agricultural sector as well. [5] By estimating the amount of pollution that occurs in the system, it will be known whether the system needs help or improvement, with an emphasis on reducing costs and meeting standards under the concept of circular economy, leading to zero-waste. This study aims to evaluate. The amount of pollution from pig farms in Nakhon Pathom Province enters the Tha Chin River Basin, and applying the concept of circular economy to pig farms through waste management situations.

## 2. Methodology

### 2.1 Study area

The target area is a pig farm located in Nakhon Pathom province in low plain areas along the river banks of the lower Tha Chin River and its tributaries. Because the canal flows into the main river, this also causes an accumulation of pollution in the Tha Chin River.

2.1.2 Questionnaire design and survey. The survey focusses on activity in the pig farm which relates to wastewater management, water quality and the number of pigs.

2.1.3 Data collection. Two types of data collection: confirmation data, which validates the research results. Analytical data, includes information on the number of pigs, pig farm wastewater management, and farm wastewater quality.

### 2.2 Material flow analysis

Pollution load calculations form the foundation for process design and control, providing insights into the required raw materials and expected product output. Initially, we began by creating a Mass Flow Diagram (MFD) and developing a standard model. Additionally, the model underwent updates through three different scenario management processes. Analysing the material flow management scenarios, encompassing both positive and negative outcomes regarding management styles and pollution in pig farms. Treatment efficiency was calculated for each model. The results of the analysis were obtained from scenarios of treatments.

## 3. Results and Discussion

This paper shows results from the calculation and wastewater management of pig farm in two parts: 1) Pollution load from pig farm, 2) Management model

### 3.1 Number of pig and pollution discharged into the environment

The number of pigs has a significant impact on pollution; the calculated loads are shown in Table 1. which loads are released into the environment in Nakhon Pathom Province from 2019 to 2022. The number of wastewater and loads per pig are based on rates from the Pollution Control Department [3]. In 2021, BOD loads after treatment in the presence of 359,709 pigs were 11,361 kg of BOD per day. However, in 2022, the BOD loads from 74,473 pigs contributed 2,352 kg of BOD per day to the discharges into the environment. The number of pigs in 2022 has been affected by the flooding situation and the epidemic situation in 2021, resulting in damage to the pig breeders from the Thai Pig Growers Association. The obtained loads were still high even after passing the treatment system. This can indicate that the presence of wastewater treatments is not functional.

Table 1. Pollutants in wastewater that will be released into the environment in Nakhon Pathom province from 2019-2022.

Year	Number of pigs	Effluent wastewater (m <sup>3</sup> /day)	Pollution (kg BOD/day)	Discharged into the environment (kg BOD/day)
2019	162,891	3,909	13,683	5,145
2020	167,192	4,013	14,044	5,281
2021	359,709	8,633	30,216	11,361
2022	74,473	1,787	6,256	2,352

Pollutant emissions in wastewater vary across districts in Nakhon Pathom Province (Table 2), with the highest emitter being Mueang Nakhon Pathom, followed by Kamphaeng Saen in second place, and Samphran in third place. Notably, in 2018, Samphran District was previously ranked third.

Table 2. Pollutants in wastewater that will be released into the environment at the district level Nakhon Pathom Province in 2022

District	Number of pigs (pigs)	Effluent wastewater (m <sup>3</sup> /day)	Pollution (Kg BOD/day)	Discharged into the environment (kg BOD/day)
Mueang Nakhon Pathom	41,554	997	3,491	1,312
Samphran	8,436	202	709	266
Kamphaeng Saen	20,388	489	1,713	644
Bang Len	3,975	95	334	126
Nakhon Chai Si	64	2	5	2
Don Tum	56	1	5	2

Total	74,473	1,787	6,256	2,352
-------	--------	-------	-------	-------

### 3.2 Management model by MFD

The current pollution management systems on pig farms are practiced according to recommendations from the Department of Livestock Development and the Pollution Control Department. Mostly farms employ a biogas system and sedimentation pond for wastewater treatment systems. However, this management approach demands significant space and involves a high initial investment, without yielding increased productivity. Within the on-farm waste management system, wastewater originating from washing and pig consumption is utilized. The biogas production system is integral to managing pig manure, yielding three primary byproducts: wastewater, biogas, and sludge. Effluent of biogas system is later treated by sedimentation ponds, which function as water retention ponds. Multiple sedimentation ponds are employed for this purpose. The treated water is subsequently recycled and released into nearby water sources at a later stage. Therefore, treated water is gradually released into the environment. Sludge from biogas systems is treated by the drying process and later used as fertilizer for growing vegetables or for sale, as shown in Figure 1.

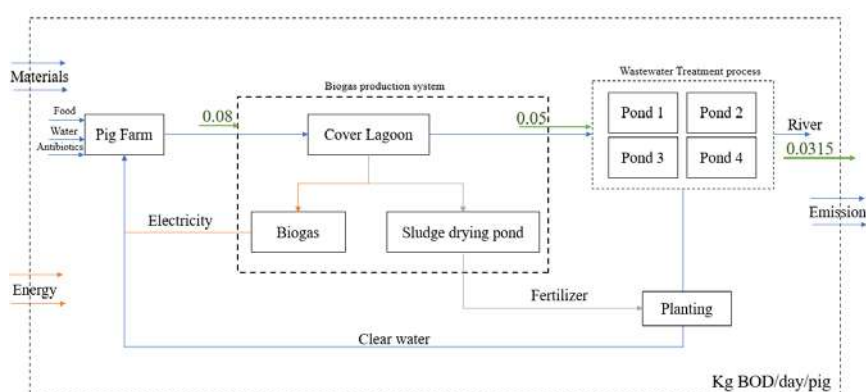


Figure 1. MFD of current pig farm waste management system in Thailand

#### 3.2.1 Guidelines for solving problems of pig farm waste management systems

1. Guidelines for adjusting large farms: This involves correcting both internal farm management, modified materials into the biogas system and add a system to help remove algae.

1.1 Guidelines for reducing water flow out of the farm: A pig farm in Kanchanaburi province has 3,000 pigs. The waste is taken through a covered lagoon process for approximately 45 days before being extracted to create fertilizer. The resulting wastewater undergoes the sedimentation process within the wastewater treatment system. Subsequently, the treated water is utilized for cultivating crops and distributed to nearby communities. The water emerging from the treatment system does not meet standard criteria in terms of chemistry and physical properties (pH=7.53, BOD=60 mg/L, COD=47 mg/L, TKN=74 mg/L [6]. However, from a biological perspective on the farm, these parameters serve as guidelines to ensure that the water does not adversely affect the health of the pigs.

1.2 Guidelines for solving the problem of modified materials into the biogas system: Modified cover lagoons are employed to reduce space usage and increase system performance biogas system. This modification simplifies the control of wastewater standards on the farm. Various principles are utilized, including air mixing and ensuring the biogas system is community-friendly. (Figure 2)

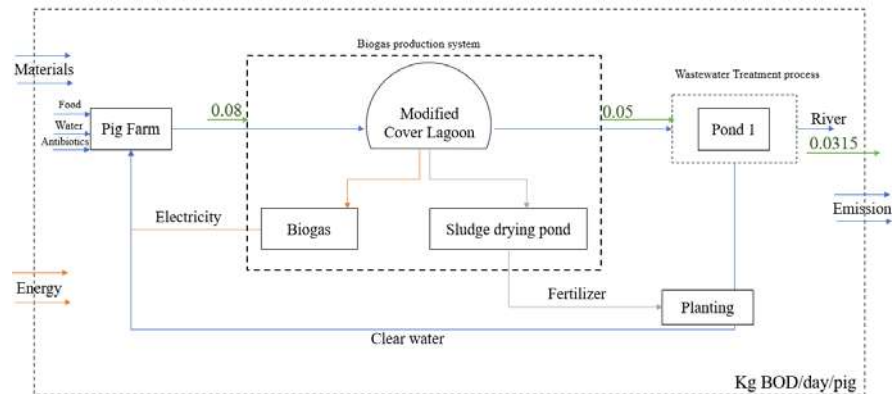


Figure 2. MFD of pig farm waste management with modified cover lagoon system

- Inserting air into the biogas system can reduce  $H_2S$  from an average level of 644 ppm to undetectable levels within 48 hours. Hydrogen sulfide in anaerobic wastewater treatment systems with high sulfate rates can result in many problems, such as rotten egg odor, high levels of This system will reduce the methane in the biogas produced from the aerated digester by up to 3.5% which can be used to produce renewable energy as usual. Economics suggests that investments in air mixing, equipment and operating costs result in an average payback period of 1.32 years over the benefits of use. [7].
- In 2008, Chiang Mai University introduced a low-cost biogas production method for households developed by the Faculty of Agriculture. This innovation aimed to address community pollution issues, utilizing an investment of no more than 2,500 baht. This approach won the 2008 Science and Technology Invention Contest under the topic 'Machinery, Energy, and the Environment for Agriculture.' It is particularly suitable for small farms [8].

Improving according to the model (Figure 2), which entails enhancing the Biogas production system, can lead to a reduction in pollutants in wastewater such as Nitrogen and Phosphorus, depending on the specific unit improved within the Cover lagoon system. Once treated in the modified cover lagoon, wastewater flows into a holding pond and eliminating the need for multiple ponds for wastewater sedimentation. Subsequently, the treated water is discharged into the environment and some of the water will return to the pig farm's barn. Sludge that comes out of the system will have more nitrogen and phosphorus, which will be beneficial for making fertilizer.

1.3 Use algae in a pig farm's waste management system: recommended for use in the wastewater pond system after leaving the cover lagoon. This system must consider adding a process to trap algae from wastewater, which is another wetland system, where green microalgae *Scenedesmus obliquus* can be used to assist in nitrogen and phosphorus treatment by incorporating it into piggery wastewater effluent process to eliminate nutrients from wastewater. Additionally, it enhances biogas production [9], this green alga can reduce nitrogen by 155 mg and phosphorus by 4 mg.

2. Modification guidelines for small farms: This involves adding pollutants to the management system.

- Magnesium-biochar can be employed to absorb phosphorus and decrease the concentration of ammonia nitrogen in wastewater. It will be introduced into wastewater treatment process, exhibiting a treatment efficiency of 62.98% for ammonia nitrogen [10]. Subsequently, the water is extracted before entering the sedimentation pond system and the water reservoir, following standard procedures.
- The capability of magnesium salt to reduce ammonia nitrogen and phosphorus through precipitation is notable. This salt is introduced into a wastewater treatment tank to enhance treatment efficiency and minimize odor. The efficiency in treating ammonia nitrogen is recorded at 78.81%, while the efficiency in treating phosphorus is 58.17% [11].
- Magnesium ammonium phosphate crystallization can be employed to reduce nitrogen and phosphorus. This compound is introduced into the treatment tank and stirred to accelerate the crystallization reaction. The highest efficiency in removing total phosphorus and ammonia nitrogen, 59.5% and 59%, respectively, was achieved with a stirring time of 30 minutes [12].
- Using Azolla plants in wastewater treatment can remove BOD up to 60-95% when planted in the wastewater treatment pond of a pig farm. The longer the wastewater stays, the more BOD Azolla plants will remove. This research recommends 14 days for the most effective results [13]. When considering the efficiency value of pollution load, the load will be reduced by 0.0015 kg BOD/day per pig.
- Floating plants such as tallow are 85.20% effective in treating BOD in pig wastewater, as the concentration level of wastewater from pig farms to the weight and nutrients of the floating plants has been determined. Water eggs are suitable for pig farmers at the farm level as they can be used in the final wastewater treatment before releasing into public water sources, and this plant can also serve as food for animals [14]. When considering the efficiency value for pollution load, the load will decrease by 0.0015 kg BOD/day per pig.

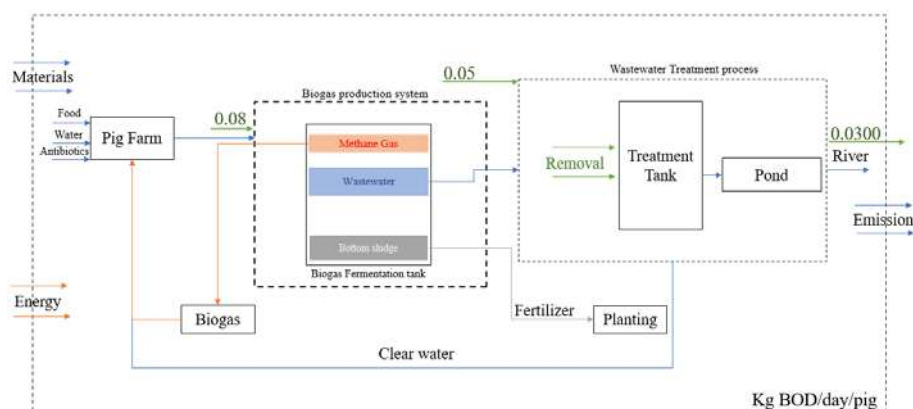


Figure 3. MFD of pig farm waste management with biogas system

Improvement according to Model 3 (Figure 3), additional wastewater treatment can lead to a reduction in the pollution level of wastewater by 0.03 kg BOD/day for 1 pig. This entails installing pollution limiters into the wastewater treatment tank. Subsequently, after treatment, the treated water is directed to the water reservoir before being discharged into the environment. Additionally, a portion of the water is returned to the farm for reuse.

### 3. Guidelines for Zero-Waste Pig Farming in Pits

- The optimal number of pigs for this type of farming is 100 on a small-sized farm, divided into pens accommodating six pigs each. The construction utilizes coconut meat as a foundation, with each pig requiring approximately 100 kilograms of coconut meat. On a daily basis, a mixture of microbial water and fruit juice is sprayed inside the pens and houses to eliminate odors and aid in the digestion of bedding material. Additionally, water is sprayed onto the bedding material to enhance water absorption and prevent runoff from the pig farming system. The use of fermented food has reduced nitrogen-induced odors from 6% to 0.8%, resulting in reduced food costs. This indicates that the microbial juice mixed with fruit fermentation contributes to a more efficient pig digestive system.
- After 5-6 months, the litter decomposes, becoming fertilizer for resale. Notably, the utilization of coconut meat has increased from 100 kg per coconut to 500 kg per coconut in last 5 months.

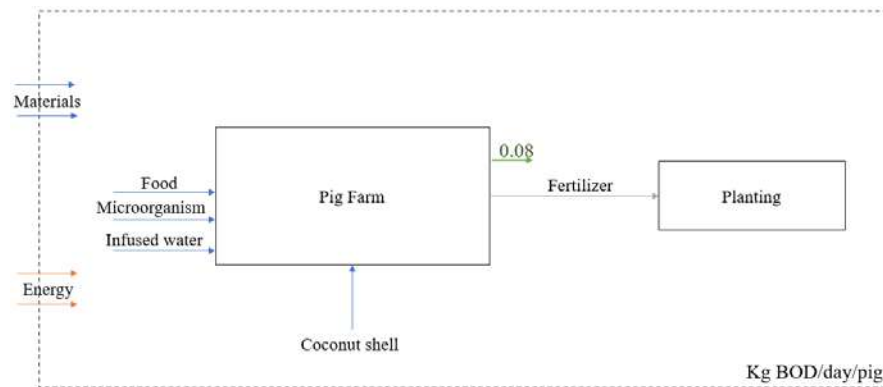


Figure 4. MFD of Pig Farming in Pits [15]

#### 4. Conclusions

Wastewater pollution from pig farms is the main source that polluted the lower Tha Chin River Basin. The current wastewater management systems in pig farms are insufficient to treat the wastewater effectively. This needs to consider the improvement of the treatment system or additional alternative system in order to meet the standards. Therefore, the use of material flow analysis for planning could be the advantage management system in order to see the circulation of materials within the farm especially Ammonia nitrogen and Phosphorus. Analysis of pollution loads reduction in each model indicates that enhancing the wastewater treatment system proves more effective than improving biogas production. The upgraded wastewater treatment system can potentially reduce pollution by 0.0015 kg BOD/day per pig. Enhancing wastewater treatment efficiency and the reuse in farm is imperative in order to meet the standards of Thailand and support the concept of the circular economy. This entails treated wastewater is reuse in the farm's greenhouses which enhancing the use of nitrogen and phosphorus for agriculture.

#### References

- [1] Pollution Control Department (2005). Pig Farm Practices. Report from Pollution Control Department. Accessed on June 8, 2023.
- [2] Pollution Control Department. (2016). Investigation and law enforcement on pollution sources in the Tha Chin River Basin. Report from Pollution Control Department. Accessed on June 8, 2023.

- [3] Pollution Control Department (2010). A guide to assess the amount of wastewater and pollution from pig farming. Report from Pollution Control Department. Accessed on June 8, 2023.
- [4] Pirom Nontasorn, & Sirilux Saihong. (2011). Wastewater Quality from Pig Farms in Western Thailand during 2008 – 2010. Veterinary Research and Development Center (Western Region), Vol 8(1685-9952), No 29.
- [5] Office of Trade Policy and Strategy. (2019). Circular Economy, the way to survive for Thailand in the era of overflowing with waste. [Online URL: [http://www.tpsoc.moc.go.th/sites/default/files/2.\\_paper\\_-\\_circular\\_economy.pdf](http://www.tpsoc.moc.go.th/sites/default/files/2._paper_-_circular_economy.pdf)] accessed on June 8, 2023.
- [6] Sunee Sutheepthum, & Pitak Siriwong. (2013). Green Farm Way: Model and Process of Environmental Management and Corporate Social Responsibility within Kanchanaburi Swine Farm of Charoen Pokphand Foods Co., Ltd. (Public). Veridian E-Journal year 6, 3.
- [7] W. Pinate. (2016). The Quality Improvement of Biogas by Air Mixing. Siam Physics Congress 2016. P 66-70.
- [8] Suchon Tangthawipat (2008). Low-cost biogas production for households. Scientific and technological invention contest for the year 2008, topic: “Machinery, Energy and Environment for agriculture” Chiang Mai University. [Online URL: [http://clinictech.ops.go.th/online/cmo/site\\_techlist\\_detail.asp?tid=331](http://clinictech.ops.go.th/online/cmo/site_techlist_detail.asp?tid=331)] accessed on January 18, 2024.
- [9] Min-Kyu Ji, Reda A. I. et al. (2013). Removal of Nitrogen and Phosphorus from Piggery Wastewater Effluent Using the Green Microalga *Scenedesmus obliquus*. JOURNAL OF ENVIRONMENTAL ENGINEERING. [https://doi.org/10.1061/\(ASCE\)EE.1943-7870.0000726](https://doi.org/10.1061/(ASCE)EE.1943-7870.0000726).
- [10] Lintong He, Dehan Wang and Zhaoyun Wu et al. (2022). Magnesium-modified biochar was used to adsorb phosphorus from wastewater and used as a phosphorus source to be recycled to reduce the ammonia nitrogen of piggery digestive wastewater. Journal of Cleaner Production 360 (2022).
- [11] Pongludda Paosiri, Weerasak Suebsoh, and Chanchainarong Songkasri. (2010). Removal Ammonia nitrogen and Phosphorus in Swine Wastewater using Precipitation with Magnesium Salt. Rajabhat Maha Sarakham University Journal; RMU.J. 6(1): January - April 2012: 129 - 137
- [12] Aditep Jumjuang, Channarong Puchongkawarin and Wipada Dechapanya.(2022). Treatment of the Swine Farm Effluent by the Magnesium Ammonium Phosphate Crystallization. Research and Innovation for SDGs in the Next Normal. Department of Chemical Engineering, Faculty of Engineering, Ubon Ratchathani University. pp. 53-64.
- [13] Natsima Tokhun, Chuleemas Boonthai Iwai and Mongkon Ta-oun. (2011). Wastewater Treatment from Piggery Farm by Using *Azolla microphylla*. The 12th Graduate Research Conference Khon Kaen University 2011. Department of Plant Science and agricultural resources, Faculty of Agriculture, Khon Kaen University
- [14] Thongphanh Lartdavong. (2021). WASTEWATER TREATMENT FROM SWINE FARM BY USING FLOATING PLANTS AS SUPPLEMENTARY FOR ANIMAL FEED. [Science in Environmental Technology, Maejo University]. <http://ir.mju.ac.th/dspace/bitstream/123456789/830/1/6204301005.pdf>
- [15] Krit Lualmai. (2022). “Pork Lum Don Rae” is definitely delicious - safe. It has been well-known in the organic farming community for a long time”. Technologychaoban. [https://www.technologychaoban.com/livestock-technology/article\\_38563](https://www.technologychaoban.com/livestock-technology/article_38563)

## Examining the connection between nutrients and water hyacinth invasion in the Lower Tha Chin River

**Chanisa Sangiampak<sup>1</sup>, Romanee Thongdara <sup>1</sup>, Trakarn Prapasongsa<sup>1</sup> and Nawatch  
Surinkul <sup>1\*</sup>**

<sup>1</sup> Department of Civil and Environmental Engineering, Mahidol University, Nakhon Pathom,  
Thailand E-mails: \* [nawatch.sur@mahidol.ac.th](mailto:nawatch.sur@mahidol.ac.th)

### Abstract

Water hyacinth (*Eichhornia crassipes* (Mart) Solms) is a rapidly proliferating aquatic plant that can double its coverage area every 62 days or increase its population from 10,000 to 600,000 plants in just eight months. Water hyacinths are biennial freshwater plants capable of both sexual and asexual reproduction. The Tha Chin River had an estimated volume of 322,852 tons, or 20 tons/m<sup>2</sup>, between October 2020 and May 2021. From February to June, water hyacinths grow at a rapid rate. Ammonia, nitrite, and total phosphorus mostly discharged from domestic uses, industry, agriculture, fisheries, transportation. The water hyacinth uses phosphorus as a nutrient when it grows quickly, which affects aquatic life as seen from a bad taste and odor of water. Ammonium is also harmful to aquatic life. Nitrogen in the form of nitrite and nitrate can cause eutrophication, which accelerates the growth of aquatic weeds and water hyacinth. In this study, surveys utilizing satellite images from remote sensing, based on past data from Landsat 8 satellite images, investigated the relationship between nutrient elements and water hyacinth invasion in the lower Tha Chin River. The overlay results indicated that station TC07, TC04, and the area between TC04 and TC01 exhibited a moderate density range of plant coverage, which was correlated with the concentration of ammonia and phosphorus in the Tha Chin River.

**Keywords:** Water hyacinth; Ammonia; Nitrite; Nitrate; Total phosphorus

### 1. Introduction

Water hyacinth, *Eichhornia Crassipes* (Mart.) Solms originated in the South American Amazon region of Brazil. They were brought to Thailand in 1901 from the Indonesian island of Java, they were planted at Sra Pathum Palace. However, due to their rapid development and spread, water hyacinths quickly turned into a significant aquatic weed. The water hyacinth is an aquatic plant with basic foliage that develops rapidly. The petiole expands out in the middle, giving the leaf a cordate appearance, and the inside is porous to support the trunk when it floats in the water. Water hyacinths can live in both clean and dirty water, as long as the water is below 34 °C and the pH value is between 4 and 6, which is ideal for their growth. Although they are not resistant to salt water, they are resistant to drought. A water hyacinth consists about 95% water, 89% leaf water, and 96.7% petioles [1]. The water hyacinth is a biennial freshwater plant that reproduces both sexually and asexually. It is an aquatic plant that grows quickly, doubling its covering area every 62 days or increasing the plant count from 10,000 to 600,000 in just eight months [2]. Water hyacinths invaded the Tha Chin River in October 2020–May 2021, weighing around 322,852 tons, or 20 tons/m<sup>2</sup>. From February to June, the water hyacinths develop at a fast rate [3]. The amount of water hyacinth blocking the water flow and hindering the weir's drainage caused a forty percent decrease in the water flow rate, which has an impact on the way the river is utilized for agriculture. Water hyacinth inhibits fish development by reducing the amount of light that can enter the water, which slows down plankton growth and causes fish to decrease in size [2].



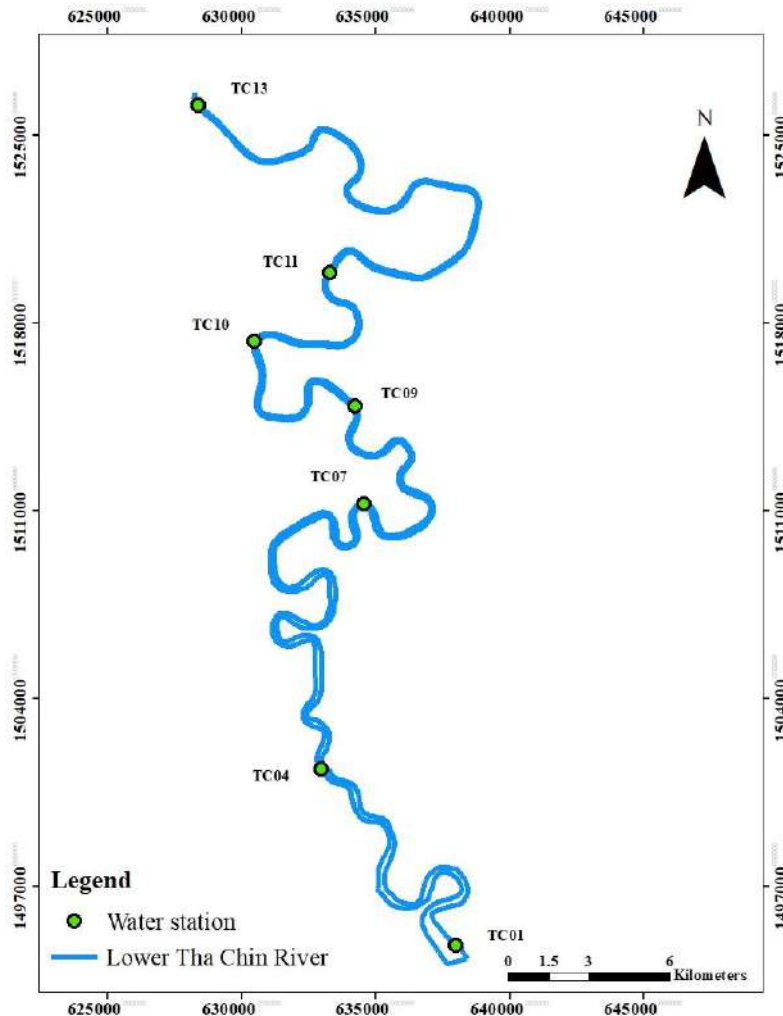
A significant water basin in Thailand's central area is the Tha Chin River. Before flowing into the Gulf of Thailand, the Tha Chin River Basin is essential to life and the environment in general, including humans, agriculture, industry, fisheries, transportation, and consumption. The presence of industrial enterprises and highly populated areas along the lower Tha Chin River puts it at risk for water hyacinth invasion and resource degradation. Consequently, it must sustain the discharge of phosphorus, a crucial nutrient for plants, and nitrogen-contaminated municipal and industrial wastewaters into the river. Nitrogen enters the river as organic compounds, or ammonium, which are harmful to aquatic life. Additionally, nitrogen enters the river as nitrate, which causes eutrophication and accelerates the growth of aquatic weeds and water hyacinth. Due to the dense covering of water hyacinths on the water's surface, sunlight is blocked and atmospheric oxygen levels are decreased, resulting in wastewater [4]. Phosphorus entering into rivers, water hyacinth has degraded the environment for investments and the hospitality and tourism sectors; toxin-producing algae can kill many fish, marine mammals, birds, and humans by causing a severe oxygen shortage that causes in a fish kill; and it increases the cost of treating water to remove taste and odor during water supply production [5,6,7].

Geographical technology is becoming increasingly significant in the areas of transportation and communication because it is advanced technology, expedient, and cost-effectiveness. Surveying water hyacinth invasion requires the use of geographic information technology to support in mapping the distribution of water hyacinths and nutrients in the river. Therefore, this study used remote sensing technology to evaluate the relationship between nutritional elements and water hyacinth invasion in the lower Tha Chin River through surveys utilizing satellite photography from remote sensing employing historical data based on Landsat 8 satellite images.

## 2. Study area and Data

### 2.1 Study area

The Tha Chin River Basin is located in the geographical middle of Thailand, to the east of the Chao Phraya River. Its boundaries are defined by latitudes 13° 10' north to 15° 30' north and longitudes 98° 15' east to 100° 10' east. The basin's 13,477.16 km<sup>2</sup> area is composed of up of 13 provinces: Bangkok, Kanchanaburi, Chainat, Nakhon Pathom, Nonthaburi, Ayutthaya, Ratchaburi, Samut Songkhram, Samut Sakon, Singburi, Suphanburi, Angthong, and Uthai Thani. The study was conducted in the lower Thachin River, measuring 82 kilometers from the river's estuary (TC01) to the Nakhon Chai Si District Office in Nakhon Pathom Province (TC13), at kilometer 0 of the Marine Department [8]. The study was conducted in the estuary of Tha Chin, Mueang District, Samut Sakhon Province, as shown in Figure 1.



**Figure 1.** Location of the study area.

## 2.2 Nutrient data

Water quality monitoring reports of the Tha Chin River by Regional Environmental Office 5 (Nakhon Pathom) and the website of the water quality database system by Regional Environmental Office 5 (Nakhon Pathom), whose water quality index is to be analyzed, serve as sources of the data collected on water quality from a total of 7 stations (TC01, TC04, TC07, TC09, TC10, TC11, TC13) in 2022. The four indices used in the analysis of the water quality index are total phosphorus, ammonia, nitrite, and nitrate, which are selected based on their nutrients that impact plant development and are established according to surface water quality standards.

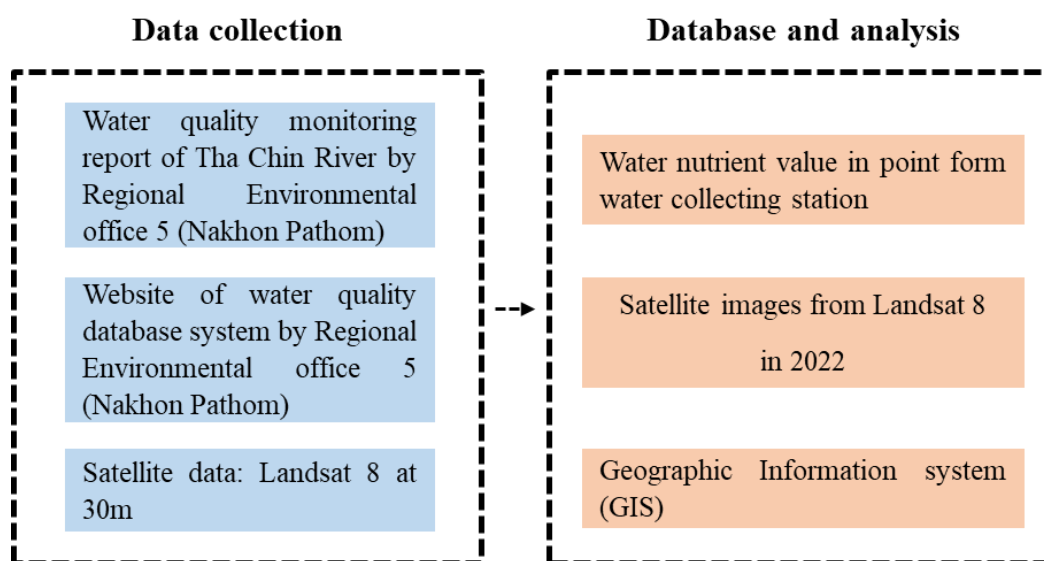
## 2.3 Satellite Image

Selecting a time period and wavelengths for collecting image data in 2022 allowed the satellite images from Landsat 8 satellite image data at 30 meters to be processed for categorization in this study. Images were chosen from satellites during clear and cloudless atmospheric conditions.

### 3. Methods

#### 3.1 Satellite Image Pre-Processing

For the purpose of analyzing the water hyacinth cover in the lower Tha Chin River in 2022, this study will examine secondary data, data including water quality data from Regional Environmental Office 5 (Nakhon Pathom), and spatial data from satellite images of Landsat 8 at 30 m. Normalized Difference Vegetation Index (NDVI) and Inverse Kriging Interpolation techniques were used in the analysis of the data, utilizing geographic information systems, as presented in Figure 2



**Figure 2.** The methodology utilized in this study to map the lower Tha Chin River and the relationship between nutrient and water hyacinth invasion. (Environmental Office 5)

The atmospheric conditions and viewing angles of the photos taken at various times fluctuate. Using an algorithm from Landsat 8, the Dark Object Subtraction adjustment was applied to make these temporal images spectrally similar to one another. After completing the aforementioned procedures, create NDVI images were generated using the Landsat 8 images taken in 2022 using the following equation 1.

$$NDVI = \frac{\rho_{NIR} - \rho_{RED}}{\rho_{NIR} + \rho_{RED}} \quad (1)$$

In this case,  $\rho$  represents the surface reflectance values for the red (R) and near infrared (NIR) spectral bands.

The Vegetation Index is a valuable tool for tracking changes in the amount of vegetation and the environmental conditions in the research region. It is calculated by taking the wavelengths associated with vegetation and assigning them a proportionality. The Normalized Difference Vegetation Index (NDVI), which is found by derived from the prevalent technique of determining the vegetation index, has a value between -1 and 1 for results interpretation, as indicated in Table 1.

Table 1. Appropriate ranges of the Normalized Difference Vegetation Index (NDVI) for the vegetation cover.

NDVI value	Vegetation class
-1.00 – 0.00	No Vegetation
0.01 – 0.30	Slightly density
0.31 – 0.60	Moderately density
0.61 – 1.00	Highly density

#### 4. Result and Discussion

##### 4.1 Water hyacinth Classification

In Table 1, the threshold values for each parameter were established. ArcGIS, the spatial analyst tool and the Reclassify tool were used to create the spatial maps. It was found that the areas with moderately density range are oceanic provinces (TC04 and TC07). These areas present intensive factories and agriculture which caused wastewater discharge as presented in Figure 3. Another factor of contributing is temperature in a tropical climate which 26.7°C is suitable for the growth of water hyacinth. Additionally, other conditions are accelerating the growth such as nutrients from wastewater sources in different places and the salinity of water sources. An excessive water hyacinth problem obstructs waterway traffic, causing small, man-powered vessels to be unable to pass through, disrupting traffic.

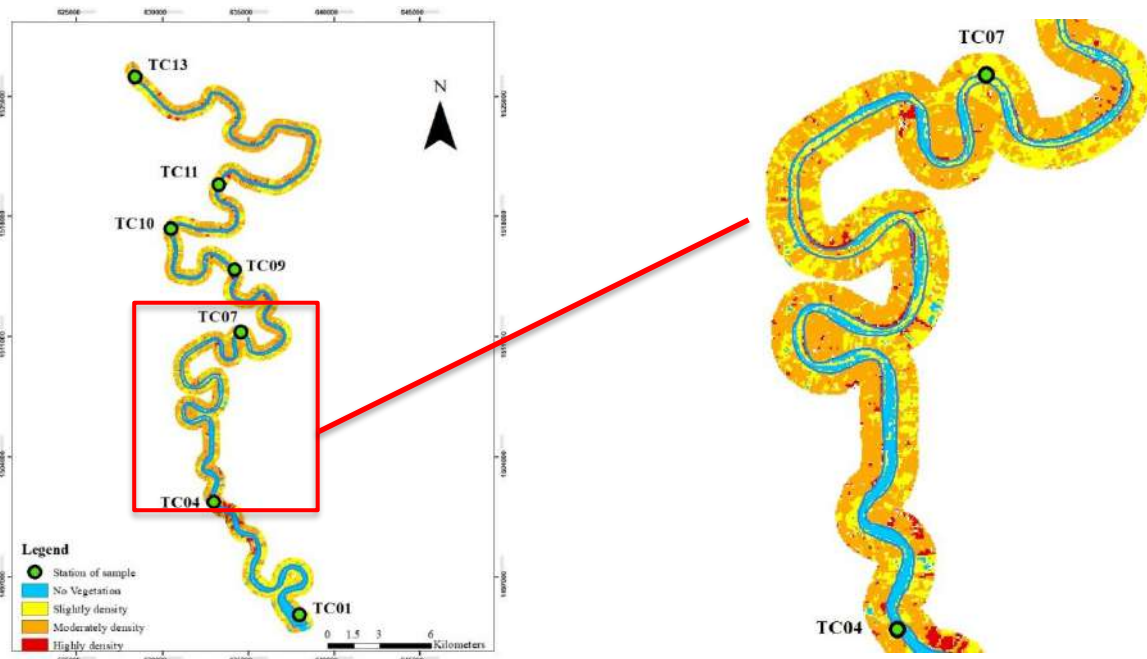
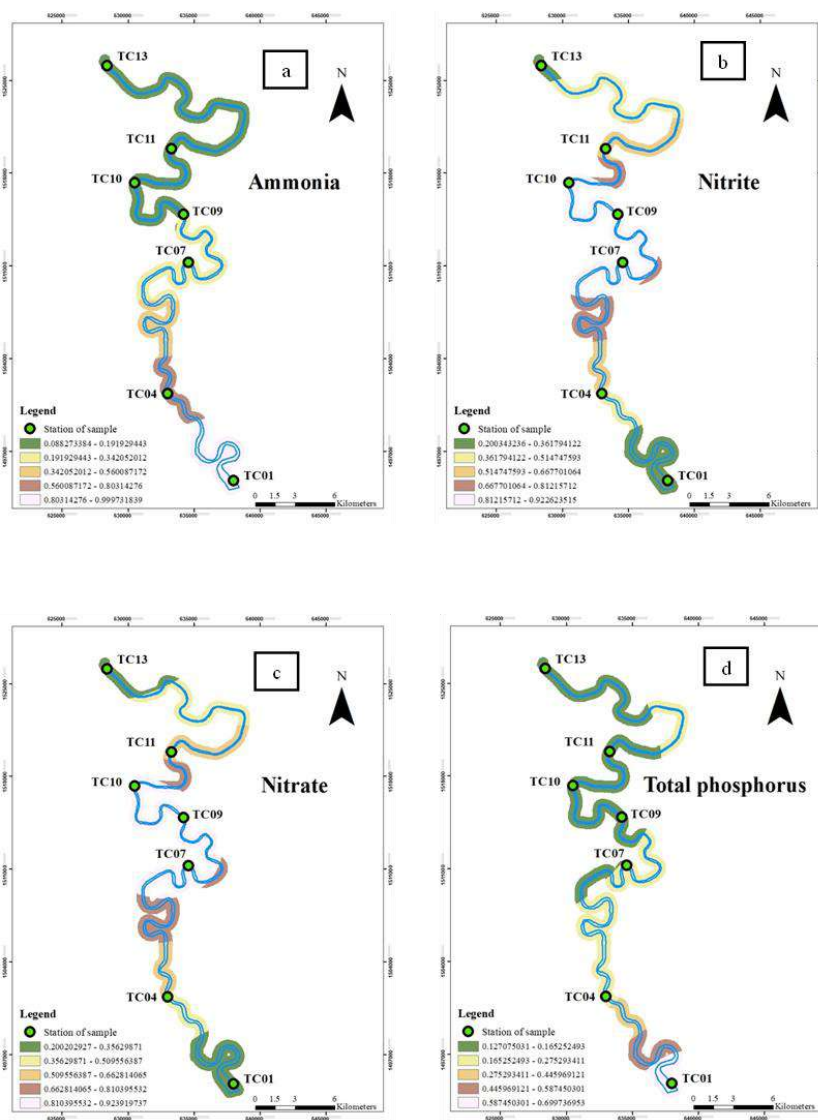


Figure 3. Map of invasion the water hyacinth in the Tha Chin River.

## 4.2 Nutrients parameter threshold

In this examination of the water hyacinth invasion of the Tha Chin River during in 2022, four water quality parameters were assessed. Interpolated data on the spatiotemporal distribution of selected parameters is shown in Figure 4.



**Figure 4.** Spatial variability of Ammonia (a), Nitrate (b), Nitrite (c), total phosphorus (d) Tha Chin River 2022

Analyzing the relationship between water hyacinth categorization and nutritional parameters, it was discovered that Figure 4 (a, c) and the region between TC07 and TC04 which are shown in the findings (Figure 3) are associated; it is a crucial nutrient for the river's water hyacinth development. Phosphorus can reach the river by runoff from agricultural and industrial areas as dissolved or particulate matter. Waves and wind have the ability to reanimate and dissolve the particle form. Wind and waves have the ability to re-suspend and re-solve the

particle form [9]. This might be the result of the basin's heavy use of ammonia fertilizer, which is then transported to the river by subbasin runoff.

The areas where high-water hyacinth coverage was the areas with high nutrient concentrations. It was also found that there were similar variations. Therefore, this reaffirmed time for the eradication of water hyacinth in water sources. Which can predict the trend of full water hyacinth coverage in water sources.

## 5. Conclusions

Nutrients as ammonia, nitrite, nitrate and phosphorus were the main factors for the relationship between nutritional components and water hyacinth invasion in the lower Tha Chin River. The results show that the area of high-water hyacinth coverage presented in the area of high nutrients concentrations. The capturing during period of time could be used for the planning of the eradication of water hyacinth. The controls of nutrients from sources and non-points sources are also very important for the control of water hyacinth invasion.

## References

- [1] Boonkrue, E. (2016). Phytoremedistion of zinc oxide nanoparticles by water hyacinth Chulalongkorn University.
- [2] Nitiset, S. (2020). *Study on Properties of Insulation Board made from Water Hyacinth* Kasetsart University.
- [3] Planning, D. o. P. W. a. T. C. (2021). *The Department of Public Works and Town & Country Planning accelerates the removal of water hyacinths in the Tha Chin River prepare for the flood season.* <https://www.thaipost.net/main/detail/101587>
- [4] Pongsak Noophan, R. C. (2014). *Effects of Nitrogen and Phosphorus on Eutrophication in Water Bodies and Nitrogen and Phosphorus Removal* (Publication Number 88)
- [5] Tirapitayanon, W. (2013). Effects of phosphorus on the environment *The Department of Science Service*, 1-3.
- [6] Zhang, T. (2019). *Phosphorus - Recovery and Recycling.* <https://doi.org/10.5772/intechopen.74920>
- [7] Ruuhijärvi, J., Rask, M., Vesala, S., Westermarck, A., Olin, M., Keskitalo, J., & Lehtovaara, A. (2010). Recovery of the fish community and changes in the lower trophic levels in a eutrophic lake after a winter kill of fish. *Hydrobiologia*, 646(1), 145-158. <https://doi.org/10.1007/s10750-010-0186-y>
- [8] (PCD), P. C. D. (2005, 6.21.2021). *Intergrated Control and Utilization of Water Hyacinth in Chachengsao Province.* <http://ptech.pcd.go.th/pcd/document/006090/006090.pdf>
- [9] Hupfer, M. G., R.; Giovanoli, R. (1995). Transformation of phosphorus species in settling seston and during early sediment diagenesis. *Aquatic Sciences* 57, 305-324.

## Predictive model for the fatigue life of a low-cost leaf cup mold

Somsak Limwongsakorn<sup>1</sup>, Hanphon Mitwong<sup>1,\*</sup>, and Wasawat Nakkiew<sup>2</sup>

<sup>1</sup> Department of Industrial Technology, Faculty of Science and Technology, Phuket Rajabhat University, Muang, Phuket 83000, Thailand

<sup>2</sup> Department of Industrial Engineering, Faculty of Engineering, Chiang Mai University, Muang, Chiang Mai 50200, Thailand

E-mail: \*Corresponding author ; mhanphon@pkru.ac.th

### Abstract

Natural, environmental and health conservation have recently been a driving trend in using natural materials for foodware, such as teak and banana leaves, instead of plastic and foams. But cup forming machine is generally expensive primarily because of mold price. This research therefore proposes a design for cup forming machine made of natural leaves, and on that basis, predicts useful lifetime of the associated low-cost molds. The design of the machine that has the capacity to form foodware by using natural leaves with diameter of 200 mm, will have the depth of 450 mm. From the experiment, it is found that the optimal factor conditions for the forming process can be achieved by using heat at 120°C for 150 seconds. In this setting, the average cost of each banana-leaf cup is estimated at 0.35 Baht, starch water weighing 10 grams (g), where estimate of cost recovery is 52 days. If applying static finite element analysis (FEA) by using mold made of stainless steels (SUS 304) weighing 360 g, fatigue damage based on thermodynamic calculation (by using software ANSYS in the prediction of fatigue life cycles) shows that it requires forces of 10-kN in order to form cups at 120°C. On this premise, there will be residual stress at the maximum level of 284 MPa on each side of the holes at the bottom of the cup, but also residual heat in the process at the maximum temperature of 84.58°C. The fatigue life prediction of the mold is estimated at 36 million cycles.

**Keywords:** Cup-formation machine; Natural-leaf cups; Fatigue life; Thermal fatigue

### 1. Introduction

Natural, environmental and health conservation plays an important role in today's life, particularly from perspective of foodware and related behavioral choices [1]. That said, choices of foodware based on natural materials has become more prevalent in local markets, especially as substitutes of plastic and foam materials, which have consequences in terms of health and well-being [2]. But across Andaman provinces in Thailand such as Phuket, Krabi, Ranong, Phang-Nga, and Trang, there exist natural alternatives such as vattayila, teak, and palm, but also almond and banana leaves that can be used as raw materials for foodware products. Such idea has indeed been widely adopted across local and regional communities considering an attractive lower-cost position that also reinforces sustainability narrative [3], especially as alternative choices for plates, cups, and bowls that all can practically be manufactured in a one-step (forming) approach [4]. However, compression molding machine is generally expensive, with price estimate of not less than 80,000 Baht each [5], primarily because of the molding and heating coils that are generally considered as critically important for the machine.

Furthermore, it is necessary to find a new design approach that fulfills engineering prerequisite while also making economic sense, for example, by using molds and SUS 304 stainless steels. For this purpose, computer-aided design (CAD) has been adopted, primarily by



using finite element analysis (FEA) [6] and simulation software ANSYS work bench [7], where the latter has been applied to the prediction of useful lifetime, especially for the components that are consistently exposed to heat, therefore most vulnerable over a long run [8]. Indeed, this study is dedicated not just to the engineering but also to the economics, such as in the sense of cost and cost recovery with the analysis that helps address such baseline [9]. Implications on the premise of the latter are wide-ranging, particularly from perspective of continual improvement process with capability and capacity to innovate on the grassroots level, but also in application of low-cost technologies that render attractive cost position both in terms of capital expenditure and operational costs. The latter is unequivocally an emphasis of such design, considering advanced capability on the premise of predictive maintenance but also total preventive maintenance system (TPM) that altogether makes sense of sustainable development in one joint narrative [10].

## 2. The objectives of this research

In order to design cup-forming machine and to predict associated useful lifetime of low-cost molds.

**Table 1** The material properties for SUS 304 stainless steel base and weld material [6].

T (°C)	C <sub>p</sub> (Jkg <sup>-1</sup> , °C)	λ (Wm <sup>-1</sup> , °C)	E (×10 <sup>11</sup> Pa)	ν	σ <sub>y</sub> base (MPa)	σ <sub>y</sub> weld (MPa)	E <sub>T</sub> /E	α (×10 <sup>-6</sup> °C <sup>-1</sup> )
20	442	15.0	2.0	0.278	230	460	0.014	19
200	515	17.5	1.85	0.288	184	367	0.014	19
400	563	20.0	1.70	0.298	132	264	0.014	19
600	581	22.5	1.53	0.313	105	209	0.014	19
800	609	25.5	1.35	0.327	77	154	0.014	19
1000	631	28.3	0.96	0.342	50	50	1×10 <sup>-4</sup>	19
1200	654	31.1	0.50	0.350	10	10	1×10 <sup>-4</sup>	19
1340	669	33.1	0.10	0.351	10	10	1×10 <sup>-4</sup>	19
1390	675	66.2	0.10	0.353	10	10	1×10 <sup>-4</sup>	19
2000	675	66.2	0.10	0.357	10	10	1×10 <sup>-4</sup>	19

T = temperature; ν = Poisson's constant; C<sub>p</sub> = specific heat; σ<sub>y</sub> = yield stress; λ = conductivity; E<sub>T</sub> = hardening modulus; E = elastic modulus; α = mean coefficient of linear thermal expansion

## 3. Materials

A 35-kg machine for forming low-cost leaf-made cups is designed with dimensions 460×646×1,100 mm (width, length, height), as depicted in figure 5A. The model is made of SUS 304 stainless steel, consisting of three components for the upper mold, and five for the bottom one. Both molds are connected by one M12-screw according to the sketch in figure 5C. The critical part of the design applies static FEA particularly to the bottom mold, while assuming that there is downward stress (von Mises) of 10 kN to the mold with the assumption of residual stress at the maximal level of 206 MPa and safety factor at 15. The design further applies Taguchi Orthogonal Array L<sub>9</sub>3<sup>3</sup> in order to optimize signal-to-noise ratio by using MiniTab program. On this premise, it is found that the most appropriate pressuring timeframe is 150 s at 120°C, where the best quality can be achieved by using 10 g tapioca starch. The based on this design calculation, the best banana-leaf quality will cost 0.35 Baht/leaf, and the

breakeven point can be achieved within 52 production-days, if assuming achievable production throughput at 24 leaves/hour [11].

#### 4. Experiments

The fatigue-based analysis of material SUS 304 (see figure 1) exhibits the characteristics in terms of signal-to-noise ratio (S-N curve), where each component in the structure is affected by the applied load continuously and in cyclical manner. Even though the magnitude of exerted forces is less than the maximal tolerance level, the cumulative level of strain, called fatigue, generally cause over 80-90% of damage. In fact, fatigue consists of two stages, where it generally starts when intensity of strain causes crack initiation. If the situation persists, the cumulative impact of fatigue will cause crack propagation. In general, strength of fatigue will determine stress at one million cycles (1,000,000) as boundary condition that in turn defines the maximal number of time that forces that can still be applied without causing damages:

$$N_f = N_i + N_p \tag{1}$$

Where;

$N_f$  = The number of time under fatigue test.

$N_i$  = The number of time that will cause crack initiation.

$N_p$  = The number of times that will extend crack until the material is completely cracked.

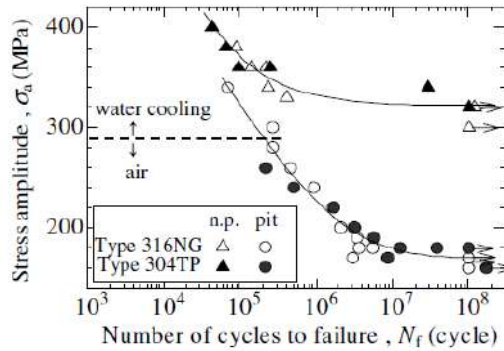


Fig. 1 The graph depicting residual stress of SUS 304 stainless steel [12].

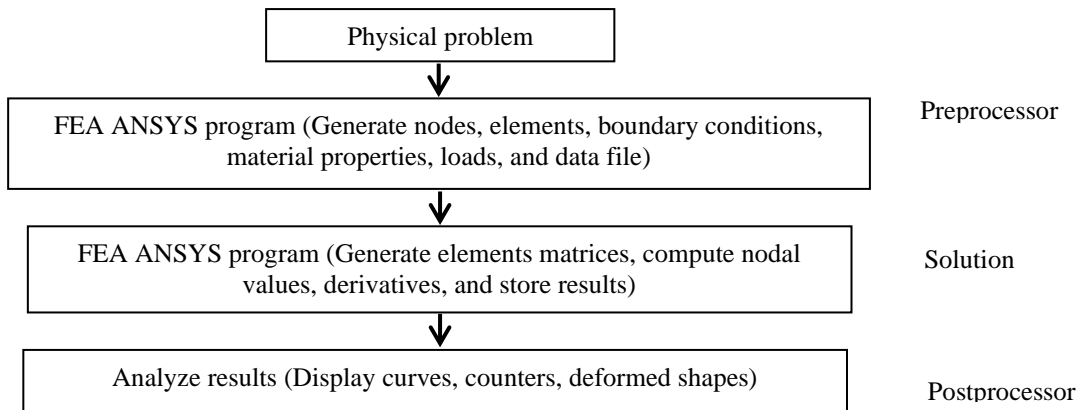


Fig. 2 The procedure for the analysis by using software ANSYS [13].

By using software ANSYS for FEA, the following steps must be fulfilled: 1) determining type of the analysis, 2) constructing the model, 3) defining types of elements, 4) locating the geometry to nodes and elements, 5) determining material properties and boundary conditions, 6) determining bolted connections and corresponding equations, 7) integration of elements, 8) correction parameters that cannot be allocated to nodes, and 9) interpretation of FEA by using software in three steps: pre-processing, problem-solving/solution-finding, and post-processing. In figure 3, there are four modules: “Transient thermal A” that requires property inputs and heat, “Transient thermal B” for determining cooling-down process, “Static structural C” for the analysis of residual stress, and “Static structural D” for fatigue analysis. After that, choose graphical representation of the Gerber mean stress correction for stress fatigue life analysis.



Fig. 3 ANSYS Work Bench schematic for solving for thermo-mechanical fatigue.

In principle, frequency (per time unit) will generally have less impact than effect of the (cumulative) number of times that the force has already been applied. This is an important premise of why the parameter “number of times” that the stress has been applied, plays a more important role than the stress/sec. That is, there will be another parameter call mean stress ( $\sigma_m$ ) that is defined as average size of the magnitude, regardless of how often such force has been/will be applied. In this sense, the definition of alternating stress shall play a critically important role, particularly with focus on the positioning of each specific stress parameter, that is, type 1 for distance and symmetry of stress being zero, type 2 for distance and symmetry of stress as non-zero, and type 3 for the case of fluctuating random strain.

#### 4.1. Variables applied in the test

The frequency is the number of rounds in the test per time unit, where hertz (Hz) is primarily used. The greater the value, the sooner the crack will occur. Stress amplitude is the amount of load applied to the test subject, which could imply either stress or strain that can be defined as [14];

$$\text{Stress Magnitude } (\sigma_a) = \frac{\text{Maximal Stress}(\sigma_{\max}) - \text{Minimal Stress } (\sigma_{\min})}{2} \quad (2)$$

Mean stress is an average value of the load exerted to the test material, which can be calculated as follows:

$$\text{Mean Stress } (\sigma_m) = \frac{\text{Maximal Stress } (\sigma_{\max}) + \text{Minimal Stress } (\sigma_{\min})}{2} \quad (3)$$

Description of load supply is characterization of the load, exerted to the test material, which is, in this case, tensile strength that can be calculated on the premise of: Stress ratio ;  $R = \frac{\sigma_{\min}}{\sigma_{\max}}$  and Amplitude ratio ;  $A = \frac{\sigma_a}{\sigma_m}$ .

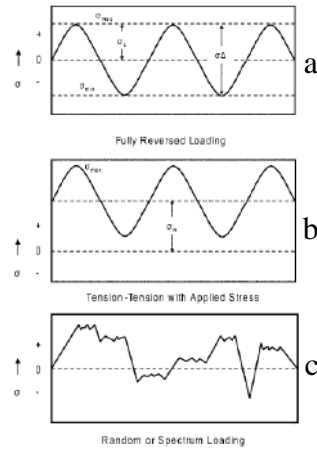


Fig. 4 Types of force frequency originated from fatigue [14].

## 4.2. Phenomenon of heat radiation

This experiment applies heating techniques by using electromagnetic induction coil, which is a method that can be applied to transfer heat from radiation. In this specific context, heat radiation refers to a process to which materials radiate electromagnetic energy that can absorb and transfer heat to other objects of similar types, all in the same heat transfer process. Mode of transfer as such will not require any specific medium, where net amount of heat radiation can be calculated by using Stefan Boltzmann's equation [15];

$$q = \varepsilon \sigma A_1 F_{12} (T_1^4 - T_2^4) \quad (4)$$

where  $q$  is the rate of heat transfer,  $\varepsilon$  being that of radiation from real objects, where the number shall lie between 0 and 1, and  $\sigma$  is Stefan Boltzmann's constant, which is approximately  $5.67 \times 10^{-8} \text{ W/m}^2 \cdot \text{K}^2$ ,  $A_1$  being the area of radiation surface 1 and  $F_{12}$  typological coefficients between radiation surface 1 and 2  $T_1$  absolute temperature on surface 1 and  $T_2$  that of surface 2.

## 4.3. Heat convection

Heat convection is defined as heat exchange as a result of temperature differences between surfaces of the solid and liquid materials. In this experiment, heat convection with water is considered as one applicable method, where such method in general can be explained by using Newton's convective heat transfer [15];

$$q'' = h(T_S - T_B) \quad (5)$$

where  $h$  is coefficient of convective heat transfer that transfers heat from temperature  $T_S$  from the surface of a solid material to the surrounding liquid counterpart at temperature  $T_B$ . In this context, the most important caveat of the aforementioned fatigue process, is the point at which fatigue kicks in, where in most cases such will depend on the geometry and the micro structure of the material, but also the type of stress being addressed by the analysis. That said, it is considered normal if the fracture starts at the highest point of the material geometry, whereas, on the other hand, the age of the fracture generally referable to the point to which the lowest point of the fatigue takes place.

#### 4.4. Mathematics thermodynamic fatigue

A great number of industrial composites are designed to work under a significant number of mechanical loads and heat, and thereby affecting the overall durability and lifetime. Such is indeed a major cause of failure, where forecast of such events with good precision will depend much on the methodology of how to respond to mechanical loads and heat with precision. To that end, the method to achieve high precision and seamless outcome as proposed by ANSYS therefore addresses the aforementioned challenge caused by thermodynamic fatigue by considering multiple inherent physical properties of the materials [7].

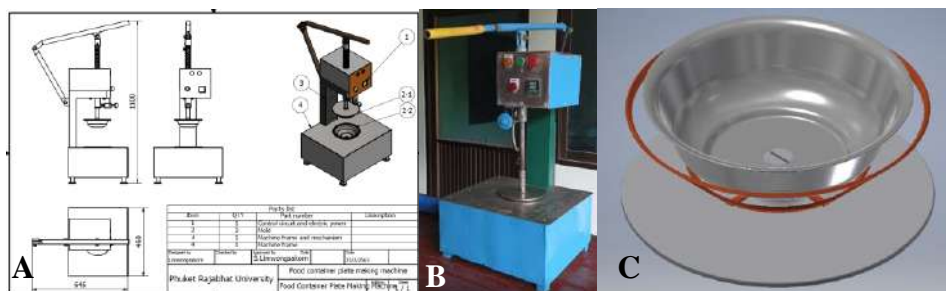


Fig. 5 The molding machine for low-cost cups.

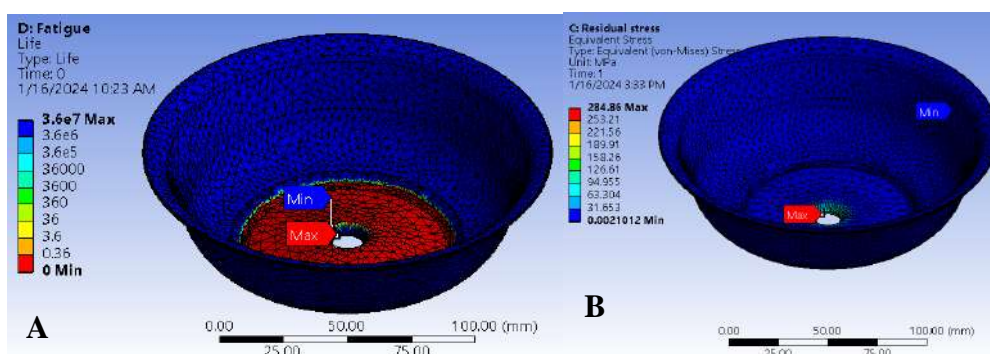


Fig. 6 (A) The foodware made of banana and (B) The teak leaves.

#### 5. The FEA Model

The design of the machine with objectives to form low-cost foodware made of natural leaves has been proposed with the following technical specification. A 35-kg machine has been successfully constructed, with the dimension of 460×646×1,110 mm, where the mold was built from SUS 304 stainless steel. The bottom mold weighs 360 g, with diameter of 160 mm, 3 mm-thickness and specific gravity at 8 g/cm<sup>2</sup>. According to figure 5, the total surface can be measured at 60,443 mm<sup>2</sup> with volume of 44,888 mm<sup>3</sup>, where the resulting leaf-made foodware has the diameter of 200 mm with 45 mm depth as shown in figure 6 [11]. In the design and modeling process, FEA method was applied, specifically by using ANSYS software in the simulation process by using parameter compressive-compression with applied stress. Furthermore, load ratio  $R = -1$  was applied, (see at figure 4b) where frequency of actual implementation was set at 3 minutes (with additional preparation at 3 minutes), and thereby exerting force of 10 kN at the support point, which is on the inner surface right in the middle of the foodware. Furthermore, static analysis with average grain size of the element was set at 3 mm, by using 3D Tetrahedral model with 111,078 nodes and 61,259 elements, where (von Mises) stress were exerted to the inner surface of cups with fixed plane at the bottom. In the experimental was used material properties at temperature 27°C such as Density=7.9 kg/dm<sup>3</sup>, Young's Modulus (E)=200 GPa, Poisson's coefficient ( $\nu$ )=0.278, Melting temperature=1,450 °C, Specific heat=442 J/kg.K, Thermal conductivity=15 W/m.K and the other properties on the

temperature range used in table 1. As a result, the maximum level of residual stress can be measured at 284 MPa from the side plane of the hold at the bottom of the cup according to figure 8, which indicates that the design can withstand loads at the anticipated level without falling apart. The designed mold can therefore be used in real-world setting, with advantages in terms of functionality, price attractiveness, and ease in handling. Furthermore, the modular design also helps facilitate self-maintenance, as long as heat applied in the forming process is set at 120°C or equivalent to 397 W/m<sup>2</sup> [16] which implies residual heat at the maximum temperature of 84.58°C and thereby substantiating predictive useful lifetime at 36 million cycles, according to figure 7.



**Fig. 7** The FEA of the mold design.

## 6. Conclusion

Development of low-cost foodware made of natural leaves has been proposed with focus on the design of a stainless-steel mold comprising 2 pieces of 360 g with 60,443 mm<sup>2</sup> surface area in total, which has been particularly optimized in order to achieve efficiency toward maximum useful lifetime. The FEA lies at heart of the aforementioned proposition, primarily by using predictive algorithm in the static analysis of the mold in the lower part (i.e., by optimizing useful lifetime on thermomechanical premise of the cumulative fatigue). In this setting (simulated by software program ANSYS), it was found that if applying 10-kN force, the maximum level of residual stress in the operational range would be 284 MPa (measurable from the side plane of the hold at the bottom of the cup), where value of such parameter at breakdown point was estimated at 540 MPa. Such is the main criteria in defining optimal operational zone that makes sense of functionality, affordability, and operability, simultaneously. On this premise, it should be emphasized that the mold is easily exchangeable therefore suitable for self-maintenance. In order to achieve that objective, however, the operational temperature should be targeted at 120°C as key premise (i.e., maximal residual heat at 84.58°C) of predictive useful lifetime at 36 million cycles. However, any operations beyond the targeted fatigue level should not exceed 1 million cycles in cumulative terms, if to win longevity perspective over the long run. It's similar to the type 304 TP line in the graph as shown in figure 1.

## 7. Acknowledgment

Authors would like to express gratitude to the research and development institute Phuket Rajabhat University that provides research funding for the year 2019 and Department of Industrial Engineering, Faculty of Engineering, Chiang Mai University for software ANSYS applied to the analysis of useful lifetime in this work.

## References

- [1] Jong, O.-K., Nasharidan, S. A., Rashid, A. H. A., Main, N. M., Mi, Y. T., Roslan, M. N., & Masrol, S. R. (2021). Factorial Analysis of Tensile Properties of Areca Leaf Sheath (ALS) Subjected to Flattening. *International Journal of Integrated Engineering*, 13(2), 82–89.
- [2] “Pro-environmental products: marketing influence on consumer purchase decision - ProQuest.” Accessed: Jan. 13, 2024. [Online]. Available: <https://www.proquest.com/docview/220137142?parentSessionId=R8N%2FD2LbkBiDnrayP0wzqr1e5Q0TAne6VqF%2FahDgYC0%3D&sourcetype=Scholarly%20Journals>
- [3] Albert C.J, Anusha P, & Shemeema U.S. (2009). *Development of technology for alternative material to areca leaf plates. kelappaji college of agricultural engineering and technology.*
- [4] Mohanty, D. P., Udupa, A., Anilchandra, A. R., Mann, J. B., & Chandrasekar, S. (2021). A study of formability of palm leaf materials using Limiting Dome Height testing. *MRS Communications*, 11(5), 662–668. <https://doi.org/10.1557/s43579-021-00094-0>
- [5] สยามไดคัท ขายเครื่องปั๊มไดคัท เครื่องปั๊มฟอยล์ เครื่องปั๊มไฮโดรลิก. (n.d.). Retrieved January 13, 2024, from <https://www.siamdiecut.com/>
- [6] Limwongsakorn, S., Nakkiew, W., & Baisukhan, A. (2016). Finite Element Analysis Model of Corrosion Fatigue for TIG Welding Workpiece. *Key Engineering Materials*, 707, 154–158. <https://doi.org/10.4028/www.scientific.net/KEM.707.154>
- [7] “thermo-mechanical-fatigue-wp.pdf.” Accessed: Jan. 15, 2024. [Online]. Available: <https://www.ansys.com/content/dam/product/structures/mechanical/thermo-mechanical-fatigue-wp.pdf>
- [8] Limwongsakorn, S., Nakkiew, W., & Baisukhan, A. (2015). Residual Stress Predictive Model of TIG Welding Process Using Finite Element Analysis. *Applied Mechanics and Materials*, 799–800, 428–433. <https://doi.org/10.4028/www.scientific.net/AMM.799-800.428>
- [9] “Design and analysis of semiautomatic paper cum arecanut plate making machine.” Accessed: Jan. 13, 2024. [Online]. Available: <https://www.irjet.net/archives/V4/i5/IRJET-V4I5853.pdf>
- [10] Sudarshan Rao, K., Pai, S., Chandan Nelli, M. K., Ambalpady, P., & Prathviraj. (2023). Design and development of semi-automatic leaf plate molding machine. *Materials Today: Proceedings*, S221478532304556X. <https://doi.org/10.1016/j.matpr.2023.08.286>
- [11] Limwongsakorn, S., Mitwong, M., & Nakkiew, W. (2566). Design the banana leaf bowl forming machine a low price. *The 8th National Conference on Science and Technology 2023: NSCIC2023 and the 1st International Conference on Science and Technology 2023: INSCIC2023*, (1), 802–810.
- [12] Masaki, K., Ochi, Y., & Matsumura, T. (2006). Small crack property of austenitic stainless steel with artificial corrosion pit in long life regime of fatigue. *International Journal of Fatigue*, 28(11), 1603–1610. <https://doi.org/10.1016/j.ijfatigue.2005.06.055>
- [13] Ansys Workbench Simulation Integration Platform. (n.d.). Retrieved January 13, 2024, from <https://www.ansys.com/products/ansys-workbench>
- [14] *Elements of Metallurgy and Engineering Alloys*. (2008). ASM International. <https://doi.org/10.31399/asm.tb.emea.9781627082518>
- [15] Ding, J. (2018). The Numerical Simulation of Thermal Fatigue Crack Propagation on Mold Steel: In *Proceedings of the 2nd International Conference on Intelligent Manufacturing and Materials* (pp. 211–217). Guangzhou, China: SCITEPRESS - Science and Technology Publications. <https://doi.org/10.5220/0007529202110217>
- [16] Mehta, N., & Shukla, D. (2015). *Thermal Fatigue Analysis of Induction Furnace Wall of Zirconia.*

## Study on Coefficient of Performance Model for Industrial Refrigeration System

**Natamorn Kamlue, Ratchanon Reaproi, Suphasan Tatami, and Surat Areerat\***

Department of Chemical Engineering, School of Engineering, King Mongkut's Institute of Technology  
Ladkrabang, Latkrabang, Bangkok, 10520, Thailand

E-mail: Surat.ar@kmitl.ac.th

### Abstract

The aim of this research was to study the composition of mixed refrigerants, specifically R32/R290, R32/1270, R134a/R290, and R134a/R1270, their impact on the coefficient of performance (COP) and global warming potential (GWP) of refrigerants. The objective was to improve the efficiency of refrigerants for industrial applications by achieving high COP and appropriate GWP. To achieve this goal, we used Aspen Plus to predict the properties of blending refrigerants. We then used the obtained data in the NIST refrigeration system simulation program (Cycle\_D-HX), which showed that the type of mixed refrigerant, composition, and behavior of the refrigerant in an azeotropic mixture affected the COP significantly. The wide phase difference reduced the COP significantly. Moreover, the composition affected the GWP. The composition of hydrocarbon in blending refrigerants that met the Montreal Protocol Standard were 0.8, 0.8, 0.9 and 0.9 for R32/R290, R32/1270, R134a/R290, and R134a/R1270, respectively.

**Keywords:** Binary refrigerant mixtures, Azeotropic, Coefficient of performance (COP)

### 1. Introduction

Nowadays, the electricity consumption of the refrigeration and air conditioning technologies estimated to be 50% in Thailand, without effective intervention, the growing energy demand will be double by 2030 [1]. It led to the development of refrigeration technology and through the negotiations under the Montreal Protocol on Substances that Deplete the Ozone Layer and limiting of GWP at 150, there has been research on new alternative refrigerant with zero (or very low) ODP (Ozone Depletion Potential), low GWP (Global Warming Potential) and high energy efficiency [2,3]. The hydrocarbon (HC) refrigerants are a group of refrigerants with very low GWP, but they have flammability properties, which limits their use [4]. Coulbourne and Espersen [5] conducted a quantitative risk assessment, finding ignition frequencies for ice cream cabinets using R290 ranged from  $2 \times 10^{-13}$  to approximately  $1 \times 10^{-8}$  per year, contrasting with the standard household refrigerator fire frequency of  $1 \times 10^{-5}$  per year. This demonstrates that the possibility of explosions or fires is minimal, and the utilization is feasible with the assurance of safe handling of HC refrigerants, achievable by implementing rules, regulations, and standards to minimize charges and adopt passive and active safety measures [4].

This research aims to investigate the blending ratios of hydrofluorocarbon (HFC) refrigerants with high GWP but high cooling efficiency, such as R32 and R134a, with HC refrigerants, which have low GWP, such as R290 and R1270 to create alternative refrigerants with low Ozone Depletion Potential (ODP) and Global Warming Potential (GWP), as well as



high Coefficient of Performance (COP) through simulation. The results obtained from the simulation will be compared to experimental data using the R410a air-conditioning system.

Table 1. Properties of refrigerants [6].

Refrigerant	R-134A	R-32	R-290	R-134A
Name	1,1,1,2-Tetrafluoroethane	Difluoro methane	Propane	Propylene
Formular	CH <sub>2</sub> FCF <sub>3</sub>	CH <sub>2</sub> F <sub>2</sub>	C <sub>3</sub> H <sub>8</sub>	C <sub>3</sub> H <sub>6</sub>
GWP	1430	675	3	2
ODP	0	0	0	0
Latent heat (J/mol)	218.97	387.07	425.07	438.66
Boiling point (°C)	-26.55	-51.60	-42.10	-47.60
Critical temperature (°C)	101.15	78.45	96.68	92.42
Critical pressure (bar)	40.64	57.54	42.47	46.65
Close flash temperature (°C)	24.98	-98.28	-96.11	-98.19
Flash temperature (°C)	-84.40	-	-	165
Auto ignition temperature (°C)	-	-	449.85	455
Safety Group	A1	A2	A3	A3

## 2. Materials and Methods

### 2.1. Vapor Compression System [7]

The vapor compression system is the most widely used system for refrigerators, air conditioning and heat pump system consist of four processes: 1) Isentropic compression process, 2) Condensation process, 3) Expansion process at constant enthalpy, and 4) Evaporation process.

#### 2.1.1. Coefficient of performance (COP)

The coefficient of performance is a measure that indicates the efficiency of heat transfer compared to the amount of electrical energy consumed.

$$COP = \frac{Q_L}{W_{comp,in}} \quad (1)$$

Where  $COP$  is the coefficient of performance of the vapor compression refrigeration system.  $Q_L$  is the heat absorption capacity of the refrigerant (kJ/kg).  $W_{comp,in}$  is the energy input into the compressor (kJ/kg).

#### 2.1.2. Compressor

The compression device compresses the refrigerant gas from a low-pressure state to a higher-pressure state. The isentropic compression process is described by the following equation:

$$W_{comp,in} = \frac{kR(T_2 - T_1)}{k-1} = \frac{kRT_1}{k-1} \left[ \left( \frac{P_2}{P_1} \right)^{\frac{k-1}{k}} - 1 \right] \quad (2)$$

Where  $k$  is the ratio of specific heat at constant pressure to specific heat at constant volume.  $R$  is the gas constant (kJ/kg·K).  $T_1$ ,  $T_2$  are the temperatures of the refrigerant entering and leaving the compressor (K).  $P_1$ ,  $P_2$  are the pressures of the refrigerant entering and leaving the compressor (bar).

### 2.1.3. Condenser

The condenser, or heat exchanger, works by converting the refrigerant from a high-pressure, high-temperature gas state to a condensed liquid state by releasing heat from the refrigerant. The equation describing this process is as following equation:

$$\dot{Q}_H = \dot{m}(h_2 - h_3) \quad (3)$$

Where  $\dot{Q}_H$  is the rate of heat release from the refrigerant (kJ/s).  $\dot{m}$  is the mass flow rate of the refrigerant (kg/s).  $h_2$  is the specific enthalpy at saturated vapor state (kJ/kg).  $h_3$  is the specific enthalpy at the saturated liquid state (kJ/kg).

### 2.1.4. Throttling valve

This is a type of pressure-reducing device that reduces pressure without requiring any work input. During the process, it is controlled by a property known as the 'Joule-Thomson coefficient,' which ensures that the enthalpy remain constant, as following equation:

$$h_4 \cong h_3 \text{ (throttling)} \quad (4)$$

Where  $h_4$  is the specific enthalpy of the refrigerant exiting the throttling valve (kJ/kg).

### 2.1.5. Evaporator

The function of evaporator is to absorb heat from areas requiring cooling, causing the refrigerant to change from liquid to vapor. The heat absorption capacity varies among different refrigerants based on their latent heat during vaporization., resulting in a decrease in temperature, as illustrated by the equation:

$$\dot{Q}_L = \dot{m}(h_1 - h_4) \quad (5)$$

Where  $\dot{Q}_L$  is the rate of heat absorption by the refrigerant (kJ/s).  $h_1$  is the specific enthalpy of the refrigerant at saturated vapor state (kJ/kg).

## 2.2. Research Methodology

To align with the objectives of this study, the research is divided into two main parts:

1. Investigation of the properties of new refrigerants developed through continuous research and development by blending refrigerants together.
2. Evaluation of the performance of vapor compression refrigeration systems when using blended refrigerants.

### 3. Results and Discussion

#### 3.1. The characteristics of the blended refrigerants

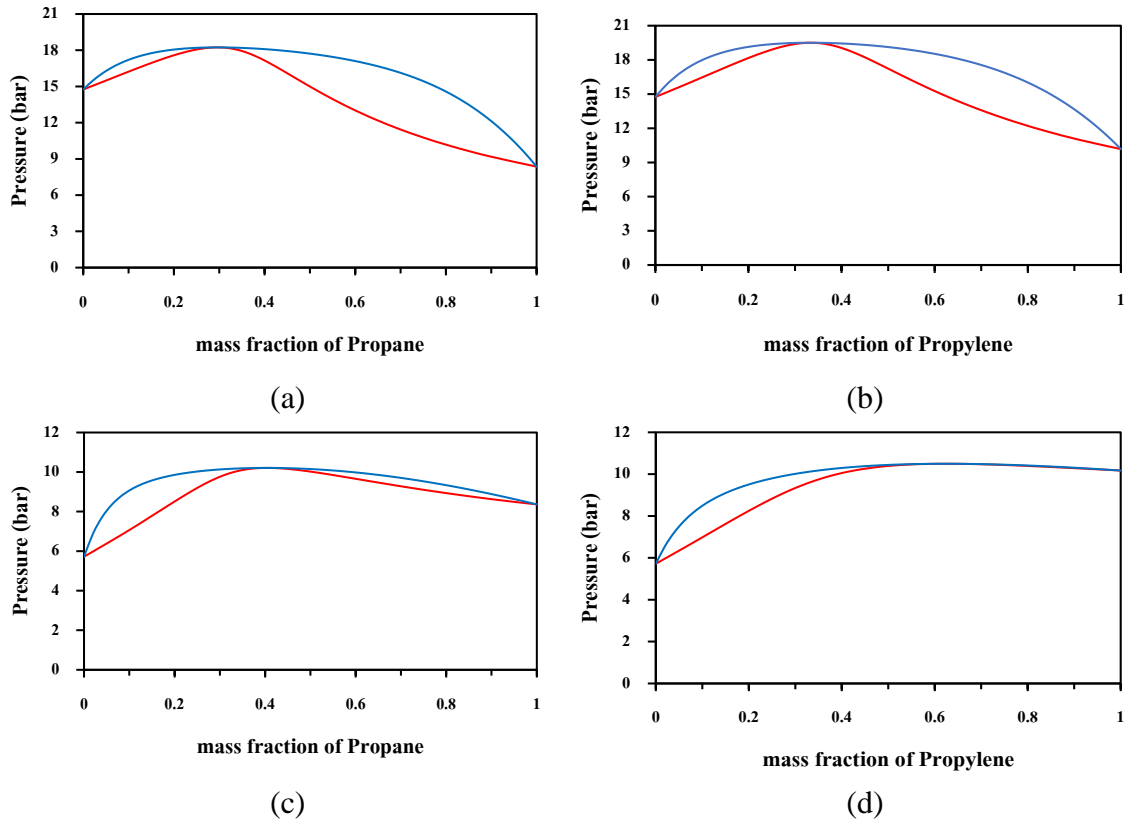
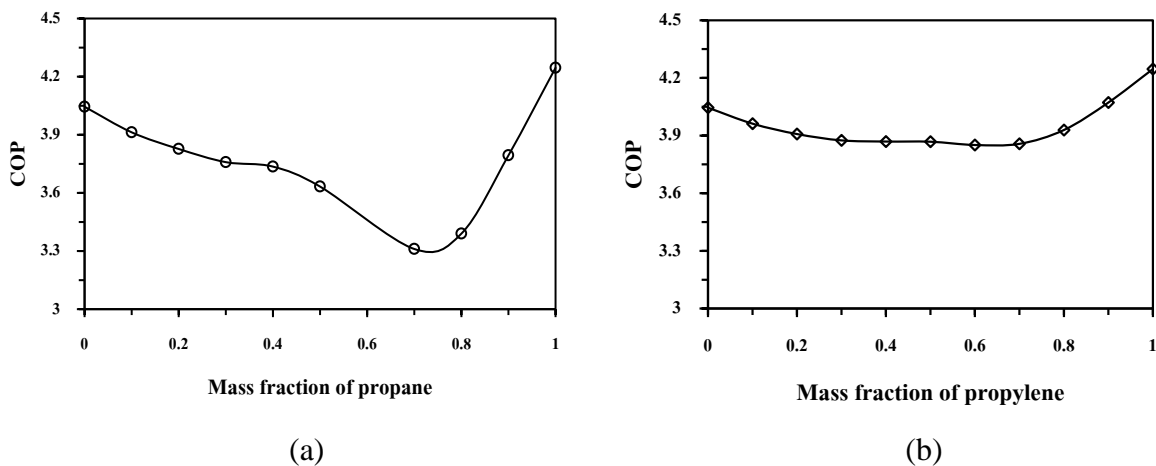


Fig. 3 P-xy diagram of: (a) R32/R290, (b) R32/R1270, (c) R134A/R290 and (d) R134A/R1270

It is possible to analyze the following results.



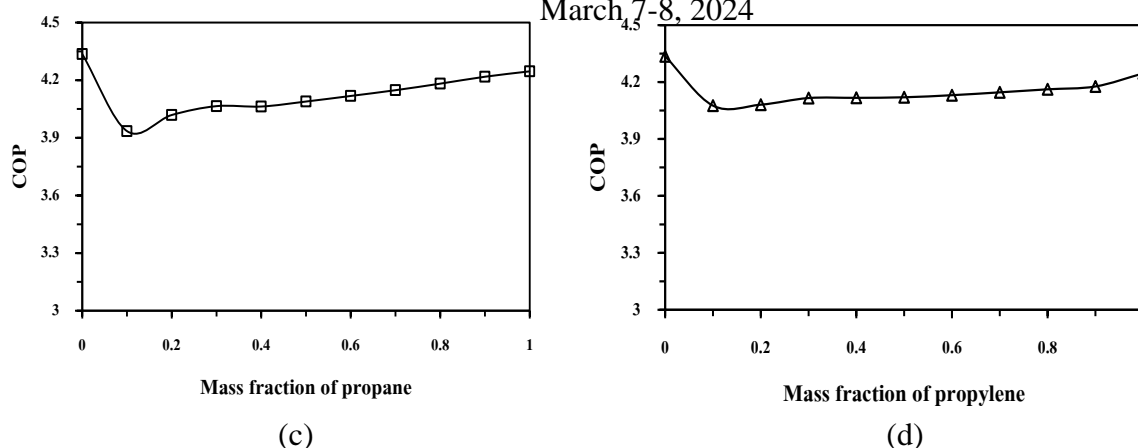


Fig. 4 Variation of COP with changing proportions of: (a) R32/R290, (b) R32/R1270, (c) R134A/R290 and (d) R134A/R1270

### 3.2. The blended refrigerant of R32/R290

When the proportion of the blended refrigerant changes, it is found that the COP of the refrigeration system decreases as the proportion of R290 increases, as shown in Fig. 4a., reaching a maximum decrease at a mass ratio of R290 around 0.7-0.75. However, the COP increases as the mass ratio of R290 reaches 0.8 and beyond. Comparing this with the phase diagram of R32/R290, it is observed that as the distance between phases increases, resulting in a significant decrease in COP.

### 3.3. The blended refrigerant of R32/R1270

It is found that although the blends refrigerant R32/R1270 and R32/R290 have similar phase diagrams, there are differences in the effect of mass ratio on the COP between them, as shown in Fig. 4b. It can be observed that the COP of the system decreases when the proportion of the R1270 increases until the proportion reaches 0.7-0.75 by mass, and the COP increases when the proportion reaches 0.8 by mass of R1270 and beyond.

### 3.4. The blended refrigerant of R134A/R290

When considering Fig. 4c, it can be observed that the COP decreases as the mass proportion of R290 increases up to 0.1. However, the COP trend increases starting from the proportion of 0.1. Comparing with the phase diagram, it is found that at the same proportion, the COP decreases significantly as the distance between phases increases.

### 3.5. The blended refrigerant of R134A/R1270

When considering Fig. 4d, it can be observed that it has similar characteristics to the R134a/R290 pair. Initially, when the mixing ratio of R1270 is at 0.1, the COP is at its lowest. As the proportion of R1270 increases, the COP increases. Compared with the phase diagram, it exhibits similar behavior to the R134a/R290 refrigerant mixture.

### 3.6. Comparing blended refrigerant

From Fig. 5, which compares the four types of mixed refrigerants R32/R290, R32/R1270, R134a/R290, and R134a/R1270, it can be observed that the type of refrigerant, the mixing ratio, and the behavior between phases of the mixed refrigerants affect the COP in the system. If the difference in phase range between the refrigerants is wide, it will result in a decrease of COP. Specifically, R32/R290 refrigerant shows a clearer trend of COP reduction compared to other types. This is because R32/R290 refrigerant has a wider phase difference range, leading to significant changes in COP. On the other hand, R32/R1270 refrigerant shows only slight changes in COP. As for R134a/R290 and R134a/R1270 refrigerants, they exhibit similar behavior with narrow phase difference ranges and wide ranges of azeotropic behavior. Consequently, when the mixing ratio of refrigerants changes, they can maintain the azeotropic state effectively.

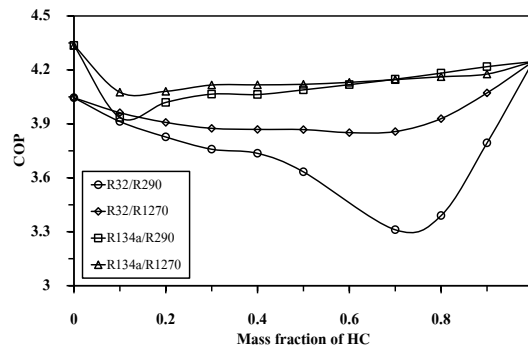


Fig. 5 The effect of mixing ratio of hydrocarbon of mixed refrigerants to COP

Furthermore, when comparing the mixing ratios of mixed refrigerants with the GWP values, as shown in Fig. 6, it is found that the mass ratios of hydrocarbons providing GWP values according to the criteria of the Montreal Protocol agreement for mixed refrigerants R32/R290, R32/R1270, R134a/R290, and R134a/R1270 are 0.8, 0.8, 0.9, and 0.9, respectively.

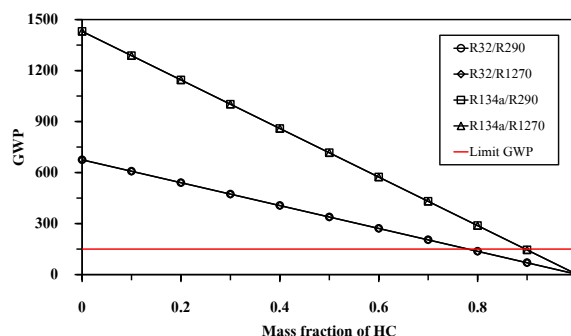


Fig. 6 The effect of mixing ratios of hydrocarbon of mixed refrigerants to GWP

### 3.7. The study and comparison of vapor compression refrigeration systems from modeling and experimental using R410A refrigerant.

From the study of the vapor compression refrigeration system based on experimental tests using R410A refrigerant, it was found that the operating time of the refrigeration system significantly affects the COP. As shown in Fig. 7, it is observed that from 12:00 AM to 6:00

AM, the COP remains constant at around 3.61. However, from 7:00 AM to 1:00 PM, the COP decreases with a minimum value of 2.96. Subsequently, from 2:00 PM to 12:00 AM, the COP tends to approach the value of 3.61.

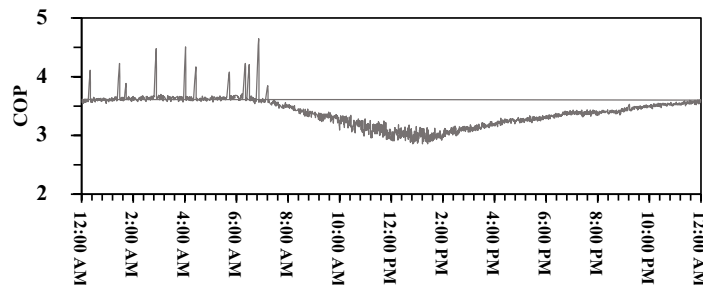


Fig. 7: Variation of COP over Time

And from the comparison of the refrigeration system using R410A refrigerant (R32/R125; 50/50) between the model and the experiment, as shown in Fig. 8, it is found that the COP from the model is 3.67, while from the experiment, during nighttime, the COP is at 3.61, resulting in a percentage difference of 0.11%. During daytime, the COP is at 2.96, resulting in a percentage difference of 18.24%.

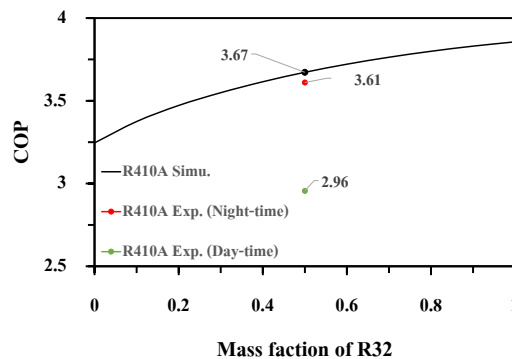


Fig. 8 Comparison of COP using R410A refrigerant between model and experiment.

#### 4. Conclusion

The type of refrigerant blend, the blending ratio, and the zeotropic behavior of the refrigerant affect the COP. When the difference between phases is high, it significantly reduces the COP. Additionally, the blending ratio also affects the GWP. The blending ratios of hydrocarbon refrigerant blends that meet the standards of the Montreal Protocol at 150 for pairs like R32/R290, R32/1270, R134a/R290, and R134a/R1270 are 0.8, 0.8, 0.9, and 0.9, respectively. Even though azeotropic behavior does not significantly affect COP, using refrigerants with azeotropic properties ensures that if a leak occurs from the system, it does not change the composition of the remaining refrigerant.

From the study and comparison of the compression refrigeration system using R410A refrigerant between the model and experimental results, it was found that the results obtained from the simulation closely to the experiment during nighttime with a COP difference of 0.11%, whereas during daytime, the difference of COP rise to 18.24%. This suggests that the operating time significantly affects the COP value, especially considering Thailand is a tropical country, which leads to high temperatures during the daytime. This makes it difficult for refrigerants to condense efficiently, resulting in a decrease in COP from its normal state.

Based on the information provided, it is evident that R134a/R1270, with a mass ratio of R1270 at 0.9, is suitable for use due to its high COP and wide range of azeotropic behavior, which maintains azeotropic properties even when the composition changes. Additionally, it meets the Montreal Protocol standards with a limiting GWP value of 150. Furthermore, considering the operating time of refrigerant cycle and geographical factors affecting COP, system designs should take these factors into account. Hence, when designing refrigeration systems, the COP value should be at least 20% higher than the operational requirements in Thailand.

## References

- [1] Philipp Pischke, Thailand Refrigeration and Air Conditioning Nationally Appropriate Mitigation Action (RAC NAMA), NAMA Facility, 2020.
- [2] Z. Yang, B. Feng, H. Ma, L. Zhang, C. Duan, B. Liu, Y. Zhang, S. Chen, Z. Yang, Analysis of lower GWP and flammable alternative refrigerants, *International Journal of Refrigeration*. 126 (2021) 12–22. <https://doi.org/10.1016/j.ijrefrig.2021.01.022>.
- [3] J.M. Calm, The next generation of refrigerants - Historical review, considerations, and outlook, *International Journal of Refrigeration*. 31 (2008) 1123–1133. <https://doi.org/10.1016/j.ijrefrig.2008.01.013>.
- [4] J.H. Koh, Z. Zakaria, A.D. Veerasamy, Hydrocarbons as Refrigerants-A Review, n.d.
- [5] D. Colbourne, L. Espersen, Quantitative risk assessment of R290 in ice cream cabinets, *International Journal of Refrigeration*. 36 (2013) 1208-1219.
- [6] Z. Lv, Z. Yang, H. Ma, Y. Chen, Y. Zhang, Flame retardant effect of the halohydrocarbons on the mildly flammable refrigerant difluoromethane, *Journal of Fluorine Chemistry*. 248 (2021). <https://doi.org/10.1016/j.jfluchem.2021.109832>.
- [7] Y. A. Çengel and M. A. Boles, *Thermodynamics: An Engineering Approach*: McGraw-Hill Education, 2019.
- [8] S. Bobbo, G. di Nicola, C. Zilio, J.S. Brown, L. Fedele, Low GWP halocarbon refrigerants: A review of thermophysical properties, *International Journal of Refrigeration*. 90 (2018) 181–201. <https://doi.org/10.1016/j.ijrefrig.2018.03.027>.
- [9] J.J. García Pabón, Phase-out of high GWP refrigerants in refrigeration systems: Status of process in Colombia, *Respuestas*. 24 (2019) 65–74. <https://doi.org/10.22463/0122820x.1832>.
- [10] J.H. Koh, Z. Zakaria, A.D. Veerasamy, Hydrocarbons as Refrigerants-A Review, n.d.
- [11] B. Gil, A. Szczepanowska, S. Rosiek, New hfc/hfo blends as refrigerants for the vapor-compression refrigeration system (Vcrs), *Energies (Basel)*. 14 (2021). <https://doi.org/10.3390/en14040946>.
- [12] M. Mohanraj, S. Jayaraj, C. Muraleedharan, Environment friendly alternatives to halogenated refrigerants-A review, *International Journal of Greenhouse Gas Control*. 3 (2009) 108–119. <https://doi.org/10.1016/j.ijggc.2008.07.003>.
- [13] B.O. Bolaji, Z. Huan, Ozone depletion and global warming: Case for the use of natural refrigerant - A review, *Renewable and Sustainable Energy Reviews*. 18 (2013) 49–54. <https://doi.org/10.1016/j.rser.2012.10.008>.
- [14] United Nations Environment Programme (UNEP), OZONACTION FACT SHEET Refrigerant Blends: Calculating Global Warming Potentials, (n.d.), Available online : [www.unep.org/ozonaction](http://www.unep.org/ozonaction). (Accessed on 15 April 2020).

## Adsorption Behavior of Industrial Dye by Activated Carbon

### Derived from Bagasse Ash

Napaporn Rasameefuengfoo<sup>1</sup>, Watcharaporn Chunwatthana<sup>1</sup>, Kannika Saengrat<sup>1</sup>,  
Khamika Khuenjuk<sup>1</sup> and Chaiyan Chaiya<sup>1,\*</sup>

<sup>1</sup>Department of Chemical and Materials Engineering, Faculty of Engineering,  
Rajamangala University of Technology Thanyaburi, Pathum Thani, 12110, Thailand

E-mail: \* Chaiyan\_c@rmutt.ac.th

#### Abstract

Activated carbon derived from bagasse ash (BC) was investigated for the adsorption efficiency and behaviour of two industrial dyes compared with commercial activated carbon (AC). Methylene blue (MB) and Congo red (CR) were varied in concentration in the range of 25 to 100 ppm and adsorption time from 0 to 80 min. Their adsorption mechanisms were analysed using four adsorption isotherms: Langmuir, Freundlich, Dubinin, and Temkin. The results showed that the adsorption behaviour fit with the Langmuir model, which proved that the BC surface had a monolayer adsorbate adduct. The calculated parameters, maximum adsorption ( $q_m$ ) of MB and CR, were 526.32 mg/g and 82.64 mg/g, respectively, due to the smaller molecule of MB influencing the mass transfer rate into the porous structure higher than CR. The results of thermodynamic adsorption revealed chemical adsorption behaviour for two reasons: the standard enthalpy ( $\Delta H^\circ$ ) calculated from the Van't Hoff equation was positive and higher than 50 kJ/mol. The differential Gibbs energy ( $\Delta G^\circ$ ) and standard entropy ( $\Delta S^\circ$ ) confirmed that both industrial dyes adsorption by BC are spontaneous processes or forward reaction.

**Keywords:** Bagasse ash; Activated Carbon; Adsorption; Methylene blue; Congo red.



## 1. Introduction

In the steam production process of a sugar plant, a sugar cane is often used as a co-fuel to heat the boiler, which results in a large amount of Bagasse Ash (BA). Normally, the BA is a 1-2 mm. particle with a composition of ash and carbon, so it often becomes a waste material that always requires removal as excrement. Based on data from the Saraburi sugar company, every year there are more than 10 tons of BA from steam processes. In the past, it was only removed by landfill method, therefore BA was tried to convert to the value material. It was separated pure carbon from ash and activated via the steam activation and finally we got the highly porous carbon material called Bagasse activated carbon (BC). The analysis results showed that BC contained a high surface area of 1,400 m<sup>2</sup>/g, which is qualify the standard of the industrial activated carbon. Previously, several research have reported the crucial of bagasse ash usages. (Srivastava et al., 2006) has developed an adsorbent from bagasse fly ash for phenol removal or (Lataye et al., 2006) experimented the adsorption of Pyridine (Py) by activated carbon from bagasse fly ash, which showed the removal efficiency up to 99%. Bagasse fly ash (FA), a byproduct of the sugar industry, was transformed to an adsorbent via hydrothermal carbonization and activation for NH<sub>3</sub> adsorption. The experimental results show that FA mixed with bamboo hydrochar has an NH<sub>3</sub> adsorption capacity of 1.02 mg-NH<sub>3</sub>/g-adsorbent, which is approximately 55% of that of the commercial adsorbent. It was also used in CO<sub>2</sub> removal applications, with an adsorption capability of 0.28 mmol-CO<sub>2</sub>/g (Ketwong et al., 2023). From that information, the application of BC is the challenge of sugar industries which are two benefits as the removal of combustion waste and recycling of waste into the value material for adsorption process. In this study, BC from previous research is experimented the removal efficiency of industrial dye including methylene blue and Congo red, which have different structural sizes and electrical properties. The experiment is carried out by batch reactor system under the constant temperature to enhance the several adsorption isotherms such as Langmuir, Freundlich, Temkin and Dubinin. Moreover, thermal adsorption is studied for explanation of thermodynamics adsorption via the Van't Hoff equation.

## 2. Materials and Methods

Bagasse activated carbon (BC) derived from KOH activation comprised of surface area 1,410.62 m<sup>2</sup>/g, pore volume 0.89 cm<sup>3</sup>/g and pore diameter 2.51 nm, was studied the adsorption behavior with two types of industrial dyes (Fig.1A). The cation dye is Methylene blue (MB, C<sub>16</sub>H<sub>18</sub>N<sub>3</sub>ClS) which has 664 nm wavelength absorbance and anion dye; Congo red (CR, C<sub>32</sub>H<sub>22</sub>N<sub>6</sub>Na<sub>2</sub>O<sub>6</sub>S<sub>2</sub>) which has 497 nm wavelength absorbance (Khan et al., 2022). The initial dye solution was varied as 25, 50, 75, 100 ppm. 1 g of BC was filled in 100 ml vessel of dye solution, stirred 50 rpm under the room temperature and the equilibrium adsorption time 80 min as shown in Fig. 1B. After that, BC was separated from solution and the amount of dye remaining in solution was analyzed by using UV-Vis Spectrophotometer. The amount of dye was calculated for plotting the four types of adsorption isotherms for identifying the adsorption behavior between BC and dyes. Each isotherm showed a different hypothesis (Dada et al., 2012) as follows in Eq.1-6.

*Langmuir isotherm:* It refers to the monolayer adsorption with no interaction between adsorbates.

$$\frac{C_e}{q_e} = \frac{C_e}{q_m} + \frac{1}{(K_L \cdot q_{max})} \quad (1)$$

Where  $C_e$  is equilibrium concentration (g/ml),  $q_e$  is equilibrium amount of adsorbed (mg/g),  $q_m$  is maximum amount of adsorbed (mg/g) and  $K_L$  is Langmuir constant (L/mg)

*Freundlich isotherm:* It refers to the adsorption on heterogeneous surface with un-constant energy site.

$$\log q_e = \frac{1}{n} \cdot \log C_e + \log K_F \quad (2)$$

Where  $C_e$  is equilibrium concentration (g/ml),  $q_e$  is equilibrium amount of adsorbed (mg/g),  $1/n$  is adsorption affinity and  $K_F$  is Freundlich constant.

*Temkin isotherm:* It refers to adsorption energy from adsorbent-adsorbate interaction or chemical adsorption.

$$q_e = \frac{RT}{B} \ln K_T + \frac{RT}{B} \ln C_e \quad (3)$$

Where  $q_e$  is equilibrium amount of adsorbed (mg/g),  $B$  heat of adsorption (kJ/mol),  $K_T$  is Temkin constant (L/g),  $R$  is gas constant (8.314 J/mol K) and  $T$  is adsorption temperature (K).

*Dubinin-Radushkevich (D-R) isotherm:* It refers to adsorption energy via micropore surface.

$$\ln q_e = \ln K_D - B\varepsilon^2 \quad (4)$$

Where  $q_e$  is equilibrium amount of adsorbed (mg/g),  $K_D$  is Dubinin constant (L/g),  $B$  is slope and  $\varepsilon$  is adsorption potential which is from,

$$\varepsilon = RT \ln \left( 1 + \frac{1}{C_e} \right) \quad (5)$$

Where  $R$  is gas constant (8.314 J/mol K) and  $T$  is adsorption temperature (K). This equation also purpose the estimation of adsorption energy as follows,

$$E = \frac{1}{(2B)^{1/2}} \quad (6)$$

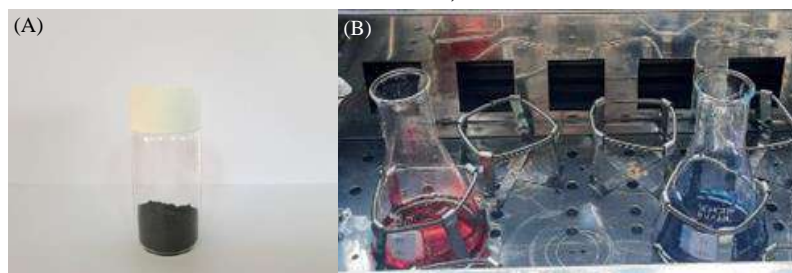
Where  $E$  is the adsorption energy on the micropore surface (kJ/mol).

Additional, 100 ppm of dye solution was adsorbed by BC under the different temperature as 30, 35, 40 and 45°C for analysis of thermodynamics phenomena of the adsorption using Van't Hoff equation as shown in Eq.7-8.

$$\Delta G^\circ = -RT \ln K_d \quad (7)$$

$$\ln K_d = \frac{\Delta S^\circ}{R} - \frac{\Delta H^\circ}{RT} \quad (8)$$

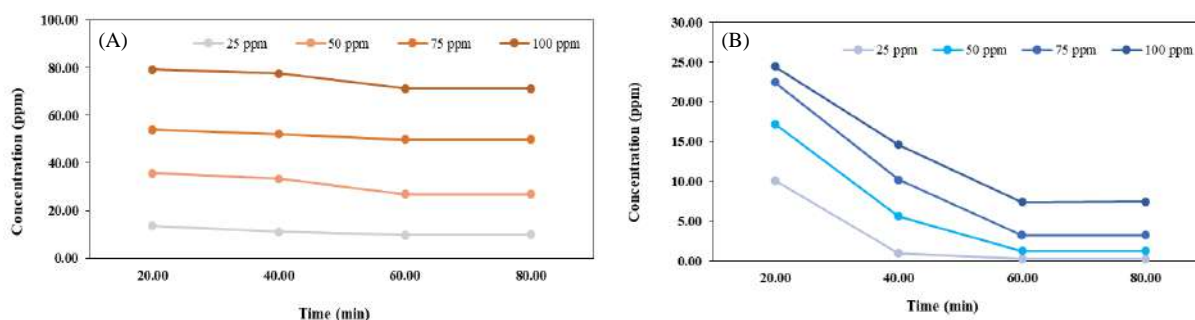
Where  $\Delta G^\circ$  is Gibb's free energy (kJ/mol),  $\Delta S^\circ$  is entropy (kJ/mol.K),  $\Delta H^\circ$  is enthalpy (kJ/mol),  $R$  is gas constant (8.314 J/mol K) and  $T$  is temperature (K).



**Fig.1.** (A) BC (B) Congo red and Methylene blue adsorption experiment.

### 3. Results and Discussion

Both industrial dyes were adsorption until equilibrium state by using BC. The results confirmed that the adsorption time reached equilibrium when was longer than 60 minutes, however this study extended to 80 min. for certainly equilibrium condition as shown in Fig.2. Under the equilibrium condition, the average removal percentage (%) of dyes were estimated in the range of concentration 25-100 ppm. The results showed that Congo red was removed as 42.30 %, whereas methylene blue was 96.14 %.



**Fig.2.** Equilibrium adsorption (A) Congo red (B) Methylene blue

The amount of adsorbed dye was measured by using UV-Vis spectrometer and calibrating with the standard data. The results were estimated the parameters for plotting adsorption isotherm. The parameters obtained from the curves were tabulated and showed in Table 1.

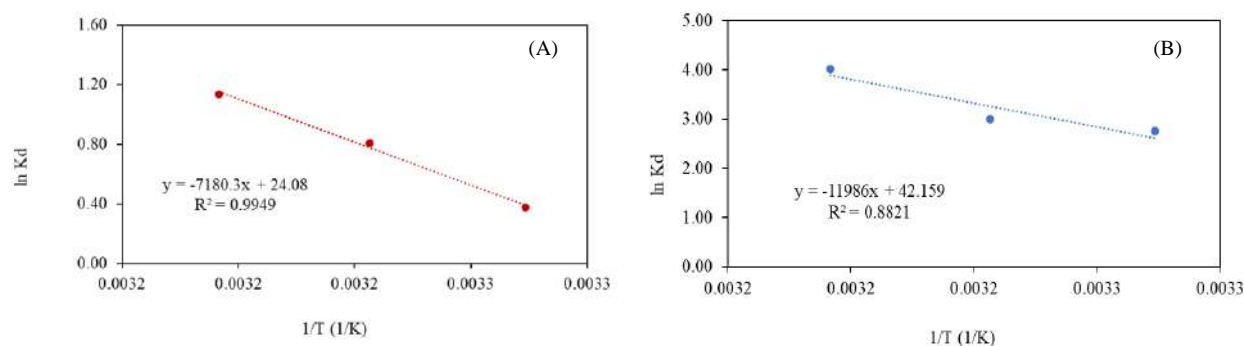
**Table 1.** Isotherm parameters from dyes adsorption by BC

Isotherm model	Parameters	Adsorbates	
		Congo red (CR)	Methylene blue (MB)
Langmuir	$q_m$ (mg/g)	82.640	526.316
	$K_L$	0.082	0.792
	$R^2$	0.99	0.99
Freundlich	$1/n$	0.316	0.400
	$K_F$	18.923	215.229
	$R^2$	0.96	0.99
Temkin	B (kJ/mol)	137.293	22.458
	$K_T$	1.049	11.136

	$R^2$	0.98	0.98
Dubinin	E (kJ/mol)	12.500	35.355
	$K_D$	76.195	461.047
	$R^2$	0.98	0.96

The results from Table 1 showed that the adsorption behavior of CR and MB agreed with the Langmuir model, which had a linearity  $R^2$  of 0.99. The maximum adsorption ( $q_m$ ) of MB and CR were 526.32 mg/g and 82.64 mg/g, respectively. It suggested that the adsorption behavior corresponded to monolayer adsorption, or that the BC surface had been covered with a layer of the dye molecule. On the other hand, the adsorption of MB exhibited a linearity  $R^2$  of 0.99 for the Freundlich model. It appears that an interaction between MB molecules happened. This behavior might be explained by the fact that MB adsorption on the BC surface occurred simultaneously with monolayer (MB on BC) and multilayer (MB with MB). MB had a greater  $q_m$  than CR. The influence of molecular size should be observed; the molecular size of MB is  $0.17 \times 0.76 \times 0.33$  nm, while the CR is  $2.59 \times 0.93 \times 0.14$  nm. The diffusion of MB molecules into the pore structure appears to be smoother than that of CR, which may be due to the huge number of dye molecules absorbed.

Generally, the Langmuir model is related to monolayer adsorption or chemical adsorption (Medhat et al., 2021). The thermodynamic adsorption experiment was used to confirm this idea. The equilibrium adsorption was collected at temperatures of 303, 308, and 313 K, and the results were plotted using the Van't Hoff equation in Figure 3.



**Fig.3.** Equilibrium adsorption under various temperature (A) Congo red (B) Methylene blue

In chemical adsorption, the adsorption efficiency decreased with increasing of adsorption temperature, theoretically. Fig.3B showed the linearity  $R^2$  was lower than 0.9, it supported the statement that the interaction between MB molecules. However, the thermal-adsorption experiment provided some interesting values, as given in Table 2. The results showed that the standard Gibbs free energy ( $\Delta G^\circ$ ) of both dye adsorption was negative at each temperature, indicating that this is a spontaneous process and does not require energy (E) input to operate (Piccin et al., 2011). Adsorptions with positive standard entropy ( $\Delta S^\circ$ ) indicate a forward process. The chemical adsorption was validated by the standard enthalpy ( $\Delta H^\circ$ ), which exceeded 50 kJ/mol (Lima et al., 2019). The  $\Delta H^\circ$  values for Congo red (CR) adsorption and Methylene blue (MB) were 59.70 and 99.65 kJ/mol, respectively.

**Table 2.** Thermodynamics parameters of adsorption

Dyes	Temperature (K)	$\Delta G^\circ$ (kJ/mol)	$\Delta S^\circ$ kJ/(mol.K)	$\Delta H^\circ$ (kJ/mol)
Congo red (CR)	303	-954.32	0.20	59.70
	308	-2,074.41		
	313	-2,953.71		
Methylene Blue (MB)	303	-6,931.51	0.35	99.65
	308	-7,670.62		
	313	-10,458.74		

#### 4. Conclusion

The bagasse ash activated carbon (BC) derived from KOH activation, showed the adsorption performance with Methylene blue (MB) and Congo red (CR) solution. The results showed the relation with Langmuir adsorption isotherm and revealed the high adsorption efficiency via maximum number of adsorbed parameters ( $q_m$ , mg/g). It was found that the  $q_m$  of MB and CR were 526.32 mg/g and 82.64 mg/g, respectively. The adsorption played the role in chemical adsorption, it was confirmed by the standard enthalpy ( $\Delta H^\circ$ ) was higher than 50 kJ/mol obtained from Van't Hoff equation.

#### Acknowledgement

This research block grants were managed under Rajamangala University of Technology Thanyaburi (FRB66E0706E and FRB67E0712), and Thailand Institute of Scientific and Technological Research (TISTR) are gratefully acknowledged.

#### References

- Dada, A. O., Olalekan, A. P., Olatunya, A. M., & Dada, O. (2012). Langmuir, Freundlich, Temkin and Dubinin–Radushkevich isotherms studies of equilibrium sorption of Zn<sup>2+</sup> unto phosphoric acid modified rice husk. *IOSR Journal of Applied Chemistry*, 3(1), 38–45.
- Ketwong, T., Cholwatthanatanakorn, N., Ding, L., Wibowo, H., & Areeprasert, C. (2023). Utilization of bagasse fly ash for the production of low-cost ammonia adsorbents in poultry farm. *Waste Management*, 172, 347–357.
- Khan, I., Saeed, K., Zekker, I., Zhang, B., Hendi, A. H., Ahmad, A., Ahmad, S., Zada, N., Ahmad, H., & Shah, L. A. (2022). Review on methylene blue: Its properties, uses, toxicity and photodegradation. *Water*, 14(2), 242.
- Lataye, D. H., Mishra, I. M., & Mall, I. D. (2006). Removal of pyridine from aqueous solution by adsorption on bagasse fly ash. *Industrial & Engineering Chemistry Research*, 45(11), 3934–3943.
- Lima, E. C., Hosseini-Bandegharai, A., Moreno-Piraján, J. C., & Anastopoulos, I. (2019). A critical review of the estimation of the thermodynamic parameters on adsorption equilibria. Wrong use of equilibrium constant in the Van't Hoff equation for calculation

- of thermodynamic parameters of adsorption. *Journal of Molecular Liquids*, 273, 425–434.
- Medhat, A., El-Maghrabi, H. H., Abdelghany, A., Menem, N. M. A., Raynaud, P., Moustafa, Y. M., Elsayed, M. A., & Nada, A. A. (2021). Efficiently activated carbons from corn cob for methylene blue adsorption. *Applied Surface Science Advances*, 3, 100037.
- Piccin, J. S., Dotto, G. L., & Pinto, L. A. A. (2011). Adsorption isotherms and thermochemical data of FD&C Red n 40 binding by chitosan. *Brazilian Journal of Chemical Engineering*, 28, 295–304.
- Srivastava, V. C., Swamy, M. M., Mall, I. D., Prasad, B., & Mishra, I. M. (2006). Adsorptive removal of phenol by bagasse fly ash and activated carbon: equilibrium, kinetics and thermodynamics. *Colloids and Surfaces a: Physicochemical and Engineering Aspects*, 272(1–2), 89–104.

## Conference Secretariat

Department of Chemical and Materials Engineering, Faculty of Engineering  
Rajamangala University of Technology Thanyaburi  
39 Moo 1, Klong 6, Khlong Luang Pathum Thani 12110 Thailand

Facebook : <https://www.facebook.com/TICHE.TICHE2024>  
website : <https://www.en.rmutt.ac.th/che>



**Smart Solution to Environmental Sustainability for Better World**